AGARD-CP-535

AGARD

ADVISORY GROUP FOR AEROSPACE RESEARCH & DEVELOPMENT

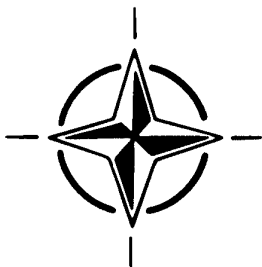7 RUE ANCELLE 92200 NEUILLY SUR SEINE FRANCE

19950302 141

AGARD CONFERENCE PROCEEDINGS 535

Wall Interference, Support Interference and Flow Field Measurements

(Les Effets de Paroi et de Support
et les Mesures des Champs d'Ecoulement)

DTIC
ELECTE
MAR 0 8 1994
F

*Papers presented and discussions recorded at the 73rd Fluid Dynamics Panel
Symposium held in Brussels, Belgium, 4th–7th October 1993.*

NORTH ATLANTIC TREATY ORGANIZATION

Published July 1994

Distribution and Availability on Back Cover

AGARD-CP-535

AGARD

ADVISORY GROUP FOR AEROSPACE RESEARCH & DEVELOPMENT
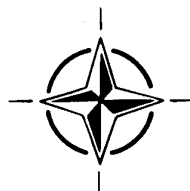
7 RUE ANCELLE 92200 NEUILLY SUR SEINE FRANCE

AGARD CONFERENCE PROCEEDINGS 535

Wall Interference, Support Interference and Flow Field Measurements

(Les Effets de Paroi et de Support
et les Mesures des Champs d'Ecoulement)

Papers presented and discussions recorded at the 73rd Fluid Dynamics Panel
Symposium held in Brussels, Belgium, 4th–7th October 1993.

Accesion For		
NTIS CRA&I		☒
DTIC TAB		☐
Unannounced		☐
Justification		
By		
Distribution /		
Availability Codes		
Dist	Avail and / or Special	
A-1		

North Atlantic Treaty Organization
Organisation du Traité de l'Atlantique Nord

The Mission of AGARD

According to its Charter, the mission of AGARD is to bring together the leading personalities of the NATO nations in the fields of science and technology relating to aerospace for the following purposes:

- Recommending effective ways for the member nations to use their research and development capabilities for the common benefit of the NATO community;

- Providing scientific and technical advice and assistance to the Military Committee in the field of aerospace research and development (with particular regard to its military application);

- Continuously stimulating advances in the aerospace sciences relevant to strengthening the common defence posture;

- Improving the co-operation among member nations in aerospace research and development;

- Exchange of scientific and technical information;

- Providing assistance to member nations for the purpose of increasing their scientific and technical potential;

- Rendering scientific and technical assistance, as requested, to other NATO bodies and to member nations in connection with research and development problems in the aerospace field.

The highest authority within AGARD is the National Delegates Board consisting of officially appointed senior representatives from each member nation. The mission of AGARD is carried out through the Panels which are composed of experts appointed by the National Delegates, the Consultant and Exchange Programme and the Aerospace Applications Studies Programme. The results of AGARD work are reported to the member nations and the NATO Authorities through the AGARD series of publications of which this is one.

Participation in AGARD activities is by invitation only and is normally limited to citizens of the NATO nations.

Recent Publications of
the Fluid Dynamics Panel

AGARDOGRAPHS (AG)

Scale Effects on Aircraft and Weapon Aerodynamics
AGARD AG-323, July 1994

Design and Testing of High-Performance Parachutes
AGARD AG-319, November 1991

Experimental Techniques in the Field of Low Density Aerodynamics
AGARD AG-318 (E), April 1991

Techniques Expérimentales Liées à l'Aérodynamique à Basse Densité
AGARD AG-318 (FR), April 1990

A Survey of Measurements and Measuring Techniques in Rapidly Distorted Compressible Turbulent Boundary Layers
AGARD AG-315, May 1989

REPORTS (R)

Missile Aerodynamics
AGARD R-804, Special Course Notes, June 1994

Progress in Transition Modelling
AGARD R-793, Special Course Notes, April 1994

Shock-Wave/Boundary-Layer Interactions in Supersonic and Hypersonic Flows
AGARD R-792, Special Course Notes, August 1993

Unstructured Grid Methods for Advection Dominated Flows
AGARD R-787, Special Course Notes, May 1992

Skin Friction Drag Reduction
AGARD R-786, Special Course Notes, March 1992

ADVISORY REPORTS (AR)

Quality Assessment for Wind Tunnel Testing
AGARD AR-304, Report of WG15, July 1994

Air Intakes for High Speed Vehicles
AGARD AR-270, Report of WG13, September 1991

Appraisal of the Suitability of Turbulence Models in Flow Calculations
AGARD AR-291, Technical Status Reveiw, July 1991

Rotary-Balance Testing for Aircraft Dynamics
AGARD AR-265, Report of WG11, December 1990

Calculation of 3D Separated Turbulent Flows in Boundary Layer Limit
AGARD AR-255, Report of WG10, May 1990

CONFERENCE PROCEEDINGS (CP)

Computational and Experimental Assessment of Jets in Cross Flow
AGARD CP-534, November 1993

High-Lift System Aerodynamics
AGARD CP-515, September 1993

Theoretical and Experimental Methods in Hypersonic Flows
AGARD CP-514, April 1993

Foreword

The question of how to improve the accuracy of windtunnel tests is of continuing interest to the aeronautics community. In the past AGARD's Fluid Dynamics Panel (FDP) has organized meetings on Wall Interference (London, 1982), Wind Tunnel Test Techniques (Cesme, 1983) and Data Accuracy Requirements (Naples, 1987).

Wall and Support Interference Effects are still an important source of error that appears to be difficult to assess in spite of significant improvements in this field since the 1982 meeting. To assess the state of the art, FDP decided to organize a meeting devoted specifically to these topics. Originally, it was anticipated to combine this with another meeting on Flow Field Measurements as "back to back" Specialists' Meetings. The mapping of the flow field has become increasingly important for improving the understanding of complicated flow structures and for the validation of CFD methods. It was, therefore, considered appropriate to review the progress in this field of activities. However, since quantitative flow field measurements are essential for modern wall interference correction methods that are based on measured boundary conditions, it was finally decided to combine the two Specialists' Meetings into one Symposium.

In formulating the programme, the Committee considered that those who use these techniques for practical applications are the first to point out recent achievements and future needs. For these reasons, Mr Frank Lynch from McDonnell Douglas Aerospace was invited to present the opening paper, and Mr Mark Goldhammer of the Boeing Co. was invited to act as the Technical Evaluator. The Symposium was also one of the first to have, through the Technical Cooperation Programme, two contributions from Moscow's Central Aero-hydrodynamics Institute. These presentations were given by Drs V. Neyland and S. Phonov.

The contributions on wall and support interference and flow field measurements covered a wide variety of topics. They present, in the view of the Programme Committee, a good cross section of current activities.

The final programme comprised:

- 9 papers on flow field measurements
- 12 papers on wall interference
- 3 papers on support interference
- 5 papers on the combined assessment of wall and support interference
  effects, including two-dimensional testing.

The Programme Committee would like to thank Professor R. Decuypere for organizing this meeting so successfully on the premises of the Ecole Royale Militaire.

<div align="right">

A. Elsenaar and D. Woodward
Programme Committee Co-Chairmen

</div>

Avant-Propos

L'amélioration de la précision des essais en soufflerie est un souci permanent du Panel AGARD de la Dynamique des Fluides. Dans le passé le FDP a organisé des réunions sur : les effets de paroi (Londres 1982), les techniques des essais en soufflerie (Cesme 1983), et la précision des données (Naples 1987).

Les effets de paroi et du support restent une source importante d'erreurs, qui semble être difficile à évaluer malgré les progrès considérables réalisés dans ce domaine depuis la réunion de 1982. Pour faire le point de l'état de l'art, le FDP a décidé d'organiser une réunion consacrée exclusivement à ces sujets. A l'origine il avait été prévu de combiner cette manifestation avec une autre réunion sur la mesure des champs d'écoulement sous la forme de deux réunions successives de spécialistes. La cartographie du champ d'écoulement devient de plus en plus important pour la compréhension des structures d'écoulement compliquées et pour la validation des codes CFD. Il a été jugé opportun de faire le point des progrès réalisés dans ce domaine. Cependant, étant donné que la mesure quantitative du champ d'écoulement est indispensable à l'élaboration des méthodes modernes de correction des effets de paroi, méthodes qui sont basées sur des conditions aux limites mesurées, il a été enfin décidé de combiner les deux réunions de spécialistes sous la forme d'un seul symposium

Lors de l'établissement du programme, le comité du programme a considéré que les personnes qui avaient l'habitude de mettre en application ces techniques devraient être les premiers à parler des besoins et des réalisations dans ce domaine. Pour cette raison, Frank Lynch du McDonnell Douglas Aerospace a été invité à prononcer l'allocution d'ouverture, tandis que les fonctions d'évaluateur technique ont été confiées à Mark Goldhammer de la Boeing Company.

Le symposium, par le biais du Programme de coopération, a été l'une des premières réunions de l'AGARD à proposer des contributions de l'Institut Central d'Aéro-hydrodynamique de Moscou. Ces communications ont été présentées par Mme V. Neyland et M.S. Phonov.

Les contributions sur les effets de paroi et de support couvrirent une large gamme de sujets. De l'avis du comité du programme, ces contributions sont une bonne représentation des activités du moment dans ce domaine.

Le programme fut le suivant :

- 9 communications sur la mesure des champs d'écoulement
- 12 communications sur les effets de paroi
- 3 communications sur les effets des supports
- 5 communications sur l'évaluation des effets combinés de paroi et de support, y compris les essais bidimensionnels.

Enfin, le comité du programme tient à remercier le Professeur R. Decuypere pour avoir si bien réussi l'organisation de cette réunion, tenue dans les locaux de l'Ecole Royale Militaire.

A. Elsenaar et D. Woodward
Co-Présidents du Comité de Programme

Fluid Dynamics Panel

Chairman: Prof. Ir J.W. Slooff
National Aerospace Laboratory NLR
Anthony Fokkerweg 2
1059 CM Amsterdam, The Netherlands

Deputy Chairman: M.C. Dujarric
ASE-Programme HERMES
Bâtiment Copernic
18 Avenue Edouard Belin
31055 Toulouse Cédex, France

PROGRAMME COMMITTEE

Ir A. Elsenaar (Co-Chairman)
National Aerospace Laboratory NLR
Anthony Fokkerweg 2
1059 CM Amsterdam - The Netherlands

Dr D. Woodward (Co-Chairman)
Superintendent AP3
Low Speed Aerodynamics Division
X80 Building
Defence Research Agency
Farnborough, Hants GU14 6TD - UK

Prof. R. Decuypere
Ecole Royale Militaire
Chaire de Mécanique Appliquée (MAPP)
Avenue de la Renaissance 30
B-1040 Brussels - Belgium

Dr L. Chan
High Speed Aerodyn. Lab. - U66
Institute for Aerospace Research
NRC Canada - Montreal Road
Ottawa, Ontario KIA 0R6 - Canada

M.J. Leynaert
Directeur Adjoint Grands Moyens d'Essais
ONERA - BP 72
92322 Châtillon Cédex - France

Prof. B. Ewald
Technische Hochschule Darmstadt
Fachgebiet Aerodynamic und Messtechnik
Petersenstr. 30
D-64287 Darmstadt - Germany

Dr G. Sideridis
Hellenic Aerospace Industry (HAI)
Tanagra - PO Box 23
GL 32009 Schmitari - Greece

Prof. M. Onorato
Dipartimento di Ingegneria Aeronautica e
  Spaziale
Politecnico di Torino
C. so Duca degli Abruzzi 24
10129 Torino - Italy

Mr F. Monge
INTA-Div. de Aerodinamica
Crta de Torrejon a Ajalvir, Km. 4
28850 Torrejon de Ardoz
Madrid - Spain

Dr V. Atli
Istanbul Technical University
Faculty of Aeronautics and Astronautics
Maslak 80626 - Istanbul - Turkey

Dr K.L. Kushman
Director of Technology
AEDC/DOT
Arnold AFB, TN 37389-5000 - United States

Mr L.J. Williams
Director, High Speed Research Div.
Office of Aeronautics
NASA Headquarters (Code RH)
Washington, DC 20546 - United States

PANEL EXECUTIVE

Mr J.K. Molloy

Mail from Europe:
AGARD–OTAN
Attn: FDP Executive
7, rue Ancelle
F-92200 Neuilly-sur-Seine
France

Mail from USA and Canada:
AGARD–NATO
Attn: FDP Executive
PSC 116
APO AE 09777

Tel: 33(1)47 38 57 75
Telex: 610176F
Telefax: 33 (1) 47 38 57 99

Contents

TECHNICAL EVALUATION REPORT

Mark I. Goldhammer
Boeing Commercial Airplane Group
P.O. Box 3707, MS 02-24
Seattle, Washington, U.S.A. 98124-2207

1. SUMMARY

An AGARD Symposium on *Wall Interference, Support Interference and Flow Field Measurements* was held in conjunction with the 73rd Fluid Dynamics Panel Meeting on 4-7 October 1993, in Brussels, Belgium. The meeting was chaired by Ir. A. Elsenaar of NLR and Dr. D. Woodward of DRA (UK). The program committee included Prof. R. Decuypere, Dr. L. Chan, Mr. J. Leynaert, Prof. B. Ewald, Dr. G. Sideridis, Prof. M. Onorato, Mr. F. Monge, Dr. V. Atli, Dr. K.L. Kushman, and Mr. L.J. Williams.

The theme of the meeting was based on the need for accuracy of wind tunnel test results. Wall interference, support interference, and the application of flow diagnostic techniques are of great practical interest in wind tunnel testing. Wall and support interference effects still represent an important source of error that appears to be difficult to assess. Quantitative flow field measurements play an increasing role in wall interference correction methods that are based on measured boundary conditions along the tunnel walls. More generally, flow diagnostic techniques like the mapping of a flow field will reveal overall flow structure that are important for an improved aerodynamic design.

The interaction between interference effects and flow field measurement techniques prompted AGARD's Fluid Dynamics (FDP) panel to address these specialists' topics in one Symposium. The significant progress that has been made in the last decade in both fields provided an interesting exchange of technical information. Topics included the routine application of these techniques in large production facilities on the one hand and the development of novel concepts that might be used in the future on the other.

2. INTRODUCTION

This technical evaluation of the AGARD Symposium on *Wall Interference, Support Interference and Flow Field Measurements* is written from the standpoint of an end user of wind tunnels as a design and validation tool. There has been considerable research and progress since the previous AGARD Symposium on these topics. However, it is important to evaluate that progress in terms of how it can improve the practical utilization of wind tunnels in the design and validation of aircraft and other fluid dynamic systems. To industrial users, the wind tunnel is one of many tools used to design and validate an aircraft (or other system). The utility of the wind tunnel in the design process is seen as a way to minimize risk, shorten flow time, minimize cost, and maximize benefit.

The wind tunnel minimizes risk by identifying problems on relatively inexpensive small scale models rather than by requiring expensive in-flight development programs on prototype test articles. Risk can also be minimized by providing accurate pre-flight estimates of airplane performance and handling characteristics. Risk minimization requires that the effects of wall and support interferences be correctable. This is a central theme to the proceedings of the Symposium.

Shortening flow time in an aircraft development program is another requirement for wind tunnels. Since little hardware design work can be initiated prior to the definition of the external shape of the aircraft, it is important that the wind tunnel development program be completed quickly and accurately. Engineers must be able to make decisions nearly in real time and cannot wait for lengthy post test analyses of data. This mandates on-line type wall and support system corrections. In addition, the decisions made during the wind tunnel development must be correct so that

lengthy in-flight programs to fix configuration deficiencies are not required.

Cost is a central issue in any aircraft development program. Airplanes cost too much today, and operators of aircraft, both commercial and military, are finding it less expensive to upgrade and maintain existing fleets rather than buying new aircraft. Efficient and accurate wind tunnel development programs can lead to cost reductions by shortening the aircraft development program and by minimizing the need to change the design after it has gone into production.

Finally, accurate wind tunnel data can lead to improved aircraft performance and handling characteristics which provide more value to the customer for the aircraft.

In order to address these practical needs for wall and support interference corrections and flow field measurement data, the AGARD FDP asked industry for its view by inviting Frank Lynch of McDonnell Douglas to present the opening overview paper (Paper 1 of the proceedings). In addition, the oral and written technical evaluations reflect Boeing experience in the industrial utilization of wind tunnels. Much of the research presented at the Symposium has been conducted in non-industrial settings, such as universities and government laboratories. The Symposium has provided the NATO aeronautical community with an opportunity to compare research being conducted in an academic setting with the pragmatic needs of industry. This should lead to improved focus and utilization of the research. However, the community should have sufficient vision to encourage broad-based research not too constrained by near term requirements or the myopic view of a profit-minded industry.

3. INDUSTRY NEEDS

With regard to *Wall Interference, Support Interference and Flow Field Measurements*, the success of the work presented at the Symposium may be measured relative to what industry perceives it needs. For wall and support interference, there are two major requirements: *correctability* and *accuracy*. For the majority of industry testing, which is to determine the best alternative among a number of configurations, wind tunnel testing is done on an incremental basis. That is, one configuration is compared to another. This type of testing is not aimed at determining absolute values of aerodynamic coefficients. Therefore it is most important that the wall effects be *correctable* for incremental

testing. A relatively small portion of industrial wind tunnel testing is used to determine absolute values of aerodynamic coefficients. This is the most stringent application of wall and support interference and requires that the data be not only *correctable* but that the corrections be *accurate* as well.

Correctability means that the influence of the walls and support systems do not distort the flow environment experienced by the model in the wind tunnel to such an extent that the basic aerodynamic behavior of the model is changed relative to the free-air environment. Generally this means that simple corrections to the flow conditions and/or forces and moments can be determined to account for the influence of the walls and support systems. However, with the advent of accurate CFD methods, more sophisticated correction techniques may be available that extend the range of correctability for wall and support interference. Information presented at the Symposium supports this observation.

Accuracy of wall and support system interference corrections means that reliable and validated methods are available for using a wind tunnel for aircraft development. Industry cannot afford to develop or debug wall and support system correction techniques during the development program of an aircraft. Generally techniques that have been developed and proven prior to a program are those that actually get implemented by industry.

It is important that wall and support interference corrections be easy to apply. A typical aircraft wind tunnel development program involves literally thousands of test conditions. A correction technique that involves extensive application of CFD or other complex methods will not be used in practice. However, general correction techniques that involve selected application of CFD or other methods will be used as long as a simple correction can be derived.

The importance of wall and support system corrections to industry have intensified in recent years because of the recognition of the need to test at higher Reynolds numbers. This need has pushed model sizes up relative to the wind tunnel test section which has increased the importance of correctability and accuracy for wall interference effects. Also, to gain Reynolds number, higher pressure wind tunnels are being used. This increases model loads which requires bulkier

support systems, increasing support tares and interferences.

A variety of sophisticated flow field measurement techniques were discussed at the Symposium. Many new capabilities were discussed, and some of these can provide additional information during a production wind tunnel test that can aid in evaluating a design. However, often it is not known in advance where on a configuration a problem will occur. It is, therefore, desirable that flow field measurement techniques are flexible enough to quickly adapt to the needs of a given wind tunnel test. Some new techniques, such as pressure sensitive paint, have this characteristic. Others, such as particle image velocimetry, may have application only to basic research tests where a well-defined need for flow field measurement exists prior to the test. There is a need for both types of techniques.

4. WALL INTERFERENCE

An excellent overview of wall interference correction techniques is given in Paper 1 by Lynch. He classifies the requirements for dealing with wall interference into model size selection, data correction techniques, and uncertainty imposed by the wall effects. Each is discussed in detail. He then reviews wall interference correction techniques and discusses their applicability relative to cruise performance testing, off-design testing, high-lift testing, stability and control testing, and unsteady testing. Numerous examples are given. The problems associated with two-dimensional airfoil testing are also discussed.

The invited paper by Dr. Ashill (Paper 12) provides an excellent overview of state-of-the-art boundary value techniques used to calculate wall interference from measured wall data and CFD models. This paper sets the stage for many of the other papers presented dealing with wall interference. It is clear from Ashill's paper that wall effects correction methods are in a stage of transition from *handbook* type corrections based on the method of images and empiricism to methods based on boundary values and CFD techniques. This transition is based on an improved understanding of the flow physics, improved mathematical and computational capability for on-line processing, improved wind tunnel instrumentation such as electronic pressure scanning, improved flow field measurement capabilities, and increased need mandated by larger models intended to provide higher test Reynolds numbers.

The paper very clearly derives the wall boundary value problems from Green's formula, both the one-variable technique and the two-variable technique. The one-variable technique is further divided into Dirichlet, Neumann, and mixed boundary value problems, and these are then discussed in terms of their applicability to porous and solid wall wind tunnels. In addition to clearly explaining the mathematics of the various wall correction strategies, Ashill cleverly examines the correctability of various wall configurations utilizing various correction techniques. He shows that the mixed boundary value approach has considerably smaller model representation errors than either the Dirichlet or Neumann approaches. He also shows the sensitivity to openness ratio of the wind tunnel and to geometry of the test section.

In discussing the two-variable technique, the concept of not needing a representation of the model to develop the wall interference corrections is discussed. This favorable aspect of two-variable techniques is countered by the need to measure normal velocities or flow angles at the tunnel boundary. The two-variable technique for wall interference correction is diametrically opposed to the method introduced in Paper 21 which uses CFD to compute wall induced increments in lift, drag, and moment. That method requires increased fidelity in the representation of the model in the CFD calculation.

Ashill discusses adaptive wall wind tunnels in detail. Computed examples showing wall interference improvements resulting from wall adaptability are shown. While there are clearly advantages to wall adaptability to reduce wall interference and reduce the uncertainty associated with wall interference corrections, to date there has not been a significant example in the application of an adaptive wall wind tunnel to the development of a production aircraft. The issues of flow time, cost, and demonstrated accuracy and reliability are probably keys as to why this is the case. The time it would take to routinely adapt the walls of the wind tunnel to the thousands of data points obtained in an aircraft development program seems prohibitive, especially near the edges of the flight envelope where wall interference will be highly non-linear. Developing confidence in the technique with airplane aerodynamicists is also a key issue. And the capital cost associated with a large scale adaptive wall facility is also a formidable obstacle. While this situation is unlikely to

change in the near future, facilities such as the TsAGI T-128 as discussed in Paper 25 by Neyland may overcome the difficulties associated with wall adaptability.

The work presented by Ashill motivates much thinking with regard to the design of new wind tunnels (or, for that matter, to the refurbishment of existing wind tunnels). With his analysis, the implications of test section cross-section, wall porosity type and distribution, and the need for wall adaptability can be assessed in terms of wall effects correctability. Additional information regarding wall porosity type and its effect on wall interference is being researched by FFA as reported by Agrell in Paper 14. This new knowledge regarding test section design can be used in the selection of new wind tunnel test section geometry and is a major outcome of the proceedings of the Symposium.

A number of papers presented expanded on the wall interference techniques summarized in both the Lynch and Ashill invited papers. In Paper 13, Kupper applies the two-variable boundary value correction technique to solid wall wind tunnels. Experimental validation using a flaps down model in two different sized tunnels presents convincing empirical evidence to the validity of the technique and to the inadequacy of classical wall interference methods.

Beutner and Celik (Paper 16) used a method of singularities along with a porous wall flow model to develop a wall interference technique that requires only sparse data on the tunnel walls. The technique is promising from the standpoint that it requires a relatively simple CFD model and only modest wind tunnel instrumentation.

A key application of the two-value boundary condition technique to transonic airfoil wall interference was reported by Freestone in Paper 19. This is an extension of earlier work presented in Reference 1. The technique initially relies on measuring normal velocity distributions in the slots of the tunnel walls using pitch/yaw probes and determining an equivalent homogeneous wall normal velocity by an averaging technique. While Reference 1 showed good results for low speed examples, problems were encountered in the more difficult transonic cases examined in Paper 19. The test cases shown were extreme in that the model was abnormally large relative to the test section. A physical/empirical model of the slot flow was developed to account for the effective amplification of the normal velocity between the wall and the wall displacement

surface. An amplification factor of approximately four was needed to account for the change in normal velocity at the slot relative to the mean normal velocity away from the wall. This was shown to provide more satisfactory results.

The work of Paper 19 is intended to develop a model that allows a two-variable method that requires only simple wall static pressure measurements. The wall normal velocity would be determined from the empirical model. If this succeeds, it would be of great practical importance. Presently, however, because wall normal velocities must be measured, the technique cannot avoid getting into the difficult flow physics associated with flows in and out of slots (or perforations). These are very complex viscous flows which are anything but homogeneous. From a practical standpoint, the flow problems associated with the wall slot flows appear to be as formidable than the flow problems associated with the airfoil being tested!

A very different approach to wall interference corrections was presented by Rueger et al in Paper 21. Rather than relying on measured wall boundary values, the technique uses a CFD model to represent the test article and the wind tunnel boundary and an empirical model for wall porosity. It is reported that the technique can implicitly correct for wall interference, support interference, and wind tunnel calibration effects. It is also reported that the technique can correct test data that, by other measures, are uncorrectable. The basis of the method is to use the CFD modeling to compute interference effects on lift, drag, and moment. These computed interferences are then applied as corrections to the measured wind tunnel data. This differs from the conventional approach of modifying the flight condition, e.g., Mach number and angle of attack. This technique is diametrically opposed to the central theme of Paper 19 which tries to eliminate the need to accurately represent the test article in the CFD model. Implicit in the technique is confidence in CFD to compute forces and moments accurately and consistently enough for the increments due to interference to be accurately determined. This point is arguable. Also, the technique may require extensive pre- or post-test CFD analysis, which could limit its usefulness to production wind tunnel testing. Results shown in Paper 21 are, nevertheless, encouraging. There is likely to be a lively debate between proponents of two-value boundary condition techniques and this force/moment correction technique for some time to come.

Paper 18 discussed ground effects wind tunnel testing, an often overlooked subject which is very important to the aircraft industry. Most flaps down testing is done in *free air*, but the needed flaps down performance for most aircraft design conditions involves flight in ground effect. Besides the ground boundary layer issues discussed in the paper, it should also be recognized that rarely do airplanes fly both close to the ground and parallel to it (unlike the racing hydrofoil example given in Paper 18). A more correct simulation requires ascent or descent near the ground, which is very difficult to simulate in the wind tunnel. These effects are not negligible, but they are normally ignored. This is an area where increased research is suggested.

Two-dimensional airfoil testing continues to be developed, as reported in Paper 26 and in comments presented by Jones of IAR at the Symposium. Clearly floor and ceiling interference issues are well-understood. Much has been learned about sidewall boundary layer issues as well, and perhaps this issue will be concluded by the next FDP meeting on this subject. The key issues seem to be sidewall boundary layer treatment (suction, blowing, etc.) and acceptable aspect ratios for the models that give nearly two-dimensional behavior. The work presented at the Symposium by ONERA and IAR were very consistent, and industry has both supported and accepted these findings. This is indicative of a good cooperative spirit between industry, universities, and government research laboratories internationally.

In addition to what *was* discussed at the Symposium, it is also important to comment on what *was not* discussed. For example, is high lift flaps down wall interference getting enough attention? Why do we tend to test large high lift models in solid wall tunnels when the flow disturbances are often larger than for the much smaller transonic models that we test in large porous wall tunnels? Flow field curvature due to wall interference may affect optimum slat/flap position and angle determination, tail behavior, etc. And our high lift model support systems tend to cause very high interference because of model loads.

Half-model testing is another key area that received little mention. Industry uses half-models extensively to increase test Reynolds number, to test engine simulators, and for a variety of other reasons. Besides all the often exaggerated normal wall interference arising from oversized half-models, the so-called plane of symmetry also

imposes a set of wall effects challenges that must be better understood. This includes splitter plate mounting systems versus tunnel wall/floor mount; boundary layer suction/blowing/offset plates; cross-flow under the model; etc.

The concept of using adaptive walls in cryogenic wind tunnels was discussed near the conclusion of the Symposium. Cryogenic wind tunnels allow testing at very high Reynolds numbers with small models by changing the properties of the fluid. Thus it is not necessary to select model sizes that are large relative to the test section. Therefore, wall interferences should be quite small and easily correctable by standard techniques, circumventing the need for wall adaptability. The mechanical complexity of adaptive walls is a formidable problem itself, but in a cryogenic environment it would seem to be an insurmountable problem. Industry does not recommend pursuing an adaptive wall cryogenic wind tunnel.

5. SUPPORT INTERFERENCE

Two major themes regarding support interference came through during the presentations at the Symposium: First is the perception that wall interference and support interference are intimately related. Second is that CFD is used extensively to develop support interference corrections. While this may be the direction of present research and may be a desirable situation, in industry reality is very different from this.

Wall interference and support interference are treated separately in most industrial wind tunnel testing. As mentioned earlier, wall interference is generally determined from classical solutions developed with the method of images, although measured boundary conditions and CFD are becoming more common. Support interference is almost exclusively determined by so-called *tare and interference* tests where a dummy mounting system is used in conjunction with the normal mounting system through an extensive incremental test program.

In addition, support interference corrections are determined only infrequently in typical aircraft development programs. The overwhelming majority of tests conducted are incremental in nature, testing a number of options and looking for the best *relative* performance. Generally only one or two (if that many) experimental determinations of interference free data occur during a major aircraft development program.

A thorough overview of the state of the art in support interference determination is given by Lynch in Paper 1. The needs and requirements for proper selection of support systems and for support interference determination are discussed at length. Issues such as selection of support systems for minimum interference and for minimum distortion of model external lines are discussed. However, industry practice is not always consistent with these recommendations because of conflicting requirements of balance installation, strength and stiffness of the support system, cost, and flow time.

Lynch also discusses support interference correction techniques. Standard empirical techniques using dummy support systems are outlined. In addition, the use of CFD for support interference corrections is discussed, and the success is characterized as mixed. Navier-Stokes codes are indicated as required for computing support interferences. This could be impractical for routine industrial wind tunnel testing and may not offer the greatest potential benefit, contrary to Paper 1 recommendations.

Results presented by Willaume of Aerospatiale in Paper 29 on 3-strut support interference for a high-lift model and by Eckert of DNW on sting interference in Paper 31 are typical of the industrial approach to support interference. Extensive wind tunnel testing for support interferences are coupled with CFD studies. While the trends predicted by CFD are somewhat in agreement with test data, experience in industry is that the agreement is not sufficient to allow replacement of testing with CFD. This is in part because the nature of the support tare and interference is a complex flow composed on both predictable inviscid phenomena (interference) and less predictable viscous phenomena (tare and interference). In addition, drag is usually most affected by support interference, and CFD methods are not able to predict small drag changes accurately. It is not clear from an industry viewpoint that enough progress will be made in this area to eliminate the need for experimental determination of support interferences.

Paper 30 by Poole of De Havilland reports on a *plate* support system that was developed for transonic testing in the IAR wind tunnel. This type of support system has been used extensively for years in the Boeing Transonic Wind Tunnel with great success. It provides a stable, repeatable, low interference support system. Its primary disadvantage is that no yaw testing or lateral controls testing can be conducted.

Research and development of support systems should not be discouraged, but the trend towards developing CFD methods to eliminate tare and interference testing is not, perhaps, the highest priority. The industry needs to make better selections of mounting systems that are most suitable to the type of testing being conducted. With the trend towards higher Reynolds number testing which generally causes higher model loads, support system size tends to be increasing. Therefore it is increasingly important to select proper low interference support systems whose influence on the model is correctable.

More testing is being done on a international basis because there are so few quality higher Reynolds number facilities and because projects are being conducted by international consortiums. It would be desirable that some type of support system consistency be developed so that users of the world's wind tunnels can obtain similar results in different wind tunnels. It is suggested that an AGARDOGRAPH on recommended wind tunnel model support systems and support interference correction techniques may be the basis for establishing this type of consistent testing methods that would benefit the overall community of wind tunnel users.

The half-model is a support system that needs more attention, as mentioned previously. While it is unlikely that half-model installations will ever be useful for anything other than incremental testing, it is still necessary to develop a good understanding to the key issues with regard to the plane of symmetry boundary layer, model sealing to the plane of symmetry, etc.

6. FLOW FIELD MEASUREMENT

The presentations and papers on *flow field measurement* techniques were generally not related to wind tunnel wall and support system interferences. It is not clear whether this was the intention of the FDP of AGARD. The *theme* of the Symposium suggested that "quantitative flow field measurements play an increasing role in wall interference correction methods." However, the Symposium *theme* also allowed for "flow diagnostic techniques like the mapping of a flow field [that] will reveal overall flow structures that are important for an improved aerodynamic design." Most of the papers on this subject fell into the latter category. Because of the growing use of measured wall boundary values in wall interference measurements, it would have been

desirable to see more applications aligned with wall and support interference issues.

What was presented on flow field measurements covered a wide variety of techniques, both intrusive and non-intrusive. Some of the presentations were applications of well-established flow field measurement techniques to specific problems while others reported on new flow field measurement techniques.

Lynch provided an excellent overview of flow field diagnostic techniques in Paper 1. The needs for flow field measurements were characterized as providing a better understanding of flow physics necessary to extrapolate wind tunnel data to flight and to understand configuration deficiencies. A thorough discussion of a wide array of techniques is included in Paper 1, including transition detection, flow separation visualization, surface pressure measurement, skin friction measurement, and off-body flow field measurements using probes and optical techniques.

New applications of intrusive flow field measurement techniques were presented, including flow angularity probes and hot wire anemometry. In Paper 3, Silva discusses the calibration of a 7-hole flow angularity probe and extensively assesses the accuracy of the calibration. Some concern was expressed in the calibration procedure since the probe was calibrated in a jet only four times the diameter of the probe. Nguyen and Ohman of IAR discuss application of 5-hole flow angularity probe measurements to a wing-mounted propeller installation in transonic flow on a commuter type aircraft in Paper 4. The data presented provide insight into the swirl effects of the propeller on the wing flow field. Significant interference of the probe installation was noted through increased power requirements for the engine simulator, however, opening the question of whether an intrusive flow field measurement technique was suitable for this application.

An extensive application of hot wire anemometry to a delta wing configuration with a canard at high angles of attack was presented in Paper 11 by Breitsamter. The investigation focused on understanding the physics of the complex vortex dominated flows rather than with the flow field measurement technique.

Other flow field measurement technique applications used to understand aircraft flow fields were also presented. These included Paper 8 by Donohoe et al of Delft University where a non-intrusive *Surface Reflective Visualization* (SRV)

technique was introduced. SRV is similar to Schlieren and shadowgraph type flow visualization except that the light bundle is directed normal to the surface of the model rather than normal to the freestream flow. This gives a more three-dimensional view of the flow above the surface. Some impressive flow visualizations were shown for the delta wing case with explanations of the flow physics as well. The SRV system was shown to be a powerful new tool in the visualization of complex flows.

Also presented were two laser doppler velocimeter (LDV) flow field measurements around aft bodies to obtain data for CFD code development (Paper 9) and to determine fuselage drag (Paper 7). LDV surveys for laminar supersonic flows were reported in Paper 5. Clearly there is considerable activity with LDV's, primarily for obtaining data for CFD development and for understanding flow physics phenomena. LDV's have not yet found their way into routine aircraft development testing, probably because optical access to production wind tunnels is poor and data acquisition is very time consuming. However, the technique continues to be promising in that it is non-interfering with the flow, unlike rakes and hot wires.

Two relatively new flow field measurement techniques were discussed by Lynch (Paper 1), particle image velocimetry (PIV) and global Doppler velocimetry (GDV). Riethmuller of VKI presented a more detailed study of PIV in Paper 2. The paper gives a thorough discussion of the principles of the technique, imaging issues, and examples. Both of these techniques hold great promise for the future, and their development is strongly encouraged by Lynch. More information on these techniques at the Symposium would have been desirable.

Phonov of TsAGI presented a very thorough report in Paper 24 on Russian developments in pressure sensitive paint. The paper deals with the physics of the process, accuracy issues, sensitivity to temperature, aging, oil, dust, etc. There is a high level of activity on pressure sensitive paint throughout the industry since the technique is seen as a near term breakthrough in terms of providing routinely increased pressure distribution information, especially for complex three-dimensional configurations. It is also seen as a possible improvement for the acquisition of loads pressure data in terms of reduced flow time and cost. Pressure sensitive paint has an advantage in that little advance planning is required for implementation, so it may be useful

for troubleshooting unanticipated problems. Pressure sensitive paint may also be useful for obtaining wall pressure data for wall interference calculations, and it may also find application in flight testing. Continued research in this area is recommended.

While a number of high leverage new flow field measurement techniques were presented in the Symposium, there were other key techniques that were not discussed. This includes boundary layer transition detection, which is a key to developing a laminar flow airplane. Infared imaging is presently receiving considerable attention in this area. Graphical wake survey techniques are also a key developing flow field measurement technology. Crowder at Boeing (Reference 2) has made considerable progress in this area and has provided both qualitative and quantitative results to improve understanding of the origins of aircraft drag. Some mention of this type of work appeared in Paper 7.

7. CONCLUDING REMARKS

The AGARD Fluid Dynamics Panel Symposium on *Wall Interference, Support Interference and Flow Field Measurements* provided an interesting forum for gathering researchers in these fields to present and discuss emerging technologies. A number of quality presentations and papers were submitted, and interesting discussions occurred during the proceedings. Significant findings were presented in several areas.

The AGARD Fluid Dynamics Panel involved the aircraft industry in this conference by having the opening paper presented by an aircraft industry representative and by having this technical evaluation prepared by another industry representative. Since the customer for much of the research presented at the Symposium is the aircraft industry, it seems appropriate to solicit input from industry experts. It is unfortunate, however, that such a small percentage of attendees at the Symposium were in fact from industry. It may be that industry participation is limited by a combination of the perception that AGARD conferences are closed to non-panel members and non-presenters (a false perception) and that much of the research presented is academic. It may also be a result of the economic condition of the aircraft industry at the present time, with both military and commercial aircraft production and development at cyclical lows.

As mentioned previously, the combination of wall/support interference and flow field measurements in the same symposium was not well-understood. The tie between the two fields was not emphasized in' the proceedings, and it seemed to be two separate symposia rather than a unified conference. Wall and support interference are sufficiently large fields to warrant a complete symposium themselves, as is flow field measurement. Nevertheless, there were significant findings presented in both areas that made attendance at the Symposium a worthwhile investment.

8. REFERENCES

1. Freestone, M.M., Mohan, S.R., and Lock, R.C.: *Interference Corrections in Wind Tunnels With SLotted Walls.* Paper 16, Proceedings of Conference on Wind Tunnels and Wind Tunnel Test Techniques, Royal Aeronautical Society, 1992

2. Crowder, J.P.: *Wake Imaging System Applications at the Boeing Aerodynamics Laboratory*, SAE 851895, Oct, 1985

9. SYMPOSIUM PAPERS

1. *The Crucial Role of Wall-Interference, Support Interference, and Flow-Field Measurements in the Development of Advanced Aircraft Configurations*, F. T. Lynch, F. C. Crites, P. W. Spaid, McDonnell Douglas Aerospace, US

2. *Particle Image Velocimetry: Principles, Current Applications and Future Prospects*, M. I. Riethmuller, von Karman Institute for Fluid Dynamics, BE

3. *Calibration and Use of a Non-Nulling 7-Hole Probe*, M.C.G. Silva, D. X. Viegas, Universidade de Coimbra, PO

4. *Applications of the 5-Hole Probe Technique for Flow-Field Surveys at IAR*, L. H. Ohman, V. D. Nguyen, Institute for Aerospace Research, NRC, CA

5. *Improvement & Validation of an LDV System to Perform Measurements in Laminar Supersonic Flows*, L. Bertuccioli, G. Degrez, von Karman Institute for Fluid Dynamics, BE

6. *Aerodynamic Investigation of the Flow-field in a 180 deg Turn Channel with Sharp Bend*, G. Rau, T. Arts, von Karman Institute for Fluid Dynamics, BE

7. *Experimental Technique for Detailed Measurements of a Transonic Field with 3D LDV - Application to the Determination of the Drag of a Fuselage*, A. Seraudie, A. Mignosi, J. B. Dor, S. Prudhomme, CERT-ONERA, FR

8. *An Investigation of Vortex Breakdown Over Delta Wings in High-subsonic Flow*, S. R. Donohoe, W. J. Bannink, E. M. Houtman, R.J.P. Boon, Delft University, NE

9. *Transonic and Supersonic Flowfield Measurements about Axisymmetric Afterbodies for the Validation of Advanced CFD Codes*, M. Burt, British Aerospace Defence; P. Miller, Miller & Wilson, UK; J. Agrell, FFA, SW

10. *The Application of Long-Range PIV and Holographic Interferometry to Transonic Flows*, P. J. Bryanston-Cross, S. Parker, University of Warwick, UK

11. *Velocity Measurements with Hot-Wires in a Vortex-Dominated Flow Field*, C. Breitsamter, B. Laschka, Technische Universitat, Munchen, GE

12. *Boundary Measurement Methods for Wall-Interference Assessment and Correction A Classification and Review*, P. R. Ashill, DRA Bedford, UK

13. *Development and Test of Wall-Correction Methods with Measured Boundary Conditions for Low-Speed Tunnels in DLR*, A. Kupper, DLR, Braunschweig, GE

14. *Computer Simulation of Slot Flows in Transonic Wind Tunnel*, Agrell, FFA, SW

15. *Estimating Wind-Tunnel Interference Due to Vectored-Jet Flows*, R. Nangia, Nangia Associates, UK

16. *Determination of Solid/Porous Wall Boundary Conditions from Wind Tunnel Data for CFD Codes*, T. J. Beutner, Z.

Z. Celik, L. Roberts, Stanford University, US

17. *Adaptive Wind Tunnel Walls vs. Wall Interference Methods in 2D Flows at High Blockage Ratios*, G. P. Russo, G. Zuppardi, M. Basciani, Istituto di Aerodinamica "Umberto Nobile," IT

18. *Development of Pneumatic Test Techniques for Subsonic High-Lift and in-Ground-Effect Wind Tunnel Investigations*, R. Englar, Georgia Technical Research Institute, US

19. *Interference Determination for Wind Tunnels with Slotted Walls*, M. M. Freestone, S. R. Mohan, City University, London, UK

20. *Interaction Effects for a Full-Scale Helicopter Rotor in the Ames 80 x 120 ft Tunnel*, P. M. Shinoda, NAS Ames Research Center, US

21. *Transonic Wind Tunnel Wall Interference Corrections*, M. Rueger, R. Crites, R. Agarwal, J. Deese, McDonnell Douglas Aerospace, US

22. *Unsteady Flow Testing in a Passive Low-Correction Tunnel*, L. Kong, G. Parkinson, University of British Columbia, CA

23. *Calculation of Low-Speed Wind Tunnel Wall Interference from Static Pressure Pipe Measurements*, L. Fernkrans, FFA, SW

24. *Optical Surface Pressure Measurements: Accuracy and Application Field Evaluation*, S. Phonov, V. Mosharov, Central Aero-Hydrodynamics Institute, Moscow, CIS

25. *Traditional and New Methods of Taking into Account Factors Distorting Flow-Fields around Wind Tunnel Models as Developed for the Large Transonic Wind Tunnels at TsAGI*, V. Neyland, Central Aero-Hydrodynamics Institute, Moscow, CIS

26. *Analysis of Test Section Sidewall Effect on 2D Aerofoils: Experimental and Numerical Investigations*, J. P.

THE CRUCIAL ROLE OF WALL INTERFERENCE, SUPPORT INTERFERENCE, AND FLOW FIELD MEASUREMENTS IN THE DEVELOPMENT OF ADVANCED AIRCRAFT CONFIGURATIONS

F.T. Lynch
McDonnell Douglas Aerospace - Transport Aircraft
3855 Lakewood Blvd.
Long Beach, California 90846
United States of America

R.C. Crites
F.W. Spaid
McDonnell Douglas Aerospace - New Aircraft & Missile Products
St. Louis, Missouri
United States of America

SUMMARY

The requirements, current technology status, and future needs for methodologies to assess wall and support interference effects, and for flow field measurement capabilities, are addressed from an aircraft industry perspective. The requirement for higher Reynolds number testing, especially for transport aircraft, places a much greater burden on the development of the respective technologies. Accurate wall interference estimation methods, including modeling of the tunnel wall flow, are required to assure that models are sized such that wall effects are correctable. Limitations of wall-interference correction methodologies, which occur as a consequence of current CFD inadequacies, are addressed. Flow field correction methods, as well as surface pressure correction methods, are covered. Three techniques for estimating model support interference are reviewed, namely, experimental using dummy stings, use of empirically-based methods for similar installations, and use of CFD-based methods. The need to design support system concepts that minimize interference, and, in the process, permit the effective application of CFD-based methods, is highlighted. Flow diagnostic techniques needed to permit extrapolation of sub-scale wind-tunnel-measured aerodynamic characteristics to full-scale conditions, and to provide the understanding to allow deficiencies to be addressed and corrected, or to guide the design of improved-performance concepts, are reviewed. Both surface flow measurement/visualization and off-body measurements are considered. Noteworthy results obtained with current intrusive devices are reviewed, but the emphasis for the future is clearly shown to reside with optical, non-intrusive techniques such as pressure sensitive paint, infrared imaging, particle image velocimetry, and Doppler global velocimetry.

1. INTRODUCTION

The primary objective of most product-development-type wind-tunnel testing and CFD application studies is to provide the information needed to permit pre-flight estimates of full scale aerodynamic characteristics. Such pre-flight appraisals are an essential element in risk management for determining if all aircraft requirements (guarantees, regulatory, etc.) will be satisfied, or, if not, to provide the basis for the definition of configuration modifications that will satisfy the requirements. To be effective, these assessments based on wind-tunnel testing and CFD applications must be reliable and accurate.

Many interrelated simulation issues must be addressed if accurate pre-flight aerodynamic assessments are to be achieved from wind tunnel testing and/or CFD applications. First, and foremost, proper viscous simulation is a must[1,2]. From a wind-tunnel-testing perspective, this requires either testing at full scale Reynolds numbers, or employing appropriate viscous simulation test techniques at less-than-flight Reynolds numbers[3,4]. While the use of these simulation techniques at sub-scale conditions has been quite successful for attached flows, especially for transonic cruise conditions, these techniques have not been successful for any of the myriad of important separated flow conditions that all aircraft encounter[2]. Consequently, it has become necessary to conduct development testing at as high a Reynolds number as possible to best represent these important separated flow conditions. Otherwise, major technical risks are incurred.

Two other wind-tunnel-testing issues that must be carefully taken into account when extrapolating wind-tunnel test results to full-scale vehicles and conditions are

wall interference and support interference effects. While it has long been recognized that these effects already contribute important sources of error, the requirement for high Reynolds number testing will lead to much greater future use of a combination of larger models and higher tunnel pressures, with correspondingly larger tunnel wall- and support-interference effects, which, in turn, need to be accurately assessed. It is also essential that these interference effects be well understood so that model installations do not produce uncorrectable data. A careful balance will have to be maintained between the desire for higher test Reynolds numbers and the associated tunnel interference effects.

Although the foregoing simulation issues are crucial in the process of obtaining reliable and accurate pre-flight estimates of full-scale aerodynamic characteristics, there is one overriding requirement that must permeate the whole process for it to be successful, whether it be experimental or CFD based. That is the need to understand the physics involved in every flow situation being addressed. Without this understanding, it is clearly not possible to make intelligent decisions regarding the following issues:

- Extrapolation of wind-tunnel test results to flight conditions.

- Establishment of aggressive but realistically achievable performance goals.

- Overcoming any performance or other deficiencies of aerodynamics characteristics.

- Determining the appropriateness of CFD predictions.

The necessary understanding of the prevailing flow physics involved in each situation can only be attained through flow diagnostic testing. This will have to involve a combination of surface flow measurement/visualization capabilities and off-body flow field measurements.

Much of the past work on flow diagnostic techniques has typically involved its use in research-type facilities where productivity and Reynolds number capability have not been a concern or an issue. However, it makes little or no sense to carry out flow diagnostic tests at low Reynolds numbers if we know or suspect that the flow physics are quite different at the high Reynolds numbers of real interest. Consequently, the focus for flow diagnostics must shift to permit its routine use in the configuration development testing that will take place in high Reynolds number, production-type wind tunnels where hourly costs are high and productivity is crucial. Likewise, the same is true for the experiments needed to obtain the data to develop turbulence models for CFD that adequately represent separated flows at high Reynolds numbers.

Hence, it is imperative that fast, efficient flow diagnostic capabilities be developed that are suitable for use in high Reynolds number production tunnels.

The intent of this paper is to document requirements from an airframe industry perspective for the wall interference, support interference, and flow field diagnostic capabilities needed to reduce the technical risk involved in the aerodynamic development of advanced aircraft. This will be followed by an assessment of the present technology status and applicability to the identified needs. Lastly, the remaining major development issues needed to achieve the required capabilities in each area will be addressed.

2. WALL INTERFERENCE

Wall interference is defined, for this assessment, as an error in the simulation of flight conditions arising from the interaction of the model flow field with the wind tunnel boundaries. The essential word in this definition is "interaction". Although there are other sources of errors associated with the walls that arise from tunnel design or operation independent of the model that "interfere" with the model flow field, these are not addressed here since they are present with or without a model. For example, the typical buoyancy correction due to the static pressure gradient through the test section is usually based on empty tunnel pressure measurements and the cross-sectional area distribution of the model. The model does not change the longitudinal pressure distribution, but simply reacts to it. However, in ventilated-wall tunnels with large models, the circulation field of the model can change the longitudinal distribution of cross-flow through the walls, and thereby change the effective pressure gradient from the empty tunnel value. The incremental change in horizontal buoyancy from the empty tunnel condition is considered a wall interference effect.

2.1 Needs and Requirements

There are three basic requirements for dealing with wind tunnel wall interference effects regardless of the type of test section or kind of model. They are:

- Ability to accurately establish maximum allowable model size for a specific test.

- Ability to reduce, or correct wall effects in any test in which the maximum allowable model size is not exceeded.

- Ability to estimate the uncertainty or accuracy of the corrections applied.

These abilities are required for a wide range of tunnel testing. For example, takeoff and landing conditions are crucial to both tactical and transport aircraft. High-lift

tests are generally performed in low speed tunnels with solid walls (or open-jet boundaries), where wall effects can easily alter maximum-lift and lift-curve slopes by ten-percent or more. For tactical aircraft, the correction procedure must be able to account for vectored jets, and/or lift fans discharging at large angles with respect to the tunnel flow.

Cruise performance requirements typically demand very accurate pre-flight estimates be derived from tunnel test results where wall effects can easily alter lift and induced drag by several percent. For example, a six-percent scale F-18 model in the 4 x 4 foot MDA Polysonic Wind Tunnel (PSWT) will experience nearly a seven-percent reduction in lift curve slope, and corresponding increase in induced drag due to wall effects. But, even though corrections for cruise performance estimates are very important, even more crucial is the requirement to understand wall interference effects at the higher angles of attack at transonic (and supersonic) conditions associated with buffet onset, etc. where current CFD capabilities cannot adequately represent the separated flow situations.

Although the major development issues and configuration integration must be resolved in 3-D testing, research into high performance airfoils, development of high-lift-system components, and some unsteady aerodynamic investigations will be conducted in 2-D tunnels. Wall interference effects (top, bottom, and side walls) have to be appropriately dealt with in these tests.

If accurate corrections could be computed for all of these applications with a single integrated wall correction method, it would require a full Navier-Stokes flow solver capable of rapidly and accurately simulating the model, model support structure, etc., and providing time accurate solutions for separation and wake development phenomena, jet/fan discharge, and the tunnel walls with accurate nonlinear cross-flow and boundary-layer displacement characteristics. Of course, if such CFD capability were available, there would be no reason for wind tunnel tests. However, since CFD cannot provide such capability, wind tunnel testing will continue, and wall interference correction requirements will have to be met by a collection of methods and techniques with various amounts of empiricism specialized for certain types of tests and specific kinds of wind tunnel walls and testing ranges.

2.1.1 Predictive Capability for Model Sizing

The first requirement obviously depends on the second. That is, the ability to establish proper maximum allowable model sizes depends on the capability of the interference correction methods being employed. An in-depth knowledge of the capabilities and limitations of the methods is an absolute prerequisite. It is fundamental that wall interference effects must be correctable. Wall-induced

aerodynamics must not change the character of the flow on the wing or any other aerodynamic surface, especially at separated flow conditions, since CFD methods do not exist that are capable of accounting for 3-D viscous separation effects.

In the past, this sizing was done by applying simple rules relating various model areas to tunnel cross-sectional area, and model wing span to tunnel width. These rules evolved from application of the method of images, and from experience with older aircraft designs. However, there is ample evidence that modern aircraft operate at conditions that invalidate the method of images. For instance, wake blockage corrections arising from separated flow can be about five times stronger than those predicted by the method of images. Also, for advanced fighter aircraft with extensive vortical flows, the "cook book" wall interference factor can badly underpredict the interference. Therefore, current model sizing criteria must be obtained either by extensive experimental testing of different sized models, or by the application of CFD using an appropriate mathematical model to predict wall behavior. Due to the time and cost involved in the experimental approach, it is likely that the CFD predictive method will become the tool of choice where accurate sizing for interference is necessary. This will be particularly true where the model size is to be maximized.

Notable efforts have been directed toward establishing the maximum allowable model size in order to achieve the highest test Reynolds numbers. Goldhammer and Steinle[5] demonstrated that the wall-induced streamwise- and spanwise-angle-of-attack and local Mach number gradient effects obtained with a semispan transport model having a span nearly 75-percent of the height of the NASA Ames 11-Foot tunnel (roughly 2.5-percent solid blockage) were quite small at typical cruise ($M_0 = 0.80$) conditions, i.e., attached flow. 3-D Navier-Stokes methods are now able to accurately predict 3-D wing surface pressure distributions at these attached flow conditions. Therefore, one of the prime justifications for continued extensive wind-tunnel testing is to evaluate aircraft characteristics at the separated flow conditions where CFD is not adequate. Consequently, one of the major questions related to wall interference effects is how large can models be made without incurring uncorrectable wall interference effects at these more extreme conditions of interest, and what kind of method is required to adequately assess the wall-induced gradients at these conditions where the flows are clearly non-linear?

Insight into the severity of the wall interference problem at buffet-onset conditions for a large transport aircraft model can be obtained by examining CFD-predicted off-surface isobars at free-air conditions. Predictions obtained with the TLNS3D Navier-Stokes code[6] for a 0.77 Mach number transport with a wing aspect ratio just over seven are illustrated in Figure 1 for two wing stations at both

M₀ = CRUISE

Cruise α   Buffet Onset

0.35 b/2

0.80 b/2
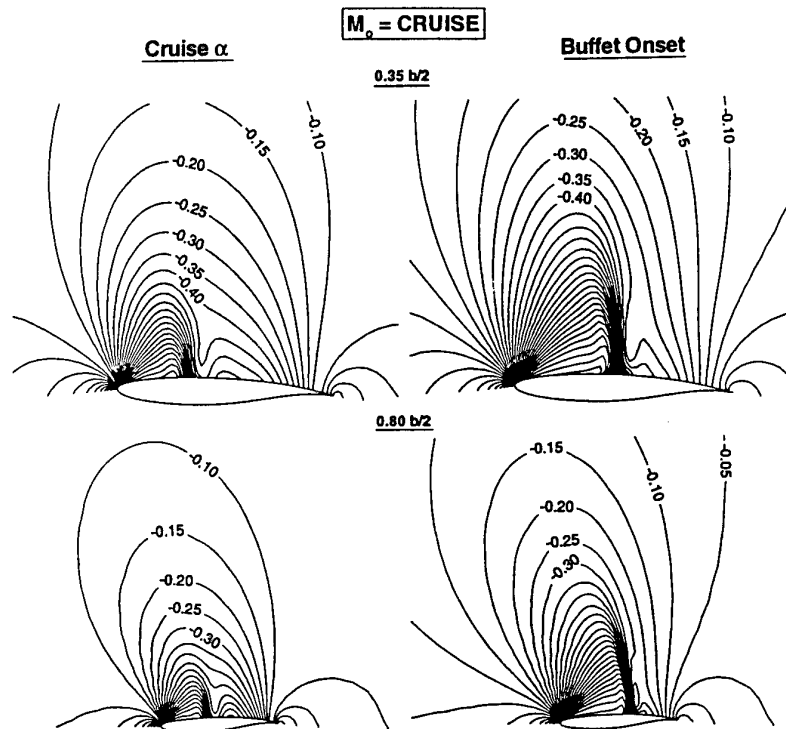
Figure 1. Predicted Off-Surface Isobars for Transport Aircraft Wing.

cruise and buffet-onset conditions. The wing flow field is noticeably more extensive at the buffet-onset condition. And, the difference is more obvious at the inboard station implying a potentially greater wall-induced spanwise gradient effect at this more extreme condition. The effect of these differences between cruise and buffet-onset conditions is small for the typical full-span model installation in a square test section when the full model span is half the tunnel width, such as NASA Langley's National Transonic Facility (NTF) installation of the same transport depicted in Figure 2. Comparisons of the predicted free-air pressures at the tunnel ceiling for this installation with the measured wall pressures are shown in Figure 3. The magnitude of the differences is small with this relatively small model installation.

However, differences are not small when considering the large semispan transport-wing-model installations being considered to provide the higher Reynolds numbers required for viscous simulation. Comparable free-air predictions of the pressures at the tunnel wall above the wing were obtained for a range of model sizes for the two tunnel configurations illustrated in Figure 4, a square cross section representative of most transonic tunnels today, and a rectangular cross section with a height-to-width ratio of 0.7. These predictions are shown in Figure 5 for the square tunnel cross section, and in Figure 6 for the rectangular section. With the square tunnel, predicted pressures become quite substantial with the larger models, with a definite increase in level and

wall pressures

b/w = 0.56
h/w = 1
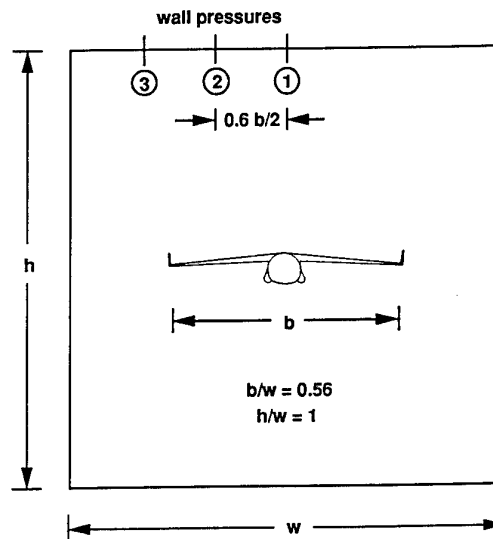
Figure 2. NTF Model and Wall Pressures Installation.

spanwise gradient observed when the angle of attack is increased from cruise to buffet-onset conditions. Hence, there appears to be reason to worry about the possibility of obtaining non-representative, uncorrectable data with these large model sizes. A significant reduction in the predicted pressure levels and gradients is observed for the

Plane of Symmetry

Cruise α

Buffet Onset

0.6 b/2
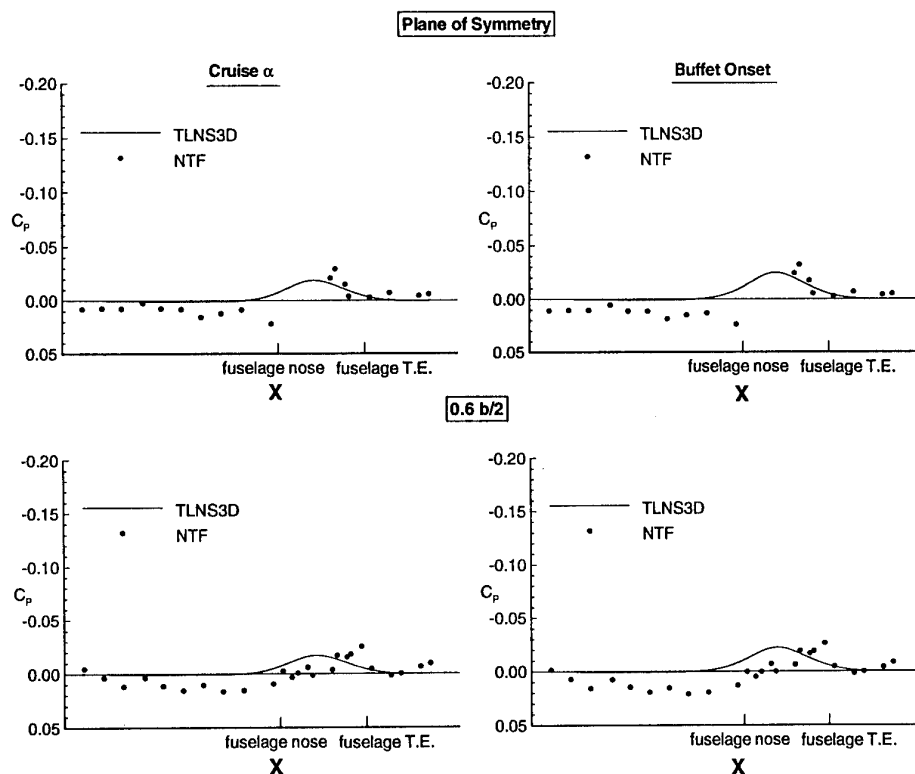
Figure 3. Measured Wall Pressures vs. Predicted Free-Air Pressures at Tunnel Ceiling Location (M_O = Cruise).

rectangular tunnel cross section (see Figure 6). This trend should be carefully considered in establishing specifications for any new transonic tunnels. However, since the existing major high-Reynolds-number, production-type transonic tunnels have square cross sections, it is imperative that wall correction methods be developed to address these non-linear conditions to avoid use of too-large models in the quest for higher Reynolds numbers. Clearly, the same holds true for tactical aircraft studies. It is important to note that the predictive methods for this objective need not be as accurate as the methods required to correct data obtained with properly sized models.

2.1.2 Prevention, Reduction, or Correction of Wall Effects

Wall interference can be prevented by either sizing the model small enough that wall effects are insignificant, or by using an adaptive wall or self-correcting wind tunnel. The first approach is not consistent with the requirement for higher Reynolds numbers for proper viscous simulation, except in cryogenic tunnels such as the NTF and the European Transonic Wind Tunnel (ETW). Both transport and tactical aircraft development testing requirements are driving the industry toward testing of large 3-D models in pressure tunnels. The transport aircraft industry requirements for high Reynolds number testing have been extensively documented[1,2,5,7-9]. Comparable requirements exist for tactical aircraft.

h/w = 1.0

h/w = 0.7
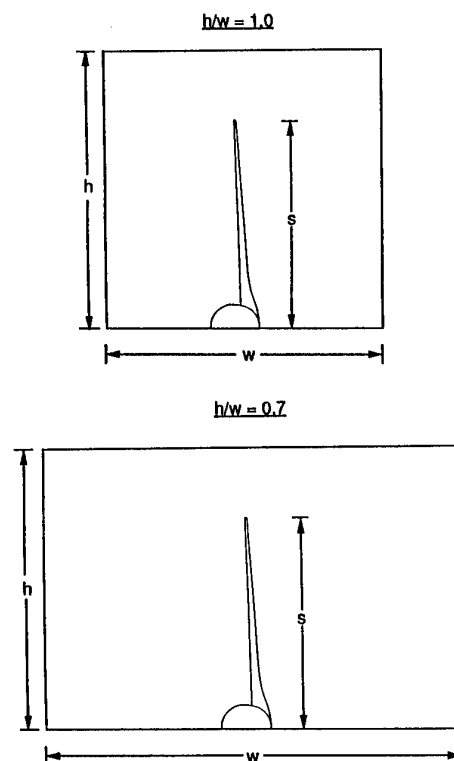
Figure 4. Large Semispan Model Installations.
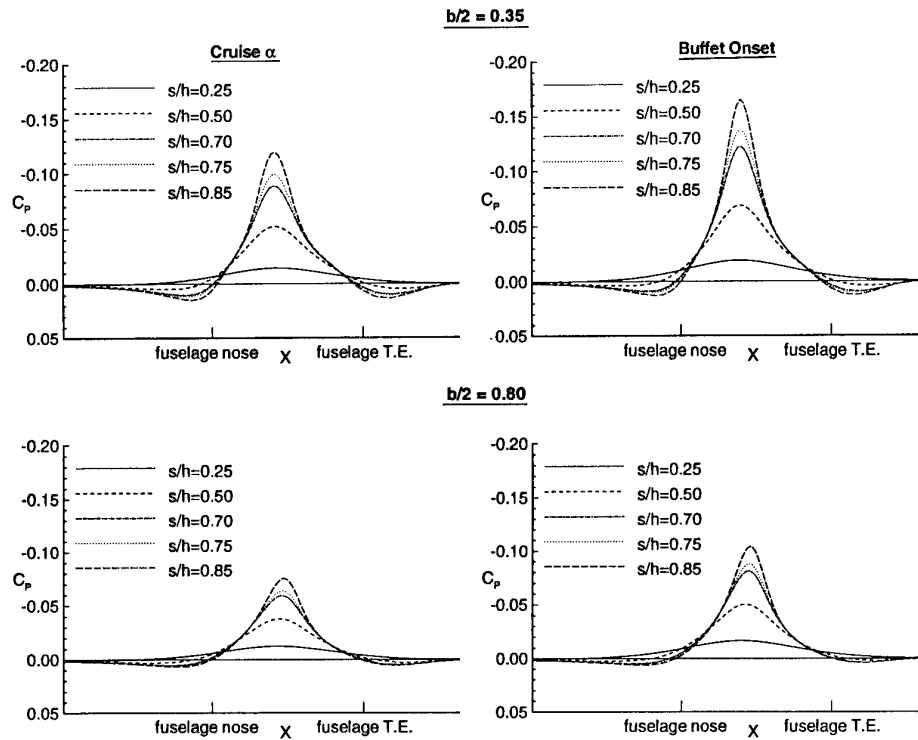
Figure 5. Predicted Free-Air Pressures at Tunnel Wall Above Wing in Square-Cross-Section Tunnel (M_O = Cruise).
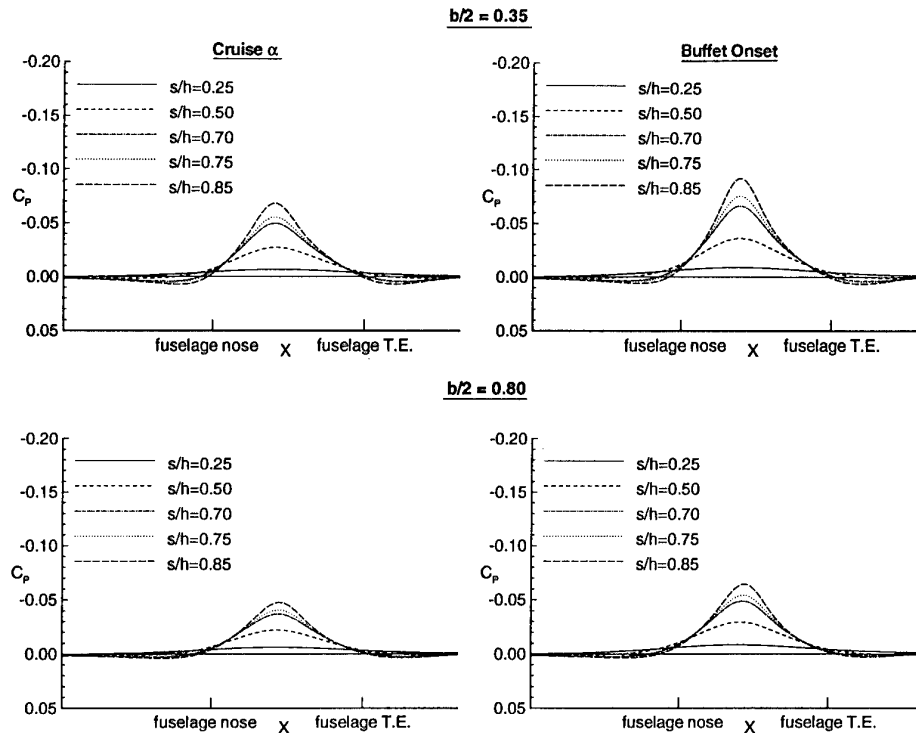
Figure 6. Predicted Free-Air Pressures at Tunnel Wall Above Wing in Rectangular-Cross-Section Tunnel (M_O = Cruise).

For development of fighter aircraft with supermaneuverability[10], it will be necessary to test aircraft designs for high lift, dynamic lift overshoot, and post stall maneuverability. These designs will use innovative, active and passive devices to maintain positive control authority over the entire flight envelope. Testing will require rapid pitch rates from 0 to at least 90 degrees, and must include simulation of large sideslip angles. Strong vortical flows, massive separation, advanced boundary-layer control devices, all involve strong viscous interaction, and are expected to be sensitive to Reynolds number. This will tend to drive the size of the model to a maximum to closely match flight Reynolds number.

Preparation for this kind of testing is beginning. Model support devices capable of pitching a three-dimensional model from 0 to 90 degrees, and back to 0, at a rate of seven cycles-per-second exist. With the exception of the self-streamlining tangential jet boundary concept[11], it seems unlikely that any adaptive wall system could be fast enough to deal with the high pitch rate conditions that will be encountered. More importantly, current large pressurized (and cryogenic) facilities do not use wall streamlining, nor is such planned for new wind tunnel facilities under consideration. This clearly places the emphasis on correction of wall effects rather than on prevention. This is not to say that adaptive wall technology[12,13] is unimportant, or doesn't have a distinct place (for 2-D testing). However, in the foreseeable future, adaptive wall technology will not play a major role in aircraft development simply because major wind tunnels will not provide this capability.

There are a small group of wall interference problems involving adverse tunnel wall viscous effects resulting from the model flow field where preventative efforts are essential. This group includes sidewall boundary-layer separation prevention for 2-D high lift and transonic airfoil development, and the prevention of separation on the tunnel wall with semispan models. Although the success achieved with the installation of a sidewall boundary-layer suction system in the NASA Langley Low Turbulence Pressure Tunnel (LTPT) to prevent wall separation during high-lift testing has been publicized[14], a considerable amount of 2-D high-lift testing is still carried out without any sidewall control. End-wall boundary-layer separation prevention with semispan model installations needs to be addressed for both low-wing and high-wing installations. For low-wing transport installations, potential separation of the floor boundary layer caused by the inboard-flap-imposed adverse pressure gradient (see Figure 7) should be considered, while, for high-wing designs, the effect of the wing upper surface flow field should not be ignored.

Since it is not feasible to prevent wall interference for realistic industry model installations in high Reynolds number production-type tunnels, accurate and practical wall interference correction techniques are needed for a wide variety of 3-D wind tunnel testing, which include the following:

- High-lift testing in solid wall and open jet tunnels.

- Cruise performance testing in ventilated tunnels.

- Buffet-onset, etc. testing in ventilated tunnels.

- Stability and control testing for all wall types.

- Sting & distortion, and tare & interference testing for all wall types.

- Unsteady aerodynamic testing.

Similar requirements exist for 2-D testing.

Landing Configuration
$\alpha = 4°$
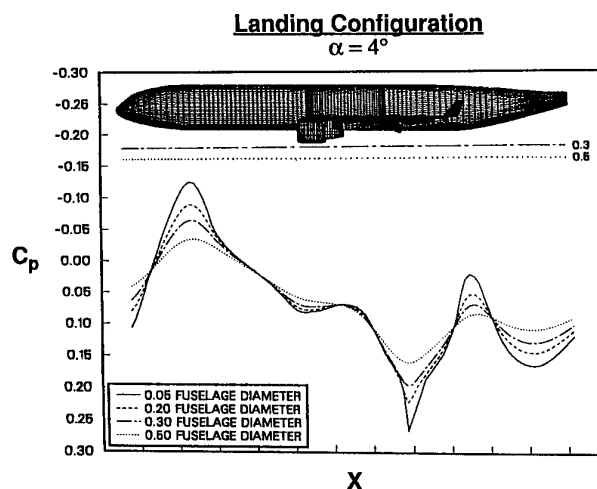
Figure 7. Predicted Pressures on End Wall for Semispan High Lift Model Installation.

2.1.3 Estimate of Uncertainty or Accuracy

Little has been done about establishing accuracy requirements, or providing for the systematic validation of various techniques. Steinle and Stanewsky[15] state that wall "correction methods should be able to assess (1) relative changes in the free-stream flow conditions and (2) changes in local flow conditions at the wing location and along the model axis caused by configurational changes" to the model. Required accuracies were given in flow inclination, and Mach number, as 0.01 degree and 0.001 respectively. These were based on the desire to resolve drag to within one drag count at (attached flow) cruise conditions.

In practice, it is difficult to assess the actual accuracy being obtained. Computing wall corrections is not like measuring pressure. There is no readily available calibration standard. The magnitude and distribution of the effect changes with model size, configuration, wall type, and in some cases, tunnel operation mode. That is why current technology correction schemes rely on measured data to establish the boundary conditions. Tunnel-to-tunnel comparisons can be helpful in indicating general validity, although wall corrections are just one of many factors involved. These can also be expensive and time consuming. Analytical approaches to estimating accuracy would also be difficult. Hence, there remains a real need to pursue development of methods to assess accuracy of wall corrections for representative installations.

2.2 Present Technology/Applicability Status

The intent of this assessment is to examine present wall correction technology in the context of current and near future wind tunnel testing needs. A comprehensive review of current work in the field is not intended, nor is any attempt made to review historical background. Newman et al.[16,17] provide excellent overviews.

There are two basic philosophies for the correction of wall interference. They are referred to herein as:

- Flow field correction methods

- Surface pressure correction methods

The flow field correction approach developed first as a consequence of limited computational capability. This perspective views wall interference as a small linear perturbation of the flow field. Corrections to the flow in terms of incremental Mach number and angle of attack are made while holding the model forces constant. The other way of looking at wall interference effects, herein called surface pressure correction methods, developed as a result of the ability to numerically calculate the pressure distribution (and thereby forces) for aircraft configurations. Serious efforts[18] to develop this approach began in the mid-1980's. The objective is to compute the incremental change in model forces that result from removing the tunnel walls. Two solutions are obtained. One simulates the model in the tunnel, while the second simulates the same model with free-air boundaries. Mach number and angle of attack remain constant. An incremental correction to model forces (lift, drag, pitching moments, etc.) is obtained as the difference between the two solutions.

All surface pressure correction methods require simulation of the model and specification of the wall boundary conditions. The wall boundary conditions can be obtained by numerical simulation of the wall, or derived from measured data (usually wall pressures). Most flow field correction methods simulate the model and obtain the wall boundary in the same way. It is most important that the users of these wall correction methods understand the assumptions inherent in each. For instance, use of the flow field correction method assumes that the wall interference is weak enough so that negligible spanwise and chordwise gradients are imposed on the model by the wall interference. Similarly, use of the pressure correction technique presumes that the flow changes imposed on the model by the wall interference can be accurately computed with available CFD techniques. This latter assumption remains our greatest concern, especially for transport aircraft applications where greater accuracy is required.

There are a few notable exceptions to methods requiring simulation of the model geometry. In one approach, flow field corrections are obtained without simulating the model in any way. Ashill and Weeks[19] demonstrated a boundary value approach in which two measured conditions near the wall (u, v) are used to generate a linear interference perturbation potential implemented as distributed sources and doublets on the tunnel walls. This allows the interrogation of the interference potential in the vicinity of the model to obtain the incremental flow field corrections.

Also, a generalized version of Hackett's method[20] is being developed by NASA LARC and the University of Tennessee Space Institute[21]. This approach uses wall pressure signatures to generate an equivalent aerodynamic body, including wakes, that would create the observed wall pressure signature if it replaced the real model in the tunnel. This equivalent aerodynamic model is numerically simulated to obtain the correction increments. Since the wall pressure signature is a far-field effect, the geometry of the equivalent aerodynamic body is much simpler than the actual model, and includes the displacement effect of wakes. In principle, either surface pressure or flow field corrections can be generated by this technique.

Empirical methods also avoid simulation of the model. These methods, like Maskell's technique[22], are commonly based on the measurement of some associated phenomena (like drag on flat plates normal to the flow), and then extended to apply to other situations (like separated wake blockage from wings). Results from empirical methods are almost always of the flow field correction type.

Flow field correction methods and surface pressure correction methods each have certain advantages and disadvantages, depending on the particular application. And, they can be complementary. In order to quantitatively assess the current status of wall interference correction technology, it is instructive to look at particular flight regimes that receive the most attention during the aircraft development testing program, and assess the status for application in each.

2.2.1 Cruise Performance

To assess the status of wall interference correction technology related to cruise performance determination, it is essential to first consider the tactical and transport aircraft industry requirements for associated tunnel testing. Issues which must be considered include:

- Accurate drag determination is of paramount importance, especially for transport aircraft.

- Extensive testing is carried out, i.e., thousands of hours for a representative transport aircraft program.

- High Reynolds numbers are needed, especially for transport aircraft.

- Flow conditions of interest are predominantly attached flow, (hopefully) very little separated flow exists on the model.

- Speed range including subsonic (M = 0.5), transonic, and supersonic.

- Testing will be conducted in transonic ventilated tunnels, with either slotted or perforated walls.

Considering these issues has major implications in establishing the role for various wall interference correction capabilities. For example, when considering flow field correction (FFC) methods versus surface pressure correction (SPC) techniques for transport aircraft, these issues lead to specific preferences as illustrated in the following table:

Issue/Consideration	Preferred Method	
	FFC	SPC
• Drag Determination	X	
• Amount of Testing	X	
• Attached Flows		X
• High Reynolds No.		X

Current CFD limitations for accurate determination of drag place the surface pressure correction techniques in the high-risk category for transport aircraft. Similarly, considering the many thousand data points typically requiring wall-interference corrections would place the surface pressure correction technique in a very-limited-use category, i.e., not practical for transport aircraft production-type testing. While these considerations clearly favor use of flow field correction methods for cruise performance testing, it must be kept in mind that

use of these methods presumes model-to-tunnel sizing that results in "weak" wall interference effects. If gradients in the interference field become noticeable, the wall effects become less like a simple change in Mach number and angle of attack. Flow field correction methods begin to yield corrections for an equivalent distorted geometry that does not correspond to any real flight condition. The wall effects become "uncorrectable" if this situation is encountered.

Surface pressure correction methods, although not well suited for the transport aircraft production testing environment, are most appropriate for providing the guidance needed to establish maximum model sizes permissible before gradients imposed on the model by the wall interference would change the character of the flow on aerodynamic surfaces. This is especially true for cruise performance conditions, since modern CFD methods can accurately predict surface pressure distributions on wings, etc. under the attached flow conditions normally present at cruise. Shmilovich[23] illustrated the application of this surface pressure correction technique to account for observed differences between free-air CFD predictions and wind-tunnel measured pressures on a large nacelle model mounted in the NASA Langley 16-Foot tunnel (with four-percent slotted walls). The results from this study are illustrated in Figure 8 where it can be seen that the predicted wall interference correction accounted for much of the observed discrepancy even though only a linear wall boundary condition was used.
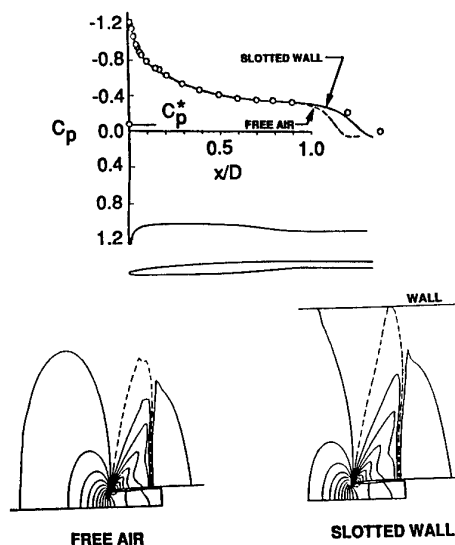

Figure 8. Effect of Wind Tunnel Wall Condition on the Pressure Distribution and Mach Number Maps for the NACA 1-85-100 Nacelle at $M_\infty = 0.96$, $\alpha = 0°$, and MFR = 0.56 (Ref. 23).

While flow field correction methods are favored for transport aircraft production testing, the surface pressure correction method is most often preferred for tactical aircraft testing. There are a number of reasons for the difference:

- Somewhat reduced accuracy required

- Better CFD success in drag predictions for (thinner) tactical aircraft wings

- Primary emphasis on maximum accuracy in the induced drag correction (for low-aspect-ratio fighters), i.e., spanwise gradients in interference induced upwash are significant

Also, surface pressure correction methods require less computational resources than flow field correction methods for cases where the model is simulated, as flow field correction techniques often require an iterative search for equivalent Mach number and angle of attack.

The major concern when using either flow field correction or surface pressure correction methods is how well the tunnel wall boundary conditions are formulated and represented. Success or failure of a correction procedure typically depends more on how well the wall boundary conditions are formulated than on the fidelity of the flow solver. The degree of difficulty involved in extracting appropriate boundary conditions clearly depends on the strength of the wall interaction. When interference effects are weak, the pressure signature induced by the model on the wall is also weak. Under these conditions the wall boundary layer is weakly affected by the presence of the model and it has been demonstrated[24] that for a perforated wall or wall with baffled slots, adequate results can be obtained by applying the classical linear boundary condition where the wall porosity factor is a function of pressure and obtained by calibration[25].

Unfortunately, this simplified approach to ventilated-wall boundary conditions will fail at a relatively low level of interaction with the model. For stronger interactions, the wall characteristics are inherently nonlinear[26,27]. Transonic ventilated wall characteristics are a function of the mode of ventilation, geometry, and a nonlinear relationship between local boundary-layer displacement thickness, local wall pressure, wall cross-flow, and the equivalent inviscid normal velocity, or flow angle. An empirical model of the nonlinear characteristics of walls with perforated 60 degree inclined holes has been demonstrated[28]. Also an empirical correlation has been developed for perforated walls that collapse the nonlinear characteristics of several different wall designs - including normal and 60 degree inclined holes[29]. There is reason to believe that this correlation would also apply to baffled slots. Efforts to improve and refine the representation of the perforated wall continues[30]. Likewise, considerable

effort has been expended on establishing minimum interference designs[31] and documenting characteristics for slotted walls[32-34]. For most transonic wind tunnel tests, especially for small tunnels[35], and large models in any tunnel, nonlinear wall characteristics must be taken into account.

The flow solver used to obtain the wall corrections must be suitable for the flow regime. For Mach numbers of 0.6 and below, corrections based on panel methods will suffice[36-39]. The boundary value approach and the wall pressure signature method would also work. The last two methods, and some of the panel code methods are intended for solid wall application. However, they can all be used with ventilated walls as long as appropriate wall boundary conditions are imposed. An attempt is in progress to modify the boundary value approach for use with slotted wall tunnels such as ETW[40]. For Mach numbers between 0.6 and about 0.9, some success has been noted for correction methods at cruise conditions based on transonic small disturbance[41-43], full potential[44], or Euler methods[45,46] (see Figure 9). However, at higher Mach numbers, inviscid representation of the model becomes questionable, and Navier-Stokes or boundary-layer interaction methods are indicated[47].
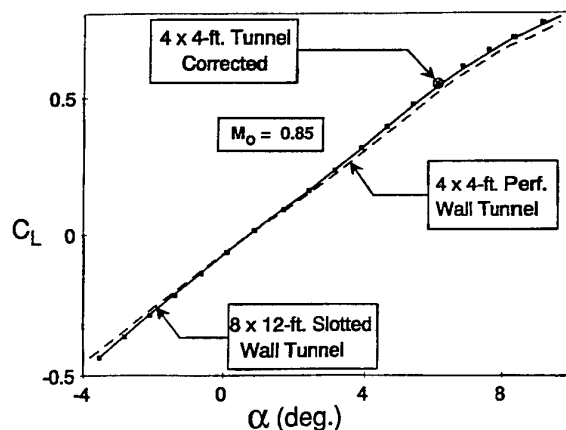
Figure 9. Euler-Based Wall Corrections for Advanced Fighter Configuration.

Previous comments about the wall boundary conditions and the potential superiority of surface pressure correction methods also apply here. The boundary value approach of Ashill and Weeks should remain valid so long as an adequate region of subsonic flow exists next to the wall. The wall pressure signature method would generate an equivalent subsonic body for evaluation. How well the incremental changes computed for this equivalent body reflect the increments for the real model with regions of supersonic flow and shocks is debatable. The upper limits should be experimentally determined, but in any case neither of these methods can be used for $M \geq 1$.

As the test Mach number approaches about 1.2, the strength of the wall interference effects sharply decrease to an insignificant level. This will certainly vary depending on model configuration, size, and tunnel operating characteristics. Our experience[48], is substantiated by Martin, Sickles, and Stanley[49] who report that wall effects for a three-percent SSLV in the 16-Foot tunnel became negligible as Mach number increased to 1.25. Their work might be called an example of "best practice" in wall corrections (for other than transport aircraft). They used a Navier-Stokes flow solver and nonlinear wall model to generate surface pressure type corrections which are validated by incremental data from two models of different size.

An empirical method of obtaining wall corrections has been demonstrated in the MDA PSWT. Experimental wall correction increments were obtained on a set of simple wing/body models to provide an interference data base for validating CFD-based corrections for an advanced fighter design. Simple scaling relations were applied to the experimental interference data base to obtain correction increments. The result was about an eight-percent increase in lift curve slope, and similar reduction in induced drag, and substantially improved data correlation with the same model in a much larger tunnel. Since then, this type of empirical correction has been applied to F-15E, F-18C, F-18E, and other advanced designs in the PSWT. This procedure seems to provide a good first-order correction - which is adequate for most advanced design testing. Application of this empirical technique to an F-15, and subsequent comparison of predicted and measured flight performance has been documented[50].

2.2.2 Buffet Onset, Post-Buffet, Etc.

Compared to predicting wall interference effects for cruise performance determination, accurately predicting these effects at buffet-onset, post-buffet, etc. conditions presents a much greater challenge. The wing flow field is much more extensive at these attitudes than at cruise angles of attack. And, the best CFD techniques are not able to represent these separated flow situations, especially 3-D effects. Compounding the problem is the realization that it is largely the determination of Reynolds number effects on these complex separated flows that is driving the aircraft industry to testing with relatively large models to achieve the higher Reynolds numbers. However, the maximum allowable model size for testing at these most important conditions will be smaller than for testing at the lower-angle-of-attack cruise conditions.

Application of a flow field correction technique to predict wall interference effects for this flight regime would likely involve use of a two-variable boundary value approach to avoid a numerical representation of the model. However,

gradients in the interference field, applied as Mach number and angle-of-attack corrections have the effect of producing a slightly modified geometry (effective changes in camber and twist). The sensitivity of flow separation characteristics on realistic wings to gradients of this kind is unknown. Any assumptions that even quite-small gradients are acceptable would represent a potentially high aircraft development risk. Attempts to utilize a surface pressure correction technique would encounter the same difficulties.

At this time, some form of empirical correction seems to be the only mechanism for meaningful wall correction in this flow regime. Unfortunately, we are not aware of any such technique. We do not question that wall corrections for these conditions can be computed by current measured boundary condition techniques. We do question the accuracy or value of such corrections.

2.2.3 High-lift Testing

Providing accurate wall corrections for high-lift testing is comparable in difficulty to that involved at transonic buffet-onset, etc. flow conditions, particularly for large model installations aimed at attaining high Reynolds numbers. Since most high-lift testing at high Reynolds numbers is commonly done in solid wall wind tunnels, specification of the tunnel wall boundary condition is much more straightforward. However, the model flow field, at conditions of primary interest, i.e., maximum lift, is governed by viscous flows with off-body wake merging and separations that are beyond the simulation capabilities of current CFD to adequately represent. The current state of the art for predicting the maximum-lift characteristics of complex 3-D aircraft high-lift systems involves the use of semi-empirical methods[51] based on an established (2-D) link between the pressure difference between the leading and trailing edges of airfoils (or components of airfoils) and the maximum-lift capability (as a function of Reynolds number and Mach number). Surface panel methods are currently used to generate the predicted 3-D pressure distributions for application of this technique.

Flow field correction techniques are currently employed to provide wall corrections for high-lift testing. Empirical methods such as Maskell's wake blockage correction, coupled with classical (method of images) upwash corrections are still used. Accuracy of these methods has been improved by further empirical refinement[52]. For application of these techniques, it is presumed that numerical representation of the model only needs to be aerodynamically correct in a far-field sense. However, to be valid, some trial and error adjustment of the simulation would be necessary to obtain agreement between measured and computed wall pressures. But, this process is likely to be highly configuration dependent.

If jets or fans are involved, it is desirable to avoid numerical simulation of the model. Application of the wall pressure signature method or the boundary value approach would be preferred. The first is still under development but the second has been demonstrated[53]. Maarsingh, Labrujere and Smith[54] report recent comparisons of corrections using model simulation and measured wall pressures, to corrections obtained using several versions of a modified two-variable boundary value method and to classical methods - method of images. The model was a simple straight wing with full-span flaps at 20 degrees. Data was obtained in a small tunnel (span/width = 0.75) and in a large tunnel (span/width = 0.20), allowing experimental determination of wall effects. The conclusions were that the two-variable boundary value method is more flexible and more accurate than the other methods. However, they note that agreement with the classical method was not bad. However, this test produced very little blockage correction - indicative of mostly attached flow. Angle of attack was limited to about 12 degrees. Our experience is that classical methods are inadequate for the large models of advanced fighter aircraft either at high angle of attack or high lift, probably due to the strong vortical flows and extensive regions of separation. Major subsonic facilities like the DRA 5-Meter tunnel, are implementing two-variable boundary value type correction methods[7]. NASA Ames is developing the generalized wall pressure signature method for the 12-Foot tunnel. It seems a safe prediction that most, if not all, major low speed and subsonic tunnels will adopt some form of measured variable correction procedure, with the two-variable boundary value approach being favored.

These methods are all flow field correction techniques. Therefore greater care must be exercised in limiting model size to insure low gradients and quality corrections. Since the favored correction methods do not lend themselves to prediction, they cannot be used directly to size the model. It is possible to estimate the extent of the interference field using modified Maskell for wake blockage and Heyson[55,56] or Joppa[57,58] for downwash corrections. The difficulty is that without a numerical simulation of the model, that at least predicts correct increments to small changes, it is difficult to judge the relative importance of the predicted interference gradients.

Consequently, a study was undertaken using the McDonnell Douglas higher-order panel method[59] to study wall interference characteristics that could be encountered with a relatively large 3-D semispan transport aircraft high-lift model installation in a solid wall subsonic tunnel. The MD-11 geometry in the landing configuration was modeled for several model-to-tunnel sizes. Various tunnel cross-sections were also included. Predicted lift curves for various model-span-to-tunnel-height functions are illustrated in Figure 10 for a floor-mounted semispan model in a tunnel with a height-to-

width ratio of 0.8. The indicated angle-of-attack corrections become quite significant for the larger model sizes. The angle-of-attack correction required at the airplane (1g) maximum-lift condition is summarized in Figure 11 for the combinations studied. It can be seen that corrections of the order of three to four degrees can be indicated. Corrections of this magnitude are worrisome.
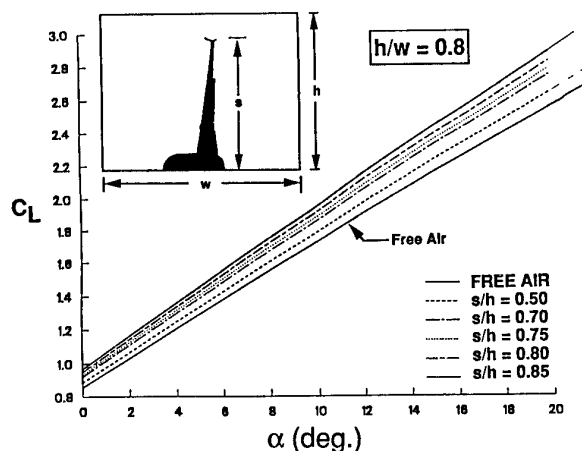
Figure 10. Panel-Method-Predicted Lift Curves for Large Semispan Model Installations in Solid Wall Tunnel.
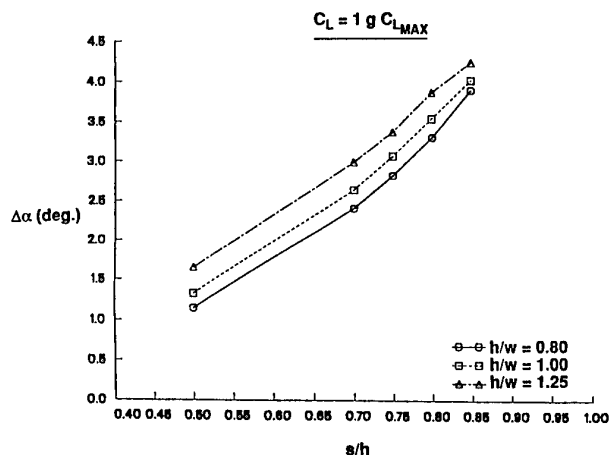
Figure 11. Predicted Angle-of-Attack Correction Required for Large Semispan High Lift Model Installations in Solid Wall Wind Tunnel.

Next, peak-pressure coefficients across the span were examined to determine how these wall interference effects might influence determination of the correct maximum-lift and/or stall characteristics. Predicted peak-pressure coefficients on the slat at maximum-lift condition for both an inboard and an outboard (span) station are depicted in

Figure 12. The predicted variations for the larger model sizes are of a magnitude to indicate that both maximum-lift levels and stall characteristics measured with these wall interferences would not be representative. Hence, use of these large high-lift models could well produce uncorrectable (unreliable) test results. The situation would be even worse for VTOL testing with powered lift fans or jets, especially at low speeds where tunnel flow breakdown is likely.

2.2.4 Stability and Control Testing

The determination of longitudinal and lateral directional derivatives are required at all speeds and over a large range of model attitude settings. High-lift devices may be employed to a varying extent - clean configuration at high speeds to full deployment at low speeds. The wing plane may not be aligned with any of the tunnel walls, and the model may be located a considerable distance from the tunnel centerline. Furthermore, some model positioning systems allow considerable vertical travel of the model during pitch sweeps. Angle of attack can be very large so that massive separation off the wings and fuselage are common. From a wall correction point of view, this kind of testing combines a lot of the most difficult aspects of performance and high-lift testing.

With the wide range of movement, orientation, and flows, it would seem that the two variable boundary value

approach, which avoids the necessity of simulating the model, is the obvious choice. However, the generalized wall pressure signature method, which generates an aerodynamically equivalent model (in a far-field sense) might also be considered. The uncertainty associated with model sizing is similar to that for high-lift testing, except that it is worse. The complex orientation and model flows would complicate Heyson's and Joppa's techniques considerably.

2.2.5 Unsteady Testing

Dynamic testing poses severe challenges. For rotary-balance and oscillatory testing, the model support structure must be massive to provide the necessary stiffness while forcing the desired model motions. These support structures lead to strong steady-state interference that for static testing could be experimentally removed. However, for dynamic testing, there is strong unsteady coupling with wall effects, and the interference cannot be "calibrated out". Dynamic loads generated on the model, interact with unsteady flows on the model support and the walls. The unsteady separated flow around the support, coupled with unsteady perturbations from the walls, communicate with the model flow field. This communication is characterized by different convective lag times. Therefore, at various discrete reduced frequencies of model motion, the coupled interference reactions can amplify or damp unsteady flows on the model.
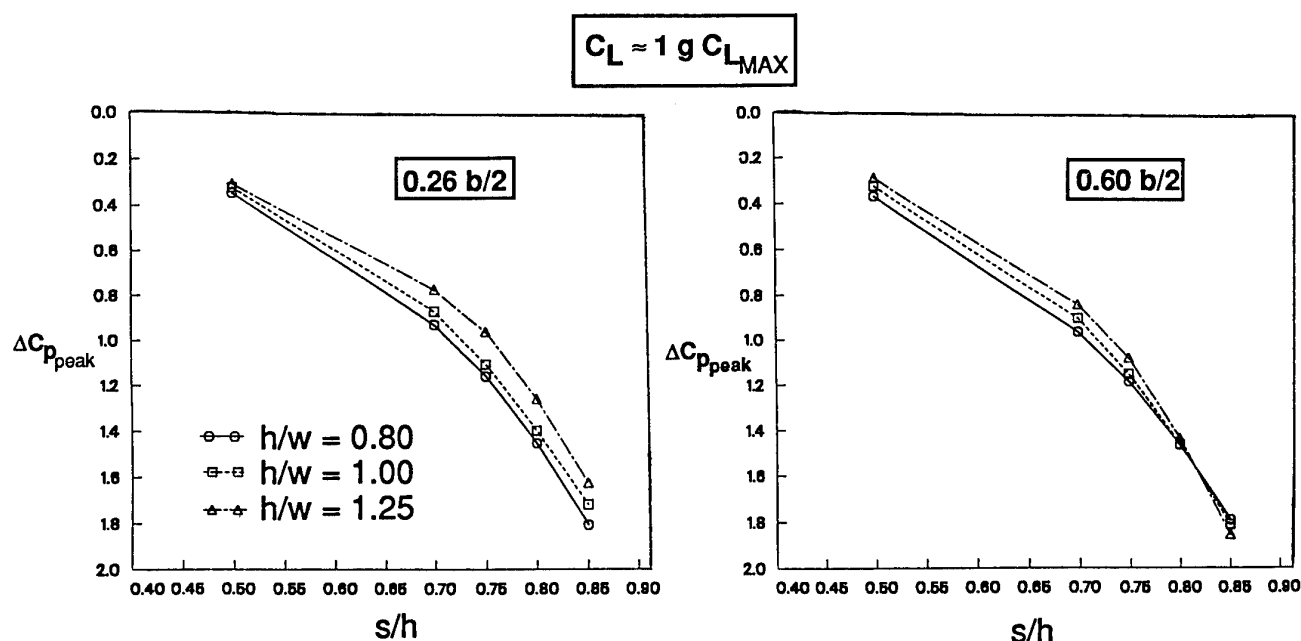

Figure 12. Predicted Reduction in Peak Pressure Coefficient on Slat for Large Semispan High Lift Model Installations in Solid Wall Wind Tunnel.

The interference effect can be strong, even for small models in big tunnels. For example, it has been observed in rotary-balance testing that the unsteady interference effect on vortex breakdown becomes a strong function of reduced roll rate[60]. When phase relations are right, the unsteady interference can alter even the qualitative nature of the aircraft maneuver characteristics. Rotary balance testing of a HIRM 2 advanced tactical aircraft model was conducted in two different tunnels at the same Reynolds number. The smaller tunnel was the 2.4 x 1.8 m (b/w = 0.6) Trisonic Wind Tunnel at DRA Farnborough. The larger tunnel was the 4 x 2.7 m Low Speed Wind Tunnel (b/w = 0.4) at DRA Bedford. It was found that unsteady interference effects completely mask a known unstable yawing-moment characteristic of the model in the smaller facility, but not the larger one[61]. This kind of problem is not unique[62]. Oscillating wing studies were conducted with the NORA wing & oscillator at several facilities. It was found that unsteady interference in smaller tunnels (DRA 3-Foot, Bedford; and DLR 1-Meter, Gottingen) suppressed oscillatory pressure spikes (shock motion) that were clearly present in larger tunnels (ONERA S2 - Modane, and NLR HST - Amsterdam). The approximate span to width ratios were 0.45 for small tunnels and 0.25 for large tunnels.

We are not aware of any unsteady correction methods currently available for general use. In addition, proper model sizing is a complex and unanswered question. Although open to debate, it would seem that empirical or semi-empirical methods hold greater promise for early application.

2.2.6 Transonic Airfoil Testing

Wall interference correction technologies for 2-D transonic airfoil testing are well advanced, and clearly more mature than the 3-D counterparts. Many of the correction schemes, such as the wall pressure signature method and the generation of aerodynamically equivalent shapes, were developed in a 2-D environment and then later extended to 3-D applications. There are two generally accepted types of correction methods to account for the displacement of the streamlines caused by the presence of the floor and ceiling in transonic airfoil testing. Both use the measured static pressure distribution on the tunnel walls as a boundary condition. The simplest, and most popular, of these methods are those that utilize the subsonic linear theory of wall corrections and apply it to the transonic range on the premise that the far fields of the subsonic and transonic flows are very similar. Typical of these methods is the procedure developed by Mokry and Ohman[63]. Although this method is based on subsonic compressible flow analysis, Chan[64] has shown by using an asymptotic transonic small disturbance analysis that the derived corrections to angle of attack and freestream Mach number are correct to the first order. The other, and more complex, type of wall correction method utilizes the

measured pressure distributions on the test airfoil together with the measured interface (wall) pressure distributions to compute an equivalent body including viscous effects by solving the "inverse" problem. This equivalent body is then used to calculate its pressure distribution in unrestrained flow, iterating on Mach number and angle of attack until a model pressure distribution is achieved which "matches" the measured one. The best known method of this type is TWINTAN[65], developed by Kemp, which is a nonlinear top and bottom wall correction method.

It has also been demonstrated[66] that it is necessary to correct transonic airfoil wind-tunnel-test data for the influence of the tunnel sidewall boundary layers. The application of sidewall-boundary-layer corrections of the type recommended by Murthy[67] or Barnwell-Sewall[68] is necessary and appropriate. There has been some lack of total satisfaction with these methods since a one-dimensional growth of the boundary layer along the sidewall is assumed, with no vertical variation. However, subsequent analysis employing a small cross-flow boundary-layer method[69] did show that the Murthy-type correction does provide the correct order of magnitude influence of the sidewall boundary layer. And, it is easy to apply. However, available sidewall boundary-layer correction methods are not appropriate for separated flow conditions such as occurs when approaching buffet onset and maximum lift[66]. Hence, test results from 2-D transonic airfoil tests are only representative for attached flow conditions. This is becoming a serious limitation since modern CFD methods are quite accurate for most of the other attached flow conditions.

Progress in 2-D adaptive wall tunnels has been quite encouraging, and useful, although eventual application of the concept to production 3-D wind tunnels appears impractical. And, it has been shown that although interference is reduced, sufficient residual remains so that correction methods are still required for accurate data[70,71]. However, utilization of the concept will continue to permit investigation of airfoil characteristics at higher Reynolds numbers than would be possible otherwise. But, the use of this concept appears to be relegated to a very limited niche.

2.3 Future Needs

Recent progress in the development of wall interference correction methods has been driven by increasing demands for improved data quality in every aspect of wind tunnel testing, and enabled by progress in computational and measurement technologies. In some areas, the newer, measured boundary condition methods are ready to be transferred to standard operations. In other areas the enabling tools are adequate, but significant development effort remains before technology transfer can occur. In a few areas, there are serious difficulties, and enabling

progress in CFD, flow measurement technology, and basic understanding are required.

There are several pressing needs at this time that need to be addressed. A suggested priority-order listing of these needs is as follows:

- Establishment of guidelines for setting the maximum size of models realistic for subsonic high-lift testing, and for the investigation of buffet-onset, post-buffet, etc. conditions at transonic conditions. It is crucial that too-large models not be used in the quest for higher Reynolds numbers. Guidelines must be established so that models are not sized that result in tunnel-wall-imposed gradients changing the character of the flow on the wing or any other critical aerodynamic surface.

- Establishment of representative semi-empirical mathematical models of the nonlinear wall characteristics of major production-type wind tunnels to provide boundary conditions for wall interference estimates. Nonlinear cross-flow and boundary-layer displacement characteristics must be accurately represented.

- Identification of benefits in terms of maximum permissible model sizes for subsonic high-lift testing by use of wall ventilation, and identification of advanced slot designs to further reduce wall interference with large models at transonic conditions.

- Continued development and implementation of practical flow field correction methods that allow more accurate wall interference predictions for 3-D models for subsonic, transonic, and supersonic testing. An example of these would be the two-variable boundary value approach for high-lift testing. However, an engineering level prediction capability is needed for wall corrections associated with typical stability and control testing.

- Establishment of stand-alone procedures to assess the quality of wall corrections obtained in practice without reference to tests of the same model in other, larger tunnels.

- Establishment of methods for damping the unsteady reaction of the wall encountered during dynamic testing. Further study is needed to identify and isolate the controlling flow physics which govern whether the interference reaction from the walls either amplifies or masks the fundamental unsteady phenomena on the model. A modification of the boundary-jet self-streamlining wall concept wherein the wall jets would be actively driven (phase locked) to model motion should be considered.

3. SUPPORT INTERFERENCE

Model support interference can typically be divided into near-field effects, and far-field effects. The strut or sector, and sting adapter, are usually bulky, but are remotely located from the model, and hence produce predominantly far-field effects at the model. It is natural then to combine these effects with the wall interference which is also normally a far-field effect. On the other hand, the sting (for sting-mounted models) produces near-field effects on the model. Likewise, the aft-end distortion of the model to accept the sting produces a near-field effect. These near-field effects are usually dominated by complex viscous interactions.

It is generally difficult to separate model support system interference from wall interference. It has been demonstrated that simulating the support system with free-air boundary conditions can result in the wrong magnitude and gradient of the interference field - at subsonic conditions[72]. This interrelationship would likely be even stronger at transonic conditions[73].

While support system interference effects have long been blamed for lack of tunnel-to-tunnel correlation[74], and for contaminating measured Reynolds number effects[75], the accurate determination/evaluation of these support interference effects is becoming even more important with the current emphasis on high Reynolds number testing. In addition to the use of larger models, increased test Reynolds numbers will be attained by expanding some current production tunnel operating limits to permit testing at higher pressures, and by establishing higher-than-current limits for all new facilities. Consequently, model loads will be increased substantially, and support systems for full-span models will grow accordingly, leading to potentially much larger support interference effects to be accounted for.

3.1. Needs and Requirements

Model support interference effects must be carefully accounted for when extrapolating wind-tunnel test results to flight conditions. Perhaps the only exception to this requirement is when the test results are being utilized to evaluate incremental or relative effects. There are several issues that must be taken into account when selecting the support system to be used for a particular test program. First, a support system must be selected that does not adversely (or favorably) impact the flow in the principal area(s) being investigated, or that does not secondarily impact the quality or accuracy of the results. An example of the latter would be using a lower-aft-fuselage support system when appraising fuselage/wing root flow

characteristics on a low wing design. In that case, the impact of upstream changes could be realized downstream on the aft fuselage. Having a support sting in this area could mask this effect. Entirely different wake structures could exist depending on whether the sting is present or not[76].

Likewise, it is important to minimize the distortion of the airplane mold lines if possible. This goal is often more achievable with transport aircraft models (relatively larger fuselages) than on tactical aircraft. Hence, the overall requirement is analogous to the model sizing/wall interference concern, i.e., the selected support system must not lead to uncorrectable support interference effects.

It is equally as important in selecting a support system to consider how the support interference effects are going to be determined. Normally, a balance between considerations of accuracy, elapsed time, and cost is sought, depending upon the particular situation. The possibilities for determining support interference effects would generally involve one of the following:

- Experimental determination using dummy stings

- Use of empirically-based methods for similar installations

- Computational methods

Accurate corrections for lift, drag, and pitching moment (as a minimum) are obviously required. Use of advanced CFD (Navier-Stokes) methods would be the desired choice based on cost and (hopefully) elapsed time. However, existing CFD limitations must again be carefully scrutinized when this option is contemplated. First, the support system installation would have to be designed to preclude any separated flow conditions. Secondly, CFD limitations for accurate determination of drag on transport aircraft would lead to concern if accurate drag corrections were part of the objective (and they usually are).

In considering the foregoing, it becomes apparent that the greatest needs/requirements are for:

- Guidelines that lead to the design of support system concepts that minimize the support interference effects and preclude any uncorrectable-data situations.

- Methodologies that permit the timely and cost-effective determination of accurate support interference corrections.

3.2 Present Technology/Applicability Status

A wide variety of model support system installations are utilized in conjunction with internal balances. These

include swept (blade) struts, aft-sting mounts, and twin-boom installations (popular for aft-fuselage-mounted engine installations). Variations of the swept (blade) strut include those that enter the top or bottom of the fuselage, either ahead of or behind the wing. Others include "vertical-tail mounts", and very thin, long chord "splitters" that enter the bottom of the fuselage and extend to (and beyond) the tunnel floor. Of all these, the "vertical-tail-mount" concept best satisfies the objective of minimizing distortion of the airplane mold lines, and avoiding flow separation. Boeing has used this installation very successfully in the NTF. The process for experimentally determining the support interference corrections with this concept is illustrated in Figure 13[77]. Applicability of this concept to new tunnel installations at much higher (50%) dynamic pressures remains to be determined. The aft-sting concept may emerge as a favorite for these very high load situations.
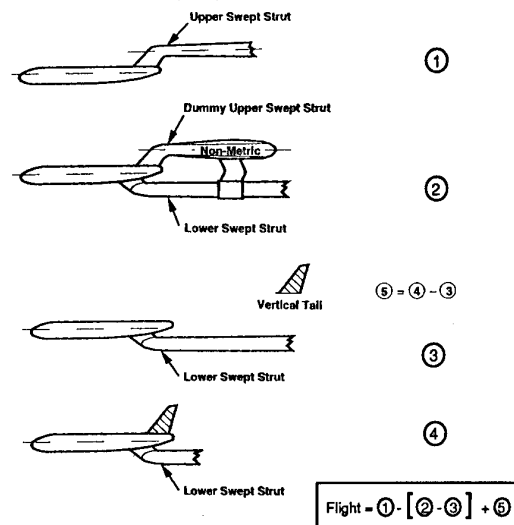
Figure 13. Tare and Interference Methodology for Vertical-Tail Mount (Ref. 77).

The concept of employing empirically-based corrections for support interference based on tests of other similar model/support system installations has not yet been widely accepted or adopted. Some attempts have been made in this direction[78] by splitting up the total support effects. While these methods may provide useful corrections for lift and pitching moment, accurate drag corrections remain a real concern due to the limited applicability.

Efforts directed toward the design of model support systems that minimize interference, and/or avoid separated flow situations that would preclude the potential use of CFD to estimate the support interference effects have increased of late. The design of a tandem strut installation with profiled fairings to minimize strut interference was

reported by Rettig and Ewald[79]. And, the vertical-tail-mount concept clearly fits in this category. Another excellent example would be the design of a model support concept for an Oblique All-Wing wind tunnel model as illustrated in Figure 14[80]. The two major considerations were to minimize the distortion of the airplane mold lines, and to facilitate testing with and without nacelles. The best flow simulation of actual flight would be achieved with the use of flow-through balances installed in the nacelles with the hollow stings in the approximate locations of the jet plumes. Of course, no nacelle-off testing would be possible. Embedding a balance deeply into the wing with a slender bulge on the underside, and a sting mount coming into the trailing edge was also considered, but the sting turned out to be quite large, and the distortion of the wing shape near the trailing edge became unacceptable. The best installation, as illustrated in Figure 14, involved completely embedding a balance in the wing, attached to a swept, slender blade on the underside of the wing, which terminates at 75-percent chord on the wing so there is no interruption of the flow along the trailing edge. At cruise lift coefficients, the streamlines are nearly straight over this segment of the wing. There is virtually no pressure gradient in the vicinity of the blade, so even viscous interactions are expected to be small.
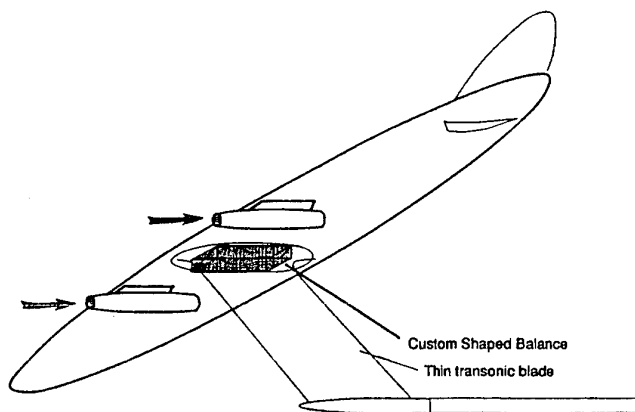

Figure 14. Model Support Concept for Oblique All-Wing Configuration.

Mixed success has been achieved to date in the use of CFD to predict support interference effects. Application of inviscid panel methods to address cylindrical aft-sting mounts did not yield representative results. But, a recently completed study by McDonnell Douglas Aerospace where a full aircraft configuration Navier-Stokes analysis was used to predict sting and distortion drag increments for a fighter aircraft in a project environment provides encouragement that this level of analysis can be a viable option for support interference predictions[81]. In the installation studied, the sting

eliminated the body closure in the inter-fairing region between the two nozzles (see Figure 15) that would exist on the flight vehicle. The resulting sting and distortion increment was derived by taking the predicted drag difference between the undistorted aircraft geometry at model scale and the distorted geometry at model scale mounted on the wind tunnel sting. The flow solver used was NASTD[82], which is a 3-D, upwind, factored algorithm, multi-zonal code capable of performing either Thin Layer Navier-Stokes (TLNS) analyses or
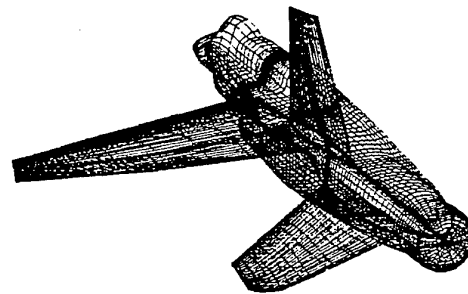
Flight Aft-End   Full Open Nozzles
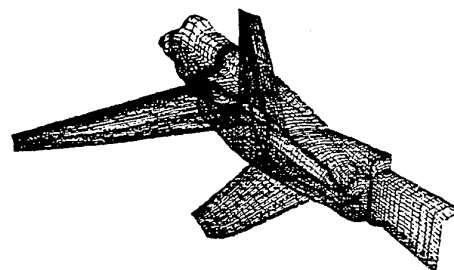
Distorted Aft-End   Sting Mounted

Figure 15. Geometries for Fighter Sting and Distortion Study.

Full Navier-Stokes (FNS) analyses. First, the actual sting and distortion drag increments were predicted. Second, an understanding of the source of these increments was needed in order to build confidence in the quality of the solutions and to gain insight into the aft end flow field. Comparison of the predicted sting and distortion drag increment with test results on a similar aircraft geometry indicated the CFD drag increment prediction was in the expected range. While much more extensive validation of this methodology is required before it can be relied upon to provide accurate predictions for a range of support interference systems, these initial results do provide a ray of hope that CFD may be able, in the foreseeable future, to perform many support interference prediction tasks which, heretofore, fell almost exclusively to expensive and lengthy wind-tunnel testing.

Analogous to the adaptive wall concept for preventing wall interference, magnetic suspension and balance systems[83] have been studied as a hope for eliminating support interference effects. However, eventual application of this concept to production 3-D wind tunnels appears impractical for a variety of reasons, not the least of which are the power requirements and model risk considerations. Again, Reynolds number is the highest priority.

3.3 Future Needs

It is imperative the model support system interference effects be accurately accounted for if wind tunnel test results are to be effectively used in providing accurate preflight estimates of full scale aerodynamic flight characteristics. At the same time, the goal of reduced design cycle times for aircraft makes it essential that these support interference effects be quantified more rapidly. Consequently, the high-priority needs at this time are as follows:

- Establishment of guidelines for the design of support system installations which minimize interference effects, and, concurrently, are amenable to CFD analysis.

- Further development, refinement, and more extensive calibration/validation, of advanced CFD (Navier-Stokes) methodologies easily applicable to a wide range of support system installation concepts.

- Development of empirically-based methods for rapidly estimating support interference effects for installations not amenable to accurate CFD assessment, such as those involving multi-element high-lift systems.

Of these, exploitation of advanced CFD methods to obtain the needed support interference estimates would provide the greatest potential benefit.

4. FLOW FIELD MEASUREMENTS

Flow diagnostic testing is typically divided into two categories - surface flow measurement/visualization and off-body flow field measurements. Several capabilities in each category are required for the aircraft configuration-development process.

4.1 Needs and Requirements

Efficient flow diagnostic capabilities which provide an accurate definition of the prevailing flow physics/conditions on and about aircraft models in high-Reynolds-number, production-type wind tunnels, or full-

scale aircraft in flight, are essential in the aircraft configuration-development process to permit:

- A knowledgeable extrapolation of sub-scale wind-tunnel-measured aerodynamic characteristics to full-scale flight conditions.

- The necessary understanding to allow deficient characteristics to be addressed and corrected, or to guide the design of concepts with improved aerodynamic characteristics.

- Appropriate definitions of steady and unsteady aerodynamic loads for efficient aircraft structural design.

It is essential that the physics involved in every flow situation being addressed be understood. In addition, flow diagnostic capabilities are needed to permit data to be obtained to guide the development of more representative turbulence models that will allow accurate CFD modeling of many critical 3-D separated flow situations at high Reynolds numbers. These measurements will, in many cases, have to be obtained using representative aircraft models in high-Reynolds-number, production-type tunnels. Although there will be times when the use of flow diagnostics in research-type wind tunnels will be necessary and appropriate, the predominant need for flow diagnostics by industry will be for use in production-type tunnels where productivity/cost issues will require the flow diagnostics to be rapid.

The following is a list of flow diagnostic requirements organized by end-data-use categories:

a. Required to enable accurate extrapolation of sub-scale tunnel results to full scale conditions:

- Transition detection (all elements)

- Skin friction measurement

- Separation/reattachment detection

- Assessment of individual drag components (parasite, induced, wave)

- Surface pressures

- Measured boundary conditions along wind-tunnel walls

b. Required for understanding of prevailing flow physics to allow deficient aerodynamic characteristics to be addressed and corrected, or to guide the design of concepts with improved characteristics:

- Transition, separation, and reattachment detection

- Surface pressures

- Surface flow visualization

- Off-body mean flow characteristics (2-D and 3-D)

Situations in which some or all of these would be required include the following:

- Multi-element high-lift system design with merging wakes and boundary layers

- Juncture-region separations

- Adverse 3-D Reynolds number effects on separation

- Laminar flow installations

- Excessive compressibility drag

- Multi-body interference situations

- Thrust reverser effects

- Vortex flows of all types

c. Required for aerodynamic loads:

- Surface pressures

- Integrated loads (steady and unsteady)

d. Required to obtain the data for development/validation of turbulence models for reliable CFD applications to a wider range of flows, with emphasis on 3-D separated flows:

- Off-body mean-flow and turbulence quantities (3-D)

- Surface pressures

- Surface flow visualization, including separation and reattachment

Flow problems where improved turbulence models are an absolute requirement before CFD predictions can be reliable include the following:

- Buffet onset/progression on 3-D wings

- Reynolds number effects on 3-D separated flows

- Maximum lift and drag prediction for multi-element high-lift systems

- Control-surface effectiveness

- Juncture flow regions

- Vortex/turbulent boundary-layer interactions

Required, for example, is a 3-D counterpart of the very successful Johnson-King nonequilibrium algebraic turbulence model[84] which was aided by flow field diagnostics on a 2-D transonic airfoil at cruise and buffet-onset conditions.

4.2 Present Technology/Applicability Status

4.2.1 Surface Flow Measurement/Visualization

The four primary surface flow measurement/visualization requirements are for transition detection, separation detection/visualization, surface pressure measurement, and skin friction determination. The status of the current diagnostic capabilities for each is assessed in the following sections in the context of current and near-future wind tunnel testing needs.

4.2.1.1 Transition Detection

a. *Sublimation*. Sublimation of a volatile material proceeds more rapidly beneath a turbulent boundary layer than beneath a laminar boundary layer; this difference is used to identify the region of transition. The china-clay technique described by Pope[85], is best suited for low-speed flows. Since sublimation rates beneath a laminar boundary layer near a leading edge are also high, sublimation patterns corresponding to transition near a leading edge can be difficult to interpret. Sublimation of a thin layer of a volatile solid material such as fluorine has been used at higher speeds. The fluorine is dissolved in an organic solvent and a thin coat is sprayed on a dark-colored model prior to a run. The location of transition is detected as in the china-clay technique. Sublimation rates associated with both techniques vary widely, depending on local flow conditions. Good results require a uniform initial coating thickness, an experienced practitioner, and/or a substantial period of trial-and-error before good results are achieved with either of these techniques. Sublimation is a time-consuming technique to use in a pressurized wind tunnel, since the model must be cleaned and resprayed for each test condition. And, the size of the pigment itself in these fluids could well influence the location of transition at the high Reynolds numbers of interest[86]. This technique is also not suitable for low temperature cryogenic conditions.

b. *Surface Hot Films*. Vacuum-deposited hot-film gages were initially developed at McDonnell Douglas by Fancher [87,88], and subsequently used in an airfoil-model transition study in the NASA Langley 0.3-Meter Transonic Cryogenic Tunnel (TCT) by Johnson et al.[89] Similar arrays of surface hot films have been used

successfully on airfoil models in the NASA Langley LTPT. Arrays of hot-film gages have the advantage that once installed, they provide continuous information as test conditions are changed. Hot-film sensor arrays, anemometers, and data acquisition systems are available commercially. Data obtained on a three-element high-lift model in the LTPT are presented in Figure 16[90]. The data are presented with the upper and lower surfaces of the three elements unwrapped about their respective leading edges, and include measurements for angles of attack from -4 to 23 degrees. The data show locations of the stagnation point, the beginning and end of transition, and separation and reattachment locations.
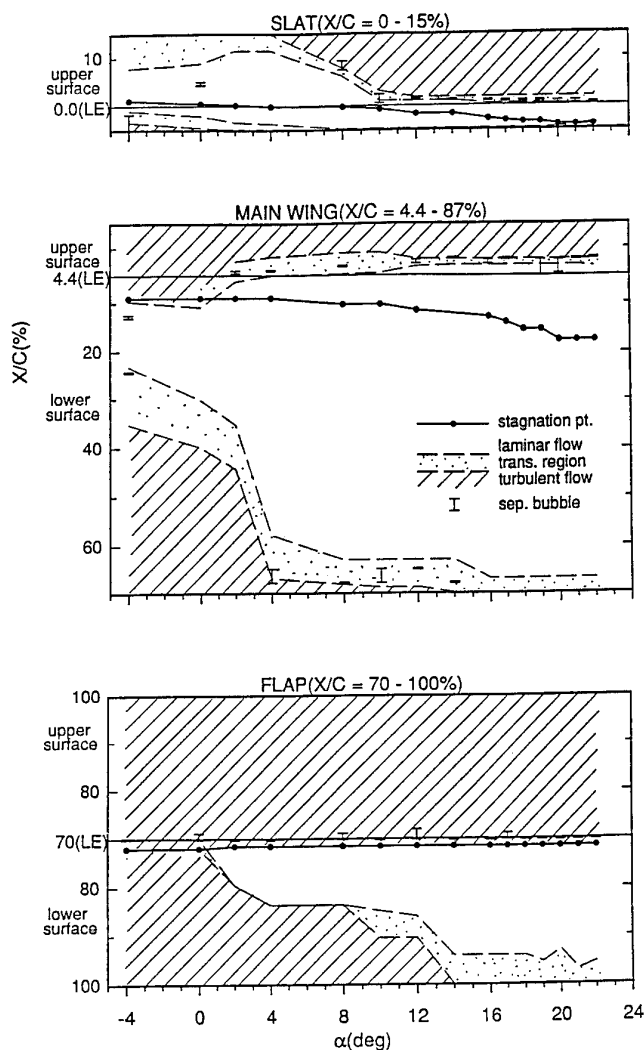
Work is in progress by Gartenberg et al.[91] to develop improved hot-film sensors for cryogenic test conditions. One of the difficulties in applying this technique at cryogenic test conditions is the need to maintain an extremely smooth surface because of the high-Reynolds-number test conditions. Three fabrication concepts are being explored. The techniques vary in reliability and frequency response of the hot films produced, ease of refurbishment, and compatibility with conventional pressure orifices and infrared imaging.

Comprehensive instrumentation of a 3-D model with hot-film arrays requires an impractically large number of channels at present. Instrumentation of a small number of wing sections and other locations is possible, with the associated risk that critical locations would remain uninstrumented.

c. *Infrared Imaging*. Gartenberg and Roberts[92] present a review of the field of infrared (IR) imaging, including subsonic to hypersonic wind-tunnel testing, space shuttle flight experiments, and propulsion testing. Gartenberg et al.[93], and Gartenberg and Wright[94], have applied this technique to boundary-layer transition detection in a cryogenic wind tunnel. The experiment was performed with an airfoil model having a fiberglass epoxy surface. A camera optimized for operation in the 8- to 12-wavelength band was used. Although the temperature range of the experiment, $170°K < T_t < 220°K$, is characterized by wavelengths in the range of 30, commercial cameras optimized for this wavelength range are not available. The recovery temperature of a turbulent boundary layer is higher than that of a laminar boundary layer, and the resulting difference in surface temperature can be used as an indication of transition. At cryogenic temperatures, reduced radiated energy at low temperatures, reduced sensitivity of the IR imager at these low temperatures, and the mismatch between the radiation wavelength and the band of wavelengths for which the imager is optimized all combine to make direct measurement of the steady-state recovery temperature distribution impractical. These difficulties were overcome by performing an experiment in which the total temperature was increased rapidly by less than one-percent of its absolute value. The increased heat transfer to the model in the turbulent region caused a temporary increase in model surface temperature relative to the laminar region. Observation of this transient process by IR imaging allowed the laminar and turbulent regions to be identified (see Figure 17).

IR imaging requires a view of the model surface through windows which transmit the appropriate wavelength range of IR radiation with tolerable efficiency. Windows made from germanium and zinc-selenide were used in the investigation described in Refs. 93 and 94. These windows attenuate IR radiation substantially in the long wavelength range characterized by cryogenic applications,

Figure 16. Summary of Hot-Film Test Results for Multi-Element Airfoil in NASA Langley LTPT.
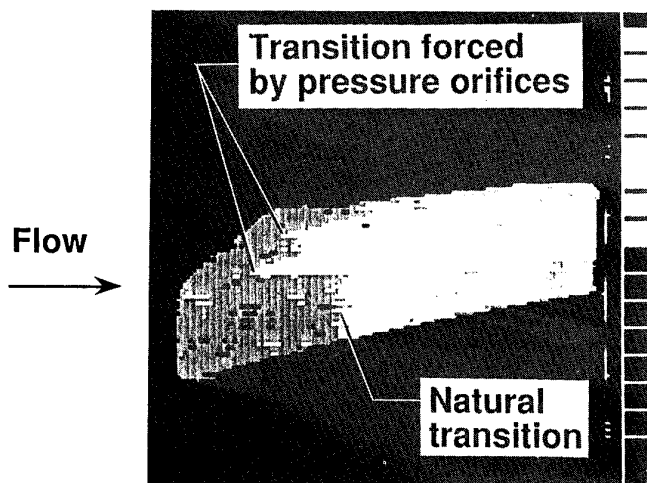
Figure 17. Transition Detection at 220°K on an Airfoil Model by IR Imaging and Image Enhancement.

and there is a need for new window materials which are more suitable for this wavelength range. In addition to optical access and improved window materials, routine use of IR imagery for transition detection will require development of imaging systems optimized for use in the long-wave band of this application, where all current systems are relatively insensitive.

d. *Liquid Crystals*. Liquid crystals combine the physical properties of a viscous liquid with optical properties of a crystalline solid. A thin layer of the material is applied to a test surface and illuminated with white light. The liquid crystal material can separate the light into colors which depend upon the shear stress and the viewing angle. The use of liquid crystals to indicate changes in surface flow properties was investigated by Margozzi[95], and as a transition indicator by Holmes et al.[96] More recently, Reda[97] performed a series of experiments demonstrating the utility of liquid crystals for indicating the magnitude and direction of surface shear stress beneath a jet. Betts and Stanfield[98] used liquid crystals in an exploratory study of transition detection on an airfoil model in the 8 x 8 foot high speed wind tunnel at DRA Farnborough. The results indicated the need for further development, particularly for crystal formulations which would combine increased viscosity and comparable shear sensitivity.

4.2.1.2 Separation Detection/Visualization

a. *Oil Flow*. This is a well-established technique for obtaining surface flow patterns, including locations of separation and reattachment. Experience with the particular test conditions is necessary to achieve good results without trial-and-error, as oil viscosity and pigment loading requirements vary widely, depending on the local dynamic pressure and total temperature. Optical access is required to avoid disturbing the pattern by tunnel shutdown transients, although high-dynamic-pressure

applications with viscous oils may result in high-quality patterns remaining on the model after a run. Oil-flow pattern images have been obtained using titanium dioxide powder as a pigment and ultraviolet light for illumination[98]. The ultraviolet light causes the titanium dioxide to fluoresce, resulting in a high-contrast image.

Because of the finite thickness of the oil streaks on the model and occasional lumps of pigment in an oil-flow pattern, the oil-flow technique can disturb flows which are sensitive to roughness. Allowable model roughness decreases with increasing unit Reynolds number. Betts and Stanfield[98] have reported lift and drag data with oil-flow patterns on the model as a function of powder (pigment) content for a delta-wing model. These results showed a significant increase in drag over the range of mixtures tested. Consequently, oil-flow techniques are currently suspect for use at the high Reynolds numbers of current interest. No such techniques have been developed for cryogenic test conditions.

b. *Mini-Tufts*. The fluorescent mini-tuft flow-visualization technique was developed by Crowder[99]. The tufts are monofilament nylon, dyed with a fluorescent dye and cemented to the model surface. The tuft pattern is photographed during a run using ultraviolet flash photography. Because of the flow disturbances introduced by the tufts, quantitative aerodynamic data should normally be obtained without the tufts. In addition, misleading results may be obtained in flow conditions where the gross flow field is sensitive to premature transition. Small-diameter tufts are desirable to minimize flow disturbances, but the minimum diameter which can be used may be dictated by visibility considerations. Larger tufts may be insufficiently responsive to local flow field gradients.

4.2.1.3 Surface Pressure Measurement

a. *Surface Pressure Orifices*. Steady surface pressures are typically measured by conventional surface pressure orifices connected to pressure-scanning devices, and unsteady pressures are measured by individual high-frequency-response transducers, either flush-mounted or mounted beneath a small orifice. These techniques are well known, and will not be discussed further here.

b. *Pressure Sensitive Paint*. An optical scheme for surface pressure measurement, known as pressure-sensitive paint (PSP) shows great promise for complementing conventional methods of pressure measurement. This scheme is based on the fact that certain compounds emit light when excited by a suitable light source (photoluminescence). The intensity of the emitted light is inversely related to the partial pressure of oxygen (oxygen quenched), and is of longer wavelength than the excitation light. A schematic diagram of this process[100] is presented in Figure 18.
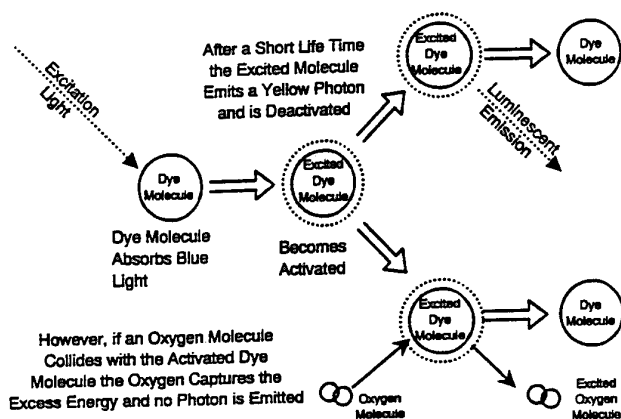
Figure 18. Oxygen Quenched Photoluminescence Schematic.

To implement this mechanism into a pressure-measurement system, a photoluminescent compound is mixed with an oxygen-permeable binder to form a pressure-sensitive paint. This paint is applied to an aircraft model and excited with a proper light source. The light source must be filtered so that it emits no light in the luminescence band. A high-resolution video camera and/or a digital camera views the model through a filter that removes all light except that emitted by the paint. The distribution of pressure over the model is computed from the measured distribution of light intensity i.e., the brighter a point in the image, the lower the pressure. A schematic diagram of a PSP measuring system is given in Figure 19.
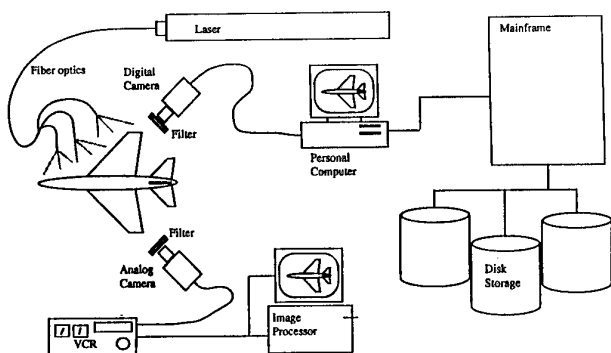

Figure 19. Schematic of PSP Measurement System.

The degree to which a PSP system provides useful results depends on several engineering details of the implementation. The sensitivity of the paint to pressure variations is such that as the pressure increases, a given change in the luminescence corresponds to a larger increase in the pressure, and the pressure resolution decreases. Subsonic wind tunnels operate at relatively high pressures, and test-section flows are associated with

small pressure differences relative to the absolute pressure level. This characteristic makes low subsonic PSP measurements particularly difficult. Other engineering difficulties in applying PSP include model motion and deformation, pressure mapping from the 2-D image plane to the model geometry, effects of temporal and spatial variations in excitation light, temporal response of the paint, and effects of paint surface temperature. Ways to minimize errors resulting from these and other sources are described in Ref. 100.

There are several groups working on development of PSP. Work performed at the Russian Central AeroHydrodynamic Institute, TsAGI, is described by Ardasheva[101], and Bukov, et al.[102] A system developed by Moscow University and TsAGI is described in detail by Vollan[103]. Kavandi et al.[104] have reported development of a PSP consisting of platinum octaethylporphrin, PtOEP, suspended in a commercial silicone polymer. The University of Washington is the only developer of PSP that (to our knowledge) has published the formulation. This work has been supported in part by NASA Ames Research Center and Boeing. McDonnell Douglas Aerospace has been developing PSP and the associated methodology since 1990. Examples of PSP applications will be taken from this work.

Results from a generic wing/body model tested in a blowdown tunnel at a Mach number of 2.0 and an angle of attack of 8 degrees are shown in Figure 20[105]. The stagnation region at the nose of the model is clearly visible in the photograph, and an extensive high-pressure region exists on the underside of the forebody. A high-pressure region is seen on the body under the wing where the wing shock intersects the body. A row of luminescence data was sampled from the side of the model and is also presented in Figure 20.
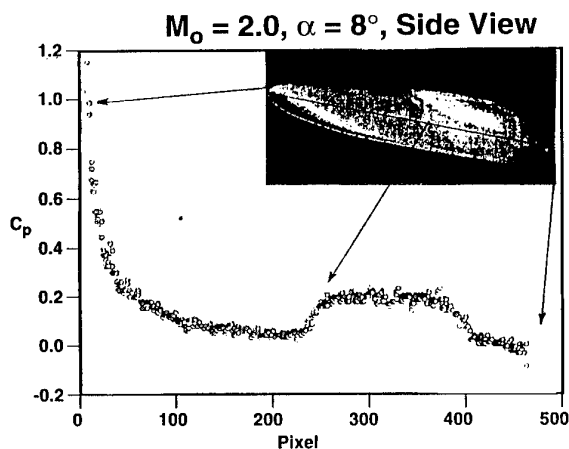

Figure 20. Pressure Distribution on Wing/Body Model at M = 2.0 Measured Using PSP (Black and White Rendering of Color Image).
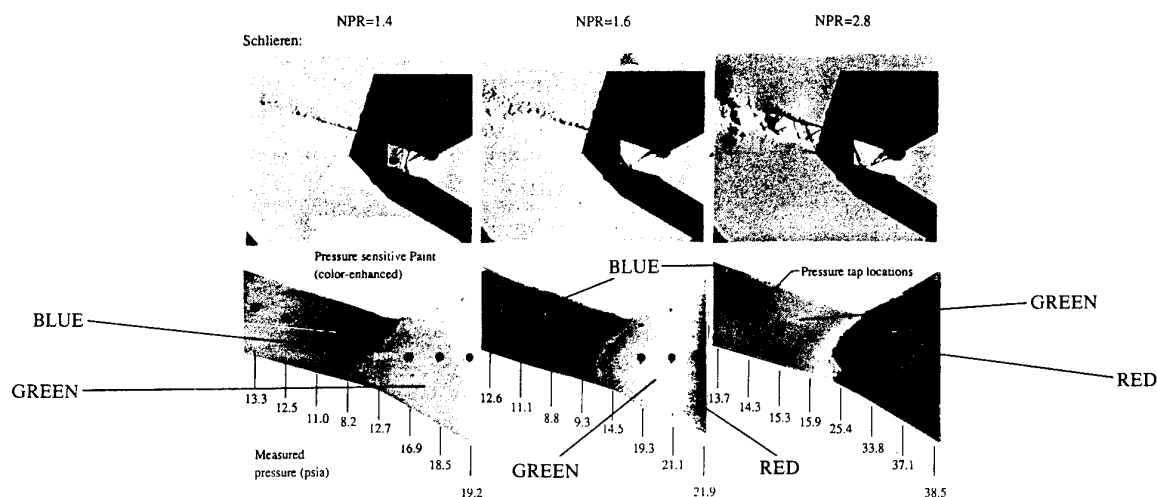
Figure 21. Schlieren Images and Pressure Distributions from 2-D C/D Nozzle Using Both PSP and Wall Orifices. (Flow is from Right-to-Left; Black and White Rendering of Color Images.)

Pressure measurements were also made in a converging-diverging nozzle at three nozzle pressure ratios. Results from this experiment are shown in Figure 21. The two-dimensional nozzle was equipped with windows for Schlieren visualization. For the paint test, one window was replaced with a solid wall painted with pressure-sensitive paint and instrumented with pressure taps. Pressures measured with wall orifices and conventional pressure transducers are included for comparison. Colors corresponding to the measured pressure correlate well between these images. A line of luminescence data was selected along the centerline row of pressure orifices, and quantitative pressure data were calculated from the luminescence data along this line. Figure 22 shows a comparison of the pressures determined by the paint with data measured by the transducers.

Pressure-sensitive paint has also been used to measure surface pressure distributions on a high-performance fighter model. Results are shown in Figure 23 for a Mach number of 1.2. The model wing was also instrumented with conventional pressure orifices. Pressure-sensitive paint in this case revealed an area of low pressure near the trailing edge at the wing tip. Because of the location and limited number of pressure orifices on the wing, wing-tip loading would be severely underestimated if only the orifice measurements were available. Samples of streamwise luminescence data from the wing were used to determine pressures. Several streamwise cuts through the wing are plotted in Figure 24. Paint calibration coefficients were determined using a linear least-squares fit to the wall orifice pressures for each cut. The agreement between results obtained from the two measurement techniques is good.
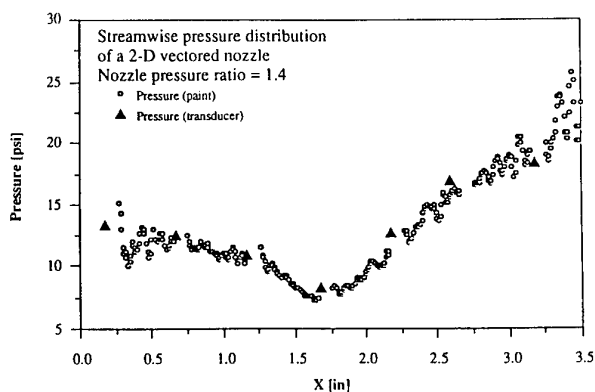

Figure 22. Comparison of Pressure Measurements Using PSP Technique and Pressure Transducers Connected to Wall Orifices.
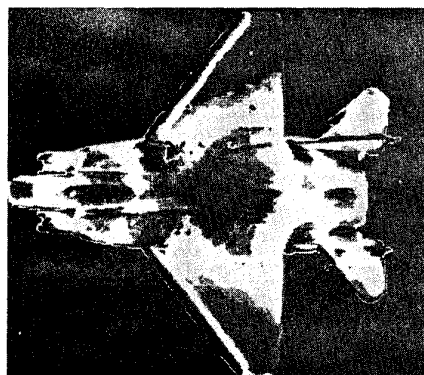

Figure 23. Pressure Distributions on a Model of a High Performance Fighter at M = 1.2 Measured with PSP. (Black and White Rendering of Color Image.)
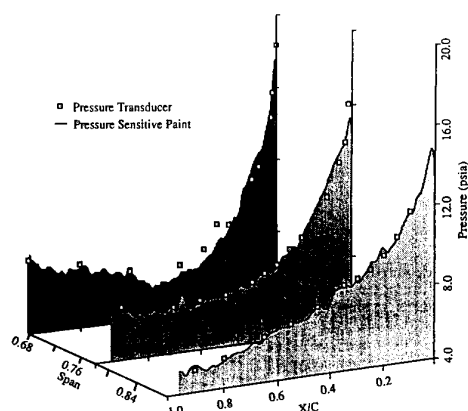
Figure 24. Comparison of Pressure Distributions on F-15 Wing at M = 1.2 Measured with PSP and Wall Orifices.

Other applications of this technique have shown that the overview provided by a pressure-sensitive paint image produces information which far exceeds expectations by revealing flow field features which were previously unsuspected. To summarize the current situation, pressure-sensitive paint can provide flow visualization, and can also provide quantitative information if data from a limited number of pressure taps are available to provide an in situ calibration.

4.2.1.4 Skin Friction Measurement

a. *Direct Methods*. Direct methods for measurement of skin friction are all variations on the floating surface element technique. Because of the limitations on the use of floating-element skin friction gauges, they are used almost exclusively in fundamental studies where skin-friction measurement is the primary objective. Data from floating-element devices is often used as a primary reference, from which calibrations of indirect methods are derived. Since the rapid increase in skin friction caused by transition is a primary indicator of transition, skin-friction measurements which have adequate spatial resolution also serve as transition-measurement techniques.

b. *Indirect Methods*. A large number of indirect techniques have been proposed. Most of these can be grouped into the categories of surface obstacles, velocity-profile measurements, heat and mass transfer analogies, and liquid surface film techniques. Surface-obstacle techniques involve identifying the characteristic pressure difference as the pressure upstream of the obstacle, or pressure measured by a forward-facing tube in contact with the surface, minus the local static pressure. Stanton tubes are very thin, razor-blade-like obstacles cemented over a pressure orifice, and are intended to remain within the innermost portion of a boundary layer where the calibration is linear or nearly so, and is essentially independent of the obstacle geometry.

Preston tubes[106] are larger, round tubes in contact with the surface. The concept underlying the Preston tube is that the pressure rise induce by a geometrically-similar group of obstacles immersed in the logarithmic portion of a turbulent boundary layer can be correlated with the local shear stress through the previously described nondimensionalization scheme. Extensive literature concerning Preston tubes exists; examples are included in Refs. 106-109. Preston tubes are among the most commonly used of the indirect methods, since they are relatively inexpensive, rugged, and insensitive to pressure gradients. The concept underlying the Preston tube has led to use of various types of obstacle blocks as skin-friction meters[110,111], including direction-sensitive devices[112].

The Clauser chart technique[113] for inferring skin friction from near-wall portions of turbulent boundary-layer velocity-profiles involves choosing a value of skin-friction coefficient such that the inner portion of the measured profile matches the law-of-the-wall velocity-profile correlation. The law-of-the-wall length scale decreases with increasing unit Reynolds number. The smallest practical boundary-layer pitot probes are 0.004 to 0.010 inches in height, independent of the scale of the experiment. As a result, velocity-profiles measured with pitot probes at high unit Reynolds number typically begin at $50<y^+<200$, and the inner region of the boundary layer is not resolved. In a region of skin friction, the logarithmic region is relatively thin, and there are few data points in the logarithmic portion of the profile upon which to base the slope and the associated value of skin-friction coefficient.

A comparison of skin-friction data obtained from a recent experiment conducted by MDA and NASA in the NASA Langley LTPT with a multi-element airfoil high Reynolds number is presented in Figure 25. Data obtained using Preston tubes by Lin[114] are compared with data obtained by Spaid and Peters[115] using the Clauser technique. The agreement between data obtained by the two techniques is very good.
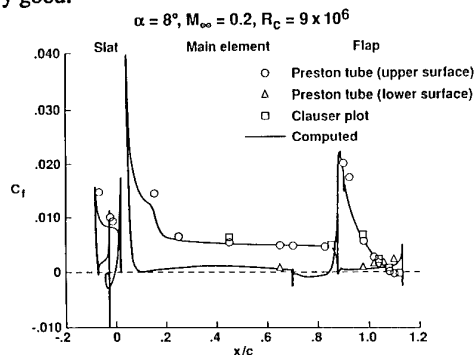

Figure 25. Skin Friction Measurements for Multi-Element Airfoil in NASA Langley LTPT.

Another popular category of skin-friction-measurement device is the heated surface wire or film, which relies on the relationship between wall shear stress and heat transfer. This is a variation of the hot-film array mentioned previously[116-118]. Although these devices are more difficult and expensive to use than Preston tubes, they can be made small and non-intrusive, can be installed on curved surfaces, and have inherently high frequency response. Mounting the heated element on a rotatable insert allows determination of the flow direction at the surface, and a multiple-wire scheme allows determination of the wall shear stress and its direction[119].

Skin friction can be deduced by observation of a thin film of oil on a surface and application of lubrication theory. Laser interferometry has been used to determine the oil-film thickness[120,121]. A new application of this technique for measuring skin-friction distributions on wind tunnel models during a single test run was recently demonstrated[122]. The method involves applying a straight, diagonal bead of oil to the airfoil surface prior to a run, and observing the fringe pattern produced by illumination of the resulting oil film with laser light. The method is particularly simple to implement, and allows determination of the skin friction distribution beneath the oil film if the absolute value of skin friction is determined at some point on the airfoil by another technique.

4.2.2 Off-Body Flow Field Measurements

Off-body flow field measurements play a major role in the aircraft-development process. Flow field measurements are used to assess drag components, to permit understanding of flow physics needed to address and correct deficient characteristics, or to guide the design of concepts with improved performance, and to obtain the data needed to develop turbulence models for CFD methods. The current status of the diagnostic capabilities relative to these needs is assessed in the following sections. Existing methodologies are grouped together as either intrusive (measurements with physical probes) or non-intrusive (optical). This grouping largely reflects past/current practices (intrusive) for aircraft production development testing versus the desired future capabilities (optical).

4.2.2.1 Single- or Multiple-Orifice Probes

a. *2-D Airfoil Momentum Rake*. Airfoil drag is typically measured with a traversing pitot probe or rake. It is desirable to obtain drag wake surveys sufficiently far downstream that the static pressure has returned to the mean value in the test section, and both turbulence level and flow angularity are small. For measurements at cruise-type conditions, simple pitot probes will often suffice. Transonic airfoil velocity-defect surveys can be effectively used to separate viscous drag and wave drag as

indicated schematically in Figure 26. A symmetric wake approach[123], based on the observation that the unequal momentum deficit profiles coming from the upper and lower surfaces of the airfoil interact very quickly through high viscous shearing forces to produce a symmetrical wake if there are no shock waves, defines the wave drag as the total integrated drag less the symmetrical part. Wave drag correlations obtained in this manner for a range of airfoil types agree with a fundamentally-based prediction method[124]. High-lift measurements, where the static pressure and flow angularity criteria are more difficult to satisfy, can be made more accurate by use of an array of five-hole probes, as in the current NASA/MDA wake rake installation in the NASA Langley LTPT.
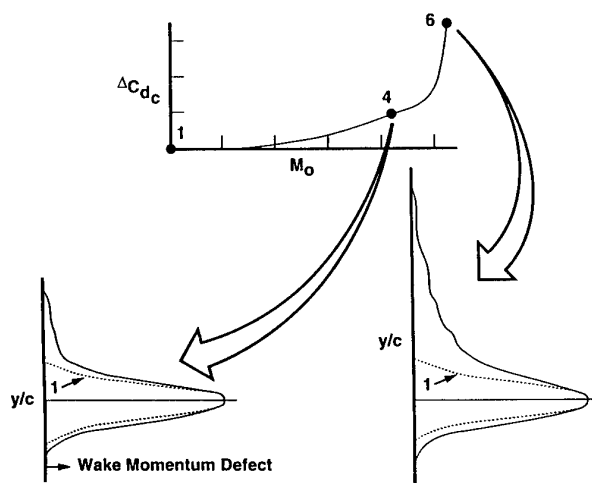
Figure 26. Drag Segregation from Airfoil Wake Profiles.

b. *3-D Wake Surveys*. The use of 3-D wake surveys for quantitative drag assessments, including distinguishing between profile drag, induced drag, and wave drag, is deceptively difficult to do accurately, since it requires determination of the local flow field velocity[125]. Quantitative wake surveys also require very accurate probe position measurements since spatial derivatives of flow velocities must be computed during data reduction[126,127]. Consequently, initial 3-D wake survey investigations focused on providing qualitative indications of features in the wake that could be correlated with drag. The leader in this area has been the Wake Imaging System (WIS) developed by Crowder at Boeing[125]. Measurements from a single traversing total pressure probe have been combined with an array of colored lights activated by the probe transducer output and a photographic system to produce color contour maps of total pressure defect superimposed on a photograph of a wind-tunnel model. This technique is particularly useful in visualizing the flow about complex three dimensional high-lift models with nacelles (including power effects).

The Boeing WIS system has been utilized in a number of large wind tunnels, including the NASA Ames 11-Foot Transonic facility. Applications presented to date have included the following:

- 3-D high-lift system analysis of drag sources

- Study of nacelle strake (vortex) flow field

- Study of aft fuselage drag sources

- Study of vortex flow fields for fighter aircraft

- Study of transonic wing shock development

- Study of wing wake at horizontal tail

Brune et al.[126,127] have subsequently illustrated the natural extension of wake imaging to quantitative three-dimensional wake surveys for drag determination using a pneumatic probe with multiple holes. Very detailed low-speed wake measurements on a simple wing model have demonstrated excellent accuracy in determination of induced drag, profile drag, and spanwise distribution of the components of drag and lift[126]. Subsequent reported applications[127] have included a 3-D high-lift configuration with and without engine simulation, and a fuselage afterbody drag study. Some results from the high-lift model study are reproduced in Figures 27 and 28. It can be seen that inboard (on left side) total pressure and velocity contours are quite different for the two nacelle configurations, but the outboard contours, including the strong vortex shed from the outer edge of the trailing-edge flap, are almost identical. Quantitative wake surveys of this type are of the utmost value in the aerodynamic design and development process for both transport and tactical aircraft.

c. _High-Lift Airfoil Flow Field Measurements_. While wake surveys provide the downstream consequences of whatever interactions occurred upstream, there are innumerable occurrences in the aircraft design and development process when it is necessary to understand the prevailing flow physics existing upstream on and about the aircraft geometry in order to guide the development of improved performance designs. One of these involves the design of high performance multi-element high-lift systems. For example, it is necessary to understand the interactions between the flow fields of the various elements in order to rig the various elements relative to each other to achieve maximum performance, or to guide the development of improved component designs, or to understand what the achievable performance limits might be.

Flow field surveys about multi-element high-lift airfoils have been undertaken previously[128], but never at and around maximum-lift conditions at high Reynolds
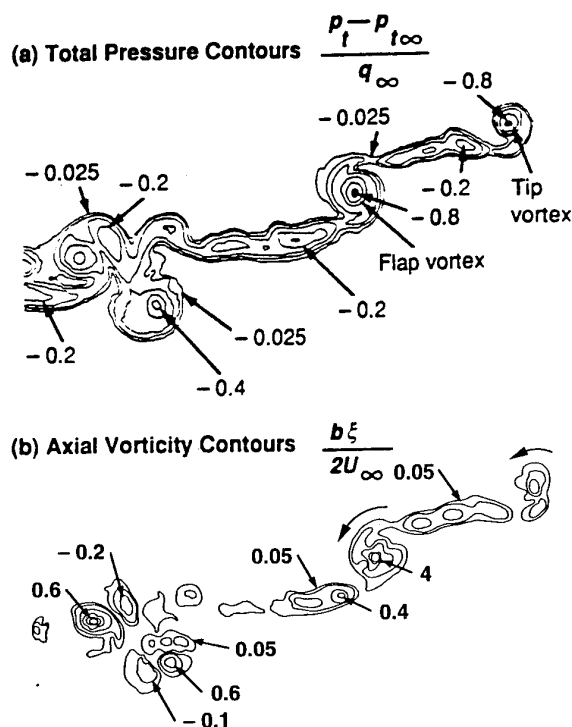

Figure 27. Wake Flow Data of Transport High-Lift Model with Flow-Through Nacelles (Ref. 127).
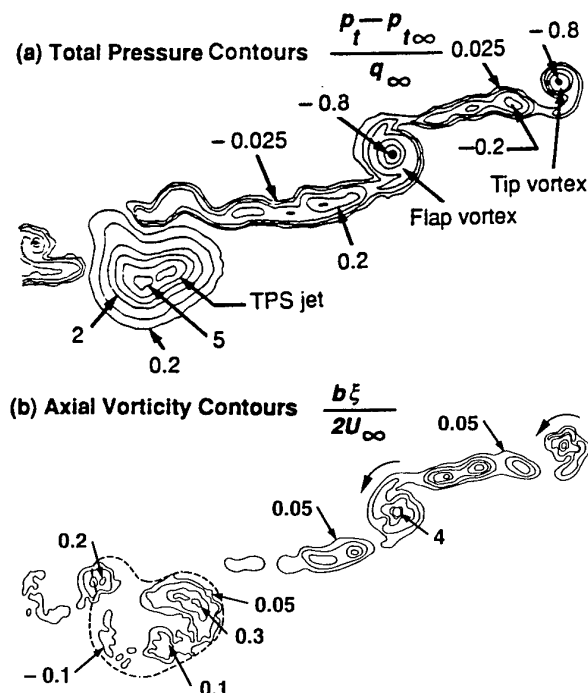

Figure 28. Wake Flow Data of Transport High-Lift Model with TPS Powered Nacelles (Ref. 127).

numbers. Typically, traverser systems employed were not sufficiently rigid to withstand the dynamics present at these high Reynolds numbers, maximum-lift conditions. To overcome this deficiency, MDA developed a unique traversing system for 2-D multi-element airfoil flow field survey testing in the NASA Langley LTPT[8]. This system is illustrated in Figure 29. Since the design of traversing units is a compromise between the conflicting requirements of rigidity, high data productivity (corresponding to multiple-axis remote traversing capability), and minimum flow field interference, a conservative approach was taken in the design of this traversing unit, in that the design incorporates remote movement along a single axis, normal to the local surface. Streamwise positioning is accomplished manually. This approach resulted in an exceptionally rigid unit, which contributes to high data quality. The system consists of a streamlined traverser which is attached to a curved wall plate by a horizontal support. An airfoil-shaped fairing surrounds the horizontal support, which can be remotely adjusted to align it with the local flow direction based on pressure measurements on the fairing. Panel method calculations were employed in the design of this system to minimize flow field interference. The traverser can be rotated about the axis of the horizontal support to align the probes (five-hole probe and flat-tube pitot probe) with the airfoil surface. It is instructive to note the complexity required in the design of this traverser system for 2-D testing at high Reynolds numbers, so that the difficulty associated with obtaining similar data on 3-D high-lift models can be put in proper perspective.
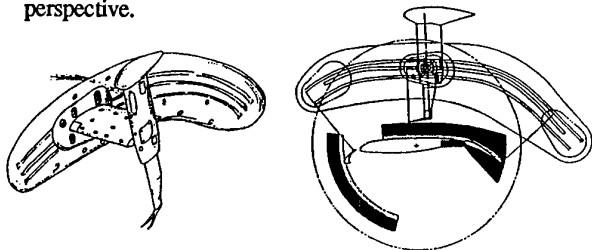

Figure 29. Traversing System for 2-D Multi-Element Airfoil Flow Field Surveys in NASA Langley LTPT.

To assess the flow field interference associated with the installation of this traverser system, individual lift curves were examine for each of the components of the multi-element airfoil with the traverser in and out of the tunnel. The results indicated that the global influence of the traverser is minimal except beyond maximum lift, where the decrease in lift with increasing angle of attack was delayed slightly.

Some initial flow field survey results about a multi-element airfoil that were obtained using this traverser system have been reported[129]. Two sets of flow field survey results are presented here to illustrate the type of

lessons learned from such testing. Both sets of results are for a three-element high-lift system, with slat and single-segment flap. In one, the effect of a small change in the flap-to-spoiler gap is shown, while the other depicts the changes occurring when the flap deflection is increased by five degrees.

The first set of flow field survey results addresses the mechanism for a loss in maximum lift at a flap deflection of 30 degrees with the reduced flap-to-spoiler gap. In this case, the flap gap was reduced to eliminate a flow separation on the flap at much lower angles of attack representative of approach conditions where noise (drag) is of crucial importance. Measured velocity profiles above the flap for both flap-to-spoiler gaps at a (stowed) chord Reynolds number of 9 x 10^6 are illustrated in Figure 30 for angles of attack below and at maximum-lift conditions. It can be seen that there is much more spreading of the wake from the main element with the smaller gap, particularly at the angle of attack for maximum lift. The corresponding increase in the equivalent displacement thickness of the wakes is shown in Figure 31. The increased displacement thickness, i.e., reduced flow turning, which leads to the reduction in maximum lift with the smaller gap is quite apparent.
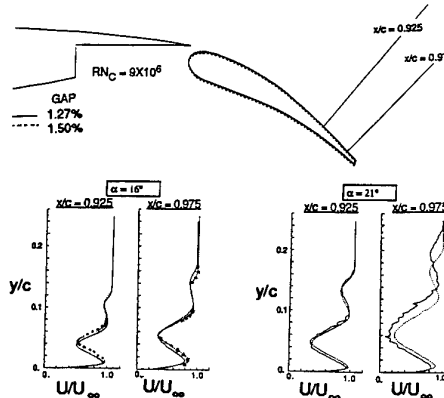

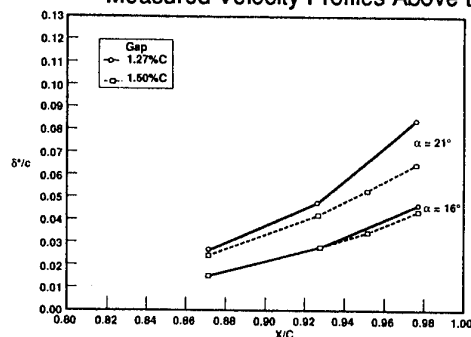Figure 30. Effect of Flap-to-Spoiler Gap Change on Measured Velocity Profiles Above the Flap.

Figure 31. Effect of Flap-to-Spoiler Gap Change on Equivalent Displacement Thickness of Wakes Above Flap.

The second set of results addresses the mechanisms that limit the increase in maximum-lift capability attained when the single-segment flap deflection was increased from 30 to 35 degrees. Measured velocity profiles above the flap for both flap deflections are presented in Figure 32. Again, much greater spreading of the wake from the main element is the culprit, most likely caused by the influence of the greater adverse pressure gradient on the flap at the higher deflection. The corresponding increase in the equivalent displacement thickness of the wakes depicted in Figure 33 is very significant, and explains the lack of benefit for the increased flap deflection.
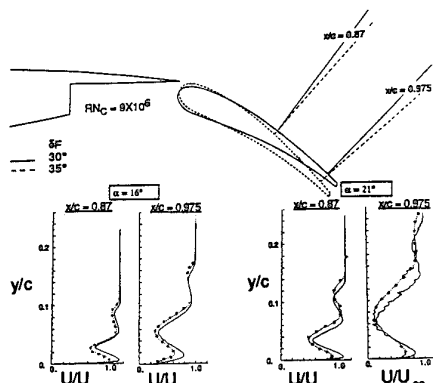

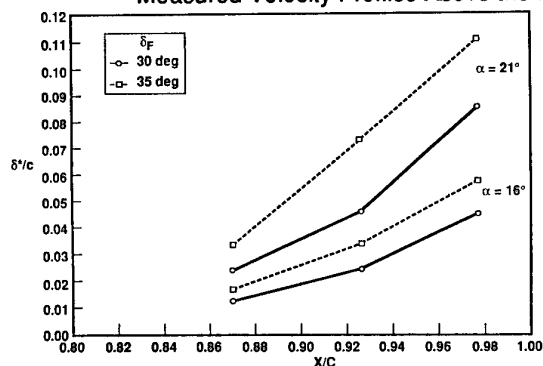Figure 32. Effect of Increased Flap Deflection on Measured Velocity Profiles Above the Flap.

Figure 33. Effect of Increased Flap Deflection on Equivalent Displacement Thickness of Wakes Above Flap.

d. *Hot-Wire or Hot-Film Probes*. Use of these probes for off-body flow field measurements involves similar considerations as in the use of multiple-orifice probes. These probes are capable of measuring unsteady velocity components and quantities such as Reynolds stress, which are needed in the development of turbulence models. They tend to be more fragile than multiple-orifice probes. Quantitative data can be obtained where the turbulence intensity is not too large, and where there is a predominant flow direction. Calibration is difficult at transonic conditions, so limited applications are seen at these speeds. For measurement of turbulence quantities in multi-element high-lift-airfoil wakes, hot-wire and hot-film probes can be used to document the wake properties prior to stagnation, and in the outer portions of the shear layers surrounding any recirculation regions.

Zaman et al.[130] have published measurements of unsteady lift on a pitching model of an NACA 0012 airfoil from wake velocity surveys. Wake vorticity data were obtained from surveys obtained with a crossed hot-wire probe. The wake survey results were found to be consistent with limited force balance data and with data from the literature.

A novel axial hot-film probe developed for the direct measurement of shock position in transonic airfoil flow fields is described by Roos[131]. Results obtained with this probe were used to correlate instantaneous upper-surface shock locations on supercritical and conventional airfoils with characteristics of the unsteady surface pressure field[132].

4.2.2.2 Optical Measurement Techniques

a. *Laser Light-Sheet Flow Visualization*. One of the simplest optical techniques, laser light-sheet flow visualization consists of seeding the flow with particles suitable for light scattering (smoke, oil droplets, water droplets, etc.), expanding a laser beam into a sheet, directing the beam to the desired plane in the flow field, and visually observing or recording the images by photography or video. The images can be analyzed by existing image-processing techniques to perform operations such as vortex tracking or mixing measurements. Automated movement of optical components synchronized with image acquisition can be used to obtain a sequence of images in parallel planes. For example, the vortical flow above a delta wing at high angle of attack was obtained by Roos[133] in the Shear Flow Facility at MDA. The technique works well in water, where reflective particles or fluorescent dyes can be used. Use of this technique by Saripalli has led to important advances in helicopter and V/STOL aircraft technology[134,135].

b. *Laser Doppler Velocimetry (LDV)*. A popular version of this technique consists of bringing two laser beams to a common focus, thereby creating a fringe pattern within a small focal volume. Light scattered by particles which pass through this volume is collected, and the frequency modulation of this scattered light is a function of the component of particle velocity normal to the fringes, the laser wavelength, and optical and geometric properties of the system. The method is nonintrusive, and requires optical access. The technique has been used extensively during the past several years for fluid dynamics research, but has been used very little for configuration-development testing in large facilities at high Reynolds

numbers, due undoubtedly the relatively poor optical access available in the production-oriented tunnels, and the extensive tunnel occupancy times required to acquire LDV data. Requirements for extensive optical access have been mitigated somewhat by the use of fiber optics for illumination, but collecting optics typically require large apertures, leading to a requirement for large windows and a wide range of viewing angles for complex models. A survey of LDV and related optical diagnostic techniques is presented by Owen et al.[136]. There is extensive literature pertaining to this technique.

One of the most important uses of LDV to date has been in obtaining building-block data to support turbulence-model development. For example, the widely used Johnson-King turbulence mode[184] was based on two sets of experimental data, the axisymmetric, transonic, shockwave/turbulent boundary-layer experiment of Bachalo and Johnson[137], and the supercritical airfoil experiment of Johnson and Spaid[138]. Mean velocity profiles and turbulence quantities were obtained with the LDV technique in the axisymmetric experiment, and the LDV measurements were complemented by pitot-probe measurements in the airfoil experiment.

c. *Particle Image Velocimetry (PIV)*. This technique consists of illuminating a particle-laden flow with two short-duration pulses of laser light. The laser beam is spread into a sheet, and the recording camera is focused on the plane of the laser sheet. The two pulses of light produce a double-exposed image of the particles. Velocities are determined from the particle displacements and the time between light pulses. Advances in this technique are being made rapidly, and it shows promise for use in large-scale production facilities. An obvious advantage is that a snapshot of data is acquired in a plane at one time, rather than the point-by-point data acquisition process which characterizes probe or LDV measurements. It is nonintrusive, and illumination can be provided with fiber optics, but optical access is required to view the laser light sheet. In most versions of the technique, there is a directional ambiguity in the data. This ambiguity may be removed by a velocity bias technique[139], or a two-color technique[140].

The practical applicability of PIV in a diverse range of flows is highlighted by Humphreys et al.[141], who present PIV data obtained from a reacting hydrogen-air flame, a low-Reynolds-number boundary layer, and hypersonic flow over a wedge. The results include quantities such as vorticity and Reynolds stress.

Efficient PIV data acquisition is demonstrated by Lourenco et al.[142] The double-exposed images were acquired using a high-resolution solid-state camera featuring a CCD array containing 1317 by 1035 pixels. Since the doubly exposed frames are acquired and stored digitally, the processing step from which the velocities are derived

follows immediately, without the need to develop and interrogate a photographic plate. The software used to compute the velocities adjusts the size of the interrogation region to trade off signal-to-noise ratio and spatial resolution, although a reasonable initial choice of pulse separation time is necessary to produce a range of particle displacements appropriate to the anticipated range of velocities. Figure 34 shows data obtained with the on-line technique for flow about a pitching NACA 0012 airfoil at a free-stream speed of 150 m/s.
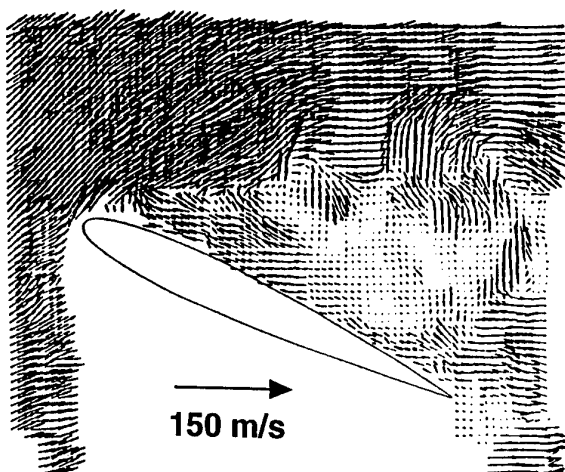
Figure 34. PIV Display of Velocity Field About Airfoil in Pitch-Up Motion.

d. *Doppler Global Velocimetry (DGV)*. Doppler Global Velocimetry is a variation of the LDV concept in which the absorption line in iodine vapor is used to produce an amplitude modulation of laser light which is a direct measure of the Doppler frequency shift[143]. This technique provides a direct measure of the scattered light Doppler shift, and does not require resolution of individual particles. The absolute intensity of the scattered light depends on numerous factors besides the degree of absorption by iodine vapor, so the frequency-dependent component of the signal is determined by taking the ratio of intensities before and after passage of the beam through the iodine vapor cell. The measurement has been extended to two dimensions by expanding the laser beam into a light sheet and using a CCD array as a collecting system. The normalized illumination intensity at each pixel of the CCD array is a direct measure of the Doppler shift of the light scattered at that point in the plane, and therefore a component of velocity.

Meyers[144] and Lee et al.[145] have presented examples of application of Doppler global velocimetry to experiments conducted in the Basic Aerodynamic Research Tunnel at NASA Langley. Results presented in Ref. 145 and reproduced in Figure 35 show vortical flow above an F/A-18 model at 25 degrees angle of attack.

Figure 35. DGV Mean Velocity Measurements of
Vortex Flow Above F/A-18 at $\alpha = 25°$.

e. *Focusing Schlieren*. A promising variation on the
traditional Schlieren flow-visualization technique known
as focusing Schlieren has been applied by Gartenberg[146]
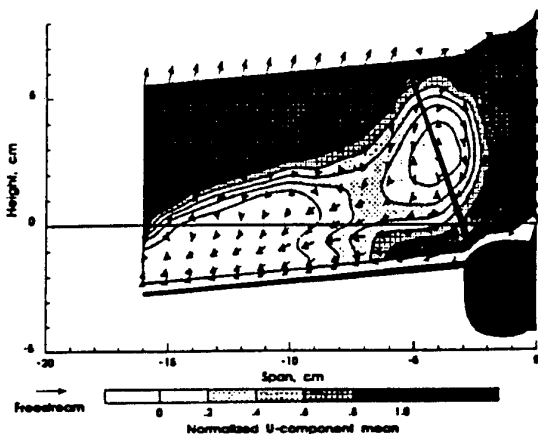to subsonic and transonic flows in the 0.3-Meter TCT at
NASA Langley. The technique allows Schlieren images
to be obtained at a sharply-focused plane within the flow
field, thus making it far more attractive than the
conventional Schlieren technique for use with three-
dimensional models. The technique replaces the knife
edge with a grid or opaque strips, and can be implemented
with low-grade windows and optical components,
allowing a low-cost installation. An example of an image
of flow about a space shuttle model obtained with this
technique is shown in Figure 36.
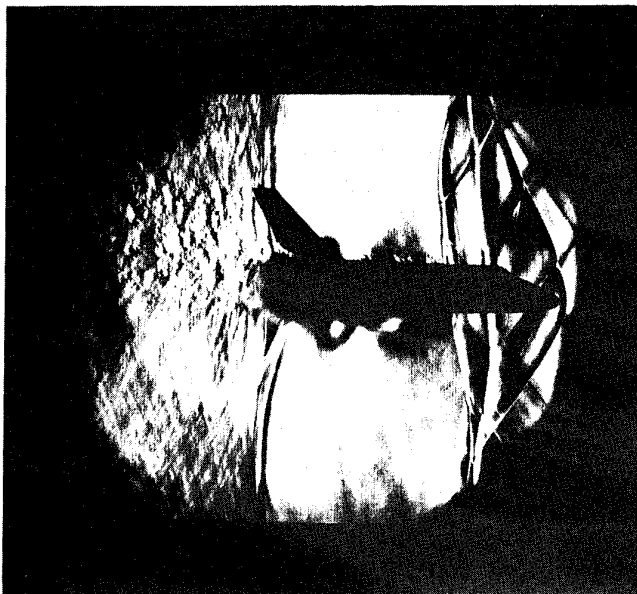
Figure 36. Focusing Schlieren Photograph of Modified
Space Shuttle in 0.3-Meter TCT at M = 1.2.

f. *Holography*. Many variations of holography have been
used in experimental fluid dynamics. Trolinger and
Havener[147] review the status of this technology. Dual-
plate holography allows reconstruction of Schlieren,
shadowgraph, or interferogram images after the experiment
has been conducted. This technique has contributed to
understanding of transonic-airfoil flow fields[148] (see
Figure 37). Application of holography to flow about a
transport aircraft model in the 2.74 x 2.44 meter transonic
wind tunnel of the Aircraft Research Association is
described by Fry and Bryanston-Cross[149]. Holographic
tomography shows promise for obtaining 3-D results.
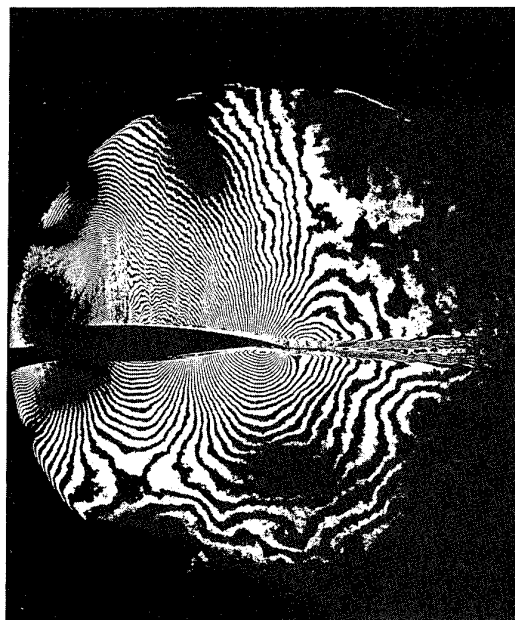
Figure 37. Interferogram of Airfoil Flow Field
Constructed Using Dual-Plate
Holography, $M_O = 0.8$.

4.3 Future Needs

Accurate, comprehensive, and efficient flow diagnostics
techniques are an absolute necessity for aircraft
configuration-development testing in high-Reynolds-
number production tunnels. Emphasis will be on
quantitative measurements, but qualitative results will
still play an important role. And, it is most appropriate
that precedence be given to optical, non-intrusive
techniques. From an aircraft developers perspective, it is
strongly urged that maximum effort be directed toward the
following four flow diagnostic techniques:

- Pressure Sensitive Paint (PSP)

- IR for Transition Detection

- Particle Image Velocimetry (PIV)

- Global Doppler Velocimetry (GDV)

Pressure-sensitive paint is an emerging technology with great promise. This technique is on the verge of providing aerodynamic loads and flow diagnostic capabilities at a fraction of the cost and elapsed time of conventional methods. The global nature of this method continues to provide information far in excess of the original test objectives in each application. Improvements are needed (and anticipated) in accuracy, conversion of pixel arrays to the 3-D model geometry, and for unsteady or impulse-facility applications. Optical access is crucial, but requirements tend to be less stringent than those imposed by other optical techniques. Potential use in cryogenic facilities is questionable, but should be pursued. However, since a vast majority of loads testing will be conducted in non-cryogenic facilities, and the application of PSP to loads testing will provide the greatest reduction in design-cycle time/cost, priority should be placed on developing the PSP process for testing in air.

Infrared imaging shows great promise for transition detection in both cryogenic and non-cryogenic environments, and should be pursued diligently. For cryogenic conditions, development of digital cameras which are optimized for long wavelengths may be a pacing technology, since the market for cameras of this type is likely to be small. The need for excellent optical access and exotic windows may be a major obstacle for cryogenic testing, but should not preclude effective use at non-cryogenic conditions, which will still constitute the bulk of the testing conducted at less-than-flight Reynolds numbers. Hot-film arrays should continue to play a meaningful role, especially for areas where optical access for IR are limited, such as occurs with some of the elements of a multi-element high-lift system.

Particle-Image Velocimetry and Doppler Global Velocimetry are clearly the most promising techniques for off-body flow field measurements if adequate optical access can be provided. Both techniques appear to be capable of providing near real-time data if state-of-the-art technology is used. The primary use of these data is likely to be qualitative, as useful results can be obtained with existing levels of accuracy. Prospects for extension of PIV and DGV to 3-D measurements depend on the requirement, whether it is for mean flow field data or simultaneous measurements of fluctuating quantities. Three components of Doppler Global Velocimetry data can be obtained in a single plane by use of three sets of receiving optics. A 3-D data set can be created by taking several sets of data sequentially in parallel planes. Extension of the PIV technique to three velocity components is being pursued as an extension of the on-line concept. Multiple

sheets will be packed sufficiently closely to obtain the third component of velocity. A 3-D set of mean velocity data could be obtained from an array of these multiple-sheet data sets. Hence, there is an established direction for obtaining 3-D *mean velocity* data from both PIV and DGV techniques that can be developed to provide the data needed for configuration-development testing. However, means need to be developed to efficiently obtain the corresponding 3-D fluctuating quantities required for development of more representative turbulence models. LDV and traversing-probe measurements will continue to be obtained, but these single-point-type techniques will not be practical for obtaining the large volume of data required from high-Reynolds-number production-type tunnels.

5. CONCLUSIONS

Requirements, current technology status, and future needs for methodologies to assess wall- and support-interference effects, and for flow field measurement capabilities, have been addressed from an aircraft industry perspective. Conclusions arising from this review include the following:

- The requirement for higher Reynolds number testing, especially for transport aircraft, is placing a much greater burden on the development of the respective technologies.

- Accurate wall interference estimation methods, including modeling of the tunnel wall, are required to establish guidelines for setting maximum model sizes for subsonic high-lift testing, and for the investigation of buffet-onset, post-buffet, etc. conditions at transonic conditions.

- Representative semi-empirical mathematical models of the nonlinear wall characteristics of major production-type wind tunnels must be established for wall interference estimation.

- CFD inadequacies must be taken into account when selecting the most appropriate wall interference estimation method for a given application.

- Increased emphasis should be placed on the design of model support systems which minimize interference effects, and, concurrently are amenable to CFD analysis.

- Emphasis should also be placed on the development/calibration/validation of advanced CFD methodologies applicable to a wide range of support systems.

- Development of flow-field diagnostic techniques should focus heavily on optical, non-intrusive techniques, rather than on intrusive devices.

- Maximum effort should be placed on transitioning pressure sensitive paint into routine use for aerodynamic loads determination in high Reynolds number production-type tunnels.

- Infrared imaging shows the greatest promise for transition detection in both cryogenic and non-cryogenic environments, and should be pursued diligently.

- Particle-Image Velocimetry and Global Doppler Velocimetry are clearly the most promising techniques for off-body flow field measurements, and directions for obtaining 3-D mean velocity data from both have been established. However, means need to be developed to efficiently obtain the corresponding 3-D fluctuating quantities needed for turbulence model development.

REFERENCES

1. Lynch, F.T., "Commercial Transports-Aerodynamic Design for Cruise Performance Efficiency", in Transonic Aerodynamics (D. Nixon, Ed.), Progress in Astronautics and Aeronautics, Vol. 81. 1982.

2. Lynch, F.T., "Experimental Necessities for Subsonic Transport Configuration Development", AIAA-92-0158, Jan. 1992.

3. "Boundary Layer Simulation and Control in Wind Tunnels", AGARD AR- 224, April, 1988.

4. Haines, A., "Experience in the Use of a Viscous Simulation Methodology for Tests in Transonic Tunnels", AIAA 90-1414, June 1990.

5. Goldhammer, M.E. and Steinle, F.W. Jr., "Design and Validation of Advanced Transonic Wings Using CFD and Very High Reynolds Number Wind Tunnel Testing", 17th ICAS Congress, Sept. 1990.

6. Vatsa, V.N. and Wedan, B.W., "Development of an Efficient Multigrid Code for 3-D Navier-Stokes Equations", AIAA 89-1791, June 1989.

7. Kirkpatrick, D. and Woodward, D., "Priorities for High-Lift Testing in the 1990's", AIAA 90-1413, June 1990.

8. Valarezo, W.O., "High-Lift Testing at High Reynolds Numbers", AIAA 92-3986, July 1992.

9. Mack, M.D. and McMasters, J.H., "High Reynolds Number Testing in Support of Transport Airplane Development", AIAA 92-3982, July 1992.

10. Gallaway, C.R., and Osborn, R.F., "Aerodynamics Perspective of Supermaneuverability", AIAA 85-4068, Oct. 1985.

11. Neyland, V. Ya. and Neyland, V.M., "Jet Boundaries - New Type of Self-Streamlining Wind Tunnel Wall", Published in "Wind Tunnels and Wind Tunnel Test Techniques", Royal Aeronautical Society, Sept. 1992.

12. Wolf, S.W.D., "Adaptive Wall Technology for Minimization of Wall Interferences in Transonic Wind Tunnels", NASA CR-4191, Nov. 1988.

13. Mokry, M., "Residual Interference and Wind Tunnel Wall Adaption", AIAA 89-0147, Jan. 1989.

14. Paschal, K., Goodman, W., McGhee, R., Walker, B., and Wilcox, P., "Evaluation of Tunnel Sidewall Boundary-Layer-Control Systems for High-Lift Airfoil Systems", AIAA 91-3243, Sept. 1991.

15. Steinle, F. and Stanewsky, E., "Wind Tunnel Flow Quality and Data Accuracy Requirements", AGARD AR-184, Nov. 1982.

16. Newman, P.A., Kemp, W.B. and Garriz, J.A., "Wall Interference Assessment and Correction", NASA CP-3020, April 1988.

17. Newman, P.A., Kemp, W.B. and Garriz, J.A., "Emerging Technology for Transonic Wind-Tunnel-Wall Interference Assessment and Corrections", SAE 881454, Oct. 1988.

18. Crites, R.C., "Transonic Wind Tunnel Interference: A Correction Method", AGARD CP-429, Oct. 1987.

19. Ashill, P.R. and Weeks, D.J., "A Method for Determining Wall-Interference Corrections in Solid-Wall Tunnels from Measurements of Static Pressure at the Walls", AGARD CP-335, May 1982.

20. Hackett, J.E., et. al., "Determination of Wind Tunnel Constraint Effects by a Unified Wall Pressure Signature Method", Part I: NASA CR 166, 186; Part II: NASA CR 166, 187, 1981.

21. Ulbrich, N., Lo, C.F., and Steinle, F.W. Jr., "Blockage Correction in Three-Dimensional Wind Tunnel Testing Based on the Wall Signature Method", AIAA 92-3925, July 1992.

22. Maskell, E.C., "A Theory of the Blockage on Bluff bodies and Stalled Wings in a Closed Wind Tunnel", Ministry of Aviation R. & M. No. 3400, 1965.

23 Shmilovich, A., "Calculation of Transonic Flows with Separation Past Arbitrary Inlets at Incidence", AIAA Journal, Vol. 28, No. 4, April 1990.

24 Steinle, F.W. Jr., NASA Ames, Unpublished work.

25 Matyk, G.E. and Kobayashi, Y., "An Experimental Investigation of Boundary Layer and Crossflow Characteristics of the Ames 2- by 2- Foot and 11- by 11- Foot Transonic Wind-Tunnel Walls", NASA-TM-73257, Dec. 1977.

26. Erickson, J.C. Jr. and Homicz, G.F., "Numerical Simulation of a Segmented-Plenum Perforated, Adaptive-Wall Wind Tunnel", AIAA Journal, Vol. 20, No. 5, May 1982.

27. Chan, Y.Y., "Wall Boundary-Layer Effects in Transonic Wind Tunnels", AGARD CP-335, May 1982.

28. Jacocks, J.L., "An Investigation of the Aerodynamic Characteristics of Ventilated Test Section Walls for Transonic Wind Tunnels", AEDC TR-77-61, 1977.

29. Crites, R. and Rueger, M., "Modeling the Ventilated Wind Tunnel Wall", AIAA 92-0035, Jan. 1992.

30. Beutner, T.J., "Determination of Solid/Porous Wall Boundary Conditions from Wind Tunnel Data for Computational Fluid Dynamics Codes", AIAA 93-0530, Jan. 1993.

31. Steinle, F.W. Jr. and Mabey, D.G., "Computer Studies of Hybrid-Slotted Working Sections with Minimum Interference at Subsonic Speeds", NASA TM 86002, Aug. 1984.

32. Kemp, W.B. Jr., "Computer Simulation of a Wind Tunnel Test Section with Discrete Finite-Length Wall Slots", NASA CR 3948, April 1986.

33. Everhart, J.L., "A Detailed Study of the Flow in the Vicinity of the Slotted Wall of a Wind Tunnel with Applications to the Homogeneous Slotted-Wall Boundary Condition", AIAA 86-0749, March 1986.

34. Everhart, J.L., "Theoretical and Experimental Analysis of the Slotted-Wall Flow Field in a Transonic Wind Tunnel", SAE 871757, 1988.

35. Crites, R.C. and Rueger, M., "Transonic Wall Interference Corrections for Small Wind Tunnels", Published in "Wind Tunnels and Wind Tunnel Test Techniques", Royal Aeronautical Society, Sept. 1992.

36. Lee, K.D., "Numerical Simulation of the Wind Tunnel Environment by a Panel Method", AIAA Journal Vol. 19, No. 4, April 1981.

37. Morky, M., Digney, J.R., and Poole, R.J.D., "Doublet-Panel Method for Half-Model Wind-Tunnel Corrections", Journal of Aircraft, Vol. 24 No. 5, May 1987.

38. Kemp, W.B. Jr., "A Panel Method for Interference Assessment in Slotted-Wall Wind Tunnels", AIAA 88-2537-CP, 1988.

39 Browne, L. and Katz, J., "Application of Panel Methods to Wind-Tunnel Wall Interference Corrections", AIAA 90-0007, Jan. 1990.

40. Freestone, M.M., Mohan, S.R., and Lock, R.C., "Interference Correction in Wind Tunnels with Slotted Walls", Published in "Wind Tunnels and Wind Tunnel Test Techniques", Royal Aeronautical Society, Sept. 1992.

41. Rizk, R.H. and Murman, E.M., "Wind Tunnel Wall Interference Corrections for Aircraft Models in the Transonic Regime", Journal of Aircraft, Vol. 21, No. 1, Jan. 1984.

42. Phillips, P.S. and Waggoner, E.G., "Transonic Wind-Tunnel Wall Interference Prediction Code", Journal of Aircraft, Vol. 27, No. 11, Nov. 1990.

43. Al-Saadi, J.A. and Dejarnette, F.R., "Wall Interference Calculation in a Transonic Test Section Including Simulation of Discrete Slots", AIAA 92-0032, Jan. 1992.

44. Tseng, W., Feinberg, E., Cenko, A., "TRANAIR Applications to Fighter Configurations", AIAA 89-2220-CP, 1989.

45. Donegan, T.L., Benek, J.A., and Erickson, J.C., "Calculation of Transonic Wall Interference", AIAA 87-1432, June 1987.

46. Deese, J.E., et.al., "Simulation of Wind Tunnel Flow Fields", AIAA 92-0034, Jan. 1992.

47. Sickles, W. and Erickson, J., "Wall Interference Correction for Three-Dimensional Transonic Flows", AIAA 90-1408, June 1990.

48. Rueger, M., et.al., "Transonic Wind Tunnel Wall Interference Corrections", AGARD "Symposium on Wall Interference, Support Interference, and Flow Field Measurements", Oct. 1993.

49. Martin, F.W. Jr., Sickles, W.L., and Stanley, S.A., "Transonic Wind Tunnel Wall Interference Analysis for the Space Shuttle Launch Vehicle", AIAA 93-0420, Jan. 1993.

50. Crites, R., Rueger, M., Evans, D., and Lehman, S., "Comparison of Transonic Wind Tunnel and Flight Data for a High Performance Fighter Aircraft", AIAA 92-3983, July 1992.

51. Valarezo, W.O. and Chin, V.D., "Maximum Lift Prediction for Multielement Wings", AIAA 92-0401.

52. Pass, C.Q., "A Wake Blockage Correction Method for Small Subsonic Wind Tunnels", AIAA 87-0294, Jan. 1987.

53. Ashill, P.R. and Keating, R.F.A., "Calculation of Tunnel Wall Interference from Wall-Pressure Measurements", Aeronautical Journal, Jan. 1988.

54. Maarsingh, R.A., Labrujere, Th.E., and Smith, J., "Accuracy of Various Wall-Correction Methods for Wind-Tunnel Testing", AGARD CP-429, Oct. 1987.

55. Heyson, H.H., "Fortran Programs for Calculating Wind Tunnel Boundary Interference", NASA TM X-1740, 1969.

56. Heyson, H.H., "Rapid Estimation of Wind-Tunnel Corrections with Application to Wind-Tunnels and Model Design", NASA TD D-6416, 1971.

57. Joppa, R.G., "Wall Interference Effects for Wind-Tunnel Testing of STOL Aircraft", Journal of Aircraft, Vol. 13, May-June 1969.

58. Joppa, R.G., "Wind Tunnel Interference Factors for High-Lift Wings in Closed Wind-Tunnels", NASA CR 2191, 1973.

59. Hess, J.L., Friedman, D.M., and Clark, R.W., "Calculation of Compressible Flow about Three-Dimensional Inlets with Auxiliary Inlets, Slats, and Vanes by Means of a Panel Method", AIAA 85-1196, July 1985.

60. Ericsson, L.E. and Beyers, M.E., "Ground Facility Interference on Aircraft Configurations with Separated Flow", AIAA 92-0673, Jan. 1992.

61. Beyers, M.E., "Unsteady Wind-Tunnel Interference in Dynamic Testing", AIAA 91-0682, Jan. 1991.

62. den Boer, R.G., Houwink, R., and Zwaan, R.J., "Requirements and Capabilities in Unsteady Wind Tunnel Testing", AGARD CP-429, Oct. 1987.

63. Mokry, M. and Ohman, L.H., "Application of the Fast Fourier Transfer to Two-Dimensional Wind Tunnel Wall Interference", Journal of Aircraft, Vol. 17, June 1980.

64. Chan, Y.Y., "A Singular Perturbation Analysis of Two-Dimensional Wind Tunnel Interference", ZAMP, Vol. 31, No. 5, 1980.

65. Kemp, W.B., Jr.: "TWINTAN: A Program for Transonic Wall Interference Assessment in Two-Dimensional Wind Tunnels", NASA TM-81819, 1980.

66. Lynch, F.T. and Johnson, C.B.: "Wind-Tunnel-Sidewall-Boundary-Layer Effects in Transonic Airfoil Testing - Some Correctable, But Some Not", AGARD CP-429, Oct. 1987.

67. Murthy, A.V., "Effect of Aspect Ratio on Sidewall Boundary-Layer Influence in Two-Dimensional Airfoil Testing", AIAA 87-0295, Jan. 1987.

68. Barnwell, R.W. and Sewall, W.G.: "Similarity Rules for Effects of Sidewall Boundary Layer in Two-Dimensional Wind Tunnels", AGARD CP-335, 1982.

69. Jones, D.J., Chan, Y.Y., and Nishimura, Y.: "A Numerical and Experimental Evaluation of the Sidewall Boundary Layer Effects on Aerofoils Tested in Wind Tunnel Facilities", Published in "Wind Tunnels and Wind Tunnel Test Techniques", Royal Aeronautical Society, Sept. 1992.

70. Mineck, R. and Green, L., "Wall Interference Assessment/Correction (WIAC) for Transonic Airfoil Data from Porous and Shaped Wall Test Sections", AIAA 90-1406, June 1990.

71. Murthy, A.V., "An Experimental Study of Wall Adaption and Interference Assessment Using Cauchy Integral Formula", AIAA 91-0399, Jan. 1991.

72. Carlin, G.J. Jr. and Bevan, D., "Prediction of Subsonic Wind Tunnel Mounting System Interference", Journal of Aircraft, Vol. 24, No. 5, May 1987.

73. Binion, T., "Wall Interference in Wind Tunnels - Technical Evaluation Report on FDP Specialists' Meeting", AGARD AR-190, 1983.

74. Rooney, E.C. and Lauer, R.F. Jr., "Wind Tunnel Predicted Air Vehicle Performance: A Review of Lessons Learned", AGARD CP-429, 1987.

75. Ericsson, L.E., "Another Look at High-Alpha Support Interference in Rotary Tests", Journal of Aircraft, Vol. 28, No. 9, Sept. 1991.

76. Britcher, C.P., "Influence of Subsonic Sting Interference on the Aerodynamic Characteristics of a Family of Slanted-Base Ogive-Cylinders", NASA CR-4299, 1990.

77. Boeing, unpublished data, 1992.

78. Eckert, D., "A Semi-Analytical Method to Correct for Support Effects on Wind Tunnel Models", Published in "Wind Tunnels and Wind Tunnel Test Techniques", Royal Aeronautical Society, Sept. 1992.

79. Rettig, K. and Ewald, B., "Minimization of Strut Interference in a Low Speed Wind Tunnel by a New Strut Design Concept", Published in "Wind Tunnels, and Wind Tunnel Test Techniques", Royal Aeronautical Society, Sept. 1992.

80. NASA Ames Research Center, unpublished data, 1993.

81. Dyer, R.S., Finfrock, G.P., and Robinson, B.A., "Transitioning Full Navier-Stokes Predictions of Sting and Distortion Increments for a Fighter Aircraft Into a Production Environment", AIAA 93-3429, Aug. 1993.

82. Bush, R.H., "A Three-Dimensional Zonal Navier-Stokes Code for Subsonic Through Hypersonic Propulsion Flowfields", AIAA 88-2830, July 1988.

83. Tuttle, M.H., "Magnetic Suspension and Balance Systems: A Selected, Annotated Bibliography", NASA TM-84661 , July 1983.

84. Johnson, D.A., "Nonequilibrium Algebraic Turbulence Modeling Considerations for Transonic Airfoils and Wings", AIAA 92-0026, Jan. 1992.

85. Pope, A., "Wind-Tunnel Testing", second edition, John Wiley & Sons, Inc., New York, 1954.

86. Lynch, F.T. and Patel, D.R., "Some Important New Instrumentation Needs and Testing Requirements for Testing in a Cryogenic Wind Tunnel Such as the NTF", AIAA 82-0605, Mar. 1982.

87. Fancher, M.F., "A Hot-Film System for Boundary-Layer Transition Detection in Cryogenic Wind Tunnels", presented to Euromech Colloquium 132 on Hot-Wire, Hot Film Anemometry and Conditional Measurement, July 1980.

88. Fancher, M.F., "Aspects of Cryogenic Wind Tunnel Testing Technology at Douglas", AIAA 82-0606, Mar. 1982.

89. Johnson, C.B., Carraway, D.L., and Stainback, P.C., "A Transition Detection Study Using a Cryogenic Hot Film System in the Langley 0.3 Meter Transonic Cryogenic Tunnel", AIAA 87-0049, Jan. 1987.

90. Nakayama, A., Stack, J., Lin, J., and Valarezo, W., "Surface Hot-Film Technique for Measurements of Transition, Separation, and Reattachment Points". AIAA 93-2918, July 1993.

91. Gartenberg, E., Scott, M.A. and Martinson, S.D., "Boundary-Layer Transition Detection with Hot Films in Cryogenic Wind Tunnels", unpublished manuscript, 1993.

92. Gartenberg, E. and Roberts, A.S. Jr., "Twenty-Five Years of Aerodynamic Research with Infrared Imaging", Journal of Aircraft, Vol. 29, No. 2, Mar. 1992.

93. Gartenberg, E., Johnson, W.G. Jr., Wright, R.E. Jr., Carraway, D.L., and Johnson, C.B., "Boundary-Layer Transition-Detection in a Cryogenic Wind Tunnel Using Infrared Imaging", AIAA J., Vol. 30, No. 2, Feb. 1992.

94. Gartenberg, E., and Wright, R.E. Jr., "Problems and Solutions for Transition Detection in Cryogenic Wind Tunnels by Infrared Imaging", The 14th International Congress on Instrumentation in Aerospace Simulation Facilities, Rockville, MD, Oct. 27-31, 1991.

95. Klein, E.J. and Margozzi, A.P., "Exploratory Investigation of the Measurement of Skin Friction by Means of Liquid Crystals", NASA TM-X-1774, 1969.

96. Holmes, B.J., Gall, P.D., Croom, C.C., Manuel, G.S., and Kelliher, W.C., "A New Method for Laminar Boundary Layer Transition Visualization in Flight - Color Changes in Liquid Crystal Indicators", NASA TM 87666, Jan. 1986.

97. Reda, D.C., Muratore, J.J. Jr., and Heineck, J.T., "Experimental Investigations of the Time and Flow-Direction Responses of Shear-Stress-Sensitive Liquid Crystal Coatings", AIAA 93-0181, Jan. 1993.

98. Betts, C.J. and Stanfield, J.H., "Wind Tunnel Flow Visualization and Measurement Techniques in Use at DRA Bedford", Published in "Wind Tunnels and Wind Tunnel Test Techniques", Royal Aeronautical Society, Sept. 1992.

99. Crowder, J.P., "Fluorescent Mini-Tufts for Non-Intrusive Flow Visualization", McDonnell Douglas Corporation, Long Beach, CA., MDC J7374, Feb. 1977.

100. Crites, R.C., "Pressure Sensitive Paint Technique", Measurement Techniques, von Karman Institute for Fluid Dynamics Lecture Series, VKILS 1993005, April 1993.

101. Ardasheva, M.M., "Measurement of Pressure Distribution by Means of Indicator Coatings", Translated from Zhurnal Prikladnoi Mekhanikii Tekhnicheskoi Fiziki, No. 4, 1985. (002-8944/85/2604-0469 - Plenum Publishing Corp.)

102. Bukov, A.P., et al., "Application of Luminescence Quenching for Pressure Field Measurements on the Model Surface in a Wind Tunnel," Published in "Wind Tunnels and Wind Tunnel Test Techniques", Royal Aeronautical Society, Sept. 1992.

103. Vollan, A. and Alati, I., "A New Optical Pressure Measurement System (OPMS)", 14th ICIASF Congress, Rockville, MD, Oct. 1991.

104. Kavandi, J., et al., "Luminescent Barometry in Wind Tunnels", Review of Scientific Instruments, 61, 11, Nov. 1990.

105. Morris, M.J., Donovan, J.F., Kegelman, J.T., Schwab, S.D., Levy, R.L., and Crites, R.C., "Aerodynamic-Applications of Pressure Sensitive Paint", AIAA J.,Vol. 31, No. 3, Mar. 1993.

106. Preston, J.H., "The Determination of Turbulent Skin Friction by Means of Pitot Tubes", J. Roy. Aeron. Soc., 58, 1954.

107. Patel, V.C., "Calibrations of the Preston Tube and Limitations on Its Use in Pressure Gradients", J. Fluid Mech., 23, Pt. 1, 1965.

108. Head, M.R. and Vasanta Ram, V., "Improved Presentation of Preston Tube Calibration", Aeron. Quarterly, Vol. XXII, 1971.

109. Keener, E.R. and Hopkins, E.J., "Use of Preston Tubes for Measuring Hypersonic Turbulent Skin Friction", NASA TN D-5544, Nov. 1969.

110. Nituch, M.J., "The Use of Congruent Obstacle Blocks for the Indirect Measurement of Turbulent Skin Friction on Smooth Surfaces", M.S. Thesis, Carleton Univ., 1971.

111. Elfstrom, G.M., Kostopoulos, C., Peake, D.J., and Fisher, D.F., "The Obstacle Block as a Device to Measure Turbulent Skin Friction in Compressible Flow", AIAA 82-589, 1982.

112. Dexter, P., "Evaluation of a Skin-Friction Vector Measuring Instrument in 3-D Turbulent Incompressible Boundary Layers", Univ. of Southampton, Dept. of Astronautics and Aeronautics, 1954.

113. Clauser, F.H., "Turbulent Boundary Layers in Adverse Pressure Gradients", J. Aero. Sci., 21, Feb. 1954.

114. Lin, J.C., Presentation at the Workshop on High-Lift Flow Physics, NASA Langley Research Center, May 1993.

115. Spaid, F.W. and Peters, D.W., Unpublished data, 1992.

116. Fage, A. and Falkner, V.M., "An Experimental Determination of the Intensity of Friction on the Surface of an Airfoil", Proc. Roy, Soc., Series A, Vol. 129, 1930.

117. Liepmann, H.W. and Skinner, G.T., "Shearing-Stress Measurements by Use of a Heated Element", Ph D. Thesis, California Institute of Technology, 1954; also NACA TN 3268.

118. Rubesin, M.W., Okuno, A.F., Mateer, G.G. and Brosh, A., "Flush Mounted Hot-Wire Gauge for Skin Friction and Separation Measurements", 6th Int. Congr. on Instrumentation in Aerospace Facilities, 1975.

119. McCroskey, W.J. and Durbin, E.J., "Flow Angle and Shear Stress Measurements Using Heated Films and Wires", J. Basic Engr., 94, 1, 1975.

120. Tanner, L.H., "The Application of Fizeau Interferometry of Oil Films to the Study of Surface Flow Phenomena", Optics and Lasers in Engr., 2, 1981.

121. Monson, D.J., Driver, D.M., and Szodruch, J., "Application of Laser Interferometer Skin-Friction Meter in Compressible Flows", Proc. Int. Congr. on Instrumentation in Aerospace Simulation Facilities, Sept. 1981.

122. Monson, D.J., Matee, G.G., and Mentor, F.R., "Boundary-Layer Transition and Global Skin Friction Measurement with an Oil-Fringe Imaging Technique", SAE 932550, Sept. 1993.

123. Elfstrom, G.M., "Extraction of Wave Drag from Airfoil Wake Measurements", AIAA 81-0291, 1981.

124. Inger, G.R., "Application of Oswatitsch's Theorem to Supercritical Airfoil Drag Calculation", J. Aircraft, Vol. 30, No. 3, 1993.

125. Crowder, J.P., "Wake Imaging System Applications at the Boeing Aerodynamics Laboratory", SAE 851895, Oct. 1985.

126. Brune, G.W. and Bogataj, P.W., "Induced Drag of a Simple Wing From Wake Measurements", SAE 901934, Oct. 1990.

127. Brune, G.W., "Quantitative Three-Dimensional Low-Speed Wake Surveys", Published in "Numerical and Physical Aspects of Aerodynamic Flows", California State University, Long Beach, CA., January 1992.

128. Nakayama, A., Kreplin, H.P., and Morgan, H.L., "Experimental Investigation of Flowfield About a Multielement Airfoil", AIAA Journal, Vol. 28, No. 1, Jan. 1990.

129. Chin, V.D., Peters, D.W., Spaid, F.W., and McGhee, R.J., "Flowfield Measurements about a Multi-element Airfoil at High Reynolds Numbers", AIAA 93-3137, July 1993.

130 Zaman, K.B.M.Q., Panda, J., and Rumsey, C.L., "Estimation of Unsteady Lift on a Pitching Airfoil from Wake Velocity Surveys", AIAA 93-0437, Jan. 1993.

131. Roos, F.W., "Hot-Film Probe Technique for Monitoring Shock-Wave Oscillations, Journal of Aircraft, 16, Dec. 1979.

132. Roos, F.W., "Some Features of the Unsteady Pressure Field in Transonic Airfoil Buffeting, Journal of Aircraft, Vol. 17, No. 11 Nov. 1980.

133. Roos, F.W. and Kegelman, J.T., "An Experimental Investigation of Sweep-Angle Influence on Delta-Wing Flows", AIAA 90-0383, Jan. 1990.

134. Saripalli, K.R., "Helicopter Design Support Testing in the McDonnell Douglas Research Laboratories Hover Research Facility", 46th Annual Forum of the American Helicopter Society, Washington D.C., May 1990.

135. Saripalli, K.R., Ferrara, P.J., Flood, J.D., Grey, R.E., and Wazyniak, J.A., "Flow Visualization Studies of the Internal Flow Characteristics in a Simulated Mixed Flow Vectored Thrust ASTOVL Engine Configuration", AIAA 91-1689, June 1991.

136. Owen, F.K., Miles, R.B., and Menon, R., "Tracking a Particle's Progress", Aerospace America, 30, 11 Nov. 1992.

137. Bachalo, W.D. and Johnson, D.A., "An Investigation of Transonic Turbulent Boundary Layer Separation Generated on an Axisymmetric Flow Model", AIAA 79-1479, 1979.

138. Johnson, D.A. and Spaid, F.W., "Supercritical Airfoil Boundary-Layer and Near-Wake Measurements", Journal of Aircraft, Vol. 20, No. 4, April 1983.

139. Lourenco, L.M., "Velocity Bias Technique for Particle Image Velocimetry Measurements of High-Speed Flows", Applied Optics, 32, 12, April 1993.

140. Post, M.E. and Goss, L.P., "Two-Color Particle-Imaging Velocimetry in Vortex Structures", AIAA 93-0412, Jan. 1993.

141. Humphreys, W.M. and Bartram, S.M., "A Survey of Particle Image Velocimetry Applications in Langley Aerospace Facilities", AIAA 93-0411, Jan. 1993.

142. Lourenco, L.M., Gogineni, S.P., and LaSalle, R.T., "On-Line PIV-An Integrated Approach", Applied Optics, in press, 1993.

143. Komine, H., Brosnan, S.J., Litton, A.R., and Stappaerts, E.A., "Real Time Doppler Global Velocimetry", AIAA 91-0337, Jan. 1991.

144. Meyers, J.F., "Doppler Global Velocimetry, The Next Generation?", AIAA 92-3897, July 1992.

145. Lee, J.W., Meyers, J.F., Cavone, A.A., and Suzuki, K.E., "Doppler Global Velocimetry Measurements of the Vortical Flow Above an F/A-18", AIAA 93-0414, Jan. 1993.

146. Gartenberg, E., "Aerodynamic Investigation with Focusing Schlieren in a Cryogenic Wind Tunnel", AIAA 93-3485, Aug. 1993.

147. Trolinger, J.D. and Havener, G., "Holograms Go with the Flow", Aerospace America, 30, 11, Nov. 1992.

148. Spaid, F.W. and Bachalo, W.D., "Experiments on the Flow about a Supercritical Airfoil Including Holographic Interferometry", Journal of Aircraft, Vol. 18, No. 4, April 1981.

149. Fry, K.A. and Bryanston-Cross, P., "The Evolution of Whole Field Optical Diagnostics for External Transonic Testing", Published in "Wind Tunnels and Wind Tunnel Test Techniques", Royal Aeronautical Society, Sept. 1992.

PARTICLE IMAGE VELOCIMETRY:
PRINCIPLES, CURRENT APPLICATIONS AND FUTURE PROSPECTS

M.L. Riethmuller
Von Karman Institute for Fluid Dynamics
72, chaussée de Waterloo 1640 Rhode St Genèse Belgium

SUMMARY

The basic principle of the technique of Particle Image Velocimetry is presented. The different methods available are discussed and advantages of each of them are exposed. The latest fully optical processing methods are compared to recent video based techniques. The extension of the measurements technique to 3D and the suppression of the directional ambiguity are presented. Examples of application in a variety of domains are discussed.

1. INTRODUCTION

Velocity measurements are probably the most important ones for a fluid dynamicist. They were first performed using pressure probes. Hot wire anemometers added the ability to follow high frequency oscillations but it is only with the advent of Laser Doppler Velocimetry (LDV) that non-intrusive velocity measurements became possible. The LDV was shown to be capable of being used in a very wide range of applications, from extremely low velocities to supersonic ones. Although it is capable of dealing with turbulent or unsteady flows it is still a single point measurement technique.

Most of the models of turbulence have been based on the interpretation of single point time wise measurements. For years, the need for a whole field velocity measurement technique was obvious and many attempts to approach it have been made: pressure probe arrays have been proposed as well as hot wire rakes. Attempts at extending the LDV technique to multiple point measurements have been made and the latest one proposed [1] is really capable of providing a complete flow field with all measurements performed simultaneously.

The Particle Image Velocimetry (PIV) benefited from the developments of LDV and constitutes a real answer to the need of Whole Field measurements. It was developed in the late 70's, was practically implemented in the early 80's and started to spread in the late 80's. It is now a fully developed technique with a large potential for new applications. The advantages of this type of instrument are found in many domains: when using intermittent facilities, flow fields may be measured without assuming perfect repeatability of testing conditions; in many instances testing times are much shorter and finally, these techniques allow the access to quantities that were otherwise impossible to determine such as instantaneous vorticity fields.

2. PRINCIPLE OF THE TECHNIQUE

2.1. Historical background

The technique now called *Particle Image Velocimetry* was born as *Laser Speckle Velocimetry*. This is due to the origins of this method of measurement that are found within the field of mechanics of solids. The specific characteristic of scattered laser light that causes the phenomenon called *speckle* was used to allow the measurement of the displacements of the surface of samples subjected to strains. The first uses of this *speckle method* are found in the late 60's. During the 70's, some fluid dynamicists thought that they could apply this technique in fluid flows. First attempts were made by Dudderar and Simpkins and are reported in [2]. Meynart [3] and [4] then started a more systematic definition of the method and of its limits. The technique was then called *Particle Image Displacement Velocimetry or PIDV* in short. About the same time, Adrian [5] also followed the same systematic approach and came with complementary proposals. This brings us within the mid 80's and time is set for the large development of what will be called *Particle Image Velocimetry* or *PIV* in short. During this period, many researchers improved many aspects of the new measurement technique, in most cases very independently and sometimes with similar findings appearing at the same time. The work of Lourenco [6] and Gauthier and Riethmuller [7] and [17] are such examples. A milestone of this development was the Lecture Series organised at the Von Karman Institute in 1988 [8]. The state of the art of PIV was presented for the first time and many researchers took this opportunity to start in this field.

The very rapid development that followed this period may be best illustrated by the evolution of the numbers of papers presented at the International Symposium of Laser Velocimetry that takes place in Lisbon (Portugal) every two year. The technique has now entered its adult age since it is no longer restricted to those who are willing to make their own developments. Several systems are now commercially available and this will probably boost the number of applications far more than ever before. PIV may be used following various methods. A synthesis of the multiple techniques presently available or under investigation is shown on fig. 1.

2.2. Basic principle

Particle Image Velocimetry is based, like Laser Doppler Velocimetry, on the measurement of the velocity of tracer particles carried by the fluid. However, rather than concentrating light in a small probe volume as in LDV, a complete plane of the flow under investigation is illuminated. This is performed by creating a narrow light sheet which is spread over the region of interest. Tracer particles are therefore made visible and images of the illuminated particles will be recorded. These recordings will either contain successive images of single tracers in time or successive frames of instantaneous images of the whole flow field. The displacement of the tracer will then be determined through the analysis of these records. The basic principle of PIV is therefore very simple: the instantaneous velocity of a fluid is measured through the determination of the displacements of

tracer particles illuminated by a sheet of light. The actual measurement is consequently performed in two successive steps: the first one is the recording of images, the second consisting in the processing of these images to determine the tracer displacements.

3. IMAGE RECORDING

3.1. Light sheet illumination

Although any light source could be used, a laser is usually the most convenient one to produce a narrow and intense light sheet. Several experiments have been performed with other types of sources but the laser is by far the most used. Laser beams constitute well-collimated sources of intense light and they can very easily be transformed in a sheet using cylindrical lenses or scanning mirrors. Continuous or pulsed lasers may be used depending on the technique to be applied. Argon Ion lasers are good choices of continuous light and Ruby or Nd-Yag lasers are chosen when a pulsed source is needed. The latter replaces more and more Ruby lasers since it allows easier focusing of cameras. The energy available is best used by creating a very narrow light sheet. This is accomplished by adding spherical positive lenses to the optical system to reduce the divergence of the laser beam.

3.2. Photographic technique

3.2.1. Fundamentals

Historically, the photographic technique, also sometimes called *silver process,* was first to be applied and it is still used in many applications. An ancestor of the PIV is the *streak photography* techniques which consists in recording traces produced by the moving particles. The disadvantage of this early method is the poor accuracy of the measurement based on an estimation of the length of the traces. This is the reason why it has been superseded by the PIV. The basic optical arrangement used in PIV is shown on figure 2. The light sheet is produced by a pulsed laser and a cylindrical lens. A photographic camera is placed perpendicularly to the light sheet to obtain a well-focused image of the illuminated tracer particles. The shutter of the camera is opened for a time long enough to pulse the laser at least two consecutive times. The tracer particles are therefore producing two images each, showing the position of the particle at the two times of firing of the laser. It is important that the light is intense enough, that the pulse duration is as short as possible to avoid any blurring of the image of the tracer, and that the film used is sufficiently sensitive for the wavelength of the laser. In most cases, a pulsed laser is used, but for relatively low speed flows (less than 2m/s) it is possible to use a continuous laser such as an Argon together with a shutter, mechanical or opto-electronical, to generate the required pulses. An example of the use of a continuous Argon laser for the measurement of the velocity field in a pump is described in [9]. Pulsed lasers that are used in PIV must be able to deliver two successive pulses separated by an adjustable time width.

In most cases, the tracer particle should be small enough to follow the flow. They will therefore only scatter a small amount of light. Furthermore, this light will be collected at 90 degrees to the incoming illuminating light. As a result, the camera will be used in most cases at its larger aperture so as to collect the largest possible amount of light. The depth of field will consequently be very small and it will be necessary to adjust the focusing of the camera with great care. Note that

this difficulty represents one of the major drawbacks of the photographic technique, since it is only after processing of the film that the quality of the resulting image will be known.

3.2.2. Tracer particles

Like the LDV, Particle Image Velocimetry is actually a technique that measures the velocity of the tracers added to the flow. It is therefore essential that these tracers genuinely follow the flow and this requires that the tracer be a very small particle. The particles used in LDV are selected for their ability to meet these constraints, they can therefore be chosen safely. They should also produce enough scattering for images to be recorded and this usually forbid the use of too small tracers. In actual practice, particles ranging from 1 to 10 micrometer are good tracers. It is important to note that the actual recorded image will not correspond to the diameter of the particle multiplied by the magnification. In this range of particle size, the image size will mostly be determined by the diffraction effect of the photographic lens. Assuming d_i is the effective dimension of the image of the tracer, it can be expressed as:

$$d_i = \sqrt{(M^2 d_p^2 + d_e^2)} \qquad (1)$$

Where M is the magnification, d_p is the particle diameter and d_e is the diffraction limited diameter of the image of the particle. The latter is given by:

$$d_e = 2.44(1 + M)f\#\lambda \qquad (2)$$

$f\#$ is the f-number of the recording optics that characterises the aperture (typically from 2.8 to 11) and λ is the wavelength of the laser used. Note that in most cases, when using small tracer particles and a magnification of the order of 1, the image diameter will approximately be given by relationship (2).

Particle concentration is one of the most important parameters that will determine the quality of the performed measurement. High tracer concentrations will lead to a mode of operation that is no longer pure PIV but is close to the original *Speckle Velocimetry* technique. Particle images can no longer be distinguished one from the other. This does not forbid velocities to be determined but the signal-to-noise ratio is significantly lower than in PIV mode. However, velocities can be measured at any point on the picture. The PIV mode is characterised by a concentration of tracers such that individual particles can still be distinguished. If the concentration is too lean, it will not be possible to measure a velocity at every location since there will not be particle images everywhere. It is therefore essential that tracer concentration is adjusted with care to be as high as possible but not too high. This upper limit is the concentration at which one enters the Speckle mode. Typically, the PIV mode requires concentrations of the order of 10^{10} to 10^{11} particles per m^3 while Speckle mode will appear if concentrations are of the order of 10^{11} to 10^{12}. In practicable terms the maximum concentration C in PIV mode will be given by the following relationship:

$$\sqrt{(1/\Delta z C)} >> d_i / M \qquad (3)$$

Where d_i is the diameter of the image as given in (1) and Δz is the thickness of the light sheet.

The lower limit of concentration is determined on the basis of the procedure used for analysing the pictures obtained. This will be treated in the chapter dealing with image processing.

In practice, tracer concentration is usually adjusted to the highest possible in PIV mode. Higher concentrations then this would lead to many problems; tracers could affect the flow, making this non-intrusive measurement technique to become more intrusive or introducing strong light absorption that would destroy the quality of the laser sheet.

3.2.3. Recording parameters

The different recording parameters to be set are the time between exposures, the choice of photographic film, the method of processing of the film, the method of post-processing of the picture and the choice of optics.

The photographic film should be selected to provide a high resolution (typically 300 line pairs per mm) but it should be sensitive enough for a good contrast of the images. The actual film selected will depend upon the type of laser used and its wavelength. The grain size of the film used should be kept to a minimum and therefore the processing of the film must be made accordingly. The rule should be that grain should always be smaller than the size of the particle images. In many cases, a copy of the original film on a high resolution, high contrast emulsion through contact printing can improve signal-to-noise ratio. This process transforms the negative into a positive.

The optics used is also a sensitive parameters. It is essential that particle images are as sharp as possible to keep the contrast to the highest possible level. A superior camera lens should be selected, a good example being a macro lens. The camera itself must be of good quality. As already stated, focusing of the camera is fundamental and a maximum of care should be exerted for this purpose.

3.3. Video technique

3.3.1. Basics of the technique

Photographic film is still the image recording method providing the highest resolution. However, video image recording has made considerable progress in the recent years. It was therefore natural that the new potential of these techniques be used in PIV. Many authors have recently described very interesting developments. Examples of these may be found in [10] and [11]. Since the PIV exists, all users reckon that the use of a photographic image recording method is its most difficult and delicate aspect. It is therefore to be expected that attempts at replacing it with video recording be made.

The main difference with photographic methods is the replacement of the photographic camera by a video equipment. A video camera is installed in the same way as in the previous method. It is usually connected to a computer equipped with a frame grabber that stores the images. It can either be used exactly like a photo camera, recording several images of each particle, or it can be used differently. In this case, series of pictures are recorded. Particle images only appear once on each picture. The series of pictures should preferably be recorded digitally on the computer rather than on a tape in analog mode. In the latter case this will result in a reduction in image quality and resolution. Note that standard video process uses two interlaced frames to reduce image flicker. The resolution of each of these frames is therefore two times coarser. Since these two frames are recorded successively in time, this mode of operation is not very suitable for PIV,

except applications that do not require a high resolution. The equipment used should be capable of working in non-interlaced mode, viewing of the resulting images being accomplished through the computer.

3.3.2. Practical interest of video imaging

In this method, the pictures containing the images of the tracers can be viewed immediately. This allows the user to immediately verify the quality of the pictures in terms of exposure, focusing and appropriate tracer concentration. The suppression of the tedious processing of the photographic film is a significant advantage. Another one is the ability to directly process the image since it is already stored under digital form in the computer.

Although the limitation of this technique could be the lower resolution of the image obtained, the actual result is far better than a first analysis would give. As shown in a previous section, because of the diffraction-limited operation of the optical system, the size of the image recorded is much larger than the magnified size of the tracer. Typically, a 2 micrometer particle would result in an image of 30 micrometer, using a magnification of 1. If we take as a reference a 35 mm photographic film with a resolution of 300 line pairs per mm, we can resolve about 10000 objects. This number is an order of magnitude larger than the resolution of an accurate video camera that will display about 1024 pixels (picture elements). This first analysis is quite wrong if we consider the actual size of the particle images. Since the tracer images are of the order of 30 micrometers, we can actually distinguish 1000 of them across a photo film, one order of magnitude less than the film resolution. The video camera, with its 1024 pixels will therefore be capable of very similar performances. The magnification and pixel size will be chosen to match the tracer image for an optimal result.

3.3.3. Advantages of the video technique

As shown before, the immediate access to the picture recorded is a considerable advantage over photo-recording. Another advantage of the video method is its very high sensitivity. It usually allows to work with less laser energy than the silver process and this sensitivity could even be boosted by the use of image intensifiers. The video mode also directly provides an image under digital form, ready for an immediate processing. Finally, in low velocity applications, series of images can be recorded and, as it will be shown later, this allows to avoid the directional ambiguity.

4. IMAGE PROCESSING

4.1. Young's Fringe Method

4.1.1. Principle

The Young's Fringe method was already applied in the Laser Speckle techniques developed in the field of solid mechanics. It consists in illuminating a small area of the negative (or positive obtained by contact-printing) of the picture recorded with a low power laser beam. The particle images illuminated will scatter the light of the beam in several ways: the images of different particles will give random diffraction images while the multiple images of the same tracers will give an organised diffraction pattern. This will result in a set of organised fringes that will be created in the Fourier plane of a lens with spacing and orientation directly related to the

distance between tracer images and their trajectory. This method is illustrated in figure 3. The fringes have an orientation perpendicular to the direction of the motion and a spacing inversely proportional to the displacement.

Assuming ΔL and Δl are respectively the displacement of a tracer particle and that of its image on the recording film, the relationship between these two quantities is

$$\Delta L = \Delta l / M \qquad (4)$$

The fringe spacing is d_f and can be expressed as

$$d_f = \lambda f_L / \Delta l \qquad (5)$$

With f_L representing the focal length of the lens used in the process. The displacement of the tracer images is therefore given by

$$\Delta L = \lambda f_L / M d_f \qquad (6)$$

The measurement of the velocity field will be made by scanning the whole picture. For each location, fringes will be created. The displacement of the tracer particles will be obtained through the determination of the fringe spacing. Relationship (6) will then convert this fringe spacing into the particle displacement. The local module of the velocity V will then be derived knowing the time width ΔT between pulses:

$$V = \Delta L / \Delta T \qquad (7)$$

The general method of image processing consists in mounting the image negative on a two-dimensional traversing mechanism for the purpose of scanning it. A computer is used to control the scanning process, to digitize fringe images and to process them. The processing hardware therefore consists in an optical bench carrying the interrogation laser, beam conditioning optics, fringe imaging lenses and traversing system

In the recent years important progress have been made in the field of fringe analysis. This step of the method used to be very time consuming and different techniques have been used to perform this task.

4.1.2. Processing of fringe images

4.1.2.1. One dimensional averaging

First methods developed to process fringes were interactive, using methods that would avoid large amount of computations. The low processing speed of computers available in these times explains the development of these techniques. Although computers available nowadays are considerably faster, it is interesting to know these early techniques since they can be alternative methods for processing difficult cases.

The initial technique developed was the *one dimensional averaging*. Early applications of it were not using any imaging process. A cylindrical lens was placed in the optical path of the Young's fringe forming system. Its purpose was to transform the fringe image into a single line. The lens was oriented manually perpendicularly to the fringes and the resulting focused image was a dotted line. This resulting image is much simpler than a fringe representation. It is actually a projection of the whole fringe image on a line perpendicular to the fringes. The speckle superimposed to the useful fringe information is almost suppressed by this process which therefore increases the Signal-to-noise ratio. All what remains to be done is to use a linear array of light receivers

which when read across, will provide a periodic waveform. The frequency of the latter is determined using a one dimensional Fourier Transform. The orientation of the receiving array can be set automatically by rotating it systematically and looking for the best signal.

The early availability of image processing systems allowed the adaptation of this method to a simpler hardware. A video camera is used to digitize the fringe image and to store it in a computer memory. The method of *one dimensional averaging* is then applied through an appropriate software. The fringe image is actually projected onto a line which is manually set perpendicular to the fringes. A Fourier Transform then provides the frequency. In this method an operator has to align manually a cursor line with the fringes. This causes the method to be excessively slow although computing time is small. The typical time of processing of each point is of the order of 20 to 30 seconds. Although incredibly slow to today's standard, this technique is still being used to process locations exhibiting very noisy fringes.

4.1.2.2. Correlation and 2D Fourier Transforms

The availability of faster and cheaper computers has lead to important changes in Young's fringe processing. The digitized fringe image can now be fully digitally processed, without any manual operation.

The method used for automatic processing of fringe images is based on the determination of the velocity components along four different axes. A convenient technique is the calculation of the auto-correlation function or its Fourier transform. The i velocity component can be computed from the relation

$$s(u) = \sum \left\{ \sum [I(i,j) I(i+u,j)] \right\} \quad -256 < u < +256 \qquad (8)$$

Where $s(u)$ is the periodic signal resulting from the correlation function for the j axis.

Algorithms written to perform this task have been proposed in [12]. The authors found that to accurately estimate the velocity, magnitude and direction, four such operations were required. The velocity vector can be determined by selecting the values of the components yielding the highest signal-to-noise ratio. This operation requires typically from 0.5 to 5 seconds, depending on processor used.

This method presents the obvious advantage of a fully automatic process since no operator is required. However, when fringe density is too low, typically less than three bright fringes, this technique will not be able to determine the velocity. In such a case, the location of the particular point at which this situation was found will be stored in memory and the velocity will be later determined using the partially manual one-dimensional averaging technique.

More recently, high performance array processors or very fast mathematical chips have become available. As a result, the fringe analysis can now be performed using two dimensional FFT algorithms. This leads to processing times of about 0.1 s per point. Further improvements require that the mechanical traversing systems used be modified to allow a faster interrogation of the PIV slide.

4.2. Full optical Processing

The Young's fringe method actually consists in performing an optical Fourier transform of the location of the PIV picture being illuminated by the interrogation beam. For many years,

attempts have been made at extending optical processing to the analysis of the fringe pattern. A photo-refractive optical correlator is described in [13]. The authors make use of a BSO crystal to perform in line recording and deleting of a hologram. The holographic record of the fringes can be analysed using an optical Fourier transform. This procedure yields an auto-correlation of the fringes. Although this process seems quite interesting, its implementation appears to be complex and user sensitive. Furthermore, the minimum time needed to delete the hologram cannot be shorter than 0.1s. Also, this method requires a very high quality of the primary PIV picture.

Another fully optical process is described in [14]. The authors make use of a Liquid Crystal Display (LCD). A CCD camera records the fringe image, and displays it on a miniature LCD computer display. A laser beam illuminates the LCD screen and after passing through it, carries the Fourier transform of the fringes. The auto-correlation of the fringes is thus obtained. Like in the previous technique, all what is necessary is to numerically determine the distance between the auto-correlation peaks. The advantage of the LCD process is that it is much cheaper than the BSO based method. It is also much simpler and easier to set up. A comparison is made in [14] with conventional Young's fringe analysis and the authors find very similar results. The optical set up used in this method is shown on figure 4.

These two fully optical processing methods probably constitute the most advanced progress in PIV. However, as it will be shown later, fully digital methods are progressing so quickly that their processing speed remains faster. Presently, optical systems allow at best an analysis of about ten vectors per second.

4.3. Full digital processing

4.3.1. General principle

Digital or "on-line" PIV refers to a full digital process. The image of the light sheet is being recorded by a Video CCD or CID camera and it is therefore directly converted into digital form. The video camera can be used either like a still or a movie camera. In the first case, multiple particle images will be recorded, while in the latter, time series of images will be registered. These digital images can directly be processed by the host computer of the image processing system. This allows an "on-line" processing that saves a significant time. The conventional photographic method also called *silver process* requires a certain number of wet processing steps that demand a significant time. Since a successful PIV measurement requires a certain amount of adjustments of parameters using a trial-and-error method, this on-line method will allow a faster setting up of the whole measurement system.

4.3.2. Multiple Particle images on a single video record

In this mode of operation, the video camera is used like a still photographic apparatus. The flow is illuminated with a light sheet produced by a pulsed light source, usually a laser. Several light pulses are produced during the opening time of the Video camera. As a result, several images of each illuminated particle are recorded on a unique frame. The image is then converted into digital form by a *frame grabber* attached to a computer. This image may directly be displayed on an appropriate screen and the operator can therefore instantaneously judge of the quality of the result. Users can re-

adjust different operating parameters such as particle concentration, focusing of the camera, aperture or laser power. Once the image is judged acceptable, it is numerically processed by the computer. Different processing schemes are available and many new developments are proposed every year, following the advances of the hardware.

One of the most successful method is described in [10]. The multiple exposed frame is processed point by point by an auto-correlation algorithm. Frames are divided into square interrogation cells of 16 pixel width or multiples of 16. Actually, the interrogation cells need not be squares. According to the type of flow, they can take the shape of elongated rectangles or any other convenient shape. A digital 2D auto-correlation of the particle image doublets is performed using an FFT algorithm. The latter can either be implemented using an array processor or multiple processors attached to the computer, or the main processor of the computer itself. Fast processors, as available now, allow the entire processing of a full frame containing about 1000 vectors in less than 4 minutes. An auto-correlation map extracted from [10] resulting from the analysis of one of these interrogation cells is shown in figure 5. The peak situated off center corresponds to the average displacement of the tracer images contained within the interrogation cell. Sub-pixel resolution is achieved using interpolation algorithms. The amplitude of the peaks is a good measure of the validity of a measurement. Only those peaks with an amplitude larger than a given threshold are considered. It is worth noting that the auto-correlation technique does not allow a determination of the sign of the displacement. This directional ambiguity has to be solved using techniques described in the sequel.

4.3.3. Time series of video images

By essence, a video camera is capable of recording time series of images at a rate of 25 images per second (30 images per second in USA). Most frame grabbers are capable of storing a number of successive frames. This feature can be used to process frames with single tracer images. Successive frames may be added and then processed as multiple exposed images. A better and more interesting technique consists in carrying out a cross-correlation of successive corresponding interrogation cells. The advantage of this method is that, unlike auto-correlations, it will retrieve the direction of the tracer displacements. In multiple exposed pictures, it is necessary that the tracers moved sufficiently between two exposures so that their images be separated by a distance large enough to avoid superposition. This means that the range of velocity that can be measured is limited in a given picture. Single exposed series do not exhibit such a limitation. It is therefore possible to cover a larger range in a single series.

Processing of these frames is very similar to the auto-correlation method. The difference is that cross-correlations are determined. There is no peak for a tracer displacement of zero and the signal-to-noise ratio is usually higher.

Although this method shows clear advantages over the multiple exposure technique, it cannot supersede it in every application because of an important limitation: the image series can only be recorded at the video rate, 25 (or 30) framed per second. This will only be satisfactory for very low speed flows, so that tracers will only move by a very small amount from one frame to the next. The technique has therefore be applied in low speed flows only, such as described in [11]. In these cases, illumination is provided by a continuous laser such as an Argon-Ion.

4.3.4. Particle tracking

A method called particle tracking is used by various authors. In the digitized picture, a tracer image is selected. Its twin, recorded at the second pulse or on the second frame, is then searched for. The method uses different algorithms for searching for the most probable tracer image to be the right one. In several cases this means the application of auto or cross-correlation. This method, is only valid for very low tracer concentration. It also has the advantage that it can be implemented on very small computers. An example of tracking procedure is shown on figure 6.

4.4. Hybrid processing

Before video techniques became sufficiently performing to be used in "in-line" PIV, a method had been proposed and commercialized. This method is described by its author in [8]. The image recording is performed using a conventional photographic still camera, but data processing does not make use of Young's fringe techniques. The multiple exposed film is interrogated like in Young's fringe method, moving it with a traversing mechanism, but the images of tracers contained within the interrogation region are digitized using a video camera. Because of the large magnification, early video equipment could be used without any loss of resolution. Further processing may be performed with the same tools as fully digital approaches. This hybrid method, making use of silver process and numerical analysis of images, can be applied in complement to other ones in certain types of applications. In most cases, the hardware used can easily be converted to conventional Young's fringe procedure.

It is also possible to digitize large parts of still pictures and then apply a digital processing. This can even be done for particle tracking approaches.

5. SOLVING DIRECTIONAL AMBIGUITY

Directional ambiguity is the conventional terminology describing the lack of a technique in being able to determine the sign of the velocity. Basic Laser Doppler Velocimetry presents a directional ambiguity since the signal yielded by the photo detector does not contain any information on the direction that particles had when crossing the probe volume. There is therefore an ambiguity of + or- 180 degrees in this direction. In Laser Doppler Velocimetry, this ambiguity is solved by adding a frequency shift to one of the illuminating beams. As a result, the fringes of the probe volume are no longer stationary, but are moving. This super-imposed overall velocity shift is selected so that it is larger than the largest negative velocities. All measured values are therefore positive. Actual velocity magnitude and sign are retrieved by subtracting the shift velocity to the data obtained.

It is not surprising that solutions to the directional ambiguity of PIV where found by researchers who had a good experience of LDV and who could therefore find similar solutions in PIV. A PIV picture carries tracer image doublets. Normal techniques do not allow to know which of the two images was recorded first, hence the directional ambiguity. The technique proposed and applied simultaneously in several laboratories of Europe and USA consists in super-imposing a *shift velocity* to the flow field. This is performed by moving the entire field of view between the exposures. The easiest and most logical method is the use of a rotating mirror. This method is not new since it was already used in the 60's to measure particle velocities in two-phase flows. In PIV, a scanning mirror is moved following a saw-tooth law. Its rotational velocity is kept constant during its useful stroke. The mirror is located in the optical path of the imaging system, still or video camera. The added velocity is determined similarly to LDV. After the whole image has been processed, the shift velocity is then subtracted at every location.

The advantage of a velocity shift is not only to allow flow direction to be measured. It also significantly increases the dynamic range of the measurement method. The velocity range contained in a single multiple exposure picture can be much larger. This is done at a cost of a certain loss in accuracy. Providing a good compromise is made, it is possible to keep this loss to reasonable magnitude. This is usually achieved if the velocity shift does not exceed 2 times the maximum reverse velocity. Figure 7 shows a typical set up using a rotating mirror to provide the shift velocity.

The scanning mirror cannot be used for very large velocity since its acceleration rate is limited due to mechanical reasons. Other techniques for producing a velocity shift have been proposed, which allow larger velocities. They all make use of electro-optics with no moving parts. One of the method proposed, uses two successive laser pulses that are polarized differently. A birefringent calcite crystal is placed in the optical path of the imaging system. Since tracer particles partially retain the polarization through scattering process, it is possible to displace the image between the two pulses. Inconveniences of this method have been identified in [10] and alternative techniques have been proposed which overcome these limitations. At present, many new development are made in this particular field of PIV. The new available electro-optical hardware opens every day new areas of investigation.

6. THREE DIMENSIONAL TECHNIQUES

6.1. Holographic techniques

Once PIV was well developed to provide two-dimensional flow fields, fluid dynamicists started asking for extensions to 3D. This move is common, to all velocity measurement techniques, whether it makes use of pressure probes, hot wire anemometers, or Laser Doppler Velocimeters. Holography can be considered as the 3D counterpart of photography. It is therefore quite normal to move towards the use of holograms. Looking at basic principles, holography presents many advantages but its implementation is still quite difficult. In the recent times, many papers have described different attempts. Usually, as described in [15] and [16], the photographic camera is replaced by a hologram. This allows the recording of tracer images illuminated in a volume. It also simplifies the problem of focusing since the hologram does not need any. After processing the hologram, the 3D flow field picture is reconstructed and the tracer images can be analysed using one of the techniques previously described. Some attempts at performing an optical analysis have been made with little success. Other approaches use methods similar to the previously described *hybrid techniques*. Another method is applying 3D particle tracking.

Also few applications of holography are reported, there is no doubt that this 3D technique will be further developed in the next future. The development of more powerful and cheaper pulsed laser certainly will help in this future move.

6.2. Stereoscopic methods and photogrammetry

Stereoscopic photography is almost as old as photography itself. Since PIV is a technique that made a large use of photographic techniques it is not surprising that advances have been made in the use of stereoscopic pairs. As shown in [17] two still cameras are used and produce two images of the same tracer particle field viewed through two different angles. Each picture is processed and the resulting data are further analysed to retrieve the third component. The latter corresponds to the transversal motion of tracers through the light sheet. The measurement of this transversal displacement can be made with quite a good accuracy as shown in [18]. The difficulty of this method is that the cameras must be set at an angle different than 90 degrees to the light sheet. Focusing becomes therefore difficult. A solution to this problem consists in using two cameras set perpendicular to the light sheet and located side by side. These cameras must have a very large field of view. The problem is then a small magnification. Nevertheless, providing these obstacles are solved, the stereoscopic method is a good 3D measurement technique. A stereoscopic arrangement is presented on figure 8.

An alternative to stereo techniques is the use of photogrammetry. In this method, two or three cameras (video or photographic) are set at right angle one to the other. Several images of the tracer field are obtained. The cross- processing of these leads to a kind of particle tracking. The 3D trajectory of the particles is determined from these multiple images. In most cases, this technique requires low tracer concentrations and is therefore only capable of low measurement densities.

7. FUTURE PERSPECTIVE

The present orientation of the evolution of PIV seems to be linked with current developments in computer and imaging hardware. Current video cameras have enhanced resolution. A capability of 1024 X 1024 pixels is common nowadays. Frame grabbers are also pursuing the same transformations and can digitize and store larger pictures in shorter times. Finally, PC computers or workstations are ever more performing with faster computational speed and larger memories. This is the reason why the fully digital technique seems to carry the present future of PIV. This method is also more user-friendly and this allows the access of this measurement technique to more and more scientists. Until recently, very few commercial systems were readily available. This is no longer the case and most companies already selling optical measuring systems and components such as LDV and lasers are now offering PIV systems including hardware and software. The PIV is also extending towards the measurement of 3 components of velocity. The silver process is not fully superseded by digital methods. It is a good complementary method for many particular flow situations.

In the field of velocity shift, further progress is to be expected. Dedicated photographic or video cameras including velocity bias hardware will soon be available.

The present processing speed of up to 100 velocity vectors per second open the way to the analysis of time dependent flows as shown in [19].

8. EXAMPLES OF APPLICATIONS

It is not the objective of these notes to present an exhaustive review of all published applications of PIV in the recent literature. However, it is interesting to briefly mention those experiments that demonstrate the potential and the advantages of this Whole Field Velocity measurement technique.

A first field in which several authors describe the use of PIV is that of **internal combustion engines**. A very complete investigation is reported in [20]. These authors made use of a Young's fringe technique with an LCD optical correlator for the fringe analysis. Their study concerns the flow around valves in a piston engine and as shown in figure 9 leads to interesting results. In the same field, an investigation of a 3D flow field is reported in [21]. Several investigations concerning **Industrial flows** are published. A study of coal flotation using Young's fringe method is described in [22]. The size of flow field under study is usually limited. The investigation of the flow around the blade of a **wind turbine** reported in [23] probably analyses the largest flow field studied with PIV. This is made possible by using large tracers. A example of results reprinted from this work is presented at figure 10. A study of waves is presented in [24]. In this investigation a comparison with LDV shows good agreement. For several decades, **turbulence** represents one of the most difficult challenges in fluid dynamics. Several investigations are under way in this field and the use of PIV gives access to spatial information otherwise not available. Low Reynolds numbers are investigated in [11] while larger Reynolds number pipe flows are studied in [25]. As shown in figure 11 and 12 these investigations lead to very spectacular results. The field of **combustion** is another domain in which PIV is extremely useful. The example shown in [26] of a study of pre-mixed turbulent flames is interesting. Like many other these authors make use of a YAG laser. PIV has become an essential tool in the field of **bio-engineering**. As an example a study of the flow in artificial heart valves is presented in [27]. Another example shown in [28] is the study of the flow in lung bifurcations in which different PIV and LDV techniques had been applied. Some results of this investigation are presented at figure 13. The technique of PIV has already been applied to **time dependent flows**. The example shown on figure 14 is extracted from [19] in which the unsteady flow past a pitching airfoil is investigated. Finally, the technique of PIV is used in the investigation of **rotating machinery**. An investigation of the flow field in a rotating pump is described in [9]. Figure 15 is extracted from this study. More recently, measurements have been performed in an axial compressor; this investigation is reported in [29].

9. CONCLUSIONS

The technique of Particle Image Velocimetry has been described. The basic principles of this Whole Field Velocimetry technique are presented and the different methods available to implement it are analysed. This relatively young measurement method is still following very quick developments and laboratories all over the world are busy improving it. Many of the future evolutions will be brought by the new developments of computer, image processing systems, image recording processes and lasers. However, whatever improvements, PIV will have, it will not replace other velocimetry techniques such as LDV. In practice, The method of PIV must be seen as a complementary measurement technique allowing other type of measurements. There is no doubt that the time resolution of a technique like LDV will never be superseded by PIV.

REFERENCES

[1] Meyers J.F.; and Komine, H. Doppler Global Velocimetry - A new way to look at Velocity, ASME 4th International Conference on Laser Anemometry, Advances and Applications, Cleveland, OH, USA, August 5-9, 1991.

[2] Dudderar T.D. and Simpkins P.G. Laser Speckle photography in a fluid medium. Nature, 1977 **270**, 45-47

[3] Meynart R. Instantaneous velocity field measurements in unsteady gas flow by speckle velocimetry. Appl. Optics , 1983, **22**, 535-540

[4] Meynart R. Mesure de champs de vitesse d'écoulements fluides par analyse de suites d'images obtenues par diffusion d'un feuillet lumineux. Phd Thesis, Univ. Libre de Bruxelles, October 1983.

[5] Adrian R.J. and Yao C.S. Development of pulsed laser velocimetry for measurement of fluid flow. Proc. 8th Symp. on Turbulence, eds. G. Patterson and J.L. Zakin, Univ. Missouri-Rola, 1983, 170-186

[6] Lourenco L.M., Velocity measurement by optical and digital processing of time exposed particle pairs, Bull. Amer. Phys. Soc., **29**, 1984, pp1531

[7] Gauthier V. and Riethmuller M.L. Application of PIDV to complex flows: Resolution of the directional ambiguity, in Particle Image Displacement Velocimetry VKI Lecture Series 1988-06 March 21-25 1988

[8] Particle Image Displacement Velocimetry VKI Lecture Series 1988-06 March 21-25 1988

[9] Paone N. Riethmuller M.L.and Vandenbraembussche R. Experimental investigation of the flow in the vaneless diffuser of a centifugal pump by Particle Image Displacement Velocimetry, Experiments in fluids **7**, 371-378 (1989)

[10] Lourenco L.M. Particle Image Velocimetry: Photographic and Video techniques, in Laser Velocimetry, VKI Lecture Series 1991-05 June 1991

[11] Westerweel J, Adrian R.J, Eggels J.G.M and Nieuwstadt F.T.M Measurements with Particle Image Velocimetry on fully developed turbulent pipe flow at low Reynolds number, in Sixth International Symposium on Applications of Laser Techniques to Fluid Mechanics and Workshop on Computers in Flow Measurements. Lisbon, Portugal 20-23 July 1992

[12] Lourenco L and Krothapalli K, Particle Image Velocimetry, Lecture notes in Engineering 45, Advances in Fluid Mechanics Measurements ed by M. Gad-el-Hak, Springer Verlag 1989

[13] Mørck T, Andersen P.E and Westergaard C.H. , Processing speed of photorefractive Optical correlators in PIV-Processing, in Sixth International Symposium on Applications of Laser Techniques to Fluid Mechanics and Workshop on Computers in Flow Measurements. Lisbon, Portugal 20-23 July 1992

[14] Vogt A, Raffel M and Kompenhans J, Comparison of Optical and Digital Evaluation of Photographic PIV Recordings, in Sixth International Symposium on Applications of Laser Techniques to Fluid Mechanics and Workshop on Computers in Flow Measurements. Lisbon, Portugal 20-23 July 1992

[15] Royer H. Contribution of Microholography to 3-D flow measurements, in Image Analysis as Measuring Technique In Flows EUROMECH Colloquium 279, 2-5 July 1991 University of Technology Delft, The Netherlands

[16] Stanislas M. et al , Particle detection criteria for automatic data reduction from micro-holograms. in Image Analysis as Measuring Technique In Flows EUROMECH Colloquium 279, 2-5 July 1991 University of Technology Delft, The Netherlands

[17] Gauthier V. and Riethmuller M.L. Application of PIDV to complex flows: Measurement of the third component, in Particle Image Displacement Velocimetry VKI Lecture Series 1988-06 March 21-25 1988

[18] Prasad A.K and Adrian R.J. Stereoscopic Particle Image Velocimetry applied to Liquid Flows. in Sixth International Symposium on Applications of Laser Techniques to Fluid Mechanics and Workshop on Computers in Flow Measurements. Lisbon, Portugal 20-23 July 1992

[19] Shih C., Lourenco L.M., Van Dommelen L. and Krothapalli A. Unsteady flow past an airfoil pitching at a constant rate, in Laser Velocimetry, VKI Lecture Series 1991-05 June 1991

[20] Lee J and Farrell P.V , Particle Image Velocimetry measurements of IC engine valve flows, in Sixth International Symposium on Applications of Laser Techniques to Fluid Mechanics and Workshop on Computers in Flow Measurements. Lisbon, Portugal 20-23 July 1992

[21] Trigui N et al, Fully automated three-dimensional Particle Image Velocimetry system applied to engine fluid mechanics research, in Optical Methods and Data Processing in Heat and Fluid Flow. The Institution of Mechanical Engineers. City Univesity London UK 2-3 April 1992

[22] Zachos A, Kaiser M and Merzkirch W, Application of Particle Image Velocimetry during froth flotation of hardcoal, in Sixth International Symposium on Applications of Laser Techniques to Fluid Mechanics and Workshop on Computers in Flow Measurements. Lisbon, Portugal 20-23 July 1992

[23] Smith G.H, Grant I. et al, A wind tunnel examination of vortices shed from a wind generator using Particle Image Velocimetry, in Sixth International Symposium on Applications of Laser Techniques to Fluid Mechanics and Workshop on Computers in Flow Measurements. Lisbon, Portugal 20-23 July 1992

[24] Zhan L.et al, An experimental study of drift velocity in progressive waves, in Sixth International Symposium on Applications of Laser Techniques to Fluid Mechanics and Workshop on Computers in Flow Measurements. Lisbon, Portugal 20-23 July 1992

[25] Adrian R.J and Offutt P.W, Investigation of turbulence structure using imaging methods, in Image Analysis as Measuring Technique In Flows EUROMECH

Colloquium 279, 2-5 July 1991 University of
Technology Delft, The Netherlands

[26] Armstrong N et al, PIV applied to premixed turbulent
flames, in Optical Methods and Data Processing in
Heat and Fluid Flow. The Institution of Mechanical
Engineers. City Univesity London UK 2-3 April 1992

[27] Lim W.L, Chew Y.T, Chew T.C and Low H.T,
Development of Particle Image Velocimetry for flow
field measurements pf prosthetic heart valves, in
Optical Methods and Data Processing in Heat and Fluid
Flow. The Institution of Mechanical Engineers. City
Univesity London UK 2-3 April 1992

[28] Corieri P, Benocci C., Paiva M. and Riethmuller M.L,
Numerical and experimental investigation of lung
bifurcation flows, in European Mechanics Colloquium
259, "Bio-Mechanical Transport Processes", Nato
workshop, Cargèse, Corsica (France) October 9-13,
1989

[29] Tisserant D. and Breugelmans F.A.E. Rotor blade to
blade measurement using Particle Image Velocimetry
Project Report PR 1993-21 von Karman Institute 1993
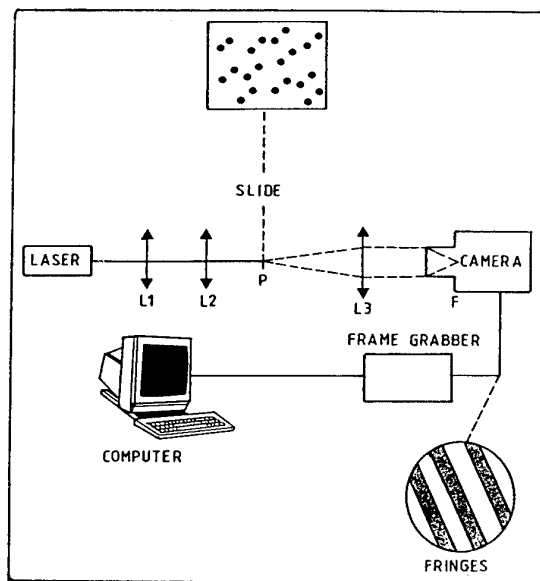
Fig. 3 Young's fringe method
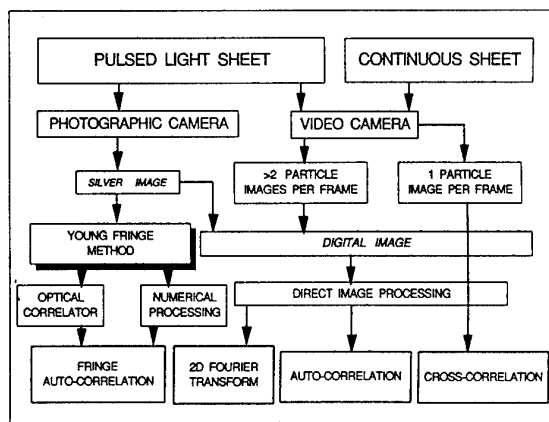
Fig. 1 Different techniques of PIV

Optical Image Processing System
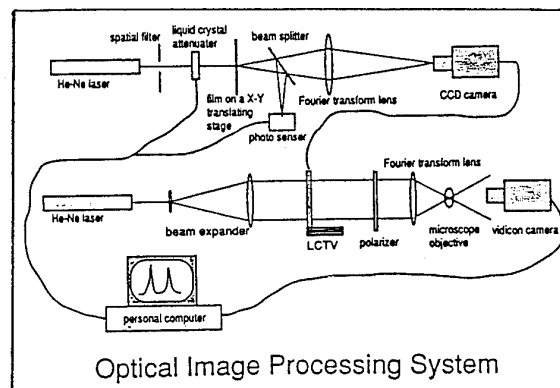
Fig. 4 Full optical processing of PIV pictures [14]
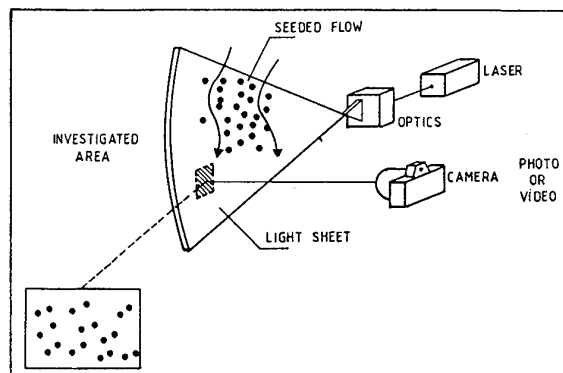
Fig. 2 Basic optical arrangement
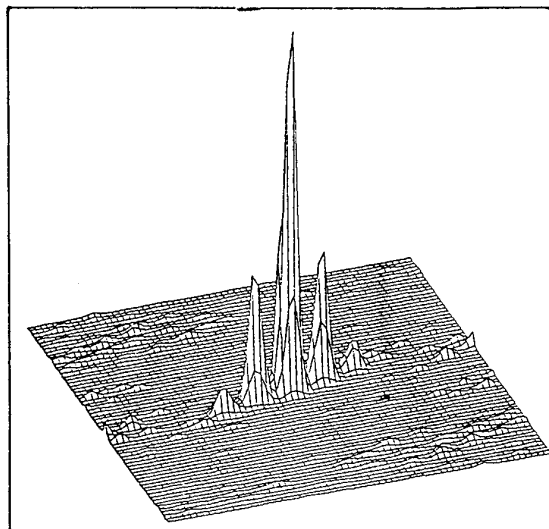
Fig. 5 Auto-correlation map [10]
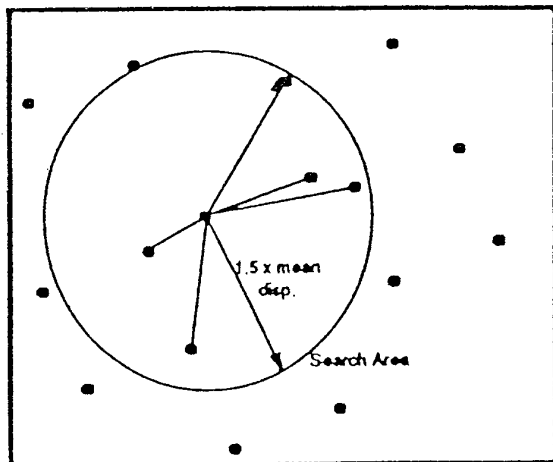
Fig. 6 Particle tracking procedure
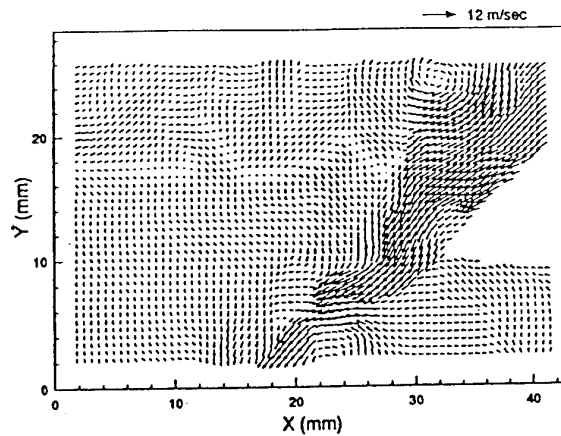
Fig. 9 Flow around valves in a piston engine [20]
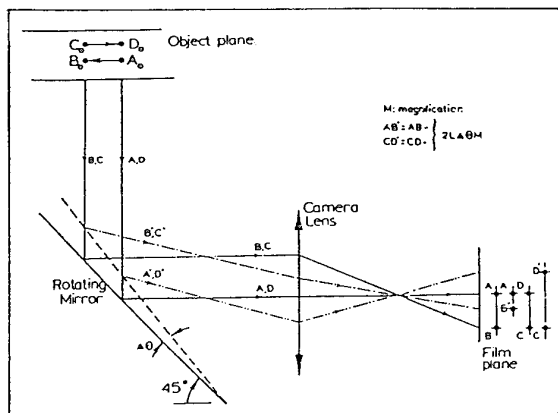
Fig. 7 Rotating mirror arrangement [10]
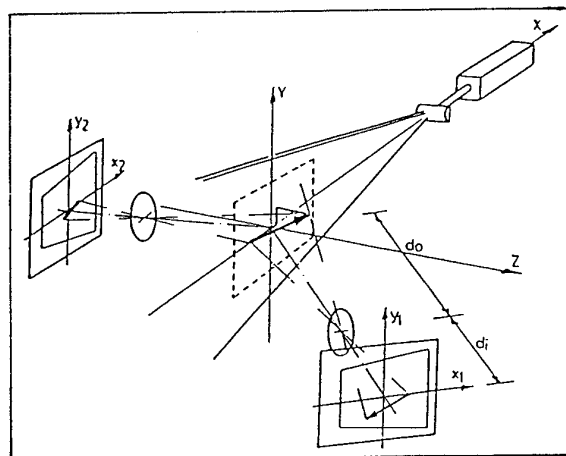
Fig. 8 Stereoscopic arrangement for 3D measurements [17]

Flow direction towards Head
Line length equivalent to 20 ms⁻¹
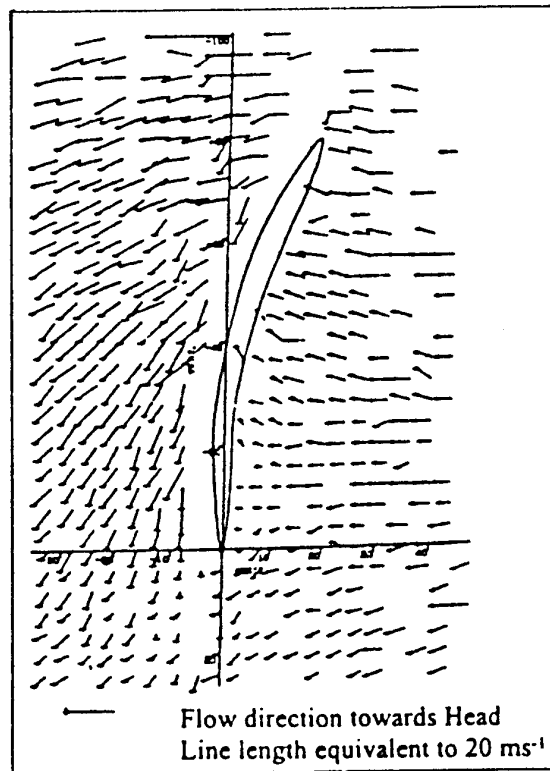
Fig. 10 Flow on the blade of a wind turbine [23]
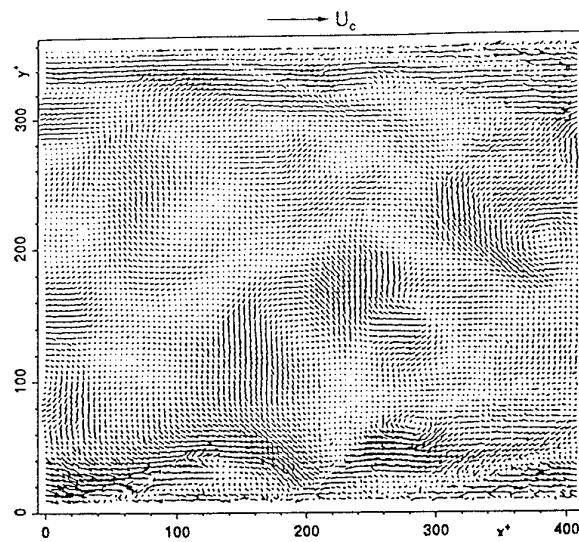
Fig. 11 Pipe flow - Fluctuating velocity [11]
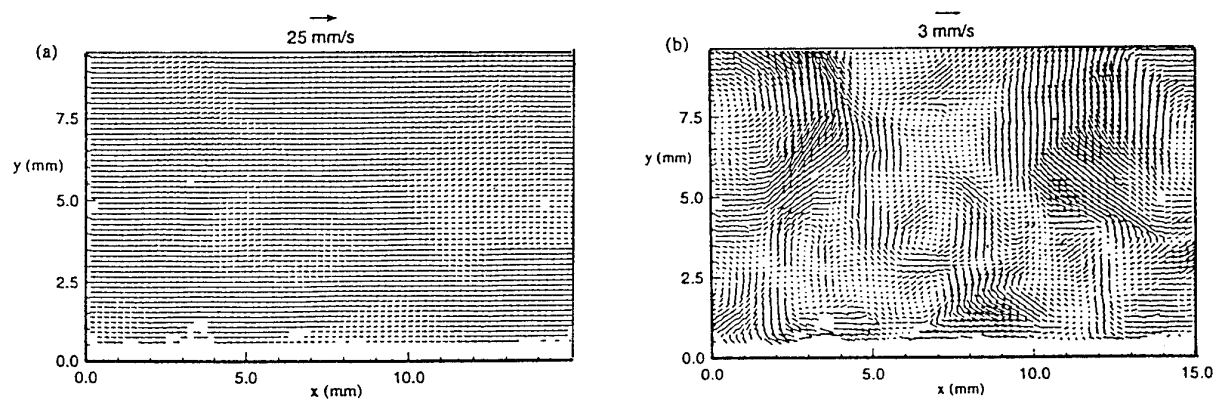
Fig. 12 Pipe flow - Absolute and fluctuating velocity [25]
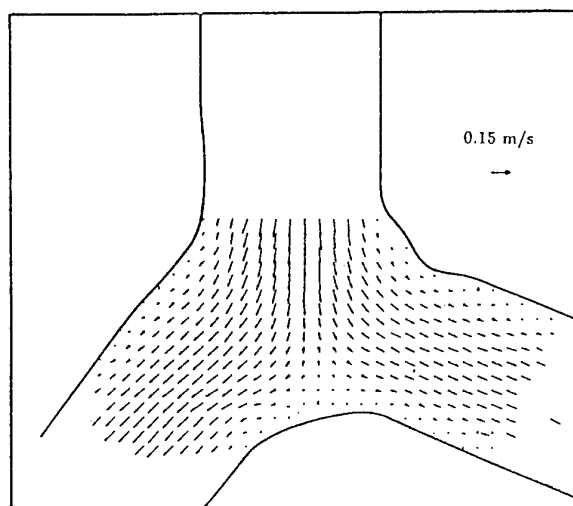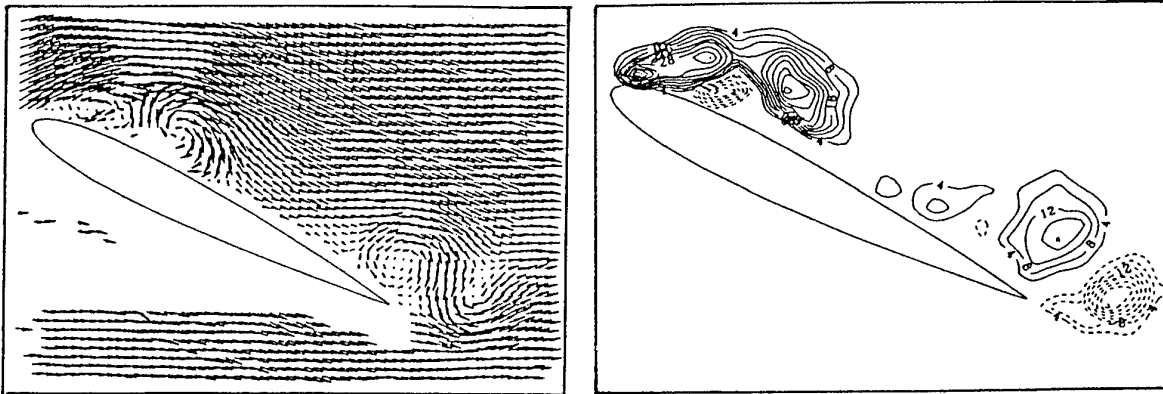

Fig. 13 Flow in a lung bifurcation [28]

Fig. 14 Flow past a pitching airfoil [19] Flow field and vorticity

Diffuser mid width
Maximum mass flow
300rpm
1mm   1m/e

-250 -150 -50 50 150 250
Ω (s^{-1}) ——►
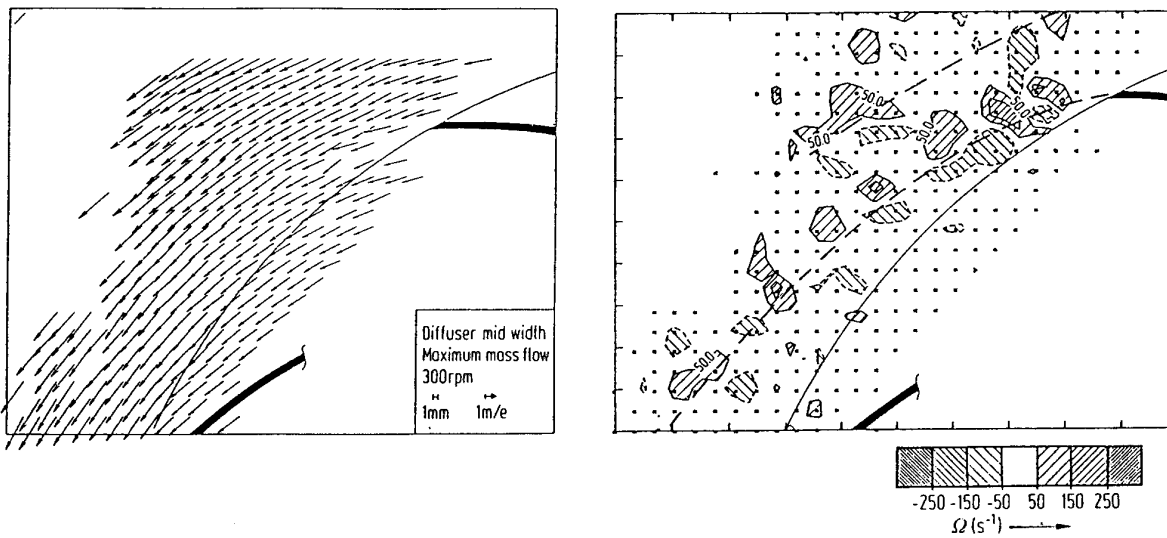
Fig. 15 Velocity field in the blade passage of a rotating pump [9]   Flow field and vorticity

Calibration and use of a non-nulling seven-hole pressure probe

M.C.G. Silva
D.X. Viegas
Grupo de Mecânica dos Fluidos, DEM-FCT
Universidade de Coimbra,
3000 Coimbra, PORTUGAL

SUMMARY
The calibration and the measuring methods associated with the use of a non-nulling seven-hole pressure probe are exposed. A detailed analysis of the error associated to the fitting process used in the calibration is presented. Some results related with the use of the probe for the determination of average local flow properties (incidence angles and dynamic pressure coefficient) in wind tunnel tests are presented.

LIST OF SYMBOLS

A	generic flow property
C_{din}	dynamic pressure coefficient
C_{α_T}	angle of attack coefficient (low angles)
C_{β_T}	angle of sideslip coefficient (low angles)
C_θ	coefficient of pitch (high angles)
C_φ	coefficient of roll (high angles)
m	total number of data points for a given sector
P	probe port pressure
V	velocity
α	angle of attack
α_T	angle of attack, tangential reference system
β	angle of sideslip
β_T	angle of sideslip, tangential reference system
θ	pitch angle, polar reference system
φ	roll angle, polar reference system
ψ	conjugated products of angular coefficients

Subscripts

i	i^{th} data point in a given sector
n	port or sector number (1-7)
n^+	adjacent port clockwise to port n
n^-	adjacent port counterclock wise to port n

1. INTRODUCTION
The directional pressure probes represent a powerful instrument in the study of the flow field around bodies. However, in the recent past, the utilization of this kind of sensors was offset by some factors related mainly with the time delay of the measuring procedures and with their restricted angular measuring fields.

The development of fast data acquisition and positioning systems and the appearance of non nulling pressure probes with large solid angles of sensivity contributed to the adoption of those sensors by different research teams.

In this paper, the results related with the calibration and the use of a seven-hole pressure probe are presented. This probe was built with the scope of studying the pressure, velocity and vorticity fields around models in wind tunnel tests.

2. CALIBRATION THEORY
The adopted geometry, as well as the general measurement method, are similar to those proposed by GALLINGTON [1]. However, some changes in the calculation process used during the calibration procedure have been introduced.

The probe was made of brass, with an external diameter in the cylindrical part of 5 mm and an internal diameter of the pressure holes of 1 mm. The opening angle of the cone is 60°. In figure 1 the port numbering convention and the system of axis associated with the probe are represented.

The measuring method of this type of non nulling pressure probes is based on analytical expressions, obtained during the calibration process, that allow the calculation of the flow properties as a function of the pressure values measured in the different ports.

Four flow properties are considered (two incidence angles, the dynamic pressure and the total pressure). The mentioned analytical expressions are fourth order polynomial expansions on two variables that relate each flow property with angular non dimensional coefficients calculated from the pressure values that were measured.
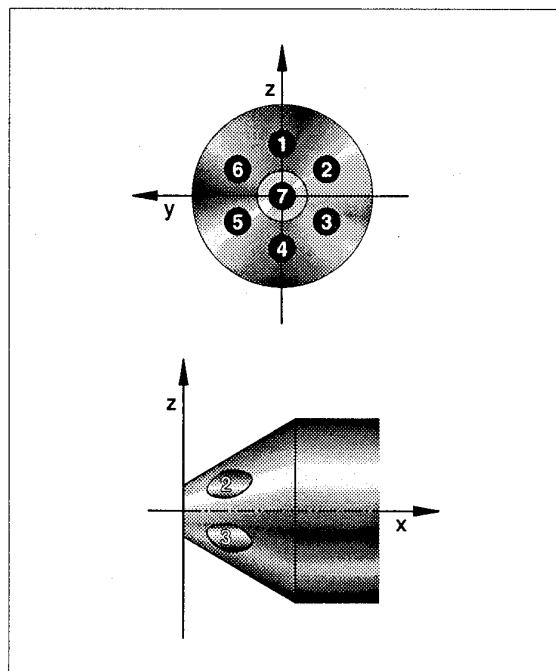

Fig. 1 - Schematic frontal and lateral views of the seven--hole probe. Actual external diameter is five millimeters.

Depending on the magnitude of the incidence flow angle, two different situations are considered. For low angles, with the maximal pressure value in the central port, a tangential reference system (fig. 2a) is used. In the case of high flow angles, that occur if the maximal pressure is measured in one of the peripherical ports, a polar reference system (fig. 2b), is more convenient.
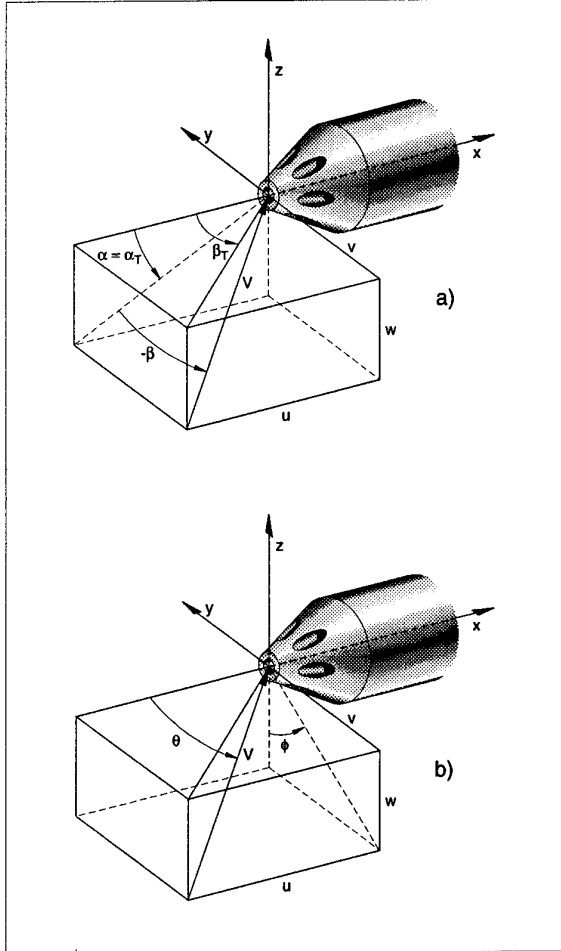

Fig. 2 - Reference system of the seven-hole probe: a) for low values of incidence flow angle; b) for high values of incidence flow angle.

The nondimensional pressure coefficients used in the analytical expressions depend, also, the flow angle. For low angles, coefficients $C_{\alpha T}$ and $C_{\beta T}$ are used. These are defined as:

$$C_{\alpha_T} = \frac{1}{3}\left(2C_{\alpha a} + C_{\alpha b} - C_{\alpha c}\right) \quad (1)$$

$$C_{\beta_T} = \frac{1}{\sqrt{3}}\left(C_{\alpha b} + C_{\alpha c}\right) \quad (2)$$

with

$$C_{\alpha a} = \frac{P_4 - P_1}{P_7 - \overline{P_{1-6}}} \quad (3)$$

$$C_{\alpha b} = \frac{P_3 - P_6}{P_7 - \overline{P_{1-6}}} \quad (4)$$

$$C_{\alpha c} = \frac{P_2 - P_5}{P_7 - \overline{P_{1-6}}} \quad (5)$$

In the case of high flow angles, the adequate coefficients are C_θ and C_φ, defined as:

$$C_\theta = \frac{P_n - P_7}{P_n - \left(P_{n^-} + P_{n^+}\right)/2} \quad (6)$$

$$C_\varphi = \frac{P_{n^-} - P_{n^+}}{P_n - \left(P_{n^-} + P_{n^+}\right)/2} \quad (7)$$

Mathematically, the calibration procedure consists, for each of the four flow properties in each of the seven sectors, on the calculation of the numerical constants of the analytical expressions that fit the space surface corresponding to the evolution of experimental data. Being A one of the four flow properties, in the situation of low flow angles, the analytical expressions take the following general form:

$$\begin{aligned}
A_i = \Big[& K_1^A + K_2^A C_{\alpha_T} + K_3^A C_{\beta_T} + K_4^A C^2_{\alpha_T} + \\
& + K_5^A C_{\alpha_T} C_{\beta_T} + K_6^A C^2_{\beta_T} + K_7^A C^3_{\alpha_T} + \\
& + K_8^A C^2_{\alpha_T} C_{\beta_T} + K_9^A C_{\alpha_T} C^2_{\beta_T} + K_{10}^A C^3_{\beta_T} + \\
& + K_{11}^A C^4_{\alpha_T} + K_{12}^A C^3_{\alpha_T} C_{\beta_T} + K_{13}^A C^2_{\alpha_T} C^2_{\beta_T} + \\
& + K_{14}^A C_{\alpha_T} C^2_{\beta_T} + K_{15}^A C^4_{\beta_T} \Big]_i
\end{aligned} \quad (8)$$

For high flow angles the expressions are similar, with C_θ and C_φ instead of $C_{\alpha T}$ and $C_{\beta T}$.

The method proposed by GALLINGTON [1] and by GERNER et al. [2] is performed according to a procedure outlined by NATTER and WASSERMAN [3] based on matrix algebra. In the present work, another solution is proposed, consisting in a different way of application of the least square method.

The equation 8, in condensed form, can be written as:

$$A_i = \left[\sum_{j=1}^{15} K_j^A \psi_j\left(C_{\alpha_{T_i}}, C_{\beta_{T_i}}\right) \right]_i \quad (9)$$

where the function ψ_j corresponds to the conjugated products of $C_{\alpha T}$ and $C_{\beta T}$. The mean quadratic error of the expression above, considering m measuring points, is:

$$E = \frac{1}{m}\sum_{i=1}^{m}\left[A_i - \left(\sum_{j=1}^{15} K_j \psi_j\left(C_{\alpha_{T_i}}, C_{\beta_{T_i}}\right)\right)\right]^2 \quad (10)$$

where the index i represents the number of the measuring point and the index j the order of the term in the polynomial expression. The minimum value of the mean quadratic error is found for:

$$\begin{aligned}
0 = \frac{dE}{dK_l} &= \frac{1}{m}\sum_{i=1}^{m}\left\{ 2\left[A_i - \left(\sum_{j=1}^{15} K_j^A \psi_j\left(C_{\alpha_{T_i}}, C_{\beta_{T_i}}\right)\right)\right] \times \right. \\
& \left. \times \left(-\psi_l\left(C_{\alpha_{T_i}}, C_{\beta_{T_i}}\right)\right)\right\} \\
&= \sum_{i=1}^{m} A_i\left(-\psi_l\left(C_{\alpha_{T_i}}, C_{\beta_{T_i}}\right)\right) + \\
& + \sum_{i=1}^{m}\sum_{j=1}^{15}\left[K_j^A \psi_j\left(C_{\alpha_{T_i}}, C_{\beta_{T_i}}\right)\psi_l\left(C_{\alpha_{T_i}}, C_{\beta_{T_i}}\right)\right]
\end{aligned} \quad (11)$$

with the derivatives taken in order to K_l, l varying from 1 to 15. That expression gives:

$$\sum_{j=1}^{15} K_j^A \left\{ \sum_{i=1}^{m} \left[\psi_j \left(C_{\alpha_{T_i}}, C_{\beta_{T_i}} \right) \psi_l \left(C_{\alpha_{T_i}}, C_{\beta_{T_i}} \right) \right] \right\} =$$

$$= \sum_{i=1}^{m} A_i \, \psi_l \left(C_{\alpha_{T_i}}, C_{\beta_{T_i}} \right) \qquad (12)$$

It is possible to write a system of equations, with one equation for each value of l, that in matricial form will come:

$$
\begin{bmatrix}
\sum_{i=1}^{m} 1 & \sum_{i=1}^{m} C_{\alpha_T} & \cdots & \sum_{i=1}^{m} C^4_{\beta_T} \\
\sum_{i=1}^{m} C_{\alpha_T} & \sum_{i=1}^{m} C^2_{\alpha_T} & \cdots & \sum_{i=1}^{m} C_{\alpha_T} C^4_{\beta_T} \\
\vdots & \vdots & \vdots & \vdots \\
\sum_{i=1}^{m} C^4_{\beta_T} & \sum_{i=1}^{m} C^4_{\beta_T} C_{\alpha_T} & \cdots & \sum_{i=1}^{m} C^8_{\beta_T}
\end{bmatrix}
=
$$

$$
=
\begin{bmatrix}
K_1^A \\
K_2^A \\
\vdots \\
K_{15}^A
\end{bmatrix}
=
\begin{bmatrix}
\sum_{i=1}^{m} A_i \\
\sum_{i=1}^{m} A_i \, C_{\alpha_T} \\
\vdots \\
\sum_{i=1}^{m} A_i \, C^4_{\beta_T}
\end{bmatrix}
\qquad (13)
$$

This system has 15 equations and 15 unknowns, whatever is the number of the m calibration points, and can be solved by one of the usual numerical methods.

3 - EXPERIMENTAL SET-UP

The calibration was performed imposing a flow with constant velocity and different known directions to the probe. A Dantec 55 D90 calibration unit was used to generate a very stable and low turbulence intensity circular jet. The seven pressure lines from the probe were connected to a Scanivalve system, the pressure being measured with an electrical Setra transducer. The voltage signal was acquired by a micro computer with an analogic-digital interface. The experimental set-up is presented in figure 3.
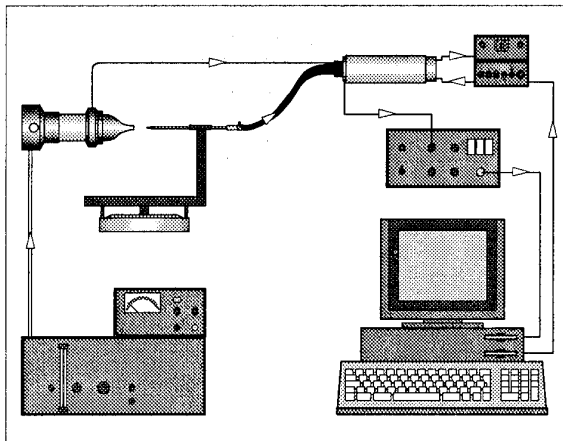
Fig. 3 - Experimental setup used in the seven-hole probe calibration.

In both situations, low and high flow angles, the two angular quantities were varied with increments of 10 degrees. For that, an angular positioning mechanism, with capacity to work in the two reference systems was built. This device is represented in figure 4 in both configurations, cartesian reference system (fig. 4a) and polar reference system (fig. 4b). The position of the probe apex was virtually unchanged in the process of rotating the probe and it was assured that the probe was always inside the potential core of the jet.
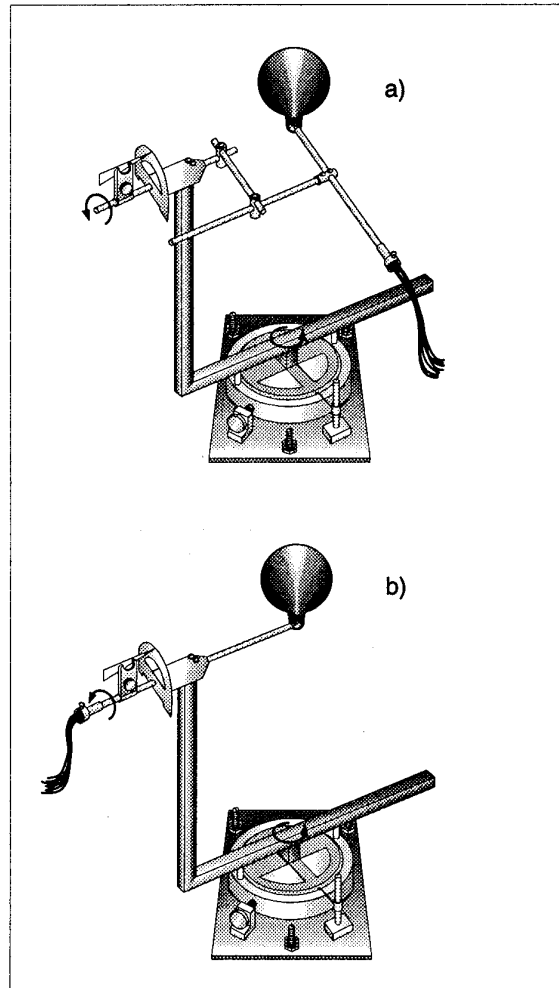

Fig. 4 - Angular positioning mechanism: a (low angles); b (high angles).

4. ERROR ANALYSIS

The analysis of the goodness of the fitting process, in the central sector, for three flow properties (α_T, β_T and C_{din}), is given in figure 5, where the values from the calibration process are compared with those corresponding to the representation of the polynomial functions that are obtained from the calculated values of the different constants. A similar representation for one of the peripheral sectors is shown in figure 6, the values of ϕ, θ and C_{din} being depicted.

For the central sector the results are clearly better than for the peripheral sector, where it seems that the fourth order polynomial function fitting process loses accuracy when there is a double curvature on the surface corresponding to the experimental data.
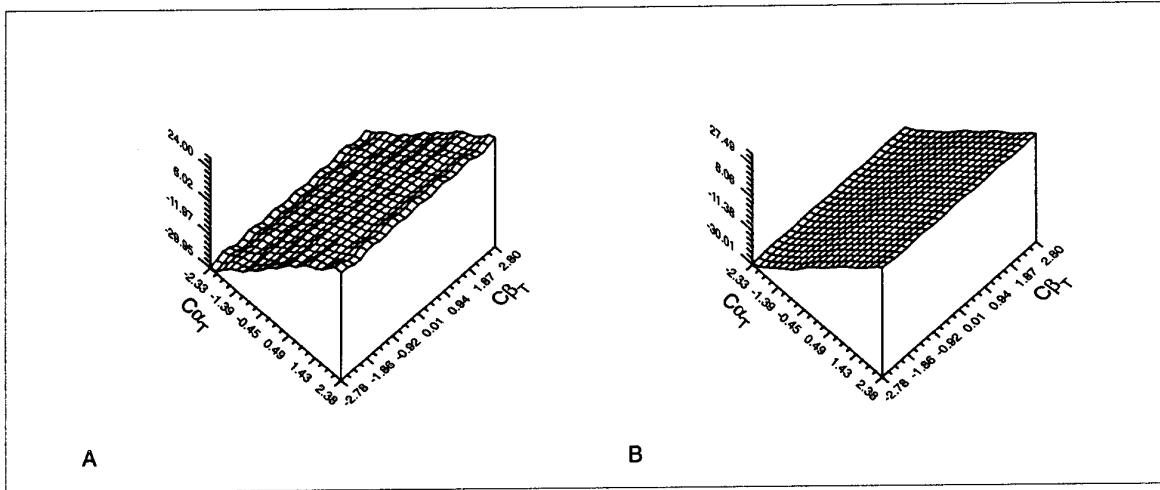
Fig. 5a - Evolution of the values of α_T, as function of the angular coefficients $C\alpha_T$ and $C\beta_T$, in the calibration process. A - experimental points. B - fitting surface.
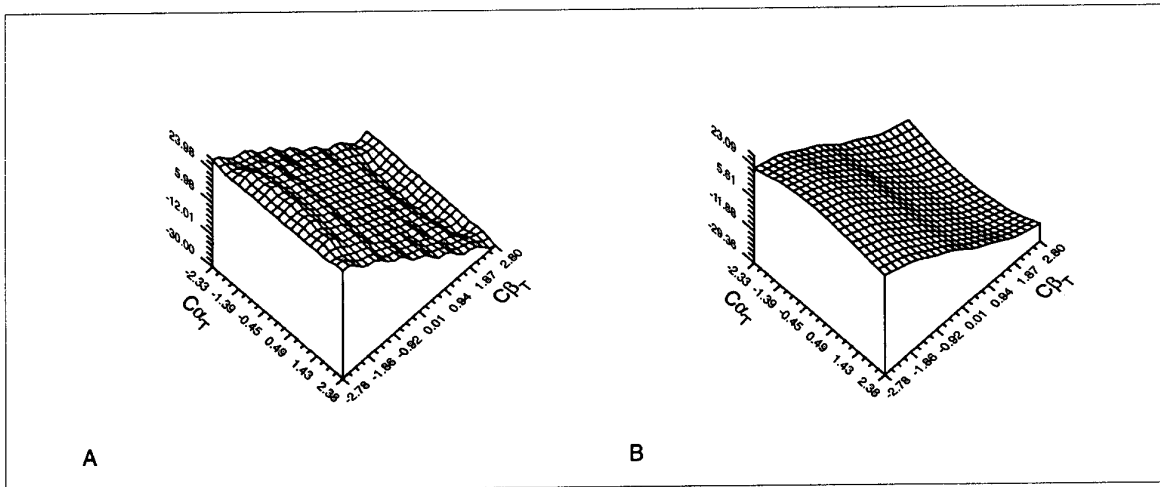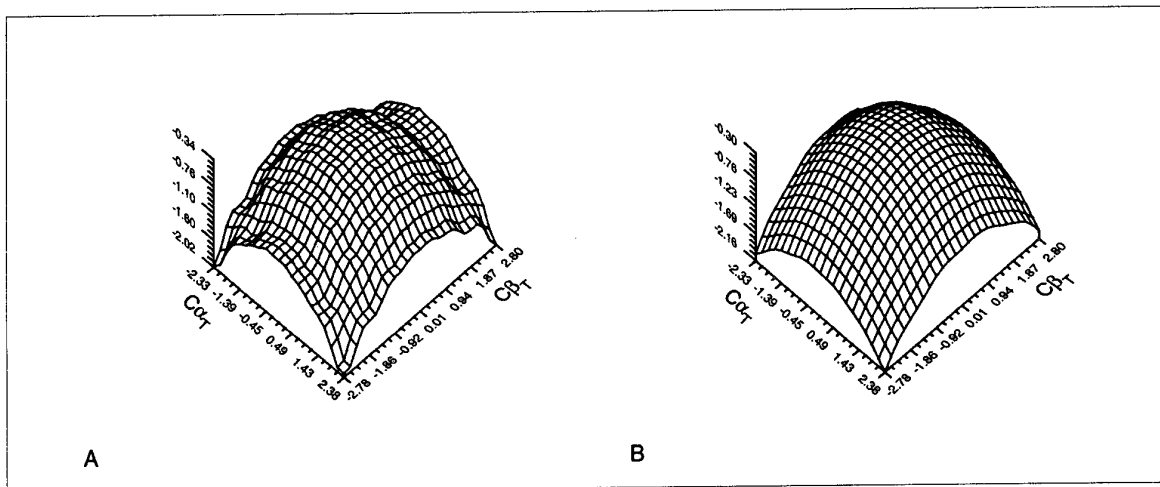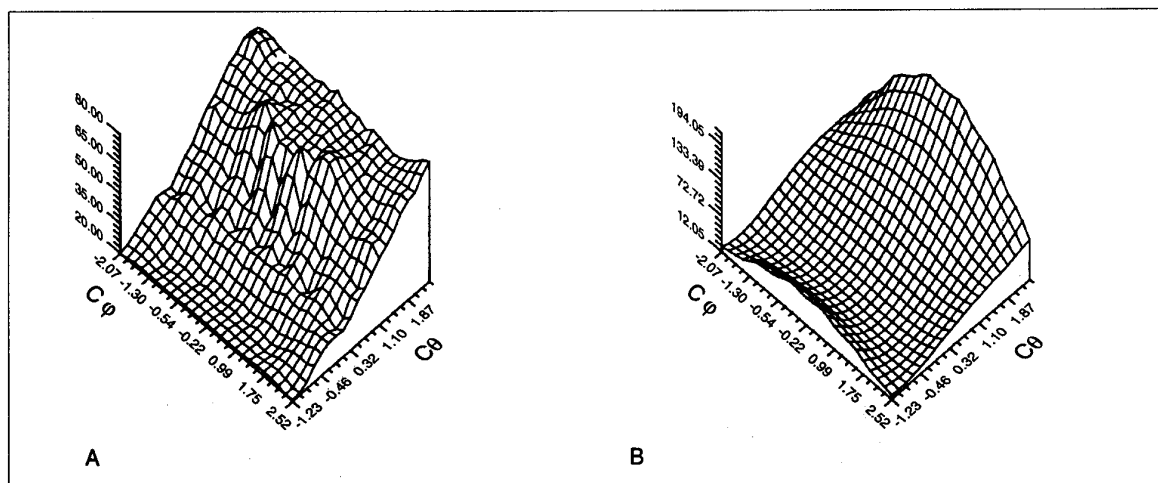

Fig. 5b - Evolution of the values of β_T, as function of the angular coefficients $C\alpha_T$ and $C\beta_T$, in the calibration process. A - experimental points. B - fitting surface.

Fig. 5c - Evolution of the dynamic pressure coefficient C_{din}, as function of the angular coefficients $C\alpha_T$ and $C\beta_T$, in the calibration process. A - experimental points. B - fitting surface.

Fig. 6a - Evolution of the value of angle θ, as function of the angular coefficients $C\varphi$ and $C\theta$, for the periphical sector nº6, in the probe calibration. A - experimental points. B - fitting surface.
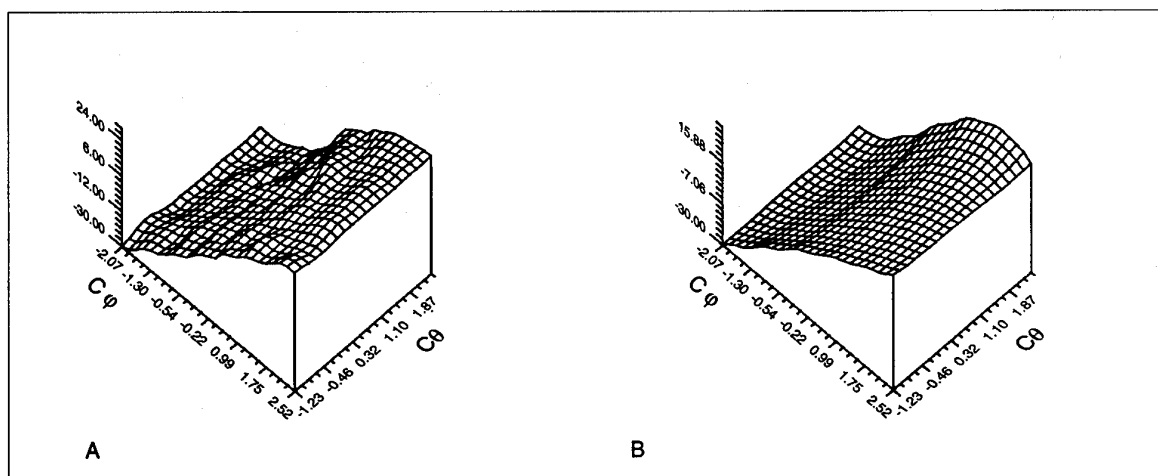
Fig. 6b - Evolution of the value of angle φ, as function of the angular coefficients $C\varphi$ and $C\theta$, for the periphical sector nº6, in the probe calibration. A - experimental points. B - fitting surface.
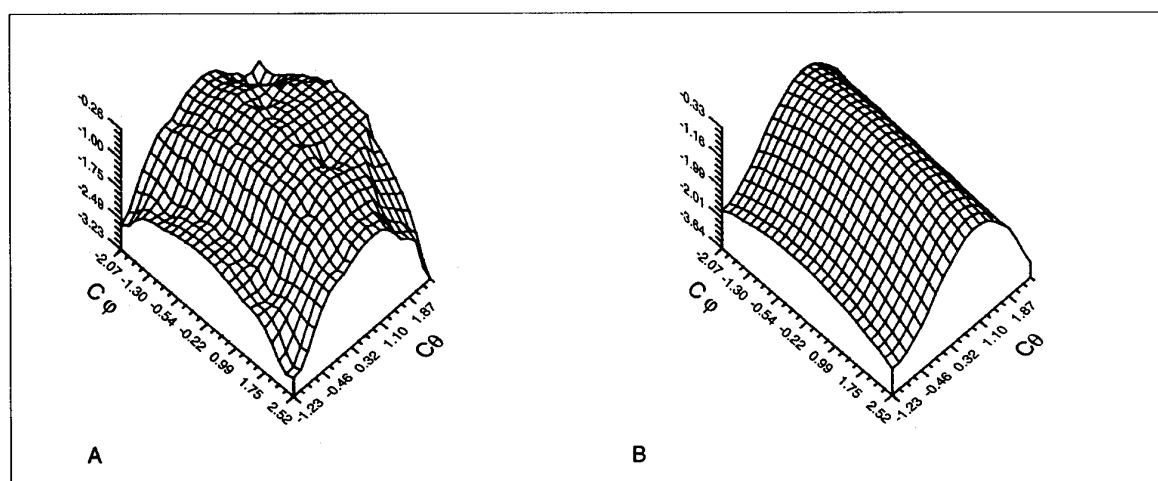
Fig. 6c - Evolution of the dynamic pressure coefficient C_{din}, as function of the angular coefficients $C\varphi$ and $C\theta$, for the periphical sector nº6, in the probe calibration. A - experimental points. B - fitting surface.

The quantification of the errors resulting from the calibration process has been done, using the following method: the values of the flow properties, that were imposed in the calibration, have been recalculated using the analytical expressions with the constants (K) determined previously and the pressure values measured in the probe during the calibration procedure. The isolines representing the absolute errors of the angular quantities and the relative error of the dynamic pressure coefficient, for the central sector and for one of the peripheral sectors, are plotted in figures 7 and 8, respectively.

The errors in the central sector are very low (typically less than 1 degree in αT and β_T and less than 1% in the dynamic pressure). In the peripheral sectors the errors are larger, as already mentioned, with maximum values of the order of 1.5 degrees for ϕ, 4 degrees for θ and 20% for the dynamic pressure, which represents an error inferior to 10% in the measurement of the velocity components.
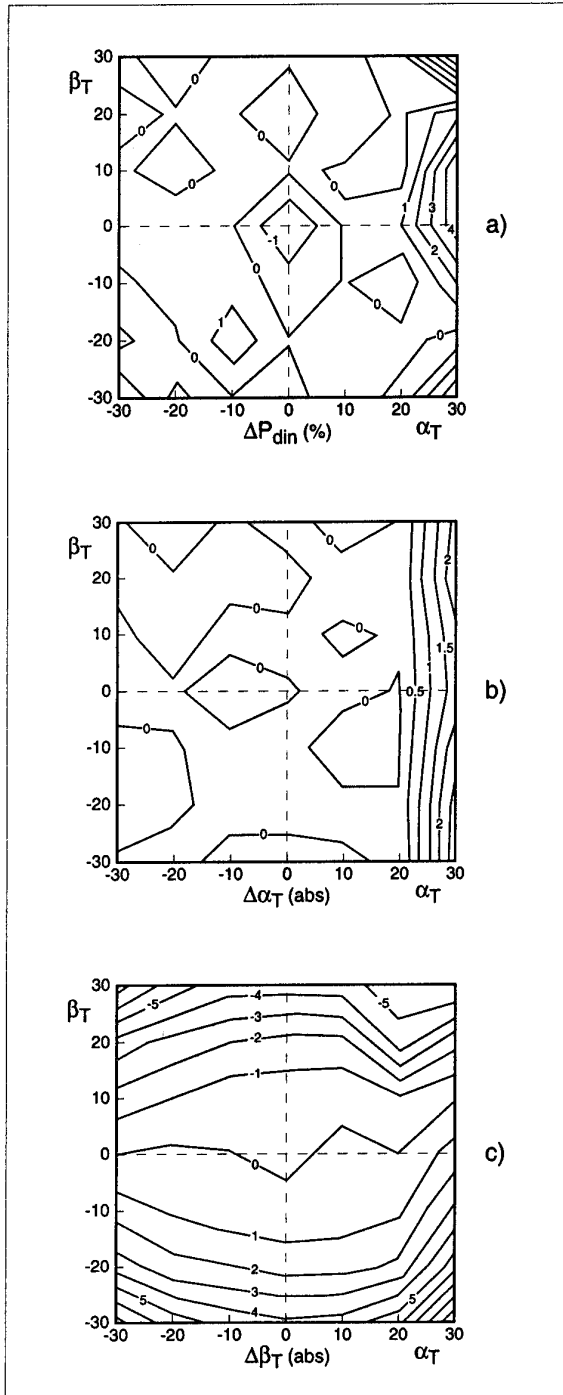
Fig. 7 - Errors introduced by the fiting process in the probe calibration, for the central sector, as function of angles α_T and β_T. a) Relative error of P_{din}. b) Absolute error of α_T. c) Absolute error of β_T.
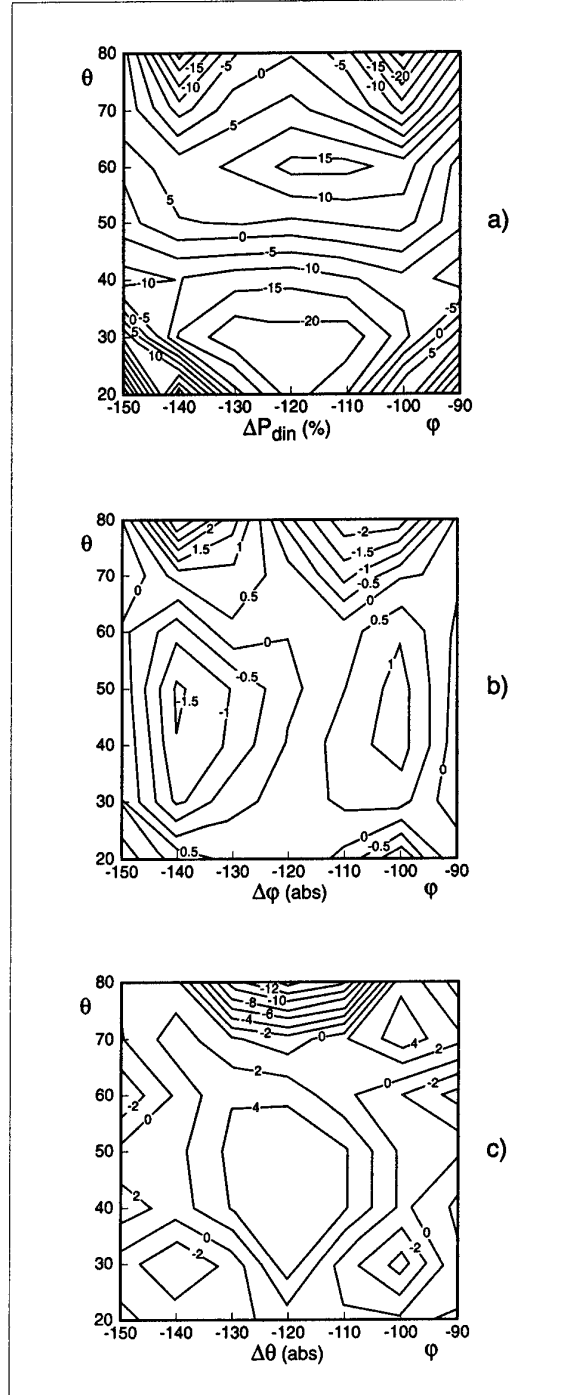
Fig. 8 - Errors introduced by the fiting process in the probe calibration, for the central sector, as function of angles φ and θ. a) Relative error of P_{din}. b) Absolute error of φ. c) Absolute error of θ.

5. EXPERIMENTAL RESULTS

Some typical results obtained with the seven-hole pressure probe concerning the study, in wind tunnel, of the flow field around a bus model are presented. A vectorial representation of the measured velocities in the mean longitudinal plane, just after the leading edge of the bus, is plotted on figure 9, while, in figure 10, the flow in a half model height plane in the near wake of the vehicle is represented.
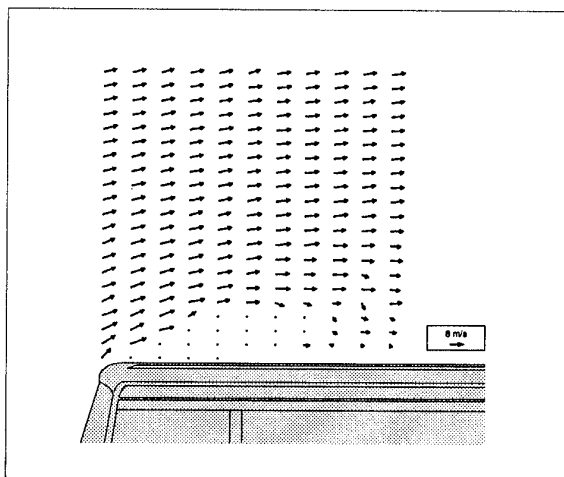

Fig. 9 - Vectorial representation of the flow velocity in the symetry vertical longitudinal plane, in the frontal zone of the vehicle.
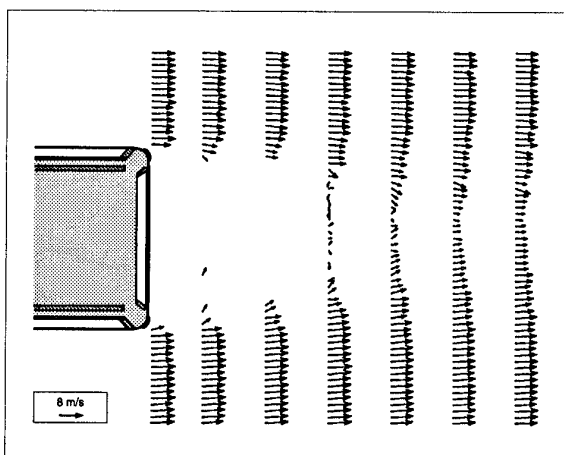
Fig. 10 - Vectorial representation of the velocity profiles in the wake of the vehicle, in a half model height horizontal plane.

6. CONCLUSIONS

A seven-hole pressure probe has been calibrated in order to be used in a non nulling measuring procedure. The method is similar to that proposed by Gallington, but has some modifications on the calculation of the constants in the calibration process.

In the error analysis it was found that the method works quite well for low incidence angles, presenting, however, a less satisfactory behaviour in the case of high incidence. A possible way to improve the accuracy is, probably, the use of a higher order fitting polynomial function, or, in alternative, the direct interpolation of the coefficients during the measuring procedure using the calibration

data. This second solution that is possible as a result of the large amount of data that nowadays, even a personal computer, can manage, could certainly improve the accuracy of the measurements performed with that kind of probes, implying, however, larger operation times.

In the near future in the evolution of the present work the study of the wall proximity and turbulence intensity effects on the probe behavior will be considered.

References

1. GALLINGTON, W.G. (1980) - Measurement of very large flow angles with non-nulling seven-hole probes. Aeronautics Digest, Spring/Summer 1980. USAFA-TR-80-17, USAF Academy, Colorado 80840, 60-88.

2. GERNER, A.A.; MAURER, C.L. and GALLINGTON (1984) - Non-nulling seven-hole probes for high angle flow measurement. Dept. of Aeronautics, US Air Force Academy, Colorado 80840, USA. Experiments in Fluids, 2,95-103.

3. NETTER, J.; WASSERMAN, W. (1975) - Simple linear regression model in matrix terms. Applied linear statistical models, pp. 200. Illinois: R.D. Irwin.

APPLICATIONS OF THE FIVE-HOLE PROBE TECHNIQUE FOR FLOW FIELD SURVEYS AT THE INSTITUTE FOR AEROSPACE RESEARCH

L.H. Ohman[1] and V.D. Nguyen
Institute for Aerospace Research
National Research Council
Ottawa, Ontario, K1A 0R6, Canada

SUMMARY

This paper deals with calibrations and uses of the five-hole probes for flow field survey. Two applications are given : one in transonic regime in the near slipstream of a powered propfan mounted on a half-model wing configuration and the other behind a generic submarine model at subsonic speeds. The acquired data have been analysed in terms of flow angles, total and dynamic pressures and Mach number and velocity vector in a probe fixed coordinate system. These parameters were necessary in determining the flow field characteristics of the studied configurations which are presented and discussed.

LIST OF SYMBOLS

First Application (Section 2.0)

AL	flow angle in the radial direction (see Fig. 4)
ALM	model and flow survey probe angle of attack
C_{pi}	pressure coefficient = $(p_i - p_\infty) / Q_\infty$, i=1,5
CP	power coefficient = power / $(Q_\infty n^3 D^5)$
D	propeller diameter, 15"
DPS	swirl angle, +ve anticlockwise looking downstream
F1	AL flow function = $(C_{p3} - C_{p1})/(C_{p5} - C_{pmin})$
F2	PS flow function = $(C_{p2} - C_{p4})/(C_{p5} - C_{pmin})$
FH	P0 flow function = $(C_{p0} - C_{p5})/(C_{p5} - C_{pmin})$
FQ	Q flow function = $C_{p5} - C_{pmin}$
FM	M flow function = $(C_{p5} - C_{pav})/(C_{p5} + 1/(0.7M_\infty^2))$
C_{pmin}	minimum of four peripheral pressures
C_{pav}	average of four peripheral pressures
M	local Mach number
M_∞	free stream Mach number
N	propeller rpm
n	propeller rps
p_i	local static pressure
p_∞	free stream static pressure
P0	local total pressure $(/p_{0\infty})$
$p_{0\infty}$	free stream total pressure
PHI	roll orientation angle of survey rake re vertical, +ve anti-clockwise looking downstream
PS	circumferential flow angle, +ve clockwise looking downstream (see Fig. 4)
Q	local dynamic pressure
Q_∞	free stream dynamic pressure

r	radial distance from propeller axis
R	propeller radius (=7.5")
rpm	revolution per minute
rps	revolution per second
Q_∞	free stream air density
	subscripts i=1,5 refer to the orifices of each probe (see Fig. 4)
	subscript min refers to the minimum value of C_{p1} to C_{p4}
	subscript av refers to the arithmetic mean of $C_{p1} + ... Cp4$

Second Application (Section 3.0)

ψ	wind tunnel turntable yaw angle
ϕ_p	rake roll angle (see Fig. 15)
θ	flow angle in the pitch-yaw plane (see Fig. 16)
ϕ	roll angle in the cross flow plane (see Fig. 16)
α	flow pitch angle in the plane of orifices one and three (see Fig. 16) = $\arctan(\tan\theta\cos\phi)$
β	flow yaw angle in the plane of orifices two and four (see Fig. 16) = $\arctan(\tan\theta\sin\phi)$
C_{pi}	pressure coefficient as previously defined
C_{pav}	average of four peripheral pressures
C_{pt}	local total pressure coefficient $(= C_{p5} + S_{cal}.P)$
Q	'beta' flow function = $(C_{p2} - C_{p4})/(C_{p5} - C_{pav})$
R	'alpha' flow function = $(C_{p3} - C_{p1})/(C_{p5} - C_{pav})$
P	dynamic pressure function = $C_{p5} - C_{pav}$
S	static pressure function = $(1- C_{p5})/(C_{p5} - C_{pav})$
S_{cal}	static pressure calibration function
P_{cal}	dynamic pressure calibration function
V_R	resultant flow velocity
V_T	wind tunnel velocity
u, v, w	local flow component
q, q_T	local and tunnel dynamic pressure
x	distance from model leading edge to a downstream measuring station
L	model total length (= 6m)

1. INTRODUCTION

The use of pressure probes for flow field investigations has been an accepted technique for many years in both wind tunnels and in flight tests, see for instance Bryer and Pankhurst (Ref. 1). In spite of the development of non-intrusive methods based on laser anemometry, the

---

convenience offered by the pressure probe technique makes it still widely accepted. In particular, the five-hole probe has become almost a standard tool since it provides data on both flow angles, total and dynamic pressures and velocity/Mach number.

The Institute for Aerospace Research (IAR, NRC) has over the years applied the five-hole probe technique to various investigations (Refs. 2, 3 and 4) and the present paper deals with two most recent applications. The five-hole probes employed in these applications were used in a fixed position or non-nulling mode and they were made differently with their distinct supports due to dissimilarity in model geometry and speed regime. This has necessitated separate calibrations of the probes in two different wind tunnels and independent interpolation and data reduction procedure was also established for each application. The following sections describe the calibration characteristics and data processing procedures, including a limited presentation of the flow field data.

2. APPLICATION IN TRANSONIC FLOW

The first application, which was part of a cooperative program between IAR and de Havilland Inc., concerned the acquisition and analysis of flow field data in the near slipstream of a de Havilland Inc 8-bladed airmotor powered propfan, nacelle mounted on a half-model wing configuration, Fig. 1 (Refs. 5 and 6). The use of the 5-hole probe technique for this type of flow field measurements seems to be an accepted technique (Refs. 7 to 10) and was the one adopted for the present investigation.

Three flow survey rakes, each with five 5-hole probes, were designed and built at the IAR (Fig. 2). The probe head had a diameter of 0.160" and was shaped in the form of a 4-sided pyramid with 90° included angle. The pressure ports had a diameter of 0.020" parallel to the probe axis.

The calibration of the flow survey rakes, an essential element of the investigation, was performed at the Lockheed Compressible Flow Wind Tunnel (CFWT), Marietta (Georgia, USA), at Mach numbers 0.6, 0.7, and 0.8 for pitch angles from -2° to 20° at every 15° roll angle setting. The pressure data were processed in the form of flow functions based on procedure developed at Lockheed as given below :

+ Flow Angle Function (pitch plane) :
$$F1 = (Cp_3 - Cp_1)/(Cp_5 - Cp_{min})$$

+Flow Angle Function (yawplane) :
$$F2 = (Cp_2 - Cp_4)/(Cp_5 - Cp_{min})$$

+Total Pressure Function :
$$FH = (Cp_0 - Cp_5)/(Cp_5 - Cp_{min})$$

+Dynamic Pressure Function :
$$FQ = (Cp_5 - Cp_{min})$$

+Mach Number Function :
$$FM = (Cp_5 - Cp_{av})/(Cp_5 + 1/0.7M^2)$$

The subscript numbers refer to the port number in the probe head (see Fig. 4), Cp_{min} is the minimum of Cp_1 to Cp_4 and Cp_{av} is the average of the sum of Cp_1 to Cp_4.

Two typical flow angle calibration maps for M=0.7 are presented in Fig. 3. Although both maps are quite regular and symmetric, the one for the outer probe (Probe 5) shows noticeable distortions, which can be attributed to the probe's proximity to the end of the probe support. Each line in the graphs represents a discrete value of the flow functions F1 and F2 from 0 to ±1 at intervals of 0.1.

For the use with the probes in flow field investigations, the calibration data were presented in the form of calibration matrices, five for each probe and Mach number. For each case, two of the matrices gave the two flow angles in degrees as function of F1 and F2 and the other three gave the functions FH, FQ and FM, again as functions of F1 and F2. The flow angles were given in a probe fixed coordinate system, see Fig. 4.

In the analysis of the flow field data, the first step was to compute the flow functions and determine the local Mach number. The other parameters such as flow angles, total and dynamic pressures were then determined by interpolation or extrapolation using corresponding flow function matrices for the three calibrated Mach numbers.

The propeller flow field survey was performed in the IAR 1.5m x 1.5m trisonic wind tunnel (Refs. 11 and 12), at Mach numbers 0.6 and 0.7 at a Reynolds number of about 7.5 million based on the 15 inch propeller diameter.

The blade angle at 75% radius was set at 52°. Two of the rakes were mounted diametrically opposite on the nacelle with the probe heads 1 inch (0.067 diameter) aft the propeller plane, giving a ¼ inch clearance to the blade trailing edges. In order to obtain a complete survey, data were acquired with the angular orientation of the rakes set at 30° intervals. The propeller rpm and model angle of attack were varied moderately at each Mach number.

The acquired data have been analysed with respect to flow angles, total pressure and Mach number. The data here discussed apply to tests at M=0.6 and a propeller rpm of 10,200 corresponding to an advance ratio of 3.048. In Fig. 5, the radial flow angle has been plotted for both the horizontal and vertical plane for the cases with and without propeller at a model incidence of 1.5°.

The figure shows that there is hardly any difference between the two cases, which implies that the radial outflow is dominated by the nacelle geometry and virtually unaffected by the propeller action.

The distribution of the circumferential flow angle and the propeller induced swirl angle, the latter defined as the difference in circumferential flow angle between the cases without and with propeller, is very non-uniform, as demonstrated in Figs. 6 and 7. Figure 6 shows the circumferential flow angle in both the horizontal and vertical plane with and without propeller. The difference between the upstroke and downstroke sides is quite pronounced. In Fig. 7, the swirl angle is plotted versus model incidence for three radial positions. The figure shows how the swirl angle decreases with incidence on the upstroke side and increases on the downstroke side with increasing incidence. This non-uniformity can primarily be attributed to the wing lift induced upwash. On the upstroke side, the effective propeller blade incidence is decreased while on the downstroke side the incidence is increased due to the upwash. A colour graphic presentation of the swirl angle given in Fig. 8 further emphasizes the non-uniformity, which has serious implications for the blade loading pattern.

Figure 9, not surprisingly, is very similar in character to that of Fig. 8 and it shows how the total pressure decreases with model incidence on the upstroke side and increases on the downstroke side. In fact, both Figs. 8 and 9 show that for a model incidence of about 2° and higher, the inner parts of the propeller blades generate negative swirl and loss in total pressure on the upstroke side, suggesting separated flow.

The difference in local Mach number between the propeller on and off cases was small, generally less than 0.03.

The flow survey has thus revealed that the blade loading can be quite non-uniform over a revolution, particularly at higher angle of attack. This oscillatory load would have to be taken into account when assessing the fatigue life of the blades. Although the propeller plane was located about one propfan diameter ahead of the wing leading edge, it is clear that the effect of the wing induced upwash was still significant at this distance.

During analysis of the power coefficient data, it was discovered that the value of the power coefficient derived from the motor power was sensitive to the angular orientation of the rakes. Furthermore, a comparison of power coefficient values for cases with and without the rakes showed that the power requirement with the rakes was considerably higher than without the rakes for the same rpm, Fig. 10. This raises the possibility that the rakes may have significant interference effects on the quantities they measure.

A follow-up investigation to determine the degree of interference was subsequently carried out on a separate propeller test rig furnished by de Havilland, with electric drive but using the same propeller and spinner-nacelle geometry, Fig. 11, as in the half-model investigation. Measurements were performed at M=0.7 and 0° angle of attack with the two rakes in the horizontal plane and also with a single 5-hole probe mounted at the same position as the most inner rake probe of one of the rakes, see Fig. 11. The single probe was considered to be virtually non-intrusive.

The swirl angle as measured by the single probe and the corresponding rake probe for a range of rpm:s are compared in Fig. 12. It shows that with the single probe, the swirl angle is 0.3° to 0.5° less than with the rakes present. The power coefficient values are also consistently lower with the single probe, Fig. 12. Although the single probe was, hopefully, considered to be interference free, the data in Fig. 12 show that there is still some residual interference, since the power coefficient values for the "clean" case, when no probes are present, are slightly lower than for the single probe case.

It is of interest to note that the probe interference effect that was found on the swirl angle in this investigation is in contrast to data presented in References 9 and 10. In Reference 9, Kooi and de Wolf reported on a low speed investigation in which flow data were acquired in the near slipstream of a 6-bladed isolated propeller, using both rakes with 5-hole probes and non-intrusive laser technique. They found that the swirl angles as measured by the 5-hole probes were consistently less than that measured by the laser technique. Similar findings were reported by Coe, Gentry and Dunham in Reference 10, from an investigation of an 8-bladed propeller. No explanation is offered in either of the references for the difference in results between the two techniques.

Why the referenced low speed investigations showed a probe-rake interference effect of opposite sign to that of the present high speed investigation is difficult to explain, unless it can be attributed to the difference in speed regime. It may be noted that the swirl angle and power coefficient data for the present investigation corroborate each other, in that a larger swirl angle is accompanied by a higher power coefficient. Had it not been for the simultaneous measurements of the power, there would have been no obvious reason to suspect that the survey rake data were subject to the degree of interference found in this investigation. Clearly great care has to be exercised in the use of 5-hole probe survey rakes for investigating swirling flow.

3. APPLICATION IN SUBSONIC FLOW

The second application of the 5-hole probe technique dealt with an extensive flow survey conducted along and immediately behind a generic submarine model in the IAR V/STOL 9m Wind Tunnel. The project was part of a research program undertaken by the Defence Research Establishment Atlantic (DREA) to develop the capability of evaluating submarine maneuvering and dynamic stability characteristics (Refs. 13 and 14).

The present investigation focussed on the shedding of complex vortex sheet formations and their associated velocity fields corresponding to the various model attitudes and configurations of the test program. The method of investigation employed the application of a visualizing medium to the surface of the hull for the purpose of observing the wall streamline pattern (which is not discussed in this paper), and the use of an array of five-hole probes in order to map the velocity field produced by the hull and the sail vortices.

The flow survey rig consisted of a 10 foot diameter annular track supported by a tubular structure (Fig. 13). This structure was fastened at its base to two longitudinal tracks on the wind tunnel floor turntable and this allowed measurements at axial locations along and aft of the model while maintaining the body-axis alignment of the survey rig and model during yaw sweeps. Two remotely controlled motorized carriages, each supporting a radial rake of eleven equally spaced five-hole probes, could be driven independently around the annular track. By radially staggering the two rakes, the radial spacing of the measurement grid could be adjusted. Details of a probe are given in Fig. 14.

The 22 five-hole probes were calibrated on the flow survey rig in the empty tunnel, i.e. with the model removed. The ring assembly was yawed through an angular range of 0° to 45° with 5° increments and the two rakes were rotated around the azimuth between 0° and 360° with 10° increments.

Figure 15 shows top and side view schematics of the flow traverse assembly and its relationship to the model and tunnel axes. The flow angles and velocities determined at a measurement point in the traverse plane swept by the rakes are shown in Fig. 16.

The important probe pressure functions, derived from the orifice pressure coefficients C_{pi} as defined in List of Symbols, are similar to those used in the previous application except a static pressure function was preferred allowing local total pressure coefficient to be computed (see Ref. 3) :

+Flow Angle Function (pitch plane) :
$$R = (Cp_3 - Cp_1)/(Cp_5 - Cp_{av})$$

+Flow Angle Function (yaw plane) :
$$Q = (Cp_2 - Cp_4)/(Cp_5 - Cp_{av})$$

+Dynamic Pressure Function :
$$P = (Cp_5 - Cp_{av})$$
+Static Pressure Function :
$$S = (1 - Cp_5)/(Cp_5 - Cp_{av})$$

The turntable yaw and rake roll angles, ψ and ϕ_p , are functions of the angle between the resultant velocity vector angle θ and the roll angle ϕ of the resultant velocity vector component in a plane normal to the probe axis. Since the last two are in turn functions of the flow pitch and yaw angles, α and β (see Fig. 16), calibrations resulted in a set of six parameters : α , β , P , S , Q and R.

A calibration software package was written by de Souza (Ref. 15) which uses two-dimensional surface spline smoothing to generate four calibration surfaces from calibration data. The program first calculates the pitch and yaw angles α and β (see expressions in List of Symbols) and then interpolates four user-selected parameters, in this case α , β , P and S, on a rectangular grid in the Q-R plane. The grid interpolation of all four parameters is performed and prepares the data to be smoothed using two-dimensional tensor product splines. The smoothed spline representations, $\alpha(Q,R)$, $\beta(Q,R)$, $P(Q,R)$ and $S(Q,R)$, are saved in appropriately named data files. Typical calibration maps of these functions are shown in Figs 17a to 17d.

Once the five pressure coefficients in an unknown flow have been determined, these four calibration functions can be used to calculate the pitch and roll angles (α and β) of the flow, as well as the longitudinal, yaw plane and pitch plane velocity components u, v and w and the local total pressure coefficient Cp_t (Ref. 15) :

$$q/q_T = P/Pcal$$
$$V_R/V_T = (q/q_T)^{1/2}$$
$$u = V_R\cos\theta$$
$$v = V_R\sin\theta\sin\phi$$
$$w = V_R\sin\theta\cos\phi$$
$$Cp_t = Cp_5 + S_{cal}.P$$

The test program for the wake survey consisted of three axial locations along the hull (x/L = 0.488, 0.722 and 0.957) for both the isolated hull (called also 'barehull') and the complete model including sail and tailfins (called 'full configuration'). The model was yawed to angles of 0, 10, 20 and 30 degrees in positive (starboard) and negative (port) directions. The individual probes were spaced at intervals of 0.22 hull diameter on each rake, with radial adjusment to half this interval. The angular interval of the rakes was 12 degrees. Maximum wind tunnel velocity was chosen to yield Reynolds number of about 22 million based on model length.

The flow parameters furnished by the probe data

reduction process are : circumferential and radial flow angles (relative to a model body-axis system), local dynamic pressure and local total pressure. Reduced data are presented in the form of velocity vector diagrams of resultant velocities in crossflow planes of the hull and color isocontours of dynamic and total pressures.

Typical velocity vector plot in the body-axis (z-y) plane are illustrated in Figs. 18 to 20. For the barehull case, Fig. 18 clearly depicts the windward side stagnation point as well as the separation points on the upper and lower portions of the body. The two distinct regions of rotational flow in the wake on the lee side represent the local imprint of a growing vortex pair developing along the length of the body. With the sail mounted in the vertical position, significant changes were observed on the top side and lee of the hull when the model was yawed. Figures 19 and 20 show velocity vector maps of the vortex flow in the wake at axial locations x/L=0.488 and 0.957. The effect of the sail, particularly at high angles of yaw, produces a strong region of rotating flow from the sail tip immediately behind the trailing edge (x/L=0.488) which has modified the body vortex pattern (Fig. 19). At the rearmost position in the propeller plane (x/L=0.957, Fig. 20), the vortex shed from the sail has moved further leeward as it convects downstream with the general flow and the body vortex has also moved outwards.A vortex system produced by the tail appendages can also be clearly identified.

Figures 21 and 22 show the colour graphic presentation of the total pressure isocontours at the rearmost plane for the barehull and the full configuration yawed at 30 degrees. The pictures confirm the remarks cited above concerning the vortex formations which were depicted in both cases.

A sample of the dynamic pressure maps is given in Fig. 23 for the full model yawed at 20°. The dynamic pressure contours show not only the vortex pattern, but also a significant region of blockage due to the supporting strut aft of the model and due to the model itself when yaw to high angles. The strut blockage effect moved to windward as the yaw angle increases and the model moved out of the way. At the highest angles of yaw, a region of low dynamic pressure surrounded the sail tip vortex and a region of high dynamic pressure, possibly from the lower body vortex separation, existed several body diameters to leeward.

4. CONCLUDING REMARKS

This paper has presented some of the features of two flow field surveys that were conducted at the Institute for Aeropsace Research (IAR, NRC) in which the five-hole probe technique has been applied. The first survey concerned a flow field investigation in the near slipstream of an eight-bladed propfan mounted on a de Havilland half-model and tested at Mach numbers of

0.6 and 0.7 while the second flow field measurement took place at subsonic speeds along and aft a generic submarine model.

It was found in the first application that the radial flow angles were primarily dominated by the nacelle geometry. The distribution of the circumferential flow angle and the propeller induced swirl angle was very non-uniform and attributable to the effect of wing lift induced upwash. The total pressure distribution was similar to that of the swirl angle. A comparison of the power coefficient values for the cases with and without the survey rakes showed that the power requirement was significantly higher than without the rakes. Swirl angle data from a single less-intrusive 5-hole probe on an isolated propeller test rig corroborated the power observation in that the swirl measured by the single probe was less than that measured by the corresponding rake probe.

In the second application, the velocity vector fields and dynamic and total pressure contours in crossflow planes have made visible the formation of leeside vortices shed from the hull. The presence of the sail resulted in a strong vortex shed from the sail tip and located along the tunnel wind vector. This vortex appeared to displace the lower hull vortex at high angles of yaw. Vortices from the tips of the vertical tail fins were also visible. The dynamic pressure contours highlighted a significant flow retardation on the windward side of the tunnel flow which was induced by the presence of the model support strut.

ACKNOWLEDGEMENT

REFERENCES

[1] Bryer D.W., Pankhurst R.C.,"Pressure Probe Methods for Determining Wind Speed and Flow Direction", National Physical Laboratory, HMSO, 1971

[2] Wickens R.H., South P., Rangi R.S., Henshaw D., "Experimental Developments in V/STOL Wind Tunnel Testing at the National Aeronautical Establishment", J. of CASI, Vol. 19, No. 4, April 1973

[3] Wickens R.H., Williams C.D., "Calibration and Use of Five-Hole Flow Direction Probes for Low Speed Wind Tunnel Applications NRC",

4-6

Aeronautical Note NAE-AN-29, NRC, July 1985

[4] Schaub V.W., Sharp C.R., Bassett R.W., "An
     Investigation of the Three-Dimensional Flow
     Characteristics of a Non-Nulling Five-Tube
     Probe", Aeronautical Report LR-393, NRC,
     February 1964

[5] Nguyen V.D., Ohman L.H., Poole R.J.D., "Wind
     Tunnel Investigation of Propfan Slipstream/Wing
     Interactions on a de Havilland Airmotor Powered
     Semispan Model at Mach Numbers 0.6 and 0.7",
     4th CASI Aerodynamics Symposium, Toronto,
     May 3-4 1993

[6] Ohman L.H., Poole R.J.D., Nguyen V.D., Beenen
     J., "Flow Field Investigation in the Near
     Slipstream of an 8-Bladed Propfan on the de
     Havilland WTEJ Half-Model at Mach Numbers
     0.6 and 0.7", 4th CASI Aerodynamics
     Symposium, Toronto, May 3-4 1993

[7] Aljabri A.S., "Measurements and Prediction of
     Propeller Flow Field on the PTA Aircraft at
     Speeds of Up to Mach 0.85", AIAA-88-0667,
     January 1988

[8] van den Borne P.C.M., van Hengst J.,
     "Investigation of Propeller Slipstream Effects on
     the Fokker 50 Through In-Flight Pressure
     Measurements", AIAA-90-3064, August 1990

[9] Kooi J.W., de Wolf W.B., "Aerodynamic
     Measurements on a 1/5 Scale Model of the
     Fokker 50 Propeller and Comparison with
     Theoretical Predictions", International Conference
     Proceedings on Advanced Propellers and Their
     Installation on Aircraft, Royal Aeronautical
     Society, September 1988

[10] Coe P.L.Jr., Gentry C.L., Dunham D.M., "Low
     Speed Wind Tunnel Tests of an Advanced Eight-
     Bladed Propeller", NASA-TM-86364, July 1985

[11] Brown D., "Information for Users of the National
     Research Council's 5FT x 5FT Blowdown Wind
     Tunnel at the National Aeronautical
     Establishment", NRC/NAE-LTR-HA-06, Sept.
     1973

[12] Ohman L.H. et al., "New Transonic Test Sections
     for the NAE 5FT x 5FT Trisonic Wind Tunnel"
     NRC/NAE Aeronautical Note AN-62, January
     1990

[13] Watt G.D., Tanguay B., Cooper K.R.,
     "Submarine Hydrodynamics in the Wind Tunnel",
     RINA Warship '91 International Symposium on
     Naval Submarines, Vol. 2, London, May 1991

[14] Watt G.D., Nguyen V.D., Cooper K.R., Tanguay
     B., "Wind Tunnel Investigation of Submarine
     Hydrodynamics - The Development of the DREA
     Static Test Rig and Some Results", Proceedings
     of the 3rd Canadian Symposium on
     Aerodynamics (CASI), Toronto, November 1991

[15] De Souza F., "A Software Package for
     Generating Two-Dimensional Smoothed Spline
     Representations; Applications for the Five-Hole
     Probe Calibration Functions", NRC/IAR-LTR-
     HA-92, May 1993
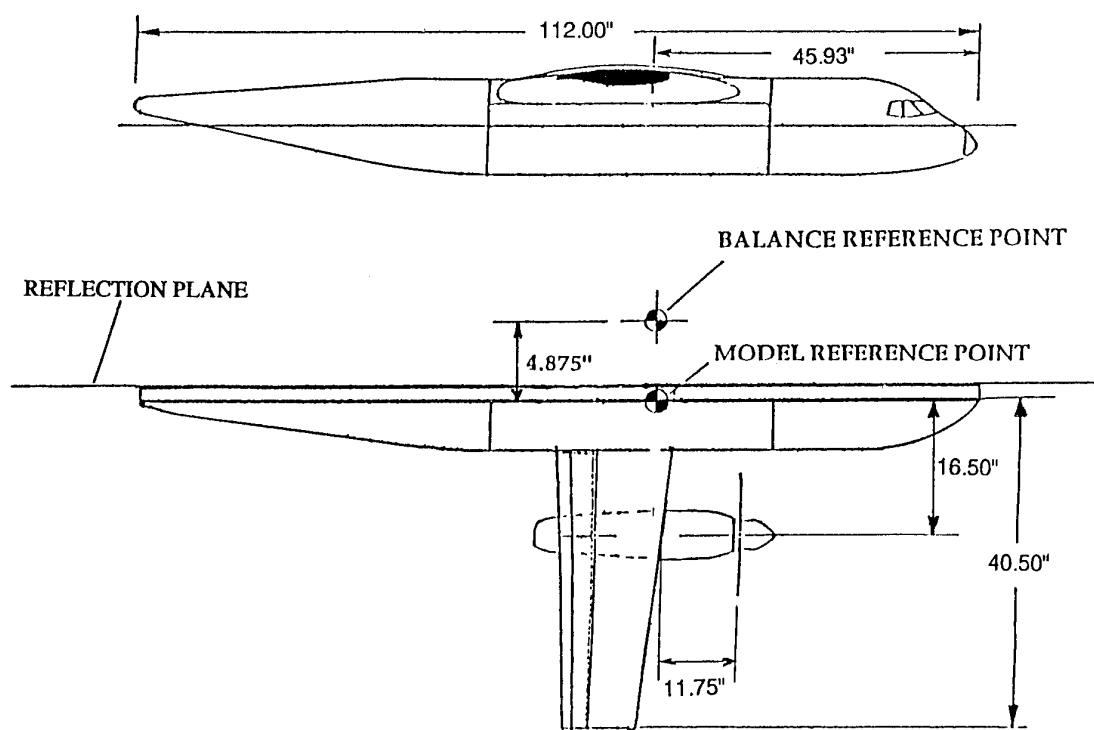
FIG. 1   DE HAVILLAND HALF- MODEL GEOMETRY

PROBE	DISTANCE PROBE ℄ TO NACELLE ℄ (r)	RATIO r/R
1	3.375	0.450
2	5.250	0.700
3	6.000	0.800
4	6.750	0.900
5	7.312	0.975

R = 7.50 INCH PROP RADIUS
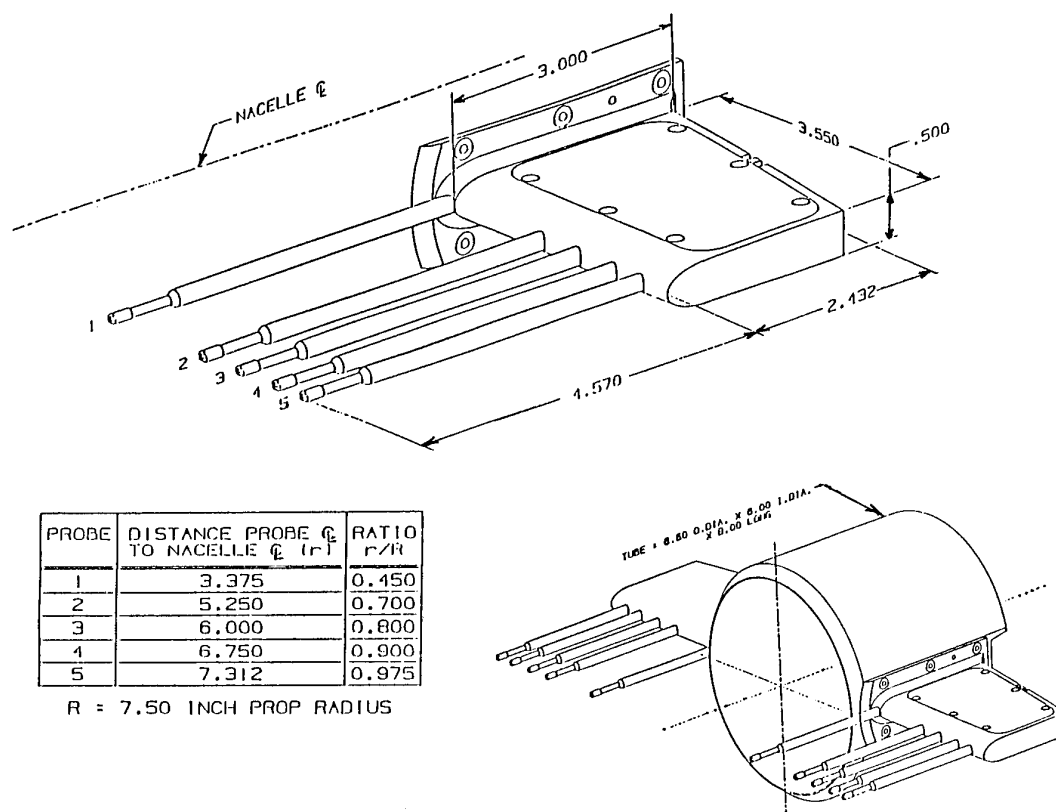
FIG. 2   FIVE-HOLE PROBE RAKE ASSEMBLY
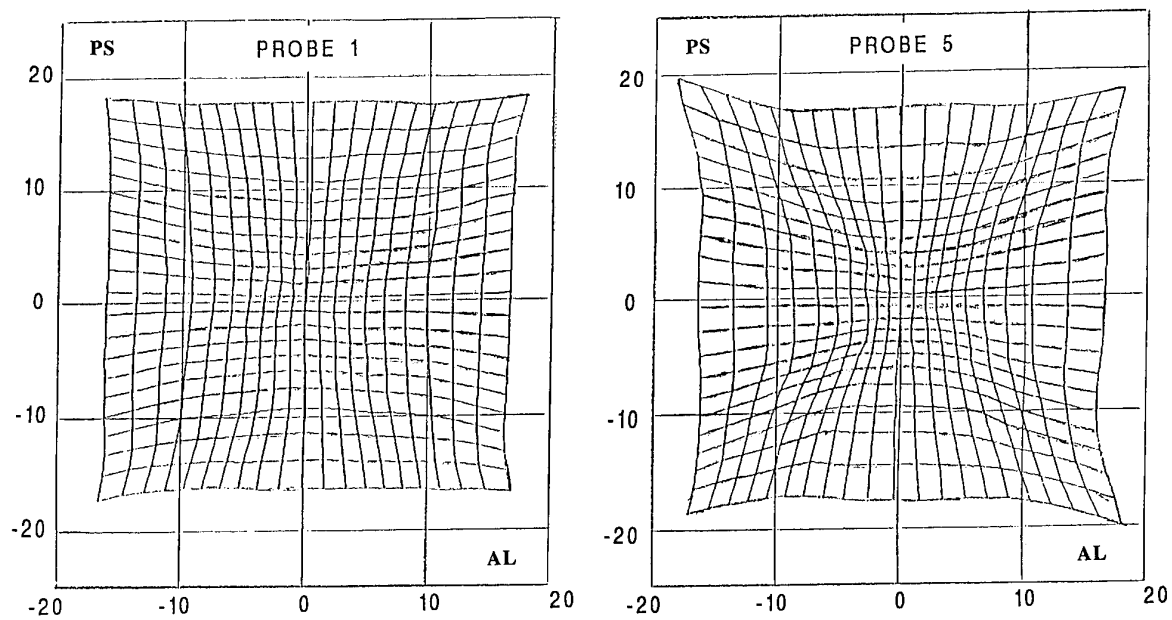
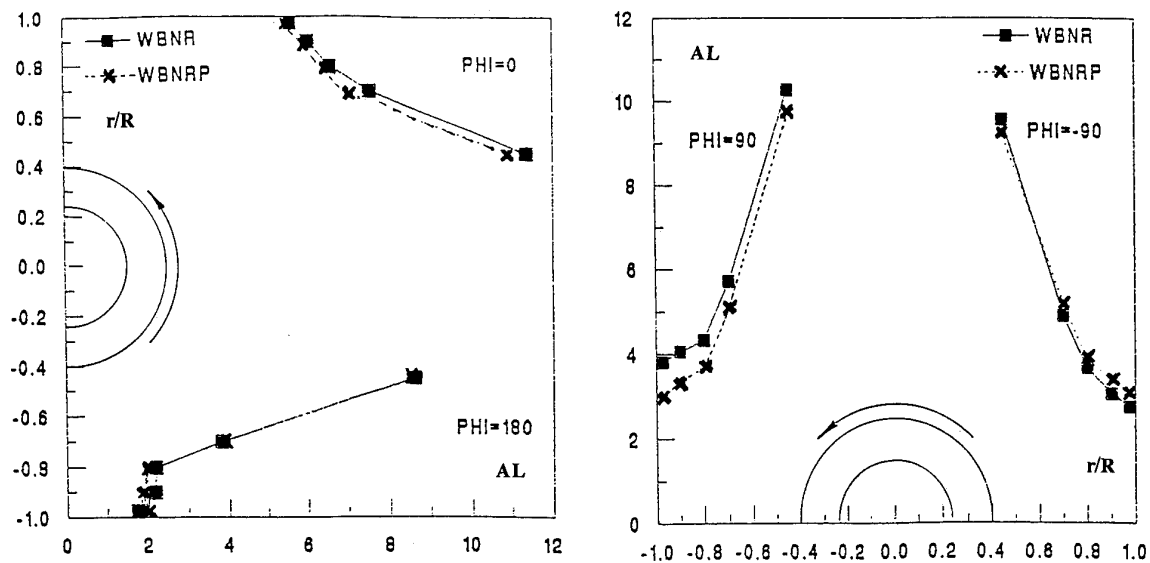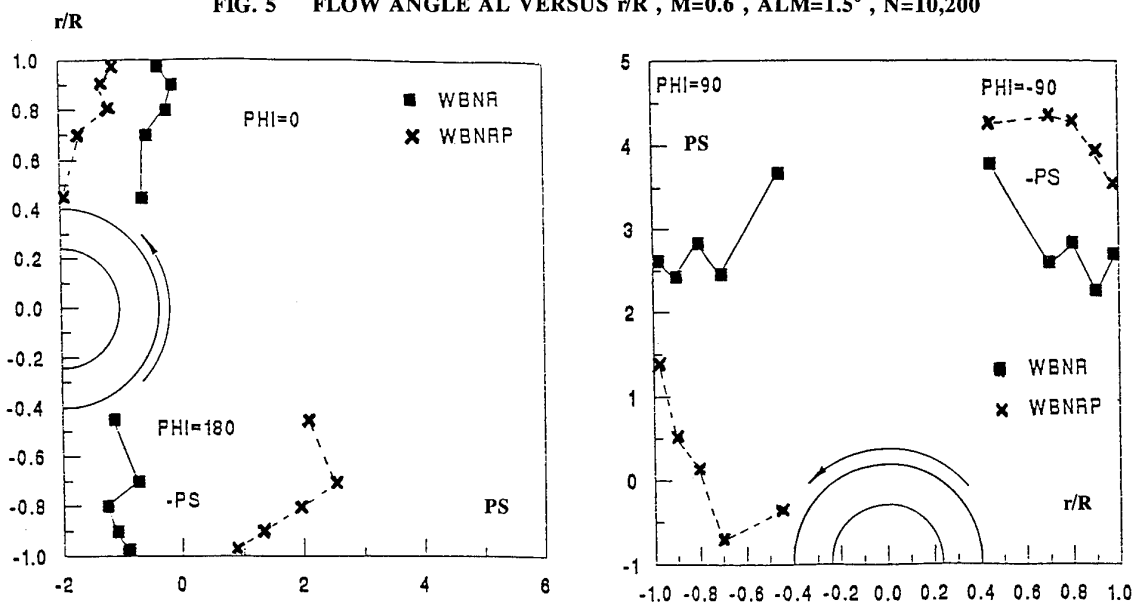**FIG. 3   SAMPLE FLOW ANGLE CALIBRATION MAPS , M=0.7**
(PS VERSUS AL)
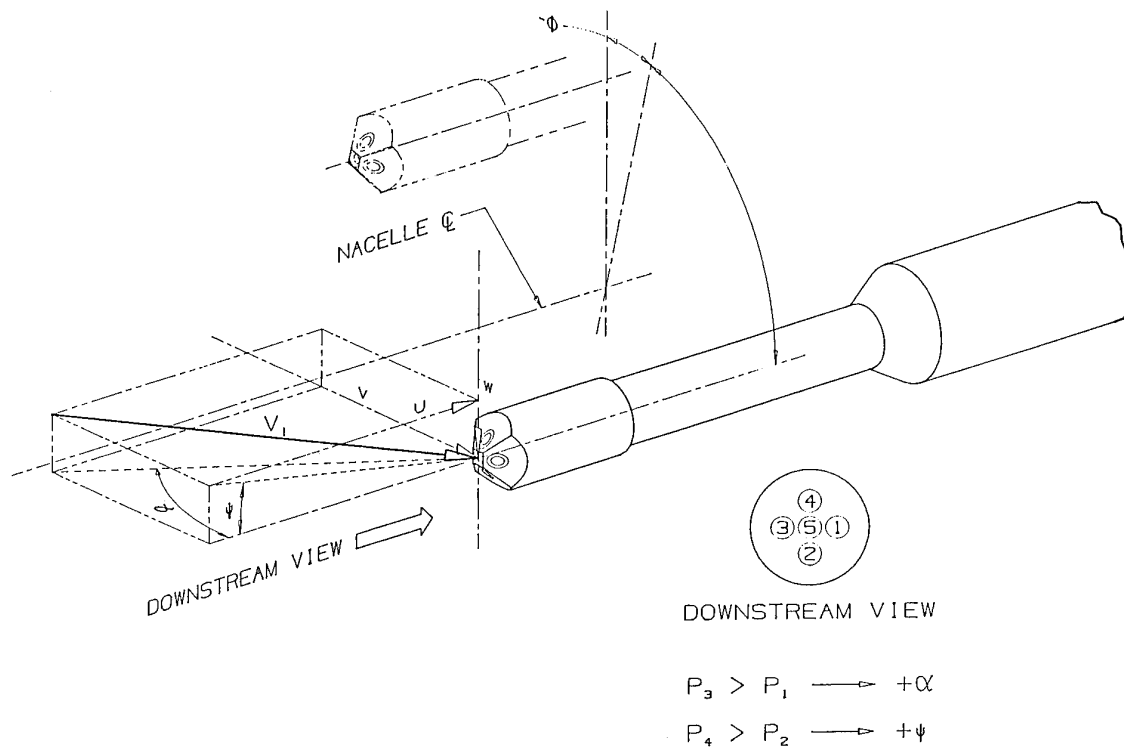
FIG. 4   FLOW ANGLES AND VELOCITY COMPONENTS IN PROBE
FIXED COORDINATE SYSTEM

FIG. 5   FLOW ANGLE AL VERSUS r/R , M=0.6 , ALM=1.5° , N=10,200

FIG. 6   FLOW ANGLE PS VERSUS r/R , M=0.6 , ALM=1.5° , N=10,200
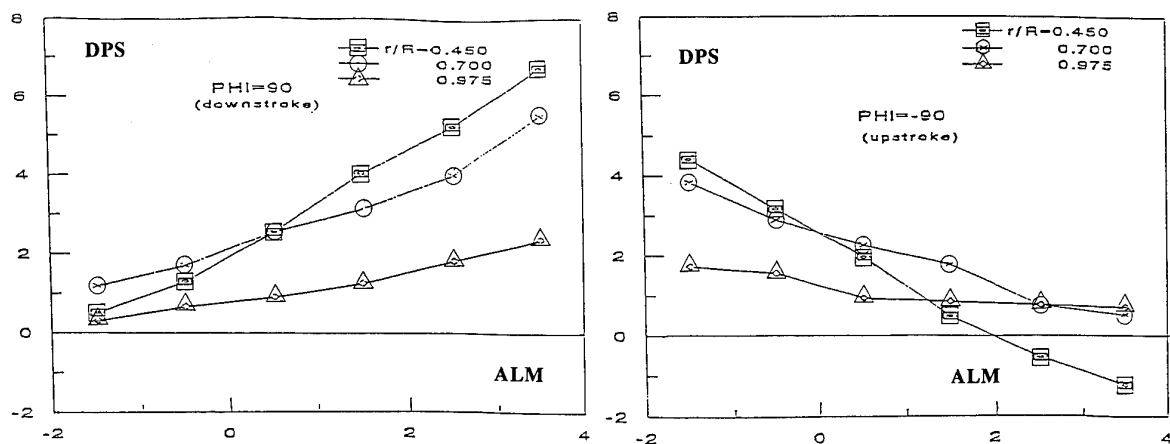
FIG. 7   PROPELLER INDUCED SWIRL ANGLE DPS VERSUS ALM ,
M=0.6 , N=10,200
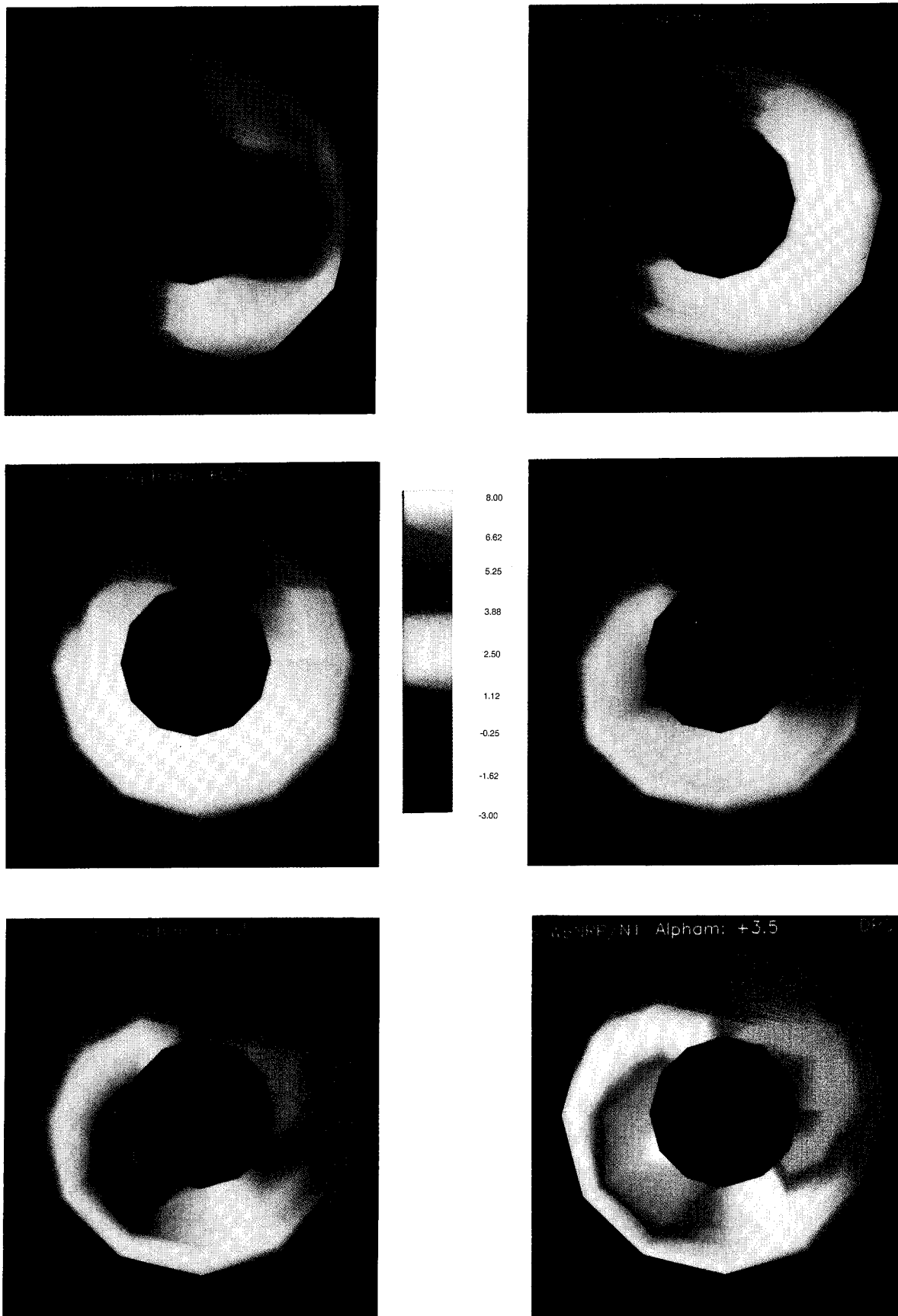
**FIG. 8   COLOUR GRAPHIC PRESENTATION OF THE SWIRL ANGLE
FOR A RANGE OF ALM , M=0.6 , N=10,200**
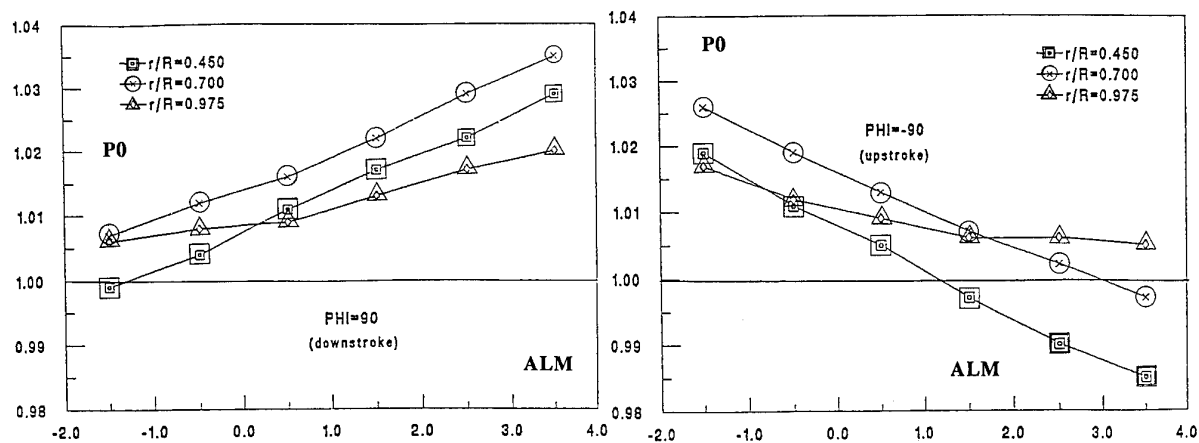
FIG. 9   NORMALIZED TOTAL PRESSURE P0 VERSUS ALM , M=0.6 ,
         N=10,200
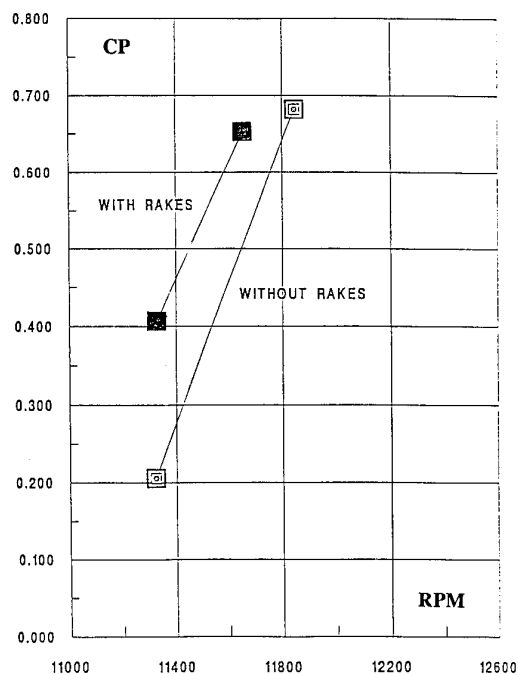
FIG. 10   SURVEY RAKE INTERFERENCE
          EFFECT ON THE POWER
          COEFFICIENT , M=0.7 , ALM=1.5°
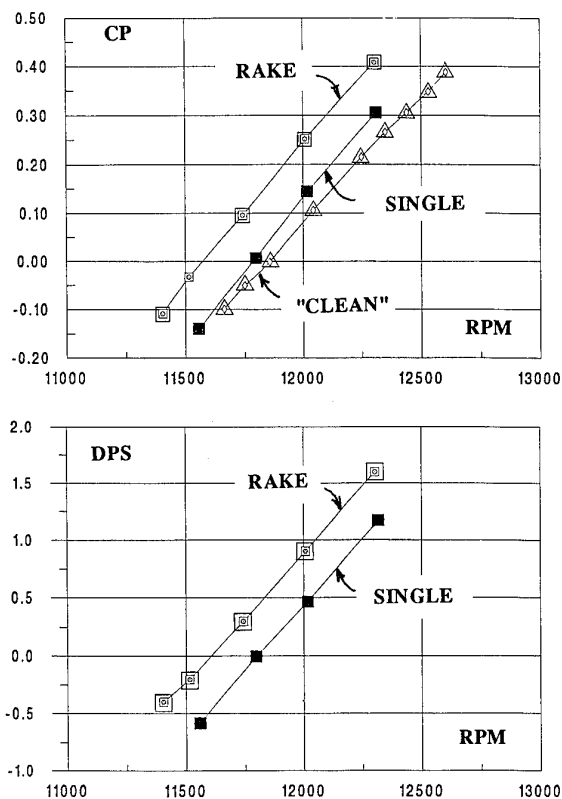
FIG. 12   SURVEY RAKE INTERFERENCE
          EFFECT ON THE POWER
          COEFFICIENT AND ON THE
          SWIRL ANGLE AT r/R=0.45 , M=0.7 ,
          ALM= 0°
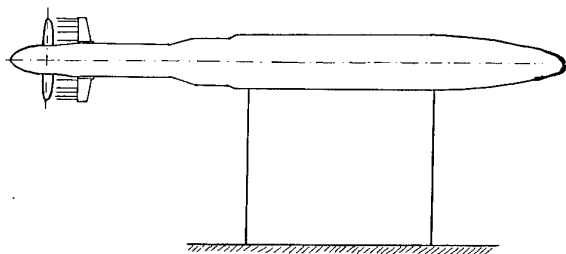
FIG. 11   PROPELLER TEST RIG
          ARRANGEMENT
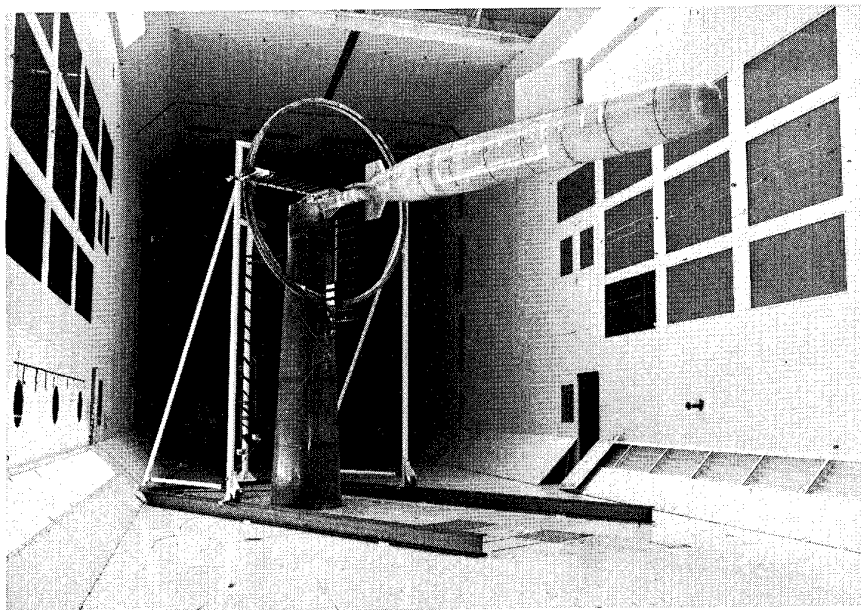
FIG. 13   THE FLOW SURVEY RIG IN THE IAR 9M WIND TUNNEL

FIG. 14   DETAILS OF THE PROBE HEAD

a) Top View of Survey Rig

a) Front View of Survey Rig
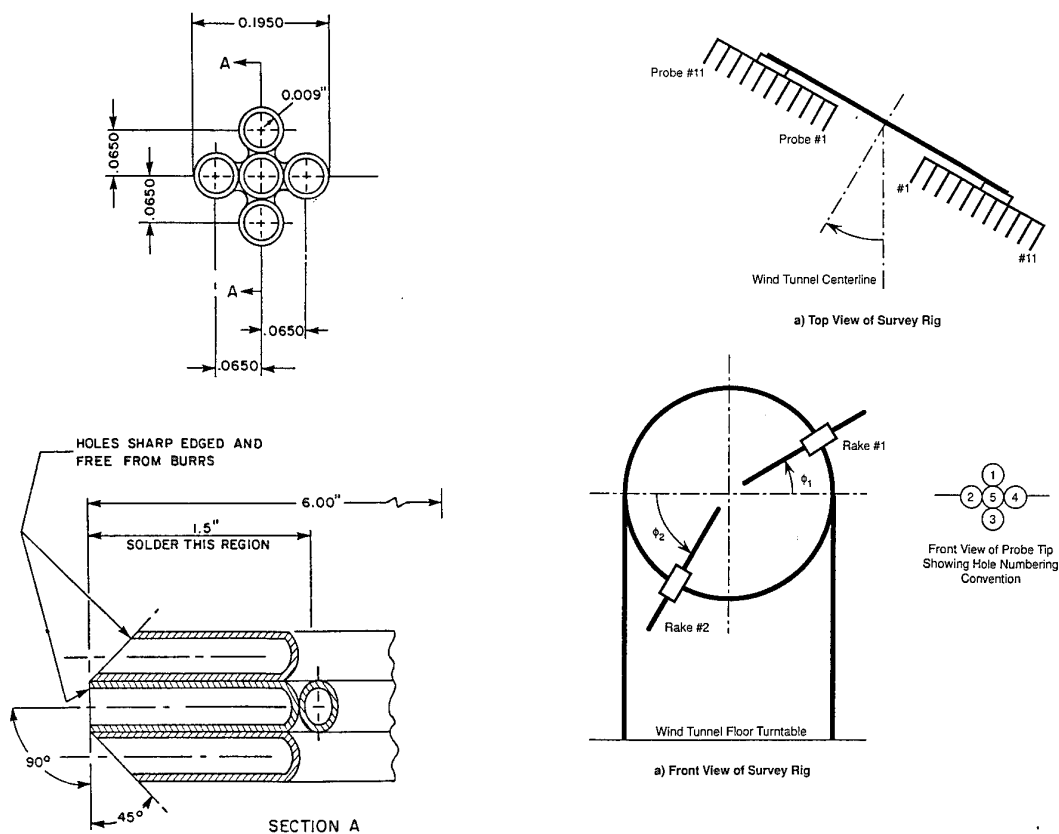
FIG. 15   TWO VIEWS OF THE SURVEY RIG
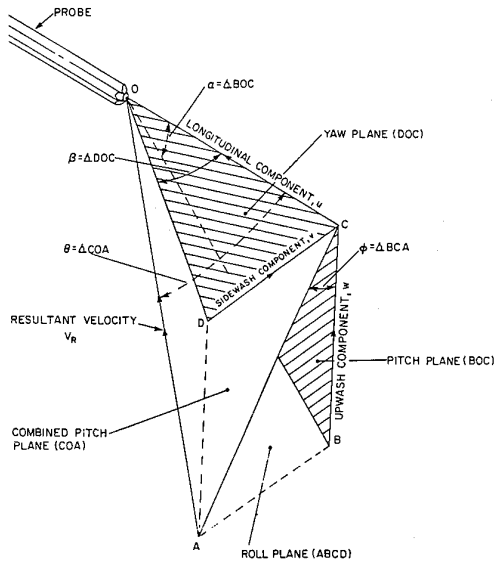
FIG. 16   DEFINITION OF FLOW ANGLES
AND VELOCITY COMPONENTS
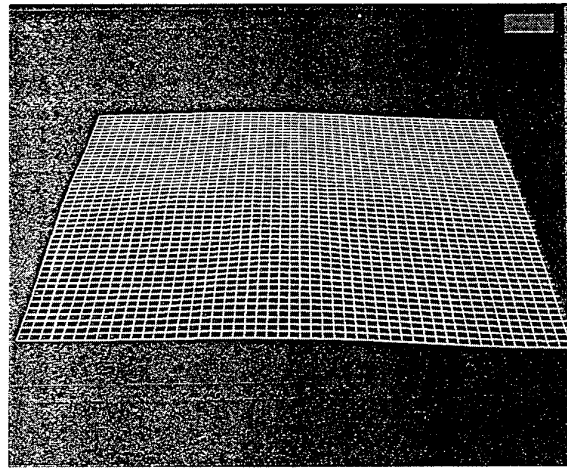
FIG. 17c (DYNAMIC PRESSURE PARAMETER P)
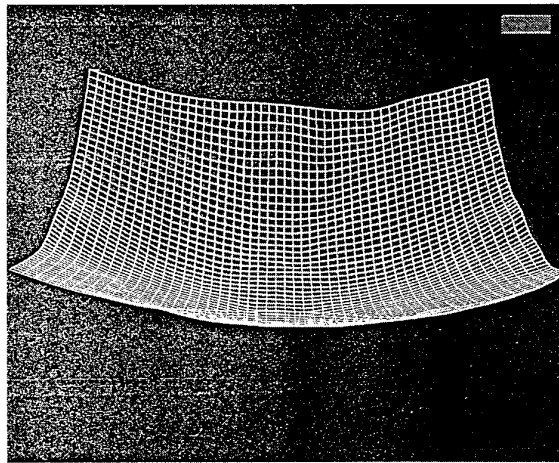
FIG. 17d (TOTAL PRESSURE PARAMETER S)

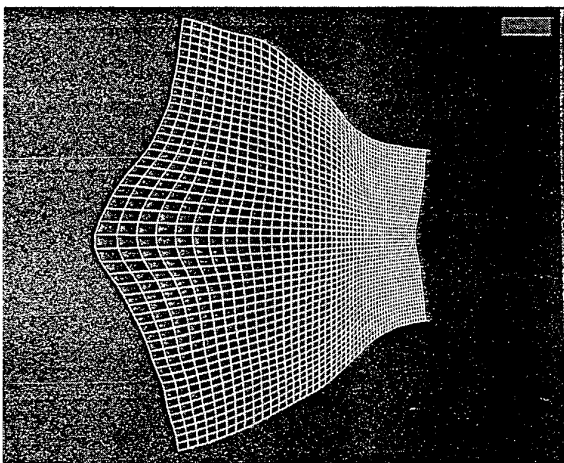TYPICAL SMOOTHED CALIBRATION SURFACES
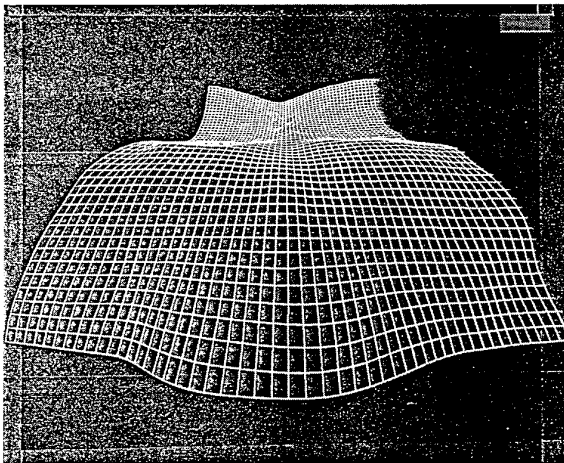
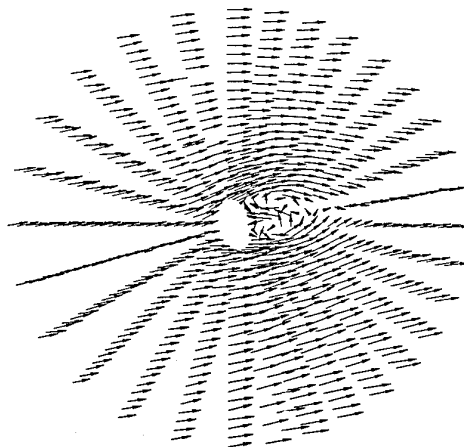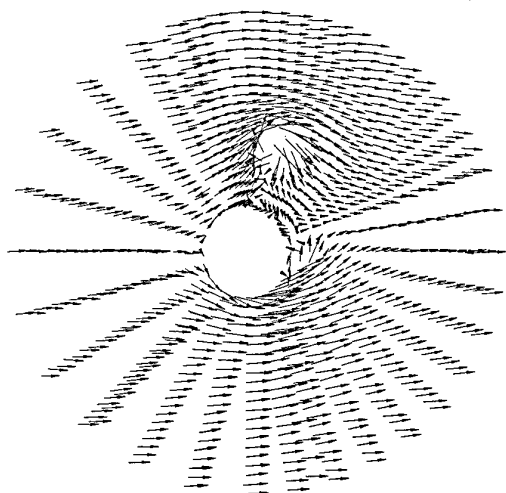FIG. 17a (RADIAL FLOW ANGLE ALPHA).

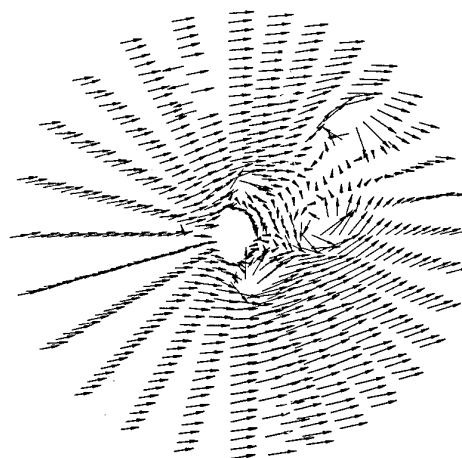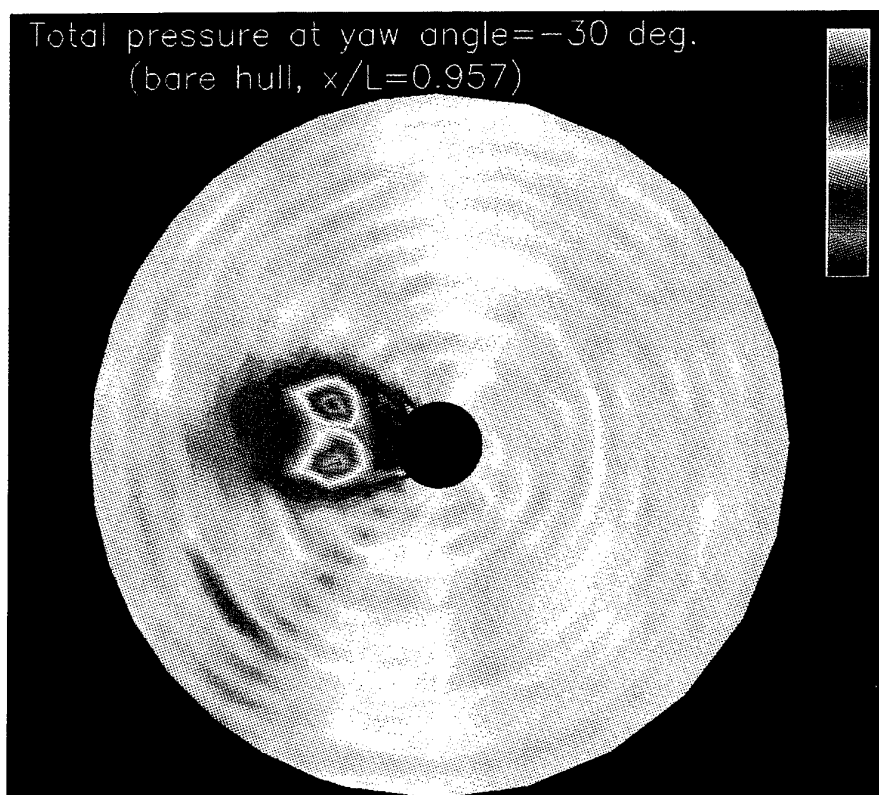FIG. 17b (TANGENTIAL FLOW ANGLE BETA)

FIG. 18   VELOCITY VECTOR PLOT IN Z-Y
PLANE (BAREHULL, x/L=0.957, yaw=20°)

FIG. 19 (FULL CONFIG., x/L=0.488, yaw=20°)   **FIG. 20 (FULL CONFIG., x/L=0.957, yaw=20°)**

VELOCITY VECTOR PLOT IN Z-Y PLANE

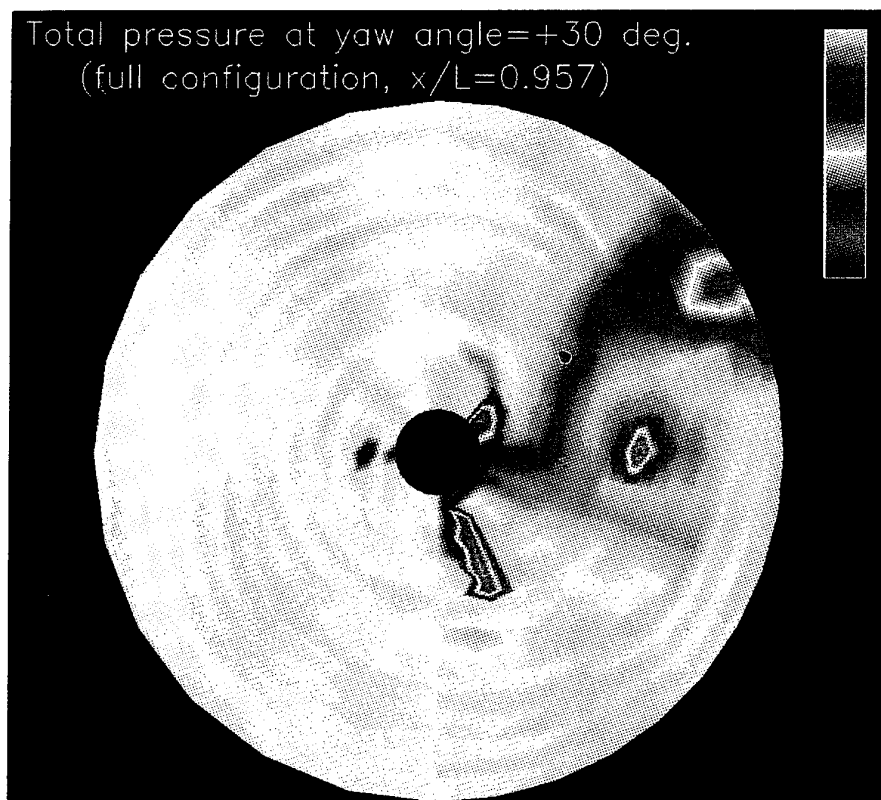**FIG. 21   COLOUR GRAPHIC PRESENTATION OF THE
TOTAL PRESSURE ISOCONTOURS**

**FIG. 22 COLOUR GRAPHIC PRESENTATION OF THE
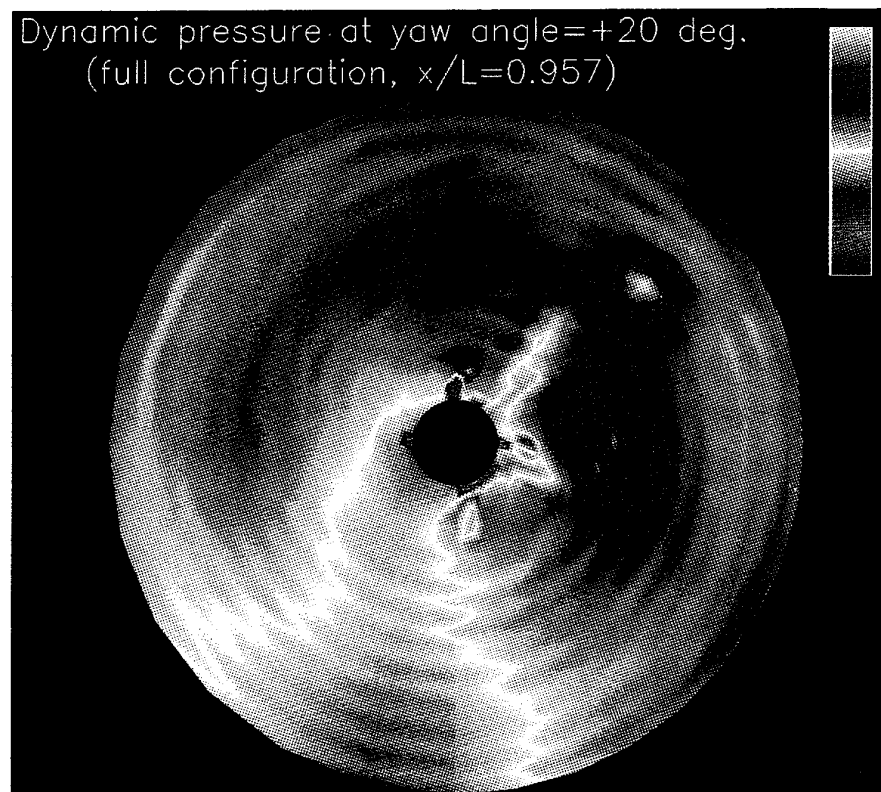TOTAL PRESSURE ISOCONTOURS**

**FIG. 23 COLOUR GRAPHIC PRESENTATION OF THE
DYNAMIC PRESSURE ISOCONTOURS**

Improvement and Validation of an LDV System to Perform Measurements in Laminar Supersonic Flows.

Luca Bertuccioli* & Gérard Degrez**
von Karman Institute for Fluid Dynamics,
72 Chaussée de Waterloo,
B-1640 Rhode-St-Genèse,
Belgium.

SUMMARY

This paper describes the optimization and systematic testing of a single component LDV system developed to perform measurements in laminar supersonic flows. The discussion concentrates on the tests carried out to validate the performance of the system and on issues which are particular to high speed LDV applications. Particular emphasis is given to issues connected to the seeding of the flow such as the constraints on the selection of a seeding material and its sizing. Oblique shock wave traverses were performed to validate the selected seeding material and the developed seeding delivery system. These tests confirmed the monodispersity of the seeding in the wind tunnel test section and showed a reasonable particle response. The oblique shock traverse results are also compared to various particle dynamics models though the comparison is inconclusive. A series of supersonic laminar boundary layer traverses were also performed. These profiles are compared to the compressible flat plate boundary layer theory of Chapman and Rubesin and the validity of this theory in the current test conditions is demonstrated. The boundary layer measurements are in good agreement with the theory, show good repeatability and do not display any signs of particle lag errors. Collectively, these experimental results clearly demonstrate the ability of the LDV system to perform accurate measurements in complex compressible flowfields.

LIST OF SYMBOLS

C_C Chapman's constant
d_p diameter of seeding particles, (μm)
f ratio of local to freestream velocity
M_∞ freestream Mach number
x, y Cartesian spatial coordinates in plate plane, (mm)
z Cartesian spatial coordinate perpendicular to plate plane, (mm)
∂ flow deflection angle for oblique shock wave traverses, (°)
σ standard deviation of measurement histogram, (%)

1. INTRODUCTION

Laser Doppler velocimetry (LDV) is a powerful, non–intrusive measurement technique which permits the investigation of highly complex flowfields, many of which cannot be explored with conventional intrusive techniques. One of the objectives of the research into LDV systems at the von Karman Institute (VKI) is to develop a tool capable of performing surveys of flowfields such as swept shock wave laminar boundary layer interactions or compressible vortical flows. Such supersonic configurations, however, represent a considerable technical challenge: the high speeds and extremely high velocity gradients as well as the presence of shock waves all contribute to the difficulties posed by such flows. In severe test conditions such as these, it is of great importance to establish the limitations of the measurement tool and its individual components.

As for any LDV application, the flow under investigation must be seeded with particles that scatter the laser light and generate the Doppler signal. For the LDV measurements to be accurate these seeding particles must "track" the flow and quickly respond to the velocity gradients imposed by the flowfield. If this is not the case and the seeding particle dynamics no longer properly represent the flowfield fluid dynamics, so called "particle lag" errors will result. The development of systems capable of providing seeding in a sufficiently controlled manner to avoid particle lag problems is, however, not trivial.

Historically, the significance and potential influence of seeding particles has, to a certain extent, been underestimated. Once the earliest studies had established the feasibility of the technique,[1, 2] researchers proceeded to investigate complex flowfields, such as those mentioned above, which could not be tackled with intrusive instruments. At the same time, most of the research into the technique concentrated on the development of optical and signal processing systems. Though it was immediately recognized that large seeding particles would not accurately follow the flow[2]—and would therefore result in particle lag errors—it was thought that this problem could be avoided simply by reducing the size of the particles used. However, traditional seeding systems—such as the atomization of liquids or the fluidization of metal oxide powders—produce broad ranges of particle sizes,[3, 4] and this is reflected in their dynamic response. LDV measurement accuracy is therefore also influenced by the size and shape distributions of the seeding materials used; this seeding characteristic must therefore also be controlled if the influence of particle dynamics is to be minimized. Finding practical solutions to these identified problems has, nevertheless, proved to be technically demanding.

The present paper describes the optimization and systematic testing of a single component LDV system developed to perform measurements in laminar supersonic flows. Issues—such as the influence of multiaxial mode laser operation—which are particular to high speed LDV applications are discussed and the tests carried out to validate the performance of the system are described in some detail. Particular emphasis is given to issues connected to the seeding of the flow such as the constraints on the selection of a seeding material and its sizing as well as a comparison of the experimental results with particle dynamics models. Results from oblique shock wave and supersonic laminar boundary layer traverses are presented and compared to theoretical profiles.

2. SYSTEM DEVELOPMENT & DESCRIPTION

2.1. Test Facility and Conditions

The experiments were carried out in the S1 supersonic windtunnel at the VKI. The S1 is a continuous, closed circuit, low pressure, Ackeret type windtunnel with a 40 cm by 40 cm test section (Fig. 1). The tests were performed at a freestream Mach number of 2.00 with a stagnation pressure of around 0.13 bar and a stagnation temperature of ≈ 300 K. These

---

*   Research Engineer
**   Associate Professor

conditions give a unit Reynolds number of $\approx 1.6 \times 10^6$ m^{-1} and a freestream velocity of ≈ 520 ms^{-1}. The boundary layer traverses were carried out on a flat plate spanning the entire test section, set parallel to the freestream, whereas the oblique shock wave traverses were performed with a wedge mounted on a sting which could be set at variable incidence. All the models were at near adiabatic wall temperature.
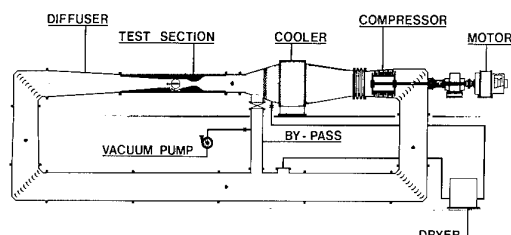
SUPERSONIC WIND TUNNEL S1

Fig. 1   Schematic diagram of S1 windtunnel.

2.2.   Seeding System

The necessity to inject seeding particles into a flow being investigated with LDV—to scatter the laser light focused into the probe volume and so generate a Doppler signal—can, in many instances, represent a weak point of the LDV technique. Since LDV measures the velocity of these seeding particles and not the fluid velocity, the relationship between the particle dynamics and the flowfield fluid dynamics becomes of obvious concern. The issue of the influence of seeding particles on LDV measurements bears particular mention since its impact has, to a large extent, been underestimated. The constraints which must be taken into consideration in selecting an appropriate seeding material are described in § 2.2.1 below.

2.2.1.   Seeding Particles

In very general terms, the requirements which seeding particles must satisfy are quite simple: Firstly, they must accurately "track" the flow, i.e., they must respond rapidly to the velocity gradients imposed by the flowfield.[1, 4-6] This effectively implies that the inertial forces acting on the seeding particle must be smaller than the aerodynamic ones. The requirement therefore translates loosely into small, lightweight particles being desirable.

The second requisite characteristic is that the particles produce large Doppler signals to facilitate signal processing and improve measurement accuracy.[1, 4, 5] The particles should therefore have a high refractive index and be as large as possible. Finding a compromise solution to these two simple yet contradictory requirements poses a significant technical problem.

The situation is further complicated when one wishes to investigate high speed, compressible flows; the presence of discontinuities and thin viscous layers results in extremely high velocity gradients which represent a particularly severe flowfield to which the seeding particles must respond. For example, the velocity gradient in the boundary layer (in the direction normal to the model surface) can be up to 600 ms^{-1} per mm in the current experimental configuration, while the velocity drop across eventual oblique shock waves can easily reach 20-30% of the freestream velocity. In these conditions, avoiding or minimizing so called "particle lag" errors, where the seeding particle velocity no longer matches the local fluid velocity, becomes increasingly difficult and the constraints on particle sizing become quite severe.[1, 7, 8]

In addition, the issue of the size and shape distributions of the seeding particles comes into play in high speed applications: Traditional seeding systems such as the fluidization of metal oxide powders or the atomization of liquids produce a broad range of particle diameters.[3, 4] Metal oxide powder particles are, furthermore, of non-uniform aerodynamic shape. In regions of the flowfield of strong de- or acceleration—such as those found in the vicinity of shock waves, in vortical structures or in boundary layers—the seeding particles of different diameter and shape (and therefore of different dynamic and aerodynamic properties) respond differently to the local fluid velocity gradients resulting in smeared and often ambiguous measurement histograms.[1, 6, 8, 9] Such "polydisperse" seeding is therefore not satisfactory for high speed applications.
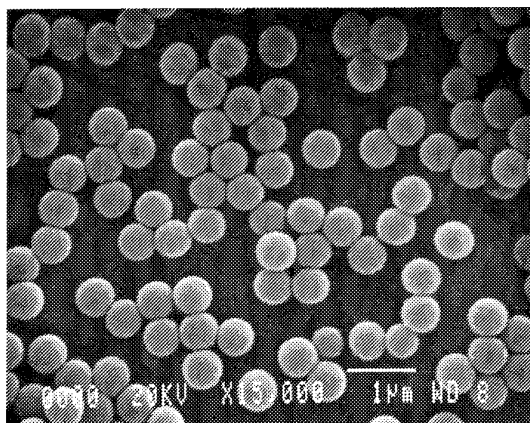

Fig. 2   Scanning electron micrograph of 0.6 μm PSL microspheres.

Taking into consideration these various constraints, polystyrene latex (PSL) microspheres were selected as the best candidate seeding material. PSL microspheres are produced by a simple controlled, emulsifier-free polymerization process developed at NASA Langley.[4, 10] These "monodisperse" particles (Fig. 2) are spherical and of a uniform diameter—between 0.6 and 2.7 μm—determined by the proportion of chemical reagents. In addition, they have a specific gravity of 1.05 as well as a high refractive index,[4, 10] making them remarkably well suited to high speed LDV applications.

The low density conditions in the S1 windtunnel coupled with high velocities create an environment in which the selection of a seeding particle size is a forced compromise between conflicting requirements: On the one hand, particle lag problems are aggravated by the reduction in aerodynamic forces caused by the low density, such that particles as small as 0.1 μm become necessary to eliminate particle lag errors. And on the other, the high velocities imply that the particle diameter cannot be reduced below ≈ 0.5 μm if the particles are to generate a Doppler signal at a sufficiently high signal to noise ratio to make measurements possible.[4, 5, 11] On the basis of calculations (described in Ref. 12, from the theory described in Refs. 1, 4, 5 & 13) of the particle size required to achieve acceptable particle response times and signal to noise ratios, 0.6 μm PSL particles were selected. [NB: The constraints described in this section apply strictly to measurements in laminar flows. In turbulent flows, if measurements of both mean and turbulent quantities are required, the constraints are considerably more complex and severe.[14]]

2.2.2.   Seeding Delivery

The PSL microspheres are produced and must be stored in an aqueous suspension since the particles agglomerate when dry. The suspension must therefore be atomized so that it can be injected into the windtunnel and the evaporation of the water surrounding the PSL must be ensured. In addition, the concentration of the suspension and the size of the droplets produced by the atomizer must be balanced such that a very large proportion of the droplets contain a single PSL particle;

this is necessary since droplets containing more than one particle would produce a larger, agglomerated particle once dried, thus reducing the monodispersity of the seeding. The final restriction imposed on the seeding delivery system—due to the low density conditions in the S1—is that the total amount of water injected into the windtunnel must be kept to a minimum to avoid condensation shocks.

In order to satisfy these requirements various aspects of the seeding delivery system were adapted: A high output atomizer functioning on the Wright jet-baffle principle[15] was designed; for a driving pressure of 2 bar, measurements carried out with an Aerometrics Phase Doppler Particle Analyzer showed that the atomizer produced an aerosol with a fairly narrow range of droplet sizes and an average droplet diameter of 2.1 μm. To ensure the evaporation of the water, the point at which the aerosol is injected into the windtunnel was moved as far upstream as possible; at this point, rough calculations of the evaporation rate of water droplets being accelerated through the nozzle, determined that the maximum permissible droplet diameter which would ensure evaporation, is 18 μm.[12] And finally, prior to injection, the aerosol is passed through a heating tube to facilitate the evaporation process.

2.3. Laser and Optics

The single component LDV system was operated in a forward scatter configuration using a 5 W Argon-ion laser (SpectraPhysics Model 2020) in multiaxial mode which gave a ≈ 2 W output power on the 514.5 nm green line. A beam expander (TSI Model 9188, 2.27 expansion factor), a final beam spacing of 34.05 mm and a 500 mm emitting lense resulted in the following probe volume characteristics:

Probe volume diameter	≈ 85 μm
Probe volume length	≈ 2.5 mm
Fringe spacing	7.43 μm ±1%

The probe volume dimensions are only approximate since they depend on the laser beam diameter which is not known precisely because it is affected by the collimation of the beam. The fringe spacing is based on a measurement of the emitting lense focusing angle, carried out by triangulation to an uncertainty of ±1%. This fringe spacing results in typical freestream Doppler frequencies of ≈ 70 MHz.

At such high Doppler frequencies, the possibility of an interaction between the Doppler signal and the various axial modes of the laser arises since the intermode and Doppler frequencies are of the same order. Theoretical studies[16, 17] showed that—for a laser operating in multiaxial mode—the range of Doppler frequencies that could be measured was limited, in principle, by the beating of the laser's axial modes and the Doppler signal when the frequencies of the two were comparable. Although this beating has been observed experimentally, its effect on LDV measurements is not clear and peculiarities, such as differences between lasers produced by different manufacturers, were reported.[17] More importantly, recently published results,[18] obtained in test conditions very similar to those in this study, indicate that the beat frequencies present in multiaxial mode do not necessarily affect the quality of the measurements and suggest that the loss of laser power caused by the installation of an etalon (in order to operate the laser in a single axial mode) results in lower data rates. The high quality, practically noise-free Doppler signal that was observed in the current tests would seem to be consistent with these findings.

2.4. Signal Processing

The Doppler signal was processed using a high speed counter type processor (TSI Model 1990A) connected to a PC via two Metrabyte PIO12 data acquisition cards. Filtering of the raw Doppler signal was kept to a minimum since the observed signal to noise ratio was high; the filters were set to eliminate the pedestal and high frequency noise while keeping as broad

a bandwidth as possible. As an example of this, Figure 3 shows a sample measurement histogram where the range shown on the velocity axis corresponds to the bandwidth of the filters used during the measurement. Typical validated data rates were 50-100 Hz in the freestream with peak rates of 600-1000 Hz achieved for high photomultiplier and counter gains. However, in order to avoid generating noise and to operate with high validation rates (95-100%) the electronic gains were limited. Data rates were lower in the boundary layers with some signal drop-out occurring close to model surfaces.
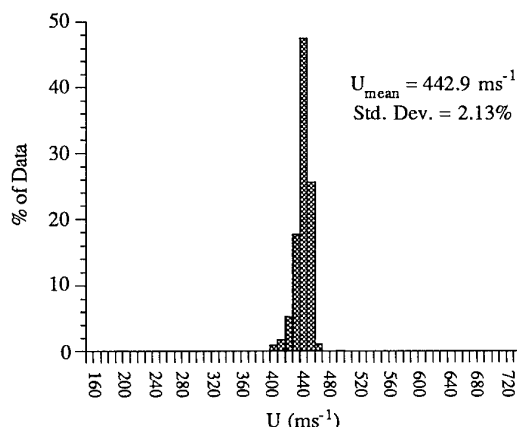
Fig. 3   Sample histogram showing filter bandwidth.

3. TESTING & VALIDATION

The systematic testing of the LDV system, by performing measurements in known flowfields, was considered a crucial part of the development of a tool intended to collect high quality data in complex compressible flowfields. Two series of tests, described separately below, were carried out to evaluate and validate different aspects of the LDV system.

3.1. Oblique Shock Wave Traverses

The flowfield through an oblique shock wave is a classical test used to evaluate the performance of seeding materials and systems under test conditions.[1, 4, 9, 13, 19, 20] The response of individual seeding particles to the step in fluid velocity created by the shock is strongly dependent upon their diameter and aerodynamic shape so that even slight variations in these characteristics will be highlighted. If the seeding in the test section consists of a distribution of sizes or of different discrete sizes, the resulting measurement histograms will be smeared or multiple-peaked respectively, and their standard deviations will rise significantly above the values found in the freestream.

The oblique shock wave traverses had three objectives: Firstly, to evaluate the particle response in order to confirm that the selected seeding was indeed appropriately sized. Secondly, to confirm the monodispersity of the seeding in the test section. The evaluation of the monodispersity in the test section is of particular importance since, as reported in the literature,[4, 6] it is possible that the seeding particles agglomerate while being injected or that the water surrounding them has not entirely evaporated leading to unexpectedly poor particle responses and/or smeared measurement histograms.

The final objective was to allow the experimental results to be compared with particle dynamics models. The flowfield created by an oblique shock wave represents a simple test-case for this comparison since the particle equations of motion reduce to a one-dimensional system (in the direction normal to the shock) and the flowfield can be completely described using the oblique shock relations.

3.1.1. Experimental Results

A wedge was mounted on a sting—which could be set at variable incidence—and the velocity component parallel to the freestream (u component, in the x-direction) was measured at various x stations at constant y and z coordinates (Fig. 4). A sample profile for a nominal flow deflection of 12° is shown in Figure 5, where the measured data and the fluid velocity, calculated according to the oblique shock relations, are plotted. To account for possible deflection of the sting or inaccuracy in the measurement of the incidence, the measured ratio of upstream to downstream velocity was used to determine the true deflection angle of the flow; by iterative calculation, this was determined to be 11.98°. The profile shows that within less than 40 mm of the shock the particles have fully relaxed to the downstream fluid velocity. Though this relaxation distance is not particularly spectacular, it seems unlikely, given the low density in the S1, that a much improved response will be feasible with particles that are still large enough to generate a visible Doppler signal.
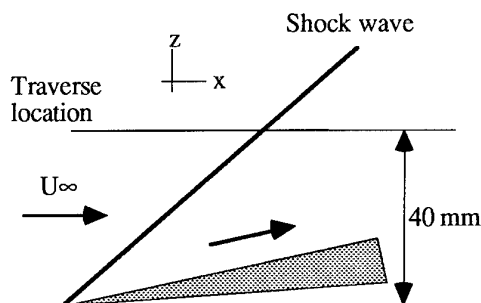
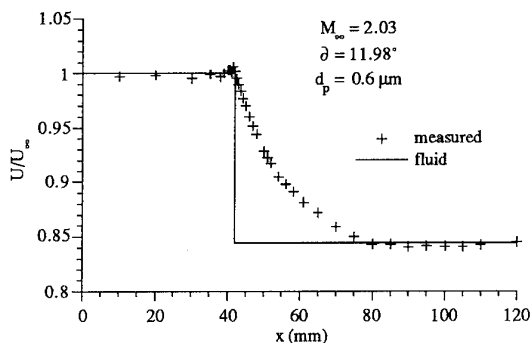Fig. 4 Schematic diagram of oblique shock wave traverse.

Fig. 5 Sample oblique shock wave traverse.

The more significant result of this traverse, however, is demonstrated by Figure 6 which shows the standard deviation of the histogram of measurements taken at each point. As can be seen in the figure, there is only a minimal increase in the measurement standard deviations—above the typical freestream value of $\approx 2\%$—in the region where the seeding "lags" the flow ($x \approx 40$ to 80 mm). This provides strong confirmation that the seeding present in the test section is indeed monodisperse since any variations in particle characteristics would result in a broadening of the measurement histograms and a consequent marked increase in standard deviation.

In order to verify that the particles generating the Doppler signals were in fact the PSL particles and not, for example, ice crystals created by the condensation of the injected water, two traverses were carried out for the same flow deflection angle using 0.6 and 0.85 μm PSL particles respectively. In between the two runs, the entire seeding delivery system was cleaned to eliminate any residual from earlier tests. The results from these traverses are shown in Figure 7 along with the

theoretical fluid velocity distributions. The sting was set for a nominal flow deflection angle of 9°—the actual deflection angles were 9.93° and 9.51° respectively—with a slight variation in the test conditions resulting in marginally different velocity drops across the two shocks.
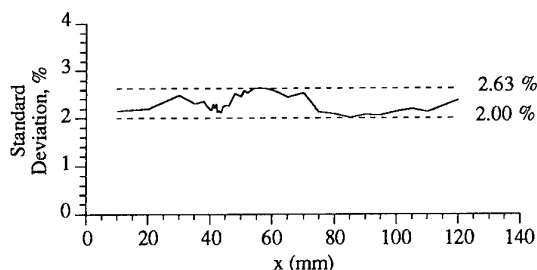
Fig. 6 Distribution of standard deviation of the local mean velocity in the oblique shock traverse.
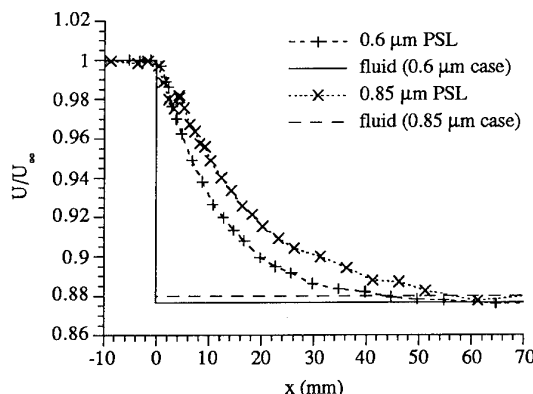
Fig. 7 Comparison of two oblique shock wave traverses using 0.6 & 0.85 μm PSL.

To compare the relaxation distances for the two particle sizes the area between the measured curve and the theoretical fluid velocity profile was calculated and normalized with respect to the velocity drop across the shock. The measured ratio of "relaxation distances" of the 0.85 μm case to the 0.6 μm case is of 1.3 which is somewhat less than the value of ≈ 1.6 expected from particle dynamics calculations (see § 3.1.2 below). Nonetheless, the slower response of the larger particles would seem to indicate that the measured signals are indeed being generated by PSL particles although a more systematic testing of this conclusion—using a broad range of particle diameters up to say 2.0 or 2.5 μm—would be quite valuable; the kink in the 0.85 μm profile and the small difference in particle diameter limit the strength of any conclusions drawn from the current tests.

3.1.2. Comparison with Particle Dynamics Models

The need to test the applicability of particle dynamics models stems from one of the main objectives of this research which is to provide experimental data for numerical code validation purposes. Since the flowfields that are of interest—e.g., swept shock wave boundary layer interactions or compressible vortical flows—contain regions of extremely high velocity gradients, it is exceedingly unlikely that the total elimination of particle lag errors will be possible. For a comparison between numerical and experimental results to be useful then, corrections for particle dynamics effects must be performed. Picking up an idea first proposed by Maurice,[7, 19] the following approach to this issue is suggested: Rather than attempting to correct the experimental data—by some complex comparison and manipulation of the measured and computed flowfields—it seems more constructive for the experimental data to be presented together with a (validated) particle dynamics model. The model could then be incorporated into computations to produce two sets of results:

the fluid flowfield and its analogous particle "flowfield". Validation could then be performed by comparing the experimental results with the computed particle "flowfield" without being dependent on the assumption that either the measured or computed flowfield is perfect (i.e., identical to the "real" fluid flowfield). To allow this however, the seeding and LDV systems and the particle dynamics model must be extensively validated and their ability to provide results in consistent good agreement with each other must be demonstrated.

For the simple geometry of the oblique shock flowfield, the various particle dynamics models described in the literature reduce, effectively, to empirical or semi-empirical modifications of Stokes drag law to extend its applicability to higher values of relative Mach and Reynolds numbers. Three such models were considered: Meyers',[4] which corrects for compressibility effects. Crowe's,[21] which includes rarefaction, compressibility and heat transfer effects. And Cunningham's correction factor[22] which accounts for rarefaction effects. (The empirical expression used for the Cunningham correction factor was taken from Ref. 23; a very similar expression can be found in Refs. 24 & 25).

As can be seen in Figure 8, the results produced by the various models are almost identical despite the differences between their respective theoretical bases. Taking advantage of this, only results from Cunningham's model are used in the comparison with experimental results in order to simplify the plots.
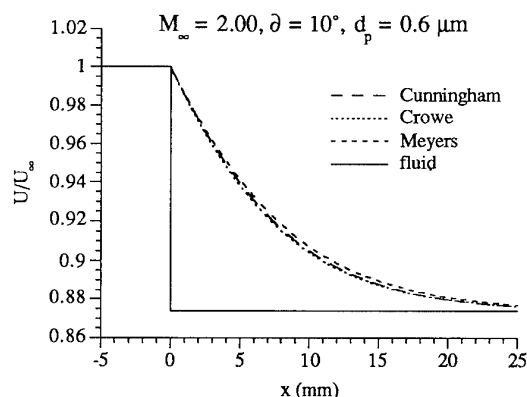

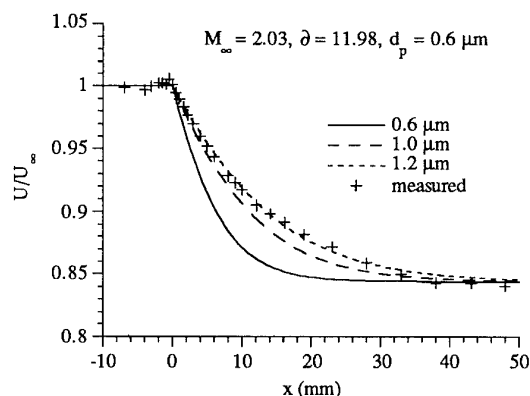Fig. 8   Sample oblique shock traverse for comparison of particle dynamics models.

Fig. 9   Oblique shock wave traverse showing measured and particle dynamics model results.

Figure 9 shows the oblique shock wave traverse already mentioned in § 3.1.1 plotted with three curves calculated for different particle diameters using Cunningham's model. The PSL used for this test was of 0.6 μm diameter. For this size seeding, the particle dynamics model predicts a significantly faster response than was measured in the windtunnel. In fact,

the measured data seem to be in reasonable agreement with the response calculated for 1.2 μm particles. However, the results from another traverse, carried out with the same seeding but a deflection angle of 8.4° (rather than 12°), are not entirely consistent (Fig. 10). Again, the measured response is slower than that predicted for 0.6 μm particles but for this case the measured data seem to agree with a profile predicted for 1.0 μm particles. Similarly, for the traverses shown in Figure 7, the models predict more rapid responses than were observed for both particle diameters.
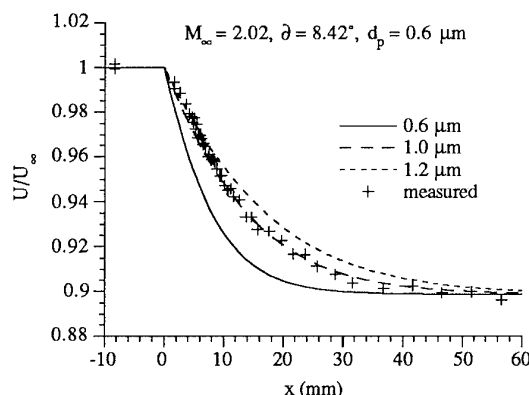

Fig. 10   Oblique shock wave traverse showing measured and particle dynamics model results.

It is as yet unclear what the cause of these discrepancies is. The slower than expected responses could perhaps be due to particle agglomeration or some other seeding effect such as the particles acting as seeds for the formation of ice crystals. However, such signs of poor control of the seeding would seem to be contradicted by the consistently low standard deviations observed and by the clear effect on the particle response seen when changing the particle diameter (see § 3.1.1 and Figs. 6 & 7). It could, on the other hand, be argued that detailed comparisons cannot be made since, for example, the 1.0 μm curve in Figure 9 lies within the experimental uncertainty band of the measurements. In practical terms however this does not resolve the issue since, if the models are to be used for code validation purposes, an uncertainty of 20% or more on the particle diameter to be used in the model would not be acceptable. Further tests in a more severe flowfield—such as a normal shock or very strong oblique shock—with a broad range of particle sizes should be performed to clarify these issues.

3.2.   Laminar Boundary Layer Traverses

The objectives of the laminar boundary layer traverses were as follows: To evaluate the accuracy of the measurements by comparing the experimental results with analytical profiles. To check for the presence of particle lag errors in a comparatively moderate flowfield that is more representative of a general flowfield than that experienced in the oblique shock wave traverses. And finally, to evaluate the wall proximity measurement capability of the LDV system. This last characteristic is of significance since many of the flows that are of interest—in particular swept shock wave boundary layer interactions—contain important features both on the scale of, and located in, the boundary layer. For these tests, typical boundary layer thicknesses were ≈ 2-3 mm making measurements very close to model surfaces necessary. The adaptations brought to the system to enhance this capability are described in Ref. 26.

3.2.1.   Theory

The compressible flat plate laminar boundary layer theory of Chapman and Rubesin[27] describes a set of self-similar profiles analogous to the Blasius profiles for the incompressible case. The profiles are derived using coordinate transformations applied to the compressible boundary layer equations. If

Chapman's approximate viscosity law is assumed, these equations can be reduced to an equivalent "incompressible" set, for the specific case of the flat plate boundary layer. The equations are integrated numerically to give a table of values for the self-similar velocity and temperature boundary layer profiles; these can then simply be scaled to fit specific test conditions.

In order to evaluate the significance of any inaccuracy introduced by the approximate viscosity law, the Chapman–Rubesin solution was compared to another self-similar solution—along the lines of that derived by Van Driest[28]—which is calculated using Sutherland's viscosity law. The basis of this solution is, in fact, very similar to that of the Chapman–Rubesin theory. However, contrary to the Chapman–Rubesin solution which depends only on the Prandtl number, the Van Driest self similar profiles depend explicitly on the freestream Mach number and temperature, such that a different solution must be computed for each set of test conditions. Figure 11 shows sample profiles for both solutions and it is clear that the differences between the two are minimal; for the comparatively low Mach number of 2.0, the error introduced by Chapman's approximate viscosity law is entirely negligible.
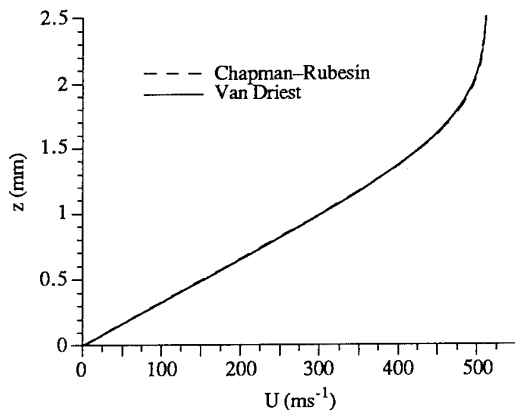

Fig. 11 Comparison of Chapman–Rubesin and Van Driest compressible flat plate laminar boundary layer profiles.

3.2.2. Experimental Results

Traverses were performed at x stations 50-200 mm from the flat plate leading edge. For each measurement point a set of 100-2000 individual velocity measurements—depending on the local data rate—was collected and averaged. The standard deviation of such data sets collected in the freestream was typically $\approx 2\%$, with this value increasing closer to the wall. This increase is, however, to be expected: The velocity gradient for the "linear" part of the boundary layer profiles ranges from 300 to 600 ms^{-1} per mm such that there is a variation in velocity between the top and bottom of the probe volume of the order of 25 to 50 ms^{-1}. This "pseudo-turbulence" [29] becomes proportionally more significant close to the wall, as the local fluid velocity becomes smaller.

A correction was performed for each profile to determine the true origin of the z coordinate. This was necessary since the origin used during the measurements was determined by visually placing the probe volume on the surface of the model while in test conditions. The correction was calculated using a sliding linear least squares fit over the lower part of each profile. This approach can be justified even though the Chapman–Rubesin profile is not perfectly linear, since deviations from linearity are extremely small in the lower part of each profile.

A sample profile, taken 200 mm from the leading edge, is shown in Figure 12 which is plotted in physical coordinates to provide a more stringent test of the measurement accuracy.

Figure 13 shows two profiles, both 75 mm from the leading edge, plotted in non-dimensional coordinates (consistent with the Chapman–Rubesin theory) to account for variations in the test conditions. The agreement between the measured data and the theoretical profiles is seen to be good, with the experimental data showing remarkably little scatter. A comparison of the gradients of the profiles at the wall, found errors in the range of 0.01-3.4% with an average of 1.2%.
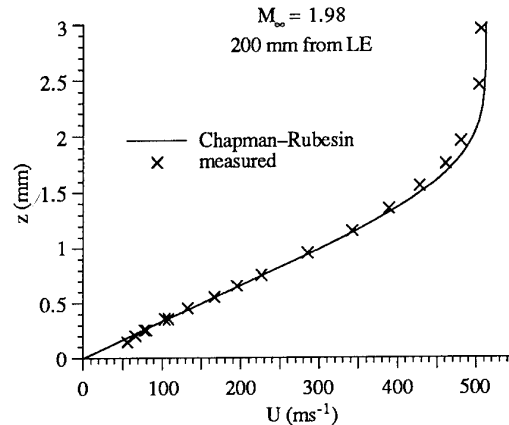

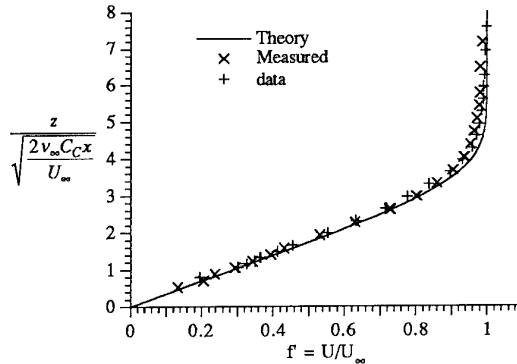Fig. 12 Laminar boundary layer profile compared to Chapman–Rubesin theory.

Fig. 13 Measurement repeatability: two boundary layer profiles (75 mm from LE) compared to Chapman–Rubesin theory.

Measurements taken below ≈ 0.3 mm from the wall (Fig. 12) show some evidence of velocity bias. Since the rate at which seeding particles pass through the probe volume is directly proportional to the local fluid velocity, the velocity variation across the probe volume caused by the velocity gradient, results in measurement histograms skewed towards the higher values.[29, 30] This velocity bias is, however, only significant where the velocity variation across the probe volume is a significant proportion of the local velocity—in practice, below ≈ 0.5 mm from the wall for the present flow conditions. Furthermore, since the profile in this region is effectively linear, a correction for the bias would, if necessary, be quite simple.[29, 30] Good measurement repeatability is demonstrated in Figure 13.

The wall proximity measurement capability was demonstrated by data collected less than 100 µm from the surface where the local fluid velocity is less than 10% of freestream. This result was subsequently confirmed—in a preliminary swept shock wave boundary layer interaction flowfield survey[26]—by measurements performed at less than 50 µm from the surface (velocity $\approx 5\%$ of freestream). In this position, the probe volume is partially reflected by the model surface; this therefore represents the lowest measuring position that can be achieved with the current optical configuration.

None of the profiles showed any evidence of particle lag effects. Particle lag errors are characterized by a reduced measured boundary layer thickness and by measured velocities in excess of theoretical values, principally in the outer part of the profile:[6, 8, 9] as the particles, travelling at the freestream velocity, enter the growing boundary layer, they are decelerated by the slower moving fluid. If they are too large, they do not rapidly relax to the lower velocity and the measurements will overestimate the fluid velocity. Neither of these applies to the current traverses where the measured profile shape is marginally (but consistently) less "full" than the theoretical one, and the measured values lie slightly below the theoretical ones in the outer part of the boundary layer. The measured freestream values however correspond to the theoretical ones within about 1%. Preliminary results of a comparison with two–dimensional Navier–Stokes computations[31] suggest that at least part of this difference in profile shape could be due to the leading edge viscous–inviscid interaction and a possible misalignment of the flat plate with respect to the freestream. Another source could be non-uniformities in the freestream flow; both these issues, as well as other possible causes, warrant further study.

An uncertainty analysis,[32] which considered—in order of importance—the standard deviation of each measurement histogram ($\pm 2\sigma = \pm$ 4% for the freestream at a 20:1 confidence level), fringe spacing, positioning errors, counter resolution, digital resolution, and the alignment of the displacement table determined the overall measurement uncertainty to be $\pm$ 4.4% (20:1). Particle lag effects were not included since these can generate very large local errors but need not affect the overall accuracy of the measurements.

4. CONCLUSIONS

The optimization and validation of a single component LDV system developed to perform measurements in laminar supersonic flows have been described. Particular emphasis has been given to the effects of seeding particle dynamics; the potentially large impact of the seeding on measurement accuracy and even feasibility, leads to the conclusion that the careful selection of an appropriate seeding material must be considered an integral and critical part of any LDV system intended for high speed applications.

Oblique shock wave traverses were carried out to evaluate the performance of the entire seeding system. These tests confirmed the monodispersity of the seeding in the test section and demonstrated a reasonable particle response. Traverses with different seeding particle diameters confirmed that the seeding present in test conditions could be controlled. In addition, the simple flowfield created by the oblique shocks was used to compare the experimental results with those calculated using various particle dynamics models. This comparison was however, inconclusive yielding inconsistent results that highlight the need for further systematic testing of the particle response achieved in test conditions.

Supersonic laminar boundary layer traverses were performed and compared to the compressible flat plate laminar boundary layer theory of Chapman and Rubesin. The validity of this theory in the current test conditions was verified by comparison with the Van Driest solution to the compressible boundary layer equations. None of the measured boundary layer profiles showed any sign of particle lag errors indicating that the selected seeding is sufficiently small to allow measurements, in comparatively moderate flowfields, without particle lag problems occurring. The experimental data showed good agreement with the theoretical profiles and good measurement repeatability was demonstrated. In addition, the wall proximity measurement capability of the LDV system was confirmed.

Together, these results indicate that the developed LDV system is capable of performing accurate flowfield surveys of complex compressible flows. However, further study of

seeding particle dynamics seems necessary especially if the experimental data are to be used for code validation purposes.

ACKNOWLEDGMENTS

REFERENCES

1. Durst, F., Melling, A., and Whitelaw, J. H., "Principles and Practice of Laser Doppler Anemometry," Academic Press, 1976.

2. Stevenson, W. H., "A Historical Review of Laser Velocimetry," in *Laser Velocimetry and Particle Sizing*, Purdue University, West Lafayette, Indiana, July 1978, pp. 1-12.

3. Crosswy, F. L., "Particle Size Distributions of Several Commonly Used Seeding Aerosols," in *Wind Tunnel Seeding Systems for Laser Velocimeters*, NASA CP-2393, NASA Langley Research Center, Hampton Virginia, March 1985, pp. 53-75.

4. Meyers, J. F., "Generation of Particles and Seeding," in *VKI Lecture Series 1991-05, Laser Velocimetry*, von Karman Institute for Fluid Dynamics, Belgium, June 1991.

5. Boutier, A., "One Component LDV System," in *VKI Lecture Series 1991-05, Laser Velocimetry*, von Karman Institute for Fluid Dynamics, Belgium, June 1991.

6. Jones, G. S., Kamemoto, D. Y., and Gartrell, L. R., "An Investigation of the Effects of Seeding in Laser Velocimeter Systems," AIAA Paper 90-0502, Jan. 1990.

7. Maurice, M. S., "Laser Velocimetry Seed Particles Within Compressible, Vortical Flows," *AIAA Journal*, Vol. 30, No. 2, February 1992, pp. 376-383.

8. Nichols, R. H., "Calculation of Particle Dynamics Effects on Laser Velocimeter Data," in *Wind Tunnel Seeding Systems for Laser Velocimeters*, NASA CP-2393, NASA Langley Research Center, Hampton Virginia, March 1985, pp. 1-11.

9. Donaldson, J. C., "Laser Doppler Velocimeter Application in Supersonic Boundary-Layer Flow," Arnold Engineering Development Center, AEDC-TR-86-44, March 1987.

10. Nichols, C. E., Jr., "Preparation of Polystyrene Microspheres for Laser Velocimetry in Wind Tunnels," NASA, TM-89163, June 1987.

11. Boutier, A., "High Velocity Measurements: Special Requirements," in *VKI Lecture Series 1981-03, Laser Velocimetry*, von Karman Institute for Fluid Dynamics, Belgium, Feb. 1981.

12. Zwicker, K., "Improvement of LDV System for Measurements in Thin Supersonic Boundary Layers," von Karman Institute for Fluid Dynamics, Belgium, VKI-PR-1991-26, June 1991.

13. Melling, A., "Particle Behaviour in Flows and Suitable Particles for LDA," in *VKI Lecture Series 1981-03, Laser Velocimetry*, von Karman Institute for Fluid Dynamics, Belgium, Feb. 1981.

14. Nichols, R. H., "The Effect of Particle Dynamics on Turbulence Measurements with the Laser Velocimeter," in *Numerical Methods for Multiphase Flows*, FED-Vol. 91, University of Toronto, Ontario, Canada, June 1990, pp. 35-45.

15. Raabe, O. G., "The Generation of Aerosols of Fine Particles," in *Fine Particles - Aerosol Generation, Measurement, Sampling, and Analysis*, edited by Liu, B. J. H., Academic Press, New York, 1976, pp. 60-110.

16. Dopheide, D., and Durst, F., "High Speed Velocity Measurements Using Laser Doppler Anemometers," in *Laser Velocimetry and Particle Sizing*, Purdue University, West Lafayette, Indiana, July 1978, pp. 357-368.

17. Melling, A., "Further Developments in Laser Anemometry," in *VKI Lecture Series 1981-03, Laser Velocimetry*, von Karman Institute for Fluid Dynamics, Belgium, Feb. 1981.

18. Wang, J. A., and Dancey, C. L., "High-Velocity Measurements via Laser Doppler Anemometer Using Single- and Multiaxial-Mode Lasers," *AIAA Journal*, Vol. 30, No. 9, Sept. 1992, pp. 2343-2344.

19. Maurice, M. S., "A Method to Quantify and Correct Particle Velocity Bias in Laser Velocimetry Measurements," AIAA Paper 92-0764, Jan. 1992.

20. Samimy, M., Abu-Hijleh, B. A. /K., and Bhattacharyya, S., "Performance of Laser Doppler Velocimeter with Polydisperse Seed Particles in High Speed Flows," AIAA Paper 88-0425, Jan. 1988.

21. Crowe, C. T., "Drag Coefficient of Particles in a Rocket Nozzle," *AIAA Journal*, Vol. 5, No. 5, May 1967, pp. 1021-1022.

22. Cunningham, E. A., *Proc. Roy. Soc*, Vol. 83A, 1910, p. 357.

23. Haertig, J., "Die Partikeln in der Laseranemometrie," Institut Saint-Louis, CO 203/79, Feb. 1979.

24. Rudinger, G., "Fundamentals and Applications of Gas-Particle Flow," in *Flow of Solid Particles in Gases*, edited by Rudinger, G., and Auriol, A., Vol. AGARD-AG-222, Oct. 1976, pp. 55-86.

25. Fuchs, N. A., "The Mechanics of Aerosols," MacMillan, New York, 1964.

26. Bertuccioli, L., and Degrez, G., "Application of LDV to Supersonic Laminar Boundary Layer Flows," AIAA Paper 93-3069, July 1993.

27. Chapman, D. R., and Rubesin, M. W., "Temperature and Velocity Profiles in the Compressible Boundary Layer with Arbitrary Distribution of Surface Temperature," *Journal of Aeronautical Sciences*, Vol. 16, No. 9, Sept. 1949, pp. 547-565.

28. Van Driest, E. R., "Investigation of Laminar Boundary Layers in Compressible Fluids Using the Crocco Method," NACA-TN-2597, 1952.

29. Leprince, F., and Riethmuller, M. L., "Skin Friction Determination by LDV Measurements in a Viscous Sublayer - Analysis of Systematic Errors," von Karman Institute for Fluid Dynamics, Belgium, VKI-TN-156, Dec. 1985.

30. Meyers, J. F., "Biasing Errors and Corrections," in *VKI Lecture Series 1991-05, Laser Velocimetry*, von Karman Institute for Fluid Dynamics, Belgium, June 1991.

31. Spazzini, P. G., Private communication, 1993.

32. Bertuccioli, L., "Improvement and Validation of an LDV System to Perform Measurements in Supersonic Flows," von Karman Institute for Fluid Dynamics, Belgium, VKI-PR-1992-16, June 1992.

Aerodynamic Investigation of the Flow Field in a 180 Degree Turn Channel with Sharp Bend

Guido RAU, Tony ARTS

Turbomachinery Department – von Karman Institute for Fluid Dynamics

Chaussée de Waterloo,72

B-1640 Rhode Saint Genèse

Belgium

1 ABSTRACT

The internal cooling of gas turbine blades is generally ensured by secondary air flowing through narrow passages existing inside the airfoils. These internal channels are usually connected by 180 deg turns with sharp bends. The aerodynamic and associated convective heat transfer characteristics observed in this type of geometry are significantly influenced by strong secondary flows and flow separations. The purpose of the present experimental effort is to give a detailed description of some aerodynamic aspects of this particular flow pattern. Detailed measurements of the three-dimensional velocity field were performed by means of a two-component Laser Doppler Velocimeter. The third velocity component was obtained by repeating the measurements at two different orientations of the emitting optics with respect to the test section.

2 INTRODUCTION

Further improvements in the performance of modern aeroengine components require a detailed and rigorous optimization of their design. In the area of high pressure turbines, the development and validation of computer programs allowing a very accurate prediction of the metal temperature are of crucial importance in order to guarantee the life time of the disks, blades and endwalls. The definition of accurate and representative test cases dealing with the aero-thermal performances of the different turbine components therefore remains a major task (Refs. 1, 2). It is one of the principal motivations for the work presented hereafter.

The classical way to improve the thermal efficiency of a gas turbine cycle is to increase the turbine entry temperature. The present HP turbine first stages mostly operate at a gas temperature much higher than the metal melting temperature. They therefore require efficient cooling schemes. One of the first techniques applied to cool turbine blades was internal forced convection. The cooling air is introduced through the hub section into the vane or blade interior and, following complicated serpentine passages, is blown out at the tip or through the trailing edge. This technique is still heavily used in combination with impingement and film cooling. An efficient design of these internal passages requires the complete understanding of the thermal and aerodynamic phenomena developing in such flows. This is even more critical when remembering that these serpentine channels are most of the time roughened with different types of ribs and pin fins to enhance the convective heat transfer rates.

A detailed investigation on a two-pass flow passage with smooth walls and a 180 degree turn with sharp bends

was therefore initiated. Detailed convective heat transfer coefficient distributions and preliminar aerodynamic results obtained in the same test section were presented in an earlier paper (Ref. 3). The present configuration is quite similar to the one used by a number of authors. Nevertheless, previous investigations (Refs. 4 - 9) on this subject often provide incomplete information on the aerodynamic characteristics of the flow. The computation of this type of flow has also been presented by a number of investigators (Refs. 10 - 13). Research still needs to progress in this area.

As already mentioned, the main objective of this work is to describe, for this known configuration, detailed local aerodynamic measurements in order to contribute to a better understanding and to the development of a data base for this type of flow. The measurements reported in the present contribution were taken in an undisturbed, smooth channel. Detailed measurements of the three-dimensional velocity field were performed by means of a two-component Laser Doppler Velocimeter. The third velocity component was obtained by repeating the measurements at two different orientations of the emitting optics with respect to the test section.
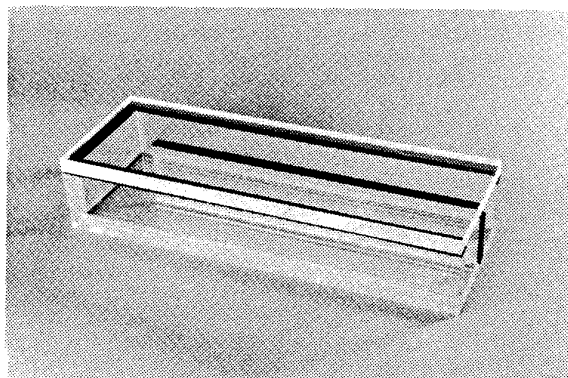

Fig. 1: 180 deg turn channel

3 DESCRIPTION OF THE MODEL

The 180 degree turn channel walls (Fig. 1) were manufactured from 15 mm thick transparent plexiglass plates and assembled with nylon bolts. A squared cross section was considered ; its hydraulic diameter was 50 mm. The overall dimensions of the test channel were 400 mm (length) × 110 mm (width) × 50 mm (height).

The air flow was aspirated at atmospheric pressure and room temperature through an inlet duct, the test chan-

nel, an outlet duct and a settling chamber by means of a small centrifugal blower. The reference velocity was controlled within the center of the test channel exit section with the help of a small Pitot probe connected to a Validyne pressure transducer. All the measurements were performed for a Reynolds number value (Re_D), based on the hydraulic diameter of the channel, equal to $3.5\ 10^4$. The velocity and turbulence fields were determined within the completely transparent test channel with the help of a two-component Laser Doppler Velocimeter system loaned by DANTEC Measurement Technology A/S. These measurements were repeated from two orthogonal directions in order to obtain, with the exception of one component of the Reynolds stresses, a three-dimensional description of the velocity field.

4 VELOCITY AND TURBULENCE DISTRIBUTIONS

4.1 Experimental apparatus

A two-component FiberFlow Laser Doppler Velocimeter system, graciously loaned by DANTEC was used to obtain, in two successive steps, the three-dimensional velocity and turbulence fields in the test channel. This system combines the accuracy of Laser Velocimetry with the flexibility of fibre optics. Today, fibre optics is a well established technology, which has also found use in Laser Doppler Velocimetry. The optical measurement chain, mounted on a DANTEC optical bench, was made of :

- a 4 W Ar-Ion Laser operated in multi-color mode (blue and green are used for the two velocity components)
- a 60X40 Transmitter Unit including a 40 MHz Frequency Shifter
- four 60X24 Manipulators connected by fibre cables to a 60X11 60 mm diameter two-dimensional probe
- three different front lenses (focal lengths = 600, 400, 310 mm). Smaller focal lengths were not available at that time and made measurements close to the walls quite difficult to perform.
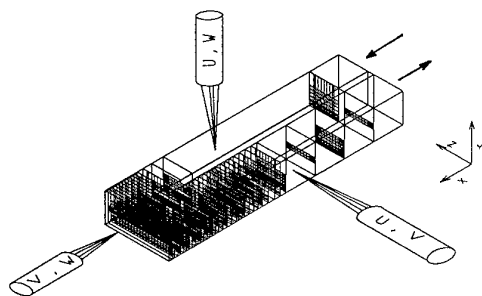- two Photomultipliers with a Color Separator, connected by a single fibre cable to the probe

Fig. 2: Laser probe position and measurement grid

The averaged size of the probe volume for the different lenses was of the order of 200μm / 3.2 μm / 4.7 μm. The Doppler signals were processed by means of two DANTEC Burst Spectrum Analysers (BSA). This approach is based on the use of a Fast Fourier transformation as the method to extract the Doppler frequency. Both Burst Spectrum Analysers were computer controlled via an IEEE-488 interface. A powerful software package provided user friendly facilities for functional tests, setup parameter control, control of data transfer, measurement control, computation of essential flow quantities such as mean value, turbulence and normal and shear stresses, and presentation of results in the form of tables and histograms.

4.2 Measurement strategy and grid

The measurements were repeated for two different orientations of the laser beams with respect to the model. The longitudinal (x) U and lateral (z) W velocity components (Fig. 2) were obtained by installing the main axis of the emitting optics perpendicularly to the bottom wall of the channel (plane y = 0) whereas it was aligned with the main axis of the channel to determine the lateral (z) W and vertical (y) V components.

In order to avoid as much as possible the problems of direct reflections and "wall cut-off" of one of the beams when measuring closely to the wall, an additional inclination of the emitting optics by 2 to 3 deg was also realized. A suitable transformation of coordinates was then necessary to correctly determine the V and W velocity components.

A very dense measurement grid was established to obtain a detailed description of the flow field: more than 5000 measurement points were considered in the test matrix. The measurement grid is presented in Fig. 2.

Six hundred samples were taken in each measurement point, unless a maximum sampling time of 4 sec was exceeded. As the averaged data rate was about 400 data/sec, the averaged sampling time was of the order of 1.5 sec. Successive measurements revealed that eventual blower fluctuations were below this time scale.

4.3 Seeding

The seeding was provided at the entrance of the test section. It resulted from the condensation of a propylene/glycol mixture. A quantitative determination of the particle size distribution revealed that 95 % of the particles had a diameter below 1 μm (Fig. 3). It was therefore assumed that the seeding distribution was as homogeneous as possible.
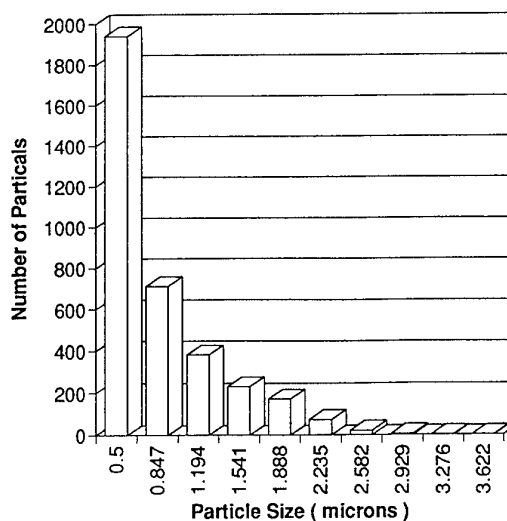

Fig. 3: Seeding particle size distribution

4.4 Measurement uncertainty

In order to take the velocity bias into account, a correction based on Ref. 14 was applied. This correction is based on the residence time of the particle in the probe volume and provides correct statistical results for all data rates, even for highly turbulent flows.

The uncertainty on the position of the measurement point, based on a 20:1 confidence level, was estimated to be of 0.5 mm in the x direction and 0.1 mm in the y and z directions. The overall uncertainties on the velocity and on the Reynolds stresses were respectively estimated at 6 % and 9 %. Repeatability was found to be of the order of 0.1 %. An averaged difference of 0.2 m/s was found when determining a velocity component from 2 different orientations (section 3.2).

4.5 Inlet conditions

The averaged flow velocity in the inlet section was 10 m/s. It corresponded to a Reynolds number value (Re_D) equal to $3.5 \ 10^4$. The inlet velocity profile (Fig. 4) was almost symmetric, although slightly higher velocities were observed close to the dividing wall. This phenomenon resulted from a small asymmetry of the inlet channel, upstream of the test section. The flow field in the latter did however not seem to be significantly influenced by this phenomenon. The averaged inlet turbulence intensity was about 6 %.
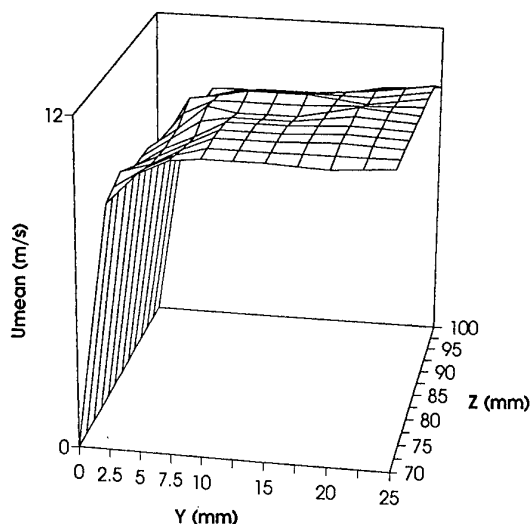

Fig. 4: Inlet velocity profile

4.6 Measurements - Results - Discussion

A complete and detailed description of all the features of this rather complicated flow goes largely beyond the scope and the size of this paper. The present discussion will therefore focus upon three particular aspects of the flow field : the separation bubble identified along the dividing wall, the flow in the first corner of the bend and the growth and decay of the secondary vortices observed in the return channel. The complete set of results (velocity components, rms-values and turbulence intensities in all measurement points) is available upon request.

4.6.1 Separation bubble downstream of the dividing wall

Figs. 5, 6 and 7 present the velocity vectors (x and z components) measured within three different "y = constant" planes respectively located at y = 2.5, 7.5 and 25 mm, i.e. the symmetry plane, from the bottom surface.
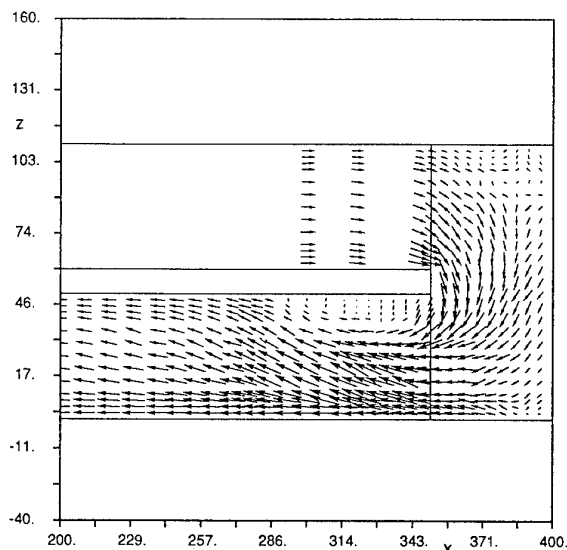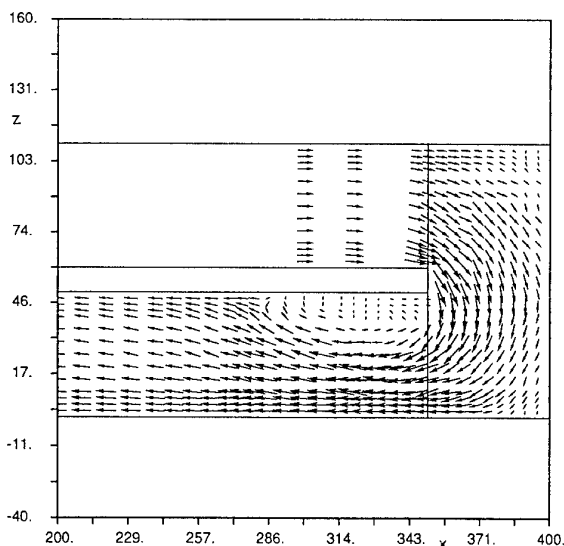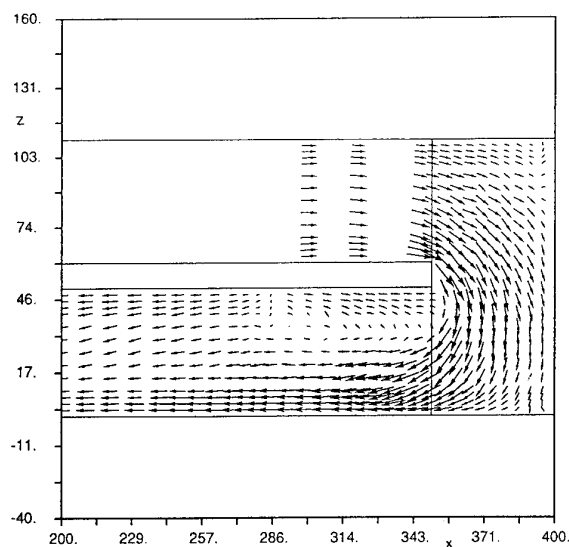

Fig. 5: UW vector plot at y = 2.5 mm

Fig. 6: UW vector plot at y = 7.5 mm

The expected recirculation bubble, developing downstream of the tip, along the dividing wall, is clearly identified. Due to the small aspect ratio of the channel and the residual turning effects, this separated region is expected to be highly three-dimensional (Ref. 5). To the authors best knowledge, its detailed description was however not yet presented in the open literature. The longitudinal and maximum lateral extensions of the bubble definitely vary along the channel height. The latter ranges from about 30 % of the hydraulic diameter for y = 2.5 mm to about 50 % of the same reference length in the symmetry plane. It is observed in a transversal section (yz plane) located at about half an hydraulic diameter downstream

Fig. 7: UW vector plot at y = 25 mm

Fig. 11: VW vector plot at x = 350 mm

of the tip. The position of the reattachement line on the dividing wall moves downstream with increasing y values, ranging between 110 % (at y = 2.5 mm) and 130 % (in the symmetry plane) of the hydraulic diameter. This recirculation bubble clearly presents a three-dimensional nature. The present results are in complete agreement with those obtained from earlier heat transfer and flow visualization experiments performed on the same model (Ref. 3).

The widening of the separation bubble can also be explained with the help of Fig. 11 (yz plane at x = 345 mm in the return channel); it demonstrates the entrainment of low momentum material towards the external lateral wall.

The turbulence intensities measured in the three xz planes at y = 2.5, 7.5 and 25 mm are presented in Figs. 8, 9 and 10. Identical conclusions are drawn about the three-dimensional development of the bubble. A high turbulence spot, whose intensity is of the order of 45 to 50 %, also spreads when moving towards the symmetry plane. Its location close to y = 0 mm coincides with that of a high heat transfer rate, due to the impinging nature of the flow (see also Fig. 5). Let us finally remark that, within the bubble, the turbulence intensity remains of the order of 15 %.

4.6.2 Flow in the first corner of the 180 deg bend

A first stagnation line is located on the endwall of the bend (yz plane at x = 400 mm), just downstream of the first corner. It results from the impingement on this endwall of the flow developing along the entrance channel. Both V-rms distributions and heat transfer coefficient results (Ref. 3) tend to indicate that this line is located at about z = 95 mm. Between this line and the lateral external wall of the entrance channel, experimental evidence indicates that the flow is deflected from the symmetry plane towards the bottom surface and that a return flow is observed along the latter. A second return flow region extends almost over half of the endwall of the bend close to the bottom wall. It appears to coincide with the observable origin of the "passage vortex" to be discussed in the next section.

These arguments are supported by Fig. 12, indicating important RMS values for the U velocity component, close
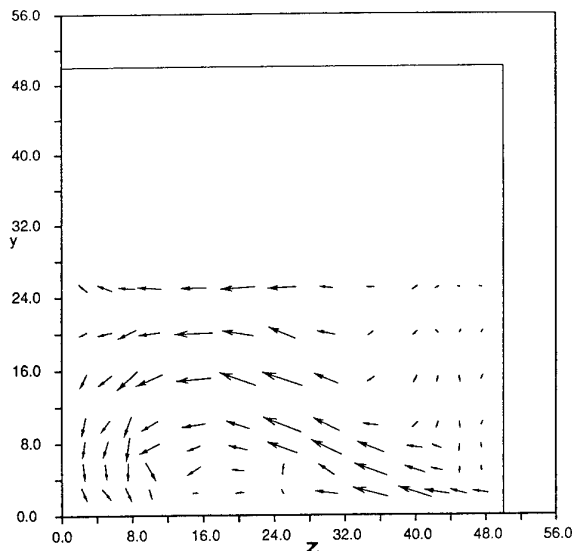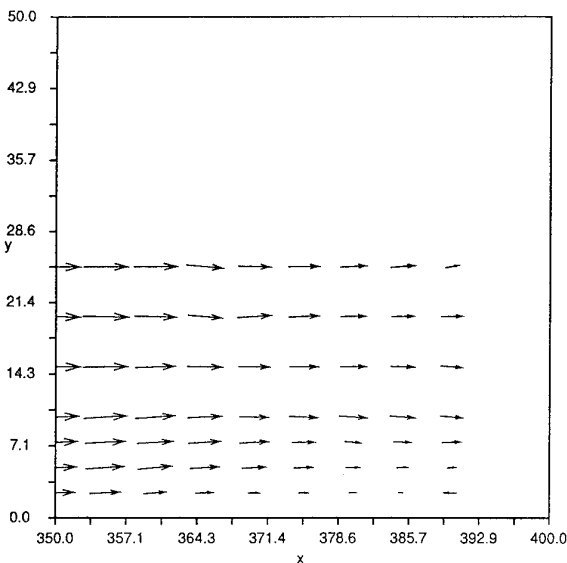
Fig. 15: UV vector plot at z = 70 mm

to the bottom wall in the considered corner, as well as by Fig. 15 presenting a U and V velocities vector plot in a xy plane located at z = 70 mm, i.e. at about half the width of the entrance channel. The negative U component is clearly visible in the endwall/bottom corner.

This low momentum return flow is strongly influenced by the pressure gradient existing between the outer and dividing walls. The air is dragged towards the low pressure tip region of the dividing wall. This is shown by the gradual shift along the bottom wall of the high Urms regions in successive yz planes at x = 390, 380 and 370 mm (Figs. 12, 13 and 14) and in Fig. 16. The latter presents the Urms values in the closest xz measurement plane (y = 2.5 mm) to the bottom wall. The shape of these isolines is an almost perfect copy of the iso-heat transfer coefficient distributions presented in Ref. 3.
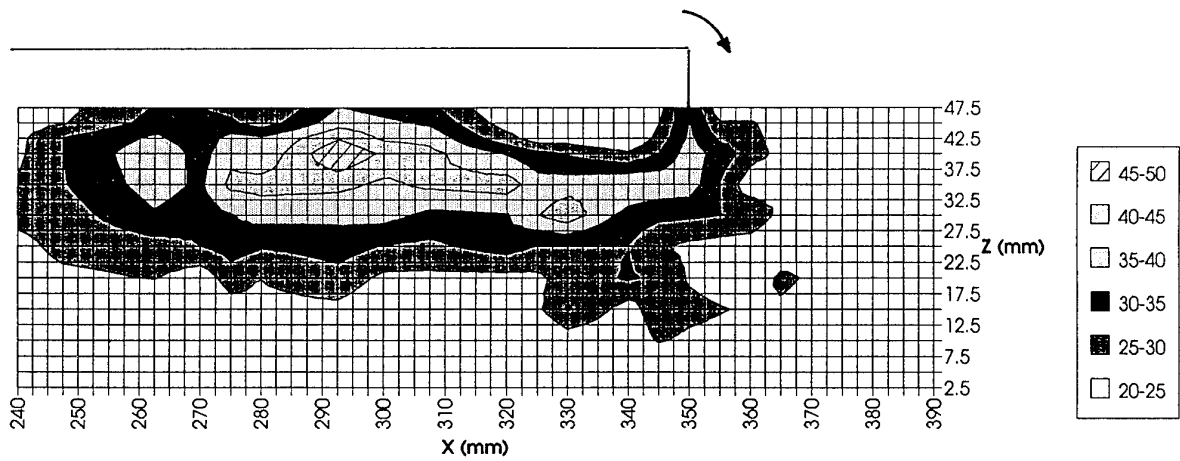
Fig. 8: Tu intensity at y = 2.5 mm
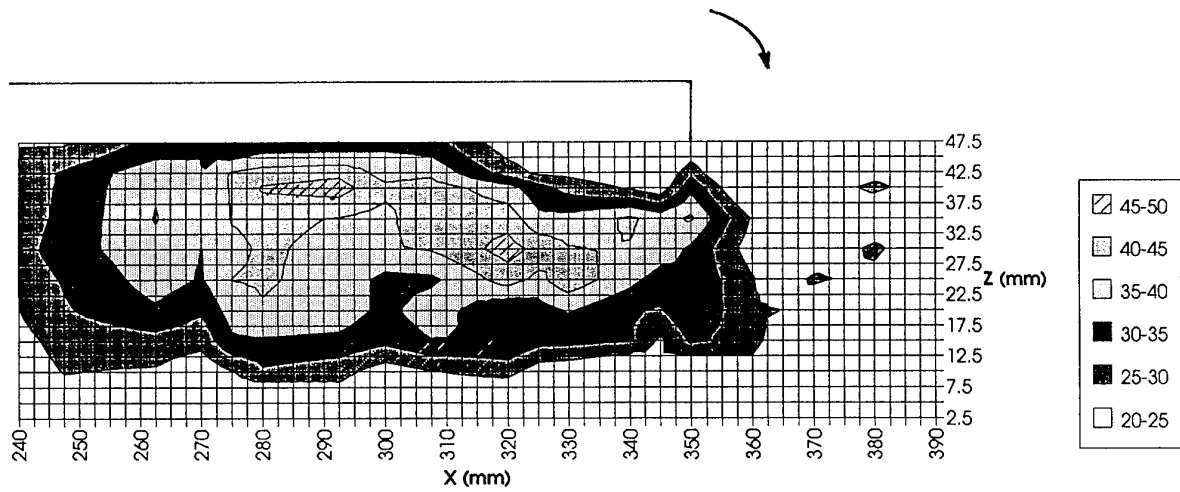
Fig. 9: Tu intensity at y = 7.5 mm
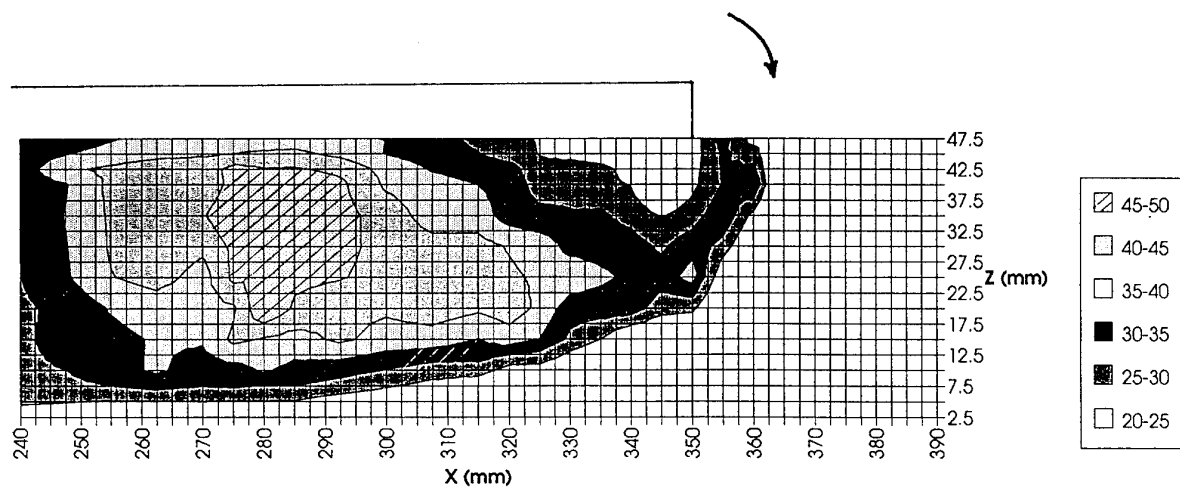
Fig. 10: Tu intensity at y = 25 mm
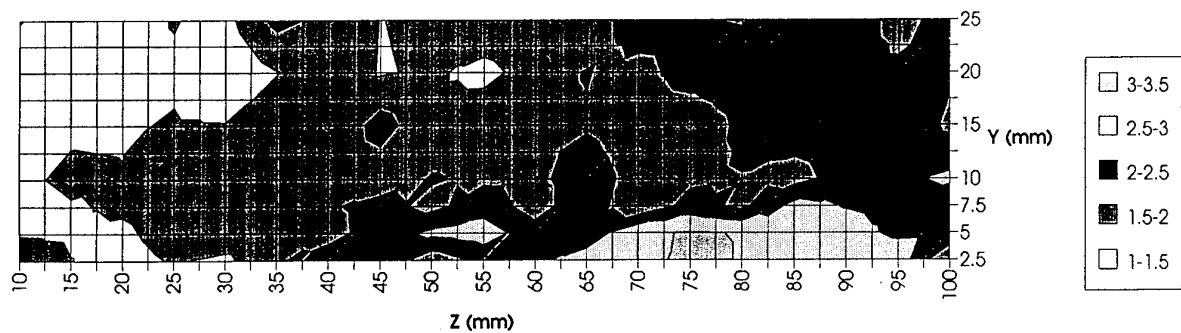
Fig. 12: Urms (m/s) at x = 390 mm
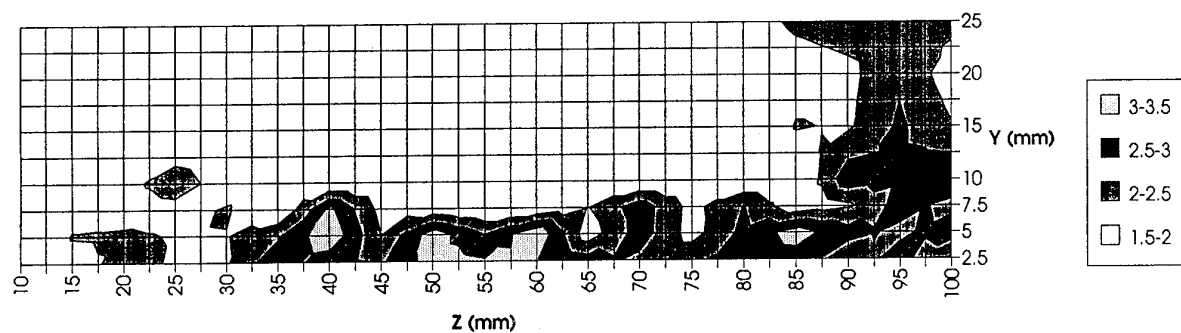
Fig. 13: Urms (m/s) at x = 380 mm
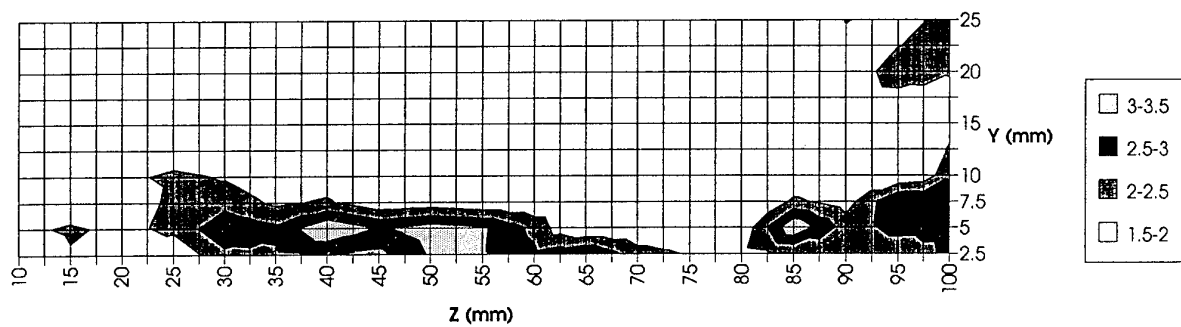
Fig. 14: Urms (m/s) at x = 370 mm
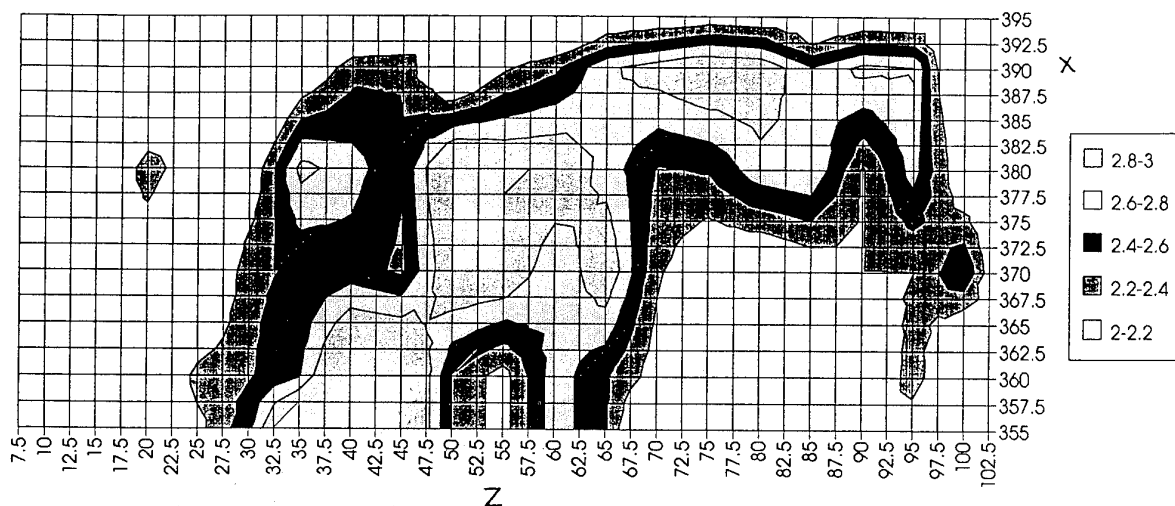
Fig. 16: Urms (m/s) at y = 2.5 mm
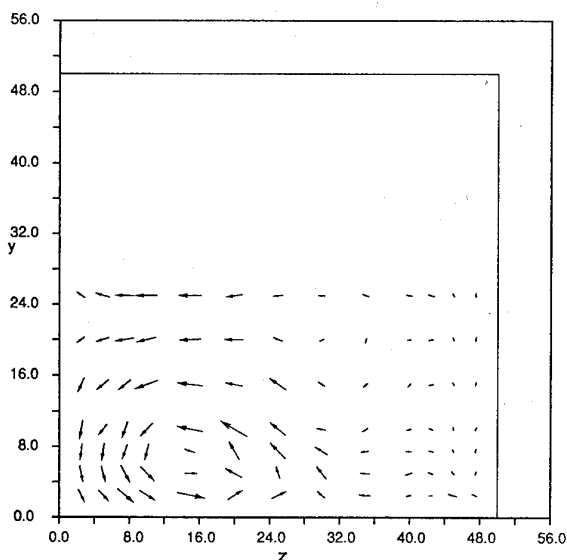
Fig. 17: VW vector plot at x = 340 mm
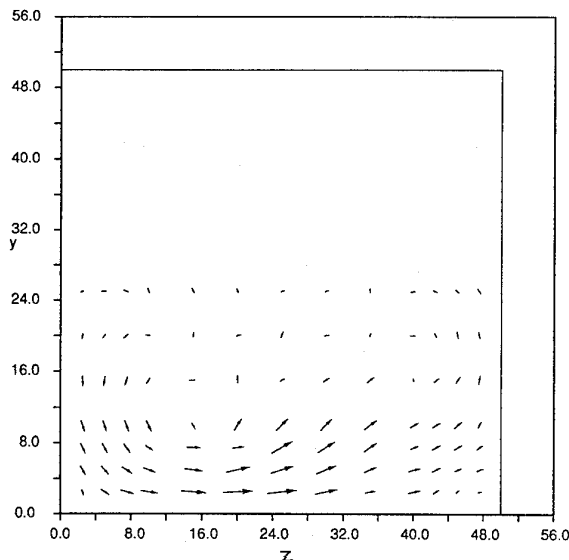
Fig. 18: VW vector plot at x = 300 mm

4.6.3 Existence of the passage vortex

The presence of the bend is responsible for the existence of strong secondary effects. The flow structure is mainly determined by the local unbalance existing, within the boundary layer, between the pressure gradient and the centrifugal forces. Two strong "passage" vortices are observed, mainly in the return channel. In order to quantify the importance of this phenomenon from an aerodynamic point of view, the "zone of influence" of these vortices is interesting to be determined.

Experimental evidence shows that the vortices start to appear at about 90 degree in the bend. This result was obtained both from smoke visualizations as from velocity vector plots. Each vortex first remains close to its bottom surface, and favours an earlier reattachement of the separation bubble. Further downstream, the passage vortices gradually evolve from their initial elliptic shape to a more and more circular one. Their strength decreases and an inward motion of their center is observed downstream of the separation region.

These arguments are supported by Figs. 17, 18 and 19. They show VW vector plots in sections located at x = 340 mm (i.e. just downstream of the dividing wall), 300 mm and 200 mm (i.e. 1 and 3 hydraulic diameters farther). It finally appears that the vortical motion has almost vanished in the last plane.

5 SUMMARY - CONCLUSIONS

Detailed measurements of the velocity and turbulence fields were performed in a 180 deg turn channel with a sharp bend and smooth walls. Some important features of this complicated flow field were pointed out. They are in good agreement with earlier heat transfer measurements performed on the same model and already reported in the technical literature. The main goals of the present contribution were to gain a better physical understanding of the flow and to obtain reliable local values to eventually use them for detailed comparisons with computations applied to a similar geometry.
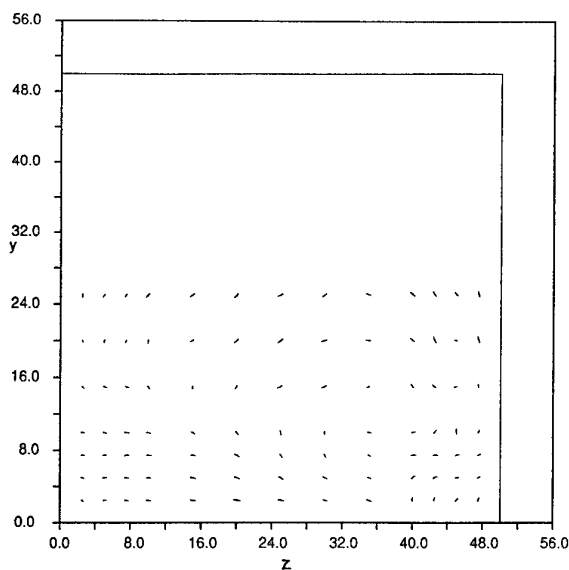
Fig. 19: VW vector plot at x = 200 mm

6 ACKNOWLEDGEMENTS

The authors wish to thank DANTEC Measurement Technology A/S to have made available the Laser Doppler Velocimetry measurement chain.

7 LIST OF SYMBOLS

D	Hydraulic diameter
Re	Reynolds number
rms	Root mean square
Tu	Turbulence intensity
U, V, W	Velocity components
x, y, z	Spatial coordinates

8 LIST OF REFERENCES

1. Fottner, L. (1989) : Overview on test cases for computation of internal flows in turbomachines. ASME Paper 89-GT-46.

2. Fottner, L.. ed. (1990) : Test cases for computation of internal flows in aeroengine components. AGARD Advisory Report 275.

3. Arts, T.; Lambert de Rouvroit, M.; Rau, G.; Acton, P. (1992) : Aero-thermal investigation of the flow developing in a 180 degree turn channel. Int. Symp. on Heat Transfer in Turbomachinery, Athens, Greece

4. Metzger, D.E. & Samh, M.K. (1986) : Heat transfer around sharp 180 degree turns in smooth rectangular channels. J. Heat Transfer, Vol 108, pp 500-506.

5. Chyu, M.K. (1989) : Regional heat transfer and pressure drop in two-pass and three-pass flow passages with 180 degree sharp turns. ASME Paper 89-GT-191.

6. Fan, C.S. & Metzger, D.E. (1987) : Effects of channel aspect ratio on heat transfer in rectangular passage sharp 180 deg turns. ASME Paper 87-GT-113.

7. Metzger, D.E.; Fan, C.S.; Plevitch, C.W. (1988) : Effect of transverse rib roughness on heat transfer and pressure losses in rectangular ducts with sharp 180 degree turns. AIAA 26th Aerospace Science meeting, Reno, Nevada.

8. Boyle, R.J. (1984) : Heat transfer in serpentine passages with turbulence promoters. ASME Paper 84-HT-24.

9. Han, J.C.; Chandra, P.R.; Lau, S.C. (1988) : Local heat/mass transfer distributions around sharp 180 deg turns in two-pass smooth and rib-roughened channels. J. Heat Transfer, Vol 110, pp 91-98.

10. Murthy, J.H. & Chyu, M.K. (1987) : A numerical study of laminar flow and heat transfer in a channel with 180 deg bend. ASME Paper 87-HT-7.

11. Wang, T.S. & Chyu, M.K. (1992) : Influence of turning geometry on convective transport in a square duct with a 180 degree sharp turn. Int. Symp. on Heat Transfer in Turbomachinery, Athens, Greece

12. Iacovides, H. & Launder, B.E. (1985) : ASM predictions of turbulent momentum and heat transfer in coils and U-bends. Proc. 4th Int. Conf. on Numerical Methods in Laminar and Turbulent Flows, Swansea, U.K.

13. Iacovides, H. & Launder, B.E. (1992) : The computation of convective heat transfer in a 180 degree pipe bend. Int. Symp. on Heat Transfer in Turbomachinery, Athens, Greece

14. Buchhave, P.; von Benzon, H.H.; Rasmussen, C.N. (1990) : LDA bias : comparison of measurement errors from simulated and measured data. 5th Int. Symp. on Application of Laser Techniques to Fluid Mechanics, Lisbon, Portugal.

Technique expérimentale de mesure en écoulement transsonique avec un système de vélocimétrie laser tridimensionnel. Application à la détermination de la traînée d'un fuselage

A. SERAUDIE   A. MIGNOSI   J.B. DOR   S. PRUDHOMME

*CERT*DERAT

Centre d'Etudes et de Recherches de Toulouse
Département d'Etudes et de Recherches en Aéro-Thermodynamique
2, avenue Edouard Belin 31055 TOULOUSE cedex
FRANCE

Abstract

Recent developments in laser anemometry have been used to design a three dimensional laser system which is in operation at the CERT ONERA's T2 wind tunnel since December 1989 : fiber optics (to lead the light between the source and the emitting optics), Fast FOURIER Transform Doppler processors (to analyse the Doppler signals), high power transmission system (to provide color separation), digital control of displacement motors and real time operation (to move the measuring point during the run). This device works well for the short run times of the T2 wind tunnel, providing a good accuracy which allows 30 to 50 measurement points during 60 to 120 seconds of the test.

After a complete description of the 3D laser velocimetry system, the present paper will develop some typical measurements which have been performed. For each case we will present some test results obtained under transonic conditions:
- shock wave probing : shape and location on the upper side of a 2D transonic model
- 3D velocity measurements in forward and backward scatter configurations with the wall approach for areas without good accessibility.

In order to obtain the drag of a fuselage, a vertical plane located dowstream of the model was measured with two devices

- laser velocimetry in order to obtain the three components of velocity
- pressure rake providing the static and total pressures.

The combination of these tmeasurements (pressure and velocity) alowed the calculation of the total drag of the 3D model.

Résumé

Les développements récents de nouvelles technologies en matière de vélocimétrie laser, ont été utilisées pour concevoir et définir le banc tridimensionnel de la soufflerie T2 du CERT-ONERA à TOULOUSE, en fonctionnement depuis la fin de l'année 1989. Les fibres optiques monomodes (conduisant la lumière entre la source laser et les optiques d'émission), les B.S.A. (analyseurs de spectre par transformée de Fourier) pour traiter les signaux Doppler, la boîte de couplage haute puissance (séparant les différentes couleurs) et le contrôle en temps réel de déplacement du banc par le calculateur de la soufflerie, sont les particularités techniques de cette installation. Cet outil, bien adapté aux rafales courtes de T2, permet d'obtenir 30 à 50 points de mesure pendant les 60 à 120 secondes que dure l'essai.

Après la description complète du banc, ce papier s'attachera à présenter les différents types de mesure qui ont été effectuées en donnant dans chaque cas un exemple précis :
- traversée de choc afin de connaître sa forme et sa position en bidimensionnel
- explorations tridimensionnelles en diffusion avant et rétrodiffusion avec approches de paroi.

Enfin, dans le but d'obtenir la traînée totale d'un fuselage d'avion de transport moderne nous avons combiné les résultats d'explorations de sillage obtenus à partir de :
- vélocimétrie laser donnant les trois composantes instantanées de la vitesse
- sondages de pression donnant les distributions de pression d'arrêt et statique.

La combinaison de ces deux informations nous a permis de calculer le coefficient de traînée totale expérimentale dans le cas d'un écoulement tridimensionnel.

1. INTRODUCTION

La soufflerie transsonique T2 (fig.1) est généralement utilisée pour les possibilités qu'elle a de faire varier le nombre de Reynolds en augmentant sa pression et diminuant sa température génératrice ; la vélocimétrie laser dont on parlera ici, n'a été utilisée jusqu'ici qu'à température ambiante.

T2 fonctionne par rafales d'environ 60 secondes nécessitant des performances élevées du système de vélocimétrie, aussi bien pour l'acquisition des données que pour le pilotage du système de déplacement. Pour satisfaire les performances souhaitées (haut de la fig.3) avec une mise en oeuvre la plus simple possible, des techniques de pointe telles que fibres optiques et électroniques rapides ont été utilisées.

- **Transonic**
- **Pressurized**
- **Self - Adaptative Walls**
- **Cryogenic**

Usual range		
0.6 <	M_0	< 0.9
1.6b <	P_f	< 3b
110K <	T_f	< 290K
3×10^6 <	R_c	< 30×10^6
100mm <	Chord	< 200mm
	Run	
0.5' <	duration	< 2'
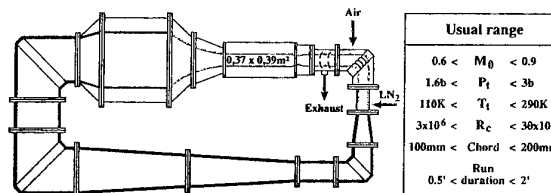
T2 Wind Tunnel   Fig. 1

L' ensemble de ce système (fig.2), équipé initialement d'un laser de 5 Watts, a été installé à la soufflerie T2 en décembre 1989 [1]. L'utilisation du vélocimètre en diffusion vers l'avant ne posait aucun problème fondamental, mais quelques essais en rétrodiffusion [4] avaient alors montré la faisabilité de ce fonctionnement à condition que la puissance lumineuse au volume de mesure soit supérieure à environ 100 mW par rayon.
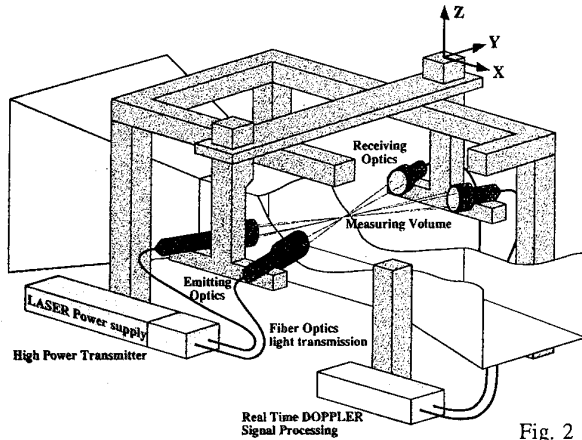

Fig. 2

Cette contrainte nous a conduit à remplacer l'ancien laser par un nouveau de 15 W et à nous équiper d'une nouvelle boîte de séparation des couleurs supportant cette puissance lumineuse. Cet ensemble a été mis en oeuvre en 1991 et 1992 pour l'étude d'écoulements autour de la partie arrière d'un fuselage et de son sillage dont quelques résultats seront présentés plus loin. Les premiers résultats ont été présentés au "Congrès français de vélocimétrie laser" à Meudon en 1990 [5] puis à Toulouse en 1992 [6].

2. DESCRIPTION DU BANC DE VELOCIMETRIE LASER 3D

Le vélocimètre laser est composé de trois sous ensemble : les parties optiques, le traitement des signaux, et les parties mécaniques.

ANEMOMETER CHARACTERISTICS

- Velocity range : -100 to 450 m/s
- Data acquisition : 60 to 90 s for 30 to 50 points
- Measurement accuracy : 1 m/s

TRAVERSING DEVICE :

- Displacements : X : 1.7m, Y : 0.4m, Z : 0.6m
- Positionning accuracy : ± 0.03 mm
- Displacement speed : 12 mm/s
    (+ 0.2 s for the starting and stopping phases)

OPTIC DEVICES :

- Argon laser source : power ligth 15 Watts
- High power transmitter :
    6 beams (3 colors), 6 Bragg cells,
    6 monomode optic fibers 10 m length
- 2 emitting optics and 2 receiving optics
    3 photodetectors
    Focal length : 800 and 600 mm
- Measuring volume diameter : 130 μm
    Interfringe : d = 5 μm

ELECTRONIC DEVICE : 3 B.S.A.

- 16 frequency bandwith : Δf from 977 Hz to 32 MHz
- 12 central frequency : Fc from 610 Hz to 64 MHz
- Samples number : N = 8, 16, 32, 64
- Accuracy on Fd : $64 \times 10^{-3} \times \Delta f/N$
- Synchronisation : measurement of arrival and
    transit times of each particule

Fig. 3

2.1 Description de la partie mécanique.

Le banc de déplacement suivant trois directions X,Y et Z qui est équipé de 5 moteurs de commande à courant continu pour 5 systèmes de translation (fig.2 et 3). Outre ces mouvements automatiques il existe des prépositionnements manuels, ainsi que des réglages grossiers et micrométriques des supports d'optiques d'émission et de réception. Les courses de déplacement sont de 1700 mm sur X, 400mm sur Y et 660 mm sur Z. Le positionnement relatif, a été contrôlé sur des courses de 400mm et l'on obtient finalement une précision de ± 0,03mm dans un cube de la veine de 400 mm de coté. Les pas élémentaires de déplacements sont de 0,25 microns, les vitesses de 12,5 mm/s, et les temps d'accélération inférieurs à 0.1 seconde [3]

L'ensemencement global de l'écoulement est réalisé par une injection de fumée d'huile dans le circuit retour de la soufflerie, la taille mesurée des gouttelettes est de l'ordre du micron.

2.2 Description du système optique actuel.

L'ensemble des composants optiques est schématisé sur les figures 2 et 4 [3]. Il comprend:
    - une source laser à argon Spectra-Physics 2040 qui fournit un rayon d'une puissance de 15 Watts sur l'ensemble des raies entre 450 et 515 nanomètres. Il est utilisée avec une ouverture de diaphragme proche de 7.
    - une boîte de transmission (fig.4) réalisée par la société Dantec, dont les fonctions essentielles sont, de séparer les couleurs du rayon multiraies provenant de la source laser, de décaler chacun des faisceaux en fréquence par six cellules de Bragg et de les envoyer vers les connecteurs des fibres optiques. Cette boîte a été testée à 15 watts et permet d'obtenir des puissances lumineuses importantes au volume de mesure comme indiqué sur le bas de la figure 4 avec un assez bon rendement optique.
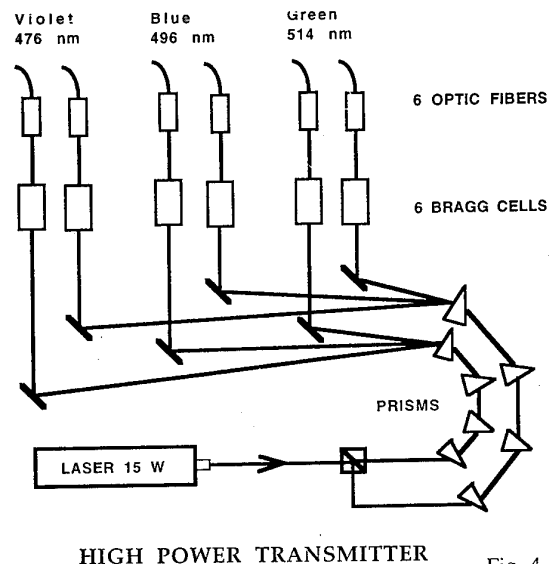
HIGH POWER TRANSMITTER   Fig. 4

    - six fibres optiques monomodes qui transmettent la lumière jusqu'aux optiques d'émission avec des rendements de l'ordre de 50%.
    - deux optiques d'émission, l'une bidimensionnelle qui comprend quatre rayons (2 bleus et 2 verts), l'autre monodimensionnelle qui utilise deux rayons violets. Ces deux optiques sont équipées de fibres de réception pour fonctionner en rétrodiffusion dans l'axe.
    - deux optiques de réception avec trois photodétecteurs (P.M.) .
    Les distances focales utilisées pour les essais étaient de 800 mm.

2.3 Réglages des parties optiques.

- Le croisement des six faisceaux au volume de mesure ($\Phi=0{,}13$ mm) est réalisé par la convergence des rayons dans un trou de 0.1 mm de diamètre en optimisant les anneaux de diffraction ainsi créés (symétrie, bonne luminosité et bon contraste). Ce réglage conditionne fortement la qualité des mesures: cadences, taux de validation, synchronisation, ... Un trou de référence est aussi utilisé pour le positionnement initial du banc servant de calage à toutes les explorations.

- Le réglage de la boîte de transmission s'effectue avec le laser à 15 W en maximisant la puissance que l'on mesure sur chaque rayon. Ces réglages sont stables sur plusieurs jours. Au cours des essais le laser n'est utilisé à 15 W que durant environ trois minutes par rafale (15 à 30 mn/jour).

- La mesure angulaire des 6 rayons en configuration de mesure est effectuée grâce à un théodolite ; cette référence angulaire est prise par rapport à la veine d'essais. Les incertitudes de mesure de ces angles sont faibles ($0{,}01°$), mais elles conduisent sur les vitesses longitudinale et verticale à quelques dixièmes de m/s d'incertitude, et plus du m/s sur la vitesse transversale.
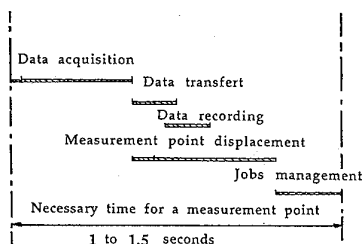
2.4 Description de l'électronique de traitement des signaux

Trois analyseurs de spectre par transformée de Fourier BSA permettent de traiter en temps réel les signaux, pour extraire la fréquence Doppler issue de chaque photomultiplicateur et de calculer grâce à l'étalonnage les trois composantes de la vitesse [3,4]. Les nombreux paramètres régissant le fonctionnement des BSA sont programmables et l'on peut retenir essentiellement que chaque BSA travaille dans une bande de fréquence donnée autour d'une fréquence centrale choisie. Sa précision est fonction de la bande d'analyse et du nombre de points d'échantillonnage choisis (fig.3).

Généralement les zones de l'écoulement explorées ont des niveaux de fluctuations non négligeables, il faut alors synchroniser les signaux acquis des photodétecteurs afin de garantir qu'ils proviennent de la même particule. Les acquisitions sont faites simultanément sur les trois voies en mesurant leur date d'arrivée afin de vérifier par un post traitement les critères de simultanéité et d'éliminer les mesures décalées dans le temps. Pratiquement si l'on se fixe un nombre de 2000 particules validées par chaque B.S.A. en chaque point de mesure, on en récupère en fait entre 900 et 1200 en diffusion avant et entre 200 et 600 en rétrodiffusion, synchronisées.

2.5 Mode de fonctionnement général

DIFFERENT PHASES FOR A MEASUREMENT POINT

Data acquisition
Data transfert
Data recording
Measurement point displacement
Jobs management
Necessary time for a measurement point

1 to 1,5 seconds

Data acquisition
500 ms for each BSA (2000 particules 4KHz)

Data transfert to the computer
150 ms (3 x 50 ms)

Data recording on magnetic tape
150 ms (3 x 50 ms)

Management of the different jobs
200 to 350 ms

Measurement point displacement
500 ms for 1mm

Fig. 5

L'organigramme des temps présenté sur la figure 5 donne les phases essentielles d'obtention d'un point de mesure: l'acquisition des données (0,5 s pour une cadence moyenne de 4 KHz), les transferts et stockages des informations (0,5 s), et le déplacement des volumes de mesure au point suivant (0,5 s). Le temps total nécessaire est essentiellement variable de 1 s à 2 s à cause des cadences d'acquisition évoluant avec les conditions d'essais : en diffusion vers l'avant, les taux d'acquisition atteignent 10 à 20 KHz, par contre en rétrodiffusion les cadences peuvent être inférieures à 1 KHz. Globalement dans une rafale de 60 s à 80 s on peut obtenir 30 à 50 points de mesure dans l'exploration d'un sillage ou d'une couche limite.

3. PRESENTATION DE RÉSULTATS EXPÉRIMENTAUX TYPIQUES.

3.1 Traversée d'une onde de choc stationnaire

Après la phase de démarrage, la première étude aérodynamique effectuée en collaboration avec la direction de l'aérodynamique à l'ONERA Chatillon, a porté sur les mesures autour du profil OAT15A [2]. L'écoulement a été analysé en bidimensionnel dans le plan de symétrie vertical de la veine, à l'extrados du modèle grâce à des sondages horizontaux et verticaux. Un test important pour le vélocimètre et l'ensemencement est constitué par la traversée d'une onde de choc. Les résultats obtenus en diffusion avant sont présentés à la figure 6 pour trois déplacements horizontaux ayant un pas entre point de mesure de 1 mm. L'onde de choc a pu être explorée sans difficulté et l'étalement mesuré, lié au ralentissement des particules, est très faible de l'ordre de 1mm.
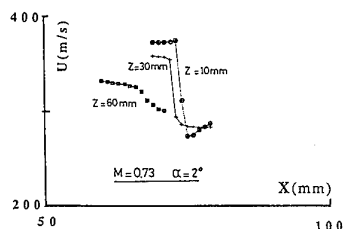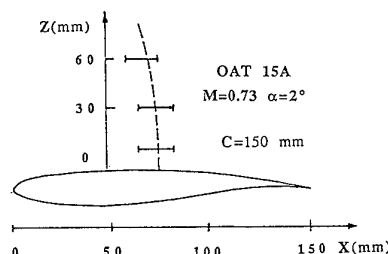
STEADY SHOCK WAVE PROBING   Fig. 6

3.2 Traversée d'une onde de choc oscillante

Sur un tel profil dans le domaine transsonique de vitesse, il suffit d'augmenter son incidence ou le nombre de Mach de l'essai pour que l'onde de choc d'extrados se mette à osciller périodiquement, on dit alors que la maquette entre dans la phase de tremblement. Sur un profil RA16 (180 mm de corde) à $M=0{,}725$ et $\alpha=2°$, ce régime a été atteint et l'on a pu, grâce à la vélocimétrie laser, avoir des informations sur la forme et l'amplitude d'oscillation de l'onde de choc [9]. Des explorations horizontales ont été effectuées à plusieurs altitudes au dessus de l'extrados de la maquette (5, 10, 35 et 60mm) et l'on a pu ainsi représenter schématiquement (fig.7) l'onde de choc en 10 points différents de la période d'oscillation ; le repère de phase était

donné par le signal d'un capteur de pression instationnaire placé à 40% de la corde. Ce résultat nous a permis de visualiser le comportement de l'onde de choc dans le phénomène de tremblement établi en bidimensionnel.

Fig. 7   Horizontal probings
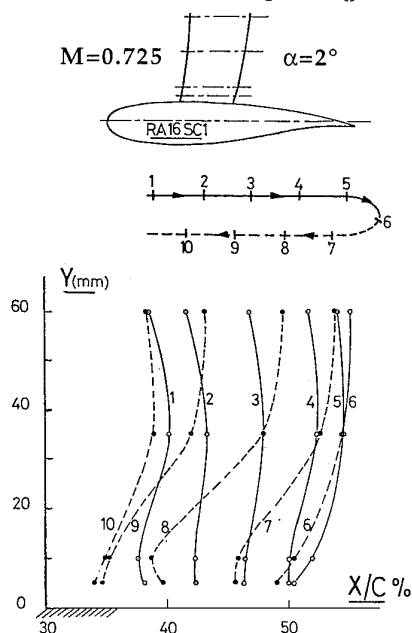
UNSTEADY SHOCK WAVE PROBING

3.3 Résultats sur les couches limites et le sillage d'un fuselage

Une application importante du banc de vélocimétrie laser 3D a porté sur l'analyse de l'écoulement transsonique tridimensionnel existant sur la partie arrière et le sillage d'un fuselage d'avion de transport. Le fuselage est maintenu près de l'axe de la veine par un mât dérive. Les parois adaptables qui équipent la soufflerie T2 sont positionnées pour annuler les interférences des parois et du support près de l'axe de la veine d'essai.

Une représentation schématique de la partie arrière du fuselage donne l'emplacement des sections dans lesquelles les mesures ont été faites (fig.8) :
- mesures de vitesse dans les couches limites et le sillage de la maquette,
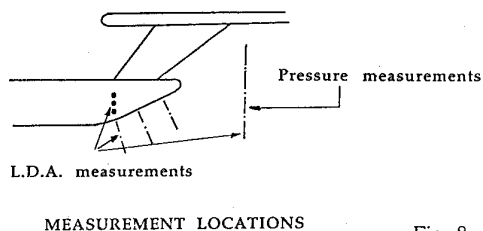- mesures de pression dans le sillage

3.3.1   Sondages des couches limites du fuselage en diffusion avant

Des profils de couche limite ont été mesurés en diffusion avant sur la génératrice basse du fuselage [6]. Les évolutions des profils de vitesse tangentielle et perpendiculaire à la paroi sont présentés à la figure 9. Les profils de vitesse normalisés par la vitesse extérieure   Ue s'épaississent en s'approchant du culot

arrière du fuselage. L' approche des parois en 3D est assez délicate et il est important de garder les six rayons laser le plus près possible du plan tangent à la surface. Ainsi l'impact d'un des rayons sur le fuselage qui éblouit les P.M. et arrête les mesures ne se produit que très près de la paroi. Avec cette condition on a pu s'approcher à environ 0,5 mm de la paroi.

Fig. 9

MEAN VELOCITY PROFILES ON THE LOWER SYMMETRY LINE
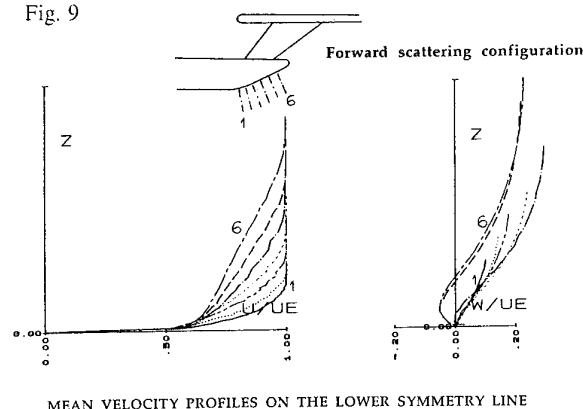
3.3.2   Approches des parois en rétrodiffusion 3D hors axe

Un sondage de couche limite de la génératrice inférieure en rétrodiffusion tridimensionnelle hors axe [6] et [8] (les P.M. étant situés à l'extérieur des optiques d'émission) a pu être effectué, la poutre support des optiques étant horizontale. L'ensemencement a été effectué au centre de la chambre de tranquillisation pour augmenter le nombre de particules localisées près de l'axe veine. Les 3 BSA ont fonctionné en mode maître avec des taux d'acquisition de 200 à 300 pt/s et un pourcentage de validation/détection variant de 25% pour le violet à 50% pour le vert.

Après synchronisation par logiciel le pourcentage de particules validées et synchronisées a atteint 15%, ce qui a permis d'obtenir un profil de couche limite que l'on a pu comparer à celui réalisé dans les mêmes conditions en diffusion avant. Les valeurs moyennes des trois composantes se recoupent de façon satisfaisante (fig.10), ainsi que les termes fluctuants. Le sondage effectué en rétrodiffusion s'arrête à 1,7 mm de la paroi lorsque les faisceaux issus des optiques horizontales interceptent le rétreint de la partie arrière de la maquette.

Fig. 10   —— Forward scattering configuration
              ---- Backward scattering configuration

MEAN VELOCITY PROFILES ON THE LOWER SYMMETRY LINE
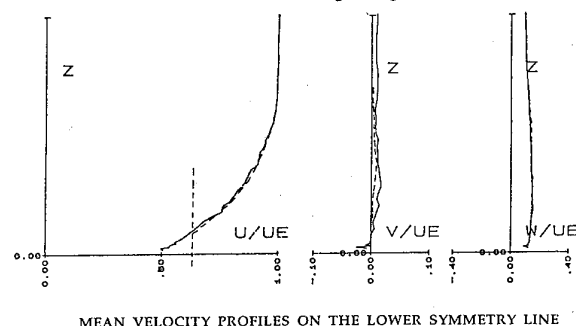
Après ce recoupement très satisfaisant sur la génératrice basse avec la diffusion vers l'avant, la rétrodiffusion a été utilisée pour explorer les couches limites se développant sur le fuselage. On donne un exemple de l'évolution azimutale des couches limites latérales dans une section déterminée du fuselage (fig.11). Les trois composantes moyennes de la vitesse sont données dans le repère local lié à la couche limite, w représentant la composante de vitesse normale à la paroi ; dans cette région de la maquette elles évoluent notablement avec la position azimutale du sondage. Dans ces explorations les approches de paroi étaient

essentiellement fonction de la position du sondage : des mesures correctes ont pu être obtenues jusqu'à presque 1mm de la paroi pour les explorations les plus basses et seulement 3 à 4 mm pour celles les plus perpendiculaires à la paroi.

Fig. 11

MEAN VELOCITY PROFILES FOR VARIOUS AZIMUTHAL LOCATIONS
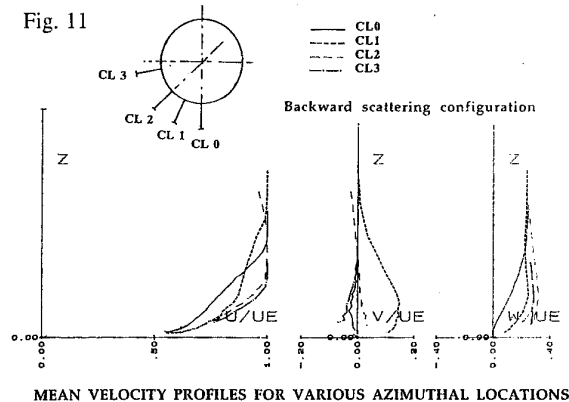
Sur la figure 12 on récapitule les différents types d'exploration qui ont été effectués du point de vue des approches de paroi. Les résultats font apparaître que plus l'approche des rayons du laser est tangentielle (angle faible par rapport à la paroi de la maquette), plus les mesures sont bonnes près de la paroi, aussi bien en rétrodiffusion qu'en diffusion vers l'avant. Lorsque les rayons arrivent presque perpendiculairement à la maquette, les mesures ne sont correctes qu'au delà de 3 ou 4mm de la paroi [7].

Fig. 12
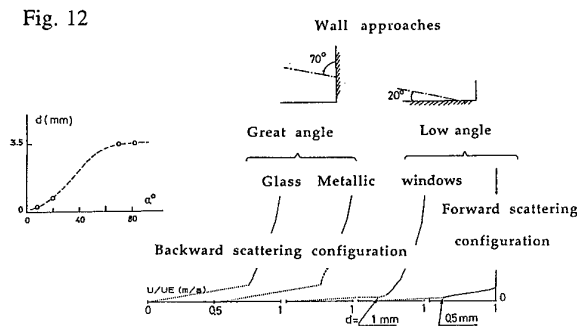
3.3.3 Résultats 3D dans le sillage d'un fuselage : mesures de vitesse

Des mesures de vitesse caractérisant le sillage ont été effectuées dans un plan vertical situé à l'aval du fuselage [6]. La grille d'exploration du vélocimètre est constituée d'un demi plan (l'écoulement étant symétrique) avec un maillage carré comportant environ 600 points. Ces mesures ont été faites en diffusion vers l'avant par des explorations essentiellement verticales donnant une trentaine de points de mesure à chaque rafale. Pour comparer aux nombres de Mach obtenus à partir des sondes de pression (fig.15) on détermine d'abord le module de la vitesse à partir des 3 composantes mesurées, le nombre de Mach étant ensuite calculé en supposant la température d'arrêt constante dans le sillage et égale à celle de la température génératrice de la veine.

Les vitesses secondaires (composantes transversales v et w) obtenues pour un autre cas par le vélocimètre sont présentées à la figure 13. La finesse de l'exploration laser met en évidence l'existence de deux tourbillons contrarotatifs probablement liés à la déportance de la partie arrière.

SECONDARY FIELD IN A 3D WAKE FLOW

Forward scattering configuration
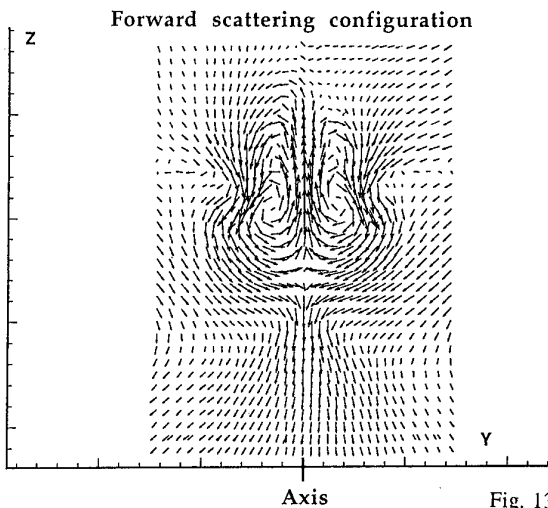
Fig. 13

3.3.4 Résultats 3D dans le sillage d'un fuselage mesures de pression

Un peigne de sillage spécifique à ces mesure a été réalisé de manière à obtenir le plus d'informations possible dans le sillage de la maquette en une seule rafale (fig.14). Il est constitué de 21 tubes de pression d'arrêt répartis en envergure, placés en quinconce sur deux lignes horizontales distantes de 15mm et de 7 sondes de pression statique disposées sur la ligne intermédiaire. La largeur totale du peigne couvre la totalité du sillage.

Front view

● 22 Pitot tubes

○ 7 Static tubes

Pressure rake for the wake measurements

Fig. 14

Ce peigne fournit au cours d'une seule rafale d'exploration du sillage, 200 points de mesures de pression statique et d'arrêt sur 21 lignes verticales. A partir de ces pressions on peut calculer le nombre de Mach de l'écoulement dans le sillage. Une comparaison entre les mesures de vitesse et de pression est présentée à la figure 15 sous forme de lignes iso-Mach montrant un bon accord entre les deux types mesures.

ISO-MACH CONTOURS IN A 3D WAKE FLOW

Pressure measurements (color levels)
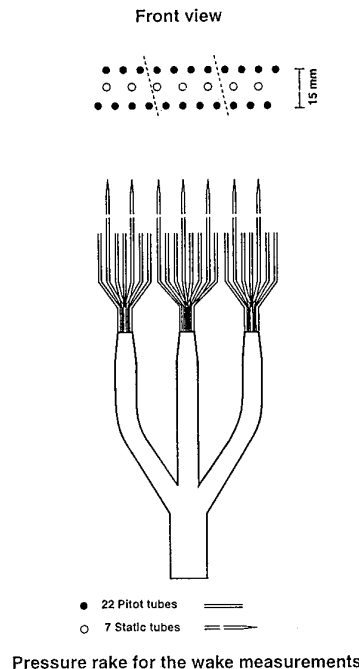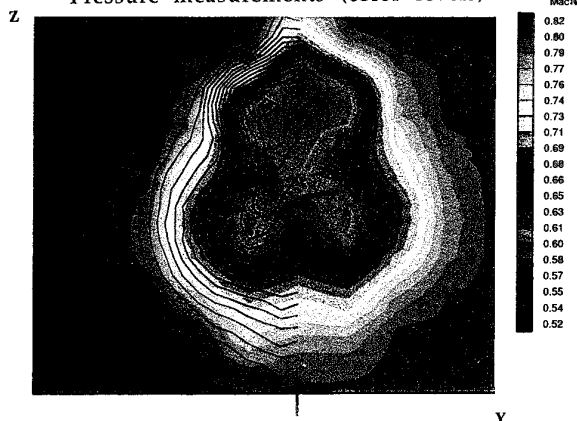

L.D.A. measurements (black lines)   Fig. 15

3.3.5 Combinaison des informations vitesse et pression

Le calcul de la traînée est basé sur un bilan de quantité de mouvement entre deux plans placés en amont et en aval de la maquette. Cette formulation fait intervenir la composante longitudinale de la vitesse u et la pression statique locale. Il est donc indispensable de procéder à des explorations de pression et de vitesse dans le sillage pour obtenir le plus rigoureusement possible la traînée expérimentale. La combinaison des sondages effectués avec le vélocimètre (une vingtaine d'essais) et ceux obtenus avec le peigne de pression (une seule rafale), a été réalisée pour obtenir la traînée totale du fuselage. L'inconvénient de ce procédé est qu'il demande un nombre important d'essais pour définir le champ de vitesse dans le plan de sillage.

A posteriori on a pu observer que les informations de pression seules, obtenues en une rafale à partir du peigne de pression, donnaient dans notre cas le coefficient de traînée de la maquette, à 1 à 2% près par défaut ; cet écart correspondant à des effets tridimensionnels. En faisant cette opération de "Cx bidimensionnel" on suppose que l'écoulement est peu tridimensionnel, que le vecteur vitesse est horizontal et l'on confond son module avec sa composante longitudinale.

Cette méthode a été utilisée à T2 pour obtenir un coefficient de traînée à chaque essai et pouvoir comparer dans une campagne d'essais le plus grand nombre de configurations. En fait chaque essai était répété un certain nombre de fois (3 à 5) afin de donner une fourchette réaliste de l'incertitude que l'on avait sur la détermination de la traînée expérimentale de la maquette; cette incertitude mesurée sur une campagne complète à partir d'une cinquantaine d'essais était d'environ DCx=$\pm$0.25 x 10-4, pour une configuration géométrique inchangée.

4 CONCLUSION

Le vélocimètre laser qui équipe la soufflerie transsonique T2 depuis décembre 89, a pu être utilisé et amélioré pour qualifier divers écoulements bi et tridimensionnels. Grâce à ces performances élevées, le système permet d'explorer de manière systématique en diffusion avant des écoulements tridimensionnels complexes du type sillage ou couches limites. Pour les zones qui ne sont pas accessibles en diffusion avant, la rétrodiffusion peut être utilisée et a été testée en tridimensionnel. Un effort reste cependant à faire pour améliorer la qualité et le nombre des signaux rétrodiffusés : ensemencement avec des particules plus grosses, réception hors axe, focales plus courtes, etc... Les approches tangentielles de parois en diffusion avant ou arrière ont pu être effectuées jusqu'à 0,6 mm, alors qu'en rétrodiffusion avec des faisceaux obliques la distance minimale est de l'ordre de 3 à 4 mm. L'utilisation du vélocimètre en cryogénie est envisagée, il semble que des hublots épais en silice puissent convenir pour permettre d'étudier, si l'ensemencement le permet, des écoulements à très grand nombre de Reynolds.

Ces mesures de vitesse, essentielles dans beaucoup de configurations aérodynamiques, n'éliminent pas celles de pression qui leur sont complémentaires dans un certain nombre de cas comme pour la mesure de la traînée totale d'une maquette tridimensionnelle.

Références

[1]   A. Séraudie, S. Prudhomme "Installation du banc de vélocimétrie laser 3D de la soufflerie T2." - Rap. Techn. DERAT n° 40/5606.23 - Mars 1990

[2]   A. Séraudie, S. Prudhomme "Application de la vélocimétrie laser à la soufflerie T2 : étude 2D de l'écoulement autour du profil OAT15A pour un bilan de traînée de choc." - Rap. Techn. DERAT n° 16/5017.19 - Juillet 1990

[3]   S. Prudhomme, A. Séraudie "Manuel d'utilisation du banc 3D de vélocimétrie laser de la soufflerie T2" - Rap. Techn. DERAT n° 43/5606.23 - Avril 1990

[4]   S. Prudhomme, A. Séraudie, M. Plazanet, M.J. Payry "Premiers essais d'optimisation du fonctionnement du banc de vélocimétrie laser 3D de T2. Mesures 3D, approches de paroi et rétrodiffusion." - Rap. Techn. DERAT n° 41/5606.23 - Août 1990

[5]   A. Séraudie, S. Prudhomme "Premiers résultats et perspectives pour le banc de vélocimétrie tridimensionnel de la soufflerie T2 utilisant les fibres optiques et le processeur à transformée de Fourier". 2ème Congres Francophone de vélocimétrie laser - Meudon 25-27 Septembre 1990

[6]   A. Mignosi, A. Séraudie, S. Prudhomme "Applications tridimensionnelles de la vélocimétrie laser en écoulement transsonique à la soufflerie T2 ". 3ème Congres Francophone de vélocimétrie laser - Meudon 21-24 Septembre 1992

[7]   S. Prudhomme, A. Séraudie A. Mignosi "A récent 3D Laser Doppler application at the T2 transonic wind tunnel: Optimisation, experimental results, measurement accuracy" - 4th International Conference on laser Anemometry - Cleveland OHIO August 5-9 1991

[8]   S. Prudhomme, J.B. Dor A. Séraudie, M.J. Payry, P. Barricau "Validation de mesures tridimensionnelles par vélocimétrie laser en rétrodiffusion à la soufflerie transsonique T2" Rap. DERAT n°46/5006.32   (Confidentiel Industrie) Fev. 92

[9]   A. Séraudie, A. Mignosi, J.B. Dor, M.J. Payry "Etude de l'écoulement instationnaire avec un système laser bicomposante dans le cas d'un phénomène de tremblement sur un profil RA16 de 180mm de corde dans la soufflerieT2." - Rap. Techn. DERAT n° 12/5017.12 - Fev.1988

The Utilization of a High Speed Surface Reflective Visualization System in the Study of Transonic Flow over a Delta Wing

S.R. Donohoe and W.J. Bannink

Faculty of Aerospace Engineering
High Speed Aerodynamics Laboratory
Kluyverweg 1, 2629 HS Delft
The Netherlands

1. Summary

An experimental study is conducted to examine the flow over a non-cambered 65° swept delta wing with a sharp leading edge in high subsonic compressible flow at various angles of attack. This flow is known to be highly three dimensional. At certain combinations of Mach number and high angle of attack, an unsteady and often non axial symmetric phenomenon known as vortex breakdown, is found to occur above the wing.

The present experimental study includes both visualizations of the flow over the model surface and of the flow field itself. The surface flow visualization study is done using a conventional oil-flow visualization technique. Flow field visualizations are done using both a traditional transmission visualization system as well as a newly developed Surface Reflective Visualization (SRV) technique. The development and application of this SRV system will be the main topic addressed in the current report.

The SRV technique provides a new perspective on the compressible flow over wings. This technique incorporates a specially designed model with a reflective surface to enable visualization of the flow over the wing in plan view. The technique has been developed and applied to the transonic flow over a delta wing presently under investigation in a vortex breakdown research program. The plan view perspective makes it possible to visualize the span-wise distribution of the shock system present in the flow field and provides confirmation of the existence of cross flow shocks for certain combinations of Mach number and angle of attack. Combining this technique with the use of a high-speed camera enables the high speed shock fluctuations associated with this flow to be assessed for the first time. The SRV system, thus, allows insight to be gained into the time scales associated with these shock fluctuations and the vortex breakdown phenomenon in general.

2. List of Symbols and Abbreviations

c_r	Wing root chord length (120 mm.)
f	Focal length of Lens
M_∞	Free stream Mach number
x	distance downstream from apex of wing
α	Angle of Attack
Λ	Leading edge sweep angle
Re	Reynolds Number
SRV	Surface Reflective Visualization

3. Introduction

In order to achieve an attractive balance between supersonic cruise performance and maneuverability at high subsonic speeds, modern aircraft designers are often led to utilize the benefits of highly swept slender wings. Examples of this trend can be seen in the Anglo-French Concorde supersonic transport first flown in 1973 and modern fighter aircraft such as the United States Navy's F-18, the European Tornado and several aircraft of the former Soviet Union . In order to obtain their high maneuverability these aircraft utilize the non-linear lift component resulting from the powerful rotating flows found on the lee-side of delta wings when operating at angle of attack. Figure 1 is an example of the complicated rotating flow field found above a simple non-cambered sharp leading edge delta wing operating at moderately high angle of attack. The flow, initially attached to the windward side of the wing, turns outward toward the leading edge where, unable to negotiate the sharp leading edge, it separates to form a free shear layer. This shear layer, under the influence of the pressure gradients existing on the lee-side of the wing, rolls up into a vortex. After the flow reattaches to the top surface of the wing at A_1, it will again move outwards towards the leading edge. Encountering an adverse pressure gradient outboard of the primary vortex core it may then again separate and form a secondary vortex. This process may repeat itself, forming a third or tertiary vortex outboard of the secondary vortex for certain configurations. The tertiary vortex is not illustrated here. The location of the separation and reattachment lines and the vortices themselves is known to be a complex function of the free stream Mach number, leading edge sweep angle, leading edge shape, surface camber and the Reynolds number.

Although complex vortical flows are currently incorporated in the design of high performance aircraft, they remain an intriguing topic of fundamental aerodynamic research. At a given free stream Mach number the lift component generated by the lee-side vortices will increase rapidly with increasing angle of attack up to the point where the vortex breaks down. Lambourne and Bryer described the phenomenon in 1962 as "a structural change from a strong regular spiral motion to a weaker turbulent motion".[1] Where in the incompressible flow regime the breakdown position is found to move gradually forward with increasing angle of attack, in the compressible regime it has been found to move suddenly upstream at a particular critical angle of attack.[2] The sudden presence of vortex breakdown above the wing, which is often non symmetric with respect to the symmetry plane of the wing, can result in severe control problems for the aircraft. The

unsteadiness of the phenomenon can also have adverse affects on such aircraft components as twin vertical tails and stabilators when the flow impinges upon them. The unsteady aerodynamic loads caused by impingement on these components can lead to structural fatigue by exciting their natural frequencies.

Much study has been done to understand vortex breakdown and the mechanisms which induce it, yet many aspects remain less than fully understood. In 1993 Rockwell[3] refers to vortex breakdown as remaining one of "the most challenging areas of fluid mechanics". The vortex breakdown process is particularly complex in the high subsonic flow regime where the vortex flow is influenced by compressible flow effects such as shock-wave/vortex and shock-wave/boundary layer interactions. Erickson[4] and Rockwell[3] have attempted to define the significant mechanisms of influence, but admit that fundamental questions remain unanswered.

The present report will present a new method of visualizing shock-wave/vortex interactions above a non-cambered delta wing and of evaluating the unsteadiness of the breakdown phenomenon. Until now the span-wise distribution of shocks perpendicular to the wing chord, which will be referred to from this point on as the trailing edge shock system, and the location of cross flow shocks in this flow regime have remained undefined. Utilizing the Surface Reflective Visualization technique allows these characteristics to be examined. Large scale fluctuations of the shock system can also be assessed by incorporating a high speed camera into the SRV system configuration. In order to gain better insight into what is being observed with the SRV technique, the results of the oil flow visualization and conventional optical transmission visualization tests will be discussed in some detail.

4. Experimental Approach

4.1 Wind tunnel
Experiments have been performed in the TST-27 transonic-supersonic wind tunnel at the High Speed Aerodynamics Laboratory of the Faculty of Aerospace Engineering at Delft University of Technology. The TST-27 is a "blow-down" type of wind tunnel with a maximum stagnation pressure of 4.0 bars and a Mach number range from 0.5 up to 4.0. The test section used for these tests has a length of 763 mm. and a solid wall cross-section of approximately 260 mm. by 280 mm. The top and bottom walls are adjustable to compensate for boundary layer growth. There are 295 mm. diameter windows located in the side walls of the tunnel to allow visual access of the test section. More information regarding the TST-27 wind tunnel's calibration and operation can be found in the internal report of Bannink and Bakker[5].

4.2 Models and supports
Three separate delta wing models are used in these experiments. One model is used to perform oil flow visualization, another model is used to make transmission flow field visualizations and the final model is for use with the SRV system. All models are non-cambered with a chord length of 120 mm., a leading edge sweep angle of 65° and a sharp leading edge. The surface oil flow visualization model is painted black to provide additional contrast with the white visualization oil and is mounted on

the side wall of the tunnel with a solid support. In order to adjust the angle of attack for this model it is necessary to raise or lower the support of the model with triangular blocks machined to a specific angle. This support configuration is chosen to allow visual access to the upper surface of the model via the side window of the tunnel while the tunnel is running. The flow field transmission visualization model is supported, in contrast, by an adjustable sting in the test section. This configuration allows a side view perspective to be obtained of the flow field above the delta wing while the tunnel is running. The SRV model is identical to the oil flow model except that it has a reflective mirror surface instead of a black upper surface. This configuration allows the visual access to the model surface while the tunnel is running required for use of the SRV system.

4.3 Experimental Set up and Testing Procedures
4.3.1 Oil Flow Visualization
Oil flow visualization are made using a white colored mixture of oil and titanium dioxide. The experimental procedure entails applying this mixture to the model surface, closing the tunnel and then running the test. Photos are made both during and after the tunnel is run. Via this procedure a footprint can be obtained which provides information on the surface topography. Differences between photos made during the run and after the run are found to be minimal except in regions which appear as foci. In these regions, there is a significant "smearing-out" of the accumulated oil during the shut down procedure of the tunnel.

4.3.2 Transmission Flow Visualization
Transmission flow visualizations are made of the flow field using both schlieren and shadowgraph system configurations. This system utilizes parabolic mirrors as the main optical components to produce, from a light source at one side of the tunnel, a parallel light bundle passing through the test section and to bring this bundle to focus again on the other side of the tunnel.

4.3.3 Surface Reflective Flow Visualization
The Surface Reflective Visualization (SRV) system is configured such that the light source is projected, via a parabolic mirror, as a parallel bundle of light into the test section. For the SRV system, however, this bundle is projected perpendicular to the model surface instead of perpendicular to the side window of the tunnel as in the transmission visualization case. The light is then reflected back along nominally the same path to the parabolic mirror and brought to focus on the image plane of the camera (see Figure 2). In order to obtain enough light for the photos it was necessary to place a tiny mirror (5 mm. diameter) at the cross point of the outgoing and returning light bundles. Initially a splitter mirror was used at this location, but preliminary tests revealed that the large losses of light (50% from the incident bundle and 50% from the returning bundle) made use of the high speed camera infeasible with that configuration. To solve this problem a tiny mirror was introduced at the junction point and the parabolic mirror and flat mirror were adjusted such that the light bundle passes just next to the tiny mirror on its return path. It was feared that the introduction of the tiny mirror, and thus the slight displacement of the incident and returning light bundles, would adversely affect the sharpness of the

visualization images. This was found to have negligible influence.

The SRV system can be configured in a similar manner as the transmission visualization system to produce either shadowgraph or schlieren visualizations. Schlieren visualizations are made by placing a knife edge in the focal plane of the parabolic mirror beyond the junction point of the outgoing and returning light bundles. Shadowgraph visualizations are made by adjusting the camera such that the focal plane is slightly above or below the upper surface of the model.

4.3.4 High Speed Camera and Nanolite
High speed photos are made using the Impulsphysik Strobodrum camera. This camera is operated by first winding the film tightly around the inner drum of the camera, bringing the inner drum up to rotational speed (maximum 3000 revolutions/minute), opening the shutter of the camera in.the dark tunnel hall and exposing images in quick succession (maximum 4500 Hz.) with a spark light source. In contrast with a normal camera, the diaphragm of the camera remains open during the exposure of the entire film. The spark light source used for these tests is an Fischer-R138 Nanolite. Characteristic of the Nanolite is the extremely high luminous density of the point shaped spark produced by the spark discharge. The duration of the spark used is nominally 18 nsec.

4.3.5 Test Matrix
Four different configurations of Mach number and angle of attack are considered in the current study. Free stream Mach numbers of 0.6 and 0.8 with angles of attack of 15° and 20°are examined (see Table I)

Mach number	Re [1/m]	15 [deg.]	20 [deg.]
0.6	2.25e7	X	X
0.8	2.75e7	X	X

Table I Test matrix

Tests at moderate angle of attack (15°) are made for the purpose of verifying the SRV system. Because SRV is a new method of visualizing the flow over delta wings it was initially unclear which features of the flow field would be revealed using the SRV system. Previous work done by Ottochian at the TU Delft High Speed Aerodynamics Laboratory[6] with the same model indicated that this angle of attack could be expected to produce a stable vortex flow pattern without the presence of vortex breakdown above the wing. Tests at high angle of attack (20°) are done to determine the usefulness of the SRV system in studying the vortex breakdown phenomenon. This angle of attack was found to exhibit vortex breakdown at both Mach numbers of 0.6 and 0.8 in the study of Ottochian referenced above.

The low Mach number (0.6) cases are chosen because it is expected that no significant shocks will be present for the moderate angle of attack configuration. In contrast, the higher Mach number (0.8) can be expected to display strong compressibility effects which will both increase the sharpness of flow visualizations and exhibit interesting shock/vortex interactions. The high Mach number case is

also expected to be highly unsteady based on previous studies made by Ottochian[6], Muylaert[2] and Schrader[7] with the same or similar configurations.

5. Results

5.1 Oil Flow Surface. Flow Visualization
Oil flow visualization studies are useful in locating such topographical characteristics as separation and reattachment lines. Figure 3 illustrates a characteristic oil flow streak pattern for the flow over a sharp leading edge delta wing with no vortex breakdown occurring above the wing and its associated qualitative pressure distribution. For a given delta wing the location and shape of the secondary and tertiary separation lines are a function of the free stream Mach number, angle of attack and the state of the boundary layer on the model surface. A turbulent boundary layer is better able to negotiate the adverse pressure gradient encountered outboard of the primary vortex core and will, therefore, tend to separate further outboard than a laminar boundary layer. The free stream Mach number and angle of attack will influence the magnitude of the adverse pressure gradient outboard of the primary vortex core and ,thus, the position of separation. These two parameters also determine whether or not the presence of conical shock waves embedded between the primary vortex and wing surface is likely. Such conical shock waves, when present, may strongly influence the position of secondary separation. In the case of vortex breakdown existing above the wing the oil flow pattern will strongly resemble that of the no breakdown case from the apex downstream to the point of breakdown. At this point the secondary separation line will move outboard suddenly and the secondary attachment and tertiary separation lines will disappear.

$\alpha = 15°$

In this study no vortex breakdown is found for the 15° angle of attack configuration at either of the two free stream Mach numbers tested. At $M_\infty = 0.6$ the secondary separation line follows a conical path downstream form the apex until $x/c_r = 0.5$. Between this point and $x/c_r = 0.65$ the secondary separation line is found to curve gradually outwards, beyond which point it again follows a conical path. This curved region can be interpreted as indication of transition zone from a fully laminar to a fully turbulent boundary layer on the surface of the model. The surface streamlines moving outboard to the secondary separation line for this configuration are seen to converge smoothly into the separation line at a small oblique angle.

For $M_\infty = 0.8$ the secondary separation line exhibits a very different shape than at $M_\infty = 0.6$ (see Figure 4). The secondary separation line again follows a conical path in the vicinity of the apex, but a sharp kink is found at $x/c_r = 0.26$, beyond which the separation line continues along a conical ray with its effective apex in front the of the apex of the actual model. The curved transition region is not observed for this configuration. For this configuration the surface streak-lines approach the separation line at a very sharp angle as compared with the $M_\infty = 0.6$ case. Erickson[4] interpreted this sharp intersection angle as an indication of a shock induced secondary separation.

α = 20°

In the high angle of attack configuration vortex breakdown is observed at both $M_\infty = 0.6$ and $M_\infty = 0.8$. At $M_\infty = 0.6$ the secondary separation line is seen to curve dramatically outboard at $x/c_r = 0.52$. Because the loss of a tight and controlled vortex structure will significantly reduce the adverse pressure gradient encountered by the outboard flowing boundary layer, this dramatic outboard curvature can be interpreted as an indication of vortex breakdown.

Dramatic outward curvature of the secondary separation line occurs at $x/c_r = 0.57$ in the $M_\infty = 0.8$ case (see Figure 5). The tertiary separation line is clearly seen to converge into the secondary separation line as the tertiary vortex lifts off the surface at this point. For the $M_\infty = 0.6$ case this separation line convergence was not clearly visible in the oil streak line pattern. This may be explained by the lower surface shear stress associated with the weaker tertiary vortex system at the lower Mach number. The joining together of the separation lines creates a sort of foci pattern at the location of vortex break down. Further attempts at defining the exact topological characteristics of the foci were given up when high speed visualization tests indicated the unsteady nature of the flow in this region. Oil flow surface visualization provides an indication of the surface shear stress integrated over the length of a run and is, thus, unlikely to yield useful information over precise topological details in the proximity of such an unsteady phenomenon as vortex breakdown.

5.2 Flow Visualization

In the interpretation of the flow field visualization results it is important to consider the three dimensional nature of the flow field and the limitations of the effectively two dimensional visualization methods used. Mair[8] has investigated the influence of length of a particular density gradient along which a light ray passes, the angle at which the ray intersects the gradient and the strength of the gradient on the final image represented by a schlieren or shadowgraph system. These optical effects result in the fact that the image represented is not simply an image of the integration of the gradients encountered by a particular light ray traversing the test section but a more complex function of the flow field. Optical influences become particularly important when considering the projection of a highly three dimensional flow. Optical effects are considered in the following qualitative interpretation of the visualization results.

5.2.1 Transmission flow visualization

$M_\infty = 0.6$

Because schlieren and shadowgraph visualization systems nominally provide an indication of the first and second derivative, respectively, of the density field perpendicular to a parallel light bundle integrated over the length of the light path, it is important to have high enough gradients present to obtain a reasonable signal/noise ratio in the resulting image. For the low Mach number case ($M_\infty = 0.6$) preliminary tests made with the video camera

in place of the high speed camera revealed that the gradients were too weak to produce a useful image. Flow accelerations over the wing were not large enough to produce a trailing edge shock observed at higher free stream Mach numbers nor were the gradients in the vortices themselves strong enough to provide a clear image of the vortices from a side view perspective. High speed transmission flow visualizations were, therefore, not conducted for this configuration.

$M_\infty = 0.8$

For the high Mach number case, on the other hand, interesting facets of the flow field could be visualized with the transmission flow field visualization system. Both the extent of the lee-side vortices and the trailing edge shock system could be visualized. It was also possible, with the use of a high speed camera, to obtain information on the fluctuations of the trailing edge shock system.

The existence of a supersonic pocket above the lee-side vortex system of a delta wing in high subsonic flow was first observed by Ottochian[6] and Houtman and Bannink.[9] Their further investigation of this supersonic pocket and the associated trailing edge shock system revealed the unsteady nature of the trailing edge shock and noted the observance of a two shock system at certain configurations of Mach number and angle of attack.

The present study reveals that at 15° angle of attack, with no vortex breakdown above the wing, the trailing edge shock system was highly fluctuating. High speed camera photos could be made at a rate of 4.5 kHz. revealed that the system fluctuated between $x/c_r = 0.6$ and $x/c_r = 0.83$ (see Figure 6). The system was found to consist at different instants in time of either one clear trailing edge shock reaching to the surface, two clear shocks or no clear shocks but, rather, a weak series of compression waves. At 20° angle of attack vortex breakdown was observed above the wing (see Figure 7). Two, apparently independently fluctuating, shock systems were observed. The first system of one, two, or no visible shocks fluctuated between $x/c_r = 0.47$ and $x/c_r = 0.57$. These shocks, when present, attached perpendicularly to the surface and then curved forward concave to the apex above the vortex system. A kink at the estimated level of the vortex core was sometimes observed. The second shock system was much more noisy, consisting of a series of waves between $x/c_r = 0.73$ and $x/c_r = 0.93$. These waves were also found to expand perpendicularly from the surface through the vortex system and then to curve upstream concave to the model apex.

Further quantitative interpretation of the results regarding shock fluctuation frequencies was not possible due to the inability of the transmission visualization system to provide information over the span wise distribution of the shock system. This uncertainty made it impossible to consistently measure the shock position at the same span-wise location over time.

5.2.2 Surface Reflective Flow Visualization

Use of the SRV system provides a new plan view perspective of the compressible flow over the delta wing. A plan view schlieren system was previously employed by

Squire[10] to investigate cross flow shocks in the wake of a delta wing in supersonic flow. It was not possible to visualize these shocks above the delta wing with this system, however, due to the obstruction of the model in the light path. Laser sheet visualization made by Erickson[4] in this flow regime provided a qualitative idea of the span-wise distribution of the vortex system but remained limited by their inability to provide a global plan view perspective on the shock systems present above the surface. The SRV system provides an image of the density gradient (or second derivative in the case of a shadowgraph configuration) perpendicular to the light bundle approaching the model at 90 deg. to the upper surface integrated over its path entering and exiting the test section.

Previous difficulties encountered in defining the span wise distribution of the shock system with the transmission visualization systems are overcome with this system. With the SRV system it is possible to visualize the primary vortices, strong cross-flow shocks and the trailing edge vortex system in plan view. Combining the SRV technique with the use of a high speed camera allows the large scale fluctuations of these phenomenon to also be considered. It is important, however, to consider the optical effects of the three dimensional flow field mentioned above when interpreting these results.

$M_\infty = 0.6$

No trailing edge shock system was observed with the SRV system at $M_\infty = 0.6$ (see Figure 8). Due to the weak compressibility effect present for the low angle of attack case (15°) it was necessary to use continuous light to make photos with an exposure time of 2 msec. In contrast, the Nanolite used with the high speed camera provides an exposure time of approximately 18nsec. With the continuous light source it was possible to increase the signal to noise ration of the image by integrating the image over time. This integration effect made it possible to clearly identify the large vortex structure above the delta wing by effectively filtering out the background noise of the tunnel.

In the high angle of attack configuration (20°) it was not necessary to use the continuous light source as the accelerations over the wing provided sufficiently high density gradients for use of the spark light source (see Figure 9). For this high angle of attack configuration it was possible to see the sudden termination of the organized vortex system at approximately $x/c_r = 0.57$ on both the port and starboard sides of the wing. This was as expected, based on the oil flow visualization results described above. The sharp line just outboard of the core of the primary vortex is expected to be an indication of a cross-flow shock. The existence of cross-flow shocks was first proposed by Muylaert[2]. The sharp angle at which the oil streak lines approach this line also supports the conclusion that the sharp line represents a cross flow shock located under and slightly outboard of the primary vortex core. That this line is located also slightly outboard of the secondary separation is explained by the existence of a shock-wave/boundary layer interaction. The pressure rise induced by the inviscid shock will propagate inboard through the subsonic boundary layer and cause surface flow

separation effectively upstream of the shock. In Squire's[10] investigation of supersonic flow over delta wings he also noted that in the case of conical shock induced separation the surface flow would indicate separation slightly ahead of the shock location. Use of a horizontal knife (parallel with the chord of the model) also revealed an interesting pattern beyond the point of breakdown which strongly resembles the spiral breakdown mechanism documented by Lambourne and Bryer[1] in the low speed flow regime (see Figure 10).

$M_\infty = 0.8$

In the moderate angle of attack configuration (15°) both spark photos and continuous light photos yielded interesting images at this Mach number (see Figures 11 and 12). Although the appearance of the main vortex structure was much the same for both exposure situations, with the continuous light photos exhibiting less background noise, there was a significant difference in the appearance of the trailing edge shock system. For the continuous light configuration no trailing edge shock system was visible. With the high speed camera/spark light configuration, on the other hand, a rapidly fluctuating shock system was visible. This difference is likely due to the relatively weak shock strength and highly fluctuating nature of the shock system which kept it from producing a clear image on the image integrated over time.

The horizontal knife edge configuration of the schlieren system used in producing these images results in the fact that a compression in the outboard direction will produce a dark tone on the port side of the wing and a light tone on the starboard side. Examining Figure 11 it is possible to see that the primary vortex is represented as an expansion gradient in the outboard flow direction on both sides of the root chord. Outboard of this region there is a neutral tone region, indicating no strong gradients in the projected surface plane, which is likely representing the vortex core. Moving further outboard a sharp line is observed on both the port and starboard sides of the wing. This line is interpreted as representation of a conical shock located below the primary vortex and inducing the secondary separation. The location of this line slightly outboard of the secondary separation line as indicated by the oil flow test is again explained by the existence of the shock-wave/boundary layer interaction mentioned above. The visualization of the secondary and tertiary vortices themselves outboard of this sharp line is not possible with the SRV due to existence of the primary vortex gradients above these embedded vortices.

The general features of the vortex system exhibited in the high speed photo of Figure 12 are very similar to the continuos light photo of Figure 11. The main difference between these two photos is that the continuos light photo has a more filtered appearance due to the averaging affect of the longer exposure time. The rough edge of the expansion region visible in the spark photo of Figure 12 it is smoothed out in the continuous light photo. This roughness in the high speed photo is possibly a representation of the feeding sheet discontinuities also observed in the laser sheet study of Erickson[4] in this same flow regime (see Figure 13) .

For the high angle of attack configuration (20°) a trailing edge shock distribution consisting of one shock system intersecting the root chord at approximately $x/c_r = 0.6$ and one at $x/c_r = 0.9$ was found (see Figure 14). The first shock is expected to be interactively effecting the breakdown procedure. This shock is concave with respect to the apex of the wing and seems to converge with the embedded conical shocks as it approaches the leading edge of the wing. This junction point strongly resembles the junction of two weak shocks visualized by Sturtevant and Kulkarny.[11] The much weaker line observed slightly upstream of this curved shock is thought to be a representation of the foremost extension of the shock above the vortex system observed in the transmission flow field visualization. This section of the shock curves gently forward and above the vortex system is likely distributed perpendicular to the root chord in the span wise direction due to the low stream wise gradients existing above the vortex system. The second shock system is indication of the acceleration of the flow again to supersonic speed beyond the point of breakdown. As with the transmission flow visualization images of this configuration the second shock system is found to be very noisy. It appears that the shocks in this region are strongly affected by their interaction with the vortex system. The non-symmetric and unsteady nature of the state of the vortices produced significantly different images within the 1.4 msec. total exposure time of the high speed camera film during a given run.

The fact that the trailing edge shock system perpendicular to the root chord can be visualized with a schlieren system configured with the knife edge parallel to the root chord has two explanations. A weak shadow-graph effect is also inherent in schlieren systems and, therefore, particularly strong secondary spatial derivatives of the density will be visible in a schlieren system regardless of the orientation of the knife edge. The second explanation of the dark trailing edge shocks visualized by this horizontal knife edge schlieren system is the effective vertical knife edge schlieren effect created by the presence of the tiny mirror in the experimental set-up. This tiny mirror would block significantly diffracted light from reaching the focal point of the parabolic mirror beyond and thus provide an effective vertical schlieren knife edge. The trailing edge shock system could induce such large diffractions.

As with the oil flow visualization, the main vortex structure in the case of vortex breakdown existing above the wing was very similar to the no vortex breakdown case from the apex downstream to the actual point of breakdown. As discussed above for the lower angle of attack at this Mach number, the outboard expansion gradients of the primary vortices, the vortex cores and conical shock waves were visible from just beyond the apex downstream to the point of breakdown. Beyond the point of vortex breakdown and, thus, the cessation of an organized vortex structure, the conical shock was observed to turn abruptly inboard. The existence of the sharp line continuing downstream slightly beyond the apparent point of vortex breakdown seems to indicate the less than chaotic nature of the flow in this region. The resemblance of the flow beyond the point of breakdown with the documented low speed spiral breakdown mechanism was less dramatic

in this configuration than at $M_\infty = 0.6$ and $\alpha = 20°$, but was still present.

6. Conclusions and Future Work

The SRV system has been shown to be a powerful new tool in the visualization of the complex and unsteady flow above a flat delta wing in transonic flow. It is noted, however, that care must be taken in the interpretation of the images produced with this system due to three dimensional optical effects. Although the oil flow visualization results do support the qualitative interpretation made in the present study, it would be useful to conduct an extensive flow field measurement study in order to quantitatively define the spatial density distribution being visualized. This is important as the significance of the optical effects of the three dimensionality of the flow field on the images produced via the SRV system remain somewhat ambiguous.

Following the above mentioned system calibration work, further applications for the SRV system will include quantitative studies of the large scale flow fluctuations leading up to and just beyond vortex breakdown for various Mach numbers. It will also be interesting to see if the difference between the well known low speed bubble-breakdown and spiral-breakdown mechanisms can be visualized with the SRV system.

7. ACKNOWLEDGMENTS

[1]Lambourne, N.C. and Bryer, D.W., "The bursting of leading edge vortices - Some observations and discussion of the phenomenon"ARC R.& M. no. 3282, 1962.

[2]Muylaert, J.M. and Wendt, J.F., "Effect of Compressibility on Vortex Bursting on Slender Delta Wings", Project Report 1980-21, von Karman Institute for Fluid Dynamics, Rhode Saint Genese, Belgium, 1980.

[3]Rockwell, D., "Three-Dimensional Flow Structure on Delta Wings at High Angle-of-Attack: Experimental Concepts and Issues", AIAA paper 93-0550, 31st Aerospace Sciences Meeting and Exhibit, Reno, NV, January 11-14, 1993.

[4]Erickson, G.E., "Wind Tunnel Investigation of the Interaction and Breakdown Characteristics of Slender-Wing Vortices at Subsonic, Transonic, and Supersonic Speeds", NASA Technical Paper 3114, November 1991.

[5]Bannink, W.J. and Bakker, P.G., "Transonic Mach Number Determination in a Blow-Down Wind Tunnel with Solid Walls and a Downstream Throat", Report LR-402, Delft University of Technology, The Netherlands, October, 1983.

[6]Ottochian, S.P., "Experimental Investigation on the Vortex Flow Above a Sharp-Edged Delta Wing in the Transonic Speed Regime", Thesis for Aeronautical Engineer, Delft University of Technology, Faculty of Aerospace Engineering, 1987.

[7]Schrader, K.F. Reynolds, G.A. and Novak, C.J., "Effects of Mach number and Reynolds number on Leading-Edge Vortices at High Angle of Attack", AIAA 88-0122, Aerospace Sciences Meeting, Reno, Nevada, January 1988.

[8]Mair, W.A., "The Sensitivity and Range Required in a Toepler Schlieren Apparatus for Photography of High-Speed Air Flow", The Aeronautical Quarterly, Vol. 4, August 1952

[9]Houtman, E.M. and Bannink, W.J., "Experimental Investigation of the Transonic Flow at the Leeward Side of a Delta-Wing at High Incidence", TU Delft, Report LR-518, August 1987.

[10]Squire, L.C., "Leading-Edge Separations and Cross-Flow Shocks on Delta Wings", AIAA Journal, Vol. 23, No. 3, March 1985.

[11]Sturtevant, B. and Kulkarny, V.A., "The focusing of weak shock waves", Journal of Fluid Mechanics, vol. 73, part 4, pp.651-671, May 1975.
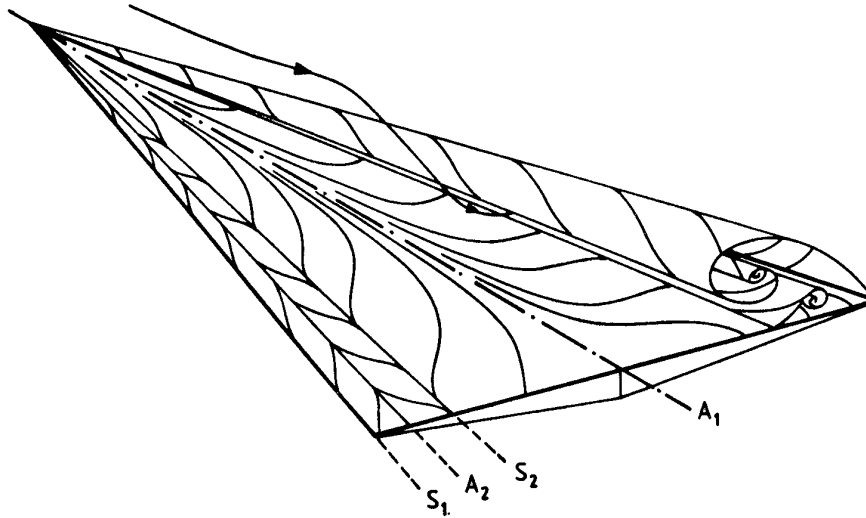
Figure 1. Schematic drawing of vortex flow above a sharp leading edge delta wing at moderate angle of attack.
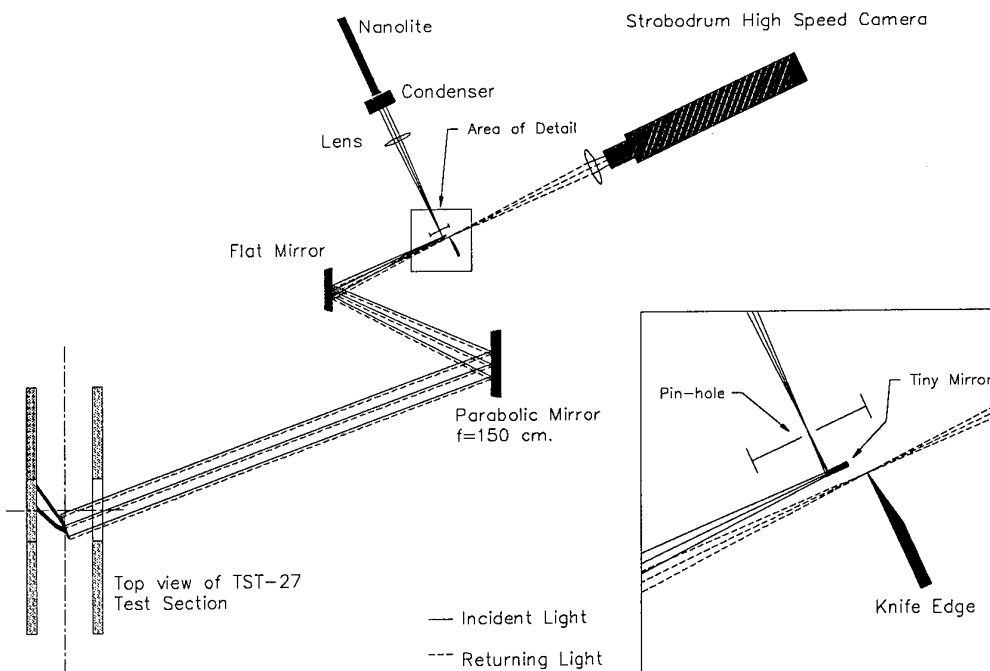
Figure 2. Surface reflective flow visualization (SRV) system configuration
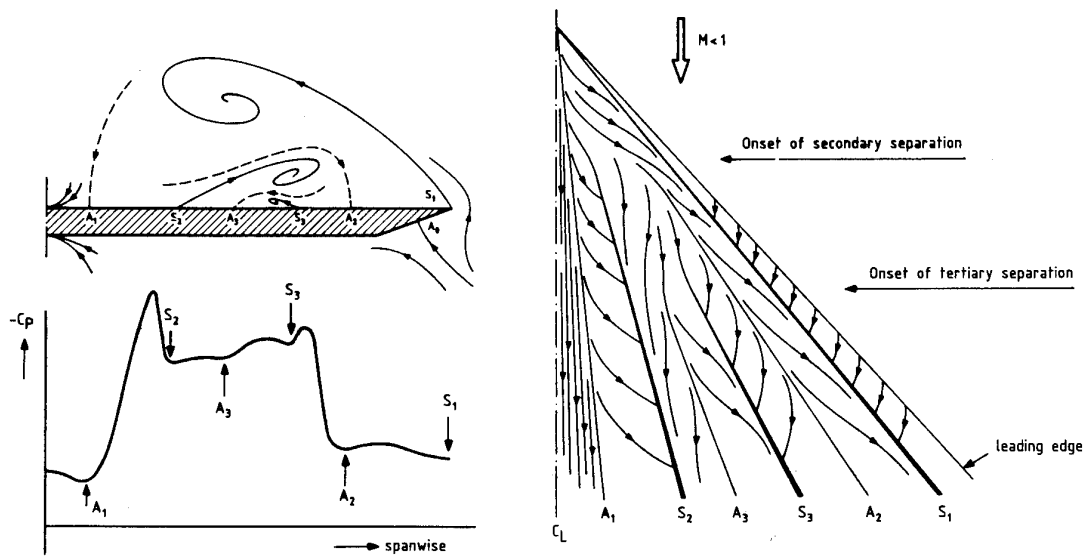
Figure 3. Characteristic oil flow surface flow visualization of the vortical flow above a sharp leading edge delta wing at moderate angle of attack and the associated qualitative pressure distribution
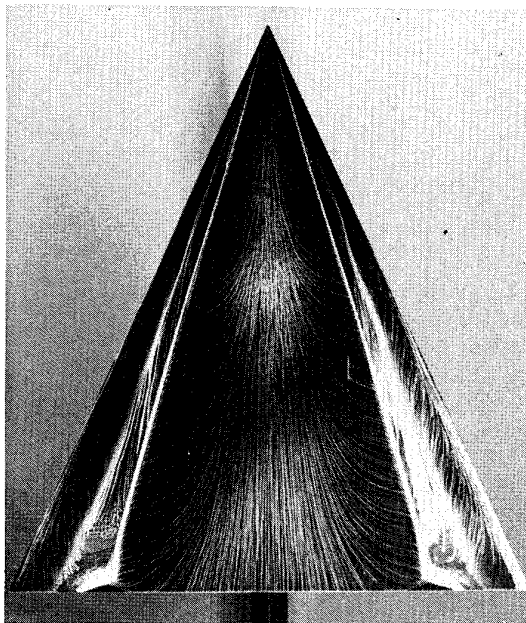

Figure 4. Oil flow surface flow visualization exhibiting no vortex breakdown above the wing at moderate angle of attack, $M_\infty = 0.8$, $\alpha = 15°$
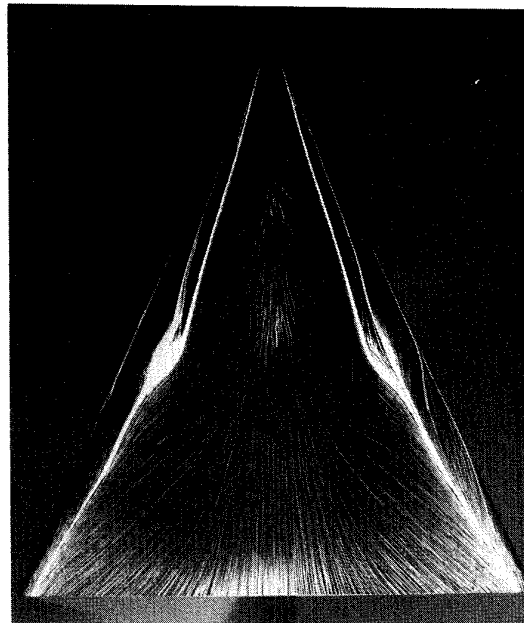
Figure 5. Oil flow surface flow visualization exhibiting vortex breakdown above the wing at high angle of attack, $M_\infty = 0.8$, $\alpha = 20°$.

Figure 6. Transmission visualization configured with schlieren knife edge perpendicular to the free stream flow direction exhibiting no vortex breakdown above the wing, $M_\infty = 0.8$, $\alpha = 15°$.
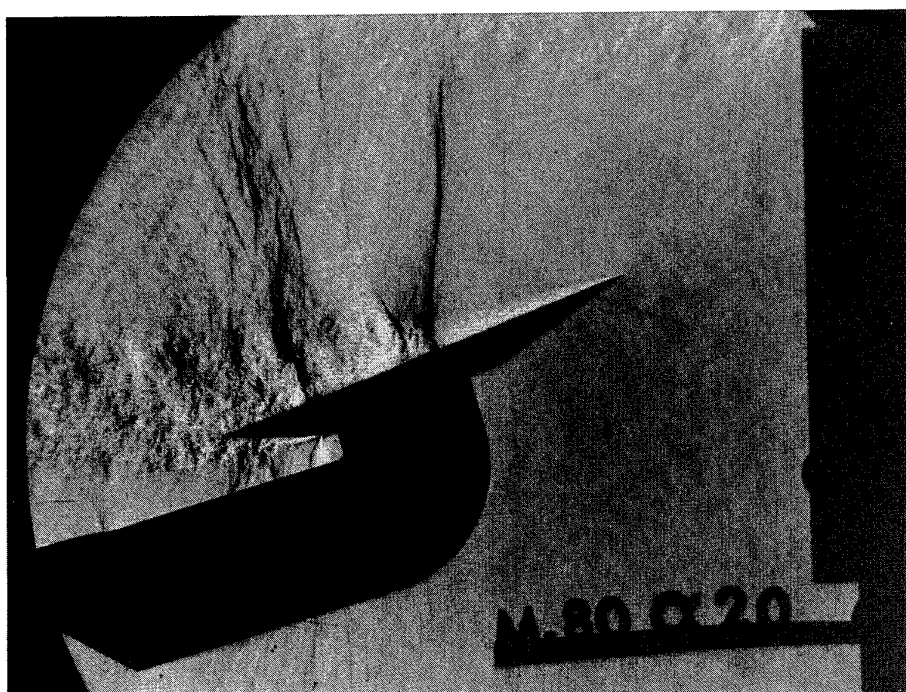

Figure 7. Transmission visualization configured with schlieren knife edge perpendicular to the free stream flow direction exhibiting vortex breakdown above the wing, $M_\infty = 0.8$, $\alpha = 20°$.

Figure 10. Schematic of Spiral vortex breakdown[1]

Figure 9. Surface reflective visualization with spark light source and schlieren knife edge parallel with the free stream flow direction exhibiting vortex breakdown above the wing and a weak trailing edge shock system, $M_\infty = 0.6$, $\alpha = 20°$.
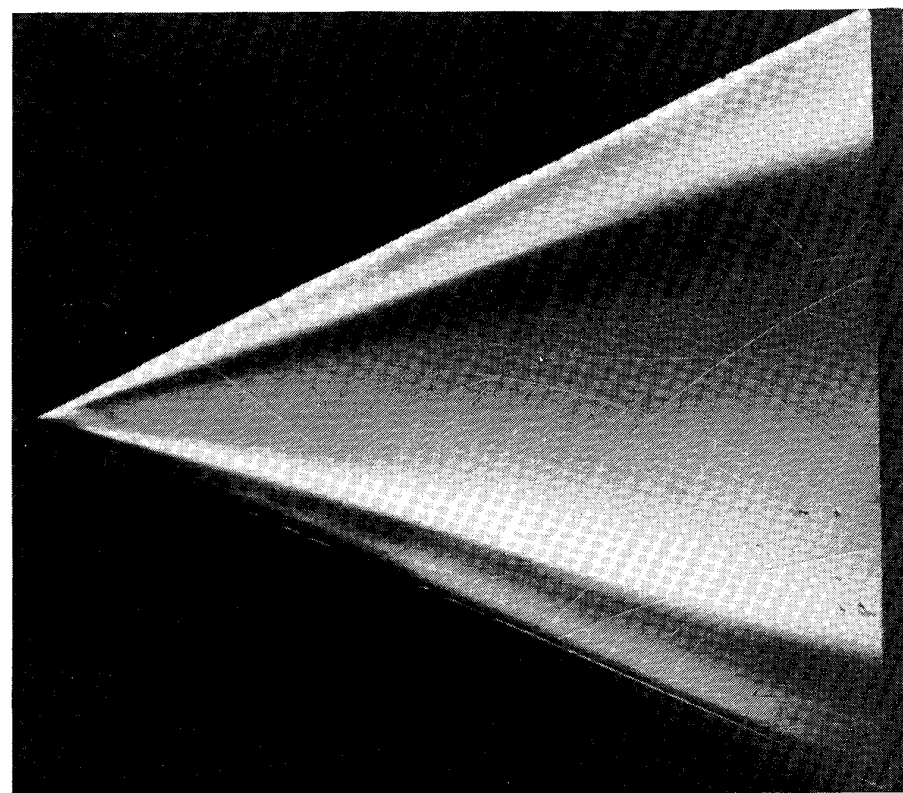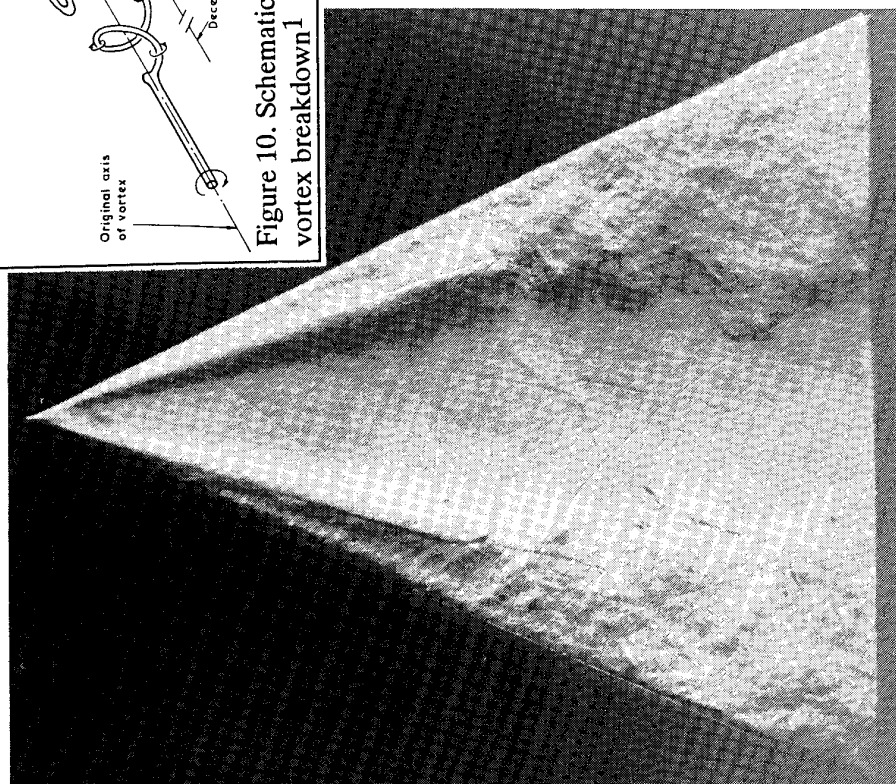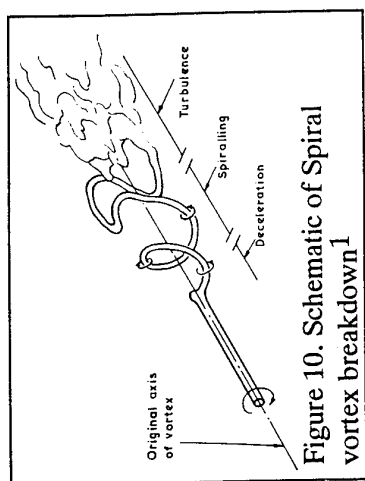

Figure 8. Surface reflective visualization configured with continuous light source and schlieren knife edge parallel with the free stream flow direction exhibiting no vortex breakdown above the wing, $M_\infty = 0.6$, $\alpha = 15°$.

Figure 13. Schematic drawing of Feeding sheet discontinuities[4]

Figure 12. Surface reflective visualization with spark light source and schlieren knife edge parallel with the free stream flow direction exhibiting no vortex breakdown above the wing and conical shocks, $M_\infty = 0.8$, $\alpha = 15°$.
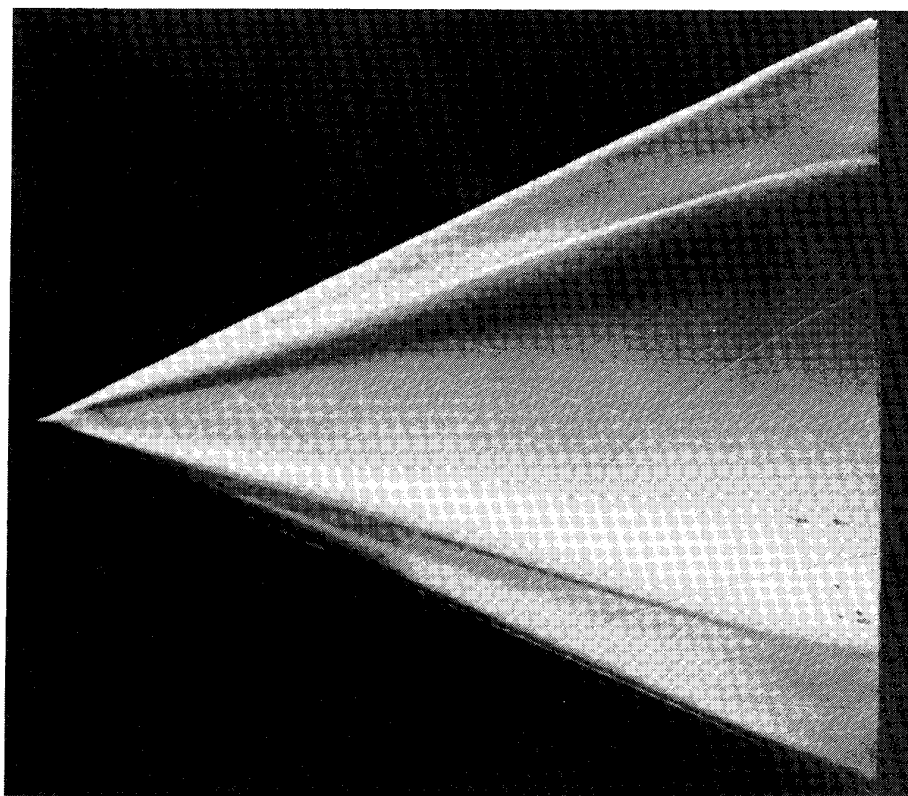

Figure 11. Surface reflective visualization configured with continuous light source and schlieren knife edge parallel with the free stream flow direction exhibiting no vortex breakdown above the wing and conical shocks, $M_\infty = 0.8$, $\alpha = 15°$.
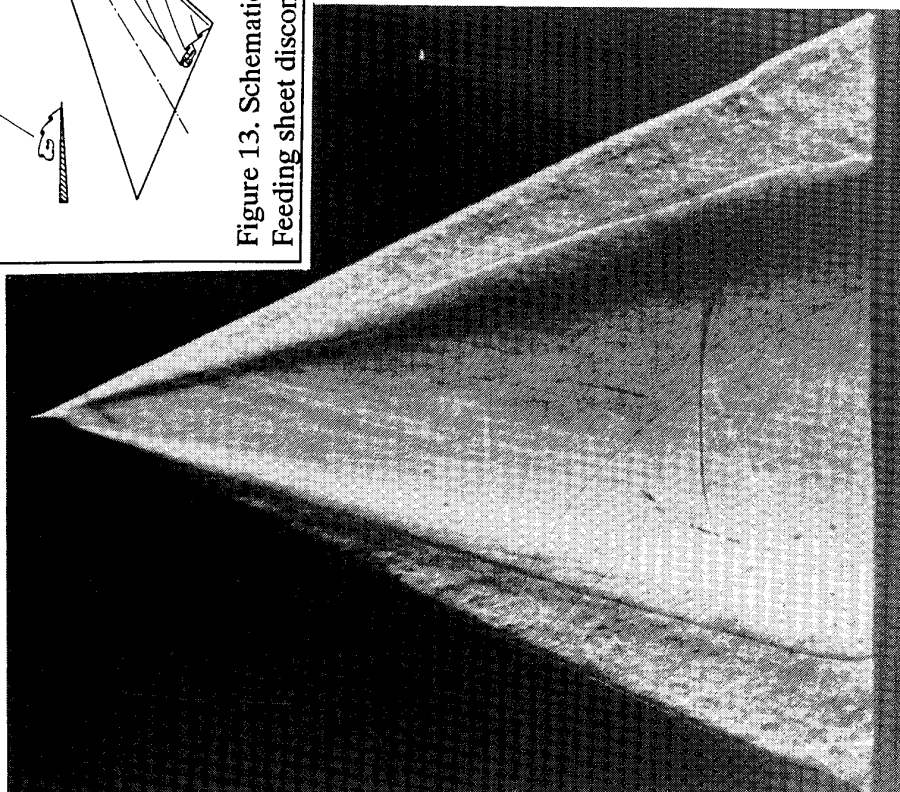
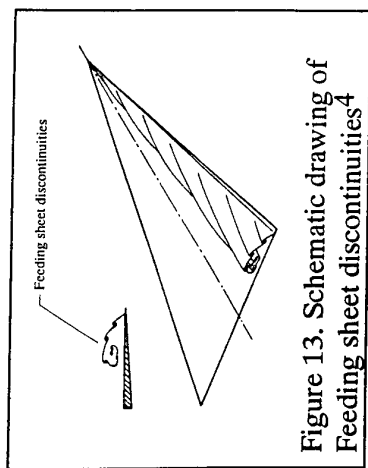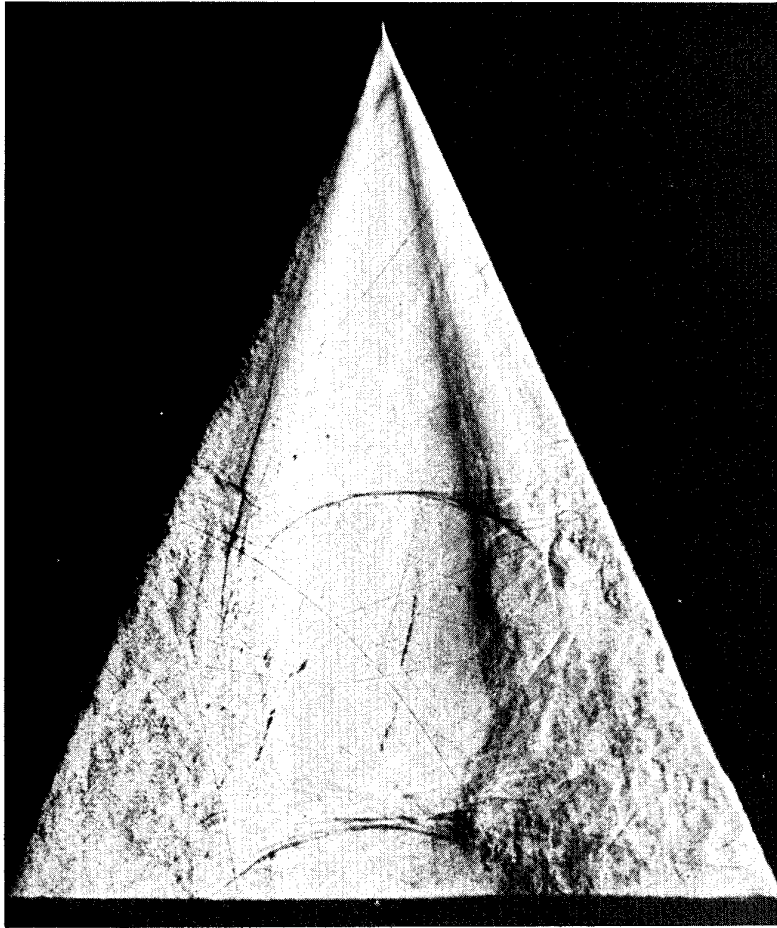Figure 14. Surface reflective visualization with spark light source and schlieren knife edge parallel with the free stream flow direction exhibiting vortex breakdown above the wing and a strong trailing edge shock system, $M_\infty = 0.8$, $\alpha = 20°$.

Transonic and Supersonic Flowfield Measurements about Axisymmetric Afterbodies for Validation of Advanced CFD Codes

Martin Burt
Aerodynamics Department, British Aerospace Military Aircraft Division
Warton Aerodrome, PRESTON, PR4 1AX
ENGLAND

Philip Miller[1]
Miller and Wilson Aerodynamics Research
Charlotte Street, BATH, BA1 2NE
ENGLAND

Johan Agrell
Aerodynamics Department, Aeronautical Research Institute of Sweden (FFA)
P O Box 11021, S-161 11, BROMMA
SWEDEN

SUMMARY

Two axisymmetric afterbody experimental programmes, aimed at providing necessary and sufficient data for CFD code validation, were conducted in the FFA S5 suckdown wind-tunnel. Flow conditions covered the range of transonic to supersonic. Mean and fluctuating flowfield velocities in a single longitudinal plane were measured using LDA along many traverses, both over the afterbody and in the jet and mixing regions. Flow separated on the boattail of the AGARD 10° and 15° geometries at all conditions tested. Separation also occurred on a conical afterbody at supersonic Mach number. Comprehensive sets of boundary condition data were also recorded, through a wide variety of techniques. Extensive error analyses have been undertaken to evaluate the accuracy of all data. Transonic Navier-Stokes computations on the configurations were performed and showed the benefit of having static pressure information along the slotted tunnel roof. An algebraic stress model of turbulence returned superior predictions of afterbody surface pressures than two more simple models, in both attached and separated flow.

NOTATION

C_p	Pressure coefficient, $p - p_\infty/q_\infty$
D	Model centrebody diameter
M	Mach number
NPR_{nom}	Nozzle pressure ratio, $P_{o\,jet}/P_{pnm}$
NPR_s	Nozzle pressure ratio, p_{jet}/p_∞
p	Static pressure
P_o	Total pressure
q	Dynamic pressure, $\frac{1}{2}\gamma pM^2$
Re	Reynolds number, $\rho U_\infty D/\mu$
u	Time-varying X component velocity
U	X component velocity
v	Time-varying Y component velocity
V	Y component velocity
X	Distance from model base, downstream
X'	Distance from model nose, downstream
Y	Vertical distance from model centreline, positive up
γ	Ratio of specific heats
μ	Dynamic viscosity
ρ	Static density

Subscripts etc.

jet	Jet conditions at nozzle
pnm	Wind-Tunnel plenum
tun	Tunnel empty nominal conditions
∞	Freestream reference conditions at onset to afterbody ("domain start")
$-$	Time-mean value

1. INTRODUCTION

The drag due to the afterbody/nozzle installation for aircraft with submerged powerplants contributes a significant proportion of the total aircraft drag at transonic and supersonic speeds[1]. The aerodynamic design of low-drag afterbody installations is a complex process requiring in general much theoretical and experimental effort. The present state of drag prediction methods for airframe-integrated afterbodies is insufficiently advanced to guarantee performance without a considerable element of wind-tunnel checking of the configuration. Even after great expense and effort in testing metrically loaded afterbody models the final results in terms of flight vehicle drag and buffet behaviour have often shown unwanted surprises[2]-[4].

Experimentally, the scaling of isolated afterbody model data to full-scale situations has created many problems. Reynolds number effects have been shown to be complex[3][5] and providing simulation of hot combustion products having the appropriate gas properties has proved difficult[6][7]. Furthermore, the construction of metric models capable of isolating the inlet, afterbody and nozzle thrust and drags, i.e. "jet-effects" models, incurs very considerable cost.

---

[1] Now at Aerodynamics & Propulsion Department, DRA BEDFORD, MK41 6AE, ENGLAND

It has long been evident that the afterbody integration process would best be achieved if an accurate and reliable predictive method was available, reducing simplified wind-tunnel tests to providing a last check on the proposed design. However, theoretical methods are often limited by their inability to reproduce the very features likely on an afterbody travelling at high speeds, especially for the transonic condition. Thus shock-boundary layer interactions, separations and viscous mixing of high speed streams all present difficulties to prediction methods that often perform well on other parts of the airframe.

With the development of CFD methodologies that provide some capability to predict viscous events and shock-capturing, plus advances in grid generation, it now appears that the afterbody design process may be becoming tractable. This would represent some real payback on the considerable investment made in evolving such methods. A key stage in the maturing of these methodologies, such as Reynolds-Averaged Navier-Stokes schemes, is the rigorous and specific validation of the algorithms for afterbody-like flows. The present paper describes high-speed experiments undertaken for just this purpose in the FFA S5 wind-tunnel. The distinctive attributes of a CFD validation experiment are also assessed and illustrated by the afterbody tests.

2. SPECIFIC AFTERBODY FLOW FEATURES

The important features of the afterbody/jet problem are shown in Figure 1 and listed below:

1) High speed onset conditions.
2) Strong shock-waves at boattail recompression.
3) Separated flow on the afterbody boattail.
4) Underexpanded plumes of high jet pressure ratio.
5) Highly sheared mixing region of jet and onset flow.

It was necessary to devise experiments that contain all of the above flow features yet also fulfil the exacting data quality requirements of a validation data-set. At an early stage it became clear that axisymmetric flow-fields would be preferable. From the experimental view it allowed a single longitudinal slice of the flow to be investigated thoroughly, rather than expending excessive effort and incurring increased costs on studying 3-D effects that were not of prime importance. Also, a similar argument could be applied in terms of the most efficient computational representation of the main flow features. Taking data over a wide Reynolds number range and with representative temperature jets would also have been desirable but the experimental facility precluded this. Similarly, the direct measurement of afterbody drag would have been a worthwhile but expensive advantage.

3. FEATURES OF CFD VALIDATION EXPERIMENTS USING LDA

3.1 General Requirements

A crucial facet of the experiments was to be the detailed velocity mapping of the different flow regions shown on Figure 1. For such a task the only technique known to be appropriate throughout the flowfield was Laser-Doppler Anemometry. A number of papers have been published in recent years that discuss the necessary experimental and accuracy attributes of validation experiments, for example Marvin[8]. Requirements of a CFD validation experiment using LDA in a wind-tunnel can be summarised:

1) A domain must be defined that suffices as both the limit of the computational boundaries and as the area covered by the experimental investigation.

2) The test conditions must be capable of being set, maintained and repeated with a high degree of accuracy because many tunnel runs will be required to map the flowfield.

3) The accuracy or uncertainty of every test condition or measured quantity must be examined and specified.

4) LDA particle seeding must be reliable and consistent.

5) The domain inflow velocities must be determined both with the LDA and another independent technique.

6) Furthermore, measurements that give confirmation of any of the LDA results should be made if at all possible.

7) The position at which LDA measurements are taken should be known relative to a model-based co-ordinate system to account for small model deflections under the aerodynamic loads.

8) Effort should be expended in acquiring LDA turbulence and shear stress data together with the mean velocities.

9) Effort should be expended in determining flow directions in regions of low speed or reversed flow.

10) The test domain should be sensibly free of other, intrusive, measuring equipment.

11) Static pressure must be recorded along all non-symmetric domain boundaries.

Many of these requirements are driven directly by the need to produce a consistent set of boundary conditions for RANS codes. In particular the measurement of static pressure around the domain can cause difficulty but without such knowledge the tunnel interference on the model is likely to invalidate the test case in all but the lowest blockage experiments. Figure 2 shows a generalised interpretation of the necessary model and domain relationship for the present class of axisymmetric afterbody experiments.

3.2 Afterbody Validation Experiments

For transonic afterbody flows, a review of the literature in 1988[9] had shown that no experiment existed at that time that met all or even most of the specific requirements listed above. Many published data-sets that have been used for limited CFD validation have either no flow data or poorly defined boundary conditions, for example refs. 10−18. Benek[19][20] and Heltsley et al.[21][22] describe two experiments that used LDA to record velocity data in afterbody flowfields and thus come closest to providing a complete validation set but there are shortcomings in the data. Benek tested an afterbody but with the jet replaced by a solid simulator and shock-induced separation conditions were avoided. Heltsley et al. used a real jet flow but presents data only at an onset Mach number of 0.6.

Lacau et al.[23] is representative of a related class of experiments in which LDA has been used to record data downstream of a blunt base body with a central jet flow. Bachalo and Johnson[24] present LDA data that has often been used for validating codes for the case of shock-induced separation but there was no jet flow and the geometry differed from an aircraft-style afterbody.

There is even less data available for the supersonic condition, but Agrell[25] describes M = 2.0 tests on a conical afterbody that have been used widely for CFD development studies. LDA data were acquired in the region of the boattail.

The report of AGARD Fluid Dynamics Panel WG 08[26] identified some of these datasets as being useful for partial validations of RANS and Euler codes, and also went some way to specifying the requirements for future tests. A further AGARD initiative in this field, Fluid Dynamics Panel WG 17, has been running over a similar timescale to the programme described in this paper. Bowers and Laughrey[27] have since extended the discussion to cover progress and requirements for development of predictions for 3-D afterbody flows.

3.3 Flowfield Measurements Using LDA

Figure 2 identifies six distinct regions for measurement with LDA that were deemed essential to the construction of a complete afterbody validation data-set:

i) Onset flow for boundary condition setting.
ii) Flow quantities along forebody to validate boundary layer growth.
iii) Boattail region for prime interest flow behaviour.
iv) Jet injection plane properties.
v) Jet plume centreline and jet mixing region.
vi) Downstream outflow boundary.

A three-component TSI LDA system was positioned on a 3-D traverse table to one side of the tunnel test section. The system was restricted to two-component measurements in the single longitudinal plane comprising the measurement domain. The blue and green beams of a 15W argon-ion laser were used, with the Doppler signal collected in backscatter mode. The measurement volume was oriented such that fringe crossings at ± 45° to the streamwise X′ direction were counted. The data processing software undertook the transformation of the mean velocities and turbulence data into the X′ and Y directions.

The laser aperture was kept small in order to maintain a gaussian beam intensity profile. Thus, for the transonic tests, only about 5W were transmitted through the 22 mm beam spacer and the x3.75 beam expander before being focused by a 762 mm lens. The resulting illuminated volume was 130 μm in diameter and 2.5 mm in length, with a fringe spacing of 5 μm. The beam spacer was 13 mm in the supersonic tests to allow for the overall higher velocities.

Bragg cells were used to provide frequency shift for the flow regions close to the model in some of the test cases. Without Bragg cells only particles with a velocity direction less than 27° from the freestream gave a sufficient number of Doppler periods (8) for the data to be validated.

The coincidence window was set to 10^{-3} seconds, with a particle transit time through the measuring volume of the order of 10^{-6} seconds. The large window was justified because the particle rate was only 100 particles/second. 1024 simultaneous samples of each component were taken at each measurement point. Both component samples were validated by a 5/8 criterion: the period time calculated from the first 5 periods was compared to the period time calculated from 8 periods; if the difference in period time was less than 1%, the measurement was validated.

The accuracy of the counter was ± 1 ns. The time for eight Doppler periods was typically 200 ns therefore any error introduced by the counter was considered negligible.

The tunnel used in the tests had a low natural particle count and forced seeding was necessary. This was achieved by injecting 500 nm (± 5 nm) latex particles in the tunnel stagnation chamber ahead of the contraction. Originally the seeding was generated by two TSI 6-jet atomisers but this was found to give an inadequate seeding rate. As the tests progressed, a seeding system designed and manufactured at FFA was installed, improving the particle count by a factor of 10. Particles of 500 nm latex were also injected into the high pressure airline supplying the jet plume, using another specially developed seeding unit. The size uniformity of both the free-stream and jet seeding particles should have eliminated any particle size

biasing of data. Particle lag effects were considered to be minimal in the parts of the flowfield investigated with the LDA.

3.4 Data Accuracy And Error Analysis

A crucial part of the production of a validation data-set is the assessment of the test data uncertainty. Test condition repeatability and test data measurement accuracy must be established[28] and specified for all boundary condition and flowfield data. This procedure is demonstrated by an example analysis for some of the test conditions later in this paper.

4. EXPERIMENTAL SET-UP

Experiments fulfilling the basic requirements outlined in ref. 26 together with the eleven specific criteria listed above, were performed in the S5 0.5 x 0.5 m suck-down wind-tunnel at the FFA Sweden. The tunnel test section has solid side walls with optical access through windows of 0.6 m diameter. For the transonic speed range $0.5 < M < 1.2$, the top and bottom walls are slotted, the test section is connected to a tunnel plenum chamber and the speed is regulated by presetting the diffuser. For supersonic operation the Mach number is set by selecting one of a range of supersonic nozzle liners.

Figures 3 and 4 show the model/tunnel relationship for test at transonic Mach number. A "hockey-stick" or blade-sting supported the model from the underside and provided the passage for the unheated air supply for the jet plume. The experimental and computational domain was situated above the model and extended to the tunnel roof. Most conventional mounting systems would introduce a degree of non-axisymmetry but it was considered the location of the blade-sting would minimise disturbances in the domain. Flowfield LDA measurements were taken in a two-dimensional plane on the model centreline through the glass side walls. Checks on the axisymmetry of the flow were made by circumferentially located pressure taps on the model.

Tunnel S5 was well suited to the task of CFD validation experiments. The test section was of reasonable size, yet, being a suck-down facility, the operating cost was nearly an order of magnitude less than blow-down or continuous running transonic tunnels. Six tunnel runs per hour, of 120 seconds duration, could be maintained indefinitely. Suck-down tunnels have naturally low turbulence levels and there is no contamination of the atmosphere with LDA seeding particles.

The one deficiency of suck-down tunnels is the limitation to moderate Reynolds number. At unity Mach number the Re/metre is about 15 x 10^6, or 0.75 x 10^6 based on the model diameter of 50 mm.

Figure 5 shows the model/support cross-sectional area variation along the tunnel test section for the transonic tests. Peak area occurs upstream of the afterbody and is a sizeable 3.32% of the tunnel cross-section. Such a high blockage level, and the resulting interference on the model pressure distribution, can be countered by the measurement of the pressure field around the entire domain. However, the longitudinal variation of blockage also caused a generally non-uniform static pressure distribution along the model forebody. An assessment of the model pressures was made for each case and the domain start boundary was positioned at a point of low streamwise pressure gradient. This location varied between extremes of $X' /D = 7.0$ and $X' /D = 8.0$.

5. TRANSONIC TESTS

5.1 Model Geometry

For the transonic tests the "AGARD-series" of afterbody models were selected as their use has been widely reported[26][29] and a range of boattail flow features can be created by choosing the appropriate model and test conditions. The 10° and 15° models were selected as being most appropriate to aircraft-style afterbody flows. The geometries are defined in ref. 29; the only deviation from the standard geometry was the adoption of a less complex internal jet-pipe contour to ease representation by computational meshes. Figure 6 shows the 15° afterbody geometry; internally the two models were identical but the 10° model had a more gentle external boattail curve.

A common forebody fitted with a 14° half-angle conical nose was used with both transonic afterbodies and for the supersonic tests. The complete transonic model had 32 pressure taps along its upper surface in the plane of the measurement domain. Ten of the taps were located forward of domain start location; the majority of the remaining 22 were concentrated in the afterbody region.

A long forebody was selected to generate a thick boundary layer at the start of the afterbody, thereby allowing a good resolution of the flow features by the LDA. Ref. 30 presents results from the AGARD models for a Reynolds number range of $0.82 - 4.11$ x 10^6 and showed no substantial change in surface pressures, although integrated drag was slightly Reynolds number dependent. It was considered that using Re $\simeq 0.75$ x 10^6 in the present tests would produce the same fundamental flow phenomena. A carborundum strip at the end of the nose section was used to force transition of the boundary layer to a turbulent state. LDA measurements in the boundary layer confirmed that transition was achieved.

5.2 Measurements Taken

In addition to the model surface pressures and the LDA flowfield information, the following test data were recorded (see Figure 4):

1) Tunnel stagnation pressure and temperature, $P_{o\ \infty}$ and $T_{o\ \infty}$.
2) Tunnel wall static pressures on centreline above model.
3) Stream static pressure variation at domain end.
4) Stagnation pressure distribution and total temperature of internal nozzle flow at $X'/D = 9.5$.

The stream static pressure variation at the domain outflow boundary was recorded by a three probe static pressure rake. A calibration of the rake revealed acceptable accuracy except at conditions close to unity Mach number[31]. However, the freestream static pressure could generally be inferred from the roof measurements and the rakes use was restricted to defining the jet plume behaviour.

A total pressure rake was built into the model jet-pipe at $X'/D = 9.5$ and a thermocouple recorded the stagnation temperature. Gauzes and straighteners were fitted upstream of the jet-pipe; nozzle exit traverses with a pitot tube revealed uniform flow over a wide NPR range[31].

Figures 7 and 8 show details of the LDA traverse lines for one of the transonic test conditions, CASE A. Approximately 500 data-points were investigated for each of the transonic tests.

5.3 Test Cases

Three basic cases were tested to produce a range of afterbody flow features, denoted in Table 1 as CASES A, B and C. CASES A and B used the AGARD 10° afterbody and CASE C used the 15° configuration. Further more limited tests were undertaken as CASES Ca − Ce in which LDA flowfield surveys were not made except to define the domain inflow plane.

CASE	Afterbody Model	M_{tun}	Re . x 10^{-6}	NPR_{nom}	Lines of LDA Trav.
A	10°	0.80	0.681	1.45	19
B	10°	0.99	0.722	6.0	17
C	15°	0.96	0.728	6.0	18
Ca	15°	0.88	0.695	6.0	1
Cb	15°	0.92	0.707	6.0	1
Cc	15°	0.98	0.730	6.0	1
Cd	15°	0.96	0.725	4.0	0
Ce	15°	0.96	0.726	7.8	0

TABLE 1: TRANSONIC TEST CASE CONDITIONS

The values quoted as M_{tun} in Table 1 are the tunnel-empty Mach numbers set according to the tunnel calibration. For CFD validation, a more detailed specification of the onset Mach number at the domain start location is required than a simple statement of M_{tun}. For this purpose, M_∞ was calculated at the domain start by considering the model surface static pressure and the stagnation conditions. M_∞ was reduced relative to M_{tun} by the effects of tunnel/model interference.

All static pressures around the measurement domain were also referenced to the domain start conditions, thus:

$$C_p = \frac{P - P_\infty}{q_\infty} \qquad [1]$$

The jet pressure ratio NPR_{nom} was defined as:

$$NPR_{nom} = \frac{P_{o\ jet}}{P_{pnm}} \qquad [2]$$

where P_{pnm} was the static pressure recorded in the tunnel plenum chamber. True nozzle pressure ratio would be significantly lower than NPR_{nom} because the boattail recompression raised the local static pressure to a higher value than P_{pnm}.

CASE A was chosen to produce an entirely subsonic flowfield and the afterbody flow was expected to be attached. CASE B used the same afterbody but at substantially higher onset flow Mach number and with an underexpanded jet. This case was expected to generate a flow separation on the afterbody. CASE C was presumed to be the severest case computationally as it was expected there would be a strong afterbody shock wave at the recompression and a large area of separated flow. CASES Ca − Ce involved running at either onset flow or jet plume conditions different to the basic CASE C.

5.4 Results

CASE A:
10° Afterbody, $M_{tun} = 0.80$, $NPR_{nom} = 1.45$

The model surface pressure distribution for CASE A is shown by Figure 9. Figure 10 shows a sketch of the flow features created after studying all the available sources of experimental information.

The freestream undergoes a gradual expansion over the afterbody shoulder followed by a strong two stage recompression. As originally intended, the freestream flow nowhere reaches sonic velocity. LDA measurements, supported by oil flow visualisation, indicated that the flow has in fact separated at the rear-end of the boattail. Surface pressure measurements

failed to show this feature as the small region of reverse flow is aft of the pressure tapped area.

A slight difference in the model and roof C_p's at the domain start location was caused by the afterbody generated pressure field. Accurate CFD boundary condition specification should account for this variation. A check on the effect the cross-stream pressure variation would have on the uniformity of the onset velocity revealed a variation of less than 1%. The maximum value of the roof C_p coincided with the region of low model and support blockage shown by Figure 8.

The thick boundary layer and ensuing separation cause a large wake region to exist in the lee of the boattail curve, see Figure 10, although the recirculating flow region barely extends downstream of the model. The Y extent of the separation is very small. The line dividing the boundary layer and the wake from the basically unaffected freestream region is positioned at an approximately constant Y value.

Figures 11 − 14 present some of the LDA data used to construct the sketch of Figure 10. $\overline{U}$ data from two cross-stream LDA traverses are shown by Figure 11. Traverse 2 coincides with the domain start and traverse 5 lies close to the trailing edge of the afterbody at $X'/D = 11.806$. Analysis of the boundary layer shape at traverse 2 showed a profile close to that of a naturally transitioning boundary layer in a zero pressure gradient. The measured freestream $\overline{U}$ velocity at traverse 2 differed by less than 1% from the value of the reference velocity U_∞ calculated from the model pressure.

At traverse 5 there is a reversed flow region, indicating the flow on the boattail has indeed separated. Figures 12 and 13 show the $\sqrt{\overline{u^2}}/U_\infty$ and $\overline{uv}/U_\infty^2$ quantities at traverse 5. Turbulence and shear stress increase as the model surface is approached.

Figure 14 shows the jet plume and mixing region some distance downstream of the exit plane. Although the pitot traverse across the exit plane undertaken to establish flow quality had shown good uniformity, the $\overline{U}$ variation immediately downstream of the nozzle had shown distinct velocity peaks near the nozzle lip location with uniform flow confined to the central 80% of the jet diameter. The presence of the velocity peaks suggests a strong lateral static pressure gradient must exist in the jet at the nozzle plane. There was some evidence that the jet-pipe convergence at exit caused the jet throat to occur a small distance downstream of the nozzle exit plane. Figure 14 demonstrates that at $X'/D = 12.275$ there is still evidence of a velocity peak at the edge of the jet. It is also clear that the remnants of the model boundary layer and separation remain present at the end of the measurement domain.

Tests on at least five nominally identical AGARD 10° afterbodies have never attracted the comment that the flow separated[29]. It is possible that the separation is unique to the present set-up due to the particular test conditions. The low Reynolds number and consequently thick boundary layer of the present tests may have produced a boundary layer marginally too thick to withstand the boattail recompression. Alternatively, it may be the case that previous investigators failed to identify the small area of separation from their surface pressure data.

CASE B:
10° Afterbody, $M_{tun} = 0.99$, $NPR_{nom} = 6.0$

Figure 15 presents the model surface pressures for CASE B and Figure 16 portrays the flowfield events established by the LDA data. The freestream flow accelerates smoothly over the afterbody shoulder to a supersonic velocity. The recompression shows the same two-stage feature as CASE A, strongly suggesting this is a characteristic of the 10° model geometry rather than particular flow conditions. A schlieren image showed the absence of an afterbody shock in the region of the recompression. Separation occurs well downstream on the afterbody and appears to be caused by a straightforward adverse pressure gradient. The separation extent is larger than for CASE A in both the X' and Y directions but still the separation covers only a small part of the complete boattail.

Operation at a higher onset Mach number caused the roof pressure distribution to show more pronounced model interference effects than for CASE A. However, the extra blockage of the underexpanded jet did not produce a noticeable effect on the roof pressures.

The jet structures for CASES B and C were similar and are described below.

CASE C:
15° Afterbody, $M_{tun} = 0.96$, $NPR_{nom} = 6.0$

The surface pressure distribution is shown in Figure 17, and Figures 18 and 19 present the schlieren image and flowfield sketch respectively. Based on the surface pressure information, the freestream flow accelerates over the afterbody shoulder to a Mach number of about 1.2. The flow is supersonic for only a short axial distance before a strong shock-wave on the afterbody shoulder recompresses the stream. The supersonic region is smaller than for CASE B with the 10° afterbody but the shock generates a much more rapid recompression. The schlieren places the shock slightly upstream of the end of the supersonic region denoted by the surface pressures. However, a traverse located just upstream of the shock, Figure 20, shows the $\overline{U}$ velocity profile to be peaky and it is clear that surface pressures are probably a poor measure of the location of off-surface features such as shock waves.

The LDA data suggest the flow separates from the surface almost immediately after the shock. The flow does not re-attach to the boattail, causing most of the afterbody flow to be separated. Even though the boat-tail surface is strongly curved, the separation bubble remains relatively thin in the Y direction and appears to follow the surface curvature. The schlieren image is not helpful in determining the separation extent.

The LDA data clearly shows the sonic throat of the jet flow occurs about $0.20D - 0.25D$ downstream of the nozzle exit plane. Figure 21 presents the $\bar{U}$ data from two cross-stream traverses located upstream of the jet Mach disk and Figure 22 displays the jet centreline $\bar{U}$ velocity. As for CASE A the nozzle exit plane pitot traverse had shown uniform nozzle total pressure, but Figure 21 shows a heavily distorted velocity profile. There appears to be substantial lateral static pressure gradient together with a strongly curved sonic line. The evidence suggests the velocity non-uniformity is a nozzle feature caused by the geometric convergence at the nozzle exit, for all of CASES A, B and C.

The underexpanded jet shows a clear Mach disk on the schlieren at $X'/D \simeq 12.3$. The LDA identifies the Mach disk at the same location, Figure 22. The behaviour of the jet centreline $\bar{U}$ velocity shows a strong expansion is present immediately the jet leaves the nozzle. A reduction in velocity gradient is evident just before the Mach disk. The post-Mach disk velocities are less than the minimum sustainable by a normal shock. Ref. 32 showed that post-Mach disk flows may be subject to a subsonic-diffusion effect that further reduces velocity.

CASES Ca – Ce

Table 1 displays the test conditions used for CASES Ca – Ce with the 15° afterbody. The surface pressure distributions for CASES Ca – Cc are shown on Figure 23 and for CASES Cd and Ce on Figure 24. The tests with differing onset flow Mach numbers, Figure 23, show a strengthening of the afterbody shock as Mach number increases and schlierens showed slight movement of the shock downstream. The surface pressure plots also show that peak pre-shock Mach numbers are higher for the higher Mach number tests. The separation region is likely to start immediately behind the shock and cover the whole boattail for all cases.

Those tests with differing jet pressure ratio and constant onset Mach number, Figure 24, show no significant effect of jet conditions on the shock location. Afterbody pressures show most effect towards the boattail rear-end.

5.5 Data Accuracy

It was demonstrated that M_{tun} was repeatable to within $\pm$ 0.003 but that small variations in the stagnation temperature of the induced air increased the repeatability error for U_∞ to $\pm$ 1.0%. Worst case deviations in the static pressure measurements equated to ΔC_p of 0.0030. Problems were encountered when trying to maintain the nozzle pressure ratio and a study of the run-log showed worst case deviations in the jet velocity of $\pm$ 6.0%.

A detailed analysis of the LDA data was undertaken to establish error limits[33], with special emphasis on errors introduced by the instrumentation. The relatively low particle count rate and generally high velocities resulted in relatively long periods of signal drop-out that may have allowed amplifier and photo-multiplier noise to affect the data quality, although this problem was serious only in the jet region. In general the results showed different error limits were applicable in the various regions of the flowfield. The findings are presented in Table 2 and are overall uncertainties including repeatability and LDA errors.

Flow Region	95% Confidence Level On:-		
	$\bar{U}$	$\bar{V}$	$\sqrt{\overline{u^2}}/U_\infty$, $\sqrt{\overline{v^2}}/U_\infty$
Undisturbed Freestream	$\pm$ 1.7% $\bar{U}$	$\pm$ 1.6 m/s	$\pm$ 1.0% $\bar{U}$
Model Boundary Layer/ Boattail Flow	$\pm$ 2.5% $\bar{U}$	$\pm$ 1.6 m/s	$\pm$ 2.0% $\bar{U}$
Separated Region	$\pm$ 10.0% $\bar{U}$	lesser of:- $\pm$ 10.0% $\bar{V}$ $\pm$ 2.0 m/s	$\pm$ 100.0% $\sqrt{\overline{u^2}}/U_\infty$
Jet Region	CASE A:- $\pm$ 3.5% $\bar{U}$ CASE B:- $\pm$ 5.0% $\bar{U}$ CASE C:- $\pm$ 5.0% $\bar{U}$	lesser of:- $\pm$ 10.0% $\bar{V}$ $\pm$ 2.0 m/s	too uncertain to quote
Wake/Mixing Region	$\pm$ 3.0% $\bar{U}$	lesser of:- $\pm$ 10.0% $\bar{V}$ $\pm$ 2.0 m/s	$\pm$ 2.0% $\bar{U}$

TABLE 2: UNCERTAINTY VALUES ASSOCIATED WITH LDA DATA FOR TRANSONIC CASES

Counter based LDA systems have a lower limit to the resolvable turbulence levels. The turbulence results in the undisturbed freestream demonstrated that the LDA was giving over-estimates of the values of $\sqrt{\overline{u^2}}$ /U_∞ and $\sqrt{\overline{v^2}}$ /U_∞. The known turbulence level in tunnel S5 is of the order of $\sqrt{\overline{u^2}}$ /U_∞ = 0.75% at transonic speeds; the LDA could not resolve below about 1.0%. This is not a serious difficulty as the prime regions of interest are the boundary layer, separation regions and mixing layers that generate turbulence many times this level. A study of the possible sources of error in the turbulence data produced an estimate that a 95% certainty on $\sqrt{\overline{u^2}}$ /U_∞ and $\sqrt{\overline{v^2}}$ /U_∞ was ± 1.0% of the local velocity magnitude (usually assumed to be $\overline{U}$).

Taking LDA data in the jet proved to be substantially more difficult than taking data in the tunnel flow. This was probably a combination of the worse repeatability of the jet pressure setting and less consistent seeding in the jet. An overall uncertainty for the jet $\overline{U}$ velocity measurements was estimated to be ± 5.0% for CASES B and C and ± 3.5% for CASE A. The mixing region between the jet and the tunnel streams proved far more amenable to investigation with the LDA and uncertainties approaching those noted previously for the onset boundary layers were attained.

It was calculated that the measurement volume was positioned within 0.15 mm of its intended location for the majority of the measurement points close to the model. For measurement points greater than about 0.5D from the model the position accuracy fell to about ± 0.3 mm. The uncertainties specified for the mean and turbulence measurements includes allowance for this magnitude of error in measurement position.

5.6 Comparison With Navier-Stokes Code

5.6.1 Introduction

The complex and viscous nature of afterbody flows demands the use of a Navier-Stokes code if the salient features are to be correctly predicted. Currently, one of the major physical modelling issues for such flows is the choice of turbulence model. A successful model will be able to predict, with adequate accuracy, all the flow features highlighted in Section 2, whilst being:

1) Affordable, in terms of:
   − grid set-up
   − computational solution time
   − computer memory requirements

2) Robust, in terms of:
   − applicable without change to a wide variety of afterbody problems
   − solution stability

5.6.2 CFD Code Description

An axisymmetric RANS code, due to Peace[34], has been further developed to now include three different formulations of time-averaged turbulence model, namely:

1) Algebraic − Baldwin-Lomax[35]   − BL
2) Eddy viscosity − Chien k-ϵ[36]   − k-ϵ
3) Algebraic Reynolds Stress
                  − Gibson and Launder[37]   − ASM

Comparison with accurate experimental data provides a mechanism by which the most appropriate method for engineering use can be chosen. The flow solver is a direct extension of the structured, cell-centre, finite volume formulation of Jameson, Schmidt and Turkel[38], cast in polar coordinate form to reduce axisymmetric afterbody flows to 2-D axial and radial sense problems. Many standard techniques are applied, such as time-marching via 4th order Runge-Kutta, central differencing, the gradual reduction of artificial dissipation within shear layers, local time-stepping based on cell characteristic speeds and the application of implicit residual smoothing. The code is blocked into two regions: the external "freestream" flow and the jet flow (both inside and external to the model). An unusual feature of the code is the adaption of the grid radially to preserve the wake dividing streamline (i.e. the common face between the external and jet blocks). This allows a dense clustering of cells in this area of high velocity shear.

Each turbulence model uses a two-layer approach, to better represent the viscous sub-layer close to the solid surfaces, and follows standard implementation practices. Further comments on the turbulence closures are:

1) Baldwin-Lomax − the model is modified following Cebeci et al.[39] to extend its applicability into the jet/wake region downstream of the afterbody.

2) Chien k-ϵ − the low Reynolds number, two-equation differential model is a standard implementation with convective terms treated using first order upwind differencing to enhance stability for a slight loss in accuracy. Values of k and ϵ are initially set according to turbulent viscosities computed from the Baldwin-Lomax model.

3) Gibson-Launder ASM − the high Reynolds number algebraic stress model requires a separate treatment in the surface viscous sub-layer. The Wolfshtein one equation model[40] was found to be more stable than the Chien model. The explicit solution method of Dimitriadis and Leschziner[41] has been adopted, as this was found to be more robust than other approaches tried.

5.6.3 Grids And Boundary Conditions

The grid used throughout is reasonably fine with 188 x 48 cells in the external block and 139 x 41 in the jet block. The near-wall cell centre is positioned at 0.000025 D normal to the surface. This gives about five cells in the laminar sub-layer. Details close to the surface of a typical post-solution grid are shown in Figure 25, showing the adaption of the dividing stream-line. The grid extends axially and radially to the full extent of the experimental measurement domain. CFD results will be presented using the radial ordinate Y together with the ordinate X measured downstream from the nozzle exit plane.

Six boundary condition types have to be applied to represent the in-tunnel flowfield: freestream inflow; tunnel roof; jet inflow; domain outflow; solid surface; and centreline. The first four boundary condition types are based on the experimental data, which have been smoothed to account for the small measurement inaccuracies that inevitably occur. The treatment of the latter four are described in Peace[34], whilst the others are now briefly explained.

1) Freestream Inflow — this follows Jameson et al.[38] in using characteristic equations. Radial velocity is set to zero as this was measured to be generally less than 1% of axial velocity and subject to scatter. LDA measurements of axial velocity do not resolve the afterbody surface boundary layer sufficiently well (especially the laminar sub-layer) to input directly into a CFD code. The measurements do, however, allow an accurate curve-fit to be generated of the velocity variation. The correlation technique of Green et al.[42] was used to derive profiles of inflow velocity and density for the measured 1/7th power law boundary layer.

2) Tunnel Roof — although the roof static pressure distribution was measured in the experiment, it is not known whether local inflows or outflows were present through the roof slots. Three different boundary condition types were tested on CASE A with the BL turbulence model, namely:

    a) Riemann Invariants, assuming freestream conditions external to the roof location.

    b) Riemann Invariants, incorporating the measured tunnel roof pressures.

    c) Rudy-Strikwerda[43] non-reflecting outflow boundary conditions, using measured tunnel roof pressures.

Predictions of afterbody surface pressures for CASE A using the above three roof boundary conditions are compared with experimental data in Figure 26. This shows large differences between the three approaches, with Rudy-Strikwerda being

notably superior. Strangely, this predicted a small amount of inflow (less than 1% of axial velocity) along part of the roof section. Nevertheless, the importance of using an appropriate boundary condition for a slotted roof, using measured static pressures and accounting for the flow between the working section and the outer plenum, is clearly illustrated. The Rudy-Strikwerda condition was used throughout all subsequent predictions.

5.6.4 Flow Simulations

Each of the turbulence models within the RANS code has been applied to CASES A, B and C.

CASE A

Afterbody surface pressure predictions are compared in Figure 27 with experimental data. There is generally good correlation between all three models at these subsonic, largely attached flow conditions. The two stage recompression on the afterbody is clearly seen, with the ASM (which models curvature effects) closest to the test data. The only noticeable difference is in the immediate vicinity of the trailing edge, where the ASM shows the reduction in pressure gradient often seen in mildly separated flows. Examination of two radial LDA traverses immediately before and aft of the trailing edge, Figure 28, show that the ASM is the only model to predict the small region of reversed flow found in the experiment. However, the ASM is apparently less successful than the other two models in predicting the shape of the boundary layer profile further forward on the geometry. Interestingly, the experimental data shows a reduction in velocity gradient close to the surface, although no turbulence model emulates this.

The non-uniform velocity at the jet exit is well predicted in Figure 28, but this feature rapidly dissipates downstream to give a uniform value across the jet, unlike that observed in the tests.

The BL model needed 4000 time-steps to reach a satisfactory level of convergence. Using this solution as initial conditions, k-ε and ASM required a further 4000 and 6000 time-steps respectively.

CASE B

Afterbody surface pressure predictions are compared in Figure 29 with experimental data and all again show generally good agreement until separation, due to the adverse pressure gradient, is reached. The ASM is closer to the experimental data in the attached flow region and clearly predicts the point of separation and the separated zone better than the k-ε model, which itself is better than Baldwin-Lomax. Velocity profiles in this region show a similar behaviour to CASE A and are not repeated. Flow characteristics in the jet were very similar to CASE C and are discussed below.

Convergence difficulties were encountered for both k-ε and ASM models. An enriched grid in the region of the Mach disk was required for k-ε to converge satisfactorily. On the finer grid Baldwin-Lomax required 4000 time-steps and k-ε a further 5000 time-steps. ASM convergence problems centred around the use of the boundary condition of the measured tunnel roof pressures, which, as expected, showed considerably more variation than CASE A. The difficulty was overcome by starting from the k-ε solution and running, initially, with freestream conditions at the roof location for 9000 time-steps. The measured values of roof pressures were then switched-in and the fourth order dissipation value doubled for a further 9000 time-steps. Whether a different sequence of running would have been more efficient has not been investigated.

CASE C

The separation generated at the foot of the boattail shock for CASE C is evident in the predictions shown in Figure 30. Again, the ASM outperforms the other two more simple models, returning a superior surface pressure prediction before and aft of the shock. A full set of velocity profiles along a radial LDA traverse off the afterbody and in the middle of the separation region is shown in Figure 31. Axial and radial velocities show the expected benefits of the ASM, with k-ε little better than Baldwin-Lomax. This finding was also supported when the normal and shear stress variations were studied. Jet centreline axial velocities are shown in Figure 32. Not surprisingly, in this largely inviscid region, the turbulence models all return similar results. The velocities are substantially overpredicted, including that at the jet exit, suggesting a small error in either the specification or the subsequent use of the internal jet boundary condition. However, the shock structure is well captured with the Mach disk correctly located and the axial length of the shock cells downstream being properly modelled. The velocity extrema are over-predicted, most probably due to the turbulence models' inability to generate turbulence, and hence dissipation, at the Mach disk.

To achieve acceptable convergence the BL model required 4000 time-steps. The k-ε model required a further 10000 time-steps after restarting from the BL solution. The ASM diverged when a similar technique was used. Convergence was procured by using 8000 time-steps when restarting from the k-ε solution.

5.6.5 Round-Up

The quality of physical prediction for afterbody flows increases with the complexity of the turbulence model employed. In particular, the ASM consistently and accurately predicts separation where the other two simpler models do not. This result has obvious attractions for the computation of afterbody drag

quantities. However, the accuracy is inversely proportional to the robustness and speed of the models, raising doubts as to the usefulness of higher order models on more complex afterbody geometries. The overall computing times are approximately in the ratio:

$$BL \, / \, k\text{-}\epsilon \, / \, ASM \; = \; 1 \, / \, 5 \, / \, 10$$

6. SUPERSONIC TESTS

6.1 Model Geometry

The gometry of the model used in the supersonic tests was the same as that tested previously[25], and selected as AGARD FDP WG 08 test cases 9 − 12[26]. This model has been used since the early 1970's for a series of tests exploring the influence of a propulsive jet emanating from the base plane.

The model construction was similar to that used in the transonic tests except for the afterbody portion. An 8° conical boattail and a cylindrical afterbody were tested, both with a convergent-divergent jet nozzle of design Mach number 2.5. Results are given only for the conical boattail model. The jet nozzle was of 20° conical divergent form and had an exit diameter of 30 mm (0.6D). The overall length of the model was 9.0D, with the afterbody occupying the last 1.0D. Figure 33 shows the model/tunnel relationship. A carborundum strip was again used to force boundary layer transition.

6.2 Measurements Taken

Figure 34 shows the overall LDA measurement domain for the supersonic tests. It consists of a number of horizontal and vertical traverse lines selected to provide information on the effects of flow expansion, separation, recirculation and plume interaction. A total of 500 datapoints were measured in the supersonic tests.

In addition to the LDA measurements a limited number of static pressures on the afterbody were recorded to allow for comparison with previous data. The wind-tunnel total pressure and temperature were also recorded. The survey of the domain boundary conditions for the supersonic flowfield was not as extensive as in the transonic cases, since the area of interest was well inside the wind-tunnel test rhombus.

6.3 Test Cases

Both afterbodies were tested at nominal freestream Mach number $M_{tun} = 2.0$ and an $NPR_s = 15.0$. A revised form of NPR definition was adopted for the supersonic tests based on the jet pipe static pressure. The 8° conical test case is denoted as CASE D.

6.4 Results

<u>CASE D:</u>
<u>8° Conical Afterbody, M_{tun} = 2.0, NPR_s = 15.0</u>

Results for CASE D will only be discussed briefly since a more extensive report is being prepared for publication. Figure 35 is helpful in clarifying the complex nature of the flowfield. This figure includes a boattail pressure distribution at NPR_s = 9.0 as well as a photo-montage of a schlieren and an oil-flow picture. The flow features such as the oncoming boundary layer on the cylindrical model body, the expansion fan at the junction of the conical afterbody, the separation shock with accumulation of oil at the separation line and traces of reversed flow downstream of the shock are clearly visible. The results shown in the following figures are for NPR_s = 15.0 resulting in a somewhat larger separated region which facilitated the LDA measurements.

Figures 36 – 38 show the development of velocity, turbulence and shear stress profiles along the cylindrical part of the model ahead of the boattail, traverses 1, 2 and 3 in Figure 34. At traverse 1 the boundary layer thickness is 5.4 mm for $\overline{U}/U_\infty$ = 0.99 and the boundary layer profile follows a power law form with an exponent of 6.0. The turbulence level is around 1% of U_∞ in the freestream, but this is a spurious result caused by system noise as explained in Section 5.5. Freestream levels measured with hot wires show $\sqrt{\overline{u^2}}/U_\infty$ = 0.0025. The turbulence level increases to about $\sqrt{\overline{u^2}}/U_\infty$ = 0.1 at 0.1 mm above the surface which is the limiting location for the LDA system. The shear stress has the same variation as observed in the transonic tests.

Figure 39 shows the mean LDA data taken at X'/D = 9.012, 0.6 mm downstream of the base plane. In Figure 39a the jet flow has an almost constant axial velocity. Outside the jet, the recirculation flow in the separated region has a maximum velocity magnitude of 10% of the freestream velocity. Above the maximum velocity point the flow accelerates continuously to the freestream value. Figure 39b shows the $\overline{V}$ velocity. A pronounced flow in the jet away from the axis is evident. The variation in the separated region is also seen. Figure 39c shows the velocity data of Figure 39a replotted as Mach number, assuming the stagnation conditions in the freestream and jet hold at the measurement location.

The flow angle at the same location is shown in Figure 40. Zero degrees represents flow in the freestream axial direction. As can be seen in the figure, the flow angle at the nozzle centreline is 0° and increases gradually to 20° close to the nozzle wall, which is the nozzle exit angle. Further outwards there is the corner expansion to nearly 50° before a change

of 180° occurs in the separated region. This information is used to create a velocity vector field just downstream of the base in Figure 41. An enlargement of the part where the flow undergoes large changes in direction is shown in Figure 42, indicating very good resolution of the flowfield.

Figure 43 shows the development of the velocity vectors along the afterbody from the start of the conical boattail to the base plane region. The extent of the separated region is clearly visible.

In Figure 44 the velocity vector field downstream of the base plane are shown. Results from the plume boundary region have not been obtained to-date, but new measurements are planned to increase the number of measured points. The wake recovery from the separated region is clearly shown in Figure 44.

7. CONCLUSIONS

A well-defined set of requirements for afterbody CFD validation tests has been drawn up after consultation with CFD developers. The requirements have defined the direction of two experimental programmes to acquire validation data.

The FFA S5 suckdown wind-tunnel and associated facilities have proved well suited to conducting experiments designed to provide detailed flowfield data for afterbody/jet flows. Good repeatability was evident over a long timescale.

The careful measurement of suitable data at all boundaries of the test domain, detailed mapping of the flowfield and surface pressure information in all significant regions, together with extensive error analyses, undertaken to evaluate the accuracy of all measurements, have confirmed these experiments have substantial advantages over many well-known and well used datasets of the past.

Flow separates on the boattail of the AGARD 10° and 15° afterbody geometries at the high subsonic and transonic conditions tested. Adverse pressure gradients caused the separation on the 10° model; shock/boundary-layer caused the separation on the 15° model. A test at M_{tun} = 2.0 with an 8° conical boattail showed a further example of shock induced separation.

Transonic Navier-Stokes computations run in conjunction with the transonic test programme have shown that:

1) Static pressure along the slotted tunnel roof must be known from the tests and applied through a computational boundary condition that accounts for porosity. Failure to specify the roof pressure would have resulted in a very poor correlation with the measured afterbody surface pressures.

2) An algebraic stress model of turbulence has returned considerably superior predictions of afterbody surface pressures than two more simple models, in both attached and separated flow. Even small regions of separated flow are well predicted. This is, however, achieved at the expense of reduced numerical robustness and an order of magnitude greater computing time.

The experimental data presented should provide a substantial contribution both to the physical understanding of simple afterbody flows and to the database for CFD validation studies.

ACKNOWLEDGEMENTS

REFERENCES

1. CAPONE F J "The Nonaxisymmetric Nozzle — It is for Real", AIAA Paper 79-1810, AIAA Aircraft Systems and Technology Meeting, New York, August 1979

2. CHAMBERLIN R and BLAHA B J "Flight and Wind Tunnel Investigation of the Effects of Reynolds Number on Installed Boattail Drag at Subsonic Speeds", AIAA Paper 73-139, AIAA 11th Aerospace Sciences Meeting, Washington D.C., January 1973

3. POZNIAK O M "A Review of the Effect of Reynolds Number on Afterbody Drag", AGARD CP-301: Aerodynamics of Powerplant Installation, Toulouse, May 1981

4. BUCCIANTINI G "Improvement of Aircraft Buffet Characteristics", AGARD AR-82: Effects of Buffeting and Other Transonic Phenomena on Manoeuvring Combat Aircraft, July 1975

5. ROBINSON C E and PRICE E A "Effect of Reynolds Number on the Nozzle Afterbody Performance of the AGARD Nozzle Afterbody and the B-1 0.06-Scale Model at Transonic Mach Numbers", AIAA Paper 75-1321, AIAA/SAE 11th Joint Propulsion Conference, Anaheim, California, September-October 1975

6. WHITE R A, AGRELL J and NYBERG S-E "Supersonic Wind Tunnel Simulation of Propulsive Jets", Journal of Spacecraft and Rockets, Vol.22 No.5, September-October 1985

7. PETERS W L and KENNEDY T L "An Evaluation of Jet Simulation Parameters for Nozzle/Afterbody Testing at Transonic Mach Numbers", AIAA Paper 77-106, AIAA 15th Aerospace Sciences Meeting, Los Angeles, California, January 1977

8. MARVIN J G "Accuracy Requirements and Benchmark Experiments for CFD Validation", AGARD CP-437: Validation of Computational Fluid Dynamics, Lisbon, May 1988

9. MILLER P "Transonic Afterbodies: A Survey of the Experimental Literature", Miller and Wilson Aerodynamics Research Report MW-TR-88-15, November 1988

10. SHREWSBURY G D "Effect of Boattail Juncture Shape on Pressure Drag Coefficients of Isolated Afterbodies", NASA TM X-1517, March 1968

11. REUBUSH D E and RUNCKEL J F "Effect of Fineness Ratio on Boattail Drag of Circular-Arc Afterbodies having Closure Ratios of 0.50 with Jet Exhaust at Mach Numbers up to 1.30", NASA TN D-7192, May 1973

12. MASON M L and PUTNAM L E "Pitot Pressure Measurements in Flow Fields Behind Circular-Arc Nozzles with Exhaust Jets at Subsonic Free-Stream Mach Numbers", NASA TM-80169, December 1979

13. ABEYOUNIS W K and PUTNAM L E "Investigation of the Flow Field Surrounding Circular-Arc Boattail Nozzles at Subsonic Speeds", NASA TP-1633, May 1980

14. REUBUSH D E "Experimental Study of the Effectiveness of Cylindrical Plume Simulators for Predicting Jet-On Boattail Drag at Mach Numbers up to 1.30", NASA TN D-7795, November 1974

15. GALIGHER L L, YAROS S F and BAUER R C "Evaluation of Boattail Geometry and Exhaust Plume Temperature Effects on Nozzle Afterbody Drag at Transonic Mach Numbers", USAF AEDC Report TR-76-102, October 1976

16. JACOCKS J L, PETERS W L and GUYTON F C "Comparison of Computational and Experimental Jet Effects", Journal of Aircraft, Vol.20 No.6, November 1982

17. PUTNAM L E and MERCER C E "Pitot-Pressure Measurements in Flow Fields Behind a Rectangular Nozzle with Exhaust Jet for Free-Stream Mach Numbers of 0.00, 0.60 and 1.20", NASA TM-88990, November 1986

18. COMPTON W B, THOMAS J L, ABEYOUNIS W K and MASON M L "Transonic Navier-Stokes Solutions of Three-Dimensional Afterbody Flows", NASA TM-4111, July 1989

19. BENEK J A "Separated and Nonseparated Turbulent Flows about Axisymmetric Nozzle Afterbodies. Part I. Detailed Surface Measurements", USAF AEDC Report TR-78-49, October 1979

20. BENEK J A "Separated and Nonseparated Turbulent Flows about Axisymmetric Nozzle Afterbodies. Part II. Detailed Flow Measurements", USAF AEDC Report TR-79-22, October 1979

21. HELTSLEY F L, WALKER B J and NICHOLS R "Transonic Nozzle-Afterbody Flow Field Measurements Using a Laser Doppler Velocimeter", AGARD CP-348: Wind Tunnels and Testing Techniques, Çesme, Turkey, September 1983

22. HELTSLEY F L and CROSSWY F L "Two-Component LDV Turbulence Measurements in an Axisymmetric Nozzle Afterbody Subsonic Flow Field with a Cold Underexpanded Jet", USAF AEDC Report TR-82-27, June 1983

23. LACAU R G, DESNOYER D and DÉLERY J "Laser Velocimetric Analysis of the Flow Downstream of Missile Aft-Bodies", AGARD CP-336: Missile Aerodynamics, Trondheim, Norway, September 1982

24. BACHALO W D and JOHNSON D A "Transonic, Turbulent Boundary-Layer Separation Generated on an Axisymmetric Flow Model", AIAA Journal, Vol.24 No.3, March 1986

25. AGRELL J "Wind Tunnel Investigation of Separated Flow Over an Afterbody in Supersonic Axisymmetric Stream Utilizing One-Component Laser-Doppler-Velocimetry", FFA TN 1983-10, February 1983

26. ANON. "Report of the Working Group on Aerodynamics of Aircraft Afterbody", AGARD AR-226, June 1986

27. BOWERS D L and LAUGHREY J A "Survey on Techniques Used in Aerodynamic Nozzle/Airframe Integration", AGARD CP-498: Aerodynamic Engine/Airframe Integration for High Performance Aircraft and Missiles, Fort Worth, Texas, October 1991

28. WHORIC J M and HOBBS R W "Hierarchy of Uncertainty Sources in Transonic Wind Tunnel Testing", AGARD CP-429: Aerodynamic Data Accuracy and Quality: Requirements and Capabilities in Wind Tunnel Testing, Naples, September-October 1987

29. FERRI A (editor) "Improved Nozzle Testing Techniques in Transonic Flow", AGARDograph AG-208, October 1975

30. ZONARS D, LAUGHREY J A and BOWERS D L "Effects of Varying Reynolds Number and Boundary Layer Displacement Thickness on the External Flow over Nozzle Boattails", AGARDograph AG-208: Improved Nozzle Testing Techniques in Transonic Flow, October 1975

31. MILLER P "Commissioning Phase of FFA Axisymmetric Afterbody Tests", Miller and Wilson Aerodynamics Research Report MW-TR-91-38, November 1991

32. BRYANSTON-CROSS P J and EPSTEIN A "Sub-Micron Particle Visualisation for PIV", Progress in Aerospace Sciences, Vol.27 No.3, 1990

33. MILLER P "FFA Afterbody Tests: A Summary and Review of Achievements", Miller and Wilson Aerodynamics Research Report MW-TR-93-51, January 1993

34. PEACE A J "A Navier-Stokes Method for the Calculation of Axisymmetric Afterbody Flows", ARA Report No.73, April 1988

35. BALDWIN B S and LOMAX H "Thin Layer Approximation and Algebraic Model for Turbulent Separated Flows", AIAA Paper 78-257, AIAA 16th Aerospace Sciences Meeting, Huntsville, Alabama, January 1978

36. CHIEN K Y "Predictions of Channel and Boundary Layer Flows with a Low Reynolds Number Turbulence Model", AIAA Journal, Vol.20 No.1, January 1982

37. GIBSON M W and LAUNDER B E "Ground Effects on Pressure Fluctuations in the Atmospheric Boundary-Layer", Journal of Fluid Mechanics, Vol.86, Part 3, June 1978

38. JAMESON A, SCHMIDT W and TURKEL E "Numerical Solution of the Euler Equations by Finite Runge-Kutta Volume Methods using Time-Stepping Schemes", AIAA Paper 81-1259, AIAA 14th Fluid and Plasma Dynamics Conference, Palo Alto, California, June 1981

39. CEBECI T, THIELE F, WILLIAMS P G and STEWARTSON K "On the Calculation of Symmetric Wakes, I -- Two Dimensional Flow", Numerical Heat Transfer, Vol.2, January-March 1979

40. WOLFSHTEIN M W "The Velocity and Temperature Distribution in One-Dimensional Flows with Turbulence Augmentation and Pressure Gradient", International Journal of Heat Transfer, Vol.12, No.3, March 1969

41. DIMITRIADIS K P and LESCHZINER M A "Modelling Shock/Turbulent Boundary Layer Interactions with a Cell-Vertex Scheme and Second Moment Closure", 12th International Conference on Numerical Methods in Fluid Mechanics, Springer-Verlag, July 1990

42. GREEN J E, WEEKS D J and BROOMAN J W F "Prediction of Turbulent Boundary Layers and Wakes in Compressible Flow by a Lag Entrainment Method", RAE TR 72231, December 1972

43. RUDY D and STRIKWERDA J "A Non-Reflecting Outflow Boundary Condition for Subsonic Navier-Stokes Calculation", Journal of Computational Physics, Vol.36, No.1, June 1980

Onset Flow

Strong Boattail
Recompression Shock

Afterbody Boundary Layer

Jet/Stream Mixing Region

Afterbody

Separation on
Boattail

Underexpanded Jet
with Complex Shock
Structure
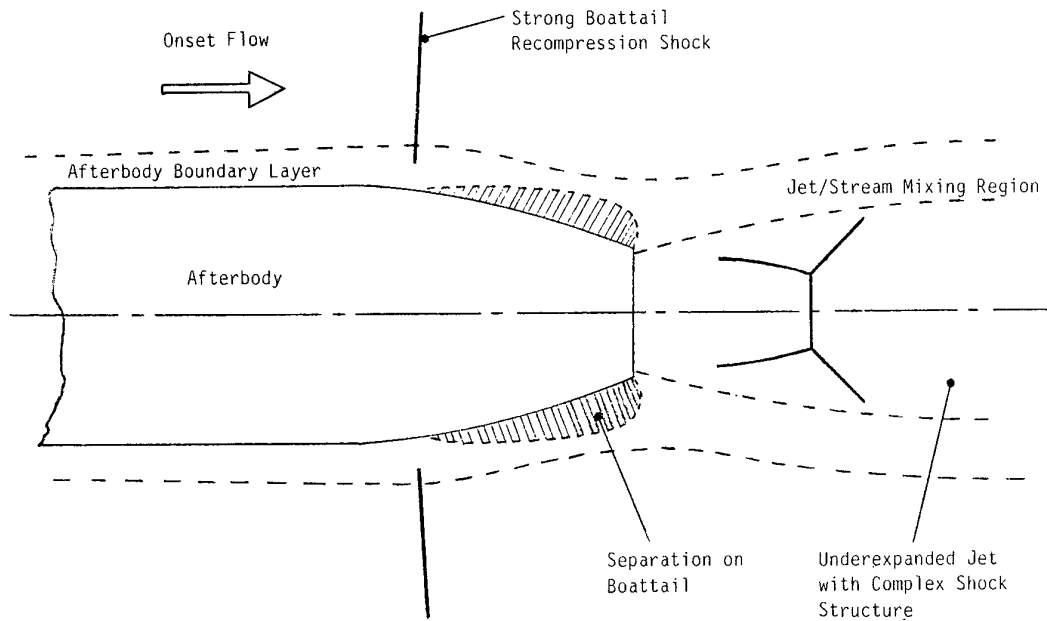
FIGURE 1: BASIC AERODYNAMICS OF AFTERBODY FLOWFIELD

Domain
Start

Domain
End

Pressure Tapped Tunnel Roof

Velocity
Profile

(i)

(vi)

Measurement and
Computational Domain

Static
Pressure
Measured

Afterbody

(ii)

(iii) (iv)

(v)
Jet Plume

Total
Pressure
Profile

Symmetry Plane

Region Key

(i)   Onset Flow
(ii)   Model Boundary Layer
(iii)   Boattail Region
(iv)   Jet Injection Plane
(v)   Plume & Mixing Region
(vi)   Downstream Outflow
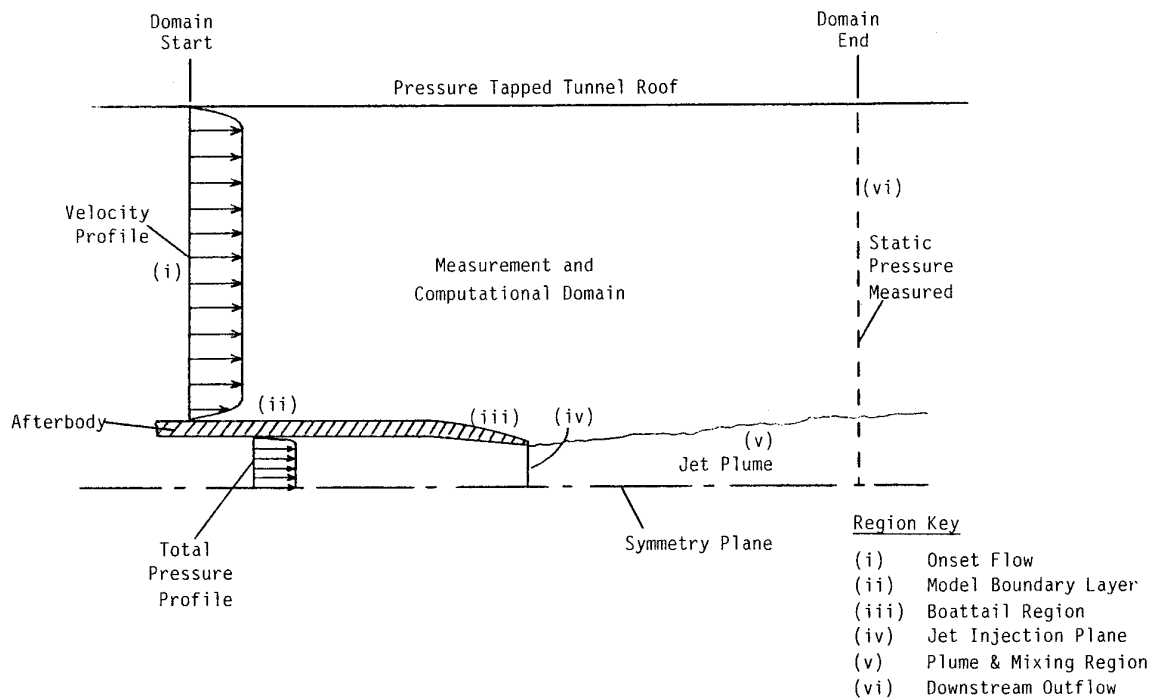
FIGURE 2: TWO-DIMENSIONAL MEASUREMENT AND COMPUTATIONAL
DOMAIN FOR AXISYMMETRIC AFTERBODY EXPERIMENTS
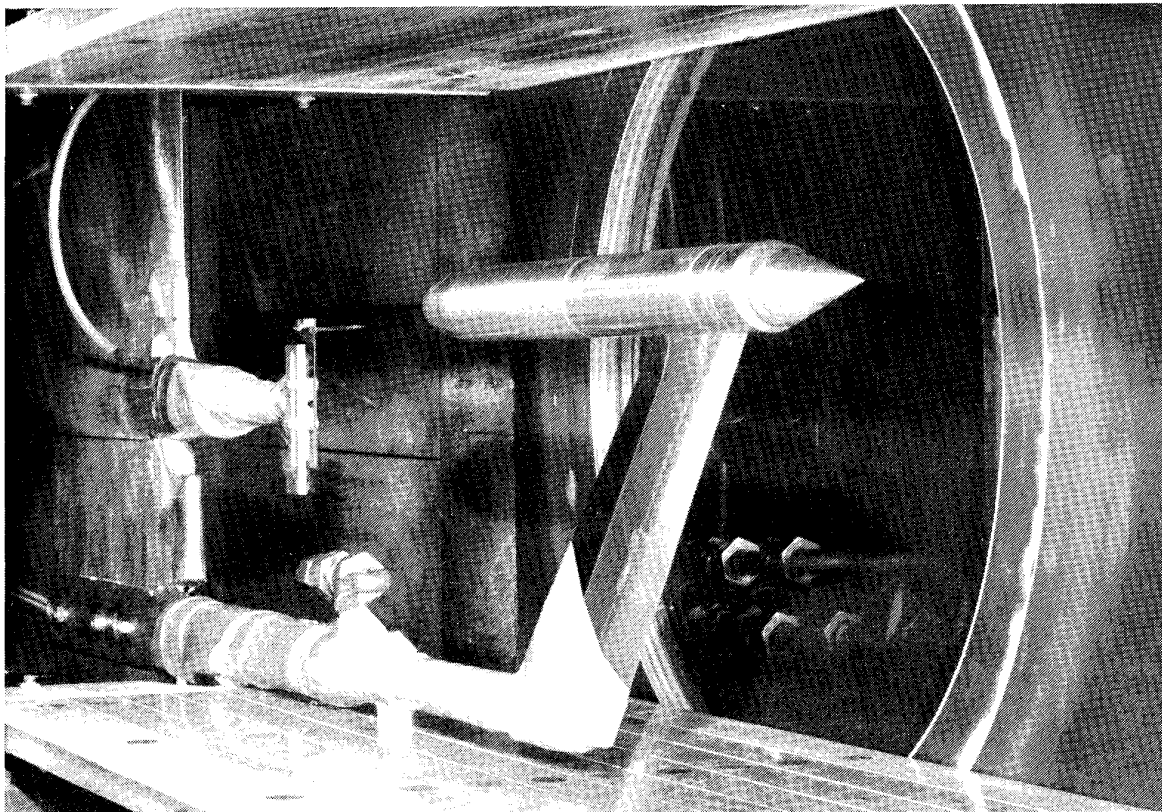
FIGURE 3: MODEL AND SUPPORT IN FFA TUNNEL S5 FOR TRANSONIC TEST
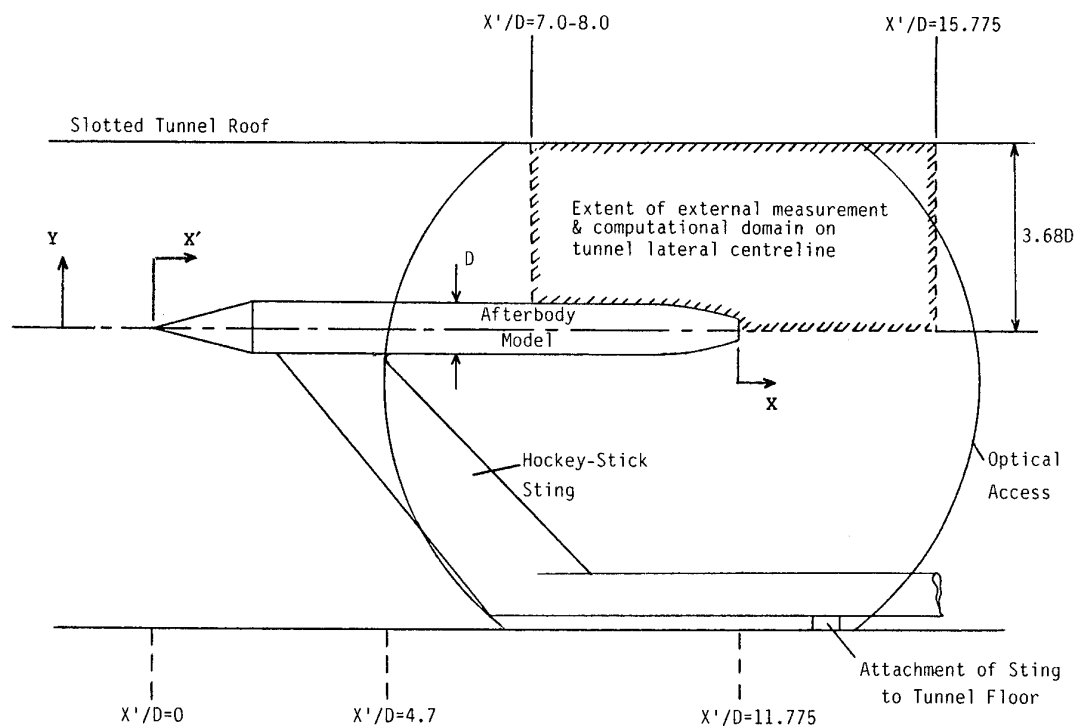
FIGURE 4: MODEL/TUNNEL RELATIONSHIP FOR TRANSONIC TEST
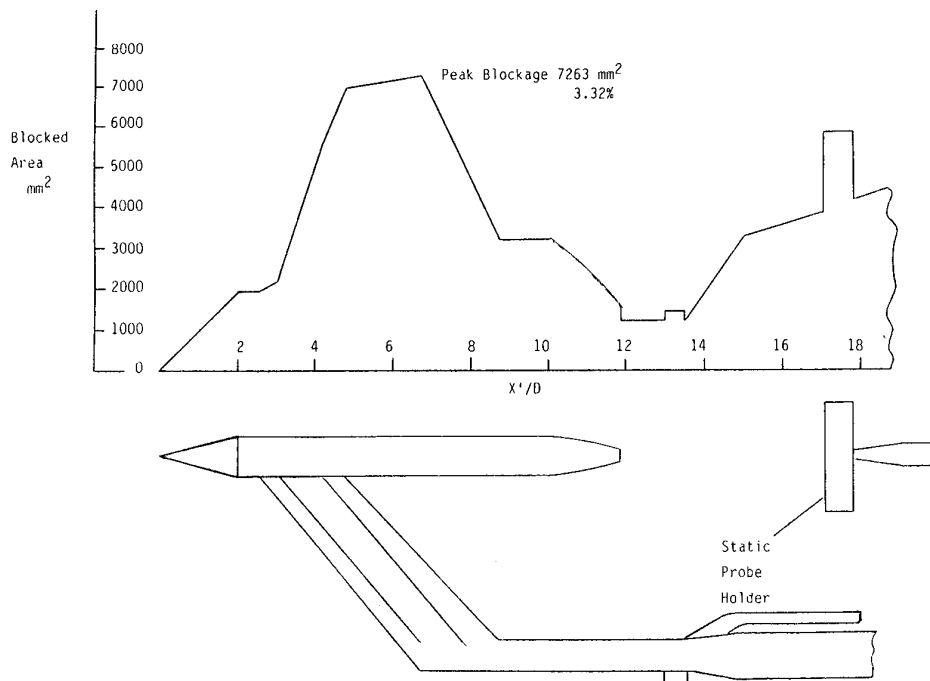
FIGURE 5: MODEL AND SUPPORT BLOCKAGE FOR TRANSONIC TEST
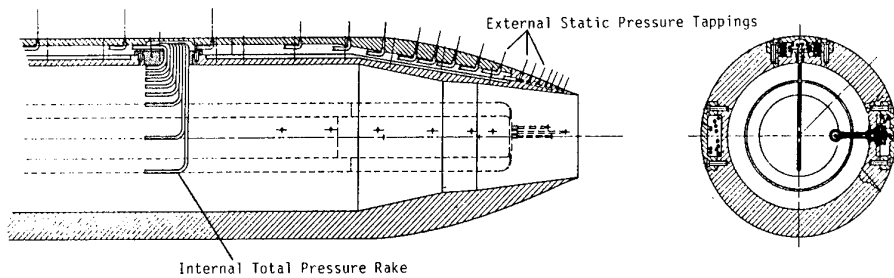
FIGURE 6: AGARD 15° AFTERBODY GEOMETRY
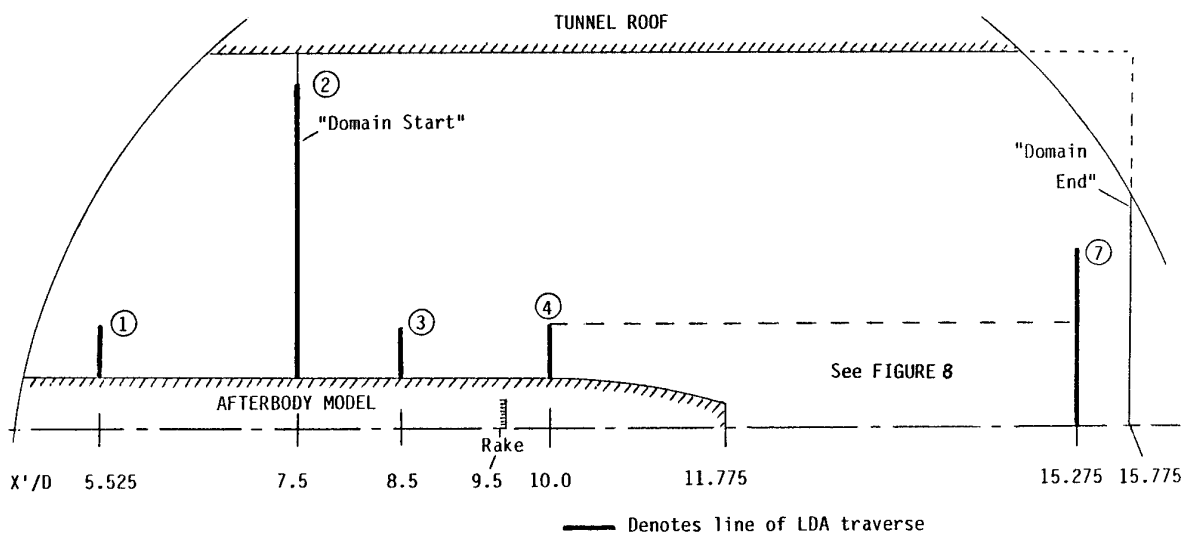
FIGURE 7: OVERALL MEASUREMENT DOMAIN CASE A

Denotes Line of LDA Traverse

X'/D=10.0

X'/D=11.775
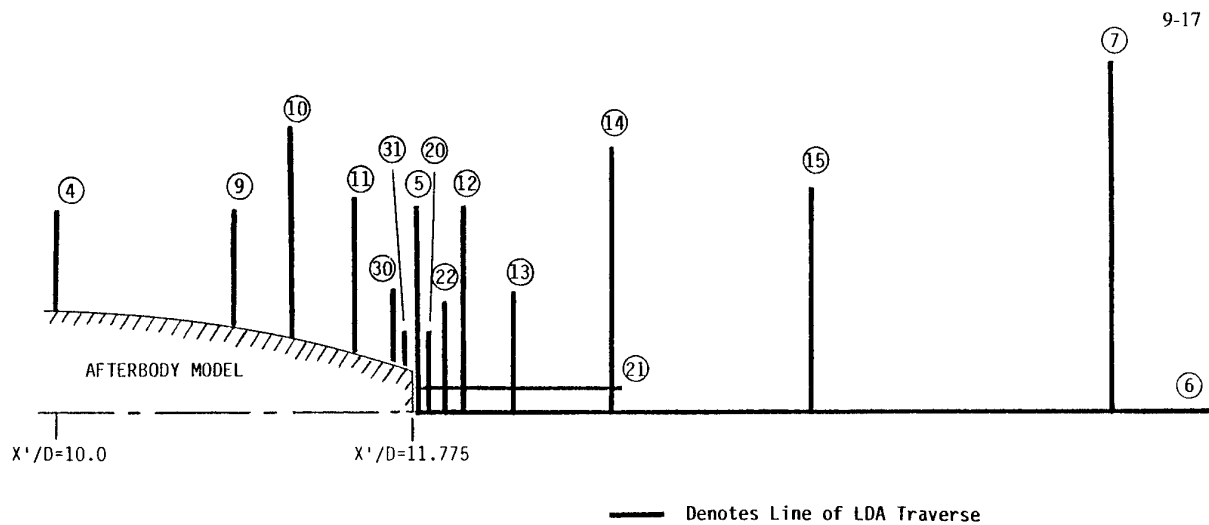
AFTERBODY MODEL

FIGURE 8: BOATTAIL/JET MEASUREMENT DOMAIN CASE A
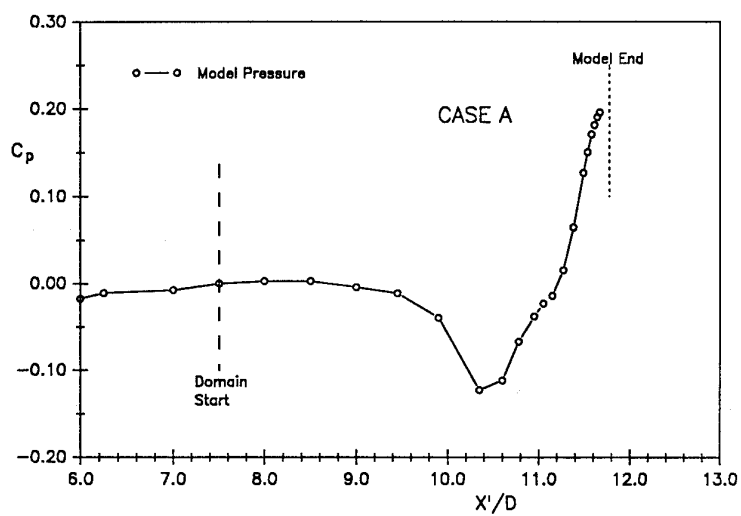
FIGURE 9: MODEL PRESSURE DISTRIBUTION CASE A
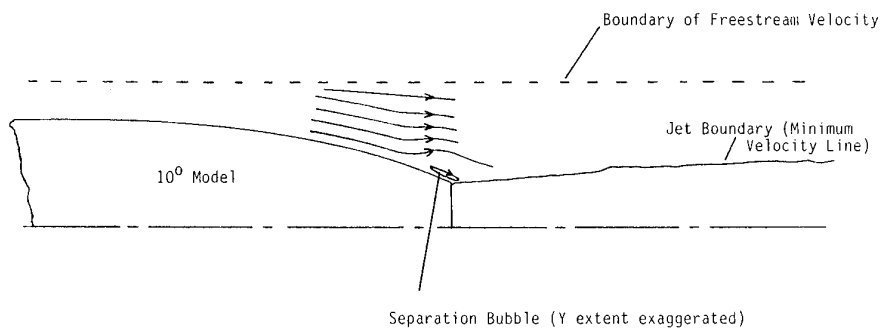
FIGURE 10: FLOWFIELD REPRESENTATION CASE A
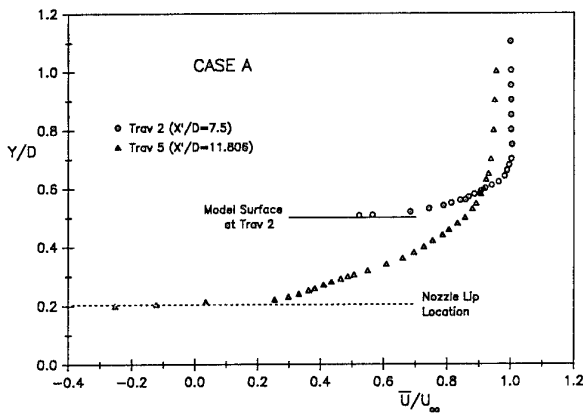
FIGURE 11: BOUNDARY LAYER DEVELOPMENT ON
MODEL   CASE A
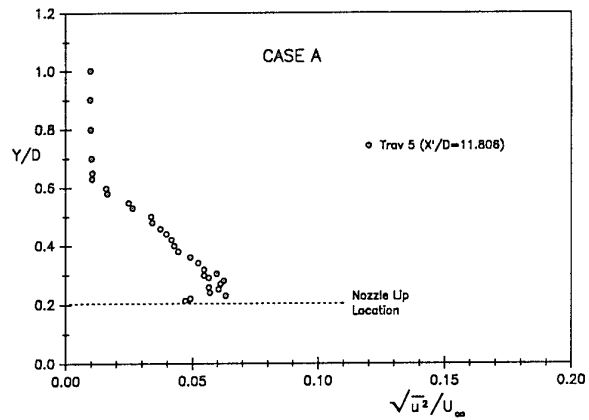
FIGURE 12: STREAMWISE TURBULENCE AT END OF
AFTERBODY   CASE A
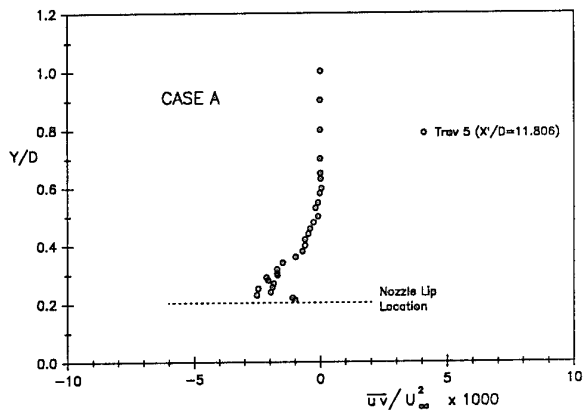
FIGURE 13: SHEAR STRESS VARIATION AT END OF
AFTERBODY   CASE A
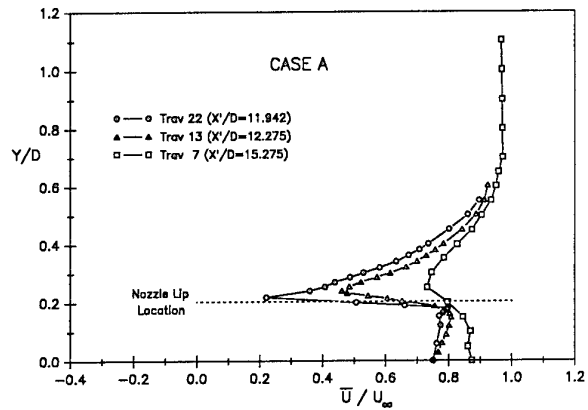
FIGURE 14: JET PLUME AND MIXING REGION
DEVELOPMENT   CASE A
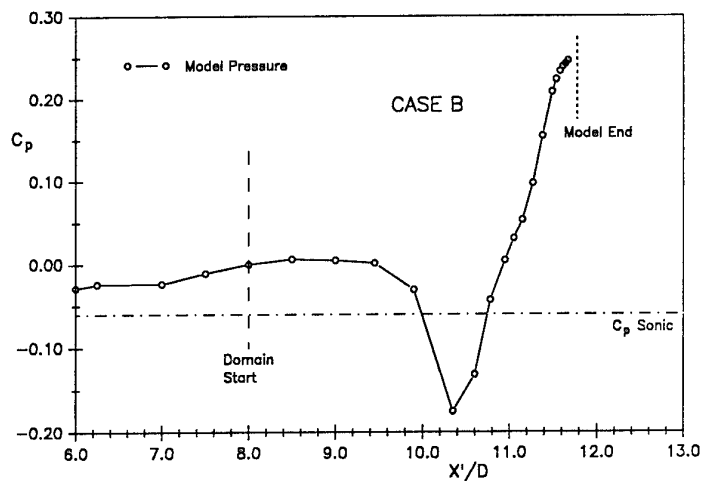
FIGURE 15: MODEL PRESSURE DISTRIBUTION CASE B
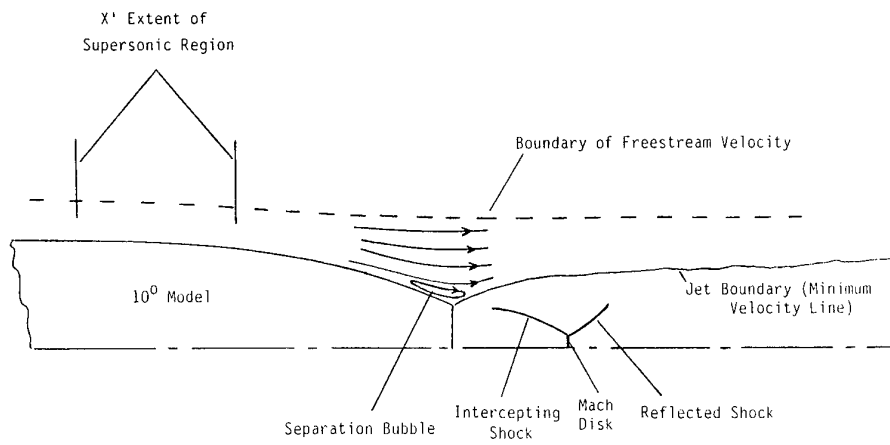
FIGURE 16: FLOWFIELD REPRESENTATION CASE B
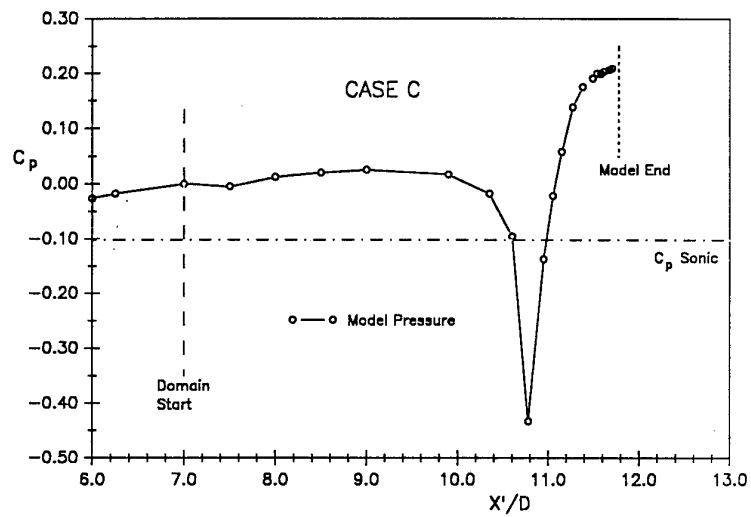
FIGURE 17: MODEL PRESSURE DISTRIBUTION CASE C
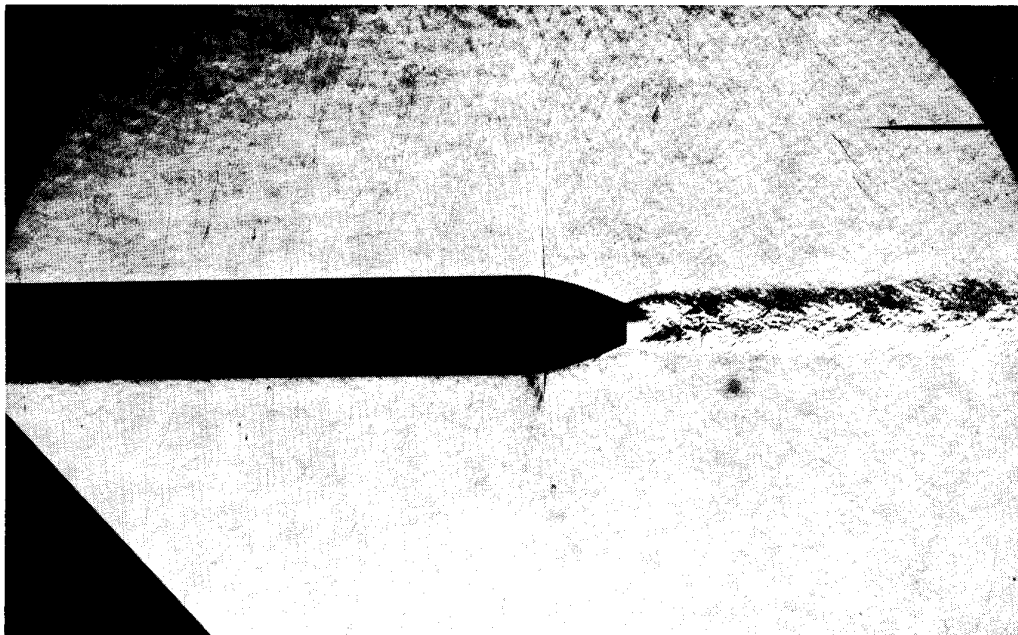
FIGURE 18: SCHLIEREN IMAGE OF CASE C
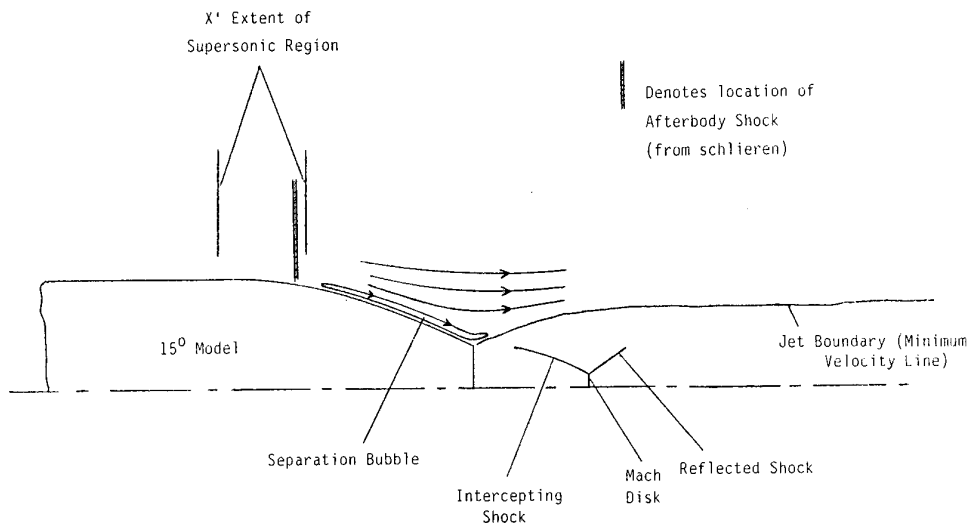
FIGURE 19: FLOWFIELD REPRESENTATION CASE C
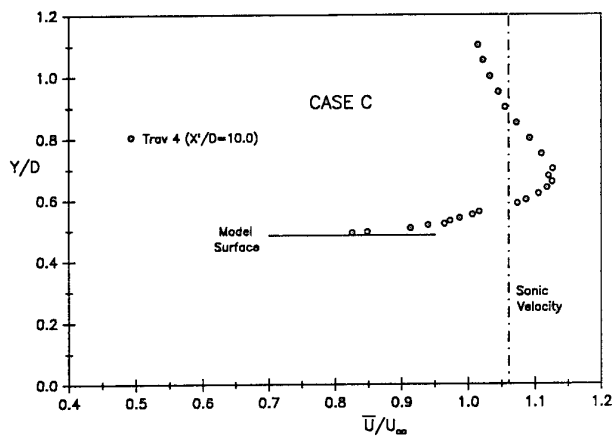
FIGURE 20: BOUNDARY LAYER ON MODEL UPSTREAM
OF AFTERBODY   CASE C
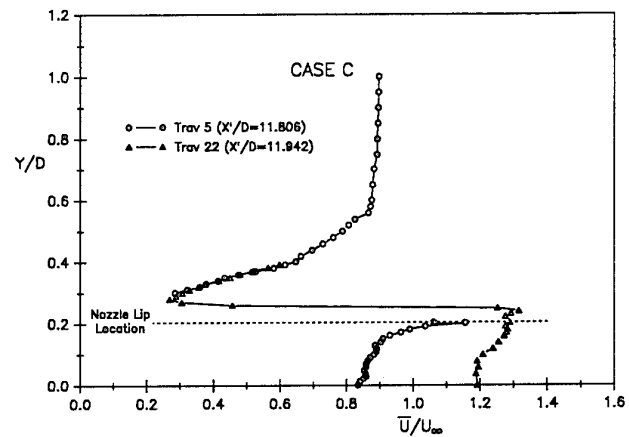
FIGURE 21: JET PLUME AND MIXING REGION
DEVELOPMENT   CASE C
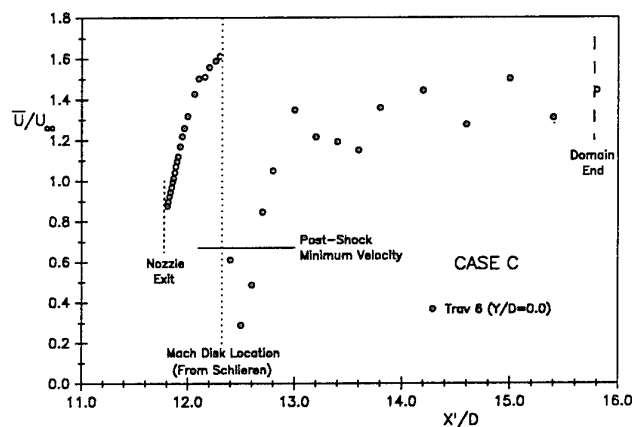
FIGURE 22: JET CENTRELINE VELOCITY VARIATION
CASE C
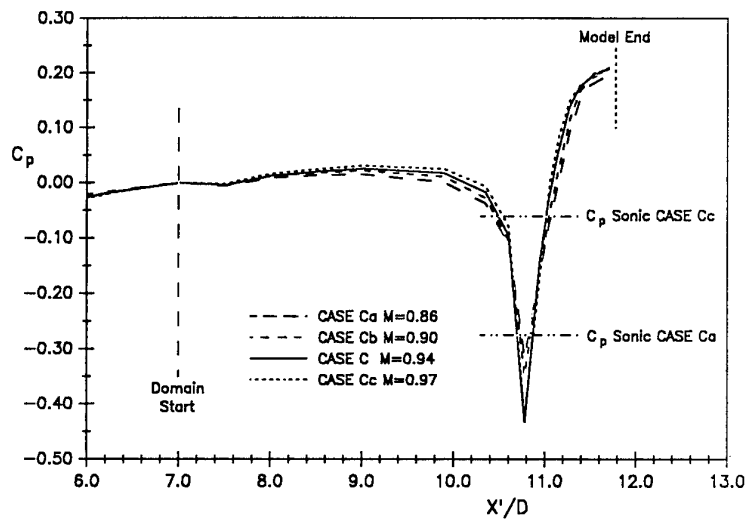
FIGURE 23: EFFECT OF ONSET MACH NUMBER ON 15° AFTERBODY
PRESSURE DISTRIBUTION
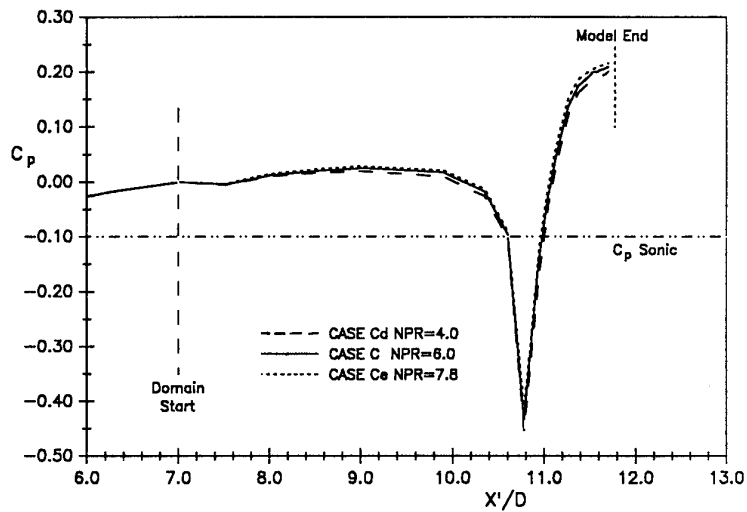
FIGURE 24: EFFECT OF NPR ON 15° AFTERBODY
PRESSURE DISTRIBUTION
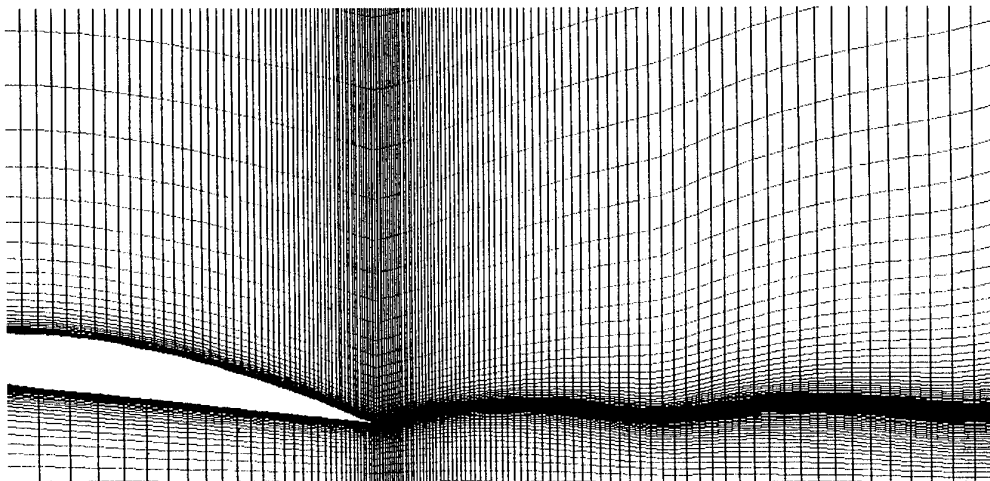
FIGURE 25: POST-SOLUTION ADAPTED GRID − CASE C
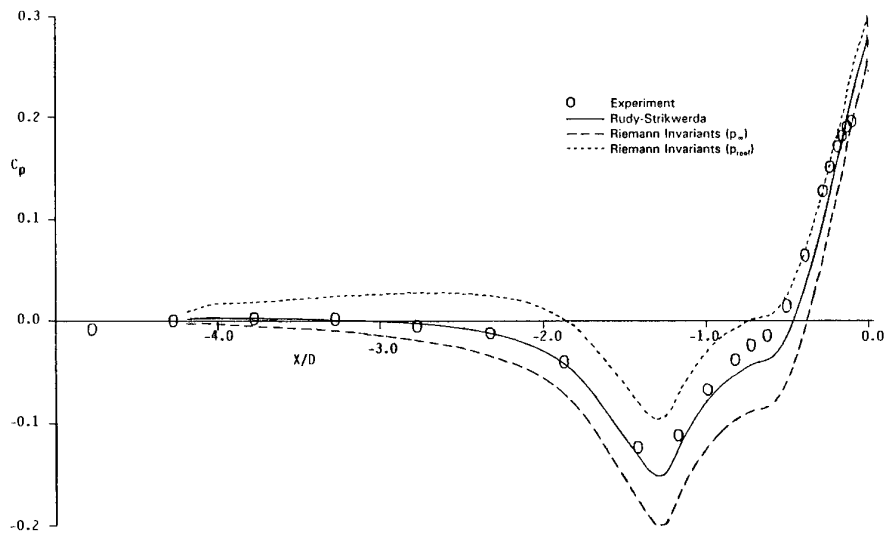
FIGURE 26: SURFACE PRESSURE PREDICTIONS USING DIFFERENT DOMAIN
UPPER SURFACE (ROOF) BOUNDARY CONDITIONS – CASE A
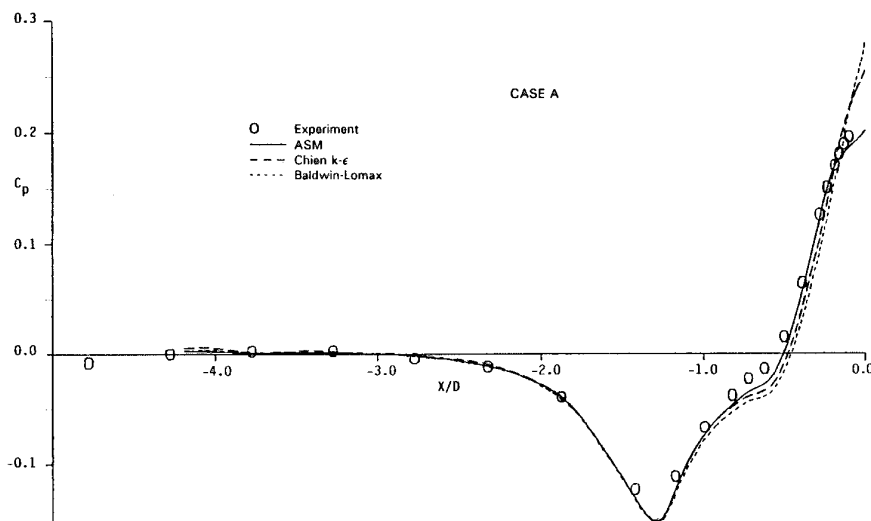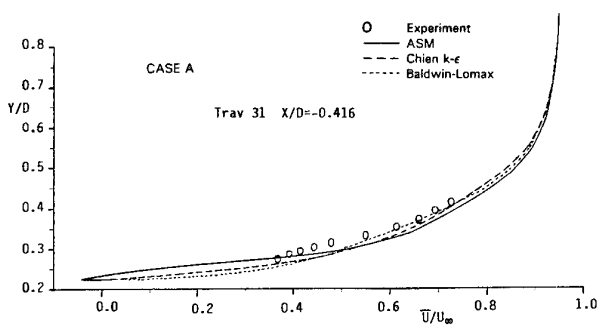

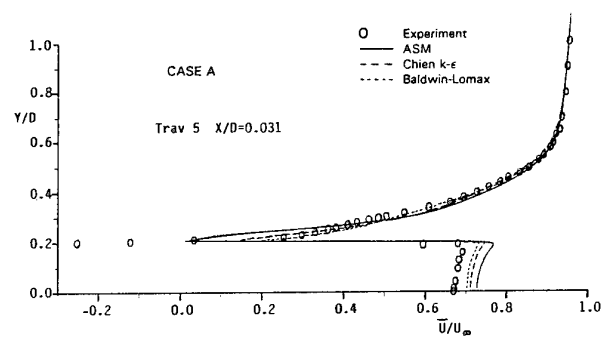FIGURE 27: SURFACE PRESSURE PREDICTIONS CASE A

FIGURE 28a

FIGURE 28b

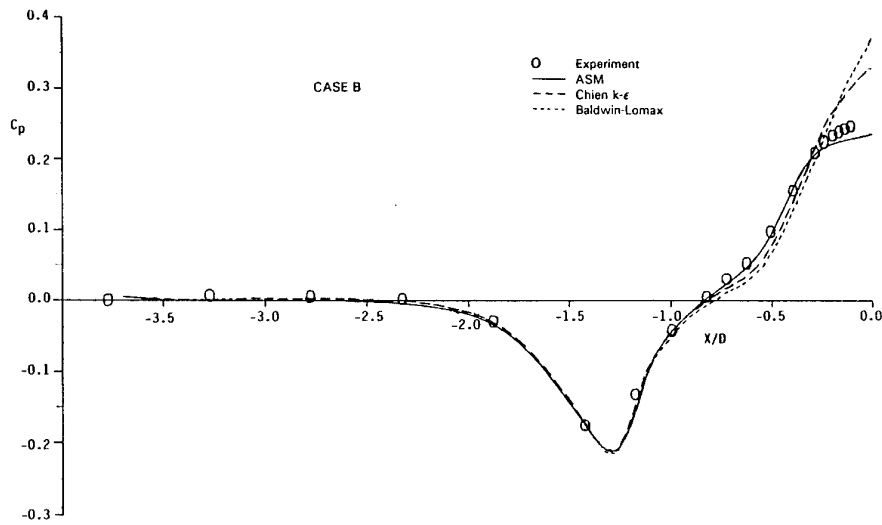FIGURE 28: $\overline{U}$ PREDICTIONS NEAR TRAILING-EDGE CASE A

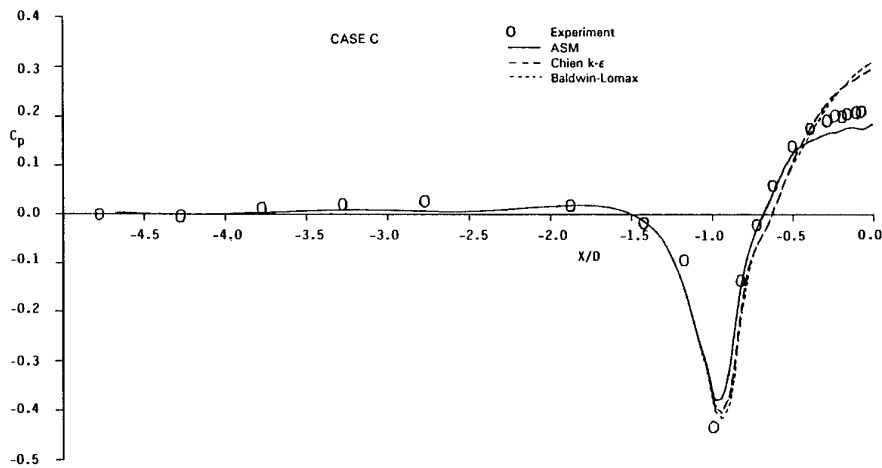FIGURE 29: SURFACE PRESSURE PREDICTIONS CASE B

FIGURE 30: SURFACE PRESSURE PREDICTIONS CASE C
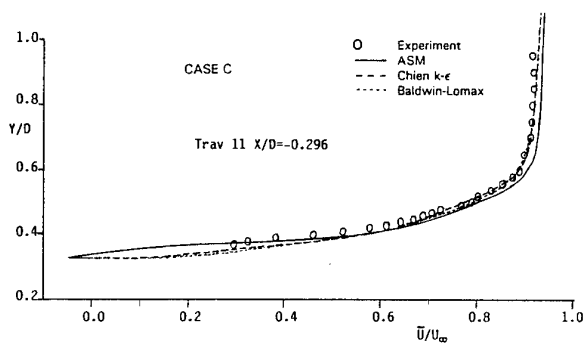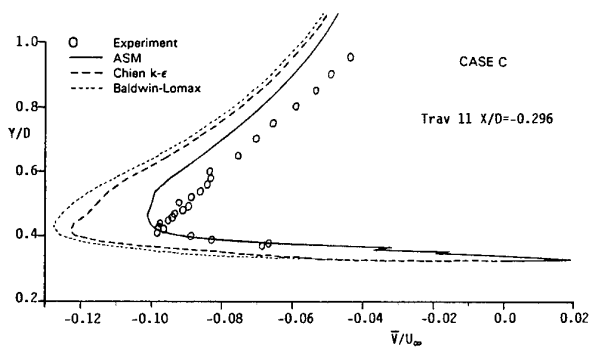

FIGURE 31a

FIGURE 31b

FIGURE 31: VELOCITY AND STRESS PREDICTIONS THROUGH
SEPARATED REGION CASE C
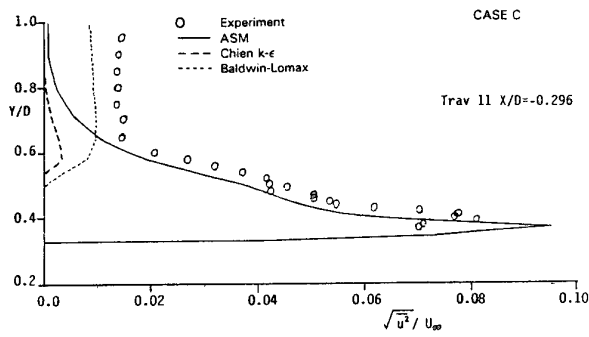
FIGURE 31c

FIGURE 31d

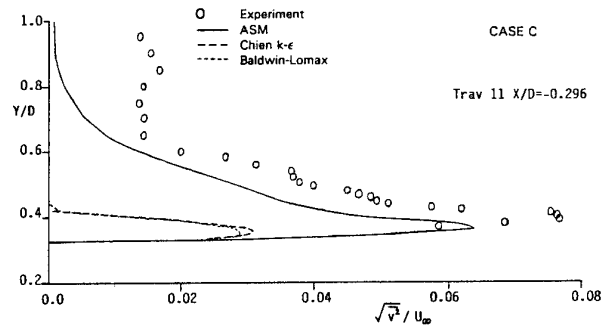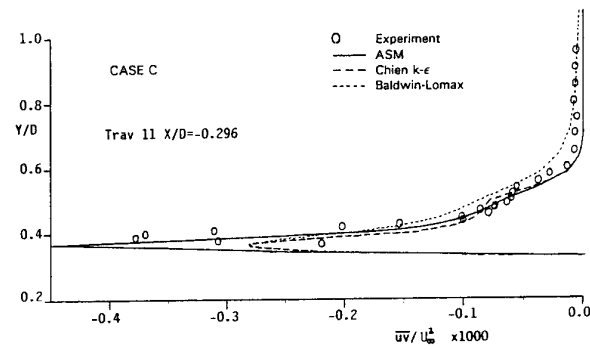
FIGURE 31e

FIGURE 31: contd.
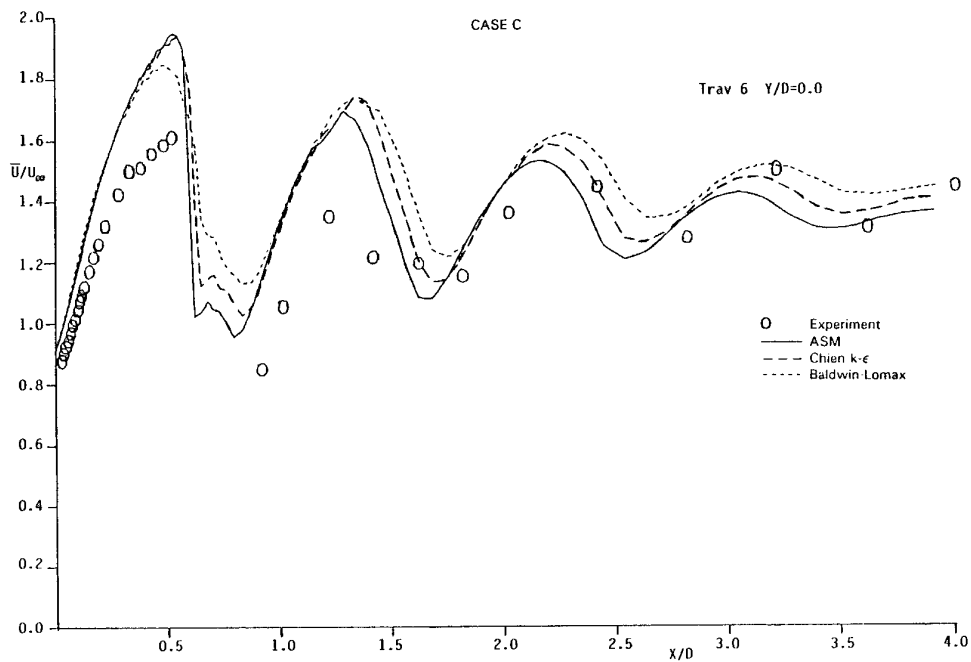
FIGURE 32: $\overline{U}$ PREDICTIONS ON JET CENTRELINE CASE C
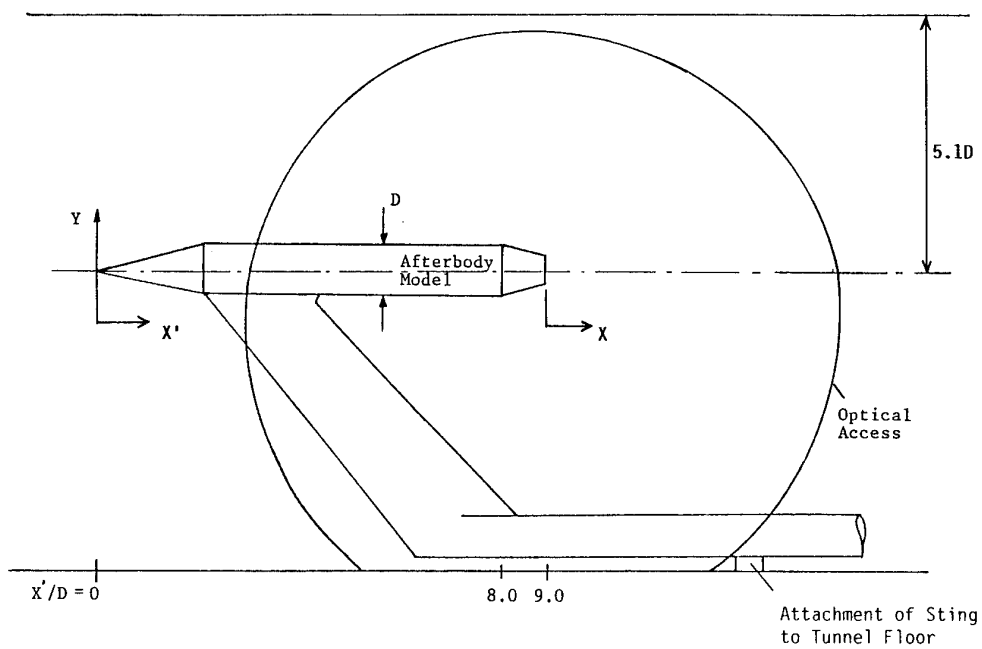
FIGURE 33: MODEL/TUNNEL RELATIONSHIP FOR SUPERSONIC TEST
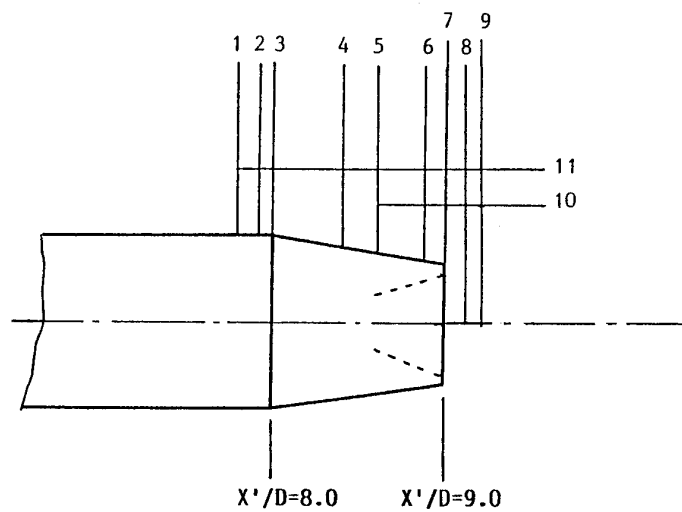
FIGURE 34: OVERALL MEASUREMENT DOMAIN CASE D
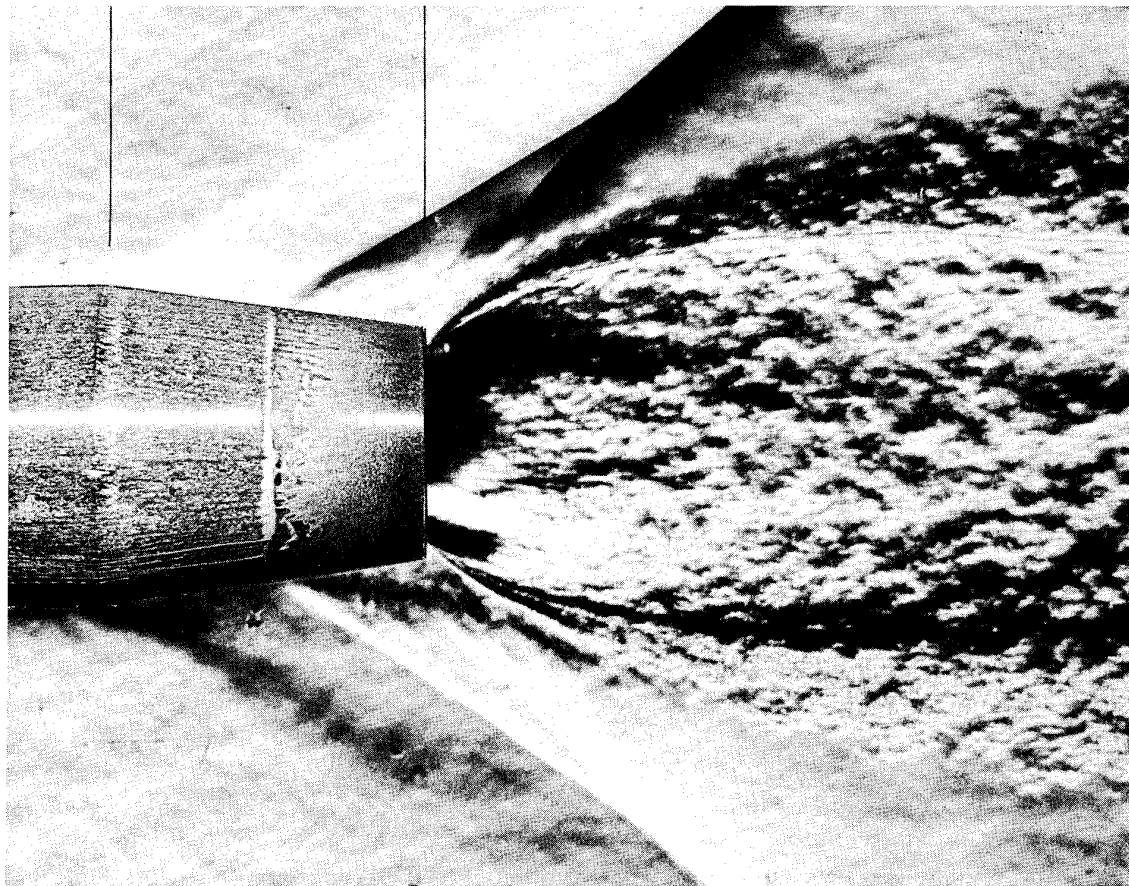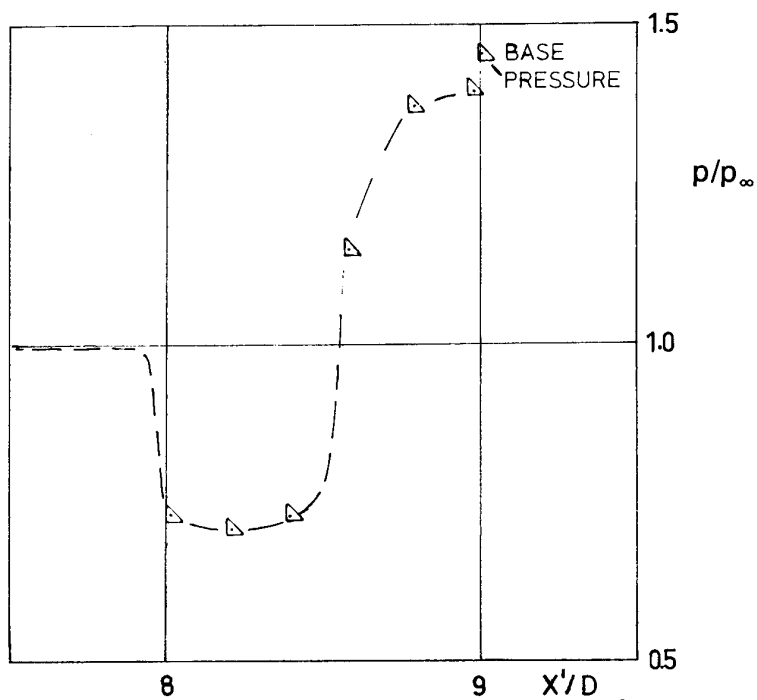
FIGURE 35: PHOTO-MONTAGE OF AN OIL FLOW AND A SCHLIEREN PICTURE
ASSOCIATED WITH THE CORRESPONDING PRESSURE DISTRIBUTION
FOR 8° CONICAL BOATTAIL
$M_{tun} = 2.0$ $M_{jet} = 2.5$ $NPR_s = 9.0$
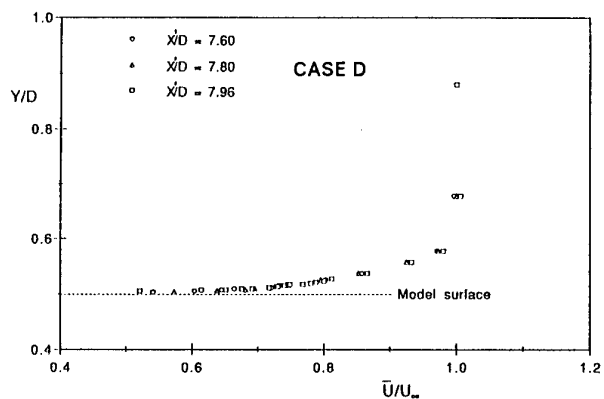
FIGURE 36: BOUNDARY LAYER DEVELOPMENT ON
CYLINDRICAL PART OF MODEL CASE D
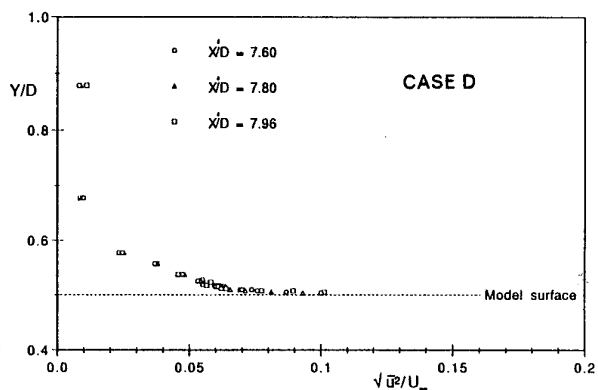
FIGURE 37: STREAMWISE TURBULENCE IN BOUNDARY
LAYER ON CYLINDRICAL PART OF MODEL
CASE D
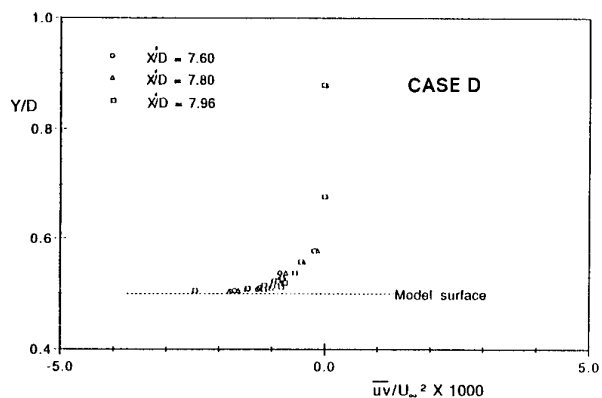
FIGURE 38: SHEAR STRESS VARIATION IN BOUNDARY
LAYER ON CYLINDRICAL PART OF MODEL
CASE D
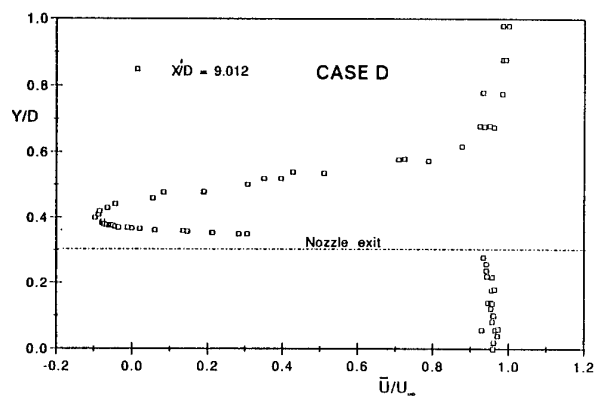
FIGURE 39a
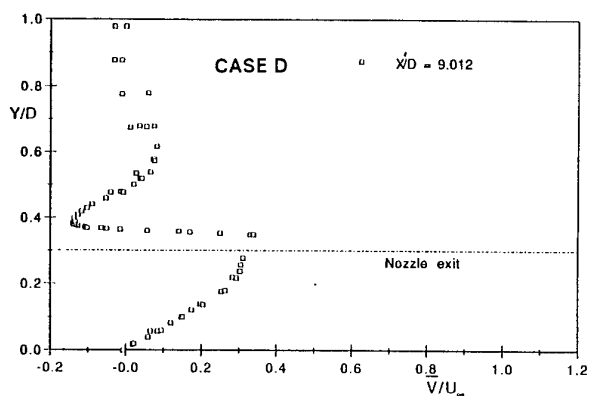
FIGURE 39b
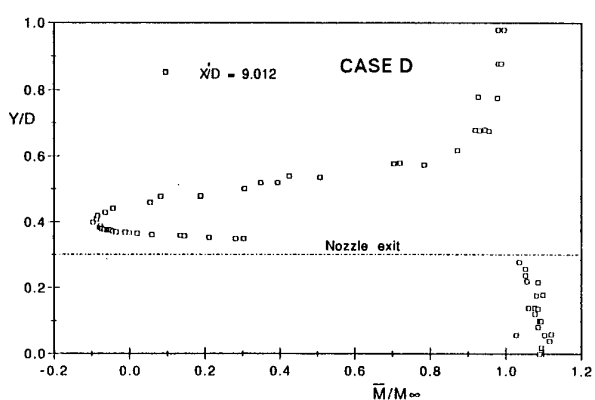
FIGURE 39c

FIGURE 39: VELOCITY AND MACH NUMBER PROFILES
AT END OF AFTERBODY CASE D
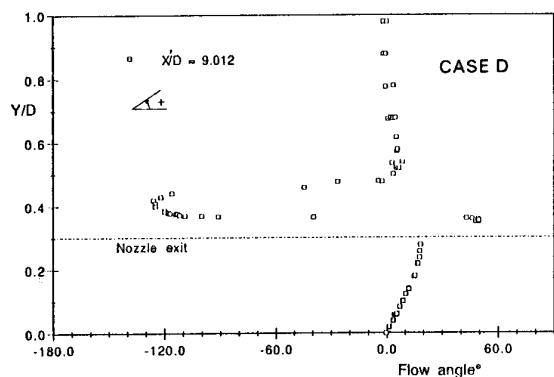
FIGURE 40: FLOW ANGLE AT END OF AFTERBODY
CASE D
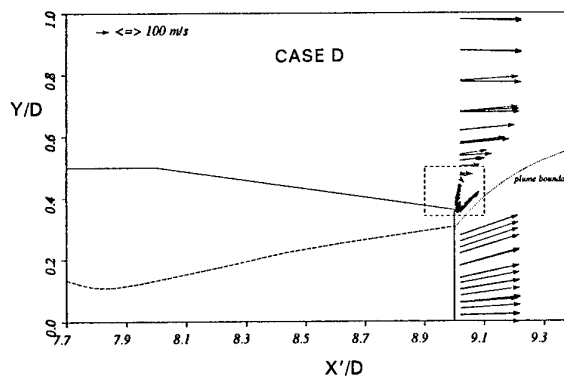
FIGURE 41: VELOCITY VECTORS AT END OF AFTERBODY
CASE D
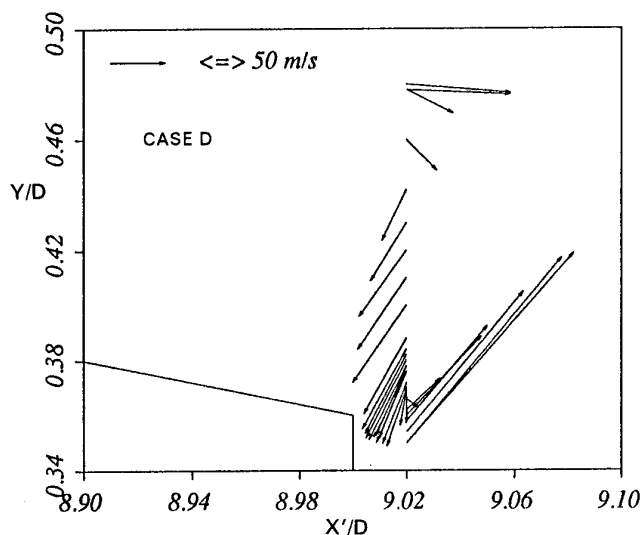
FIGURE 42: VELOCITY VECTORS AT END OF AFTERBODY
ENLARGED CASE D
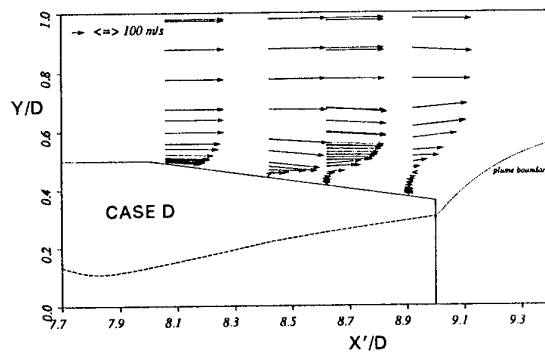
FIGURE 43: VELOCITY VECTORS ALONG AFTERBODY
CASE D
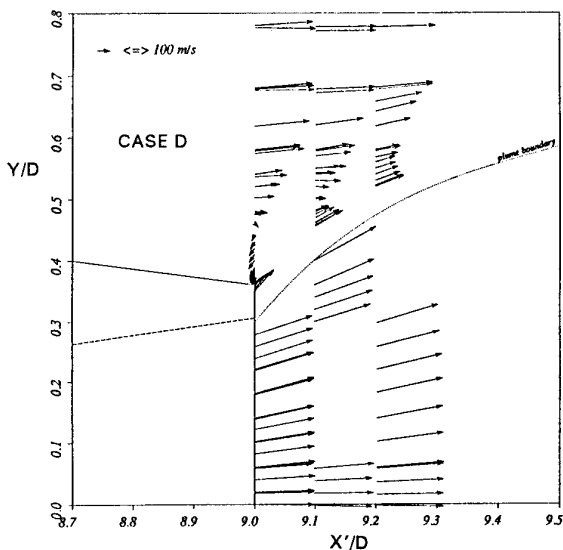
FIGURE 44: VELOCITY VECTORS IN PLUME AND
MIXING REGION CASE D

VELOCITY MEASUREMENTS WITH HOT-WIRES IN A VORTEX-DOMINATED FLOWFIELD

Christian Breitsamter and Boris Laschka
Lehrstuhl für Fluidmechanik, TU München
Arcisstrasse 21, 80290 München, Germany

SUMMARY

Selected results from a quantitative experimental investigation documenting the low-speed flow environment over a 75° swept delta wing and over a delta-canard-configuration are presented. The hot-wire measurement techniques using cross-wire and triple-wire probes are described. Results obtained include detailed flowfields of the time-dependent velocity components for angles of attack from 12.5 deg to 31.5 deg at a test Reynolds number of 1.0×10^6. The structure of the highly turbulent vortex dominated flow is clearly shown by time-averaged, root-mean-square and spectral distributions. Thus the delta wing vortex substructure organized by discrete vortices and vortex breakdown characteristics are analyzed. With increasing incidence both the wing and the canard leading-edge vortices move inboard resulting in increase of the velocity fluctuations due to the bursting of these vortices. At the delta-canard configuration strong interference effects between the canard and the wing vortex systems are found. Peaked velocity spectra are detected in the vorticity sheets at burst flow conditions related to a narrow-band concentration of kinetic turbulent energy in the flow of the wing/canard vortex sheets.

NOMENCLATURE

|	
c_r	wing root chord
E_1, E_2, E_3	anemometer output voltage of hot-wire 1, 2, 3
f	frequency (Hz)
k	reduced frequency, $k = f l_\mu / U_\infty$
l_μ	wing mean aerodynamic chord
Re	Reynolds number, $Re = U_\infty l_\mu / \nu$
s	(local) wing half span
U	streamwise calibration velocity
U_c	calibration velocity
U_∞	freestream velocity
V	lateral calibration velocity
u, v, w	streamwise, lateral and vertical velocity components (wind tunnel-axis system)
$\overline{u}, \overline{v}, \overline{w}$	streamwise, lateral and vertical mean velocity
u', v', w'	fluctuation part of u, v, w
u_{rms}, v_{rms}, w_{rms}	root-mean-square values of the fluctuating components of velocity, $u_{rms} = \sqrt{\overline{u'^2}}$, $v_{rms} = \sqrt{\overline{v'^2}}$, $w_{rms} = \sqrt{\overline{w'^2}}$
$u_{xz_{rms}}$	root-mean-square value of the streamwise and vertical fluctuating components
Y, Z	non-dimensionalized coordinates in the measurement plane, referred to s, origin at the mid section
x, y, z	streamwise, lateral and vertical coordinates of the wind tunnel-axis system
α	aircraft angle of attack
α_c	calibration pitch angle
β_c	calibration yaw angle
φ_W	wing leading-edge sweep
φ_C	canard leading-edge sweep
Λ	wing aspect ratio
λ	wing taper ratio
ν	kinematic viscosity

Abbreviations:

rms	root-mean-square

INTRODUCTION

Combat aircraft of delta and canard-delta wing type at angle of attack generate leading edge vortices which produce substantial increases in lift. This is utilized to achieve enhanced manoeuverability in the high-α flight domain. The aircraft structure, however, experience unsteady vortex flows that cause problems such as tail buffeting [1−5] and lateral instability [6], in particular, when vortex bursting occurs. The physics of the corresponding three-dimensional and separated flow is, therefore, of high interest for aeronautical research work [7].

At moderate angle of attack the fluid separates at the leading edges of a slender wing, forming a free shear layer which curves upward and rolls into a core of high vorticity. This results in the formation of large bound counter-rotating spiral-shaped vortices above the upper surface of the wing. A strong outflow of the attached flow beneath the vortex on the wings upper surface is induced. Each of these concentrated primary vortices also contain axial flow components in the central core regions, around and along with the fluid spirals attaining velocities up to three times the freestream value. Thus the primary vortices produce a large suction force due to the vortex-induced velocities. The corresponding pressure distribution has two distinct peaks refering to the vortex axis [8]. The associated lift increase causes the well-known non-linear characteristic exhibited by slender wings.

Outboard of the primary vortex the flow on the surface encounters an adverse pressure gradient between the

pressure minimum and the leading edge. This causes boundary layer separation leading to an associated small counter rotating secondary vortex. The main effect of the secondary vortex is to displace the primary vortex upwards and inwards. The development of the secondary vortex is dependent on a laminar or turbulent boundary layer. Outboard of the secondary vortex the flow reattaches and approaches the leading edge. At the leading edge the flow again separates and joins the flow from the lower surface in the shear layer. The size and strength of the primary vortices increases with angle of attack. It becomes the dominant steady flow feature through a wide range of practical flight attitudes.

At high angle of attack the delta wing performance is limited, however, by a phenomenon known as vortex breakdown or vortex bursting. This rapid change of the vortex structure is associated with a stagnation of the core flow. It is characterized by a sudden increase in vortex diameter followed by large scale turbulent dissipation, and a decrease in the core's axial and circumferential velocity [9]. This then causes a loss of lift and hence a limitation of maneuverability. The position of vortex breakdown is dependent on angle of attack, angle of sideslip, Reynolds number and wing geometry. Vortex breakdown has inspired many studies on leading-edge configurations [9 − 12].

As noted two types of vortex breakdown are classified, the bubble and spiral type, which are extremes in a continuum of breakdown forms. The bubble breakdown is characterized by a stagnation point on the vortex axis followed by an oval shaped recirculation zone with a nearly axisymmetric upstream half and an open and irregular downstream half. Downstream of the bubble the vortex is turbulent and diffuses rapidly with distance. The spiral breakdown is characterized by a rapid deceleration of the core flow followed by an abrupt kink at which point the core flow takes the form of a spiral which persists for one or two turns before breaking up into large scale turbulence [11]. The type of vortex breakdown is primarily a function of Reynolds number, circulation and pressure gradient. There is still a lack of knowledge into the exact mechanism for vortex breakdown.

Due to the extremely complex flow structure delta and delta-canard configurations have been investigated for a long time, and there exist a large number of published experimental work on this topic [13]. At present, however, there is a lack of systematic instantaneous flowfield data to get detailed insight into the turbulent flow structure of vortex-dominated aircraft configurations associated with the severe random aerodynamic loads arising from the impact of vortical flows on the structure. As a contribution to fill this gap, a research program on a delta wing and a typical high performance delta-canard model was initiated at the Institute of Fluid Mechanics of the Technical University Munich. The approach adopted here is to measure the fluctuating velocity components. Statistical analysis will be applied to show whether significant frequencies are present in the vortex dominated flow.

Experimental Technique and Test Program

Facility

All experiments were carried out in the Technical University of Munich low-speed wind-tunnel. This is a closed-return facility powered by a 85 kW electric motor. The

$2s = 0.335$ m	$\varphi_W = 75°$
$l_\mu = 0.447$ m	$c_r = 0.670$ m
$\Lambda = 1.0$	$d_{max} = 0.057$ m
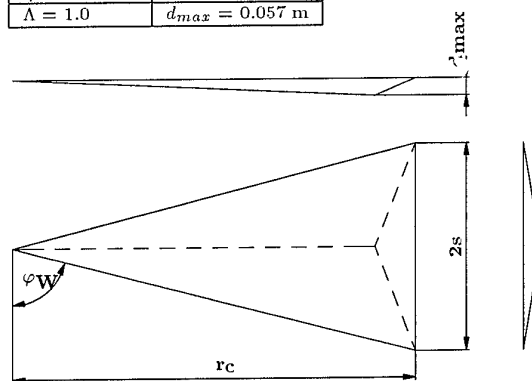
a) **Delta wing**

$2s = 0.740$ m	$\varphi_W = 50°$
$l_\mu = 0.360$ m	$\varphi_C = 45°$
$\Lambda = 2.45$	$\lambda = 0.14$
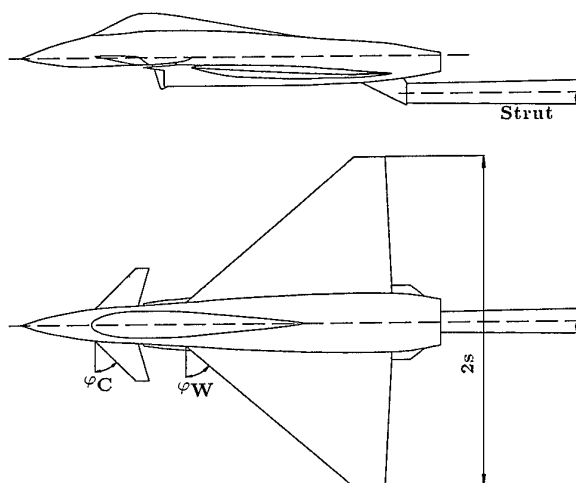
b) **Delta-canard configuration**

Fig. 1 Wind tunnel models.

nozzle diameter is 1.5 m, the length of the open test section is 3 m. Maximum usable velocity is 55 m/s. Turbulence intensity is known to be under 0.3% − 0.4% over the speed range of interest. The minimum step sizes of the three-degree-of-freedom probe-traversing system in the streamwise, spanwise and normal directions were ±0.2 mm.

The tunnel is equipped with an automated data acquisition and control system. A personal computer with a high-speed board is used for data acquisition of the hot-wire, pressure and temperature signals as well as for the control of the wind tunnel, the 3-axis probe-traversing system and the 3-axis model support. Flowfield parameters are required to ensure that the experiment is progressing properly and to evaluate reference quantities. Data acquisition software has been developed which allows fully automated surveys of flowfields around models of arbitrary geometrical shape. A second computer sys-

tem is required for data storing, reduction and processing by statistical means of the huge amount of data during instantaneous measurement cycles. This is done by on-line data transfer and communication with a CONVEX C1 which realizes then a completely automatic process of flowfield measurements.

Wind-tunnel models

In the experimental study a very stiff model of a delta wing and of a delta-canard configuration is used. The delta wing is a 75° swept sharp-edged wing with a flat surface and a triangular cross section, Fig. 1a. The delta-canard model is the model of a high performance fighter configuration, Fig 1b. In this model tested, the leading- and trailing-edge flap deflections were set at zero deg. The canard setting angle has also been fixed at zero deg. The models were sting mounted on its lower surface by a computer-controlled moving support strut providing an incidence range from 0 − 31.5 deg. This setting up guarantees flowfield measurements over the wing and in a possible fin region as far as possible free from interference. The models may be yawed and rolled up to 360 deg to ensure accurately positioning in the test section. The maximum blockage of the delta-canard configuration at 31.5 deg angle of attack is under 7.5%.

Hot-wire Anemometry

The hot-wire probes are operated by a DISA C three-channel constant-temperature anemometer system. Signal conditioner modules transform the bridge output voltages into a suitable range for the sixteen-channel simultaneous-sampling 12 bit A/D converter of the personal computer board. The total sampling frequency is limited to 130 kHz. The probes used are cross-wire probes (DISA 55A32 and 55P61) and triple-wire probes (DISA 55P91). The sensors consist of 5-μm–diam platinum-plated tungsten wires giving a length/diameter ratio of 250. The cross-wires form a measuring volume of approximately 0.8 mm in diam. and 0.5 mm in height. The sensor angle of 45 deg was chosen assuming that the best angular resolution will be obtained with pairs of perpendicular wires. An additional temperature probe is used to correct the anemometer output-voltages if ambient flow temperature varies.

The use of cross-wire configuration generally assumes some knowledge of the flowfield, such as a known flow direction with which the probe must be aligned. The nature of the vortex-dominated flow precludes any knowledge on the direction of the velocity vector everywhere in the field, save for the axial component which is assumed to be always in the positive x-direction. In order to fully determine all three velocity components (u, v, w) the probe has to be rotated around its axis by 90 deg to adjust the wire plane (once horizontal and once vertical) against the main flow direction. Thus at least two traverse sweeps are necessary to obtain the streamwise (u), lateral (v) and vertical (w) components respectively. With the calibration technique described below the magnitudes and the direction of all three velocity components can be derived considering the correction methods of Cutler and Bradshaw [13].

Using the triple-wire probes all velocity components can be obtained at one sweep. The disadvantage is a reduced unique angle range as well as the enlarged measurement volume of about 3 mm.
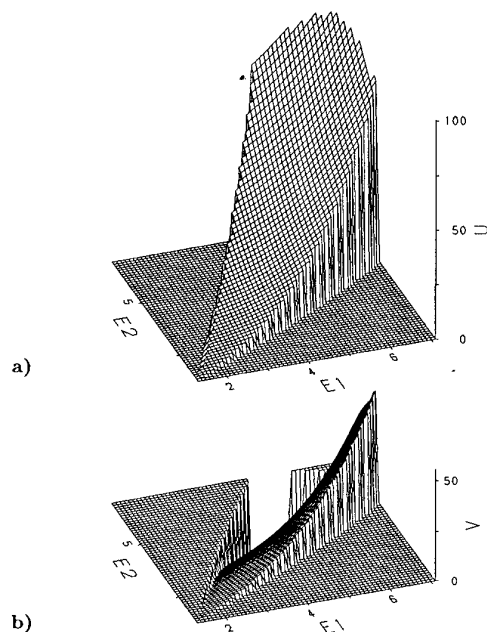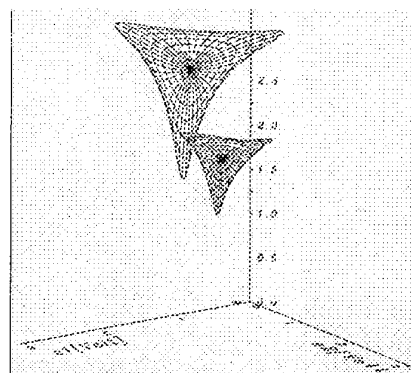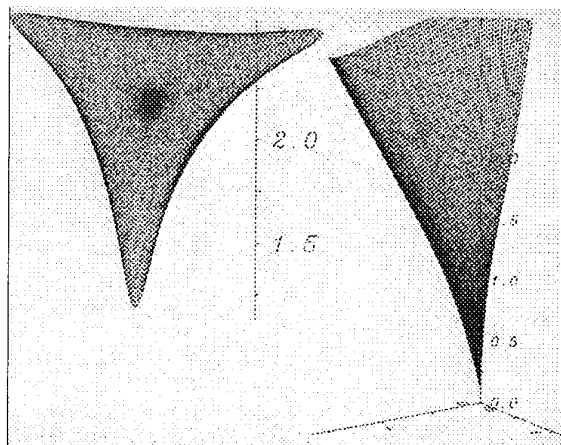

a)

b)

Fig. 2 X-probe look-up table surface; a) Streamwise velocity plane; b) Lateral velocity plane

a) Part of calibration grid

b) Cuts through refined look-up room

Fig. 3 Look-up-room of a triple-wire probe

Calibration and Evaluation Procedure

To calibrate the hot-wire probes a computer-aided fully automated procedure is developed based on a velocity and flow-angle dependent, temperature corrected method [15]. A cross-wire calibration surface is achieved by pitching the probe in the freestream of the flow at different velocities. This results in an unique voltage pair E_1 and E_2, for each pitch angle α_c and velocity magnitude U_c. The pitch angle range was ±45 deg, the velocity magnitude ranges from 1.5 m/s to 52 m/s. The calibration of triple-wire probes requires additional yawing of the probe to get a unique voltage triple E_1, E_2 and E_3, for each pitch angle α_c, yaw angle β_c and velocity magnitude U_c. The triple-probe was calibrated in a pitch and yaw angle range from −35 deg to +35 deg at a velocity range from 1.5 m/s to 52 m/s.

Using this technique actual experimental flow conditions, i.e. varying flow angle and velocity magnitude are considered during the calibration procedure. Consequently the interference between prongs and wires and the wires itself is also covered as manufacturing inaccuracy and divergence from the ideal probe geometry, and within a certain time interval the different soiling of the single wires. For this direct calibration method there is no need of simplifying assumptions concerning the sensor characteristics or about physical laws governing the sensor cooling and no yaw or pitch angle factors have to be introduced.

The calibration grid itself is too rough to determine the magnitudes and the associated directions of the measured velocity vector exactly. Therefore, the calibration grid is processed to a highly refined grid called look-up table. For the generation of look-up tables several modified and refined numerical methods are implemented in the hot-wire measurement system [16 − 19]. Fig. 2 gives an example to refine cross-wire raw calibration data with cubic spline or polynomial regression fits. The plots show the look-up table velocity surfaces of the components U and V as functions of anemometer output-voltages E_1 and E_2. Fig. 3 shows an example of refinement of the triple-probe calibration grid using an interpolation procedure in the whole look-up table room. The refined look-up room is depicted by a plane with constant velocity and a plane with constant pitch- and yaw angle combinations.

The evaluation of the instantaneous velocity vector is done for each value of the stored timeseries of E_1, E_2 and E_3 respectively. A search algorithm is used to determine the closest look-up table voltage pair/triple relevant to the measurement voltage pair/triple. The velocity magnitude and the associated flow direction are then calculated by interpolation between the voltage pair/triple of the measurement point and the adjacent look-up table point.

Description of the Tests

Flowfield measurements were made in planes perpendicular to the model x-axis, Fig. 4a,b. The delta-wing tests were conducted for three angles of attack (12.5, 25 and 30 deg) at a freestream reference velocity U_∞ of 37 m/s. Results are shown only for $x/c_r = 0.9$. The delta-canard tests were made for seven angles of attack (0, 15, 20, 25, 28, 30 and 31.5 deg) at a freestream reference velocity U_∞ of 40 m/s. This gives a Reynolds number of approximately $Re = 1.0 \times 10^6$ based on the wing mean aerodynamic chord for all the results presented. Further test section

a) $x/c_r = 0.9$

b) $x/c_r = 1.125$
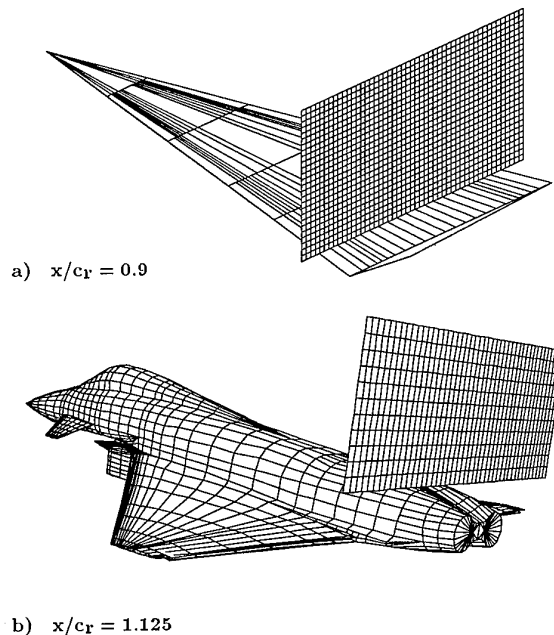
Fig. 2 Location and discretization of the measurement planes.

conditions were ambient static pressure and room temperature. As the wing leading-edge was sharp free transition was used.

The sampling frequency for each channel was set to 3 kHz. The anemometer signals were low pass filtered at 1 kHz before digitization to satisfy the Nyquist criterion. This is due to the check that no other significant flowfield phenomena are present in the higher frequency domain. The sampling time for each measuring point is 26.4 s depending on stable, time-averaged auto-spectra due to the turbulent flow structures. The values based on the fundamentals of random error evaluation methods [20] relate to an accuracy of 0.2%, 1% and 3% which are desired for mean and standard deviation and the spectral density, respectively.

A typical survey plane of the delta wing measurements contained 47 evenly spaced points spanwise and 26 evenly spaced points vertically giving a grid resolution of 0.022 based on the wing span. The grid increments of the delta-canard survey planes were set to 0.020 spanwise and 0.014 vertically at each station, Figs. 4a,b. Ref. 21 and Ref. 22 contain the complete results of these investigations.

Results and Discussion

75° Swept Delta Wing

Mean Velocity Distributions

Fig. 5 gives a general view about the development of the vortex dominated flowfield from moderate to high angle of attack showing the cross flow $(\overline{v}, \overline{w})$ velocity vectors. In addition Fig. 6 shows contours of mean velocities $\overline{u}/U_\infty$, $\overline{v}/U_\infty$, $\overline{w}/U_\infty$ for $\alpha = 12.5$ and 30.0 deg.

The leading edge vortices with increasing velocities towards its center as well as the accompanied secondary vortices, having the opposite sense of rotation, are clearly depicted, Fig. 5a. The secondary vortex is rather small because the boundary layer on the wing beneath the pri-

a) $\alpha = 12.5$ deg

b) $\alpha = 25.0$ deg

c) $\alpha = 30.0$ deg
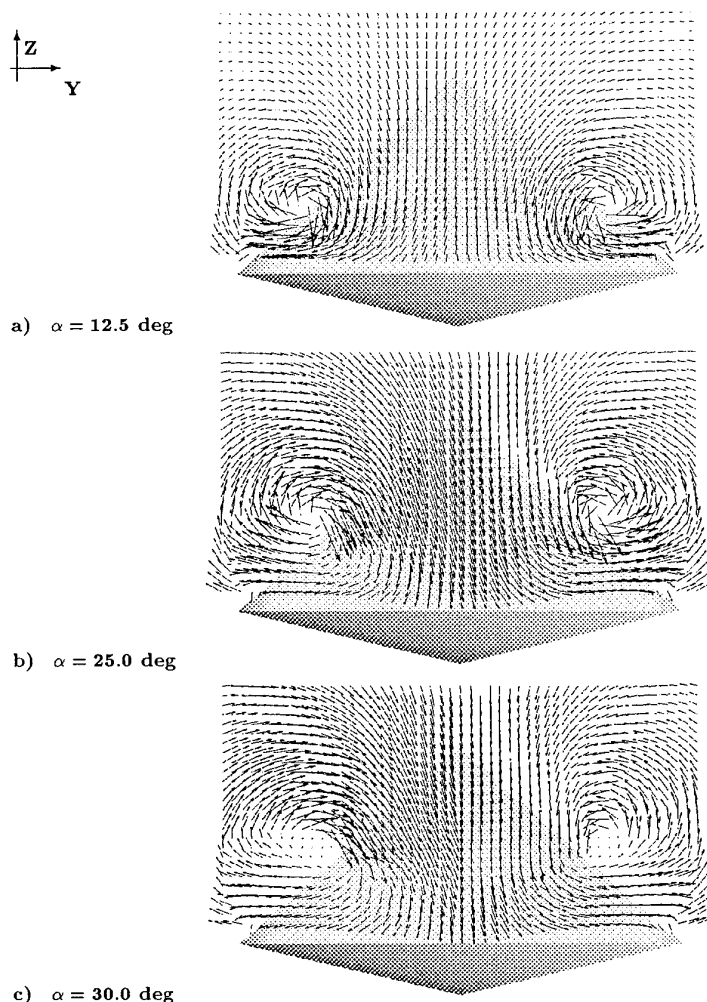
Fig. 5   Crossflow vectors in the measuring plane at $\alpha = 12.5$ deg, $\alpha = 25$ deg and $\alpha = 30$ deg.

mary vortex is turbulent [21]. For this reason, secondary flow separation occurs rather close to the leading edge. The streamwise flow, of velocity $\bar{u}$, shows a very strong overvelocity on the axis, with the ratio $\bar{u}/U_\infty$ reaching a value of 2, Fig. 6a. Such an axial acceleration is typical of concentrated delta wing vortices, which can be extremely vigorous. The boundary layer between the primary vortices as well as the region of the secondary vortices are indicated by a decrease in streamwise velocity.

The maxima of transverse velocities $\bar{v}$ and $\bar{w}$ near the core, which practically represent the rotation component of the motion, reach the freestream value, Fig. 6b,c. The increase of transverse velocity on a line from above the primary vortex through its center is stopped at the border, where viscous effects starts to dominate the flow. Thus there are three distinct vortex regions: An internal viscous core where the motion is like that of a rotating solid body, an external area where the flow is irrotational and the vortex is of the potential type and an intermediate region where the flow is rotational and inviscid. At this incidence the flow is not completely dependent on the vortex formation over the wing. The streamwise velocity in the flowfield above the boundary layer and between the two vortices is $\bar{u}/U_\infty = 1.0$ corresponding to the freestream value.

When the angle of attack is increased to 25 deg there is

a marked increase in both size and strength of the primary vortices, Fig. 5b. The leading edge vortices move inboard and upwards above the wing. Large downwash components are induced between these two vortices. Now the complete flowfield of the measurement plane is dominated by the primary vortices.

At $\alpha = 30$ deg the flow structure has altered significantly, Fig. 5c. This is due to the onset of vortex breakdown slightly upstream of this plane. The abrupt disorganization of the vortex with occurence of a stagnation point on the axis is clearly indicated by the expansion of a region with very low velocity quantities, Fig. 6d. Thus the streamwise velocity shows two distinct regions. One is the displaced vortex core just after the kink at the vortex breakdown point which is characterized by the highest streamwise velocity. The ratio $\bar{u}/U_\infty$ reaches a level of 2.5. This indicates already a reduction against the core value at 25 deg angle of attack, where the velocity has peaked at $\bar{u}/U_\infty = 2.68$ [21]. The other is the very low velocity region underneath the high velocity subcore directly behind the stagnation point of the kink. The streamwise velocity decreases to 40% of the freestream value. The lateral and vertical velocity components also indicate a strong reduction in velocity reaching levels of 10% of the freestream value, Fig. 6e,f. Thus a very steep gradient between this close change from flow acceleration
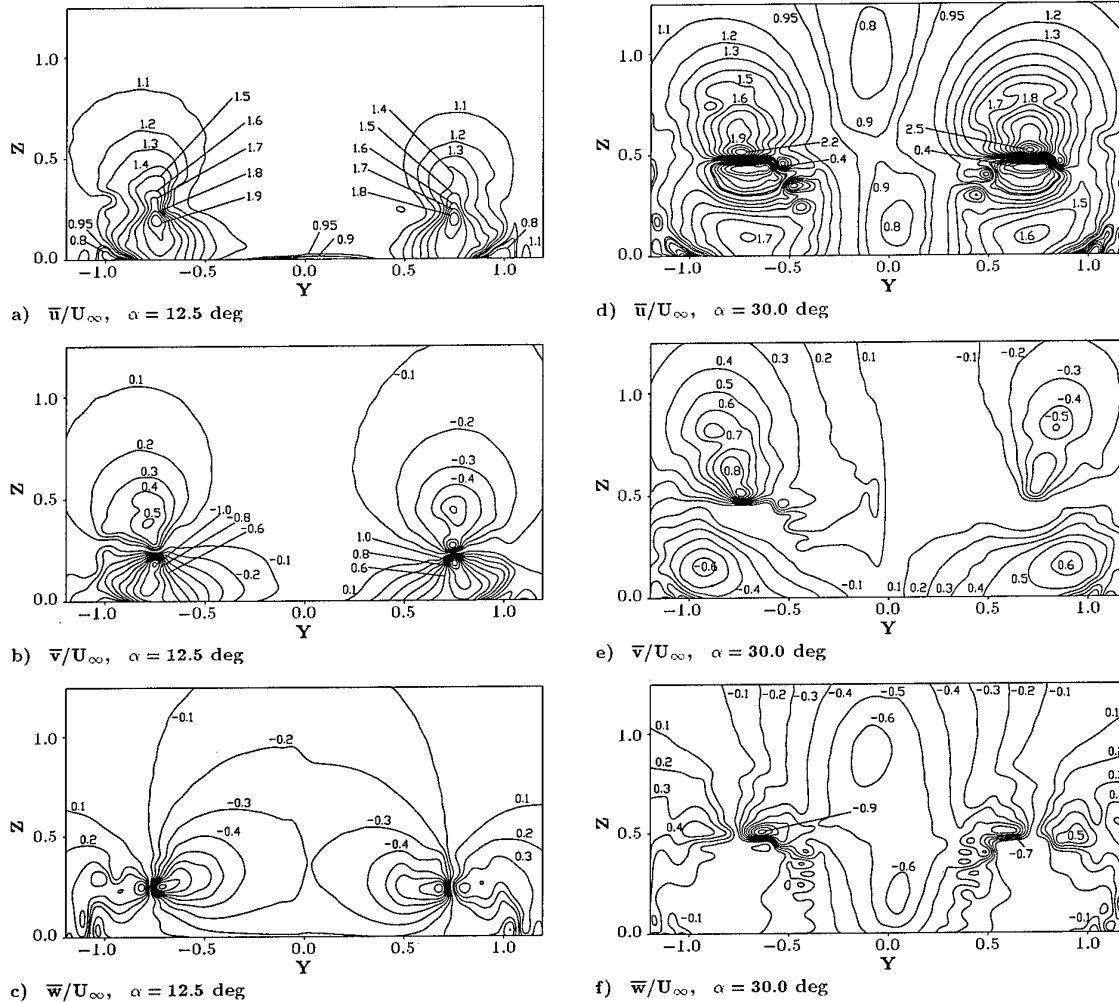
a) $\overline{u}/U_\infty$, $\alpha = 12.5$ deg

b) $\overline{v}/U_\infty$, $\alpha = 12.5$ deg

c) $\overline{w}/U_\infty$, $\alpha = 12.5$ deg

d) $\overline{u}/U_\infty$, $\alpha = 30.0$ deg

e) $\overline{v}/U_\infty$, $\alpha = 30.0$ deg

f) $\overline{w}/U_\infty$, $\alpha = 30.0$ deg

Fig. 6 Contours of mean velocity $\overline{u}/U_\infty$, $\overline{v}/U_\infty$, $\overline{w}/U_\infty$ at $\alpha = 12.5$ deg and $\alpha = 30.0$ deg.

to deceleration is evident leading to a rapid diffusion of the vortex subcore. The transition from a small jet-flow subcore to an enlarged wake-flow core determines the development of the vortex structure at breakdown conditions.

Similar results were reported in Ref. 8 and 10. As noted in Ref. 10 the intrusive method may have a significant influence on breakdown onset and the breakdown location, in particular, near the trailing edge. In this case flow visualization and surface pressure measurements show that vortex breakdown occurs at this plane at 30 deg angle of attack [21]. The probe influence is mainly visible by a disturbed location of the inboard shear layer.

Root-mean-square Velocity Distributions

The turbulent flow structure is quantified by the root-mean-square values of the velocity fluctuations. Fig. 7 presents carpet plots of the rms-distribution for all three velocity components. Figs. 8 and 9 contain the contour values.

At $\alpha = 12.5$ deg, the vortex structure is clearly depicted by an increase in the turbulence intensity level. The vis-

ous subcore is represented by local rms maxima of 10 - 15%, Figs. 7a, 8a, 9a, indicating the center of the primary vortex, which is at $Y = \pm 0.72$ and $Z = 0.2$. The diameter of the subcore is calculated to 0.07 referred to the local wing span. Good correlation is evident for the comparison between the mean and rms plots for position and size of the viscous core. The subcore turbulence intensity is greater in the lateral and vertical direction compared to the streamwise direction due to the higher gradient of the transverse velocity components in the core region, Fig. 6b,c. Local rms maxima of about 5% indicate the region of the secondary vortices at $Y = 0.94$ and $Z = 0.02$.

The vortex shear layer is characterized by the formation of discrete vortices represented by local maxima of turbulence intensity of all three velocity components, Fig. 7a,b,c. The appearance of discrete vortices in the shear layer was observed also at flow visualization experiments [9]. This proves that large vortices on delta wings originate as a series of smaller vortices shed from the leading edge of the airfoil. It was found [23] that the growth of such shear layers is the result of a pairing process between neighbouring discrete vortices. The mutual induction of
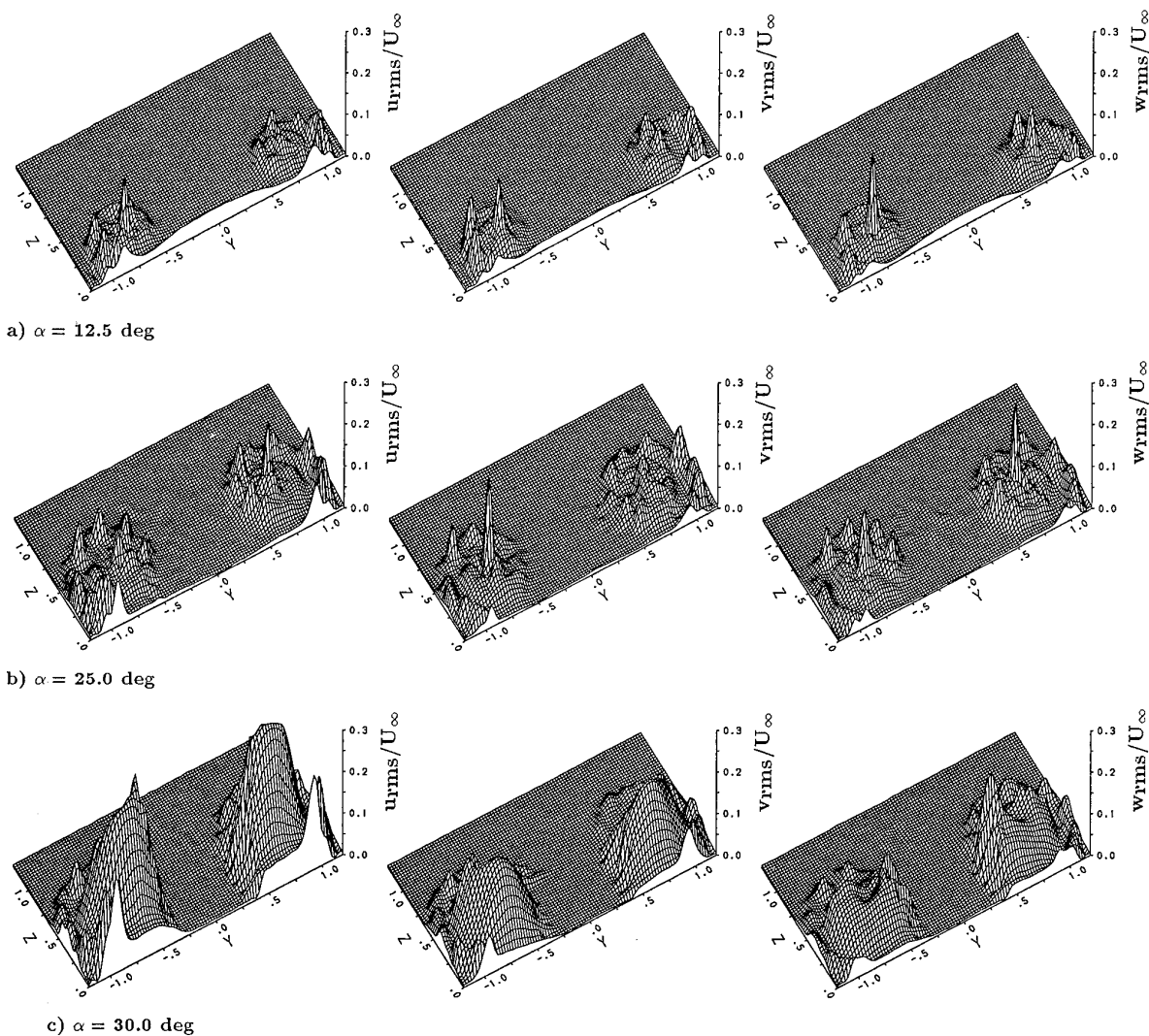
a) $\alpha = 12.5$ deg

b) $\alpha = 25.0$ deg

c) $\alpha = 30.0$ deg

Fig. 7 Carpet plots of streamwise, lateral und vertical rms velocity, u_{rms}/U_∞, v_{rms}/U_∞, w_{rms}/U_∞, at $\alpha = 12.5$ deg, $\alpha = 25$ deg and $\alpha = 30$ deg.

one vortex on the other caused them to begin to rotate around each other amd merge to form a single vortex of larger diameter.

With increasing angle of attack to 25 deg the growth of the vortex system is depicted by the enlargement of the turbulent flow region, Figs. 7b, 8b, 9b. The subcore has moved to $Y = 0.69$ and $Z = 0.37$ due to the upward and inboard shift of the leading edge vortices when the angle of attack is increased. The core diameter is calculated to 0.11 referred to the local wing span. Again the subcore turbulence levels of the lateral and vertical velocity components are significantly increased against the streamwise component, Fig. 7b. The maximum core rms values reach levels of 15%, 22% and 20% for the streamwise, lateral and vertical components, respectively. The increase in the core turbulence intensity is due to much stronger velocity gradients when the vortex grow in strength with increased angle of attack. The secondary vortex is detected by local rms maxima of 5% at $Y = 0.94$ and $Z = 0.01$.

The values for v_{rms} and w_{rms} in fact represent an overall oscillation of the vortex structure in directions normal to the axis. The result is an apparent turbulence, which is particularly strong, because of the rapid variations of mean velocity $\bar{v}$ and $\bar{w}$ as a function of the radius in the vicinity of the vortex axis. The turbulence intensity in the shear layer is only slightly increased. The rms distribution shows the structure of the vortex shear layer consisting of the discrete vortices which rolls up around the viscous core well. There is a considerable increase in the number of the discrete vortices when the angle of attack is increased.

At $\alpha = 30$ deg the onset of vortex breakdown is clearly depicted by the vehement increase and expansion of turbulence intensity in the core region, Fig. 7c, 8c, 9c. Levels of about 30% and steep rms gradients are detected for the streamwise component. The lateral and vertical turbulence intensity reach levels of 20%, Fig. 7b, 7c. At the onset of vortex breakdown it is now the streamwise rms component that takes on by far the highest values.
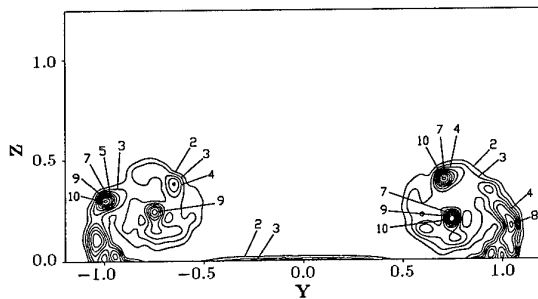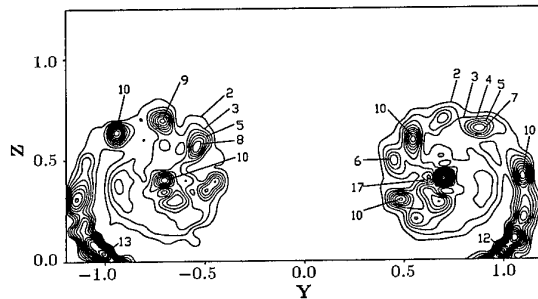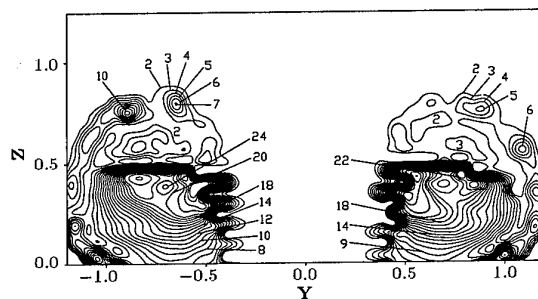
a) $\alpha = 12.5$ deg

b) $\alpha = 25.0$ deg

c) $\alpha = 30.0$ deg

Fig. 8 rms velocity contours $u_{XZ_{rms}}/U_\infty$ (sum of streamwise and vertical component) at $\alpha = 12.5$, 25.0 and 30.0 deg; (Values in percent)

a) $\alpha = 12.5$ deg

b) $\alpha = 25.0$ deg

c) $\alpha = 30.0$ deg

Fig. 9 rms velocity contours v_{rms}/U_∞ at $\alpha = 12.5$, 25.0 and 30.0 deg; (Values in percent)

This is a reversal of the tendency described above for the subcore of concentrated leading edge vortices. The extreme velocity gradient between the neighboured high and low velocity region above and below the initial core position is the reason for this maximum in streamwise turbulence intensity. As noted in Ref. 11 the point of origin of the breakdown goes through a large-amplitude longitudinal fluctuating motion that also cause a peak in u_{rms}.

The large area of high turbulence levels corresponds with the low velocity region of Fig. 6d. This depicts the transition into a fully turbulent flowfield after the onset of vortex breakdown. There is also an effect between the highly turbulent low velocity flow region and the delta wing. The large area of high turbulence seems to be compressed into an oval shape between the delta wing and the high velocity gradient between maximum and minimum velocity. The turbulence level of the discrete vortices in the shear layer is reduced due mainly to the change to a large low velocity highly turbulent region from a small high velocity viscous core.

The rms diagrams also clearly depict the interference pat-

tern associated with the lateral movement of the probe. This occurs at approximately $Y = \pm 0.45$. There is a strong velocity gradient in the lateral direction across the shear layer which is extremely sensitive to intrusive flowfield measurements.

Delta-Canard Configuration

Mean Velocity Distributions

The flowfield of the measurement plane (Fig. 4b, $X/L = 1.125$) is characterized by the interaction of several vortex systems, mainly produced by the canard and the delta wing. Fig. 10 shows contours of mean velocities $\bar{u}/U_\infty$, $\bar{v}/U_\infty$, $\bar{w}/U_\infty$ for $\alpha = 15$ and 30 deg.

The canard vortices can be clearly identified in the measuring plane near the fuselage. The axial velocity $\bar{u}$ in the core of the canard vortex system has decelerated to approximately 85% of the freestream value, Fig 10a. This considerable decrease in the canard vortex core indicates that even for moderate angles of attack the vortices are strongly influenced by viscous effects. The lateral and vertical velocity components reach levels of 12.5% of

a) $\bar{u}/U_\infty$, $\alpha = 15.0$ deg

d) $\bar{u}/U_\infty$, $\alpha = 30.0$ deg

b) $\bar{v}/U_\infty$, $\alpha = 15.0$ deg

e) $\bar{v}/U_\infty$, $\alpha = 30.0$ deg

c) $\bar{w}/U_\infty$, $\alpha = 15.0$ deg

f) $\bar{w}/U_\infty$, $\alpha = 30.0$ deg

Fig. 10 Contours of mean velocity $\bar{u}/U_\infty$, $\bar{v}/U_\infty$, $\bar{w}/U_\infty$ at $\alpha = 15.0$ deg and $\alpha = 30.0$ deg, Ref. 1.

the freestream value, Fig. 10b,c.

When the angle of attack is increased to $\alpha = 30$ deg the wing's primary vortices move inboard towards the fuselage and upwards above the wing, Fig. 10d-f. The flowfield is then completely dominated by the wing leading-edge vortices. With higher angle of attack the intensity of the vortex induced cross-flow velocities has increased. Because of the strong inward and downward velocity the canard vortex system cannot be resolved any more. Severe flow deceleration occurs at the lower edges of the measuring plane, resulting in strong velocity gradients. The change from flow acceleration to deceleration is evident due to the bursting of these vortices. The burst wing vortices increase in its radial extension what leads to a big vortex core which was also observed at the single delta wing. This inner part of the vortex is characterized by very small velocity quantities, Figs. 10d,e,f. The increase of the vortex core is connected with the decrease of velocity to meet the continuity equation, but it is obvious that strong viscous effects dominate the flow in a rather large area around the center of the primary vortex. Although the core becomes very large, a well-structured swirling flow pattern can be observed around it. When the angle of attack is increased the borders of the primary vortices move closer together. In connection with the induced circumferential velocities a nozzle effect appears in the mid section, Fig 10f.

Root-mean-square Velocity Distributions

Figs. 11 and 12 contain the rms contours of the sum of the streamwise and vertical velocity component as well

as of the lateral component.

At moderate angle of attack, $\alpha = 15 - 20$ deg, the canard leading-edge vortices are indicated by local rms humps of approximately 6% – 10% around the mid section, Figs. 11a,b, 12a,b. This complies with the axial velocity drop seen in Fig. 10a and with the velcoity jumps of Figs. 10b and 10c, respectively. There is also an evident increase in the fluctuation intensity at the lower cross section edges which are related to the wing primary vortex sheets as well as very steep gradients in the rms-distribution in the sheet itself. The maximum rms values reach levels of approximately 21%.

At $\alpha = 25$ deg, Figs. 11c, 12c, the turbulent region has grown considerably in both size and strength. The lower part of the measuring plane is dominated by large rms values which are due to the wing primary and the canard vortex sheets. With increasing angle of attack the canard vortex system passes the wing leading edge relatively high above the wing. It consists of the canard's leading-edge and its trailing-edge vortex. This vortex system keeps its structure downstream still behind the wing trailing edge [22]. From the comparison of Figs. 11a, 12a ($\alpha = 15$ deg) and Figs. 11b, 12b ($\alpha = 20$ deg) it can be inferred that through wing influence the canard vortex system is moved above the wing inward towards the fuselage and also downward towards the wing surface. At 25 deg angle-of-attack the interaction between the vortex systems of the wing and the canard is such that the canard vortex sheet belonging to the trailing vortex starts to move upwards away from the wing while the canard leading-edge vortex is moved inwards and down-

a) $\alpha = 15.0$ deg
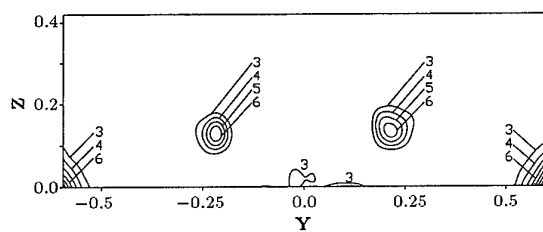
a) $\alpha = 15.0$ deg
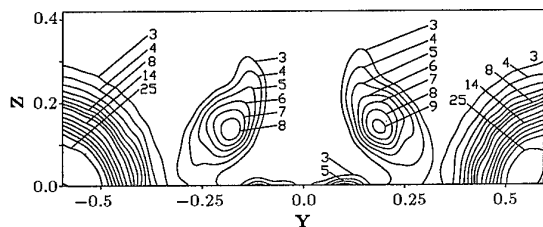
b) $\alpha = 20.0$ deg

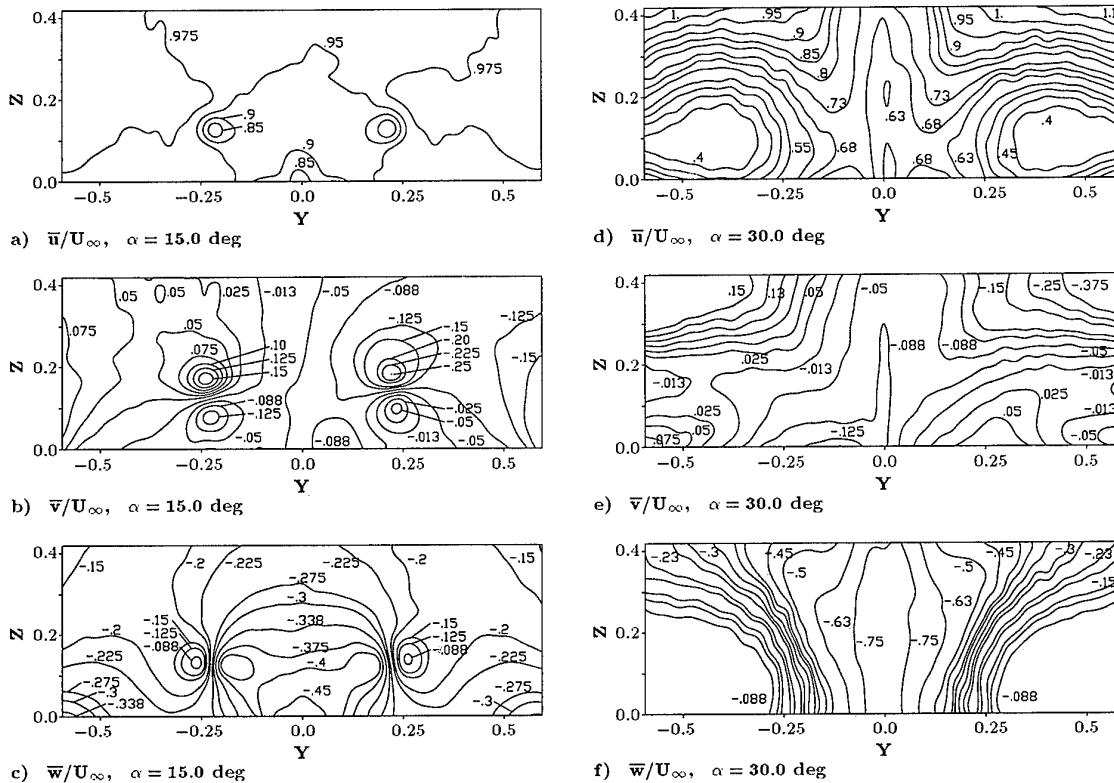b) $\alpha = 20.0$ deg
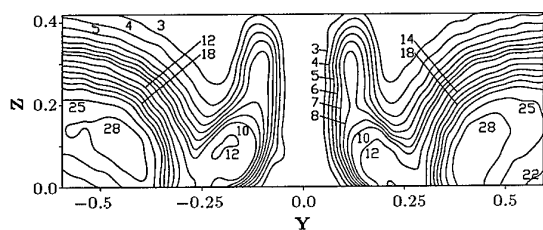
c) $\alpha = 25.0$ deg

c) $\alpha = 25.0$ deg
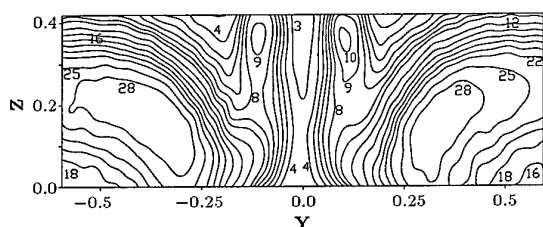
d) $\alpha = 28.0$ deg

d) $\alpha = 28.0$ deg
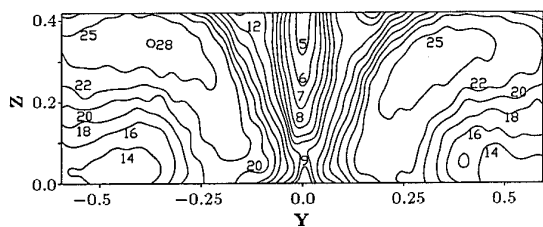
e) $\alpha = 31.5$ deg

e) $\alpha = 31.5$ deg

Fig. 11 rms velocity contours $u_{xz_{rms}}/U_\infty$ (sum of streamwise and vertical component) at $\alpha = 15.0 - 31.5$ deg; (Values in percent), Ref. 1.
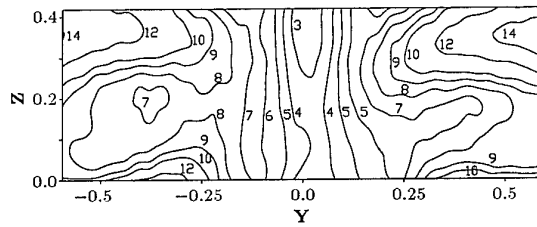
Fig. 12 rms velocity contours v_{rms}/U_∞ at $\alpha = 15.0 - 31.5$ deg; (Values in percent), Ref. 1

wards to merge with the sheets of the wing primary vortices.

With a further increase to $\alpha = 28$ deg, the rms values of all three components become still larger again, Figs. 11d, 12d. The canard leading-edge vortex sheets are completely merged in the wing leading-edge vortices. The upper part of the canard's vortex system referring to the trailing-edge vortices remains separate from the wing's primary vortex sheets. The maxima of the rms velocity

fluctuations go up to 31%, 15% and 28% for the u, v and w components, respectively.

The vortex regions of the wing primary vortices reveal that the maxima of the rms velocities are concentrated in an annular-like structure around the core. It is related to the vortex sheet (shear layer) due to the swirling pattern. The inner part of the core has, however, a decrease in local rms. The reason for lower rms values in the core is the loss of mean velocity as well as the low velocity gra-

a) $\alpha = 15$ deg

b) $\alpha = 15$ deg, $Z = 0.05$

c) $\alpha = 28$ deg

d) $\alpha = 28$ deg, $Z = 0.13$
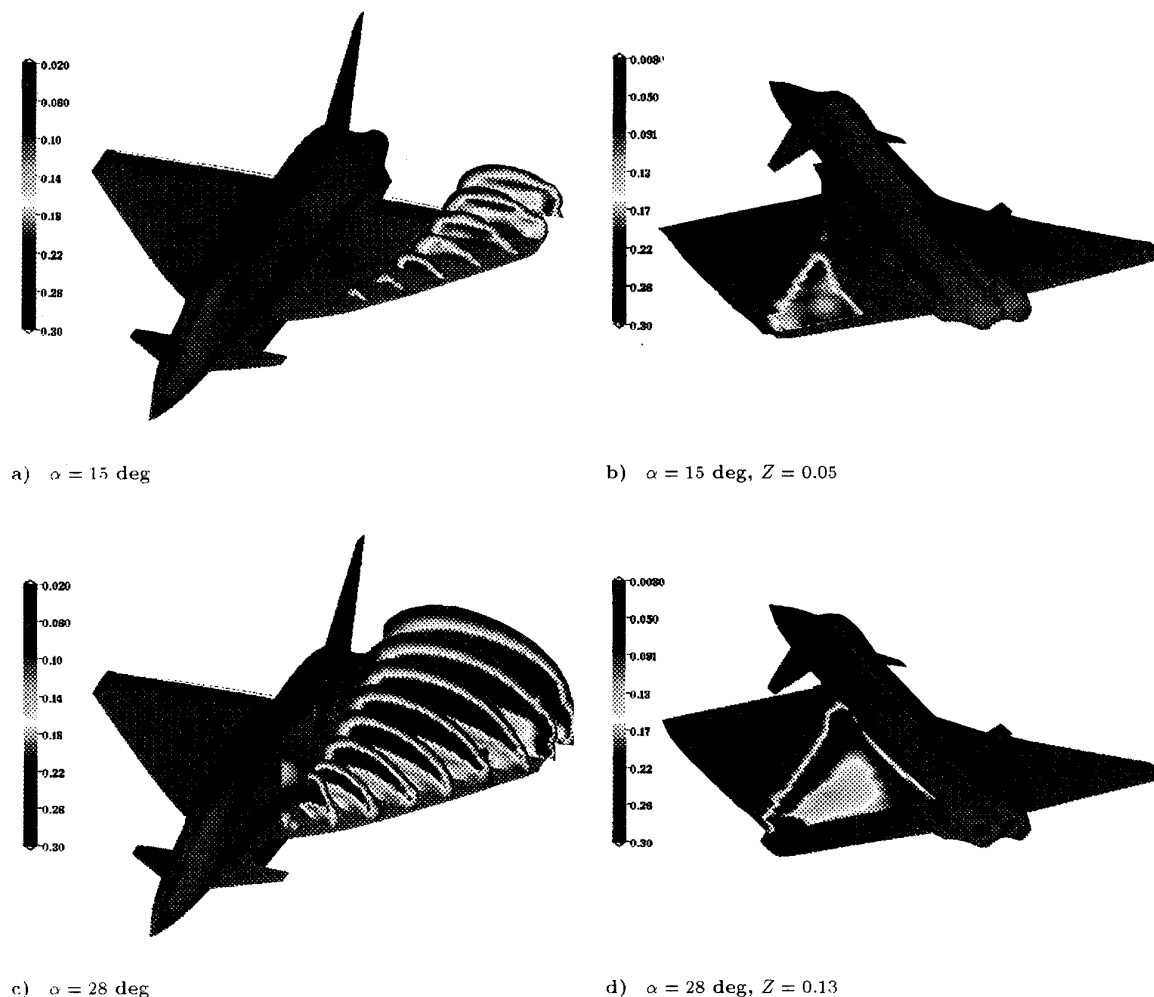
Fig. 13 Streamwise rms velocity distribtution at $\alpha = 15$ deg and $\alpha = 28$ deg.

dient within the core which reduces the turbulence level. The very steep gradients of the vortex sheet's rms distribution outside the core do not change with increasing angle of attack.

Although at $\alpha = 31.5$ deg, Figs. 11e and 12e, the maximum rms values of the velocity fluctuations have not grown considerably, their region of influence has. There is an increase to much higher rms values in the mid section which is caused by the inward shift of the wing primary and combined canard vortex sheets. This explains the severe increase of lateral rms velocity fluctuation in the mid section at high-α flow conditions.

The complete development of the delta-wing primary vortices is depicted by the streamwise rms-distribution at $\alpha = 15$ deg and $\alpha = 28$ deg, Fig. 13. The measurement volume contains 18 planes downstream with 33 points spanwise and 16 points vertical. At $\alpha = 15$ deg, Fig. 13a, the rms-values of planes normal to the wing surface show the rapid appearance of high turbulence levels when vortex breakdown occurs. The change from jet-flow to wake-flow during the breakdown process leads to large streamwise velocity fluctuations, see Fig. 6c. Moving downstream the strong enlargement of the highly turbu-

lent vortex core region can be observed. The rms distribution of the last planes shows a first annular-like structure of the rms-maxima described above. In the plane $Z = 0.05$, Fig. 13b, the rms distribution is characterized by a first region with increased rms values followed by a second region with a very high rms core due to the development of the bubble breakdown process. The location with the absolute rms maxima may be near the locus of reverse flow at vortex breakdown which cannot be detected with this conventional hot-wire probes.

At $\alpha = 28$ deg, Fig. 13c, vortex breakdown occurs very close to the wing apex. A first region with maximum rms values can be detected at the second station. Moving downstream the region with maximum rms values becomes very large. It is extended over the whole wing half span. In the first planes also a part of the canard vortex system can be detected. In the plane $Z = 0.13$, Fig. 13d, the rms-distribution depicts two separated regions of rms maxima downstream of the vortex breakdown location. This is the most noticeable change against the 15 deg case showing a distinct displacement of the domain where the turbulence intensity is strongest. The maximum rms values are now to either side of the initial vortex axis in a region that coincides with the mean

a) Spectra of the left side (−Y)

b) Spectra of the right side (+Y)
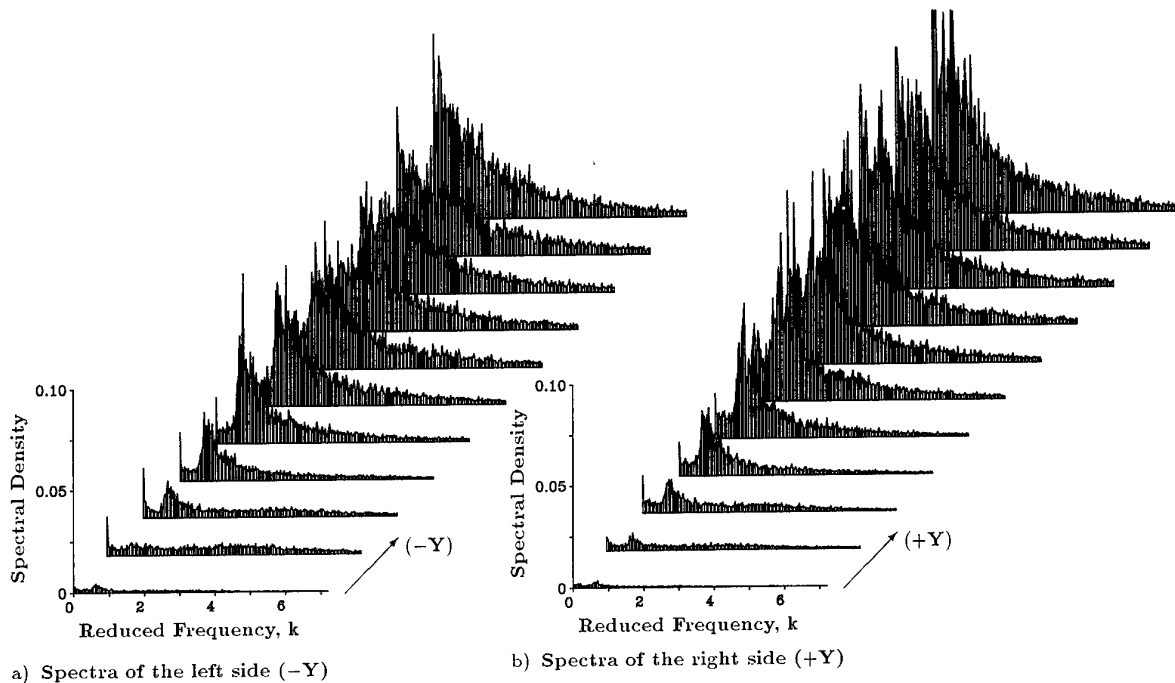
Fig. 14 Spectra of the lateral velocity component v, left and right of the plane of symmetry at Z = 0.21 and α = 28 deg, Ref. 1

boundary of the very low velocity region.

Spectral analysis
Spectral analysis gives the magnitude and the frequencies for structural excitation levels.

Character of the Spectral Content at High Angle of Attack
Results shown for α = 28 deg only, give a general view of the distribution of kinetic turbulent energy at high-α. Two staggered density spectra plots of the lateral velocity component both of the left and right side of the cross section are shown in Fig. 14.

The power spectrum density increases strongly in spanwise direction, Figs. 14a and 14b, what is directly related to the vortex shear layer and core position. For the outboard locations corresponding to the wing primary vortex core the spectra have a pronounced and broad frequency hump ranging from $k = 0.5$ to $k = 1.2$. The turbulence level reaches values of approximately 13%.

At middle stations of the left or right side of the measurement plane, however, a strong narrow-band frequency peak which is closely associated with the pronounced velocity fluctuations in the vortex sheet is observed. The spectral energy is accumulated in this limited frequency range. This may indicate a periodic or quasiperiodic fluctuation which is due to the swirling vortex pattern. Roughly 75% of the turbulent energy is concentrated within this narrow band.

The power spectrum density values near the mid section are appreciably small. The kinetic turbulent energy decreases by an order of magnitude, but the spectra show a concentration of kinetic turbulent energy in the specified frequency range again. It is obvious that by the induced concentration of turbulent energy into a limited fre-

quency range the vortex sheet affects the flow conditions even in the surrounded region.

Conclusions

The time-average and root-mean-square of the velocity components in a turbulent flowfield caused by a vortex-dominated configuration have been studied from moderate to high angles of attack. The used hot-wire techniques employing cross-wire and triple-wire probes are described. The frequency contents of the fluctuating flowfield are also presented. Major results of these investigation are as follows:

1) Size and turbulence level of the viscous subcore of concentrated leading edge vortices are determined.
2) The delta wing vortex shear layer originates as a series of discrete vortices shed from the leading edge which rolls up and merge to form a single vortex of larger diameter. The discrete vortices are clearly indicated by local rms maxima in the vortex sheet.
3) Already at moderate angles of attack the wing and canard vortex systems are strongly influenced by dissipation giving an increase in the turbulence levels.
4) When the angle of attack is increased, the wing vortex system moves inboard towards the mid section and upwards. The vortices grow continuously both in size and strength.
5) At the onset of vortex breakdown two neighboured regions of high and low streamwise velocity are present leading to a severe velocity gradient. Thus streamwise turbulence intensity is much higher than in the lateral and vertical direction. A significant enlargement of the high turbulent low velocity region characterizes the breakdown process.
6) Downstream of the breakdown point the vortices in-

creases in their radial extension leading to a large highly turbulent vortex core. This is emphasized by a strong decrease of the axial- and azimuthal velocity.

7) A strong increase of the turbulence level for all three velocity components characterizes the vortex flowfield downstream of the breakdown location. Steep gradients separate the vortex sheet region from the outer flowfield. The maxima of rms values shows an annular structure which are assigned to the vortex sheet while in the vortex core a local rms decrease occurs.

8) For moderate angles of attack ($\alpha < 20$ deg) it is shown that above the wing through wing influence the canard vortex-system is moved towards the mid section and also downward towards the wing. At an angle of attack $\alpha \approx 20$ deg the interaction between the wing and canard vortex systems makes the canard trailing-vortex sheet to move upwards whereas the canard leading-edge vortex sheet merges with the wing primary vortex. The merged vortex sheets are indicated by a significant increase in the turbulence level.

9) The spectra of the vortex sheets at burst flow conditions show a distinct narrow-band peak whereas the vortex core region depicts a broader frequency hump. The narrow-band concentration of kinetic turbulent energy indicates a strong periodicity in the flow.

Acknowledgements

References

1. Breitsamter, C. and Laschka, B., "Turbulent Flow Structure Associated with Vortex-Induced Fin Buffeting", *Journal of Aircraft*, (accepted for publication)

2. Becker, J., "Bewegungsinduzierte Luftkräfte bei abgelöster Strömung und ihre Übertragung auf die Ermittlung der Strukturresponse", Dissertation, TU Braunschweig, 1982.

3. Mabey, D. G. and Pyne C. R., "Fin Buffeting at High Angles of Incidence on a Model of Slender Wing Aircraft," International Forum on Aeroelasticity and Structural Dynamics, Paper 91-129, 1991, pp. 552-561.

4. Wentz, W. H., "Vortex-Fin Interaction on a Fighter Aircraft", AIAA-87-2474, AIAA 5th Applied Aerodynamics Conf., Monterey, CA, Aug. 1987.

5. Lee, B. H. K. and Brown, D., "Wind-Tunnel Studies of F/A-18 Tail Buffet," *Journal of Aircraft*, Vol. 29, No. 1, 1992, pp. 146-152.

6. Brandon, J. M. and Nguyen, L. T., "Experimental Study of Effects of Forebody Geometry on High Angle-of-Attack Stability", *Journal of Aircraft*, Vol. 25, No. 7, 1988, pp. 591-597.

7. Ashley, H., Rock, S. M., Eggers, Jr., A. J., Digumarthi, R. V. and Chaney, K., "Active Control for Fin Buffet Allevation", Mid-Year Report, RANN, Palo Alto, California, Jan. 1993.

8. Hummel, D., "On the Vortex Formation Over a Slender Wing at Large Angles of Incidence", AGARD CP 247, October 1978, Paper 15.

9. Hummel, D., "Untersuchungen über das Aufplatzen der Wirbel an schlanken Deltaflügeln", Z. Flugwiss. 13, Heft 5, 1965, pp. 158 -168.

10. Payne, F. M., Ng, T. T. and Nelson, R. C., "Visualization and Flow Surveys of the Laeding Edge Vortex Structure on Delta Wing Planforms", AIAA Paper 86-0330, January 6-9, 1986.

11. Payne, F. M., Ng, T. T. and Nelson, R. C., "Experimental Study of the Velocity Field on a Delta Wing", AIAA Paper 87-1231, June 8-10, 1987.

12. Pagan, D. and Solignac, J. L., "Experimental Study of the Breakdown of a Vortex Generated by a Delta Wing", *Recherche Aerospatiale*, 3, 1986, pp. 29-50.

13. Oelker, H.-Chr. and Hummel, D., "Investigations on the Vorticity Sheets of a Close-Coupled Delta-Canard Configuration", *Journal of Aircraft*, Vol. 26, No. 7, 1989, pp. 657 - 666.

14. Cutler, A. D., and Bradshaw, P. "A crossed hot-wire technique for complex turbulent flows", *Experiments in Fluids* Vol. 12, No. 1, 1992, pp. 17-22

15. Breitsamter, C., "Messungen und Analyse der zeitabhängigen Geschwindigkeiten im wirbeldominierten Strömungsfeld eines Hochleistungsflugzeuges, Teil 1," FLM-91/22, Lehrstuhl für Fluidmechanik, Technische Universität München, 1991.

16. Johnson, F. D., and Eckelmann H., "A variable angle method of calibration for X-probes applied to wall-bounded turbulent shear flow," *Experiment in Fluids* Vol. 3, No. 2, 1984, pp. 121-130.

17. Lueptow, R. M., Breuer, K. S., and Haritonidis J. H., "Computer-aided calibration of X-probes using a look-up table," *Experiments in Fluids*, Vol. 7, No. 6, 1988, pp. 115-118.

18. Samet, M., and Einav, S., "A hot-wire technique for simultaneous measurement of instantaneous velocities in 3D flows," *J. Phys. E: Sci. Instrum.*, Vol. 20, 1987, pp. 683-690.

19. Browne, L. W. B., Antonia, R. A., and Chua, L. P., "Calibration of X-Probes for turbulent flow measurements," *Experiments in Fluids*, Vol. 8, No. 7, 1989, pp. 201-208.

20. Bendat, J. S., and Piersol, A. G., "Random Data: Analysis and Measurement Procedures," J. Wiley & Sons, Inc. Ney York, 1971.

21. Breitsamter, C., "Experimentelle Untersuchung der zeitabhängigen Geschwindigkeiten im Strömungsfeld eines Deltaflügels", FLM-93/17, Lehrstuhl für Fluidmechanik, Technische Universität München, 1993.

22. Breitsamter, C., "Messungen und Analyse der zeitabhängigen Geschwindigkeiten im wirbeldominierten Strömungsfeld eines Hochleistungsflugzeuges, Teil 2," FLM-91/54, Lehrstuhl für Fluidmechanik, Technische Universität München, 1991.

23. Gad-el-Hak, M. and Blackwelder, R. F., "The Discrete Vortices from a Delta Wing", *AIAA Journal*, Vol. 23, No. 6, 1985, pp. 961-962.

BOUNDARY-FLOW MEASUREMENT METHODS FOR WALL INTERFERENCE ASSESSMENT AND CORRECTION - CLASSIFICATION AND REVIEW

P.R. Ashill
Defence Research Agency
Bedford, MK41 6AE, UK

SUMMARY

The development of methods of determining wind-tunnel wall interference from measurements of the flow at a boundary adjacent to the wind-tunnel walls has required the collaboration of theoreticians and experimenters. After these methods are classified and reviewed, techniques for making the measurements are discussed and the concept of correcting wind-tunnel flows to equivalent free-air conditions is examined. Three classes of method are identified, two needing a model representation ('one-variable' and 'wall-signature' types) and a third needing no simulation of the flow around the model ('two-variable' methods). All three classes are related and the need for accuracy in the model representation in 'one-variable' methods can be relaxed by a suitable choice of 'mixed' boundary conditions. Further work is needed to establish non-intrusive techniques and to develop improved methods for determining the normal component of velocity at or just away from the measurement surface. The need for research to establish allowable limits on variations in wall-induced velocity in the region of the model is highlighted.

SUFFIXES

e	outer edge of wind-tunnel wall boundary layer
F	equivalent free-air flow
I	wall-induced flow
i,j	differentiation with respect to either x,y or z in either case
R	fictitious region outside region contained within S
S	measurement surface
T	adjacent to wind-tunnel walls
U, D	upstream and downstream faces
V_0	volume integration in the fictitious region R
∞	conditions far upstream

LIST OF SYMBOLS

a_0, a_1, a_2	
$A_0, A_1, A_2,$	empirical constants
A, B, C	
B	breadth of working section of equivalent wind tunnel of rectangular section
C_p	static-pressure coefficient
G, G_D, G_F	Green's functions
G_N, G_{DN}	
H	height of working section of equivalent wind tunnel of rectangular section
ℓ	length of open jet part of working section
M	Mach number
n	normal inward towards working section in transformed (Prandtl-Glauert) space
P	point within region bounded by S
R	fictitious region outside the region bounded by S
R_1	slot resistance coefficient
S	measurement surface in transformed space
T	wall shape factor for doublet
u	streamwise velocity perturbation
U	stream speed
V	model volume
V_w	mass flow parameter, ie mass flow through hole or slot per unit area, made non dimensional with respect to density and speed of flow just outside boundary layer
x,y,z	cartesian coordinate system (Fig 1)
X,Y,Z	transformed coordinates, = (x,ßy,ßz)
α	angle of incidence
ß	Prandtl-Glauert factor, = $\sqrt{(1 - M_F^2)}$
δ_0, δ_1	lift interference parameters, Ref 1
ΔC_p	rise in static pressure coefficient across walls
Δ	increment due to wall effect
Φ	velocity potential
φ	perturbation velocity potential
η_a, η_p, η_u	parameters defining flow through slots

1 INTRODUCTION

The subject of wind-tunnel wall interference on the steady flow about aircraft models at subsonic speeds has for a long time been of concern to both theoreticians and experimenters. The theoreticians' efforts were needed because of the challenging mathematical problems involved, while the experimenter was called upon to provide data, fully corrected for wall constraint, for application to aircraft design. For a long while, there was a gulf between what the theoreticians could provide and what the experimenter needed. In many cases, the theoretical solutions were unreliable, owing to their failure to model the flow physics properly. Of concern to the experimenter was the validity of the modelling of the wall boundary conditions in wind tunnels with perforated or slotted walls and the failure of the linear-theory simulation of flows in which non-linear effects play an important part (eg transonic flows). It is not surprising, therefore, that experimenters developed empirical modifications to the theory based on experience in the wind-tunnel[1].

In the 1970's developments took place which were to lead to a more reliable basis for calculating wind-tunnel-wall interference corrections. The first significant development was that of the adaptive-wall wind tunnel[2]. In this concept the walls are shaped, or the flow at the tunnel walls adjusted, until wall interference is substantially removed. The algorithms needed to perform the wall adaptation required the

measurement of the velocity vector of the flow at a control surface in the neighbourhood of the walls, and these measurements enabled residual wall interference to be determined. At about the same time researchers at Lockheed[3,4,5] were striving to improve the accuracy of wall corrections for tests on high lift and V/STOL models in solid-wall tunnels. They adopted a method based on the measurement of wall pressures. The idea of measuring flow quantities at the walls was not new then, having been proposed during the 1940's to provide the basis for more accurate corrections in tests at high subsonic speeds in solid-wall tunnels[1]. Similarly, adaptive-wall wind tunnels had begun to be used at the National Physical Laboratory, England in the late 1930's[2]. A probable explanation for resurgence of interest in the 1970's of wall-flow measurement and adaptation is the rapid development of the digital computer during this period. The arrival of powerful digital computers dedicated to the wind tunnel made it possible to contemplate 'on-line' correction for, or elimination of, tunnel-wall interference using boundary-flow measurements.

A key advantage of making flow measurements at a surface close to the walls is that the wall corrections derived are directly linked to the actual flow in the working section of the wind tunnel rather than to some idealised flow. Thus, for a slotted-wall tunnel, for example, these measurements allow the effects of the flow through the slots to be properly represented. Consequently, 'pseudo' Reynolds-number effects, arising from incorrect simulation of the viscous flow through the slots, are eliminated. In the case of solid-wall tunnels, wall pressures provide information which may be used to improve the far-field representation of the flow around the model or to eliminate the need for a model representation altogether, as will be described in Section 2.

The subject of boundary-flow measurement methods has been extensively and thoroughly reviewed in recent years[6,7,8,9] and so another review may seem unnecessary. However, previous reviews have tended to concentrate on the theoretical methods; the present review, on the other hand, reflects the combined efforts of theoreticians and experimenters towards the development of boundary-flow measurement methods. First, a classification and review of various methods is presented in Section 2. A unified approach is adopted in which these methods are shown to be derived from a single equation. Emphasis is placed on methods in which the wall-induced flow is assumed to satisfy the Prandtl-Glauert equation, but it is argued that this assumption does not necessarily restrict the study to small-perturbation flows. The significance of the type of boundary conditions used is considered, and a strategy is proposed to minimise the influence of model representation in the calculated wall-induced velocities by combining different types of boundary conditions. In Section 3 both direct and indirect methods for determining the velocity vector at the measurement surface are reviewed and, where appropriate, compared. This is followed in Section 4 with a discussion of the concept of correcting wind-tunnel flows to an equivalent free-air flow. For various reasons, adaptive-wall tunnels do not remove tunnel-wall constraint altogether, and so it is important to consider the meaning of the concept. The present paper concludes with a summary

and recommendations for the directions of future work. The mutual interference between a model and the sidewall boundary layer, as occurs when the model is mounted from sidewalls, is a problem of some importance, perhaps deserving a separate review paper: this aspect, however, is outside the scope of the present paper.

2 CLASSIFICATION AND REVIEW

2.1 Basics

Before the various methods are classified and reviewed, it is useful to set the scene by considering basic aspects of methods for calculating wall interference from boundary flow measurements.
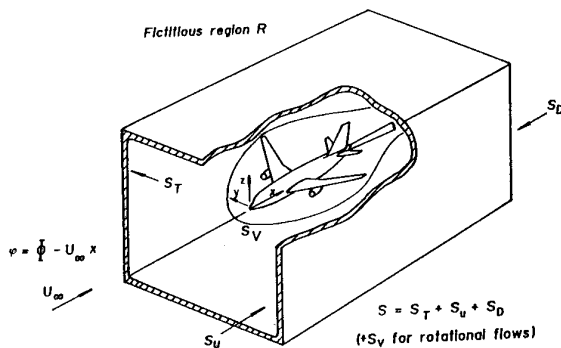
Fig 1 Model in wind tunnel

Consider the subsonic flow about a model of an aircraft in a wind tunnel (Fig 1). Suppose, initially, that the flow everywhere in the working section is irrotational, implying that any shock waves are weak and that the turbulent shear layers are thin. The flow may therefore be defined uniquely by the velocity potential Φ or the perturbation velocity potential $\varphi = \Phi - U_\infty x$, where U_∞ is the speed of the notional flow far upstream, usually determined by calibration of the empty test section. This flow satisfies the exact potential equation[10], which may be written in the form

$$\beta^2 \varphi_{xx} + \varphi_{yy} + \varphi_{zz} = f(\Phi_i , \Phi_{ij} , U_F ; M_F) , \qquad (1)$$

where $\beta^2 = 1 - M_F{}^2$ and M_F is the Mach number corrected for blockage, ie the free-stream Mach number of an equivalent 'free-air' flow. The corrected Mach number and the corresponding corrected free-stream speed, U_F, are preferred in equation (1) to the corresponding conditions far upstream because the former quantities determine the character of the flow in the near field of the model. Suffixes i and j, respectively, refer to differentiation with respect to either x, y or z. The function f is a term which is non-linear in the derivatives of Φ and which becomes significant in transonic-flow regions near the model.

The Prandtl-Glauert transformation may be used to replace equation (1) by

$$\nabla^2 \varphi = f (\Phi_i , \Phi_{ij} , U_F ; M_F)/\beta^2, \qquad (2)$$

where

$$\nabla^2 \varphi = \varphi_{XX} + \varphi_{YY} + \varphi_{ZZ}$$

and

$$(X, Y, Z) = (x, \beta y, \beta z).$$

$$\varphi_F = \Phi_F - U_F x - U_F \Delta\alpha z$$
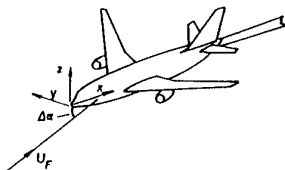
Fig 2 Free-air flow about same model

Consider now the 'free-air' flow about the same model at the free-stream speed U_F and at an angle of attack differing from the geometric angle of attack of the model in the tunnel by $\Delta\alpha$ (Fig 2). This flow is characterised by the perturbation potential

$$\varphi_F = \Phi_F - U_F \; x - U_F \; \Delta\alpha \; z$$

and satisfies the equation

$$\nabla^2 \varphi_F = f\left[(\Phi_F)_i \; , \; (\Phi_F)_{ij} \; , \; U_F \; ; \; M_F\right]. \tag{3}$$

If either

a) the two flows are identical· ($\Phi = \Phi_F$) in the region near the model, so that the tunnel flow may be corrected to an equivalent 'free-air' flow,

or b) the perturbations in the flow induced by the model are 'small' everywhere,

or c) the Mach number of the flow is everywhere close to zero, ie the two flows are essentially incompressible,

then the right-hand sides of equations (2) and (3) are either identical but non-zero, or negligible. This being the case, subtraction of equation (3) from equation (2) leads to the expression

$$\nabla^2 \varphi_I = 0, \tag{4}$$

where

$$\varphi_I = \varphi - \varphi_F$$

is the wall-interference potential. Since, by equation (4), this potential is harmonic within the working section, it is possible to use Green's formula to write for the point P in the (transformed) working section[11]

$$4\pi\varphi_I \; (P) = -\int_S \left[\frac{\partial\varphi_I}{\partial n}G - \varphi_I \frac{\partial G}{\partial n}\right] dS,$$

$$= -\int_S \left(\left[\frac{\partial\varphi}{\partial n} - \frac{\partial\varphi_F}{\partial n}\right]G - (\varphi - \varphi_F)\frac{\partial G}{\partial n}\right) dS. \tag{5}$$

Here n is the normal inward towards the working section and the integration is performed over the measurement or boundary surface S, comprising a surface at or close to the walls, S_T, with faces at the upstream and downstream extremities of the working section, S_U and S_D, (Fig 1). G is a Green's function that is harmonic everywhere within the measurement region except at the point P, near which it behaves like $1/r$, where r is the distance between the point P and a variable point in the region.

For the wall interference potential to be harmonic everywhere within the volume bounded by S means that $(\varphi - \varphi_F)$ must be single-valued there, ie the difference in circulation between the two flows around any circuit within the working section must be zero, and

$$\int_S \left(\frac{\partial\varphi}{\partial n} - \frac{\partial\varphi_F}{\partial n}\right) dS = 0,$$

ie, to the accuracy of linear theory, the net flux of the wall-induced flow across S must be zero. These conditions need to be borne in mind in any numerical method for determining wall interference based on equation (5).

The analysis above may, with certain restrictions, be extended to rotational flows. The first restriction is that the vorticity is confined to a region surrounding the model, as illustrated in Fig 1, where it is shown to be bounded by the surface S_v. The surface S in equation (5) then has to include the surface S_v. However, if the wind tunnel flow may be corrected to an equivalent free-air flow, the analytical continuation of the wall-interference potential is harmonic within the rotational-flow region, and hence, by Green's theorem[11], the contribution of the extra term vanishes. Thus, in this circumstance, equation (5) applies to rotational flows as well.

To determine the wall-interference potential at a point in the working section by using equation (5), it is necessary to know both the wall interference potential itself and its normal gradient at the measurement surface. This, in turn, means that perturbation potential of the wind-tunnel flow and its normal gradient have to be determined at the surface; furthermore, a satisfactory representation of the free-air flow around the model has to be derived. Thus at first sight, it appears that three independent variables are required, two from flow measurements at the surface S and a third, the model free-air flow, by calculation. However, the number of variables needed can be reduced to two by using the freedom to choose an appropriate Green's function for the boundary-value problem. Depending on the choice of Green's function, the two variables can either comprise one defining the flow at any one part of the measurement surface and another specifying the free-air flow or two defining the conditions at the measurement surface. Kraft[12] suggested that a measure of merit of any technique is how well the two independent

quantities are evaluated. Following Mokry[9], the two types of method are, respectively, called 'one-variable' and 'two-variable' methods. As the name of the former class of methods implies, it needs the measurement of only one flow variable at the measurement surface, but it does require a representation of the free-air flow about the model. The second class, on the other hand, requires two variables to be measured, but it does not need a simulation of the model flow. A third class exists - a hybrid - which uses a complete knowledge of one flow variable, or an assumed relationship between the two flow variables, at the measurement surface, together with limited measurements of a second flow variable on the same surface. In these 'wall-signature' methods, a model representation is used, and the 'signature' of the second variable is used to define either the strengths of the singularities representing the model or the values of a parameter linking the two flow variables. In the remainder of this section the three types of methods are reviewed, with a discussion of the hybrid, 'wall-signature' methods falling in a section between reviews of one-variable methods (Section 2.2) and two-variable methods (Section 2.4).

2.2 One-variable methods

2.2.1 Dirichlet, Neumann and mixed boundary value problems

For the Dirichlet problem, where the interference potential is specified on S, the appropriate Green's function is one that vanishes on the measurement surface leaving

$$4\pi \varphi_I(P) = \int_S (\varphi - \varphi_F) \frac{\partial G_D}{\partial n} dS. \qquad (6)$$

With the appropriate Green's function, G_D, defined, the integral can, in principle, be evaluated once the perturbation potentials φ and φ_F are known on S. The perturbation potential φ can, in principle, be inferred from

i) measurements of static pressure at the outside surface S_T by appropriate integration of the linearised version of Bernoulli's equation.

$$\frac{\partial \varphi}{\partial x} = - \frac{U_\infty C_p}{2} \qquad (7)$$

provided that the magnitude of the pressure coefficient C_p is sufficiently small for second order terms in Bernoulli's equation to be ignored (See Section 3.1), and

ii) a knowledge of the way the perturbation velocity potential varies across the upstream and downstream faces S_U and S_D. If these surfaces are perpendicular to the tunnel axis this variation can be determined by measurement of the upwash component of velocity at these faces. However, for sufficiently long working sections, where the two faces are far removed from the model, this is probably unnecessary because the contributions of the integrals over these faces can reasonably be ignored.

The integration of equation (7) has been avoided in existing methods of the 'Dirichlet' type, which are based on the streamwise velocity increment $u = \partial\varphi/\partial x$ instead of the perturbation velocity potential φ. However, in these methods, a further integration is needed to determine the wall-induced upwash, and the constant of integration is determined from a measurement of the upwash at the upstream measurement station. The alternative expressions have been derived for cylindrical boundary surfaces and, for these types of surfaces, a comparable expression may be derived from equation (6) by differentiating each side of this equation by X. Mokry and Ohman[13], in two dimensions, and Mokry[14], in three dimensions, used Fourier transform techniques, in effect, to determine the required Green's function. Later, Mokry et al[15] used a doublet-panel method, in which the doublet distribution on the measurement surface satisfying the boundary condition for the wall-induced increment in streamwise velocity is determined. In all these methods, the influence of the upstream and downstream faces can, in principle, be accommodated provided information about the variation of the streamwise increment in velocity across them is available (see Section 3.1). In an analysis of the two-dimensional problem in a working section of infinite length, Capelier et al[16] used complex-variable theory to solve the equivalent Schwarz problem[6], and this method was later extended to the case of a semi-infinite working section by Paquet[17], who specified boundary conditions for the streamwise velocity increment on an upstream measurement face.

Methods using either wall interference potential or streamwise velocity are autocorrective in that calculations by them of corrected stream speed automatically compensate for errors in the reference-pressure measurement.

2.2.2 Neumann problem

In the case of the Neumann problem, where the normal gradient of the interference potential, or the normal component of the wall-induced velocity, is given on the boundary, the required Green's function, G_N, is one with vanishing normal gradient on S giving

$$4\pi \varphi_I(P) = - \int_S \left(\frac{\partial \varphi}{\partial n} - \frac{\partial \varphi_F}{\partial n} \right) G_N dS. \qquad (8)$$

The term $\partial\varphi/\partial n$ in equation (8), implies that the normal component of velocity or the flow angle has to be specified on S. This aspect is considered in more detail in Section 3.2. However, it may be noted, in passing, that the measurement of flow angle causes no significant problems for wind tunnels with solid, though possibly, flexible walls, since the flow angle is essentially defined by the condition of no flow through the walls. On the other hand, for porous or slotted walls, flow angle needs either to be measured or to be deduced from wall and plenum pressure measurements by using elaborate theoretical models, as described in Section 3.2. Measurement of flow angle with the required accuracy is extremely difficult. For this reason, methods of the 'Neumann' type are not favoured for porous or slotted-wall wind tunnels. Indeed, the use of the wall-induced streamwise velocity as a boundary condition,

was originally proposed by Capelier et al[16] with just this problem in mind.

Where the difference in normal velocity is used as the boundary condition, as for equation (8), the technique is autocorrective in that errors in measurements of normal velocity or flow angle far upstream of the model are compensated for by the method.

2.2.3 Mixed problem

In some cases, where the normal velocity is well defined on parts of the boundary and the streamwise velocity increment or the perturbation potential on other parts, a mixture of types of boundary condition may be appropriate. An example of where such a treatment might be used is for a case with solid sidewalls and upper and lower walls that are either perforated, slotted or flexible. In such cases, the boundary S_T may be divided into S_1 and S_2, on which conditions of the 'Dirichlet' and 'Neumann' types are, respectively, applied, and if, for example, the effects of the upstream and downstream faces are ignored, the solution for the interference potential may be expressed as:

$$4\pi\varphi_I(P) = \int_{S_1} (\varphi - \varphi_F) \frac{\partial G_{DN}}{\partial n} dS$$

$$- \int_{S_2} \left(\frac{\partial\varphi}{\partial n} - \frac{\partial\varphi_F}{\partial n} \right) G_{DN} dS, \qquad (9)$$

This approach has been used to determine residual wall interference for adaptive wall wind tunnels with flexible upper and lower walls and straight, solid sidewalls[16,18,19]. In these studies, the working section was assumed to be cylindrical and of infinite length; the wall-interference potential, φ_I, was expressed as the sum of contributions due, respectively, to the model, an infinite array of images of the model simulating the solid sidewalls and a remainder to allow for the flexible roof and floor. The last contribution was determined by separation of variables and Fourier transforms of the resulting set of two-dimensional, partial-differential equations. Smith[20,21] used mixed boundary conditions in his treatment, by a panel method, of wall interference on the flow over two-dimensional aerofoils in a working section that was slotted in one part and solid upstream and downstream of it. Boundary pressures were measured only over a part of the working section, which extended beyond the slotted region. He applied conditions of the 'Dirichlet' type to this part (S_1) and 'Neumann' type conditions to the solid regions upstream and downstream of it (S_2).

Mokry et al[6] noted that some care needs to be taken with mixed boundary conditions at any line or point where the conditions change from one sort to another. They also raised concerns about the uniqueness of the solution which, in the case considered by Smith[20], is presumably ensured by satisfying the condition of smooth flow at the two joins.

2.2.4 Minimisation of model representation errors

As noted before, the terms φ_F and $\partial\varphi_F/\partial n$ in equations (6), (8) and (9) require some form of model representation. In

principle, this may be accomplished by using suitable distributions of potential singularities so long as the flow is subcritical at the tunnel walls. The problem is to determine the strengths of the singularities. Smith[20] noted the importance of accurate model representation, arguing that errors caused by inaccurate modelling could be as large as the interference quantity itself. For subcritical flows over wings or bodies at low angles of incidence, linear theory can be used with allowance for model thickness or cross-sectional area[1] and with other modifications, as described below. However, for transonic flows or for flows with large regions of separation, the problem is much less easily solved owing to the non-linear character of the flow in the near field of the model. Numerical methods have been developed, in which various approximations to the Navier-Stokes equations have been solved for aerofoils and wing-body configurations[22,23,24]. However, these methods require both the wind tunnel and 'free-air' flows to be calculated, and, as far is the author is aware, they have not been used to calculate the strengths of the equivalent potential-flow singularities. Methods of this type are expected to be of particular value when there are supercritical-flow patches at the wall, but it is unlikely it will be possible to correct such flows to 'free-air' conditions except in adaptive-wall tunnels (see Section 2.4).

If numerical calculations of transonic flows, or, indeed, any other complex flows, are to be avoided, three possible approaches may be used to minimize errors due to model representation:

i) Exploit an observed tendency for different types of boundary condition to have different levels of sensitivity to model representation errors (see below).

ii) Make use of experience from testing in solid-wall wind tunnels.

iii) Obtain more accurate estimates of singularity strengths using asymptotic expansion or other approximate methods,

In the first approach, it may be noted that the contribution of the model representation term to the wall interference potential can be determined for each type of boundary condition by setting $\varphi = 0$ in equation (6) and $\partial\varphi/\partial n = 0$ in equation (8), while, for equation (9), it follows by setting $\varphi = 0$ on S_1 and $\partial\varphi/\partial n = 0$ on S_2. This implies that, for wind tunnels with long, cylindrical working sections, the respective contributions due to model representation in methods of the 'Dirichlet' and 'Neumann' type can be inferred from classical results for tunnels with open-jet and solid walls and, for mixed boundary conditions, by a combination of wall types. In this respect, it is useful to think of a wind tunnel having a working section with the same cross section as the measurement surface and with classical wall boundary conditions, hereafter referred to as the 'equivalent wind tunnel'.

The observations in the last paragraph are not merely of academic interest, since they allow extensive experience with classical wall-interference methods to be used to assess the contribution to wall-induced velocities from imperfect model representation. In the past, particular emphasis has been placed on determining the strength of the doublet representing the volume effect of the model and its associated supercritical

flow in the far field. The reason for this is that non-linear effects of compressibility affect doublet strength in a way that cannot be predicted by linear theory, and, consequently, this is a possible source of error. It is therefore interesting to compare the wall corrections associated with a source-sink doublet placed on the tunnel axis in various equivalent wind tunnels of rectangular cross section. Results for the wall shape factor for the doublet

$$T = \frac{(BH)^{\frac{3}{2}}}{V} \frac{u_I^m}{U_F}$$

are plotted in Fig 3 against (effective) working section breadth to height ratio B/H, where u_I^m is the wall-induced or blockage increment in streamwise velocity at the model and V is model volume.
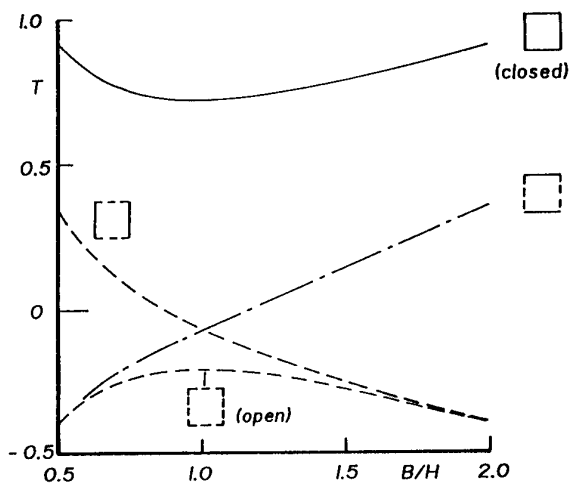
typical length in modern high-speed tunnels. Some calculations have therefore been performed for a long axisymmetric body that is mounted on a sting on the centre line of equivalent wind tunnels of square section, and results for the distribution along the model axis of the blockage increment in Mach number are shown in Fig 4. In the way suggested by Evans, the model has been represented by an axial distribution of sources and sinks, and the Prandtl-Glauert factor is based on the 'corrected' Mach number 0.82. Results are shown for the 'Neumann' (closed), 'Dirichlet' (open jet) and 'mixed' cases, as indicated in the figure. The magnitude of the maximum increment in Mach number obtained with the 'mixed' case is about 9% of that of the 'Neumann' case, ie similar to that found with the doublet, and is less than 0.001, so that, in this case, large errors in source strength could be tolerated without the influence on Mach number being serious.
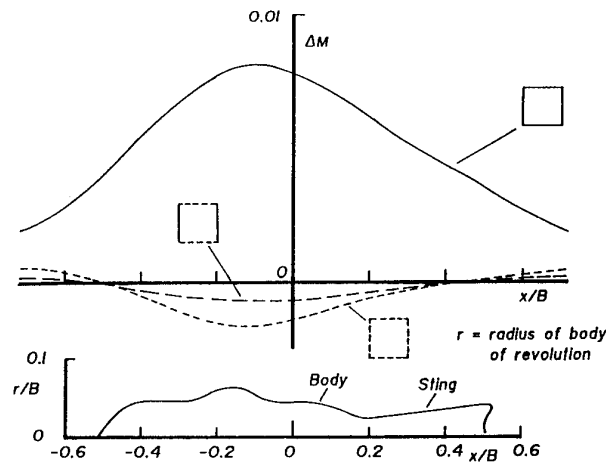

Fig 3 Wall-shape factor T for doublet placed on axis of equivalent wind tunnel of rectangular cross section

Fig 4 Axial distribution of blockage increment along model axis (tunnel centre-line) in equivalent wind tunnels of square section (B/H = 1)

Shown in the figure are cases with working sections that are i) fully-closed (Neumann), ii) fully-open (Dirichlet), iii) mixed, open sidewall and closed roof and floor and iv) mixed, open roof and floor and closed sidewalls. Results for the fully-closed and fully-open cases have been gleaned from Ref 1, while the results for the two 'mixed' cases have been calculated by the author. For values of B/H close to unity, the 'Dirichlet' case gives a wall shape factor that is only 28% of the magnitude of that of the 'Neumann' approach, indicating that the 'Dirichlet' approach is to be preferred to the 'Neumann' approach from the point of view of minimising model-representation errors. For B/H = 1 the 'mixed' approach gives an even lower value, with a magnitude of only 10% of that of the 'Neumann' value. The 'mixed' approach also yields zero blockage (due to model representation) for mixed conditions of type iii) above with B/H = 1.17 or of type iv) with B/H = 1/1.17 = 0.85. These are significant results which could have an important bearing on where and how to apply wall boundary conditions with one-variable methods.

As noted by Evans[25], and later confirmed by Vaucheret[26], a doublet is not a satisfactory way of representing a model of

Fig 5 shows the variation of maximum value of wall-induced Mach number with corrected Mach number for the model and wind-tunnel geometries of Fig 4, illustrating the relatively-low value for the correction of the 'mixed' case over a wide range of Mach number for a measurement section with B/H = 1. This shows that the use of conditions of the 'Dirichlet' type on the roof and floor and 'Neumann' type conditions on the sidewalls (or vice versa) would lead to relatively-small errors in Mach number correction due to imperfect model representation over a wide range of Mach numbers for a square section. It is interesting to record that mixed conditions of this type would be appropriate for wind tunnels with slotted roof and floor and solid sidewalls, as is planned to be the case with the European Transonic Wind tunnel (ETW) (B/H = 1.2) and as is already the case with the National Transonic Facility (NTF) (B/H = 1). It should be noted in Fig 3, however, that the magnitude of the blockage increment with mixed 'Dirichlet' type conditions on the roof and floor and 'Neumann' type conditions on the sidewalls increases with B/H for values of B/H above 1. Consequently, the blockage increment for this type of 'mixed' condition is greater for B/H = 1.2 than for B/H = 1. Thus, for a wind tunnel such as ETW, it might be worth considering how to reduce the open-area ratio of the equivalent wind tunnel.
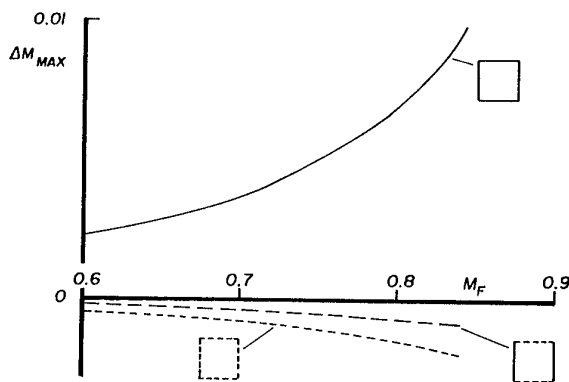
Fig 5   Variation with Mach number of maximum value of blockage increment in Mach number in equivalent classical wind tunnels of square section for body of Fig 4.

With this concern in mind, it should be remembered that the porous or slotted region does not necessarily occupy the whole length of the working section. It may, therefore, be possible to exploit this feature by using, as Smith[20,21] has done, boundary conditions which differ from one part of the working section length to another. It may be possible to decrease the open-area ratio of the equivalent wind tunnel by applying 'Neumann' type conditions where the wall is solid upstream (and downstream) of the slotted or perforated region. For slotted-wall tunnels, it may be possible to apply the solid-wall condition on parts of the slats between the slots to reduce the sensitivity to model representation errors. Kemp[27] applied boundary conditions in this way in his method for three-dimensional models in a slotted-wall tunnel, but for the different reason that he was limited by the number of slat pressure measurements that were available.

Using complex-variable theory, Woods[28] was able to derive an expression for the solid blockage associated with a two-dimensional doublet in a working section with mixed solid and open-jet boundary conditions, as shown in Fig 6. This figure also includes a graph derived from Woods' theory showing the variation of solid blockage with length of the open-jet region. Zero blockage is obtained when the length of the open-jet or 'Dirichlet' part, $\ell = 1.513\beta H$. This means that the length of working section giving least sensitivity to model representation errors depends on, and decreases with, Mach number. This example should be contrasted with the case illustrated in Fig 3 for boundary conditions that are mixed only in sections normal to the tunnel axis. In this case, Mach number does not enter into the relationships describing the effect of the walls.

To summarise this discussion of the influence of type of wall boundary condition on Mach-number correction, the reader is referred to Fig 7. This shows a simplified, schematic view of the effect of the open-area ratio of the equivalent wind tunnel on the contribution of model representation to Mach-number correction. As a rough rule, this contribution vanishes for a certain value of open-area ratio of the equivalent wind tunnel for a given effective working section shape and Mach number. This shows that it is possible, in principle at least, to minimise the errors in

Mach-number correction due to imperfect model representation by suitable choice of the way the boundary-value problem is tackled. It is important to emphasise that this argument applies to the way the boundary conditions are applied and not to the type of tunnel walls, although the type of walls may constrain the way the boundary-value problem may be tackled. As noted by Smith[20], the errors associated with model representation are independent of the type of tunnel walls for a given type of boundary-value problem.
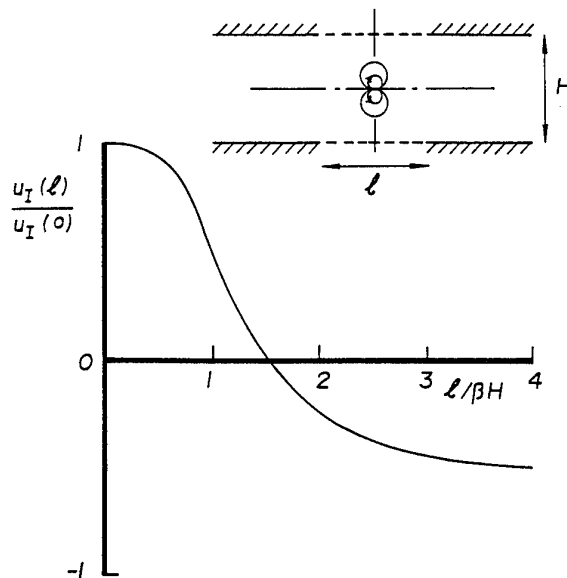
Fig 6   Blockage associated with 2D doublet placed at centre-line of working section with part open jet and part closed boundaries (Woods, Ref 28).
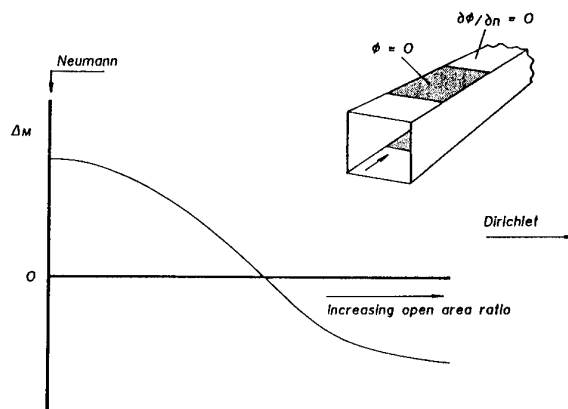
Fig 7   Blockage increment in Mach number versus open-area ratio of equivalent wind tunnel for a given model and Mach number.

Results for lift-interference parameters of a 'small' wing are shown in Fig 8 for various types of classical boundary conditions[1]. For a square tunnel the smallest values of the classical parameters δ_0 and δ_1 are obtained with the walls of the equivalent wind tunnel open at the sides and closed in the roof and floor, for which $\delta_0 = 0$. This means that, if an

accurate estimate of lift interference is the overriding consideration and there are doubts about the accuracy of the representation of the model lift distribution, 'Dirichlet' type conditions should be applied at the sidewalls and 'Neumann' type conditions at the roof and floor. Plainly, this is an unattractive option for tunnels with a slotted roof and floor such as ETW and NTF.
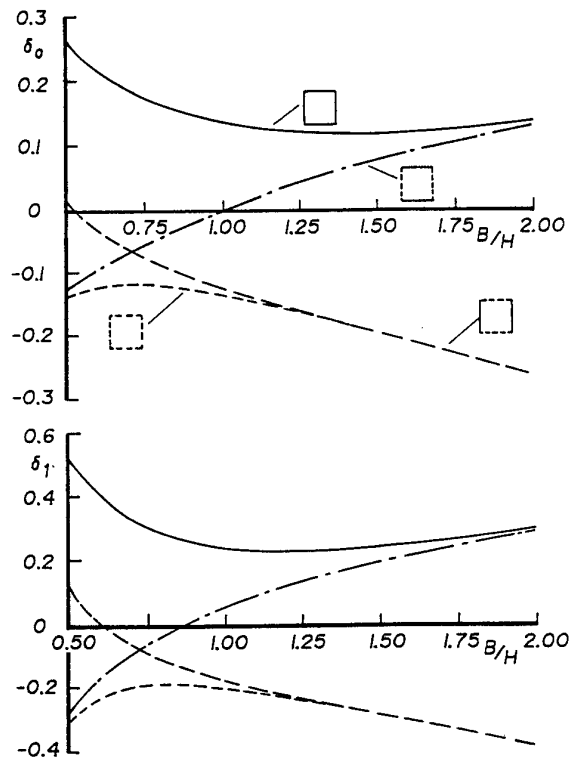
Fig 8   Lift interference for 'small' wings
         wings on axis of equivalent wind tunnels of
         rectangular section (after Garner, Ref1).

Basing his ideas on the earlier work of Davis[29], Schairer[30] developed a method for two-dimensional tests in which the influence of model representation was eliminated altogether by using measurements of one flow variable, normal velocity, at two separate surfaces. Schairer found that he was unable to obtain wall-induced velocities of adequate accuracy owing to the limited range of the measurements along the working section. The method does not seem to have been adapted to three-dimensions, but studies by Davis[29] suggest that the method is much more complicated for three-dimensional flows.

Using the second approach to minimise model representation errors mentioned above, Evans[25] was able to make significant progress. As well as drawing attention to the importance of representing body length for typical models, he showed the significance of using the corrected Mach number in the Prandtl-Glauert factor when determining the strengths of the sources and sinks representing a body. This important point, which does not appear to have been fully grasped in some later work, is illustrated in Fig 9 showing comparisons between calculation and measurement of wall pressure measurements in the RAE 10ft x 7ft Tunnel for a series of bodies. Since the correction is not known a priori,

this implies an iteration process. However, if, as is often the case, the corrections are calculated 'on line' during the test, the nominal Mach number can be adjusted until the corrected Mach number corresponds with the desired value. Evans concluded that an error in the solid blockage at drag-rise conditions could be reconciled with an increase in the effective volume of the model, and he suggested that this error is directly proportional to the rise in drag coefficient. Although plausible and based on comparisons with wall pressure measurements, this result does not have a rigorous theoretical basis.
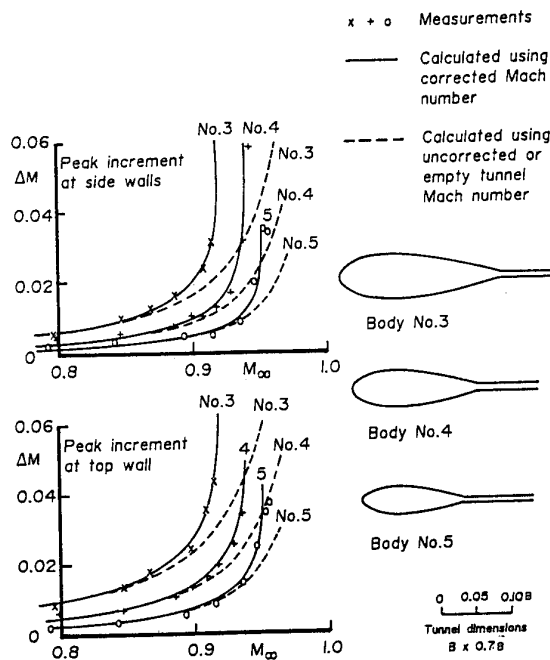
Fig 9   Comparison of measured and calculated peak
         increments in wall Mach numbers for three bodies
         (3,4,5) (after Evans, Ref 25).

This leads to the third approach for establishing accurate estimates for singularity strengths. Using the method of matched asymptotic expansions, Chan[31,32] established a correction for compressible non-linear effects to doublet strength for two-dimensional aerofoils. For the same problem, Smith[33] used Green's formula to obtain an estimate of the doublet strength. As far as the author is aware, these approaches have not yet been extended to three dimensions. No correction is needed to vortex strength for compressibility if the spanwise distribution of local lift coefficient of a wing is known either from pressure measurements or can be inferred from overall-force measurements.

2.3 Wall-signature methods

As noted earlier, there are two variants of the wall-signature method. In the first, one component of velocity is known and the other is measured at a limited number of points on the measurement boundary. By matching calculation to measurement at this boundary it is then possible to determine the strengths of the singularities representing the model. The best known application of this type of method is to solid-wall wind tunnels, for which the normal-velocity component may be taken to be zero at the walls. Therefore, with the

measurement boundary taken to coincide with the walls, the solution to the Neumann problem, equation (8), may be used to obtain:

$$4\pi\,\varphi_I(P) \;=\; -\int_S \frac{\partial\varphi_F}{\partial n}\,G_N\,dS. \qquad (10)$$

After differentiation by X, equation (10) may be re-expressed as:

$$4\pi[u(P) \,-\, u_F(P)] \;=\; -\int_S \frac{\partial\varphi_F}{\partial n}\,\frac{\partial G_N}{\partial X}\,dS,$$

or as

$$u(P) \;=\; u_F(P) \,-\, \frac{1}{4\pi}\int_S \frac{\partial\varphi_F}{\partial n}\,\frac{\partial G_N}{\partial X}\,dS. \qquad (11)$$

Here the differentiation with respect to X has been taken under the integral sign because G_N is smooth and continuous within the region of integration. If the point P is taken to be limitingly close to the walls, the left-hand side of equation (11) may then be defined by static-pressure measurements at the walls, together with the linear Bernoulli equation (6), at N points. Thus, if the model is represented by a distribution of N singularities, equation (11) may be regarded as a linear (integral) equation for the unknown singularity strengths. For a wind tunnel with a cylindrical working section of length that is sufficiently large to be assumed infinite, the integral in equation (11) may be replaced by a doubly-infinite sum for each singularity, representing the image effect of the tunnel walls.
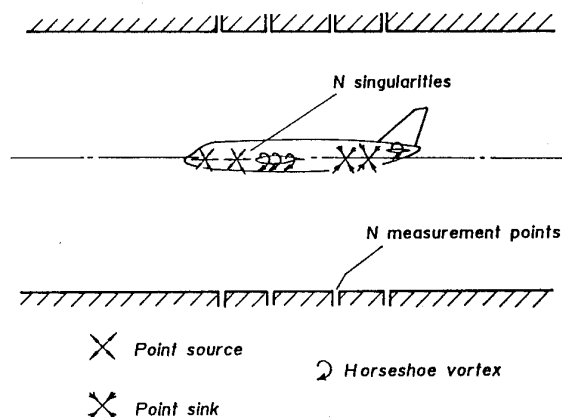

Fig 10 Sketch illustrating 'Wall-Signature' methods for solid-wall wind tunnels.

The idea behind this approach, which is illustrated in Fig 10, goes back to the 1940's when the problems of testing at high subsonic speed in solid-wall tunnels were first addressed. Mokry et al[6], reviewing various early methods for two-dimensional flows, described a simple procedure to determine the strengths of a doublet, vortex and source representing a lifting aerofoil from static-pressure measurements at three points on both the roof and floor of the working section. They argued that methods of this type are superseded by two-variable methods, to be described later, which need no model representation. A contrary view is that wall-signature methods are to be preferred in some applications because they need relatively-few measurement points compared with two-variable methods. Smith[20], using a method similar to that described by Mokry[34], suggested that an aerofoil with a chord to working section height ratio of about 0.2 could probably be represented adequately in the far field by about ten singularities placed at a single point, requiring ten measurement points. Evans[25] found that it was possible to represent a body of revolution by a point source and point sink, in each case placed at a fixed distance from the centre of volume of the body on its axis, indicating the need for two measurement points. These numbers of measurement points would be considered much too low for a two-variable method. However, where the model flow field is complex and not easily represented by singularities, two variable methods are probably to be preferred (see Section 2.4). Nevertheless, the wall-signature strategy has been used to determine wall corrections for models with separated flows[3,4,5] and jets in cross flow[35] by Hackett and his colleagues.

Le Sant and Bouvier[19] found that the matrix inversion needed to solve equation (11) is ill-conditioned owing to the insensitivity of the flow at the walls to details of the model. They suggested that this problem could be overcome by gathering singularities into groups with fixed relative strengths. A method similar to this is routinely used to determine the blockage for tests at subsonic speeds in the 8ft x 8ft (solid-wall) Wind Tunnel at the Defence Research Agency (DRA), Bedford[36]. The axial source distribution representing model volume is assumed to be represented adequately by linear theory and the theory is used merely to determine the ratio between the mean value of the streamwise velocity increment at four points on the walls (two on the roof and two corresponding ones on the floor) and the blockage increment at a reference point on the model. Measurements of the change in static pressure coefficient between the empty tunnel case and the case with the model in the wind tunnel at these same points provide sufficient information to determine the blockage at the model reference point. Experience has suggested that the method is reliable[36].

If comprehensive measurements could be made of static pressures at the measurement boundary, a similar procedure to that described above could, in principle, be developed using, instead, the 'Dirichlet' approach, together with limited measurements of flow angle to give normal velocity at the boundary. This approach may be useful for wind tunnels with perforated or slotted walls but, as far as the author is aware, it has not yet been tried.

The second variant of the method uses a 'wall' pressure signature to establish or check the value or values of a parameter linking the flow variables at the measurement surface. This approach has been used by Vaucheret[26], who used a validated model representation, along with wall pressure measurements, to infer the porosity of the roof and floor liners of the ONERA S2Ma Tunnel. In a similar way Goldhammer and Steinle[37] made static pressure measurements on four rails to verify the porosity factor used in a simulation

of slotted walls. As with Vaucheret's method, a model representation is used.

2.4 Two-variable methods

In section 2.2.4 it was shown that the contribution of the model representation term to a particular component of wall-induced velocity at a point on the model could be eliminated by a suitable mixture of types of boundary condition on S. Equation (5) indicates that the contribution of model representation terms vanishes identically when

$$0 = \int_S \left(\frac{\partial \varphi_F}{\partial n} G - \varphi_F \frac{\partial G}{\partial n} \right) dS. \tag{12}$$

This suggests that the Green's function satisfying this condition is that for an interference-free, equivalent wind tunnel. In turn, this suggests that the appropriate Green's function is:

$$G = G_F = \frac{1}{r},$$

the free-space Green's function[6], which, in aerodynamic terms, may perhaps be called the 'free-air' Green's function. For this Green's function, Green's formula gives

$$\int_S \left(\frac{\partial \varphi_F}{\partial n} \frac{1}{r} - \varphi_F \frac{\partial}{\partial n} \left(\frac{1}{r} \right) \right) dS$$

$$- \int_{V_0} \frac{1}{r} \nabla^2 \varphi_F \, dV = 0, \tag{13}$$

where V_0 refers to volume integration in the fictitious region, R, outside the measurement region (Fig 1). Thus, provided that the perturbations in the free-air flow outside the working section are 'small', the perturbation potential φ_F may be considered harmonic in this region with the consequence that

$$\int_S \left(\frac{\partial \varphi_F}{\partial n} \frac{1}{r} - \varphi_F \frac{\partial}{\partial n} \left(\frac{1}{r} \right) \right) dS = 0.$$

Thus, for flows of this type, the Green's function G_F satisfies equation (12) to give, in place of equation (5), an expression no longer containing model-related terms

$$4\pi \varphi_I(P) = - \int_S \left(\frac{\partial \varphi}{\partial n} \frac{1}{r} - \varphi \frac{\partial}{\partial n} \left(\frac{1}{r} \right) \right) dS. \tag{14}$$

This expression was derived by Ashill and Weeks[38] in a somewhat different way to the way presented here and it appears in a number of references[7,8,39], Mokry[8] giving a particularly elegant derivation. Corresponding expressions have been obtained for plane, two-dimensional flows, using, variously, Fourier transforms[40], Green's formula in the plane[39,41] and Cauchy's integral formula[20,42,43].

The price that is paid for not having to know anything about the flow around the model is that it is necessary to measure both components of velocity at all parts of the measurement boundary. The first term under the integral sign in equation

(14), recognised as the contribution of sources of strength $\partial \varphi / \partial n$, requires the normal component to be known at S, while, for the second term, which is the contribution of source doublets, the streamwise velocity increment on S is needed. For solid-wall tunnels, including certain types of adaptive-wall wind tunnels with flexible liners, this poses no significant problems, since the normal component is effectively defined by the condition of no flow through the walls. For other types of walls, however, the measurement of normal velocity over the whole measurement boundary is much more difficult. As a result, the method has largely been restricted, up to now, to solid-wall tunnels[38,44], although significant progress is being made in determining the normal component in perforated and slotted wall tunnels, as described in Section 3.2.

A major enhancement that was made possible with two-variable methods is the calculation of wall interference for complex flows in solid-wall tunnels, eg those for high-lift configurations, helicopters and other V/STOL aircraft. Here the ability to ignore the flow around the model is an important advantage. One area which has been known to cause difficulties in the past is the calculation of blockage for aircraft configurations at high angles of attack, where the flow over the lifting surface is partially separated. In particular, experience in various establishments with Maskell's semi-empirical method for calculating blockage[1] was not entirely favourable. This method was considered the 'standard' in UK until the advent of boundary-flow measurement methods. However, it was found that, in many cases, Maskell's method gives an overestimate for blockage correction with a consequential underestimate in maximum lift coefficient. This view was confirmed for a combat-aircraft configuration[44,45] and for a civil transport model[46] by calculations using the DRA two-variable method. A careful and thorough assessment of a two-variable method for tests at low speed and high lift has been made by Maarsingh et al[47].

Another area where two-variable methods have been used is in the calculation of residual wall interference in adaptive-wall tunnels[48,49], where, as noted before, it is routinely necessary to measure both flow angle and static pressure at the measurement boundary. Typical results for wall-induced upwash and blockage increment, calculated by the DRA two-variable method, for tests on an arrowhead (half) wing in the adaptive-wall wind tunnel at Southampton University are shown in Figs 11 and 12. In this wind tunnel the working section is square in cross section and comprises solid sidewalls and a roof and floor that are flexible in single curvature. Thus, as shown in the figure, complete removal of wall interference is not possible; however, wall adaptation does reduce the variation of wall-induced velocities in the plane of the model considerably if these velocities are kept constant along a suitable 'target' line, as indicated on the figures. Mokry[9] showed how equation (14) may be manipulated to give a convergence formula to allow the shape of the of the walls of an adaptive-wall wind tunnel to be altered in one step to give nominally interference-free flow. He also proved that two-variable methods are autocorrective in character.
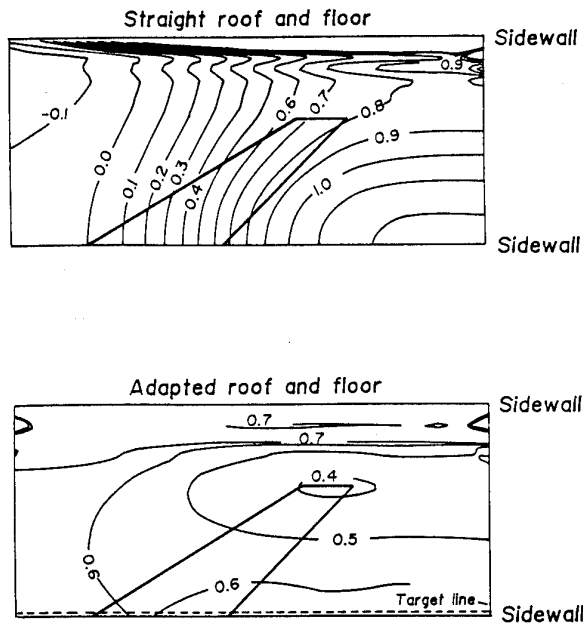
Fig 11 Calculated wall-induced upwash (% free-stream speed) in plane of half arrowhead wing in adaptive-wall wind tunnel (B/H = 1) with straight and adapted roof and floor $M_\infty = 0.7$, $\alpha = 4°$ (Ref 48).
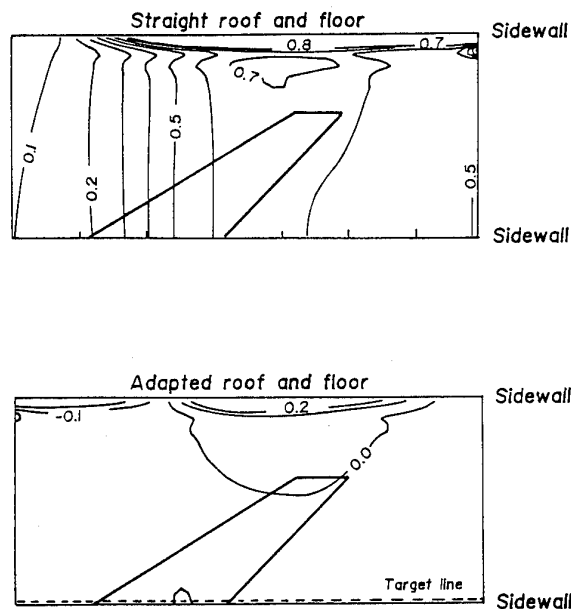

Fig 12 Calculated wall-induced blockage increment in velocity (% free-stream speed) in plane of half arrowhead wing in adaptive-wall wind tunnel (B/H = 1) with straight and adapted roof and floor, $M_\infty = 0.7$, $\alpha = 4°$ (Ref 48).

Since the Green's function in equation (14) is known, special techniques for determining the function, or equivalent techniques, are unnecessary in two-variable methods. Methods of this type can, therefore, be applied to measurement boundaries of irregular shape with relative ease. In this respect, two-variable methods may be favourably contrasted with one-variable methods.

If the free-air perturbation potential in the fictitious region R is not harmonic, equation (5), with G replaced by $1/r$, and equation (13) show that equation (14) must be replaced by

$$4\pi\varphi_I \, (P) \; = \; - \int_S \left(\frac{\partial\varphi}{\partial n}\frac{1}{r} \; - \; \varphi \; \frac{\partial}{\partial n}\!\left(\frac{1}{r}\right) \right) dS$$

$$+ \int_{V_0} \left(\frac{1}{r}\right) \nabla^2 \varphi_F \; dV. \tag{15}$$

It may be thought that this is an extreme situation and, as mentioned before, that it would not be possible to correct such flows to equivalent free-air conditions. However, flows of this type are found in adaptive-wall tunnels at high subsonic speeds[48,50], and it has therefore been necessary to establish the magnitude of the residual corrections for wall constraint[50]. For practical reasons, it might be convenient to avoid eliminating tunnel-wall interference altogether in adaptive-wall wind tunnels, concentrating, instead, on ensuring that the wind-tunnel flow may be corrected to equivalent free-air conditions. For example, savings in wind-tunnel power might be achieved by performing tests with the Mach number of the flow far upstream of the model lower than that of the equivalent free-air flow. This situation is illustrated in Fig 13.
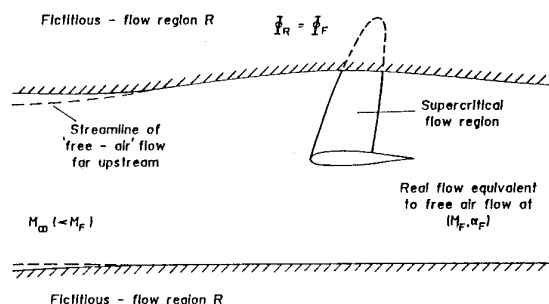
Fig 13 Sketch illustrating use of adaptive-wall wind tunnel to provide a free-air flow with a corrected free-stream Mach number that is higher than that far upstream.

A problem with equation (15) is that it requires the source term or volume integral in the fictitious region R outside the measurement region to be calculated. This requires a (transonic) flow-field calculation as well as the evaluation of the integral. To avoid the latter difficulty it is useful to think of a flow in the fictitious region R with a velocity potential Φ_R that is identical to the free-air flow velocity potential in the near field of the model (Fig 13). This implies that the difference in perturbation potentials $(\varphi_F - \varphi_R)$ is harmonic in this region. Thus, if Green's formula is applied to the perturbation potential φ_R in the same way as was done to

obtain equation (13), and the resulting expression is combined with equation (15), it is found that

$$4\pi\,\varphi_I(P) = -\int_S \left(\left(\frac{\partial\varphi}{\partial n} - \frac{\partial\varphi_R}{\partial n} \right) - (\varphi - \varphi_R)\,\frac{\partial}{\partial n}\!\left(\frac{1}{r}\right) \right) dS$$

$$+ \int_{V_0} \left(\frac{1}{r}\right) \nabla^2(\varphi_F - \varphi_R)\,dV,$$

$$= -\int_S \left(\left(\frac{\partial\varphi}{\partial n} - \frac{\partial\varphi_R}{\partial n} \right)\frac{1}{r} - (\varphi - \varphi_R)\frac{\partial}{\partial n}\!\left(\frac{1}{r}\right) \right) dS. \quad (16)$$

Mokry[9] refers to this variant of the two-variable approach as an 'interface - discontinuity method', expressing the fact that the equation contains discontinuities in the normal velocity and perturbation potential across the measurement boundary.

For a solid-wall tunnel

$$\frac{\partial\varphi_R}{\partial n} = \frac{\partial\varphi}{\partial n},$$

and thus equation (16) reduces to

$$\varphi_I(P) = \frac{1}{4\pi}\int_S (\varphi - \varphi_R)\frac{\partial}{\partial n}\!\left(\frac{1}{r}\right) dS.$$

This expression is recognised as the potential at P due to a distribution of source doublets of strength (φ - φ_R) on S, and, for a cylindrical measurement surface, the integral may be rewritten in terms of a distribution of horseshoe vortices[9]. The strength of each of these vortices is directly proportional to the local wall loading. Judd (unpublished research, Southampton University) derived the corresponding expression for two-dimensional flows which was used by Goodyer and Wolf[51] to determine residual corrections in the flexible-wall tunnel at Southampton University. This method was later extended to three dimensions by the Southampton-University group[49]. For the study of aerofoils at transonic speeds in the same wind tunnel, Lewis[50] performed calculations of the fictitious flow (effectively to determine either φ_R or $\partial\varphi_R/\partial x$) using a transonic small-perturbation method. Since the boundaries of the fictitious flow are cylindrical or planar, this calculation is less demanding than that for the free-air flow about the model at transonic speeds, particularly in three dimensions.

If the external flow is solved as a Dirichlet problem so that

$$\varphi_R = \varphi$$

at the measurement surface, equation (16) reduces to

$$\varphi_I(P) = -\frac{1}{4\pi}\int_S \left(\frac{\partial\varphi}{\partial n} - \frac{\partial\varphi_R}{\partial n}\right)\frac{1}{r}\,dS,$$

which is the potential due to a distribution of sources of strength ($\partial\varphi/\partial n$ - $\partial\varphi_R/\partial n$). This approach was suggested by Rebstock and Lee[52].

3 BOUNDARY-FLOW MEASUREMENTS

3.1 Streamwise velocity increment

All the methods described in Section 2 require the streamwise velocity increment to be known on at least part of the measurement surface. As was noted in Section 2.1, this velocity increment is usually derived from static-pressure measurements by using the linearised version of Bernoulli's equation. Systematic errors may therefore arise from the neglect of the higher-order terms in the velocity-pressure relationship. Fig 14 shows plots of the error in streamwise-velocity increment against static-pressure coefficient for flows on the working section roof or floor in two-dimensional, plane flows (and flows at planes of symmetry in three-dimensional flows). For the sake of simplicity, the normal component is ignored. The figure indicates that the errors are most significant for tests at low speed and at high lift or with large blockage. So long as the magnitude of static-pressure coefficient is below 0.1, the errors are unlikely to be serious, especially at high Mach number where the consequences of errors in streamwise velocity are most serious. In fully three-dimensional flows, the problem of allowing for non-linearities becomes more difficult, since it is then necessary to solve Euler's equations on the measurement surface, given the static-pressure distribution. Comparisons between results of calculations of wall-induced velocity obtained in this way and by the linear equation are given in Ref 45. Unfortunately, this extra complication results in a significant increase in computing time[47]. Thus, except in the most extreme cases, methods based on the linear Bernoulli equation are likely to be preferred for on-line data reduction. Where there are doubts, some post-test analysis would be desirable using a method with the non-linear terms included.
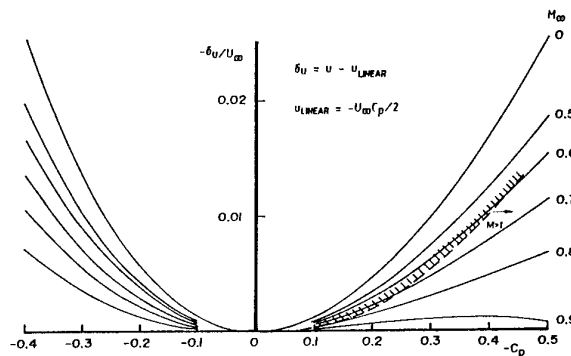
Fig 14 Error in streamwise velocity increment for flow on roof and floor in two-dimensional, plane flows resulting from use of linearised Bernoulli equation.

For solid walls, the measurements of static pressure are usually made in the conventional way with orifices in the walls. Bias errors due to hole size and imperfections, as well as the influence of geometry of the wind tunnel walls not precisely modelled in the wall-correction method, can be accounted for by subtracting the empty-tunnel pressures from the corresponding pressures with the model in the wind tunnel. This procedure also accounts for the major part of the effect of the streamwise growth of the wall boundary

layers on the wall pressures. Thus, with the flow in the empty tunnel at the usual position of the model calibrated and the wall-induced velocities determined using the pressure differences, the free-stream speed is properly corrected for these effects. Further hole-size errors arising from the fact that the wall boundary layer with the model in the working section is different from that with the tunnel empty are unlikely to be significant.
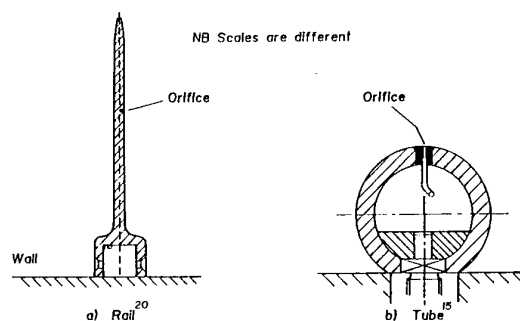

Fig 15 Devices for measuring static pressure in slotted and perforated-wall wind tunnels.

For slotted or perforated walls, the flow near the wall can be highly three dimensional, and thus the meaning of static-pressure measurements made in this region is less certain than for solid walls. This problem has encouraged a different approach in which the measurements are made away from the walls in the 'homogeneous' flow region, using either 'rails'[20] or tubes[15]. Examples of the two types are shown in Fig 15. While such devices are practical and have been used with apparently satisfactory results, they have two possible disadvantages:

i) since they have to be mounted away from the wall they reduce the effective area of the working section, placing increased emphasis on the accuracy of the model representation[20];

ii) they may interfere with, or the flow over them may be influenced by, the lateral flow in the working section.

Smith[20] suggested that a 'safe' distance for a row of static pressure tappings from the wall of a slotted-wall wind tunnel is probably the distance between the slot centre-lines. Data from measurements by Firmin and Cook[53] of the flow near a slotted liner in an otherwise two-dimensional flow, confirm that this is a reasonable estimate for a slot width to slat width ratio 0.11. On the other hand, these data suggest that it might be possible to use the measurement of static pressure on the slat centre-line to determine the boundary condition for streamwise velocity increment in the homogeneous flow. Theoretical studies[54] indicate that a correction has to be applied to this measurement to allow for the far-field effect of the source-sink flow near the slot. Freestone et al[55] found that, in low-speed tests on an aerofoil in a slotted section with plenum-chamber suction, this correction was, generally, negligible. Smith[20], on the other hand, reported systematic differences between wall corrections obtained using i) static-pressure measurements on a slat centre-line and ii) measurements away from the wall

by a rail. It is possible that these discrepancies become less important where efforts are made to reduce the strength of the returning flow by, for example, plenum chamber suction, since this has been shown to reduce significantly the growth of the slat boundary layer in the region of the slot[56]. The differences may also cease to be important for three-dimensional models at low to moderate lift coefficients, where the slot normal velocities are likely to be significantly lower than in two dimensions. In view of the need to avoid measurement methods which intrude into the working section, this is a worthwhile area for future study.

Another major source of bias errors in pressure-measurement methods arises from using an inadequate number of sensing points and/or inaccurate techniques for interpolating the data at the measurement surface. The number of measurements that are made in the streamwise direction is usually adequate, but there remains some concern about the number of measurements made in sections normal to the working-section axis in tests on three-dimensional models. Mokry[14] proposed a method that uses the periodic nature of the solution for wall induced velocities with a measurement boundary comprising a circular cylinder. The technique was applied with measurements made of static pressure along just four lines at the boundary of the cylinder, and Mokry demonstrated the accuracy of the method, when used with this number of measurement lines, by comparison with an exact test case. He pointed out, however, that the technique is limited to wind tunnels of circular, octagonal or square cross section. Later, when determining the wall interference associated with a half model in square-section wind tunnel (equivalent to a complete model in a working section with B/H =2), Mokry et al[15] made use of measurements on six axial lines. Le Sant and Bouvier[19] utilised the periodic nature of the solution in the spanwise direction for a rectangular wind tunnel with solid sidewalls. They showed that, with the model simulated by a doublet, only the two-dimensional (or zeroth) harmonic and the first harmonic make significant contributions to wall-induced velocities. In addition, they showed that pressure measurements made on the roof and floor at ±¼B and ±¾B do not sense the small contribution of the second harmonic. These are interesting examples of how improvements to accuracy can be made by forethought being given to the position and number of static pressure measurements. Other examples of preparatory work of this sort can be found in Refs 20, 38 and 45.

Bias errors may arise from the way the data are treated at the upstream and downstream extremities of the measurement region or beyond. Smith[21] has reviewed three possible procedures, as illustrated in Fig 16. Apart from obvious errors in extrapolations (Fig 16a) arising from the inadequacy of the assumed form of the extrapolation, errors may occur if too much weight is placed on data close to the ends of the measurement region when determining the extrapolation. Smith gave an illustration of the consequences of such errors at the downstream end of a measurement zone. He found that blockage increment in the vicinity of the model calculated by the DRA (then RAE) two-variable method is remarkably insensitive to gross extrapolation errors. Considerations of the balance of streamwise momentum within the working section, together with measurements of drag, should make it possible to establish the asymptotic behaviour of static pressure far downstream[44].
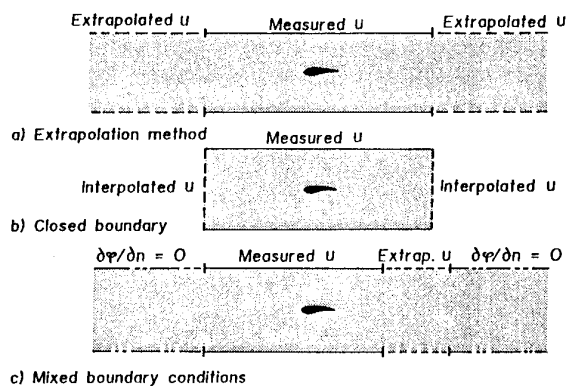
a) Extrapolation method

b) Closed boundary

c) Mixed boundary conditions

Fig 16 Different ways of handling streamwise-velocity data at or beyond measurement region.

A second method, used for example by Mokry and Ohman[13], closes the measurement surface with faces at the upstream and downstream ends (Fig 16b). Here it is necessary to interpolate the static pressure between opposite sides of each face, which Mokry and Ohman did with a linear interpolation. Clearly, errors from this source become less important the smaller the difference in static pressure between the two sides, as is the case if the two faces are sufficiently far from the model.

A third method, employed by Smith (Fig 16c), avoids the use of either streamwise extrapolation to upstream and downstream infinity or interpolation across the end faces. He used the fact that the walls of the NLR Pilot Tunnel are solid upstream and downstream of the slotted region to replace the streamwise-velocity condition with the condition of zero normal velocity away from this region, except for a small patch, as shown in the figure. As with the data at the streamwise surface, errors resulting from the way the data are handled at or beyond the measurement region can be minimised by careful selection and validation of the technique used.

Allied to the problem of the way the data are dealt with at or beyond the measurement region, is the study of errors in the measurement of the reference static pressure. For solid walls this measurement is usually made some distance upstream of where the model is normally situated, while, for slotted walls, the measurement may be made in the plenum surrounding the working section. In both cases, the measurements may be influenced by the flow induced by the model, together with the associated wall effect. The 'autocorrective' nature of some of the theoretical methods referred to previously, makes it possible, in principle, to ensure that these errors do not affect the corrected Mach number. However, numerical approximations in the treatment of the data at or beyond the measurement region, may lead to errors in the corrected Mach number. Le Sant and Bouvier[19] considered the effect on the accuracy of the autocorrective compensation in a two-dimensional flow of truncation of the measurement region without either allowing for interpolation at the end faces or extrapolation. They found that a one-variable method (of the 'Dirichlet' or 'Schwarz' type) gave more accurate compensation for errors in reference static pressure than the two-variable method.

However, allowance for the end effects or extrapolation in two-variable methods should ensure that the compensating corrections are much more accurate than without this allowance.

3.2 Normal velocity component

As noted before, the normal velocity component can be determined at the measurement surface with some confidence for solid-wall wind tunnels, including adaptive wind tunnels with flexible walls, after allowance for the displacement effect of the wall boundary layers (see below).

For slotted or perforated wall working sections, the problems are more difficult. In response to the practical difficulty of using conventional yawmeters, various alternative systems have been developed. One example is the Calspan pipe[57,58], comprising a pipe of circular section mounted with its axis parallel to the wind tunnel axis. Static pressure holes are drilled in the tube in a plane that is perpendicular to the measurement surface, and the difference in pressure provides a measure of the gradient of axial velocity normal to the surface. The condition of irrotationality then provides the axial gradient of normal velocity, and the normal velocity component follows by integration in the axial direction. An advantage of this method is that it allows static pressure to be measured with good precision and spatial resolution[58]. The main disadvantage concerns the reduction it causes in the effective size of the working section, referred to in Section 3.1. Smith[59] noted difficulty in achieving satisfactory repeatability with the technique, which he attributed to unsteadiness in the wind tunnel flow. He pointed out that the problem would not have been as serious if the pipe pressures had been measured simultaneously, which they were not in his tests. With the current trend towards solid-state scanning, problems of this sort should be eased considerably. The implications of the increased scanning speed of solid-state devices, compared with that of the earlier rotary devices, for the application of the DRA two-variable method in the DRA 5m Wind Tunnel are described in Ref 46.

Use has also been made of laser velocimeters[30,60] to determine both components of velocity at the measurement surface. Although perhaps the ultimate non-intrusive measurement method, it is doubtful if the technique will find application for the routine determination of wall interference in large, industrial wind tunnels, at least in the near term. Considerable development is needed before the method will be able to provide measurements at the many points required with sufficient rapidity to satisfy the need for high productivity.

Recognition of the difficulties noted above has resulted in alternative approaches being developed, in which use is made of a deduced or assumed relationship between the two components of velocity at the measurement surface or at a surface defining the outer edge of the homogeneous flow. The simplest forms of these relationships are linear and are given below:

1) Wall boundary layers[61] and jets (or wakes) in solid-wall wind tunnels[62].

$$\frac{\partial \varphi}{\partial n} \approx \frac{K}{\beta} \frac{\partial^2 \varphi}{\partial x^2}.$$

$K > 0$ for boundary layers and jets with a total head less than free-stream total head.

2) 'Ideal' porous wall[1].

$$\frac{\partial \varphi}{\partial n} = -\frac{p}{\beta} \frac{\partial \varphi}{\partial x},$$

where p is the porosity factor.

3) 'Ideal' slotted wall[1].

$$\frac{\partial \varphi}{\partial n} = -\frac{\varphi}{\beta FB},$$

where F is a slot parameter.

Boundary layers on solid walls, 1), effectively relieve the wall interference to some extent (auto-adaptation). However, limited experience with two-dimensional, adaptive-wall tunnels has been that the effect is not significant when a two-variable method is used and for flows with mild pressure gradients at the walls[38]. In more extreme cases, notably where a shock wave reaches the wind tunnel walls, the effect on wall-induced velocities is likely to be much more serious, and more complex treatments of the boundary layer than that implied in 1) become necessary. Lewis[50], for example, used the Lag-Entrainment method[63], in combination with measured pressure distributions, to calculate the turbulent boundary layers on the walls in such a case.

For porous-wall wind tunnels, 2), Vaucheret[26] determined the porosity factor for the porous roof and floor of the ONERA S2-Ma Wind Tunnel by using validated model representations and wall pressure measurements. He found that, in order to obtain a good match between calculated and measured wall pressures, a constant value of porosity factor sufficed for variations along the centre-line of the wind tunnel. However, for spanwise variations it was necessary to allow for a spanwise variation in the porosity factor. Neiland[64] described a similar approach used in the TsAGI T-128 Wind Tunnel. For some while[65] it has been known that the relationship between the two velocity components is non-linear, depending on factors such as flow direction, hole diameter and depth and inclination. Vaucheret[66] noted that this fact explains why the porosity obtained by the linear relationship in 2) above varies from one test condition to another. This suggests that the linear relationship is likely to be of limited use.

A more fundamental approach for perforated-wall wind tunnels has been described by Freestone and Henington[67,68]. For a given hole geometry and inclination they established a correlation of the form

$$V_w = f\left(\Delta C_p , M_e , \delta^*/d \right), \qquad (17)$$

where V_w is a mass-flow parameter, ie mass flow through the hole per unit area made non-dimensional with respect to the density and speed of the flow at the outer edge of the boundary layer. δ^*/d is the ratio of boundary-layer displacement thickness to hole diameter and ΔC_p is the rise in pressure coefficient across the wall. Suffix e refers to the conditions at the outer edge of the boundary layer. For plane flows the normal velocity of the equivalent inviscid flow in the transformed space is given by:

$$\frac{\partial \varphi}{\partial n} = \frac{1}{\beta} \left(U_e V_w + \frac{1}{\varrho_e} \frac{\partial (\varrho_e U_e \delta^*)}{\partial x} \right). \qquad (18)$$

The last term, representing the displacement effect of the wall boundary layer, is important, and is determined in the calculation of turbulent boundary layers with blowing through the wall. The normal velocity component in the equivalent inviscid flow, so derived, along with the streamwise velocity increment derived from static-pressure measurements, have been used in calculations by the DRA two-variable method of wall interference for a NACA 0012 aerofoil in a perforated wall wind tunnel.

Related, but possibly simpler, methods of determining the relationship between velocity components have been developed by Chan[69] and Crites and Rueger[70], who, respectively, suggested correlations of the following form:

$$\frac{\partial \varphi}{\partial n} = \frac{U_e}{\beta} \left(A_0 V_w + \left[A_1 V_w^2 + A_2 \right]^{1/2} \right),$$

$$\frac{\partial \varphi}{\partial n} = \frac{U_e}{\beta} \left(a_0 + a_1 V_w + a_2 V_w^2 \right),$$

where A_0, A_1, A_2, a_0, a_1 and a_2 are empirically-derived coefficients. Both groups developed correlations similar to that of equation (17), except that the latter authors included terms to allow for the effect of hole inclination. Chan pointed out that the empirical coefficients depend on the configuration of the wind-tunnel walls and therefore need to be established for each wind tunnel. In both methods, the correlations are combined with equation (18) to obtain the solution for normal velocity.

The intention of the last two studies was to provide a (non-linear) wall boundary condition relating streamwise velocity increment and normal velocity component for use with a model-representation method. Methods of this type do not routinely require boundary-flow measurements, as such, and are therefore, strictly, outside the scope of the present paper. It should be noted, however, that measurements of static pressure on or close to the walls at a sufficient number of points, would, together with the inferred normal velocity, supply all the information needed for a two-variable method. It could be that the requirements for numbers of static-pressure measurements for a two-variable method cannot be met for practical reasons. Even so, users of methods which determine a relationship between the two velocity components should be encouraged to make some wall static-pressure measurements, if only to check the validity of their method. This is the strategy adopted in

certain types of wall-signature method, as noted previously.

The condition for the 'ideal' slotted-wall wind tunnel given in 3) above might conceivably be used, together with empirically-derived values of the parameter F, to establish the normal velocity condition for the homogeneous region in slotted-wall wind tunnels. However, as with perforated walls, the relationship between the two velocity components is known to be non-linear, in general. This fact is recognised in the work of Berndt and Sorensen[71], who have derived non-linear expressions for use as boundary conditions in a model representation method. Recently, these expressions have been used, with minor modification, by Freestone and his group[55,72]. They have adapted these expressions to provide the normal velocity condition for the homogeneous flow from measurements of static pressure on the slat and in the plenum. The method has been used to supply both flow variables for the DRA two-variable method and has been applied to the two-dimensional flow about an aerofoil model mounted between solid sidewalls. The equations solved are as follows:

$$\frac{d\,(\,C\,V_w\,)}{d\,\xi} = A\,\Delta C_p - B\,V_w^2\,, \qquad V_w < 0, \qquad (19)$$

$$\frac{d\,(\,C\,V_w\,)}{d\,\xi} = A\,(\Delta C_p - R_1\,V_w), \qquad V_w > 0, \qquad (20)$$

where ξ is the axial distance from the leading edge of the slot made non-dimensional by slot length, L, and A and B are constants for a given slot geometry. C is a function of an auxiliary parameter η_p, which is related to the coordinate of a flow boundary where plenum total pressure is supposed to be reached. This coordinate changes with distance along the slot, and thus the parameter η_p has to be determined by integrating the equation

$$\frac{d\eta_p}{d\xi} = \frac{L}{a}\frac{v_p\,V_w}{\eta_u^2\eta_a^2}. \qquad (21)$$

Here a is slot width,

$$v_p = 1 - 2\,\exp\left(\,-2\,(\,1\,+\,\pi\,\eta_P\,)\,\right),$$

and the constants η_a and η_u are empirically-derived to allow for the effects on slot effective width and streamwise speed of the slot boundary layer. The term on the right-hand side of equation (20) that is linear in V_w is a modification to allow for the resistance of the slot to flow into the working section, and it contains an empirical resistance coefficient R_1. The increment in pressure coefficient ΔC_p here refers to the rise in pressure between the slat centre-line and the plenum. The mass-flow parameter is determined by simultaneous integration of equations (19) or (20) with equation (21). Once the mass-flow parameter is known, the normal velocity condition for the homogeneous flow is determined by a) ignoring the boundary layers on the slats, and b) taking a lateral average of the slot normal velocity over the width of the working section.

In the tests performed by Freestone et al the roof and floor were either solid or slotted. In the latter case they measured the mass-flow parameter, slat centre-line pressures and plenum pressure, and Fig 17 shows comparisons of predictions by their method and measurement of mass-flow parameter. Particular values of the empirical constants were used in the calculations but the results for mass-flow parameter were found to be remarkably insensitive to their precise values. Following a study of accuracy requirements for the prediction of wall-induced upwash, Freestone et al[55] concluded that the agreement is tolerably good for the two lowest angles of incidence, but, at the highest angle, the agreement is unsatisfactory. Thus, before the method can be used with confidence in an industrial wind tunnel, further development is needed. In the meantime, it may be possible to provide wall-induced velocities which satisfy accuracy requirements using a limited number of flow angle measurements in each slot, perhaps as little as four[55]. Extensions of this work to high subsonic speed are to be reported to this Symposium[73].
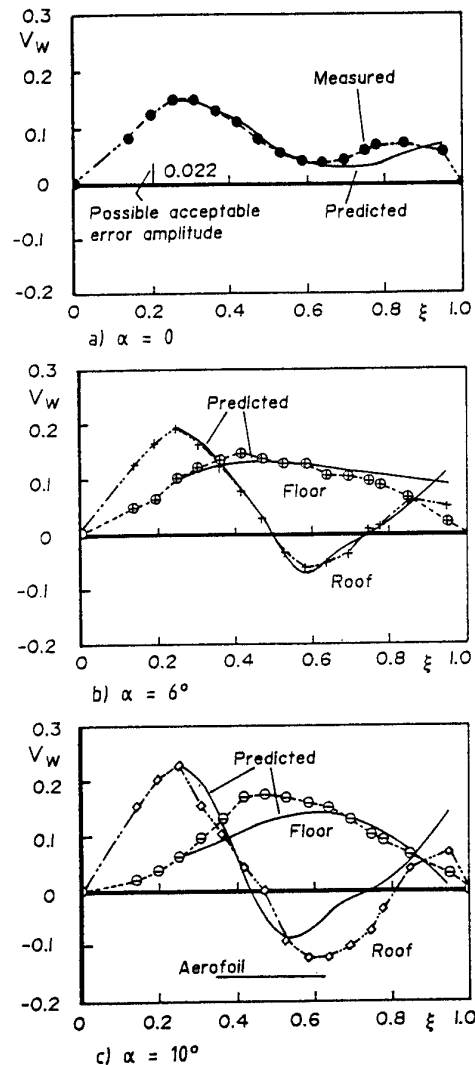

Fig 17 Comparisons of measured and predicted slot mass-flow parameter (Ref 55).

It remains to be seen if the method proposed by Freestone et al can be applied successfully in three dimensions. One important aspect is the lateral extent of the region over which the mass flow should be averaged to give the normal velocity condition. Since the normal velocity of the equivalent inviscid flow at the walls is close to zero near the slat centre line, it may be worth limiting the region over which the slot mass flow is averaged to an area close to the slots.

4 VALIDITY OF WALL CORRECTIONS

A flow over a model is said to be 'correctable' provided there is a free-air flow about the same shape which corresponds exactly to that in the wind tunnel. In reality, wall-induced velocity will always vary by a certain amount in the region of the model, raising the question about the acceptability of the variations. This question does not yet have a complete answer.

It might be argued that the use of adaptive-wall wind tunnels makes the need to answer this question unnecessary, since these tunnels are able to remove wind-tunnel wall interference altogether. In response, the following points may be made:

i) Residual variations of wall-induced velocity have been found in two-dimensional, adaptive-wall wind tunnels[38]. These variations may or may not be significant depending on the type of flow.

ii) Owing to the difficulty of providing complete wall adaptation for three-dimensional flows, compromise solutions have been sought[48,49], eg with two flexible walls and the others held fixed, which give rise to residual variations of wall-induced velocities (Figs 11 and 12).

These comments are made not to devalue the considerable achievements of those who have developed adaptive-wall wind tunnels, but merely to point out that adaptive-wall tunnels do not necessarily provide a complete answer. On the other hand, adaptive-wall wind tunnels are the best available solution for minimising variations in wall-induced velocity, while offering an ideal opportunity to investigate this aspect in more detail. They allow systematic studies to be made of the effect of residual variations on, for example, wing pressure distributions and drag. This would appear to be a fruitful area for future study.

In the absence, for the present, of such information it is necessary to use data from theoretical studies such as those of Steinle and Stanewsky[74] who, on behalf of the AGARD Fluid Dynamics Panel, performed a survey of requirements for flow quality and data accuracy. They investigated the effect of streamwise variations of wall-induced upwash and Mach number on drag and of spanwise variations of wall-induced upwash angle on spanwise loading and induced drag. They suggested that 0.03° should be the upper limit to the variation along the chord of an aerofoil or a wing, while, for the spanwise variation, they suggested an upper limit of 0.1°. For Mach number they proposed that the variation over the length of the model should be less than $0.0006M_\infty$. With these values in mind, it is interesting to study Figs 11 and 12 for the wall-induced velocities

associated with the arrowhead half wing mounted on a sidewall in the adaptive-wall wind tunnel at Southampton University, previously referred to in Section 2.4. Fig 11 shows that, with the roof and floor straight or unadapted, the chordwise variation of wall-induced upwash is an order of magnitude greater than that which may be inferred from the upper limit noted above. On the other hand, the variation is comfortably within the limit with the roof and floor adapted. The variation of wall-induced upwash across the span for the unadapted case is a factor of 4 greater than that required, while the adapted-wall case is just within limits. Significant reduction in the spanwise variation may be effected by changing the target line to one that roughly follows a wing generator[48,49]. This might result in an increase in the chordwise variation, and thus a balance may have to be found between the two variations. For high aspect ratio wings typical of modern transport aircraft, the variation along the chord is unlikely to be a problem, and, in this case, it may well be possible to concentrate on reducing the spanwise variation. Furthermore, it appears that the situation as regards spanwise variation is much better for a complete wing in a wind tunnel with B/H ≈ 1 than it is for half wing in the same wind tunnel[49]. It may be possible to tailor the variation to accommodate the change in wing twist due to aeroelastic distortion that would be found, for example, in a pressurised wind tunnel over a range Reynolds number. I am indebted to Prof M J Goodyer for pointing this possibility out to me.

Turning to Mach number variations, Fig 12 shows that, with straight walls, the variation is outside the stated limit while, with the walls adapted, the variations are well inside. These results may be considered encouraging but further detailed studies are needed to determine more precisely the limits for different types of flow. It should also be noted that this assessment is made in the plane of the wing. To be certain, variations should also be checked in other planes, particularly for flows with extensive supercritical regions or large areas of separated flow.

5 SUMMARY AND CONCLUDING REMARKS

This paper has considered theoretical and experimental aspects of boundary-flow measurement methods. Theoretical methods have been classified and reviewed. It has been shown that the methods may be derived from Green's formula for the wall-interference potential in the measurement region, after application of the Prandtl-Glauert transformation. This formula is valid for calculating wall-induced velocities so long as the wall-interference potential is harmonic in this region. Flows satisfying this requirement are those that may be corrected to free-air conditions, small perturbation flows and flows at low Mach number.

Three classes of method have been reviewed. Methods of the one-variable type require some form of model representation, the sensitivity to model-representation errors depending on the type of boundary condition on the measurement surface. It has been shown that reliance on the accuracy of model representation may be minimised by using a suitable mix of types of boundary condition at the measurement surface. The relevance of this property to the calculation of wall interference in wind tunnels with slotted roof and floor, such as ETW and NTF, has been noted.

Wall-signature methods also require a model representation. However, for solid-wall wind tunnels, wall signatures can, in principle, be used to define the model flow.

Two-variable methods do not need a model representation but require a second flow variable to be measured at the measurement surface.

The relative advantages of the various methods depend on the type of application. Thus two-variable methods are favoured for adaptive-wall wind tunnels because, first, the boundary-flow measurements required are, in any case, needed for the wall-adaptation process, and, second, these methods do not need a model representation. Furthermore, two-variable methods offer significant advantages for complex flows in solid-wall wind tunnels. On the other hand, wall-signature methods are likely to be preferred in solid-wall wind tunnels where the flow around the model can easily be represented by singularities (eg for attached flows over wings), because of the modest requirements of these methods for wall-pressure measurements. For other applications, the relative advantages of the various methods are less clear cut. At present, it is not possible to draw definitive conclusions because further work is needed on a number of aspects, including model representation for one-variable methods (perhaps using the benefits of 'mixed' boundary conditions mentioned above) and the accurate determination of the normal velocity component in two-variable methods (see below). The parallel development of different types of methods should be encouraged.

Consideration has been given to methods of measuring the streamwise and normal components of the perturbation velocity at the measurement surface. Techniques for measuring the former component have been shown to be well advanced. However, further efforts are needed to make it possible to infer this component from measurements of static pressures on the slats of slotted-wall wind tunnels rather than from intrusive devices such as 'rails' or 'tubes'. The accurate determination of the normal component for wind tunnels with slotted walls remains a goal for the future, since laser velocimetry is not yet a viable proposition for making routine measurements with the required rapidity. Some encouraging progress is, however, being made with methods for inferring the normal component from measurements of static pressure on the walls.

Comments have been made about the concept of 'correctable' flows, ie flows that can be corrected to an equivalent 'free-air' condition, and it has been concluded that more work is needed to place the limiting factors on a firmer foundation. In this connexion, a possible future role for adaptive-wall wind tunnels has been noted.

The paper began with reference to a gulf that has existed between theoreticians and experimenters in the field of wind-tunnel wall interference. Boundary-flow measurement techniques have largely bridged that gulf by involving both groups actively in the determination of wind-tunnel wall interference. It is interesting to record that the author of the formula, George Green, was born 200 years ago this year in Nottingham, England. He was both a miller and an applied mathematician[75] (Fig 18)*. Thus Green can be said to have appreciated the problems of aerodynamics both from the

applied and theoretical points of view. It is appropriate, therefore, that the formula, which is the basis for boundary-flow measurement methods in three dimensions, bears his name.
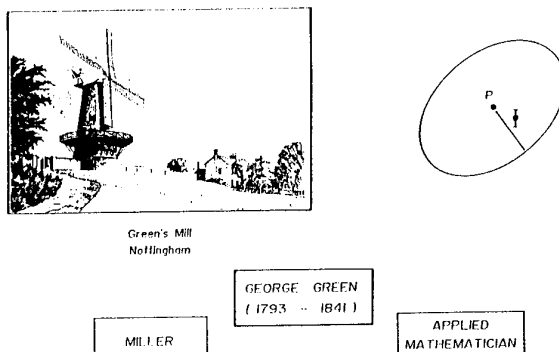

Fig 18 George Green, Miller and Mathematician.

ACKNOWLEDGEMENT

REFERENCES

1. Garner, H.C., Rogers, E.W.E., Acum, W.E.A. and Maskell, E.C., "Subsonic wind tunnel wall corrections.", AGARD-AG-109, October 1966.

2. Goodyer, M.J. (ed.) "The aims and history of adaptive wall wind tunnels." AGARD-AR-269, pp.1-7, April 1990.

3. Hackett, J.E. and Wilsden, D.J., "Determination of low speed wake-blockage corrections via tunnel-wall static pressure measurements." AGARD-CP-174, pp.22.1-22.9, October 1975.

4. Hackett, J.E. and Wilsden, D.J., "Estimation of tunnel blockage from wall pressure signatures: a review and data correlation." NASA CR-152241, March 1979.

5. Hackett, J.E., Wilsden, D.J., and Stevens, W.A., "A review of the wall pressure signature and other tunnel constraint correction methods for high angle-of-attack tests." AGARD-R-692, February 1981.

6. Mokry, M., Chan, Y.Y., Jones, D.J. and Ohman, L.H. (ed.), " Two-dimensional wind tunnel wall interference." AGARD-AG-281, 1983

7. Binion, T.W. Jr. and Kraft, E.M., "A review and update of the FDP Specialists' Meeting in London on wall interference in wind tunnels." AGARD-CP-348,

---

* A museum dedicated to Green's contributions to mathematical physics, based on the windmill in which he worked at one time, can be found in the district of Sneinton in Nottingham.

pp.6.1-6.12, February 1984.

8. Mokry M. (ed.) "Limits of adaptation, residual interferences." AGARD-AR-269, pp.66-90, April 1990.

9. Mokry, M. "Residual interference and wind tunnel wall adaptation." USA AIAA-89-0147, January 1989.

10. Küchemann, D. "The aerodynamic design of aircraft." London, Pergamon Press, 1978.

11. Weatherburn, C.E. "Advanced vector analysis." London, G.Bell & Sons Ltd., 1978.

12. Kraft, E.M. "An overview of approaches and issues for wall interference assessment/correction." NASA CP-2319, pp.3-20, January 1983.

13. Mokry, M. and Ohman, L.H. "Application of the Fast Fourier Transform to two-dimensional wind tunnel wall interference." Journal of Aircraft, Vol.17, No.6, June 1980, pp.402-408.

14. Mokry, M. "Subsonic wall interference corrections for finite-length test sections using boundary pressure measurements." AGARD-CP-335, pp.10.1-10.15, 1982.

15. Mokry, M., Digney, J.R. and Poole, R.J.D. "Doublet-panel method for half-model wind-tunnel corrections." Journal of Aircraft, Vol.24, No.5, May 1987, pp.322-327.

16. Capelier, C., Chevallier, J.P. and Bouniol, F., "Nouvelle methode de correction des effets de parois en courant plan." La Recherche Aerospatiale, 1978-1, Jan.-Feb.1978, pp.1-11

17. Paquet, J.B., "Perturbations induites par les parois d'une soufflerie, methods integrals." These Doc.Ing., Universite de Lille, June 1979.

18. Chevallier, J.P., "Survey of ONERA activities on adaptive-wall applications and computation of residual corrections." NASA CP-2319, pp.43-58, January 1983.

19. Le Sant, Y., and Bouvier, F., "A new adaptive test section at ONERA Chalais-Meudon." Proceedings of European Forum on Wind Tunnels and Wind Tunnel Test Techniques, Southampton University, 14-17 September 1992, Paper 41.

20. Smith, J., "A method for determining 2D wall interference on an aerofoil from measured pressure distributions near the walls and on the model." Holland NLR TR 81816 U, 1981.

21. Smith, J., "Measured boundary condition methods for 2D flows." AGARD-CP-335, pp.9.1-9.15, 1982.

22. Kemp, W.B. Jr., "Towards the correctable-interference transonic wind tunnel." Proceedings of the AIAA 9th Aerodynamic Testing Conference, 7-9 June 1976, pp.31-38.

23. Newman, P.A. Kemp, W.B. Jr. and Garriz, J.A., "Emerging technology for transonic wind-tunnel-wall interference assessment and corrections." USA SAE Paper 881454, October 1988.

24. Rizk, M.H. and Smithmeyer, M.G., "Wind tunnel wall interference corrections for three-dimensional flows." Journal of Aircraft, Vol.19, No.6, June 1982, pp.465-472.

25. Evans, J.Y.G., "Corrections to velocity for wall constraint in any 10 x 7 rectangular subsonic wind tunnel." ARC R&M 2662, 1949

26. Vaucheret, X., "Amelioration des calculs des effets de parois dans les souffleries industrielles de l'ONERA." AGARD-CP-335, pp.11.1-11.12, 1982, (English translation in NASA TM-76971).

27. Kemp, W.B. Jr., "A panel method procedure for interference assessment in slotted-wall wind tunnels." USA AIAA-88-2537, 1986.

28. Woods, L.C., "The theory of subsonic plane flow." Cambridge University Press, 1961

29. Davis, S.S., "A compatibility assessment method for adaptive-wall wind tunnels." AIAA Journal, Vol. 19, No. 9, Sept. 1981, pp.1169-1173.

30. Schairer, E.T., "Two-dimensional wind-tunnel interference from measurements on two contours." Journal of Aircraft, Vol.21, No.6, June 1984, pp.414-419.29.

31 Chan, Y.Y., "A singular perturbation analysis of two-dimensional wind tunnel interferences." Journal of Applied Mathematics & Physics, Vol 31, 1980, pp.605-619.

32. Chan, Y.Y., "Lift effect on transonic wind tunnel blockage." Journal of Aircraft, Vol.17, No.12, December 1980, pp.915-916.

33. Smith, J., "A transonic model representation for two-dimensional wall interference assessment." Holland NLR TR 86026 U, 1986.

34. Mokry, M., "Higher order theory of two-dimensional wall interference in a perforated wall wind tunnel." Canada NRC LR-853, October 1971.

35. Wilsden, D.J.and Hackett, J.E., "Tunnel constraint for a jet in crossflow." NASA CP-2319, pp.273-290, January 1983.

36. Isaacs, D., "Calibration of the RAE Bedford 8ft x 8ft wind tunnel at subsonic speeds, including a discussion of the correction to the measured pressure distribution to allow for the direct and blockage effects due to the calibration probe." ARC R&M 2777, 1969.

37. Goldhammer, M.I. and Steinle, F.W., "Design and validation of advanced transonic wings using CFD and

12-20

very high Reynolds number wind tunnel testing." ICAS 90-26.2, 1990.

38. Ashill, P.R. and Weeks, D.J., "A method for determining wall-interference corrections in solid-wall tunnels from measurements of static pressure at the walls." AGARD-CP-335, pp.1.1-1.12, 1982.

39. Labrujere, Th.E., "Correction for wall interference by means of a measured-boundary-condition method." Holland NLR TR 84114 U, November 1984.

40. Lo, C.F., "Tunnel interference assessment by boundary measurements." AIAA Journal, Vol.16, No.4, April 1978, pp.411-413.

41. Ashill, P.R. and Weeks, D.J., "An experimental investigation of the drag of thick supercritical aerofoils - a progress report." RAE TM Aero 1765, 1978.

42. Kraft, E.M. and Dahm, W.J.A., "Direct assessment of wall interference in a two-dimensional subsonic wind tunnel." USA AIAA-82-0187, January 1982.

43. Ashill, P.R. and Weeks, D.J., "Techniques developed in Europe for tunnel-wall corrections using measured boundary conditions." Unpublished Proceedings of the AGARD FDP Subcommittee on Wind Tunnels and Testing Techniques Meeting on 'Integration of Computers and Wind Tunnel Testing', RAE Bedford UK, 18-19 February 1981.

44. Ashill, P.R. and Keating, R.F.A., "Calculation of tunnel wall interference from wall-pressure measurements." Aeronautical Journal, Vol.92, No.911, January 1988, pp.36-53.

45. Ashill, P.R. and Keating, R.F.A., "Calculation of tunnel wall interference from wall-pressure measurements." RAE TR 85086, 1985. (This report provides a more detailed account of the work referred to in Ref.42).

46. Kirkpatrick, D.L.I. and Woodward, D.S., "Priorities for high-lift testing in the 1990s." USA AIAA-90-1413, 1990.

47. Maarsingh, R.A., Labrujere, Th.E., and Smith, J. "Accuracy of various wall-correction methods for 3D subsonic wind-tunnel testing." AGARD-CP-429, pp.17.1-17.13, September 1988

48. Lewis, M.C., Taylor N.J. and Goodyer, M.J., "Adaptive wall technology for three-dimensional models at high subsonic speeds and aerofoil testing through the speed of sound." Proceedings of the Royal Aeronautical Society Symposium 'Wind Tunnels & Wind Tunnel Test Techniques', Southampton University, 14-17 October 1992, Paper 32.

49. Lewis, M.C. "Two-dimensional wall adaptation for three-dimensional flows." Proceedings of the International Conference on Adaptive Wall Wind Tunnel Research and Wall-Interference Correction (ICAW), June 1991, Paper A2.

50. Lewis, M.C. "Aerofoil testing in a self-streamlining flexible walled wind tunnel." NASA CR-4128, May 1988

51. Goodyer, M.J. and Wolf, S.W.D., "The development of a self-streamlining flexible walled transonic test section." USA AIAA-80-440-CP, 1980.

52. Rebstock, R. and Lee, E.E. Jr., "Capabilities of wind tunnels with two adaptive walls to minimize boundary interference in 3D model testing." Transonic Symposium: theory, application, and experiment, NASA Langley, April 1988, NASA CP-3020 Vol.1, Part 1, pp.891-910, March 1989

53. Firmin, M.C.P. and Cook, P.H., "Disturbances from ventilated tunnel walls in aerofoil testing." AGARD-CP-348, pp.8.1-8.15, February 1984.

54. Berndt, S.B. "Inviscid theory of wall interference in slotted test sections." AIAA Journal, Vol.15, No.9, September 1977, pp.1278-1287.

55. Freestone, M., Mohan, S.R. and Lock, R.C., "Interference corrections in wind tunnels with slotted walls." Proceedings of the Royal Aeronautical Society Symposium 'Wind Tunnels & Wind Tunnel Test Techniques', University of Southampton, 14-17 October 1992.

56. Wu, J.M. and Collins, F.G., "Investigations of flow field perturbations induced on slotted transonic-tunnel walls." NASA CP-2319, pp.119-142, January 1983

57. Erickson, J.C. Jr., Whittliff, C.E. and Daughtry, D.C., "Further investigations of adaptive-wall wind tunnels." USA AEDC-TR-80-34, October 1980 (AD-A091 774).

58. Parker, R.L. and Erickson, J.C. Jr., "Development of a three-dimensional adaptive wall test section with perforated walls." AGARD-CP-335, pp.17.1-17.14, September 1982.

59. Smith, J., "Two-dimensional wall interference assessment using Calspan pipes." Holland NLR TR 85065 U, April 1985.

60. Schairer, E.T., "Methods for assessing wall interferences in the 2- by 2-foot adaptive wall wind tunnel." NASA TM-88252, June 1986.

61. Adcock, J.B. and Barnwell, R.W., "Effect of boundary layers on solid walls in three-dimensional subsonic wind tunnels." NASA CP-2319, pp.205-218, January 1983.

62. Neiland, V.Ya. and Neiland, V.M., "Jet boundaries - new type of self streamlining wind tunnel wall." Proceedings of the Royal Aeronautical Society Symposium 'Wind Tunnels & Wind Tunnel Test Techniques', University of Southampton, 14-17 October 1992, Paper 40.

63. Green, J.E. and Weeks, D.J., "Prediction of turbulent boundary layers and wakes in compressible flow by a

lag-entrainment method." ARC R&M 3791, January 1973.

64. Neiland, V.M., "Adaptive wall wind tunnels with adjustable permeability experience of exploitation possibilities." Proceedings of the International Conference on Adaptive Wall Wind Tunnel Research and Wall-Interference Correction (ICAW), June 1991, Paper A3.

65. Goethert, B.H., "Transonic wind tunnel testing." AGARD-AG-49, 1980.

66. Vaucheret, X., "Vortex lattice code for computation of wind tunnel and support effects on models." La Recherche Aerospatiale, 1991-2, 1991, pp.40-51.

67. Freestone, M.M. and Henington, P., "A scheme for incorporating the viscous effects of perforated windtunnel walls in two-dimensional flow calculations." City University Res.Memo Aero 78/7, 1979.

68. Freestone, M.M. and Henington, P., "Incorporation of viscous effects of perforated windtunnel walls in two-dimensional flow calculations." City University Res.Memo Aero 81/1, 1981.

69. Chan, Y.Y., "Wall boundary-layer effects in transonic wind tunnels." AGARD-CP-348, pp.6.2-6.12, February 1984.

70. Crites, R.C. and Rueger, M., "Transonic wall interference corrections for small wind tunnels." Proceedings of the Royal Aeronautical Society Symposium 'Wind Tunnels & Wind Tunnel Test Techniques', Southampton University, 14-17 October 1992, Paper 18.

71. Berndt, S.B. and Sorensen, H., "Flow properties of slotted walls for transonic test sections." AGARD-CP-174, pp.17.1-17.10, 1975.

72. Freestone, M.M., Lock, R.C. and Mohan, S.R., "Determination of wind tunnel interference due to slotted wall liners." City University, Department of Mechanical Engineering, MED/AERO Rept.179, Vols.1 & 2.

73. Freestone, M.M. and Mohan, S.R., "Interference determination for wind tunnels with slotted walls." Paper 19 to be presented to AGARD FDP Symposium "Wall Interference, Support Interference and Flow Field Measurements." Brussels 4-7 Oct. 1993

74 Steinle, F. and Stanewsky, E., "Wind tunnel flow quality and data accuracy requirements." AGARD-AR-84, November 1982.

75. Whitrow, G.J., "George Green (1793-1841): a pioneer of modern mathematical physics and its methodology." Annali dell'Instituto e Museo di Storia dela Scienza di Firenze, Vol.9, No.2, 1984.

WALL CORRECTION METHOD WITH MEASURED BOUNDARY CONDITIONS
FOR LOW SPEED WIND TUNNELS

A. Küpper
DLR
Deutsche Forschungsanstalt
für Luft- und Raumfahrt e.V.
Lilienthalplatz 7, D-38108 Braunschweig

SUMMARY

In the wind tunnel division of DLR in Braunschweig a wall correction method based on measured boundary conditions was developed. The verification of the method was made with theoretically calculated boundary conditions and with experimental test data. The calculation of the wall interferences from theoretical boundary conditions are in good agreement with exact reference data of the wall interferences. The advantage of the wall pressure correction method is shown by the results of the experimental tests where the measured coefficients of the force and the moments are compared with the corrected coefficients and the coefficients of free-flight. In this comparison the classical correction method is shown too. The wall correction method is easy to use because no information of the model is required and can be applied into an on-line processing. Particular attention should be paid to the wall pressure measurement system because wrong wall pressure data can have an influence on the calculated wall interferences.

LIST OF SYMBOLS

b	span of the wing
B	width of the test section
C_A	lift coefficient
C_m	pitching moment coefficient
C_p	pressure coefficient
C_W	drag coefficient
H	height of the test section
R	distance of the wall and the observed point in the test section
$R_1, \ldots, R_{12}$	wall pressure row 1 to 12 in the NWB
S	surface of the test section
u_W, v_W, w_W	wall induced velocity components
U_∞	undisturbed stream velocity
V_N	velocity component in normal direction
x, y, z	coordinates
α	angle of attack
φ	potential of small disturbances
φ_W	wall induced potential
σ	span ratio

INTRODUCTION

To transform the results of wind tunnel measurements to free flight the measured data must be corrected for the amount of the wind tunnel interferences. The wind tunnel interferences result from the boundaries of the wind tunnel flow which constrain the infinite expansion of the model induced disturbances. To calculate the interferences in the test section mainly the "classical correction method" is used. In this the model is represented by a system of vortices, doublets, sources and sinks. These singularities are then arranged in an image system in such a way that the boundary conditions on the wind tunnel walls are accomplished and can determine the wind tunnel interferences at the location of the model. Yet, the disadvantage of the "classical correction method" is the difficulty of an exact model representation particularly for complex models, for the representation of the wake and for separated regions. Instead of calculating the wind tunnel interferences with the aim of models composed of singularities by the potential theory wall pressure correction methods for wind tunnels with closed and slotted test sections are in further development which are able to calculate the interferences based on the measured boundary conditions. The measured boundary conditions includes exactly the wall interferences and the model induced disturbances with the effect of separated regions and the wake.

At the wind tunnel division of DLR in Braunschweig a wall pressure correction method (WPCM2) was developed. In this method the calculation of the wall interferences is based on the solution of Green's integral where the velocity of the disturbances at the walls are calculated from the measured pressures. To determine the surface integral over the test section the velocities over the four test section walls are needed. A great advantage of WPCM2 is that no model representation is required and the wall interferences can be easily calculated at any point in the test section. This means that the distri-

bution of the wall interferences over the model can be calculated and a statement can be made about the admissibility of the correction. The numerical treatment of the method is expensive and could not be calculated in sufficient time by the wind tunnel computer till recently. But the exploding development in computer technology makes it possible to calculate the corrections by a work-station or a fast personal computer during the on-line data processing of wind tunnel measurements.

The first step to verify the correction method were "theoretical measurements". This means that the wall pressure was calculated for singularities by an image system. The reference data without wall interferences were also calculated by the image system in order to qualify the correction method.

In the second step of the verification measurements in the low speed wind tunnel Braunschweig (NWB) (Ref 1) and a small subsonic wind tunnel Braunschweig (MUB) (Ref 2) were performed with the "Subsonic Wall Interference Model" (SWIM) of NLR. The span ratio in the NWB is 18% and in the MUB 73%. The measurements in the NWB were taken as reference data with nearly wall interference free data to qualify the wall pressure correction methods applied to the measurements in the MUB.

CALCULATION OF WALL INTERFERENCES

To calculate the wall interferences from a wall pressure distribution on the surface of a closed test section a method was developed by Ashill and Weeks in (Ref 3). The wall pressure distribution represents the resultant potential of disturbances in the test section which is composed of the disturbances by the model and the walls. To determine the potential of the walls only the integration over the surface of the test section is required. The derivation of Ashill and Weeks leads to

$$\varphi_W = -\frac{1}{4\pi} \iint_S \left\{ \frac{\partial \varphi}{\partial N} \frac{1}{R} - \varphi \frac{\partial}{\partial N}\left(\frac{1}{R}\right) \right\} ds' \quad (1)$$

where φ is the potential of disturbances and φ_W the potential of the wall disturbances at a point P (x,y,z) in the test section. The integration over the surface S will be divided into integration over panels. R is the distance between the center of the panel and the point P (x,y,z)

in the test section. $\partial \varphi / \partial N$ is the derivative of the potential φ to the normal direction of the panel. Ashill and Weeks show in their examination that the potential of the model will be eliminated in the solution of equation (1).

The wall induced velocities at the point P (x,y,z) will result by differentiating the potential of the wall φ_W to the components of the axe-system, i.e.

$$u_W = \frac{\partial \varphi_W}{\partial x} \quad (2)$$

$$v_W = \frac{\partial \varphi_W}{\partial y} \quad (3)$$

$$w_W = \frac{\partial \varphi_W}{\partial z} \quad (4)$$

The surface integration in equation (1) must be made over the closed volume of the test section, i.e. also over the cross-section at the entrance and the exit of the test section. If the distance between model and cross-section is far enough their part of the surface integration can be neglected.

The general solution of the surface integration was discussed by Holst (Ref 4). He describes in detail the calculation of the wall induced velocities in the test section.

For a closed test section with straight walls equation (1) becomes

$$\varphi_W = \frac{1}{4\pi} \iint_S \varphi \frac{\partial}{\partial N}\left(\frac{1}{R}\right) ds \quad (5)$$

because there is no velocity normal to the walls, i.e.

$$\frac{\partial \varphi}{\partial N} = v_N = 0 \quad (6)$$

BOUNDARY CONDITIONS

The determination of the wall induced velocities u_W, v_W, w_W at a point P (x,y,z) in the test section will be made with the formulae given by Holst (Ref 4). Therefore the potential φ and its velocities u, v and w at the walls are required. They must be de-

termined by the measured pressure distribution on the walls. The measured C_p-value includes the pressure difference of model influence and wall influence. Provided that the Laplace-equation for a potential field with small disturbances is accomplished the u-component of the velocity can be determined by the linearised Bernoulli-equation.

$$\frac{u}{U_\infty} = -\frac{C_p}{2} \qquad (7)$$

The small disturbances potential on the panels will result by an integration of the u-values in x-direction.

$$\varphi = \int u dx \qquad (8)$$

In a closed test section the velocity perpendicular to the wall is zero, see equation (6). The third velocity component can be determined with the equations for a potential flow field without rotations. This means

$$\frac{\partial v}{\partial x} = \frac{\partial u}{\partial y} \quad (horizontal \quad wall) \qquad (9)$$

$$\frac{\partial w}{\partial x} = \frac{\partial v}{\partial z} \quad (vertical \quad wall) \qquad (10)$$

The potential and the velocities over the cross-section will be calculated by an interpolation of the values at the entrance and the exit of the test section. Usually the part of the surface integral over the entrance can be neglected.

The walls are divided in small panels. The surface integration results from an integration over each panel, where the solution of each panel will be added to the final result. The panels should be small enough because the potential φ is taken constant on the panel. In practice this means the boundary conditions at the center of the panels must be calculated by an interpolation because the pressure holes on the walls are not always identical with the center of the panels. The interpolation method of Harder and Desmarais (Ref 5) uses surface splines. It is based upon the small deflection equation of an infinite plate. The main advantages of the surface spline are that the coordinates of the known points need not be located in an rectangular array and the function may be differentiated to find slopes.

VALIDATION OF WPCM2 FOR CLOSED TEST SECTIONS

The computer program is written on a Personal Computer in FORTRAN77. In the first step of the verification the solution of the surface integral of equation (2), (3) and (4) were performed. Therefore the wall pressure data was calculated for simple singularities by the image system. Also the wall interference velocities in the test section were calculated by the image system which would be taken as reference data. From the calculated wall pressure the wall interference velocities in the test section were determined with the wall pressure correction method (WPCM2) and will be compared with the reference data.

The dimensions of the NWB were used. The test section is 3.25m wide and 2.8m high, pressure tappings are over a distance of about 6.5m. The center of the model is located in the center of the test section. The calculated wall pressures were at the same positions as in the NWB. Each wall of the NWB has three wall pressure rows. One on the center line of the wall, the two others are in a distance of $\pm$ 0.82m from the center line. In Fig 1 a sketch of the cross section of NWB is shown where the position of the wall pressure rows (R_1, ..., R_{12}) upon the circumference of the cross section are listed.

On each row are 64 pressure holes with 0.1m space between the holes. For the "theoretical" measurements the pressure coefficient C_p was calculated only at 24 holes each row. With these pressure coefficients the u-velocity of the small disturbances at the walls can be determined by

$$u = -C_p/2 \qquad (11)$$

For the surface integration the test section walls are divided into panels. 36 panels streamwise and 9 panels in lateral direction, i.e. 324 panels on each wall. The u-velocities at the center of the panels are calculated by using the surface interpolation of Harder and Desmarais. With the well-known boundary conditions the wall induced velocities in the test section can be determined. The wall interference method was verified with two simple singularities, a doublet and a horseshoe vortex. With the doublet the wall induced blockage effect, i.e. the wall induced u-velocity, and with the horseshoe vortex the wall induced upwash, i.e. the wall induced

w-velocity, in the test section were checked.

Fig 2 shows the result of the wall induced u-velocity in the main cross section which includes the origin of the doublet. The doublet is shown by a hatched circle and takes 15% of the cross section area of the tunnel. The calculated u-velocity of the wall interference is shown by the continuous lines, the reference data of the image system by the dashed lines. In the area of the model the results are in a good agreement, only near the walls are small differences.

In Fig 3 the upwash velocity w of the wall interference is shown. A horseshoe vortex was chosen as model which has a span ratio $\sigma = {}^b/B = 0.73$. The horseshoe vortex has a constant circulation and the examination in Fig 3 was made for the lift coefficient $C_A = 1.7$. The model is placed with its origin in the center of the test section. The continuous lines represent the wall induced upwash calculated by the wall pressure method. The dashed lines are the reference data calculated by the image system.

The upwash interference is calculated for the main cross section of the tunnel which includes the origin of the model. In the center of the cross section is the greatest displacement between the reference data and the data calculated with the wall pressure method. The displacement will become smaller over the span. The error of the displacement in the center makes a difference in the incidence correction of 0.02°.

The differences between the wall pressure method and the reference data are caused in the error of the calculated wall pressure distribution by the image system because it is a finite system. Another reason for the differences is the short length of the test section so that the influence of the cross section at the entrance and the exit of the test section cannot be neglected.

The second step of the verification measurements were made with the Subsonic Wall Interference Model (SWIM) in the NWB and the MUB (Ref 6 and Ref 7). A sketch of the model is given in Fig 4. The model can optionally be mounted with a flap (K) and a horizontal tail (H). The angle of the flap is 20°. There are four model configurations
- RF   fuselage (R) and wing (F)
- RFK   fuselage (R), wing (F) and flap (K)
- RFH   fuselage (R), wing (F) and horizontal tail (H)
- RFKH   fuselage (R), wing (F), flap (K) and horizontal tail (H)

The ratio of the cross-section of the NWB and the MUB with SWIM is shown in Fig 5. This figure illustrates that the expected wall interferences in the MUB will be large and in the NWB will be very small. Examination in the NWB shows that no appreciable wall interference exists because span ratio of SWIM in the NWB is $\sigma = 0.18$. Large wall interferences are expected in the MUB because the span ratio of SWIM is there $\sigma = 0.74$. In the MUB the wall pressure distribution was measured on half of the test section circumference because the model is symmetric and no asymmetric tests were made. The wall pressure holes cover a length of 2.5m. On half of the top and half of the bottom wall are 3 tappings each. On one side wall are 5 tappings. From the wall correction method the wall pressure distribution of half the test section will be reflected to the other test section half. The result of the experimental examination is shown for the model configuration RFKH in the following three figures. In Fig 6 the lift coefficient C_A is drawn against the incidence α. The difference between the measured data in the NWB and the MUB shows the great influence of the wall interferences. The measured data of the MUB were corrected with the classical correction method and the wall pressure correction method WPCM2. The dotted-pointed line marks the classical correction and the dotted line marks the correction of WPCM2. The corrected lift coefficient C_A coincides with the reference data of the NWB whereas the correction with the classical method gets worse with the increasing angle of incidence. In the region of maximum lift coefficient the classical correction method fails, i.e. the region of separated flow is not considered in the right way. Particularly in this region the advantage of the wall pressure method is to be seen. The influence of the wall interference to the drag coefficient is shown in Fig 7. There the lift coefficient C_A is drawn against the drag coefficient C_W. The two correction methods lead to the same result up to a lift coefficient of $C_A = 1.9$ but don't coincide with the reference data. For a drag coefficient $C_W > 0.2$ the classical correction method fails whereas the data corrected with WPCM2 are nearly the reference data. In Fig 8 the lift coefficient is drawn against the pitching moment coefficient C_m. The quality of the two correction methods are the same as in the foregoing two figures.

Also in particular the classical correction method failed for regions with separated flow whereas the wall correction method shows good results compared with the reference data.

The theoretical and experimental examination of the wall pressure correction method WPCM2 show the quality of the method and the progress in the development of wall interference correction methods.

PROGRESS OF WALL PRESSURE CORRECTION METHOD

Planned activities of DLR in research and development of wall pressure correction method are in a cooperation with the DNW. For this cooperation the DLR built a model like SWIM in their workshops. The model is called Correction Model (COMO) and a sketch of the model is given in Fig 9. With COMO wall pressure measurements will be made in the closed and slotted test section of the NWB. The span of COMO is b = 2.4m and for an optional version the span is b = 2.6m, i.e. the span ratio is $\sigma = 0.74$ respectively $\sigma = 0.8m$.

From measurements with COMO in the DNW the reference data will result. With the data of DNW and NWB wall pressure correction methods for closed and slotted test section can be verified.

REFERENCES

1. Kausche, G., Otto, H., Christ, D. and Siebert, R., "Der Niederge-schwindigkeits-Windkanal der DFVLR in Braunschweig", DFVLR-Mitt. 88-25, Okt. 1988.

2. Müller, R., "Beschreibung des Modell-Unterschallwindkanals (MUK) zum 'Großen Unterschallkanal' (GUK). Erstellung, Inbetriebnahme, erste Ergebnisse", DFVLR Braun-schweig IB 151-75/14, 1975.

3. Ashill, P.R. and Weeks, D.J., "A method for determining wall-interference corrections in solid-wall tunnels from measurements of static pressure at the walls", AGARD-CP-335, May 1982, pp 1-1. - 1-12.

4. Holst, H., "Verfahren zur Bestim-mung von dreidimensionalen Wind-kanalinterferenzen und Wandadap-tionen mit Hilfe gemessener Wand-drücke bei kompressibler Unter-schallströmung", DLR-FB 90-46, May 1990.

5. Harder, R.L. and Desmarais, R.N., "Interpolation Using Surface Splines", Journal of Aircraft, Vol. 9, No. 2, February 1972, pp 189 - 190.

6. Küpper, A., "Kraft- und Wanddruck-messungen an einem subsonischen Wandinterferenz-Modell im Nieder-geschwindigkeits-Windkanal Braun-schweig", DLR Braunschweig IB 19111 - 93 A 02, March 1993.

7. Küpper, A., "Kraft- und Wanddruck-messugen mit einem subsonischen Wandinterferenzen Modell im Modell-Unterschallwindkanal Braun-schweig, DLR Braunschweig IB 19111 - 93 A 08, May 1993.
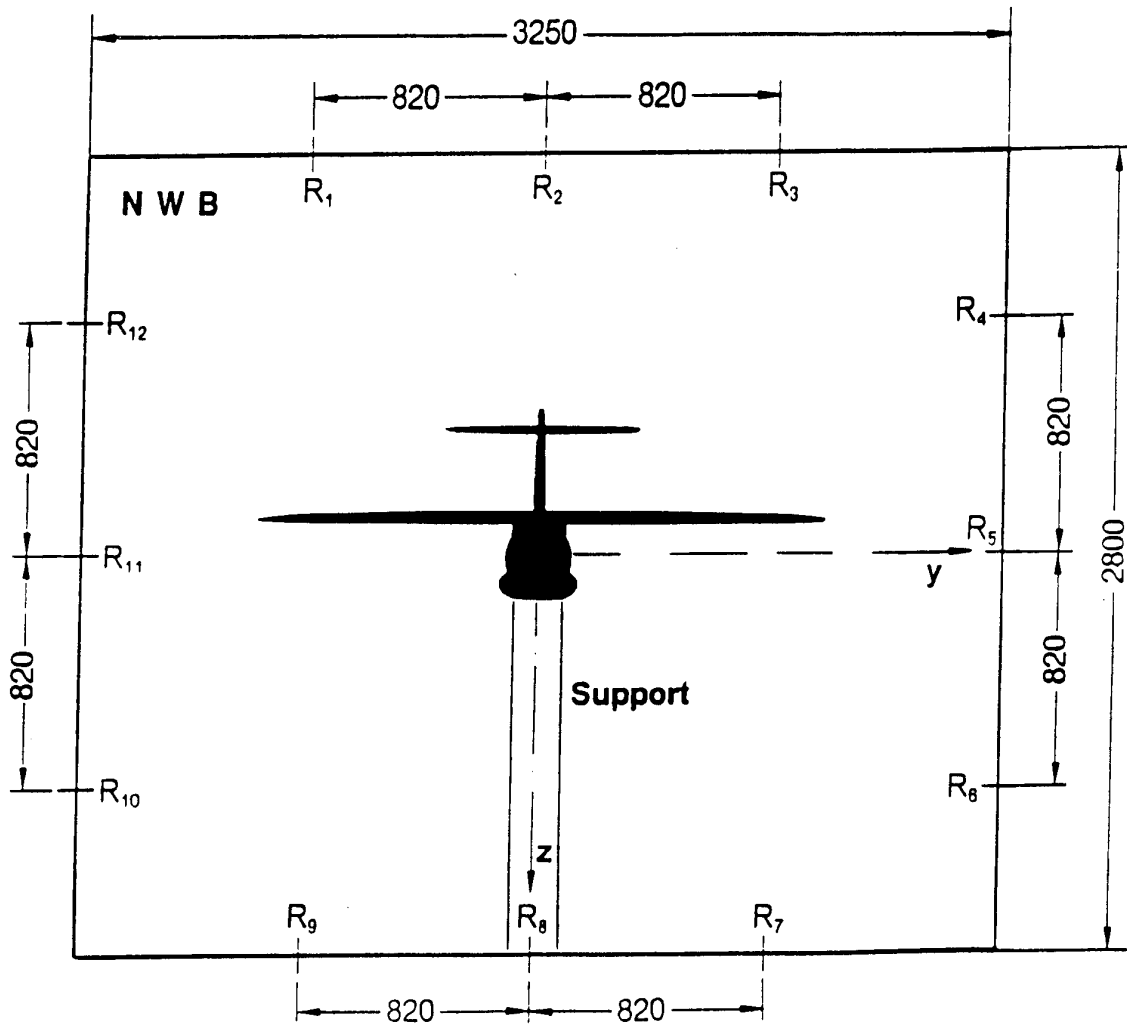
Figure 1 Cross-section of the NWB with the location of the tappings
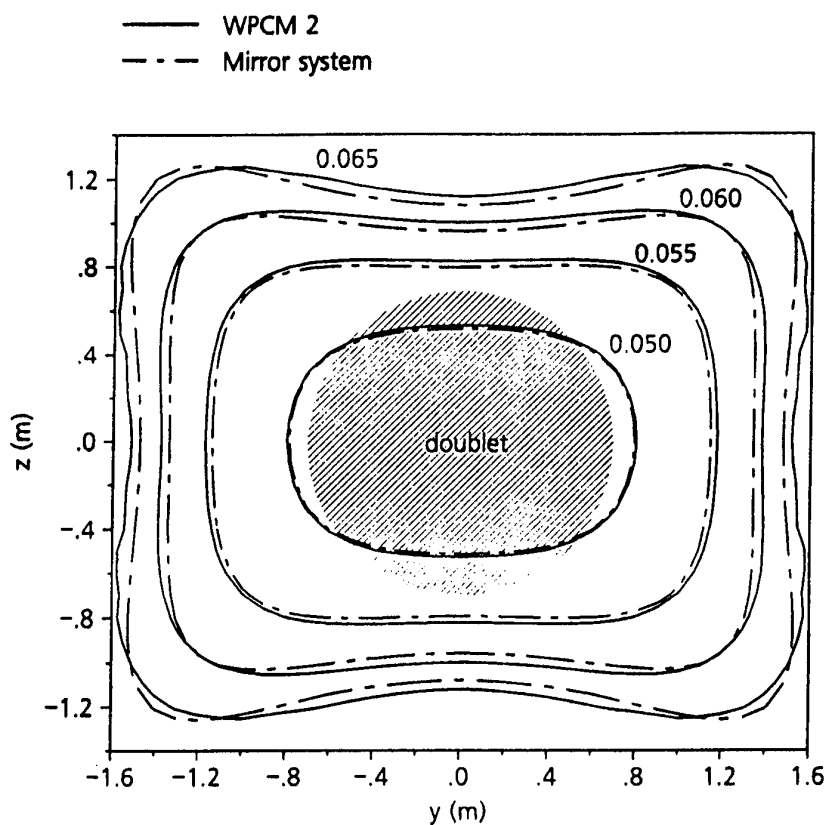
Figure 2   Wall induced u-velocity for a doublet in the main cross-section of NWB test section
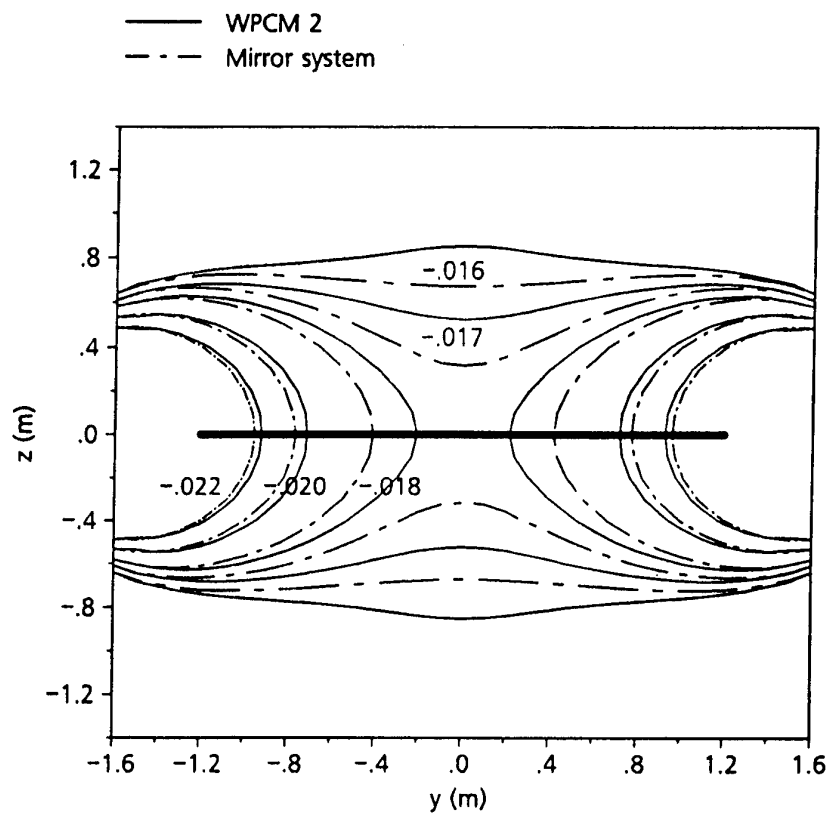

Figure 3   Wall induced w-velocity for a horseshoe vortex with the span ratio $\sigma = 0.73$ in the main cross section of the NWB test section
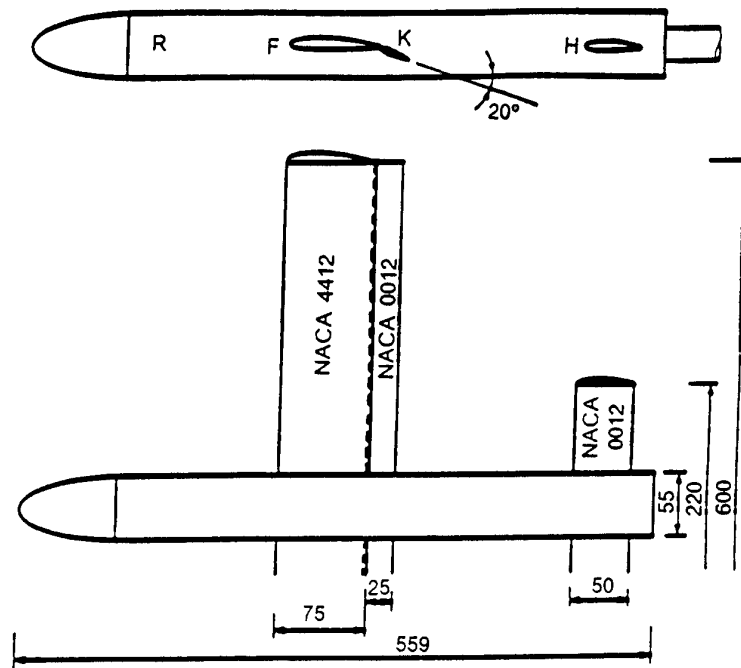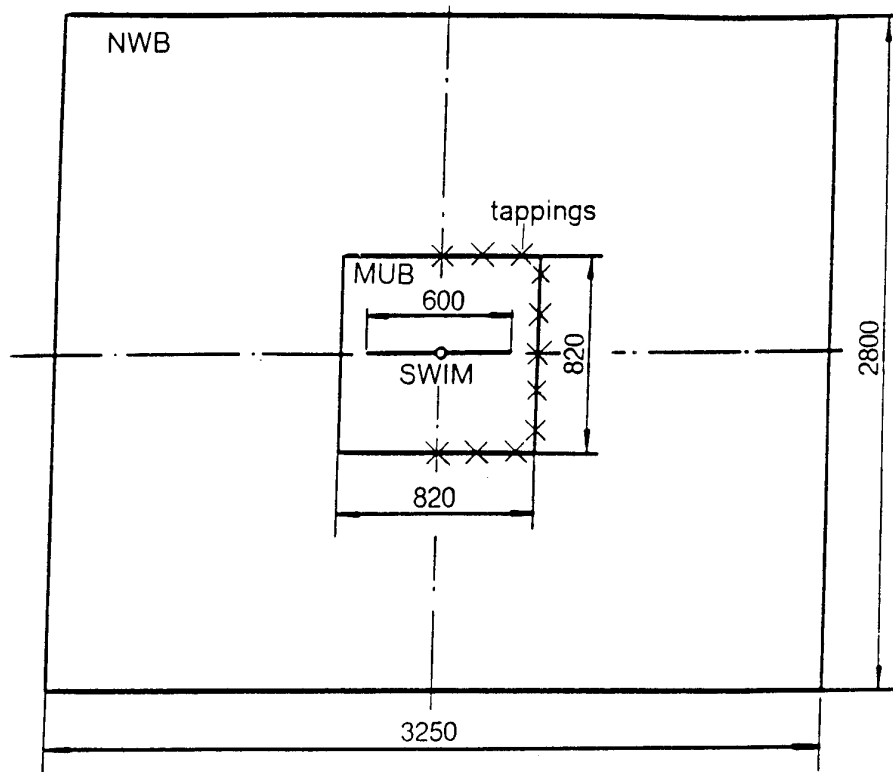
Figure 4   Sketch of SWIM

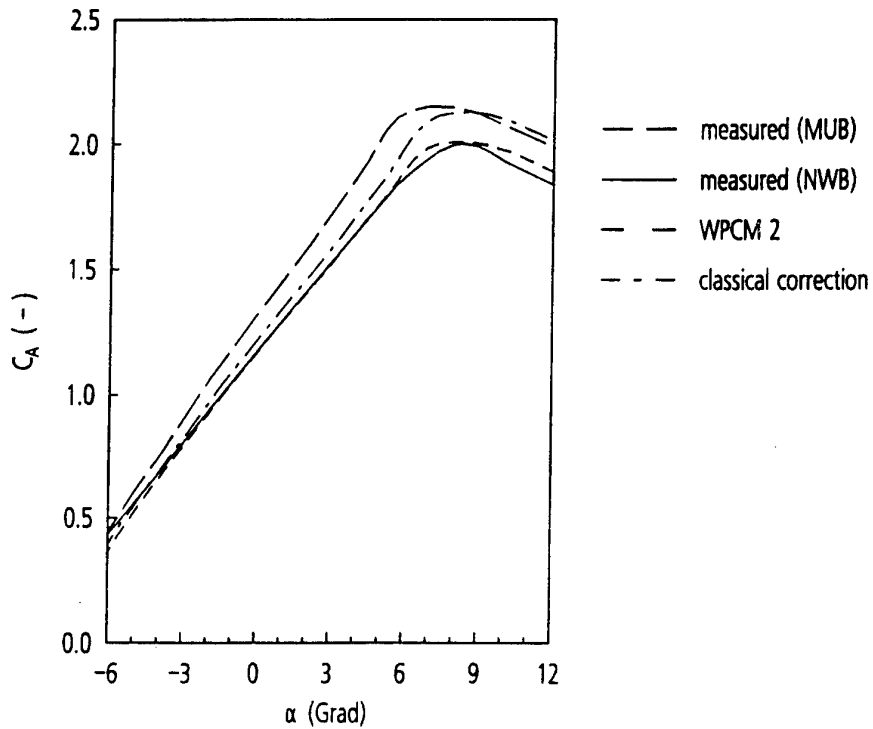**Figure 5**   Ratio of the tunnel cross-sections of NWB and MUB with SWIM
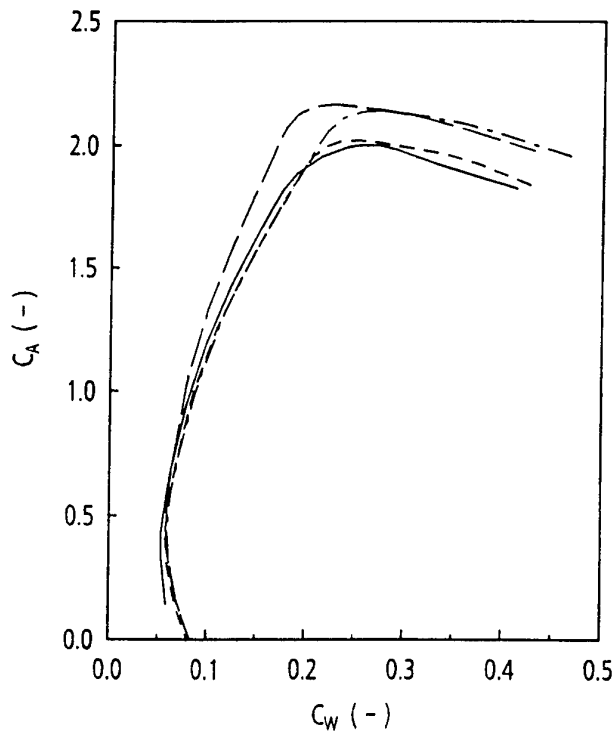
Figure 6   Lift coefficient C_A over incidence α

Legend:
- — — measured (MUB)
- —— measured (NWB)
- – – WPCM 2
- – · – classical correction

Figure 7   Lift coefficient C_A over drag coefficient C_W
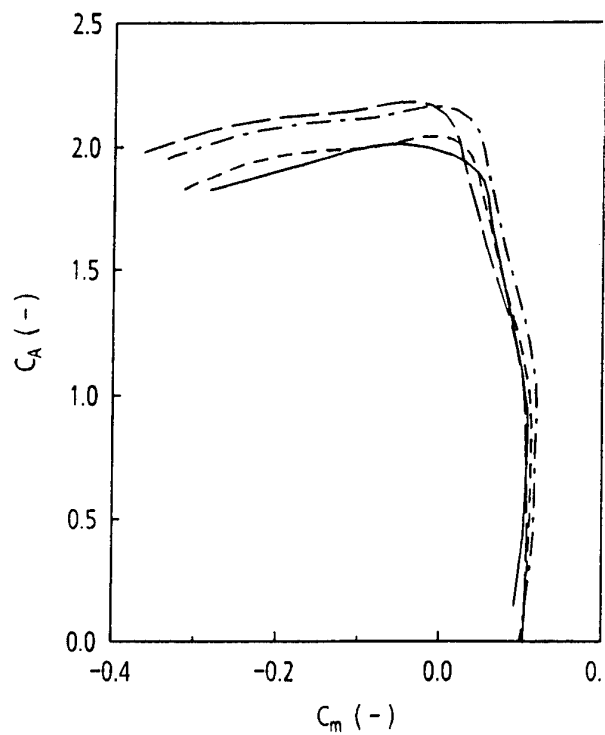
Figure 8   Lift coefficient C_A over pitching moment coefficient C_m

Correction - Model **COMO**
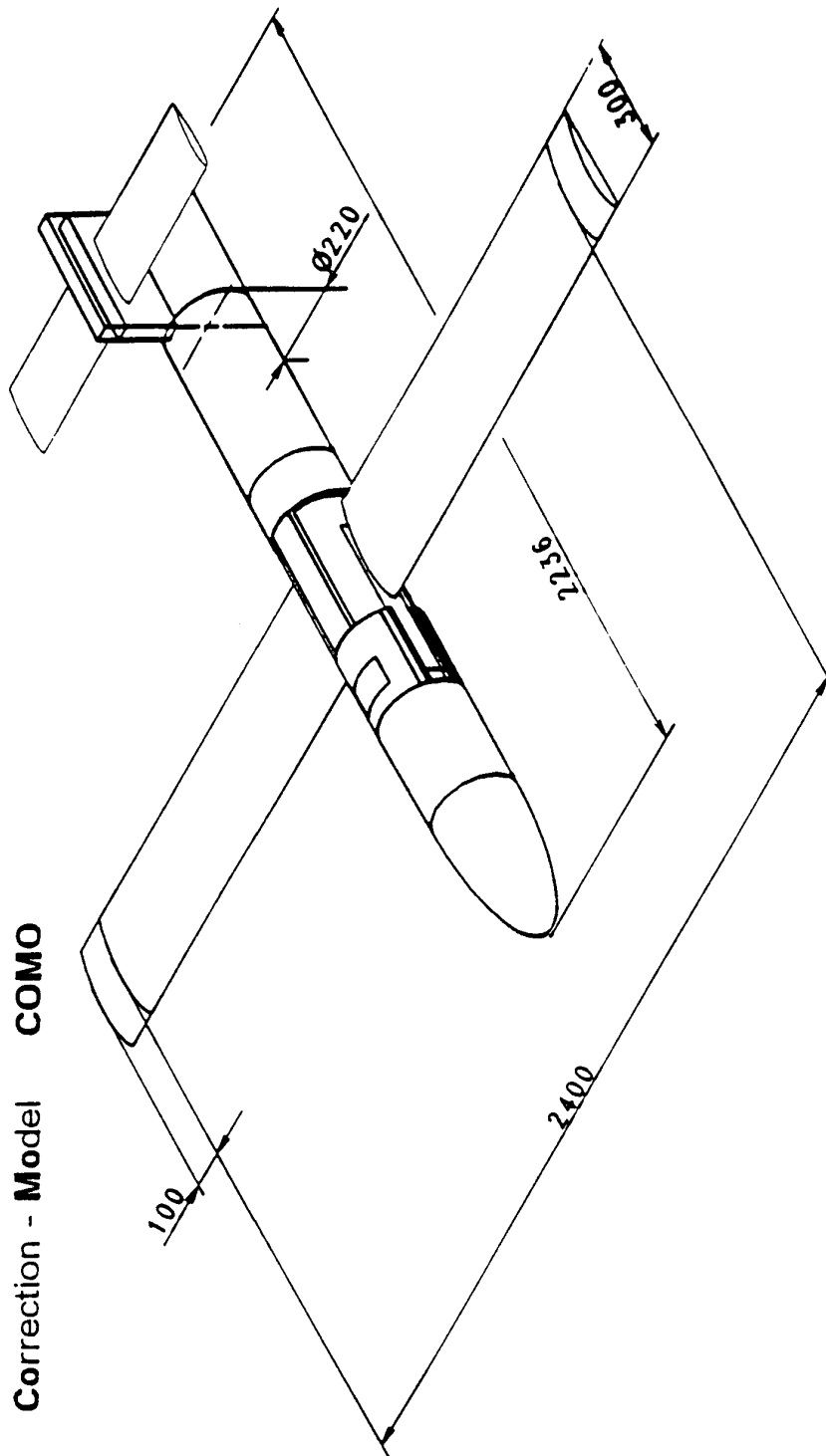
Figure 9   Sketch of COMO

Computational Simulations for Some Tests in Transonic Wind Tunnels

Nada Agrell
Aerodynamics Department
FFA, Aeronautical Research Institute of Sweden
P.O.Box 11021, S-161 11 BROMMA
SWEDEN

SUMMARY

Two large models with swept wings have been investigated in two rather similar tunnels, whose cross sectional areas differ by a factor of 9. The tunnels are configured with slotted walls. The larger of the tunnels has a ventilation of 8.3%, while the ventilation of the smaller tunnel has been varied between 4.2% and 8.3% for this investigation. The blockage of the tested models in the tunnels varied from approximately 0.2% to 1.7%. For the case with the blockage of 1.7% the ratio of span to the width (equals to the height) of the tunnel was 0.8.

For the configuration blocking 0.6% in the larger of the two wind tunnels the comparison of Mach number signatures on the tunnel walls between experiments and computations is very good at both Mach numbers, 0.9 and 0.95, and both angles of attack, 0° and 10°. The position of the 'shock' is very well predicted in the computations.

Most of the computational simulations for the model blocking 1.7% in the smaller of the two tunnels have so far been performed at Mach number 0.8 and at angles of attack of 0° and 2°. This presentation has been concentrated on Mach number 0.8 and angle of attack of 2°. However, a limited number of comparisons is given for other cases, like Mach number 0.8 with angle of attack 5° and Mach number 0.95 with angle of attack 2°. As can be seen the agreement is excellent for all Mach numbers and related angles of attack that have been investigated.

LIST OF SYMBOLS

x, y, z	Cartesian co-ordinates
b	semi span
q	flux per unit length
y_p	pressure surface
M	Mach number
α	angle of attack
ϕ	disturbance potential
η_a	correction factor for slot width
η_U	correction factor for axial velocity
FTI	Figure of Tunnel Interference

1. INTRODUCTION

All high speed wind tunnels at FFA can be operated with slotted or perforated walls at transonic speeds. One of these tunnels, T1500, is a modern wind tunnel recently taken into operation. However, for a long time FFA had only rather small wind tunnels and the possibility to run a relatively large (> 0.4 - 0.7% blockage) model in those tunnels became important. The question was in which sense a model designed for a large wind tunnel could be tested in a relatively small wind tunnel. Could the wind tunnel itself be modified to give less interaction with the model tested? Could a reliable evaluation be made for the wall interference effects?

There is a series of articles [1] on wall interference that have been published in Sweden until 1980. A new effort was initiated in the mid-80s in order to develop computational codes capable of estimating the wall interference, designing 'optimal' slots and finally, if possible, suggesting the necessary tunnel parameters in order to minimise the wall interference for the tested model. The work aimed mainly at improving the status of the FFA small wind tunnels but when the decision was taken to build the modern transonic wind tunnel facility, T1500, the developed methods were used for the design of the slots.

At an early stage of the research and development it was important to approach the wall interference problem with well tested and reliable computational method that could easily (and cheaply) be modified and run on a computer. This together with the requirement that the method could be used in the transonic range of Mach numbers caused the

Transonic Small Perturbation (TSP) method to be chosen.

2. COMPUTATIONAL METHOD

The physical model for the slot flow, schematically shown in Figure 1., is basically inviscid and based on a 2D cross-flow theory [2]. Two reduction factors, η_a for the slot width $a(x)$ and η_U for the axial velocity U, are used in order to correct for viscous effects in slot flow. These reduction factors are assumed to be constant and typical values used are 0.6-0.8 [3]. The slot flow equations [4,5] consist of two relations, one essentially based on the 2D cross-flow mass flux equation which determines the plenum pressure surface $y_p(x)$ and the other which gives the pressure difference across the slot in terms of the slot flux $q(x)$ per unit length, the slot width $a(x)$ and the plenum surface position $y_p(x)$. The slot flux q is a priori unknown and must be determined as a part of the total solution including the interaction with the interior test section flow generated in the wind tunnel.

The field equation used for simulation of the interior test section flow is given by the non-linear small perturbation potential equation:

$$(1- M^2)\, \phi_{xx} + \phi_{yy} + \phi_{zz} = 0 \qquad (1)$$

Here ϕ is the disturbance potential and M the approximate local Mach number. (x, y, z) is a fixed Cartesian co-ordinate system with x pointing downstream in the direction of the tunnel axis. Equation (1) is written in finite-difference form and solved by an over-relaxation procedure. On the walls between the slot strips, which are as many as the slots but wider, the normal velocities are given by the turbulent wall boundary layer displacement thickness and the actual wall inclination. No boundary layer has been evaluated so far for the wind tunnel test model.

On the slot strips a local slot boundary condition [4] is applied giving $\phi(x, 0, z)$ in terms of the slot flux (see Figure 2). The slot flux q is found assuming a mass flux balance for each slot and is evaluated in terms of the normal flow as computed from Eq.(1) and then integrated along the wall strip. It is corrected for the wall boundary layer.

3. DESCRIPTION OF THE TUNNELS

The wind tunnels used in this investigation were two high speed wind tunnels, T1500 and TVM500 at FFA. T1500 is a pressurised injector driven tunnel while TVM500 is a blow-down tunnel. T1500 has a square cross section of 1.5×1.5 m^2 and TVM500 of 0.5×0.5 m^2. Both tunnels are equipped with up to 4 slots on each wall. Pressure taps along the centre line of each wall are part of the instrumentation of both tunnels. The operational ventilation of the T1500 is at present 8.3%. The ventilation of the TVM500 tunnel can be varied up to 8.3% as there are several easily interchangeable slots that can be used. The 16 original slots provide the TVM500 tunnel with a ventilation of at most 4%, while the recently milled slots, copies of the slots of T1500, provide up to 8.3% ventilation. Active suction from the plenum chamber can be applied in both tunnels. A schematic drawing of the tunnels together with the position notations used throughout this paper can be seen in Figure 3.

It should be pointed out that the slots used were neither designed for the PT8-99 configuration nor any other large model. The slots have originally been designed for 'regular' size models and are simply scaled down from T1500 to TVM500 tunnel.

4. DESCRIPTION OF THE MODELS

For the B3LA configuration (an abandoned attack-trainer project from the late 70's), which can be seen in Figure 4, only total forces could be measured together with the pressures on the walls of the tunnel. Because the tail has not been simulated in the computations only Mach number signatures on the walls are compared. B3LA has been blocking around 0.6% in T1500 tunnel.

The PT8-99 model, see Figure 5, is one in the series of swept wings tested at FFA and has pressure taps at 4 different sections at constant $y/b/2$ on one of its wings, Figure 6. The model was blocking almost 0.2% in T1500 tunnel and more than 1.7% in the TVM500 tunnel. The tests in TVM500 tunnel have so far been limited to the recordings of the pressures on the two outermost sections of the wing and on the top and side walls of the tunnel. The ventilation of the tunnel was varied between 4.2% and 8.3%. 4.2% ventilation was obtained by creating solid side walls by closing the side wall slots. Two somewhat different shapes of slots have been tested for the two amounts of ventilation.

5. COMPUTATIONAL AND EXPERIMENTAL RESULTS

5.1 General

The computational method used is valid for small disturbances which means that only small angles of attack should be considered. When a small model (blocking around 0.5%), to be simulated computationally, is tested in a wind tunnel at small angles of attack then very high resolution in experimental data is needed in order to make the comparisons meaningful. The main attention when comparing experimental and computational results has been given to the pressures obtained at the centre line of each wall along the x-axis of the tunnel (see positions A, B and F in Figure 3).

The aim of the computations is to simulate conditions under which the configurations are tested in a wind tunnel. It is known that a higher Mach number can be obtained by either increasing the Mach number itself or increasing the suction by decreasing the plenum pressure. When suction is increased the Mach number curve is mainly moved to a higher level except for the limited region at the 'shock' where the 'shock' is moved somewhat along x-axes as demonstrated in Figure 7.

5.2 B3LA in T1500

One of the configurations tested in the wind tunnel T1500 at an early stage of the wind tunnel's existence was a B3LA configuration, which has a swept main wing and a tail. This configuration was blocking around 0.6% in the T1500 tunnel and the ventilation of the tunnel was 8.3%. The ventilation was provided by four identical slots on each wall of the test section.

In the computational simulations for the B3LA configuration in T1500 tunnel the main wing was located on the body at the same position as for the wind tunnel model but the tail was omitted.

Wall pressures have been recorded in T1500 tunnel for the B3LA configuration at Mach numbers 0.9 and 0.95 and several angles of attack. Figure 8 shows the Mach number signatures obtained experimentally and computationally on the centre of the side wall at Mach number 0.9 and at two angles of attack, 0° and 10°, while Figure 9 shows the same for Mach number 0.95.

As the computations have been carried out at Mach numbers and angles of attack which almost never coincide with the values obtained experimentally the adjustment of the Mach number level (by a constant value throughout the test section) for experiments has been performed for the results shown in both Figures 8 and 9. The original Mach number difference between the experimental and computational levels on the walls close to the entrance to the test section was small. The correction applied to the Mach number level was smaller than 0.01.

The agreement demonstrated in Figs 8 and 9 between the experimental and computed results for the B3LA configuration in T1500 is very promising.

Finally a computational comparison was made at a relatively large angle of attack of 10° for two different slots called **a** and **g** for the T1500 wind tunnel and the result can be seen in Figure 10. Slot **a** was the actual slot shape in the T1500 tunnel at the time B3LA was tested there.

5.3 PT8-99 in T1500

A limited test program was carried out in T1500. The model had been tested extensively earlier in FFA HT tunnel [6] which was a slotted octagonal high speed wind tunnel, and the model was blocking around 0.6% in that tunnel. The results were considered as almost free from the wall interference effects and the tests were supposed to confirm that fact as the model's blockage was only around 0.2% in T1500.

Figure 11 shows the comparison of the pressure coefficients at Mach number 0.8 and angle of attack of 2° on the wing as obtained experimentally in T1500 and computationally with the TSP-method at the free stream condition.

5.4 PT8-99 in TVM500

During the autumn of 1993 a series of tests have been performed with PT8-99 in TVM500 tunnel. The model can be seen in this tunnel in Figure 5. The ratio of the span of the configuration to the width, and height, of the tunnel was 0.8 and the blockage was more than 1.7%.

As the outcome of the tests in TVM500 tunnel was uncertain the computations were mainly limited to Mach number 0.8 and lower. Only small angles of attack were planned to be investigated mainly due to the large blockage of the model in this tunnel but also because of the limitations in the computational simulation (the TSP-method). Therefore, in this paper, the main emphasis is put on comparisons at Mach number 0.8.

Figure 12 shows the slots that are available at present for the TVM500 wind tunnel. The PT8-99 configuration has so far been tested with the two of these slots, denoted s1 and s2. In the same Figure 12 the position of the PT8-99 configuration relative to the slots can be seen. The size of PT8-99 is represented in right length to span scale while the width of the slots is not.

Figure 13 shows the comparisons at position B along the centre line of the top wall, see also Figure 1, between experiments and computations for Mach number signature for PT8-99 with four different tunnel wall configuration at $M_{\bullet} = 0.8$ and $\alpha = 2°$. It can be seen that the agreement is very good up to the maximum Mach number level while the differences vary depending on the slots used. The 'best' overall agreement is reached with 16 slots of the type s2, see Figure 12, and the 'poorest' with 8 slots of the type s1.

The results shown in Figure 13 call for a closer look at the slot flow conditions. Figure 14 is a plot of the computed slot fluxes for the slots number 2 and 4 on the top wall (see Figure 3) for all the cases shown in Figure 13. It can be seen that a flow from the plenum chamber into the test section exists in all slots on the top wall.

In Figure 15 the corresponding comparisons as in Figure 13 are made at position F on the centre line of the side wall. The overall agreement is excellent. The main discrepancies are to be found well behind the position of the model.

All computations for the PT8-99 model in TVM500 tunnel have been performed with a total number of 6×10^5 points covering the complete test section. Only a very few cases have been computed with 50×10^5 points. The Mach number distribution on the walls is almost unchanged when increasing the number of the computational points. However, the pressure distribution on the model itself is changed especially in the leading edge region as the suction peak is more pronounced in the computations with the finer mesh and is quite close to the suction peak obtained in experiments. This can be seen in Figure 16, where the results from the computations with the two meshes and from the experiments have been compared for two of the outermost sections on the PT8-99 wing.

The upper part of Figure 17 is showing Mach number distribution for Mach number 0.8 and alpha 5° at the entrance part of the tunnel at positions B and F (see Figure 3) for 16 slots of type s1. The lower part of the same figure is showing the corresponding distribution for the arrangement with 8 slots of the same type. From Figure 17 one can see that in the case of the solid side walls (8 slots) the Mach number is somewhat lower at the centre line of the side wall than at the centre line of the top wall. This difference is the same in experiments and in computations and indicates the existence of the Mach number gradient. This gradient is obviously created by the solid side walls in the wind tunnel.

In Figure 18 a Mach number signature is given for just one wall configuration, 16 slots of the s1 type, at a Mach number 0.95 and alpha 2°. The agreement is very satisfactory. A more thorough investigation for Mach numbers larger than 0.8 will be done in the near future.

Finally some attention has been paid to the possibility of correcting the forces measured by using the computed values. This investigation has only been performed at Mach number 0.8 and alpha 2°. In Table 1. below the relevant values from computations and interpolated values from experiments for lift coefficients can be found. The interference is quantified using relative numbers called Figures of Tunnel Interference. For lift it is FTI$_L$ as follows:

$$FTI_L = ((C_L)_t - (C_L)_f)/(C_L)_f \qquad (2),$$

where index t indicates tunnel data and index f unbounded free stream data. For experiments free stream means tests for PT8-99 in T1500 wind tunnel.

6. CONCLUSIONS

From the material presented in this paper it is seen that for angles of attack investigated (in some cases up to an angle of attack of 10°) good predictions can be made of Mach number signatures at the walls of the wind tunnel. That this was possible for a 'normal' size of the model and small angles of attack

has been shown earlier [7] but it is very encouraging to find such a good agreement for very large models, high Mach numbers and angles of attack around 10°.

Table 1. shows that perceptual quantitative corrections are almost the same for computations and experiments. This means that the corrections for the lift coefficient should be possible using the computations as a correcting tool. Through Table 1. it is easy to see that the 'best' - giving least interference - tunnel configuration is one with 16 slots of s2 type while the 'poorest' one is one with 8 slots (4 slots on each of the top and the bottom walls) of s1 type. One can now also see the correlation of large deviations from free stream values in Table 1. and the severe flow from the plenum chamber back into the test section as seen in Figure 12.

The Mach number gradient that appears in the wind tunnel with solid side walls, Figure 17, should be especially considered when testing large models.

7. ACKNOWLEDGEMENTS

8. REFERENCES

1.   Nyberg, S.-E., A Review of Some Investigations in the Wind Tunnel Wall Interference Carried out in Sweden in Recent Years, AGARD Fluid Dynamics Panel Meeting, Neubiberg, Germany, May 1980.

2.   Berndt, S.B., Inviscid Theory of Wall Interference, in Slotted Test Sections, AIAA J., Vol. 15, Sept. 1977, pp 1278-1287.

3.   Sedin, Y.C-J., Sörensen, H., Computed and Measured Interference in Slotted-Wall Test Section, AIAA J., Vol. 24, March 1986, pp 444-450.

4.   Sedin, Y.C-J., Agrell, N., Zhang, N., Computation of Transonic Wall-Interference in, Slotted-Wall Test Sections of Wind Tunnels, ISCFD, Tokyo, Sept. 1985.

5.   Agrell, N., Pettersson, B., Sedin, Y.C-J., Numerical Design Parameter Study for Slotted Walls in Transonic Wind Tunnels, ICAS-86-1.6.2, London, Sept. 1986.

6.   Torngren, L., Transonic Wind Tunnel Tests of a Swept Supercritical Wing-Body Model, PT8, FFA TN 1982-24, Stockholm 1985.

7.   Agrell, N., Pettersson, B., Sedin, Y.C-J., Numerical Computations and Measurements of Transonic Flow in a Slotted-Wall Wind Tunnel, AIAA paper 87-2610, Monterey, 1987.

Slot shape	No. of slots	Vent. [%]	Experiments C_L	FTI$_L$ [%]	Calculations C_L	FTI$_L$ [%]
Free stream - ref. value			0.1961	0	0.1931	0
s 1	16	8.3	0.2085	6	0.2033	5
s 1	8	4.2	0.2151	10	0.2104	9
s 2	16	8.3	0.1976	1	0.1926	0
s 2	8	4.2	0.2076	6	0.2028	5

Table 1. Lift coefficients for PT8-99 in TVM500 wind tunnel at Mach number 0.8 and alpha 2°.
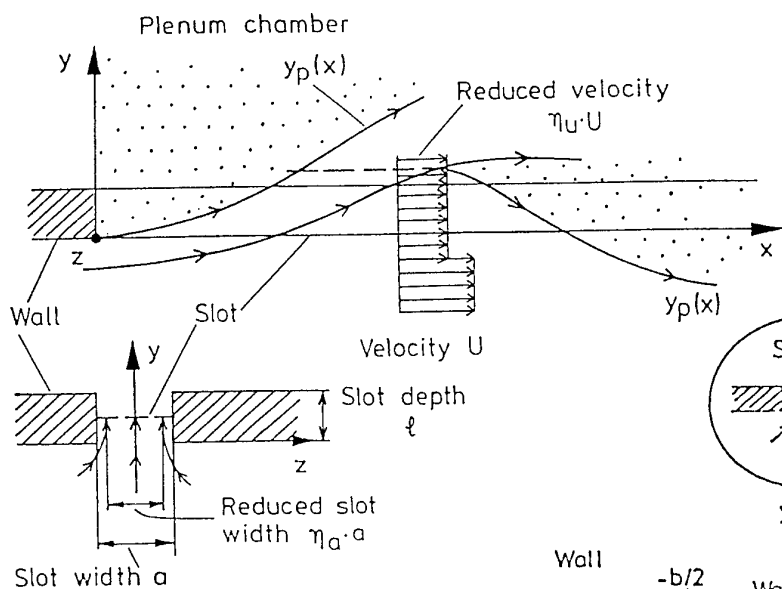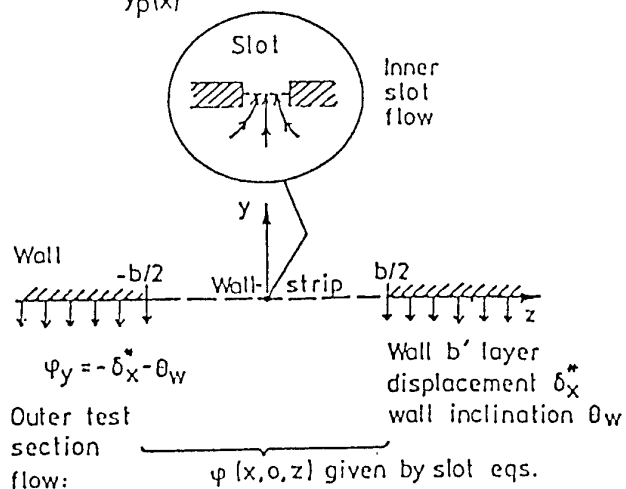
Figure 1. Slot flow model

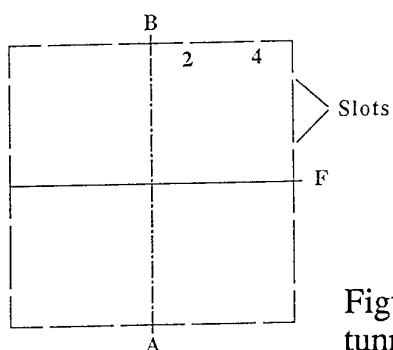Figure 2. Local slot boundary condition.

Figure 3. Schematic cross section of the wind tunnels. Pressure measurements at A, B and F.
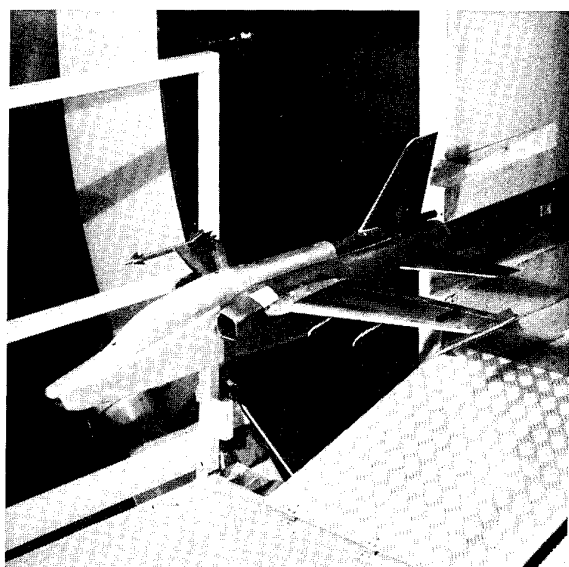

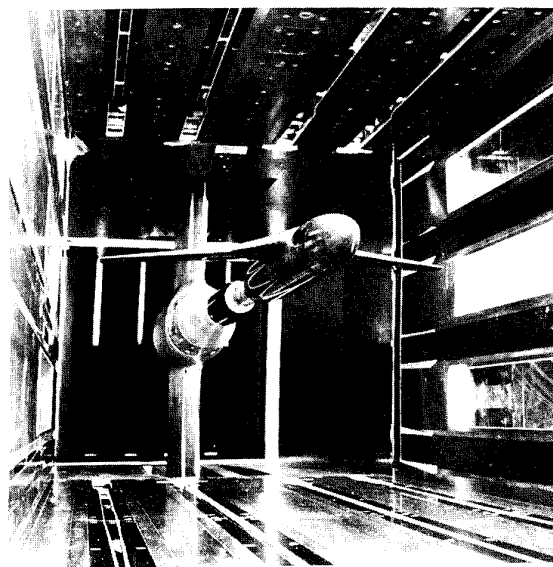Figure 4. B3LA prepared for testing in T1500 wind tunnel.
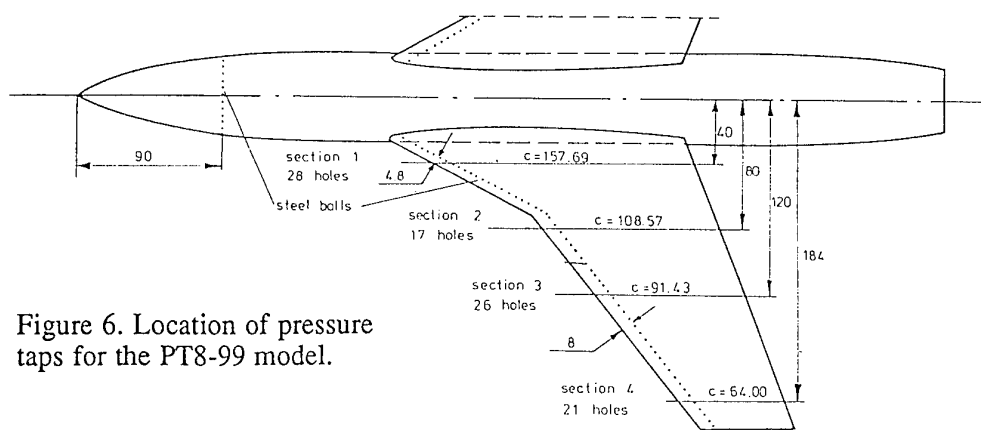

Figure 5. PT8-99 in TVM500 wind tunnel.

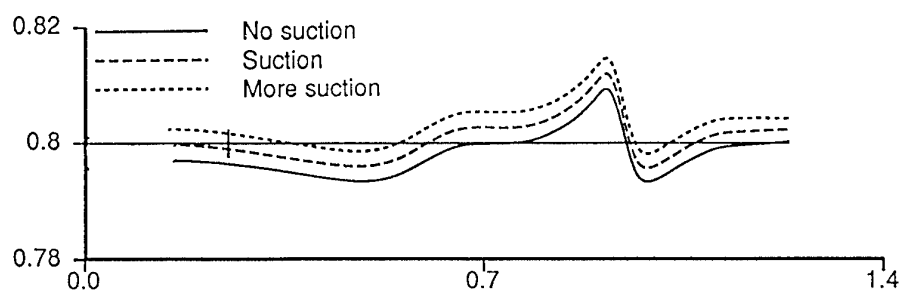Figure 6. Location of pressure
taps for the PT8-99 model.

Figure 7. Suction effect on the Mach number signature at the side wall.
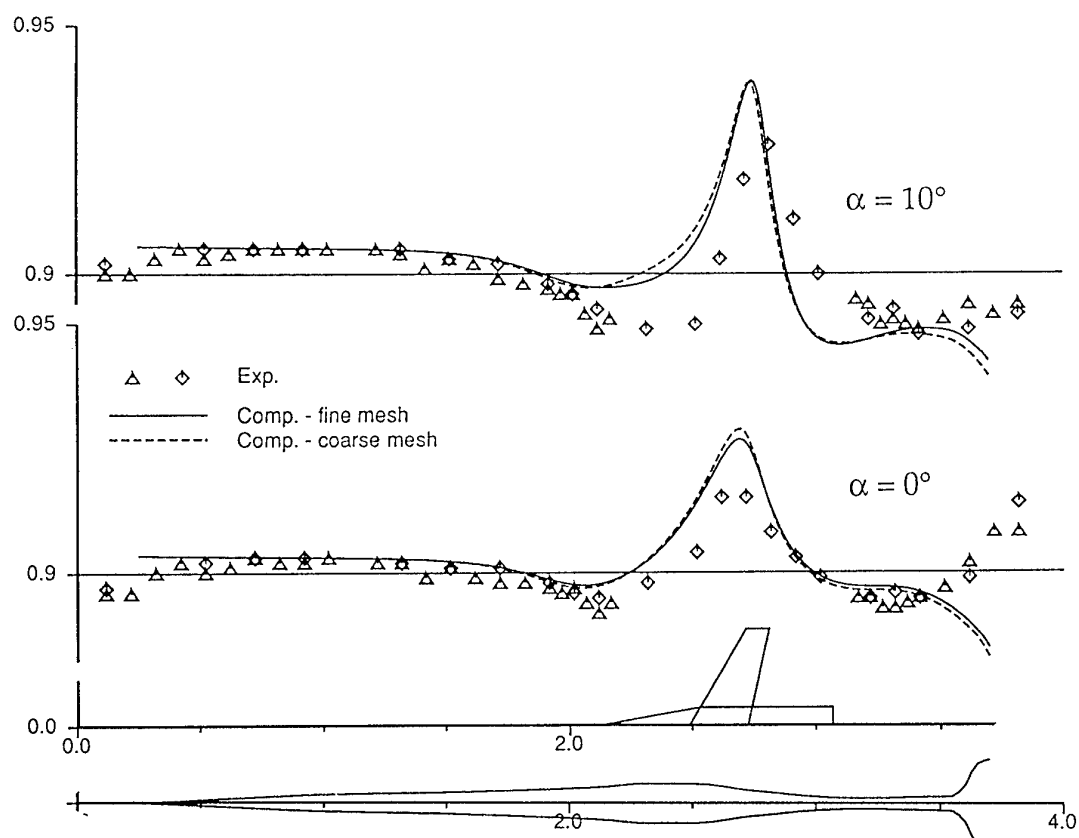

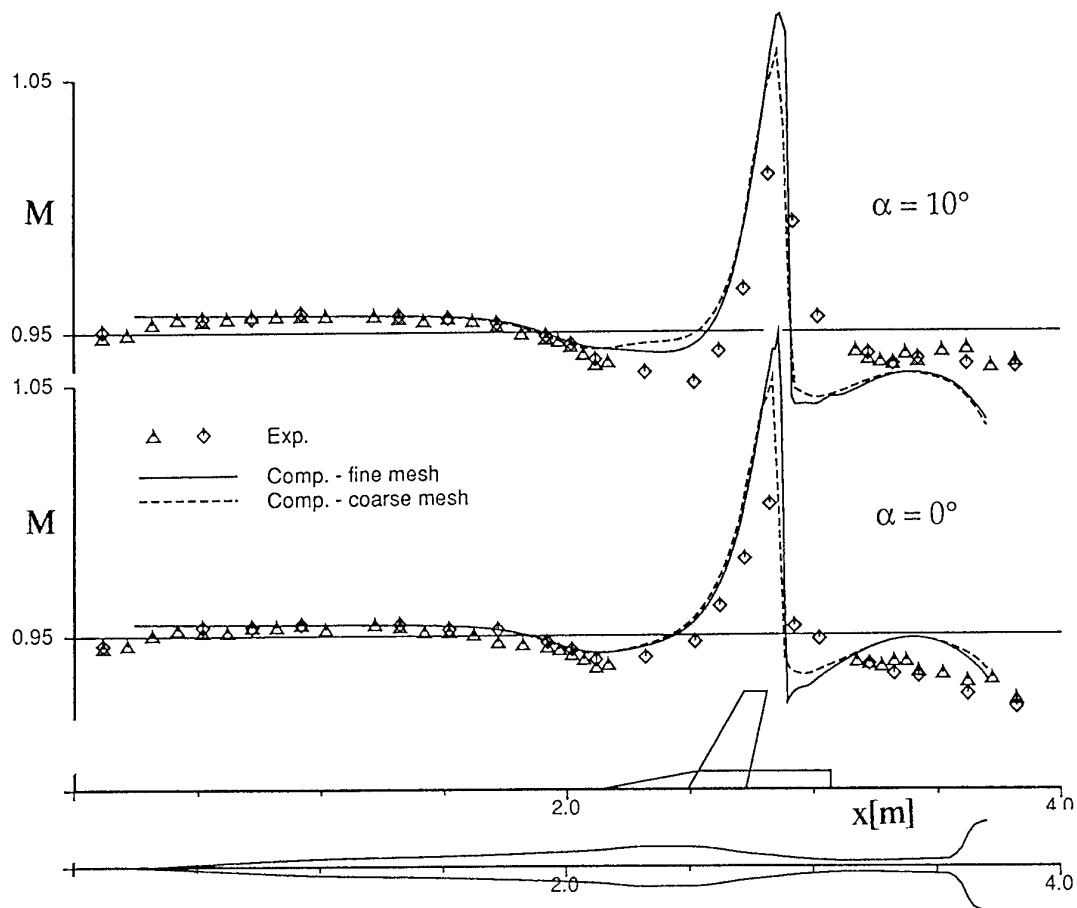Figure 8. M(x) at position F for B3LA at M_∞ = 0.9 and α = 0° and 10°.

Figure 9. M(x) at position F for B3LA at $M_\infty = 0.95$ and $\alpha = 0°$ and $10°$.
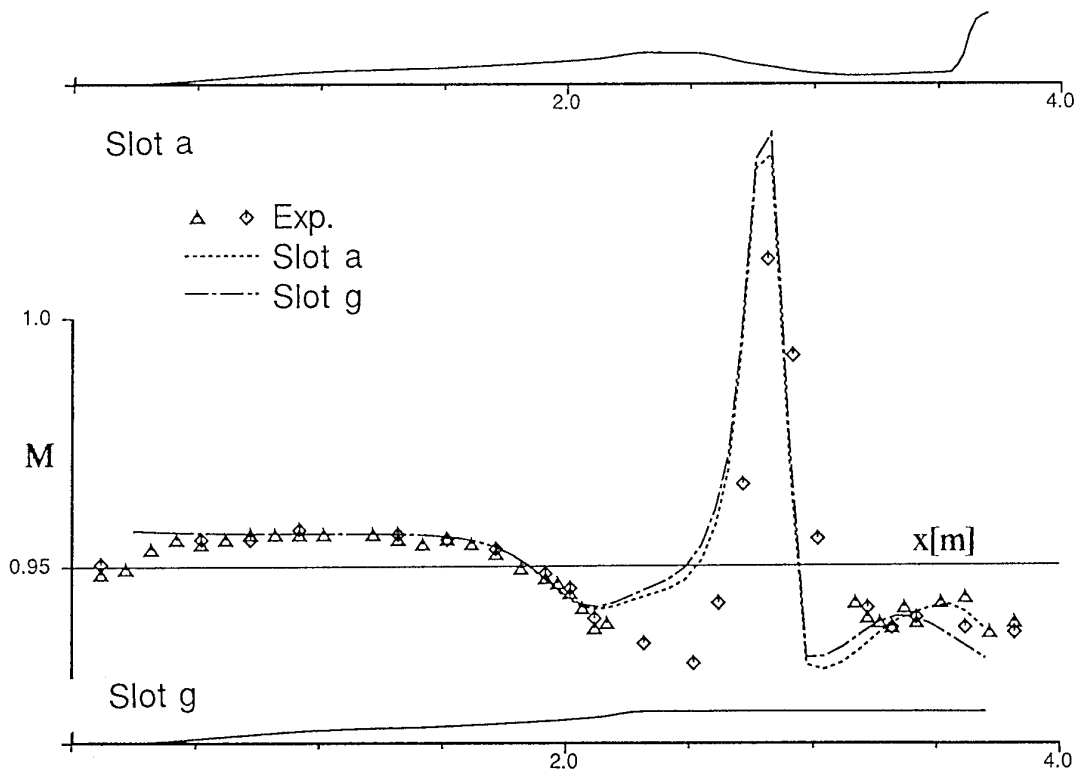
Figure 10. M(x) at position F for $M_\infty = 0.95$ and $\alpha = 10°$ - different slots.
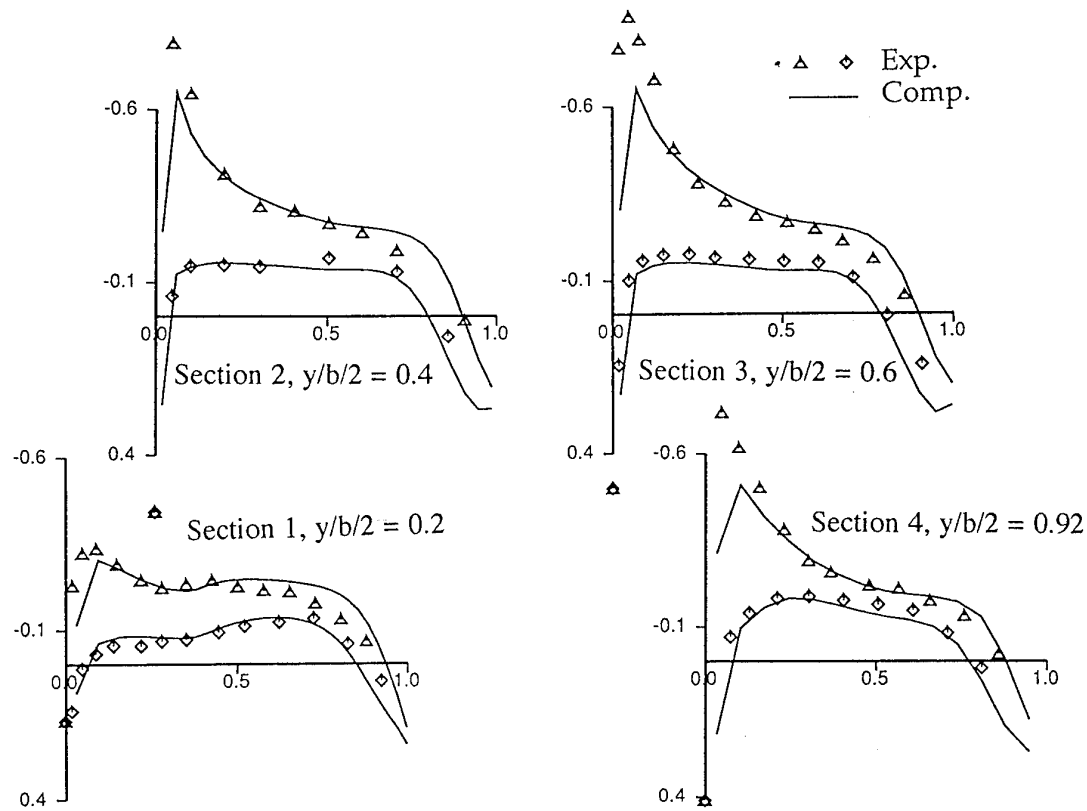
Figure 11. Pressure distribution for PT8 in T1500 at $M_\infty = 0.8$ and $\alpha = 2°$.
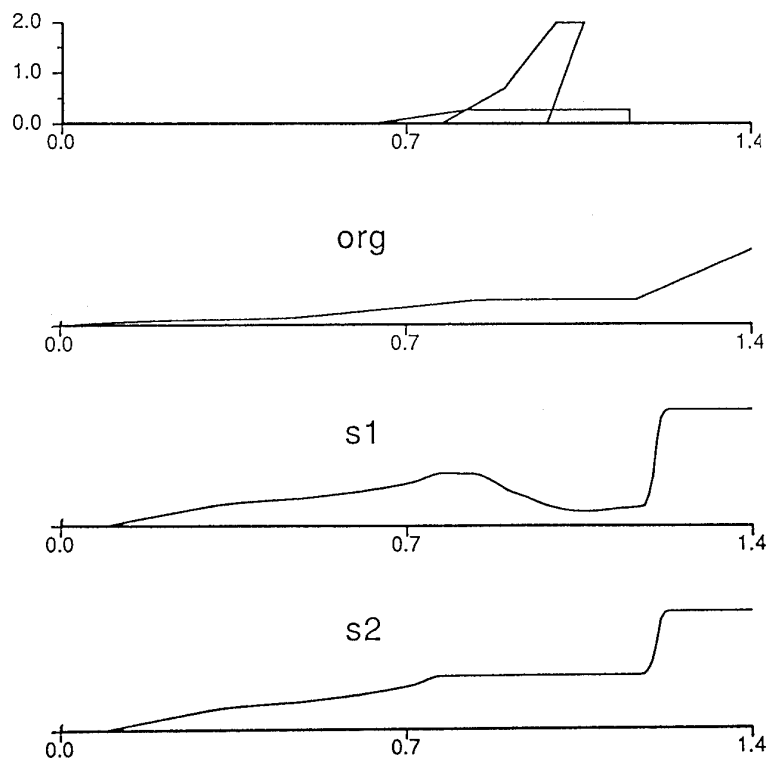
Figure 12. Different slots and PT8-99 model's location in TVM500 wind tunnel.
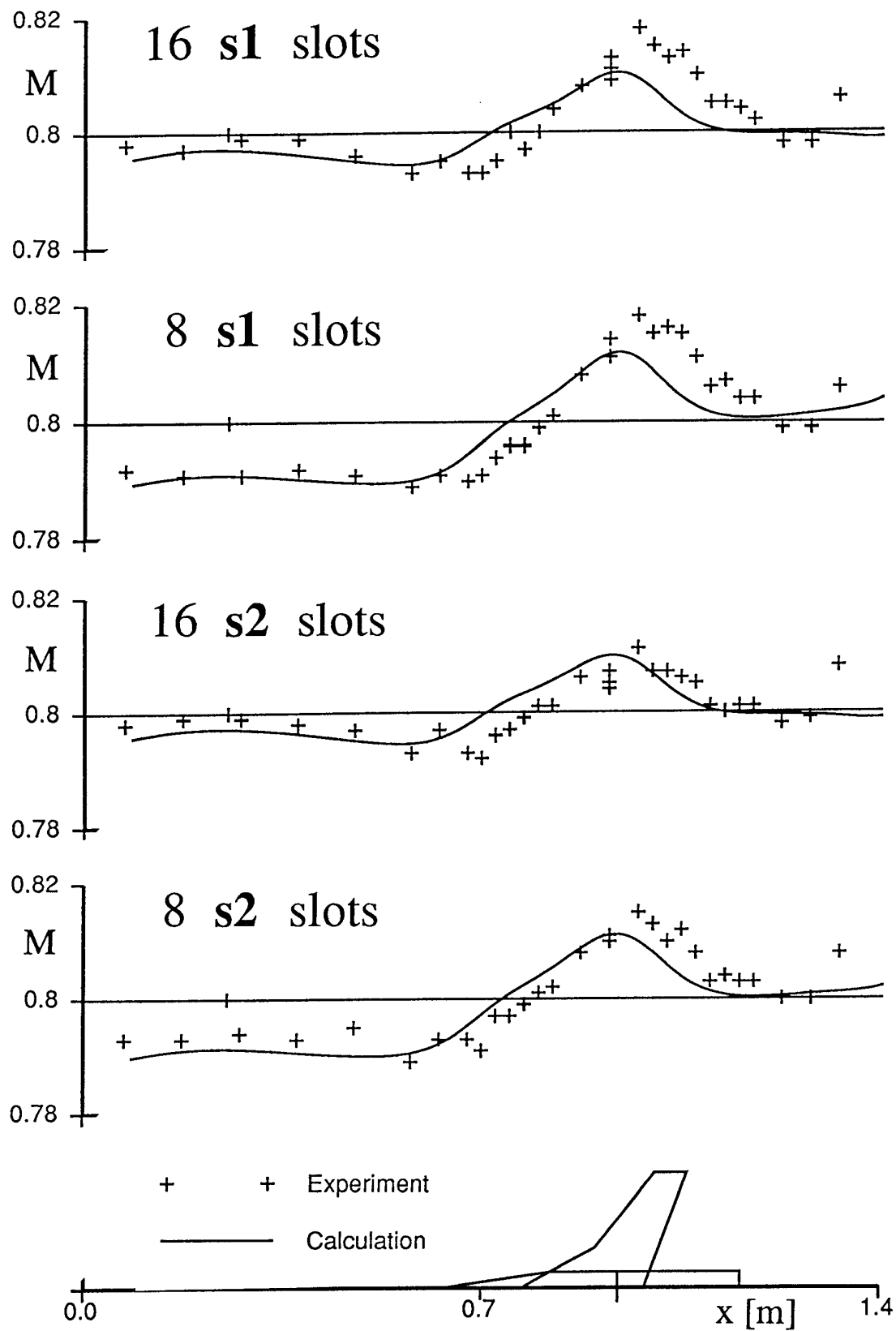
Figure 13. M(x) at position B for PT8-99 in TVM500 at $M_\infty = 0.8$ and $\alpha = 2°$.
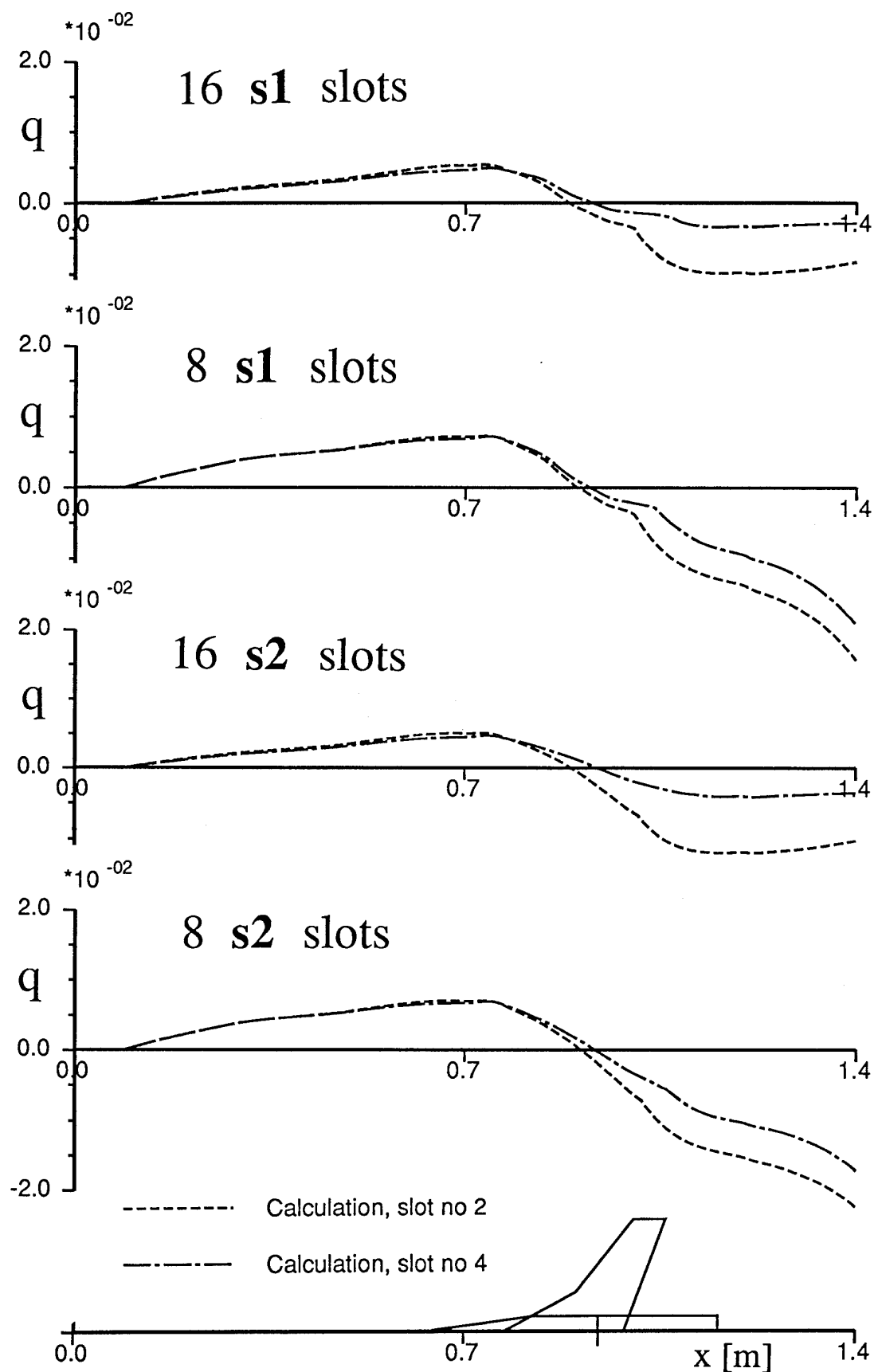
Figure 14. Slot fluxes for slots on the top wall for PT8-99 in TVM500 at $M_\infty = 0.8$, and $\alpha = 2°$.

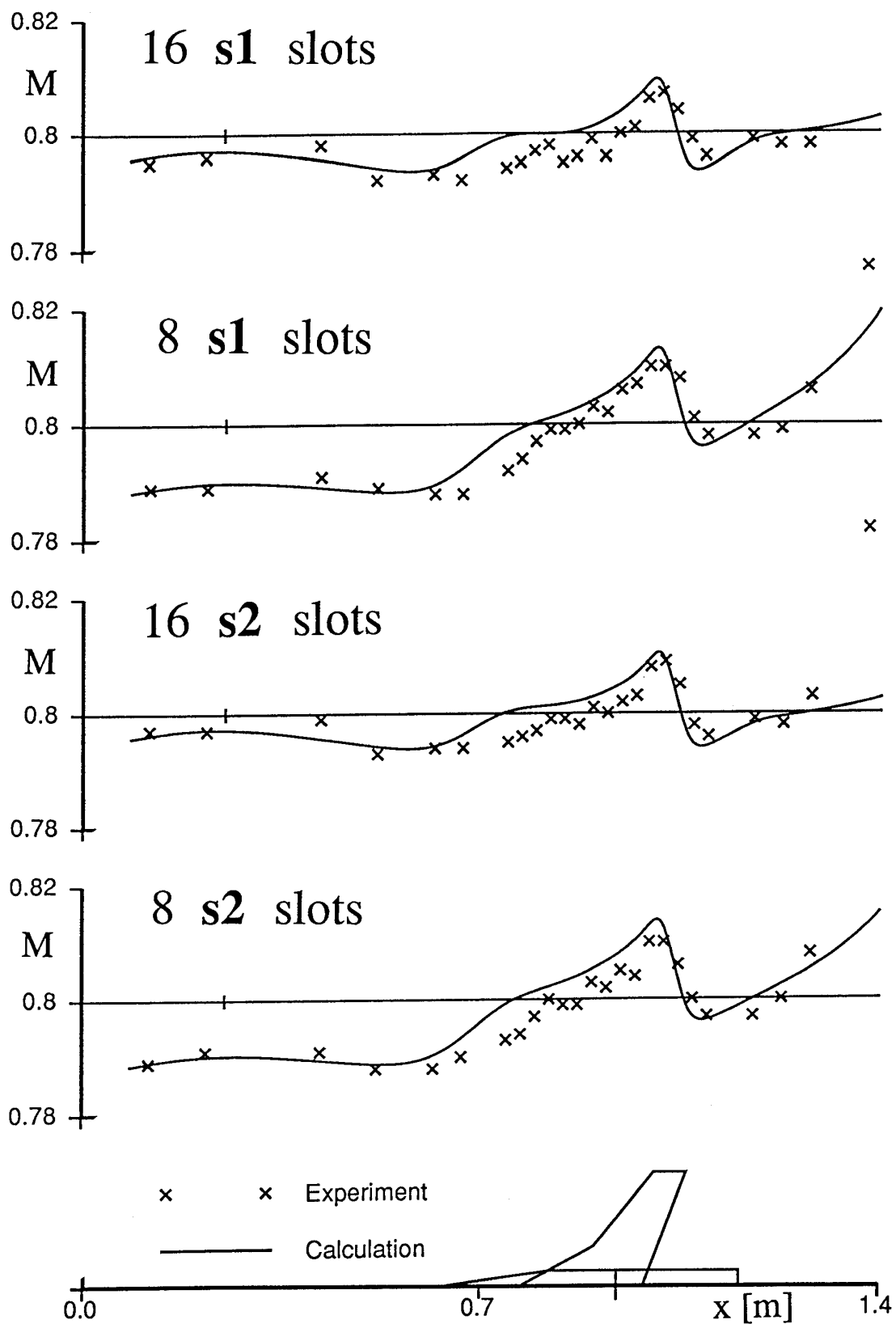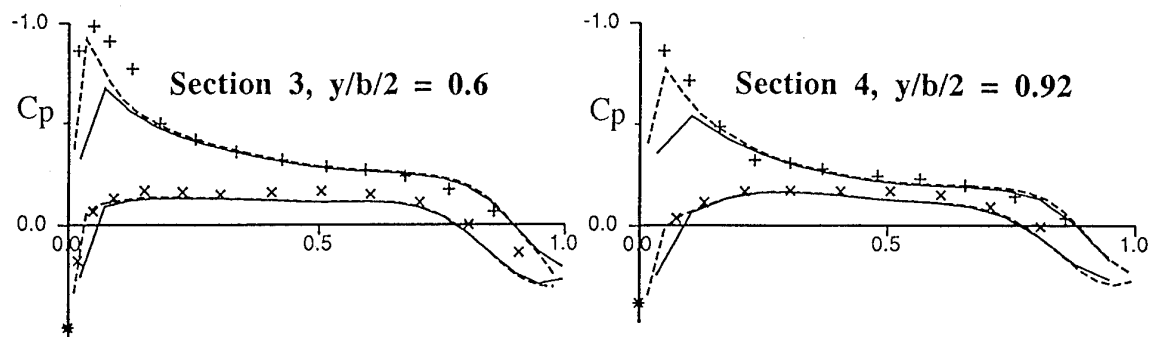Figure 15. M(x) at position F for PT8 in TVM500 at $M_\infty = 0.8$ and $\alpha = 2°$.

Figure 16. Pressure distribution for the two outermost sections of PT8-99
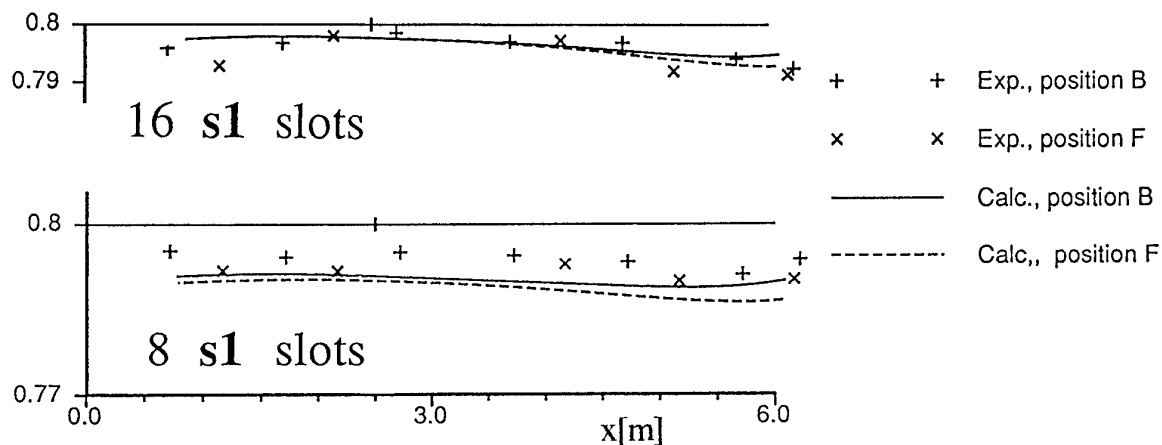in TVM500 with 8 slots of s1 type

Figure 17. M(x) at the entrance to the TVM500 tunnel at positions B and F
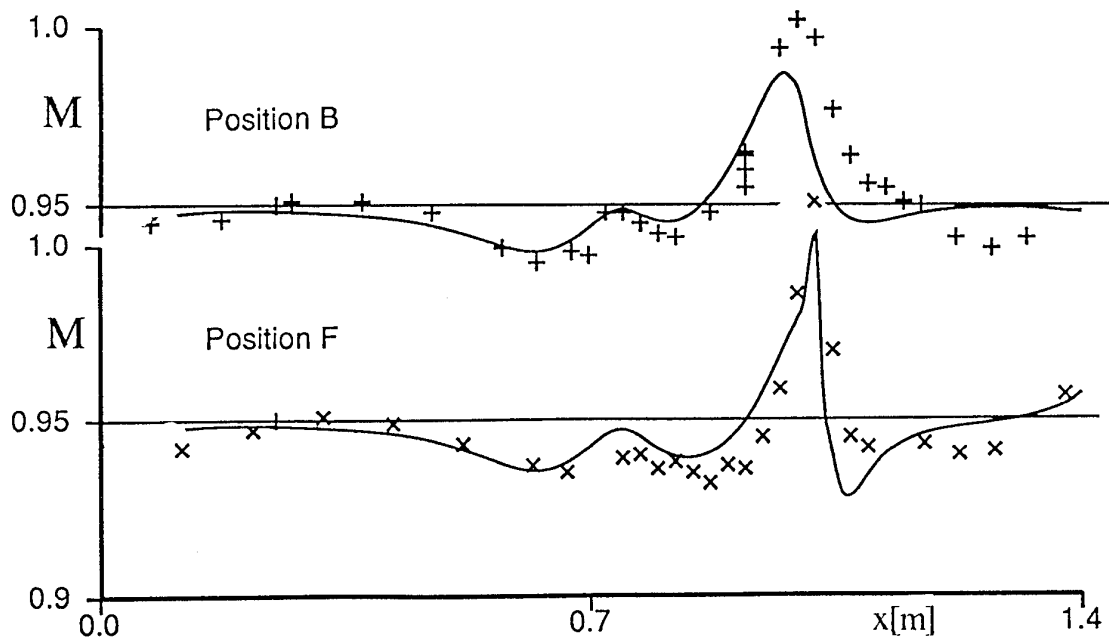for PT8-99 and $M_\infty = 0.8$, $\alpha = 5°$.

Figure 18. M(x) at positions B and F for PT8-99 in TVM500 tunnel with
8 slots of s1 type and at $M_\infty = 0.95$ and $\alpha = 2°$.

ESTIMATING WIND TUNNEL INTERFERENCE DUE TO VECTORED JET FLOWS

Dr. R. K. Nangia

Consulting Engineer
Nangia Aero Research Associates
Maggs House,
78-Queens Road,
Bristol, BS8 1QX, UK

SUMMARY

An important consideration in the testing of aircraft models with vectored jets is the allowance to be made for wind tunnel interference on jet flows. Depending on the cross-section dimensions, the wind tunnel interference, can be particularly severe at high incidences or for high jet velocities and large jet deflections. For assessment of these effects, either "Wall pressure signature" or "Direct" methods can be used. The wall pressure methods, although requiring dedicated instrumentation, have the advantage that model flow simulation is not required. The direct methods allow calculations of interference prior to the tests and can therefore assist in optimisation of model geometry for a particular wind tunnel.

A "Direct" method for estimating wind tunnel interference due to jet flows is described. A semi-empirical model of the jet plume, imaged in walls has been used to represent the tunnel constraint. Comparisons with results from a "wall pressure signature" method are very encouraging.

The results emphasise the large magnitudes of effects which can arise, particularly in experiments with 2, 3 or 4 vectoring nozzles on multi-surface aircraft configurations. For 4 nozzles with jet velocity ratio near 10, the vertical velocity flow angle can be near 6°- 8°.

The present technique offers the capability of guiding the design of acceptable experiments, or for checking the validity of existing information. Several aspects of future work have been proposed.

1. INTRODUCTION

The accurate prediction of vectored jet-induced effects on wing and wing+body+tail (or canard) configurations, Fig.1 (Refs.1-3) during transition phase and manoeuvres constitutes an important aspect in the understanding, design, control and operation of such aircraft.

In the past, progress on this subject has been relatively slow because of the evident need to proceed mainly on an experimental basis and the high cost and time factors implicit in wind tunnel tests or full-scale trials. The experiments have ranged from exploring fundamental jet flows to more specialised ones investigating a particular configuration. The current project scene is naturally more "paced" and it focusses on cost and time reductions, emphasising the need for reliable predictive techniques. Extended time-scales could allow changes in emphasis and requirements leading to several stages of configuratuion evaluation.

© *Dr. R. K. Nangia 1993*

The main features of a jet in arbitrary cross-flow and neighbouring surface interference have been appreciated and described by several workers for a long time now. A jet issuing from a surface deforms under the cross-flow forming counter-rotating vortices (Fig.2). The dominant features are, therefore, the entrainment by the jet shear layer and the concentration of vorticity on the downstream side of the jet.

As yet, the detailed vectored-jet models using CFD field (Navier-Stokes) formulations have not reached sufficient maturity to become tools for routine design and analysis. There is a need, therefore, for an "effective" (in time, cost and flexibility) semi-empirical jet model which can be used to assess, in the first instance, the jet-induced effects on aircraft configurations and secondly, give a reasonable approximation to the tunnel constraint effect.

In this context, the author has been involved in analysis of experimental data and setting up a theoretical model to enable an understanding and assessment of the main flow effects on general 3-D configurations. A semi-empirical modelling of the jet is used within the framework of subsonic singularity methods. This enables jet interference over the configuration to be calculated and encouraging agreement with experimental data has been found. Highlights of the programme were reported at the AGARD FDP 72nd meeting held at Winchester, UK in April 1993, Ref.4.

A recurring and important consideration in the testing of aircraft with vectored jets and subsequent validation, is the allowance to be made for wind tunnel interference on jet flows. Depending on the cross-section dimensions, the wind tunnel interference can be particularly severe at high angles of attack or for high jet velocities and large jet deflections. For assessment of these effects, either "Wall pressure signature" or "Direct" methods can be used. The wall pressure methods have the advantage that model flow simulation is not required. The direct methods allow calculations of interference prior to the tests and can therefore assist in optimisation of model geometry for a particular wind tunnel.

Emphasis in This Paper & Topics Covered

The primary objective of the work reported is to develop and evaluate a "direct method", that gives, *a priori*, the tunnel constraint and blockage to be included in the experimental analysis. The direct approach has been assessed against an existing indirect method. This led to a secondary objective of the programme: to improve the understanding of the jet flows and produce, therefore, a better semi-empirical jet model.

Overall, the emphasis of this paper is on predicting the wind tunnel jet interference effects rather than dwelling on the fine detail of the jet empirical model which has been progressively developed with improvements arising from experience of continuing applications. A Fortran77 computer programme embodying the techniques has been written. This is applicable to wind tunnels of rectangular or near rectangular cross-sections.

2. DIRECT & WALL PRESSURE SIGNATURE METHODS FOR TUNNEL CONSTRAINT CORRECTIONS

2.1. Direct Methods of Estimation

The most well known attempt to directly estimate the wall interference on jets has been the Vortex-Source-Doublet (VSD) method of Hackett (Ref.5). This uses an empirical flow model for a round jet in cross-flow based on the work of Fearn and Weston (Refs.6-9). Fig.3 shows the main features and assumptions. The source and doublet terms are for the blockage effects in the tunnel. Full details of the method are not available and it is open to conjecture as to how the method will cope with flows in which there is a significant interference between the jet and neighbouring lifting surfaces. The principle of the method is, however, worthy of further development.

It follows that direct methods do enable experiments to be designed and planned with a good idea of the practical flow limits i.e. when the corrections become large and unacceptable.

2.2. Wall Pressure Signature Measurements

It has been recognised that wall-pressure measurements can assist in the calculation of wall interference in solid-wall tunnels and several methods have been proposed. Ashill and Keating (Ref.10) mention that these methods may be classified into two categories; one requiring the simulation of the model perturbation flowfield and needing a relatively limited number of static-pressure measurements at or close to the walls ("model representation") and the other not requiring a model representation but calling for knowledge of two components of flow velocity at the outer boundary ("two-component"). These components are that normal to the boundary and that in the streamwise direction. Of the two categories, the "two-component" appears better suited for low-speed wind tunnels, mainly because model representation is not required and this is clearly an advantage for the substantial range of complex flows commonly encountered. Moreover, for tunnels with solid walls and "thin" wall boundary layers, the outer boundary of the "two-component" methods may be taken to coincide with the tunnel walls and the normal component assumed to be zero. Hence only the streamwise component is required for tunnels of this type, and this component can be inferred from static-pressure measurements at the walls.

Ashill and Keating have applied the "two-component" technique to simple jets in cross-flow with some success in the DRA 13x9 wind tunnel. They mention that the number of pressure measurements required is not "excessive" (115 are sufficient).

2.3. Usage of Corrections

In practice, compared with "direct" methods, there may be some reservations to the use of wall pressure methods since the latter involve dedicated computer and instrumentation and although the number of measurements are not excessive, the extrapolations downstream are extensive.

In practice, a prior knowledge of jet interferences is required for sizing models for wind tunnel experiments which emphasises the need to develop the "direct" methods.

3. BRIEF DESCRIPTION OF APPROACH

The aim is to provide velocity flowfield and constraint corrections at a series of (desired) points in the wind tunnel test section. The proposed corrections are to be based on one isolated jet. This is not a great restriction for an aircraft model application, since the wing does not influence the jet very much and the wing influence and measured lift is accounted for by the usual constraint factors. Wing interaction on the jet-jet interferences are small and do not influence the overall momentum change so that the **correction to the correction** is minute.

A convenient simplification is that we use a pre-specified path for the constrained jet in the wind tunnel, avoiding iteration. This is reasonable as we are not considering the actual effects of jet impingement on the walls.(MEP)

Existing information, model and wind tunnel data are used for validation of the model. In addition, the position of impingement of the jet is calculated on the basis of an unconstrained jet. This allows an assessment to be made if the impingement is likely to upset the flow in the tunnel or if it is too close to the jet nozzle, questioning any meaningful calculations with simple images representing the wall constraint.

A semi-empirical model of the jet plume for free air (Ref.4) is the starting point before considering the tunnel wall constraint effects.

3.1. Jet Model in Free Air

For building up the jet model (Ref.4), the basic proposition is that the cross-flow momentum is transferred to a streamwise vorticity in a gradual manner, releasing the volume of air as an expiration. The strength of the jet is modelled with doublets for lifting effects and momentum changes, sources to represent the volume displacement of the injected mass flow and sinks to represent the jet plume. The vortex path is described empirically.

A re-examination of data on the jet plume (Jordinson, Ref.11, Fearn and Weston, Refs.6-9) has led to a formulation of a semi-empirical jet model depicted in Fig.4. This takes into account the work of Keating (unpublished work at RAE, 1989), Bradbury (Ref.12), Kuchemann (Ref.13), Smy & Ransom (Ref.14), Hackett (Ref.5), Wooler et al (Ref.15), Ashill & Keating (Ref.10) and others (Refs.16, 17, 18). As emphasised in Ref.4, the experience suggests that the applicability of the model is in "practical" geometries where the neighbouring surface is about one jet diameter away from the nozzle. This does not, however, preclude cases where this may not be entirely satisfied; because the effects are localised near the nozzle. As experience builds up, limiting of induced velocities can be introduced. Ref.4 also considers other qualifications of the empiricism e.g. neglecting the local viscid interactions present upstream and downstream of the jet.

A line doublet located along the vortex-line of the jet gives a circular displacement surface with the stagnation lines similar to those found in experimental data (Fearn and Weston, Refs.6-9) as

shown in Fig.5. The model therefore implies the imaging effect of the flat plate. However, in relation to the approximations involved in setting up the basic model of the jet, the effect of the images is relatively small.

For a jet of diameter D and velocity ratio $R = V_j/V$ issuing normally ($\Theta_{j0} = 90°$) from the nozzle face at the origin, the jet vortex path (Fig.4) is given by adapting the Jordinson (Ref.11) cosh formula:

$$(x/D).F/R^2 = \cosh[(z/D).F/R^2] - 1 \qquad (1)$$

The scaling factor F is taken as 10 for R near 8. Fig.6 shows jet vortex paths for different jet velocity ratios R, $\Theta_{j0} = 90°$. Different values of F may be substituted for improving the correlation with experiment at different values of R. The factor F can be varied to describe the jet path.

For the jet issuing at $\Theta_{j0} < 90°$, the jet path can be derived, imagining a virtual jet origin ($\Theta_{j0} = 90°$) displaced forward from the real jet origin ($\Theta_{j0} < 90°$).

Several analytical Forms for the doublet strength $\mu_T(\Theta_j)$ were investigated. As an example, Forms 1 and 2 are depicted in Fig.7. Experimental results from papers by Fearn et al and Thompson are also indicated. The Form 2 agreeing more closely with Fearn and Weston results was considered more plausible and the doublet strength μ_T was generalised in terms of the jet parameters: D and Θ_j. Alternatively, numerical forms for the doublet strength may be used.

To introduce the source effects, we need, at the nozzle origin, a source σ_{v0} which is a function of nozzle area and $\cos\Theta_{j0}$ plus a line of sinks along the vortex path (distance along jet vortex curve: s) of strength $\sigma_v(\Theta_j,s)$ and an allowance for entrainment effects.

To fit the beginning and end of the displacement flux ($\Theta_{j0} \leq \Theta_j \leq 0$), a plausible (but unproven) expression for the displacement flux, m, (excluding entrainment) is of the form:

$$m \text{ (equivalent at } \Theta_j) = A V \frac{R \cos\Theta_j}{R \cos\Theta_{j0} + \sin\Theta_{j0}} .$$

This can be related to the elemental source strength $\sigma_v(\Theta_j,s)$ by differentiating along the vortex curve of the jet (variable s).

For an axial jet ($\Theta_{j0} = 0°$), the doublets disappear and a source strength at the jet origin σ_{v0} remains. There is an entrainment of air into the jet stream represented by a long string of sinks. An example of these effects in a wind tunnel is given in Ref.10. In free air, however, there is a lack of suitable information.

The elemental sources σ_v along the jet vortex path are not easy to integrate in an analytic manner and a numerical discretisation technique is required.

For the R = 8 jet, Fig.8 illustrates the effect of varying jet deflection angle Θ_{j0} on the streamwise variations of the jet parameters: height, Θ_j , doublet strength μ_T and source strength σ_v. The source term σ_v depends strongly on the variation of Θ_j with respect to s. Consequently this term decreases sharply with decreasing jet deflection angle Θ_{j0}. The term is appreciable for jet deflection angles Θ_{j0} between 75° to 90° but very small for $\Theta_{j0} < 75°$. The σ_{v0} term is also small for relatively small jet nozzles and for Θ_{j0} near 60°.

Early Validation - Pressures Induced Due to Jet on Flat Plate

The velocity (cartesian components: u,v,w in x,y,z system) induced at a general point in space due to doublet and source distributions along the jet can be written following the potential flow equations derived in a standard text such as Ref.19.

For early trials, a suitable test case was the prediction of C_p contours induced on a flat plate due to a jet issuing normally ($\Theta_{j0} = 90°$).

Assuming that the vertical velocity induced by the jet is cancelled by its image in the flat plate, the total C_p follows by doubling up the expression for C_p from the non-dimensional velocity components u and v calculated for one jet as:

$$\text{Total } C_p \text{ (2 Jets)} = 2 C_p \text{ (1 jet)} = 2 (-2u-u^2-v^2).$$

The C_p contours (Fig.9) from the present doublet jet model have been compared against Fearn's experimental data (Refs.6-9). It must be mentioned that this comparison is really an extreme case and a rather critical check of the theoretical model since we are estimating the effects due to a jet which is not displaced from the surface and high induced velocities are implied (C_p near -4.0 at the edge of the nozzle). Further, wake effects of the jet on the flat plate surface are also present.

There is, overall, a fair to good agreement between the theory and experiment over the region of the flat plate where the jet and surface boundary layer interaction can be considered minimal (i.e. over a 135° sector measured from the upstream direction) The agreement is particularly good for low values of R when the contours are relatively "asymmetric" about the spanwise axis. At higher R, the contours tend towards "symmetry" about the spanwise axis as the jet vertical extent increases. The predictions are once again acceptable for large R and away from the jet and surface boundary layer interaction zones.

These induced C_p comparisons, as well as the favourable comparisons on jet stagnation lines, have given confidence to pursuing further work. If necessary in the future, improved correlations between theory and experiment for given R may be obtained by varying the factor F. In the current work, we are concerned with "practical" flows where the jet nozzle is displaced from the wing plane by one or two nozzle diameters.

3.2. Jet Model with Wind-Tunnel Constraint

Next we need a suitable model for the jet geometry under tunnel wall constraint. The jet deforms due to the presence of the wall prior to touching or impingement at the wall. For high jet strengths, and when the jet touches or impinges on the walls of the tunnel, the flow pattern becomes complex with rolled-up vortex sheets. If the impingement angle is less than 30° to the normal then a "scarf vortex" occurs.

Since the jet model refers to the vortex path and that the accuracy of the constraint calculated will deteriorate to an unknown extent when a scarf vortex occurs; a distorted vortex path is used for the images, with only small errors likely, as long as the impingement is far downstream in the test section.

To account for the distortion effects, z is replaced by z' in the "cosh" Equation (1) describing the jet path:

$$(x/D).F/R^2 = \cosh[(z'/D).F/R^2] - 1 \qquad (2)$$

From empirical argument and experimental observations, z' is:

$$z' = z/[1 - G z^2/h^2] \qquad (3)$$

where

h represents the distance of the nozzle jet plane from the wall.

G is a constant that defines the limiting distance from the wall.

The value of G dictates the limiting height z_{max} in Equation (2) as:

$$z_{max}/h = 1/\sqrt{G}. \qquad (4)$$

Asymptotic distance away from the wall is given by:

$$h_{wall}/h = (1 - 1/\sqrt{G}) \qquad (5)$$

Choosing a typical value for G = 1.25, gives z_{max}/h of the order of 0.9. Fig.10 illustrates the principle.

Equations (2) to (5) then provide the z - x relationship for the vortex path of the jet as an image in the walls and not a representation of the jet at the wing. The height z remains less than h. As h becomes large, z' tends to z.

Jet Deflection Θ_{j0} less than 90°

For the jet issuing at angle Θ_{j0} less than 90°, the jet path can be derived on the principle that asymptotic distance away from the wall, Equation (4), is maintained. The analysis (Fig.11) is enabled by imagining a virtual origin of the jet (Θ_{j0} = 90°) displaced from the actual jet origin (Θ_{j0} < 90°). A solution is found by iterating for a corresponding value for G to give the same h_{wall}. For a given h, G reduces as Θ_{j0} decreases.

Impingement on a Wall

Since the images in the wall do seem to influence the jet path substantially, it is easy to predict the impingement point for a single jet and the computer programme produces a warning of both the position of the impingement point and when the "scarf vortex" occurs. "Harder" warnings are generated if the impingement occurs too near the jet nozzle which would indicate flow breakdown in practical situations more akin to tests in ground proximity on VSTOL aircraft.

The present technique enables simplification of the images of the jet. Nevertheless a problem for deeper analysis has been posed. The present model will therefore need to be extended with a suitable modelling of the wall impingement flow field.

Representing the Jet

As for the free-air case, the jet is represented by doublets for lifting effects and momentum changes, sources to represent the volume displacement of the injected mass flow, and sinks to represent the jet plume. Since the images are well displaced from the region of interest in the tunnel, the actual form of the images is not as critical as the problem of wing-jet interference covered in Ref.4.

3.3. Representing Tunnel Walls

There are two choices for representing tunnel walls; the first one relies on a vortex lattice network representing the walls while the second one uses images of the jet in the walls. The first one is more general and can be adapted to different types of wind tunnel cross-sections. The second one is perhaps more expedient but relies on tunnel cross-sections in which image locations can be predetermined. The levels of images to be used can be one or two or more. There is a reasonable background on both these choices in the literature. The consensus is that predicted results with both techniques are essentially equivalent, provided certain conditions are fulfilled e.g. reasonable panelling is used in the vortex lattice network and the images are properly organised for the imaging technique. For the present work, in the interests of simplicity, the choice adopted was the latter one i.e. using images to represent rectangular cross-section wind tunnel.

The image locations can be selected by specifying the number of levels in y and z directions. The periodicity of the images is $2z_t$ for the z direction and $2y_t$ in the y-direction, as shown in Fig.12. Thus for the nozzle located at spanwise dimension: a and height: b measured from the centre of the tunnel, the images lie along:

$$a,(2y_t-a),(-2y_t+a),(4y_t-a),(-4y_t+a) \ldots(n_y \text{ images})$$

and

$$b,(2z_t-b),(-2z_t+b),(4z_t-b),(-4z_t+b) \ldots(n_z \text{ images})$$

Convergence studies based on velocities induced due to images of the jet have shown that because the jet flowfield lies in essentially one portion of the wind tunnel cross-section, n_y is to be an odd integer and n_z an even integer. The integer n_z being even, the doublet strength of alternate levels are either up or down in pairs. The rate of convergence as n_z is increased is then very rapid. The source images are not "handed" (directional) but converge more slowly being an inverse square function (not an inverse cube).

To help with convergence with respect to increasing n_y and n_z , bearing in mind, the potential flow far-field considerations (Ref.20), two velocity correction terms are required. The first one is related to a continuous sheet of sources required to be placed outside the grid of images in the manner pioneered by Glauert. The second term refers to a balancing sink at infinity related inversely to the cross-section of the wind tunnel.

An empirical expression for the flow entrainment into the jet is introduced as a function of jet angle. Entrainment increases as jet angle decreases or tunnel cross-section size increases (Ref.20).

4. VALIDATION OF JET MODEL IN "FREE-AIR", COMPARISONS WITH EXPERIMENT

Before proceeding with wall interference, the empirical free-air jet model was incorporated in a body+lifting surfaces, sub-critical method (Ref.4).

Fig.13 shows the effect of varying jet velocity (R=Vj/V) on a wing (Aspect ratio 3.4) + body configuration for two nozzle positions (forward and aft). Lift loss is predicted for both nozzle locations. Comparisons with experiment show very encouraging correlation. The spanwise loads shown for one data point depict good agreement.

Several other examples are covered in Ref.4 which emphasise that the empirical jet model is capable of providing very encouraging comparisons against experiments on fairly general 3-D configurations. There are some notable restrictions that apply however with regard to jet closeness to surfaces, as mentioned in Ref.4.

5. EXPERIMENTAL DATA AVAILABLE ON WIND TUNNEL INTERFERENCE

The only readily available data is that of Ashill and Keating (Ref.10) on Jet nozzle experiments carried out in the DRA 13x9 ft wind tunnel (Figs.14-16).

Geometry Details

Fig.14 shows the half-model set up. This implies that a full model of the aircraft with starboard and port nozzles has been set up in a "Duplex" wind tunnel (i.e. $2W_T$ x H_T, width 18 x height 13 ft in the direction of the jet). The corner fillets are neglected. Non-dimensionalisation of length is carried out in terms of half height $H_{ref} = 0.5H_T$ ie 6.5 ft. This is considered reasonable as the jet nozzle is usually near the centre of the tunnel. The z-axis lies in the direction of the jet.

The nozzle diameter is 6.107% of the reference dimension, $H_{ref} = 6.5$ ft. The nozzle is set away from the wall as illustrated in Fig.15. The non-dimensional distances are: $y/H_{ref} = 0.168$, $z/H_{ref} = 0.072$. The nozzle has been set $x/H_{ref} = 0.154$ downstream of the centre of the tunnel.

The sampling points lying along the axis of the 18 x 13 ft wind tunnel.

Fig.16 shows results obtained by Ashill and Keating. The streamwise and vertical interference velocities: u/V and w/V have been shown for jet nozzle angle Θ_{j0} variation. A nozzle thrust of $C_T = 0.119$ corresponds to R = 7.33. Note that the sampling points etc. have been presented with slightly different notation (x/b etc.) The velocities are for **two nozzles**. The distance x is measured from the centre of the tunnel and the non-dimensionalising length is $H_T = 2H_{ref}$ ie. 13 ft.) The nozzle is located 0.077 H_T downstream of the centre of the wind tunnel section and the jet impingement on the wall is likely to lie a reasonable distance downstream. It is interesting to observe the "large" gradients of vertical velocity. For example, for the two 90° nozzles, the vertical velocity varies from near zero to about 2.3° between x/b=-0.5 to 0.5. For four nozzles, as on a typical VSTOL configuration, the vertical velocity gradients would be doubled.

6. THEORETICAL PREDICTIONS OF WIND TUNNEL INTERFERENCE & COMPARISONS

The process leading to the theoretical prediction of wind tunnel interference is described next.

6.1. Modelling of Geometric & Flow Details

The geometric details of the tunnel and jet are as mentioned in Section 5. Most of the early work was carried out with Jet Velocity Ratio R = 7.33. Effects due to **one** nozzle are presented here. For a two-nozzle set-up, the induced velocities u and w would be doubled.

6.2. Ascertaining Number of Image Levels Required

The first problem is to ascertain the required number of image levels in the computation ensuring acceptably small errors in the value of the constraint. The computer code allows for any set of images, arranged only in levels leading to a clear convergence as the number of images increases.

Fig.17 shows the 5 different sets of image levels given by integers, n_y (y varies) and n_z (z varies). The combinations shown are: n_y x n_z = 3 x 2, 5 x 4, 7 x 6, 9 x 8 and 11 x 10. The nozzle is displaced in y- and z— directions ($y/H_{ref} = 0.168$, $z/H_{ref} = 0.072$) and the image locations are therefore not symmetric. Studies showed that for demonstrating convergence, (because the jet is near the middle of the tunnel in the y-direction and in one half of the tunnel in the z-direction) n_y should be an odd integer and n_z should be an even integer.

Consider the case of $\Theta_{j0} = 90°$.

Fig.18 shows the jet height, doublet strength ($\mu_T(\Theta_j)$) and source strength ($\sigma_v(\Theta_j,s)$) for the jet velocity ratio R = 7.33. The height and doublet strength have been presented against x/H_{ref}.

Fig.19 shows the induced velocities u and w due to one nozzle in the Duplex tunnel for various combinations of image levels (n_y x n_z). Note that convergence in the induced velocity w is reached with only (7 x 6) Level. For the induced velocity u, convergence is a little slower but acceptable at levels above (9 x 8).

We take, and recommend, 11 x 10 levels of images in further discussion and proceed to consider parametric variations of jet interference.

6.3. The Effect of Θ_{j0} Variation

Fig.20 shows the effect of Θ_{j0} variation (3° to 90°) on jet height, doublet strength, and source strength for the jet velocity ratio R = 7.33. Note that the restraining effect of the wall on the jet height decreases as Θ_{j0} decreases.

To gain an understanding of the relative magnitudes of velocities induced due to the doublet and source representation on the jet, Fig.21(a,b,c) has been presented. Fig.21(a) shows the calculated induced velocities u and w due to doublet effects from one nozzle. Fig.21(b) refers to the source effects and finally Fig.21(c) represents the total effects. Note that source effects give a very small contribution to w. On the other hand, u terms are more significant with the source distributions.

In Fig.22, the u/V and w/V results of Fig.21(c) have been compared with selected results (Fig.16) of the Ashill & Keating wall pressure signature experiment (Ref.10, re-interpreted in terms of **one** jet nozzle and for the present axes and reference length system). Agreement with the constraint jet model is remarkably encouraging. The u and w calculations predict the nature but magnitudes are slightly smaller than the experiment. The differences in u suggest that further improvements are possibly needed in the entrainment effects and source-sink combinations. We must not, however, forget that the measurements also assume certain levels downstream of the model which are known to be slightly unreliable. It would be of interest therefore to have access to further detailed measurements in due course (including if possible, using different wind tunnels).

6.4. The Effect of Jet Velocity Ratio R Variation

Fig.23 shows the effect of jet velocity ratio R variation on jet height and doublet strength for jet diameter 6.11% H_{ref}. Note the restraining effect of the wall on the jet height as R increases (c.f. shapes of Fig.6 in free air). Fig.24 shows the calculated induced velocities u and w due to **one vertical** nozzle. The sampling points lie along the central wind tunnel axis. The induced velocities increase as R increases. Note the emphasised drop in the velocity u near the jet origin.

6.5. The Effect of Jet Diameter D Variation

Fig.25 shows the effect of jet nozzle diameter variation on jet height and doublet strength for R=7.33. Fig.26 shows the calculated induced velocities u and w due to **one vertical** nozzle. As for the previous cases, the sampling points lie along the central wind tunnel axis. The induced velocities increase as D increases. Near the jet origin, there is a drop in the velocity u.

Figs.22, 24 and 26 emphasise the large magnitudes of effects which can arise, particularly in experiments with 2, 3 or 4 vectoring nozzles on multi-surface aircraft configurations. For 4 vectoring nozzles (R = 8 to 10), the vertical velocity flow angle can amount to 6° – 8°. We infer therefore that the present technique has the capability of guiding the design of acceptable experiments, or for checking the validity of existing information.

7. IMPLICATIONS & FUTURE WORK

In this work we have focussed mainly on the cases where the jet does not strike the walls. Indeed a restraining function has been introduced to avoid the impingement of strong jets. It is realized that this is not a full description of the phenomenon in which rolled-up vortex (or "scarf") sheets are likely to be present. Nevertheless, in the vicinity of the centre of the tunnel, the present simplified model of the jet has provided encouragement towards improved understanding and numerical confidence. This has opened the subject for several future investigations. A few are mentioned as follows:

- Typical geometry variations for continued validation e.g. R and θ_{j0} variations for different jet locations. More wind tunnel measurements, or access to data already existing will be needed to assess the jet interferences which can alter significantly.

- Application to wind tunnels of different cross-sections. Experimental data will help in improving the tunnel constraint model.

- Jet striking the wall. Modelling of rolled-up "scarf" vortex sheets in addition is needed.

- Improved entrainment model for cross-flow jets.

- Preliminary work for the case of a model at high incidence with jets at differing offsets from the wind tunnel axis has suggested large variations in tunnel induced interference. This implies, of course, that the wind tunnel corrections need to be applied over the whole flow-field. An aircraft model is therefore subject to tunnel induced variation gradients of u/V, v/V and w/V over the whole volume occupied. This is analogous to extra wing camber and twist effects along the span as well

as changes in control effectiveness. Alternatively, an implication is that aircraft modelling should also include tunnel representation from the begining.

- Studies with non-circular jets. To a first approximation, equivalent diameter is generally a useful approximation. This needs to be verified for more complex nozzles with "swept" exits and vanes.

8. CONCLUDING REMARKS

One of the important considerations in the testing of aircraft models with vectored jets is the allowance to be made for wind tunnel interference on jet flows. Depending on the cross-section dimensions, the wind tunnel interference, can be particularly severe at high angles of attack or for high jet velocities and large jet deflections.

For assessment of these effects, either "Wall pressure signature" or "Direct" methods can be used. The wall pressure methods although requiring dedicated instrumentation, have the advantage that model flow simulation is not required. The direct methods evaluate, *a priori*, the tunnel constraint and blockage to be included in the experimental analysis, for designing an acceptable experiment in a particular tunnel, or for checking the validity of existing information.

This paper has described a "Direct" method for estimating wind tunnel interference due to jet flows. A semi-empirical model of the jet plume has been used with its images in walls to represent the tunnel constraint. Comparisons with existing "wall pressure signature" test results of Ashill and Keating depict very encouraging agreement.

The results emphasise the large magnitudes of effects which can arise, particularly in experiments with 2, 3 or 4 vectoring nozzles on multi-surface aircraft configurations. For 4 vectoring nozzles (R = 8 to 10), the vertical velocity flow angle can amount to 6° – 8°.

The present technique offers the capability of guiding the design of acceptable experiments, or for checking the validity of existing information.

Several aspects of future work have been proposed, including jet geometry variations and validation in different wind tunnel cross-sections. Such studies will lead to improvement of the semi-empiricisms.

A Fortran77 computer programme embodying the techniques mentioned has been written. This is applicable to wind tunnels of rectangular or near rectangular cross-sections.

REFERENCES

1. SEVERAL SPEAKERS, "Towards Harrier III", RAeS Conference, See Report by J.M.RAMSDEN, RAeS, Aerospace, Feb.1991.

2. HARRIS, A.E., WILDE, G.L. & SMITH, V.J., MUNDELL, A.R.G. & DAVIDSON, D.P., "ASTOVL Model Engine Simulators for Wind Tunnel Research", Paper 15, AGARD CP-498, October 1991.

3. LAUGHREY, J.A. & MOORHOUSE, D.J., "Propulsion Integration Results of the STOL Manoeuvre Technology Demonstrator", Paper 30, AGARD CP-498, October 1991.

4. NANGIA, R.K., "Vectored Jets-induced Interference on Aircraft, Prediction & Verification", AGARD FDP 72nd Symposium "Computational & Experimental Assessment Of Jets In Cross Flow", Winchester, UK, April'93.

5. HACKETT, J.E., "Living with Solid-Walled Wind Tunnels", AIAA-82-0583, 1982.

6. FEARN, R.L. & WESTON, R.P., "Vorticity Associated with a Jet in a Crossflow", AIAA J. of Air., Vol.12, No.12, pp.1666-71, Dec.1974.

7. FEARN, R.L. & WESTON, R.P., "Induced Velocity Field of a Jet in a Crossflow", NASA TP-1087, 1978.

8. FEARN, R.L. & WESTON, R.P., "Velocity Field of a Round Jet in a Crossflow for Various Jet Injection Angles and Velocity Ratio", NASA TP-1506, (1979).

9. FEARN, R.L., "Velocity Field of a Round Jet in a Crossflow for Various Jet Injection Angles and Velocity Ratio", Proceedings of Conference held at University of Stanford in 1983, Published in "Recent Advances in Aerodynamics", Springer Verlaag, 1986.

10. ASHILL, P.R. & KEATING, R.F.A., "Calculation of Tunnel Wall Interference from Wall-Pressure Measurements", Euromech Colloquium 187, Oct.1984, DFVLR, Gottingen, (See also RAE TR 85086, 1985).

11. JORDINSON, R., "Flow in a Jet Directed Normal to the Wind", A.R.C. R & M 3074, 1958.

12. BRADBURY, L.J.S., "Some Aspects of Jet Dynamics and their Implications for VTOL Research", AGARD-CP-308, 1981.

13. KUCHEMANN, D. "The Aerodynamic Design of Aircraft", Pergamon, 1980.

14. SMY, J.R. & RANSOM, E.C.P., "Structure of Single Jets at Large Angles to Cross-Flow", BAe Kingston Internal Report, 1976.

15. WOOLER, P.T., KAO, H.C., SCHWENDAM, M.F. & ZIEGLER, H., "VSTOL Aircraft Aerodynamic Prediction Methods", AFFDL-TR-72-26, 1972.

16. THOMPSON, A.M. " The Flow induced by Jets Exhausting Normally from a Plane Wall into an Airstream", PhD Thesis, Univ. of London, 1971.

17. TOY, N. & SAVORY, E., "An Experimental Study of a Jet in Cross-flow", Surrey University, Guildford, Dec.1988.

18. HANCOCK, G.J., "A Review of the Aerodynamics of a Jet in a Cross Flow", The RAeS Aeronautical Journal, Vol.91., No.905, pp. 201-13, May 1987.

19. ANDERSON, J.D., "Fundamentals of Aerodynamics", McGraw Hill, 1984.

20 NANGIA, R.K., "Development of a Method for Estimating Wind Tunnel Interference Due to Jet Flows", Unpublished Report, 1990.

LIST OF SYMBOLS

A	$= \frac{1}{4} \pi D^2$, Nozzle cross-section Area
C_{LL}	Local lift Coefficient
C_p	Pressure Coefficient
C_T	$= T/(q\,C)$, Thrust Force Coefficient
D, d	Jet Nozzle Diameter
F	Scaling Factor, Jet path in free air
G	Scaling Factor, Constrained Jet path h Distance of Nozzle plane from the Wall
h_{wall}	Distance of Jet from the Wall, infinite distance downstream
H_{ref}	$= 0.5\, H_T$, Reference Dimension measured in Jet path plane, e.g. = 6.5 ft in 13x9 ft Tunnel
H_T	Wind Tunnel Height measured in Jet path plane, (eg = 13 ft in 13x9 ft Tunnel)
L	Lift Force
q	$= 0.5\, \rho\, V^2$, Dynamic Pressure
R	$= V_j/V$, Jet Velocity Ratio
s	wing semi-span
s	jet path variable
T	Nozzle Thrust
u,v,w	perturbation or induced velocities in x,y,z direction
V	Airstream Velocity
V_j	Nozzle Jet Velocity
W_T	Tunnel Width measured in plane normal to the Jet path plane (eg = 9 ft in 13x9 ft Tunnel)
x,y,z	Orthogonal Co-ordinates, x measured from jet nozzle face location
z_j	Distance along z, from jet nozzle face
μ	Doublet Strength
σ_v	source strength along jet
σ_{v0}	source strength at jet origin
Θ_{j0}	Nozzle Jet Deflection angle
Θ_j	Jet path Deflection angle
η	$= y/s$, Non-dimensional spanwise Distance
ρ	Air Density
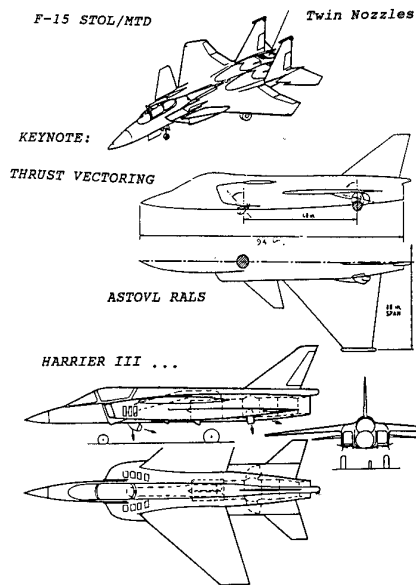
FIG. 1 TYPICAL AIRCRAFT CONFIGURATIONS WITH VECTORING JETS
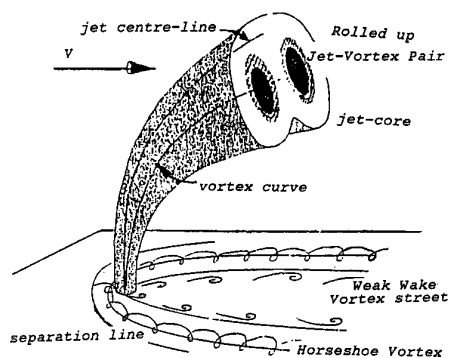
FIG. 2 SKETCH OF JET IN CROSS-FLOW
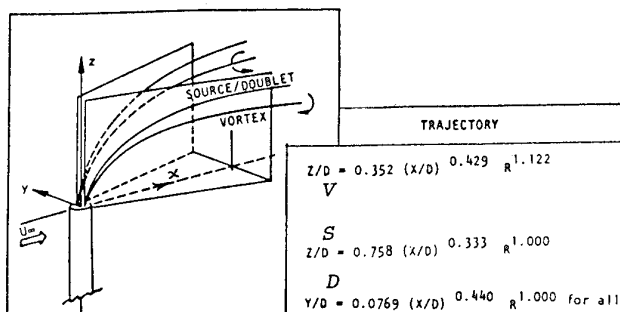
FIG. 3 FEATURES OF "VSD" JET IN CROSS-FLOW (HACKETT)
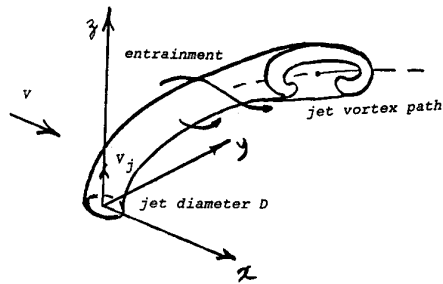

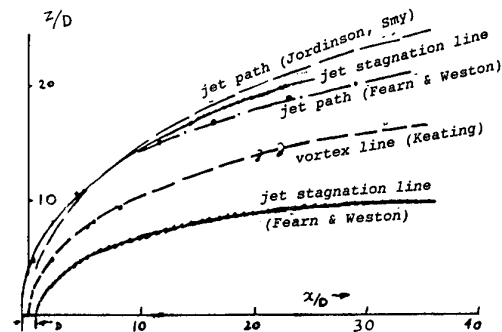FIG. 4 JET DEFORMING IN CROSS-FLOW, SEMI-EMPIRICAL MODELLING, FREE AIR

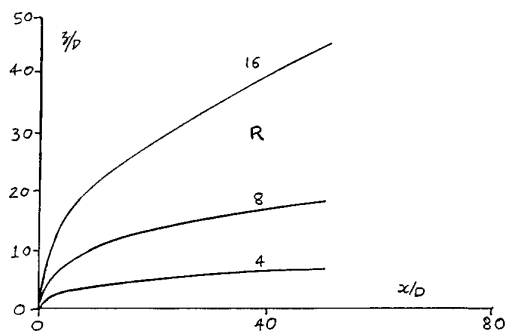FIG. 5 COMPARISONS OF JET PATHS, $R = 8$, $\theta_{jo} = 90°$ (BASED ON WORK BY KEATING)

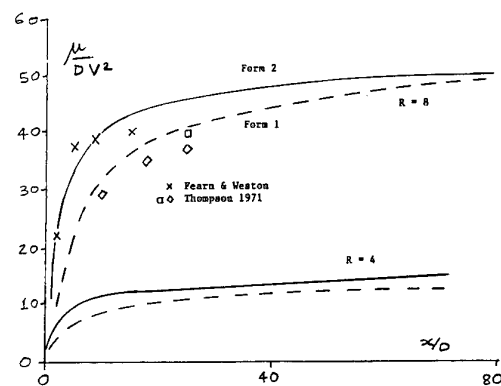FIG. 6 JET VORTEX PATHS FOR DIFFERENT VALUES OF R, $\theta_{jo} = 90°$, FREE AIR

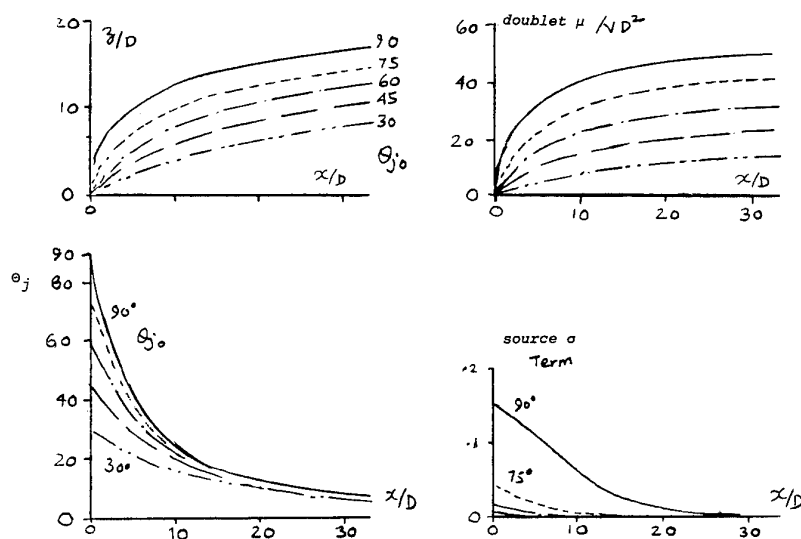FIG. 7 DOUBLET STRENGTH OF JET, FREE AIR $\theta_{jo} = 90°$, $R = 4$ & 8

FIG. 8   EFFECT OF Θ_{jo} VARIATION ON JET PARAMETERS IN NEAR-FIELD, $R = 8$, FREE AIR

FEARN & WESTON EXPT.(1975)   PRESENT MODEL
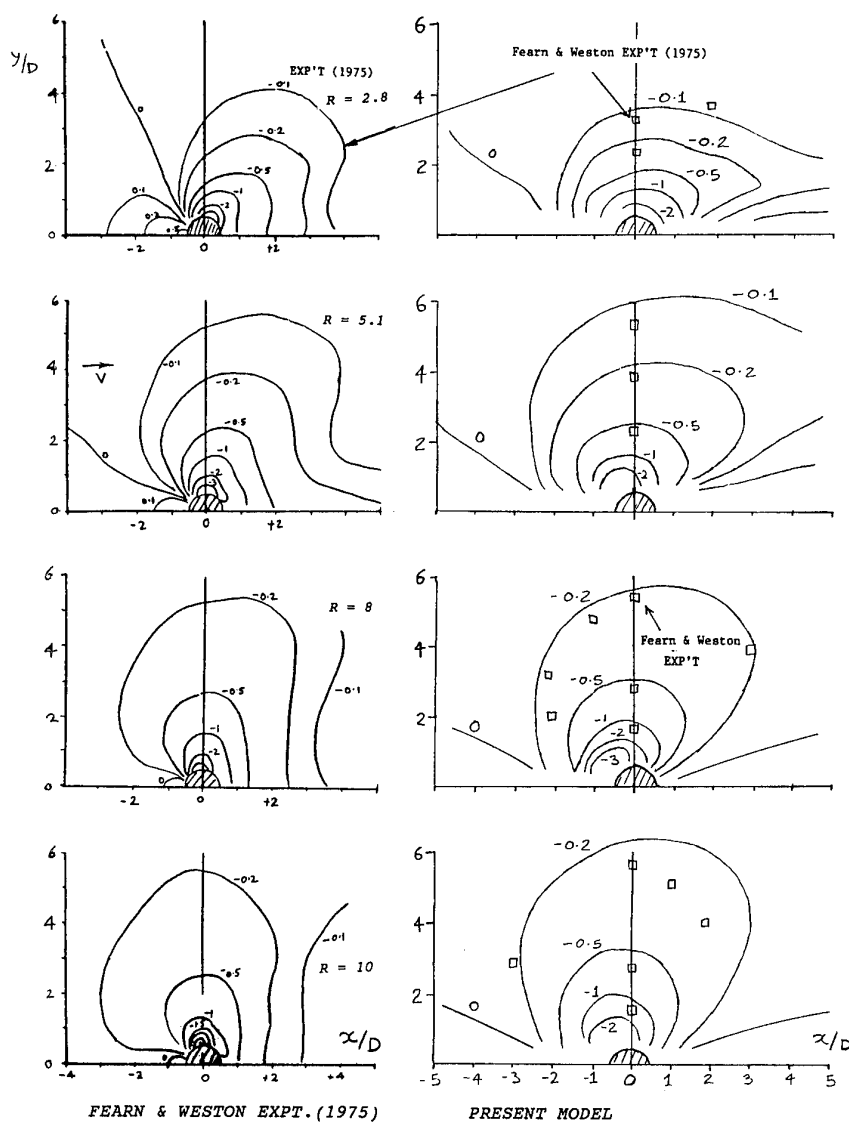
FIG. 9   COMPARISONS OF C_p CONTOURS ON A FLAT PLATE DUE TO JET, R VARIES , FREE AIR
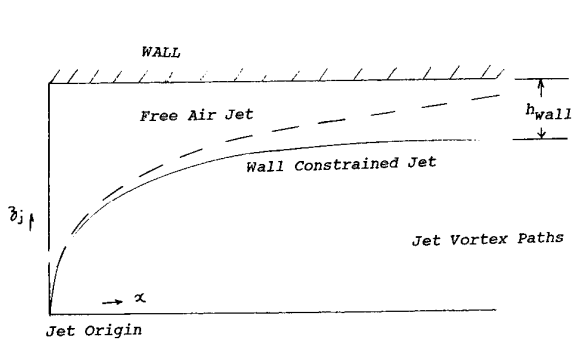
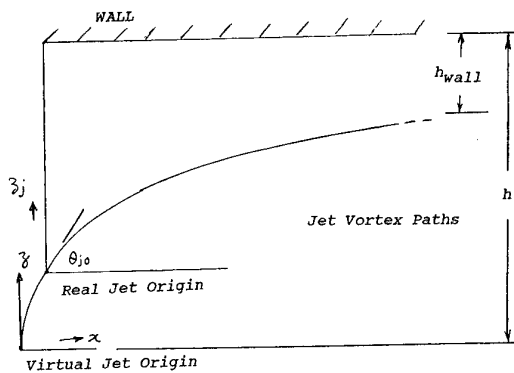FIG. 10 WALL CONSTRAINT ON THE JET HEIGHT
FOR JET ISSUING NORMAL TO THE WALL

Spanwise Jet-induced Loading, R=4.585,
AFT Nozzle

FIG. 11 WALL CONSTRAINT ON THE JET HEIGHT
FOR JET DEFLECTION LESS THAN 90°
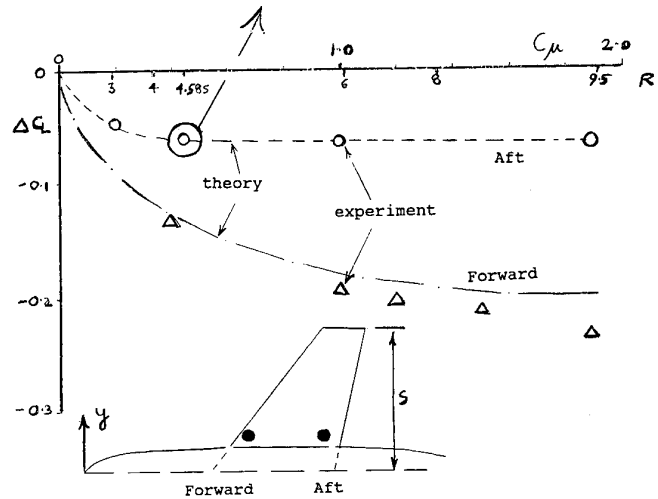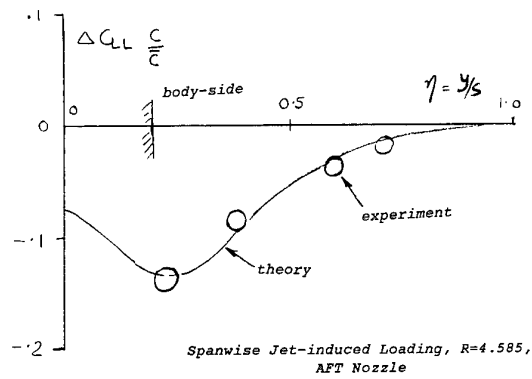
FIG. 13 LIFT LOSS DUE TO FORWARD or AFT
JETS FROM NOZZLES ON A MODEL, FREE AIR,
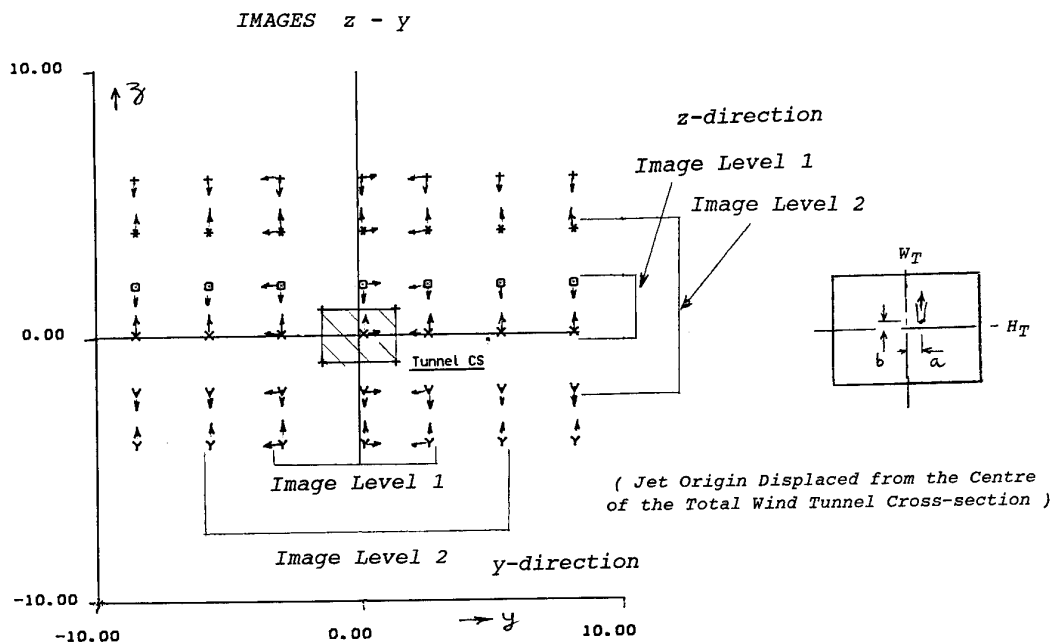$\theta_{jo} = 60°$, R (& C_μ) VARY

IMAGES z - y

z-direction

Image Level 1

Image Level 2

Image Level 1

Image Level 2   y-direction

(Jet Origin Displaced from the Centre
of the Total Wind Tunnel Cross-section)

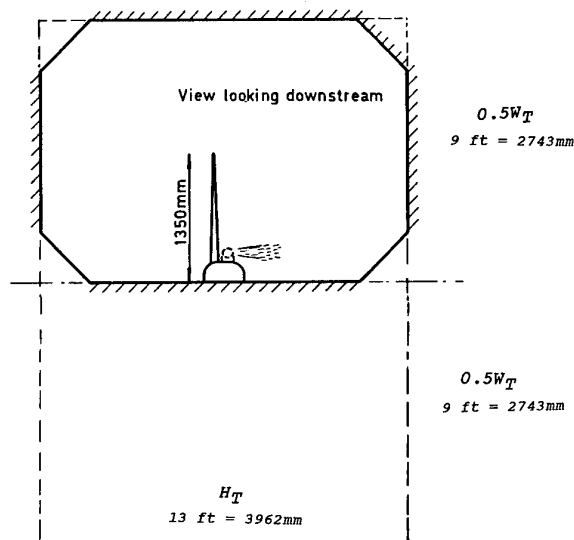FIG. 12 IMAGES IN TUNNEL WALLS
Showing IMAGE LEVELS Occur in Pairs

FIG. 14 A HALF-MODEL SET-UP WITH JETS IN A WIND-TUNNEL (EFFECTIVE WIND TUNNEL (W_T x H_T): 18 ft wide x 13 ft high, TWO JETS)
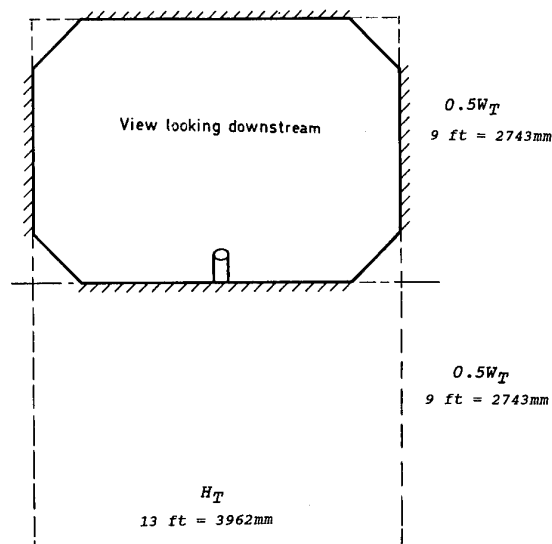

FIG. 15 JET NOZZLE IN A 13x9 ft WIND TUNNEL, (EFFECTIVE WIND TUNNEL (W_T x H_T): 18 ft wide x 13 ft high, TWO JETS)
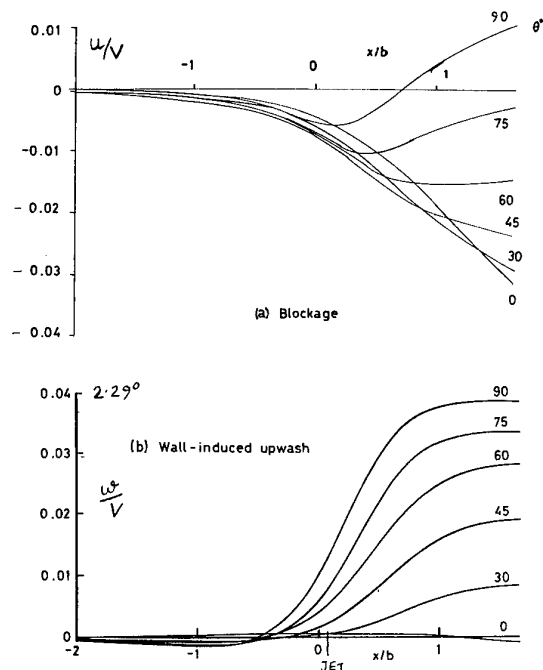

FIG. 16 u/V & w/V DUE TO TWO NOZZLES, R = 7.33, C_μ = 0.119, RESULTS OF ASHILL & KEATING. b=2H_{ref}

(Jet Origin Displaced from the Centre of the Total Wind Tunnel Cross-section)
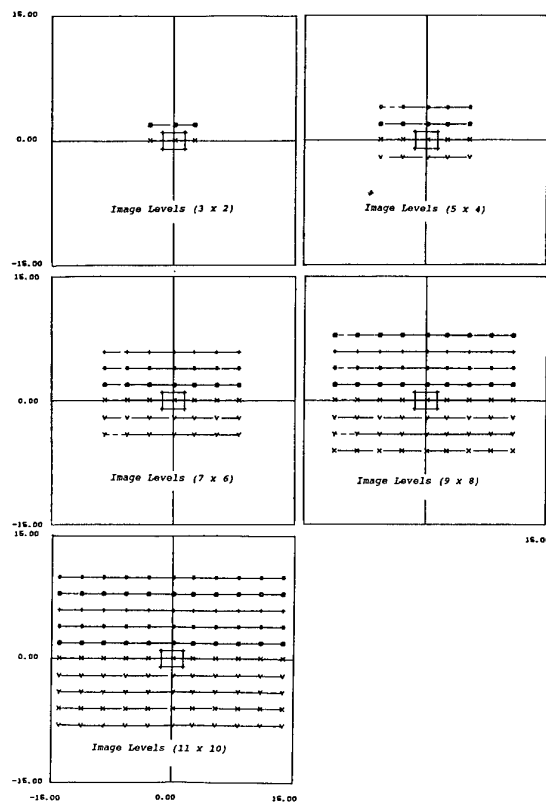

FIG. 17 DIFFERENT SETS OF IMAGE LEVELS (n_y x n_z) IN 18x13 ft SECTION, One Jet Nozzle at y/H_{ref}=0.168, z/H_{ref}=0.072

FIG. 19 u/V & w/V DUE TO ONE NOZZLE,
DIFFERENT IMAGE LEVELS, SOURCE & DOUBLET
EFFECTS INCLUDED
Nozzle at $y/H_{ref} = 0.168$, $z/H_{ref} = 0.072$
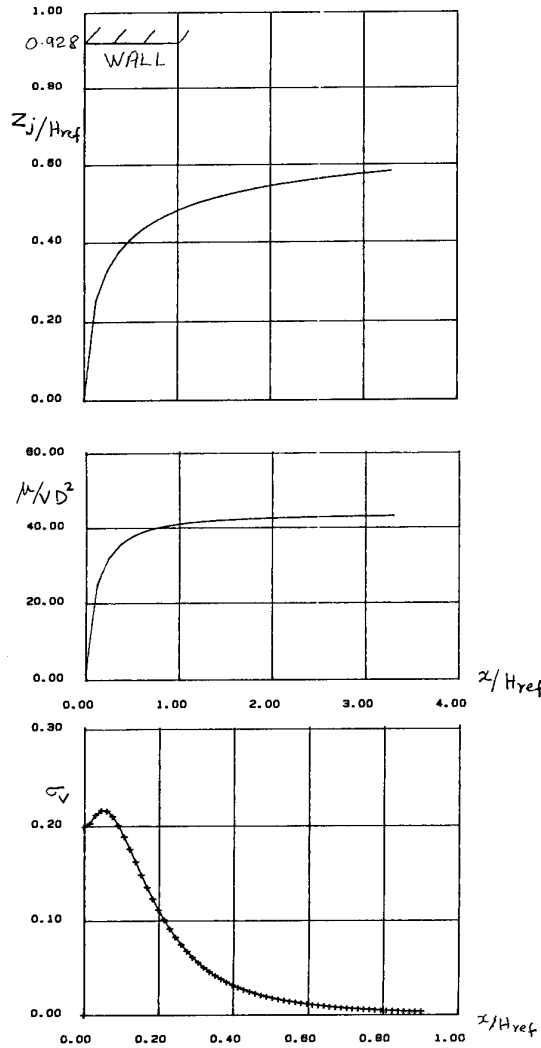Diameter $0.0611\ H_{ref}$, $R = 7.33$, $\Theta_{j0} = 90°$

FIG. 18 JET PARAMETERS: HEIGHT, DOUBLET &
SOURCE STRENGTH,
Nozzle at $y/H_{ref} = 0.168$, $z/H_{ref} = 0.072$
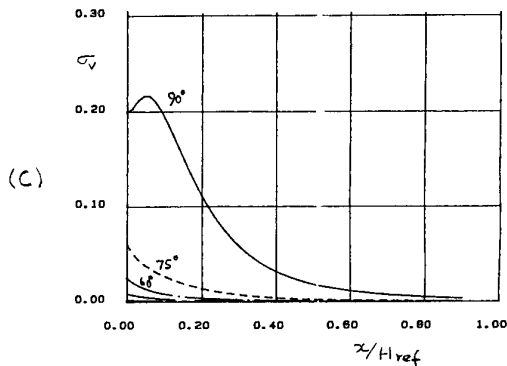Diameter $0.0611\ H_{ref}$, $R = 7.33$, $\Theta_{j0} = 90°$

FIG. 20 EFFECT OF Θ_{j0} VARIATION ON JET
PARAMETERS: HEIGHT, DOUBLET & SOURCE
STRENGTH
Nozzle at $y/H_{ref} = 0.168$, $z/H_{ref} = 0.072$
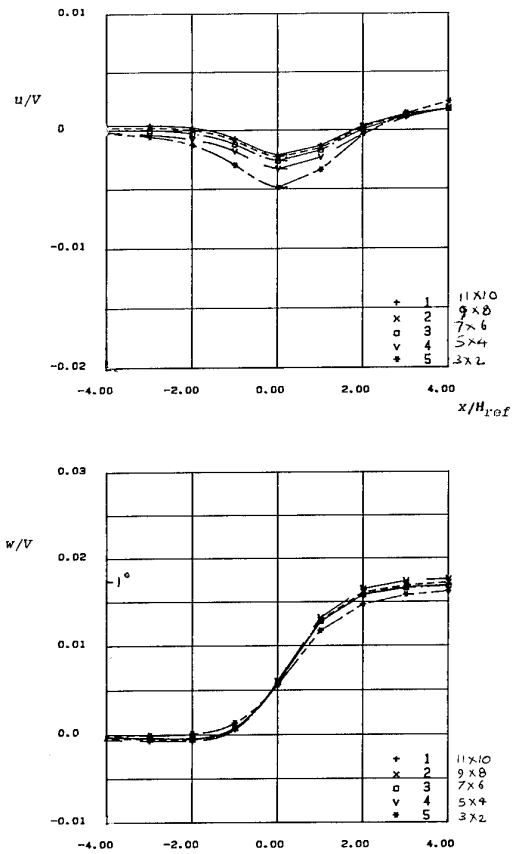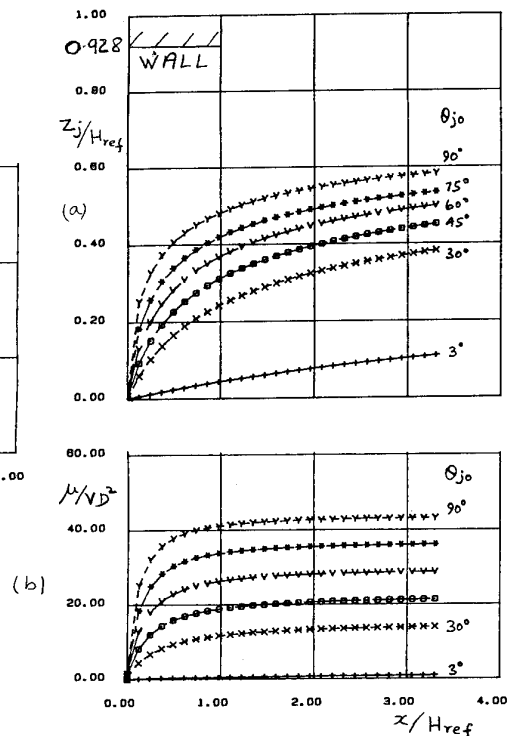Diameter $0.0611\ H_{ref}$, $R = 7.33$

(a) Due To Doublet Distribution   (b) Due To Source Distribution   (c) Due To Doublet & Source
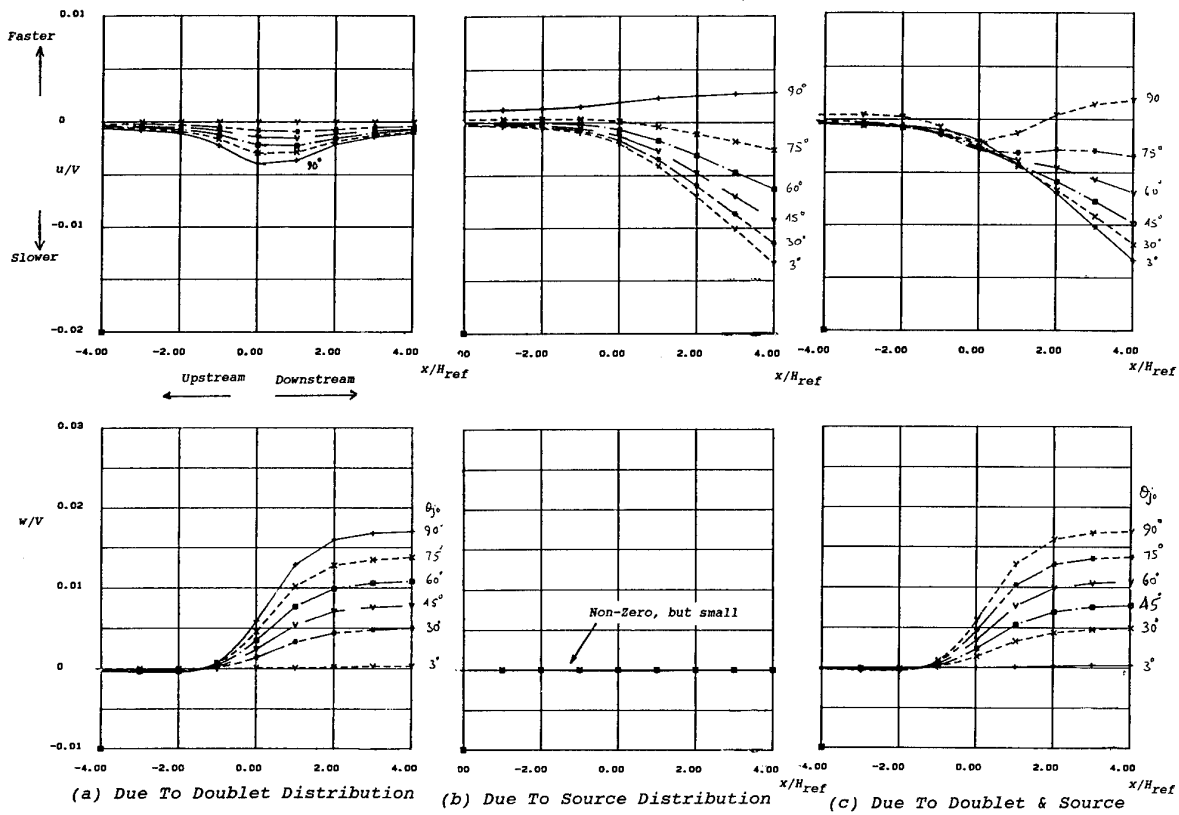
FIG. 21   CONSTRAINT OF SINGLE NOZZLE IN DUPLEX TUNNEL, u/V & w/V DUE
NOZZLE, Θ_{j0} VARIATION, IMAGE LEVELS (11x10),
Nozzle at y/H_{ref} = 0.168, z/H_{ref} = 0.072, Jet Diameter 0.0611 H_{ref}, R = 7.33

FIG. 22   PREDICTED WIND-TUNNEL INDUCED
INTERFERENCE VELOCITIES u/V & w/V DUE TO
SINGLE JET, COMPARED WITH u/V & w/V
DEDUCED FROM WALL PRESSURE MEASUREMENTS OF
ASHILL & KEATING, DEFLECTION VARIED

Nozzle at y/H_{ref} = 0.168, z/H_{ref} = 0.072
Diameter 0.0611 H_{ref}, Θ_{j0} = 90°
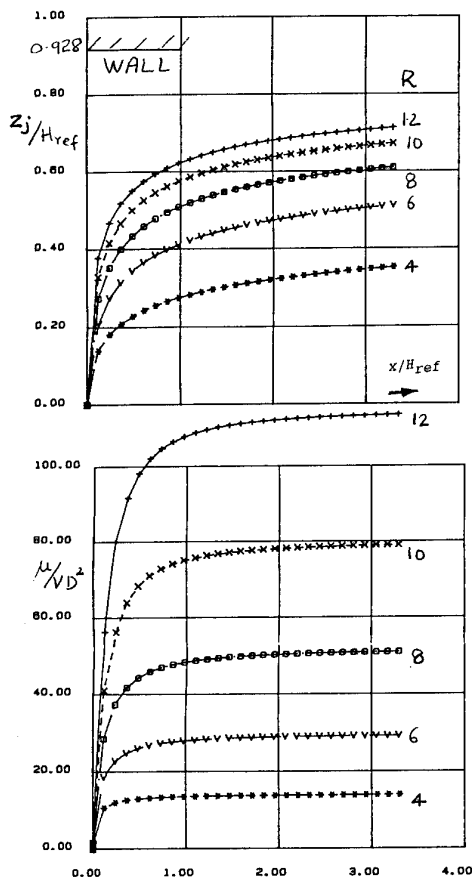
FIG. 23   EFFECT OF R VARIATION ON JET
PARAMETERS: HEIGHT & DOUBLET STRENGTH
Nozzle at $y/H_{ref} = 0.168$, $z/H_{ref} = 0.072$
Diameter 0.0611 H_{ref}, $\Theta_{j0} = 90°$

FIG. 24   EFFECT OF R VARIATION ON u/V &
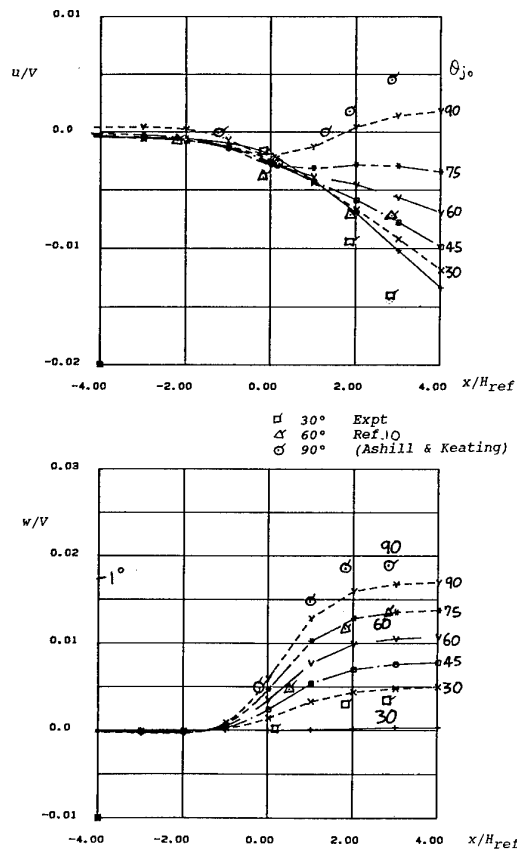w/V DUE TO ONE JET, IMAGE LEVELS (11 x 10)
Nozzle at $y/H_{ref} = 0.168$, $z/H_{ref} = 0.072$
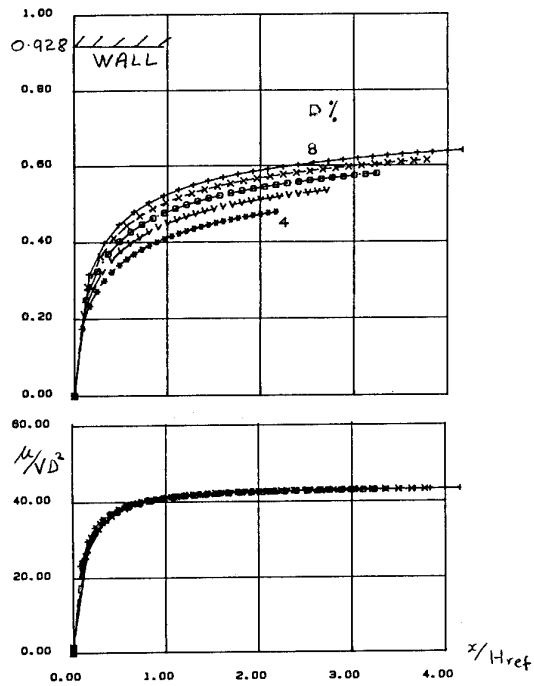Diameter 0.0611 H_{ref}, $\Theta_{j0} = 90°$

FIG. 25   EFFECT OF JET DIAMETER D ON
VARIATION ON PARAMETERS: HEIGHT & DOUBLET
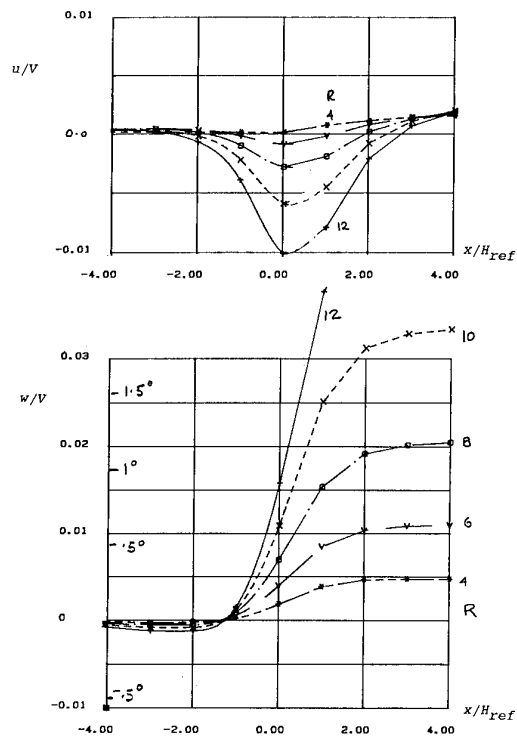Nozzle at $y/H_{ref} = 0.168$, $z/H_{ref} = 0.072$
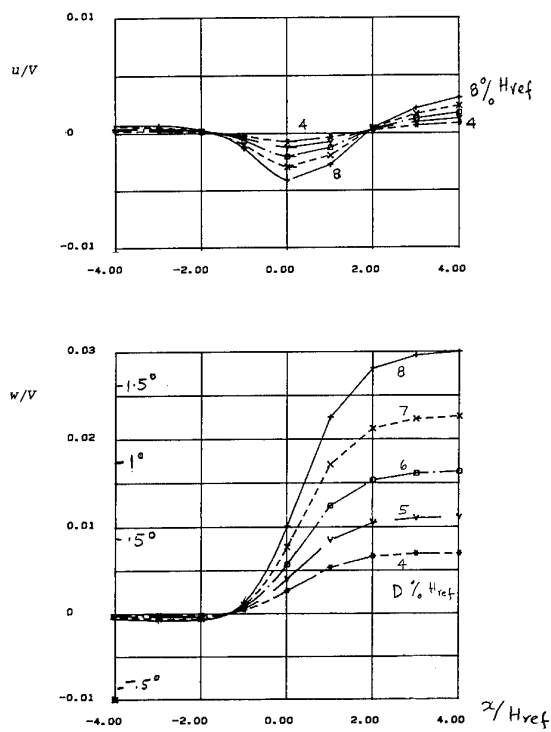$R = 7.33$, $\Theta_{j0} = 90°$

FIG. 26   EFFECT OF JET DIAMETER D
VARIATION ON u/V & w/V DUE TO ONE NOZZLE,
IMAGE LEVELS (11 x 10)
Nozzle at $y/H_{ref} = 0.168$, $z/H_{ref} = 0.072$
$R = 7.33$, $\Theta_{j0} = 90°$

DETERMINATION OF SOLID/POROUS WALL BOUNDARY CONDITIONS FROM WIND TUNNEL DATA FOR COMPUTATIONAL FLUID DYNAMICS CODES

Thomas J. Beutner
Aero-Instrumentation Group, WL/FIME
Wright-Patterson Air Force Base, OH 45433, United States
Zeki Z. Celik
Leonard Roberts
Department of Aeronautics and Astronautics
Stanford, CA 94305, United States

SUMMARY

A computational and experimental study has been undertaken to investigate methods of modelling solid and porous wall boundary conditions in computational fluid dynamics (CFD) codes. The procedure utilizes experimental measurements at the walls to develop a flow field solution based on the method of singularities. This flow field solution is then imposed as a pressure boundary condition in a CFD simulation of the internal flow field. The effectiveness of this method in describing the boundary conditions at the wind tunnel walls using only sparse experimental measurements has been investigated. Verification of the approach using computational studies has been carried out using an incompressible flow solver. The current work demonstrates this technique for low speed flows and compares the result with experimental data obtained from a heavily instrumented variable porosity test section. Position and refinement of experimental measurements required to describe porous wall boundary conditions has also been considered for application to other porous wall wind tunnels. The approach developed is simple, computationally inexpensive, and does not require extensive or intrusive measurements. It may be applied to both solid and porous wall wind tunnel tests. Some consideration is given to the extension of this method to three dimensions.

LIST OF SYMBOLS

c	airfoil chord, wing chord
Cp	pressure coefficient
Cp_{Plenum}	plenum pressure coefficient
h	wind tunnel test section height
m	line source strength
M	Mach number
n	outward normal coordinate direction
p	pressure
p_∞	free stream pressure
P	porosity parameter
P_U	porosity of upper wall
P_L	porosity of lower wall
U_∞	free stream velocity
u, v	two-dimensional Cartesian velocity components; u is streamwise component, v is vertical component
u,v,w	three-dimensional Cartesian velocity components; u is streamwise component, v is spanwise component, w is vertical component
W	tunnel width
V_0	empty tunnel normal velocity at walls

x, y	two-dimensional Cartesian coordinates, origin at airfoil leading edge ($\alpha=0$), x is the streamwise coordinate, y is the vertical coordinate
x, y, z	three-dimensional Cartesian coordinates, origin at wing root leading edge ($\alpha=0$), x is the streamwise coordinate, y is the spanwise coordinate, z is the vertical coordinate
x_0, y_0	position of two-dimensional singularities
α	angle of attack
β	$\sqrt{1 - M^2}$
ϕ	perturbation velocity potential
γ	two-dimensional vortex strength
Γ	horseshoe vortex strength
μ	two-dimensional x-doublet strength
σ	two-dimensional source strength
ω	two-dimensional y-doublet strength

1. INTRODUCTION

Ventilated wall wind tunnels have been in use for several decades and have been useful in reducing wall interference effects at subsonic and transonic speeds and allowing for testing through Mach 1. A series of improvements have been made to the earliest ventilated wind tunnels leading to modern porous wall test sections.

It has long been recognized that the corrections to wind tunnel data for open and closed test sections were of opposite signs [1]. Theodorsen suggested that a wind tunnel might be constructed which would reduce wind tunnel wall interference by using a partially open wall [2]. Wright and Ward tested one of the first successful ventilated wall wind tunnels which used several streamwise slots in the tunnel walls [3]. As predicted, they found that blockage interference was reduced. Wright and Ward also found that ventilated walls alleviated the choking problems at transonic speeds and permitted testing through Mach 1. This work led to other transonic wind tunnels, also using streamwise slots to ventilate the test section walls. It was soon realized, however, that streamwise slots allowed for reflection of shock and expansion waves from the tunnel walls [4]. Porous wall tunnels alleviated this problem by significantly reducing the shock and expansion wave reflections from the walls [5]. The porous wall was constructed with a pattern of small, discrete holes in the wall. The differential resistance wall was a further refinement to the porous wall

concept, using holes with the hole axis inclined to the normal. The differential resistance wall was found to provide cancellation of both shock and expansion waves from the model and allowed for inflow and outflow resistance of the wall to be balanced [1].

Motivation for Modelling the Porous Wall Boundary Condition

As high speed computers have increased the flexibility and capability of computational modelling of flow fields, a new emphasis has been placed on obtaining wind tunnel data which may be used to calibrate and validate CFD codes [6]. Increasingly, there has been a trend toward modelling entire wind tunnel flow fields, including support struts and wind tunnel walls [7, 8]. This has led to an increased use of solid wall wind tunnels in transonic testing. The simplicity of modelling a solid wall boundary condition has made their use attractive despite the disadvantages of substantial wall interference [9]. Increased emphasis on high Reynolds number testing in existing facilities [10,11], and increasing use of CFD codes for high Reynolds number applications [12], however, are creating a renewed incentive for porous wall wind tunnel testing. While solid wall tunnels are used for these tests, wall interference can become a limiting condition on the size of models. Additionally, ventilated wall tunnels are useful for low speed tests where significant wall interference is present [13].

Porous walls may eliminate shock boundary layer interactions on the walls and reduce such interactions on the model by reducing the number of reflected shocks from the walls. Thus, the use of porous wall data in CFD validation may reduce the grid refinement required near the wind tunnel walls while providing a more realistic assessment of the applicability of a turbulence model to free air calculations.

Some attempts have been made to model discrete slots in CFD codes either by modelling the slots in an approximate manner or by solving coupled equations to describe the boundary condition [14, 15]. Porous walls pose a more difficult problem, however, because of the large numbers and fine scale of the holes in the walls. Porous walls are often intricate in design and may include layered walls designed to allow variations in porosity, screens to reduce oscillatory flow in the holes, and inclined holes designed to balance the wall resistance to inflow and outflow and reduce shock wave reflections. Since the porous wall wind tunnel may have several thousand holes on the walls, modelling the individual holes and the viscous effects associated with each hole in a CFD grid is not possible given the current limitations on computer speed and memory. Thus, the effect of the porous walls must be dealt with either by correcting the test data to free air conditions, or by modelling the porous wall by appropriate means in the CFD code.

Wall Interference Corrections

Numerous approaches for correcting porous wall data to free air conditions have been proposed.

These methods use a variety of approaches, based on model pressure and force measurements [16], wall boundary pressure or velocity measurements, or pressure rail measurements [1, 17]. These methods generally produce a global correction to the velocity and angle of attack. Additional corrections to drag and moment coefficients and Mach number are sometimes included. These methods are generally based on classical reflection techniques incorporating a linearized boundary condition to account for the porous wall. This approach results in a useful comparison of bulk flow measurements, such as lift and drag coefficients, but these methods are of limited use in performing CFD validations and calibrations because they have the effect of altering the entire flow field. When performing CFD validations, it is desirable to compare as much of the flow field as possible [6]. In addition, attempts to correct wind tunnel data to free air conditions before comparing it to the CFD calculations may result in errors caused by such corrections being falsely attributed to the CFD code or turbulence model.

Modelling the Porous Wall

Other approaches have sought to develop a boundary condition which may be used at the ventilated wall boundary in the CFD code. These methods have depended on either a simple, universal boundary condition, [1, 5] or on detailed measurements of the boundary conditions during wind tunnel tests which are then imposed as a boundary condition in the CFD code [18-22].

A universal boundary condition for porous walls has proven difficult to determine experimentally and to implement computationally. The linear boundary condition proposed by Baldwin [1, 5] has proven useful in performing corrections to porous wall data and gives some insight into the behavior of the porous wall, but it does not appear adequate to describe porous walls in a CFD code. The porosity parameter in this boundary condition may be different for otherwise identical top and bottom walls, and it may depend on Mach number, stagnation pressure, model size and orientation [23]. This may result in extensive measurements being required for each test condition in order to determine an appropriate value for the porosity parameter. Additionally, there is evidence that the linear relationship between pressure coefficient and flow inclination implied by such a boundary condition does not exist over the entire wall [20]. This casts doubt on the appropriateness of applying such a linear boundary condition in CFD simulations. Furthermore, such a boundary condition may be destabilizing in CFD codes and can actually prevent convergence [24]. Still, the linear boundary condition gives some valuable insight into the nature of the flow near a porous wall.

Some current efforts in ventilated wall interference research have been directed toward making detailed measurements of the flow near the walls and using these measurements to prescribe a boundary condition in CFD codes. King and Johnson used detailed pressure measurements on a surface midway between the model and wall to prescribe a pressure boundary conditon in a two-dimensional CFD

simulation of a slotted wall test [18, 19]. Jacocks used a detailed calibration of a porous wall tunnel, along with detailed measurements during wind tunnel tests to develop an equivalent inviscid normal velocity profile based on an integrated boundary layer analysis [20]. An extension of this method was used by Crites and Rueger for limited three-dimensional problems [21,22]. These approaches required detailed measurements of the wall boundary conditions and large amounts of dedicated test time for calibration at each plenum pressure, Mach number and Reynolds number, making them costly in practice. In most practical cases, the extensive measurements and calibrations required at each test condition limit these techniques to two-dimensional flows.

Current Approach

The approach presented here represents an attempt to describe the effects of a porous wall boundary in a CFD code based on sparse measurements of the flow field in the wind tunnel. The usefulness of this approach is demonstrated by carrying out wind tunnel experiments in a heavily instrumented variable porosity research tunnel and performing CFD simulations of some of the experiments.

The theoretical approach to describing the porous wall boundary utilizes the classical porous wall boundary condition as a means of interpolating boundary conditions measured during wind tunnel tests. A solution for the flow near the walls, based on the method of singularities, is developed using measurements made on the walls during wind tunnel tests. The singularity solutions used in this method satisfy the classical porous wall boundary condition. The method of singularities solution is then used to predict the pressure at CFD boundary point locations. This approach requires very few measurements to determine the flow field solution, though it makes use of all available data and accuracy improves with the number of measurements used. It does not require extensive calibrations of the wind tunnel walls, and uses pressure measurements from the walls, which may be obtained simply and quickly during wind tunnel tests.

The current work consists primarily of two-dimensional, low speed studies. Experimental work was conducted in the Stanford Low Speed Wind Tunnel and computational studies were performed using an incompressible flow solver. Although the Mach number range of the research tunnel used for this work was very low, some consideration was given to the implementation of this method for higher speed flows. Extensions of this method to three dimensions were considered and limited three-dimensional data is presented here.

2. EXPERIMENTAL FACILITIES

This research used a low speed, heavily instrumented, variable porosity test section which was built and tested at the Stanford University Low Speed Wind Tunnel (see Figure 1). This test section was used to conduct both two-dimensional and three-dimensional half-span tests. Nominal free stream velocity for these tests was 24. m/s and the Reynolds number based on chord was 3.2×10^5 for the airfoil and 2.4×10^5 for the three-dimensional wing.

The test section was .457 m. x .457 m. and the porous portion of the test section was .76 m. long. An atmospheric breather section was located at the end of the test section. The porous walls of the test section were layered in a design which used porous inserts between two longitudinally slotted layers of the wall. The outer slotted layer of each wall could be slid laterally to vary the open area ratio of the wall from a solid wall condition to an open area ratio of 9-percent. Figure 2 shows an exploded view of this wall design. An atmospheric plenum was used for all porous wall tests. The test section top and bottom walls were adjustable and were inclined normal to the free stream to compensate for boundary layer growth through the test section.

For two-dimensional testing, variable porosity top and bottom walls were used and solid side walls were used with the airfoil model mounted to the side walls. The airfoil used in the tests was a Boeing Advanced Transport Airfoil and may be seen in Figure 3. The model had a flap and spoiler which were in the retracted position for these tests. The airfoil chord was .203 m. Measurements of the model coordinates were made with a Leitz Precision Measuring Machine with an accuracy of 2.54×10^{-6} m., or approximately .00125-percent of the airfoil chord. Grit was applied to the airfoil between 2.5 and 5.0-percent of the chord. Nominal grit diameter was 3.18×10^{-4} m. Oil flow studies were undertaken to ensure the two-dimensionality of the flow field and to ensure that the grit applied to the model successfully triggered transition on the airfoil.

The wing used in the three-dimensional testing was a half-span, unswept wing with a constant length chord and a constant NACA 0018 cross section. The wing chord was .152 m. and the span was .229 m. The wing had a rounded tip with diameter based on local thickness of the cross section. As with the two-dimensional model, grit was applied between 2.5 and 5.0-percent of the chord and oil flow studies were performed to ensure that the grit successfully triggered transition. In the three-dimensional half-span tests, the wing was mounted on a solid side wall and the opposing side wall was a porous wall similar to the porous top and bottom walls.

The test section was instrumented with 78 static pressure tappings on the centerlines of the upper and lower walls and a total of 640 static pressure tappings distributed on the top, bottom and side walls. Pressure tappings were also located on both models. The test section design also allowed five hole probe access near the upper and lower walls and on the inflow and outflow planes. The five hole probe was used to determine flow inclinations and velocity perturbations on these planes.

Static pressure data was acquired by three Scanivalves and two computers. A maximum of 540 static pressure measurements could be made with the Scanivalves on each run. The Scanivalves were

calibrated on each run against a secondary standard which was traceable to the National Bureau of Standards. Overall errors in pressure measurements due to calibration uncertainties, sensitivity limits and non-linearity were less than 1.0-percent. Errors in pressure coefficient measurements as a function of pressure coefficient may be seen in Figure 4.

3. COMPUTATIONAL METHODS

Navier-Stokes Solver

A two-dimensional, incompressible, Reynolds averaged Navier-Stokes solver developed at NASA Ames Research Center was used in this study [25]. This CFD code solved the incompressible Navier-Stokes equations using the method of artificial compressibility. The method of artificial compressibility adds a pseudo-time derivative of pressure to the continuity equation. This results in a hyperbolic system of equations which may be marched in pseudo-time to a steady state solution [26]. A Baldwin-Barth turbulence model [27] was used and the transition point was fixed at the airfoil leading edge. This code was fully implicit, used locally upwind spatial differencing, and was modified to allow for an experimental static pressure profile to be imposed as a boundary condition for internal flow calculations. Velocity components at the wall boundaries were obtained by the method of characteristics.

Grids used in this flow solver conformed to the boundaries of the test section (see Figure 5) and were developed using GRIDGEN software [28]. All computations were performed on the CRAY Y-MP at NASA Ames Research Center.

Method of Singularities

As a means of describing the wind tunnel wall boundary conditions in a wind tunnel experiment, a potential flow solver based on the method of singularities was developed.

The boundary condition of Equation 1 has been proposed as a theoretical description of a porous wall boundary [1].

$$\frac{\partial}{\partial x}\phi + \frac{1}{P}\frac{\partial}{\partial n}\phi = \frac{1}{P}\frac{V_0}{U_\infty} - \frac{1}{2}C_{P_{Plenum}} \qquad (1)$$

The boundary condition of Equation 1 assumes an analogy between flow through the porous wall and flow through a pipe. Velocities normal to the wall are assumed to be linearly related to the pressure difference existing across the wall. The pressure differences across the wall are, in turn, related to the perturbations in the tangential velocity at the wall. The right hand side terms in Equation 1 account for the flow through the wall which is observed during empty tunnel runs. In theory, $V_0 = 0$ when holes are normal to the tunnel wall. However, porous wall tunnels generally use holes inclined to the normal direction in order to balance inflow and outflow resistances. Inclined holes may have the effect of inducing a velocity, V_0, through the walls even during empty tunnel tests. In practice, however,

V_0 may be negligibly small. The second term on the right hand side of Equation 1 accounts for the pressure difference created by the porous wall plenum. If the plenum pressure is chosen to be the free stream static pressure, the second term is zero. If the right hand side terms in Equation 1 are neglected, the homogeneous boundary condition of Equation 2 results.

$$\frac{\partial}{\partial x}\phi + \frac{1}{P}\frac{\partial}{\partial n}\phi = 0 \qquad (2)$$

As mentioned earlier, the porosity parameter, P, in Equation 2 must be determined from experimental measurements. It is generally assumed that the porosity parameter is constant over the length of the porous wall. Some of the limitations of this boundary condition have already been mentioned and these limitations make direct application of Equation 2 as a boundary condition in CFD codes questionable.

Despite the difficulties in applying Equation 2 directly as a boundary condition in porous wall CFD simulations, the insight it provides into the nature of the flow near a porous wall makes it useful for interpolating experimental data.

Analytic solutions for the perturbation velocity potentials due to a source, a vortex and doublets in the presence of porous walls described by Equation 2 have been developed [1] and are shown in Equations 3-12.

$$\text{Source:} \quad \phi_\sigma = \frac{\sigma}{\beta}\left[B(Z) + E(Z) + \chi(P_U)\chi(P_L) \right] \qquad (3)$$

$$\text{Vortex:} \quad \phi_\gamma = i\,\gamma\left[B(Z) - E(Z) \right] \qquad (4)$$

$$\text{X-Doublet:} \quad \phi_\mu = \frac{\mu}{\beta^2 h}\frac{d}{dz}\left[B(Z) + E(Z) \right] \qquad (5)$$

$$\text{Y-Doublet:} \quad \phi_\omega = \frac{i\,\omega}{\beta h}\frac{d}{dz}\left[B(Z) - E(Z) \right] \qquad (6)$$

Where:

$$Z = \frac{x}{\beta h} + \frac{i\,y}{h} \qquad (7)$$

$$Z_0 = \frac{x_0}{\beta h} + \frac{i\,y_0}{h} \qquad (8)$$

$$B(Z) = \frac{1}{2}\frac{\exp\left[\pi\,\dfrac{\tau_U + \tau_L}{2}(Z - Z_0)\right]}{\exp\left[\pi\,(Z - Z_0)\right] - 1} \qquad (9)$$

$$E(Z) = \frac{-1}{2}\frac{\exp\left[\pi\,\dfrac{\tau_U + \tau_L}{2}(Z - \overline{Z}_0)\right]}{\exp\left[\pi\,(Z - \overline{Z}_0)\right] + 1} \cdot \\ \exp\left[i\,\pi\,\dfrac{\tau_U - \tau_L}{2}\right] \qquad (10)$$

$$\chi(P_U)\chi(P_L) = \begin{cases} 1, & \text{if } P_U = P_U = 0 \\ 0, & \text{otherwise} \end{cases} \quad (11)$$

$$\tau_{U,L} = \frac{2}{\pi} A \tan \frac{P_{U,L}}{\beta} \quad (12)$$

The approach used in this research was to use experimental pressure data to develop a potential flow solution. Streamwise velocity profiles were developed from measured pressure profiles and were used to develop a potential flow solution by the method of singularities. The singularities used were a point source, a point vortex and derivatives in the streamwise direction of the point source and point vortex. Up to four derivatives were retained in the potential flow solution. Singularity strengths were determined by making a least squares error match of the velocity profiles due to the singularities and the streamwise velocity profiles inferred from static pressure measurements on the wind tunnel walls. The potential flow solution was then used to prescribe pressure boundary conditions in the CFD code. Thus, sparse data could be interpolated and extrapolated using the method of singularities. While the singularities used in this method satisfied the boundary condition of Equation 2, only the pressure profile resulting from the potential flow solution was specified in the CFD code. Thus, the difficulties of using Equation 2 as a boundary condition in CFD calculations could be avoided.

This method may also be applied in three dimensions. Although analytical solutions for the perturbations due to a source and vortex in the presence of porous walls as described by the boundary condition of Equation 2 are not available, these solutions may be obtained by simple numerical methods once the free air solutions are known. If ϕ_1 is the free air potential due to a singularity and ϕ_2 is the wall interference potential, then the combined free air and interference potentials, denoted by ϕ must satisfy Equation 2.

$$\phi = \phi_1 + \phi_2 \quad (13)$$

In the case of three-dimensional solutions, the porosity parameter in Equation 2 may take on different values on each wall. Substituting Equation 13 into Equation 2 and rearranging terms gives the following boundary condition:

$$\frac{\partial}{\partial x}\phi_2 + \frac{1}{P}\frac{\partial}{\partial n}\phi_2 = -\left(\frac{\partial}{\partial x}\phi_1 + \frac{1}{P}\frac{\partial}{\partial n}\phi_1\right) \quad (14)$$

Once the free air potential is known, it remains to solve for the interference potential ϕ_2 which satisfies the boundary condition of Equation 14.

In this work, a panel method was used to solve for the interference potentials from a horseshoe vortex, a line source, and derivatives of these singularities with respect to x, y_0 and z. The potential due to a horseshoe vortex centered at the origin with a span of $2y_0$ is given by Equation 15.

$$\phi_V = \frac{\Gamma}{4\pi}\left[A \tan\left(\frac{(y+y_0)}{z}\right) - A \tan\left(\frac{(y-y_0)}{z}\right)\right.$$
$$+ A \tan\left(\frac{x(y+y_0)}{z\sqrt{x^2+(y+y_0)^2+z^2}}\right)$$
$$\left. - A \tan\left(\frac{x(y-y_0)}{z\sqrt{x^2+(y-y_0)^2+z^2}}\right)\right] \quad (15)$$

The potential due to a line source centered at the origin with a span $2y_0$ is given by Equation 16.

$$\phi_S = \frac{m}{4\pi}\log\left[\frac{(y-y_0)+\sqrt{x^2+(y-y_0)^2+z^2}}{(y+y_0)+\sqrt{x^2+(y+y_0)^2+z^2}}\right] \quad (16)$$

The paneling method used an array of 12 by 32 constant strength doublet panels to cover each wall. The porous wall boundary condition described in Equation 2 was enforced at the control points. Velocities at intermediate points were found using bicubic spline fits to the velocities at the control points.

Once the interference potentials due to simple singularities were found with the panel method, the potential flow solutions could be superimposed and the singularity strengths determined by least squares matching in the same manner as described for the two-dimensional case.

Boundary Conditions

In the two-dimensional CFD validations performed in this research, the top and bottom wall boundary conditions were static pressure boundary conditions. The static pressure profiles on these walls were determined by the method of singularities described above. The outflow plane also used a static pressure boundary condition based on the breather section pressure. For both the walls and the outflow plane, the remaining flow variables were solved for by the method of characteristics.

On the inflow plane, the velocity profile was specified. This velocity profile was based on a cubic polynomial fit to the five hole probe velocity measurements on the inflow plane. Pressure on the inflow plane was determined by the method of characteristics.

A no-slip boundary condition was used on the airfoil, and averaging was used on the wake cut.

Evaluation of Method

Previous work by the authors with a transonic CFD code has demonstrated, by computational studies, the consistency of the pressure boundary condition as a means of describing a wall boundary condition in a flow

field containing shocks. In that work, as in the current work, pressure was specified as a boundary condition with the remaining flow variables solved for by the method of characteristics. That work also showed that the method described here is relatively insensitive to changes in the porosity parameter, P [29]. The value of P in this work was determined by the minimizing root-mean-square error.

The evaluation of this technique for describing a wind tunnel boundary condition was broken into three parts. First, the method of singularities was evaluated in a series of computational studies. Second, the method was used to perform CFD validations using experimental data obtained from the variable porosity test section. Third, three-dimensional singularities were used to fit data from the half-span wing tests.

The computational studies were centered on evaluating the number of data points and the number of singularities required to adequately describe the boundary conditions. This study was performed by using a CFD simulation in which slip wall boundary conditions were used at the tunnel wall boundaries. This CFD simulation was treated as a pseudo-wind tunnel experiment and data samples which were representative of measurements obtainable from wind tunnel tests were taken from the boundaries of this CFD simulation. Various numbers of data points were used to develop potential flow solutions, and these potential flow solutions were then compared to the original, complete velocity profiles from the CFD simulation. Using a computational study for this evaluation had the advantage of allowing more detailed comparisons of the boundary conditions on the walls than would be possible using experimental data only.

The second part of the evaluation of this method involved using experimental wall pressure profiles from both solid and porous wall tests to develop flow field solutions with the method of singularities. These flow field solutions were then imposed as a pressure boundary condition in the CFD code. CFD simulations were carried out for solid wall and porous wall (9-percent open area ratio) tests at 5, 6, 7, 8, 9, 10 and 11 degrees angle of attack. These simulations used boundary conditions developed by the method of singularities using a source, a vortex and 4 derivatives of each to develop a pressure profile based on a total of 77 pressure measurements on the wind tunnel walls.

As a further test of this method, the method of singularities was used to develop pressure profiles based on very sparse data. For these cases, a total of 8 data points from the wind tunnel tests were used to develop the method of singularities solution. This solution was then imposed as a boundary condition in the CFD code and the resulting pressure profiles on the airfoil were compared with the results obtained using more complete data from the wind tunnel tests. This allows for an evaluation of the effect of using sparse data in this method.

Finally, a limited study of three-dimensional data was undertaken. Pressure profiles from both porous and solid wall tests of the half-span wing were used to develop flow field solutions using the method of singularities and the three-dimensional singularities described earlier. These flow field solutions are compared to the experimental pressure profiles on the walls. No CFD simulations of the three-dimensional tests were performed.

4. RESULTS

Two-Dimensional Case

Figure 6 shows the pressure profiles on the walls as predicted by the CFD simulation using slip wall boundary conditions for an angle of attack of 5 degrees. This simulation was used to determine the effects of refining the number of data points used to develop the potential flow solution.

Figure 7 shows the root-mean-square error resulting when various numbers of data points were used to develop the potential flow solutions. These data points were distributed as uniformly as grid spacing would allow over the top and bottom walls. The root-mean-square errors were based on a comparison of the pressure predicted by the CFD simulation and the pressure predicted by the potential flow solver at each grid point on the upper and lower walls. As may be seen in Figure 7, a relatively small number of measurement locations was sufficient to develop a potential flow solution. In addition, a small number of singularities was adequate to describe the far field flow with good accuracy.

Additional singularities required additional data points to produce acceptable fits to the velocity profiles. It was found that the number of data points required to produce a good fit to the velocity profiles was approximately twice the number of singularities retained in the potential flow solution.

The next step in evaluating this method was to use it to perform validations of a series of wind tunnel tests. The tests were conducted in the variable porosity tunnel described above. The pressure profiles measured on the walls in these tests may be seen in Figures 8a-g. These figures show data from both the solid wall tests and the porous wall tests with a 9-percent open area ratio. Data is shown for angles of attack of 5-11 degrees. Also shown in Figures 8a-g are the potential flow solutions based on this data. These potential flow solutions were developed using the 77 measurements on the wind tunnel walls and a total of 10 singularities. As can be seen in these figures, the potential flow solutions showed excellent agreement with the experimental data. Typical root-mean-square errors in matching wall pressure coefficient profiles were approximately 1-percent of peak pressure coefficient values.

The potential flow solutions shown in Figures 8a-g were imposed as boundary conditions in the Navier-Stokes solver and the resulting pressure profiles obtained on the airfoil are shown in Figures 9a-g. Also shown in Figures 9a-g are the pressure profiles obtained in the wind tunnel tests. Experimental and computational results compared very well. The largest discrepancies were approximately 6-percent of the peak values. These

discrepancies occurred at the location of the grit transition strip on the model. At locations away from the grit strip, however, agreement was much better with typical discrepancies of approximately 1-percent of peak values. A comparison of airfoil pressure profiles from the solid wall and porous wall tests showed that this method predicted the qualitative effect of a porous wall very well. As the porosity of the wall was varied, the trend in pressure profiles on the airfoil was duplicated in the CFD simulations by imposing the potential flow solution as a pressure boundary condition in the Navier-Stokes solver.

Also of interest in Figures 9a-g are the slight deviations seen in the pressure profiles on the airfoil between x/c=.75 and x/c=.80. These deviations may be seen on both the upper and lower surfaces and are present in both the experimental and CFD data. They are the result of small ridges on the airfoil model between the main airfoil and the retracted flap.

Figures 10 and 11 show typical results obtained by using sparse data to develop the potential flow solutions. Figure 10a shows the potential flow solution developed using 8 data points from the solid wall test at 5 degrees angle of attack. Figures 10b-g show similar results for 6-11 degrees angle of attack and Figure 11 shows similar results using porous wall data. In these cases, only first derivatives were retained in the singularity solution, resulting in a total of 4 singularities being used to develop the pressure profiles shown. In both Figure 10 and 11, the complete wind tunnel data is shown for reference, as well as the potential flow solutions based on the complete wind tunnel data. The potential flow solutions based on 8 data points show close agreement with the potential flow solutions based on 77 data points. Typical root-mean-square errors in matching the complete experimental pressure coefficient profiles using the method of singularities solution based on 8 data points was approximately 10-percent of peak values. Although these errors were higher than the cases in which 77 data points were used to develop the solution, the trend of the pressure profiles is still captured using very sparse data. This agreement indicates that this method was robust enough to allow for a good description of the boundary conditions on the walls even when only very sparse data is available from the wind tunnel walls.

The pressure profiles shown in Figures 10 and 11 were imposed as boundary conditions in the CFD code and the resulting pressure profiles on the airfoil are shown in Figures 12 and 13. For reference, the airfoil pressure profiles which resulted by imposing the boundary conditions of Figure 8 in the CFD code are also shown in Figures 12 and 13. This allows a comparison of the effect on the airfoil of using sparse data to develop the wall boundary conditions. As can be seen in these figures, the method of singularities provided a means of describing boundary conditions which was sufficiently robust so that little effect was seen on the airfoil from significantly reducing the number of measurements used to develop the boundary conditions. Typical root-mean-square errors between the pressure coefficient profiles shown in Figures 12 and 13 was 1.5-percent or less of the peak values.

Three Dimensional Case

Limited three-dimensional data is also available. No CFD validations were performed for the three-dimensional data, however, the method of singularities was used to develop fits to the data measured on the walls.

Figures 14, 15 and 16 show the pressure profiles on the top, side and bottom walls from the three-dimensional solid wall tests of the half-span wing at 20 degrees angle of attack. Also shown in these figures are the pressure profiles developed by the method of singularities using 342 data points and 16 singularities to match the data. Figures 17-19 show similar results for the porous wall tests.

As can be seen in these figures, the agreement of the method of singularities fit to the experimental data is better in two dimensions than in three dimensions. This is in part due to the finite test section effects near the inflow plane and outflow plane. The abrupt change in boundary conditions associated with the breather section and inlet of the wind tunnel test section caused flow anomalies which the method of singularities could not adequately model. Only data from the central region of the test section is shown in Figures 14-19. The root-mean-square errors based on a comparison of experimental pressure profiles and those predicted from the method of singularities are 4.5-percent of the peak pressure coefficient for the solid wall case and 7.6-percent of the peak pressure coefficient for the porous wall case. Over the central region of the test section, the method of singularities captured the general trend in pressure profiles on all three walls.

5. CONCLUDING REMARKS

A method for describing porous wall boundary conditions based on sparse, nonintrusive measurements of flow quantities at the wall boundary has been developed. This method utilized a potential flow solution based on least squares matching of singularity strengths to measured experimental data. The consistency of imposing a pressure boundary condition based on this method with other means of describing a wall boundary condition has been demonstrated in computational studies. This method has been shown to provide a good description of the entire wall boundary condition even when only sparse data is available. The ability of this method to predict the effects of changing porosity in a wind tunnel test has been demonstrated by simulation of experiments performed in a variable porosity test section.

This method has been extended to three-dimensional porous wall testing. In three dimensions, the method of singularities allowed the porous wall boundary condition to be modelled without the need for normal velocity perturbation measurements and without the need for extensive calibrations of the wall. An experimental study has shown that the method was capable of capturing the trends in pressure profiles existing on the walls in three dimensional porous and solid wall tests.

In these low speed tests, the method of singularities has been found to be rather insensitive to the value of the porosity parameter specified. This allowed for the porosity parameter to be found by means of least squares matching. While changes in the porosity parameter did have a strong effect on the singularity strengths, the effect on the overall match to the pressure profile was minimal. Since the porosity parameter was not specified as a boundary condition in the CFD code, and no corrections were made to the wind tunnel data, this method eliminated many of the concerns associated with the classical linear porous wall boundary condition. This method also allowed for a simulation of the entire flow field and direct comparison of the flow field to wind tunnel data without the need for corrections to the experimental data.

6. ACKNOWLEDGMENTS

7. REFERENCES

1) AGARD Report AG-281, "Two-Dimensional Wind Tunnel Wall Interference," 1983.

2) Theodorsen, T., "The Theory of Wind-Tunnel Wall Interference," NACA Technical Report 410, 1931.

3) Wright, R.H. and Ward, V.G., "NACA Transonic Wind-Tunnel Test Sections," NACA Technical Report 1231, 1956

4) Ritchie, V.S. and Pearson, A.O., "Calibration of the slotted Tests Section of the Langley 8-Foot Transonic Tunnel and Preliminary Experimental Investigation of Boundary Reflected Disturbances," NACA RM L51K14, July 7, 1952.

5) Baldwin, B.S., Turner, J.B., and Knechtel, E.D., "Wall Interference in Wind Tunnels with Slotted and Porous Boundaries at Subsonic Speeds," NACA TN 3176, May 1954.

6) Marvin, J.G., "Accuracy Requirements and Benchmark Experiments for CFD Validation," AGARD CP 437, May 1988.

7) Lan, C.E. and Thomas, J.P., "Application of Computational Aerodynamics to Assessment/Correction in Wind Tunnel Testing," KU-FRL-887-1, The University of Kansas Center for Research, Inc., Sept. 28, 1990.

8) Levy, L.L., "Experimental and Computational Steady and Unsteady Transonic Flows about a Thick Airfoil," AIAA Journal, Vol. 16, No. 6, June 1978, pp. 564-572.

9) Potsdam, M. and Roberts, L., "A Numerical Study of the Effects of Wind Tunnel Wall Proximity on an Airfoil Model," JIAA TR-99, Stanford University, Department of Aeronautics and Astronautics, Sept. 1990.

10) Lynch, F.T., "Experimental Necessities for Subsonic Transport Configuration Development," AIAA Paper 92-0158, January 1992.

11) Olson, L.E., "Future Experimental Needs in Low Speed Aerodynamics," AIAA Paper 92-0157, January 1992.

12) O'Lone, R.G., "Final Assembly of 777 Nears," Aviation Week and Space Technology, pp 48-50, Oct. 12, 1992.

13) Shujie, W., Yuan, R. and Ruiqin, C., "Investigation of Wall Interference at High Angle of Attack in a Low Speed Wind Tunnel with Slotted Wall," AIAA Paper 87-2611, 1987.

14) Agrell, N. and Pettersson, B., "Numerical Computations and Measurements of Transonic Flow in a Slotted-Wall Wind Tunnel," AIAA Paper 87-2610, 1987.

15) Al-Saadi, J.A., and DeJarnette, F.R., "Wall Interference Calculation in a Transonic Test Section Including Simulation of Discrete Slots," AIAA Paper 92-0032, Jan. 1992.

16) Rizk, M.H. and Lovell, D.R., "Euler Procedure for Correcting Two-Dimensional Transonic Wind-Tunnel Wall Interference," AIAA Journal, Vol. 26, No. 12, December 1988.

17) Gopinath, R., "Wall Interference Evaluation from Pressure Measurements on Control Surfaces," AIAA 82-4301, Journal of Aircraft, Vol 19, No. 12, pp1097-1098, December, 1982.

18) King, L.S. and Johnson, D.A., "Calculations of Transonic Flow About an Airfoil in a Wind Tunnel," AIAA Paper 80-1366, 1980.

19) King, L.S. and Johnson, D.A., "Transonic Airfoil Calculations Including Wind Tunnel Wall-Interference Effects," AIAA Journal, Vol 24, No. 8, August 1986.

20) Jacocks, J.L., "An Investigation of the Aerodynamic Characteristics of Ventilated Test Section Walls for Transonic Wind Tunnels," Phd Dissertation, The University of Tennessee, December 1976.

21) Crites, R. and Rueger, M., "Modelling the Ventilated Wind Tunnel Wall", AIAA Paper 92-0035, January 1992.

22) Rueger, M. and Crites, R., "Wind Tunnel Boundary Interference Prediction and Correction," AIAA Paper 92-0036, Jan. 1992.

23) Smith, J. "A Method for Determining 2D Wall Interference on an Aerofoil from Measured Pressure Distributions Near the Walls and on the Model," NLR TR 81016 U, January 1981.

24) Cooper, G.K. and Sirbaugh, J.R., "PARC Code: Theory and Usage," Arnold Engineering Development Center, AEDC-TR-89-15, December 1989.

25) Rogers, S, "Numerical Solution of the Incompressible Navier-Stokes Equations," NASA TM 102199, November 1990.

26) Peyret, R. and Taylor, T.D., "Computational Methods for Fluid Flow," © 1983, Springer-Verlag New York, Inc.

27) Baldwin, B. and Barth, T., "A One-Equation Turbulence Transport Model for High Reynolds Number Wall-Bounded Flows," NASA TM 102847, Aug. 1990.

28) WRDC-TR-90-3022, "The GRIDGEN 3D Multiple Block Grid Generation System, Vol. 1 and 2," 1990.

29) Beutner, T., Celik, Z., and Roberts, L., "Modelling of Solid/Porous Wall Boundary Conditions for the Validation of Computational Fluid Dynamics Codes," AIAA Paper 92-0033, January 1992.
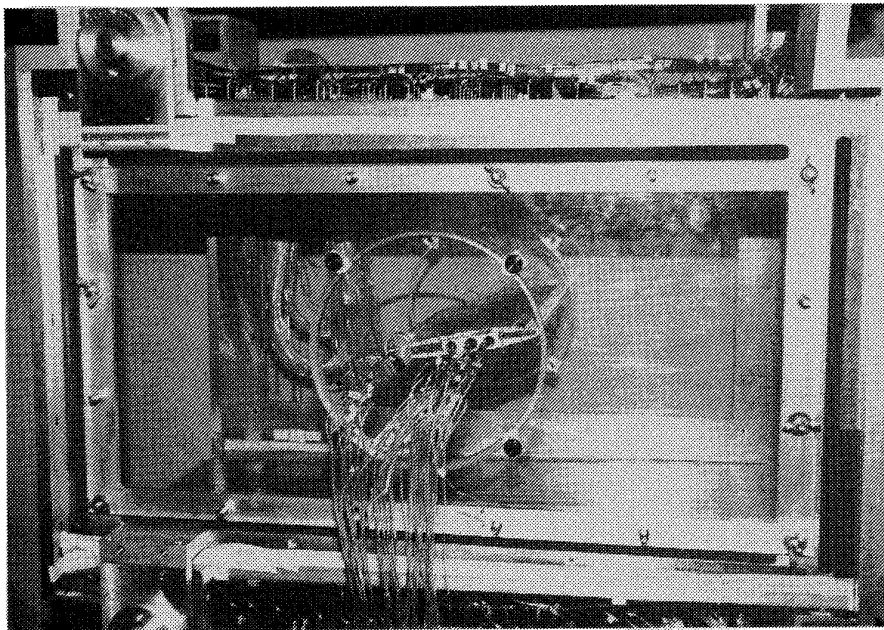
Figure 1 Variable porosity test section. Two-dimensional airfoil model is shown installed.
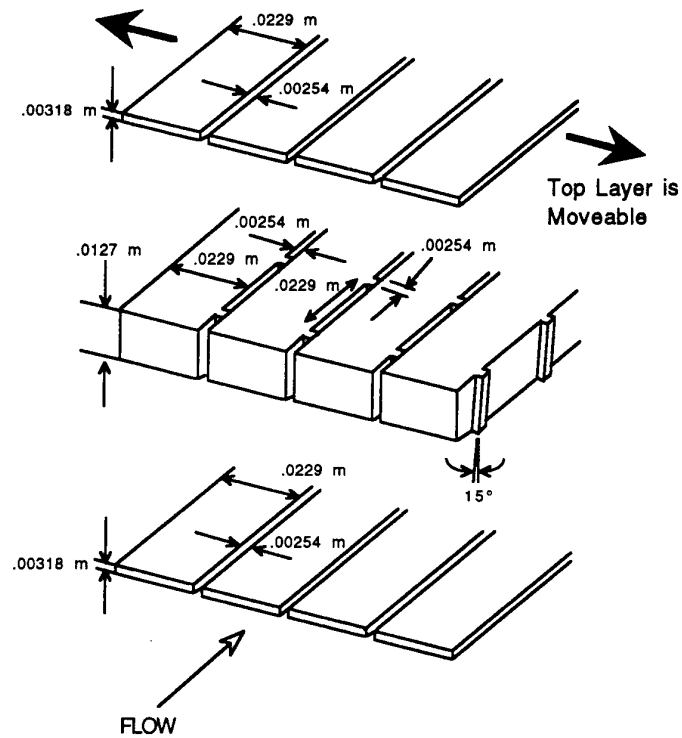
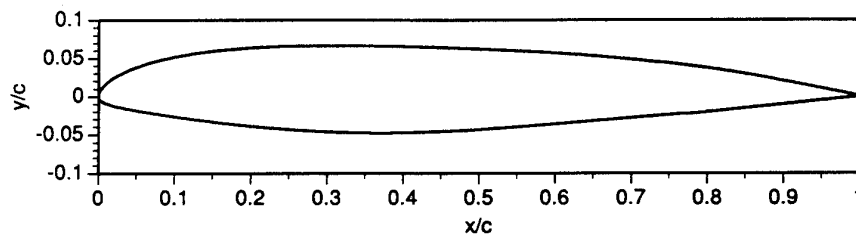**Figure 2** Exploded diagram of variable porosity wall.

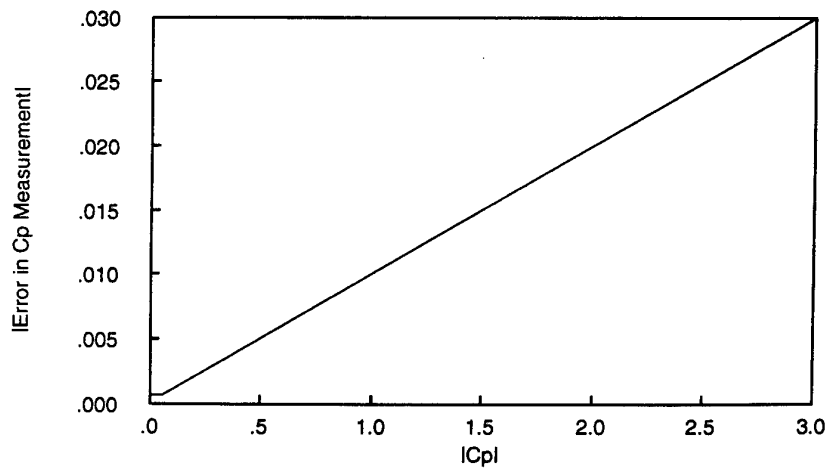**Figure 3** Boeing Advanced Transport airfoil cross section.

Figure 4 Uncertainties in the measurement of the pressure coefficient as a function of the pressure coefficient.
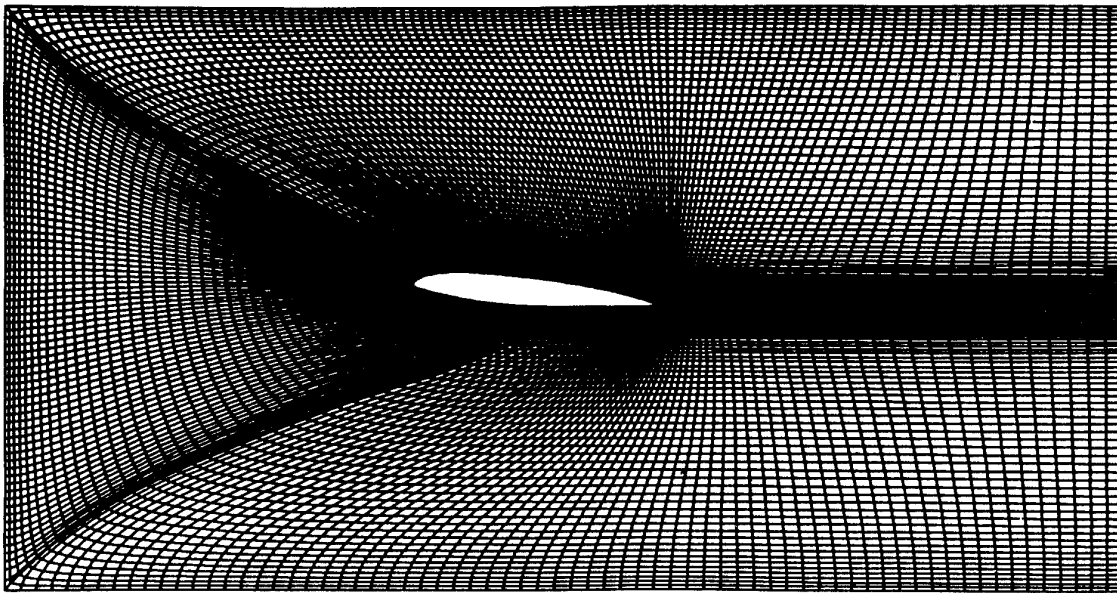
Figure 5 Grid used in two-dimensional CFD simulations for $\alpha = 5$ degrees.
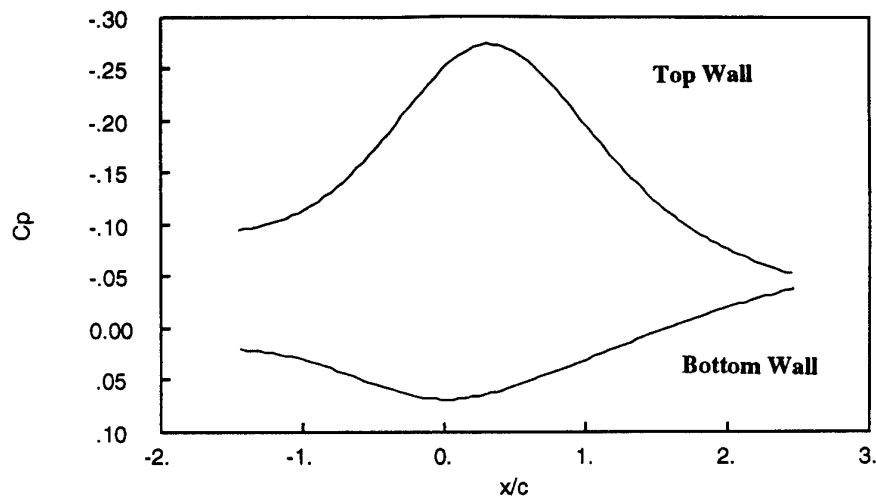

Figure 6 Velocity perturbation profiles on the top and bottom walls predicted by Navier-Stokes solver using a slip wall boundary condition.
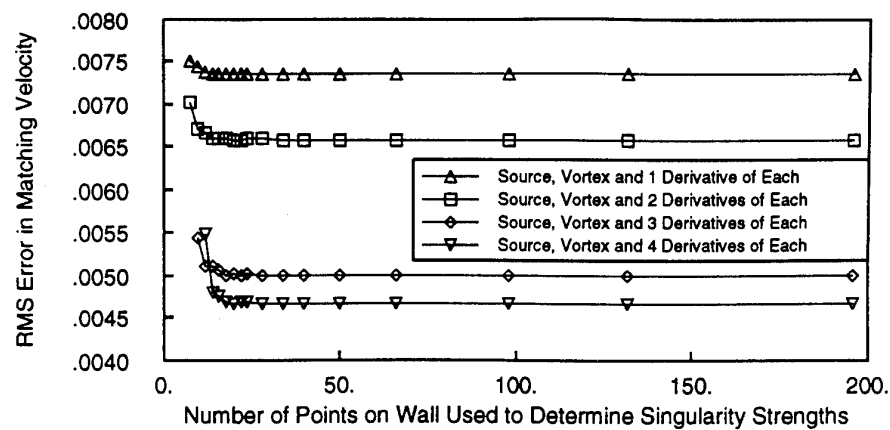

Figure 7 Root-mean-square errors as a function of the number of data points used to develop the method of singularities solution.
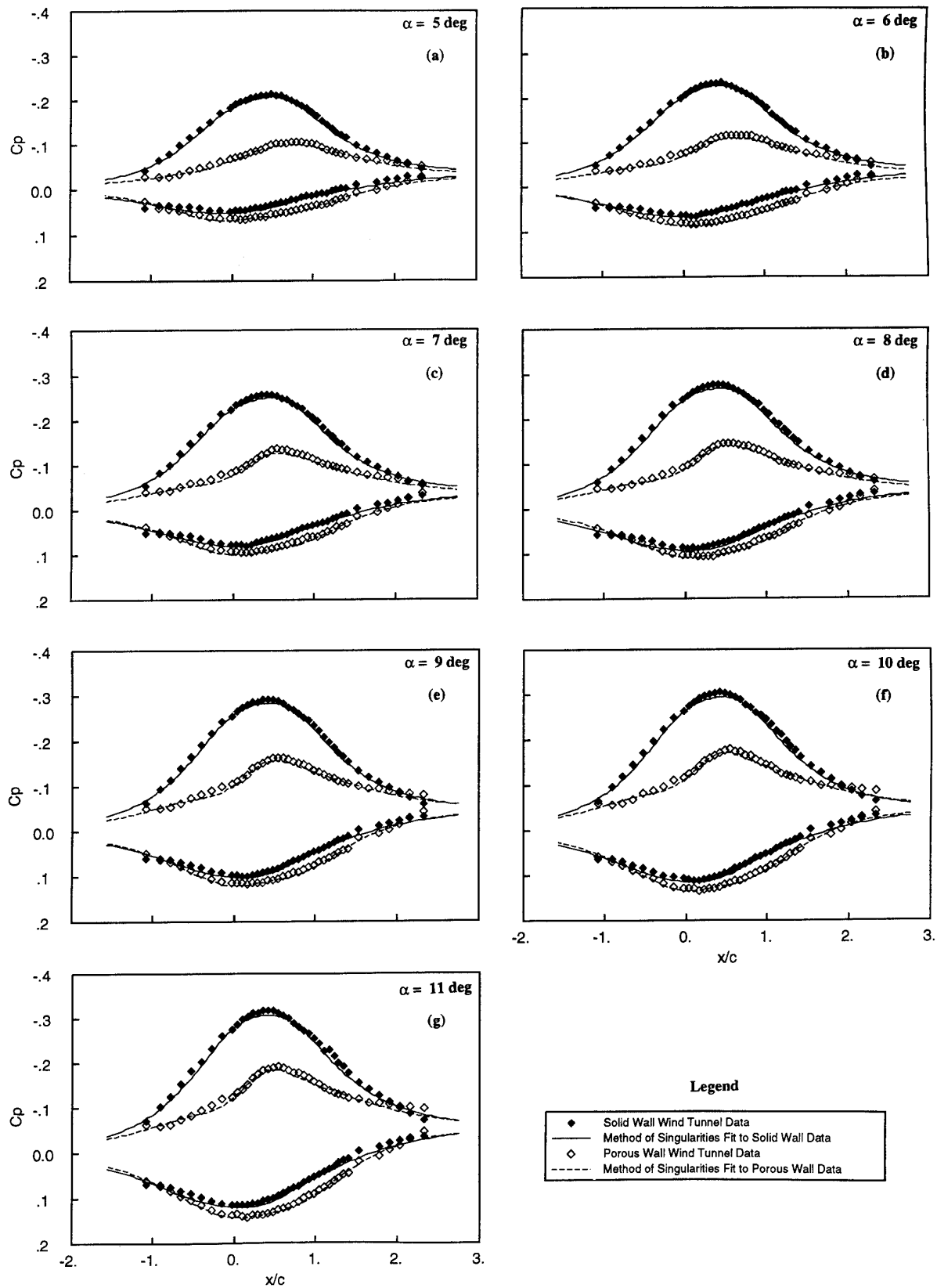
Figure 8 Method of singularities matches to pressure profiles on the wind tunnel walls for airfoil tests at α = 5-11 degrees. U_∞ = 24. m/s, Re = 3.2 x 10^5, h/c = 2.25.
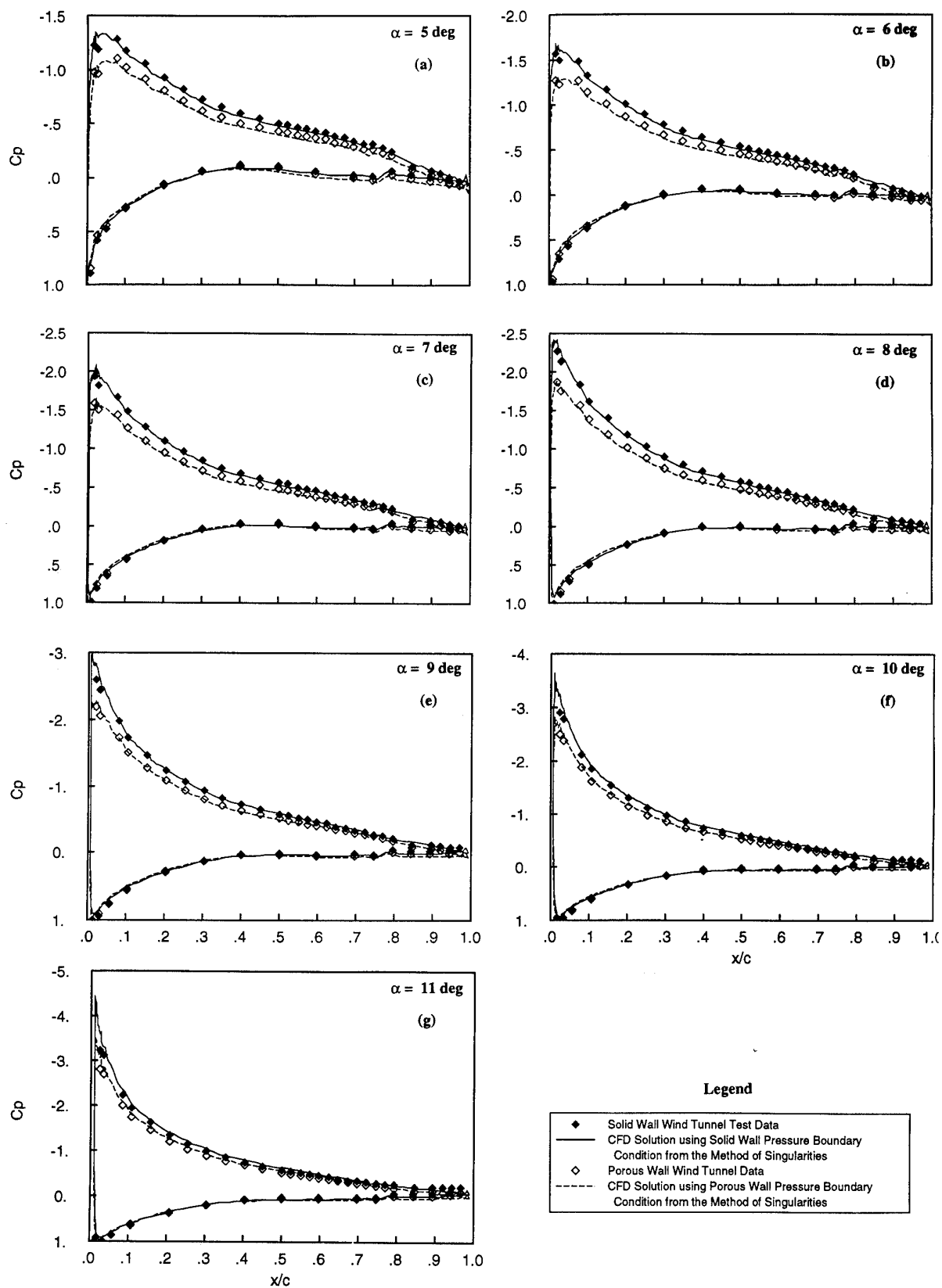
Figure 9 Comparison of experimental and CFD pressure profiles on the airfoil for α = 5-11 degrees. U_∞ = 24. m/s, Re = 3.2 x 10^5, h/c = 2.25.
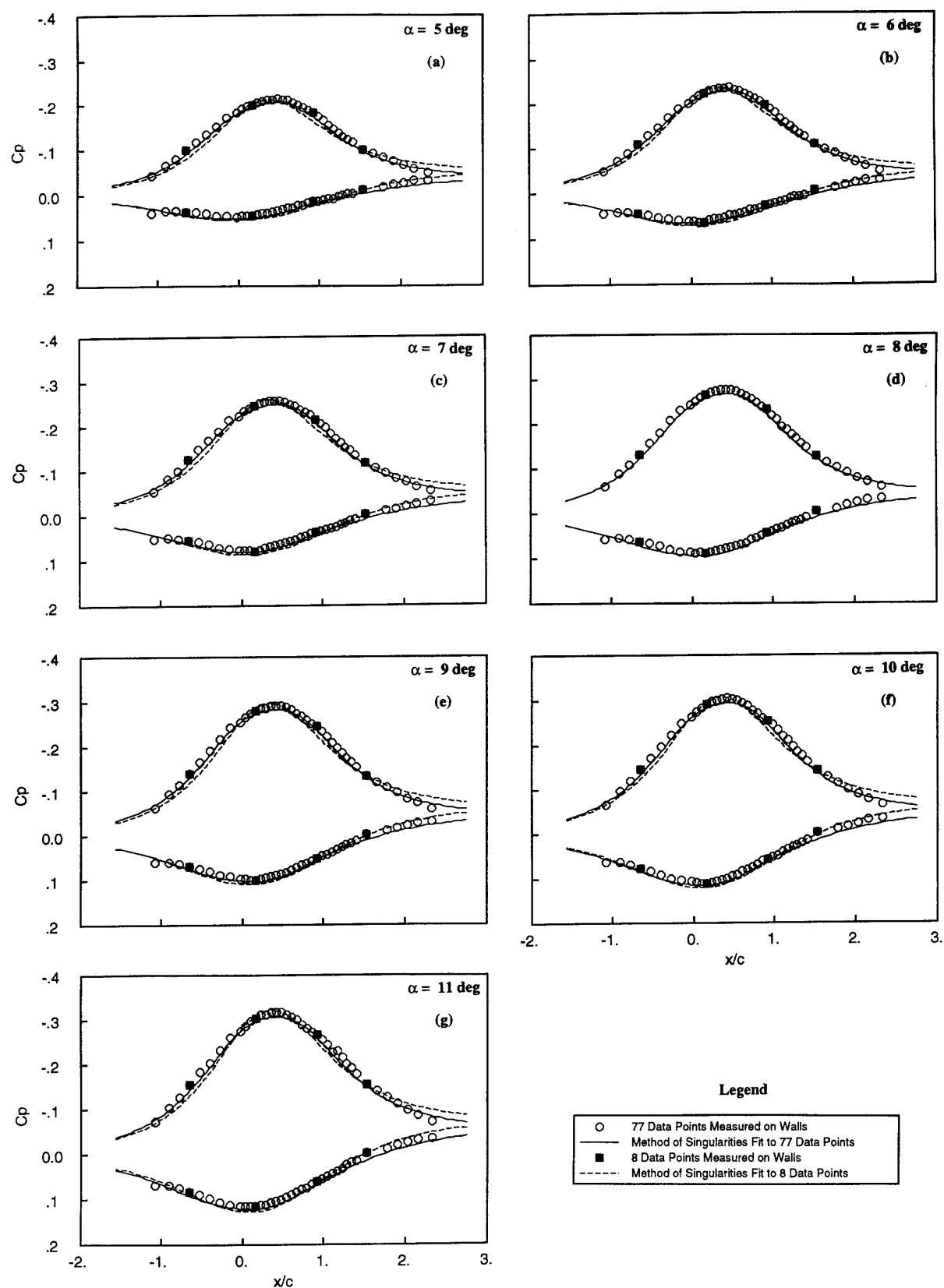
Figure 10 Method of singularities fits to sparse and fine pressure data on the wind tunnel walls for solid wall airfoil tests at α = 5-11 degrees. U_∞ = 24. m/s, Re = 3.2 x 10^5, h/c = 2.25.
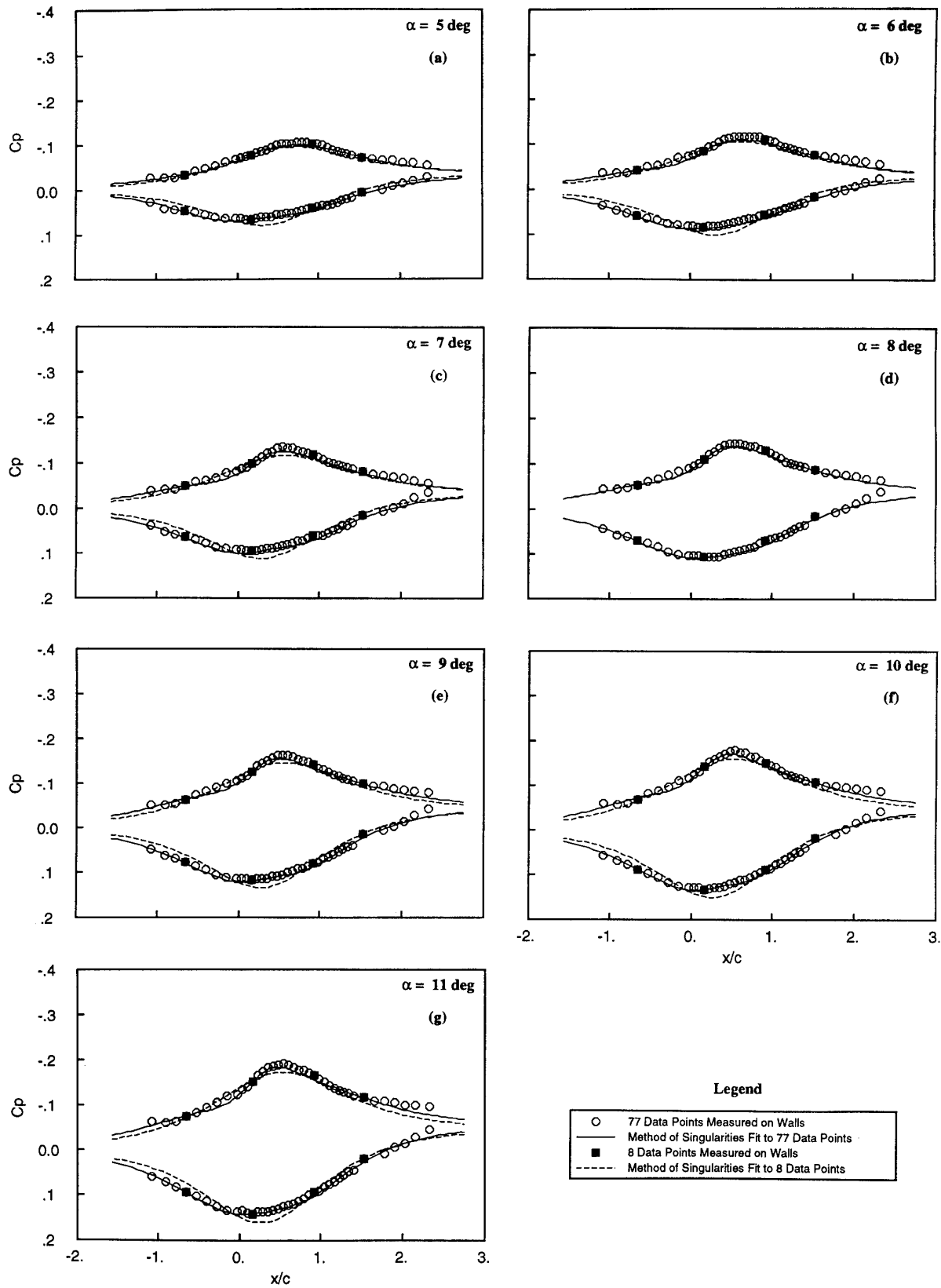
Figure 11 Method of singularities fits to sparse and fine pressure data on the wind tunnel walls for porous wall airfoil tests at α = 5-11 degrees. U_∞ = 24. m/s, Re = 3.2 x 10^5, h/c = 2.25.

Figure 12 Comparison of CFD airfoil pressure profiles obtained using the boundary conditions developed from sparse and fine data, shown in Figure 10. $U_\infty = 24.$ m/s, Re $= 3.2 \times 10^5$, h/c $= 2.25$.
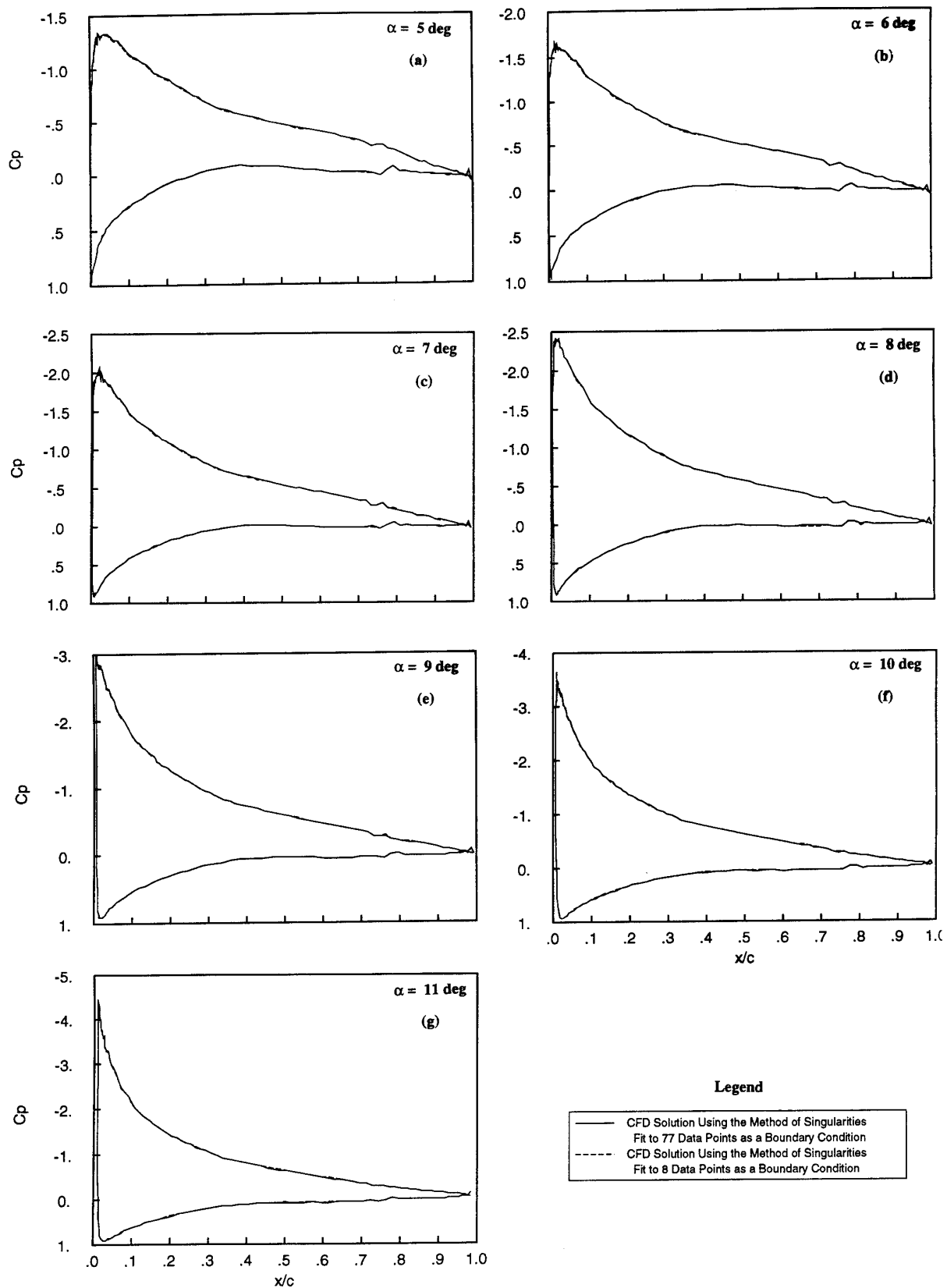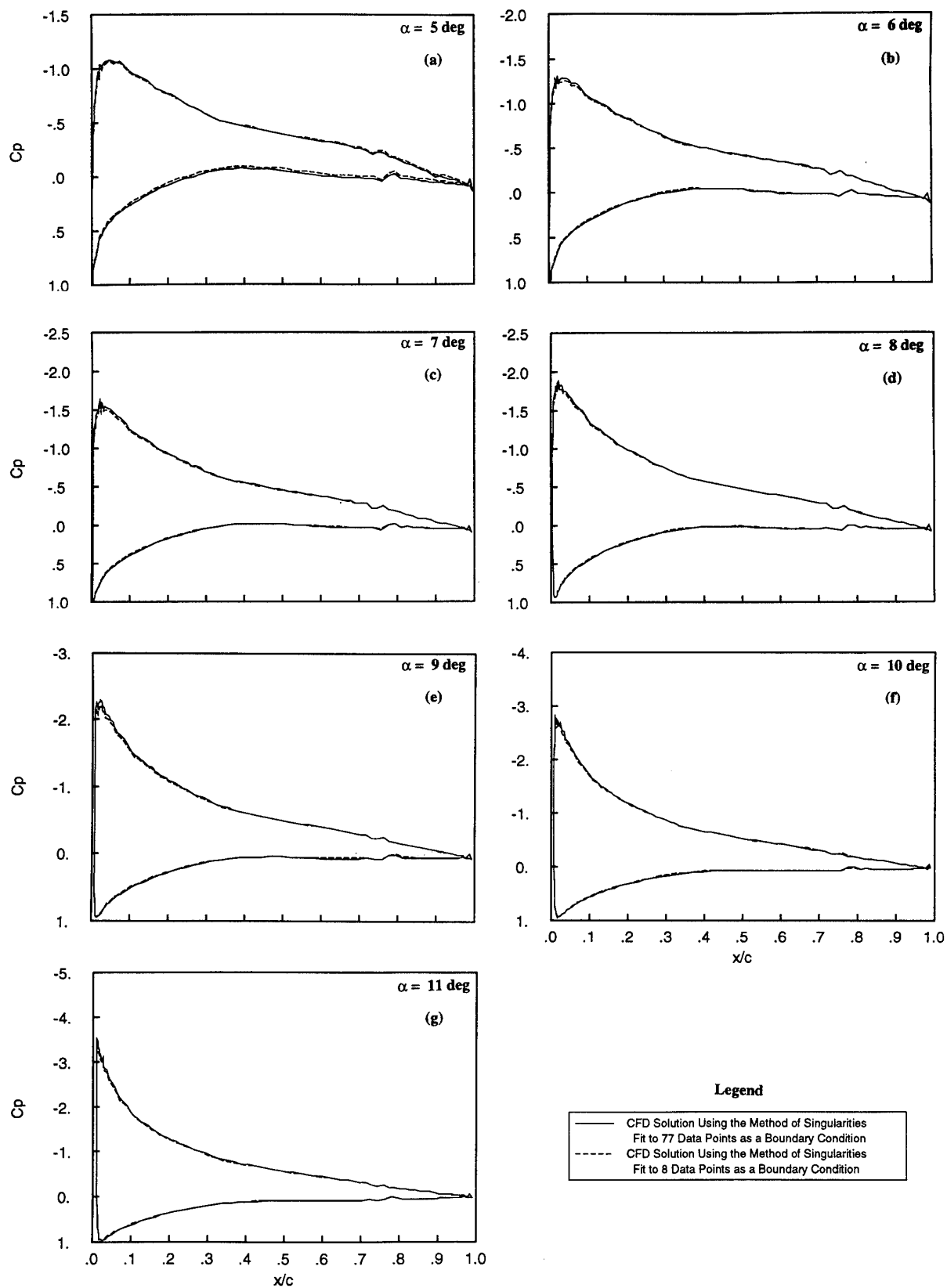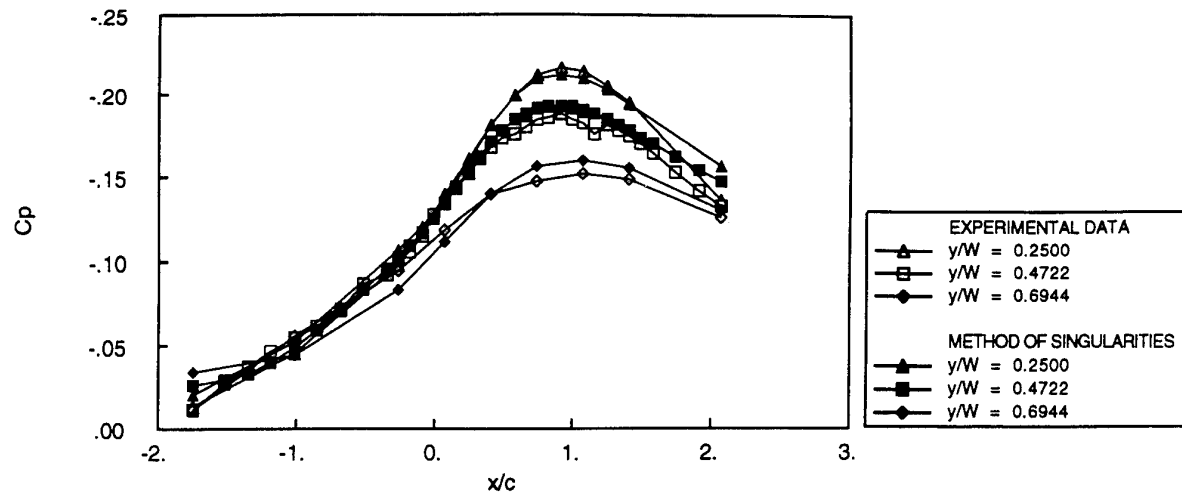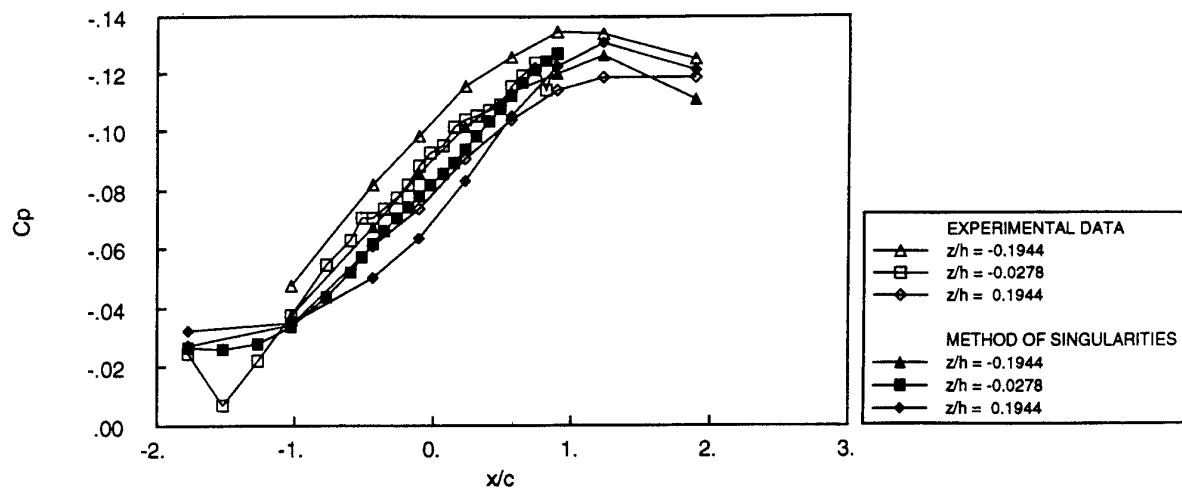
Figures 13 Comparison of CFD airfoil pressure profiles obtained using the boundary conditions developed from sparse and fine data, shown in Figure 11. $U_\infty = 24.$ m/s, Re = 3.2×10^5, h/c = 2.25.

Figures 14 Experimental data and the method of singularities fit to data from the top wall of the solid wall test of the three-dimensional wing.

Figures 15 Experimental data and the method of singularities fit to data from the side wall of the solid wall test of the three-dimensional wing.
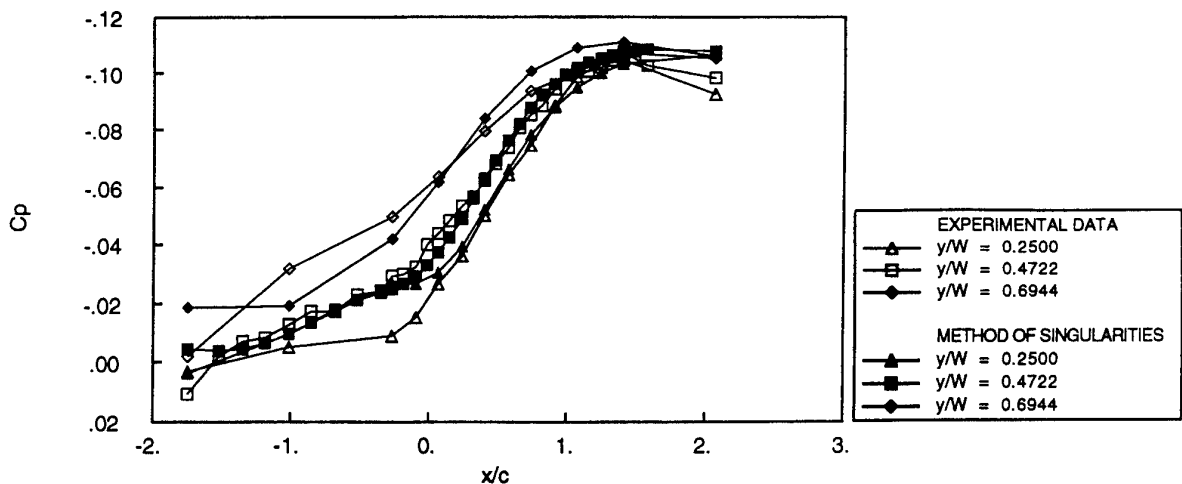
Figures 16 Experimental data and the method of singularities fit to data from the bottom wall of the solid wall test of the three-dimensional wing.

Note: Data is shown with symbols. Lines on these figures are for reference only.

Figures 17 Experimental data and the method of singularities fit to data from the top wall of the porous wall test of the three-dimensional wing.

Figures 18 Experimental data and the method of singularities fit to data from the side wall of the porous wall test of the three-dimensional wing.

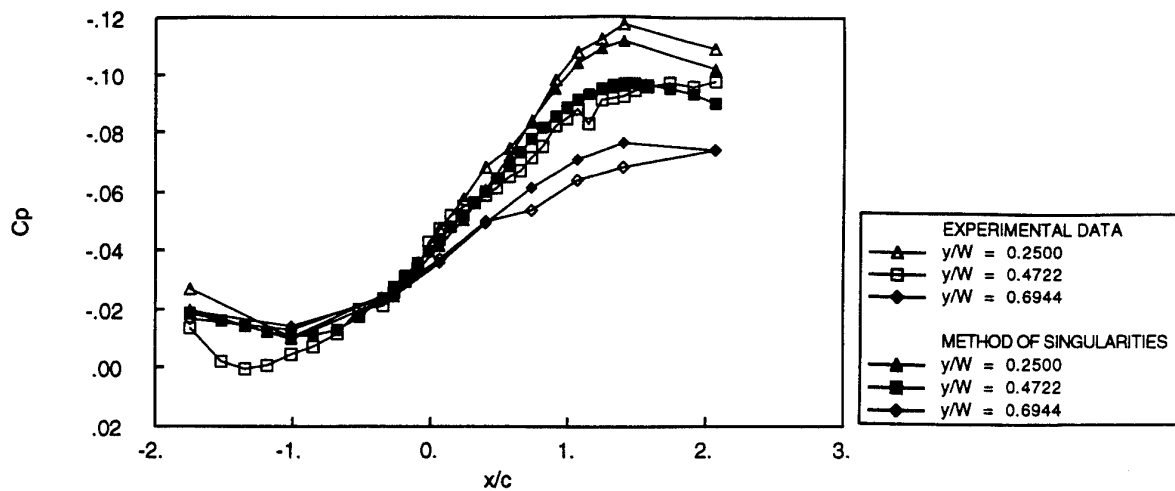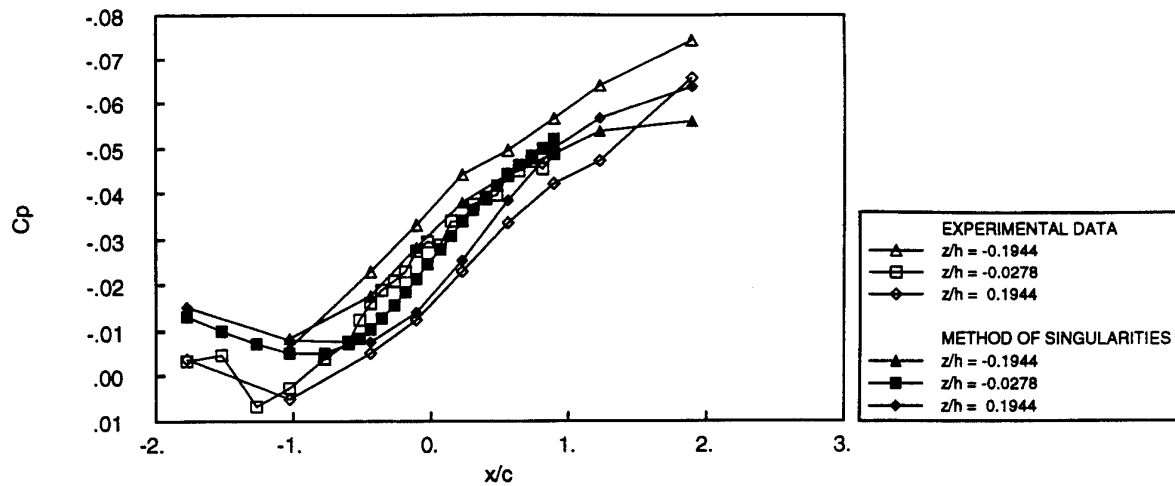**Figures 19** Experimental data and the method of singularities fit to data from the bottom wall of the porous wall test of the three-dimensional wing.
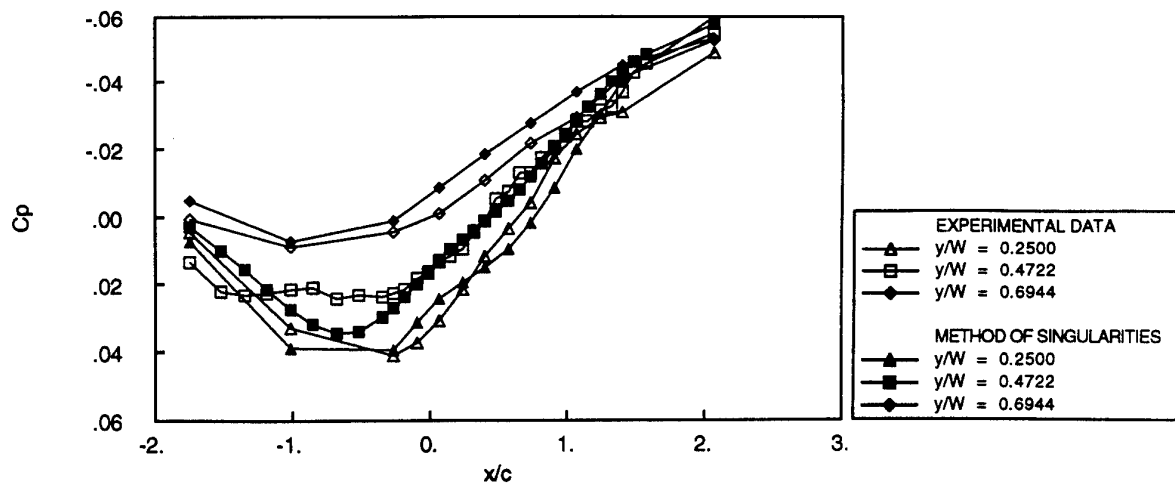
Note: Data is shown with symbols. Lines on these figures are for reference only.

Adaptive Wind Tunnel Walls Vs Wall Interference
Correction Methods in 2D Flows at High Blockage Ratios

G.P. Russo, G. Zuppardi, M. Basciani
Istituto di Aerodinamica "Umberto Nobile"
Universita' degli Studi di Napoli "Federico II"
Piazzale Tecchio, 80
80125, Napoli, Italia

SUMMARY

The aim of the present work is to compare the effectiveness of the adaptive-wall approach with the capabilities of WIAC (wall interference assessment and correction) methods in reducing wall interference effects in wind tunnel testing. Tests have been made in the 20 cm x 20 cm subsonic Adaptive Walls Wind Tunnel in Naples. Three different models having a chord of 100 mm, 150 mm and 200 mm have been used. The corresponding blockage ratios at $\alpha = 0°$ are 6%, 9% and 12%, respectively. Results of the tests show that wall adaptation and measured boundary condition WIAC methods are equivalent in correcting wall interference at moderate angles of incidence and/or with medium size models (i.e. at moderate blockage ratios). Furthermore adaptive walls wind tunnels can give data *correctable* with a WIAC method also at very large blockage ratios as high as 4 times the blockage ratio used in conventional wind tunnels.

LIST OF SYMBOLS

c = chord of the airfoil
c_l = lift coefficient
c_d = drag coefficient
c_m = moment coefficient
c_p = pressure coefficient
H = height of the test chamber
M = Mach number
p = pressure
u, v, w = velocity components
V = velocity

α = angle of incidence
γ = specific heat ratio
Φ = velocity potential

Subscripts:
∞ = undisturbed stream
m = model
w = wall

1. INTRODUCTION

The aim of the present work is to compare the effectiveness of the adaptive-wall approach with the capabilities of WIAC (wall interference assessment and correction) methods in reducing wall interference effects in wind tunnel testing. The comparison is made using as reference data those obtained in experimental tests considered as free from wall interference. Usually WIAC methods are tested using as a reference the data obtained by CFD but in this case it is difficult to take into account the effects of boundary layer on the model, sepa-

ration and wake. Residual interferences in adaptive-walls strategies are usually evaluated by global criteria (wall loading) or by residual interferences at model locations as induced incidence and camber or, in the best cases, a comparison is made with WIAC methods.

Obviously the procedure adopted in the present work is valid only if experimental interference-free data are available, as in the case of well-known standard models, and hence cannot be applied in the study of new model geometries. Nevertheless when good results are obtained, or, at least, limitations in the adopted technique, WIAC or adaptive-wall, are known it can be used with confidence also for different models whose *free-flight* behaviour is not known a priori.

For this reason the NACA 0012 airfoil has been selected as test specimen. The pertinent reference data are those reported in [1] that can be considered as free from wall interference being obtained at low blockage ratio (3% at $\alpha = 0°$) and subsequently corrected for wall interference.

Three different models having a chord of 100 mm, 150 mm and 200 mm, performing values of c/H=0.5, 0.75 and 1.0 have been used. The corresponding blockage ratios at $\alpha = 0°$ are 6%, 9% and 12%, respectively. The aims of the tests were:

- to establish the maximum blockage ratio for which the WIAC and the adaptive wall techniques are still valid

- to increase the maximum allowable blockage ratio for adaptive walls wind tunnels applying a WIAC method to the adapted data.

Several wall interference correction methods have been compared starting from the image methods, where the model is represented with singularities and images of the singularities are considered in order to satisfy the boundary conditions at the wall, up to the most recent measured boundary condition methods where no model representation is needed since the methods are mostly based on Cauchy principal value.

2. WIAC METHODS

2.1 Global methods

If the dimensions of the model are not large with respect to the test chamber and if incidence is not very large the wall effects can be divided in lift interference, whose effect is a change in stream direction and model curvature, and in the blockage effect consisting in a modification of the speed.

The model is represented as a distribution of singularities (vortices and/or doublets); images of the singularities are produced by the walls and hence interference is given by the potential that summed to the model potential satisfies the boundary conditions:

$$\Phi = \Phi_w + \Phi_m$$

If the airfoil thickness is zero it can be represented by a vortex distribution on the chord; in a closed test chamber this will result in a potential corresponding to an infinite array of vortices. Interference will depend on height of the test chamber, h, Mach number, M, lift distribution, angle of incidence, α, and on the distance of the model from the walls.

The problem needs the evaluation of the normal velocity component induced by the system of image vortices. The induced velocity is needed to correct incidence, lift and pitching moment.

Linear theory is only valid for thin airfoils at low incidence and at low Mach numbers. If it is not $\alpha \cong 0$ then conformal transformations are needed also for s = 0.

If the airfoil is thick a distribution of doublets is needed and lift interference will interact with blockage.

Obviously the global methods cannot take into account the boundary layer on the model being based on the assumption of potential flow.

2.1.1 Corrections of O(c/H)²

Allen and Vincenti [2] proposed the following corrections for incidence, lift coefficient and moment coefficient considered to be valid up to c/H = 0.15:

$$\Delta\alpha = \frac{\pi}{96\beta}\left(\frac{c}{h}\right)^2 (c_l + 4c_m)$$

$$\Delta c_l = -\frac{\pi^2}{48}\left(\frac{c}{\beta h}\right)^2 c_l$$

$$\Delta c_m = \frac{\pi^2}{192}\left(\frac{c}{\beta h}\right)^2 c_l$$

2.1.2 Corrections of O(c/H)⁴

Tomotika [3,4] used a series of conformal transformations to obtain lift and pitching moment of a plate at incidence α in an incompressible flow in a rectangular test chamber with the middle point on the centreline of the wind tunnel.

$$\Delta\alpha = \beta c_l\left[\frac{\pi}{96}\left(\frac{c}{\beta h}\right)^2 - \frac{41\pi^3}{92160}\left(\frac{c}{\beta h}\right)^4 + O\left(\frac{c}{\beta h}\right)^6\right]$$

$$\Delta c_l = c_l\left[-\frac{\pi^2}{48}\left(\frac{c}{\beta h}\right)^2 + \frac{7\pi^4}{3072}\left(\frac{c}{\beta h}\right)^4 + O\left(\frac{c}{\beta h}\right)^6\right]$$

$$\Delta c_m = c_l\left[\frac{\pi^2}{192}\left(\frac{c}{\beta h}\right)^2 - \frac{\pi^4}{15360}\left(\frac{c}{\beta h}\right)^4 + O\left(\frac{c}{\beta h}\right)^6\right]$$

These corrections can be applied for c/H ≤ 0.5.

2.2 Boundary measured condition methods

More rigorous methods to calculate wall interference require the measurement of two variables over a control surface (two-variable methods or Cauchy-type methods in 2-D flows) or the measurement of one flow variable and additional model data (one-variable methods or Schwarz-type methods in 2-D flows) [5,6].

Denoting by Φ the disturbance velocity potential $\nabla^2\Phi = 0$ is satisfied in linear regions. For an infinitesimal model Φ is split in two contributions $\Phi = \Phi_m + \Phi_w$ where Φ_m is referred to the model in free air and Φ_w is due to wall interference

$\nabla^2\Phi_m = 0$ is satisfied outside the model
$\nabla^2\Phi_w = 0$ is satisfied everywhere in the test section, model included

For a finite size model there is coupling of interferences between the wall and the model and Φ_w may have singularities inside the model.

The derivatives of Φ_w on the model are interpreted as global corrections:

$$\Delta M = \left(1 + \frac{\gamma-1}{2}M^2\right)M\frac{\partial\Phi_w}{\partial x}$$

$$\Delta\alpha_y = \frac{\partial\Phi_w}{\partial y}; \quad \Delta\alpha_z = \frac{\partial\Phi_w}{\partial z}$$

Local corrections to local c_p or M are more rigorous but less practical.

Among these methods the Ashill and Weeks method [7] and the Labrujère method [8] are two-variable methods and make use of pressure measurements on the walls.

3. ADAPTIVE-WALLS WIND-TUNNELS

The method is based on the measurement of two independent flow quantities near the wall such as static pressure and flow direction. A "fictitious external flow", tangential to the walls, with the same free-stream velocity as the real flow in the wind-tunnel and undisturbed conditions at infinity, is assumed to exist outside the physical boundaries of the test chamber. Under the assumptions that the flow is subsonic near the walls and that the streamlines deflections are sufficiently small, induced flow disturbances can be described by the linearized potential equation; pressure is calculated by means of analytical or numerical solutions starting from the measured flow direction and compared with the measured pressure. Similarly the measured pressure can be used to determine the stream surface or inclination that corresponds to the same conditions of external uniform flow at infinity.

With an iterative procedure the wall boundary conditions are adjusted until they correspond to an interference-free flow. The adjustment is based again on the comparison of data

measured and calculated along a control surface near the test section wall. This did provide the basic principle for the adaptive-wall technique that is based on the premise that if streamlines near the wind tunnel wall may be allowed to take their interference-free shape then the entire flow in the working section is free of wall interference and the force and pressures on the model would represent free-air data.

4. THE WIND TUNNEL

A detailed description of the AWWT in Naples is reported in [9]. The AWWT is an open return, indraft, continuous wind tunnel with a 0.2 m x 0.2 m x 1 m closed test chamber. Adaptation is obtained by modifying the shape of the flexible horizontal walls of the test chamber (Fig. 1). Maximum Mach number in empty wind tunnel is 0.55. Maximum unit Reynolds number is about 10^7 m^{-1}. The wind tunnel is powered by a 50 Kw a.c. motor driving a centrifugal fan. The choice of a centrifugal fan is due to the high total head loss in the circuit (= 5.5 KPa); stepless variation of speed from zero to the maximum value is achieved through inlet vane control which changes the angle at which the airstream approaches the impeller.

Two diffusers, formed of 3 mm steel, are provided, one upstream (with a 4° divergence semiangle) and one downstream (6° semiangle) of the centrifugal fan to reduce to a minimum the loss of kinetic energy at the exit. Antivibrating joints are interposed between the two diffusers and the fan which in turn stands on antivibrating supports.

In order to achieve a low turbulence level both a honeycomb with exagonal elements with L/D = 10 and a low-turbulence gauze screen have been installed in the settling chamber. A high contraction ratio (= 25) has been used to minimise losses through the honeycomb and the screen and to help turbulence reduction. The settling chamber and the contraction are formed of 5 mm steel.

The open return configuration has been chosen because it is free from the need of cooling the airstream (a critical problem in closed-circuit wind-tunnels); the pressure in the test chamber is therefore well below atmospheric pressure and this means that plenum chambers vented to the airstream must be provided to alleviate pressure loads on the two horizontal flexible walls.

One of the vertical walls of the test chamber is made with a 20 mm thick steel plates, the other one is made with a 30 mm Plexiglas plate to make all the interior of the test chamber and of the two plenum chambers visible in order to allow continuous checking of the integrity of the displacement system of the flexible walls; two Plexiglas port-holes with a diameter of 300 mm are inserted at the centre of the side walls; the hub of 2-D models is fixed to the two port-holes.

Steel plates, 0.6 mm thick, have been used for the flexible walls; the upstream ends are fixed to the last part of the contraction, the downstream ends are free; this allows both the shortening of the plate due to wall contouring and a good ventilation between plenum chambers and airstream.

Vertical displacements of the flexible walls are obtained by rotation of 2 x 16 screw jacks aligned on the centreline of the walls. In every station the jack is linked to a transversal yoke linked in turn to two supports fixed to the flexible plate. With this system transmission of moments is inhibited. Control of the twist of the wall is relied to transversal ribs. Maximum outward excursion of the walls is 26 mm.

Since the linkage between jacks and walls cannot be rigid, as it must allow the longitudinal displacement of the walls during adaptation, it is not sufficient to move jacks but is mandatory to control the true wall displacements. This task will be performed in the future automated version of the wind tunnel by position transducers; presently in each control station has been inserted a little staff, hold against the wall by a spring, that, passing through the external wall of the test chamber, shows on a scale the displacement of the flexible wall with respect to the reference position.

Control stations are 40 mm apart in the model zone and 80 mm apart upstream and downstream of the model in order to allow a more accurate control of the shape of the walls in the proximity of the model where deformations are more pronounced.

A pressure tap has been inserted in each control station; 2x16 pressure holes are therefore provided on the centreline of the horizontal flexible walls of the test chamber. The values of pressure at the entrance and exit stations have been obtained by interpolation of the values measured on the walls. This approach can be considered correct due to the quite high length/height ratio of the test chamber (L/H = 5).

The downstream end of each flexible wall is linked to a 17th dummy jack to prevent vibration. Rubber seals are inserted on the lateral edges of the walls to prevent leakage between airstream and plenum chambers.

The models are made in aluminium alloy (Fig.2); 41 pressure taps on the model surface aligned along the centreline of the model (1 on the leading edge, 20 on each side) less spaced in the leading edge zone where pressure variations are more severe, allow an accurate detection of c_p distribution. By integration of c_p curves lift coefficient and pressure drag coefficient can be obtained.

Profile drag coefficient can be obtained from wake survey through a rake made with 16 Φ = 2 mm Pitot tubes 5 mm apart.

A Pitot-static tube has been inserted in the upstream end of the test chamber to measure the test Mach number.

Besides the 32 pressure taps drilled on the flexible walls several static pressure holes have been drilled on the vertical Plexiglas test chamber wall in order to increase knowledge of stream quality:

-n. 2 static holes in the two plenum chambers to monitor the effectiveness of venting to the airstream

-n. 3 static holes at the downstream end of the test chamber to integrate the total pressure measurements made by the wake rake

All the pressures are measured by a 2 x 48 ports Scanivalve, the data are sent through an A/D converter to a microprocessor.

5. THE TESTS

An adaptation strategy based on a Cauchy two-variable method [3] has been used to streamline the two 1 m long flexible top and bottom walls via the 2 x 16 jacks. The adaptation strategy has been stopped when the required displacements of each jack was less then the minimum displacement obtainable with the present manual operation (about 0.5 mm).

In one test (C = 200 mm at $\alpha = 8°$ and M = 0.5) the adaptation was terminated before completion because the maximum allowed displacement was reached.

Two rigid walls with 2 x 16 pressure taps have been used in tests intended to simulate a conventional wind tunnel in order to apply the WIAC methods.

Tests have been performed at angles of incidence, α, varying from zero to the maximum value allowed for tests with rigid walls by the need of obtaining the desired test Mach number and for the tests with adaptive walls by the need of not trespassing the maximum allowable displacement (Table 1).Tests have been performed for the three models at 2° interval in incidence and for Mach numbers M = 0.2, 0.3, 0.4 and at the maximum Mach number allowed by the combination model, angle of attack (typically $0.43 \leq M \leq 0.47$).

TABLE 1- Test Mach numbers for nominal $M_\infty = 0.3$

Chord	c = 100 mm		c = 150 mm		c = 200 mm	
α	Rigid walls	Adapt. walls	Rigid walls	Adapt. walls	Rigid walls	Adapt. walls
0°	0.301	0.305	0.307	0.307	0.307	0.305
2°	0.304	0.303	0.301	0.305	0.308	0.303
4°	0.304	0.302	0.300	0.303	0.306	0.302
6°	0.300	0.308	0.306	0.303	0.303	0.302
8°	0.300	0.302	0.305	0.307	0.303	0.303
10°	0.304	0.302	0.304	0.304	0.307	
12°	0.300	0.302	0.302	0.304		
14°	0.303	0.308	0.307			

TABLE 2- Test Mach numbers for nominal $M_\infty = 0.5$

Chord	c = 100 mm		c = 150 mm		c = 200 mm	
α	Rigid walls	Adapt. walls	Rigid walls	Adapt. walls	Rigid walls	Adapt. walls
0°	0.470	0.508	0.457	0.508	0.495	0.500
2°	0.481	0.507	0.461	0.499	0.470	0.497
4°	0.462	0.499	0.431	0.494	0.454	0.497
6°	0.443	0.495	0.415	0.480	0.439	0.498
8°	0.425	0.484	0.410	0.471	0.429	0.487
10°	0.425	0.479		0.462		
12°	0.409	0.476		0.438		
14°		0.455				

6. RESULTS OF THE TESTS

6.1 c_p distribution on the model

A good pedagogical example of what happens in a conventional subsonic (M = 0.3) wind tunnel with rigid walls when the blockage ratio increases is represented in Fig. 3: the behaviour of walls interference is shown by the regular increase of the deviation of the c_p curves from the free-flight data with increasing blockage ratio.

Walls interference is more dramatically put in evidence when Mach number (M = 0.4) and incidence ($\alpha = 8°$) are increased (Fig. 4). In all tests, and on the reference data as well, supersonic flow is present: increasing the blockage ratio the supersonic region extends to larger parts of the airfoil, from the 5% of the reference data up to 10%, 18% and 22%. The pressure peaks are more pronounced for the 150 and 200 mm models.

Using the adaptive walls option residual interference is strongly reduced at low Mach number (M = 0.3) and low incidence ($\alpha = 4°$) as is shown in Fig. 5.

Increasing Mach number (M = 0.45) and incidence ($\alpha = 8°$) adaptation is quite good except for the 200 mm chord model (Fig. 6) for which the adaptation procedure has not been completed due to the limitation in the maximum allowable outward displacement of the flexible walls.

From Fig. 7 it can be seen that also for $\alpha = 6°$, where adaptation has been considered complete, the residual interference for the c = 200 mm model is still significant; a supersonic region has not been removed which is not present in the reference data. This combination of blockage, angle of incidence and Mach number is out of field of validity of the adaptive walls approach. Intrinsic limitations of the adaptive walls concept are the finite number of jacks and of pressure taps on the flexible walls and the approximate nature of adaptation algorithms

In Fig. 8 the c_p distribution on the adapted walls is reported. The knowledge of these data is needed at each step of the adaptation procedure and can become a useful by-product if used as an input for a measured boundary condition WIAC method in order to correct residual wall interference.

In Fig. 9 the displacement of the adaptive walls is reported. The vertical scale is 2.5 times larger than the horizontal one.

6.2 Lift curves

To test the effectiveness of the various approaches to correct or eliminate wall interference a comparison is made among:

- the experimental $c_l = f(\alpha)$ curve as measured in the wind tunnel with straight walls

- the $c_l = f(\alpha)$ curves obtained applying a classical correction method, in particular the Tomotika [3,4] method. The dynamic pressure has been corrected to take into account the effect of the solid blockage of the model and then corrected values of $\Delta\alpha$ and Δc_l have been calculated.

- the $c_l = f(\alpha)$ curve corrected with a wall pressure measurement method, in particular the Labrujère [8] method .

- the $c_l = f(\alpha)$ curve obtained with adapted wind tunnel walls.

- a reference curve obtained from the data reported in AGARD AR-138 [1].

For the smallest model (c = 100 mm) also at the higher Mach number (Fig. 10) the rigid walls data are quite good, the Labrujère and the adaptive walls methods show an equivalently good approximation to the reference data. The Tomotika method overcorrects data.

For the c = 200 mm model at M = 0.3 (Fig. 11) both the Labrujère method and the adaptive walls wind tunnel strongly reduce walls interference. The Tomotika method is not adequate.

Still worse is the case of the same model at higher Mach number (Fig. 12). The case is complicated by the decrease in

the $c_l(\alpha)$ curve slope that is not yet present in the reference data.

From these results it is evident that a blockage ratio of 12% can be considered as out of the limits of validity of both WIAC methods and adaptive walls wind tunnels also in the subsonic field. The validity of the adaptive walls approach can nevertheless be extended, in principle, if a suitable WIAC method is applied to correct the adapted data.

This approach has been followed in Fig. 13 for M = 0.3, and in Fig. 14 for M = 0.5. At both Mach numbers the adapted data corrected with the Labrujère method perfectly fit the reference data. The Tomotika method overcorrects data since its validity extends only up to c/H = 0.5.

7. CONCLUSIONS

Among the WIAC methods, as expected, those based on pressure measurements on the walls are superior to global correction methods based on image technique that can be relied upon only at low angles of incidence, Mach numbers and blockage ratios since they are strictly valid only for potential flows. Both boundary measured correction methods and wall adaptation strategies, where no model representation is needed, are based on the less stringent assumption that only at a distance from the model (near the walls boundary and at the entrance and exit sections of the test chamber) the flow is irrotational and free from discontinuities.

A good agreement at moderate angles of incidence is obtained between the reference data and the data obtained both in the adapted test chamber and with the Labrujère correction method based on measured wall pressures. The classical correction methods show large deviations from the reference data: in particular the correction method of Tomotika is to be considered not valid in the present case since it is based on the assumption that c/H << 1.

Results of the tests show that wall adaptation and measured boundary condition WIAC methods are equivalent in correcting wall interference at moderate angles of incidence and/or with medium size models (i.e. at moderate blockage ratios). Furthermore adaptive walls wind tunnels can give data *correctable* with a WIAC method also at very large blockage ratios as high as 4 times the blockage ratio used in conventional wind tunnels. This approach makes therefore a more efficient use of the wind tunnel (higher Reynolds number at low power and low cost).

8. REFERENCES

[1] Thibert, J. J., Grandjacques, M. and Ohman, L.H., "NACA 0012 Airfoil", AGARD-AR-138, Report of the AGARD FDP WG-04 on "*Experimental Data Base for Computer Program Assessment*", May 1979.

[2] Allen, H.J. and Vincenti, W.G., "Wall Interference in a Two-Dimensional Wind Tunnel, with Consideration of the effect of compressibility", NACA Report 782, 1944.

[3] Tomotika, S., "The Lift of a Flat Plate Placed in a Stream between Two Parallel Walls and some Allied Problems", Aero. Res. Inst. (Tokyo) Report 101, 1934.

[4] Tomotika, S., "The Moment of the Fluid Pressures Acting on a Flat Plate Placed in a Stream between Two Parallel Walls and some Allied Problems", Aero. Res. Inst. (Tokyo) Report 170, 1938.

[5] Mokry, M. "Residual Interference and Wind Tunnel Wall Adaptation", AIAA-89-0147, Jan. 1989.

[6] Mokry, M. (editor), Erickson, J. C., Goodyer, M. J., Mignosi, A., Russo, G. P., Smith, J.,Wedemeier, E., and Newman, P. A.(NASA LaRC), "Limits of Adaptation, Residual Interferences", Chapter 6 of the AGARD-AR-269, Fluid Dynamics Panel WG-12 on "Adaptive Wind Tunnel Walls: Technology & Applications", April 1990.

[7] Labrujère Th. E., "Correction for Wall-Interference by Means of a Measured Boundary-Condition Method", NLR TR 84114 U, November 1984.

[8] Ashill, P.R., Weeks, D.J., "A Method for Determining Wall Interference Corrections in Solid-Wall Tunnels from Measurements of Static Pressure at the Walls", AGARD FDP Specialists' Meeting on Wall Interference in Wind Tunnel, London, 19-20 May 1982.

[9] Russo, G.P., Zuppardi, G., Basciani, M, "Evolution of the Adaptive Walls Wind Tunnel", Proceedings of the Sixth International Conference on Computational Methods and Experimental Measurements (CMEM93)", Siena 3/5 May 1993, pp.395-410.

[10] Everhart, J.L., "A Method for Modifying Two-Dimensional Adaptive Wind-Tunnel Walls Including Analytical and Experimental Verification", NASA TP-2081, February 1983.
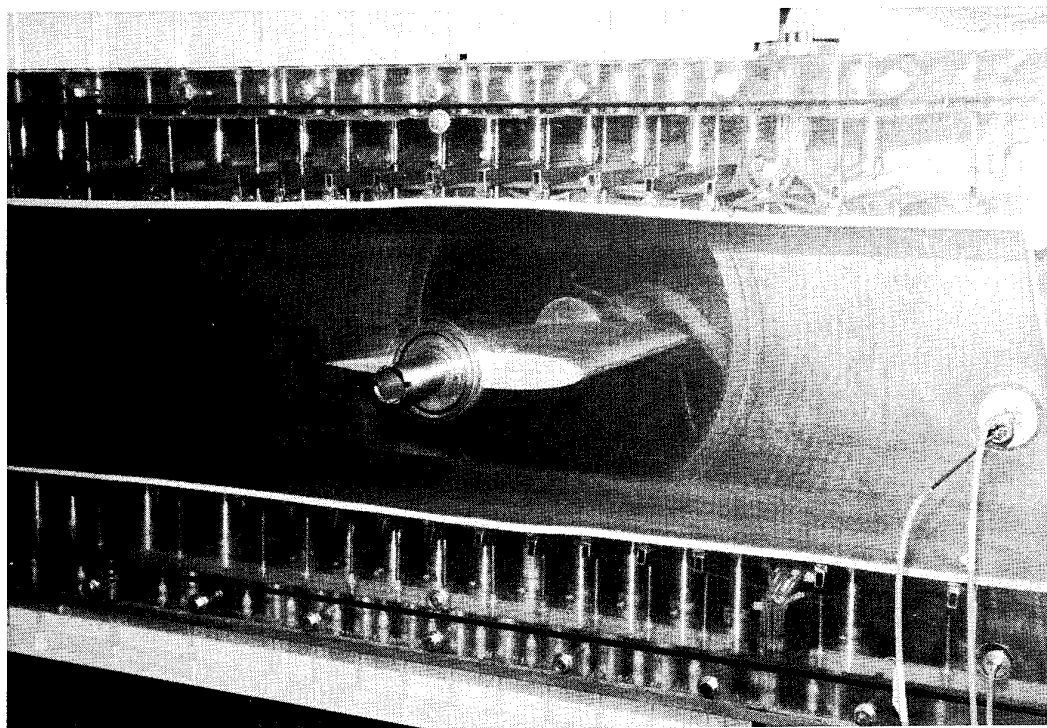
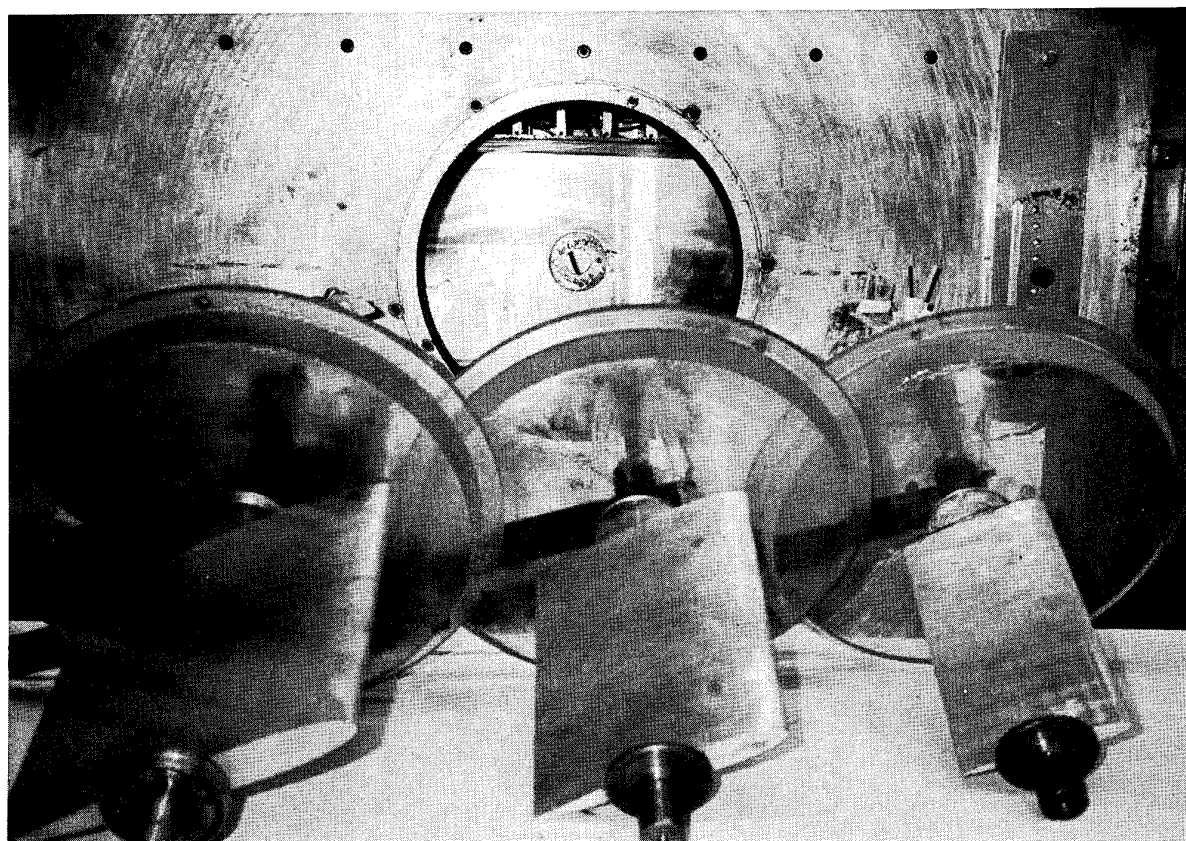Fig. 1- The test chamber of the Adaptive-Walls Wind Tunnel in Naples.

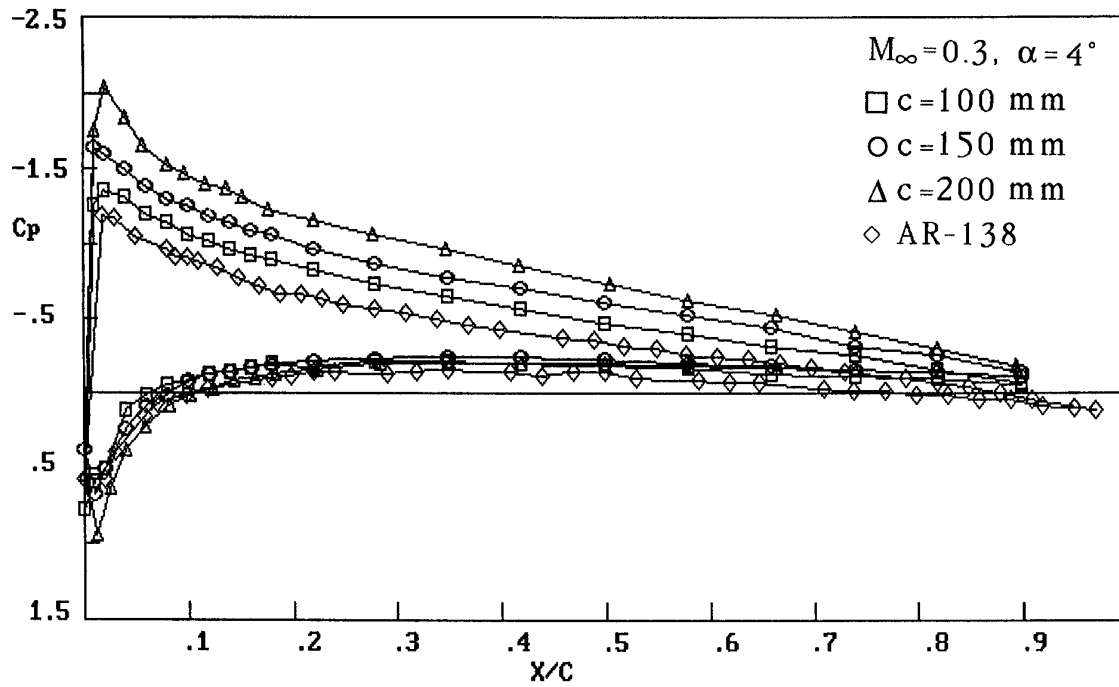Fig. 2- The three tested models (c = 100 mm, c = 150 mm and c = 200 mm) of the NACA 0012.

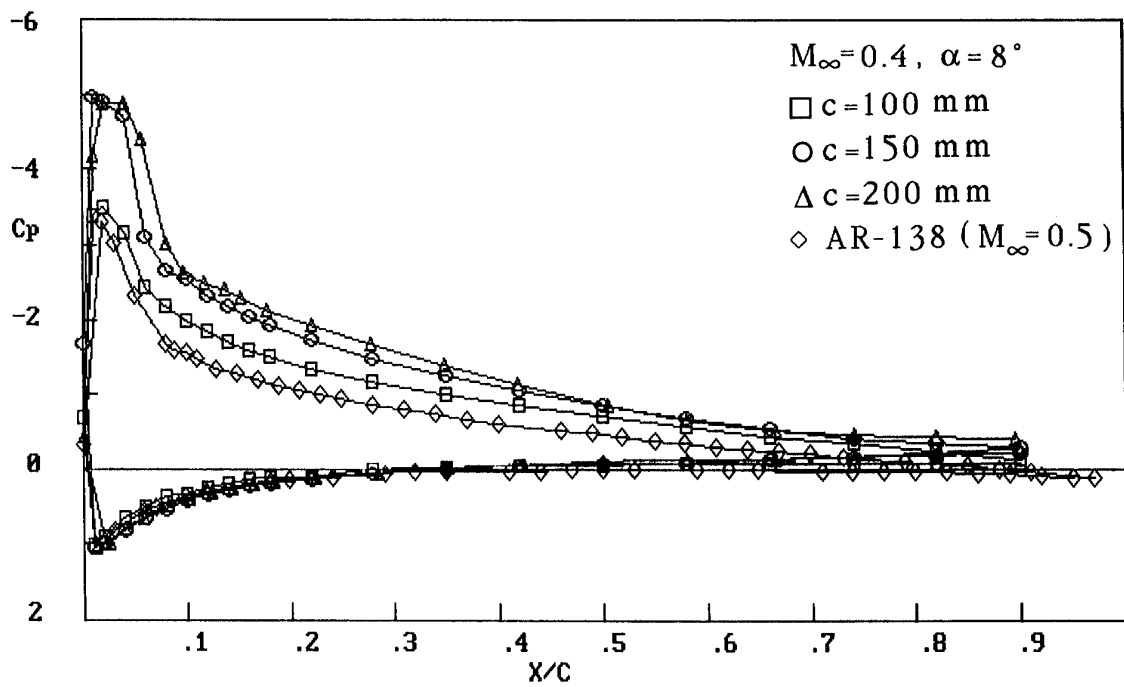Fig. 3- Effects of increasing the blockage ratio on the c_p distribution on the model at M = 0.3 and α = 4°.

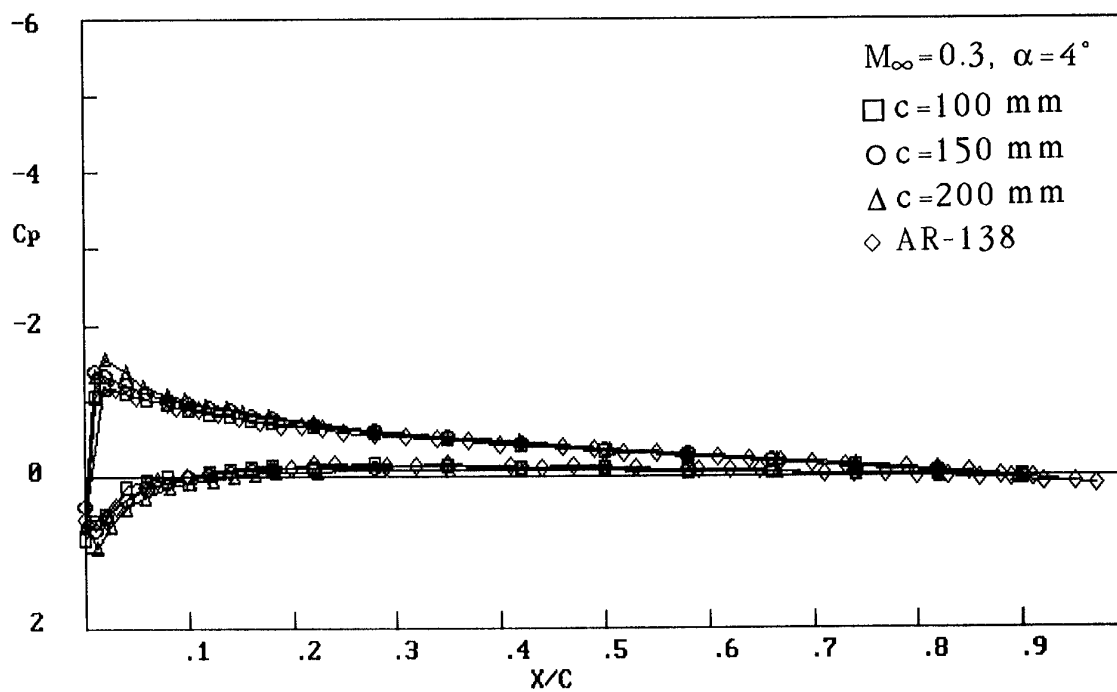Fig. 4- Effects of increasing the blockage ratio on the c_p distribution on the model at M = 0.4 and α = 8°.

Fig. 5- Effects of walls adaptation on the c_p distribution on the model at M = 0.3 and α = 4°.
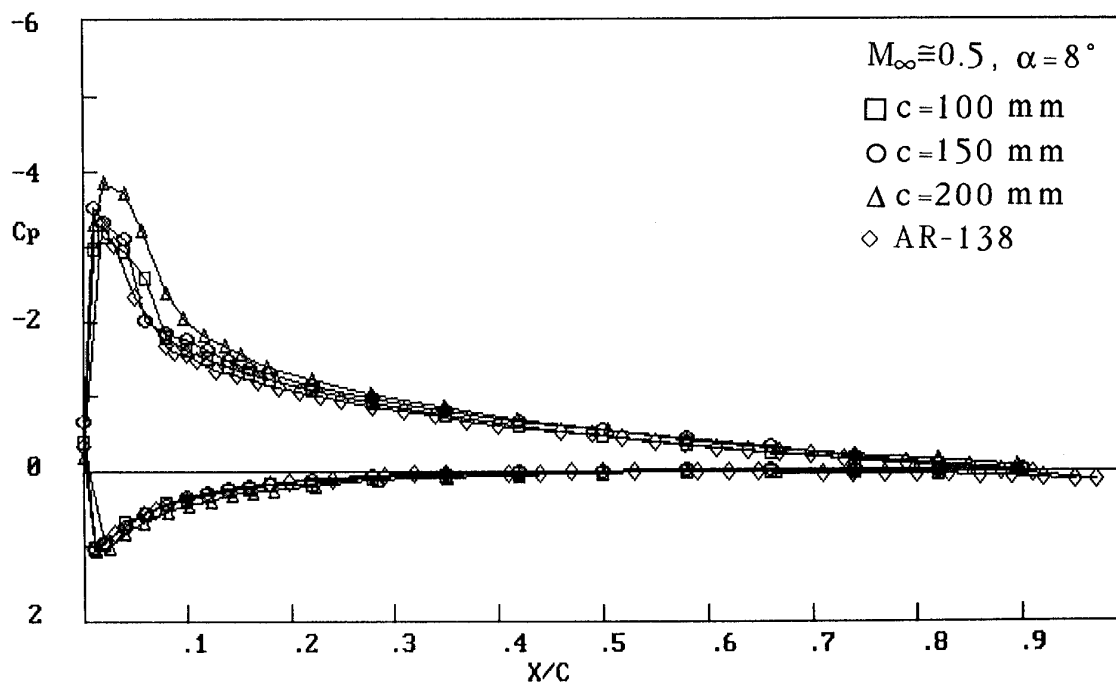
Legend: $M_\infty = 0.3$, $\alpha = 4°$; $\square$ c =100 mm; $\bigcirc$ c =150 mm; $\triangle$ c =200 mm; $\diamond$ AR-138

Fig. 6- Effects of walls adaptation on the c_p distribution on the model at M = 0.5 and α = 8°.

Legend: $M_\infty \cong 0.5$, $\alpha = 8°$; $\square$ c =100 mm; $\bigcirc$ c =150 mm; $\triangle$ c =200 mm; $\diamond$ AR-138
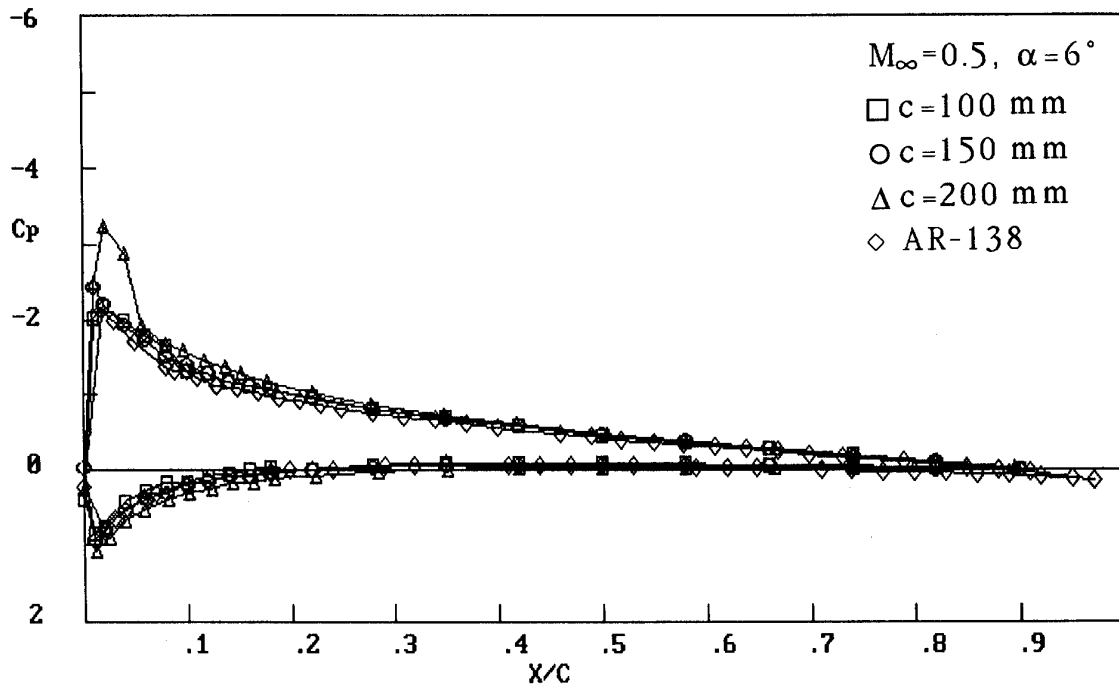
Fig. 7- Effects of walls adaptation on the c_p distribution on the model at M = 0.5 and α = 6°.

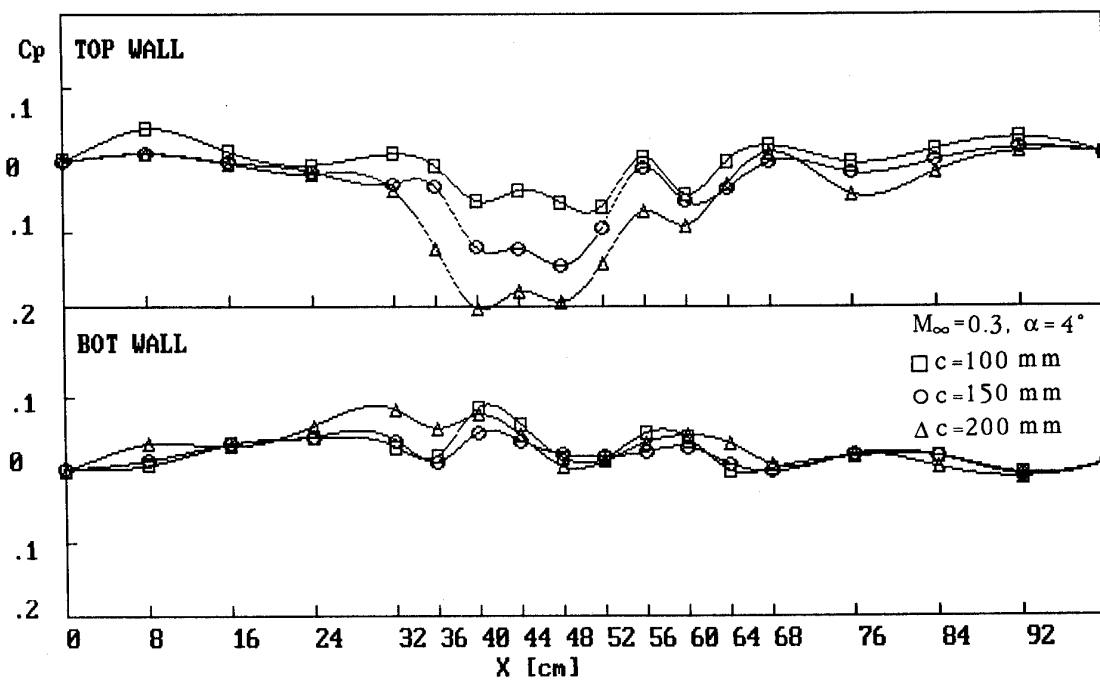Fig. 8- A sample c_p distribution on the adapted walls at M = 0.3 and α = 4°.
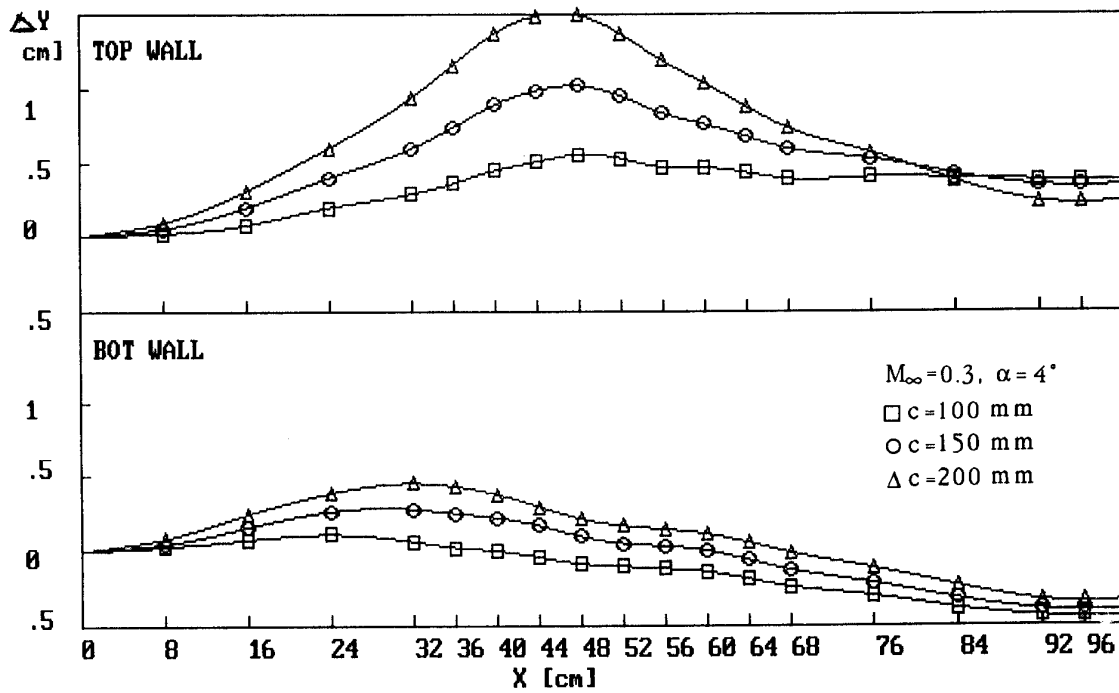
Fig. 9- Sample displacements of the flexible walls after adaptation at M = 0.3 and $\alpha = 4°$.

Fig. 10- Comparison of WIAC methods and adaptive walls in correcting lift data obtained in a wind tunnel with rigid walls at M = 0.45 and c = 100 mm.

Fig. 11- Comparison of WIAC methods and adaptive walls in correcting lift data obtained in a wind tunnel with rigid walls at
M = 0.3 and c = 200 mm.

Fig. 12- Comparison of WIAC methods and adaptive walls in correcting lift data obtained in a wind tunnel with rigid walls at
M = 0.45 and c = 200 mm.

Fig. 13- Comparison of WIAC methods in correcting lift data obtained in a wind tunnel with adapted walls at M = 0.3 and
c = 200 mm.

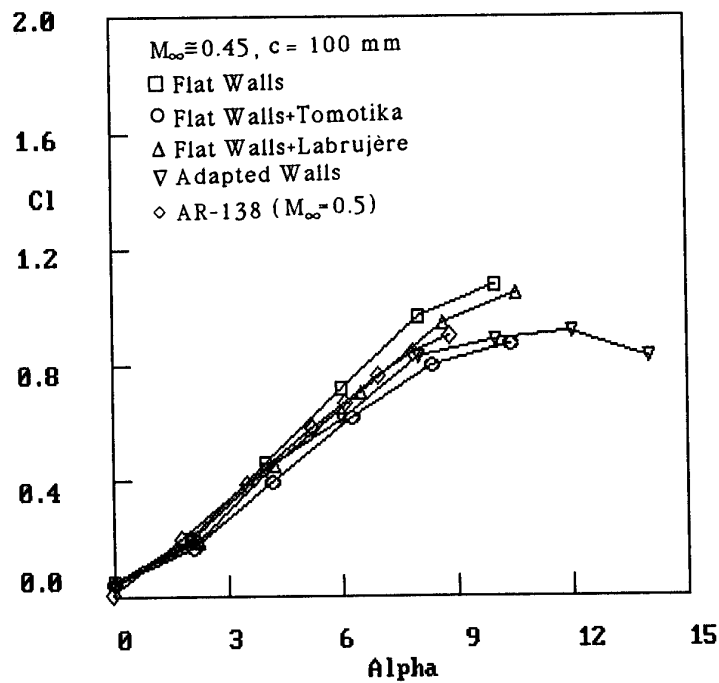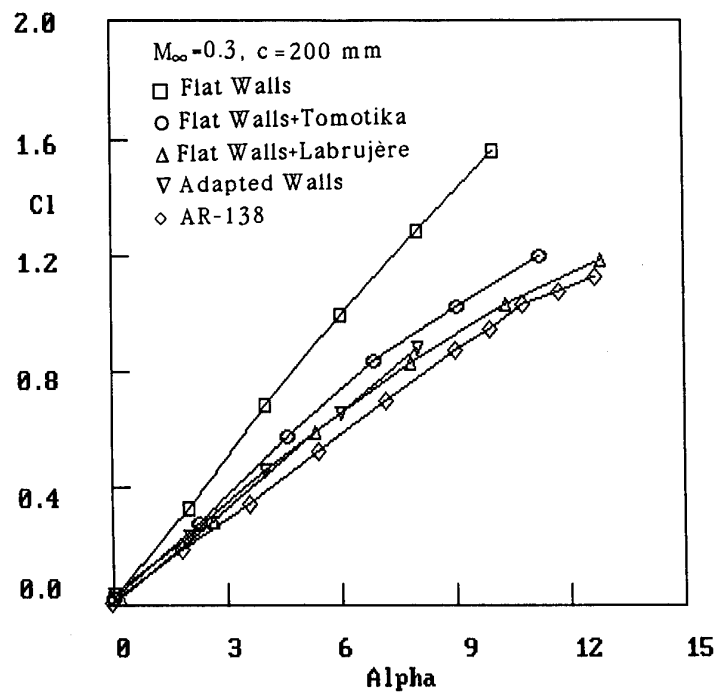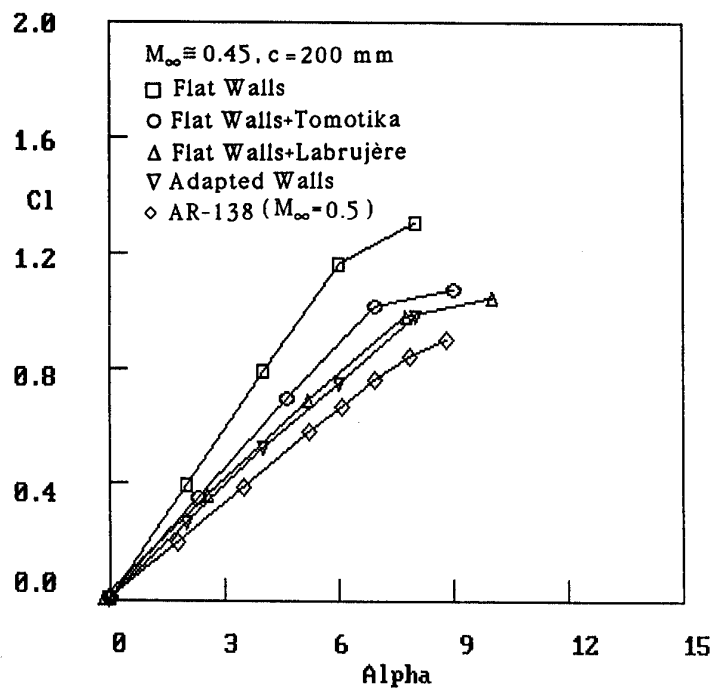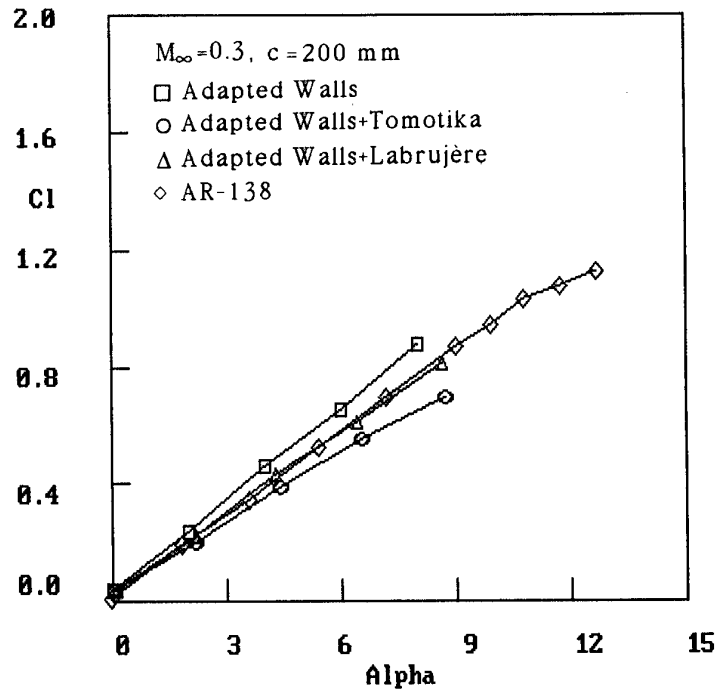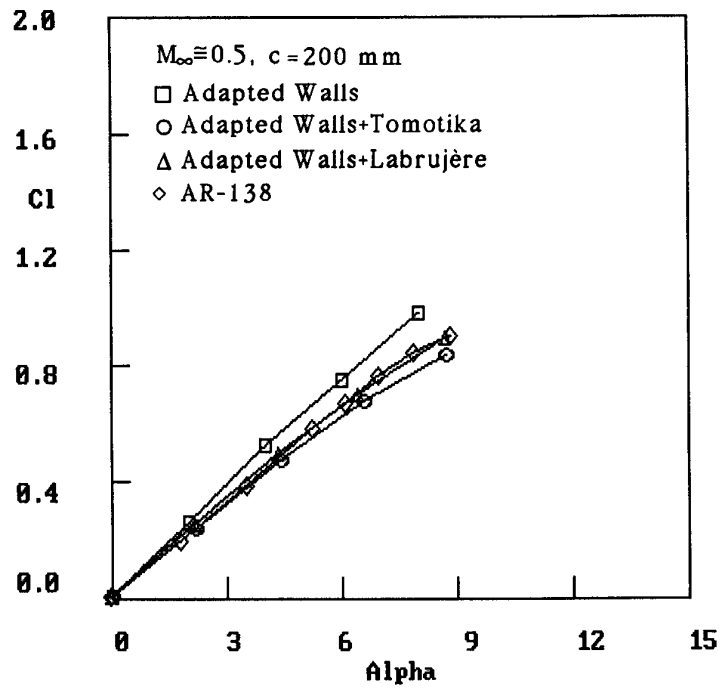Fig. 14- Comparison of WIAC methods in correcting lift data obtained in a wind tunnel with adapted walls at M = 0.5 and
c = 200 mm.

DEVELOPMENT OF PNEUMATIC TEST TECHNIQUES FOR SUBSONIC HIGH-LIFT AND IN-GROUND-EFFECT WIND TUNNEL INVESTIGATIONS

Robert J. Englar
Senior Research Engineer, Aerospace Laboratory
Georgia Tech Research Institute
Georgia Institute of Technology
Atlanta, GA 30332-0800, USA

1. SUMMARY

Wind tunnel evaluations of two-dimensional high-lift airfoils and of vehicles operating in ground effect near the tunnel floor require special test facilities and procedures. These are needed to avoid errors caused by proximity to the walls and interference from the wall boundary layers. Pneumatic test techniques and facilities were developed for GTRI aerodynamic research tunnels and calibrated to verify that these wall effects had been removed. The modified facilities were then employed to evaluate the aerodynamic characteristics of blown very-high-lift airfoils and of racing hydroplanes operating in ground effect at various levels above the floor. The pneumatic facilities, techniques and calibrations are discussed and typical aerodynamic data recorded both with and without the test-section blowing systems are presented.

2. INTRODUCTION

Tunnel wall interference and model support interaction can present significant difficulties in subsonic wind tunnel evaluations when the model is displaced from the test-section centerline or comes in close proximity to the walls. These problems can occur because of the presence of wall boundary layers and their associated velocity/momentum deficits. If not corrected, their interaction with the model flowfield can produce significant inaccuracies. This has been encountered in two types of research programs currently underway at the Georgia Tech Research Institute (GTRI) Aerospace Laboratory: high-lift airfoils and vehicles in ground effect.

Accurate testing of 2-D high-lift airfoils (both blown and unblown) poses a significant problem when setting up a test facility free of the non-uniform flow caused by interaction between the wind-tunnel wall boundary layer (BL) deficits and the adverse pressure gradients generated on the model. This interaction can cause strong vorticity at the wall/model junction, yielding non-uniform local angle of attack and aerodynamic loadings varying with the distance from the walls. Due to vortex-induced downwash, the true angle of attack may be less than the geometric value, even when corrected for conventional tunnel interference. The results are not high-quality two-dimensional data. If balance data are recorded, a significant portion of the 2-D lift force is missing and an enormous streamwise component is added as induced drag. Clearly, these problems must be prevented in order to obtain accurate 2-D data and meaningful aerodynamic trends. This is especially important if 2-D data are to be compared against computational fluid dynamics (CFD) calculations.

Testing of models in ground effect is also affected by these boundary-layer deficits, which will normally result in under-prediction of the ground effect. Evaluations of aircraft in takeoff and landing configurations (especially very-high-lift STOL aircraft) and of vehicles such as Unlimited-Class racing hydroplanes, which operate almost entirely in ground effect, will be erroneous if the BL interaction isn't properly treated.

Researchers at the GTRI Aerospace Laboratory have developed pneumatic systems for wall boundary-layer control to adequately evaluate both of these types of aerodynamic configurations. The following sections will provide: brief discussions of the concepts to be tested and their specific test requirements; a description of the test facilities developed and their calibrations; and results of the experimental evaluations, both with and without the pneumatic test systems operating.

3.0 SPECIFIC TEST REQUIREMENTS

3.1 Blown High-Lift Airfoils

Tangential blowing over trailing-edge contours has been shown to offer significant benefits in terms of high-lift augmentation at low blowing rates and with a minimum of mechanical complexity (See, for example, References 1 and 2). The Circulation Control Wing (CCW) concept, which employs blowing over a rounded trailing edge, has been applied to the flight-demonstrator aircraft shown in Figure 1, and has produced more than a doubling of usable lift over that of the conventional mechanical flap. This results in a 35 percent reduction in terminal-area velocities, and up to 65 percent reductions in takeoff/landing ground rolls (Reference 2). Recent improvements (Figure 2, Reference 3) have added camber from a short-chord rounded flap and a blown leading-edge device to the CCW airfoil. However, as can be seen from these pressure distributions, the extreme suction peaks from the high supercirculation yield severe adverse pressure gradients at both the leading and trailing edges. If not addressed, these will yield strong interactions with the

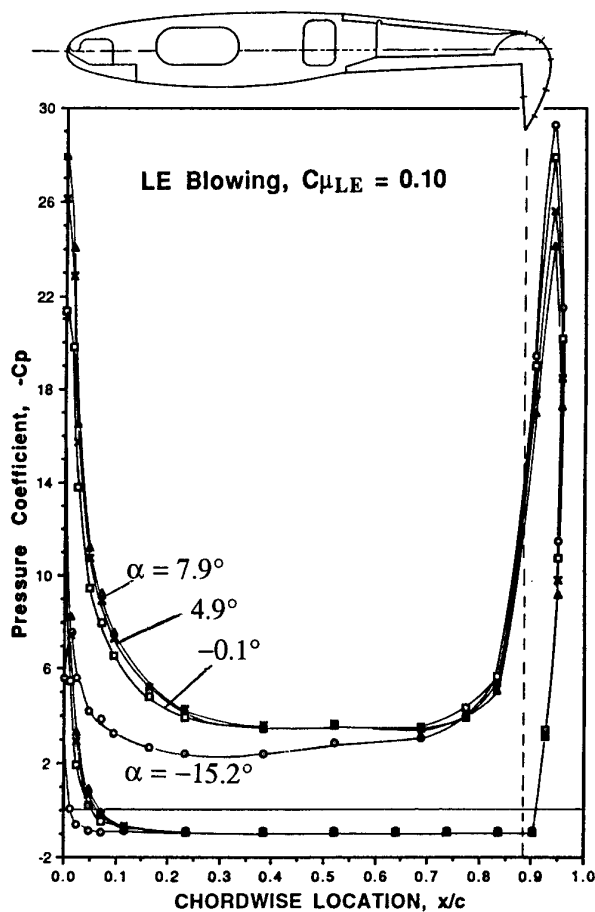Figure 1 - A-6/Circulation Control Wing Flight Demonstrator Aircraft

Figure 2 - Chordwise Static Pressure Distributions for Dual-Slot, Dual-Radius CCW Airfoil with Leading Edge Blowing

tunnel wall BL momentum deficits and resulting strong vorticity at the wall/model junction. This will produce non-uniform 2-D results, incorrect angle of attack, reduced lift and erroneous drag. Thus, proper treatment of the wall boundary layer is essential, and has been addressed by GTRI in a research program conducted for NASA Langley Research Center (Reference 3).

3.2 Racing Hydroplanes in Ground Effect
Current Unlimited-Class racing hydroplanes powered by gas turbine engines (Figure 3, from Reference 4) are able to reach competition speeds exceeding 200 mph. Because of the increased aerodynamic lift produced by operation in ground effect, the majority of the boat is out of the water, and the hydrodynamic drag is greatly reduced. At the resulting higher speeds, the vehicle cruises just above the water surface, and aerodynamic forces predominate over the hydrodynamic ones as a delicate force and moment balance is established. Unfortunately, current hydroplane designs can become aerodynamically unstable when disturbed from their normal racing attitudes. Wind gusts or rough water conditions can cause the boats to pitch up and rise above the water surface. These perturbations can be large enough to trigger aerodynamic instability. This often leads to a phenomenon known as "blowover," where the racing boat transitions from waterborne to airborne, frequently pitching or rolling wildly, and eventually crashing back to the water surface. (Videotapes of these events show blowovers with pitchup of 360° or more and

Figure 3 - Current Unlimited-Class Racing Hydroplane Operating at Speed in Ground Effect (Ref. 4)

the resulting crashes). Frequently, the existing aerodynamic surfaces are unable to restore control. Obviously, this type of airborne "maneuver" can be extremely damaging to the boat and very dangerous to the drivers. Properly conducted wind-tunnel evaluations can provide valuable data for control system design.

To address the above problem areas, an experimental research and development program was undertaken by the GTRI Aeronautics Research Branch under contract to Douglas Ford Engineering, consultant for development of racing hydroplanes. The prime objective of the program was to evaluate the aerodynamic and stability characteristics of a baseline 1/8-scale Unlimited hydroplane boat model by using a subsonic research wind tunnel that had been suitably modified to simulate the air/water interface and the associated strong ground effect. An essential part of that program was the development of an adequate test procedure to properly record these aerodynamic characteristics virtually on the surface of the water (the tunnel floor).

The following sections will discuss the development at GTRI of two research facilities designed to address the specific test requirements above.

4.0 EXPERIMENTAL APPARATUS, MODELS, AND TEST PROCEDURES

4.1 In-Ground-Effect Test Facility
Experimental simulation of ground effect in subsonic wind tunnels typically poses two significant problems not experienced in more conventional testing. First, the boundary layer produced by freestream flow over the tunnel floor results in velocity and momentum deficits that do not properly simulate the conditions experienced by the vehicle moving relative to the ground or water surface (see Reference 5, for example). Second, to

properly evaluate operation in ground effect, a wide range of heights above the ground must be examined, with smaller increments available as the ground is approached. In conventional tunnels, this is sometimes attempted by inserting false floor planes at various heights below the model, an awkward procedure at best when a number of heights are desired. It also splits the freestream flow into channels above and below the floor, creating the problem of unsymmetrical blockage and making determination of corrected freestream velocity at the model difficult.

To resolve these issues, a subsonic research wind tunnel operated by GTRI (and previously fitted with a moving ground plane) was modified to more efficiently simulate the essential ground/air interface and the required variation in height above the ground. This 30- by 43-inch Model Test Facility (MTF) wind tunnel was originally developed by Lockheed-Georgia Company's Advanced Flight Sciences Department as a research facility with multiple test capabilities, including the moving-belt ground plane of Figure 4 (from Reference 5) for automotive testing. It and numerous other aerodynamic and acoustic research facilities were donated in 1989 to the GTRI Aerospace Laboratory, and are now operated by ex-Lockheed personnel (including the author) who are members of the GTRI research staff. However, as Figure 5 shows, a combined blown/moving ground plane was previously required in this facility to eliminate the momentum deficit in the floor boundary layer at 20.5" from the test section entrance. (Here, H is total head at each point in the profile and y is distance from the floor.) This blowing system was not totally adequate, as further downstream at the test section center the deficit was not fully eliminated. Also, since this complex system with flexible belt could prohibit testing the hydroplane models extremely close to the floor, and since the slot in the belt center could leak ground-effect overpressure, it was decided to develop a simplified tangential floor blowing system to replace these existing devices.

Based on considerable past experience of GTRI researchers in development of pneumatic high-lift systems (References 1, 2, 3, and 6), a tangential single-slot system with a fixed ground plane was designed to replace the previous complex system. This revised blown system was designed to energize and entrain the floor boundary layer until its displacement thickness was reduced to zero at the center of the test section. Figure 6 shows the growth of the untreated MTF tunnel floor boundary layer and its displacement thickness δ^* at several positions downstream of the entrance to the test section (x = 0.0"). These data were taken using a boundary layer probe
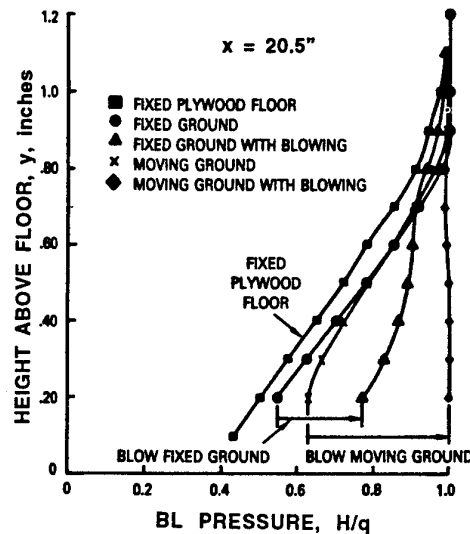

Figure 5 - Variation in Tunnel Boundary-Layer Profiles Produced by Original MTF Ground Plane Treatment (from Reference 5)
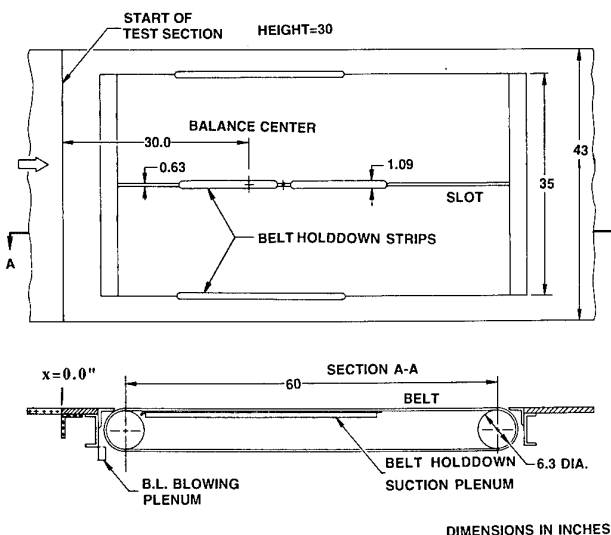

Figure 4 - Moving-Belt Ground Plane and Original Floor-Blowing Installation in the Model Test Facility Wind Tunnel (from Reference 5)
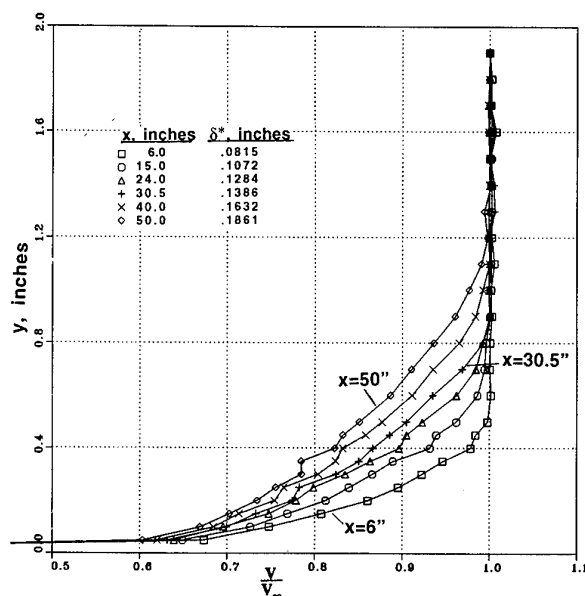

Figure 6 - Growth of Tunnel Floor Boundary Layer Downstream of the Test Section Entrance, x=0.0", q=15 psf, $C\mu$=0.0
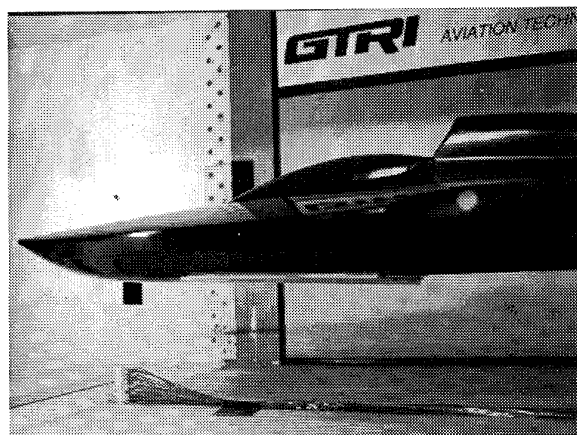
Figure 7 - Hydroplane Installation, Showing Boundary-Layer Probe and Tangential Floor-Blowing Slot at Test Section Entrance (x=0.0")
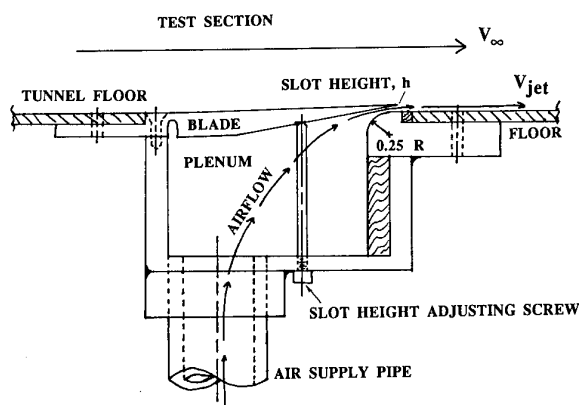

Figure 8 - Tangential-Blowing Boundary-Layer-Control System in MTF
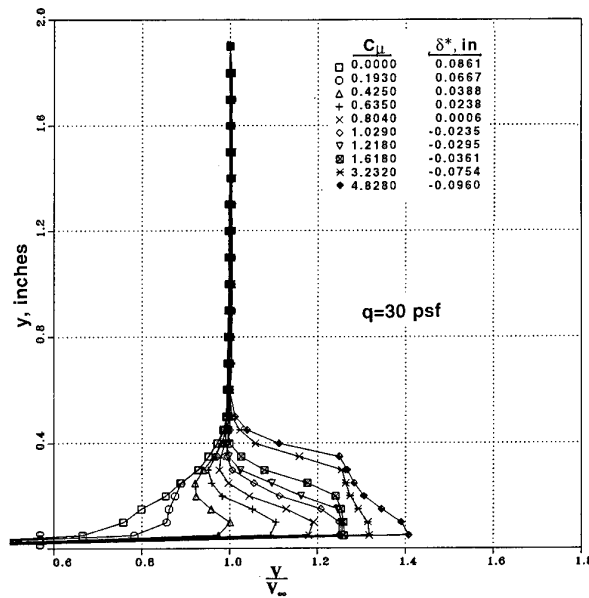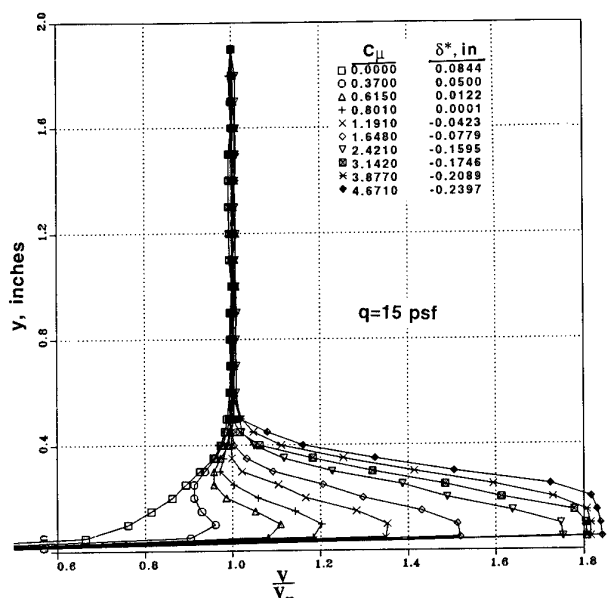
Figure 9 - Effectiveness of Tangential Blowing System in Modifying the MTF Upstream Boundary Layer at x=6.0" (h=0.02")

installed in the otherwise empty test section. (Figure 7 shows a later test point with both the BL probe and the hydroplane model installed.) Similar data taken over a range of dynamic pressures showed little variation with Reynolds number in the floor boundary layer profiles and displacement thickness values. Since values of model height above the ground as low as 0.01" were desired, it was clear that boundary-layer profiles approaching 1 inch thick near the test section centerline (x = 30") would not be acceptable. From this data, the need for a boundary layer control of some sort was evident.

The single-slot tangentially blown system (Figures 7 and 8) was installed at the entrance to the MTF test section. Both the blowing slot height (h) and the plenum pressure were variable. The air supply pipe was connected to a high-pressure air source through an in-line flow meter which was used to determine blowing mass flow rate $\dot{m}$.

Blowing jet velocity V_j was calculated isentropically (Reference 6) and the blowing momentum coefficient C_μ was calculated as

$$C_\mu = \frac{\dot{m}V_j}{qS}$$

For this application, the reference area S was taken as that of the floor-blowing turning surface (diameter x span) rather than a model wing area (or chord, c, for 2-D airfoils). This small diameter thus yields the seemingly large C_μ values to be presented below.

To establish the necessary blowing values required to reduce the boundary layer displacement thickness δ^* to zero, boundary layer surveys were taken at various test section locations and dynamic pressures. Figures 9 and 10
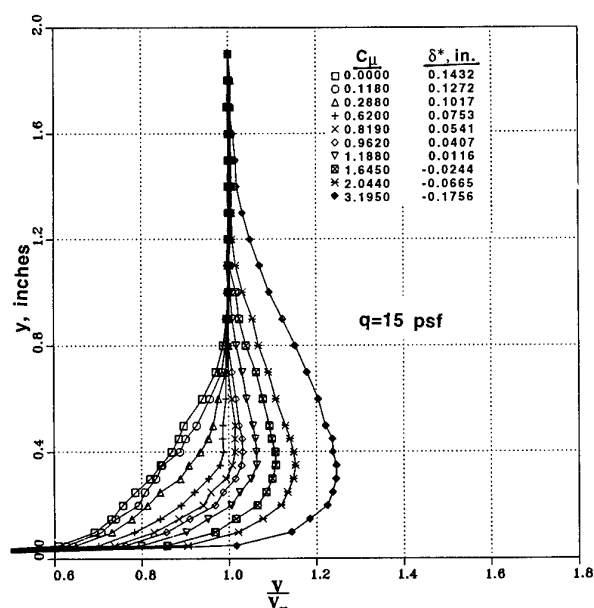
Figure 10 - Effectiveness of Tangential Blowing System in Modifying the Boundary Layer at the MTF Test Section Centerline at x=30.5" (h=0.02")
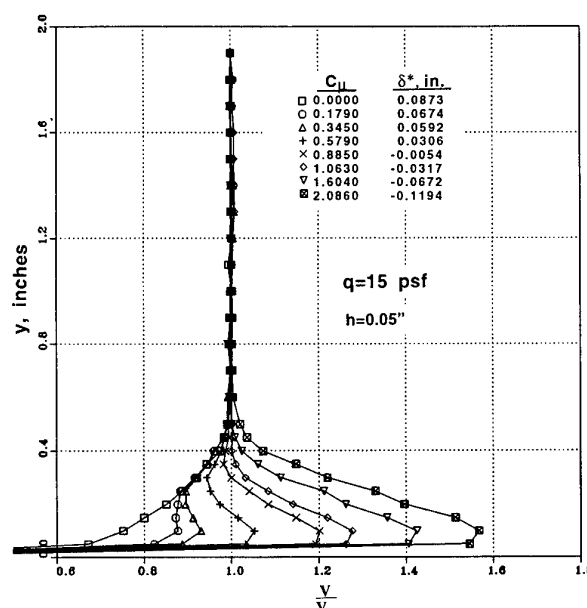
Figure 12 - Effectiveness of Floor Blowing System with Increased Slot Height (h = 0.05") in Modifying MTF Test Section Boundary-Layer Displacement Thickness (q=15 psf, x = 6.0")
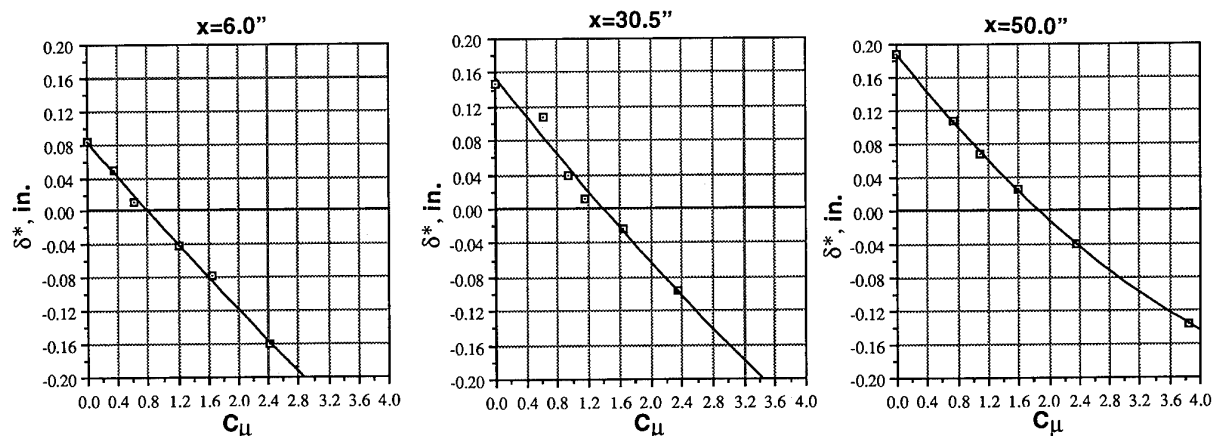
Figure 11 - Effect of Floor Blowing System on MTF Test Section Boundary-Layer Displacement Thickness (slot height = 0.02", q=15 psf)

show the effectiveness of this floor-blowing system at two locations and two dynamic pressures. Note in Figure 9 the non-dimensionalizing effect of the blowing parameter C_μ: even though the dynamic pressure q is doubled, the C_μ required to yield $\delta^*=0$ is virtually the same (≈ 0.80) and the BL profiles are duplicated. (At high C_μ, the similarity appears to break down, but this is irrelevant as the BL deficits have already been eliminated.) The flow-energizing capability of the blown slot is seen, as is the possibility of applying too much blowing (negative values of δ^* represent a velocity and momentum excess). Figure 11 summarizes the family of surveys by displaying the C_μ required to reduce δ^* to zero at different locations in the test section. It is seen that the increased

boundary layer thickness downstream requires increased blowing momentum to reach the desired $\delta^* = 0$ condition. The results did not vary with dynamic pressure. Similar investigations were done with variation in jet slot height (h). Figure 12 shows the profiles with h increased to 0.05", which virtually duplicates Figure 9 for q=15 psf. To yield the same C_μ, smaller slot heights required less mass flow but higher jet velocity and pressure ratio. This positive effect of increased V_j led to the decision that a 0.02" slot height value was more suitable for this application. Based on this data, the blowing rate was adjusted to reduce δ^* to zero at the test section center (x = 30") for the following ground-effect investigations.
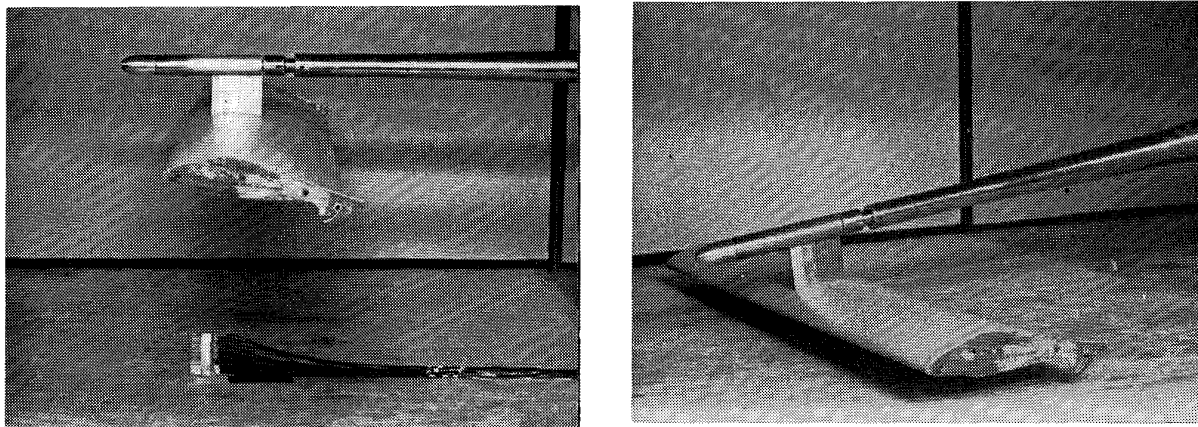
Figure 13 - Flapped Wing Test in Ground Effect to
Evaluate Floor Blowing System

Hg, inches	Hg/c
□ 11.60	1.57
O 7.40	1.00
△ 5.55	0.75
+ 3.70	0.50
X 2.78	0.38
◇ 1.85	0.25
▽ 1.48	0.20
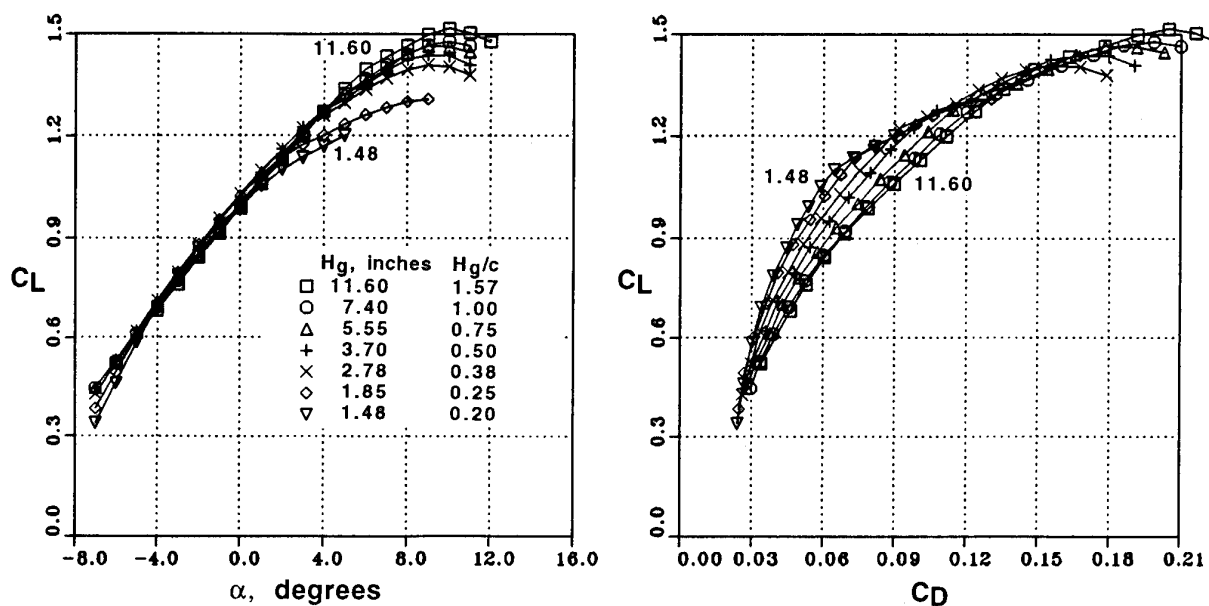
Figure 14 - Wing-In-Ground-Effect Aerodynamic Char-
acteristics without Floor Blowing ($C\mu=0.0$,
20-deg Flap)

4.2 Wing-In-Ground-Effect Tests

To calibrate the effectiveness of the above technique for ground effect tests, a generic rectangular-planform wing was evaluated in this facility. Figure 13 shows the test setup, where an aspect-ratio 3.9 wing with a 20-degree plain flap was mounted on a sting via an upper surface blade. The sting assembly, containing a 6-component balance, was mounted on a hydraulic table below the tunnel floor, which allowed an infinite number of heights above the ground (Hg) to be obtainable. Angle of attack, α, was variable via an automated pitch mechanism. Boundary layer surveys were also taken with the wing installed. Figure 14 depicts the unrealistic results produced when no floor treatment ($C\mu= 0$) was used in the test section with the wing in ground effect. For an angle of attack of 5°, the 3-D wing at 0.2 chords above the ground loses as much as 10% of the out-of-ground-effect

value. This is contrary to works such as Reference 7, which indicate 20-25% lift gain for 2-D airfoils at this ground height. However, the application of the floor blowing value required for $\delta^* = 0$ from Figure 11 yields the proper trends shown in Figure 15, with 3-D lift increases of 10-15% at the 0.2 chord height. Figure 16 shows a direct comparison with and without blowing for two ground heights, verifying that there is no effect from floor blowing when the model is away from the floor. A significant effect does exist in close proximity to the ground, and can be corrected by floor blowing. Thus the desired test conditions and techniques needed for proper evaluation of models operating in ground effect were confirmed for the modified facility.

Figure 15 showing CL vs α, degrees (left) and CL vs C$_D$ (right) with labels 1.48, 11.60.

Legend:

	Hg, inches	Hg/c
□	11.60	1.57
○	7.40	1.00
△	3.70	0.50
+	2.78	0.38
×	1.85	0.25
◇	1.48	0.20
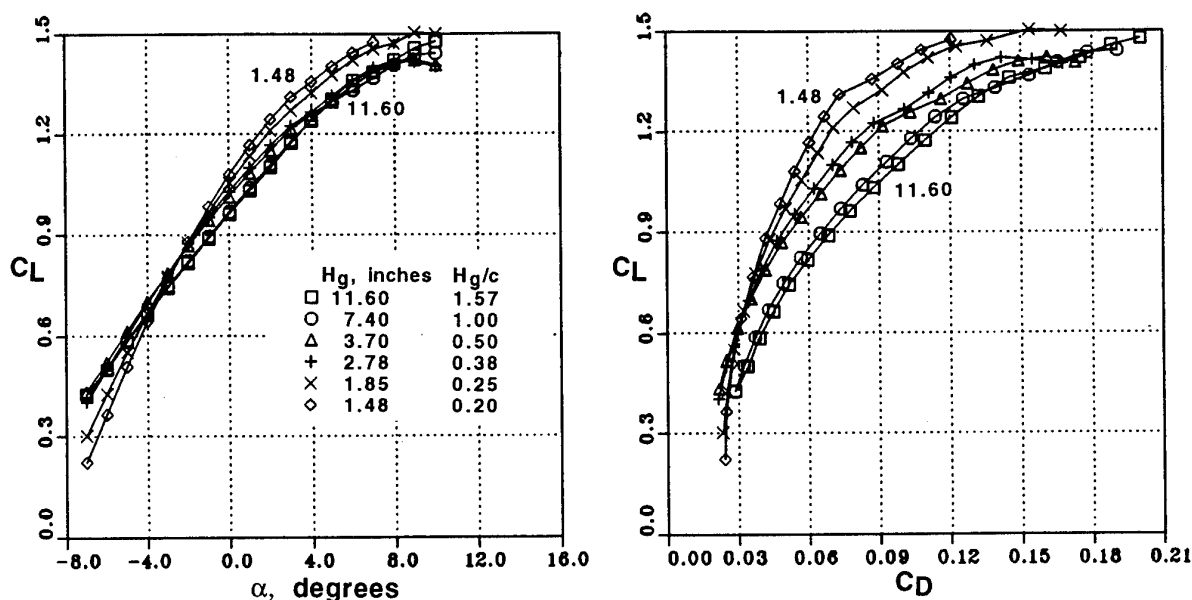
Figure 15 - Wing-In-Ground-Effect Aerodynamic Char-
acteristics with Tangential Floor Blowing
(Cμ=1.33, 20-deg Flap)

Figure 16 showing CL vs α, degrees (left, labels 0.25, 1.00) and CL vs C$_D$ (right, labels 0.25, 1.00).

Legend:

	Hg, inches	Hg/c	Cμ
□	7.40	1.00	0.00
○	7.40	1.00	1.30
△	1.85	0.25	0.00
+	1.85	0.25	1.30
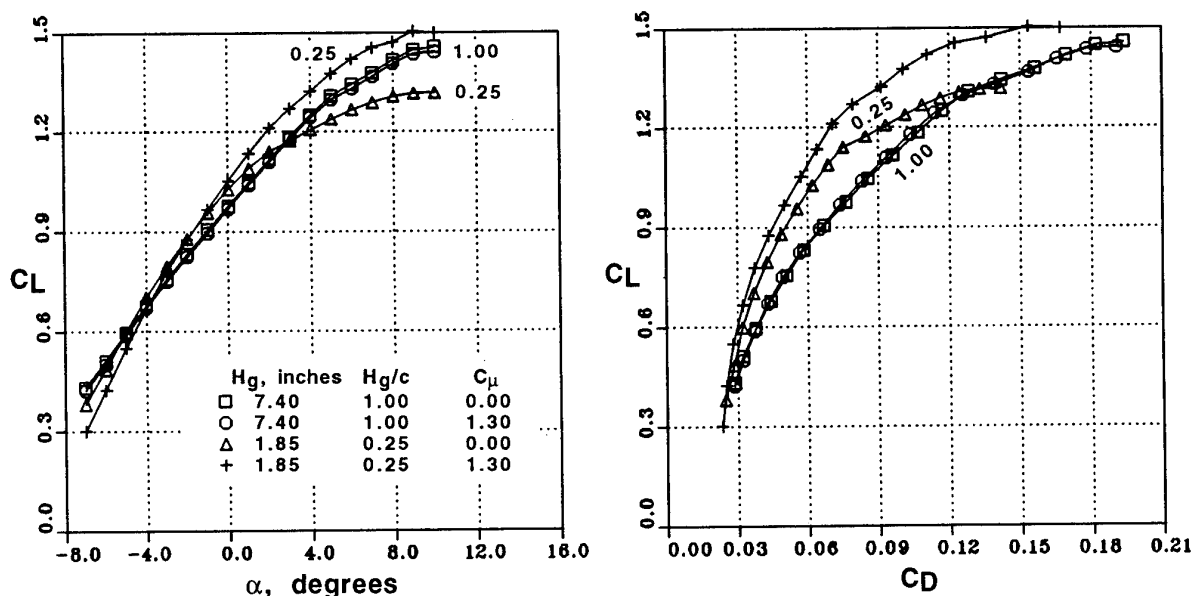
Figure 16 - Effect of Floor Blowing and Ground
Proximity on Aerodynamic Characteristics of
20-deg Flapped Wing

4.3 Hydroplane Models and Setup

Using the test procedures and techniques described above, several racing hydroplane models were evaluated in the modified MTF facility with a larger-range balance and a hydraulic table below the test section to vary their height above the simulated water. Figure 17 shows this setup and the installation of a 1/8-scale model of the *Miss Budweiser* Unlimited-Class hydroplane. The moving balance and strut allowed the model height to be varied from undisturbed freestream values (near the tunnel vertical centerline) down to direct contact with the floor, and any values in between. The strut also allowed variation in angle-of-attack. The six-component balance was mounted between the model strut and the hydraulic table and rode up and down with the model, remaining below the tunnel floor and always a constant distance from the model. Tares removed the aerodynamic loads on the varying exposed length of the support strut. Figure 7 shows a close-up of the model hydroplane, the boundary layer probe (which was removed after preliminary surveys) and the floor-blowing slot at the test section entrance.

For these investigations, and for the 3-D flapped wing test above, standard test section blockage and wall interference corrections (Reference 8) were deleted from the data reduction routines because it was desired to test the vehicle
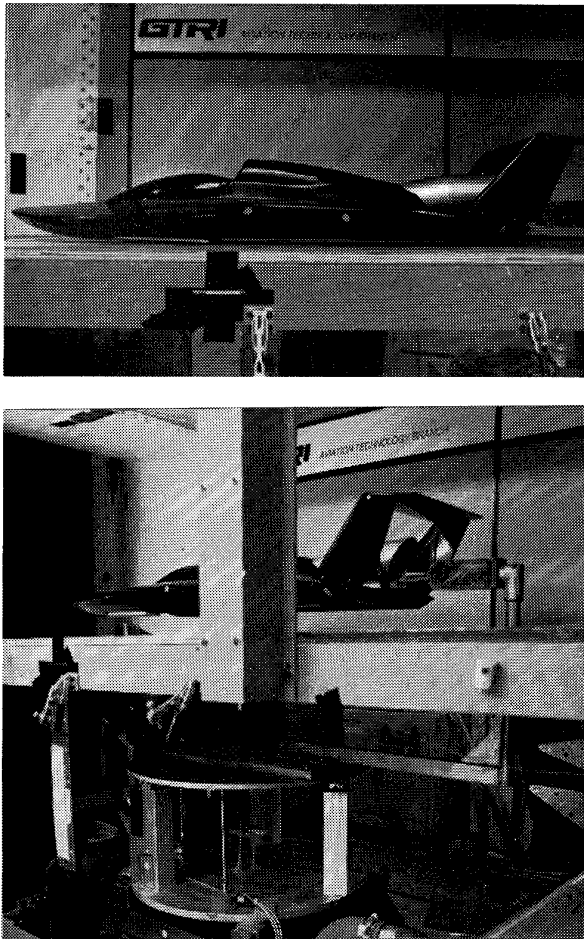
Figure 17 - Hydroplane Model Mounted in MTF Test
Section on Hydraulic Actuator Table and Six-
Component Below-Floor Balance

near the MTF floor to determine the effect of the ground
(water surface) on the performance of the boats. Since
these corrections are normally used to remove the
constraining effects of the floor and tunnel walls, their use
would have been counter to one of the main objectives of
the test. However, the variation in freestream dynamic
pressure as the model approached the floor was recorded,
and a calibration was used to determine the effective value
at each height for non-dimensionalizing the force and
moment coefficients.

The basic test procedure used was to set a geometric angle-
of-attack for the boat and then acquire a range of data by
varying the height from the freestream value down to 0.01
inches above the floor. Data were acquired, corrected,
reduced and displayed in real time on a color terminal and
then cross-plotted later to yield variation with angle-of-
attack at constant height. Some model deflection due to
air load at higher angles-of-attack was detected. This was
measured and then input as a curve fit so that data plotted
as a function of angle-of-attack was automatically
corrected to the effective value.

4.4 Hydroplane Results
A 400-hour wind-tunnel evaluation was conducted on three
hydroplane configurations using the above techniques.
Strong ground effect was confirmed with the boats
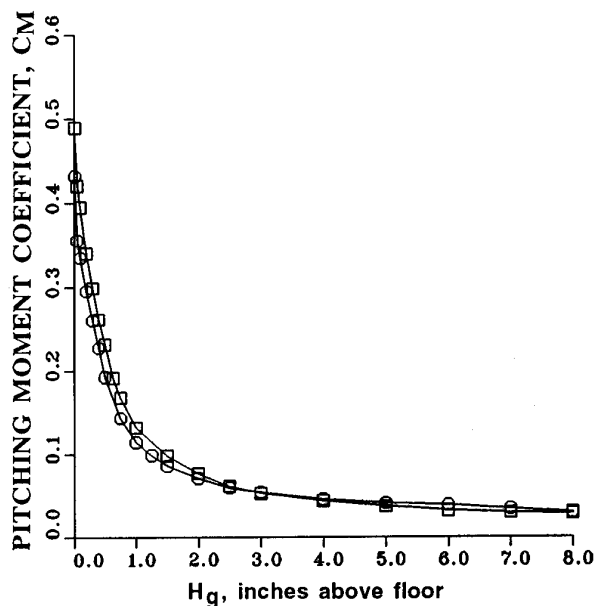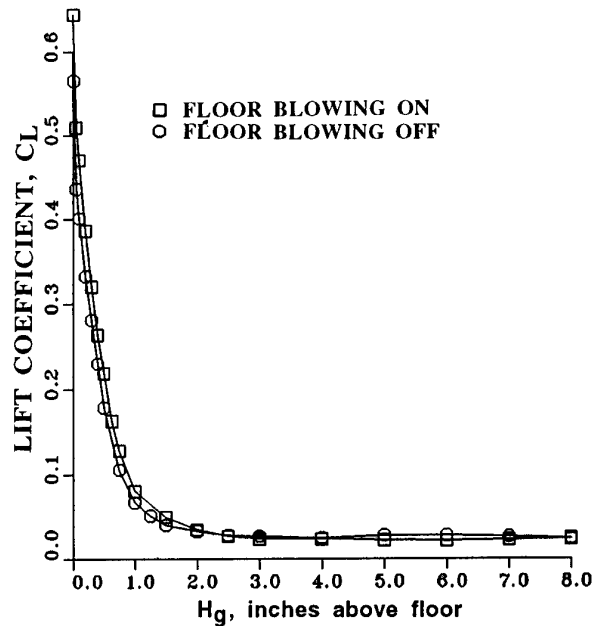

Figure 18 - Effect of Boundary Layer Blowing on
Aerodynamic Characteristics of Baseline
Hydroplane Model at α=0.3 degrees

operating at low angle-of-attack (Figure 18), with lift
values increasing to 10-15 times those recorded in the
undisturbed freestream. Significant drag and nose-up
pitching moments accompanied these lift increases. (Here,
the moments are resolved about the propeller at the aft
transom of the boat, since this is the rotation point of the
boat when water-borne.) Note also the 15-23 percent
increase in lift at fixed lower values of height as floor
blowing was introduced to energize the boundary layer.
Thus the use of the floor-blowing system captured the
ground-effect over-pressure which would otherwise have
been missed; this would have caused large under-prediction
of the lift, drag and moment for the vehicle. The original

goals of determining the causes of boat instabilities and providing effective remedies were met, and a better understanding of the aerodynamic phenomena affecting the performance of these ground-effect racing vehicles was obtained. Control surfaces developed during these investigations have recently been installed and raced on full-scale Unlimited-Class hydroplanes.

4.5 2-D Airfoil Experimental Test Setup
Development of advanced CCW airfoils was desired for application to commercial transport aircraft (Reference 3). Aerodynamic development can be done most meaningfully with a carefully conducted two-dimensional airfoil investigation. Accurate 2-D experimental evaluation of blown high-lift airfoils is not a trivial undertaking, and considerable care must be expended to perform this effort properly. The primary problem which must be overcome is the interaction between the momentum deficits in the tunnel-wall boundary layers and the severe adverse pressure gradients on the blown airfoil downstream of both the leading-edge and trailing-edge flaps or blowing slots. If left uncorrected, this yields strong vorticity at these junctions and nonuniform downwash all along the airfoil span; non 2-D results occur, and the true angle of attack is far less than the nominal geometric value.

For the present investigations conducted in the GTRI Model Test Facility research tunnel, the tangential wall blowing system previously developed to improve ground-effect investigations was modified to provide combined floor and ceiling blowing (Figure 19). The tangential floor-blowing system used in the above ground-effect test was duplicated in the tunnel ceiling. As Figure 19 shows, these two plenums are now located in the effective sidewalls when the 2-D airfoil is mounted on a floor balance. A range of wall blowing pressures was run to determine the minimum blowing required to remove the wall BL interference. The significant effects on lift, drag and pitching moment are seen in Figure 20, where the parameter Cμ corresponds to airfoil blowing, and the abscissa is the wall blowing pressure applied. As the wall boundary layer is energized and the deficits removed, the drag is reduced and lift is increased. This corresponds to elimination of the non-uniform spanwise pressure distribution and vorticity near the wall, and increase of
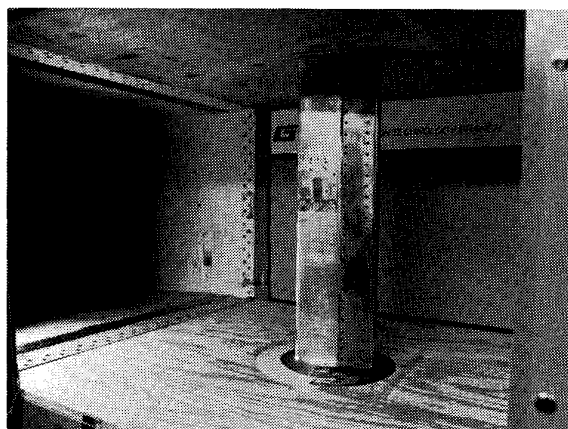
Figure 19 - Baseline 2-D CCW Airfoil in MTF Test Section; Floor and Ceiling Wall Blowing Slots in Entrance (x=0.0")
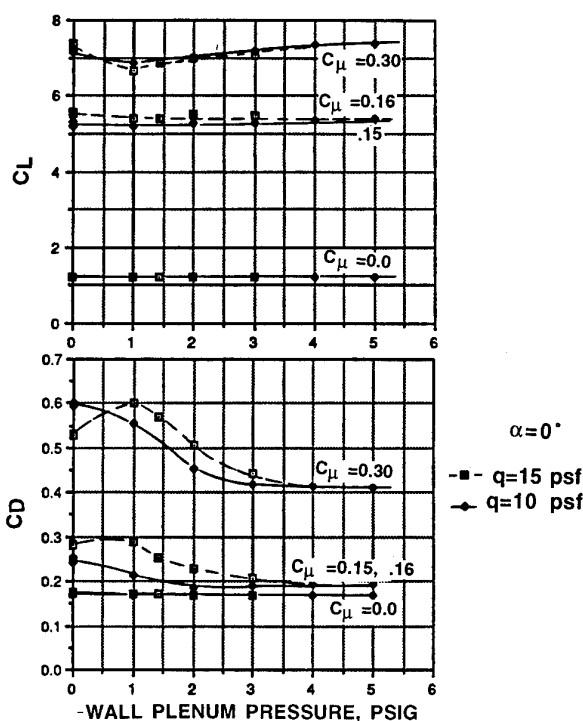
Figure 20 - Effect of Wall Blowing in Eliminating Tunnel Boundary-Layer Interaction Effects on 2-D CCW Airfoil

angle of attack to the proper geometric value. The greatest effect is seen for higher airfoil Cμ, where the airfoil pressure gradients are strongest and interactions with the wall BL deficits are greatest. Static pressures measured along the model span also confirmed this blowing value as returning the spanwise flow to a near-uniform value from floor to ceiling.

In addition to these spanwise pressures, chordwise static pressure measurements were taken on the model surface at midspan for comparison to CFD analytical results. Force and moment coefficients were recorded by a floor balance. The CCW model spanned 30" from tunnel floor to within 1/16" of the tunnel ceiling, and was mounted on a 12-inch diameter base plate attached to the floor balance system. A thin endplate separated the ceiling end of the model from the wall, allowing only enough space to prevent model grounding. After the previously-conducted calibration of the ceiling blowing system, drag tares were taken on the base plate with wall blowing activated, and a blown tare as a function of dynamic pressure was determined. This increment was subtracted from all floor-balance data.

4.6 CCW Airfoil Results
The airfoil of Figure 2 was evaluated in this facility using these special 2-D test techniques. This configuration had previously been evaluated in the MTF tunnel as part of a powered-lift STOL program (Ref. 9) Those tests were conducted using a semi-span 3-D model with a constant-chord wing having this same airfoil section and extending 26" from the tunnel floor, yielding an aspect ratio=5.5 configuration. A confirmation of the 2-D test procedure is

$\alpha = 0.0°$

	C_μ	C_l
— Computed	.114	3.81
o Experimental	.102	4.07

Figure 21 - Comparison of CFD and Experiment for 2-D CCW Airfoil at α=0 degrees

Figure 22 - Comparison of 2-D Airfoil and 3-D Semi-Span Lift Results for the Dual-Radius CCW Model at α=0 degrees

seen in Figure 21, which compares experimental pressure data with CFD results (from Ref. 3). The close agreement for this highly viscous flowfield implies that the wall BL has not induced any large angle of attack variation due to non-uniform flow.
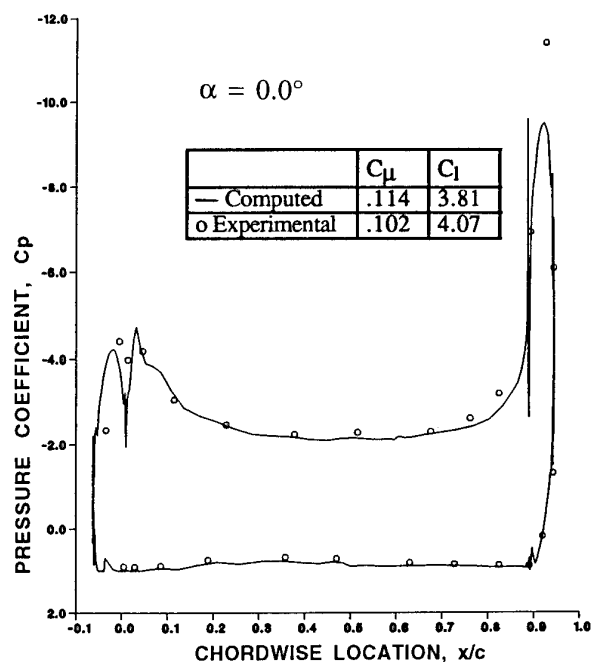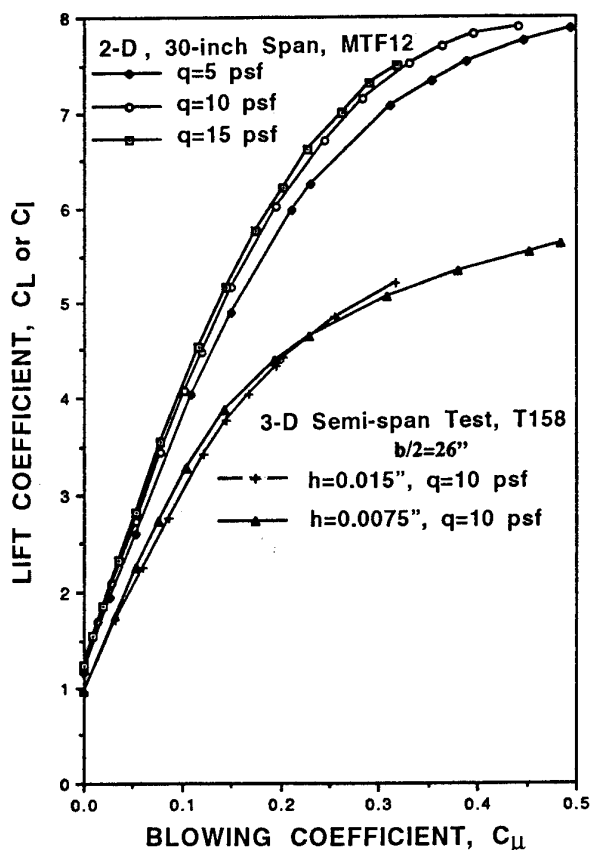
Figure 22 shows reduced and corrected balance data for this 2-D airfoil (labelled "MTF12") in comparison to the data previously recorded for the semi-span version of the same configuration (labelled "T158"), all taken at a geometric incidence of $\alpha = 0°$. 2-D airfoil lift increases of 26 to 43% (at momentum coefficients of 0.0 and 0.30, respectively) are seen relative to the semi-span model, primarily due to the elimination of the strong tip vorticity and improved test setup. Corresponding to this elimination of the induced finite-span effects is a 21 to 68 percent reduction in measured drag coefficient.

5.0 CONCLUSIONS

Experimental evaluations of airfoils and vehicles operating near tunnel walls require special facilities and test techniques to avoid errors caused by wall boundary-layer interference. Test programs at GTRI to investigate 2-D blown high-lift airfoils and racing hydroplanes in ground effect have been affected by these conditions. To rectify these problem areas, pneumatic wall-blowing systems have been designed, evaluated, and are now in operation. Also, a hydraulic system to allow multiple variations in model height above the tunnel floor has been added. Test results for a representative flapped wing in ground effect have shown a very significant reversal in ground effects when the floor blowing system was activated, and ground-effect overpressure beneath a racing hydroplane was shown to increase aerodynamic data by up to 23 percent with floor blowing. The revised facility and test techniques were thus shown to be effective tools for evaluating the performance and stability of these unique racing ground-effect vehicles, and for developing control surfaces to take effect in these non-conventional flowfields. Also, 2-D high-lift airfoil experimental data showed an increase in lift and a dramatic decrease in drag when two blown sidewall plenums were activated. The spanwise static pressure distributions became uniform from wall to wall, and comparison to CFD results was excellent. It is concluded that wall BL interference elimination is essential to these types of experimental aerodynamic evaluations, and that a pneumatic tangentially-blown system is very effective, while being quite simple to install and operate. Its combination with a hydraulic system to vary model height above the floor can provide a very excellent test facility for hydroplanes, automobiles, and aircraft operating in ground effect.

6.0 ACKNOWLEDGEMENTS

Appreciation is also expressed to Mr. Douglas A. Ford of Doug Ford Engineering who sponsored the hydroplane wind-tunnel evaluation in conjunction with the *Miss Budweiser* racing hydroplane team, which by necessity led to the development of the in-ground-effect test capability.

7.0 REFERENCES

1. Englar, R. J. and C. G. Huson, "Development of Advanced Circulation Control Wing High-Lift Airfoils," AIAA Paper 83-1847, July 1983. Also, in AIAA *Journal of Aircraft*, July 1984, pp. 476-483.
2. Pugliese, A. J. and R. J. Englar, "Flight Testing the Circulation Control Wing," AIAA Paper 79-1791, August 1979.
3. Englar, R. J., M. J. Smith, S. M. Kelley, R. C. Rover, "Development of Circulation Control Technology for Application to Advanced Subsonic Transport Aircraft," AIAA Paper 93-0644, Jan. 1993.
4. Unlimited Racing Commission, "1990 Media Guide for the HFC Hydroplane Series," American Power Boat Association, April 1990.
5. Hackett, J. E., et al, "On the Influence of Ground Movement and Wheel Rotation in Tests on Modern Car Shapes," SAE Paper 870245, February 1987.
6. Englar, R. J. and C. A. Applegate, "Circulation Control - A Bibliography of DTNSRDC Research and Selected Outside References (January 1969 through December 1983)," David Taylor Naval Ship R&D Center Rpt 84/052, September, 1984.
7. Nuhait, A. O. and D. T. Mook, "Numerical Simulation of Wings in Steady and Unsteady Ground Effects," AIAA Paper 88-2546, June 1988.
8. Pope, A., Wind Tunnel Testing, John Wiley and Son Inc., New York, 1954.
9. Englar, R. J., "The Application of Circulation Control Pneumatic Technology to Powered-Lift STOL Aircraft," SAE Paper 872335, Dec. 1987; also in SAE P-203, *Proceedings of the International Powered Lift Conference*, Feb. 1988.

INTERFERENCE DETERMINATION FOR WIND TUNNELS WITH SLOTTED WALLS

by

M.M. Freestone and **S.R. Mohan**
Centre for Aeronautics
The City University
Northampton Square
London EC1V 0HB
United Kingdom

SUMMARY

The effectiveness of a 'two-variable' scheme, for evaluating wall interference with slotted liners installed, is assessed. Test data from transonic wind tunnel tests with a two-dimensional model geometry are utilised. In these tests untypically high levels of wall interference are produced. In the first tests, solid wall liners were used, in order to establish a standard. Selected results from two further series of tests, in which slotted roof and floor liners were fitted, are then presented and analysed. In the first of these, divergent liners were used, and it was found that the slot flows generated large disturbances in the wall shear region, causing the normal velocity of the equivalent inviscid flow to be amplified in relation to the normal velocity in the slot. An allowance therefore had to made in the proposed interference scheme to account for this amplification. With convergent wall liners, large disturbances were avoided, and no such allowance was needed. Implications of the investigation for tests in large slotted liner wind tunnels are discussed.

1.   NOTATION

a slot width

C_L lift coefficient

C_p pressure coefficient

c aerofoil chord

d lateral spacing between slots in roof and floor

H working section height, at model mid-chord location

h slot depth

L slot length

M_c local Mach number, corrected for wall interference, evaluated on test section centre line

$\bar{M}_c$ mean value of M_c (i.e. average over aerofoil chord)

M_∞ Mach number in undisturbed stream

p local static pressure

p_0 total pressure

U_{ref} axial velocity corresponding to $\bar{M}_c$

v laterally averaged normal (vertical) velocity component, positive upwards

x longitudinal (axial) coordinate; $x=0$ corresponds to aerofoil leading edge

a_c aerofoil incidence, corrected for wall interference, evaluated at mid-chord location

a_g geometric aerofoil incidence

a_i induced upwash angle, resulting from wall interference, evaluated on test section centre line

2.   INTRODUCTION

For some years work has been conducted at City University (with support from the UK Department of Trade and Industry) with the object of establishing a method for the accurate determination of interference velocity fields in transonic wind tunnels with slotted wall liners. Very precisely known interference levels may be needed for wind tunnels of this type, such as the European Transonic Wind Tunnel (ETW), especially for tests on advanced civil aircraft configurations, where error levels as low as 0.001 for blockage increment in Mach number and 0.01 deg in upwash are the aim.

In order to avoid the limitations implicit in those methods which require accurate representation of the flow around the model under test, a method utilizing only measured boundary conditions has been adopted. Such methods have already been shown to be capable of yielding highly accurate interference velocities in solid liner wind tunnel tests. These methods require the axial and normal velocity components of the effective inviscid flow (EIF) to be specified over a bounding surface, which, for convenience, is generally taken to be a right-angled 'box' coinciding, approximately, with the test section boundary. The axial component distributions may be found from wall liner pressure measurements, and for solid liners the corresponding normal velocity distributions are

effectively determined by the shape of the walls. These normal velocity values are ideally 'corrected' by using measured or calculated wall boundary layer developments to yield the normal transpiration velocity field (of the EIF) generated by streamwise variation in the wall boundary layer displacement surface. In the present work the method of Ashill and Weeks (Reference 1) has been used for determination of the interference flow from the measured wall boundary conditions. In common with other methods of this type, it requires the EIF disturbances near the walls to be sufficiently small to be adequately represented by a subsonic linear potential equation, with an appropriate value of Mach number.

For slotted liner wind tunnels the process of determining the EIF axial velocity components is similar to that for solid liners, (although a small adjustment to allow for the slot flow has to be incorporated) but determination of the normal velocity distributions is clearly more complex. From analysis of aerofoil tests carried out at low Mach numbers in a specially constructed slotted liner wind tunnel (see Reference 2), it was established that the normal velocity component distributions of the EIF could be found to a good accuracy, for a range of lift coefficients, by means of slot traverses with a pitch/yaw probe. The mean, or equivalent 'homogeneous' wall normal velocity, was evaluated by averaging the slot flows laterally, over the sum of the slot and slat widths. Disturbances to the wall boundary layer generated by the slot flows were sufficiently modest not to introduce significant errors in this process of obtaining the EIF normal velocity distributions. An example of the effectiveness of the scheme at low speed is shown in Figure 1, where slotted-liner aerofoil pressures, corrected by using interference velocities evaluated from applying the scheme, are compared to well-established solid-liner data. Furthermore, it was found that the variation of slot flow mean normal velocity along the length of a slot was adequately specified by a relatively small number of probe measurements made along a slot centre line. For low lift coefficient cases the slot flow was also well predicted by a theory developed from the work of Berndt and Sorensen (Reference 3).

The work presented here extends this low speed investigation to high subsonic speeds. A two-dimensional model geometry was again chosen in order to simplify the process of assessing interference. The aerofoil had the NACA0012 profile. The first tests were conducted with solid liners. These provided data for the same Reynolds number based on aerofoil chord, and related to the same means of transition fixing and the same model

surface finish and stream turbulence levels as those of the later slotted liner tests. At high speed there are additional limitations imposed on the methods of determining interference and applying corrections, due to the restricted validity of the assumption of the near-wall flow being governed by a linear potential. Thus the high speed solid liner tests were expected to be more revealing than the earlier tests at low speed. Although it was expected that non-uniform interference fields would place rather more severe limitations on the correctability of the tests, no particular difficulties, associated with increasing the test Mach number, were expected to arise in relation to applying the same scheme for determining interference in the slotted test section as had proved successful at low speed.

Following an outline of the approach adopted for assessing the proposed method of determining interference, the experimental considerations are presented in Section 4. In Section 5 the solid liner tests are described and discussed. Tests with the solid roof and floor of the wind tunnel test section replaced by slotted liners are then presented (Sections 6 and 7). Following analysis, it was found that the first series of these tests indicated a serious deficiency in the scheme for evaluating interference (in its original form) for, in some situations, the EIF near the slotted liners was clearly very different from that predicted on the simple basis of laterally averaging the slot flow probe measurements. This was found to be due to a rapid growth in the viscous flow layers forming over the slotted liners in the areas where air of low total pressure returns from the plenum chambers into the test section. It is shown that the large disturbances may either be taken into account, or measures taken to avoid them.

The significance of the findings for large slotted liner wind tunnels is discussed in Section 8.

3. APPROACH FOR ASSESSING SCHEME FOR DETERMINING SLOTTED LINER INTERFERENCE

Here the steps taken to assess the proposed scheme for determining interference in wind tunnels with slotted liner test sections are presented. Use is made of two main computational 'tools', (a) a scheme for implementing the two-dimensional method of Ashill and Weeks, Reference 1, and (b) a code implementing the viscous-inviscid interaction scheme known as VGK, References 4 and 5. The relevant performance of this code is referred to in Section 5.

The main steps for assessing interference in wind tunnels with slotted liner test sections are:

(1) Conduct aerofoil tests in a solid liner wind tunnel, for which both aerofoil and wall pressure distributions are determined.

(2) Utilise the Ashill and Weeks scheme to determine interference velocity distributions in the region of the aerofoil.

(3) Determine free air aerofoil pressure distributions, using VGK, corresponding to relevant 'corrected' wind tunnel conditions of Mach number, Reynolds number, incidence and camber. Transition trips should also be taken into account.

(4) Establish, if possible, that, for a range of conditions to be determined, the solid liner tests are 'correctable' and are as close to VGK predictions as is compatible with the known performance of this code. The object of this step is to provide a means of checking whether interference levels in the subsequent slotted liner tests have been correctly evaluated.

(5) Conduct tests on the same aerofoil in the wind tunnel with slotted roof and floor replacing solid liners. In these tests determine slot flow normal velocity distributions, in addition to aerofoil and wall pressures.

(6) Utilise the Ashill and Weeks scheme to determine interference in the model region.

(7) Conduct Step (3) corresponding to the 'corrected' slotted liner conditions.

(8) By comparing measured values of aerofoil pressures with those predicted, determine whether or not the interference levels obtained in Step (6) appear to be sufficiently accurate.

(9) Investigate the causes of any inadequacy revealed in Step (8), and evaluate their significance.

In the proceeding Sections the approach is described.

4. EXPERIMENTAL CONSIDERATIONS

As with the low speed tests described in Reference 2, it was decided to use an aerofoil having a larger chord relative to the test section height than would normally be employed in order to simplify the task of assessing interference effects (so far as possible). A limit on model size is necessary, however, since excessively large models present difficulties, both because the interference fields generated in the region of the model would become highly non-uniform, and because uniform wind tunnel flows far upstream and far downstream of the model could not then be effectively defined, as required by methods of interference determination such as those of Ashill and Weeks (Reference 1). (This latter reason would not apply to methods which use a finite closed measurement surface, together with measurements or interpolations at the 'end faces'.) For the current tests a NACA 0012 aerofoil model of 127mm chord (c) was used. The aerofoil spanned the 254 mm width of the test section. The test section height varied along its length, depending on the angle of divergence or convergence of the 'roof' and 'floor'. In the solid liner configuration the roof and floor walls diverged by 1.5 deg (total), giving a value of height at mid-chord, H, equal to 198mm. The 'low' value of H/c, 1.56, which results, produces untypically high levels of interference and places unusually demanding conditions on any method of interference determination. With slotted roof and floor liners fitted, initial tests utilised the same divergence angle as provided for the solid liners. Subsequently, further tests were conducted with the slotted liners converged at an angle of 2.2 deg. The geometry of the test section with slotted liners fitted is shown in Figure 2.

In order to maintain a nearly two-dimensional type of flow, shaped vertical plates were mounted on the aerofoil model at a distance of 25mm from each sidewall, see Figure 3. These plates serve to isolate the model, to some extent, from the influence of variations in the sidewall boundary layers. The mean growth of the wall boundary layers has an effect on the pressure gradient over the test section length, and, as such, is largely taken into account by a method of interference determination (such as that of Reference 1) which utilises measured wall conditions.

Tests were made at values of M_{ref} between 0.6 and 0.8, for geometric incidence values of 0, 1, 2, 4 and 6 deg, although here only a few results corresponding to $a_g = 2$ and 4 deg are presented. In each test run, pressures from 43 aerofoil locations, and from 44 wall locations (22 on the roof and 22 on the floor) were recorded. Care was taken to keep the pressure

holes, or 'taps' in good condition, so that high accuracy of pressure recording could be maintained. Slot normal velocity distributions were obtained using a miniature five-hole pitch/yaw probe which could be traversed along the majority of the length of a slot in the floor. Slot flows corresponding to the roof slots were found with the floor traverse by setting the symmetrical aerofoil model at negative incidence. Check measurements of liner pressures indicated the validity of this procedure. Separate check tests were made with the probe mounted on a slender static support, and these also indicated that the data obtained with the traversed probe were reliable. In separate tests, the probe was mounted at various locations within the test section, in order to check the assumption relating the slot normal velocity to the mean normal velocity in the 'inviscid' near-wall region.

5.   SOLID LINER TESTS AND COMPARISON WITH PREDICTIONS

In Figure 4, the interference results for nine runs, all for $a_c = 2$ deg, are shown corresponding to the solid liner configuration. It is seen that there is a significant Mach number variation over the length of the aerofoil, as well as a variation in upwash, for all these runs, and that these variations become more marked as the (mean) Mach number increases. The fact that the local corrected Mach numbers are lower at the more aft positions, indicates that the wall divergence used has more than compensated for the growth in boundary layer displacement thickness. It has been shown that a nearly linear variation of upwash over the chord can be accounted for by imposing an induced parabolic camber on the aerofoil, see, for example Reference 1 or 5, but no similar method has been found to account for a simultaneous non-uniformity of the longitudinal velocity component, in terms of relating the actual aerofoil pressures to those on an aerofoil in an infinite flow. However local pressures, expressed in terms of pressure ratios, p/p_0, do seem generally to correlate well with the local corrected Mach number, see, for example, Reference 6, provided variation of this Mach number is small. As a result, comparison of the measured aerofoil pressures with those predicted for free air flows is possible at least in some cases where the interference is non-uniform, but may require careful interpretation.

In Figures 5, 6 and 7, aerofoil surface pressures predicted using the VGK code are compared with measured values from three runs, having mean corrected Mach numbers of 0.606, 0.669, and 0.721 respectively. In Figure 8 the correponding measured wall pressures are shown. In each case the VGK

results presented allow for the induced upwash by means of a change in incidence, together with an imposed camber, in such a way as to produce the same distribution of local incidence along the chord as that determined using the method of Reference 1 for the corresponding test. For each run two VGK results are shown, one for the lowest and one for the highest value of corrected Mach number determined along the chord. It is clear that the aerofoil pressures in the region around the 'ballotini' transition strips, which extend from about 7 to 7.8 percent of the chord on both upper and lower aerofoil surfaces, are influenced by the local surface irregularities. It is probable that the aerofoil boundary layers, in addition to being changed from a laminar to a turbulent state in the vicinity of the strips, are also somewhat thickened, and a small increment in boundary layer momentum thickness has been incorporated into the VGK calculations so as to take approximate account of this, (although the detailed representation of the irregular pressures in the transition region would still not be expected to be good). One further point should be made in considering comparisons of VGK calculations and observed pressures. This concerns the fact that the VGK code does not include higher order terms in calculating the boundary layer development. Such higher order terms are normally of relatively little importance provided the boundary layers are not close to separation, see Reference 5, especially if comparisons of surface pressures are made at the observed lift coefficient. However, for the present comparisons, where it is important to assess the accuracy of corrections to incidence, errors in VGK at a given incidence are relevant. It was determined from comparisons with a code which did include higher order terms, that VGK generally tended to overpredict the lift at given incidence, by an amount which varied somewhat according to the flows involved, but which for the flows shown in Figures 5, 6 and 7 was close to 4 percent.

With these comments in mind, it is apparent that the observed aerofoil pressures of Figures 5 and 6 are closely compatible with the values calculated using VGK, especially when the variations in local Mach number along the chord (see Figure 4) are taken into account. On the other hand, the observed flow shown in Figure 7, for which the mean corrected Mach number is 0.721, appears to be affected by a general lowering (by about 0.1) of the Mach numbers upstream of the upper surface shock which results in this case, and this is attributed to a 'non-correctable' wind tunnel interference effect. Comparisons at higher mean corrected Mach numbers, and higher incidence values, (not shown), indicate that these 'non-correctable' interference

effects are associated with the flow between the aerofoil upper surface and the solid roof liner approaching a 'choked' condition. Clearly such a condition would be avoided, and a margin of 'safety' retained, in any tests other than those in which interference itself was the major interest.

It may be concluded that the observed solid liner aerofoil pressures are fairly well predicted by a code such as VGK, provided that

(a)   some allowance is made for non-uniform blockage interference,

(b)   non-uniform induced upwash is taken into account in the way described,

(c)   choking is avoided by an adequate margin.

6.   INITIAL SLOTTED LINER TESTS AND COMPARISON WITH PREDICTIONS

In Figure 9 are shown the measured liner pressure distributions (Figure 9a), and normal slot flows (Figure 9b), corresponding to two runs with $a_g = 4$ deg, with the slotted liners in their initial, diverged configuration. The data of Figure 9, used as input to the code embodying the method of Ashill and Weeks, produce the interference velocity distributions shown in Figure 10. These distributions are expressed in terms of local (corrected) Mach number, and local induced incidence. In contrast to the solid liner distributions, those for the slotted liner show virtually no variation of corrected Mach number over the length of the chord. Also, the calculated induced incidence values at mid-chord are larger than, and of the opposite sign to, the solid liner ones, although the sign of the induced camber is unchanged. Consequently, the calculated values of a_c for the slotted liner tests at $a_g = 4$ deg are within a degree of the solid liner values corresponding to $a_g = 2$ deg. In Figures 11 and 12 the measured aerofoil pressures for the two slotted liner runs are compared with predictions found using the VGK code. Only one VGK result is shown in each Figure, since, as remarked, the calculated corrected Mach number hardly varies over the chord. From Figure 11 it is seen that, even where there is no supersonic flow, there is a marked overprediction of the aerofoil lift, and from Figure 12 it is apparent that this overprediction becomes rather greater at $\bar{M}_c = 0.691$, in which case a small region of supersonic flow is observed. Because of the close agreement noted in Section 5 between observed and predicted pressure distributions (at corrected conditions) found for otherwise similar solid liner runs, it may be

concluded that the interference velocity fields calculated for the slotted liner tests are significantly in error.

In one sense, the large magnitude of the differences between predicted and observed pressures in Figures 11 and 12 is encouraging, since it suggests that the approach for checking the validity of the scheme for determining interference is sufficiently sensitive. If a much smaller aerofoil model had been utilised it is doubtful whether any errors would have appeared as important. However, when the differences were first noted, they were not viewed in this light. Following (a) an investigation into moderate changes to the far field extrapolations used in applying the method of Reference 1, (b) a number of minor changes to the wind tunnel configuration, and (c) checks on the accuracy of the normal velocity measurements, all of which revealed only negligible effects, it became clear that the cause of the disagreement must be fundamental.

It was eventually suspected, and then confirmed by measurement, that over relatively short lengths of the slots (in particular those in the roof) where air was flowing into the test section, rather than out of it, that this flow was causing a local rapid growth of the mean boundary layer displacement surface. This in turn resulted in an effective amplification of the normal velocity between the plane of the wall liner and the displacement surface. Similar disturbances had been observed earlier by Firmin and Cook (Reference 7). A few rather sparse surveys, made with the five-hole flow probe, indicated that a magnification factor of about 4.0 was needed to convert the mean normal velocity at the slot into the mean normal velocity relevant to the EIF bounding surface, over the lengths of these returning flow portions. Elsewhere this magnification factor appeared to be close to unity. In Figures 13 and 14 comparisons are shown between observed aerofoil pressures and those predicted by VGK utilising interference velocity values revised to take into account of such an amplification effect. The results of using values for the magnification factor of 4 and 5 (over the returning flow extent) are both shown. For simplicity, the VGK calculations are shown for a single value of Mach number, i.e. $\bar{M}_c$, in each Figure, although in both cases there is a small calculated variation in M_c along the chord. It appears from Figures 13 and 14 that a value for the magnification factor equal to 5.0, or thereabouts, produces agreement between predicted and observed pressures which is similar to that found for the solid liner runs (Figures 5,6 and 7). It is of interest that the data of Crites and Reuger (Figure 7 in Reference 8), for a perforated plate test section liner, show that where flow is returning to the test

section, magnification factors, with values of about 3 to 4, must be applied in order to convert the mean normal velocity at the plate into the normal velocity at the edge of the boundary layer. The values of this factor appear to increase with the magnitude of the normal velocity.

7. FURTHER SLOTTED LINER TESTS AND COMPARISONS WITH PREDICTIONS

The depth of the slots in the liners used in the current tests is relatively small, and it is largely because of this that there is only a limited 'reservoir' of air with a total pressure near that of the free stream to feed back returning air to the test section without producing significant shear layer disturbances. Deeper slots, and higher test Reynolds numbers, may be expected to lead to reduced disturbance levels in the returning air regions, and thus to generally lower effective amplification factors. In some situations it may be possible to avoid producing large shear layer disturbances, by removing, or limiting, the returning air flow. For this reason, it was of interest to see if the proposed interference scheme would prove to be accurate in a situation where there was no returning flow, i.e. where there was no need to apply an amplification factor.

To do this with the liners used in the present tests, it was decided to converge the slotted liners by 2.2 deg. Preliminary tests, in which a smaller amount of convergence was also employed, showed that such an angle of convergence was necessary in order to remove the regions of returning flow when the aerofoil was set at an angle of incidence of 2 deg. To have removed the returning flow regions at higher incidence, would have required even higher angles of convergence. Unfortunately, the alternative approach, of having 'plenum chamber suction' to augment the 'diffuser suction', and thus to remove additional air flow from the plenum chambers, would have entailed a considerable amount of engineering effort. However, such an augmented plenum suction would be desirable, since the wall convergence applied leads not only to a reduction in the extent and degree of the returning flow, as desired, but also to a significant positive gradient in the corrected Mach number over the chord of the aerofoil.
The same test procedure that was carried out for the series of tests using the diverged slotted liners was repeated with the liners converged. Geometric incidence values, a_c, equal to 1 deg and 2 deg were used. Following evaluation of interference velocities, using the proposed scheme, the VGK code

was used to determine predicted aerofoil pressure distributions, in the same way as had been done for the earlier solid and slotted liner tests. Results for four runs with $a_g = 2$deg are presented. Figures 15 and 16 show the measured wall pressures and normal velocity distributions respectively. From Figure 16 it is seen that, for all but the highest speed run presented, there is no returning flow. Even for the highest speed run the amount of returning flow is negligibly small. Computed interference on the test section centre line for the four runs is shown in Figures 17 and 18, in terms of M_c and a_i. Comparisons of measured and predicted aerofoil pressures are shown in Figures 19 to 22. In each case, predictions are shown for two Mach numbers, namely the corrected Mach number at the leading edge location (which in these tests is the lowest value over the chord extent), and that at the trailing edge, where the highest values of M_c occur. It is clear that the agreement between measured and observed pressure distributions is satisfactory when the gradient of corrected Mach number is taken into account. It is also apparent, comparing Figures 7 and 22, that this satisfactory agreement extends to rather higher values of $\bar{M}_c$ for the slotted liner tests, than for the earlier solid liner tests. This is not surprising, as it reflects the main objective of slotted liners, that of obtaining correctable test data for transonic flows. In the present context, however, the important conclusion is that use of measured wall pressures and slot flows appears to lead to as accurate a determination of interference for slotted liners tests as the use of pressures alone does for solid liners.

In principle, further assessment of the accuracy of interference determination may be made by comparing aerofoil pressure data, from both solid and slotted liner tests, 'corrected' to a common Mach number, incidence and induced camber. The 'corrections' to be applied should account for differences in surface pressure occurring as a result of any differences between the test conditions and the selected 'common' Mach number, incidence and camber. With non-uniform test conditions, there is no simple and reliable way of determining these corrections. They may be estimated, however, using VGK (for example) to yield the variations of p/p_0, for each aerofoil pressure location, due to separate variations in M_∞, incidence and magnitude of induced camber. The local effect of a change in M_c may be assumed to be the same as that from an equal change in M_∞. The total corrections may then be found as sums of appropriate amounts of the separate effects due to changes in M_c, incidence and magnitude of camber. Applying corrections in this way, for two 'pairs' of solid and slotted liner runs, resulted in the data shown in Figure 23 (for

$M_\infty = 0.606$, $a_c = 2$ deg and zero camber) and Figure 24 (for $M_\infty = 0.674$, $a_c = 2$ deg and zero camber). In Figure 23 the corrected data agree very closely (except for one point which appears to be influenced by a transition strip), but the comparison at the higher Mach number (Figure 24) shows several points on the upper surface where there is significant disagreement. It would appear probable that the rather large corrections applied to obtain the data of Figure 24 are not determined sufficiently accurately by VGK in the area of low pressure just aft of the upper surface transition strip, and that this is at least a contributory cause of the disagreement noted between the corrected solid liner data and slotted liner data in Figure 24. However, it is also possible that there are errors in the interference velocities determined for the slotted liner test at this higher Mach number, resulting from a shear layer growth occurring near the slots in the roof liner in this case, since, as is seen in Figure 16, there were some measurements near $x/c = 0.6$ where 'returning' flow is indicated. Further investigation of this point is intended.

8. DISCUSSION AND CONCLUSIONS

Procedures which use measured flow boundary conditions, in order to determine accurate levels of wall interference, are well established for solid liner wind tunnels, for both two and three dimensional configurations. To reach the same level of confidence in employing similar procedures to slotted liner wind tunnels, entails careful study of the sources of error that may arise. The procedures require as input the axial and normal velocity components of the effective inviscid flow (EIF) over a boundary surface. Determining the axial component with sufficient accuracy presents little difficulty, but over the regions where the liners are slotted, the normal velocities are affecte d by the slot flows, and by any secondary viscous influences which these flows may introduce. Provided the slot flows introduce only slight disturbances to the wall shear layers, then the homogeneous wall condition, which effectively averages the slot normal velocity laterally, is applicable, and the present tests (with converged slotted liners) indicate that its use with the interference procedure of Ashill and Weeks (Reference 1) may be satisfactory. However, where the slot flow returns to the test section, large disturbances are produced, and the accuracy is impaired. Flow surveys indicated that the effect of the normal slot flow on the EIF is amplified, by a factor of about 4 in the present tests. Taking this amplification effect into account in the interference procedure resulted in much improved agreement between predicted and measured aerofoil flows, this

agreement then being very similar to that found for the solid liner tests.

The present work by itself does not show that the use of measured boundary flow conditions for slotted liner tunnels can unequivocally yield the accuracy of interference determination desired for wind tunnels such as ETW. However, based on analysis, or measurement, of the range of slot flows likely to be generated in specific tests, it should be possible to avoid the development of large secondary viscous disturbances, such as those found in the present tests with divergent slotted liners. The necessity of determining the degree of amplification (i.e. the magnification factor), and of demonstrating its effectiveness in practice, would then be avoided. The effects of any residual small disturbances could be assessed by a boundary layer analysis, which could in turn be checked for adequacy by a relatively few measurements. A previous analysis, reported in Reference 2, suggested that the permissible error in a mean normal slot flow, for an upwash error of 0.01 deg at the model, corresponded to an error in slot flow angle of the order 1 to 2 deg. Such an accuracy should be achievable, and could possibly be achieved with very few (or even no) slot flow measurements being made on a routine basis. The use of a theoretical model of slot flow, such as that presented in Reference 2, should assist with this objective.

Implications associated with tests on three-dimensional models, as compared with the two-dimensional configurations of the tests described here, also need to be considered. A study of interference produced by a swept wing model partly spanning a slotted liner tunnel is currently in progress.

9. ACKNOWLEDGEMENTS

19-8

11. REFERENCES

1. ASHILL, P.R. A method for determining wall-
   WEEKS, D.J. interference corrections in sold-wall
   wind tunnels from measurements of
   static pressure at the walls.
   Paper 1, AGARD Conference
   Proceedings CP 335, 1982.

2. FREESTONE, M.M. Interference corrections in wind
   MOHAN, S.R. tunnels with slotted walls.
   LOCK, R.C. Paper 16, Proceedings of conference
   on 'Wind tunnels and wind tunnel
   test techniques'. Royal Aeronautical
   Society, 1992.

3. BERNDT, S.B. Flow properties of slotted walls for
   SORENSEN, H. transonic test sections.
   Paper 17, AGARD Conference
   Proceedings CP 174, 1975.

4. COLLYER, M.R An extension of the method of
   Garabedian and Korn for the
   calculation of transonic flow past an
   aerofoil to include the effects of
   boundary layer and wake.
   RAE Technical Report 77104, 1977.

5. ASHILL, P.R. An improved, semi-inverse version of
   WOOD, R.F. the viscous, Garabedian and Korn
   WEEKS, D.J. method (VGK).
   RAE Technical Report 87002, 1987.

6. FREESTONE, M.M. Determination of corrections to be
   applied to tests in transonic wind
   tunnels with perforated liners.
   Report MED/AERO 189, The City
   University, 1986.

7. FIRMIN, M.C.P. Disturbances from ventilated tunnel
   COOK, P.H. walls in aerofoil testing.
   RAE Tech. Memo AERO 1971, 1983.

8. CRITES, R.C. Transonic wall interference
   RUEGER, M. corrections for small wind tunnels.
   Paper 18, Proceedings of conference
   on 'Wind tunnels and wind tunnel
   test techniques'.
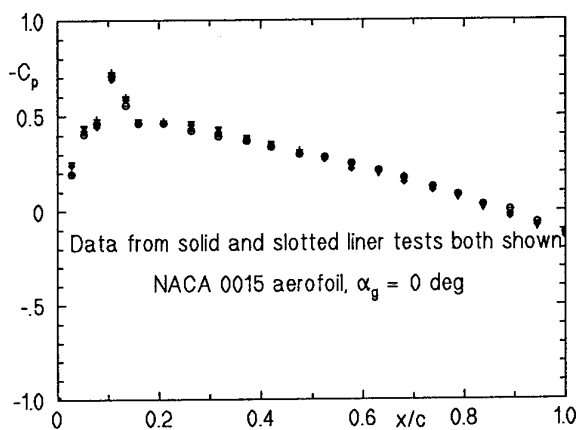   Royal Aeronautical Society, 1992.

Figure 1 (a) Corrected pressures from low speed tests,
solid and slotted liner data. α_g = 0 deg.
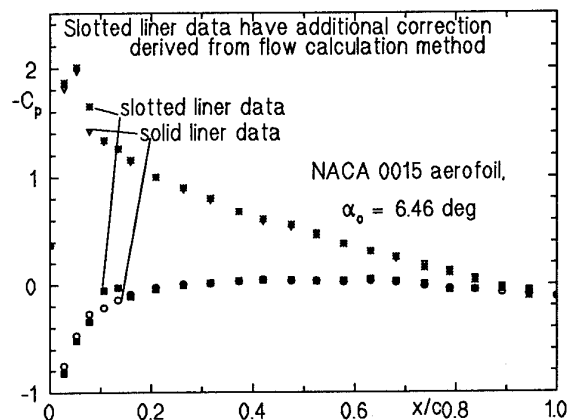

Figure 1(b) Corrected pressures from low speed tests,
solid and slotted liner data, α_o = 6.46 deg.

Test section width 254 mm
Slot width 7.9 mm
Slot depth 3.5 mm
Plenum depth 89 mm
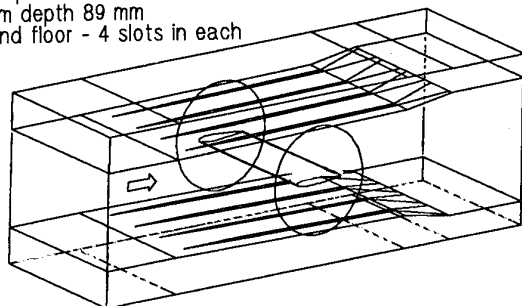Roof and floor - 4 slots in each

Figure 2 Geometry of test section -with aerofoil location

Aerofoil NACA 0012 section
Chord 127 mm
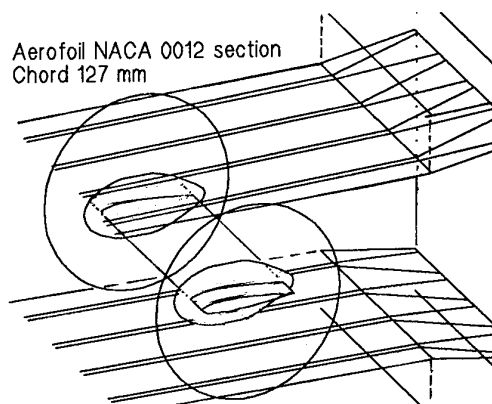
Figure 3 Aerofoil and boundary layer plates
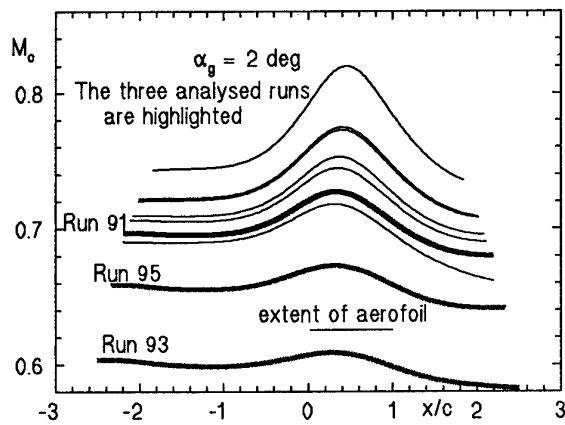
Figure 4(a) Variation of M_o for nine solid liner runs
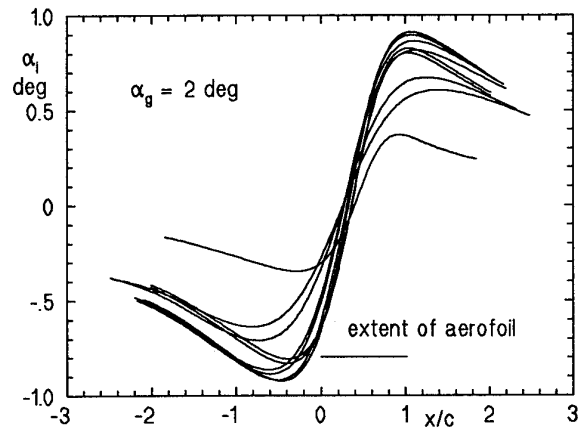
Figure 4(b) Variation of α_i for nine solid liner runs
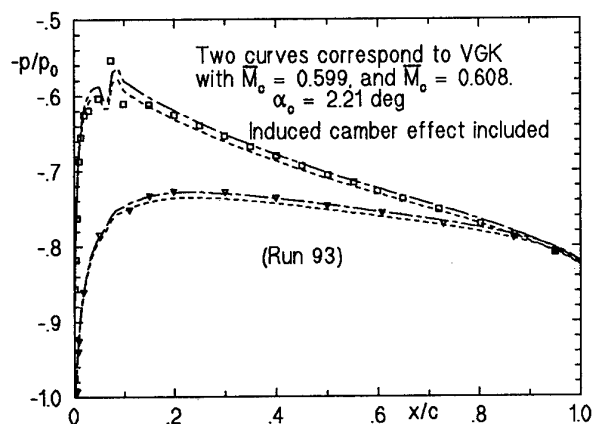
Figure 5 Comparison of measured and predicted
aerofoil pressures, solid liners, $\overline{M}_o = 0.606$
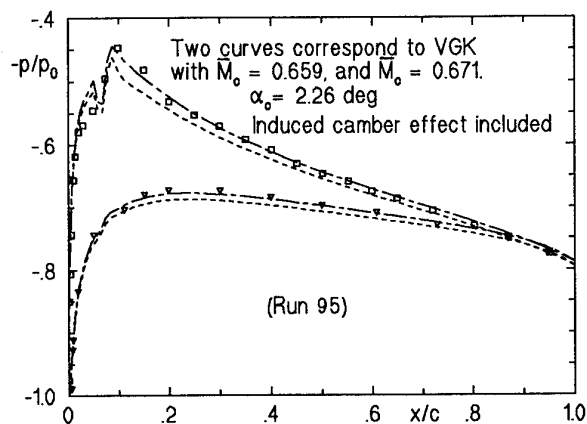
Figure 6 Comparison of measured and predicted
aerofoil pressures, solid liners, $\overline{M}_o = 0.699$
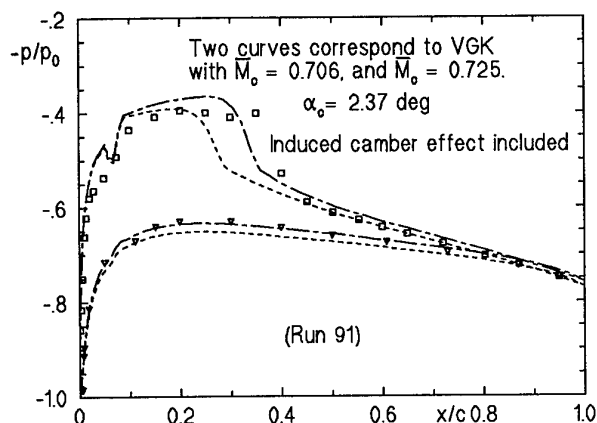
Figure 7 Comparison of measured and predicted
aerofoil pressures, solid liners, $\overline{M}_o = 0.721$
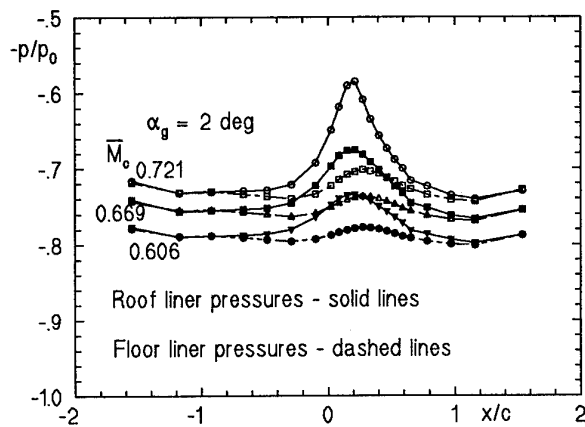
Figure 8 Roof and floor liner pressures for the three runs
corresponding to Figures 5, 6, and 7
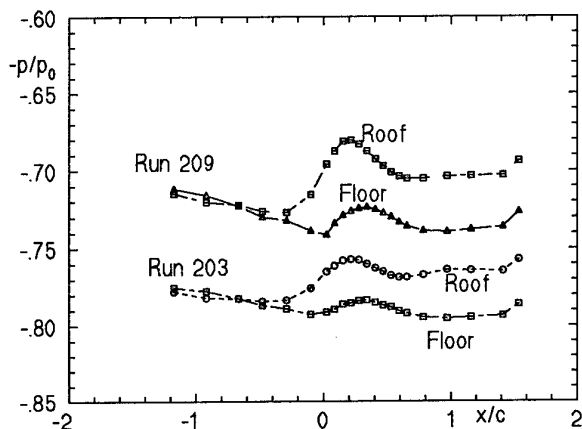
Figure 9(a) Measured liner pressure distributions, diverged slotted liners
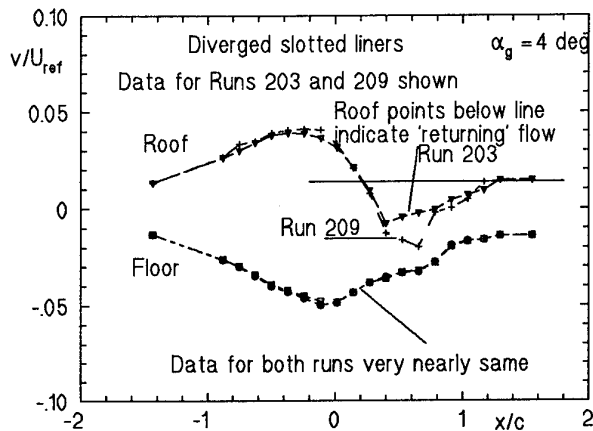
Figure 9(b) Normal velocity distributions deduced from slot flow traverses
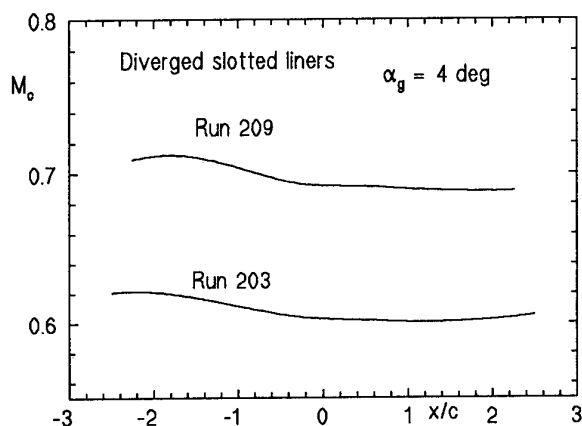
Figure 10(a) Calculated centre line interference, local corrected Mach number
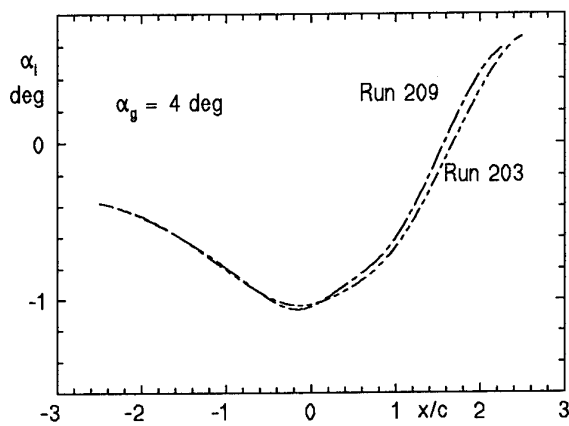
Figure 10(b) Calculated interference, local induced incidence
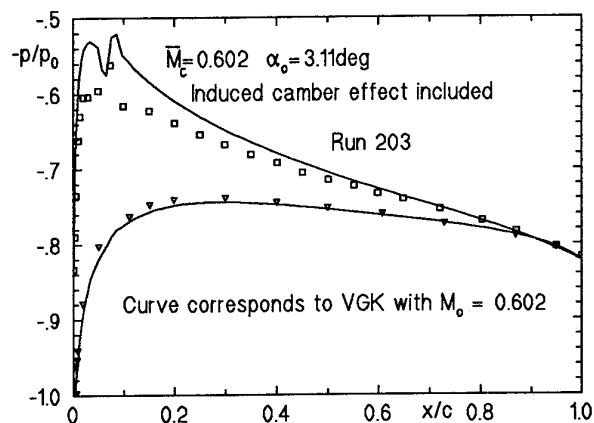
Figure 11 Measured and predicted aerofoil pressures, diverged slotted liners, $\overline{M}_o$ = 0.602
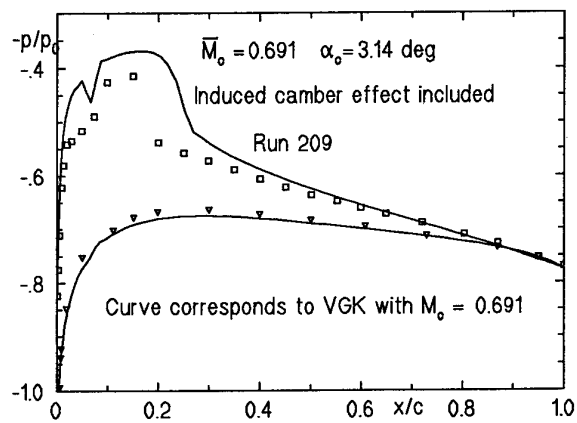
Figure 12 Measured and predicted aerofoil pressures, diverged slotted liners, $\overline{M}_o$ = 0.691
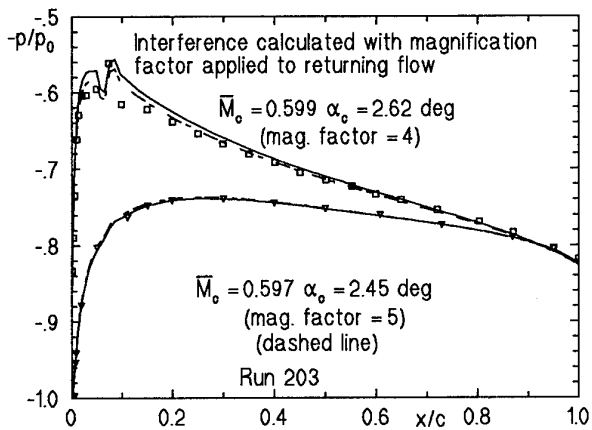
Figure 13 Measured and predicted aerofoil pressures,
amplification of returning flow
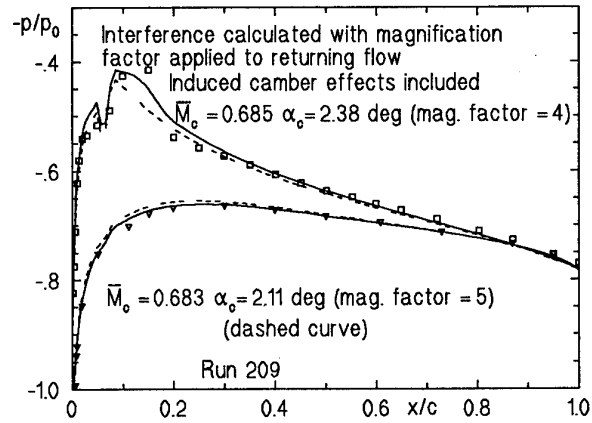
Figure 14 Measured and predicted aerofoil pressures,
amplification of returning flow
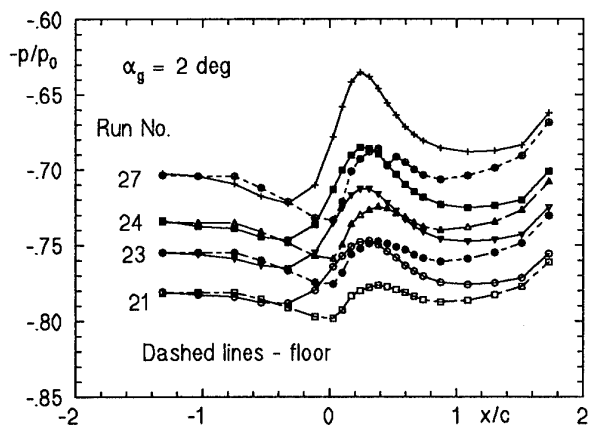
Figure 15 Measured liner pressure distributions,
converged slotted liners
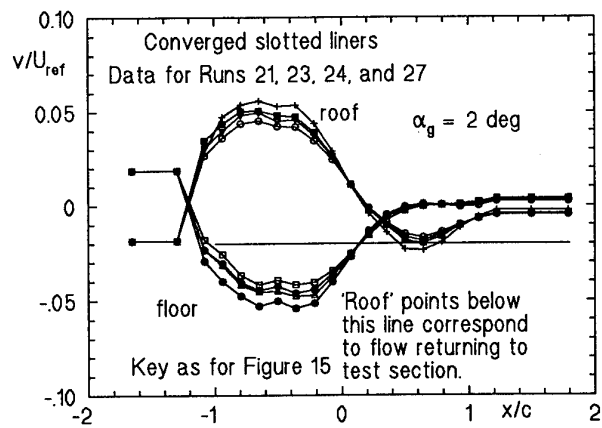
Figure 16 Normal velocity distributions-
deduced from slot flow traverses
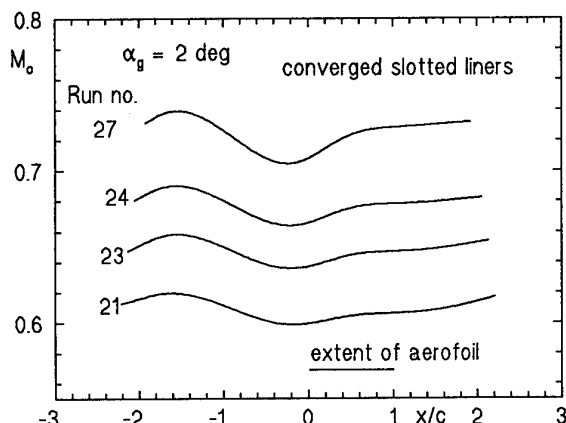
Figure 17 Calculated centre line interference,
local corrected Mach number
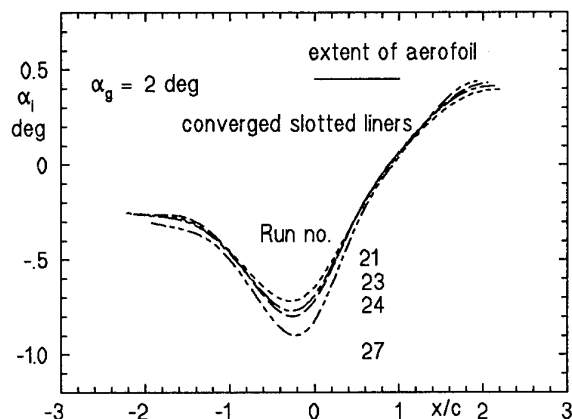
Figure 18 Calculated centre line interference,
local induced incidence
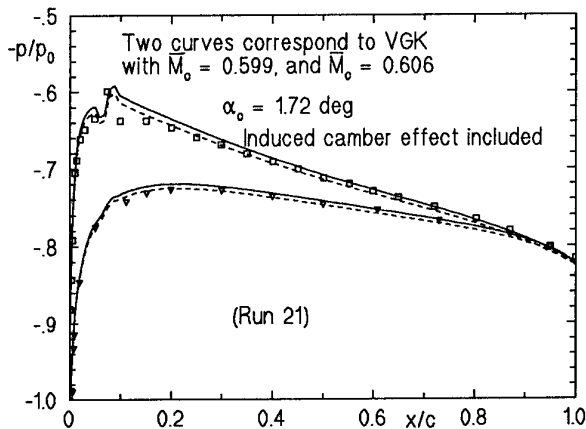
Figure 19 Measured and predicted aerofoil pressures, converged slotted liners, $\bar{M}_o$ = 0.604
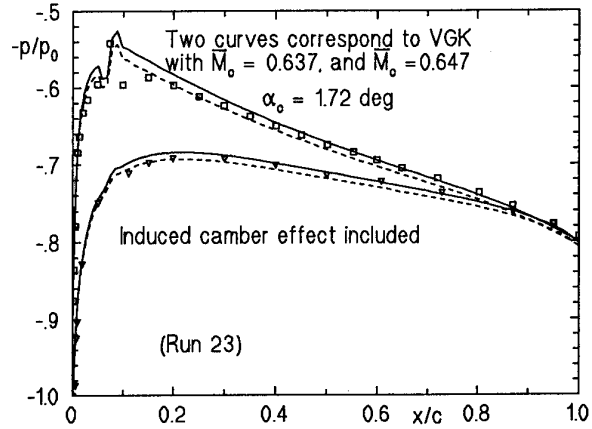
Figure 20 Measured and predicted aerofoil pressures, converged slotted liners, $\bar{M}_o$ = 0.643
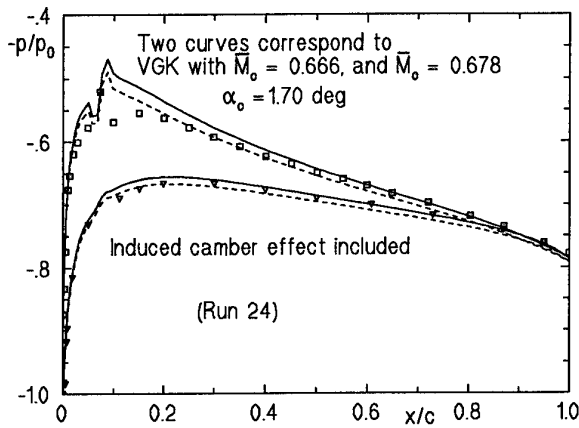
Figure 21 Measured and predicted aerofoil pressures, converged slotted liners, $\bar{M}_o$ = 0.674
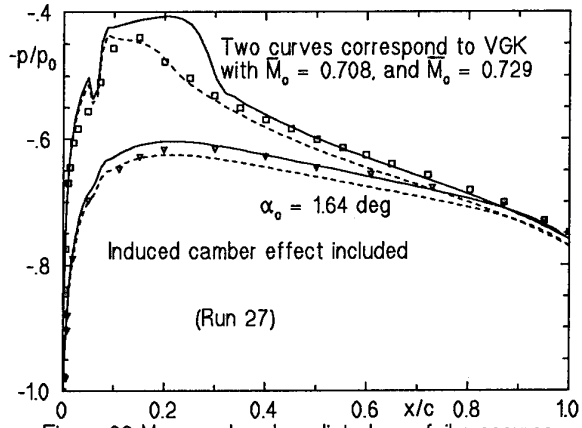
Figure 22 Measured and predicted aerofoil pressures, converged slotted liners, $\bar{M}_o$ = 0.721
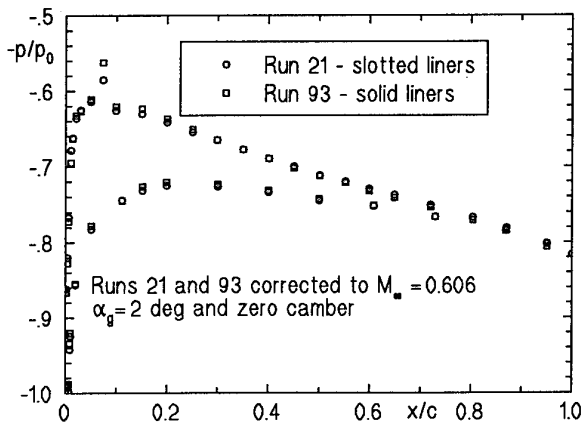
Figure 23 Corrected aerofoil pressures, solid and slotted liners, $M_\bullet$ = 0.606
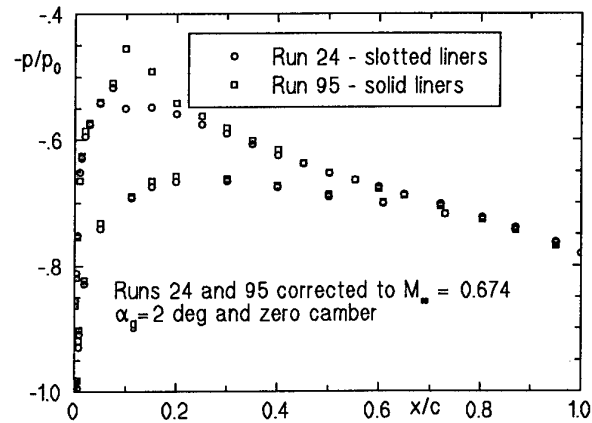
Figure 24 Corrected aerofoil pressures, solid and slotted liners, $M_\bullet$ = 0.674

WALL INTERACTION EFFECTS FOR A FULL-SCALE HELICOPTER ROTOR IN THE NASA AMES 80- BY 120-FOOT WIND TUNNEL

Patrick M. Shinoda
US Army Aviation RD&E Center - ATCOM
and
NASA Ames Research Center
Moffett Field, California 94035-1000

SUMMARY

A full-scale helicopter rotor test was conducted in the NASA Ames 80- by 120-Foot Wind Tunnel with a four-bladed S-76 rotor system. This wind tunnel test generated a unique and extensive data base covering a wide range of rotor shaft angles-of-attack and rotor thrust conditions from 0 to 100 knots. Three configurations were tested: empty tunnel; test stand body (fuselage) and support system; and, fuselage and support system with rotor installed. Empty tunnel wall pressure data are evaluated as a function of tunnel speed to understand the baseline characteristics. Aerodynamic interaction effects between the fuselage and the walls of the tunnel are investigated by comparing wall, ceiling, and floor pressures for various tunnel velocities and fuselage angles-of-attack. Aerodynamic interaction effects between the rotor and the walls of the tunnel are also investigated by comparing wall, ceiling, and floor pressures for various rotor shaft angles, rotor thrust conditions, and tunnel velocities. Empty tunnel wall pressure data show good repeatability and are not affected by tunnel speed. In addition, the tunnel wall pressure profiles are not affected by the presence of the fuselage apart from a pressure shift. Results do indicate that the tunnel wall pressure profiles are affected by the presence of the rotor. Significant changes in the wall, ceiling, and floor pressure profiles occur with changing tunnel speeds for constant rotor thrust and shaft angle conditions. Significant changes were also observed when varying rotor thrust or rotor shaft angle-of-attack. Other results indicate that dynamic rotor loads and blade motion are influenced by the presence of the tunnel walls at very low tunnel velocity and, together with the wall pressure data, provide a good indication of flow breakdown.

LIST OF SYMBOLS

|	
A	rotor disk area, πR^2, ft^2
b	number of rotor blades
c	airfoil chord length, ft
C_P	test section wall pressure coefficient, $(P_W - P_{SCLT}) / Q_{PSF}$
C_S	speed of sound, ft/s
C_T	rotor thrust coefficient, perpendicular to tip-path-plane, $T/A\rho(\Omega R)^2$
C_T/σ	rotor thrust coefficient divided by rotor solidity, $T/\rho(\Omega R)^2 S_R$
M_{TIP}	rotor tip Mach number, $\Omega R/C_S$
P_{SCLT}	calculated test section centerline static pressure referenced to outside ambient pressure based on P_R and P_S, lb/ft^2
P_R	test section total pressure referenced to outside ambient pressure, lb/ft^2
P_S	test section static pressure referenced to outside ambient pressure, lb/ft^2
P_W	test section wall pressure (west wall, east wall, tunnel ceiling, tunnel floor) referenced to outside ambient pressure, lb/ft^2
Q_{PSF}	test section free-stream dynamic pressure, lb/ft^2
R	rotor radius, ft
S_R	rotor blade area, bcR, ft^2
T	rotor thrust, positive up, lb
V_∞	free-stream velocity, ft/s
x	distance upstream of rotor centerline, ft
α_F	fuselage angle, positive nose up, deg
α_S	rotor shaft angle ($\alpha_F = \alpha_S$), positive aft of vertical, deg
μ	advance ratio, $V_\infty/\Omega R$
ρ	free-stream air density, slug/ft^3
σ	rotor solidity, bc/πR or S_R/A
σ	standard deviation
Ω	rotor rotational speed, rad/s

1.0 INTRODUCTION

Wind tunnel testing has been extensively used in the development and improvement of rotorcraft designs, in addition to providing a data base for refinement of theoretical predictions. However, in the low-speed flight regime (0 to 60 kt) of rotorcraft wind tunnel testing (small-scale and specifically full-scale), there is no significant rotor performance, rotor loads, or rotor control state data base with which prediction codes can be validated. Some of the major reasons for this lack of information are: 1) the inability to properly account for wind tunnel wall corrections when the rotor produces large downwash angles at low speed/high thrust conditions; 2) the difficulty in identifying the onset of flow breakdown (the point at which standard wall corrections can no longer correct to free air) for a given rotor and wind tunnel test section size; 3) the difficulty in accounting for Reynolds number effects for small-scale rotors; and, 4) the inability of the tunnel to operate at low speeds for certain size rotors.

There have been wind tunnel tests to establish certain facilities' capabilities / limitations for testing rotorcraft in the low-speed flight regime. Studies have been conducted at the University of Washington (Refs. 1 - 3) and Boeing Vertol Company (Refs. 4, 5) to understand the flow breakdown phenomenon in a wind tunnel with a rotor present. These studies provided some guidelines in determining when flow breakdown will occur for a given size rotor and wind tunnel cross-section, and insights into identifying when flow breakdown occurs. All of these investigations used small-scale rotors.

A full-scale Sikorsky S-76 rotor test was recently conducted in the NASA Ames 80- by 120-Foot Wind Tunnel. In Ref. 6 the facility was evaluated for hover testing and rotor forward flight performance data were correlated with analytical results and other test data. The wide-field shadowgraph technique was evaluated for visualizing full-scale rotor wakes from this test in Ref. 7. One of the main objectives of this test was to establish a data base of information documenting the tunnel's capability to operate a full-scale rotor system throughout its low-speed flight

envelope, including into the tunnel flow breakdown region. This data base will assist in establishing wall corrections for future rotor tests in this facility (using Glauert (Ref. 8), Heyson (Refs. 9-12), Joppa (Refs. 13-14), or Hackett and Wilsden (Ref. 15), Hackett, Wilsden, and Lilley (Ref. 16) methodologies or a combination of them), establish the flow breakdown region for this general size rotor system and wind tunnel, and assist in refinement of theoretical predictions for rotor systems in the low-speed flight regime.

The focus of this paper is to investigate the interaction between the S-76 rotor and the wind tunnel walls. The approach in this investigation was to: (1) acquire empty tunnel wall pressure data and evaluate the baseline characteristics as a function of tunnel speed; (2) acquire data for the fuselage alone and support system configuration to investigate aerodynamic interaction effects between the fuselage and the walls of the tunnel for different tunnel speeds and fuselage angles-of-attack; (3) acquire data for the fuselage with the rotor installed configuration to evaluate rotor inflow and wake effects (by varying tunnel speed, shaft angle, and thrust condition) on wind tunnel test section wall and floor pressures; and, (4) establish the criteria for flow breakdown for this rotor and wind tunnel cross-sectional area.

This paper presents a brief description of the experiment. Wall pressure measurements are discussed and evaluated with the tunnel empty, with the fuselage present, and with the fuselage and rotor present. Various rotor conditions are explored including the flow breakdown regime. Finally, concluding remarks of the research results are presented.

2.0 DESCRIPTION OF THE EXPERIMENT

NASA Ames 80- by 120-Foot Wind Tunnel

The 80- by 120-Foot Wind Tunnel is part of the National Full-Scale Aerodynamics Complex (NFAC) located at the NASA Ames Research Center. The tunnel has an open circuit with a closed, rectangular test section. The maximum test section flow speed is approximately 100 knots. Figure 1 shows a schematic of the wind tunnel circuit. The 80- by 120-Foot Wind Tunnel shares a portion of the flow circuit with the 40- by 80-Foot Wind Tunnel; both tunnels share a single drive system. The drive system consists of six fans rated 135,000 maximum combined horsepower (101 MW). When operating in the 80 x 120 mode, a system of vanes and louvers are positioned so that the 40 x 80 circuit is closed off and the 80 x 120 leg forms a through-flow wind tunnel (Fig. 1). The drive fans pull outside air in through the 80 x 120 inlet and exhaust the air back to the atmosphere through louvers in the tunnel wall downstream of the tunnel fan drive system.

The test section is 80 ft high, 120 ft wide, and 193 ft long. The east wall of the test section has two doors that provide an access opening of approximately 80 ft in height by 120 ft in width. This opening provides room for the tunnel crane to move into the test section for installation of various size wind tunnel models.

General Hardware

The experiment used a production Sikorsky Aircraft S-76 rotor system. The rotor was mounted on NASA's modified Rotor Test Apparatus (RTA). Figure 2 shows the model installed in the wind tunnel. The rotor system is four-bladed with coincident flap and lag articulation provided at the blade root by elastomeric bearings. Blade pitch is also permitted by the same bearing through the rotor spindle. Table 1 lists the S-76 main rotor parameters. The rotor system, including the hub, spindles, blades, and swashplate is identical to the production model.

The RTA is a special-purpose test stand used for operating helicopter rotors in the NFAC. The test stand was originally built in the mid-1970's. The RTA houses two electric-drive motors, a right-angle transmission, a new rotor balance with 22,000 lb thrust capability (installed in 1992) along with primary and dynamic control systems. The primary control system consists of three electro-hydraulic servo-actuators with an on-board hydraulic system with accumulators. The dynamic control system is integrated into the primary control system and provides time varying perturbation capability to the non-rotating swashplate. The RTA was first built as a body of revolution that was 33.3 ft in length and had a maximum diameter of 5.83 ft. In 1991, the RTA was modified to incorporate a fairing on top to enclose the raised rotor control system and the new balance. The new fairing on top of the RTA is 15.96 ft in length and has a maximum cross-section (3.5 ft wide by 4 ft tall) located near the rotor shaft .

The RTA was mounted in the wind tunnel on a three-strut (two main struts and one tail strut) support system placing the rotor hub nominally one rotor diameter above the wind tunnel floor. The model angle-of-attack was varied by changing the height of the gimballed tail strut. All data presented in this paper were acquired with the first harmonic flapping trimmed to near zero.

Instrumentation

The new RTA rotor balance provides increased accuracy in measuring rotor hub loads. This five-component rotor balance measures rotor lift, drag and side forces, together with the rotor pitching and rolling moments. Also incorporated is an instrumented flex coupling to measure rotor torque. Both rotor balance and flex coupling are designed to measure static and dynamic loads. Table 2 lists the general capabilities of the rotor balance.

To understand the interaction effects between the rotor and the wind tunnel at various test conditions, the walls, ceiling, and floors were instrumented with static pressure taps: 21 taps on both east and west walls at mid-height, 21 taps on the centerline of the ceiling, and 18 taps on the floor forward of the rotor shaft and 2 ft to starboard from the centerline of the rotor and tunnel. Refer to Figs. 3-4 for streamwise pressure tap locations. Table 3 lists the general capabilities of the pressure transducers used in this experiment.

Test Configurations and Conditions

Three basic test configurations were investigated: empty tunnel (speed sweep), fuselage and support system (speed sweep at specific fuselage angles-of-attack), and fuselage and support system with the rotor installed (speed sweeps at specific thrusts and rotor shaft angles-of-attack, and thrust sweeps at specific speeds and shaft angles-of attack). The full range of test conditions for each configuration is shown in Tables 4-7. Since the 80 x 120 is an open circuit wind tunnel, outside winds can affect the tunnel test section conditions. To alleviate this concern, the majority of low speed testing was performed when the ambient outside wind speeds were less than 5 kt and the air speed through the test section was less than 4 kt (based on tunnel dynamic pressure measurements).

Wall Pressure Data Reduction and Uncertainty Analysis

The primary parameter used to quantify the effects of the fuselage and rotor on the tunnel walls is the pressure coefficient, C_P.

The wall pressure coefficients were obtained using the following equation,

$$C_P = \frac{(P_W - P_{SCLT})}{Q_{PSF}} \tag{1}$$

Given that $P_{SCLT} = (P_R - P_S) (-1.1936)$, the equation is expanded to

$$C_P = \frac{(P_W - (P_R - P_S) (-1.1936))}{Q_{PSF}} \quad (2)$$

An uncertainty analysis, based on Refs. 17-18, was performed to determine the error estimate for the wall pressure coefficients. The analysis requires the partial derivative of C_P with respect to each measurement parameter in Eq. 2; in addition, the estimate of the standard deviation is needed for each parameter. The error estimate for C_P is represented by,

$$\sigma_{C_P} = \left[\left(\frac{\partial C_P}{\partial P_W}\right)^2 \sigma^2_{P_W} + \left(\frac{\partial C_P}{\partial P_R}\right)^2 \sigma^2_{P_R} + \left(\frac{\partial C_P}{\partial P_S}\right)^2 \sigma^2_{P_S} + \left(\frac{\partial C_P}{\partial Q_{PSF}}\right)^2 \sigma^2_{Q_{PSF}} \right]^{\frac{1}{2}} \quad (3)$$

where

σ_{P_W} = standard deviation of the wall pressure

= calibration accuracy / 2

σ_{P_R} = standard deviation of the test section total pressure

= calibration accuracy / 2

σ_{P_S} = standard deviation of the test section static pressure

= calibration accuracy / 2

$\sigma_{Q_{PSF}}$ = standard deviation of the free-stream dynamic pressure

= calibration accuracy / 2

Uncertainty analysis results for wall pressure coefficients at various tunnel speeds are shown in Table 8. As expected, the uncertainty level increases with decreasing tunnel speeds; this was caused primarily by the uncertainty in Q_{PSF} at low speeds.

3.0 EMPTY TUNNEL RESULTS

The purpose of acquiring the empty tunnel wall pressure data was to establish the baseline wall pressure distribution of the tunnel as a function of tunnel speed. Repeat empty tunnel runs were performed to document the repeatability of the measurements for various tunnel speeds.

Effects Of Tunnel Velocity On Cp Values

The effects of tunnel velocity on the west wall C_P values are presented in Fig. 5. The data show tunnel velocity has no effect on the west wall pressure distribution profile except for minimal offsetting in the pressure distribution. The measurements on the east wall, ceiling and floor are similar and within uncertainty levels for the various tunnel speeds.

Repeatability of Empty Tunnel Run Data

Figure 6 demonstrates the repeatability of pressure coefficient data along the west wall at tunnel velocities of 100 kt and 20 kt. At 100 kt, the total variation in the wall pressure coefficient from pressure tap to pressure tap is quite small (less than 0.04) and the individual pressure tap variation is even smaller (less than 0.01). The 20 kt case shows a slight increase in random fluctuations (up to 0.03) between the individual transducers for a given distribution. However, the overall pressure distribution is similar to the

100 kt profile except for a mean offset. This can probably be attributed to error in the measurement system. The east wall, ceiling, and floor pressures all show similar results as the west wall pressures.

4.0 FUSELAGE ALONE EFFECTS ON WALL PRESSURES

One of the objectives of this test was to investigate the aerodynamic interaction between the fuselage (including the support strut system) and the walls of the tunnel. This was done by comparing the empty tunnel wall pressure data with data acquired with the fuselage installed at various angles-of-attack.

Effect of Fuselage on Tunnel Wall Pressures

Figures 7 and 8 present the effect of the fuselage and support struts on the tunnel west wall and floor pressure distributions, respectively, for a tunnel speed of 100 kt and a fuselage angle-of-attack of -2 deg. Results for the east wall and ceiling are similar to the west wall.

The shape of the pressure profile for the west wall with the fuselage installed, shown in Fig. 7, does not vary significantly from the empty tunnel data. However, the pressure distribution does shift in a negative direction. According to Hackett et al (Ref. 16), a local reduction in area caused by the presence of a body in the tunnel free-stream should create a local reduction in wall pressure in the vicinity of the fuselage / support struts, but not an entire profile shift as shown in the figure. The shift may be attributed to a blockage effect from the body and support struts causing more than just a local effect on the tunnel wall pressures. However, the blockage for $\alpha_F = -2$ deg is estimated to be approximately 2 percent.

The floor pressure profile, shown in Fig. 8, shows there is a significant effect when the fuselage and support struts are present. When the fuselage is present, the pressure coefficient at the furthest upstream location matches closely to the empty tunnel floor pressure coefficients. As the rotor centerline is approached, the pressure coefficient becomes more positive and reaches its maximum value near the rotor centerline. Aft of the rotor shaft centerline, the pressure becomes less positive and more closely matches the empty tunnel floor pressures in this location. This can be attributed to the proximity of the pressure taps on the floor to the right main strut fairing. The main strut fairings are 3.5 ft thick by approximately 8.5 ft in chord length at the floor. The 3-strut support system creates a blockage effect causing the air to flow between the wall and the support system. This causes a low-velocity, high-pressure region forward of the struts where the floor pressures are measured.

The effect of tunnel speed on the tunnel wall pressures with the fuselage present was also analyzed. The pressure profiles for 60 kt were similar to the 100 kt profiles. For velocities less than or equal to 40 kt, the measurements showed consistent negative shifts. These indicated shifts in wall pressure distributions below 40 kt can be partially attributed to limitations of the measurement capabilities of the transducers. Another cause of this shift may be a blockage effect from the body and support struts causing more than just a local effect on the tunnel wall pressures.

Effect of Fuselage Angle on Tunnel Wall Pressures

The effect of fuselage angle-of-attack on a west wall pressure tap is shown for 100 kt in Fig. 9. The data are taken from a representative pressure tap located at the longitudinal station nearest to the test section turntable centerline (turntable centerline is zero in Fig. 3). A similar location was chosen to evaluate the east wall and ceiling

pressure data; for the floor, the pressure tap furthest upstream was chosen.

In Fig. 9, the differences in Cp between the fuselage installed and the empty tunnel is at a maximum when $\alpha_F = 10$ deg then decreases as the fuselage angle decreases and becomes nearly zero at $\alpha_F = -15$ deg. This trend indicates that the blockage effect of the fuselage and support system can be minimized by selecting an appropriate fuselage angle-of-attack. The strut-blockage effect appears to be counteracted by the fuselage as the angle-of-attack is decreased to -15 deg. The east wall, ceiling, and floor pressure coefficient values show similar results as the west wall data. For speeds less than 100 kt, the effects of the fuselage on the west wall and the other wall pressures were similar to the 100 kt condition. The lower speed conditions, however, exhibited an increase in uncertainty (as shown in Table 8).

5.0 ROTOR/FUSELAGE EFFECT ON WALL PRESSURES

The following section discusses the effect of the combined rotor / fuselage configuration on the wind tunnel wall pressures. The wall pressures are evaluated for different rotor advance ratios, thrust levels, and shaft angles. These three parameters influence the strength and location of the rotor wake.

Effect of Advance Ratio

Figures 10 - 13 present the effect of the rotor wake on the tunnel walls, ceiling, and floor as the advance ratio is varied. The rotor thrust coefficient-to-solidity ratio is 0.10 and the rotor shaft angle is tilted forward 2 deg during this advance ratio sweep.

The west wall pressure coefficients are shown in Fig. 10. The wall pressure profiles for $\mu \geq 0.06$ (24 kt) are similar to the empty tunnel profiles except for a mean offset. However, for $\mu < 0.06$ (24 kt), a low pressure region begins to appear; the region increases in size and magnitude and moves forward towards the rotor centerline as advance ratio is decreased. Norman and Yamauchi (Ref. 19) observed similar results for a full-scale helicopter rotor (46 ft diameter) in the NASA Ames 40- by 80-Foot Wind Tunnel.

The east wall pressure profile, Fig. 11, is similar to the west wall profile except for a few differences and in general, agrees with observations of Rae (Ref. 1) and Norman and Yamauchi (Ref. 19). The east wall low pressure region appears at an advance ratio of $\mu = 0.06$ (24 kt) and the peak low pressure region is slightly forward in position and greater in magnitude than the west wall pressure (compare Fig. 10 and Fig. 11). These differences are caused by the variation in wake strength and shape due to the direction of rotor rotation; the east wall is on the advancing blade side of the rotor and the west wall is on the retreating blade side of the rotor.

The strength, size and location of the low pressure regions and peaks shown in Figs. 10 and 11 are directly related to the rotor wake skew angle (a function of rotor inflow ratio and advance ratio) and rotor height in the tunnel. As advance ratio decreases the rotor wake skew angle decreases, which moves the rotor wake impingement on the floor further upstream underneath and closer to the rotor. This means the rotor wake rollup along both walls moves upstream, therefore, causing the peak low pressure region on both walls to move upstream closer to the rotor. As observed by Rae (Ref. 1), this condition can cause flow recirculation in the tunnel and the onset of reverse flow on the tunnel side walls as the peak low pressure region moves closer to the rotor centerline (see $\mu = 0.03$ (12 kt) case in Fig. 11).

Figure 12 shows the tunnel ceiling pressure distribution is affected by the rotor system throughout the advance ratio range studied but to a lesser degree than the east and west walls. Above $\mu = 0.113$ (45 kt), the pressure signature is relatively small in magnitude upstream of the rotor and still compares well with the empty tunnel pressure profile. The pressure signature becomes more pronounced as the advance ratio is decreased below 0.113 (45 kt). However, contrary to expectations, the low pressure regional peak does not move downstream as advance ratio is decreased. For hover condition, the peak should be directly above the rotor. Recirculation effects may be influencing the rotor inflow.

In Fig. 13, advance ratio does not have an affect on the floor pressure profile above $\mu = 0.113$ (45 kt). However, as the advance ratio is decreased to 0.06 (24 kt), a positive shift in the pressure level occurs with no significant change in profile. This positive shift can be partially attributed to the measurement system uncertainties. However, the majority of the shift may be attributed to the increasing influence of the rotor wake as the tunnel speed is decreased. In particular, the rotor wake may cause a partial blockage (this blockage is a function of skew angle) resulting in a reduction in the local free-stream velocity below and in front of the rotor relative to the surrounding region. For $\mu = 0.04$ (16 kt), a very small profile distortion occurs upstream of the rotor centerline possibly representing the beginning of a small ground vortex. At $\mu = 0.03$ (12 kt), a large profile distortion is generated further upstream of the rotor. At this point, the downwash of the rotor begins to strongly interact with free-stream air below the rotor creating a ground vortex and a large low pressure region. Also, the large positive pressures beneath the rotor are caused by the impingement of the wake on the floor. Evidence of ground vortices have also been observed by Rae (Ref. 2) and Sheridan and Wiesner (Ref. 4). These results are further discussed in the section on flow breakdown. These studies showed that the vortex becomes stronger and moves upstream as tunnel speed is decreased.

Effect of Rotor Thrust

The effect of rotor thrust on the tunnel walls (east and west) and ceiling pressure distributions are shown in Figs. 14, 15, and 16, respectively. The advance ratio is fixed at 0.05 (20 kt) and the rotor shaft angle is tilted forward 2 deg during this thrust sweep.

Both west and east wall show a low pressure region forming aft of the rotor at $C_T/\sigma = 0.08$. This low pressure region expands in size and strength with increasing thrust. In addition, the low pressure region peak moves upstream closer to the rotor centerline as the thrust is increased. This behavior was also observed by Norman and Yamauchi (Ref. 19). Again when comparing the east and west wall pressure profiles for a given thrust condition, the east wall pressure profile distortion is larger and closer to the rotor than the west wall.

The strength, size and location of the low pressure regions and peaks shown in Figs. 14 and 15 can once again be directly related to the rotor wake skew angle and rotor height in the tunnel. As the thrust increases, the rotor wake skew angle decreases which moves the rotor wake impingement on the floor further upstream. Thus, the location where the wake flows up the walls also moves upstream and gains strength due to increased thrust. Subsequently, the peak low pressure region on both walls becomes stronger and moves upstream closer to the rotor. Note that increasing thrust has the same effect on the location of the low pressure region peak as decreasing advance ratio.

The effect of thrust on the ceiling pressure profile is shown in Fig. 16. The ceiling pressure profile is affected for all

thrust levels at this advance ratio. The magnitude of the low pressure regional peaks increase with thrust as expected, however, the peaks remain stationary instead of moving downstream with increasing thrust. This expected movement in peaks may exist but was not observed possibly due to coarse spacing of pressure taps.

Effect of Rotor Shaft Angle

The effects of rotor shaft angle on the tunnel west wall, east wall, ceiling and floor pressure distribution profiles are shown in Figs. 17 - 22 for $C_T/\sigma=0.10$ at fixed advance ratios. The side walls and ceiling profiles are shown at $\mu=0.05$ (20 kt) and the floor pressures at $\mu=0.03$ (12 kt).

Figures 17 and 18 show the east and west wall pressures have similar profiles and that shaft angle has a minimal effect on the wall pressure profiles. As noted in earlier sections of this paper, the east wall low pressure region is more clearly defined, of greater magnitude, and further upstream than the west wall. The strength, size and location of the low pressure regions and peaks shown in Figs. 17 and 18 are also related to the rotor wake skew angle, rotor shaft tilt, and rotor height in the tunnel. As the shaft angle is increased from -10 deg to 5 deg, the rotor wake impingement on the floor is expected to move further upstream, together with wake roll-up, toward the rotor. This would cause the low pressure region and the peak to move upstream closer to the rotor and have a greater magnitude. However as discussed earlier, this is not occurring.

The ceiling pressure profiles, shown in Fig. 19, are similar in shape for each shaft angle. For any given shaft angle, the low pressure region peaks remain stationary instead of moving downstream with increasing shaft angle; this was also observed with rotor thrust sweeps discussed earlier.

The cause for the side wall peaks not moving upstream and ceiling peak downstream with decreasing shaft angle may be due to the coarse distribution of pressure taps, or more extreme shaft angles are required to cause movement of the low pressure region of the wall and ceiling profiles.

A review of the ceiling pressure profile data indicates a relationship between the pressure distortion peak strength and shaft angle for a given advance ratio. Figures 20 and 21 show this relationship in absolute magnitudes for advance ratios of 0.03 - 0.06 (12 - 24 kt), 0.10 (40 kt), and 0.25 (100 kt). The pressure peak magnitude on the ceiling increases with increasing rotor shaft angle for all advance ratios. Even though the uncertainty estimates are large at these low advance ratios, there is a definite trend.

Figure 22 presents the effect of the rotor shaft angle on the tunnel floor pressure distribution at $\mu=0.03$ (12 kt). This speed was chosen since no effects on tunnel floor pressure distribution occurred at $\mu=0.05$ (20 kt) (see Fig. 13). However, as shown earlier in this section, there is a significant effect at $\mu=0.03$ (12 kt). Figure 22 shows the general pressure profile does not change with rotor shaft angle but there is an indication that the low pressure region moves forward with increasing shaft angle which is expected.

6.0 FLOW BREAKDOWN

The results from the previous section showed the effect of the rotor on the wind tunnel. Ultimately, the goal is to determine what effect the wind tunnel has on the rotor and to determine (for this size rotor system) at what condition (rotor thrust, rotor shaft angle-of-attack, and tunnel speed) the wind tunnel environment becomes an inadequate substitute for the free-air environment. The other term commonly used to describe this condition is flow breakdown: where wall corrections are no longer sufficient to correct to free air conditions (Ref. 2). Establishing this

flow breakdown envelope for this size rotor will assist future test programs in establishing a proper test matrix that avoids this area of rotor / tunnel operation.

Flow breakdown usually occurs at a tunnel speed where the rotor wake begins to create a ground vortex, placing the rotor in-ground effect (Refs. 2 and 4). For full-scale testing, installing a rotor out of ground effect for a hover condition in a wind tunnel is rarely possible. Sheridan and Wiesner (Ref. 4) describe how deviations in the steady-state rotor controls and rotor power appear as tunnel speed is reduced to a ground effect or flow breakdown condition. The data from this investigation do not reveal such deviations. However, floor pressure results presented in Figs. 13 and 22 do indicate the presence of a ground vortex; in addition, Figs. 10 and 11 show strong wall pressure distribution distortions at the same advance ratio of $\mu=0.03$ (12 kt). These changes in the floor and advancing blade side-wall pressure distribution were also observed in Rae's tests (Refs. 1-3). The following discusses some of the dynamic rotor loads and blade motion results that show indications of flow breakdown that correspond to the floor pressure and wall pressure results.

Dynamic (1/2 peak-to-peak) rotor loads and blade motion results are shown in Figs. 23 and 24, respectively, for three thrust conditions and a rotor shaft angle of -2 deg.

Rotor thrust 1/2 peak-to-peak loads, shown in Fig. 23, increase with decreasing tunnel speed and peak between 30 and 40 kt (depending on the fixed thrust condition) and then decrease until 12 to 16 kt is reached. This vibratory load could be expected to continually decrease to a lower value in hover. Instead, the unsteady thrust is found to increase to a higher level and almost matches the same vibratory condition at 30 to 40 kt. Similar results are seen in other dynamic rotor and blade loads data. This is probably due to an unsteady and strong rotor wake recirculation caused by the enclosed test section walls.

Figure 24 shows a similar trend for rotor blade 1/2 peak-to-peak flap motion. The blade flap motion reaches a minimum at 70 kt as advance ratio is decreased from 100 kt. As the velocity is further decreased, the flapping motion gradually increases and peaks between 30 and 40 kt, and then decreases until 12 to 16 kt is reached. As the velocity is reduced further, the flapping motion increases to a much higher level.

The data shown in Figs. 23 and 24 correlate well with the west and east wall pressure data and floor pressure data (Figs. 10, 11, and 13, respectively) presented earlier in this paper. The east and west wall pressure profiles begin to show a strong low pressure peak at $\mu= 0.04$ (16 kt) and even a stronger one at $\mu= 0.03$ (12 kt). These results are similar to Rae's experiments (Refs. 1 and 3) but at different advance ratios; the level of distortion in the pressure distribution seen in Fig. 11 at $\mu= 0.04$ (16 kt) and below is what Rae considered to be indicative of flow breakdown. The floor pressure distribution shows this large change in pressure profile at $\mu= 0.03$ (12 kt) also indicating a ground vortex formation upstream of the rotor, again similar to Rae's experiment (Ref. 2). The ground vortex in combination with the rotor wake recirculation in the test section, shown in the pressure data, grows and causes an increase in rotor unsteadiness manifested in both rotor loads and blade motion as the tunnel speed is decreased. The 12 - 16 kt region corresponds to the inflection point of the rotor 1/2 peak-to-peak thrust data and blade flapping motion data. Therefore, wall pressures as well as rotor oscillatory loads indicate flow breakdown occurs at or below $\mu= 0.04$ (16 kt) for a shaft angle of -2 deg at these particular thrust conditions for this facility.

7.0 CONCLUDING REMARKS

A full-scale helicopter rotor test was conducted in the NASA Ames 80- by 120-Foot Wind Tunnel with a four-bladed S-76 rotor system. This wind tunnel test generated a unique and extensive data base covering a wide range of rotor shaft angles-of-attack and rotor thrust conditions from 0 to 100 knots. Three configurations were tested: empty tunnel; test stand body (fuselage) and support system; and fuselage and support system with rotor installed. The study has resulted in the following observations.

Empty Tunnel

Wall pressure coefficient values and profiles are not affected by tunnel speed. The mean offsets in wall Cp profiles are well within the uncertainty estimates.

Wall pressure data show good repeatability within the uncertainty analysis calculations.

Fuselage Alone

Wall pressure data with the fuselage installed are similar when compared with empty tunnel data. However, the fuselage does have an effect by shifting the pressure distribution profile relative to the empty tunnel profile. The magnitude of this shift depends on the body angle-of-attack and tunnel speed.

Minimum blockage of the wind tunnel does not occur at 0 deg fuselage angle-of-attack but at -15 deg.

Fuselage and Rotor

The east wall, west wall and floor pressures are affected by the presence of the rotor only at low speeds. An effect of rotor thrust was also observed but to a lesser degree.

The ceiling pressures are affected by the presence of the rotor at all speed and shaft angles at high thrust conditions. The magnitude of this effect is a function of shaft angle, speed, and thrust condition.

Flow Breakdown

The dynamic rotor loads, dynamic blade flapping motion, and wall and floor pressures indicate flow breakdown occurs at or below $\mu = 0.04$ (16 kt).

ACKNOWLEDGEMENTS

REFERENCES

1. Rae, W. H., Jr., "Limits on Minimum-Speed V/STOL Wind-Tunnel Tests," *Journal of Aircraft*, Vol. 4, No. 3, May-June 1967, pgs. 249-254.

2. Rae, W. H., Jr., "An Experimental Investigation of Wind Tunnel Wall Corrections and Test Limits for V/STOL Wind-Tunnel Tests," U.S. Army Grant No. DA-ARO-31-124-G-809, Project No. 4506-E , AD-764 255, Dept. of Aeronautics and Astronautics, Univ. of Washington, July 1973.

3. Rae, W. H., Jr. and Shindo, S., "An Experimental Study of Alleviating the Limits on Minimum Speed V/STOL Wind Tunnel Tests," University of Washington, Dept. of Aeronautics and Astronautics, Report No.68-1, 1968.

4. Sheridan, P. F. and Wiesner, W., "Aerodynamics of Helicopter Flight Near the Ground," American Helicopter Society 33rd Annual Forum, Washington D.C., May 1977.

5. Harris, F. D., "Aerodynamic and Dynamic Rotary Wing Model Testing in Wind Tunnels and Other Facilities," Advisory Group for Aerospace Research and Development (AGARD) Lecture Series No. 63, May 1973.

6. Shinoda, P. M, and Johnson, W., "Performance Results from a Test of an S-76 Rotor in the NASA Ames 80- by 120-Foot Wind Tunnel," AIAA Paper 93-3414, AIAA Eleventh Applied Aerodynamics Conference, Monterey, CA, August 1993.

7. Swanson, A., "Application of the Shadowgraph Flow Visualization Technique to a Full-Scale Helicopter in Hover and Forward Flight," AIAA Paper 93-3411, AIAA Eleventh Applied Aerodynamics Conference, Monterey, CA, August 1993.

8. Glauert, H., " The Interference on the Characteristics of an Airfoil in a Wind Tunnel of Rectangular Section," R & M 1459, 1932.

9. Heyson, H. H., "Linearized Theory of Wind Tunnel Jet Boundary Corrections and Ground Effect for VTOL-STOL Aircraft," NASA TR R-124, 1962.

10. Heyson, H. H., "Jet-Boundary Corrections for Lifting Rotors Centered in Rectangular Wind Tunnels," NASA TR R-71, 1960.

11. Heyson, H. H., "Use of Superpositions in Digital Computers to Obtain Wind-Tunnel Interference Factors for Arbitrary Configurations, With Particular Reference to V/STOL Vehicles," NASA TR R-302, 1969.

12. Heyson, H. H., "General Theory of Wall Interference for Static Stability Tests in Closed Rectangular Test Sections and in Ground Effect," NASA TR R-364, 1971.

13. Joppa, R. G., "A Method of Calculating Wind Tunnel Interference Factors for Tunnels of Arbitrary Cross Section," NASA CR-845, 1967.

14. Joppa, R. G., " Wind Tunnel Interference Factors for High-Lift Wings in Closed Wind Tunnels," NASA CR-2191, February 1973.

15. Hackett, J. E. and Wilsden, D. J., "Determination of Low Speed Wake Blockage Corrections via Tunnel Wall Static Pressure Measurements," AGARD CP 174, Paper 23, October 1975.

16. Hackett, J. E., Wilsden, D. J., and Lilley, D. E., "Estimation of Tunnel Blockage from Wall Pressure Signatures: A Review of Data Correlation," NASA CR 152,241, March 1979.

17. Kline, S. J. and McClintock, F. A., "Describing Uncertainties in Single-Sample Experiments," *Mechanical Engineering*, January 1953.

18. Schenk, H., Theories of Engineering Experimentation, McGraw-Hill, 1979.

19. Norman, T. R. and Yamauchi, G. K., "Full-Scale Investigation of Aerodynamic Interactions Between a Rotor and Fuselage," American Helicopter Society 47th Annual Forum, Phoenix, AZ, May 1991.

Table 1. Main Rotor Parameters

Parameter	Value	
Radius	22	ft
Nominal Chord	15.5	in
Solidity Ratio	.0748	
Number of Blades	4	
Airfoils	SC1095	
	and SC1095R8	
Flapping Hinge offset	3.70%	radius
Lock No.	11.6	
100% RPM	293	
100% tip speed	675	fps

Table 2. RTA Rotor Balance Calibration Accuracy

Parameter	Maximum Capacity		Std. Deviation of Error Value		% Capacity
Normal Force	22,000	lbs	25	lbs	0.12
Side Force	4,400	lbs	7	lbs	0.16
Axial Force	4,400	lbs	12	lbs	0.27
Pitching Moment	694,000	in-lbs	324	in-lbs	0.05
Rolling Moment	694,000	in-lbs	504	in-lbs	0.07
Torque	36,083	ft-lbs	--		--

Table 3. Pressure Transducer Accuracies

Parameter	Maximum Capacity		2 Std. Deviation of Error Value		% Capacity
P_W(West Wall)	0.36	psid	0.00036	psid	0.10
P_W(East Wall)	0.36	psid	0.00036	psid	0.10
P_W(Ceiling)	0.36	psid	0.00036	psid	0.10
P_W(Floor)	1.00	psid	0.00100	psid	0.10
P_R	0.19	psid	0.00019	psid	0.10
P_S	1.00	psid	0.00080	psid	0.08
Q_{PSF}	262	psf	0.20000	psf	0.10

Table 4. Empty Tunnel Test Matrix

Tunnel Velocity, kt	4, 8, 12, 16, 20, 24, 28, 32, 36, 40, 50, 60, 70, 80, 90, 100

Table 5. Fuselage Alone Test Matrix

Fuselage Angles, α_F	-15°, -10°, -5°, 0°, 5°, 10°
Tunnel Velocity, kt	0 - 100

Table 6. Speed Sweep Test Matrix
V_∞ = 0-100 kt
M_{TIP} : 0.605 (675 fps)

α_S	THRUST, lb		
	8,000 (C_T/σ=.065)	9,850 (.080)	12,320 (.100)
10°		X	X
5°	X	X	X
0°		X	
-2°	X	X	X
-5°	X	X	
-10°	X	X	X

Table 7. Thrust Sweep Test Matrix
C_T/σ=0.03-0.125
M_{TIP} : 0.605 (675 fps)

VKTS	μ	α_S					
		10°	5°	0°	-2°	-10°	-15°
20	0.050				X		
32	0.080			X			
40	0.100	X	X		X	X	X
50	0.125	X	X				
60	0.150	X	X		X	X	X
80	0.200	X	X		X	X	
100	0.250	X	X		X	X	X

Table 8. Wall Pressure Uncertainties
(+- 2σ)

VKTS	Approx Q_{PSF}	μ	West Wall Cp	East Wall Cp	Ceiling Cp	Tunnel Floor Cp
100	33.90	0.25	.004	.004	.004	.0053
80	21.67	0.20	.006	.006	.006	.0086
60	12.19	0.15	.011	.011	.011	.0153
40	5.41	0.10	.024	.024	.024	.0347
32	3.46	0.08	.037	.037	.037	.054
20	1.35	0.05	.095	.095	.095	.137
16	0.86	0.04	.157	.157	.157	.222
12	0.48	0.03	.308	.308	.308	.423
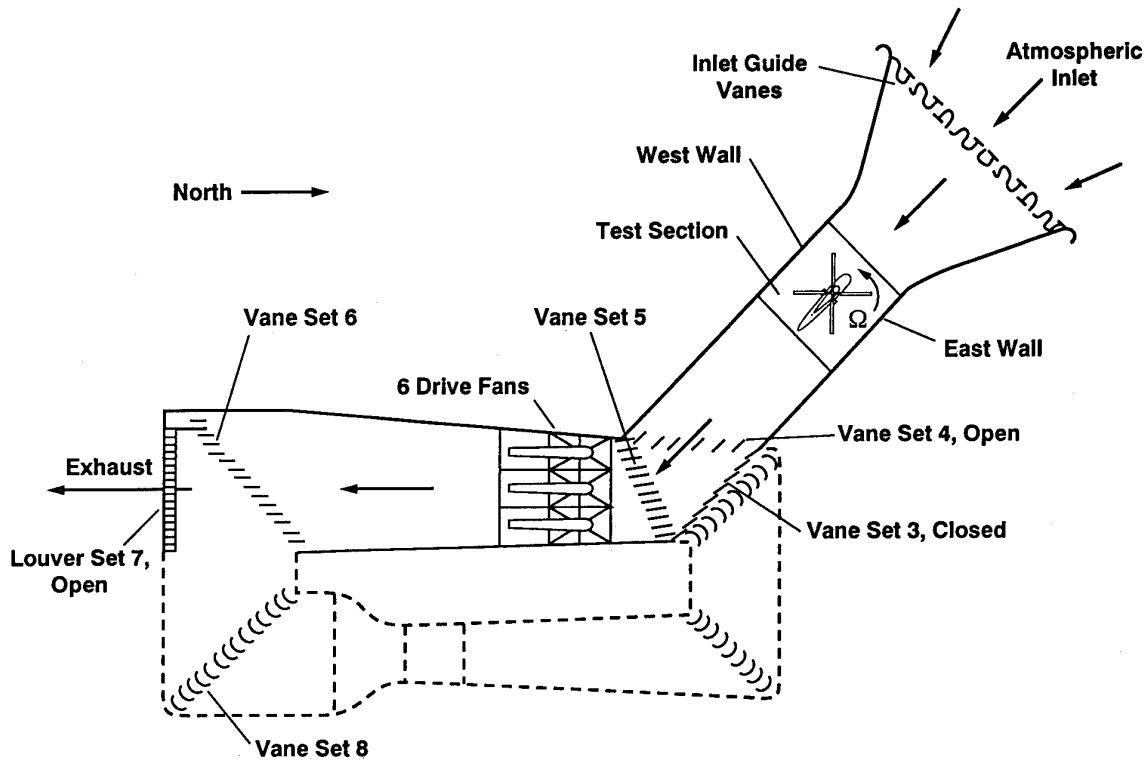
Fig. 1   80- by 120-Foot Wind Tunnel circuit.
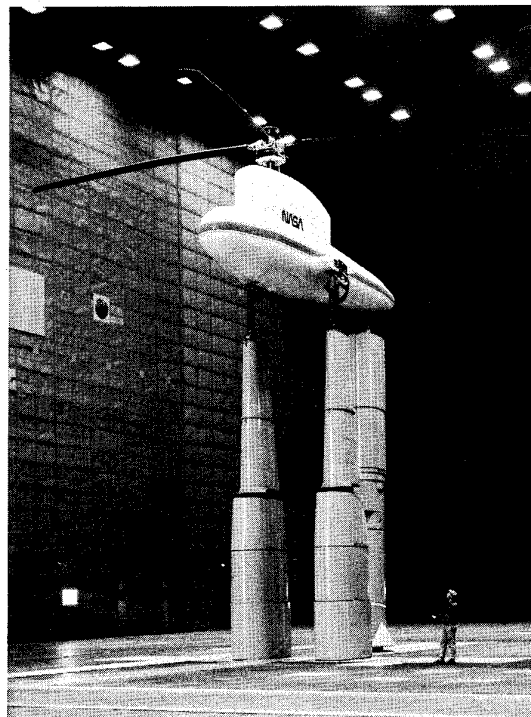
Fig. 2   S-76 Rotor System installed on Rotor Test Apparatus in the Ames 80- by 120-Foot Wind Tunnel.
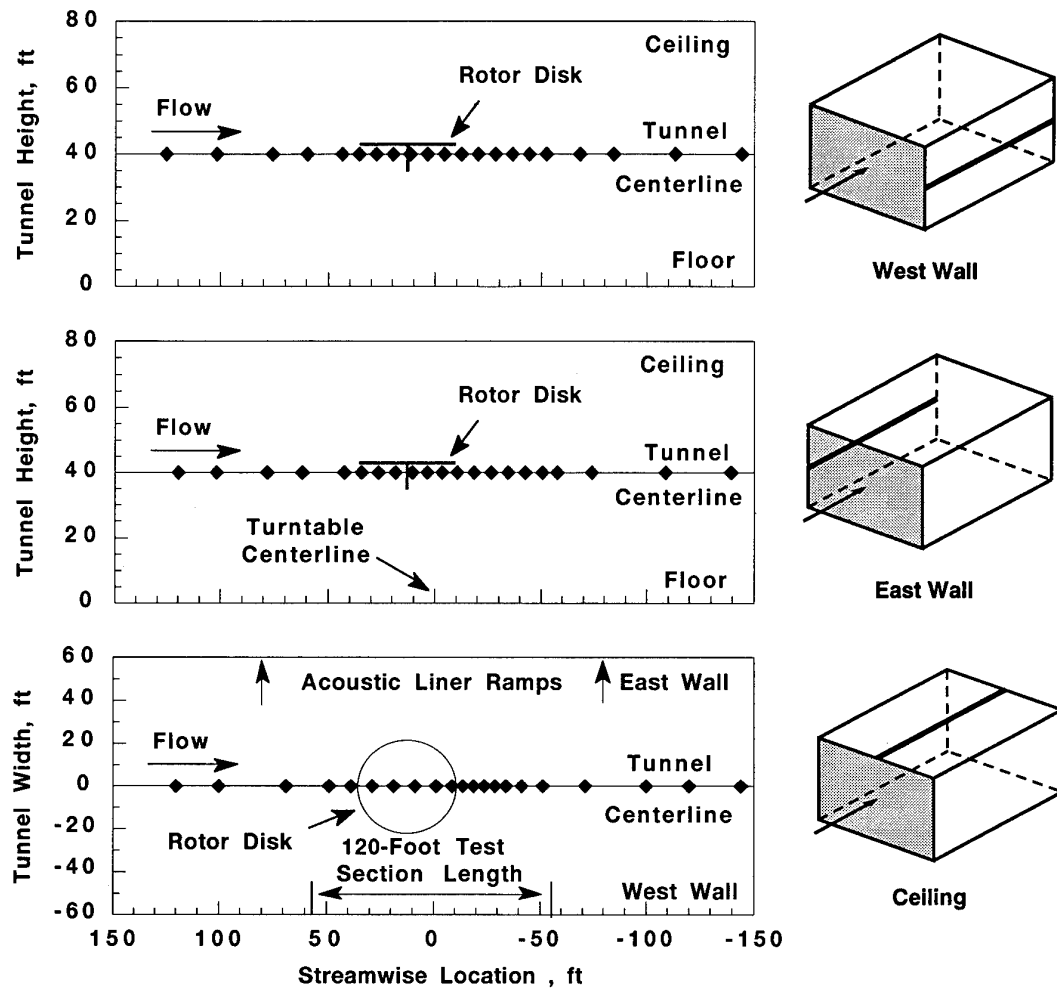
Fig. 3   West wall, east wall, and ceiling pressure tap locations in the wind tunnel.
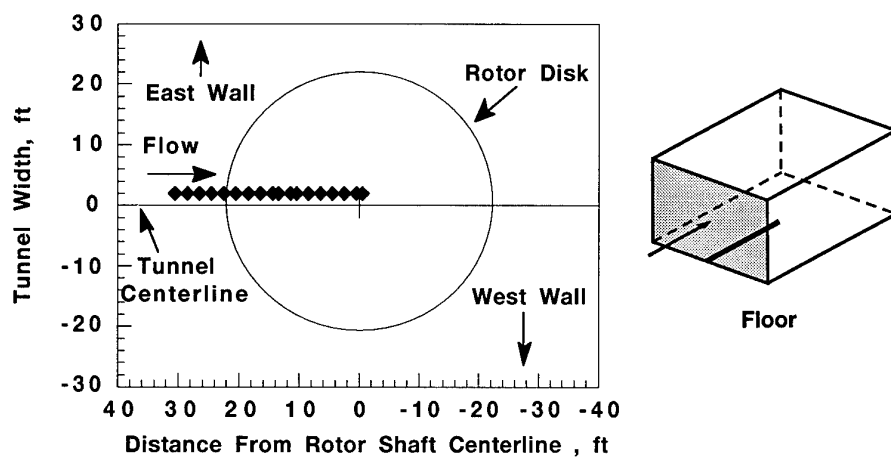
Fig. 4   Floor pressure tap locations in the wind tunnel.
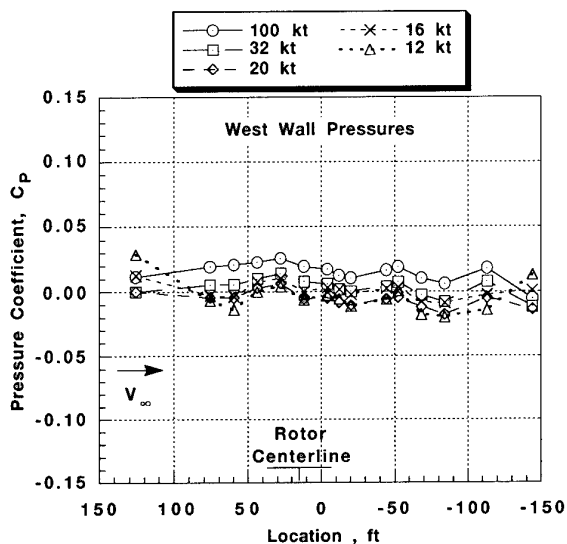
Fig. 5   Effect of tunnel speed on empty tunnel west wall pressures.
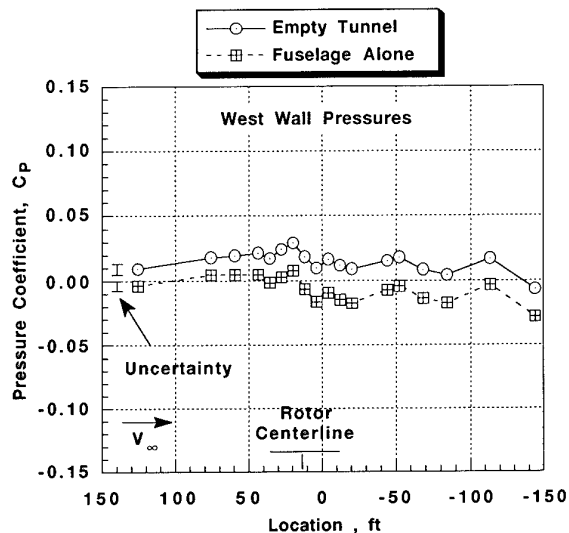
Fig. 7   Effect of fuselage on wind tunnel west wall pressures, V_∞=100 kt, α_F= –2 deg.
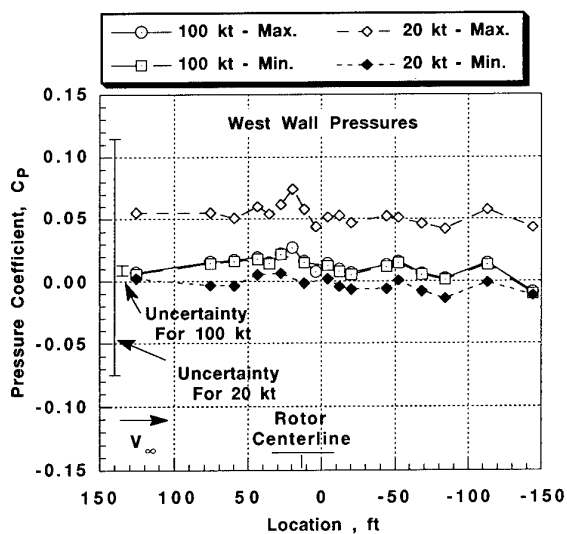
Fig. 6   Empty tunnel west wall pressure repeatability at 100 kt and 20 kt.
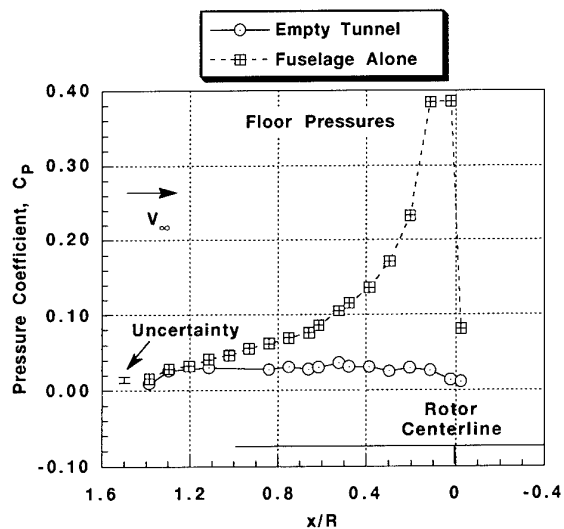
Fig. 8   Effect of fuselage on wind tunnel floor pressures, V_∞=100 kt, α_F= –2 deg.
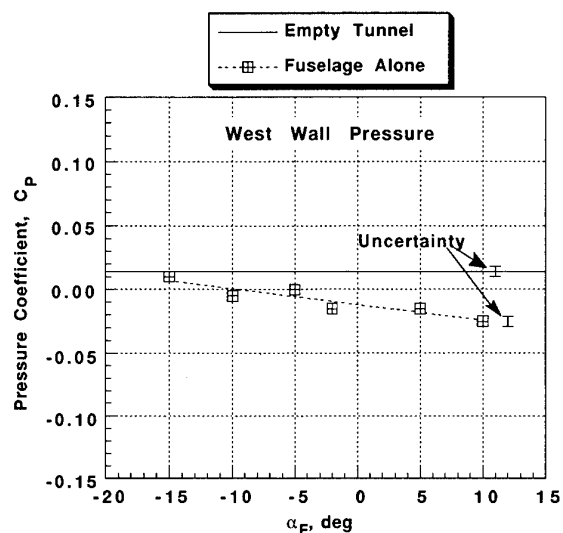
Fig. 9   Effect of angle-of-attack of fuselage on west wall pressure at 100 kt.
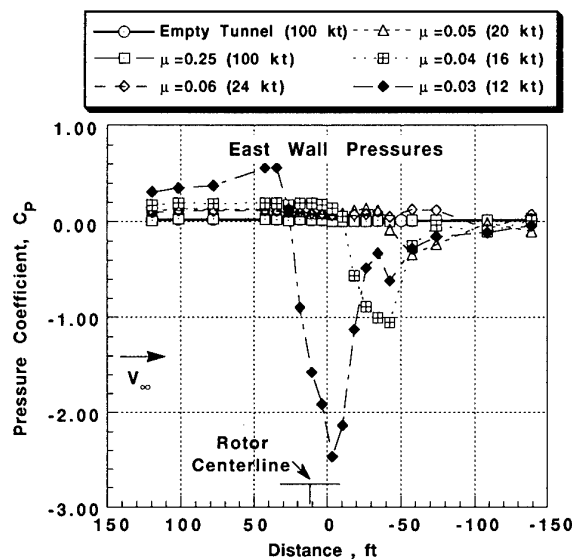
Fig. 11   Effect of advance ratio on tunnel east wall pressures; α_s= -2 deg, C_T/σ=0.100.
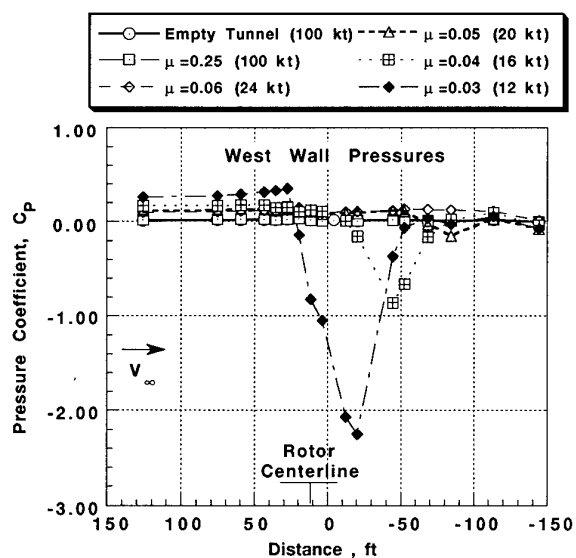
Fig. 10   Effect of advance ratio on tunnel west wall pressures; α_s= -2 deg, C_T/σ=0.100.
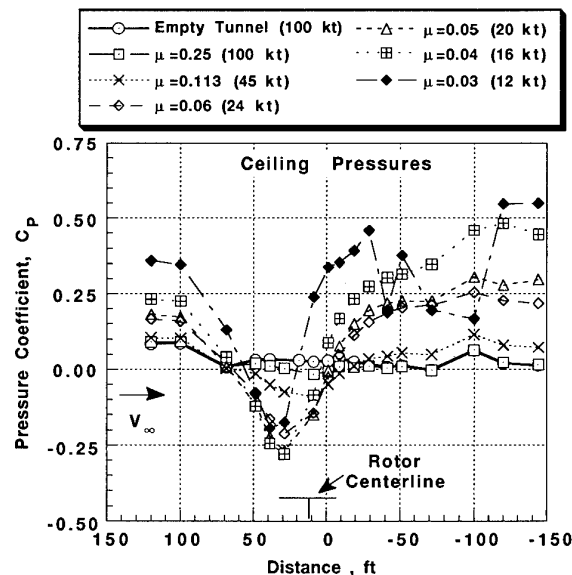
Fig. 12   Effect of advance ratio on tunnel ceiling pressures; α_s= -2 deg, C_T/σ=0.100.
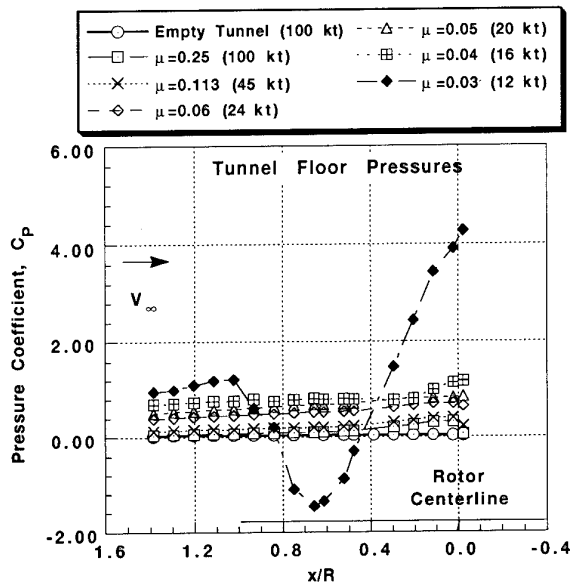
Fig. 13   Effect of advance ratio on tunnel floor pressures;
α_S= -2 deg, C_T/σ=0.100.
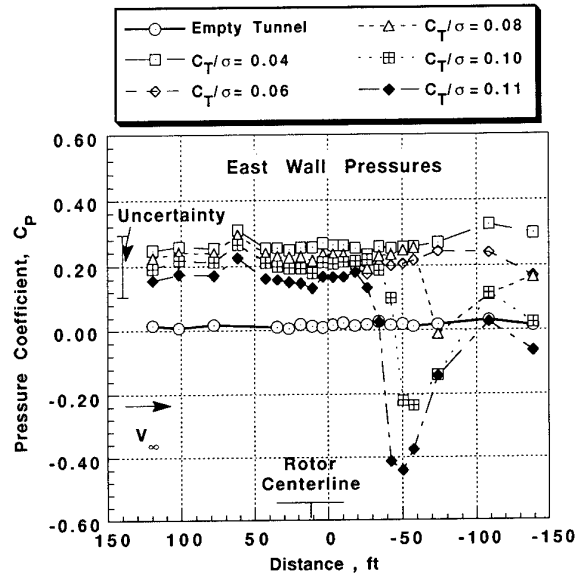
Fig. 15   Effect of rotor thrust on tunnel east wall pressures;
α_S= -2 deg, μ= 0.05 (20 kt).
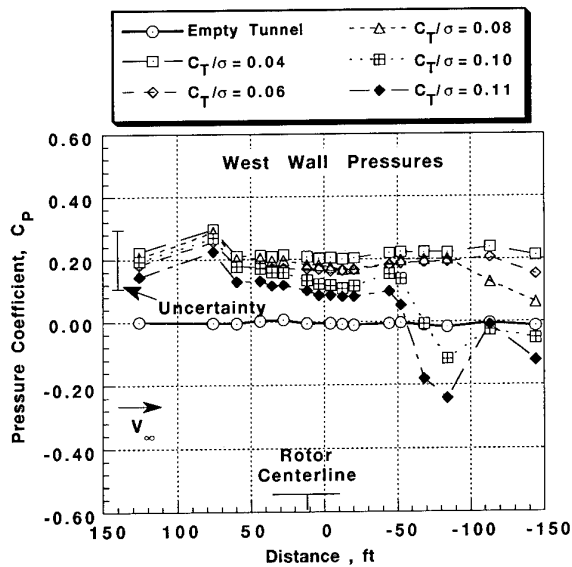
Fig. 14   Effect of rotor thrust on tunnel west wall pressures;
α_S= -2 deg, μ= 0.05 (20 kt).
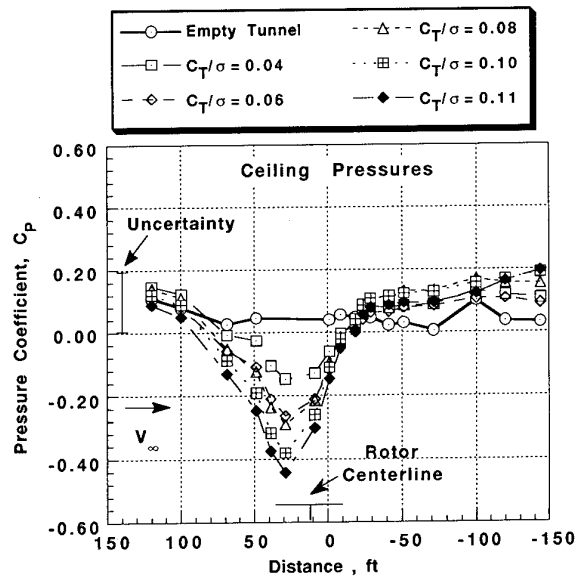
Fig. 16   Effect of rotor thrust on tunnel ceiling pressures;
α_S= -2 deg, μ= 0.05 (20 kt).
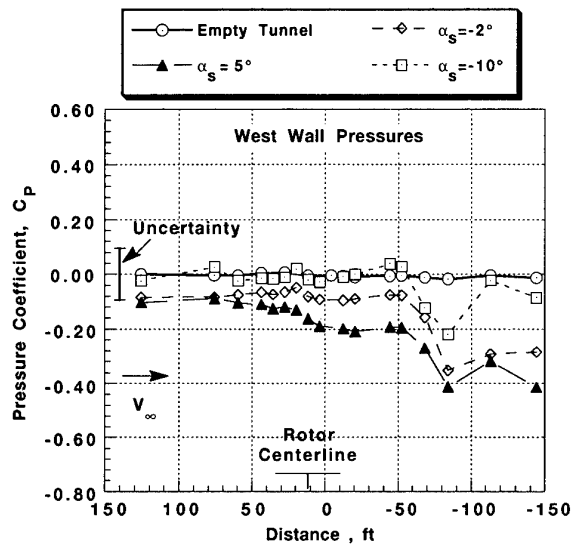
Fig. 17 Effect of rotor shaft angle-of-attack on tunnel west wall pressures; $C_T/\sigma=0.100$, $\mu= 0.05$ (20 kt).
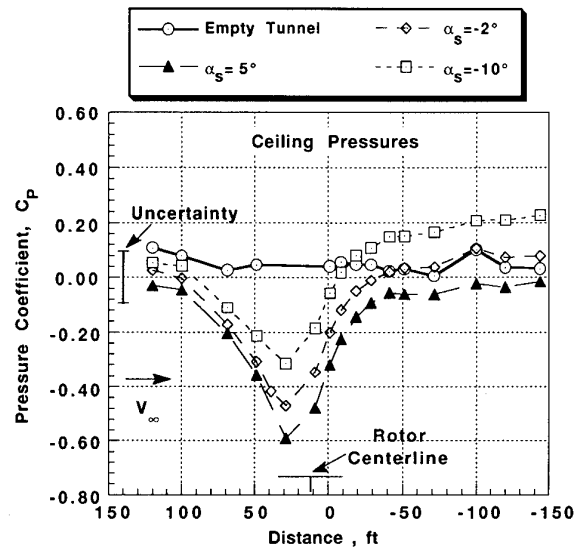
Fig. 19 Effect of rotor shaft angle-of-attack on tunnel ceiling pressures; $C_T/\sigma=0.100$, $\mu= 0.05$ (20 kt).
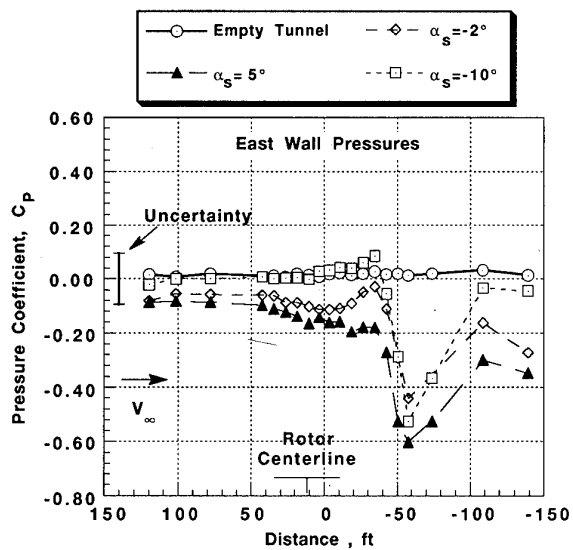
Fig. 18 Effect of rotor shaft angle-of-attack on tunnel east wall pressures; $C_T/\sigma=0.100$, $\mu= 0.05$ (20 kt).
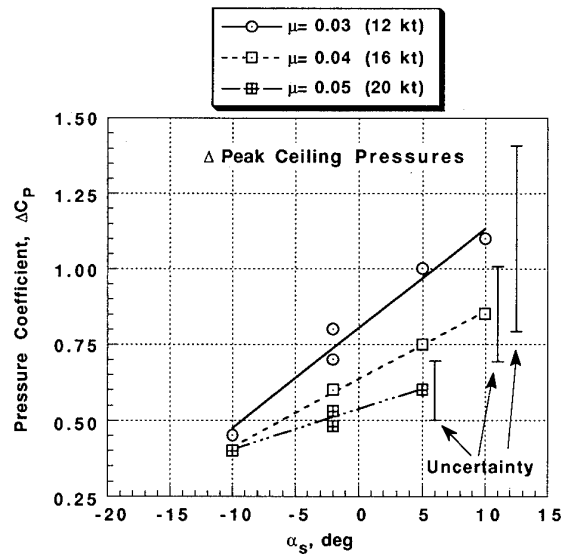
Fig. 20 Effect of rotor shaft angle-of-attack on tunnel ceiling peak wall pressures; $C_T/\sigma=0.100$, $\mu= 0.03$ (12 kt) to 0.05 (20 kt).
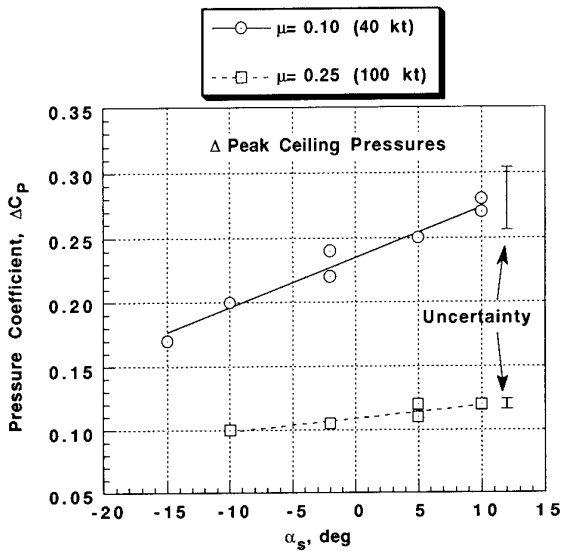
Fig. 21   Effect of rotor shaft angle-of-attack on tunnel ceiling
peak wall pressures; C_T/σ=0.100, μ= 0.10 (40 kt),
0.25 (100 kt).

Fig. 23   Effect of advance ratio on rotor 1/2 p-p thrust; α_S= -2
deg, C_T/σ=0.065, 0.080, 0.100.

Fig. 22   Effect of rotor shaft angle-of-attack on tunnel floor
pressures; C_T/σ=0.100, μ= 0.03 (12 kt).
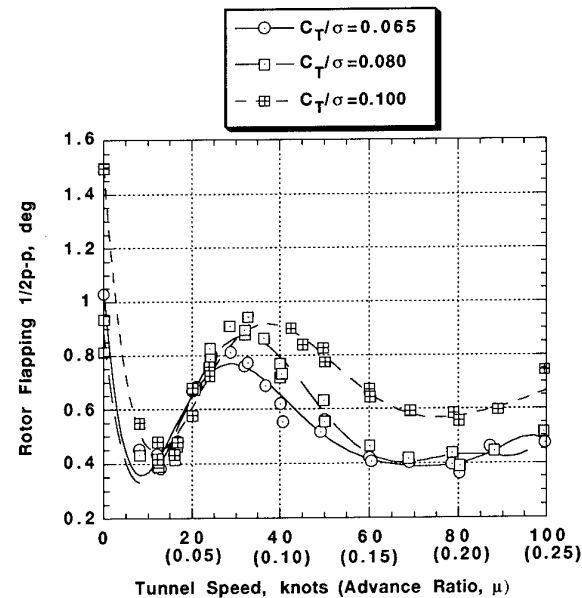
Fig. 24   Effect of advance ratio on rotor 1/2 p-p blade flapping;
α_S= -2 deg, C_T/σ=0.065, 0.080, 0.100.

TRANSONIC WIND TUNNEL BOUNDARY INTERFERENCE CORRECTION

M.L. Rueger, R.C. Crites, R.F. Weirich, F. Creasman, R.K. Agarwal, J.E. Deese
McDonnell Douglas Aerospace
McDonnell Douglas Corporation
P.O. Box 516
St. Louis, Missouri 63166
USA

Export Authority # 22 CFR 125.4(b)(13)

1. SUMMARY

A continuous effort in the area of transonic boundary interference correction has been underway at McDonnell Douglas Aerospace for over 6 years. A method of interference correction based on force and moment increments computed from CFD solutions was proposed in 1986. An extensive validation database has been acquired of transonic wind tunnel data for a set of geometrically similar models of different sizes. An empirical model of the flow at a porous transonic wind tunnel wall has been used in conjunction with panel codes and Euler solvers to yield corrections at a variety of conditions in both the MDA Polysonic Wind Tunnel (PSWT) and the MDA Trisonic Wind Tunnel (TWT).

LIST OF SYMBOLS

α = Angle of Attack
C_L = Lift Coefficient
C_D = Drag Coefficient
C_{Do} = Drag Coefficient at $C_L = 0$
C_M = Pitching Moment Coefficient
$\Delta\alpha$ = Angle-of-Attack Correction Increment
ΔC_L = Lift Correction Increment
ΔC_D = Induced Drag Correction Increment
ΔC_M = Pitching Moment Correction Increment
C_P = Pressure Coefficient $\dfrac{(P-P_\infty)}{q_\infty}$

P = Static Pressure
P_∞ = Free-stream Static Pressure
q_∞ = Free-stream Dynamic Pressure
C_{PW} = Wall Pressure Coefficient $\dfrac{(P_e-P_p)}{q_\infty}$

P_e = Static Pressure on the Wind Tunnel Wall
P_p = Plenum Pressure
C_d = Plate Discharge Coefficient
η = Wall Porosity Factor
d = Porosity Hole Diameter

L = Wall or Plate Thickness
δ^* = Boundary Layer Displacement Thickness
θ = Porosity Hole Inclination Angle
V_W = Dimensionless Mass Flux through the Wall
V_N = Equivalent Normal Velocity on the Inviscid Wall Boundary
X = Distance in Flow Direction
k_1 = Angle-of-Attack Interference Factor
k_2 = Induced Drag Interference Factor
k_3 = Pitching Moment Interference Factor

2. INTRODUCTION

Aircraft development programs continue to encounter discrepancies in transonic wind tunnel data acquired from different facilities. As a result, redundant testing in large expensive facilities is required. The ability to obtain high quality data from smaller less expensive facilities could have a significant impact in reducing the cost and cycle time of aircraft development programs. This is only possible through the proper correction of wall and support interference effects.

Conventional approaches to interference correction attempt to determine an equivalent angle-of-attack and Mach number for the observed force and moment coefficients. In a situation where interference effects are large, gradients over the model result in a change in force and moment coefficients such that no equivalent angle-of-attack and Mach number exists. Such conditions are typically termed "uncorrectable". In 1986 MDA initiated the development of a correction procedure based on computational fluid dynamics to correct wind tunnel data in the presence of such gradients[1].

3. OVERVIEW OF APPROACH

The procedure is designed to correct wind tunnel data for the effects of boundary interference. Boundary interference is here defined as consisting of the

following:

Wall Interference - The presence of the wind tunnel walls distorts the flow field. In a transonic porous wall wind tunnel, a classical "Method of images" approach is inadequate to describe this distortion.

Support Interference - The presence of the model support system can cause a distortion of the flow field from the desired condition. In a situation where the support system is close coupled, it may be impossible to account for this effect independently of the wall effects.

Tunnel Calibration Effects - A transonic tunnel is typically calibrated through the use of a "static pipe" placed along the centerline of the tunnel. The flow field generated with a model in place, may be distorted from this calibrated condition enough that the tunnel control system induces errors in an attempt to compensate. An example would be buoyancy effects induced by increased mass-flow through the tunnel walls at higher blockage conditions. Once again such effects are intimately tied to the wall interference and separate accounting may not be possible.

The MDA interference correction procedure is based upon computational simulation of the model in the wind tunnel, which when compared to a simulation in free-air, results in increments in forces and moments that may be applied as a correction directly to the wind tunnel data. This process is shown schematically in Figure 1. The incremental nature of the correction means that inaccuracies in the absolute levels of the forces in the computational model tend to cancel. In order to implement this boundary interference correction scheme, a three part wind tunnel test plan was devised:

Force and Moment Validation - A set of wind tunnel data, preferably from more than one facility in which the interference effects can be discerned, was essential to evaluating the success of the correction procedure.

Wall Pressure Measurements - In order to properly simulate the walls and evaluate the quality of the CFD solutions, wall pressure measurements corresponding to the validation data were required.

Wall Cross-Flow Model - Obtaining a quality CFD solution for the model in the tunnel requires the proper boundary conditions at the wind tunnel wall. Because of the porous nature of the wind tunnel walls it is necessary to account for the mass-flow into and out of the plenum. This transpiration, coupled with the boundary layer development at the wall, leads to a complex condition that is difficult to model analytically. Since direct measurement of the flow angle at the wall is difficult, an empirical relationship between equivalent normal velocity at the wall and the pressure distribution on the wall was required. A set of test data was needed to allow a generalized empirical relationship to be determined.
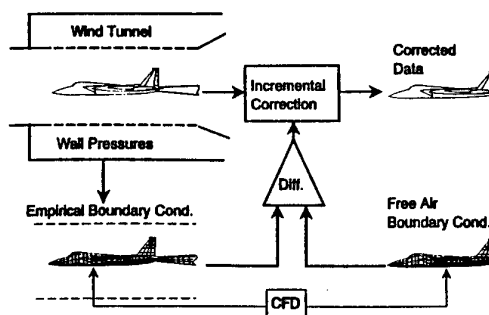
Figure 1.
Boundary Interference Correction Method

4. TESTING

4.1 Validation Data

Validation of the boundary interference correction approach required a database where boundary interference effects could be determined independently over the whole transonic Mach number range. A plan was set upon whereby geometrically similar models of different sizes would be tested in different facilities. The force and moment data from such tests should yield interference effects and a proper boundary interference correction scheme should be able to collapse these data.

Initial efforts (Ref. 1) used a set of models constructed with a conical nose, cylindrical body and biconvex delta wing configuration. The large base area of these models gave them excessive drag, making tunnel operation with the larger models difficult. Also, the large contribution of base pressure to the overall drag led to inaccuracies in the data and was difficult to model computationally.

A new set of models was constructed with a more aerodynamically clean configuration. A boat-tail was added to reduce drag, and base area was reduced to a value more typical of wind tunnel models. Four models were constructed, the dimensions of which are given in Figure 2.

Initially the models were tested in the MDA Polysonic Wind Tunnel (PSWT) and the MDA Trisonic Wind Tunnel (TWT). The PSWT is an intermittent "blow-down" facility with a 4 ft. by 4 ft. test section. Transonic testing takes place in a porous walled test section surrounded by an enclosed plenum. Mach number is controlled through active plenum pumping. The TWT is similar to the PSWT but has only a 1 ft. by 1 ft. test section. In the TWT Mach number is controlled by a turning vane at the downstream choke position.
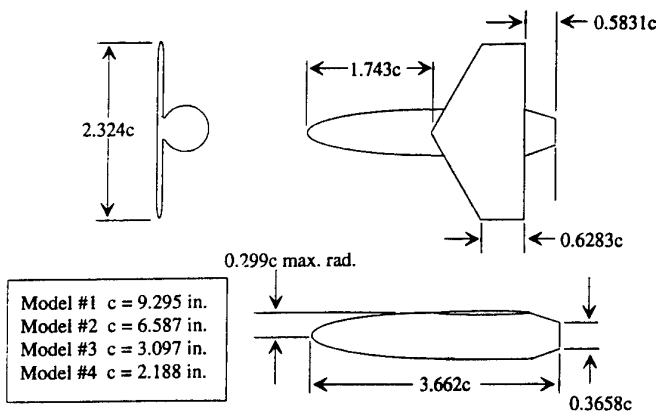
Figure 2.
Interference Model Dimensions

Model #1 c = 9.295 in.
Model #2 c = 6.587 in.
Model #3 c = 3.097 in.
Model #4 c = 2.188 in.

Figure 4.
PSWT Interference Effects at Mach 0.9

Over a period of two years these models were tested in varying combinations in three separate facilities. Figure 3. shows the wing area blockage of each model in the facilities where they were tested.

The models were tested at conditions typically ranging in Mach number from 0.6 to 1.2 and at several unit Reynolds numbers. Transition was fixed through the use of transition strips. Corrections have been applied to all the data presented here for flow angularity and protuberance drag from the transition strips. Angles-of-attack ranged from -4 to 10 degrees. Averaged data was taken to allow for wall pressure measurements. Typically data was acquired at two degree increments in angle-of-attack.

Typical results of the validation testing are shown in Figures 4 to 6. Comparisons are shown for model #1 in the NASA Ames 11 ft. tunnel was well as in the PSWT. The blockage of model #1 in the Ames tunnel is negligible so that the observed differences are presumed to be due to boundary interference effects in the PSWT. The reduced lift curve slope, increased induced drag, and de-stabilizing effect on pitching moment are typical of the results over the transonic range.

Figure 5.
PSWT Interference Effects at Mach 0.9

$$Blockage = \frac{Model\ Reference\ Area}{Tunnel\ Cross-Section}$$

	Model #1	Model #2	Model #3	Model #4
NASA Ames (11ft. x 11 ft.)	0.01108	-	-	-
MDA PSWT (4 ft. x 4 ft.)	0.08381	0.04191	0.009306	0.004651
MDA TWT (1ft. x 1 ft.)	-	-	0.1489	0.07442

Figure 3.
Interference Model Tests
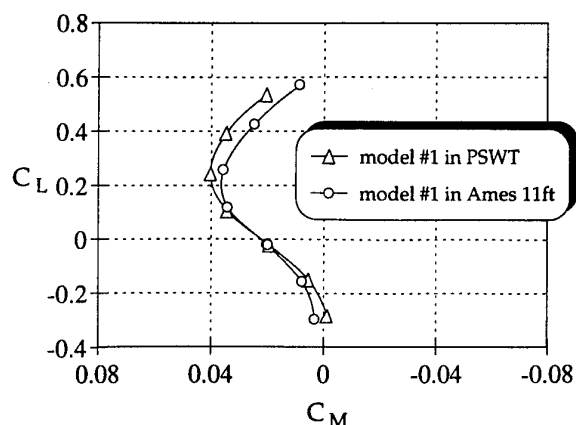
Figure 6.
PSWT Interference Effects at Mach 0.9

The examination of the large amount of validation data requires a more compact means of display than the plots shown in figures 4 through 6. If a suitable baseline exists, the data in question can be subtracted from it to yield increments as a function of lift. After examination of the validation data it was determined that the increments could be meaningfully expressed in equations of the following form:

(1) $\Delta \alpha = k_1 C_L$

(2) $\Delta C_D = k_2 C_L^2 + \dfrac{\Delta \alpha}{57.3} C_L$

(3) $\Delta C_M = k_3 C_L$

The constants in the equations (k_1, k_2, k_3) are termed interference factors and are determined through suitable curve fitting of the increments. These constants can then be plotted against Mach number to show the character of the interference effects over the transonic range.

The assumed linear relationship between the increments and lift (C_L^2 for ΔC_D) is indicated by the data. An angle-of-attack increment is used rather than ΔC_L to allow comparisons with more conventional correction procedures. Note that as long as $\Delta \alpha$ is computed from the difference in C_L there is no loss in generality. The equations above are used primarily for display of the indicated interference in the wind tunnel data and of the computed corrections. The interference correction process is not dependent upon these relationships and other formulations may be equally valid.

Figures 7 through 9 show the interference factors for both models #1 and #2 in the PSWT. All three plots show similar trends in that the interference effects steadily increase as Mach 1 is approached. The maximum value is reached at Mach 0.9 or 0.95 and the effects reduce rapidly as the flow becomes supersonic. Model #2 shows less interference than model #1. This is consistent in that the reference area and blockage of model #2 is half that of model #1.

Figures 10 through 24 show the same comparisons for models #3 and #4 in the TWT. The relative size of model #3 in the TWT is much larger than that of model #1 in the PSWT and the interference effects are correspondingly larger as well. Also, interference effects in the TWT are complicated by the close coupling of the vertical support structure to the model.
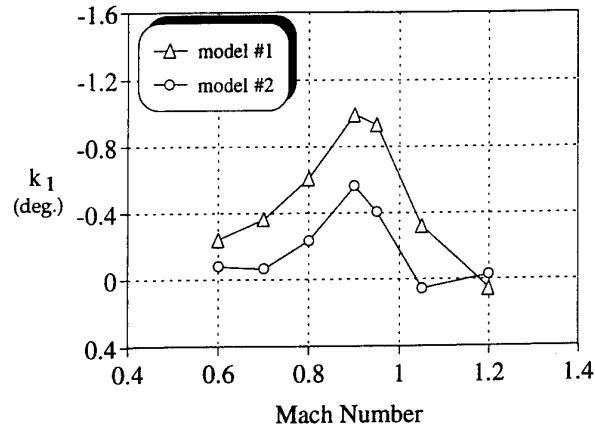
Figure 7.
Angle-of-Attack Interference Factor in the PSWT
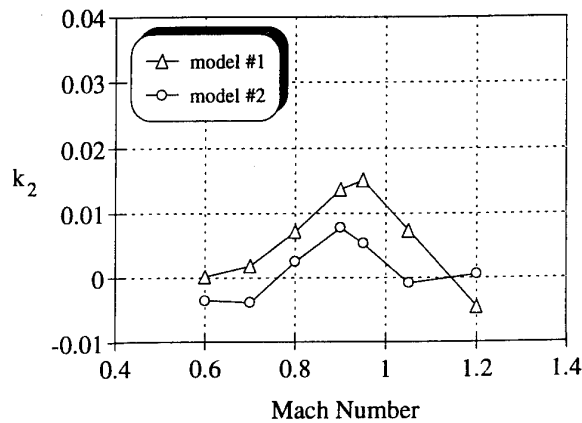
Figure 8.
Induced Drag Interference Factor in the PSWT
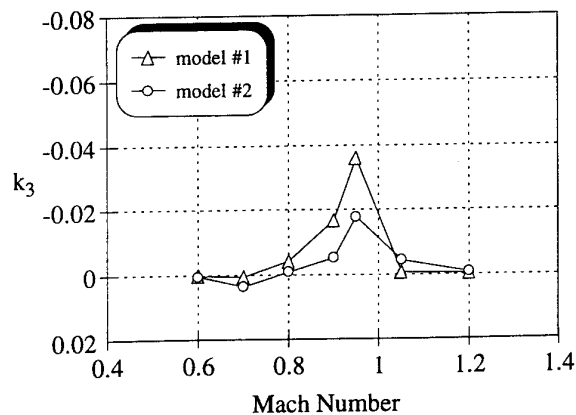
Figure 9.
Pitching Moment Interference Factor in the PSWT
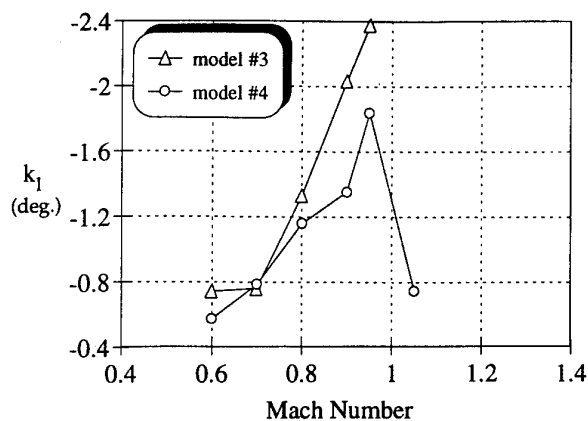
Figure 10.
Angle-of-Attack Interference Factors in the TWT
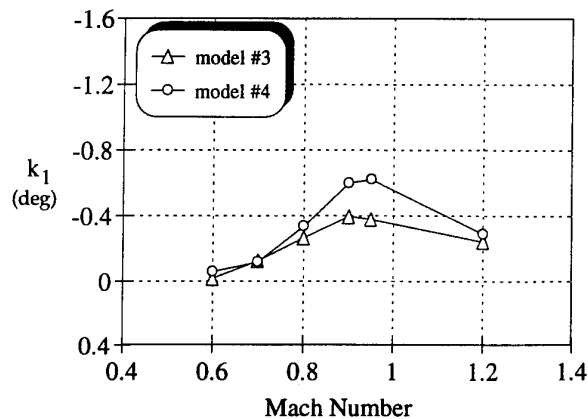
Figure 13.
Angle-of-Attack Interference Factors in the PSWT
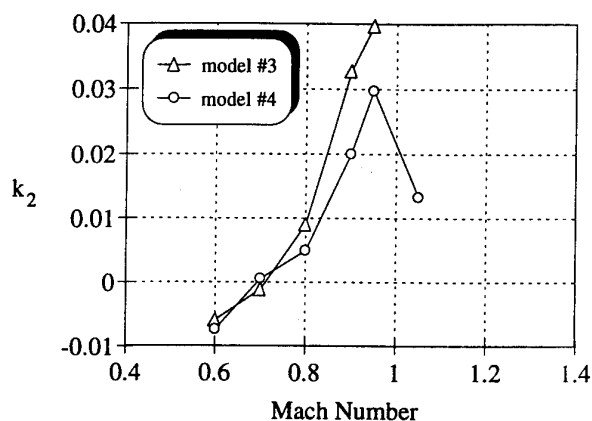
Figure 11.
Induced Drag Interference Factors in the TWT
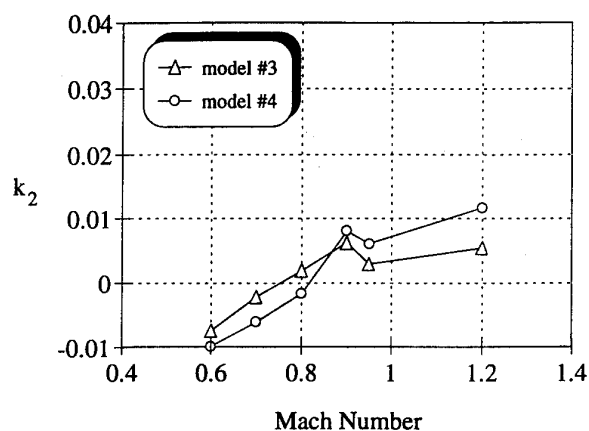
Figure 14.
Induced Drag Interference Factors in the PSWT
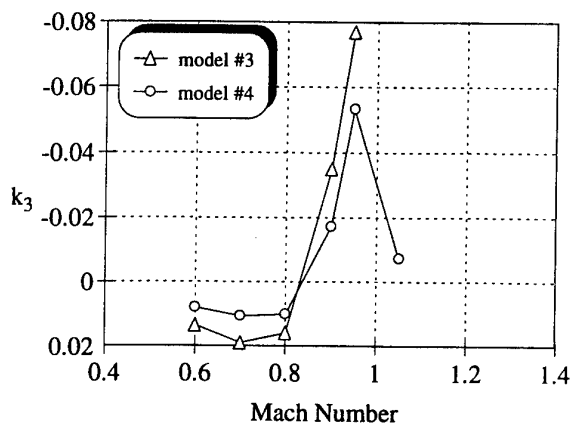
Figure 12.
Pitching Moment Interference Factors in the TWT
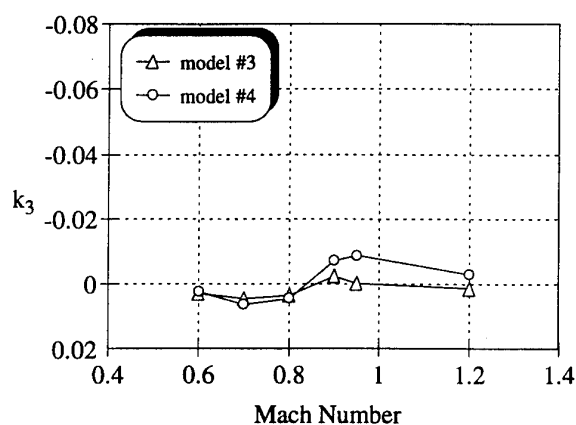
Figure 15.
Pitching Moment Interference Factors in the PSWT

As in the case of model #1 in the Ames facility, models #3 and #4 in the PSWT have negligible blockage and wall effects are presumably absent. The same can not be said of sting interference effects however. In fact, the relative size of the sting support is greater for models #3 and #4 than for model #1. The effects of this sting interference for models #3 and #4 can be seen in figures 13 through 15. Note that the significant interference effects observed are greater for the smaller of the two models because the relative size of the sting is larger.

4.2 Wall Pressures

Accurate wall pressure measurements were essential to evaluating the quality of initial CFD solutions and to establishing the wall boundary condition. Initial efforts to measure static pressures on the wind tunnel walls were hampered by several factors. The pressure excursion from free-stream at the walls is extremely small, typically on the order of .02 in pressure coefficient (C_p). A large number of highly accurate transducers were required. Also, the pressure measurement proved to be extremely noisy, presumably as a result of edge-tones from the porous wall. Because both the PSWT and TWT were "blow-down" facilities, long term averaging was not possible. Lastly, the measured pressure was extremely sensitive to tap orientation, quality of the tap orifice, and the location of the tap relative to the surrounding porosity holes.

Figure 16 is a schematic drawing of the wall pressure measurement system. The electronically scanned pressure measurement system (EPS) was referenced to a plenum tap to allow the use of low-range transducers for improved accuracy. The plenum reference was isolated from the tunnel during scanning through the use of a solenoid valve, and the reference pressure was measured independently. Because of the strong high frequency noise content of the pressure signal and limited sampling rate, digital filtering was subject to aliasing. Pneumatic filtering techniques were used to remove the high frequency components.

Although extensive efforts were made to reduce the tap sensitivity problem through minimizing orifice size and quality machining, relatively large tap sensitivity effects remained. Figure 17 shows a typical wall pressure distribution acquired during validation testing. A common approach to removing tap sensitivity effects from such data would be to make measurements with the tunnel empty, and subtract these from the measurements made with the wind tunnel model in place. There was concern however that in removing the empty tunnel distribution, some of the gradients that are to be accounted for in the correction procedure would be lost. As a result, a means of curve-fitting the empty tunnel

data based on a Fourier series approach that does not remove continuous gradients was devised. This procedure is outlined in more detail in a previous paper[2].

Wall pressure data was acquired for all the validation tests listed. The most extensive use of wall pressures was in the TWT where over 500 wall and plenum pressures were acquired and processed. Figure 18 shows the same pressure distribution as in figure 17 but with the tap sensitivities removed.
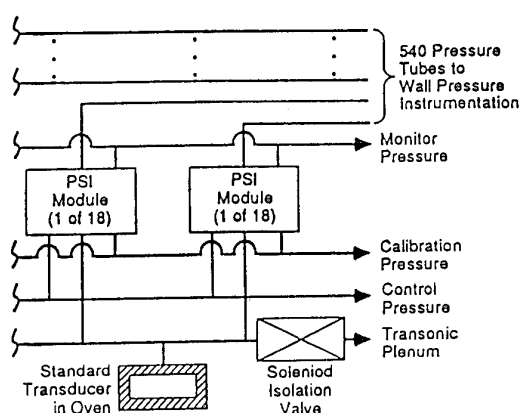
Figure 16.
Wall Pressure Measurement System
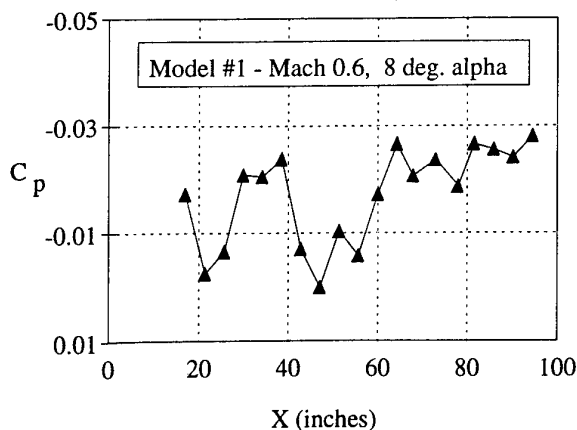
Figure 17.
Uncorrected Wall Pressure Measurements
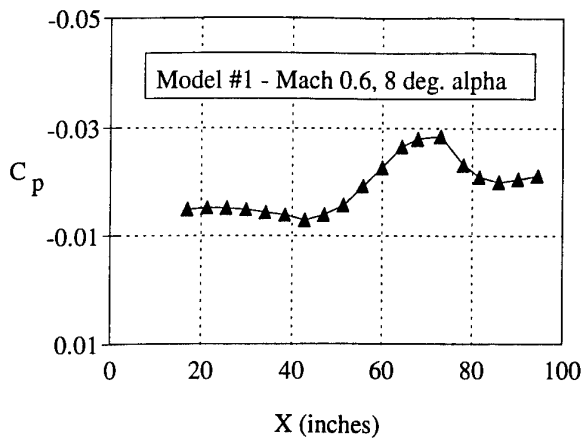
Figure 18.
Corrected Wall Pressure Measurements

normal velocity at the inviscid wall in the computation, to the transpiration velocity. These two relationships, used in conjunction with the continuity relationship from integral boundary layer theory, result in a system of algebraic and non-linear differential equations that can be solved numerically through the use of a Runge-Kutta scheme. These equations are summarized below:

For $V_W \geq 0$

$$(4) \quad \frac{V_W}{\eta C_d \cos^2(\theta)} = -1.557 \Delta C_P - 0.2242 \sqrt{\Delta C_P}$$

For $V_W \leq 0$

$$(5) \quad \frac{V_W}{\eta C_d \sqrt{\frac{L}{d} \cos^2(\theta)}} = -2.047 \Delta C_P - 0.0304 \sqrt{\Delta C_P}$$

$$(6) \quad \Delta C_P = \dot{C}_P - \dot{C}_P|_{V_W = 0}$$

$$(7) \quad \dot{C}_P = C_{P_W} \sqrt{\frac{\delta^*}{d}}$$

$$(8) \quad V_N = 0.0045 + 2.26 V_W + 49.4 V_W^2 + 120 V_W^3$$

$$(9) \quad \frac{d\delta^*}{dX} = V_N - V_W + \frac{\delta^*}{2} \frac{dC_P}{dX}$$

These equations allow an equivalent normal velocity to be computed based on a wall pressure distribution and initial boundary layer displacement thickness. Conversely, if the normal velocity is known, the pressure distribution can be computed. Both these methods have been used in the computational process.

4.3 Wall Cross-Flow

An accurate means of implementing the proper wall boundary condition is critical to the success of the computational simulation. An empirical relationship based on experiment results seemed to be the only way to achieve this.

An experiment was designed whereby a section of the plenum was isolated in a chamber. Mass-flow into and out of this chamber was precisely measured through the use of a set of calibrated venturis. The chamber was mounted such that the face was flush with the surrounding wind tunnel wall. A set of face plates was made so that several different porosity patterns and wall thicknesses could be examined. Provision was made for injection and suction through a portion of the wall ahead of the plate to allow the boundary layer thickness to be varied. Pressures were measured in the chamber and on the face of the plates. Boundary layer rakes were installed to measure the boundary layer development across the plate as a function of tunnel free-stream conditions and mass-flow through the plate. Figure 19 shows a schematic of the test set-up.

Results of the test indicated that a $\sqrt{P}$ type of relationship held for all the plates with the tunnel off. With the tunnel on however, the relationship between pressure change across the plate and mass-flow through the plate was completely different. Information about each plate is given in figure 20 and some typical results are shown in figure 21.

An empirical relationship was derived that collapses the data from these plates[3] (Fig. 22). In addition, a single variable function was determined relating the equivalent

Figure 19.
Wall Flow Test Set-up
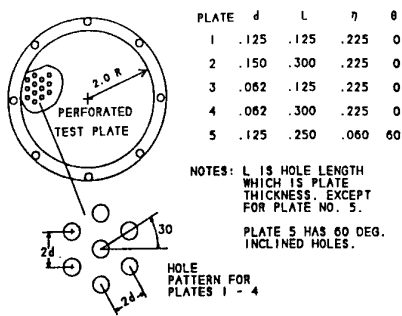
Figure 20.
Wall-Flow Test Plates

PLATE	d	L	η	θ
1	.125	.125	.225	0
2	.150	.300	.225	0
3	.062	.125	.225	0
4	.062	.300	.225	0
5	.125	.250	.060	60

NOTES: L IS HOLE LENGTH WHICH IS PLATE THICKNESS. EXCEPT FOR PLATE NO. 5.

PLATE 5 HAS 60 DEG. INCLINED HOLES.
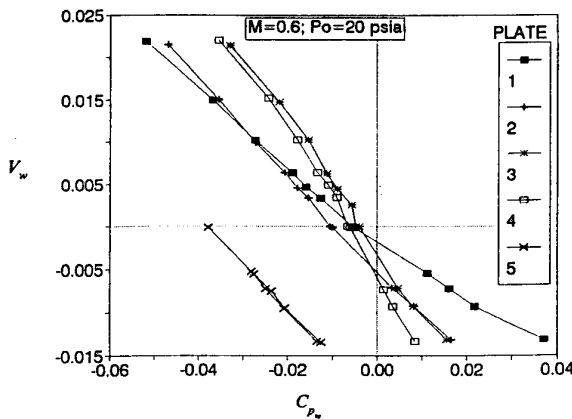
Figure 21.
Wall Flow Test Results
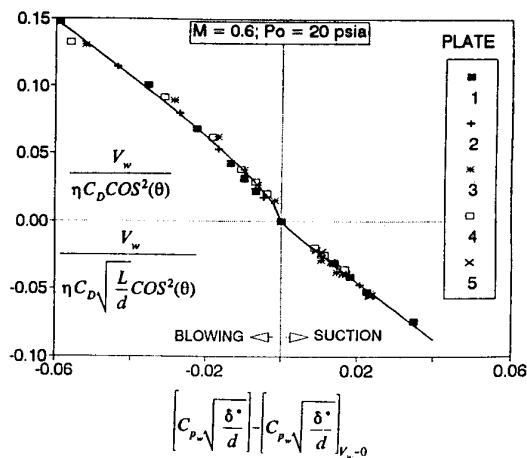
Figure 22.
Wall Flow Test Results

5. CFD RESULTS

5.1 TWT

In order to allow CFD solutions to be obtained in a minimum time period and at a minimum cost, Work concentrated on finding the least complex flow-solver applicable to the flow field conditions and our needs. Initial work at Mach 0.6 began with panel codes. These required only a surface grid and solution times are an order of magnitude less than for typical Euler solutions. At higher Mach numbers where shock waves are present, Euler solutions were required.

Initial efforts in computing corrections were made in the TWT. The observed interference effects were much larger than for the PSWT data and a more extensive set of wall pressure data had been acquired.

The panel code chosen for this work was a developed at MDA. DACVINE is a higher order panel code that uses an iterative solver[4]. It was selected primarily because it was capable of handling the large number of panels required to properly simulate the wind tunnel, wind tunnel model, and support structure.

A grid consisting of approximately 850 panels was constructed for the interference model configuration. The support sting was modelled for the in-tunnel solutions and a conical body wake was used in place of the sting for free-air solutions. The vertical support structure was not modelled. A typical panel distribution is shown in figure 23. The modelling of the wind tunnel walls added another 1200 panels to the simulation. Figures 24 through 26 show a comparison of DACVINE free-flight results with wind tunnel data.
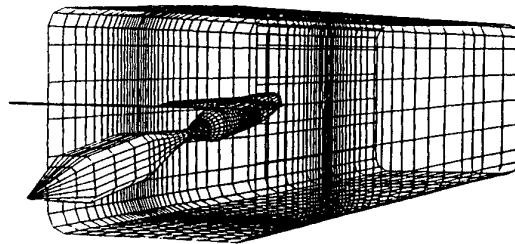
Figure 23.
Typical Panel Distribution - Model #3 at 8 deg.
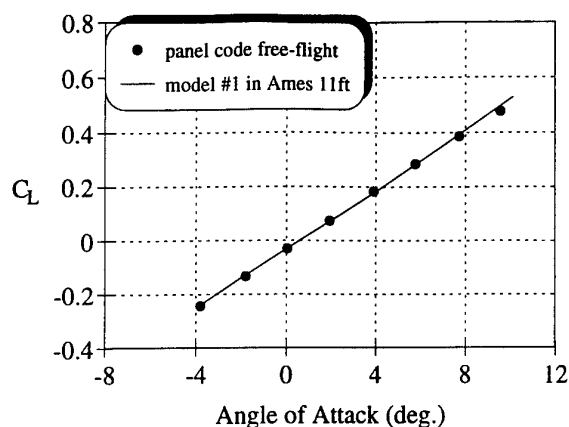
Figure 24.
Free-Flight Panel Code Results - Mach 0.6
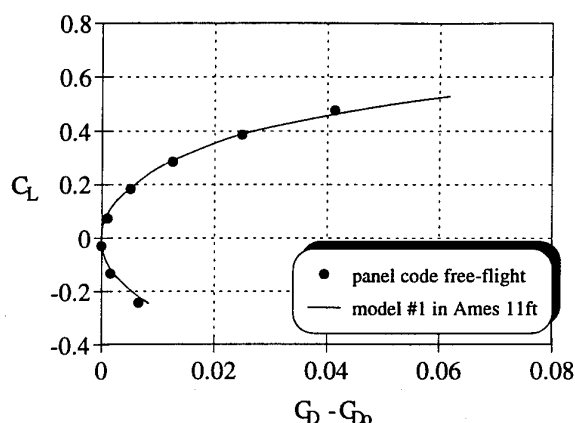
Figure 25.
Free-Flight Panel Code Results - Mach 0.6
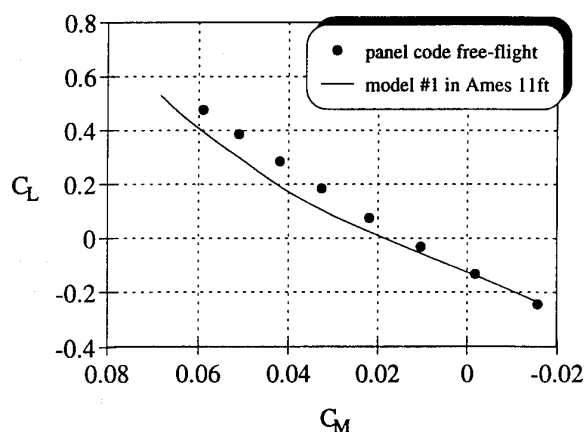
Figure 26.
Free-Flight Panel Code Results - Mach 0.6

Initial application of the wall-flow model was straight forward. After the wall pressures had been processed according to the methods referred to in section 5, they were input into the wall-flow model. The resulting normal velocity distribution was then used as a boundary condition in the panel code on the wind tunnel walls.

Investigations indicated that some adjustment of the pressure levels going into the wall-flow model was required in order to obtain reasonable results, After determining this "offset" in C_p through trial and error, agreement of the wall pressures from the panel code with the measurements was quite good (figure 27). In order to develop the correction both free-air and in-tunnel solutions were computed at 0 and 4 degrees angle-of-attack. Corrections were made at higher angles for some cases to confirm the linear nature of the computed corrections.

Results of the panel code based corrections for the TWT were moderately successful. Excellent agreement in terms of the angle correction were achieved for both model #3 and model #4 at Mach 0.6 (figure 28). The pitching moment correction also matched the wind tunnel data reasonably well. The drag correction was unsatisfactory however (figures 29 through 30).

The use of a normal velocity boundary condition with the panel code had shown an extreme sensitivity to small offsets in C_p. After discussions with Jacocks at AEDC and others, it was determined that pressure might be used as a boundary condition directly as long as the regions where flow moved from the plenum into the test section were small. Because an extensive set of wall pressure measurements were available from the TWT, corrections were made by using the measured pressure directly as a boundary condition.

The Euler code used for simulation of the TWT was developed at MDA. It is a single zone finite volume Euler solver[5]. Euler solutions were computed at both Mach 0.6 and 0.9 for model #3. Results were similar to those encountered with the panel code. The angle-of-attack correction was in good agreement with the wind tunnel data at both Mach 0.6 and 0.9. The drag correction exhibited the right trend with Mach number but value at the low Mach number was still incorrect. This was also true of the pitching moment correction. Interference factors for both the panel code and Euler based corrections are compared to wind tunnel data in figures 28 through 30. The effect of the Euler based corrections at Mach 0.9 are shown in figures 31 through 33.

The vertical strut support was not modelled in the TWT simulations for the panel code or the Euler code. Subsequent free-air investigations with the panel code at Mach 0.6 indicated that the strut created an interference effect comparable in magnitude to that of the walls. Because the presence of the strut undoubtedly effects the wall pressures, forcing agreement with the wall pressures without the strut would introduce an error. It was felt that this might be one possible explanation for the poor drag correction in light of the excellent results for the angle-of-attack correction.
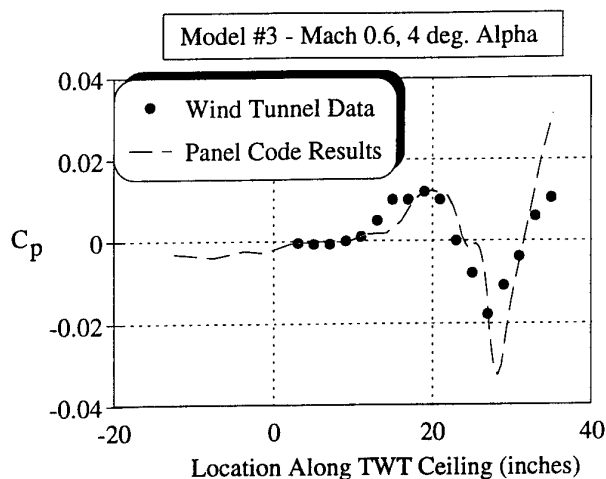
Figure 27.
Wall Pressure Distribution on TWT Ceiling - Centerline
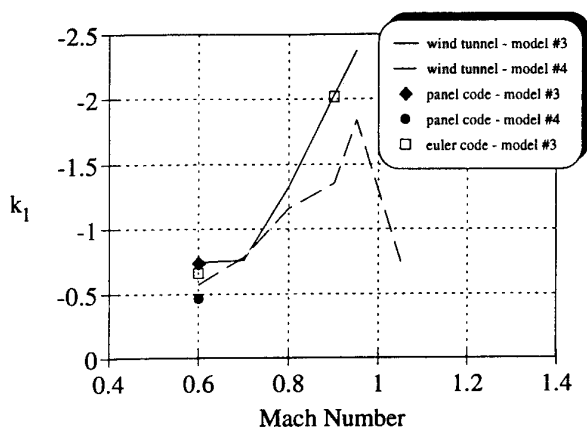
Figure 28.
Angle-of-Attack Interference Factor in the TWT
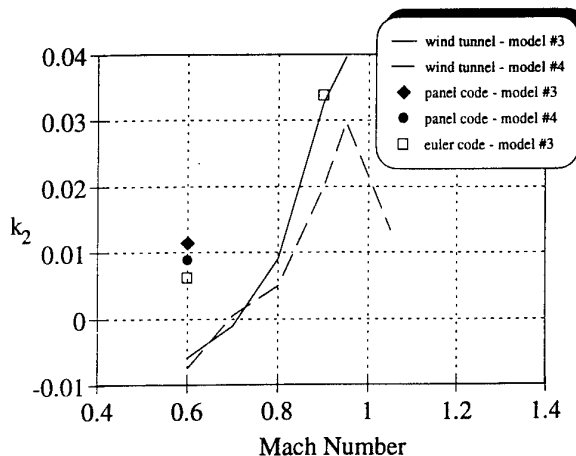
Figure 29.
Induced Drag Interference Factor in the TWT
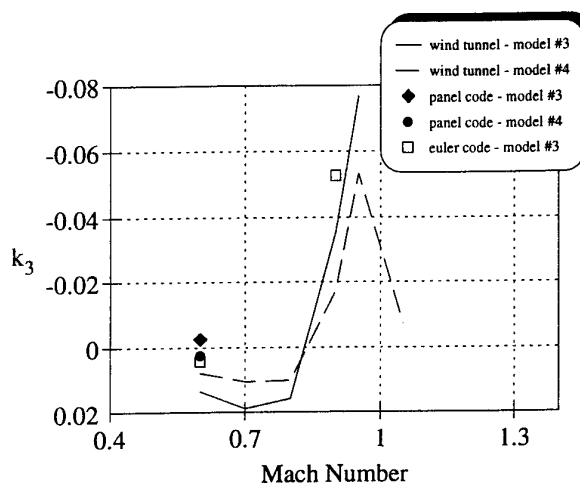
Figure 30.
Pitching Moment Interference Factor in the TWT
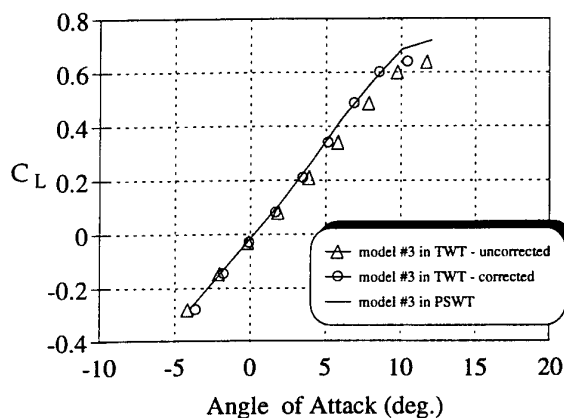
Figure 31.
Euler based Correction of TWT Data
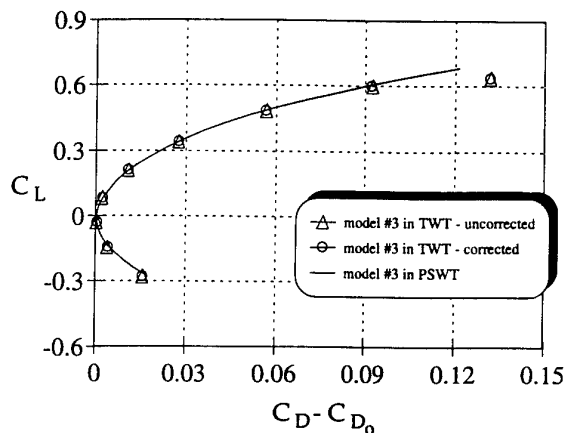
Figure 32.
Euler based Correction of TWT Data
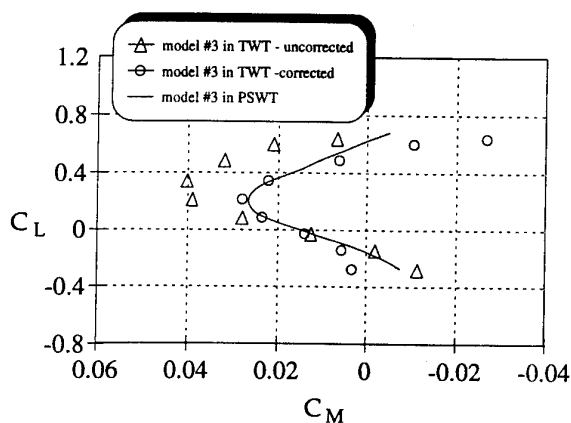
Figure 33.
Euler based Correction of TWT Data

5.2 PSWT

Initial testing in the PSWT involved over 500 wall pressures. The acquisition and reduction of so much wall pressure data was not practical for production testing however. An effort was made to greatly reduce the number of wall pressure measurements required for corrections.

Since pressure measurements were less extensive in the PSWT, solutions based solely on measured pressures would be less accurate. Also, since the conditions modelled in the simulation are invariably different in some way from the actual conditions in the tunnel (e.g. the missing strut in the TWT simulation), a simulation based on measured wall pressures alone would to some degree be in error. If the empirical wall flow model is used, a simulation containing interference effects specific to the geometry being simulated can be obtained and the reliance on wall pressure reduced.

The application of the wall-flow model is an iterative process outlined in figure 34. Rather than computing normal velocities, the model is used in reverse to compute pressures from velocities. This proved to be a more stable means of iteration. Typically the initial pressure distribution is determined by interpolation from approximately 40 measurements.
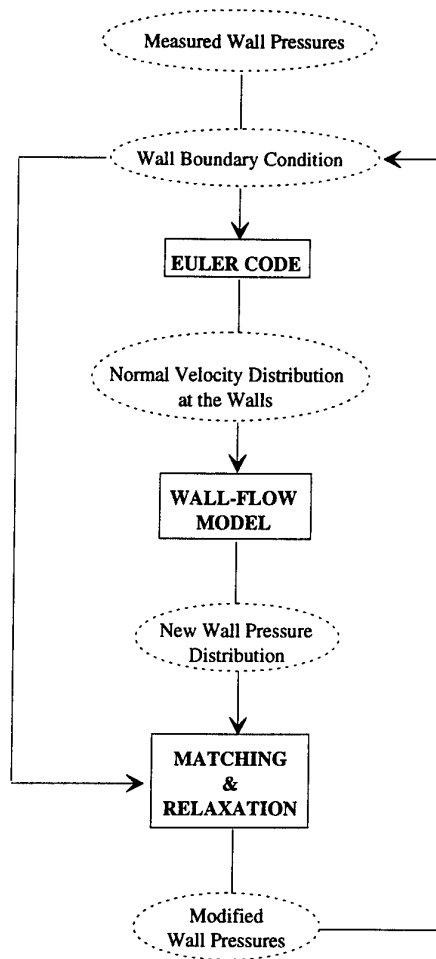
Figure 34.
Euler Code / Wall-Flow Model Iteration Procedure

The Euler code used for simulation of the PSWT is a multi-block code that was specifically modified to accept pressure as a boundary condition and to output normal velocities at the wall boundary[6,7].

As interference correction efforts for the PSWT got underway, some additional validation data became available. Data from a large transonic tunnel was obtained on a 5% scale model of a modern fighter configuration. The blockage of the model was minimal

so this provided a baseline for comparison. Corresponding PSWT data was available on the same configuration (with wall pressure measurements).

Corrections using the approach outlined above were computed at two Mach numbers. In figure 35 an iteration history of lift is shown in which the wall flow model iterations can be discerned. Three or four applications of the wall flow model and subsequent iteration of the Euler code were required to reach convergence. Note the difference in lift between the final converged value and the value at the initial application of the wall flow model.
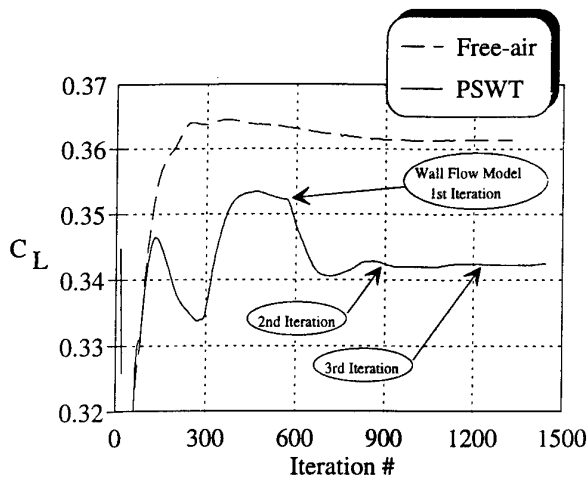
Figure 35.
Lift Iteration History

Both panel code and Euler code solutions were obtained at Mach 0.6 and an Euler based correction was obtained at Mach 0.85 as well. The corrections were much more successful than those made for the TWT. These results are shown in figures 36 through 38. The panel code still has problems with the induced drag correction. One possible explanation for this is the lack of wake iteration in the panel code solutions. efforts are being made to improve the panel code results. There is also a problem with under prediction of the pitching moment correction at the higher Mach number condition. This is thought to be due to some over simplifications made in the empennage grid and is being addressed as well.

Figure 39 through 41 show the actual increments between the baseline and PSWT plotted as a function of angle-of-attack. The linear nature of the angle and pitching moment corrections can be clearly discerned as well as the quadratic nature of the induced drag interference. Note that the interference effects have been virtually eliminated for angle-of-attack and drag once the CFD based corrections are applied.
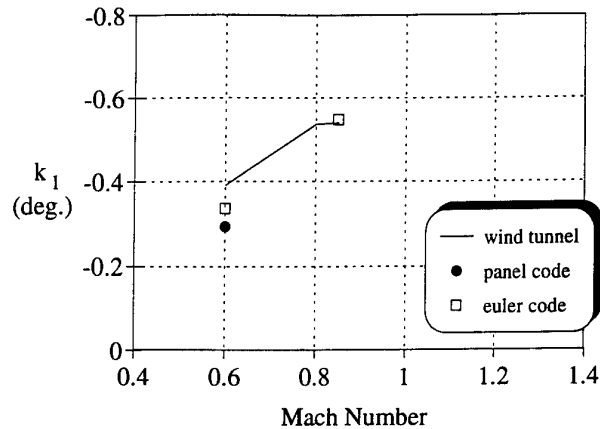
Figure 36.
Angle-of-Attack Interference Factor in the PSWT
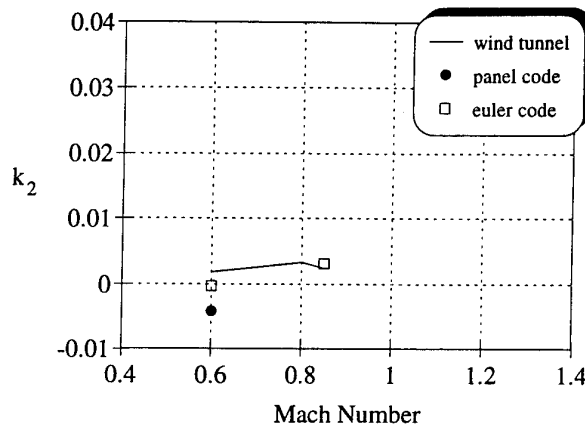
Figure 37.
Induced Drag Interference Factor in the PSWT
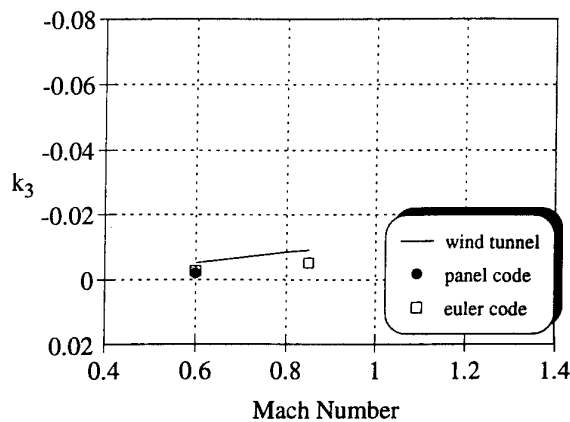
Figure 38.
Pitching Moment Correction Factor in the PSWT
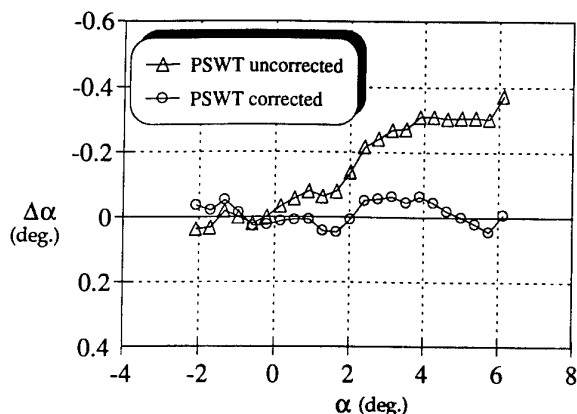
Figure 39.
Euler based Correction of Modern Fighter Data
Mach 0.85
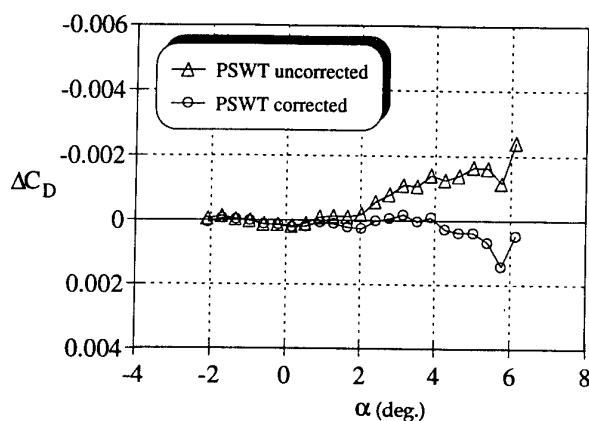
Figure 40.
Euler based Correction of Modern Fighter Data
Mach 0.85
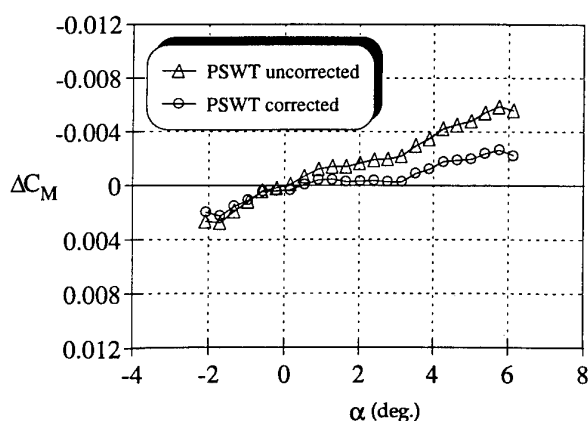
Figure 41.
Euler based Correction of Modern Fighter Data
Mach 0.85

6. CONCLUSIONS

A strong effort in the area of transonic boundary interference correction has been underway at MDA for over 6 years. Significant advances have taken place in three main areas:

Validation Database - A set of models has been constructed which allow the interference effects in small transonic wind tunnels to be determined experimentally. An extensive set of wind tunnel data has been acquired over the full transonic range in several wind tunnels. This provides a database suitable for validation of a boundary interference correction procedure.

Wind Tunnel Simulation - Through extensive testing a generalized empirical model of the flow at a porous transonic wind tunnel wall has been developed. This wall flow model has been used successfully with both panel codes and Euler solvers. At first moderately successful corrections were generated through reliance on extensive wall pressure measurements. The method has been improved to the point where accurate corrections have been generated using limited measurements as starting conditions.

Application of Corrections - Corrections have been generated over a wide range of Mach numbers. It is probable that near Mach 1 and at angles-of-attack near C_{Lmax}, viscous solutions would be required. The available wind tunnel data, and the success of the current corrections indicate that for performance testing, Euler codes can provide accurate boundary interference corrections. The application of Euler code generated corrections to aircraft development programs has already taken place for the PSWT.

It should be possible to generate useful corrections for configurations for which no wind tunnel data exists. Currently, the method relies on wall pressure measurements only for starting conditions. Our latest results indicate that corrections can be computed by starting with a uniform wall pressure. By examining the effects of such parameters as blockage, wing span, and tail length on interference corrections a database of interference effects can be developed so that corrections can be applied during production testing without reliance on extensive CFD solutions.

7. REFERENCES

1. Crites,R.C., "Transonic Wind Tunnel Boundary Interference - A Correction Procedure," AGARD CP-429, Sept. 1987, pp. 15-1 through 15-16.

2. Rueger, M.L., and Crites, R.C., "Wind Tunnel Boundary Interference Prediction and Correction," AIAA 92-0036

3. Crites, R.C., and Rueger, M.L., "Modelling the Ventilated Wind Tunnel Wall," AIAA 92-0035

4. Hess, J.L., Friedman, D.M., Clark, R.W., "Calculation of Compressible Flow about Three-Dimensional Inlets with Auxiliary Inlets, Slats, and Vanes by Means of a Panel Method," NASA CR-174975, June 1985

5. Deese, J.E., Johnson, J.G., Agarwal, R.K., and Soni, B.K., "Simulation of Wind Tunnel Flow Fields," AIAA 92-0034

6. Jameson, A., and Baker, T.J., "Solution of the Euler Equations for Complex Configurations," AIAA Paper No. 83-1929, July 1983

7. Creasman, S.F., Agrawal, S., and Lowrie, R.B., "Development and Engineering Applications of a Multizone Euler Solver," 4th International Symposium on Computational Fluid Dynamics Proceedings, Vol. 2, Davis, CA, September 1991, pp. 735-740.

UNSTEADY FLOW TESTING IN A PASSIVE LOW-CORRECTION WIND TUNNEL

L. Kong

G.V. Parkinson

Department of Mechanical Engineering

The University of British Columbia

Vancouver, BC V6T 1Z4 CANADA

SUMMARY

A passive low-correction wind tunnel designed for two-dimensional testing has a test section consisting of transverse airfoil-slatted side walls separating it from outer plenum chambers. The uniform spacing of the airfoil slats determines the open-area ratio (OAR). The tests described were on two sizes of NACA0015 airfoil in plunging oscillation, and instantaneous pressure distributions were measured for different values of airfoil reduced amplitude and frequency, and over a full range of tunnel OAR. It was found that, despite the relatively large sizes of test airfoil, values of pressure, lift, and moment coefficient close to theoretical free-air values were obtained for $0.6 < OAR < 0.8$, whereas values were much too high in the presence of solid walls and much too low in open-jet testing. Test Reynolds numbers were in the range $(2.5\text{-}8.0)10^5$.

1. INTRODUCTION

Some years ago the second author and a graduate student presented, at an AGARD Symposium on Wind Tunnel Design, a paper (Ref. 1) on a passive low-correction wind tunnel test section designed for two-dimensional low speed airfoil testing. The low-correction capability was achieved by replacing the solid test section wall opposite the suction side of the test airfoil by a uniformly spaced row of airfoil slats at zero incidence so that the tunnel air flow could pass between the slats into and out of a plenum on the other side. The airfoil slats operate within their unstalled range of angle of attack, and potential flow modelling can be used to obtain a preliminary estimate of the best open area ratio (OAR), defined by

$$OAR = \frac{g}{c + g}$$

where c is the slat chord and g the gap between slats. It was predicted and confirmed experimentally that OAR in the 60-70% range would produce test airfoil pressure distributions and lift coefficients requiring very little correction (typically less than 1%) for a wide range of test airfoil sizes, profiles and angles of attack, including values beyond the stall.

Other versions of the concept have been developed in recent years, including one for two-dimensional bluff body testing (Fig. 1 and Ref. 2), and one for wind engineering testing of buildings and road vehicles (Ref. 3). Among flow phenomena examined by Hameury in the 2D bluff body testing was wake Strouhal number S (Ref. 4) and it was found again that for a certain OAR correction-free data could be obtained even for very high blockage ratios (bluff body transverse dimension ÷ test section width). These results are shown in Fig. 2 for three sizes of normal flat plate, and in Fig. 3 for four sizes of circular cylinder. The results are quite remarkable. The values of S, the dimensionless wake vortex shedding frequency, are seen to be much too large in the presence of solid test section walls ($OAR=0$), with the effect increasing with blockage ratio to as much as 87% for the normal plate and 26% for the circular cylinder at 33.3% blockage, while the values in the open jet tests ($OAR=1$) are correspondingly seen to be much too low.

However, in the flat plate tests at $OAR=0.67$ two of the three plates give $S=0.142$, the generally accepted free-air value, and the third, with 33.3% blockage, gives $S=0.147$, only 3.5% high, and even this lack of agreement is apparently a consequence of the extreme blockage of the largest normal plate having caused some of the airfoil slats to stall. Further, in the circular cylinder tests the values of S for three of the four cylinders converge at $OAR=0.56$ to $S=0.185$, within the range of accepted free-air values at the test Reynolds number, while the fourth cylinder gives $S=0.189$, only 2% high. These results suggested that this passive form of test section could be used to produce low-correction data in more general unsteady flow testing, and so led to the present investigation.

2. THE WIND TUNNEL

The basis of the concept of airfoil-slatted test section walls was to make use of the compensating corrections inherent in partly solid, partly open boundaries while

avoiding the separated jet flows occurring with the widely used longitudinally slotted walls. Since the airfoil slats operate within their unstalled range of angle of attack there are no separated wakes or empirical base pressure coefficients in the flow through the slatted boundaries. This feature makes the flow less sensitive to the details of the test model, so that it is possible to find an OAR that will lead to low-correction data for a considerable range of sizes and shapes of test models of the same class. The original version of the airfoil-slatted test section used only one slatted wall, facing the suction side of the test airfoil because of its greater importance. However, for the oscillating airfoil of the present tests both surfaces are equally important, so the symmetrical version of Fig. 1, designed for 2D bluff body testing, was used.

The test section is a two-dimensional insert in an existing low-speed closed circuit tunnel. The insert is 915 mm wide by 388 mm deep in cross-section, and 2.59 m long. Test airfoils are mounted vertically at the middle of the test section. The two slatted side wall mountings have external plenums 300 mm wide by 388 mm deep, and 2.44 m long. The airfoil slats are of NACA0015 section at zero incidence and have 89 mm chord. They are uniformly spaced, and by changing the number of slats the full range of OAR can be tested. The test section velocity is spatially uniform within 0.3% outside the floor and ceiling boundary layers, whose displacement thickness is of the order of 8 mm at the location of the test airfoils. The freestream turbulence intensity is less than 0.1%.

3. THE EXPERIMENTS

It was decided to test the capability of the airfoil-slatted test section to deal with boundary corrections to the pressure loading on an oscillating body under closely two-dimensional conditions. The NACA0015 airfoil at zero incidence in low-amplitude plunging oscillation was selected as the test model. The unseparated flow would presumably produce loadings close to the predictions of potential flow, and the experimental results could be compared with the free-air values from the familiar thin-airfoil theory of Karman and Sears (Ref. 5). Two models were used, one of chord C=305 mm and the other of C=610 mm, so that the boundary interference parameters C/H where H is the test-section width were 0.333 and 0.667 respectively. Both models were instrumented with surface pressure taps in the center plane. In the tests these taps were connected by plastic tubing to a Scanivalve and Barocel transducer, whose output was corrected, using calibration curves, for attenuation in the tubing. Airfoil displacement was measured with a linear transducer. The surface pressure at a particular tap and the airfoil displacement were measured and

recorded very nearly simultaneously at successive time increments, and the process was repeated for each pressure tap using the Scanivalve, so that complete pressure distributions as a function of time over the oscillation cycle were obtained for each test condition.

The test airfoil was mounted vertically on an oscillating table under the test section, with supporting struts from the table to the bottom and around the test section to the top of the model. The connecting struts moved through transverse slots in the test section floor and ceiling, which were at small clearances from the model. The oscillation mechanism was a simple slider-crank in which, because of the small airfoil amplitudes tested, the offset was very small in comparison to the connecting-rod length so that the airfoil oscillation was always satisfactorily close to sinusoidal. Airfoil oscillation amplitude η_o and circular frequency ω could be adjusted and free stream flow velocity U controlled so that in the tests reduced frequency

$$\mu = \frac{\omega C}{2U}$$

apparent angle of attack amplitude

$$\alpha_o = \frac{\omega \eta_o}{U}$$

and Reynolds number R were in the ranges

$$0.25 < \mu < 0.55, 0.2^o < \alpha_o < 2.2^o,$$

$$2.5(10)^5 < R < 8.0(10)^5.$$

4. RESULTS

The theory of Ref. 5 predicts that the phase angle ϕ by which the oscillatory free-air lift, treated as a rotating vector, leads or lags the quasi-steady lift is quite small over the range of μ covered in the present experiments (Fig. 4) and the experimental results indicated this to be true also for the confined flow. Therefore, the effects on phase are ignored and the effects on lift and moment amplitude only are considered. By varying μ and α_o for the two airfoil models 7 different oscillation conditions were tested over the full range of OAR, as recorded in Table 1. The values $\bar{\mu}$ and $\bar{\alpha}_o$ in Table 1 are averages for each oscillation condition, since it was difficult to set frequency ω to the same value for each of the tests at from 4 to 7 different OAR values.

From the oscillatory pressure traces for each tap time-averaged amplitudes were extracted and converted to coefficients C_P. From these the difference in loading distribution amplitudes between lower and upper surfaces $(C_{PL} - C_{PU})$ vs X/C was determined and integration gave lift and moment coefficient

amplitudes C_L and C_M. Fig. 5 gives a sample of plots of $(C_{PL} - C_{PU})$ vs X/C for several OAR values in one of the model test conditions. The curve from the linear theory of Ref. 5 is also shown for comparison. It can be seen that the experimental curves become progressively lower with increasing OAR, and that the curve for $OAR=0.526$ lies close to the theoretical curve. Also the experimental curve for the open jet case $(OAR=1.0)$ is far more irregular than the others indicating an appreciably lower flow quality for that test section configuration. Integration of the curves of Fig. 5 (plus 3 curves for other OAR values not shown on Fig. 5) gives the values of lift coefficient C_L and pitching moment coefficient C_{M_o} (with respect to mid-chord) plotted vs OAR in Figs. 6 and 7.

The figures show a monotonic decrease of C_L and C_{M_o} with increasing OAR, as would be expected in steady-flow applications of the airfoil-slatted test section from the results of Refs. 2 and 3, and in agreement with the unsteady-flow Strouhal number results of Figs. 2 and 3. As previously indicated by the results in Fig. 5, the experimental C_L for $OAR=0.526$ agrees closely with C_{L_f}, the theoretical free-air value in Fig. 6. However, Fig. 7 seems to show a large discrepancy for C_{M_o}. This is misleading because of the scale of the plot. C_P values, from which C_L and C_{M_o} are obtained, provide the true scale for comparisons and since C_L is given by direct integration of the C_P distributions its scale should be used for C_{M_o} also as is commonly done for airfoil data. In Fig. 7 the difference between the theoretical free-air value 0.0367 and the experimental value at $OAR=0.526$, 0.0245 is $\Delta C_M=-0.0122$ or only 8.3% of $C_{L_f}=0.147$, a reasonable result probably attributable to typical boundary-layer effects on pitching moment.

Figs. 5, 6, 7 all represent the same test conditions of C/H, μ, α_o and R. The other 6 combinations of parameters tested yielded similar results, and it is useful and convenient to present all the results in a collapsed form. To avoid congestion Figs. 8 and 9 present results from the 4 test series in which μ was near 0.5, and Figs. 10 and 11 give the corresponding results from the 3 series in which μ was near 0.3. Moment is presented with respect to the airfoil quarter-chord, $C_{M_{c/4}}$, as in conventional steady-flow practice and to emphasize the apparent-mass effect on the oscillatory loading, and both C_L and $C_{M_{c/4}}$ are given as fractions of C_{L_f}. In Figs. 8 and 10, lift and moment are plotted vs OAR to the same scale, and in Figs. 9 and 11, moment is plotted to an expanded scale to show more detail. The degree to which the lift and moment data in Figs. 8 and 10 collapsed to narrow bands, monotonically decreasing with increasing OAR for lift and increasing for moment, was surprising. Indeed, if all of the data had been

superimposed on one figure the lift and moment bands would not have been significantly wider, so that the method of collapse removed most of the effect of reduced frequency μ from the results. The effects of model size C/H and displacement amplitude η_o/C were qualitatively more or less as expected. At $OAR=0$ (solid walls) the larger airfoil at its highest amplitude gave the highest value of C_L/C_{L_f} and the small airfoil at its lowest amplitude gave the lowest C_L/C_{L_f}. On the other hand, at $OAR=1$ (open jet) the reverse was true. This is in accord with conventional boundary correction theory. However, the values of the required corrections are unexpectedly large, for lift of the larger airfoil as much as -70% for solid walls and +45% for open jet.

In the middle range of OAR the lift data all lie close to the theoretical free-air value at $C_L/C_{L_f} = 1$. More precisely, in the range $0.6 < OAR < 0.8$ the average value of C_L is 2.7% higher than C_{L_f}, and at $OAR=0.708$ the average value for the 7 test conditions is within 1% of C_{L_f}, although individual values range from 7% high to 9% low. The moment data of Figs. 8 and 10, plotted to the same scale as the lift data, fall within a very narrow band. Presented on an expanded scale in Figs. 9 and 11 it can be seen, despite some scatter in both figures, to increase with OAR from negative values of the order of -0.1 at $OAR=0$ to near zero values at $OAR=1$. The theoretical thin-airfoil free-air values are shown as shaded bands as a result of the dependence on μ, which varied slightly over the test range. In the mid-range of OAR the moment values are seen to be more nearly constant, and in general smaller than the theoretical values.

5. DISCUSSION

The data for the smaller airfoil was obtained by the first author as part of his master's research (Ref. 6). The results were obviously interesting and encouraging, but the unexpectedly large corrections indicated for the tests in the presence of solid walls and the open jet were puzzling. The authors searched for corroborative evidence in the aerodynamics literature, but there seems to be relatively little experimental data on the plunging oscillation of airfoils. However, some was found and a report by Halfman (Ref.7) proved useful. He suggested that serious deviations from theoretical predictions could result both from too low Reynolds numbers and too low oscillation amplitudes, and that the ratio of the boundary layer thickness to the oscillatory displacement amplitude was an important parameter if amplitudes were small.

The tests on the smaller airfoil were performed at a constant Reynolds number of $2.5(10)^5$, above the lower

limit of $1.5(10)^5$ suggested by Halfman, but certainly the displacement amplitudes, η_o/C=0.0052, 0.0104, were small. It was therefore decided to perform similar tests on a larger airfoil model to obtain higher Reynolds numbers, and to modify the oscillation mechanism to permit higher displacement amplitudes and exactly sinusoidal motion. The larger airfoil, with C/H=0.667, of course posed a stiffer challenge for boundary corrections. For this second test series $R = 7.3(10)^5$ and $8.0(10)^5$, and displacement amplitudes η_o/C were 0.026 and 0.039. However, again to our surprise, the test results were essentially the same. The actual lift coefficients C_L were much larger, but not as a fraction of their corresponding C_{L_f}. Instead, as shown in Figs. 8 and 10, the new data showed the same trends with OAR and fell in the same narrow scatter bands as the previous data. Certainly 2 of the 3 tests on the larger airfoil at OAR=0 and all 3 tests at OAR=1 showed larger required corrections to C_L/C_{L_f} than for the smaller airfoil, but those corrections were again unexpectedly large. One favourable effect of the new test conditions is seen in Figs. 9 and 11 where, over the mid-range of OAR, the moment data points for the larger airfoil lie closer to the theoretical band than those for the smaller airfoil. This could be a result of suppression of the boundary-layer effects mentioned by Halfman.

Further reassurance on the validity of the data seemed desirable, so the experimental method and the instrumentation were re-examined. The details of the method appeared satisfactory, and it had been shown to produce consistent data with plausible trends. The instrumentation was given routine checks, but was also given two additional test cases. In one it was used to measure the steady-flow pressure distribution at $\alpha_o = 10^o$, $R = 5.0(10)^5$ on the larger airfoil model at OAR=0. This was compared with data obtained by Malek (Ref.8) for the same airfoil and test conditions, but with different instrumentation, and the two C_P distributions were essentially identical. In the other test case the instrumentation was used to measure the oscillatory pressure on the sides of a square-section prism in two tests of forced plunging oscillation under two-dimensional conditions, with the parameters of wind speed and oscillation amplitude and frequency closely matching two of the observed test conditions for free flow-induced vibration reported by Bearman et al (Ref.9). In both examples, the present instrumentation produced values slightly lower than those of Ref. 9, but quite acceptably close in view of the difficulty of matching test conditions.

It was therefore concluded that the present data is valid, and the puzzle remains as to the reason for the high values of boundary correction for the plunging airfoil loadings in the presence of solid walls or open jet. However, it should be noted that Halfman's two-dimensional data in Ref. 7 shows values of $C_L > C_{L_f}$ by more than 15% in the presence of solid walls, for the same range of μ as the present data but for the very low (in terms of wall corrections) C/H of 0.20. Finally, then, the present results indicate that the test section configuration of Fig. 1 can be used for two-dimensional testing of oscillating airfoils, with acceptably low boundary corrections for $0.6 < OAR < 0.8$, and that a fixed slatted-wall configuration with OAR=0.7 should give the best results.

ACKNOWLEDGMENT

REFERENCES

1. Williams, C.D. and Parkinson, G.V., "A Low-Correction Wall Configuration for Airfoil Testing," Proc. AGARD Symp. Windtunnel Design and Testing Techniques, London, October 1975, Paper 21.

2. Parkinson, G.V. and Hameury, M., "Performance of the Tolerant Tunnel for Bluff Body Testing," J. Wind Eng. Ind. Aero., 33, 1990, pp 35-42.

3. Parkinson, G.V., Kong, L., and Cook, N.J., "Configuration Criteria for a Blockage-Tolerant Wind Tunnel", J. Wind Eng. Ind. Aero., 40, 1992, pp 215-219.

4. Hameury, M., "Development of the Tolerant Wind Tunnel for Bluff Body Testing", Ph.D. Thesis, University of British Columbia, 1987.

5. von Karman, T. and Sears, W.R., "Airfoil Theory for Non-Uniform Motion," J. Ae. Sci., 5, 10, August, 1938, pp 379-390.

6. Kong, L., "Experimental Investigation of the Tolerant Wind Tunnel for Unsteady Airfoil Motion Testing", M.A.Sc. Thesis, University of British Columbia, 1991.

7. Halfman, R.L., "Experimental Aerodynamic Derivatives of a Sinusoidally Oscillating Airfoil in Two-Dimensional Flow," NACATR1108, 1952.

8. Malek, A.F., "An Investigation of the Theoretical and Experimental Aerodynamic Characteristics of a Low-Correction Wind Tunnel Configuration for Airfoil Testing," Ph.D. Thesis, University of British Columbia, 1983.

9. Bearman, P.W., Gartshore, I.S., Maull, D.J., and Parkinson, G.V., "Experiments on Flow-Induced Vibration of a Square-Section Cylinder," J. Fluids and Structures, 1, 1987, pp 29-34.

Symbol	C/H	$\bar{\mu}$	$\overline{\alpha_o^o}$	$R \times (10)^{-5}$
●	0.333	0.52	0.62	2.5
▼	0.333	0.52	0.31	2.5
◆	0.333	0.37	0.44	2.5
▲	0.333	0.37	0.22	2.5
○	0.667	0.48	2.16	7.3
▽	0.667	0.48	1.44	8.0
△	0.667	0.28	0.82	8.0

Table 1: Airfoil Model Test Conditions

Figure 2: Variation of Strouhal Number as a Function of OAR for 3 Sizes of Flat Plate Model positioned at the Center of the Test Section (Hameury, Ref. 4).

Figure 1: Test Section Configuration for Oscillating Airfoil Tests
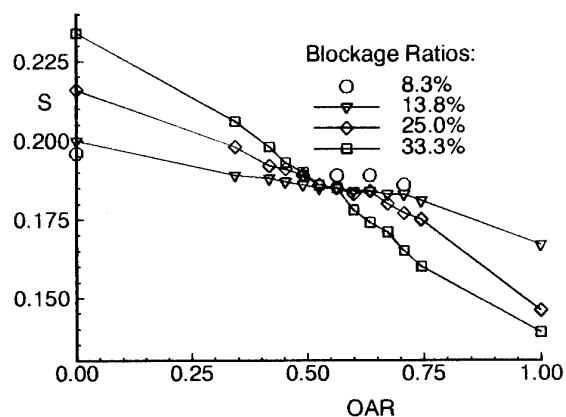
Figure 3: Variation of Strouhal Number as a Function of OAR for 4 Sizes of Circular Cylinder Model positioned at the Center of the Test Section (Hameury, Ref. 4).
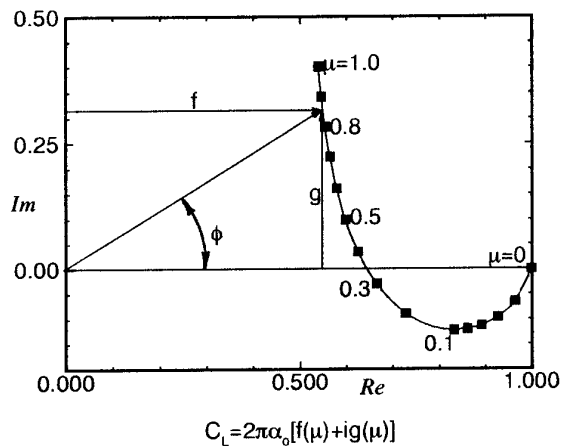
Figure 4: Loci of the Real and Imaginary Components of Unsteady Lift $C_L/2\pi\alpha_o$ on a Flat Plate in Plunging Oscillation as a Function of Reduced Frequency (Ref. 5).
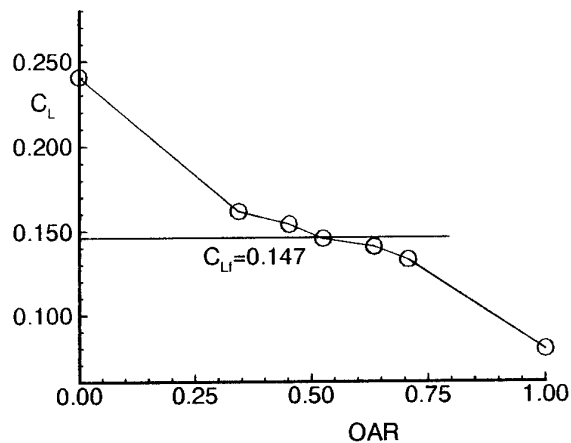
Figure 6: Lift Coefficient Amplitude vs OAR for $C/H = 0.667$, $\alpha_o = 2.16°$, $\mu = 0.48$, $R = 7.3 \times 10^5$
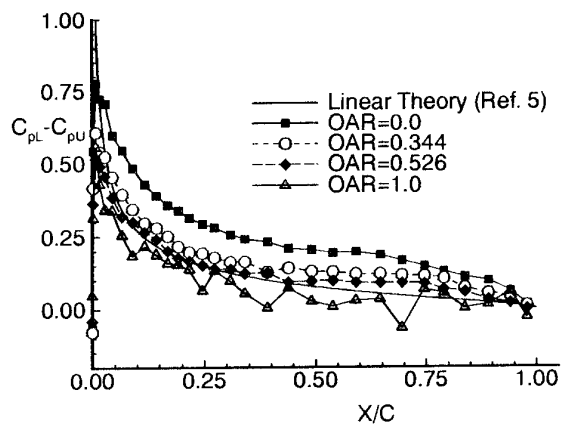
Figure 5: Pressure Difference Distribution along the Airfoil Chord for $C/H = 0.667$, $\alpha_o = 2.16°$, $\mu = 0.48$, $R = 7.3 \times 10^5$
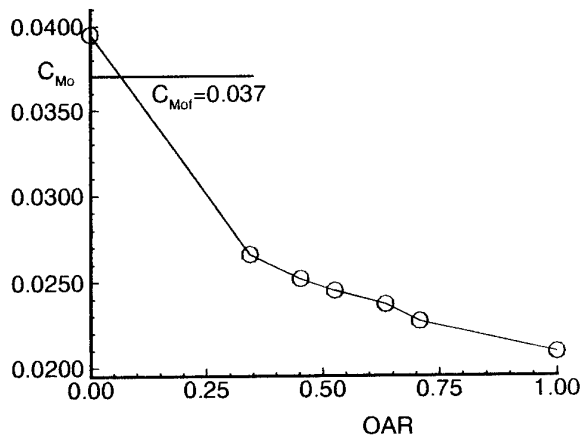
Figure 7: Moment Coefficient Amplitude vs OAR for $C/H = 0.667$, $\alpha_o = 2.16°$, $\mu = 0.48$, $R = 7.3 \times 10^5$
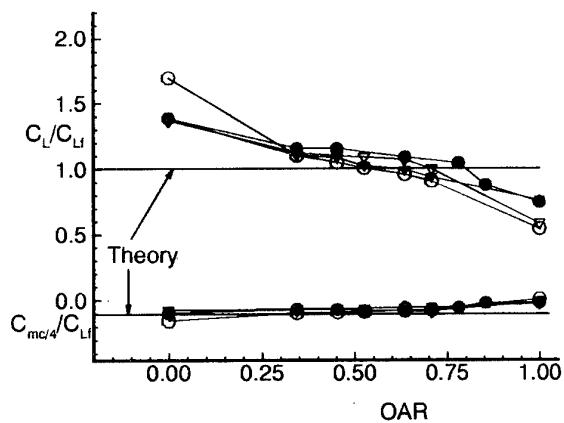
Figure 8: Collapsed Lift and Moment Data for Tests with μ near 0.5
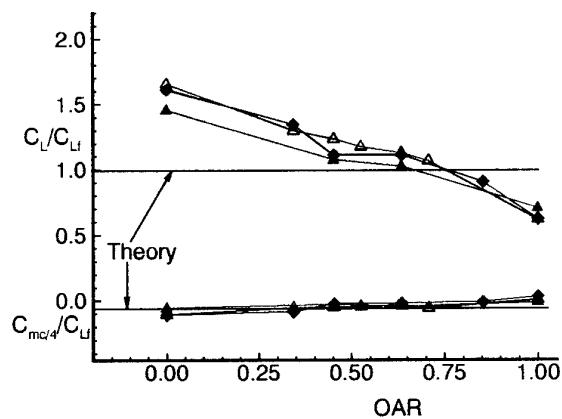
Figure 10: Collapsed Lift and Moment Data for Tests with μ near 0.3
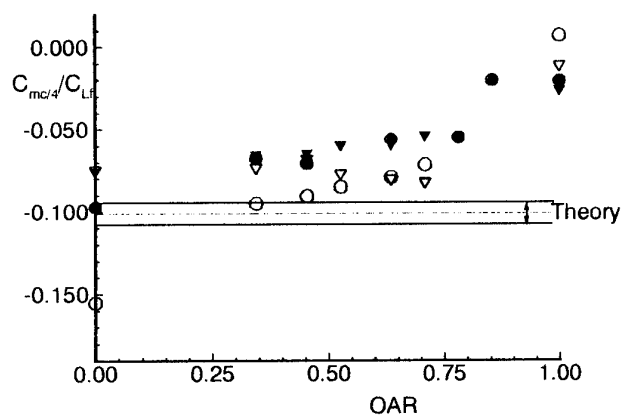
Figure 9: Collapsed Moment Data for Tests with μ near 0.5
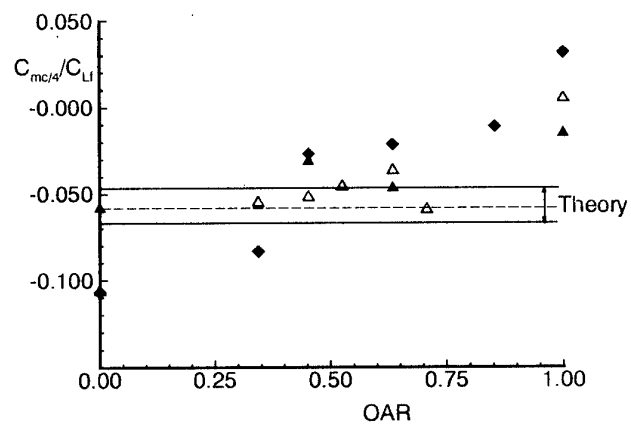
Figure 11: Collapsed Moment Data for Tests with μ near 0.3

CALCULATION OF LOW SPEED WIND TUNNEL WALL INTERFERENCE FROM STATIC PRESSURE PIPE MEASUREMENTS

Lars Fernkrans
FFA, The Aeronautical Research Institute of Sweden
P.O. Box 11021, S-161 11 Bromma
Sweden

SUMMARY

A wall interference prediction tool based on a boundary condition method is developed. The correction method, based on Green's theorem, gives the interference velocity potential field in the control volume from the velocities on a control surface around the model of interest without the need to model the flow field.

The boundary velocities around separated wake flows are measured with static pressure pipes. This is done with both solid and partially open test section walls. The results are used for validation of the tool and to evaluate the possibilities to use static pressure pipes in low speed flows as a means to get the perturbation velocities needed to calculate blockage effects in nonsolid walls cases.

This paper also describes some problems in estimating flow properties that are not measured.

The results presented show that if the static pressure measurements are made carefully it is possible to resolve small cross flow velocities with the necessary accuracy for the correction method.

LIST OF SYMBOLS

B	test section diameter
C	wind tunnel cross sectional area
C_d	drag force coefficient
C_p	pressure coefficient
D	drag force
M	Mach number
N	vector normal to control surface element
q	free stream dynamic pressure
Δq	perturbation dynamic pressure
$\hat{q}$	normalised perturbation dynamic pressure, $\Delta q/q$
r	static pressure pipe radius, also model pressure orifice radial position
R	vector from point (x,y,z) to control surface element, also circular plate radius.
S	model reference area
dS	area of control surface element
U	axial flow velocity
V	horizontal cross flow velocity
W	vertical cross flow velocity
u	axial perturbation velocity rel. to freestream
Δu	axial wall interference velocity rel. to freestream
v	horizontal cross flow velocity rel. to freestream
w	vertical cross flow velocity rel. to freestream

x,y,z	Cartesian coordinates, origin at tunnel entrance of centre line
x'	=x/B, x'=0 at model reference point
β	$\sqrt{1-M^2}$
ϕ	perturbation velocity potential
$\Delta\phi$	interference velocity potential

subscripts

c	corrected value
u	uncorrected value
free	interference free conditions
∞	free stream conditions
$+\infty$	far down stream value

1. INTRODUCTION

There is an increasing interest in low speed tests in which large wake blockage interference is involved. Examples of such tests are high angle of attack tests of modern military aircraft, wing profiles at stalled conditions and highly loaded wind turbines. This emphasises the need of wall interference correction methods. Several methods exist today that can predict the wall interference from solid and wake blockage in wind tunnels with solid walls. The presented method has the advantage of not requiring modelling of the internal flow field. This is of special interest in the above mentioned cases since important flow field characteristics are often unknown during the performance of such tests.

The method chosen is suitable for use in wind tunnels with solid or nonsolid walls. It requires measurements of velocities on the tunnel boundaries. Only axial velocities is needed for solid wall tunnels, while in tunnels with perforated or partially open walls it is necessary to measure both axial and cross flow velocity components to solve the problem. A way to do this is to use static pressure pipes. The use of static pressure pipes for cross flow measurements has earlier proved to give good results in high speed wind tunnels. The fact that the magnitude of the pressures used for calculation of cross flow velocities at a static pressure pipe are of an order lower than the pressures used for axial velocity calculation may create difficulties in low speed wind tunnels. A part of the present work has been to evaluate its usefulness at dynamic pressures typical for low speed wind tunnels.

2. THE METHOD

2.1 Wall interference

The theory of the interference prediction method which is based on Green's theorem and Gauss divergence theorem is previously described in [1]. Here only the equations that are of interest to this work will be described. From the theory it is found that if the flow inside a control surface can be described by a velocity potential the interference perturbation potential inside that surface can be written :

$$\Delta\Phi(x,y,z) = -\frac{1}{4\pi}\iint_{S_2}\left\{\frac{\partial\phi}{\partial N}\frac{1}{R} - \phi\frac{\partial}{\partial N}\left(\frac{1}{R}\right)\right\}dS,$$

where S_2 is the control surface and N is positive facing into the control volume. The first part of the integral contains the perturbation velocities perpendicular to the control surface. This can be neglected if the control surface coincides with a solid wall. The second part is found from integrating the axial perturbation velocities at the control surface. Since these properties cannot easily be found at the entrance and exit surfaces of the control volume they are treated separately. In the described tests the entrance surface is far enough upstream to be undisturbed by the model and therefore Φ is set to zero at the entrance. If the exit surface is placed far enough down stream of the model, the influence from it will become negligible. The problem reduces to a question of how the perturbation velocities decreases from the most down stream point measured in the wind tunnel to an undisturbed value far down stream.

2.2 Cross flow velocities

The theory of the method for calculating the perturbation cross flow velocities from the pressures measured at static pressure pipes is described in [2] and [3]. In the theory it is assumed that the flow around the pipe can be described by a velocity potential. This means that there is an inviscid flow outside a thin boundary layer surrounding the pipe. This also means that there is a limit in local angle of incidence for the theory, above which the boundary layer may separate. Under these conditions the assumption is that the pressure difference across the pressure pipe is caused by a curved flow field and one can prove that the velocity gradients can be written:

$$dv/dx = (C_{P2} - C_{P4})/8r$$
$$dw/dx = (C_{P3} - C_{P1})/8r$$
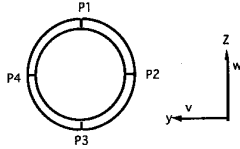
where v and w are normalised with the free stream velocity. Cp1 is on the upper, Cp2 is on the right, Cp3 is on the lower and Cp4 is on the left side of the static pipe facing down stream. r is the static pipe radius. The axial flow disturbance velocity is calculated directly from the pressure coefficients by

$$u = \frac{\sqrt{1-\beta^2\overline{C_P}}-1}{\beta^2},$$

$$\overline{C_P} = (C_{P1} + C_{P2} + C_{P3} + C_{P4})/4$$

2.3 Estimation of down stream conditions

Even though all surface conditions that are needed for the method can be measured, this is not practical in all cases. Therefore some important assumptions has to be made. This is the case at the outflow surface of the control volume. A way to avoid the problems involved in an estimation of the velocities at the outflow surface is to estimate the velocities at the walls down stream of the test section to a point where the influence from the outflow surface is negligible. This may be somewhat simpler but still needs some care if high accuracy is desired.

A commonly accepted assumption is that there is a x-station where the axial perturbation velocities has reached a constant value. The fact that this x-station often is in the wind tunnel diffuser or even further down stream may rise doubts about the usefulness of this procedure. Still it is a way that can be used with good result. The assumption also implies that this velocity is constant far enough away from the model that the velocities here have little effect on the model flow. If the pressure at this point has reached its final value caused by the total energy loss over the model it can be calculated from

$$C_{P-\infty} = \frac{D}{qC}$$

In this work it is found that the pressure rises to a constant value somewhere 0.5 to 1.5 tunnel diameters behind the model depending on the model size. In the presented preliminary work a very simple model of the pressure is used where it increases linearly from the most down stream measured value at x'=0.7 to a value corresponding to $C_{P-\infty}$ at x'=1.4 for all models as shown in figure 1. For the cross flow velocities an exponential function is used.
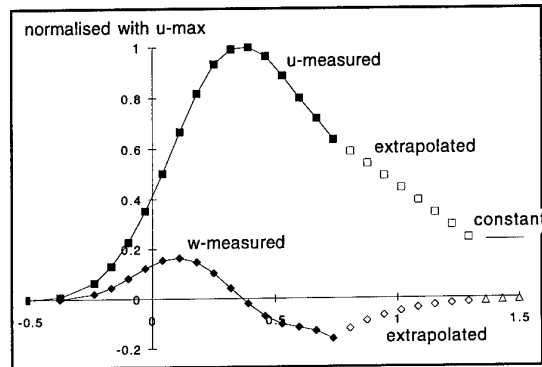
Figure 1. Estimated data added to measured points.

3. TEST EQUIPMENT

3.1 Test section

The FFA low speed wind tunnel LT1 is a closed test section, return type tunnel with atmospheric pressure. It has two 3.6 metre diameter circular test sections in file. The total length of the test sections is 8 meter. The rear test section can partially be opened in the roof and in the floor to

fit different sets of model supports. The size of the openings is approximately 3.5 m² when fully opened, which is comparable to an average porosity of 14 %. The centre of the openings are at the same x-position as the model reference point for the rear test section. Their shapes are shown in figure 2. The rest of the wind tunnel has solid walls so any air leaving the test section through the upstream openings will re-enter through the downstream openings.
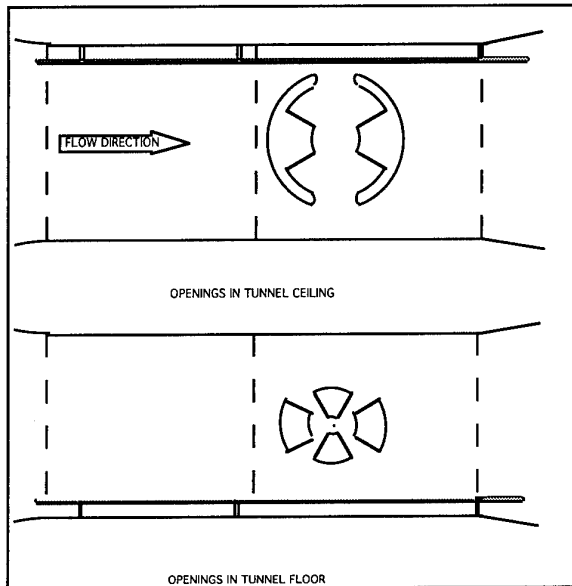
Figure 2. Wind tunnel test sections with openings and static pressure pipe at port wall (facing upstream). Flow is from left to right.

3.2 Models and support

The models chosen for this first validation phase are circular plates normal to the free stream. Five different sizes of plates were tested corresponding to relative tunnel blockages of 1.23, 2.78, 4.5, 6.0 and 7.5 %. The measurements presented here are made at a tunnel speed of 60 m/s except for the largest model which is tested at 50 m/s.

In order to keep the support interference at a minimum level the models were connected to a sting via a small balance. As most wind tunnel balances are not made for this type of models the larger plates experienced substantial vibrations which may have reduced the accuracy of the drag measurements. The sting was suspended by thin wires from the tunnel walls to the centre line.

4. MEASURING TECHNIQUE

4.1 Pressure measurements

One static pressure pipe with 22 measuring stations were manufactured. Each station has four pressure orifices at 90 degrees displacement (up, down, port and starboard). The pipe was mounted 260 mm from the test section wall at four circumferential stations, the floor, the ceiling and port and starboard walls. This means that the measurements could not be made simultaneously at the four walls which of course adds uncertainties to the results. In the forward test

section the streamwise distance between each station is 500 mm, and in the rear test section it is 250 mm. The pipe diameter is 60 mm, which is 1.7 % of the tunnel diameter. The total length of the pipe is 8 meters stretching through both test sections. The pressures are averaged from 1000 samples during 10 s measuring time.

4.2 Data conditioning

To avoid influence of tunnel flow irregularities on the results, all measured pressures were reduced with the corresponding empty tunnel pressure signature. There has been no curve fitting or interpolation of the measured data in order to obtain values between the measuring points for the integrations.

5. RESULTS AND DISCUSSION

5.1 Measurement accuracy

The axial velocities causes large pressure drops which makes them possible to be measured with high accuracy. The cross flow velocities are more difficult to measure but are fortunately of less importance for the final result. The pressure differences across the pipe from which the cross flow velocities are integrated were typically less then five Pascal for the smallest model. This is of the same order as the scatter in the pressure data for the empty tunnel. The pressure differences can of course be made larger by using a larger pipe diameter. The pipe will however at the same time become a larger and unwanted obstruction in the tunnel. Figures 3-4 show the magnitude of the axial- and cross flow velocities measured at the ceiling for the solid and open cases respectively.
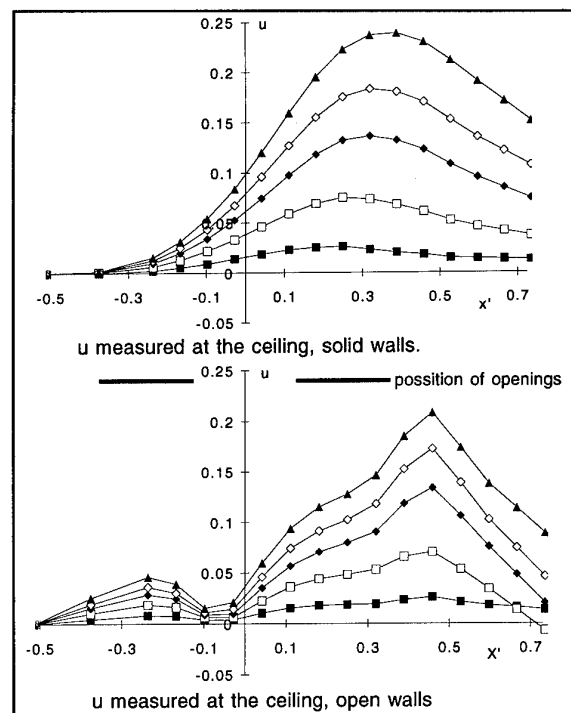
Figure 3. Axial flow velocities at the ceiling pressure pipe measured with solid and open walls. The relative blockage is 1.2, 2.8, 4.5, 6 and 7.5 %.

For the larger models in the open wall case the cross flow angles very likely exceed the limit where the theory no longer holds. One reason for these large cross flow angles may be separation of the flow returning into the test section through the rear opening.
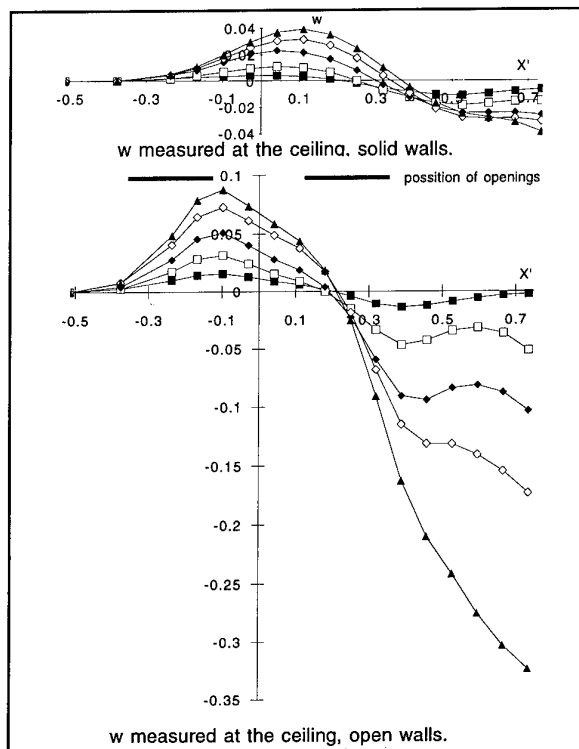
Figure 4. Cross flow velocities at the ceiling pressure pipe measured with solid and open walls. Positive values are towards the ceiling. The relative blockage is 1.2, 2.8, 4.5, 6 and 7.5 %.

A total error span for the cross flow velocities is shown in figure 5. The graph is created by adding and subtracting the standard deviation to the measured data, based on four different readings with 1000 samples each.
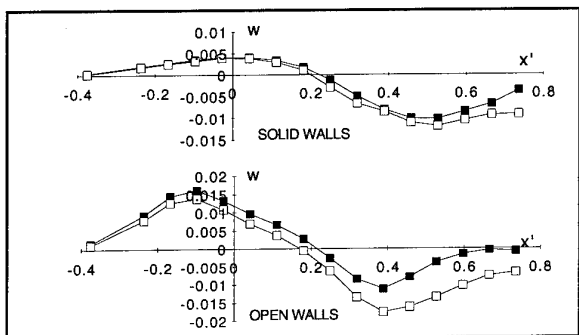
Figure 5. Cross flow velocities for the smallest model ± standard deviation.

For comparison with measured data a potential flow calculation has been made for the solid wall case. The model is represented by a source and a sink at x/B=0.15 respective 0.5. The wake is represented by a source at x/B=0.45. The perturbation velocities of the wall

interference are found by solving the interference problem (Laplace equation) in cylindrical coordinates for a three dimensional source placed at the centre line of a circular cylinder. This is applied to the three singularities. All velocities are solved for a line at the relative tunnel radius of 0.85 where the pressure pipe is placed. Since the measured axial disturbance velocities are assumed to be reliable, the strengths of the singularities are adjusted to give axial velocities that matches those measured. The output information from the theoretical calculation then reduces to the shape of the curves and the ratio between velocity components. The result is shown in figure 6 Here all data are normalised with the maximum value of the axial velocity. Only data between x/B=0.5 and 0.75 are measured. For this specific measurement the agreement is quite good up to x/B=0.6.
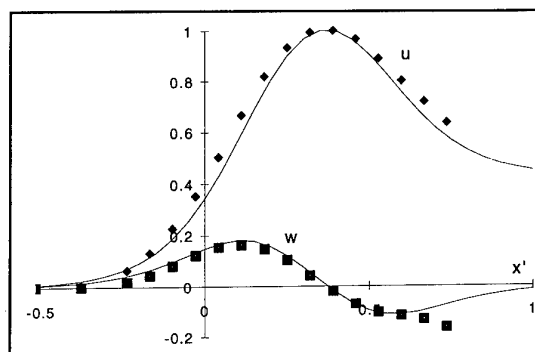
Figure 6. Comparison between measured velocities (symbols) and calculated velocities (lines) at pressure pipe position normalised with u_{max}. S/C=0.075.

The agreement in this comparison varies depending on which static pipe reading that are chosen since the measured flow fields, despite the axisymmetric test setup, were not totally axisymmetric. There may also be an interaction with the wall boundary layer that is not taken into account in the singularity method.

5.2 Dynamic pressure correction

In the scope of this work, only the axial interference velocities at the tunnel centreline are studied. The calculated results are shown in figure 7 and 8. For comparison the interference velocities are also calculated without using the wall normal velocities.
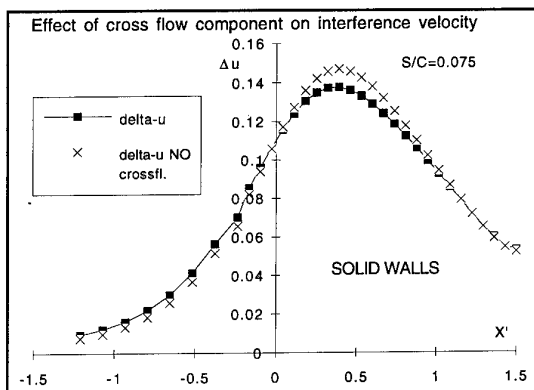
Figure 7. Wall interference velocities at tunnel centre line for the solid wall case. Calculation made with and without using the measured velocities normal to the wall.

The relative change of the calculated interference velocities shows the sensitivity of the method to errors in the cross flow velocity measurements. It does not represent the gain in accrue obtained from using the two variable method instead of only using the method for one variable. In the solid wall case, wall pressures would give equivalent results except that it does not compensate for wall boundary layer deformation due to pressure gradients at the walls. In the nonsolid wall case, static pressures measured close to the wall would give another axial velocity profile that would partially compensate for the lack of cross flow velocity information.
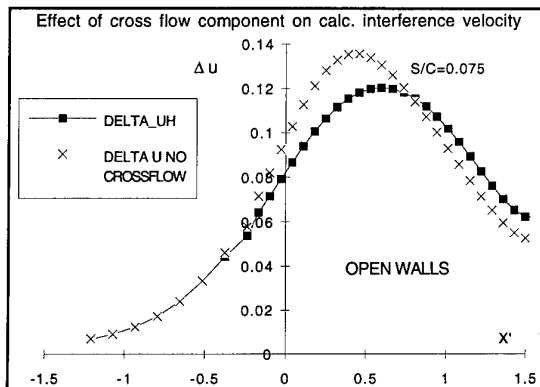
Figure 8. Wall interference velocities at tunnel centre line for the non solid wall case. Calculation made with and without using the measured velocities normal to the wall.

The drag coefficients are corrected by using a global correction of the dynamic pressure in the following way:

$$C_{dc} = C_{du} / (1 + u_{max})^2$$

where u_{max} is the maximum interference velocity found on the centre line. It is found by others that using this value and not the corresponding value at the model position gives far better correction. The reason for this is probably to be found in the fact that for this type of flow the wake pressure, which determines the base pressure, has a large effect on the drag. At the same time the wake pressure suffers much more from wall interference than the pressure on the wind side of the model. As the wake bubble and the maximum Δu position is at approximately the same x-station this is the reason it should be used. A more appropriate procedure would be to correct the pressures and integrate these. The question of choosing $\hat{q}$-values for correction of the different parts of the flow will still remain in cases of separated wakes.

Figure 9 shows the drag coefficients vs. S/C, for solid and open test section support doors. The difference between the two cases is rather small. In fact the measured drag forces were almost identical but the calibrated empty tunnel dynamic pressure were 1.5 % higher in the open door case.
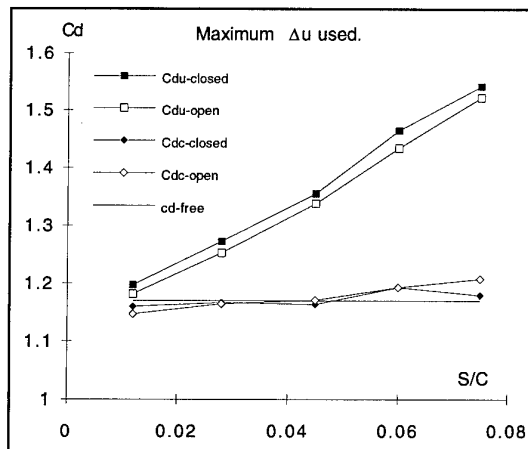
Figure 9. Corrected and uncorrected C_d values for different blockage made with $\hat{q}_{max}$ at tunnel centre line.

For three of the models the method gives a good compensation for the flow through the tunnel walls despite the few numbers of pressure pipes used. For the other two models the difference remains.

5.3 Model surface pressure

The models were equipped with four pressure orifices at the relative radius stations 0.3, 0.5, 0.7 and 0.9 except for the smallest plate for which the mounting plate covered the 0.3 radius orifice.

The purpose of measuring the model surface pressures was to see if the deformation of the flow field due to wall interference could be detected in the pressures at the models. The flow around a flat plate is of course not very sensitive to flow field pressure gradients. In particular the base pressure ought to be nearly constant in all cases.

To achieve corrected pressure coefficients from pressure measurements, both dynamic pressure and free stream static pressure were corrected, since they are both influenced by the walls. The dynamic pressure was corrected as mentioned above. The static pressure at the model position is assumed to decrease by the same value as the dynamic pressure have increased. The C_p correction becomes

$$C_{p_c} = \frac{C_{p_u} - 1}{\hat{q}} + 1$$

The result of correcting pressure coefficients are shown in figure 10.
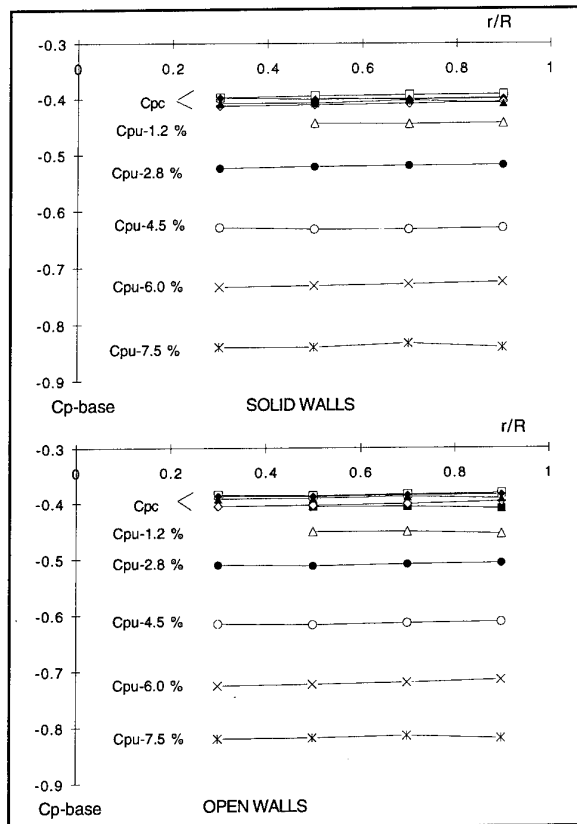
Figure 10. Uncorrected and corrected pressure coefficients at lee side of the five different plates.

Corrected and uncorrected Cp$_{base}$ vs. S/C in figure 11 show a slight overcorrection in the open wall cases.
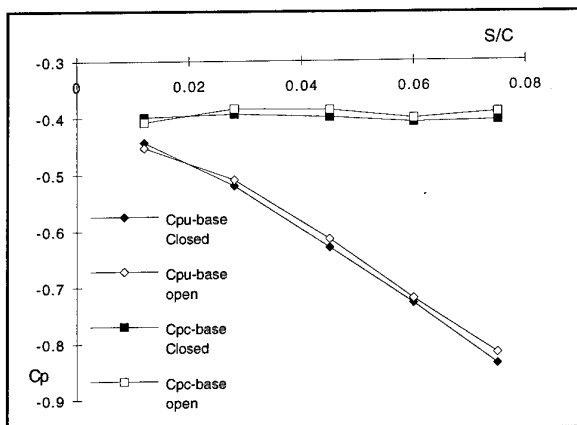
Figure 11. Average base pressures in solid and open wall cases.

6. CONCLUSIONS

The paper has considered the possibilities and limitations associated with both the interference prediction method and the measurement technique.

The results obtained from this preliminary work demonstrate that:

- The correction method is very robust and that good results is possible to achieve even with a few numbers of measured points across the wall openings.

- It is possible to calculate reliable cross flow velocities in low speed flows using relatively small static pressure pipe diameters providing that the pressure measurements are accurately performed.

- Despite a significant change in the flow close to the walls in the non solid wall case, the result of correcting dynamic pressure is very close to the corresponding result from the solid wall case.

The different unsolved problems indicate that the following areas that should be investigated further.

- The problem of predicting the boundary velocities down stream the test section in the general case is not satisfactory solved. This is particularly true for the cross flow velocities in cases where large values can be expected outside the measured boundary.

- The method to calculate the cross flow velocity derivatives from pressures on the static pressure pipes are based on theoretical grounds. An experimental investigation of the pipe pressures at different cross flow angles should show to what extent the cross flow affects the results. With such results available it may be possible to separate the effects of cross flow from that of cross flow derivatives and hence increase the accuracy.

- Even with a method that in theory is capable of producing interference velocities in the whole flow field it is not jet fully understood how these data affects the measured forces in complicated flow cases. Examples of such flows are partially separated flows from solid models and flows through propellers and wind turbines.

In a future work to extend the capabilities of the interference prediction tool and to verify it, experimental investigations should consist of measurements with models with lifting wings and complex geometry's, preferably with surface pressure measurements. It is also important to do simultaneous measurements on all walls to increase the accuracy.

7. ACKNOWLEDGEMENT

8. REFERENCES

1. Ashill, P.R., Keating, R.F.A. "Calculation of Tunnel Wall Interference from Wall-Pressure Measurements", Aeronautical Journal, Jan 1988.

2. Nenni, J.P., Erickson, J.C Jr and Wittliff, C.E. "Measurement of Small Normal Velocity Components in Subsonic Flows by Use of a Static Pipe", AIAA Journal Vol. 20, No. 8, August 1982.

3. Smith, J.,"2D Wall Interference Assessment Using "Calspan Pipes". Holland NLR TR 85065 U, April 1985.

4. Hackett, J.E., Wildsen, D.J., and Stevens, W.A., "A Review of the Wall Pressure Signature and other Tunnel Constraint Correction Methods for High Angle-Of-Attack Tests." AGARD-R-692, February 1981.

OPTICAL SURFACE PRESSURE MEASUREMENTS: ACCURACY AND APPLICATION FIELD EVALUATION.

A. Bukov, V. Mosharov, A. Orlov, V. Pesetsky, V. Radchenko, S. Phonov, S. Matyash
Central AeroHydrodynamic Institute (TsAGI), Jukovsky, Moscow region, Russia
M.Kuzmin, N.Sadovskii
Moscow Lomonosov University, Russia

ABSTRACT

Optical Pressure Measurement (OPM) is a new pressure measurement method rapidly developed in several aerodynamic research centers: TsAGI (Russia), Boeing, NASA, McDonnell Douglas (all USA), DLR (Germany).

Present level of OPM−method provides its practice as standard experimental method of aerodynamic investigations in definite application fields. Applications of OPM−method are determined mainly by its accuracy. The accuracy of OPM−method is determined by the errors of three following groups:

1. Errors of the Luminescent Pressure Sensors (LPS) itself, such as uncompensated temperature influence, photo degradation, temperature and pressure hysteresis, variation of the LPS parameters from point to point on the model surface, etc.

2. Errors of the Measurement System, such as noise of the photo detector, non linearity and non uniformity of the photo detector, time and temperature offsets, etc.

3. Methodological errors, owing to displacement and deformation of the model in an airflow, a contamination of the model surface, scattering of the excitation and luminescent light from the model surface and test section walls, etc.

OPM−method allows to get total error of measured pressure not less then 1%. This accuracy is enough to visualize the pressure field and allows to determine total and distributed aerodynamic loads and to solve some problems of local aerodynamic investigations at transonic and supersonic velocities. OPM is less effective at low subsonic velocities (M<0.4), and for precise measurements, for example, an airfoil optimization.

Current limitations of the OPM−method are discussed on an example of the surface pressure measurements and calculations of the integral loads on the wings of canard−aircraft model. The pressure measurement system and data reduction methods, used on these tests, are also described.

1. Introduction

Pressure field measurement on the surface of the aircraft model is one of the largest problems in experimental aerodynamics. Classical technique, i.e., building a model with a vast amount of pressure taps for surface pressure distribution measurements is quite time−consuming, complex and expensive. The availability of a rapid and economical procedure to obtain these measurements stimulates development of the new methods. Now one can say about appearance of the Optical Pressure Measurement Method [2−20].

The pressure measurement technique by Luminescence Pressure Sensor (LPS) technology is based on deactivation of photo−excited molecules by oxygen contained in the air. The model surface is covered by thin (thickness about 2−100 mkm) polymer layer containing luminophore molecules and penetrable for oxygen. Appropriate light source is used for luminescence excitation. Exited luminophore molecules can lose energy by light radiation luminescence or by transfer this energy to oxygen molecules without light

radiation. The part of energy lost by non radiation deactivation (luminescence quenching) is proportional to oxygen concentration in the polymer layer and oxygen mobility. In accordance with Henry's law, concentration of oxygen in polymer layer is proportional to oxygen partial pressure on its outer boundary. As a consequence, luminescence output is inversely proportional to oxygen partial pressure above polymer surface and if the partial pressure of oxygen in the air is proportional to air pressure, the effect of luminescence quenching can be used for measurement of the air pressure. The luminescence intensity is proportional to excitation illumination and is a function of the layer thickness.

A Luminescence quenching phenomenon is well known as a mean of measuring the partial pressure of various gases. Peterson and Fitzgerald [1] used fluorescent dye for flow visualisation. However the idea of application luminescence quenching for pressure field measurements in aerodynamic test credits to Newsky and Pervushin from TsAGI [2−4]. Our group began their works with the pressure sensitive paint formulation from Newsky and Pervushin in the middle of eighties, but soon in cooperation with photo chemist from Moscow University we developed another pressure sensitive paints [5,6,11,14,15,17,20]. In the end of eighties Boeing Company with Washington University began analogous investigations [7,8,10]. After our demonstration experiment in the Boeing wind tunnel, McDonnell Douglas Research Laboratory targeted this area for independent research and development effort. The impressive results were obtained [13,16,18,19].

We have in our disposal now the next pressure sensitive paint formulations:
LPS L2 − − PSP with ultraviolet excitation for stationary transonic and supersonic flows,
LPS R1 − − PSP excited with visible blue light for stationary transonic and supersonic flows,
LPS F1 − PSP excited with ultraviolet for non stationary flows, for example flows in a shock tube, or near oscillating wings. Table 1 shows the main technical performance data.

Table 1

PSP Type	LPS L2	LPS R1	LPS F1
P max.,Bar	5	2	5
Sensitivity.[a] %/Bar	75	65	60
Temp. range. °C	20−70	10−70	10−40
Temperature sensit[b],%/°C	−0.3	−0.1	−0.1
Responce time, sec.	0.3	0.3	0.005
Thickness, mkm	20	20	2
Exitation, nm	320−340	400−500	320−340
Emission, nm	425−550	500−700	425−550

a). Sensitivity − (dI/dP)/I·100%, P = 1Bar, T = 20°C.
b). Temperature sensitivity − (dI/dT)/I·100%, P = 1Bar.

2. Measurement accuracy of the PSP method.

The measurement errors of the PSP method can be divided in three groups. The first — the errors of the pressure sensitive transducer. The second — the errors of the measurement system. The third — the methodological errors, attributed to particulars of the PSP applications in the aerodynamic test.

2.1. The errors of PSP Method

These errors have not been considered in any published work, but by our opinion transducer errors define the place of the PSP technique in aerodynamic experiment. Let's consider the most substantial PSP errors.

2.1.1. Non linearity of the PSP calibration characteristic.

PSP operation is based on the well–known phenomenon of a luminescence oxygen quenching of some luminophore. An intensity of luminescence is inversely proportional to the air pressure:

$$I \cong J\Omega/[A(T)+B(t)p] \qquad (1)$$

where: I — luminescence intensity,

J — excitation intensity,

Ω — some proportional coefficient,

A(T), B(T)— temperature dependent coefficients,

p — air pressure.

Let I_0— luminescence intensity at some known pressure p_0, then one can write:

$$I_0/I \cong A(T)+B(T)p. \qquad (2)$$

The calibration characteristic can be derived from above equation:

$$F(I_0/I,T) \cong a_0(T)+a_1(T)I_0/I.+a_2(T)(I_0/I)^{2+}. \qquad (3)$$

A formula (2.1) is only some approximation and real calibration characteristic is nonlinear (plots on Figure 1)
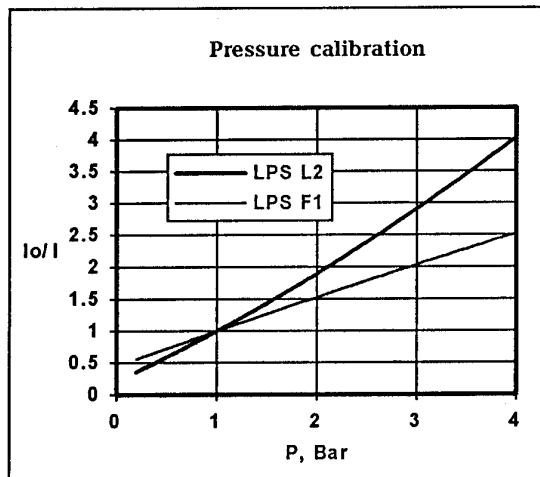
Figure 1. Pressure calibration curves for LPS L2 and LPS F1.

Practically second or third order approximation gives approximation error about 0.2% in the pressure range from 0.3 to 1.5 bar.

The first conclusion from calibration curve is that ambient light bends calibration curve. So it is necessary carefully eliminate all possible sources of ambient light in the wind tunnel, for example, light scattered by test section walls.

The second, PSP is transducer of the absolute pressure, so it is very difficult measure the small pressure variations.

2.1.2. The spread of PSP characteristics on the model surface.

One can suggest, what calibration curve obtained in calibration chamber for PSP sample can be used for total painted surface of the model. Practically, there is some spread of characteristic, that can be estimated as:

$$\Delta_r = \frac{\underset{R1,R2}{Max}\{F_{R1}(I_0/I,T) - F_{R2}(I_0/I,T)\}}{\overline{F}(I_0/I,T)}, \qquad (4)$$

where R_1 and R_2 arbitrary points on the model surface,

$\overline{F}(I_0/I,T)$-averaged by total surface calibration characteristic. The value of this spread is not larger then 0.3% for all working pressure and temperature ranges.
The source of this spread can be explained by polymerization environment distinction of luminophore bending material: the thickness variation of the PSP layer, evaporation velocity of the solvent, the temperature of the model surface, etc. It is very difficult to reduce this spread for pressure transducer being thin sprayed polymeric layer. Sometimes it is possible to calibrate PSP for all points of the model surface directly in the test section of the wind tunnel. Some types of the wind tunnels give one possibility to control pressure level in the test section, but this procedure is very expensive especially in the large wind tunnel, and calibration by temperature creates additional problems.

2.1.3. The temperature sensitivity of PSP.

The PSP temperature sensitivity can be defined as:

$$\Delta_T = \frac{1}{I} * \frac{\partial I}{\partial T}, \qquad (5)$$

and is ascribed to two factors:
1. the temperature dependence of the luminophore quantum yield:

$$\varphi = \frac{A}{A + A_0 \exp(-E_0/kT)}, \qquad (6)$$

where: A and A_0 the probabilities of radiation and non radiation transitions in the luminophore molecule,
E_0 — activation energy of the non radiation transition,
k — Boltzmann constant,
2. the temperature dependence of the bending polymer permeability for the oxygen molecules:

$$\mu = \mu_0 \exp(-E_p/kT), \qquad (7)$$

where E_p— permeability activation energy.
These factors have different temperature dependence and some times can compensate each other in the desired temperature range.

Taking into account temperature influence, the PSP calibration characteristics can be approximated by the next formula:

$$F(I_0/I,T) = \sum_{k,m=0}^{k=2,m=2} \chi_{k,m}(I_0/I)^k T^m, \qquad (8)$$

As a result, the temperature field on the PSP layer is required. The possible way to evaluate this field will be discussed later. The plots on Figure 2 show temperature calibration curves for our paints.

Temperature calibration
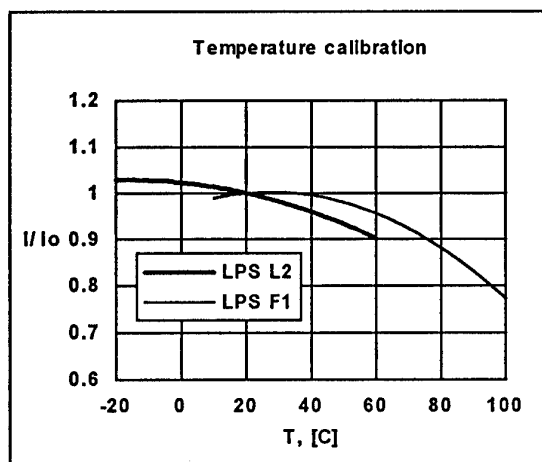
Figure 2. Temperature calibration curves for LPS L2 and LPS F1.

2.1.4. The temperature hysteresis of the PSP.

The temperature hysteresis is due to polymer structure modification with temperature variation. Relaxation time at heating is significantly smaller then at cooling, that is why hysteresis is observed mainly in the heating—cooling cycle. The hysteresis value is function of the polymer type and is large for glasslike polymer then for high elastic polymers. The hysteresis significantly increases about polymer glasslike temperatures.

The hysteresis can arise at ultimate luminophore concentration in the polymer due to luminophore molecules association.

For all PSP presented in the table heating—cooling hysteresis at temperature range $20-70^{\circ}C$ does not increase 0.5%.

2.1.5. PSP Pressure Hysteresis

Oxygen dissolving in polymer can change polymer structure, what can be source of some pressure hysteresis. The hysteresis value is defined by polymer used for luminophore bending. The lowest pressure hysteresis is for high elastic polymer. The hysteresis is significant for pressure changing from some value to vacuum.

For PSP presented the hysteresis at pressure range 0.5 — 5.0 Bar does not increase 0.5% and is comparable with replicatability of calibration curve obtained in laboratory environment.

2.1.6. Spatial Resolution.

PSP spatial resolution is determined by gas flow in active layer when pressure gradient is presented on the upper boundary. Gas flow in polymer is very small in comparison with gas flow on the upper boundary, so it does not effect on the pressure distribution on the boundary.

Spatial resolution was estimated theoretically by Laplas equation solution for gas concentration in thick layer with shock wave liked boundary condition. Calculated gas concentration distribution in active was used for luminescence intensity distribution. The results obtained indicate that 99% variation of intensity occurs on length about 5 thicknesses of the active layer what corresponds to spatial resolution about 0.1 mm for LPS L2, LPS R1, and 0.01 mm for LPS F1. It is enough for most experimental applications.

2.1.7. Time resolution

PSP time resolution is determined by a time required for oxygen concentration transition to a steady state in the active layer while pressure variation on the upper layer boundary.

Concentration transition time can be estimated by solving appropriate diffuse equation. Well—known solution for concentration distribution can be presented by series with the specific relaxation time:

$$\tau = \frac{4h^2}{\pi^2 D},$$ (9)

where: **h** — — active layer thickness,

D— specific diffusion of the bending polymer. Luminescence output is integral across boundary layer, and digital estimations show that luminescence transition time to 99% intensity level is about 3τ

The experimental investigation showed very well agreement with these estimations. Time resolution for LPS L2 and LPS R1 is 0.3 sec, and for LPS F1 — 0.005 sec.

2.1.8. PSP reaction on oscillating pressure.

The gas dissolving in the polymer layer goes throw sorption—dissorption process on the polymer boundary. Sorption and dissorption velocities can differ, what in the case of oscillating pressure can shift mean luminescent intensity and pressure value measured.
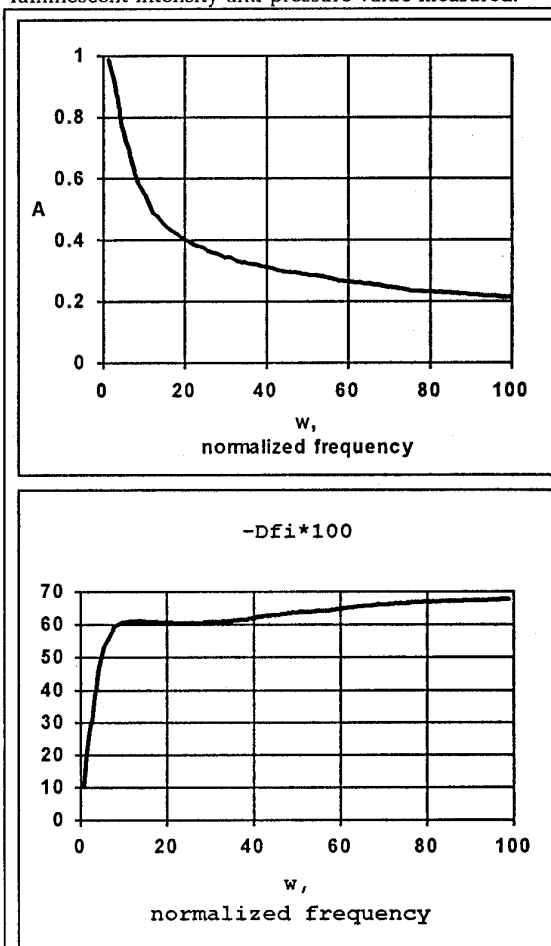
Figure 3. Amplitude (A) and phase (Dfi) caracteristics of LPS L2

Integration across active layer of the diffusion equation solution with harmonically pressure boundary condition gives frequency characteristic of PSP transducer. Calculated amplitude and frequency characteristics of LPS L2 and LPS F1 are presented on Figure 3 as function of non dimensional frequency

$w = 2\omega h^2/D = \pi^2 \omega \tau/2$ for optical densities 0.5. Frequency bandwidth is 0.2 Hz for LPS L2 , and 12 Hz for LPS F1 (phase lag 0.1 rad, for 99% amplitude level). It is worth mentioned what for PSP under consideration sorption and dissorption velocities are equaled.

2.1.9. Long time relaxation of PSP characteristics.

PSP calibration characteristics slightly vary after application on the model surface. For our paint formulations this age process is signuficant in the first day and ascribed to the polymerization of the active layer. For PSP under consideration the value describing aging is:

$$\Delta_a = \frac{1}{F(I_o / I, T)} * \frac{dF(I_o / I, T)}{dt}, \qquad (10)$$

and is about 5%/day. The time of the initial aging process can be reduced by some heating−cooling cycles. Upon completion of polymerization process PSP characteristics vary with significantly smaller velocity. For example aging parameter for above mentioned PSP does not increase 0.05%/day.

There are a lot of causes of this slow aging: polymer aging, oxidation, luminophore molecules association, luminophore molecule drift in the screen layer. The significance of each factor depends on PSP type.

In order to minimize this error testing have to be started 24 hours later the paint application and PSP calibration has to be done just before experiment or during experiment.

2.1.10. The Luminophore Photo destruction.

The luminophore photo destruction takes place under the action of the excitation radiation. The photo destruction reduces absolute luminescence output, but, usually, calibration curve $F(I_r, T)$ does not change significantly. A photo destruction velocity V is proportional to the intensity of the excitation and for PSP under consideration is about 1%/hour for excitation level 0.1 mwatt/cm^2. Corresponding pressure measurement error is:

$$\delta p_{phd} \cong \frac{\partial F}{\partial I_r} * Vt; \qquad (11)$$

where t − total exposure time.

2.1.11. The oil influence.

This question is under consideration because of air flow in the wind tunnel usually contaminated by oil drops.

Oil film on the PSP surface absorbs excitation light and fluoresces itself what is the source of additional error.

Active layer can absorb the oil and oil can quench luminescence. Unfortunately oil absorption is irreversible and oil influence takes effect on the leading edges

Testing of PSP sample LPS L2 in TWT ARA (England) wind tunnel showed what oil contamination creates pressure measurement error rate about 1 − 3%/hour (depend on wind tunnel operation regime).

This error rate is due to luminescence quenching. The influence on the calibration curve slope is smaller Δ <0.1%/hour. The oil influence on LPS F1 is identical, but experiments show LPS R1 is insensitive to the oil.

The possible way to diminish oil contamination influence is additional acquisition of the reference image and reduction of the test duration.

In conclusion of this topic it is worth saying that total pressure measurement error with LPS L2 can be reduced up to 1% if the run duration is not larger then 20 minutes, and temperature field uncertainty on the model surface is smaller then 3 degrees Celsius. More exact determination of the temperature field, air filtering, taking into account experimental particularities of the wind tunnel can slightly improve situation, but there is another source of the measurement errors − errors of an acquisition system.
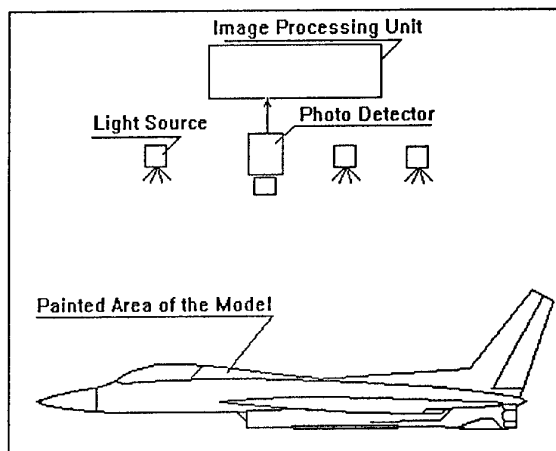
Figure 4. Optical Pressure Measurement System

2.2. The errors of the measurement system.

A prototype of the optical pressure measurement system is shown in Figure 4. A model is illuminated by the excitation light field and luminescence distribution on its surface is acquired by photo detector. A photo detector output (analogous or digital) is connected with an image processing unit. The excitation field is created by one or multiple light sources.

2.2.1. Stability and uniformity of the excitation light field.

The luminescence intensity is proportional to the intensity of the excitation light. Thus non stability δJ of excitation field J is the source of the pressure measurement error:

$$\delta p_J \cong \sqrt{2} \frac{\partial p}{\partial I_r} * \frac{\delta J}{J}; \quad I_r = \frac{I_o}{I}; \qquad (12)$$

Development of the light source with non stability better then 1% is the complex and expensive task. The standard solution is the measurement of the light source output and normalizing the luminescence signal on this value.

Dust and water vapor in the illumination light field due to light scattering and absorption create additional measurement error. The possible and practically tested solution of the entire problem of illumination field stability is measurement normalizing signal from Reference Luminescence Marks (RLM) applied on the surface under study. The luminescence output of RLM is independent of the air pressure and

temperature or has approximately the same temperature sensitivity coefficient as LPS. By using appropriate number of RLMs one can compensate large scale fluctuation of the illumination field. The main disadvantage − − the lost information about pressure field on RLM zones.

2.2.2. Photo detector parameters influence.

The main photo detector inputs in the measurement error are conversion parameter non stability, electronic noise and non uniformity of pixel to pixel gain. Influence of the noise was detail discussed in the work [], and in the best case signal to noise ratio (SNR) restricted by quantum noise and saturation chargи of cooled scientific−grade CCD matrix is about 600−800.
Input in the pressure error due to limited SNR is:

$$\delta p_{SNR} \cong \sqrt{2}\,\frac{\partial F}{\partial I_r} * \frac{1}{SNR}; \qquad (13)$$

Further improvements of SNR can be reached by spatial and frame averaging with the lost of the time and spatial resolution. Standard integration time for model with character scale about 1 m painted with LPS L2 and nitrogen laser ($P_{output} \approx 200$ mwatt) illuminated is about 0.2...1 sec.(depend on pressure range during the test, relative objective ratio required). ADC conversion (sampling rate − −200 KHz) and digital data transfer requires about 1−4 sec for CCD matrix having 1000 by 1000 pixels resolution. Total acquisition rate is in the range 1 to 5 sec per frame. Frame averaging improves SNR proportionally square root from number of frames and time consuming to be used for large scale model.

The variation of the CCD gain for scientific grade matrix not worse then 2%. When the image of the model under study does not move relative to matrix, the variable gain does not influence on relative intensity measurement. However, if the image displaces relative reference one on CCD matrix, the gain non uniformity K_{CCD} can create a significant part of the measurement error:

$$\delta p_K \cong \frac{\partial F}{\partial I_r} * (d_{xy} grad K_{CCD}) / K_{CCD}, \qquad (14)$$

where d_{xy} − − displacement vector in CCD plane.
A standard procedure is used to correct non uniformity of the gain − − flat−field calibration [19]. The CCD is illuminated with a uniform field of light, using, for example, integration sphere. The image acquired is used to generate correction coefficient field. Really, when relative displacements d_{xy} are small, only small scale fluctuations of K are significant, for measurements of relative intensities. In order to provide this procedure we supply our CCD camera with near uniform light source. Special computer controlled unit is used to generate a set of different intensity levels. The calibration procedure can be done directly during the test. Additional information about true conversion function of the CCD matrix is used to compensate offset and gain variations in the total acquisition channel.

2.3. Methodology Errors.
2.3.1. Re reflection of luminescence.
During the measurements on the model having complex shape, for example, wing with pylon, wing−winglet, luminescence light re reflection can take place
Total luminescence registered at point 1 can be presented as:

$I = I_1 + rI_2$, where r−PSP surface reflection coefficient, I_1 and I_2−luminescence levels at point 1 and point 2 accordingly (luminescence radiation is assumed isotropic). The pressure measured is:

$$p = F[(I_{01} + rI_{02})/(I_{p1} + I_{p2})] \qquad (15)$$

Considering only the first order components, corresponding pressure measurement δ_{rr} error can be estimated:

$$\delta_{rr} = r(I_2/I_1)*(p_2 - p_2) \qquad (16)$$

The r value is about 4%, ratio I_2/I_1 is about 0.5..2, $p_2 - p_1$ is about dynamic pressure. This estimation shows that the pressure measurement error related to dynamic pressure can be about 2−8%, and model components must be painted and tested separately.

2.3.2. Model displacement and deformation.
Model displacement and deformation create additional pressure measurement error. The error may be subdivided into two constituents:
1. Error determined by the necessity of comparison of images, registered with and without air flow. The intensity distribution of excitation light varies with deformations of the model and mechanical stand. Moreover, as the image of the model is shifted along the photo detector, then there is some sensitivity discrepancy over the cathode surface.
2. Error determined by the necessary identification process of deformed surface points.
Let model, which surface is described by $Z(x,y)$ function, is illuminated by point light source located point R_s, which has axial intensity distribution $I(0)$. Model surface illuminance distribution may be represented as:

$$J_{ex}(r_z) = I(0)\cos(\psi)/|R|^2 \qquad (17)$$

where: $\cos(\psi) = (Rn)/(|R||n|)$, $R = R_s - r_z$, $r_z = (x,y,Z(x,y))$ − radius vector of point on the model surface, $n=(n_x,n_y,n_z)$ − normal vector at R point, and $\cos(0) = (R_s R)/(|R_s||R|)$. Objective lens accomplishes the projective transformation of the luminescent intensity distribution, proportional to $J(r_z)$, on the model surface into luminescent intensity $J(x',y')$ on the photo detector surface. After photo electric conversion, the output signal $U(x',y')$ may be represented as:

$$U(x',y') = K_{CCD}(x',y')J(x',y') \qquad (18)$$

where $K_{CCD}(x,y) =$ function, circumscribing signal conversion by photodetector

Spatial irregularity of the output signal is mainly governed by the model geometry (ψ angle), by the intensity distribution $I(0)$ of the light source , by a distance length R between light source and model, by unevenness of LPS layer on the model surface and by the $K_{CCD}(x',y')$ function. Clearly it is impossible to provide a uniform signal if the surface of the model is quite curvilinear (i.e., at great variations of ψ angle) when one uses single a point source of light. Finally, it is necessary to compensate the $K_{CCD}(x',y')$ function irregularity.

Assume model shifting for some reasons, e.g., due to the aerodynamic loads. Let $d = (d_x, d_y, d_z)$ − the linear displacements vector of surface points. R−direction component of d vector, $d_r = (Rd)/|R|$ changes the distance from the model to the source of light and, hence, the luminescent intensity level by the value:

$$\Delta J/J = -2d_r/|R|. \qquad (19)$$

This is the source of pressure measuring error − − measured pressure is a ratio function of luminescence intensity "before test" − no loads effect, and "during test" − the loads and displacements are

present. When the model undergoes only parallel displacement and

$$d_x \ll s_x, \quad d_y \ll s_y,$$

$(s_x, s_y$ — characteristic scale factors of illuminance irregularity in x, y directions), one can determine d_r and consequently the relative intensity increment with the help of "before test" and "during test" model or LRM dimensions measurement.

Lets consider image plane component of displacement, i.e. $d_{xy} = (d_x, d_y)$ vector. The photo detector output signal "during test" is described by:

$$U(x',y') = K_{CCD}(x',y')J(x'+\mu d_x, y'+\mu d_y),$$

where μ — image scale factor. Therefore, contribution to relative intensity is:

$$\Delta J/J = \mu(d_{xy} \text{grad}J)/J. \tag{20}$$

The contributed value may be substantial even when $|d_{xy}|$ value is small, but there is huge luminescence intensity gradients. For the determination of the above mentioned relative intensity it is necessary to match the image taken "before test" with one taken "during test":

$$U_d(x',y') = K_{CCD}(x'-\mu d_x, y'-\mu d_y)J_1(x',y'),$$

here $J_1(x,y) = J(x+\mu d_x, y+\mu d_y)$, but this is the case when irregularity of video detector conversion coefficient yields additional error:

$$\Delta J/J = -\mu(d_{xy}\text{grad}K_{CCD})/K. \tag{21}$$

2.3.3. Influence of the temperature variation on the model surface.

Temperature response of PSP is additional source of the measurement error. Usually, a model temperature before test differs from the temperature distribution during the wind tunnel run. PSP temperature before test is the model temperature and this temperature can be measured. In the flow the PSP temperature approximately corresponds to local recovery temperature on the model surface especially then PSP is applied to the intermediate screen layer. The recovery temperature can be estimated from the pressure distribution field with a some assumption about a boundary layer state. Due to the comparatively low temperature sensitivity coefficients of our LPSs the requirements to the accuracy of this estimation are not very high. The recovery temperature T_w on a flat adiabatic wall can be used for the first iteration:

$$T_w = T_0 \frac{1 + (\kappa - 1)rM^2/2}{1 + (\kappa - 1)M^2/2}, \tag{22}$$

where: T_0 — —flow stagnation temperature,

M — local Mach number on outer boundary of the boundary layer, estimated from local pressure coefficient.

r — recovery coefficient.

These estimations show what temperature variations on the model surface are about $6-8^\circ C$ for transonic flows. Temperature field T_w is used for recalculation of the pressure field. Application of this procedure increase data processing time but can reduce temperature contribution to the pressure measurement error up 0.1 − 0.3%.

2.3.4. Dusting of the model surface

There is a dust in the air flow, what sediments on the model surface during the run. Dust layer absorbs the excitation and luminescent light and increase the measurement error. A dusting rate varies during the run with the maximums just after the beginning of the wind tunnel run and after the stop. The dust layer is non uniform especially on a leading edge zone or zones under a vortex flow. It is worth mentioned what dust in

a wind tunnel carries the large amount of ferroxides and hydroferroxides and has brown color. Absorption and scattering are wavelength dependent with minimum in a red spectral region.
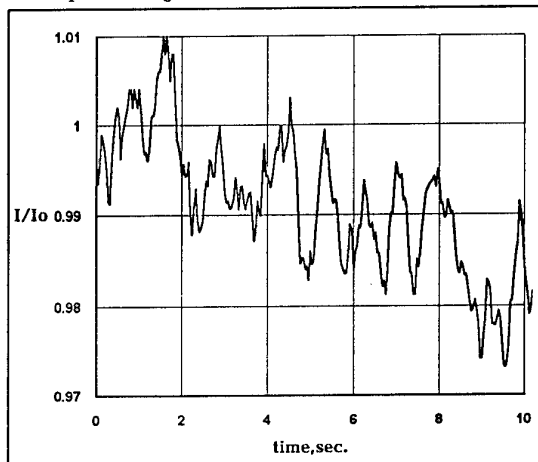
Figure 5. Dusting of the model surface.

Figure 5 shows the dusting process — normalized luminescence output of LPS L2 as function of time, in some region near the wing leading edge during T− 128 wind tunnel run.

The influence of the dust can be diminished by more frequent reference image acquisition. LRM, fabricated from the same bending polymer as pressure sensitive paint, reveals the same dusting properties, but can be used only for large scale compensation due to limited number of the marks.

2.3.5. Light scattering in an air flow.

Light scattering in the air flow takes place on the turbulent density pulsation's and on an aerosol. The main source of aerosol in a wind tunnel is a water vapor condensation. The density of the water vapor at supersonic flow regimes or in the vortexes can be large enough to obscure the model and to stop measurements.

The LRM at low vapor densities can slightly compensate this effect.

An air drain or air heating is desirable to prevent condensation. Wind tunnel must be equipped with an optical system for condensation diagnostics.

3. Prospects of PSP Method development
3.1. PSP improvement.

By our opinion the next generation of PSP will be two colours luminescent paint, one color component − pressure sensitive, the second − luminescent reference marks spread evenly over the surface. The perspectives of two colour PSP are discussed in the work [18]. The main requirement to the two colors PSP is constant intensity ratio of two luminescent components at fixed pressure and temperature levels for all points on the painted surface. The relative intensity field is obtained from the images simultaneously acquired at two wavelength ranges. The influence of illumination unevenly and non stability, the model deformation and displacement can be excluded in this case. The dust and scattering influence reduced only partly due to wavelength dependency of the absorption coefficients.

There are some disadvantages of two colors PSP, in particular oil, water, photo distraction lead to degradation of the paint, but degradation of each color component will differ.

Luminescence Pressure Sensors with the measurement and reference luminescent components, having resembling in light spectrum, but different in decay times, are more perspective. The dust and light scattering influence in these compositions will be totally compensated.

In the work [18] an idea of three components luminescent sensor was suggested. The third color channel is exclusively temperature sensitive and the problem of the temperature field evaluation can be solved. By our opinion this idea is practically non realizable due too large (factor $10-100$) lost in luminescence output. The main difficulties in work out of the three colors' sensors, is suppression of the inter channel influence and attainment of uniformity in the luminescence output ratios between channels.

3.2. Decay time measurements.

The more promising direction of the PSP technology development is transfer from the luminescence intensity measurements to the evaluation of the luminescence decay time. The decay time τ is governed only by quencher pressure and temperature:

$$\tau = \frac{\tau_0(T)}{1+C(T)P},$$ (21)

where: τ — decay time in the absence of the quencher,
$C(T)$ — some temperature dependent constant.
The temperature can be measured with the help of the second luminophore, without pressure sensitivity. These luminophores can be embedded in a single polymer matrix, or be implanted in the different layers. The luminescence channels can be separated by absorption or luminescence spectrums, or, by time, if luminophore decay times differ significantly.

Our first experience of practical wind tunnel application of PSP method was related with measurements of luminophore decay time. A model surface painted with appropriate paint was scanned in a single line along the model axis with a laser beam. Laser output was synchronized with a triggered photo multiplier to avoid photo multiplier saturation during laser pulse. Decay signal from photo multiplier was digitized and processed in the computer controlled system. The results obtained were in good agreement with the digitally evaluated pressure field. The future progress of decay time measurements' method is hold down by difficulties met in development of the measurement system.

4. Application field evaluation.

Initial experience of wind tunnel application of the Pressure Sensitive Paint method in TsAGI was obtained in transonic and supersonic wind tunnels: T−112 with test section dimensions 0.6·0.6 m, T−106 − − test section diameter 2.3 m, T−128 with test section dimensions 2.4·2.4 m. The models tested were: aircraft models−4 types, wing models −3 types, wing with winglet model, space shuttle model, etc. Discrepancy in C_p values was about $3-5\%$ for flows with Mach number $0.6-1.5$. The main sources of errors were attributed to low signal to noise ratio and stability of intensified CCD cameras used, the model dusting and uncompensated influence of the model deformations and displacements. Usually we have not any problems with the calibration parameters and stability of the paint itself. Summarizing the estimations of the errors, previously mentioned, one can say that the accuracy obtained corresponds them.

All PSP users found much value in the flow visualization provided by PSP method [9,12,13,20]. This application can be done by using comparatively inexpensive acquisition system, including intensified CCD camera coupled throw a frame grabber with the personal computer. Real time or near real time presentation (depend on efficiency of the frame grabber) gives one possibility to visualize very small pressure disturbances, a vortex flow near the surface, the shock wave position and the low frequency oscillations. Digital image processing procedures, including normalizing, spatial filtering, etc., improves the quality of these images and gives additional information. While studying flow around wing−winglet configuration [20], shock wave oscillations were noticed and power spectrum analysis applied to the data series, obtained from the successive video frames, resolved the oscillation frequency about 1 Hz
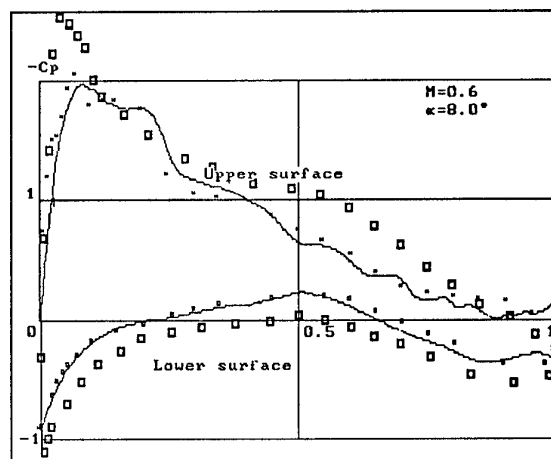
Figure 6. Pressure Distributions on the Profile GAW−1, obtained be OPM−solid lines, taps−×, ■, and panel method−□.

An information fullness of the OPM method may be more when the numerical methods' results used. For instance, the pressure field visualization does not give information about flow velocity vector on the body that may result in wrong interpretation of experimental results. Besides the OPM method does not give space flow pattern that is important for investigation of the flow and body interaction. The numerical results may be used for the prediction of the boundary layer separation. The example of the numerical method using for the interpretation of the OPM experimental data and standard pressure tap technique is shown on the Figure 6. In that case the profile model with the aspect ratio $\lambda=5$, angle of attack $\alpha=8°$, M=0.6 and the GAW−1 profile was tested into T−106 wing tunnel of TsAGI. The numerical data was made by "SPRUT" panel program for inviscid flow with the correction by Prandtl Glauert formula for compressible gas. The comparison of numerical results without separation of the boundary layer and the experimental data shows the separation of the boundary layer on the upper surface of the model, that makes the difference of pressure at the trailing edge, besides the pressure distributions for the upper and down surfaces were moved to each other and the lift force was decreased. In that experiment the separation of boundary layer was predicted before the experiment by using of the numerical inviscid flow data and the numerical method of calculation of the boundary layer separation. The numerical calculation information is necessary to complete the OPM experimental data.
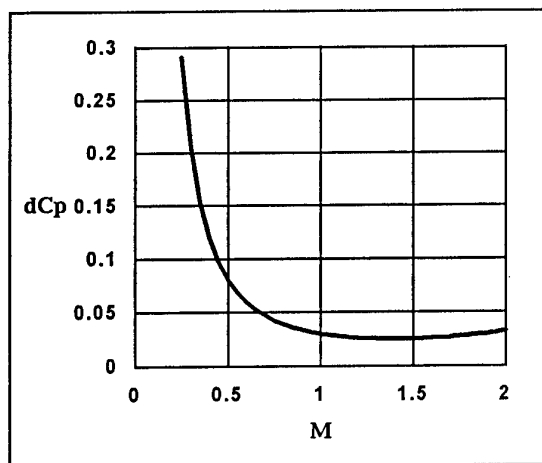
Figure 7. Error dC_p of pressure coefficient measurement with LPS L2. $(P_0=1Bar, \delta P=1\%)$

As mentioned above, up to date accuracy of the pressure measurements due to paint limitations, noise, uncompensated model displacement, dusting, etc., can not be better than 1% (relative standard pressure). One percent in the pressure measurement error for the PSP formulations governed by Stern— Volmer equation leads to the dynamic pressure measurement error shown on the plot (Figure 7) as Mach number function. Really, our PSP are suitable only for transonic and supersonic Mach number ranges. In this range, for one point measurement PSP accuracy approximately 3—10 times worse than standard pressure taps. The main OPM advantages are: the amount of information—up to 100000 or larger pressure measurement points, the remote measurements, time resolution—up to 0.005 sec, the cost of the model. Figure 8 demonstrates time resolution posibilities of OPM — the pressure distribution field obtained on the model in the shock tube.
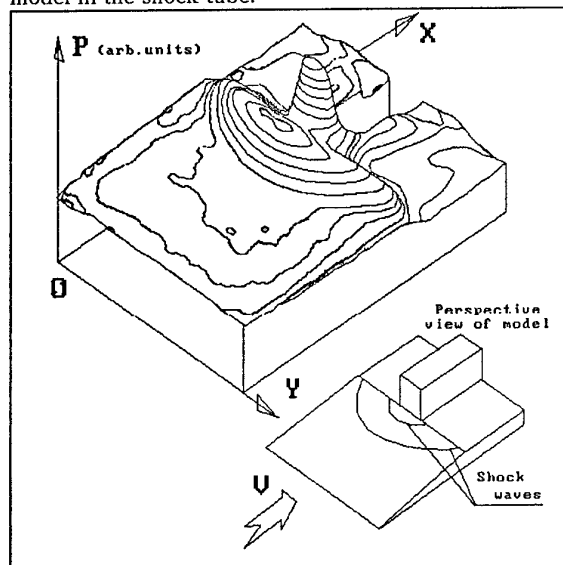
Figure 8. Pressure Distribution on the model in the Shock Tube. (M=8).

Another significant OPM application is calculation of the loads acting on the model elements. The plot on Figure 9 shows comparison of normal forces acting on a canard, measured by the internal balance system and calculated from pressure distributions for

upper and lower surfaces of the model wings covered by PSP.
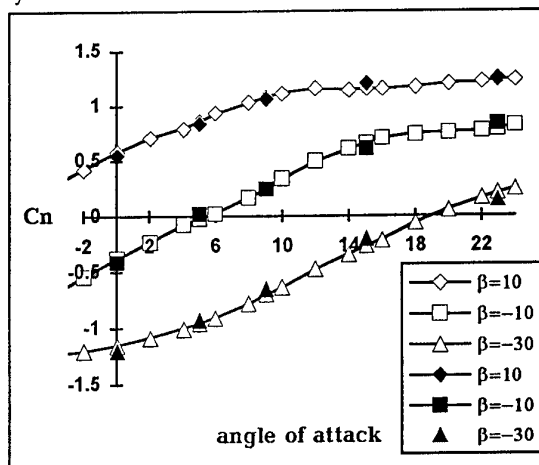
Figure 9. Comparison of C_n, obtained with OPM (black markers) and internal balance system, on canard at different deflection angles β.

Conclusion.

Pressure distribution field shows the physical nature and details of the flow, aircraft designer is more interested in integral loads on specific components of the model especially on the earlier stages of an airplane design and choice of the optimal aerodynamic arrangements. These two directions, by our opinion, define the main application fields of the Pressure Sensitive Paint.

References.

1. Peterson J.I.,and Fritzgerald V.F. "New Technique of surface flow visuslization based on oxygen quenching of Fluorescence", Rev. Sci. Instrum.,Vol.51(5),May 1980, pp.670—671.

2. Первушин Г.Е.,Невский Л.Б. "Состав для индикаторного покрытия (его варианты)." Авторское свидетельство СССР СУ 1065452 А, приоритет 09.10.81.

3. Ардашева М.М., Невский Л.Б., Первушин Г.Е. "Методика визуализации распределения давления по поверхности модели с использованием органических люминофоров." Сб. докладов на 3—й Всесоюзной школе по методам аэрофизических исследований. 1982г., с.103—107.

4. Ардашева М.М., Невский Л.Б., Первушин Г.Е. "Методика измерения распределения давления с помощью индикаторного покрытия.", ПМТФ, N4, 1985.

5. Мошаров В.Е., Орлов А.А., Петунин А.Н., Радченко В.Н., Розанов Н.Н., Талыков В.В., Фонов С.Д., Чикин И.И. "Люминесцентное покрытие для исследования распределения давления на поверхности моделей в аэродинамических трубах." Труды ЦИАМ, N1232, 1988.

6. Мошаров В.Е., Орлов А.А., Петунин А.Н., Радченко В.Н., Фонов С.Д., "Применение люминесцентых преобразователей давления (ЛПД) в аэродинамическом эксперименте." Труды ЦИАМ, N1258, 1989.

7. Kavandi J., Callis J., Gouterman M., Khalil G., Wright D., Green E., Burns D., McLachlan B. "Luminescent Barometry in Wind Tunnels.", Rev. Sci. Instruments, 61(11), pp. 3340—3347, November 1990.,

8. Crowder J.P. "Flow Visualization In Flight Testing" AIAA 90−1273, 5th Biannual Flight test Conference, May 22−24, 1990/Ontario, CA,

9.Kavandi J.L.,Crowder J.P. "Pressure Indicating Paint for Aerodynamic Surface Pressure Measurements", AIAA 90−1516, June 1990.,

10.Gouterman M., Callis J., Burns D.,Kavandi J., Gallery J., Khalil G., Green E., McLachlan B., Crowder J.,"Luminescence Imaging for Aerodynamic Testing.", Proceedings of the ONR/NASA Workshop on Quantitative Flow Vizualization, Purdue University,

11. Vollan A., Alati L., "A New Optical Pressure Measurement System", 14th ICIASF Congress, October 27−31,1991, Rockville, MD.,

12. Engler R. H., Hartmann K.,Schulze B. "Aerodynamic Assessment of an Optical Pressure Measurement System (OPMS) by Comparison with Conventional Pressure Measurements in High Speed Wind Tunnel",, 14th ICIASF Congress, October 27−31,1991, Rockville, MD.,

13. Morris M.J., Donovan J.F., Kegelman J.T., Schwab S.D., Levy R.L., Crites R.C. "Aerodynamic Applications of Pressure−Sensitive Paint." AIAA 90−0264, Jan. 1992.,

14. Troyanovsky I., Sadovskii N., Kuzmin M., Mosharov V., Orlov A., Radchenko V., Phonov S. "Set of Luminescence Pressure Sensors−LIPS for Aerospace Research.", 1st European conference on optical chemical sensors and biosensors, Graz, Austria 12−15 April 1992.,

15. Bukov A.P., Orlov A.A., Mosharov V.E., Pesetsky V.A., Sorokin A.V., Phonov S.D., Alaty L., Colucci V. "Application of Luminescence Quenching for Pressure Field Measurements on the Model Surface in a Wind Tunnel", conference "Wind Tunnels and Wind Tunnel Testing Techniques", Sauth Hempton, September 1992.,

16. Crites R.C., Benne M.E., Morris M.J., Donovan J.F. "Optical Surface Pressure Measurements: Initial Experience in the MCAIR PSTWT",conference "Wind Tunnels and Wind Tunnel Testing Techniques", Sauth Hempton, September 1992.,

17. Andreev A.O., Bykov A.P., Ipatov M.W., Kabin S.V., Nushtaev P.D., Orlov A.A., Mosharov V.E., Radchenko V.N., Pesetsky V.K., Phonov S.D., "Pressure Fields Investigation by LPS Technology on the Aerospacecraft Model" Preprint TsAGI N ,1993. Submitted "Journal de Physics III".

18. Donovan J.F., Morris M.J., Pal A., Benne M.E., and Crites R.S. "Data analysis Techniques for Pressure and Temperature−Sensitive Paint", AIAA 93−0176, 1993.

19. Morris M.J., Benne M.E. Crites R.S., Donovan J.F.,"Aerodynamic Measurements Based on Photoluminescence", AIAA 93−0175, 1993.

20. .Lifshitz Yu., Morozov A., Orlov A., Pesetzki V.,.Phonov S., Radchenko V. "A study of transonic wing−winglet flow with Light Intensity Pressure Sensors" Preprint TsAGI N78.,1993.

The traditional and new methods of accounting for the factors distorting the flow over a model in large transonic wind tunnels

V.M.Neyland

Deputy director of aerodynamics department

TsAGI

140160 Zhukovsky Moscow region

Russia

ABSTRACT

The report presents a brief review of the investigation methods and results obtained for the key problems of the test procedure in the industrial sub- and transonic TSAGI wind tunnels. Among these are the flow calibration in "empty wind tunnels", the wall interference minimization, the interference with supporting devices. These problems can be solved only in the combination of the calculation and theoretical investigations with the tests carried out first in pilot facilities and then in large wind tunnels.

As examples are given the results of the flow calibration both in the conventional conditions of a uniform test section flow and in a flow with the side wall boundary layer suction which is typical for two-dimensional model tests.

The flow boundary influence is investigated by the calculation and experimental method of corrections which works well at angles of attack up to 50° at M = 0.9. Good results are also obtained owing to the application of the adaptive perforation to reduce the wall interference on a large-scale civil plane model (blockage is 3.16%).

The introduction of corrections for the sting-induced flow distortion over the model afterbody is discussed shortly.

1. INTRODUCTION

The Central Aerohydrodynamic Institute (TSAGI), the greatest world aeronautical research center, possesses more than 60 aerodynamic facilities [1]. The present report is based mainly on the results of the methodical investigations carried out in the T-128 wind tunnel and partly in the T-106 wind tunnel.

The T-128 wind tunnel is in essence a great research complex combining five removable test sections of different destinations in one wind tunnel. This wind tunnel shown schematically in Fig.1 is a closed-circuit facility having a 2.75x2.75x7.2m test section and a compressor driven by a 100Mwt motor. The wind tunnel circuit pressure can be increased up to 4atm, as a result the characteristic Re number can obtain 12×10^6. The dependence Re for the T-128 wind tunnel is compared with those for other similar facilities in Fig.2.

Five removable test sections are intended for:

- tests of three dimensional models on the sting (stationary and nonstationary)

- tests of half-models

- tests of 2-d models with the wake probing

- tests of aeroelastic and flutter models

- various flow visualizations (colour oil film, thermography, fast evaporation, pressure indicating films and so on).

One of the important peculiarities of the T-128 wind tunnel is the adaptive controlled wall perforation which serves to minimize the flow boundary interference.

2. FLOW CALIBRATION IN AN "EMPTY WIND TUNNEL"

In each new or modernized test section, the flow is calibrated before the beginning of tests. The purpose of these investigations is to provide a gradientless flow by varying those parameters as the wall perforation, the test section wall divergence angle. If the test section design does not allow an ideally uniform flow it is necessary to estimate its nonuniformity and to include it in the form of respective corrections.

The second purpose of the flow calibration is to set up a correspondence of the flow parameters along the wind tunnel axis in the model zone to those which are taken by the measuring system as nondisturbed flow parameters.

Along with the static characteristics, the fluctuation flow components are also measured during the flow

calibration (turbulent mass flow fluctuations and noise spectrum and level). Typical results of the flow calibration in the T-128 wind tunnel are given below.

Fig.3 presents a rake used to measure stationary wind tunnel flow field characteristics. The rake is fitted with static pressure probes and inclinometers that are calibrated in advance in a small wind tunnel to estimate the sensitivity coefficients. The rake can rotate about the longitudinal axis by 180° and move along the wind tunnel length, thus scanning the flow core.

It is easy to see that this rake is an expensive and sophisticated device whose development and adjustment has taken several years. Unfortunately, the high quality results of the flow field measurements by using this rake were not obtained. The matter is that the rake design must satisfy two mutually exclusive requirements: on the one hand, it must be sufficiently rigid so that the elastic deformation of the rake ends in the flow should not distort the local sidewash measurements; on the other hand, it must be sufficiently thin so that the rake profile should not produce the buoyancy force during the local static pressure measurements. As a result, it was possible to obtain only relative characteristics, i.e., the variation in the static pressure along the wind tunnel axis during the flow scanning, the pressure at the point where the rake motion initiates being taken as 0 (Fig.4). As far as the sidewash is concerned, only the data of the central probe that is subject to least deformations proved to be reliable (Fig.5).

Of interest are the results obtained during the measurements of turbulent fluctuations along the wind tunnel axis using a hot-wire anemometers(Fig.6) according to the technique of [2]. The fluctuation level increasing appreciably with ε did not return to the reference value $\varepsilon = 0.2\%$ at the end of the run. This mass flow fluctuation behaviour is found to correlate with the behaviour and fluctuations of the flow temperature (Fig.7). Therefore, it is assumed that the fluctuation hysteresis in Fig. 6 is related to the rise in the so-called entropic fluctuation mode caused in turn by the rise in the flow temperature field nonuniformity as the wind tunnel operation time increases and the difference in the temperatures of the air flow in the wind tunnel and the cooling fluid in the wind tunnel cooler increases.

Another interesting example of the flow field calibration in the test section N3 aimed at testing airfoils is considered below. The airfoil is placed horizontally between the side walls. The side wall boundary layer influence distorting the flow two-dimensionality is eliminated by the controlled boundary layer suction through the upstream perforated windows. In spite of relatively small mass flows of the gas being sucked the flow field turns out

to be rather sensitive to this distorting action. Bearing in mind the negative results of the rake application a thin static probe along the wind tunnel axis is chosen to investigate the static pressure fields in the model zone (Fig.8).

Fig.9 presents the static pressure distributions over the wind tunnel walls and the probe at different suction rates. It is seen that the flow pattern changes abruptly even at a small suction rate (K=1 corresponds to the elimination of 70% of δ^*).

The wavy pressure behavior is explained easily assuming that the sink lines with a uniform intensity lie on the places of the suction system windows. Then the pressure along the wind tunnel axis is described by the formula:

$$Cp(x) = - \frac{K\,H}{4\pi\,(X_1-X)} \ln \left| \frac{(X_2-X)^2+\frac{H^2}{4}}{(X_1-X)^2+\frac{H^2}{4}} \right| \quad (1)$$

Where H is test section width, X_1, X_2 - coordinates of suction area beginning and end.

It is easy to see that the behaviour of this curve shown by the solid line in Fig.9 coincides qualitatively with the test data. The difference in the region $X \geq 0.5$ is related to the perforated horizontal test section walls which violates the assumption on the flow two-dimensoniality underlying the relation (1).

When testing the airfoils in the flow field similar to that shown above it is necessary to introduce corrections to the M number.

3.FLOW BOUNDARY INFLUENCE

This problem plays an important role in the tests of both civil airplane models and military objects. In the first case, the main attention is paid to the reliability of the determination of the airplane drag in cruise. In the second case, the moment characteristics at high angles of attack prove to be critical. There is also a third class of vehicles sensitive to the boundary influence at M~1. They are every possible spacecraft starting as part of launcher systems. In this case, the climb and sonic speed loads are critical, and sometimes the possibility of putting spacecraft with payloads into an orbit depends on the accuracy of the determination of spacecraft component characteristics in ground facilities.

All above typical situations were investigated in detail at TSAGI; as a result, a complex approach to the solution of the wall interference problem has been developed [3]. For example, it is shown that by varying the wall perforation rate f from a very small value of the order of 1-2% to a maximum possible value f=18% (the T-128 wind tunnel design allows a real-time f variation) it is possible to cover the whole range of the boundary conditions from an

almost closed wall to an almost free jet. If the model characteristics with f variation then the model is sufficiently small and the interference-free flow takes place.

The "scatter" of the characteristics with respect to f indicates an appreciable wall influence on the flow over the model. In this case, two approaches are possible: the introduction of corrections (correctable case) and the application of the adaptive perforation (uncorrectable case). The method developed in the T-128 wind tunnel makes it possible to introduce corrections based on the linear subsonic theory but with taking account of real aerodynamic characteristics obtained experimentally. Thus, it is possible to correct even separated flows over models at high angles of attack.

Fig.10 presents an example of those corrections in the form of the dependence of the pitching moment of a modern fighter on α^o. Three upper curves correspond to the reference data obtained for three wall perforation ratios. Three lower curves present the same data but corrected for the wall interference. The essential coincidence of lower curves shows that the interference is eliminated for angles of attack up to $50°$. The increase in the random point scatter in the range of $40°$ is caused by the model vibration in the separated flow condition.

A similar example of the investigation of the flow boundary influence on the civil airplane model is shown in Fig.11 where the airfoil polars also obtained for different wall perforation ratios are presented. The greatest scatter here is 25 drag counts. The introduction of corrections reduces the scatter down to 12-13 drag counts, and the data for f=10% and 4% coincide practically at the level of the interference-free value of f. However, at f=2% and especially at f=0% the data are not corrected by only introducing the corrections for interference (uncorrectable case). The investigations show that in this case at a small wall perforation ratio a gradient flow field occurs due to the model-boundary layer interaction on the wind tunnel walls. After rather complicated calculations the corrections for this effect were also introduced. However, the results of the tests with closed walls at such high velocities are, as a rule, distorted and uncorrectable.

The case of the uncorrectable wall influence can often be remedied by applying the adaptive controlled wall perforation. The details of the development and application of this technology are presented in [3,4]. Recall only that the adaptation process consists in setting up a local wall perforation corresponding to the infinite flow conditions over the model. This correspondence is achieved by real-time iterations where the difference between the pressure measured on the test section walls and that predicted in the calculations of the flow over the given model in

an infinite atmosphere is used as a governing parameter.

The model for the calculations of far fields corresponding to the distance to the walls may be presented rather schematically which simplifies noticeably the problem. The classical scheme of matching the flow in the wind tunnel with an imaginary external infinite region is performed at the boundary of the potential flow core in the wind tunnel, i.e., the iteration process should include the influence of the wind tunnel walls boundary layer. The investigations show that at a relatively small wall perforation ratio (f=4÷6 %) the corrections for the wall boundary layer influence are not great. However, at f=10% this problem becomes serious.

As an example of the application of this technology, consider the results for a civil airplane halfmodel tested in the test section N2 of the T-128 wind tunnel. The flow blockage by the model is 3.16% which is much higher than that recommended for conventional facilities. In this case, the great model dimensions only improve the adaptation accuracy since a considerable level of the disturbed wall pressure that can be measured and controlled rather accurately. The model arrangement in the test section is shown in fig.12, where the rectangles indicate the controlled perforation sections and the dotted line denotes the line along which the pressure was checked. These tests are discussed in more detail in [5].

The results obtained in the course of the tests are given in Fig.13. Presented here are the pressure distribution on the upper wing surface at several sections. The dotted lines with a shadow region inside them show Cp with the scatter boundaries for a small geometrically similar model which were taken in this case as most close to the interference-free results. The dashed line corresponds to the pressure on the surface of a large model before the adaptation. The difference between these two cases is very great especially in the root and central wing parts. The distributions of Cp obtained after the adaptation are shown by the solid line that essentially coincides with Cp for a small model. The lower wing surface responds somewhat worse to the adaptation but as a whole the above data can be considered to be satisfactory.

Fig.14 shows the behaviour of the total characteristics corresponding to the above results. It should be noted that the adaptation to perforation was performed only for the polar branches with negative α where the curves C_L coincide appreciably for a great and a small model which can not be noticed for the right-hand polar part. The results obtained were verified by introducing the corrections for the wall interference according to the standard technique used in the T-128 wind tunnel. After that all curves in the left polar part coincided

while at $\alpha > 0$ the slope of the curve C_L for a small model remained noticeably less. The cause of this difference is being investigated by the specialists of TSAGI and the Boeing company, the latter being the customer of the tests carried out.

4. STING INFLUENCE

Most commomly used means of attaching models tested in subsonic wind tunnels are all possible stings. All they distort the flow over the afterbody and very often the model afterbody geometry itself. The introduction of corrections for these effects is a very cumbersome, expensive and not always successful measure. The only experimental approach used in these cases is the method of dummy sting which requires that the number of tests be doubled and at times even tripled. Along with the expensiveness, the disadvantage of this approach is that in the case of the slightest non-axiality of the model and the dummy sting the latter causes a considerably greater distorting action than the load-carrying sting imitated by the dummy sting.

For the analytical estimations of the sting influence an approach has been developed in TSAGI based on the linear subsonic theory. In some cases, this approach is effective. For example, Fig.15 compares the corrections ΔC_D determined by the method of dummy sting in the T-106 wind tunnel with the data calculated according to the above technique. The model was mounted on the wire suspension that in this case was a load-carrying one, and the dummy sting was attached by butt joint to the model face end on the non-load-carrying strut. A special measuring system checked the axiality of the model and the dummy sting. It should be noted that this dummy sting imitated the flow pattern over the external strain gage balance having very great dimensions. The considerable corrections ΔC_D due to this sting supported it. The calculated values show a reasonable agreement sufficient for first estimations in the cases when accurate measurements of the above corrections are not required.

In conclusion, the author wishes to thank the specialists of TSAGI A.P.Gorbushin, A.I.Ivanov, A.V.Semenov, O.K.Semenova, V.V.Troitsky, N.N.Khozyayenko for providing the materials for this review, as well as the Boeing and the British Aerospace companies for a kind permission to use the data obtained during the tests of their models in TSAGI.

REFERENCES

1. Neyland V.Ja.
   "Review of TSAGI Wind Tunnels."
   Proceeding of the International Conference on Wind Tunnels and Wind Tunnel Test Technique. 14 -17 September 1992, Southampton UK.

2. ElizarovaE.I., Ponomareva V.S., Troitzkij V.V. "Experimental Study of the Disturbances in the Boundary Layer and Flow Core in a Supersonic wind Tunnel at M = 2,3,4."
   Trudi TsAGI issue 1715, Moscow, 1975.

3. Neyland V.M., Semenov A.V., Semenova O.K., Glazkov S.A., Ivanov A.I., Khozyaenko N.N. "Testing Technique Features of the Experiments in the Wind Tunnel with Adaptive Perforated Walls."
   Preprint TSAGI N47, 1991.

4. Neyland V.M.
   "Adaptive Wall Wind Tunnels with Adjustable Permeability - Experience of Exploitation and Possibilities of Development."
   Proceedings of International Conference on Adaptive Wall Wind Tunnel Research and Wall Interference Corrections. 10-14 June 1991, Xian, Shuanxi, China.

5. Neyland V.M., Semenov A.V., Semenova O.K. "Operation of the Adaptive - Wall Wind Tunnel of TSAGI",
   Moscow. To be published in " Symposium on Aerodynamics and Aeroacoustics ". Chapter 9, 1993.

Re2 (mln)

12.0

9.0

6.0

3.0

Mach number

0.00 0.40 0.80 1.20 1.60 2.00

T-128
AEDC
SIMA
11:NASA
14:NASA
12:NASA
16:NASA
16:NASA
7:NASA
ONERCC
BOEING
CALSPAN
RAE
FFA
NLR
NAL

Fig.2 Re number referred to $0.1\sqrt{S_{fs}}$ versus M number

1. Refrigerator.
2. Pressure up and down inside the tunnel shell.
3. Compressor.
4. Deturbulising screens.
5. Subsonic nozzle.
6. Supersonic nozzle.
7. Test section.
8. Movable leaves.
9. Turning blades.
10. Honeycomb.
11. Settling chamber.
12. Hatch for test section change.
13. Section.
14. Blowing up.
15. Diffuser.
16. Protecting screens.

Fig.1 T-128 wind tunnel scheme
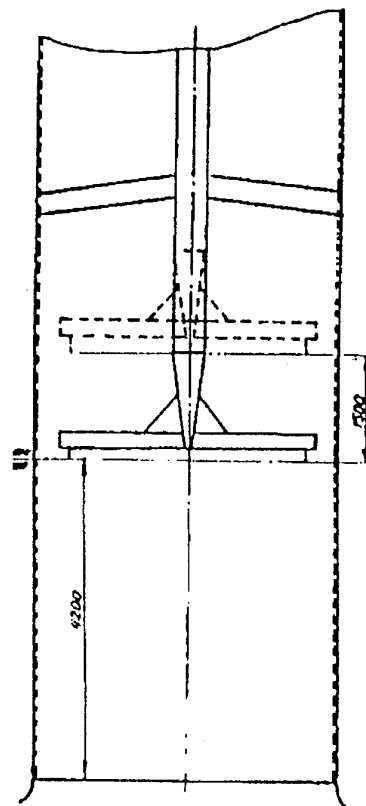
Fig.3 Flow calibration rake location in test section N 2 of T-128

PROT.7775 M=0.7

AL=0.5 F=STANDARD

PO=1 GAMMA=-90

dCp

Fig.4 Relative pressure gradient along X-axis (test section N 2)
Different markers mean different pressure probes on the rake span.
Arrow shows random scatter of data
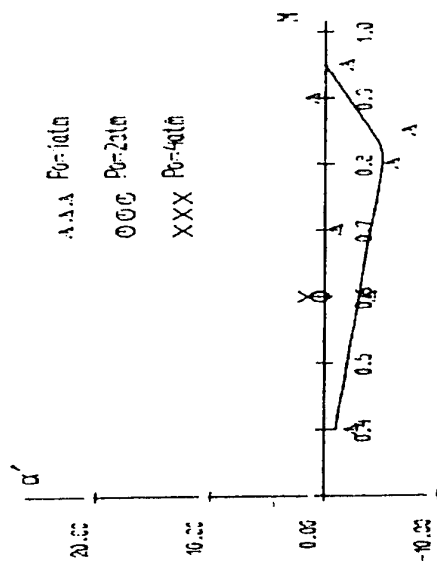
Fig.5 Flow upwash at the test section N 2
centerline

Fig.7b Total temperature fluctuations
corresponding to fig.6

Fig.7a Total temperature corresponding to fig.6

Fig.6 Mass flow fluctuation in test section
N 1 of T-128
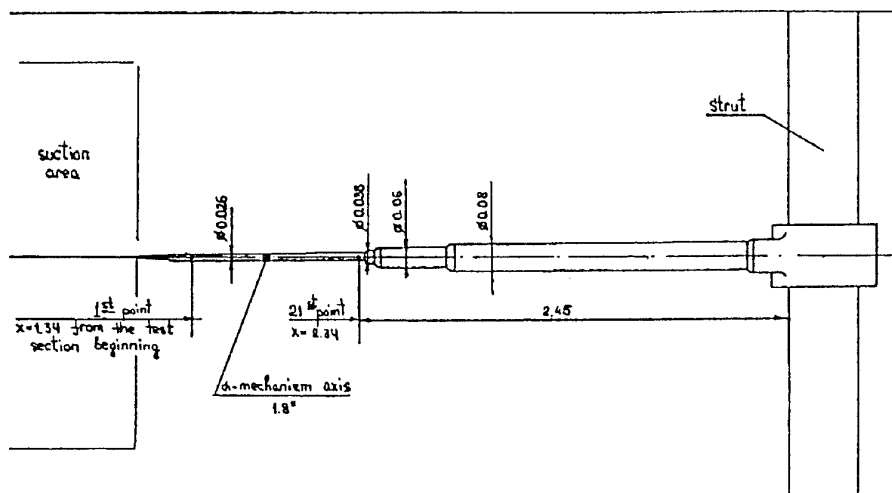
Fig.8 Static probe location in test section N 3
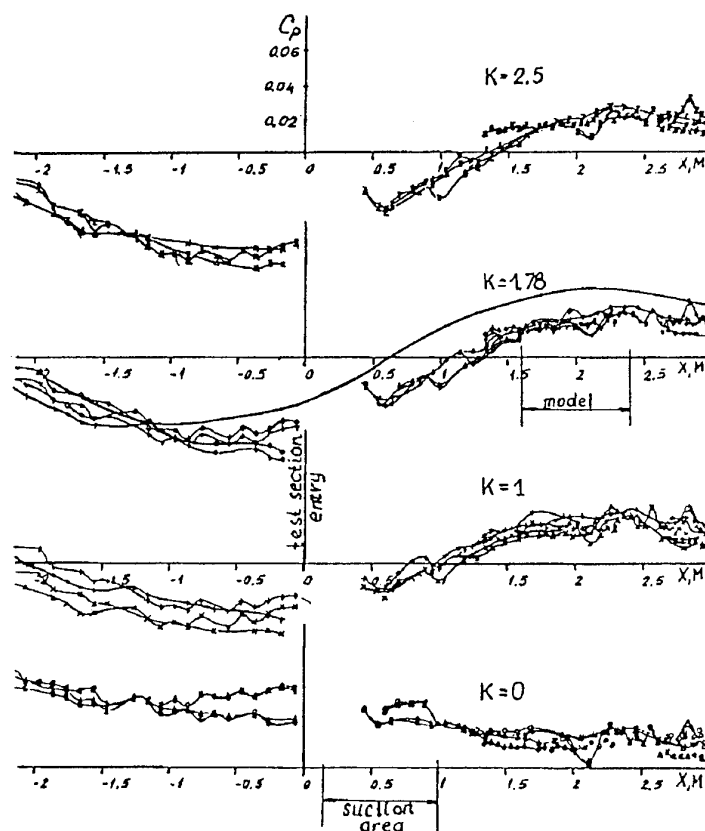
Fig.9 Pressure field in the "empty" test section N 3 with and without side wall boundary layer suction
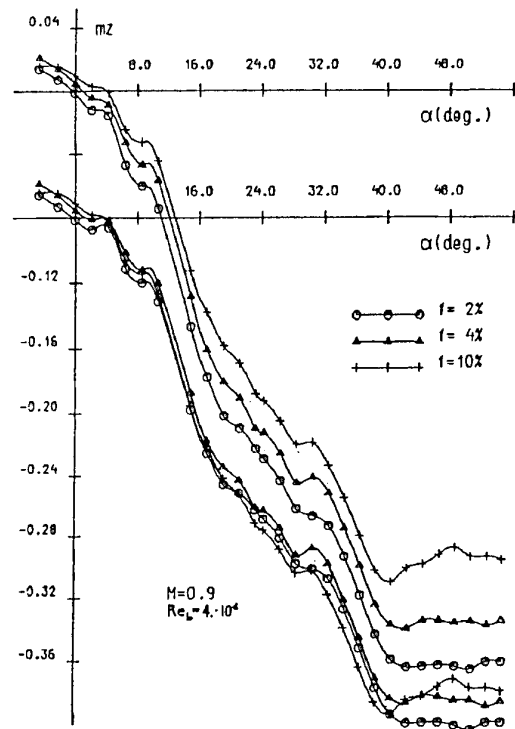
Fig.10 Pitch moment of modern fighter model
before and after corrections for wall
interference.
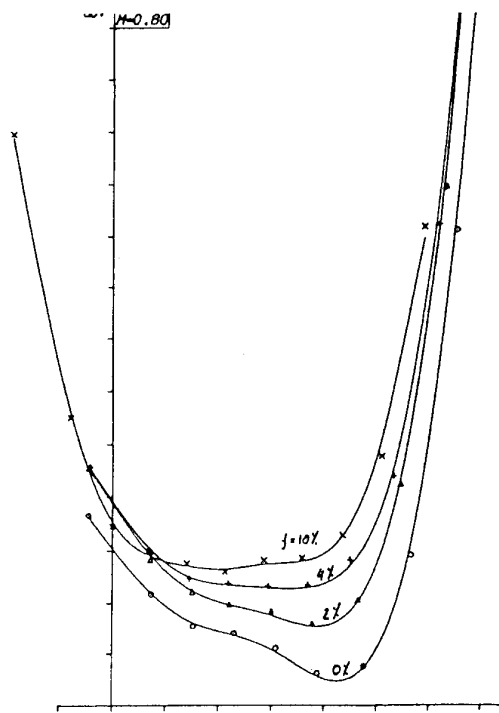
Fig.11a Drag polar of modern civil aircraft
model
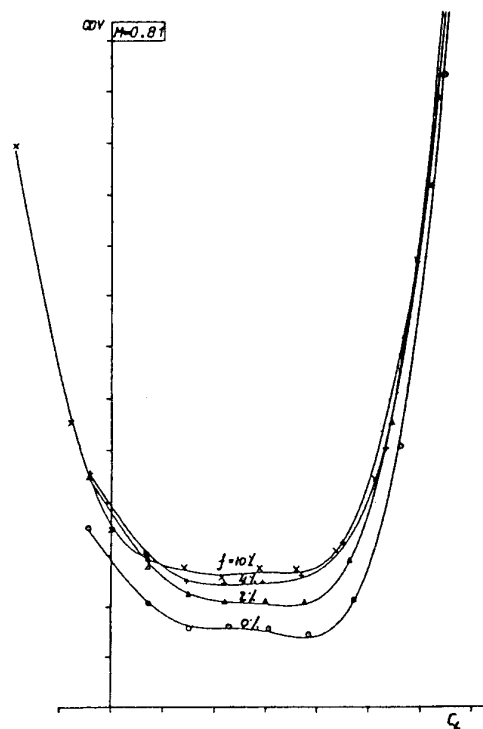
Fig.11b Drag polar of modern civil aircraft model
(with wall interference corrections)
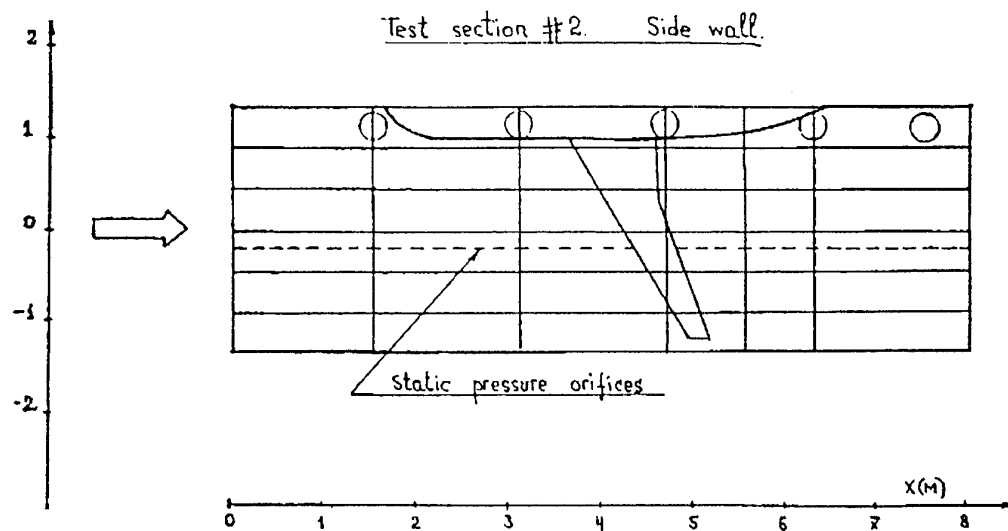
Fig.12 Half-model location in test section N 2 of T-128
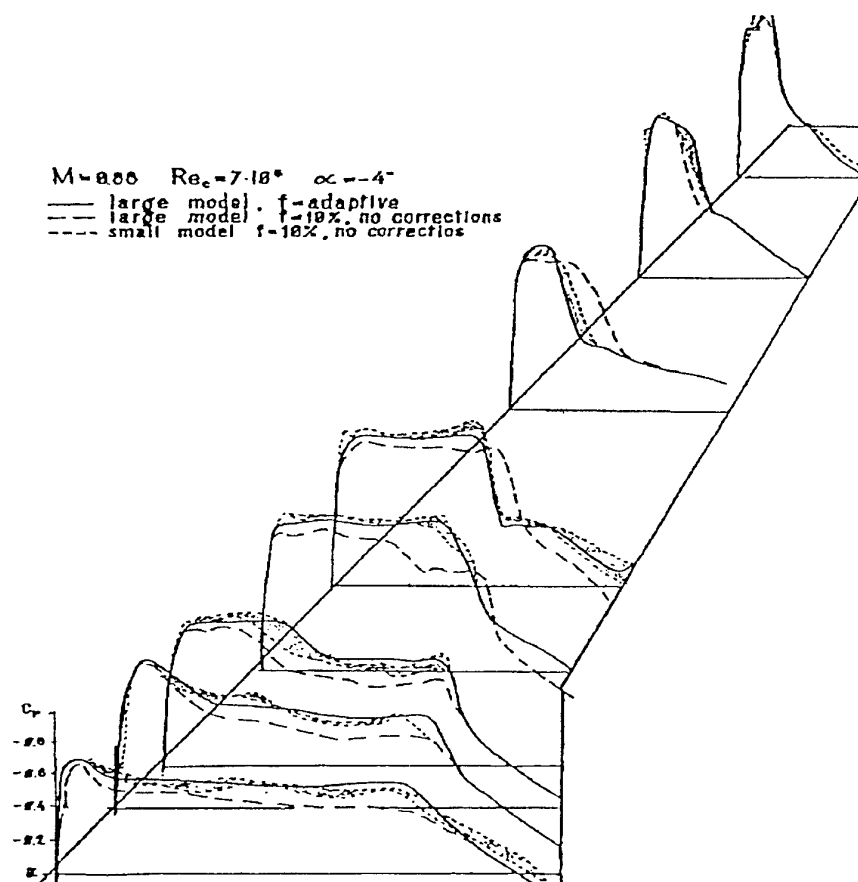
Fig.13 Pressure distribution over upper wing surface

Fig.15 Sting interference corrections (civil aircraft model)

Fig.14 Lift curve of two geometrically similar half-models.

EFFETS LATERAUX DANS UNE VEINE D'ESSAIS AUTOUR D'UN PROFIL D'AILE BIDIMENSIONNEL : ETUDES EXPERIMENTALE ET NUMERIQUE

J.P. ARCHAMBAUD, J.F. MICHONNEAU, A. MIGNOSI

Centre d'Etudes et de Recherches de Toulouse
Département d'Etudes et de Recherches en Aéro-Thermodynamique
avenue Edouard Belin 31055 TOULOUSE cedex
FRANCE

SUMMARY

Sidewall effects affect the pressure field around a 2D airfoil tested in wind tunnel, even on its central section. Firstly, laser measurement results show the 3D boundary condition near sidewalls. Then, another experimental investigation points out on the model the perturbation due to sidewall effects.

In the second part a numerical method is described (coupling between inviscid flow and sidewall boundary layer computations) which allows to take into account sidewall effects. Comparisons with experiments are shown. Finally, the numerical method is used to estimate the Mach number correction due to sidewall effects.

RESUME

Les effets latéraux affectent le champ de pression autour d'un profil d'aile bidimensionnel testé dans une soufflerie. D'abord, des mesures au laser montrent la condition tridimensionnelle imposée près des parois latérales. Puis une autre étude expérimentale met en évidence l'influence des effets latéraux sur le profil lui-même.

Dans la deuxième partie est décrite une méthode numérique (couplage entre calculs de fluide parfait et de couche limite latérale) prenant en compte les effets latéraux. Des comparaisons avec des résultats expérimentaux sont faites. Enfin, cette méthode numérique sert à estimer la correction du nombre de Mach due aux effets latéraux.

NOTATIONS

b,	largeur de la veine
c,	corde du profil.
C.L.L.,	Couche Limite Latérale.
C_Z,	coefficient de portance.
Cp,	coefficient de pression.
M_∞,	nombre de Mach infini.
M,	nombre de Mach local.
ΔM_∞,	correction du nombre de Mach infini.
X,	coordonnée longitudinale.
Y,	coordonnée transversale.
Z,	coordonnée verticale.
α,	angle d'incidence
δ^*,	épaisseur de déplacement tridimensionnelle (écoulements longitudinal + transversal)
δ_0^*,	épaisseur de déplacement tridimesionnelle dans la veine vide
2D,	bidimensionnel.
3D,	tridimensionnel.

1.   INTRODUCTION

Lors d'essais en soufflerie, l'écoulement entourant la maquette est perturbé par les interférences dues aux parois de la veine. Les interférences de parois sont plus ou moins intenses selon la géométrie relative veine-maquette et selon les conditions aérodynamiques de l'essai.

La minimisation des interférences de parois ou leur prise en compte est obligatoire pour assurer la précision attendue sur les résultats. L'adaptation des parois haute et basse (parois flexibles adaptées, poreuses ou à fentes) permet de s'affranchir d'une partie plus ou moins importante des interférences dues à ces deux frontières. Cette opération étant réalisée, les interférences produites par les parois latérales subsistent tout de même.

Les perturbations dues aux parois latérales peuvent être divisées en deux composantes : d'une part l'effet de convergence des parois latérales de la veine vide, dû au développement de couches limites sur celles-ci ; cette composante à caractère monodimensionnel peut être facilement corrigée par une divergence du même ordre de grandeur des parois latérales, ou même des parois haute et basse lorsqu'elles sont flexibles. D'autre part, ces Couches Limites Latérales (notées désormais C.L.L.) prennent un caractère tridimensionnel sous l'effet des gradients de pression dus à la présence de la maquette. Cette tridimensionnalité des C.L.L. est source de perturbations que nous appellerons désormais "Effets Latéraux", et dont l'étude constitue le sujet de cet article. Nous nous intéresserons uniquement au cas d'un profil d'aile bidimensionnel fixé aux parois latérales, cas dans lequel les effets latéraux sont très importants.

Cet article aborde d'abord la caractérisation expérimentale de ces perturbations, puis leur simulation numérique. La majorité du travail présenté ici a été réalisé dans le cadre d'une thèse de doctorat par Mr. Jean-François Michonneau [1] au sein d'une coopération avec le département de Mr. Stanewsky, au DLR Göttingen.

2.   EFFETS LATERAUX AUTOUR D'UN PROFIL D'AILE

Essayons de comprendre tout d'abord ce qui se passe sur la paroi latérale. La figure 1 schématise la géométrie tridimensionnelle de la C.L.L. autour de l'emplanture d'un profil d'aile, côté extrados uniquement, où les variations sont les plus importantes. La surface hachurée représente l'évolution de l'épaisseur de déplacement de la couche visqueuse. Sous l'effet de l'accélération de l'écoulement, en aval du bord d'attaque, la C.L.L. s'amincit. Puis, dans la zone d'interaction avec le choc, elle s'épaissit fortement, et cet épaississement se poursuit tout en devenant plus modéré. La cartographie de l'épaisseur de déplacement tridimensionnelle δ^* sur la paroi latérale présente donc, de l'amont vers l'aval, un creux suivi d'une bosse. D'autre part, cette géométrie creux-bosse s'étale sur une surface plus grande tout en diminuant d'intensité au fur et à mesure que l'on s'éloigne du profil, vers le haut de la paroi. Cette géométrie de la C.L.L. a donc un caractère très
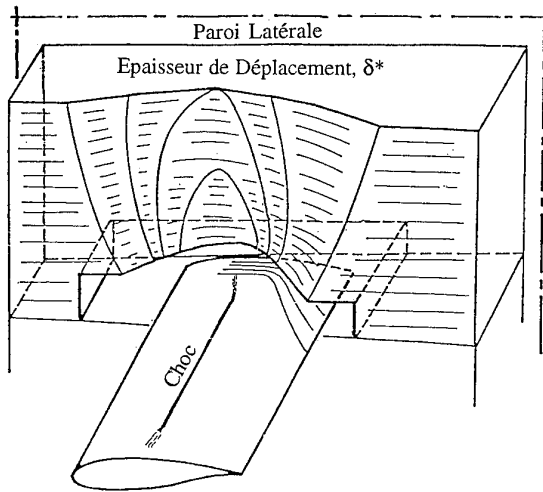
Fig.1 Cartographie de la couche limite latérale

tridimensionnel, qui joue le rôle de condition latérale pour le fluide parfait de la veine d'essai.

Il s'ensuit des variations de déviation du fluide et de largeur locale du canal. Ces perturbations latérales se propagent vers l'intérieur de la veine en diminuant d'intensité, mais cette propagation dépend de façon complexe du nombre de Mach local [2]. Dans ces conditions, si les effets latéraux sont importants, ils perturbent l'écoulement dans toute la veine d'essai ; s'ils sont moins sévères ou si la veine d'essai est large par rapport à la corde du profil, ils perturbent seulement les zones proches des parois latérales. Signalons tout de même que dans des veines de dimensions classiques, les effets latéraux "ne sont pas vus" de façon significative par les prises de pression des parois haute et basse comme l'ont montré deux essais spéciaux réalisés dans chacune des veines citées dans le chapitre suivant. Dans ces conditions, l'effet latéral n'est pas pris en compte par l'adaptation des parois haute et basse, hypothèse qui a été faite dans l'étude présente.

Dans tous les cas, la distribution de pression mesurée sur la section centrale du profil ne correspond pas obligatoirement aux conditions nominales de l'essai, nombre de Mach M_∞ et angle d'incidence α. D'où l'intérêt de prédire l'intensité des perturbations dues aux effets latéraux dans toute la veine d'essai, et si possible d'estimer leur influence en terme de correction du nombre de Mach et de l'angle d'incidence nominaux. Il faut pour cela bien caractériser expérimentalement les effets latéraux afin de valider ensuite une méthode numérique.

3. QUALIFICATION EXPERIMENTALE DES EFFETS LATERAUX

Deux séries d'essais ont permis de mettre en évidence les conditions latérales tridimensionnelles imposées par les C.L.L. et leur influence sur l'écoulement dans la veine et sur le profil lui-même.

3.1 ESSAIS EFFECTUES DANS LA SOUFFLERIE T2

La première série d'essais a été réalisée dans la soufflerie T2 du CERT/ONERA à Toulouse, en 1990 [3],[1]. Elle a consisté à qualifier l'écoulement entourant la maquette à l'aide d'un laser à 3 composantes.

3.1.1 Installation

La soufflerie T2 est de type circuit fermé [4], transsonique et cryogénique, fonctionnant par induction, par rafales de 2 minutes environ. La veine de cette soufflerie a 0,39 m de large, 0,37 m de haut et 1,40 m de long (fig.2). Les parois flexibles haute et basse sont adaptées à chaque essai [5], supprimant ainsi quasiment les interférences qu'elles induisent.

Les essais sont effectués à température ambiante, à la pression totale de 1,7 bars.

Les essais sont réalisés autour du profil supercritique OAT15A de l'ONERA. La maquette bidimensionnelle de 0,15 m de corde est montée entre deux hublots partiellement transparents. L'unique configuration aérodynamique étudiée dans le cadre des effets latéraux est définie par $M_\infty = 0,754$ et $\alpha = 1,15°$, correspondant à un écoulement transsonique avec un choc relativement fort sur le profil, mais sans décollement arrière.

Les trois composantes de la vitesse sont mesurées en diffusion avant à l'aide d'un laser argon 3D de puissance 5W [6], l'analyse des signaux étant faite par des appareils BSA (Burst Spectrum Analyser). Une mesure en un point de l'écoulement est le résultat de l'acquisition des signaux de 2000 particules (gouttelettes d'huile de diamètre 1 μm environ), réalisée en moins de 2 secondes. Trente à quarante points de mesures correspondants à autant de points de l'écoulement sont ainsi effectués en une même rafale. Des mesures sont réalisées suivant des droites orientées dans les trois directions, longitudinale, transversale et verticale, afin d'établir des cartes de vitesse suivant des droites et dans des plans, ainsi que des sondages de C.L.L..
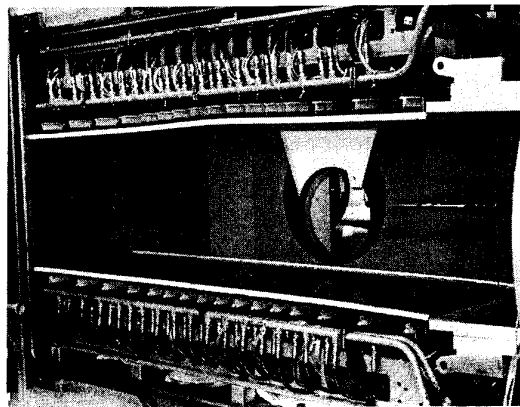
Fig.2 Veine de la soufflerie T2 (CERT/ONERA)

3.1.2 Résultats

L'ensemble des résultats de cette campagne est compilé dans la référence [3]. Nous nous contenterons ici de montrer deux des résultats les plus typiques.

Tout d'abord, des mesures de vitesse ont été réalisées dans un plan vertical, parallèle à la paroi latérale, et distant de cette paroi de 20 mm, soit légèrement supérieur à l'épaisseur moyenne de la C.L.L.. Ces sondages fournissent donc une vraie cartographie de la condition à la limite du fluide parfait. La figure 3 présente les vecteurs vitesses transversale et verticale mesurés suivant deux droites horizontales situées à Z=33 mm et 53 mm au dessus du profil. La courbe tracée en trait pointillé indique l'étendue de la poche supersonique. En décrivant la droite de sondage Z=33 mm dans le sens de l'écoulement, on observe tout d'abord des valeurs négatives de la composante transversale (dirigée vers la paroi latérale), c'est à dire un amincissement de la C.L.L.. Puis la composante transversale passe par une valeur nulle (minimum du creux de la C.L.L., au milieu de la zone supersonique). Plus en aval, la vitesse est dirigée vers le centre veine, correspondant à un épaississement de la C.L.L.. On observe les mêmes tendances sur la ligne supérieure (Z=53 mm), mais les évolutions sont moins marquées du fait de l'éloignement par rapport à la maquette. L'ensemble ici présenté, complété par des sondages de couche limite, qualifie assez bien la condition latérale tridimensionnelle en terme de déviation de fluide et de variation de la largeur locale de la veine.
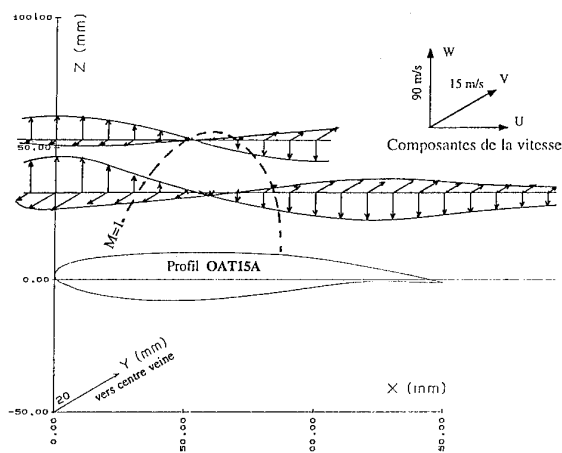
Fig.3   Vitesse transversale à 20 mm de la paroi latérale

La figure 4 présente les résultats de sondages laser dans un plan transversal coupant la veine d'essais à 40 mm en aval du bord de fuite du profil (25% de corde). Une différence essentielle apparaît dans l'écoulement secondaire, près de la paroi latérale, entre le canal supérieur (au dessus du sillage) et le canal inférieur. La composante transversale de la vitesse V est faible dans le canal supérieur alors qu'elle est importante sous le sillage qui apparaît comme une surface de discontinuité. D'autre part, dans le canal inférieur, la déviation transversale du fluide vers la paroi ne s'atténue que très progressivement vers le centre veine (Y=195 mm), qui n'a malheureusement pas pu être atteint à cause de l'accès optique réduit au niveau des hublots.
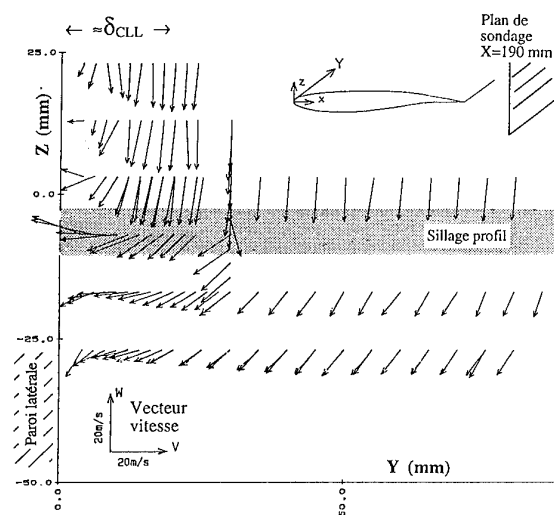
Fig.4   Vitesse transversale en aval du profil

Enfin, de fortes déviations vers la paroi apparaissent, très près de celle-ci.

3.2   ESSAIS EFFECTUES DANS LE LUDWIEG TUBE (DLR, Göttingen)

La deuxième série d'essais a été effectuée dans le tube à choc du DLR à Göttingen, plus connu sous le nom de Ludwieg Tube, ou KRG (KryoRohrwindkanal Göttingen) [7]. Ces essais ont principalement consisté à mesurer la distribution de pression sur plusieurs sections d'un profil.

3.2.1   Installation

Le Ludwieg Tube est une soufflerie transsonique et cryogénique, pressurisable jusqu'à 10 bars. La veine est alimentée en amont par un tube de stockage haute pression de 130 m de long et 0,8 m de diamètre. La veine d'essai a 0,4 m de large, 0,35 m de haut et 2 m de long. Les parois haute et basse sont planes et légèrement divergentes pour compenser l'effet d'encombrement des couches visqueuses. Dans ces conditions, les interférences de ces parois ne sont pas annulées et elles rendent l'écoulement entourant directement la maquette plus sensible au nombre de Mach et à l'angle d'incidence. La rafale dure environ 1 seconde et la partie utile n'excède pas 0,3 seconde.

La maquette utilisée est le profil supercritique CAST7 [8] (fig.5). Cette maquette a 0,15 m de corde et 1 m d'envergure. Elle peut être déplacée suivant l'envergure, entre deux rafales, afin d'amener une des deux sections de mesure à l'endroit désiré dans la veine.

La transition est déclenchée à 5% de corde sur les deux faces du profil, par une bande de caractères Letraset de 12 µm d'épaisseur. Les essais sont effectués à température ambiante et à deux bars de pression totale.
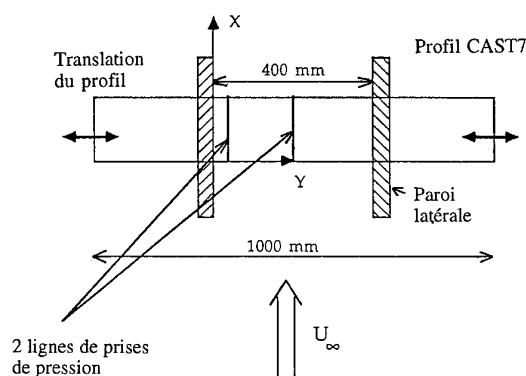
Fig.5   Montage du profil CAST7 dans le Ludwieg Tube

3.2.2   Résultats

De nombreux essais ont été effectués, pour différents angles d'incidence (α=-1°, 0°, 1°, et 2°), dans une large gamme de nombre de Mach (M_∞=0,40 0,475 0,52 0,57 0,65 0,70 0,75 0,78). Ces essais vont de cas subsoniques sans choc aux cas transsoniques avec décollement de la couche limite entre le choc et le bord de fuite, en passant par le cas transsonique sans décollement arrière.

La figure 6 présente les distributions de Cp relatives à M_∞=0,653 et α=-1°, pour différentes sections en envergure. On observe un net étagement des courbes : A l'extrados et sur la moitié amont de l'intrados, le niveau du nombre de Mach diminue au fur et à mesure que la section de prises de pression se rapproche de la paroi latérale. Cette évolution est déjà effective entre le centre de la veine (Y=200 mm) et le quart de l'envergure (Y=100 mm). Les deux sections situées à 20 mm et 10 mm de la paroi sont respectivement à la limite et dans la C.L.L..

La figure 7 présente une comparaison analogue des distributions de Cp sur les différentes sections dans un cas transsonique : M_∞=0,65 et α=2°. On retrouve le même étagement des courbes que celui décrit précédemment. De plus, le choc recule de façon très nette lorsque la section de mesure se rapproche de la paroi latérale (10% de corde) ; ce mouvement du choc semble être très sensible aux effets latéraux, et pourrait constituer un paramètre utile pour la caractérisation de ces effets. On remarquera que les différentes courbes se coupent approximativement en un même point, autant sur l'extrados (X/C=87%) que sur l'intrados (X/C=53%). Enfin, aucun décollement arrière n'est présent dans ce cas, si ce n'est sur les sections Y=20 mm et Y=10 mm qui se trouvent à la limite de la C.L.L. et dans celle-ci.
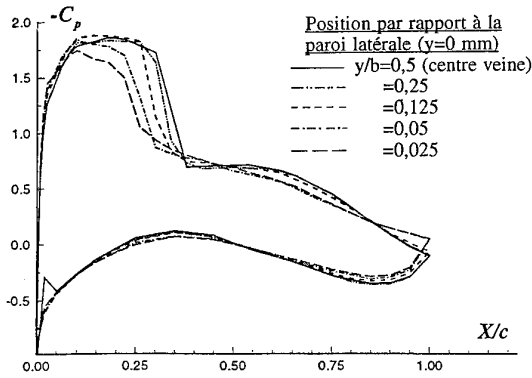
Fig.6 Distributions de pression sur le profil CAST7 - M_∞=0,653 et α= -1°
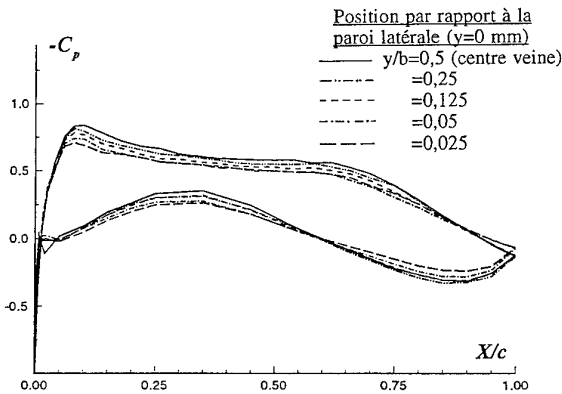
Fig.7 Distributions de pression sur le profil CAST7 - M_∞=0,650 et α= 2°
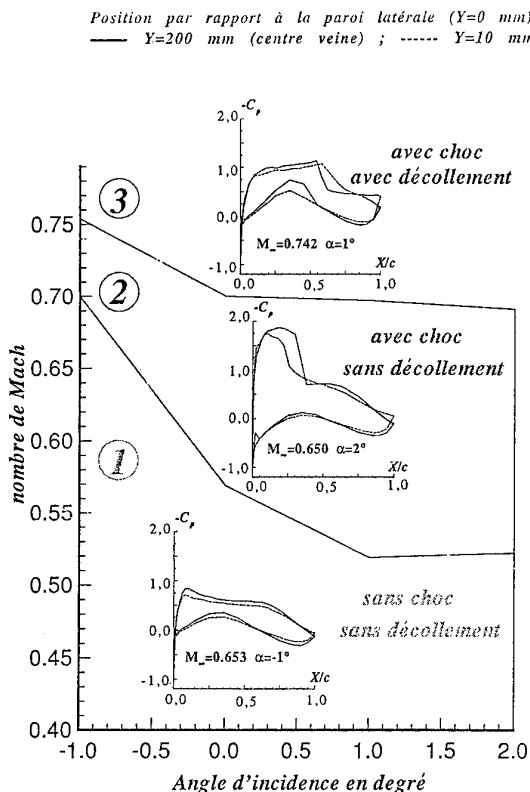
Fig.8 Classification des configurations d'essais

Après analyse de tous les essais effectués, les différentes configurations ont été classées en trois catégories, à partir de la distribution de pression à l'extrados (fig.8). La zone 1 correspond à des écoulements sans choc. La zone 2 comprend les cas avec choc mais sans écoulement de retour. La zone 3, relative à de fortes valeurs du nombre de Mach, rassemble les configurations avec choc et avec décollement arrière. On peut penser raisonnablement pouvoir corriger des effets latéraux les essais contenus dans les zones 1 et 2 seulement. La méthode de correction mise en œuvre pour cela va être décrite au chapitre 4.

4. METHODE NUMERIQUE DE PREDICTION DES EFFETS LATERAUX

Une méthode numérique [1] a été développée au CERT/ONERA afin de calculer l'écoulement entourant la maquette, en prenant en compte la géométrie réelle de la C.L.L. comme condition à la limite. Il s'agit d'un couplage entre deux méthodes tridimensionnelles de fluide parfait et de couche limite, qui converge en quelques itérations. La géométrie étudiée est toujours celle d'une aile bidimensionnelle fixée entre parois.

4.1 METHODE NUMERIQUE

La figure 9 présente l'organigramme de la méthode décrite. La première étape est celle d'un calcul de fluide parfait "bidimensionnel" ; les frontières latérales du maillage sont planes et parallèles, et ce calcul donne le même résultat en toute section. Ce résultat constitue le cas bidimensionnel de référence relatif aux conditions nominales M_∞ et α.

A partir de la distribution de pression obtenue par le calcul précédent sur les plans latéraux du maillage, la méthode de couche limite fournit la géométrie de la C.L.L., et notamment la cartographie de l'épaisseur de déplacement tridimensionnelle δ^* [9].

Les deux plans latéraux du maillage du calcul de fluide parfait sont alors déformés de l'épaisseur de déplacement δ^*, et un nouveau calcul de ce fluide parfait est réalisé, prenant en compte la géométrie latérale réelle. C'est le début de la deuxième itération.

Les calculs de fluide parfait et de couche limite s'enchaînent ainsi sur 4 ou 5 itérations (avec facteur de relaxation) avant de converger sur la définition d'un écoulement tridimensionnel, relatif aux conditions nominales M_∞ et α, mais qui tient compte des effets latéraux.
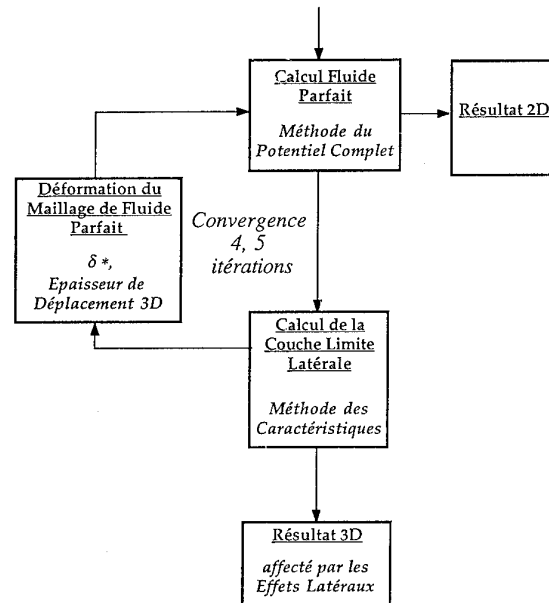
Fig.9 Organigramme de la méthode numérique

Après avoir décrit le déroulement du processus, mentionnons quelques explications supplémentaires.

• Le code de fluide parfait utilise une méthode de potentiel complet tridimensionnel [10], traité sous sa forme conservative par éléments finis. Le maillage, de type H (fig 10), reproduit l'allongement b/c du profil. Le nombre de mailles sur le profil a été optimisé de façon à observer des déplacements naturels du choc relatifs à de faibles variations du nombre de Mach infini ($\Delta M_\infty \approx 0,001$). En envergure, les mailles sont plus ressérées près des frontières latérales afin de bien schématiser ces zones qui sont le siège des perturbations.

• La couche limite latérale est calculée par une méthode des caractéristiques nommée 3C3D et originaire du CERT/ONERA [11]. La C.L.L. est considérée comme turbulente depuis la section d'entrée de veine. Le maillage utilisé est constitué par les centres des mailles du calcul fluide parfait, dont on ne considère que la frontière latérale (fig.11). Lors du calcul, certaines zones sont abandonnées lorsque la déviation des lignes de courant est trop forte ou le gradient de pression trop sévère. En conséquence, une étroite bande demeure non calculée autour de l'emplanture du profil, ainsi que le sillage qui la prolonge (fig 12 haut). En pratique, l'étroite bande non calculée est estimée à partir des zones qui l'entourent, et un nouveau calcul de couche limite est initialisé au niveau du bord de fuite du profil, calculant ainsi la zone correspondant au sillage. La couche limite est finalement connue sur toute la paroi latérale.

• En réalité, le couplage entre les deux méthodes s'effectue non pas avec l'épaisseur de déplacement tridimensionnelle $\delta^*(X,Z)$, mais avec la différence $\delta^*-\delta_0^*(X,Z)$, $\delta_0^*(X)$ correspondant à la veine vide. On ne prend ainsi en compte que les variations tridimensionnelles de la C.L.L., qui correspondent à la présence de la maquette. La figure 11 présente un exemple de cartographie de la variable $\delta^*-\delta_0^*$, sur laquelle on peut distinguer, côté extrados, un creux suivi d'une bosse, ainsi que la géométrie assez complexe du sillage.

• La prise en compte de la géométrie de la C.L.L. pour déformer le maillage du calcul de fluide parfait se fait progressivement, à l'aide d'un facteur de relaxation.

4.2 VALIDATION DE LA METHODE NUMERIQUE

Certaines comparaisons avec des résultats expérimentaux acquis à la soufflerie T2 (chapitre 3) ont permis de valider la méthode numérique.

Fig.12 Lignes de frottement calculées (haut) et visualisées expérimentalement (bas)

Fig.10 Maillage du calcul de fluide parfait

Fig.11 Maillage du calcul de couche limite
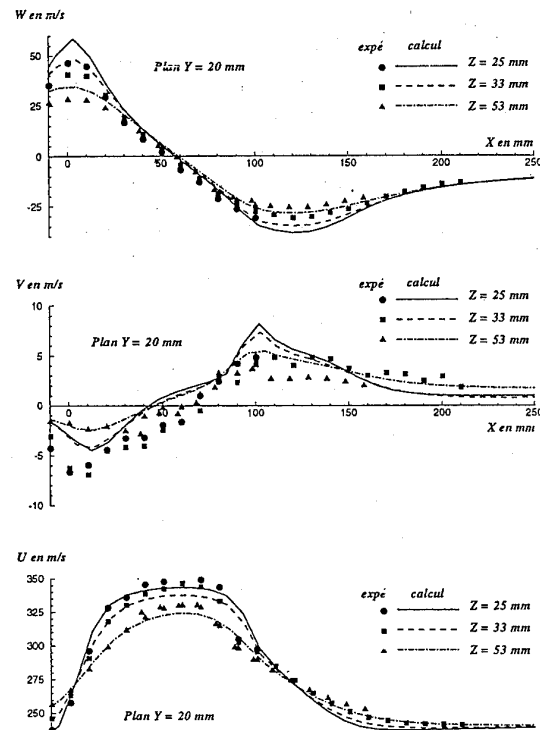
Fig.13 Comparaison calcul-expérience des composantes de la vitesse à Y=20 mm de la paroi latérale

La figure 12 montre la comparaison entre les lignes de frottement pariétal de la couche limite calculée par la méthode 3C3D et celles visualisées par bouillie sur la paroi latérale de la veine d'essai. On constate une grande similitude de forme, même dans les zones de forte évolution comme à l'extrados du profil, et dans le sillage où l'on retrouve par le calcul la forme typique en "queue de poisson".

La figure 13 présente une comparaison calcul-expérience fondée sur les trois composantes de la vitesse le long de trois droites longitudinales. Ces droites forment un plan vertical situé à Y=20 mm de la paroi latérale. Les mesures au laser des composantes de la vitesse constituent les données expérimentales. L'accord est satifaisant entre les évolutions calculées et mesurées, ce qui prouve que la méthode reproduit assez bien la tridimensionnalité de l'écoulement.

Une comparaison des écoulements secondaires dans un plan transversal situé en aval de la maquette montre que le calcul retrouve assez correctement les évolutions complexes des vecteurs vitesses mesurés (fig 14).
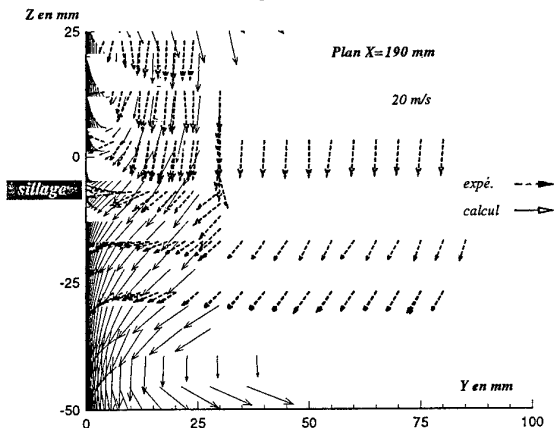
Fig.14   Comparaison calcul-expérience de la vitesse transversale en aval du profil

4.3   RESULTATS

La figure 15 (bas) présente le résultat de la méthode numérique dans un cas avec choc correspondant aux conditions suivantes : largeur de veine, b=0,4 m ; corde du profil CAST7, c=0,15 m ; b/c=2,67 ; M_∞=0,71 et α=2° ; ce cas est comparé sur la même figure (haut) au cas expérimental M_∞=0,69 et α=2°, qui possède une distribution de Cp analogue, notamment en position de choc. L'ajustement du nombre de Mach est nécessaire pour pallier les deux différences existantes entre calcul et expérience : le calcul ne tient pas compte de la couche limite sur le profil et l'expérience est réalisée entre parois solides non adaptées.

Le résultat calculé a été obtenu en quatre itérations. On constate que la méthode numérique prédit assez bien le gradient de pression suivant l'envergure, uniquement dû aux effets latéraux. Le choc se déplace vers le bord d'attaque et le niveau supersonique s'affaiblit lorsque la section considérée du profil se rapproche de la paroi latérale. Le débattement de la position du choc est très similaire à celui mis en évidence expérimentalement.

D'autres configurations ont été calculées, allant du cas sans choc au cas précédemment décrit, en passant par des configurations avec un choc plus faible et placé plus en amont sur l'extrados. Dans toutes ces configurations, les effets latéraux sont seuls responsables de la tridimensionnalité de l'écoulement. En conclusion, ces divers calculs montrent le fonctionnement très satisfaisant du code numérique, qui prédit qualitativement et quantitativement la perturbation de l'écoulement suivant l'envergure, provoquée par les C.L.L..

Cette méthode numérique nous permet maintenant d'étudier l'influence de différents paramètres agissant sur l'importance des effets latéraux et leur propagation dans la veine d'essais.
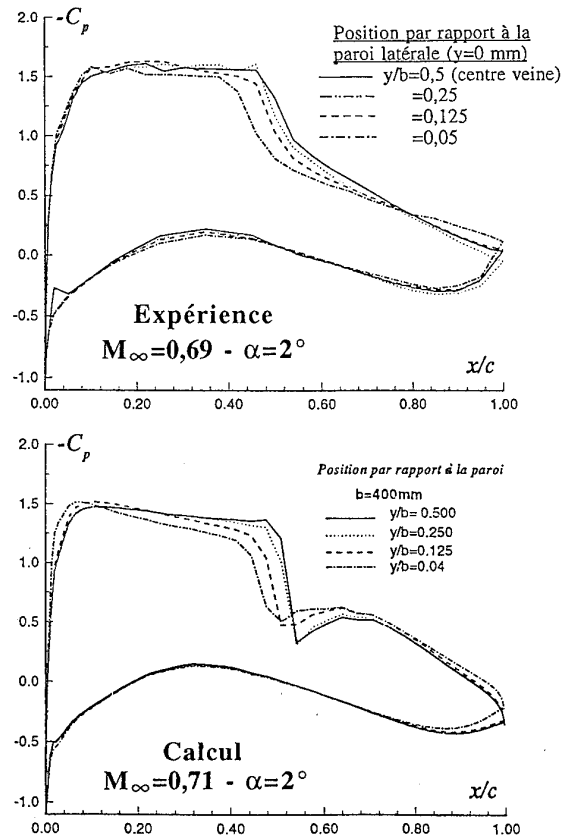
Fig.15   Comparaison calcul-expérience des distributions de pression sur le profil CAST7

Un premier paramètre influant est bien sûr l'allongement b/c (largeur veine/corde profil). Prenons le cas précédent comme cas de base (b/c=2,67 ; c=0,15 m) et multiplions cet allongement par 2, 4 et 6 en considérant que la largeur de la veine croît et que la corde du profil reste constante ; dans ce cas, la géométrie des C.L.L. varie peu d'un cas à l'autre et les effets latéraux également, mais ces C.L.L. s'éloignent de plus en plus de la section centrale. La figure 16 présente les distributions du nombre de Mach sur la section centrale du profil, relatives aux différents allongements. Lorsque la veine s'élargit, la position du choc tend vers la position notée 2D qui correspond à un cas bidimensionnel, c'est à dire à une veine infiniment large. Mais il faut atteindre des valeurs importantes de b/c, de l'ordre de 16, pour que la distribution sur la section centrale corresponde au cas bidimensionnel pour les mêmes conditions M_∞ et α.
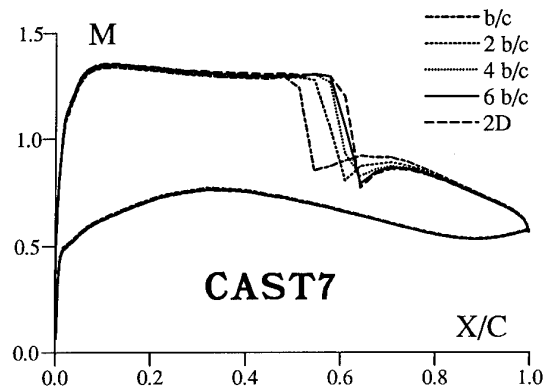
Fig.16   Influence de l'allongement (b/c) sur l'action des effets latéraux au centre veine

Une deuxième étude, qui n'a pas encore été entreprise, est celle de l'influence de la corde, à largeur de veine constante. Si la corde est diminuée, les gradients de pression sont intensifiés près de l'emplanture, mais sur une étendue plus restreinte. Ces évolutions n'étant pas obligatoirement linéaires, cette étude n'est pas identique à la précédente. La courbe de l'influence des effets latéraux au centre veine en fonction de la corde sera une information très intéressante à connaître.

4.4 METHODE DE CORRECTION DES EFFETS LATERAUX

La démarche de l'estimation de la correction des effets latéraux est la suivante (fig.17, haut), sachant que l'on ne s'intéresse qu'à la section centrale du profil. Un premier calcul bidimensionnel effectué dans les conditions nominales
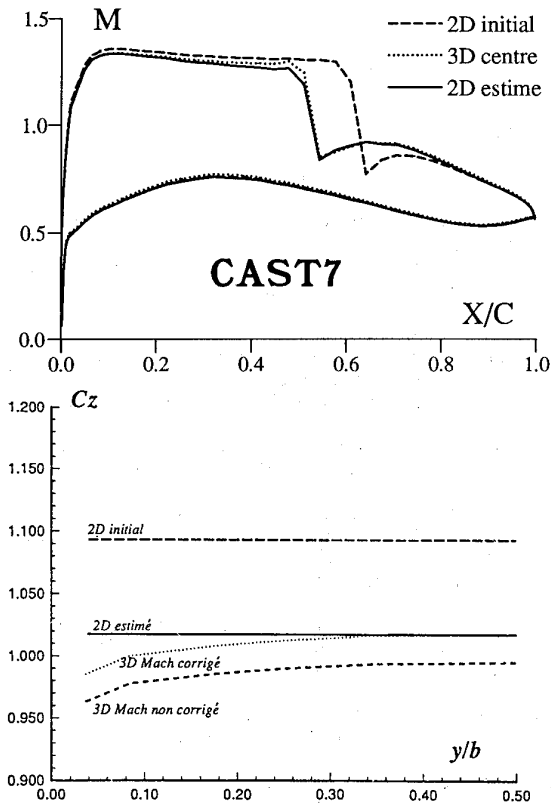
Fig.17 Correction des effets latéraux

$M_\infty=0,71$; $\alpha=2°$

$M_\infty=0,702$; $\alpha=1,94°$
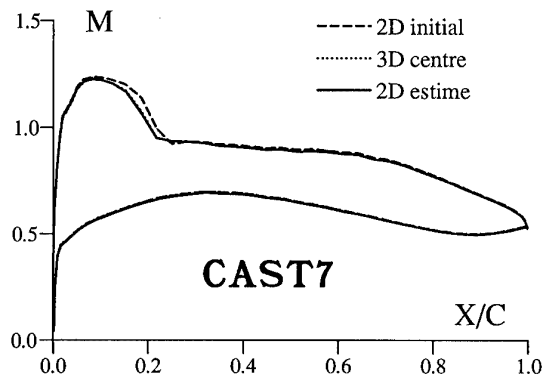
Fig.18 Correction des effets latéraux

$M_\infty=0,650$; $\alpha=2°$

$M_\infty=0,645$; $\alpha=2°$

$M_\infty=0,71$ et $\alpha=2°$ fournit le résultat non perturbé par les effets latéraux. Pour les mêmes conditions d'essai, le calcul tridimensionnel itératif donne la courbe du nombre de Mach notée 3D, sur laquelle le choc a avancé à cause de la perturbation due aux effets latéraux. Cherchons maintenant à recouper au mieux cette distribution perturbée notée 3D par un calcul bidimensionnel (appelé 2D estimé) réalisé avec des conditions d'essai légèrement modifiées ; dans le cas de la figure 17, ces conditions sont $M'_\infty=0,702$ et $\alpha'=1,94°$. Nous appellerons "correction des effets latéraux", la correction des conditions de l'essai suivante : $\Delta M_\infty=M'_\infty-M_\infty$ et $\Delta\alpha=\alpha'-\alpha$. Les figures 17 et 18 présentent cette démarche dans deux configurations différentes, les résultats étant résumés dans le tableau suivant :

Figure	Conditions d'essai	Corrections
17	$M_\infty=0,71$	$\Delta M_\infty\approx -0,008$
	$\alpha=2°$	$\Delta\alpha\approx -0,06°$
18	$M_\infty=0,65$	$\Delta M_\infty\approx -0,005$
	$\alpha=2°$	$\Delta\alpha\approx 0°$

La figure 17 montre également dans sa partie inférieure le bon accord sur le coefficient de portance au centre veine, entre les cas 2D estimé et 3D perturbé, à condition de tenir compte de la correction du nombre de Mach pour ce dernier.

On constate que la correction des effets latéraux semble modifier principalement le nombre de Mach infini, la correction sur l'angle d'incidence étant faible et difficile à estimer, au moins dans les cas comportant un choc.

La précision d'une telle estimation de la correction est de l'ordre de $\Delta M_\infty\approx\pm0,001$. La position du choc jouant un grand rôle dans l'estimation de la correction de cas transsoniques, il est important, pour obtenir une telle précision, que le maillage soit suffisamment fin sur le profil pour laisser bouger librement l'onde de choc, sans discontinuité de mouvement due à la répartition des mailles.

4.5 ABAQUE DE CORRECTION

Nous pouvons maintenant chiffrer la correction des effets latéraux sur le nombre de Mach pour différents allongements relatifs à une même corde de profil. La figure 19 montre le résultat de cette étude. Dans le cas comportant un choc sur le profil ($M_\infty=0,71$ et $\alpha=2°$), la correction du nombre de Mach croît en valeur absolue de façon non linéaire avec la réduction de la largeur veine. Notons la valeur $|\Delta M_\infty|\approx0,01$ pour un allongement de 2. Par contre, dans un cas d'écoulement entièrement subsonique ($M_\infty=0,60$ et $\alpha=1°$), la correction $|\Delta M_\infty|$ semble conserver une valeur très faible de l'ordre de 0,001, même pour b/c=2. Une étude plus poussée de cas intermédiaires est nécessaire pour mieux comprendre et valider ce comportement.
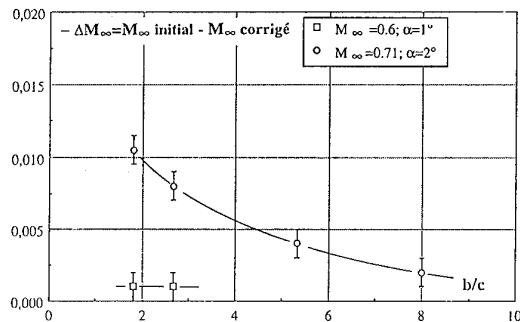
Fig.19 Evolution de la correction du nombre de Mach infini ΔM_∞ en fonction de l'allongement b/c

De nombreuses configurations ayant été calculées, il est maintenant possible de construire un abaque fournissant la correction du nombre de Mach au sens de l'influence des effets latéraux, pour un profil et un allongement donnés. La figure 20 présente un tel abaque pour le profil CAST7 et l'allongement b/c = 2,67. La courbe inférieure est la limite de formation de l'onde de choc. Sous cet arc de courbe, la correction est faible ($|\Delta M_\infty| \leq 0,002$). L'arc de courbe supérieur représente la limite d'apparition du décollement arrière, dans l'expérience. Au delà de cet arc de courbe, toute correction s'avère impossible actuellement. Entre ces deux portions de courbes extrêmes sont tracées des lignes iso-correction du nombre de Mach. Un tel abaque peut être utile pour corriger de nombreux essais ou pour prédire la valeur de la correction avant l'essai et ajuster le nombre de Mach nominal en conséquence. Actuellement, le tracé de cet abaque demande la connaissance de la correspondance entre les conditions nominales du calcul et celles de l'expérience qui lui ressemble au sens de la distribution du nombre de Mach sur l'extrados du profil. Cette étape est plutôt délicate. L'introduction prochaine de la couche limite sur le profil devrait résorber en partie l'écart entre ces deux ensembles de conditions nominales.
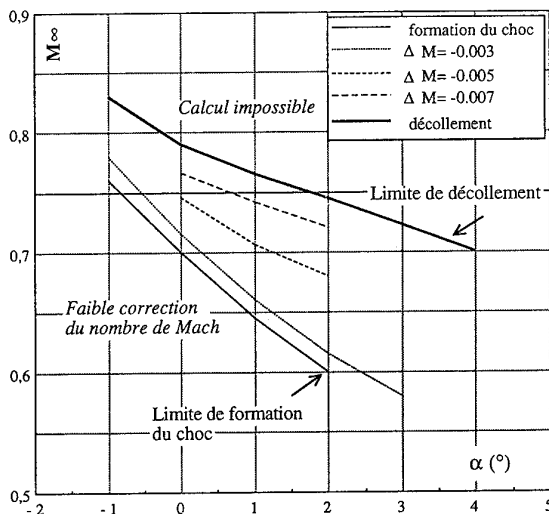
Fig.20 Abaque de correction du nombre de Mach infini ΔM_∞ pour le profil CAST7 (allongement, b/c=2,67)

5. CONCLUSION

Les effets latéraux (composante 3D de la géométrie des couches limites latérales) perturbent les essais en soufflerie, même entre parois haute et basse adaptées. Ils sont particulièrement importants autour d'un profil bidimensionnel, configuration de l'étude présente.

La qualification expérimentale de l'influence de ces effets latéraux, d'une part dans l'écoulement, d'autre part sur le profil, a mis en évidence son action significative dans une veine classique.

La méthode numérique qui a été développée a permis de calculer l'écoulement réel dans la veine d'essais en présence des couches limites latérales et de retrouver les gradients de pression suivant l'envergure. Cette méthode, une fois validée par rapport à l'expérience, a été utilisée pour prédire une correction du Nombre de Mach infini relative à la présence des effets latéraux. Un abaque de correction a pu être établi.

Il reste à utiliser la méthode numérique pour d'autres profils, à étudier l'importance de certains paramètres, à optimiser le processus de recherche des corrections de nombre de Mach et d'incidence.

6. REFERENCES

[1] Michonneau J.F., "Analyse des perturbations induites par les couches limites latérales d'une soufflerie sur un profil en régime transsonique", Thèse de doctorat de l'ENSAE, CERT/ONERA Toulouse, 17 mars 1993.

[2] Fournier R., Michonneau J.F., "Etude théorique des effets latéraux sur un profil, essais de compensation par déformation de la paroi haute réalisés à la soufflerie T2", Projet de DEA, CERT/ONERA, DERAT Sep.1989.

[3] Archambaud J.P., Dor J.B., Michonneau J.F., Breil J.F., "Etude des effets latéraux autour d'un profil bidimensionnel dans la soufflerie T2. Mesures par vélocimétrie laser et utilisation de différents contrôles actifs", R.T. OA n°15/2891 AN 169 D (DERAT N° 15/5015.24), Oct. 1991.

[4] Mignosi A., Faulmann D., Séraudie A., "La soufflerie transsonique à induction T2 : fonctionnement à température ambiante et adaptation cryogénique", La Recherche Aérospatiale, 1981-3.

[5] Archambaud J.P., Mignosi A.,"Two-dimensional and three-dimensional adaptation at the T2 transonic wind tunnel of CERT/ONERA", 15th Aerodynamic Testing Conference, San Diego, May 1988.

[6] Prudhomme S., Séraudie A., "Premiers essais d'optimisation du fonctionnement du banc de vélocimétrie 3D de T2. Mesures 3D, approches de paroi, rétrodiffusion", Rapport Technique DERAT n° 41/5606.23, Sep. 1990.

[7] Hefer G., "The cryogenic Ludwieg Tube Tunnel at Göttingen", AGARD Report n°774, June 1989.

[8] Stanewsky E., Zimmer E., "Entwicklung und Windkanalerprobung von drei überkritische Tragflügelprofilen für Verkerrsflugzeuge", Z. Flugwiss.23, 1975.

[9] Cousteix J., "Analyse théorique et moyens de prévision de la couche limite turbulente tridimensionnelle", TP ONERA 157, 1974.

[10] Bredif M., "A fast finite element method for transonic potential flows", AIAA Paper 83-0507, 1983.

[11] Houdeville R., "Calculs de couches limites tridimensionnelles, description et mode d'emploi du code 3C3D", Rapport Technique DERAT n° 43/5625.41, Fév. 1992.

CALCULS DES EFFETS DE PAROIS
DANS DES VEINES A PAROIS PERFOREES
AVEC UN CODE DE SINGULARITES SURFACIQUES

par
J.F. Piat
ONERA
Centre d'Essais de Modane-Avrieux
B.P. n° 25, 73500 Modane, France

RESUME

Des hypothèses simplificatrices restrictives sont inhérentes à la méthode analytique utilisée auparavant pour obtenir les effets perturbateurs des parois des veines d'essai.
Afin d'éliminer ces hypothèses un nouveau code fondé sur la méthode des singularités surfaciques a été developpé. Il autorise des veines non cylindriques de forme de section quelconque, et des zones locales perforées de caractéristiques de perte de charge non linéaires.

Ce code a été utilisé pour calculer les effets de parois dans la veine transsonique de la soufflerie S3MA de section 0,78 m x 0,56 m et équipée de 2 ou de 4 parois perforées.
Les porosités des parois, ont été ajustées de sorte que les répartitions de pression calculées coïncident au mieux avec les répartitions mesurées sur les parois.
La validité des corrections des effets de parois calculées par le code a pu être contrôlée par comparaison des coefficients de traînée CX corrigés obtenus dans S3MA et dans S2MA, soufflerie de section beaucoup plus grande, avec des effets de parois minimes.

ABSTRACT

Simplifying assumptions are inherent in the analytic method previously used for the determination of wall interferences on a model in a wind tunnel.
To eliminate these assumptions, a new code based on the vortex lattice method was developed. It is suitable for processing any shape of test sections with limited areas of porous wall, the characteristic of wich can be nonlinear.

Calculation of wall effects in S3MA wind tunnel, whose test section is rectangular 0,78 m x 0,56 m, and fitted with two or four perforated walls, have been performed.
Wall porosity factors, have been adjusted to obtain the best fit between measured and computed pressure distributions on the test section walls.
The code was checked by measuring nearly equal drag coefficients for a model tested in S3MA wind tunnel (after wall corrections) and in S2MA wind tunnel whose test section is seven times larger (negligible wall corrections).

PRINCIPALES NOTATIONS

A	Amplification de la vitesse normale à la paroi $A = \dfrac{w_e}{w_w}$
Apq	Coefficient d'influence de la facette q sur la facette p
CP	Coefficient de pression
CX	Coefficient de traînée de la maquette
M	Nombre de Mach
P	Pression statique locale
q	Pression cinétique
R	Paramètre de porosité de la facette perforée $R = \dfrac{2\, w_e / U_e}{\left(P_w - P_{cai}\right)/q_e}$
U	Vitesse totale en x
w	Vitesse de perturbation normale à la paroi
x, y, z	Coordonnées cartésiennes
X, Y	Coordonnées x, y en axes veine
β	$= \sqrt{1 - M^2}$
δ*	Epaisseur de déplacement de la couche limite
ρ	Densité
η	Perméabilité (géométrique)
μ_q	Intensité de la facette q
φ	Potentiel de perturbation

Indices

e   : condition à la frontière de la couche limite

w ou   : condition à la paroi de la veine
veine

cai   : condition dans le caisson

H   : relatif aux parois perforées horizontales

V   : relatif aux parois perforées verticales

ecl   : relatif à l'éclatement de veine

1 - INTRODUCTION

Pour se trouver dans la même situation qu'un avion en vol, une maquette en soufflerie devrait être essayée dans un écoulement uniforme (champ propre exclu). Cette situation idéale n'est pas réalisée ; en réalité la maquette se trouve placée dans un écoulement perturbé qui a été rendu inhomogène par les effets de parois et de support et par les défauts éventuels de veine. Cet écoulement doit être connu pour pouvoir restituer des résultats en atmosphère illimitée.

Parmi les effets parasites, celui des parois va être examiné plus particulièrement dans cet article. Bien qu'ayant déjà fait l'objet d'une multitude d'études depuis l'origine des souffleries, sa connaissance reste toujours à améliorer étant donné les précisions de plus en plus fines exigées.

Les premiers essais en soufflerie qui avaient lieu en veine guidée étaient affectés d'erreurs importantes sur le nombre de Mach (blocage) et l'incidence pour les tailles de maquette habituellement utilisées (1 % d'obstruction).

C'est pourquoi de nombreuses veines perméables, à fentes ou perforées, ont été construites. La possibilité pour l'écoulement de s'échapper et de revenir à travers les parois a permis de réduire sensiblement les effets de parois ; aussi, dans un premier temps, de nombreux essais ont pu être effectués sans apporter de corrections aux résultats.

Plus tard, compte tenu des précisions accrues requises, en particulier pour établir les bilans de traînée à la croisière, les corrections sont devenues nécessaires.

Une illustration de l'importance des effets de parois pouvant encore exister dans des veines perméables est donnée figure 1. Sur celle-ci ont été reportées les répartitions de CP mesurées en amont d'un dard dans la veine transsonique de la soufflerie S3MA, de section 0,78 m x 0,56 m, ventilée sur environ 2 m de longueur et équipée soit de 2 parois perforées, soit de 4 parois perforées (voir paragraphe 3.1).
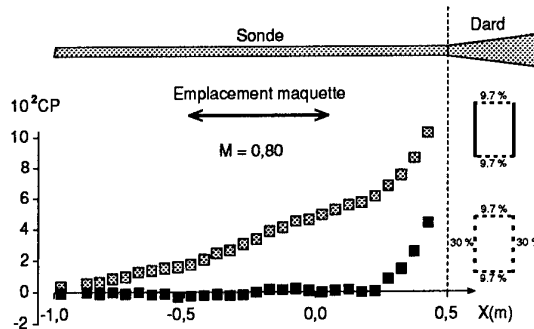
Fig 1 : Champ d'un dard mesuré dans 2 types de veine

L'extinction du champ du dard apparaît très rapide dans la veine à 4 parois perforées tandis qu'elle est très lente dans la veine à 2 parois perforées ; ainsi la maquette placée habituellement en amont de ce dard voit sa traînée CX modifiée par la seule présence du dard de 0 % ou de 15 % selon le type de parois.

Les corrections des effets de parois à l'ONERA ont été longtemps obtenues par la méthode analytique [1]. Une double transformée de Fourier en X et Y était utilisée et les vitesses de perturbations résultaient d'intégrales en général non résolubles analytiquement et qui devaient être calculées par méthode numérique [2].
Cependant la méthode analytique avait l'inconvénient d'être très restrictive sur le type de veine d'essai, nécessairement :

- de section rectangulaire s'étendant à l'infini,

- avec des zones perforées limitées à 2 parois, de perméabilité uniforme jusqu'à l'infini et possédant des caractéristiques de pertes de charge linéaires.

Aussi pour traiter le cas de veines de formes et de caractéristiques variées, une nouvelle procédure de calcul des corrections des effets de parois et de support s'est avérée nécessaire. La méthode des singularités surfaciques a été retenue. Elle a été developpée à l'ONERA à partir de 1984 [3].

2 - METHODE DES SINGULARITES SURFACIQUES

2.1 - Historique

La méthode des singularités surfaciques, fondée sur la théorie des équations intégrales de Fredholm, permet de déterminer le potentiel des vitesses φ, solution de l'équation de Laplace Δφ = 0, en satisfaisant certaines conditions limites sur la frontière d'un objet.

La mise en oeuvre de cette méthode a été développée en 1962 par Hess et Smith [4] avec une répartition de sources surfaciques, de densité constante par facette, sur la surface de l'objet fermé.

L'application au cas des veines d'essai guidées en soufflerie en vue de calculer des corrections d'incidence dues aux parois, en incompressible, a été initiée en 1967 par Joppa [5].

L'extension de la méthode Joppa au cas des parois ventilées de veines cylindriques a été proposée en 1972 par Borovik [6]. Les singularités utilisées sur les parois de la veine étaient des facettes doublets d'intensité constante μ par facette équivalentes à des tourbillons linéiques μdl concentrés sur le pourtour de la facette ("vortex lattice method"). Seules les corrections d'incidence étaient recherchées.

Le code utilisé ici reprend la discrétisation de Borovik en l'élargissant au cas des veines de formes quelconques, aux écoulements compressibles et aux corrections de blocage.

2.2 - Description de la méthode

Les parois de la veine sont découpées en Q facettes quadrilatères. Chaque facette q est modélisée par une répartition surfacique de doublets d'intensité μq constante (équivalent à 4 tourbillons linéiques $\mu_q dl$ sur le pourtour de la facette).

Au point de contrôle, situé au centre d'une facette p sont calculées :

- les vitesses $\mu_q \overrightarrow{A_{pq}}$ induites par les quatre tourbillons de chacune des facettes (q de 1 à Q) selon la loi de Biot et Savart. Les intensités μq sont inconnues pour l'instant,

- les vitesses $\overrightarrow{V_M}$ et $\overrightarrow{V_S}$ induites par les singularités modélisant respectivement la maquette et le support. Leur intensité est déjà connue, fonction de la géométrie et des conditions d'essai.

La vitesse de perturbation totale $\overrightarrow{V_p}$, qui se superpose à l'écoulement veine vide, s'exprime alors :

$$\overrightarrow{V_p} = \sum_{q=1}^{Q} \mu_q \overrightarrow{A_{pq}} + \overrightarrow{V_M} + \overrightarrow{V_S}$$

et doit satisfaire à une des 2 conditions limites suivantes :

- si la facette p est pleine : $\overrightarrow{V_p} . \vec{n} = 0$

- si la facette p est ventilée : $R . \overrightarrow{V_p} . \vec{t} + \overrightarrow{V_p} . \vec{n} = 0$

avec $\vec{t}$ et $\vec{n}$ respectivement les vecteurs unitaires tangentiel et normal à la facette ;
et R : paramètre de porosité affecté à la facette.

Dans le cas d'un coefficient de pression caisson non nul, l'expression plus générale suivante est utilisée :

$$R . \left(\overrightarrow{V_p} . \vec{t} + CP_{caisson} / 2 \right) + \overrightarrow{V_p} . \vec{n} = 0$$

A noter que pour tenir compte de l'évolution longitudinale de l'intensité des tourbillons μ discrétisée par des valeurs constantes par facette, une correction de la composante tangentielle de la vitesse $\overrightarrow{V_p} . \vec{t}$ préconisée par Borovik [6], est effectuée.

Celle-ci est proportionnelle au saut d'intensité d'une facette à l'autre :

$$\Delta \left(\overrightarrow{V_p} . \vec{t} \right) = \left(\mu_{j+1} \Delta X_{j+1} - \mu_{j-1} \Delta X_{j-1} \right) / 4 \left(X_{j+1} - X_{j-1} \right)$$

Si le maillage est assez fin, ceci revient au même que l'utilisation d'une intensité variant linéairement avec x par facette.

L'écriture des conditions limites pour les Q points de contrôle (p de 1 à Q) conduit à un système de Q équations linéaires à Q inconnues (les μ_q) que l'on résoud par inversion de la matrice des coefficients d'influence de taille Q x Q. Cette opération s'effectue par la méthode directe de Gauss qui consiste à remplacer le système de départ par un système triangulaire équivalent.

L'écoulement de perturbation (maquette + support + facettes) est alors totalement identifié.
L'effet seul des Q facettes d'intensité μ_q qui ont été "excitées" par les singularités maquette et support fournit le champ de vitesse induit par les parois dans toute la veine et plus particulièrement à l'emplacement de la maquette.

2.3 - Application aux écoulements compressibles

L'écoulement de perturbation peut être décrit par l'équation linéarisée du potentiel :

$$\beta^2 \frac{\partial^2 \varphi}{\partial x^2} + \frac{\partial^2 \varphi}{\partial y^2} + \frac{\partial^2 \varphi}{\partial z^2} = 0$$

sous réserve que :

- le nombre de Mach subsonique de l'écoulement "veine vide" ne soit pas trop voisin de 1. Les calculs effectués à M = 0,8, présentés par la suite, sont considérés respectant cette condition ;

- les vitesses de perturbation restent faibles vis à vis des vitesses "veine vide". Cette condition est généralement vérifiée quand il s'agit d'effets de parois, les vitesses induites par les singularités étant déjà bien atténuées au niveau des parois (champ lointain).

Le changement de coordonnées classique (X = x, Y = βy, Z = βz) ramène l'équation linéarisée à l'équation de Laplace $\Delta \varphi = 0$, équation de base de la méthode des singularités surfaciques.

Par ailleurs la valeur de β n'est pas prise constante, l'écoulement "veine vide" étant déjà souvent loin d'être uniforme (convergent, divergent...). A cha-

que singularité (indice S) et à chaque point de calcul (indice C) sont affectés une valeur de β locale qui résulte à la première itération d'un calcul de Mach monodimensionnel et aux itérations suivantes du Mach calculé à cet emplacement à l'itération précédente. Ainsi les distances d s'expriment :

$$d^2 = (x_c - x_{s'})^2 + (\beta_c\, y_c - \beta_s\, y_s)^2 + (\beta_c\, z_c - \beta_s\, z_s)^2$$

3 - APPLICATION A DES ESSAIS DANS LA SOUFFLERIE S3MA - DESCRIPTIFS

L'utilisation du code surfacique pour le calcul des effets de parois lors d'un essai de maquette de missile dans la soufflerie S3MA va être présentée dans la suite de cet article.

Plus précisément on va s'intéresser aux corrections de blocage, essentielles pour une bonne connaissance de la traînée ; les corrections de portance quant à elles sont plus modestes étant donné les faibles surfaces portantes de la maquette considérée.

L'incidence maquette α est proche de 0° et le nombre de Mach M est de 0,80.

3.1 - Veine d'essai

La veine transsonique de la soufflerie S3MA est rectangulaire, de hauteur 0,78 m et de largeur 0,56 m. Elle est entourée par un caisson dans lequel s'établit une pression proche de la pression statique veine.

A l'abscisse X = 0,8 m, le caisson et la veine se rejoignent (éclatement de veine) pour former un seul conduit de section 0,805 m x 0,76 m (figure 2).
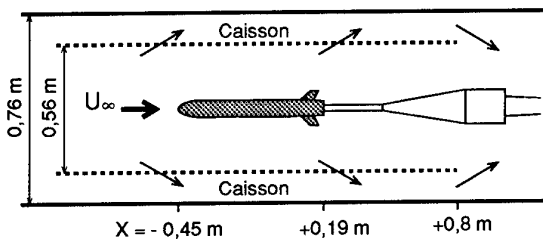
Fig. 2 : Schéma de la veine d'essai

Les caractéristiques des parois perforées horizontales et verticales de la veine sont indiquées figures 3 et 4.

La perméabilité η des parois horizontales, obtenue avec des trous droits de diamètre 3 mm, est faible. Elle évolue de $\eta = 0$ à $\eta = 9,7\ \%$ entre X = -1,47 m et X = - 1,05 m puis elle est constante $\eta_H = 9,7\ \%$ pour - 1,05 m $\leq$ X $\leq$ + 0,80 m.

La perméabilité η des parois verticales, obtenue avec des trous droits de diamètre 11 mm, est par contre importante. Elle évolue de $\eta = 0$ à $\eta = 30\ \%$ entre X = - 1,6 m et X = - 0,9 m puis elle est constante $\eta_V = 30\ \%$ pour - 0,9 m $\leq$ X $\leq$ + 0,8 m. A noter que ces parois peuvent être remplacées par des parois pleines.
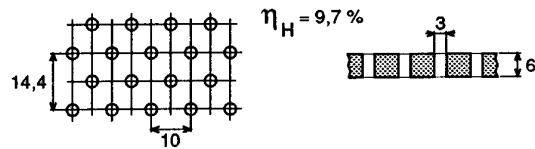
Fig. 3 : Perforations des parois horizontales
(distances en mm)
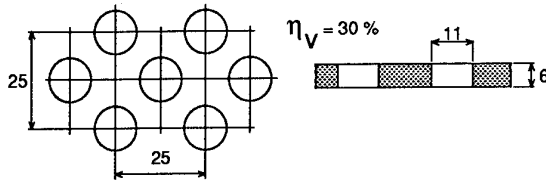
Fig. 4 : Perforations des parois verticales
(distances en mm)

Une vue d'ensemble des perforations de la veine est donnée figure 5.
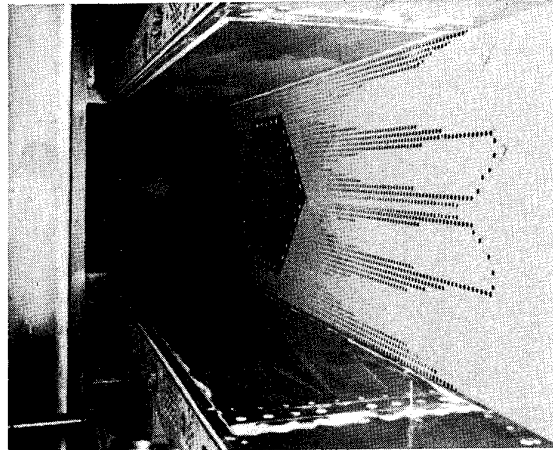
Fig 5 : Veine d'essai S3MA

Le maillage de la veine s'étend de X = - 7 m à X = + 7 m (figure 6) il comporte 2200 facettes dont 700 facettes perméables sur les parois horizontales et 864 facettes perméables sur les parois verticales (si perforées). Les facettes sont placées sur les parois ; une amélioration consisterait à soustraire les épaisseurs δ^* de couche limite constatées .

L'éclatement de veine a été positionné avec 2 mailles en X sur l'intervalle [+ 0,8 m, + 0,93 m], il est représenté avec 88 facettes perméables.
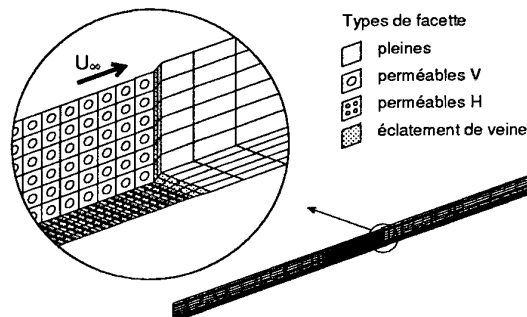
Fig. 6 : Maillage du 1/4 veine S3MA

3.2 - Maquette et dard

La maquette a une longueur de 0,637 m ; son nez est situé à l'abscisse X = - 0,45 m en axes veine et elle présente une obstruction de 1,3 %. Elle est pesée par une balance à 6 composantes et tenue au culot par un dard droit (figure 7).
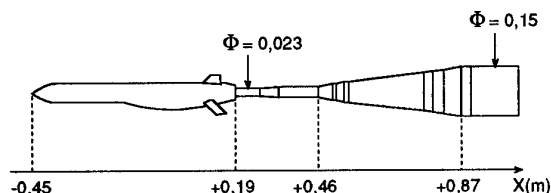
Fig. 7 : Montage maquette + dard

L'ensemble maquette + dard est modélisé à l'aide de 60 singularités source ou puits d'intensité proportionnelle à la variation de section en X. Les perturbations de l'écoulement induites par la présence de la veine autour de cet ensemble (= effets de parois) et calculées par le code surfacique sont intégrées sur la maquette seule pour corriger les résultats des pesées.
Pour accéder à des résultats en atmosphère illimitée il resterait à corriger de l'effet direct du dard droit, ce qui n'est fait ici que de façon rudimentaire avec des singularités ponctuelles inadaptées pour calculer un champ proche (maquette et dard sont jointifs). Ce point constitue un autre sujet d'étude non abordé dans cet article où seule une bonne évaluation des effets de parois a été recherchée.

La qualité de la modélisation des objets en veine conditionne fortement la validité des effets de parois calculés.
La modélisation simple qui est utilisée est suffisante pour simuler le volume d'objets allongés, sensiblement de révolution et peu inclinés par rapport au vent tels que ceux présents en veine (fuselage, dard droit). La mauvaise prise en compte des discontinuités maquette (entrée d'air, culot) par la discrétisation a peu d'importance dès que l'on s'intéresse à l'effet à une certaine distance, comme sur les parois (champ lointain).
Les sillages ont aussi été simulés avec une source d'intensité proportionnelle au CX située au culot maquette et une autre source située au culot du dard.

Pour contrôler la modélisation des objets en veine, une méthode couramment utilisée consiste à comparer sur les parois d'une veine guidée les répartitions de pression calculées et mesurées. Ce contrôle avait déjà été effectué avec des maquettes et des dards de formes comparables dans des veines de plus grande dimension (S1MA, S2MA) et un bon accord avait été constaté. Il n'a pas été repris pour cet essai à S3MA.

A noter enfin qu'une autre configuration, une simple sonde de révolution fixée sur le dard (figure

8),très facile à modéliser, a aussi été essayée dans la veine de S3MA ; cela, uniquement pour la recherche des porosités des parois perforées.
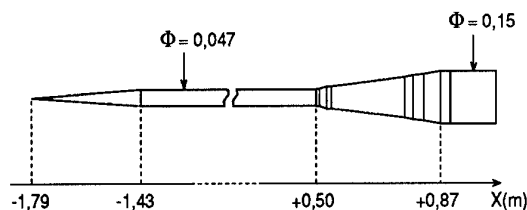
Fig. 8 : Montage sonde + dard

4 - DETERMINATION DES POROSITES DES PAROIS PERFORES DE S3MA

4.1 - Méthode

Il s'agit de connaître le paramètre de porosité

$$R = \frac{2\, w_e / U_e}{(P_w - P_{cai})/\, q_e}$$ affecté à chaque facette ventilée.

La vitesse normale à la facette à prendre en compte est celle, w_e, à la frontière extérieure de la couche limite (figure 9).
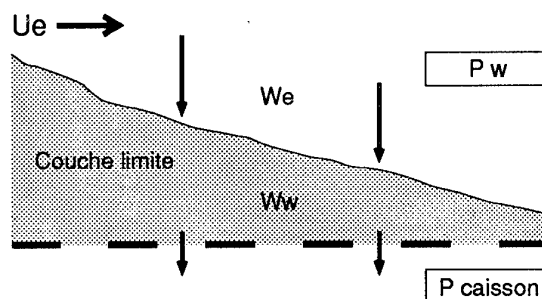
Fig 9 : vitesses normales à la paroi

Elle est fonction de la vitesse effective de traversée de paroi w_w qui peut être déterminée à partir de mesures de débit dans une portion de caisson dans laquelle on fait varier la pression [7] et de l'épaisseur de déplacement $\delta*$ de la couche limite suivant la relation suivante (conservation de la masse) :

$$\rho_e w_e = \rho_w w_w + \frac{d}{dx}\left(\rho_e\, U_e\, \delta*\right)$$

Etant donné les faibles gradients dU_e/dx constatés et en considérant que ρ_w est voisin de ρ_e , la relation se réduit à :

$$w_e = w_w + U_e . \frac{d\delta*}{dx}$$

w_w est essentiellement fonction de l'écart de pression à travers la paroi ; U_e . $d\delta*/dx$ l'est aussi en bonne partie mais dépend de plus d'autres paramètres, tels $\delta*$, dU_e/dx.

L'amplification $A = w_e/w_w$ par la couche limite de la vitesse normale est importante en soufflage ($P_{caisson} > P_w$), la référence [8] indique la valeur $A = 3,25$; par contre elle est réduite en aspiration ($P_{caisson} < P_w$), avec des valeurs beaucoup plus proches de l'unité [7] et [8].

Les répartitions de pression statique mesurées sur les parois de la veine qui seront présentées paragraphes 4.2 et 4.3 nous indiquent, avec des CP_w en forte majorité positifs, un fonctionnement des parois avec aspiration des couches limites. La vitesse $U_e . d\delta^*/dx$ est à priori modeste devant w_w, ce qui sera contrôlé avec des mesures de couche limite présentées paragraphe 4.4, aussi on peut admettre en n'introduisant qu'une faible erreur sur w_e que la vitesse $U_e . d\delta^*/dx$ n'est fonction que de l'écart de pression ($P_w - P_{caisson}$) et qu'en conséquence w_e ne dépend plus aussi que de cet écart.

Enfin on admettra étant donné les faibles plages de CP_w observées en essai ($- 0,01 \leq CP_w \leq + 0,08$) la linéarité de la loi w_e/U_e ($\Delta p/q_e$).

Il ressort de cette discussion que toutes les facettes d'un même type de paroi seront caractérisées par une valeur R identique : R_H pour les parois horizontales, R_V pour les parois verticales.

Une difficulté apparaît pour les facettes situées sur les perforations les plus en amont où la perméabilité η vaut entre 0 et la valeur nominale η_H ou η_V. Pour ces facettes, le paramètre R_η a été pris proportionnel à la perméabilité η locale :

$$R_\eta = R_{H \text{ ou } V} \cdot \frac{\eta}{\eta_{H \text{ ou } V}}$$

Une autre difficulté apparaît pour les 88 facettes d'éclatement de veine. La porosité R_{ecl} qui leur a été affectée est celle qui fournit un débit calculé rentrant (du caisson vers la veine), à travers ces 88 facettes, égal au débit calculé sortant (de la veine vers le caisson) dans la partie amont de la veine ($X < + 0.8$ m). Une étude paramétrique avec différentes valeurs R_{ecl} est nécessaire pour arriver à cette égalité.

La détermination de la valeur inconnue R_H ou R_V a lieu en faisant calculer par le code surfacique les répartitions de pression statique sur une paroi horizontale, sur une paroi verticale et éventuellement sur la sonde (si présente) pour différentes valeurs de R. La valeur retenue sera celle qui fournira le meilleur accord avec les répartitions de pression effectivement mesurées.

Pour identifier les 2 inconnues R_H et R_V cette opération doit s'effectuer en deux temps :

Veine à 2 parois perforées⟶ détermination de R_H (paragraphe 4.2)

. Veine à 4 parois perforées ⟶ utilisation de la valeur R_H précédente et détermination de R_V (paragraphe 4.3).

Cette méthode requiet une grande précision sur les mesures de pression, aussi, comme c'est l'usage, les répartitions veine vide ont été systématiquement soustraites afin d'éliminer les erreurs dues aux défauts de prise.
Les faibles gradients observés veine vide autorisent la superposition de l'écoulement veine vide et de l'écoulement de perturbation.

4.2 - Détermination de R_H

5 planches de comparaison de répartitions de pression mesurée et calculées dans la veine à 2 parois perforées obtenues pour les 2 types d'objets en veine (sonde + dard, maquette + dard) et sur les différentes génératrices (paroi horizontale, paroi verticale, sonde) sont présentées figure 10. A noter que, par définition, toutes les courbes des planches paroi horizontale passent par CP = 0 à l'abscisse $X = - 1,17$ m de la prise de référence.

Les répartitions de pression mesurées mettent en évidence :

- un écoulement sensiblement monodimensionnel dans la veine, les pressions étant voisines sur les différentes génératrices,
- des coefficients de pression CP quasiment partout positifs ; l'objet le plus volumineux, le dard, imposant le ralentissement de l'écoulement devant lui dans toute la veine,
- la remontée très en amont du champ des objets (jusqu'à $X = - 1$ m pour le dard). Ce phénomène est révélateur des faibles échanges à travers les parois perforées.

Sur chaque planche trois répartitions de pression calculées ont été tracées ; elles ont été obtenues avec les porosités.

- $R_H = 0,15$; valeur qui a été trouvée fournissant le meilleur accord (globalement, pour les 5 planches de la figure 10) avec la répartition mesurée. Elle sera retenue comme porosité moyenne des parois horizontales ;
- $R_H = 0,08$ et $R_H = 0,30$; valeurs environ deux fois plus faible et deux fois plus forte que la valeur nominale $R_H = 0,15$. Les répartitions correspondantes ont été tracées afin de donner une idée de la sensibilité des CP au paramètre R.

La courbe $R_H = 0,08$ apparaît dans tous les cas bien décalée. Par contre la situation de la courbe $R_H = 0,30$ apparaît plus confuse ; en présence de la maquette elle se confond sur une grande plage de X avec la courbe nominale $R_H = 0,15$; elle ne s'en
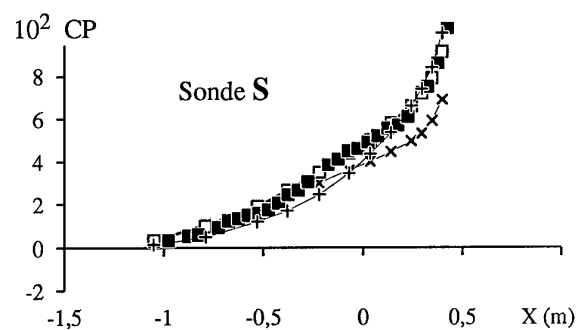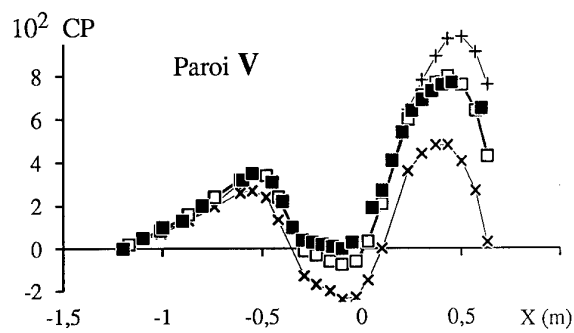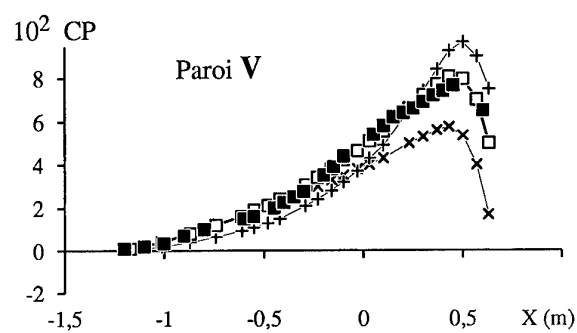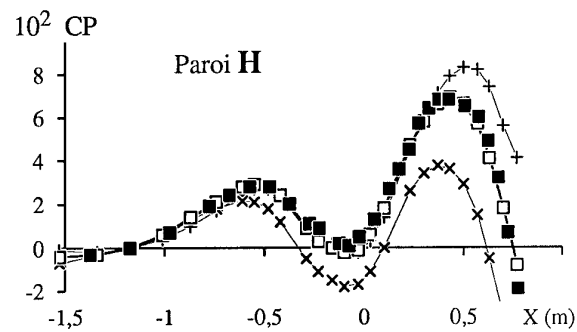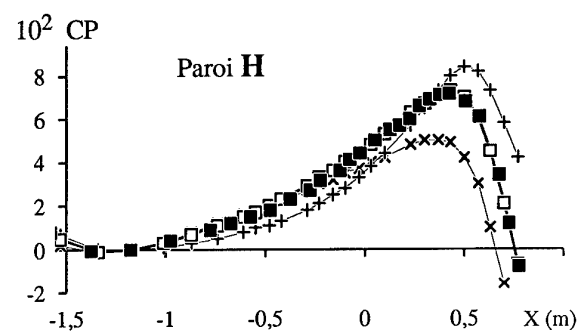
10a : sonde + dard   10b : maquette + dard
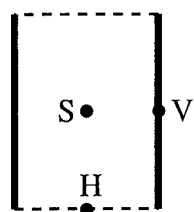
Figure 10 :   Pressions parois et sonde mesurées et calculées
dans la veine 2 parois perforées - M = 0,80 α = 0°

distingue franchement qu'à proximité du dard (X ≈ 0,5 m ; CP les plus élevés).

L'accord répartition mesurée - répartition calculée avec la valeur R_H = 0,15 est, quant à lui, correct. Pour les 5 planches les écarts sont en majorité comparables à la précision des mesures de CP ($\approx 2.10^{-3}$) ; seuls des écarts significatifs de 5 à 10 millièmes subsistent en présence de la maquette et au niveau du maître couple (X ≈ - 0,1 m) ; curieusement ils apparaissent pour les CP les plus faibles ce qui suggérerait une évolution dδ*/dx de la couche limite différente (soufflage ?) à cet endroit , qui se traduirait par une valeur locale R différente de R_H = 0,15.
Néanmoins, étant donné la localisation de ces écarts et leur amplitude modérée (10 % du CP maximum), la modélisation des parois effectuée avec l'approximation d'une porosité R_H unique, qui a été retenue paragraphe 4.1, reste acceptable.

4.3 - Détermination de R_V

Comme pour la veine précédente, 5 planches de comparaison de répartitions de pression mesurée et calculées existent pour la veine à 4 parois perforées. Elles sont présentées figure 11.

On constate :
- des niveaux de CP deux à trois fois plus faibles que dans la veine à 2 parois perforées,
- des extinctions des champs perturbateurs des objets en veine très rapides (dès X = + 0,25 m pour le dard). Ce phénomène est révélateur des forts échanges à travers les parois,
- une monodimensionnalité de l'écoulement moins marquée que dans la veine à 2 parois perforées.

Sur chaque planche trois répartitions de pression calculées ont été tracées. Elles ont été obtenues avec la porosité des facettes horizontales R_H = 0,15 déterminée au paragraphe précédent et avec les porosités des facettes verticales suivantes :

- R_V = 1,6 ; valeur trouvée fournissant le meilleur accord global mesure - calcul. A noter que cette porosité est sensiblement 10 fois plus élevée que la précédente R_H = 0,15 (pour un rapport 3 sur les perméabilités η),
- R_V = 0,8 et R_V = 3 ; valeurs environ deux fois plus faible et deux fois plus forte que la valeur nominale.

La courbe R_V = 0,8 apparaît dans tous les cas bien décalée avec des variations de CP plus marquées.
La courbe R_V = 3 présente des variations de CP plutôt moins marquées que celles mesurées mais ce phénomène n'est vraiment net que sur la paroi verticale.

L'accord répartition mesurée - répartition calculée avec la valeur R_V = 1,6 est, quant à lui, convenable. Pour les 5 planches les écarts en CP ne dépassent pas quelques millièmes.

Il faut préciser que cette valeur R_V = 1,6 de même que la valeur R_H précédente est entachée d'une incertitude importante, de l'ordre de 20 %, du fait que l'accord mesure-calcul n'est pas parfait et qu'il y a un certain arbitraire dans le choix du "meilleur ajustement". La méthode utilisée ne permet pas une détermination fine de la porosité d'une paroi perforée.
Un calcul d'effets de parois effectué avec une valeur R_H décalée de 20 % modifie le CX de la maquette de 1,5 % dans la veine à 2 parois perforées (minime dans l'autre veine). Pour R_V, un décalage de 20 % a une influence plus limitée, de 0,5 % sur le CX.

4.4 - Couches limites sur les parois

Afin de connaître l'ordre de grandeur de l'amplification A = w_e /w_w de la vitesse normale à la paroi, des mesures de couche limite ont été effectuées pour la configuration maquette + dard et veine vide à 3 emplacements.

- sur une paroi horizontale à X = - 1,7 m et X = + 0,63 m ;
- sur une paroi verticale à X = + 0,63 m.

4.4.a) Veine à 2 parois perforées

Les épaisseurs de déplacements δ* mesurées sont indiquées figure 12.
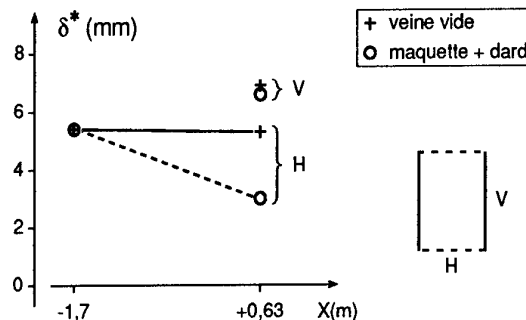
Fig 12 : Epaisseurs δ* de couche limite
(veine à 2 parois perforées)

Sur la paroi verticale pleine, la couche limite apparaît peu affectée par la présence de la maquette.
Sur la paroi horizontale, par contre, l'aspiration de la couche limite entre X = - 1,7 m et X = + 0,63 m, déjà présente veine vide, est fortement accentuée en présence de la maquette. La diminution de δ* est de 2,3 mm, ce qui équivaut, en considérant une distance d'aspiration de 1,9 m à une vitesse normale moyenne rapportée à U_e de : dδ*/dx = $1,2.10^{-3}$
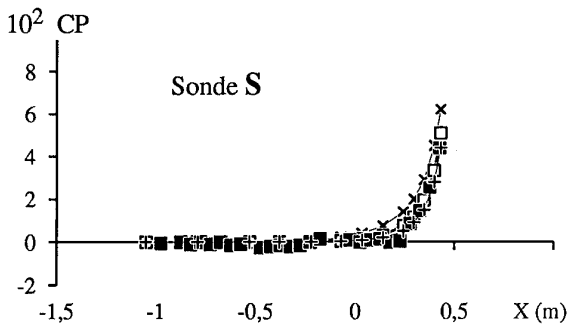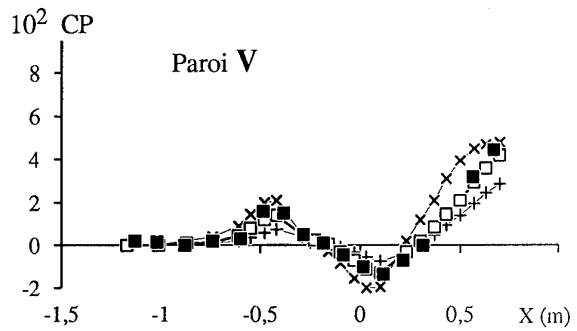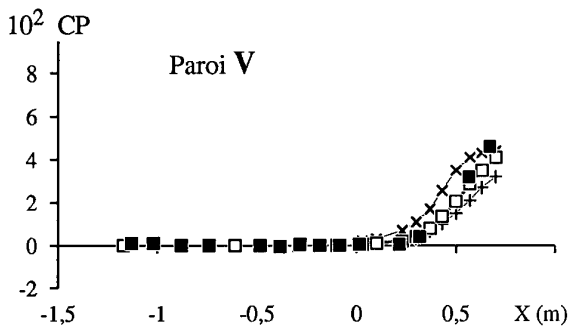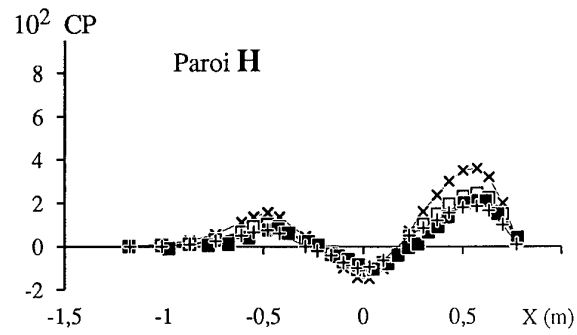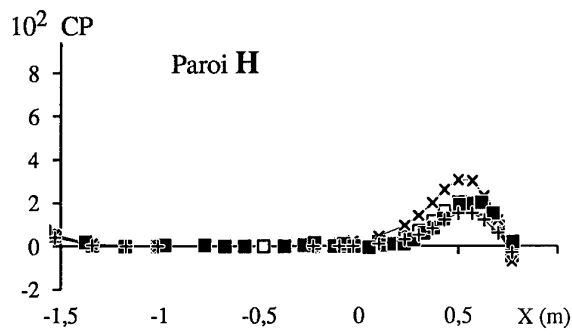
11a : sonde + dard

11b : maquette + dard
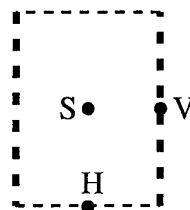
Figure 11 : Pressions parois et sonde mesurées et calculées
dans la veine 4 parois perforées - M = 0,80 α = 0°

Par ailleurs, la vitesse normale totale $w_e/U_e = (R_H/2) \cdot (CP_{veine} - \Delta CP_{cai})$ vaut $3,6.10^{-3}$ en utilisant les valeurs $R_H = 0,15$, $CP_{veine\ moyen} = 2,5.10^{-2}$ et $\Delta CP_{cai} = -2,3\ 10^{-2}$ (la présence de la maquette et du dard a modifié la pression caisson).

D'où la vitesse normale effective de traversée de paroi $w_w/U_e = w_e/U_e - d\delta^*/dx$ qui vaut $2,4.10^{-3}$ et l'amplification moyenne A = 1,5.

Le rôle de la couche limite n'apparaît pas négligeable. En réalité A n'est pas constant (ce que la modélisation avec R_H unique suppose) et il est probable que ses variations locales expliquent en bonne partie les écarts résiduels en CP entre mesure et calcul observés par endroits figure 10.

4.4.b) veine à 4 parois perforées

Les diminutions de δ^* en présence de la maquette, présentées figure 13, apparaissent faibles.
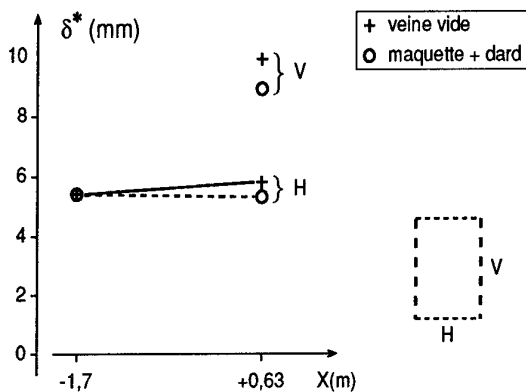
Fig 13 : Epaisseurs δ^* de couche limite
(veine à 4 parois perforées)

- Pour la paroi horizontale, avec un $CP_{veine\ moyen}$ de $0,4.10^{-2}$, un ΔCP_{cai} nul , une porosité $R_H = 0,15$ et une amplification A = 1,5, la diminution de δ^* attendue est de 0,2 mm pour une diminution constatée de 0,5 mm. On ne peut en conclure que R_H a changé car ces faibles valeurs de δ^* sont voisines de l'incertitude de mesure.

- Pour la paroi verticale, la diminution de δ^* est de 1 mm ; ce qui avec un $CP_{veine\ moyen}$ de $0,6.10^{-2}$, un ΔCP_{cai} nul et $R_V = 1,6$ conduit à une amplification A = 1,1. Cette valeur, là aussi est assez imprécise étant donné les faibles niveaux de CP et de $\Delta \delta^*$, néanmoins elle reste faible. Le rôle de la couche limite apparaît modeste, ce qui conforte la modélisation avec une porosité R_V unique qui a été utilisée.

5 - COMPARAISON DES CX OBTENUS DANS 3 VEINES

La validité des corrections de parois calculées par le code surfacique a pu être contrôlée en comparant les coefficients de traînée CX de la maquette mesurés par la balance et obtenus :

- dans les 2 veines de S3MA,
- dans la veine transsonique de la soufflerie S2MA de section 7 fois plus grande (figure 14) ; induisant ainsi des effets de parois minimes.
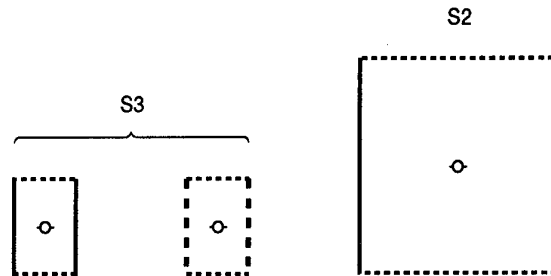
Fig 14 : Maquette dans les 3 veines

La maquette était montée sur le même dard droit pour les 3 essais.

Les modifications de pression statique CP induites par la présence des parois et calculées à l'emplacement de la maquette sont présentées figure 15. A l'arrière de la maquette les CP apparaissent très différents, négatifs en 4 parois perforées, fortement positifs en 2 parois perforées.
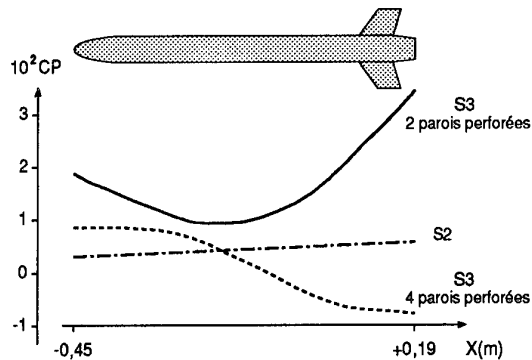
Fig 15 : CP induits par les parois dans les 3 veines

Les corrections en CX sont obtenues :

- en recalant le nombre de Mach et la pression cinétique,
- en calculant une poussée d'Archimède par intégration (monodimensionnelle) des CP sur le volume de la maquette.

Elles sont importantes (atteignant 10 % du CX mesuré) étant donné les forts niveaux de CP. Leurs valeurs sont visibles (en pourcentage) sur la figure

16 où ont été pointés pour les 3 veines les niveaux de CX obtenus avant et après correction des effets de parois.
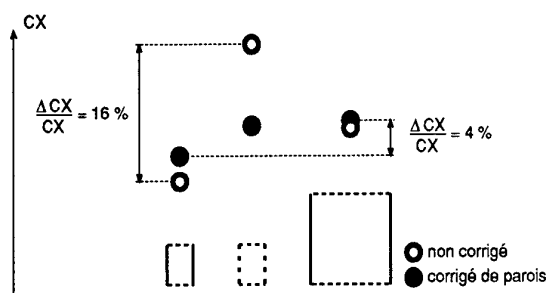
Fig 16 : CX mesurés dans les 3 veines

La dispersion des CX de 16 % initialement a été fortement réduite, à 4 %, après application des corrections. En regardant de plus près on note l'accord excellent, à mieux que 1 %, du CX de la veine S3 à 4 parois perforées avec celui de S2 (niveau de référence) tandis que le CX de la veine S3 à 2 parois perforées est plus faible de 4 % ; décalage qui reste au delà de la fidélité des mesures estimée à ± 1 %. Le fait que, figure 10, les CP calculés soient plus faibles que les CP mesurés à X ≈ 0 a probablement pour conséquence une sous-estimation de la correction ΔCX. Une meilleure prise en compte des porosités R locales sur les parois perforées devrait permettre un regroupement encore meilleur des trois CX.

6 - CONCLUSIONS

Pour le calcul des effets de parois dans des veines d'essai de section quelconque comportant des parois localement perforées de perméabilité différente sur les côtés horizontaux et verticaux, un code employant des singularités surfaciques disposées sur les parois de la veine a été développé.
Il a été utilisé dans le cadre des essais d'une maquette de missile dans la veine transsonique de la soufflerie S3MA équipée de 2 ou de 4 parois perforées pour :
- évaluer les paramètres de porosité moyens R des deux types de parois,
- évaluer les effets de parois.

Les principaux résultats de cette étude sont résumés ci-dessous :

1 - Des effets de parois très importants ont été constatés dans les veines à parois perforées de S3MA, modifiant de l'ordre de 10 % le CX d'une maquette d'obstruction 1,3 %. Des corrections sont indispensables. Non calculables par la méthode analytique classique, elles ont justifié la mise au point du code surfacique.

2 - Une fois le code de calcul disponible, la difficulté consiste à lui indiquer quelle porosité R est affectée à chaque facette veine.
D'une manière générale R dépend de la géomé-

trie de la paroi, du niveau de pression et de la couche limite et on peut s'attendre à autant de valeurs R que de facettes. Un concept de porosité unique par type de paroi a cependant été retenu.
Des valeurs moyennes R_H = 0,15 et R_V = 1,6 ont pu être obtenues pour les 2 types de parois perforées à partir de la comparaison des répartitions de pression mesurées et calculées. Elles ont été déterminées avec une certaine incertitude (de l'ordre de 20 %) et tenant compte des développements de couche limite, elles sont à reconsidérer pour des essais où le champ de pression serait nettement différent dans la veine.

3 - Des amplifications par la couche limite de la vitesse normale à la paroi non négligeables, voisines de 1,5 et de 1,1 ont été observées. Elles restent cependant modérées comme on pouvait s'y attendre avec $P_W > P_{caisson}$ majoritairement dans la veine (aspiration de la couche limite). Cela explique le succès relatif du concept de porosité unique.

4 - Les corrections des effets de parois calculées par le code ont fortement réduit la dispersion des CX (16 % au départ).
Les écarts avec le niveau de référence (S2) ont été ramenés à moins de 1 % pour la veine à 4 parois perforées et à 4 % pour la veine à 2 parois perforées.

Dans le futur, pour perfectionner la connaissance des veines de S3MA, il est envisagé :

- un étalonnage direct des parois perforées pour accéder à la loi w_w/U_e ($\Delta P / q_e$),

- des essais avec une maquette d'avion portante pour disposer dans la veine d'une large zone $P_W < P_{caisson}$ (soufflage de la couche limite). Les porosités R des parois seraient redéterminées et la validité des corrections d'incidence serait contrôlée.

REFERENCES

1 - VAUCHERET X - "Recent progress in wall interference calculations for industrial wind tunnels" La Recherche Aerospatiale, 1988-3

2 - VAUCHERET X - "Corrections de parois en soufflerie transsonique. Porosité équivalente" Publications ONERA 1977-3

3 - VAUCHERET X - " Vortex lattice code for computation of wind tunnel and support effects on models" -
La Recherche Aérospatiale, 1991-2

4 - HESS J.L et SMITH A.M.O. - "Calculation of potential flow about arbitrary bodies" Progress in Aeronautical Sciences, vol 8, Pergamon Press, New York (1966)

5 - JOPPA R.G - "A method of calculating wind-tunnel interference factors for tunnels of arbitrary cross-section", NASA CR 845 (1967)

6 - WASSERSTROM E., BOROVIK Y., HAZA-NOVSKY D. ET ROM J - "Calculation of lift interference correction due to wind tunnel test section boundaries by the vortex- lattice-method", Technion Israel Institute of Technology, Report 124 (1971)

7 - CRITES R., et RUEGER M. - "Modeling the ventilated wind tunnel wall", 1992, AIAA-92-0035

8 - CHAN YY - "Analysis of boundary layers on perforated walls of transsonic wind tunnels", Journal of Aircraft, juin 1981, vol 18, n° 6.

EVALUATION OF COMBINED WALL- AND SUPPORT-INTERFERENCE ON WIND TUNNEL MODELS

M. Mokry

High Speed Aerodynamics Laboratory
Institute for Aerospace Research
National Research Council Canada
Ottawa, Ontario, Canada, K1A 0R6

Summary

Coupled interference effects of model support systems and ventilated test section walls on stream parameters at the model are calculated using a subsonic source panel method. The configurations discussed are the movable sting support system and the model plate mount in the IAR 1.5m×1.5m perforated-wall wind tunnel, and an automobile model in the DSMA slotted-wall wind tunnel.

List of symbols

C_D	drag coefficient
C_p	pressure coefficient
$\mathbf{i}$	unit vector in the direction of x axis
H	wind tunnel height
K	slot parameter
M	Mach number
N	coordinate along $\mathbf{N}$
$\mathbf{N}$	unit outward normal vector in physical space
n	coordinate along $\mathbf{n}$
$\mathbf{n}$	unit vector along the outward normal to S
P	porosity parameter
$\mathbf{r}$	position vector
R	radius of semi-infinite body
R_W	radius of cylindrical test section
S	boundary of flow region in transformed space
X, Y, Z	Cartesian coordinates in physical space
x, y, z	Cartesian coordinates in transformed space
α_Y, α_Z	flow angles in X, Y and X, Z planes (deg)
β	Prandtl-Glauert factor $(= \sqrt{1 - M_o^2})$
γ	ratio of specific heats $(= 1.4)$
Δ	interference correction
ν	angle between vectors $\mathbf{n}$ and $\mathbf{i}$
σ	source density
ϕ	disturbance velocity potential in physical space
φ	disturbance velocity potential in transformed space

Sub/super-scripts

j, k	collocation point
o	upstream end of test section
∞	far downstream

1. Introduction

The prominent effects of the wind tunnel interference associated with a model support system, as discussed by Young and Pankhurst[1], are:
(a) increment of velocity due to solid blockage,
(b) increment of velocity due to wake blockage,
(c) longitudinal pressure gradient,
(d) flow curvature, and
(e) mutual interference at the support/model junction.

Items (a)-(d), which are similar to wall interference induced by the model only, can be analyzed using potential flow techniques. Item (e) is an interactive viscous-flow problem, affecting the base pressure and drag, which has largely eluded theoretical description. An experimental approach is also heavily relied upon when studying the support interference in dynamic tests[2].

The development of a method to calculate the combined model support - wall interference effects on aircraft models at subsonic speeds was initiated at the IAR (formerly NAE) about 10 years ago, shortly after the first successful applications of panel methods to complex configurations in closed-wall test sections were reported elsewhere[3,4]. The objective was to analyze the effect of the asymmetry of the model support system, Fig.1, on flow in the 1.5m×1.5m perforated wall test section of the IAR Blowndown Wind Tunnel. However, the method was found to underestimate the experimentally observed differences in zero-lift angles for the upright and inverted model tests, and the results remained unreported at that time.

In 1984-85 the method was modified to compute an inviscid flow past automobile models inside closed or slotted wall test sections. A reasonable agreement with experiment, verifying the slotted wall concept of an automotive wind tunnel, designed by DSMA International, was obtained at that time[5,6].

A renewed interest in the method has emerged in 1987, with the design of a new roll drive system[7] for the IAR 1.5m×1.5m test section. The new system, which permits higher model loads and speeds of rolling, has a bulkier roll drive housing than the original one, leading to an inreased interference.

In 1990 the method was applied to estimate interference effects of the newly designed plate mount for the de Havilland aircraft model tests in the IAR test section.

A source panel method was chosen since at low incidences the model support system is essentially a nonlifting body and the wind tunnel walls can also be treated as nonlifting surfaces. A study on closed wall interference[4], performed earlier at British Aerospace, showed that the first-order panel method, based on the use of piecewise-constant source distributions, works remarkably well for closed tunnel walls. The 'leakage', which is due to the fact that the boundary condition is enforced only at a single point of each source panel, but the air is free to leak around, was found to be relatively small, not altering significantly the mass flux down the wind tunnel. The present paper extends the source panel method to perforated and slotted wind tunnel walls.

A similar application of a vortex lattice method has recently been reported by Vaucheret[8]. Use of higher-order panel methods or other advanced CFD methods to assess the effects of model support systems and working section modifications have also been reported in Refs.9-13.

2. Governing Equations

Items (a)-(d) discussed in Introduction can be quantified using linear potential theory. Experience shows that the walls provide, in the averaged sense, a 'low perturbation' environment so that linearization of the potential equation in the adjacent flow regions applies up to high stream Mach numbers, $M_o < 1$. With some limitations, the same can be adopted to a model support, designed to minimize the perturbations to the free stream.

The governing equation for the disturbance velocity potential is

$$\beta^2 \frac{\partial^2 \phi}{\partial X^2} + \frac{\partial^2 \phi}{\partial Y^2} + \frac{\partial^2 \phi}{\partial Z^2} = 0, \qquad (1)$$

where X is the coordinate in the direction of the wind tunnel axis and $\beta = \sqrt{1 - M_o^2}$.

Assuming the stream velocity vector to be of unit magnitude, the boundary condition of no flow through the model or its support system is

$$\frac{\partial \phi}{\partial N} = -\mathbf{i} \cdot \mathbf{N}. \qquad (2)$$

The wall interference effects are accounted for using the following linear boundary conditions:

a) closed (solid) walls

$$\frac{\partial \phi}{\partial N} = 0, \qquad (3a)$$

b) perforated (porous) walls

$$\frac{\partial \phi}{\partial N} - P \frac{\partial \phi}{\partial X} = 0, \qquad (3b)$$

c) longitudinally slotted walls

$$\frac{\partial \phi}{\partial N} - \frac{1}{K}(\phi - \phi_o) = 0, \qquad (3c)$$

d) open jet walls

$$\frac{\partial \phi}{\partial X} = 0. \qquad (3d)$$

The porosity parameter P and the slot parameter K, which are functions of wall geometry, openness ratio, and local flow conditions, need to be obtained experimentally[14-17]. The value ϕ_o, referring to the upstream end of the test section, is a constant of integration[9] of the Davis-Moore boundary condition[18].

The compressibility transformation

$$x = \frac{X}{\beta H}, \quad y = \frac{Y}{H}, \quad z = \frac{Z}{H}, \quad \varphi = \beta \frac{\phi}{H}, \qquad (4)$$

reduces Eq.(1) to Laplace's equation and in Eqs.(3) amplifies P by the inverse of β and normalizes K by the test section height H. The resultant relationships between the disturbance velocity components in the physical and the transformed (incompressible) plane,

$$\frac{\partial \phi}{\partial X} = \frac{1}{\beta^2} \frac{\partial \varphi}{\partial x}, \quad \frac{\partial \phi}{\partial Y} = \frac{1}{\beta} \frac{\partial \varphi}{\partial y}, \quad \frac{\partial \phi}{\partial Y} = \frac{1}{\beta} \frac{\partial \varphi}{\partial y}, \qquad (5)$$

are consistent with Goethert's extension[19] of the Prandtl rule.

184 PANELS

VIEW

X = −100.00
Y = −150.00
Z = 50.00
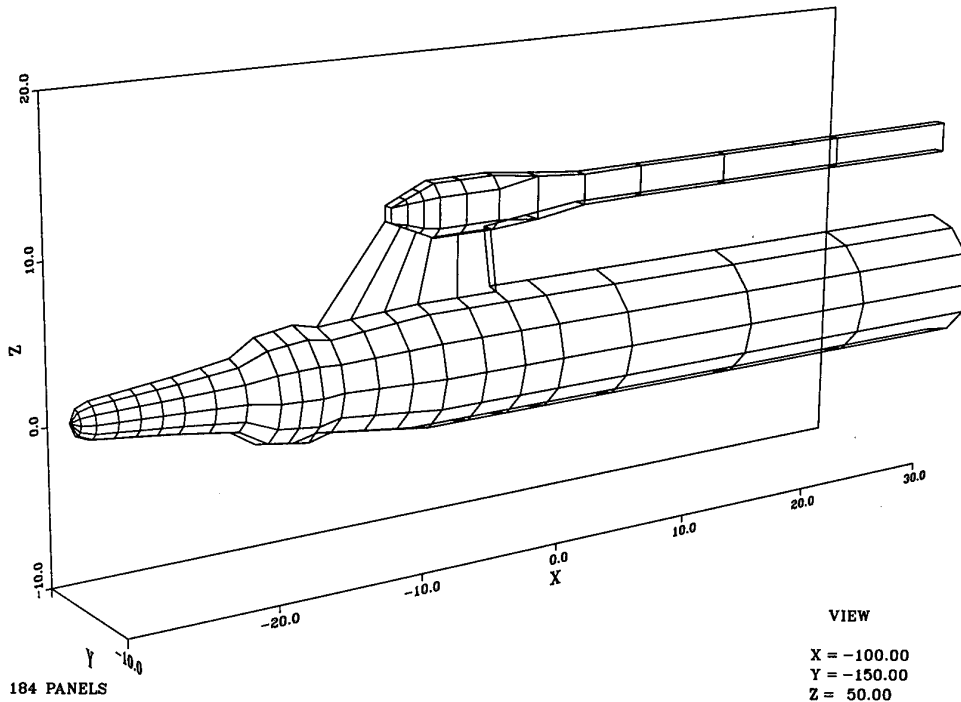
Fig.1 NAE old model support system.

3. Integral Equation Formulation

In the transformed space, the linearized disturbance velocity potential for nonlifting flows can be represented by the potential of the simple layer

$$\varphi(\mathbf{r}_k) = -\iint_S \sigma(\mathbf{r})\frac{1}{4\pi|\mathbf{r}_k - \mathbf{r}|}dS, \qquad (6)$$

where σ is the source density and $\mathbf{r}_k = (x_k, y_k, z_k)$ and $\mathbf{r} = (x, y, z)$ are position vectors of the observation and source points respectively. The integration surface S comprises the surfaces of the model support system and walls.

The gradient of φ is given by

$$\nabla\varphi(\mathbf{r}_k) = \begin{cases} \displaystyle\iint_S \sigma(\mathbf{r})\frac{\mathbf{r}_k - \mathbf{r}}{4\pi|\mathbf{r}_k - \mathbf{r}|^3}dS, & \mathbf{r}_k \notin S; \\[2ex] \displaystyle\frac{1}{2}\sigma(\mathbf{r}_k)\mathbf{n}_k + \barint_S \sigma(\mathbf{r})\frac{\mathbf{r}_k - \mathbf{r}}{4\pi|\mathbf{r}_k - \mathbf{r}|^3}dS, & \mathbf{r}_k \in S, \end{cases}$$

$$(7)$$

where $\mathbf{n}_k$ is the unit normal to S at $\mathbf{r}_k$, pointing into the flowfield. The bar across the integral sign in the lower part of Eq.(7) indicates that a small (circular) neighbourhod of the point $\mathbf{r}_k$ is excluded from the surface integral; its contribution has already been accounted for by the preceding isolated term.

The Neumann boundary condition to be satisfied on the model or its support in the transformed space is

$$\frac{\partial\varphi}{\partial n_k}(\mathbf{r}_k) = -\cos\nu_k, \qquad (8)$$

where ν_k is the angle between $\mathbf{n}_k$ and the x-direction (direction of flow). Substituting from Eq.(7), we obtain

$$\frac{1}{2}\sigma(\mathbf{r}_k) + \barint_S \sigma(\mathbf{r})\frac{\mathbf{n}_k \cdot (\mathbf{r}_k - \mathbf{r})}{4\pi|\mathbf{r}_k - \mathbf{r}|^3}dS = -\cos\nu_k. \qquad (9)$$

With respect to the unknown source density σ, Eq.(9) represents a Fredholm integral equation of the second kind, which is known to have a well-behaved solution.

The perforated wall boundary condition (3b) in the transformed space takes the form

$$\frac{\partial\varphi}{\partial n_k}(\mathbf{r}_k) - \frac{P(\mathbf{r}_k)}{\beta}\frac{\partial\varphi}{\partial x_k}(\mathbf{r}_k) = 0, \qquad (10)$$

where $\partial/\partial n_k$ denotes the derivative in the direction of the unit vector $\mathbf{n}_k$, normal to the wall and pointing into the flowfield. The closed wall and open jet boundary conditions are contained in Eq.(10) as the limiting cases $P/\beta \to 0$ and $P/\beta \to \infty$ respectively.

Substituting from Eq.(7) in (10), we obtain

$$\begin{aligned} &\frac{1}{2}\sigma(\mathbf{r}_k) + \barint_S \sigma(\mathbf{r})\frac{\mathbf{n}_k \cdot (\mathbf{r}_k - \mathbf{r})}{4\pi|\mathbf{r}_k - \mathbf{r}|^3}dS \\ &\quad - \frac{P(\mathbf{r}_k)}{\beta}\iint_S \sigma(\mathbf{r})\frac{\mathbf{i} \cdot (\mathbf{r}_k - \mathbf{r})}{4\pi|\mathbf{r}_k - \mathbf{r}|^3}dS = 0, \end{aligned} \qquad (11)$$

which retains the character of a Fredholm equation of the second kind supposed that P/β is not very large.

The slotted wall boundary condition (3c) in the transformed space takes the form

$$\frac{\partial\varphi}{\partial n_k}(\mathbf{r}_k) - \frac{H}{K(\mathbf{r}_k)}[\varphi(\mathbf{r}_k) - \varphi(\mathbf{r}_k^o)] = 0, \qquad (12)$$

where $\mathbf{r}_k^o = (x^o, y_k, z_k)$ and x^o is the x-coordinate of the upstream end of the test section. The closed wall and open jet boundary conditions are included in Eq.(12) as the limiting cases $H/K \to 0$ and $H/K \to \infty$ respectively.

Substituting from Eqs.(6) and (7) in Eq.(12), we obtain

$$\begin{aligned} &\frac{1}{2}\sigma(\mathbf{r}_k) + \barint_S \sigma(\mathbf{r})\frac{\mathbf{n}_k \cdot (\mathbf{r}_k - \mathbf{r})}{4\pi|\mathbf{r}_k - \mathbf{r}|^3}dS \\ &\quad + \frac{H}{K(\mathbf{r}_k)}\iint_S \sigma(\mathbf{r})\left(\frac{1}{4\pi|\mathbf{r}_k - \mathbf{r}|} - \frac{1}{4\pi|\mathbf{r}_k^o - \mathbf{r}|}\right)dS = 0, \end{aligned}$$

$$(13)$$

which again retains the character of a Fredholm equation of the second kind provided that H/K is not very large. We note that for a very large H/K Eq.(12) would specify a Dirichlet boundary condition, for which a double layer distribution (doublets) would be more appropriate than a simple layer distribution (sources).

4. Source Panel Method

The surface S is approximated by an assembly of quadrilateral and triangular panels S_j with a piecewise constant source density,

$$\sigma(\mathbf{r}) = \sigma_j, \qquad \mathbf{r} \in S_j.$$

For the wall panels, similarly,

$$P(\mathbf{r}) = P_k \quad \text{or} \quad K(\mathbf{r}) = K_k, \qquad \mathbf{r} \in S_k.$$

Satisfying boundary conditions at each panel centroid results in a system of linear algebraic equations

$$\sum A_{kj}\sigma_j = b_k \qquad (14)$$

in unknown source densities.

From Eq.(9) we obtain for k on the model support

$$A_{k,j} = \begin{cases} \displaystyle\frac{1}{2}, & j = k \\[2ex] \displaystyle\iint_{S_j}\frac{\mathbf{n}_k \cdot (\mathbf{r}_k - \mathbf{r})}{4\pi|\mathbf{r}_k - \mathbf{r}|^3}dS, & j \neq k \end{cases}$$

$$b_k = -\cos\nu_k = -\mathbf{n}_k \cdot \mathbf{i} \qquad (15)$$

Similarly, from Eq.(11) on a perforated wall

$$A_{k,j} = \begin{cases} \displaystyle\frac{1}{2}, & j = k \\[3ex] \displaystyle\iint_{S_j}\frac{\mathbf{n}_k \cdot (\mathbf{r}_k - \mathbf{r})}{4\pi|\mathbf{r}_k - \mathbf{r}|^3}dS \\ \displaystyle\quad - \frac{P_k}{\beta}\iint_{S_j}\frac{\mathbf{i} \cdot (\mathbf{r}_k - \mathbf{r})}{4\pi|\mathbf{r}_k - \mathbf{r}|^3}dS, & j \neq k \end{cases}$$

$$b_k = 0 \qquad (16)$$

and from Eq.(13) on a slotted wall

$$
A_{k,j} = \begin{cases}
\dfrac{1}{2}, & j = k = k^o \\[2mm]
\dfrac{1}{2} + \dfrac{H}{K_k} I_k \\[2mm]
\quad - \dfrac{H}{K_k} \displaystyle\iint_{S_j} \dfrac{1}{4\pi|\mathbf{r}_k^o - \mathbf{r}|} dS, & j = k \neq k^o \\[4mm]
\displaystyle\iint_{S_j} \dfrac{\mathbf{n}_k \cdot (\mathbf{r}_k - \mathbf{r})}{4\pi|\mathbf{r}_k - \mathbf{r}|^3} dS, & j \neq k = k^o \\[4mm]
\displaystyle\iint_{S_j} \dfrac{\mathbf{n}_k \cdot (\mathbf{r}_k - \mathbf{r})}{4\pi|\mathbf{r}_k - \mathbf{r}|^3} dS \\[2mm]
\quad + \dfrac{H}{K_k} \displaystyle\iint_{S_j} \dfrac{1}{4\pi|\mathbf{r}_k - \mathbf{r}|} dS \\[2mm]
\quad - \dfrac{H}{K_k} I_j, & k^o = j \neq k \\[4mm]
\displaystyle\iint_{S_j} \dfrac{\mathbf{n}_k \cdot (\mathbf{r}_k - \mathbf{r})}{4\pi|\mathbf{r}_k - \mathbf{r}|^3} dS \\[2mm]
\quad + \dfrac{H}{K_k} \displaystyle\iint_{S_j} \dfrac{1}{4\pi|\mathbf{r}_k - \mathbf{r}|} dS \\[2mm]
\quad - \dfrac{H}{K_k} \displaystyle\iint_{S_j} \dfrac{1}{4\pi|\mathbf{r}_k^o - \mathbf{r}|} dS, & k^o \neq j \neq k \neq k^o
\end{cases}
$$

$$
b_k = 0. \tag{17}
$$

Index k^0 corresponds to the upstream panel centroid $\mathbf{r}_k^0$. The value

$$
\begin{aligned}
I_j &= \iint_{S_j} \frac{1}{4\pi|\mathbf{r}_j - \mathbf{r}|} dS \\
&= \frac{1}{2\pi}\left(a \ln \frac{b + \sqrt{a^2 + b^2}}{a} + b \ln \frac{a + \sqrt{a^2 + b^2}}{b} \right)
\end{aligned}
$$

applies to a rectangular wall panel S_j of sides a and b. Although closed form solutions can also be constructed for the remaining integrals, it is more efficient to evaluate them numerically, for example by dividing the panels into sub-panels.

If the paneled surface S possesses a plane of symmetry, the system of Eqs.(14) can be reduced by one half, at the cost of a slightly increased complexity of the matrix coefficients, which then include the contributions of the 'image' panels.

As indicated earlier, there is a problem concerning the ill-conditioning of the matrix when $P/\beta \to \infty$ or $H/K \to \infty$. Accordingly, by approaching the open jet conditions the computation becomes inaccurate and sensitive to small changes in input data and, eventually, breaks down completely.

5. Corrections to Stream Parameters

Once the system of linear equations has been solved, the components of disturbance velocity can be evaluated from Eqs.(5) and (7). Assuming that the stream Mach number M_o is measured at the reference station X_o, Y_o, Z_o, the correction to M_o at an arbitrary flowfield point X, Y, Z is obtained as

$$
\Delta M \simeq \left(1 + \frac{\gamma - 1}{2} M_o^2\right) M_o \left[\frac{\partial \phi}{\partial X}(X,Y,Z) - \frac{\partial \phi}{\partial X}(X_o,Y_o,Z_o) \right] \tag{18}
$$

The incremental corrections to angles of incidence are

$$
\Delta \alpha_Y \simeq \frac{180}{\pi} \frac{\partial \phi}{\partial Y}(X,Y,Z) \quad \text{and} \quad \Delta \alpha_Z \simeq \frac{180}{\pi} \frac{\partial \phi}{\partial Z}(X,Y,Z). \tag{19}
$$

6. Results

The feasibility of the described source panel program for modeling flows past slender support systems in the wind tunnel environment was first tried on a point-source body surrounded by a cylindrical wall. Denoting by R_∞ the body radius far downstream, the disturbance velocity potential of the body-generating source is

$$
\phi = -\frac{R_\infty^2}{4\sqrt{X^2 + Y^2 + Z^2}}
$$

and the radial and axial coordinates of the body surface are[20]

$$
R \equiv \sqrt{Y^2 + Z^2} = R_\infty \cos \frac{\theta}{2}, \quad X = R \cot \theta, \quad 0 < \theta \leq \pi.
$$

Using the vertical plane of symmetry, the port side of the body is approximated by 270 panels on interval $-0.5R_\infty \leq X \leq 40R_\infty$. The downstream end of the body was kept open. Similarly, the port side of the wall of radius $R_W = 3R_\infty$ was approximated by 640 panels on interval $-40R_\infty \leq X \leq 40R_\infty$. A central portion of the paneling is shown in Fig.2.
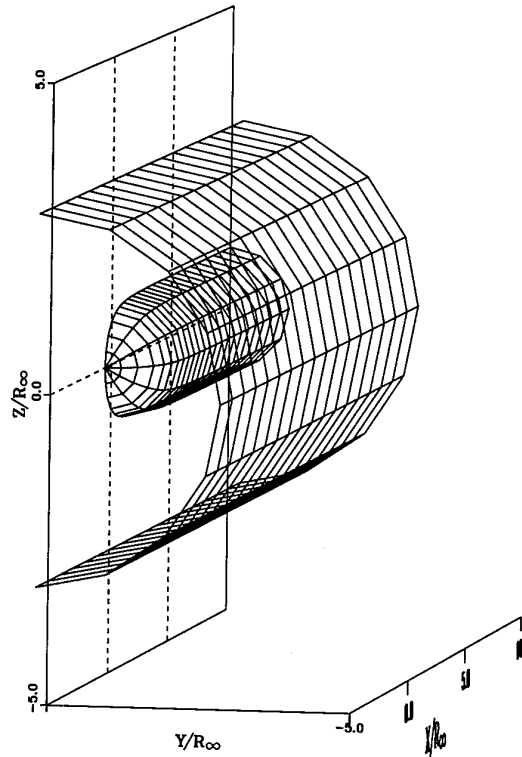
Fig.2   Point-source body inside a cylindrical test section.
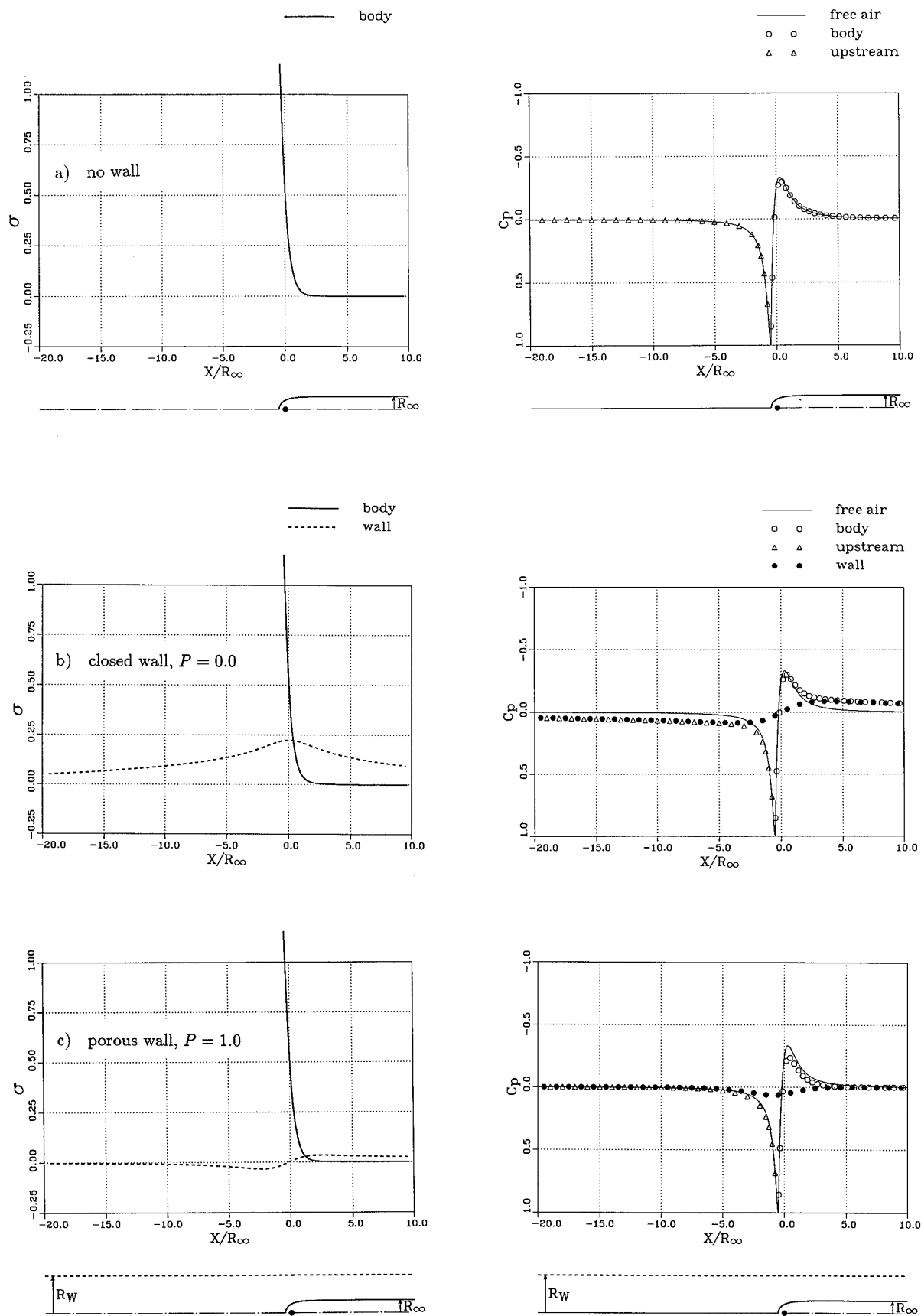
Fig.3.   Point-source body and wall pressures.

First, free air flow past the body (no wall) was considered. The surface source density and pressure coefficient distributions, obtained by the panel method are plotted in Fig.3a. It is seen that σ decays rapidly with the distance from the body nose. It can also be confirmed that

$$\iint_S \sigma(\mathbf{r})dS \simeq \pi R_\infty^2.$$

This suggests that on elongated cylindrical bodies, such as stings, the paneling does not have to extend very far downstream provided that it remains open-ended at the rear. The computed pressure coefficients are compared with the exact values

$$C_p = -\frac{X R_\infty^2}{2(X^2 + Y^2 + Z^2)^{1.5}} - \frac{R_\infty^4}{16(X^2 + Y^2 + Z^2)^2}$$

along the dividing streamline (streamsurface). The circles are the surface values computed at the panel centroids, the triangles are the computed axial values upstream of the body; the solid line represents the exact values. Apart from the nose region, where the paneling for a first-order panel method is perhaps too coarse, there is an excellent overall agreement. The upstream influence of nonlifting, slender support systems can be evaluated by a source panel method quite confidently.

Interpretation of wall interference calculations by the same method is somewhat more complex. Fig.3b shows the evaluated σ and C_p on the body and a solid wall of radius $R_W = 3R_\infty$. The source density on the wall is seen to decay very slowly with the distance from the body nose, indicating that an open-ended test section surface should not be truncated too close to the model. The variation of the wall pressure near the model is symptomatic of wake blockage in a closed-wall test section: the pressure established some distance upstream of the model decreases as we move towards the model and further decreases as we continue to move downstream of the model. For an infinitely long wind tunnel, different pressure levels should be attained far upstream and downstream. The correction to pressure coefficient at the source point ($X = 0$) relative to the flow far upstream is then half the difference. For a point source of strength πR_∞^2 inside an infinite tube of radius R_W it is[21]

$$\Delta C_p = -\left(\frac{R_\infty}{R_W}\right)^2 \simeq -0.111.$$

The calculated wall pressure coefficients undergo changes of a correct magnitude in the vicinity of the model nose but, because the paneling is only finite, tend to zero both upstream and downstream. Accordingly, the correction has to be evaluated from a difference of wall-induced pressures at the model and a finitely distant upstream station, where the reference static pressure is measured.

Fig.3c shows similar calculation results for the same geometry, assigning the porosity parameter of the cylindrical test section wall the value $P = 1.0$. The source density function along the wall displays now a different shape and decays faster with the distance from the model nose than was the case for $P = 0$. The wall pressures become undisturbed at much shorter distances from $X = 0$, which is consistent with porous wall theory[21]. We may also note that at this intermediate wall porosity the pressure coefficient at $X = 0$ is larger than that upstream, indicating a correction of opposite sign to that obtained for a fully closed wall.

Following the outlined guidelines, the (new) model support system of the IAR 1.5m×1.5m Blowdown Wind Tunnel has been paneled as shown in Fig.4. The port side of the system is approximated by 172 panels, the corresponding half of the perforated wall test section is described by 210 panels and

its closed-wall continuation by 56 panels. The entrance and exit planes are left open; the boundary condition is satisfied on the inner faces of wall panels. A sting, which connects the support system with the model, has not been considered in this study.

With respect to the motion of various components of the system, four types of panel corner points have been identified:
1. model points (pitched),
2. strut points (translated vertically),
3. link points(translated horizontally and vertically), and
4. wall points (fixed).

Consequently, the panels formed by differently moving points were treated as "stretchable".

The corrections ΔM and $\Delta \alpha$ were calculated for a range of Mach numbers, support incidences and wall porosities (over the perforated-wall portions of the test section). An example is given here for $M_o = 0.7$, $\alpha = -15^o, 0^o, 15^o$ and $P = 1.0$. In Fig.5 compared are the interference effect of the support only and the combined effect of the support and test section walls, evaluated along the model support axis and plotted as a function of distance from the "pitch pin". The dotted vertical line indicates the intersection of the support system axis and the wind tunnel axis, where the aerodynamic centre of a tested model is normally located. To what extent these corrections may affect the test data depends on the size of the tested model and its closeness to the model support system. The source panel method did not detect any appreciable effect of the model support asymmetry.

The same method has also been applied to investigate the interference effects of a proposed plate mount for the de Havilland aircraft model tests. Again, the model was to be installed and tested in the IAR 1.5m×1.5m Blowdown Wind Tunnel. A full description of the plate mount and its effects on the measured model force coefficients are given in Ref.22.

In the preliminary stage of the investigation, the test section and a simplified plate mount were approximated by 370 panels, as illustrated in Fig.6. The arrows, which identify the perforated-wall panels, were generated as normal vectors in a control routine which is used to check the sequence of corner points specifying each panel. The calculations were performed for a range of Mach numbers and porosity parameters. One of the results is shown in Fig.7, where compared are the evaluated wall/plate mount and plate mount only corrections along the test section centreline. Since a major flow disturbance occurs near the plate mount nose (vertical dotted line), the mount had to be eventually designed to reach well upstream of the model[22]. The wall induced effect at intermediate wall porosities was found to be relatively minor, but in order to quantify it more precisely, the porosity parameter for a given wall geometry (open area ratio) and flow conditions (Mach number, stagnation pressure, etc) has to be known in the first place.

For higher blockage ratios, the pertinent parameters characterizing flow through ventilated walls can be obtained by correlating the measured and computed wall pressures. An example of this procedure is given here for the DSMA low speed wind tunnel tests of an automobile model[6].

Fig.8 shows the paneling of a generic car model, developed by the Motor Industry Research Association (MIRA), inside the DSMA slotted-wall wind tunnel. The rear end of the automobile surface was left open, in order to simulate
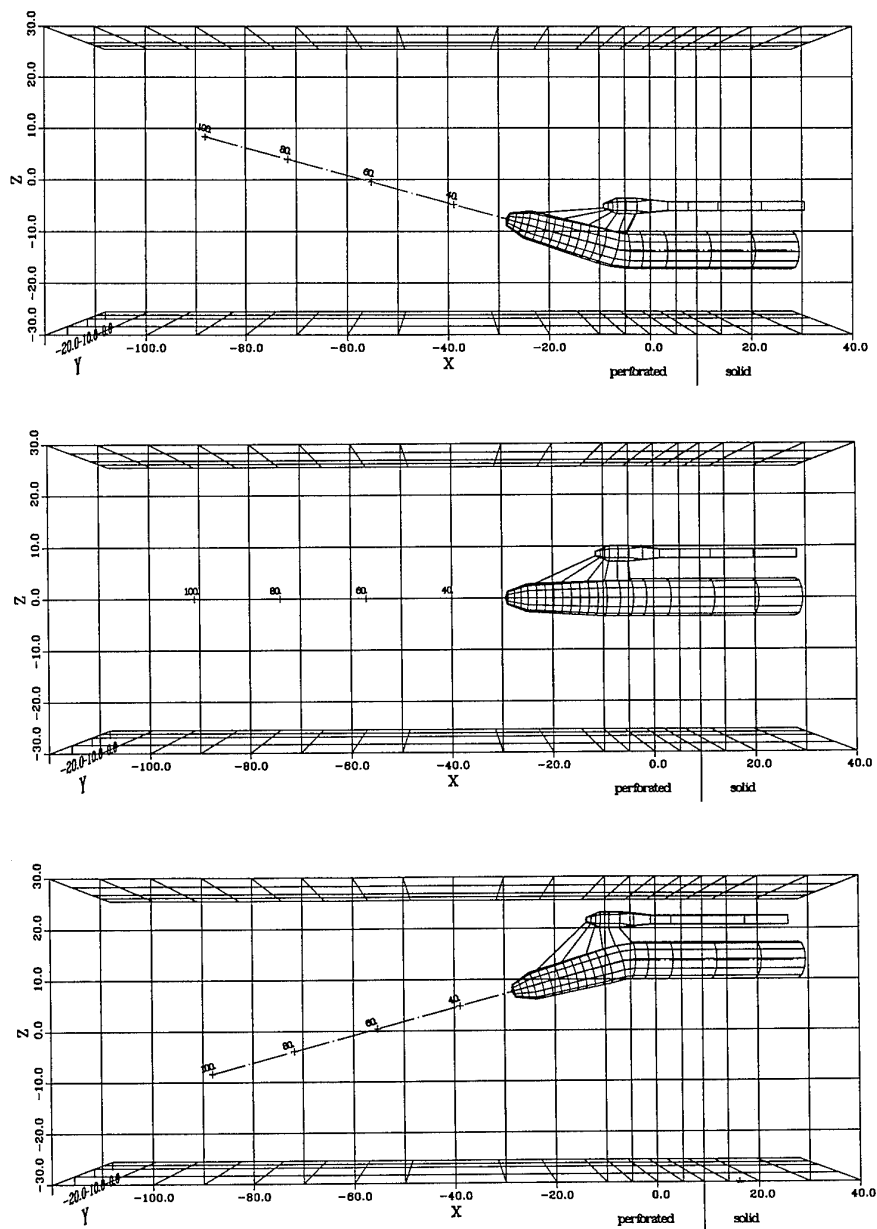
Fig.4.   IAR model support and test section.
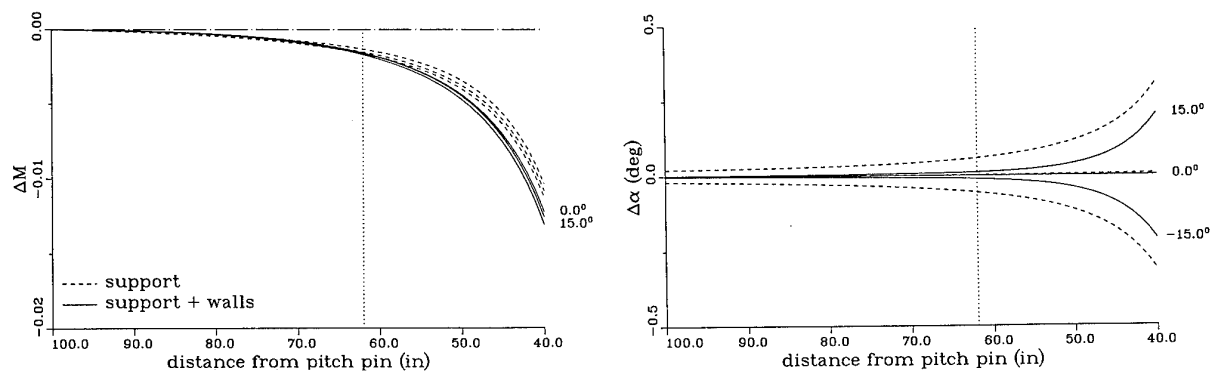
Fig.5.   Model support/wall corrections, $M_o = 0.7$, $P = 1.0$.
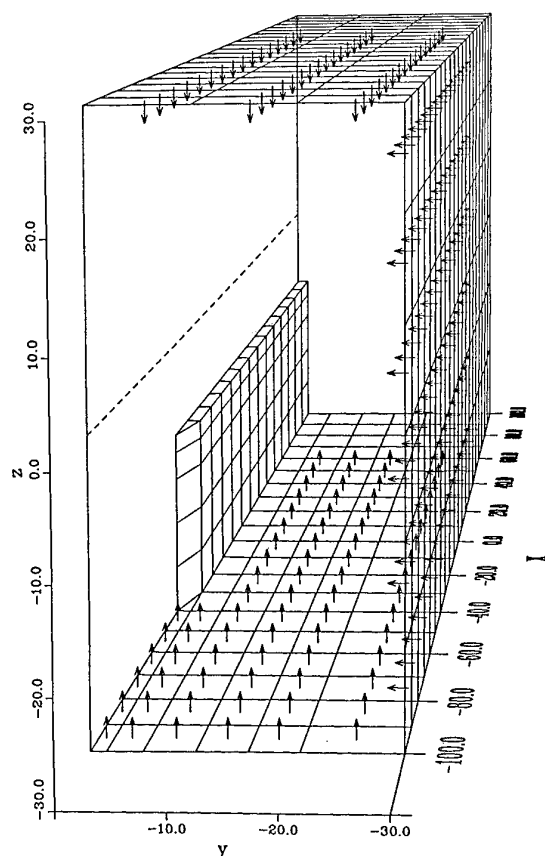
Fig.6. Plate mount and test section.
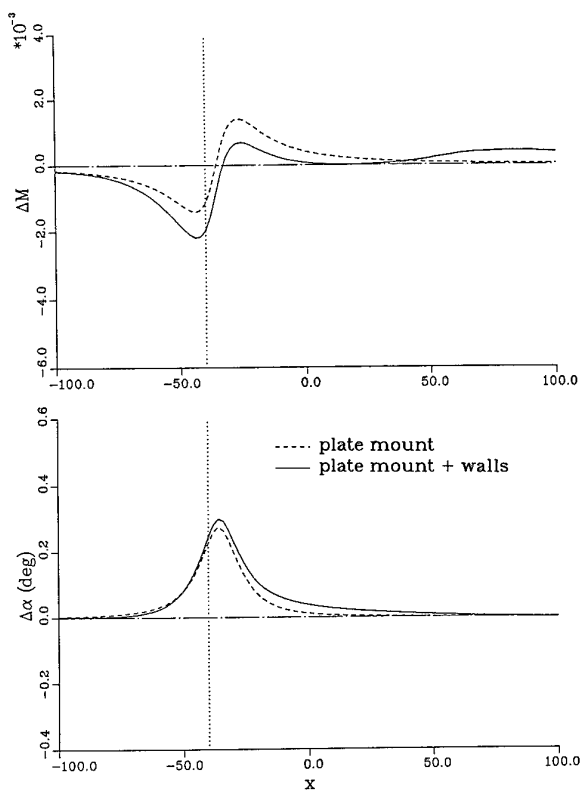
Fig.7. Plate mount/wall corrections, $M_o = 0.6$, $P = 1.0$.

the wake blockage effect by the net flux from the source panels. The ground effect was taken into account by considering the floor of the test section as a horizontal plane of symmetry. A detailed description of the models, test sections and their instrumentation is given in Ref.5.

In Fig.9 compared are the ceiling and sidewall pressures, measured along the slat centrelines, with those computed by the source panel method. The verical broken lines indicate the extent of the DSMA slotted-wall test section. The experimental pressures (symbols), obtained with slotted walls at 30% open area ratio (OAR), were found to match closest the calculations performed at $K/H \simeq 0.5$, which in turn were very close to those performed for free air conditions. The inability of the theoretical curves to better match the experimental wall pressures downstream of the model is attributable[23], in part, to external interference from a structural beam inside the plenum chamber, whose location is indicated in Fig.9 by the vertical dotted lines.

Fig.10 shows the wall induced pressures, ΔC_p, at the beltline height of the model, calculated by considering the wall panels only. The obtained values were then used to evaluate the drag coefficient corrections, which take into account the change of dynamic pressure at the model position and compensate for the wall induced buoyancy force[23].

Similar calculations were performed for a range of slot parameters and model sizes with respect to the wind tunnel, listed in Table 1. The upper portion of Fig.11 illustrates the relative sizes of the full-scale car model with respect to three closed-wall test sections of the German-Dutch Wind Tunnel (DNW), and of three subscale car models with respect to the slotted-wall test section of the DSMA wind tunnel. The attached symbols are used to identify the corresponding drag coefficient corrections in the lower portion of Fig.11. The ratio $\Delta C_D/C_D$, where $C_D = 0.278$ is the free-air drag coefficient obtained by correcting the DNW 2.1% blockage experiment, is plotted there as a function of the slot parameter to test section height ratio, K/H. It is seen that ΔC_D decreases monotonically with K, from positive values for the 3/4 open test section to (large) negative values for the closed test section. With 30% OAR slotted walls, characterized by $K/H \approx 0.5$, the experiment is practically interference-free even at high blockage ratios.

This last example was used to illustrate that the described wall interference assessment may indeed be useful in supplementing experimental findings or confirming the soundness of newly designed wind tunnel test sections or components. Based on a predominantly experimental work, several wind tunnels with longitudinally slotted test sections have been built or designed by DSMA since: Volvo (1986), Porsche (1986), Hyundai (1991), and VAZ-Lada (1993).

Table 1. Sizes of test sections and car models

facility (m×m)	model scale	blockage (%)
DNW 9.50×9.50	1.00	2.06
DNW 8.00×6.00	1.00	3.87
DNW 6.00×6.00	1.00	5.16
DSMA 1.24×0.72	0.20	8.32
DSMA 1.24×0.72	0.25	13.00
DSMA 1.24×0.72	0.30	18.71
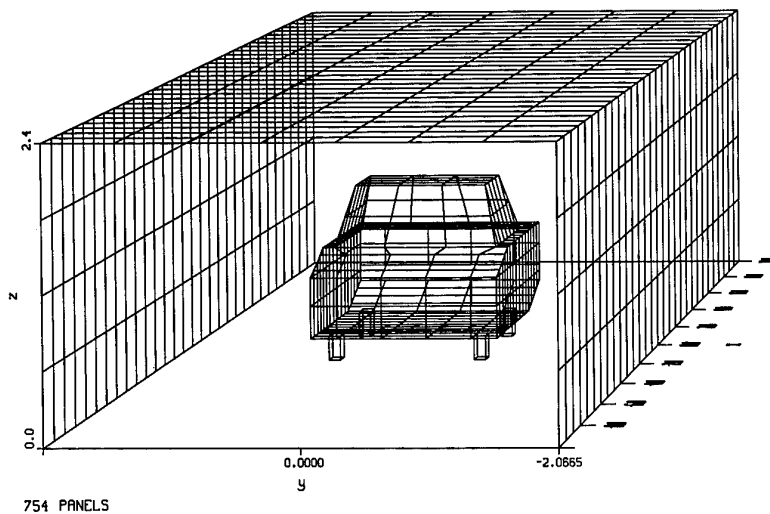
Fig.8.   MIRA notchback car model and test section.
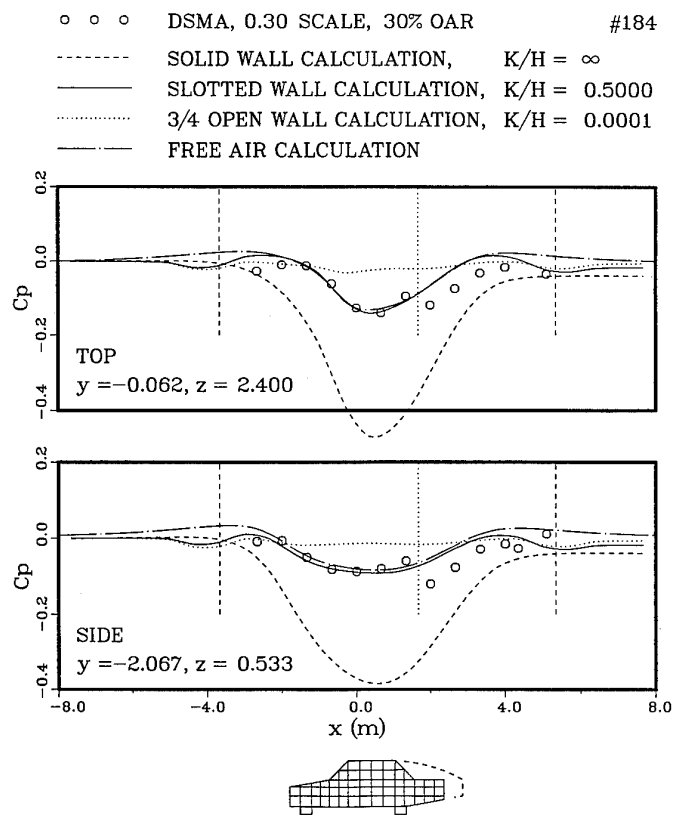
Fig.9.   Ceiling and sidewall pressures.
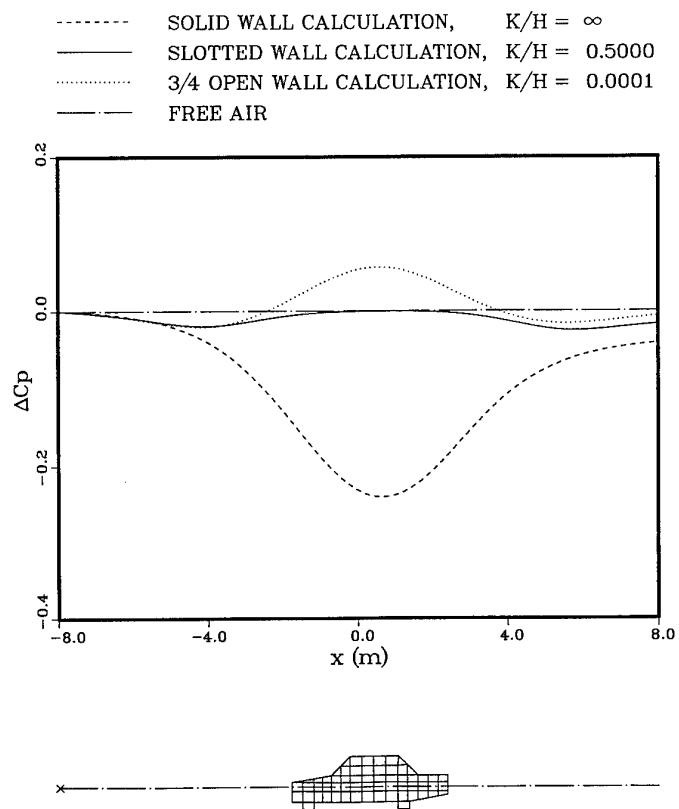
Fig.10. Wall induced pressures at beltline height.
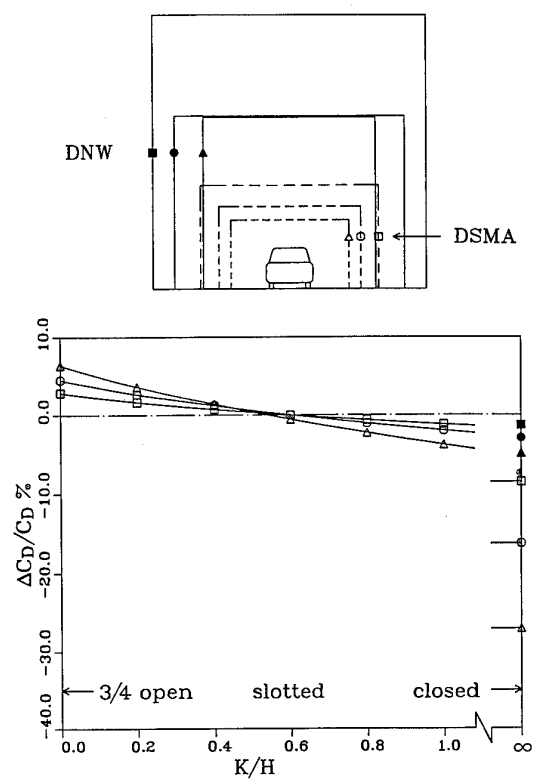
Fig.11. Correction to drag coefficient.

7. Concluding Remarks

The method described here is capable of predicting the combined interference due to model support systems and wind tunnel walls. Since the underlying source panel technique is based on linearized subsonic potential theory, the method is best suited for cases where compressibility or vortex shedding phenomena are relatively unimportant. In the form presented here, it is strictly applicable to nonlifting bodies and closed or partially open wind tunnel walls. The pertinent wall parameters specifying the linear boundary conditions are expected to be established experimentally.

Acknowledgements

References

1. Young, A.D. and Pankhurst, R.C., "Support Blockage Interference in Wind-Tunnel Tests," Aeronautical Research Council 19,903 F.M.2646, Feb.1958.

2. Ericsson, L.E. and Reding, J.P., "Review of Support Interference in Dynamic Tests," AIAA Journal, Vol.21, Dec.1983, pp.1652-1666.

3. "Round Table Discussion on Wall Interference in Wind Tunnels," Contribution of J.C.Vayssaire, AGARD-CP-335, May 1982, RTD.1-10.

4. Holt, D.R. and Hunt, B., "The Use of Panel Methods for the Evaluation of Subsonic Wall Interference," AGARD-CP-335, May 1982, pp.2.1-2.16.

5. Templin, J.T. and Raimondo, S., "Experimental Evaluation of Test Section Boundary Interference Effects in Road Vehicle Tests in Wind Tunnels," Journal of Wind Engineering and Industrial Aerodynamics, Vol.22, 1986, pp.129-148.

6. Mokry, M. and Templin, J.T., "A Source Panel Method for the Calculation of Boundary Interference on Automobile Models in Solid and Slotted Walls and 3/4-Open Jet Wind Tunnels," Development of Adaptive Slotted Wall Wind Tunnel Concepts for Aerodynamic Testing of Road Vehicles, NRC/DSMA Rept. 974/R216, April 1988.

7. "Roll Drive System for the NAE 5ft. Trisonic Wind Tunnel," Rept. 4077/R200, DSMA International Inc.

8. Vaucheret, X., "Vortex Lattice Code for Computation of Wind Tunnel and Support Effects on Models," Recherche Aérospatiale, n° 1991-2, English edition, pp.39-51.

9. Lee, K.D., "Numerical Simulation of the Wind Tunnel Environment by a Panel Method," AIAA Journal, Vol.19, April 1981, pp.470-475.

10. Snyder, L.D. and Erickson, L.L., "PAN AIR Prediction of NASA Ames 12-Foot Pressure Wind Tunnel Interference on a Fighter Configuration," AIAA-84-0219, 1984.

11. Stanniland, D.R., "The Use of Computational Fluid Dynamic Methods to Assess the Effects of Model Support Systems and Working Section Modifications on the Flow Around Wind Tunnel Models, "AGARD-CPP-429, October 1987, pp.16.1-16.16.

12. Krynytzky, A.J., "Mach Number Corrections for a Two-Foot Propeller Rig in Solid and Slotted Test Sections," AIAA 15th Aerodynamic Testing Conference, May 1988, pp.392-401.

13. Vaucheret, X., "Recent Progress in Wall Interference Calculations for Industrial Wind Tunnels," Recherche Aérospatiale n° 1988-3, English edition, pp.45-57.

14. Goethert, B.H., Transonic Wind Tunnel Testing, Pergamon Press, New York, 1961.

15. Jacocks, J.L., "An Investigation of the Aerodynamic Characteristics of Ventilated Test Section Walls for Transonic Wind Tunnels," Doctoral Thesis, The University of Tennessee, Knoxville, Dec.1976.

16. Everhart, J.L. and Barnwell, R.W., "A Parametric Study of the Interference Effects and the Boundary-Condition Coefficient of Slotted Wind-Tunnel Walls," Paper 78-805, AIAA 10th Aerodynamic Testing Conference, 1978.

17. Berndt, S.B., "Measuring the Flow Properties of Slotted Test-Section Walls," FFA Rept.135, The Aeronautical Research Institute of Sweden, May 1982.

18. Davis, D.D., Jr. and Moore, D., Analytical Study of Blockage- and Lift-Interference Corrrections for Slotted Tunnels Obtained by the Substitution of an Equivalent Homogeneous Boundary for the Discrete Slots, NACA RM L53E07b, 1953.

19. Goethert, B., "Ebene und räumliche Strömung bei hohen Unterschallgeschwindigkeiten (Erweiterung der Prandtlschen Regel)," Lilienthal Gesellschaft, Bericht 127, 1940, English transl. NACA TM 1105, Oct.1946.

20. Vallentine, H.R. Applied Hydrodynamics, 2nd ed., Butterworths, 1967, pp.244-246.

21. Wright, R.H., "The Effectiveness of the Transonic Wind Tunnel as a Device for Minimizing Tunnel-Boundary Interference for Model Tests at Transonic Speeds," AGARD Rept.294, March 1959.

22. Poole, R.J.D. and Galway, R.D., "Interference Corrections for a Centre-Line Plate Mount in a Porous-Walled Transonic Wind Tunnel," AGARD 73rd Fluid Dynamics Panel Symposium on Wall Interference, Support Interference and Flow Field Measurements, Brussels, Paper No.30, October 1993.

23. Mokry M, "Wall Interference Correction to Drag Measurements in Automotive Wind Tunnels," to be published in Journal of Wind Engineering and Industrial Aerodynamics.

INTERACTION D'UN SUPPORT DE TYPE 3 MATS SUR LES CARACTERISTIQUES AERODYNAMIQUES D'UNE MAQUETTE D'AVION CIVIL

par

J. WILLAUME
AEROSPATIALE Toulouse
316 route de Bayonne, 31060 Toulouse Cedex 03, France

C. QUEMARD
ONERA
Centre d'Essais du Fauga-Mauzac, 31410 Noë, France

A. BONNET
ENSAE
10 Avenue Edouard Belin, 31055 Toulouse Cedex, France

SUMMARY

The interference effects of a three strut support system on the longitudinal aerodynamic characteristics of a model is mainly due to the guards.

Our purpose is to describe two theoritical methods allowing to gain access to the level of correction to apply to the wind tunnel gross measurements. The first one is a well known panel method which provides a global correction of the forces; the second one is a simplified method which calculates separatly both the displacement effect (thickness) of the guards and the mutual lift effect between them and the wing.

The validity of these theoretical results has been checked by specific tests in wind tunnel F1 (ONERA) on a model of the AIRBUS A310.

The experimental interference due to the struts and the influence of the model on the strut tares are also discussed.

RESUME

L'influence d'un support de type 3 mâts sur les caractéristiques aérodynamiques longitudinales d'une maquette est dû essentiellement à l'effet des carénages de ces mâts.

L'exposé présente deux méthodes théoriques permettant d'accéder au niveau de correction à appliquer aux mesures brutes. La première de ces méthodes est une méthode classique de singularités surfaciques qui fournit une correction globale des efforts; la seconde est une méthode simplifiée qui permet de quantifier le niveau des corrections dû d'une part aux effets de volume, et d'autre part aux effets liés aux interférences mutuelles des lois de circulation.

Les résultats théoriques sont validés à l'aide de résultats expérimentaux issus d'une campagne d'essais spécifique dans la soufflerie F1 de l'ONERA sur une maquette d'A310.

L'exposé présente enfin l'influence des lames du montage, ainsi que l'effet de la maquette sur le tarage, qui ne peuvent être raisonnablement obtenus aujourd'hui qu'au travers d'une détermination expérimentale.

INTRODUCTION

Un des objectifs essentiels des grandes souffleries pressurisées à basses vitesses, telles que la soufflerie F1 de l'ONERA, est d'accéder aux performances absolues des avions civils grâce à la grande taille des maquettes (représentation fine des formes) et à la possibilité d'extrapoler avec une faible marge d'erreur les résultats expérimentaux établis aux nombres de Reynolds de la soufflerie vers ceux du vol.

Cet objectif, pour être rempli, a nécessité au cours des dernières années un effort accru pour limiter les incertitudes des résultats d'essais liées aux interactions des parois et des supports de maquettes.

Nous allons nous interesser ci-après, plus particulièrement au montage 3 mâts, utilisé dans la soufflerie F1 pour la détermination des caractéristiques aérodynamiques longitudinales.

Un montage de ce type est constitué de mâts profilés, supports proprement dits, fixés à la maquette au niveau de la voilure et de la pointe arrière du fuselage; le mât arrière pénètre légèrement à l'intérieur de celui-ci alors que chacun des deux mâts amont est solidaire de la maquette par l'intermédiaire d'attaches situées à l'intrados de l'aile, à l'emplacement d'un carénage d'hypersustentateur modifié à cet effet. Le tout est relié au plateau supérieur de la balance de paroi placée sous le plancher de la veine d'essais.

Afin de minimiser les forces qui s'exercent sur le support uniquement, une partie importante des mâts est abritée de l'action du vent à l'aide de carénages fixes, encore appelés pantalons, qui ne présentent aucune connexion avec la balance: leurs extrémités supérieures sont ouvertes afin d'assurer un libre passage des mâts et d'éviter ainsi tout contact qui perturberait les mesures; leurs bases sont simplement fixées sur le plancher de la soufflerie (figure 1).

Les modifications de l'écoulement induites par ce type de montage sont essentiellement dues aux carénages, assez volumineux; le niveau des perturbations propre à la partie des mâts visible entre ceux-ci et la maquette, encore appelée lame ou sabre, est faible. D'autre part, la balance de paroi fournissant les efforts aérodynamiques appliqués à l'ensemble maquette + lames, il est nécessaire de déterminer la tare du montage avant toute utilisation, ainsi que l'influence de la maquette sur ce tarage.

Ces corrections peuvent être complètement déterminées en effectuant des essais spécifiques de pesée d'une maquette tenue par un dard en présence, puis en l'absence d'un mannequin du support 3 mâts. Cependant, ces essais étant coûteux en temps et en argent, il est souvent préférable de s'orienter vers une détermination théorique de son influence, au moins en ce qui concerne la participation des carénages.

L'étude théorique peut être menée à l'aide d'une méthode classique de singularités surfaciques, valable en écoulement de fluide parfait, incompressible, irrotationnel et stationnaire. L'un des inconvénients de cette méthode, en
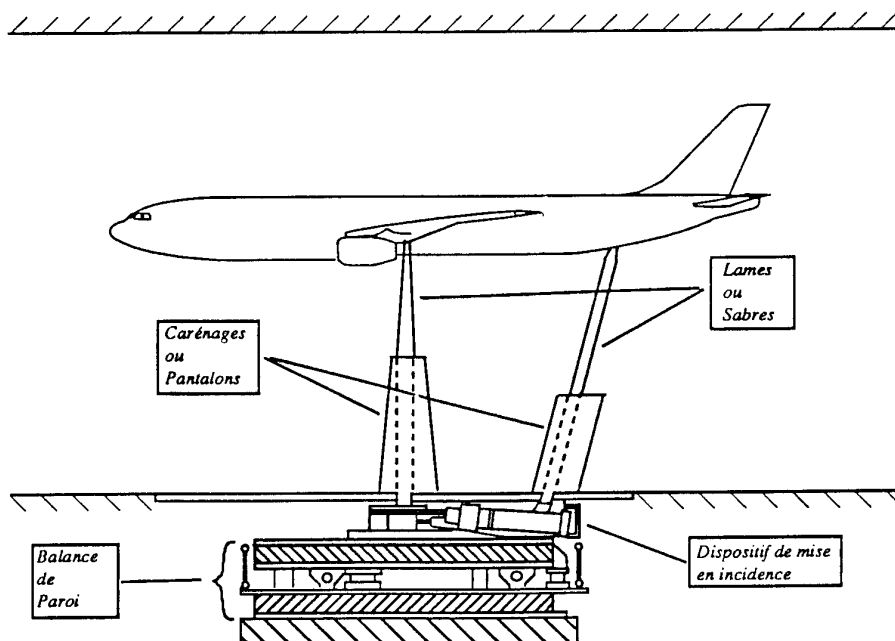
Figure 1 - Schéma d'un montage de type 3 mâts (ref. [1])

dehors de son aspect relativement complexe et onéreux, est qu'elle donne accès à une correction globale du montage. Une méthode simplifiée a donc été développée afin de mettre en évidence et de quantifier les différents phénomènes intervenant dans le processus d'interaction, et de pouvoir ainsi juger de la prépondérance d'un effet par rapport à un autre.

Le but de cet exposé est de présenter deux méthodes théoriques d'un niveau d'élaboration différent pour le calcul de l'influence des carénages, en nous limitant au cas d'une maquette en configuration lisse sans empennage horizontal. Les essais en soufflerie étant le moyen privilégié pour la justification de la validité des résultats, tous les calculs réalisés s'inscriront dans le cadre d'une campagne d'essais visant à déterminer l'effet du support 3 mâts de la soufflerie F1, sur une maquette au 1/14ème de l'Airbus A310. Ces essais nous permettront de plus d'avoir accès à l'effet expérimental des lames, ainsi qu'à l'influence de la maquette sur le tarage.

A. INFLUENCE THEORIQUE DES CARENAGES DU SUPPORT 3 MATS

A.1. APPLICATION D'UNE METHODE DE SINGULARITES SURFACIQUES

Il s'agit de la méthode AM37 d'AEROSPATIALE. Les résultats issus de ces calculs sont constitués, pour une incidence et un nombre de MACH donnés, soit des caractéristiques locales de l'écoulement en un point quelconque de l'espace et en particulier au niveau de la maquette, soit des coefficients aérodynamiques globaux Cz, Cx et Cm par intégration des pressions à la surface de l'obstacle.

L'influence du montage est alors obtenue par la différence entre un calcul avec support et un calcul en leur absence. Supposant que cette correction, basée sur des calculs fluide parfait, se conserve en fluide réel, les résultats bruts de soufflerie sont corrigés de cet effet de support ce qui permet d'accéder aux efforts en la seule présence des parois, situation qualifiable de "classique".

Les bases théoriques de cette méthode sont rappelées succintement ci après (ref. [2] à [4]).

1. Bases théoriques de la méthode des singularités

1.1. Discrétisation des obstacles et répartition des singularités

Si on considère un domaine fluide D limité par une frontière F pouvant comporter les surfaces de un ou plusieurs obstacles, la vitesse de l'écoulement dépend d'un potentiel Φ, solution de l'équation de LAPLACE et satisfaisant à des conditions de type NEUMANN. Grâce à la troisième identité de GREEN, il est possible d'exprimer le potentiel Φ sous la forme d'intégrales de surface sur la frontière des obstacles; si r désigne le rayon séparant le point d'observation $P(x,y,z)$ appartenant au domaine D du point d'intégration $Q(x,y,z)$ situé sur la frontière des obstacles, l'équation intégro-différentielle pour Φ peut se mettre sous la forme:

$$(1) \qquad -4\pi T\Phi_P = \iint_F \frac{1}{r}\vec{n}_Q \nabla \Phi_Q dS_Q - \iint_F \Phi \, \vec{n}_Q \nabla_Q\left(\frac{1}{r}\right)dS_Q$$

avec $T = A/2\pi$, où A désigne l'angle solide sous lequel la surface S_Q est vue du point P; T est nul si P est à l'extérieur du domaine D, T vaut 1/2 si P est sur la frontière de D et T est égal à 1 si P est à l'intérieur de D.

La première intégrale de surface est interprétée comme le potentiel d'une répartition surfacique de singularités de type source d'intensité $\sigma = \vec{n}\nabla\Phi$; la seconde intégrale de surface peut s'interpréter comme le potentiel d'une répartition surfacique de doublets d'intensité $\mu = \Phi$.

A la traversée de la surface, la vitesse induite par une répartition de sources subit une discontinuité de sa composante normale. Compte tenu des conditions aux limites, une distribution de sources compatible avec le problème de NEUMANN est fournie par la résolution d'une équation intégrale de FREDHOLM de deuxième espèce:

$$(2) \qquad 2\pi \sigma_P - \iint_F \sigma_Q \, \vec{n}_P \nabla_P\left(\frac{1}{r}\right)dS_Q = 4\pi\vec{n}_P\left(\vec{V}_P - \vec{V}_\infty\right)$$

De la même façon, l'équation de base relative aux vitesses induites par une répartition surfacique de doublets, caractérisés par une discontinuité de leur composante tangentielle, se présente sous la forme d'une équation de FREDHOLM de première espèce pour l'inconnue μ:

$$(3) \qquad -\iint_F \mu_Q \, \vec{n}_P \nabla_P\left(\vec{n}_Q \cdot \nabla_Q\left(\frac{1}{r}\right)\right)dS_Q = 4\pi \, \vec{n}_P\left(\vec{V}_P - \vec{V}_\infty\right)$$

La résolution numérique de ces équations s'effectue aisement si on considère des éléments plans recouverts de singuiarités d'intensité constante. Les frontières des obstacles sont ainsi discrétisées en un nombre fini d'éléments surfaciques quadrilatères ou triangulaires constituant le maillage, dont une des contraintes est de fournir une représentation correcte des corps du point de vue géométrique. Le principe de la méthode consiste alors à itérer sur les distributions des singularités jusqu'à obtenir une solution compatible avec les conditions aux limites qui devront être satisfaites en des points de contrôle affectés à chacune des surfaces élémentaires. De plus, l'écriture des conditions de JOUKOWSKI impose de considérer une répartition de doublets normaux sur les nappes tourbillonnaires des éléments portants équivalente à une répartition de tourbillons en fer à cheval.

1.2. Mise en forme du système d'équations et resolution

La condition de tangence, écrite aux N points de contrôle des panneaux composant l'obstacle, permet de déterminer les intensités σ_j des N sources:

(4)
$$\vec{n}_P \vec{V}_\infty + \sum_{j=1}^{j=N} \vec{n}_P \sigma_j \vec{V}'_{j(S/S)} + \sum_{k=1}^{k=n} \vec{n}_P \Gamma_k \vec{V}'_{k(D/S)} = 0$$

Le second terme de l'équation (4) représente la somme des projections sur la normale en P des vitesses dues aux N panneaux de sources σ_j (y compris le panneau P lui-même). Les vitesses $\vec{V}'_{j(S/S)}$ sont obtenues en calculant les vitesses induites par des panneaux plans de source unitaire. Cette opération, effectuée pour les N points de contrôle, permet d'aboutir à un premier système d'équations qui peut s'écrire sous la forme matricielle suivante:

$$\left[A_{ij} \right]\left[\sigma_j \right] = \left[V_{i(S/S)} \right]$$

où $\left[A_{ij} \right]$ est la matrice $N \times N$ des coefficients d'influence des sources sur les sources et où $\left[V_{i(S/S)} \right]$ représente le vecteur des vitesses normales totales induites par les sources sur chacun des panneaux i.

Le troisième terme de l'équation (4) représente quant à lui la somme des projections sur la normale en P des vitesses dues aux n bandes de doublets et à leurs tourbillons en fer à cheval associés; chacune des "bandes + tourbillons" est caractérisé par une intensité Γ_k et une vitesse $\vec{V}'_{k(D/S)}$, somme des contributions de chacun des panneaux composant une bande du squelette à laquelle est ajoutée la vitesse induite par le tourbillon en fer à cheval associé. Ces vitesses sont calculées pour une intensité de doublet unitaire par application successive de la formule de BIOT-SAVART.

La projection de ces vitesses suivant la normale en P fournit les coefficients d'influence des n doublets sur la source σ en P. Cette opération doit être effectuée pour les N points de contrôle d'où le second système:

$$\left[R_{ik} \right]\left[\Gamma_k \right] = \left[V_{i(D/S)} \right]$$

où $\left[R_{ik} \right]$ est la matrice $N \times n$ des coefficients d'influence des doublets sur les sources et $\left[V_{i(D/S)} \right]$ le vecteur des vitesses normales totales induites par les doublets sur chacun des panneaux i.

Compte tenu du choix des singularités qui conduit à des vitesses infinies en bordure des panneaux, l'application de la condition de JOUKOWSKI s'effectue au voisinage immédiat du bord de fuite des éléments portants. Une condition de glissement supplémentaire est ainsi écrite pour chaque tranche d'aile dans le prolongement du squelette:

(5)
$$\vec{n}_F \vec{V}_\infty + \sum_{j=1}^{j=N} \vec{n}_F \sigma_j \vec{V}'_{j(S/D)} + \sum_{k=1}^{k=n} \vec{n}_F \Gamma_k \vec{V}'_{k(D/D)} = 0$$

Le second terme représente la somme des projections sur la normale au point F des vitesses induites par les N panneaux de sources tandis que le troisième terme est la somme des projections sur cette même normale des vitesses induites par chaque bande portante. L'écriture des conditions de JOUKOWSKI permet ainsi d'obtenir deux systèmes d'équations supplémentaires:

$$\left[B_{ij} \right]\left[\sigma_j \right] = \left[V_{i(S/D)} \right]$$

avec $\left[B_{ij} \right]$ matrice $n \times N$ des coefficients d'influence des sources sur les doublets et $\left[V_{i(S/D)} \right]$ vecteur des vitesses normales totales induites par les sources σ_j en chaque point de JOUKOWSKI

et:
$$\left[S_{ik} \right]\left[\Gamma_k \right] = \left[V_{i(D/D)} \right]$$

avec $\left[S_{ik}\right]$ matrice $n \times n$ des coefficients d'influence des doublets sur les doublets et $\left[V_{i(D/D)}\right]$ vecteur des vitesses normales totales induites par les doublets Γ_k en chaque point de JOUKOWSKI.

Finalement, le système complet d'équations à résoudre se présente sous la forme matricielle suivante:

$$\begin{pmatrix} A_{ij} & R_{ik} \\ B_{ij} & S_{ik} \end{pmatrix} \begin{pmatrix} \sigma_1 \\ \vdots \\ \sigma_j \\ \vdots \\ \sigma_N \\ \Gamma_1 \\ \vdots \\ \Gamma_n \end{pmatrix} = - \begin{pmatrix} \vec{V}_\infty \cdot \vec{n}_1 \\ \vdots \\ \vec{V}_\infty \cdot \vec{n}_j \\ \vdots \\ \vec{V}_\infty \cdot \vec{n}_N \\ \vec{V}_\infty \cdot \vec{n}_{N+k} \\ \vdots \\ \vec{V}_\infty \cdot \vec{n}_{N+n} \end{pmatrix}$$

2. Calcul des efforts

La connaissance des intensités des sources et des doublets, issue de la résolution du système linéaire, permet d'accéder à la vitesse totale $\overrightarrow{V_{tj}}$ de l'écoulement en tout point de contrôle de l'obstacle, égale à la somme des contributions de chaque élément à laquelle est ajoutée la vitesse à l'infini amont. La loi de BERNOULLI fournit alors les coefficients de pression, soit:

$$Kp_j = 1 - \left|\vec{V}_{ij}\right|^2 \Big/ \left|\vec{V}_\infty\right|^2$$

d'où finalement la résultante des efforts due aux forces de pression sur le corps, en nommant S_j la surface élémentaire d'un panneau:

(6)
$$\vec{F} = -\frac{1}{2}\rho V_\infty^2 \sum_{j=1}^{j=N} Kp_j \, \vec{n}_j \, S_j$$

et le moment associé par rapport à un point de référence A:

(7)
$$\vec{M}_A = -\frac{1}{2}\rho V_\infty^2 \sum_{j=1}^{j=N} \overrightarrow{AP} \wedge (Kp_j \cdot \vec{n}_j) \, S_j$$

A.2. ELABORATION D'UNE METHODE SIMPLIFIEE

1. Définition du problème

L'étude peut être décomposée en trois parties:

→ *Résolution du problème P1*

Etude de l'écoulement autour de la maquette en veine d'essais en présence des carénages du montage 3 mâts.

Le champ de vitesse total est défini par:
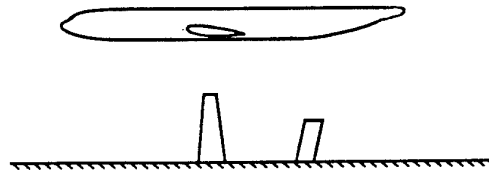
$$\vec{V}_1 = \vec{V}_\infty + \vec{V}_{Maquette} + \vec{V}_{3\,Car\acute{e}nages} + \delta\vec{V}_{3\,Car\acute{e}nages\big/Maquette} + \delta\vec{V}_{Maquette\big/3\,Car\acute{e}nages}$$

où: • $\vec{V}_\infty$ désigne la vitesse de l'écoulement à l'infini amont

• $\vec{V}_{Maquette}$ désigne le champ de vitesse induit par la maquette en présence des parois de la veine d'essais; il est obtenu en sommant les champs propres de la voilure et du fuselage, soit:

$$\vec{V}_{Maquette} = \vec{V}_A + \vec{V}_F$$

- $\vec{V}_{3\ Carénages}$ désigne le champ de vitesse induit par les 3 carénages en veine. Les champs de vitesse induits par le carénage amont gauche et le carénage amont droit ne seront pas différenciés dans la mesure où ces deux obstacles sont géométriquement semblables et qu'ils sont situés symétriquement de part et d'autre du plan de symétrie de la maquette.

Nous aurons ainsi, avec $\vec{V}_{Pa}$ et $\vec{V}_{Pr}$ relatifs aux champs de vitesses induits respectivement par les carénages amont et le carénage arrière:

$$\vec{V}_{3\ Carénages} = \vec{V}_{Pa} + \vec{V}_{Pr}$$

- $\delta\vec{V}_{3\ Carénages/Maquette}$ représente l'influence des 3 carénages sur l'écoulement autour de la maquette, qui peut être décomposée comme suit:

$$\delta\vec{V}_{3\ Carénages/Maquette} = \delta\vec{V}_{Pa/A} + \delta\vec{V}_{Pa/F} + \delta\vec{V}_{Pr/A} + + \delta\vec{V}_{Pr/F}$$

- Enfin, $\delta\vec{V}_{Maquette/3\ Carénages}$ représente l'influence de la maquette sur l'écoulement autour des carénages, soit:

$$\delta\vec{V}_{Maquette/3\ Carénages} = \delta\vec{V}_{A/Pa} + \delta\vec{V}_{A/Pr} + \delta\vec{V}_{F/Pa} + \delta\vec{V}_{F/Pr}$$

→ *Résolution du problème P2*

Etude de l'écoulement autour de la maquette en veine d'essais en l'absence des carénages du montage 3 mâts.

Le champ de vitesse total se présente sous la forme:

$$\vec{V}_2 = \vec{V}_\infty + \vec{V}_{Maquette}$$

ou encore:

$$\vec{V}_2 = \vec{V}_\infty + \vec{V}_A + \vec{V}_F$$

→ *Résolution du problème P3*

Etude de l'écoulement autour des carénages du montage en veine d'essais en l'absence de la maquette.

Le champ de vitesse total est défini par:

$$\vec{V}_3 = \vec{V}_\infty + \vec{V}_{3\ Carénages}$$

soit:

$$\vec{V}_3 = \vec{V}_\infty + \vec{V}_{Pa} + \vec{V}_{Pr}$$

Le but de cette étude est de déterminer les modifications du champ des vitesses de la maquette en veine, induites par la présence des 3 carénages, c'est à dire

$$\vec{V}_1 - \vec{V}_2 = \vec{V}_{3\ Carénages} + \delta\vec{V}_{3\ Carénages/Maquette} + \delta\vec{V}_{Maquette/3\ Carénages}$$

ou encore:

$$(8) \qquad \vec{V}_1 - \vec{V}_2 = \vec{V}_3 - \left(\vec{V}_\infty - \delta\vec{V}_{3\ Carénages/Maquette} - \delta\vec{V}_{Maquette/3\ Carénages} \right)$$

L'effet des carénages sur une maquette en veine se présente donc comme la somme:
  • d'un terme représentant le champ propre de ces carénages, lié à un effet de volume: l'écoulement étant parfaitement symétrique par rapport au plan $y = 0$, la présence des carénages se traduit au droit de la maquette, d'une part par des vitesses de perturbations longitudinales auxquelles correspondent une modification du champ de pression statique, et d'autre part par des vitesses de perturbations verticales qui modifient en direction la vitesse de référence.
  • d'un terme représentant les interactions entre les deux obstacles: lorsque la maquette et les carénages sont mis en présence l'un de l'autre, le niveau des perturbations liées à l'effet de volume décrit ci-dessus est modifié. De plus, il existe un phénomène d'interférence de portance entre la voilure et les carénages amont, dû à leur conception géométrique (aile verticale en flèche) et à leur position en veine (décalage par rapport au plan de symétrie de la maquette). Cet effet résulte des vitesses transversales induites par la voilure sur les carénages plaçant ainsi ces derniers à une certaine incidence; ils sont alors soumis à une portance ou plus précisemment à une force latérale d'où l'apparition d'un sillage en bord de fuite. Ces tourbillons induisent à leur tour des déflexions de l'écoulement au niveau de l'aile qui se traduisent par une modification de la loi de circulation.

La méthode simplifiée développée ci-après est basée sur la décomposition de l'effet global des carénages en un effet de volume et un effet d'interférence mutuelle de portance.

2. Modélisation des obstacles

En terme de potentiel, en notant Φ_1, Φ_2 et Φ_3 le potentiel total de l'écoulement relatif respectivement aux problèmes P1, P2 et P3, la formulation exacte du problème à résoudre est:

(9)
$$\begin{cases} \Delta\Phi_j = 0 \\ \left[\nabla\Phi_j \cdot \vec{n}\right]_{S_i} = 0 \\ \left[\nabla\Phi_j^+ \cdot \vec{v}\right]_{\Sigma_i} = \left[\nabla\Phi_j^- \cdot \vec{v}\right]_{\Sigma_i} = 0 \\ \left[p^+\right]_{\Sigma_i} = \left[p^-\right]_{\Sigma_i} \\ \nabla\Phi_j \to \vec{V}_\infty \qquad \text{à l'infini amont} \end{cases} \quad j = 1, 2, 3$$

où S_i désigne la surface de chacun des obstacles i dont le vecteur normal est noté $\vec{n}$, et Σ_i les surfaces de glissement des éléments portants caractérisées par la normale $\vec{v}$.

Etant donné la complexité du problème, nous allons faire appel aux théories linéarisées classiques de la dynamique des fluides, l'écoulement étant supposé permanent, incompressible et irrotationnel de fluide parfait. Nous choisissons ainsi d'appliquer d'une part la théorie des corps élancés pour traiter le potentiel de perturbation induit par le fuselage, et d'autre part la théorie de la surface portante pour définir les potentiels dus à l'aile et aux trois carénages, ces derniers pouvant être assimilés à des ailes verticales.

Le repère considéré est le repère aérodynamique $Oxyz$ défini comme suit:
  • l'origine O est situé au nez du fuselage
  • l'axe des x est confondu avec l'axe de la veine d'essais, et dirigé comme la vitesse à l'infini amont
  • l'axe des y est normal à la vitesse à l'infini amont et à l'envergure de l'aile, et est dirigé de l'intrados vers l'extrados
  • l'axe des z complète ce repère pour en faire un repère orthonormé

Dans la théorie de la surface portante (ref. [5]), la formulation linéarisée des conditions de glissement, basée sur l'hypothèse que les composantes du champ des vitesses de perturbations sont d'ordre $o(\varepsilon)$ (profils minces placés à incidence faible), entraîne la linéarité complète du problème, d'où la possibilité de décomposer celui-ci en un problème épais symétrique et un problème squelettique. Les conditions de vitesse normale nulle prennent la forme suivante:

  • *sur l'aile*

(10)
$$\begin{cases} \left[v(x, H_A^\pm, z) = V_\infty \delta_A^\pm(x, z) = V_\infty \left[\pm\delta_{eA}(x, z) + \delta_{sA}(x, z)\right]\right]_{S_A} \\ \left[v(x, H_A^+, z) = v(x, H_A^-, z) = V_\infty \delta_{nA}(x, z)\right]_{\Sigma_A} \\ \left[u(x, H_A^+, z) = u(x, H_A^-, z)\right]_{\Sigma_A} \end{cases}$$

Dans cette expression, u et v désignent respectivement les composantes longitudinale et verticale de la vitesse totale induites sur l'aile; $\delta_A^\pm(x, z)$ est la loi de pente des profils composant la surface S_A de l'aile, chacun de ceux-ci étant décomposé en un profil épais symétrique de pente $\pm\,\delta_{eA}(x, z)$, et un profil squelettique antisymétrique de pente

$\delta_{sA}(x,z)$. La loi de pente de la nappe tourbillonnaire, de surface Σ_A, s'échappant du bord du fuite de la voilure, est notée δ_{nA}. Cette condition est écrite à travers un plan d'ordonnée constante $y = H_A^{\pm}$, ordonnée que nous choisissons égale à celle du point situé à 25% de la corde moyenne aérodynamique.

• *sur les carénages amont*

Les carénages amont, situés à une distance $z = \pm d$ de part et d'autre du plan de symétrie de la maquette, sont composés d'une suite de profils symétriques et homothétiques de corde variable, de pente $\delta_{epa}(x,y)$. Ce sont des éléments portants; δ_{npa} est la loi de pente de leur surface de glissement Σ_{Pa}.

La condition de glissement linéarisée fait intervenir la composante transversale de la vitesse totale induite; elle s'écrit, pour le carénage amont gauche:

(11)
$$\begin{cases} \left[w(x,y,d^{\pm}) = \pm V_{\infty}\delta_{epa}(x,y) \right]_{S_{Pa}} \\ \left[w(x,y,d^{+}) = w(x,y,d^{-}) = V_{\infty}\delta_{npa}(x,y) \right]_{\Sigma_{Pa}} \\ \left[u(x,y,d^{+}) = u(x,y,d^{-}) \right]_{\Sigma_{Pa}} \end{cases}$$

• *sur le carénage arrière*

(12)
$$\left[w(x,y,0^{\pm}) = \pm V_{\infty}\delta_{epr}(x,y) \right]_{S_{Pr}}$$

Le carénage arrière, situé dans le plan de symétrie de la maquette, est un obstacle non portant dont la surface S_{Pr} est constituée d'un profil unique symétrique de pente $\delta_{epr}(x,y)$.

La formulation linéarisée des conditions de glissement et la décomposition du problème complet en un problème épais et un problème squelettique, conduisent à considérer des répartitions surfaciques de singularités de type sources σ sur l'aile et les 3 carénages et de type doublets ω, de direction y sur l'aile et de direction z sur les carénages amont; les nappes de l'aile et des carénages amont sont modélisées à l'aide de tourbillons en fer à cheval Γ.

Le fuselage, dont l'axe de révolution à incidence nulle est supposé être confondu avec l'axe de la veine d'essais, est modélisé à l'aide de la théorie des corps élancés (ref. [5]); la linéarisation de la condition de glissement est basée sur le fait que les perturbations de vitesse suivant la direction longitudinale sont négligeables devant les perturbations suivant y et z, et que R/L est supposé être d'ordre $o(\varepsilon)$, R et L désignant respectivement le rayon et la longueur du fuselage.

Dans un repère de coordonnées cylindriques (x,r,θ) lié à ce corps, il vient, dans le cas du problème complet P3:

(13)
$$\left[\frac{\partial \varphi_F}{\partial r} = V_{\infty}\cos\alpha R'(x) - V_{\infty}\sin\alpha\cos\theta - \frac{\partial \varphi_A}{\partial r} - \frac{\partial \varphi_{Pa}}{\partial r} - \frac{\partial \varphi_{Pr}}{\partial r} \right]_{r=R(x)} \quad \begin{cases} \forall x: 0 \le x \le L \\ \forall \theta: 0 \le \theta \le 2\pi \end{cases}$$

Une solution consiste à définir le potentiel du fuselage comme la somme d'un potentiel de l'écoulement longitudinal indépendant de θ, déterminé à l'aide d'une répartition linéique de sources sur l'axe de révolution du corps et d'un potentiel de l'écoulement transversal dépendant de θ, obtenu à l'aide d'une répartition de doublets.

Compte tenu de ce qui précède, la formulation complète des conditions de vitesse normale nulle sur la voilure, les carénages amont et le carénage arrière, montre:

1/ que les intensités des sources dépendent uniquement de la géométrie des obstacles et non pas de l'environnement dans lequel ils se situent. Nous aurons ainsi, pour la résolution des problèmes P1, P2 et P3:

(14)
$$\begin{cases} \sigma'_A(x,z) = 2V_{\infty}\delta_{eA}(x,z) & \text{sur l'aile} \\ \sigma'_{pa}(x,y) = 2V_{\infty}\delta_{epa}(x,y) & \text{sur les carénages amont} \\ \sigma'_{pr}(x,y) = 2V_{\infty}\delta_{epr}(x,y) & \text{sur le carénage arrière} \end{cases}$$

2/ que les problèmes épais et squelettique ne peuvent plus être résolus indépendamment l'un de l'autre; sous forme condensée, les conditions de vitesse normale nulle permettant d'accéder aux intensités des doublets et des tourbillons, prennent une forme du type:

$$(15) \quad \text{P1} \quad \begin{cases} V_\infty \delta_{sA}(x,z) = p_1(\omega'_A, \Gamma_A, \sigma'_1, \sigma'_2) + p_2(\omega'_p, \Gamma_p) + e_1(\sigma'_A, \sigma'_0) + e_2(\sigma'_{pa}, \sigma'_{pr}) \\ 0 = p'_1(\omega'_A, \Gamma_A, \sigma'_1, \sigma'_2) + p'_2(\omega'_p, \Gamma_p) + e'_1(\sigma'_A, \sigma'_0) + e'_2(\sigma'_{pa}, \sigma'_{pr}) \\ \sigma'_1 = d_1(\omega'_A, \Gamma_A) + d_2(\omega'_p, \Gamma_p) + d_3(\sigma'_A, \sigma'_0) + d_4(\sigma'_{pa}, \sigma'_{pr}) \\ \sigma'_2 = d'_1(\omega'_A, \Gamma_A) + d'_2(\omega'_p, \Gamma_p) + d'_3(\sigma'_{AH}, \sigma'_0) + d'_4(\sigma'_{pa}, \sigma'_{pr}) \end{cases}$$

$$(16) \quad \text{P2} \quad \begin{cases} V_\infty \delta_{sA}(x,z) = p_1(\omega'_A, \Gamma_A, \sigma'_1, \sigma'_2) + e_1(\sigma'_A, \sigma'_0) \\ \sigma'_1 = d_1(\omega'_A, \Gamma_A) + d_3(\sigma'_A, \sigma'_0) \\ \sigma'_2 = d'_1(\omega'_A, \Gamma_A) + d'_3(\sigma'_A, \sigma'_0) \end{cases}$$

$$(17) \quad \text{P3} \quad \left\{ p'_2(\omega'_p, \Gamma_p) + e'_2(\sigma'_{pa}, \sigma'_{pr}) = 0 \right.$$

Le but de cette étude est d'élaborer une méthode simple en vue de limiter les temps de calcul sur ordinateur, d'une part en faisant appel à des théories peu sophistiquées, et d'autre part en ne traitant que les termes principaux du processus d'interaction. Ceci nous amène naturellement à négliger les termes de sources qui interviennent dans la détermination des intensités des doublets et des tourbillons, afin de pouvoir traiter séparement les problèmes épais et portant.

D'autre part, la théorie de la surface portante ne permettant pas de conserver un caractère analytique aux résultats, nous choisissons d'employer la théorie de la ligne portante de PRANDTL pour la résolution du problème portant, pour laquelle nous ferons l'hypothèse que les vitesses induites par les doublets répartis sur le fuselage peuvent être négligées.

3. Détermination des effets liés au volume des carénages

Les notations employées sont les suivantes:

$$(18) \quad \text{P}[X,Y,Z] = X^2 + Y^2 + Z^2$$

$$(19) \quad \iint_S \frac{\sigma'(x_0,z_0)[X,Y,Z]}{4\pi \text{P}[X,Y,Z]^{3/2}} dx_0 dz_0 = \iint_S f[\sigma'(x_0,z_0),X,Y,Z] dx_0 dz_0$$

$$(20) \quad \int_C \frac{\sigma'(x_0)\left[-3XY,(X^2 - 2Y^2 + Z^2),-3YZ\right]}{4\pi \text{P}[X,Y,Z]^{5/2}} dx_0 = \int_C h_y[\sigma'(x_0),X,Y,Z] dx_0$$

$$(21) \quad \int_C \frac{\sigma'(x_0)\left[-3XZ,-3YZ,(X^2 + Y^2 - 2Z^2)\right]}{4\pi \text{P}[X,Y,Z]^{5/2}} dx_0 = \int_C h_z[\sigma'(x_0),X,Y,Z] dx_0$$

3.1. Préliminaire: modélisation des parois de la veine d'essais

H_v et L_v désignent respectivement la hauteur et la largeur de la veine d'essais; les demi-envergures de la voilure et des carénages sont notées b_A, b_{Pa} et b_{Pr}.

Pour que les parois verticales et horizontales situées respectivement en $z = \pm L_v/2$ et $y = \pm H_v/2$ soient simultanément surfaces de courant, il faut considérer une infinité d'images de chacun des obstacles, dont les intensités des singularités vérifient:

• $\sigma'_{vl}(x_0,z_0) = \sigma'_A\left[x_0,(-1)^v(z_0 - vL_v)\right]$ sur les images de l'aile définies par:

$$\begin{cases} x_{BA}(z_0) \le x_0 \le x_{BF}(z_0) \\ y_0 = lH_v + (-1)^l H_A \\ vL_v - b_A \le z_0 \le vL_v + b_A \end{cases}$$

• $\sigma'_{vl}(x_0,y_0) = \sigma'_{Pi}\left[x_0,(-1)^l(y_0 - lH_v)\right] = \sigma'_{Pi}\left[x_0,(-1)^l\left(y_0 - (4l-1)\frac{H_v}{2}\right)\right]$

avec $i = a,r$ respectivement sur les images des carénages amont et du carénage arrière définies par

$$\begin{cases} x_{BA}(y_0) \le x_0 \le x_{BF}(y_0) \\ 2lH_v - \dfrac{H_v}{2} - b_{Pi} \le y_0 \le 2lH_v - \dfrac{H_v}{2} + b_{Pi} \\ z_0 = \pm d + vL_v \ \Big\} \quad \begin{cases} \text{sur les carénages amont} \\ z_0 = vL_v \ \ \Big\} \quad \text{sur le carénage arrière} \end{cases} \end{cases}$$

$$\bullet \ \left. \begin{array}{l} \sigma'_{0vl} = \sigma'_0(x_0) \\ \sigma'_{1vl} = (-1)^l \sigma'_1(x_0) \\ \sigma'_{2vl} = (-1)^v \sigma'_2(x_0) \end{array} \right\} \quad \text{sur les segments images du fuselage soit:} \quad \begin{cases} 0 \le x_0 \le L \\ y_0 = 0 \\ z_0 = vL_v \end{cases}$$

Dans les expressions ci-dessus, v et l sont des entiers non nuls variant de $-\infty$ à $+\infty$. Si on pose $t_0 = (-1)^v(z_0 - vL_v)$ sur l'aile et $u_0 = (-1)^l(y_0 - (4l-1)H_v/2)$ sur les carénages, le champ de vitesse total induit en un point quelconque de la veine par les différents obstacles, est la somme:

• de la contribution de l'aile:

$$(22) \quad \sum_{v,-\infty}^{+\infty} \sum_{l,-\infty}^{+\infty} \iint_{S_A} f_A\left[\sigma'_A(x_0,t_0), x - x_0, y + (-1)^{l+1} H_A - lH_v, z + (-1)^{v+1} t_0 - vL_v\right] dx_0 dt_0 \qquad S_A \begin{cases} x_{BA}(t_0) \le x_0 \le x_{BF}(t_0) \\ -b_A \le t_0 \le b_A \end{cases}$$

• de la contribution du fuselage:

$$(23) \quad \sum_{v,-\infty}^{+\infty} \sum_{l,-\infty}^{+\infty} \left\{ \int_0^L f\left[\sigma'_0(x_0), x - x_0, y - lH_v, z - vL_v\right] dx_0 + \int_0^L h_y\left[(-1)^l \sigma'_1(x_0), x - x_0, y - lH_v, z - vL_v\right] dx_0 \right.$$
$$\left. + \int_0^L h_z\left[(-1)^v \sigma'_2(x_0), x - x_0, y - lH_v, z - vL_v\right] dx_0 \right\}$$

• de la contribution des carénages amont:

$$(24) \quad \sum_{v,-\infty}^{+\infty} \sum_{l,-\infty}^{+\infty} \left\{ \iint_{S_{Pa}} f_{Pa}\left[\sigma'_{pa}(x_0,u_0), x - x_0, y + (-1)^{l+1} u_0 - (4l-1)H_v/2, z - d - vL_v\right] dx_0 du_0 \right.$$
$$\left. + \iint_{S_{Pa}} f_{Pa}\left[\sigma'_{pa}(x_0,u_0), x - x_0, y + (-1)^{l+1} u_0 - (4l-1)H_v/2, z + d - vL_v\right] dx_0 du_0 \right\} \qquad S_{Pa} \begin{cases} x_{BA}(u_0) \le x_0 \le x_{BF}(u_0) \\ -b_{Pa} \le u_0 \le b_{Pa} \end{cases}$$

• de la contribution du carénage arrière:

$$(25) \quad \sum_{v,-\infty}^{+\infty} \sum_{l,-\infty}^{+\infty} \iint_{S_{Pr}} f_{Pr}\left[\sigma'_{pr}(x_0,u_0), x - x_0, y + (-1)^{l+1} u_0 - (4l-1)H_v/2, z - vL_v\right] dx_0 du_0 \qquad S_{Pr} \begin{cases} x_{BA}(u_0) \le x_0 \le x_{BF}(u_0) \\ -b_{Pr} \le u_0 \le b_{Pr} \end{cases}$$

3.2. Intensites des singularités sur le fuselage

Dans l'expression (13), le potentiel φ_F représente la somme du potentiel du fuselage origine et des potentiels des fuselages images. Au voisinage du corps, les expressions approchées des potentiels de sources et de doublets du fuselage origine sont (ref. [5]):

$$(26) \quad \varphi_0 = \int_0^L \frac{\sigma'_0(x) - \sigma'_0(x_0)}{4\pi|x - x_0|} dx_0 \ - \ \frac{\sigma'_0(x)}{4\pi} \log[4x(L-x)] \ + \ \frac{\sigma'_0(x)}{2\pi} \log r$$

pour le potentiel de sources et

$$(27) \quad \varphi_{D1} = \frac{\sigma'_1(x)}{2\pi r} \cos\theta \qquad\qquad \varphi_{D2} = \frac{\sigma'_2(x)}{2\pi r} \sin\theta$$

pour les potentiels de doublets.

La condition de corps élancés permet d'autre part de définir une formulation approchée du potentiel des images; tous calculs faits, le comportement du potentiel de sources de l'ensemble des images du fuselage se présente sous la forme d'une fonction de x uniquement, qui s'écrit:

$$(28) \quad \varphi_{oi}(x,r,\theta) \underset{r\to 0}{\approx} f_{0i}(x) = \int_0^L \frac{-\sigma_0'(x_0)}{4\pi}\left[\sum_{-\infty,\nu\neq 0}^{+\infty}\frac{1}{\sqrt{P(x-x_0,0,\nu L_\nu)}} + \sum_{\nu,-\infty}^{+\infty}\sum_{-\infty,l\neq 0}^{+\infty}\frac{1}{\sqrt{P(x-x_0,lH_\nu,\nu L_\nu)}}\right]dx_0$$

La relation suivante, permettant de déduire le potentiel des doublets répartis sur les images:

$$\varphi_{Di} = \frac{\partial\varphi_{0i}}{\partial r}\left(\nu_2\cos\theta + \nu_3\sin\theta\right) + \frac{\partial\varphi_{0i}}{r\partial\theta}\left(-\nu_2\sin\theta + \nu_3\cos\theta\right)$$

montre en particulier que ces doublets n'induisent aucune vitesse transversale au voisinage du fuselage origine.

Enfin, exprimés dans le repère curviligne, les champs de vitesse induits par l'aile et les carénages en veine fournissent, avec r/L d'ordre $o(\varepsilon)$:

$$(29) \quad \frac{\partial\varphi_A}{\partial r}(x,R,\theta) = \cos\theta f_A(x) \qquad \frac{\partial\varphi_{Pa}}{\partial r}(x,R,\theta) = \cos\theta f_{Pa}(x) \qquad \frac{\partial\varphi_{Pr}}{\partial r}(x,R,\theta) = \cos\theta f_{Pr}(x)$$

avec:

$$(30) \quad f_A(x) = -\frac{V_\infty}{2\pi}\sum_{\nu,-\infty}^{+\infty}\sum_{l,-\infty}^{+\infty}\iint_{S_A}\delta_{eA}(x_0,z_0)\frac{lH_\nu + (-1)^l H_A}{\left[P(x-x_0,lH_\nu+(-1)^l H_A,(-1)^\nu z_0+\nu L_\nu)\right]^{3/2}}\,dx_0$$

$$(31)\ f_{Pa}(x) = -\frac{V_\infty}{2\pi}\sum_{\nu,-\infty}^{+\infty}\sum_{l,-\infty}^{+\infty}\iint_{S_{Pa}}\delta_{epa}(x_0,y_0)\left[\frac{(-1)^l y_0+(4l-1)H_\nu/2}{\left[P(x-x_0,(-1)^l y_0+(4l-1)H_\nu/2,\nu L_\nu+d)\right]^{3/2}} + \frac{(-1)^l y_0+(4l-1)H_\nu/2}{\left[P(x-x_0,(-1)^l y_0+(4l-1)H_\nu/2,\nu L_\nu-d)\right]^{3/2}}\right]dx_0$$

$$(32) \quad f_{Pr}(x) = -\frac{V_\infty}{2\pi}\sum_{\nu,-\infty}^{+\infty}\sum_{l,-\infty}^{+\infty}\iint_{S_{Pr}}\delta_{epr}(x_0,y_0)\left[\frac{(-1)^l y_0+(4l-1)H_\nu/2}{\left[P(x-x_0,(-1)^l y_0+(4l-1)H_\nu/2,\nu L_\nu)\right]^{3/2}}\right]dx_0$$

La condition de vitesse normale nulle sur le corps (13) montre finalement que le potentiel du fuselage est obtenu à l'aide d'une répartition linéique de sources d'intensité identique à celle qui serait obtenue dans le cas de l'étude d'un fuselage isolé en milieu infini:

$$(33) \quad \sigma_0'(x) = 2\pi R(x)R'(x)V_\infty\cos\alpha$$

et d'une répartition de doublets de direction y, d'intensité

$$(34) \quad \sigma_1'(x) = 2\pi R^2(x)\left[V_\infty\sin\alpha + f_A(x) + f_{Pa}(x) + f_{Pr}(x)\right]$$

3.3. Calcul de la variation de pression cinétique induite par les carénages

La connaissance de la composante longitudinale de la vitesse totale induite sur la maquette en présence et en l'absence des carénages permet d'obtenir la pression cinétique de référence vraie notée q_b, à laquelle doivent être ramenés les coefficients aérodynamiques, afin de leur restituer leurs valeurs exactes en dehors de toute interaction. La résolution du problème épais fournit ainsi une correction du champ de pression statique, basée sur une notion de perturbation moyenne.

Si u_b et u_c désignent les composantes longitudinales de la vitesse sur la maquette respectivement en présence et en l'absence des carénages, la pression cinétique q_b régnant au droit de celle-ci en présence du support s'écrit au premier ordre:

$$(35) \quad q_b = \frac{1}{2}\rho_\infty\left[V_\infty + u_b\right]^2 \approx q_\infty\left[1 + \frac{2}{V_\infty}u_b\right]$$

en notant q_∞ la pression cinétique de référence correspondant à la vitesse infini amont V_∞.

q_c désigne d'autre part la pression cinétique qui règnerait au droit de la maquette en l'absence des carénages. Elle correspond à la pression cinétique à laquelle sont ramenés les coefficients mesurés sur la maquette en présence du support alors que celle-ci baigne dans une atmosphère q_b; on a:

$$(36) \quad q_c = \frac{1}{2}\rho_\infty\left[V_\infty + u_c\right]^2 \approx q_\infty\left[1 + \frac{2}{V_\infty}u_c\right]$$

Il vient alors, avec $\Delta u = u_b - u_c = (u_A + u_F)_b - (u_A + u_F)_c$ représentant la variation totale de la vitesse longitudinale:

(37)
$$\frac{\Delta q}{q_\infty} = \frac{q_b - q_c}{q_\infty} = \frac{2}{V_\infty} \Delta u$$

En faisant intervenir l'expression des coefficients de pression statique en théorie linéarisée, soit:

$$Cp_{eA} = -2\frac{u_A}{V_\infty} \quad \text{sur l'aile} \quad \text{et} \quad Cp_F = -2\frac{u_F}{V_\infty} - \frac{v_{rF}^2}{V_\infty^2} - \frac{v_{\theta F}^2}{V_\infty^2} \quad \text{sur le fuselage,}$$

on obtient finalement:

(38)
$$\frac{\Delta q}{q_\infty} = -\frac{1}{S_{ref}} \left[\iint_{S_A} \Delta Cp_{eA}(x, H_A, z) dS + \int_0^L \int_0^{2\pi} \Delta Cp_F(x, \theta) dx d\theta \right]$$

S_{ref} est la surface de référence de la maquette; $\Delta Cp_{eA}(x, H_A, z)$ et $\Delta Cp_F(x, \theta)$ sont obtenus à l'aide des formules (22) à (25). Les intensités des sources réparties sur les obstacles n'étant fonction que de leur géométrie respective, la variation de pression statique induite par les carénages sur l'aile est la somme de la contribution de ces carénages et de leur influence sur les intensités des doublets y de l'axe du fuselage.

3.4. Calcul de l'ascendance induite par les carénages

De la même façon, l'ascendance moyenne $\Delta\alpha$ induite par les carénages est obtenue en intégrant les variations vitesses verticales fournies par un calcul de l'écoulement sur la maquette en présence puis en l'absence des carénages.

4. Détermination des interférences mutuelles de portance

La résolution du problème portant est effectuée à l'aide de la théorie de la ligne portante de PRANDTL; nous rappelons que cette théorie repose sur une modélisation simplifiée à l'aide de tourbillons en fer à cheval d'un corps portant et de sa nappe tourbillonnaire; elle consiste à supposer l'écoulement autour de chaque section normale des obstacles assez voisin de l'écoulement plan pour appliquer la théorie de JOUKOWSKI, et assurer ainsi une vitesse finie au bord de fuite, en considérant cependant les conditions aérodynamiques réelles, c'est à dire la vitesse et l'incidence effective attaquant chacun des profils.

Les notations employées par la suite sont définies comme suit:

(39) $P[X,Y,Z] = 1 + X(X^2 + Y^2 + Z^2)^{-1/2}$ $Q[X,Y,Z] = (X^2 + Y^2 + Z^2)^{3/2}$ $R[Y,Z] = Y^2 + Z^2$

(40)
$$\int_a^b \frac{\Gamma(t)(-Y, X, 0)}{4\pi Q(X,Y,Z)} dt + \int_a^b \frac{\Gamma'(t)(0, Z, -Y)\, dt}{4\pi R(Y,Z)} P(X,Y,Z) = \int_a^b f_A[\Gamma(t), \Gamma'(t), X, Y, Z]\, dt$$

(41)
$$\int_a^b \frac{\Gamma(t)(Z, 0, -X)}{4\pi Q(X,Y,Z)} dt + \int_a^b \frac{\Gamma'(t)(0, Z, -Y)\, dt}{4\pi R(Y,Z)} P(X,Y,Z) = \int_a^b f_{Pa}[\Gamma(t), \Gamma'(t), X, Y, Z]\, dt$$

4.1. Modélisation des obstacles et définition des champs de vitesse

Chaque section de l'aile normale à Oz est réduite à son point de rencontre avec cet axe. L'aile est assimilée au segment $x = X_A$, $y = H_A$, $-b_A \leq z \leq b_A$; elle est le siège de segments tourbillonnaires d'intensité $\Gamma_A(z_0)$. Sa nappe est constituée par les branches semi-infinies des tourbillons en fer à cheval d'intensité $\Gamma'_A(z_0)dz_0$; PRANDTL fait l'hypothèse que cette surface est plane et rectangulaire.

Les carénages amont sont considérés comme des ailes verticales d'envergure $2b_{Pa}$. Ils sont assimilés aux segments $x = X_A$, $-b_{Pa} \leq y \leq b_{Pa}$, $z = \pm d$ (l'origine du repère est prise au niveau du plancher de la veine) et sont porteurs de tourbillons $\mp\Gamma_P(y_0)$. Leurs nappes sont constituées par les lignes tourbillons semi-infinies d'intensité $\mp\Gamma'_P(y_0)dy_0$.

La modélisation des parois de la veine est obtenue comme précedemment à l'aide de la méthode des images. Les parois seront surfaces de glissement si les lois de circulation vérifient:

$\bullet \ \Gamma_{vl}(z_0) = \Gamma_A\left[(-1)^v(z_0 - vL_v)\right]$ et $\Gamma'_{vl}(z_0) = (-1)^v\Gamma'_A\left[(-1)^v(z_0 - vL_v)\right]$

sur les segments images de l'aile: $x = X_A$, $y = 2lH_v + H_A$, $vL_v - b_A \leq z_0 \leq vL_v + b_A$

$\bullet \ \Gamma_{vl}(z_0) = -\Gamma_A\left[(-1)^v(z_0 - vL_v)\right]$ et $\Gamma'_{vl}(z_0) = (-1)^{v+1}\Gamma'_A\left[(-1)^v(z_0 - vL_v)\right]$

sur les segments images de l'aile: $x = X_A$, $y = 2lH_v - H_A$, $vL_v - b_A \leq z_0 \leq vL_v + b_A$

$\bullet \ \Gamma_{vl}(y_0) = \Gamma_P\left[(-1)^l(y_0 - 2lH_v)\right]$ et $\Gamma'_{vl}(z_0) = (-1)^l\Gamma'_P\left[(-1)^l(y_0 - 2lH_v)\right]$

sur les segments images des carénages amont: $x = X_A$, $2lH_v - b_{Pa} \leq y_0 \leq 2lH_v + b_{Pa}$, $z = vL_v + d$

$\bullet \ \Gamma_{vl}(y_0) = -\Gamma_P\left[(-1)^l(y_0 - 2lH_v)\right]$ et $\Gamma'_{vl}(z_0) = (-1)^{l+1}\Gamma'_P\left[(-1)^l(y_0 - 2lH_v)\right]$

sur les segments images des carénages amont: $x = X_A$, $2lH_v - b_{Pa} \leq y_0 \leq 2lH_v + b_{Pa}$, $z = vL_v - d$

Les champs de vitesse induits respectivement par l'aile et les deux carénages amont se mettent finalement sous la forme suivante:

$$(42) \quad \vec{V}(x,y,z) = \sum_{v,-\infty}^{+\infty} \sum_{l,-\infty}^{+\infty} \left\{ \int_{-b_A}^{b_A} f_A\left[\Gamma_A(t_0),(-1)^v\Gamma'_A(t_0),x - X_A, y - H_A - 2lH_v, z + (-1)^{v+1}t_0 - vL_v\right]dt_0 \right.$$
$$\left. + \int_{-b_A}^{b_A} f_A\left[-\Gamma_A(t_0),(-1)^{v+1}\Gamma'_A(t_0),x - X_A, y + H_A - 2lH_v, z + (-1)^{v+1}t_0 - vL_v\right]dt_0 \right\}$$

$$(43) \quad \vec{V}(x,y,z) = \sum_{v,-\infty}^{+\infty} \sum_{l,-\infty}^{+\infty} \left\{ \int_{-b_{Pa}}^{b_{Pa}} f_{Pa}\left[-\Gamma_P(u_0),(-1)^{l+1}\Gamma'_P(u_0),x - X_A, y + (-1)^{l+1}u_0 - 2lH_v, z - d - vL_v\right]du_0 \right.$$
$$\left. + \int_{-b_{Pa}}^{b_{Pa}} f_{Pa}\left[\Gamma_P(u_0),(-1)^l\Gamma'_P(u_0),x - X_A, y + (-1)^{l+1}u_0 - 2lH_v, z + d - vL_v\right]du_0 \right\}$$

4.2. Equation intégro-différentielle de PRANDTL pour l'aile et les carénages amont

Si on considère d'une part que les vitesses induites sont faibles devant la vitesse de l'écoulement à l'infini, et d'autre part que les angles induits sont petits, on obtient les expressions des circulations sur l'aile et les carénages amont qui s'écrivent, d'après la théorie bidimensionnelle:

$$(44) \quad \Gamma_A(z) = -k_A(z)l_A(z)V_\infty\left[\alpha + \alpha_{vA}(z) - \alpha_{0A}(z) + \frac{Vy_A(z)}{V\infty}\right] \qquad \text{sur l'aile}$$

$$(45) \quad \Gamma_P(y) = -k_{Pa}l_{Pa}(y)Vz_{Pa}(y) \qquad \text{sur les carénages}$$

Dans les expressions ci-dessus:
- α représente l'incidence aérodynamique de la maquette en veine
- $\alpha_{vA}(z)$ désigne la loi de vrillage des profils de l'aile
- $\alpha_0(z)$ est la loi donnant l'angle d'incidence de portance nulle
- les coefficients k caractérisent la géométrie des profils; ils sont égaux à la moitié du gradient de portance de chaque profil
- l est la corde réelle du profil de la tranche considérée
- les termes Vy_A et Vz_{Pa} sont liés aux angles induits supplémentaires

Ces équations sont résolues en cherchant à représenter les circulations sous la forme d'un développement en série de FOURIER, compatible avec une circulation nulle aux extrémités, soit:

$$(46) \quad \Gamma_A(\theta) = -4b_A V_\infty \sum_{n=1}^{\infty} A_n \sin n\theta \qquad \text{sur l'aile, avec } z = b_A \cos\theta, \ 0 \leq \theta \leq \pi$$

$$(47) \quad \Gamma_P(\eta) = -4b_{Pa} V_\infty \sum_{m=1}^{\infty} C_m \sin m\eta \qquad \text{sur les carénages, avec } y = b_{Pa} \cos\eta, \ 0 \leq \eta \leq \pi$$

Finalement, les lois de circulation seront complètement déterminées par la résolution du système d'équations suivant (écrit pour le carénage amont gauche sens pilote), obtenu en portant les changements de variable définis ci-dessus dans les expressions (42) à (45):

(48)
$$\begin{cases} \sum_{n=1}^{\infty} A_n\, PMA(\theta,n) = \alpha + \alpha_{vA}(\theta) - \alpha_{0A}(\theta) + \sum_{m=1}^{\infty} C_m\, SMAPA(\theta,m) \\ \sum_{m=1}^{\infty} C_m\, PMP(\eta,m) = \sum_{n=1}^{\infty} A_n\, SMPA(\eta,n) \end{cases}$$

Le terme $PMA\ (\theta,n)$ représente l'influence de l'aile sur elle-même ainsi que l'influence des parois tandis que le terme $SMAPA\ (\theta,m)$ fournit l'effet des carénages amont en veine sur celle-ci; ils sont définis de la façon suivante:

(49)
$$PMA(\theta,n) = \frac{4b_A}{k_A(\theta)l_A(\theta)}\sin n\theta + n\frac{\sin n\theta}{\sin \theta}$$

$$- \frac{n}{\pi}\left\{ \sum_{-\infty,v\neq 0}^{+\infty} \int_0^{\pi} \frac{(-1)^v \cos n\theta_0 d\theta_0}{Z} + \sum_{v,-\infty}^{+\infty}\sum_{-\infty,l\neq 0}^{+\infty} \int_0^{\pi} \frac{(-1)^v \cos n\theta_0 Z d\theta_0}{Z^2 + (2lH_v/b_A)^2} - \sum_{v,-\infty}^{+\infty}\sum_{l,-\infty}^{+\infty}\int_0^{\pi} \frac{(-1)^v \cos n\theta_0 Z d\theta_0}{Z^2 + ((2lH_v - 2H_A)/b_A)^2} \right\}$$

où $\ Z = \cos\theta + (-1)^{v+1}\cos\theta_0 - vL_v\,/\,b_A$

(50)
$$SMAPA(\theta,m) = \frac{m}{\pi}\sum_{v,-\infty}^{+\infty}\sum_{l,-\infty}^{+\infty}\int_0^{\pi}(-1)^l \cos m\eta_0 \left[\frac{Z1}{Y^2 + Z1^2} - \frac{Z2}{Y^2 + Z2^2}\right]d\eta_0$$

où $\ Y = (H_A - 2lH_v)\,/\,b_{Pa} + (-1)^{l+1}\cos\eta_0$, $\ Z1 = (b_A\cos\theta - vL_v + d)\,/\,b_{Pa}$, $\ Z2 = (b_A\cos\theta - vL_v - d)\,/\,b_{Pa}$

De la même façon, le terme $PMP\ (\eta,m)$ représente l'influence totale des carénages en veine sur le carénage amont gauche et le terme $SMPA\ (\eta,n)$ fournit l'influence de l'aile:

(51)
$$PMP(\eta,m) = \frac{4b_{Pa}}{k_{Pa}l_{Pa}(\eta)}\sin m\eta + m\frac{\sin m\eta}{\sin \eta}$$

$$- \frac{m}{\pi}\left\{ \sum_{-\infty,l\neq 0}^{+\infty} \int_0^{\pi} \frac{(-1)^l \cos m\eta_0 d\eta_0}{Y} + \sum_{l,-\infty}^{+\infty}\sum_{-\infty,v\neq 0}^{+\infty} \int_0^{\pi} \frac{(-1)^l \cos m\eta_0 Y d\eta_0}{Y^2 + (vL_v/b_{Pa})^2} - \sum_{v,-\infty}^{+\infty}\sum_{l,-\infty}^{+\infty}\int_0^{\pi} \frac{(-1)^l \cos m\eta_0 Y d\eta_0}{Y^2 + ((2d - vL_v)/b_{Pa})^2} \right\}$$

où $\ Y = \cos\eta + (-1)^{l+1}\cos\eta_0 - 2lH_v\,/\,b_{Pa}$

(52)
$$SMPA(\eta,n) = \frac{n}{\pi}\sum_{v,-\infty}^{+\infty}\sum_{l,-\infty}^{+\infty}\int_0^{\pi}(-1)^v \cos n\theta_0 \left[\frac{Y1}{Y1^2 + Z^2} - \frac{Y2}{Y2^2 + Z^2}\right]d\theta_0$$

où $\ Y1 = (b_{Pa}\cos\eta + H_A - 2lH_v)\,/\,b_A$, $\ Y2 = (b_{Pa}\cos\eta - H_A - 2lH_v)\,/\,b_A$, $\ Z = (d - vL_v)\,/\,b_A + (-1)^{v+1}\cos\theta_0$

D'autre part, les coefficients A_n et C_m sont écrits sous la forme d'une fonction de l'incidence de la maquette, afin d'obtenir une solution générale correspondant à une incidence quelconque (ref. [5]):

(53)
$$\begin{cases} A_n = \alpha\, a_n + b_n + c_n \\ C_m = \alpha\, p_m + q_m + r_m \end{cases}$$

Dans ces expressions, les coefficients b_n et q_m d'une part, c_n et r_m d'autre part sont respectivement dépendant des lois de vrillage et d'incidence de portance nulle de l'aile.

La résolution numérique est alors effectuée en limitant les développements des séries de FOURIER à leurs N et M premiers termes, et en écrivant les équations pour N et M valeurs distinctes de θ et η. La première itération, pour laquelle on pose $p_m = q_m = r_m = 0$, fournit les lois de circulation sur l'aile en présence uniquement des parois de la veine d'essais (correspondant à la résolution de la partie portante du problème P2).

4.3. Effet de la circulation des carénages sur les coefficients aérodynamiques de l'aile

Les expressions des coefficients aérodynamiques longitudinaux de l'aile établies dans le cadre de cette théorie sont fournies ci-après:

a) *Expression du coefficient de portance*

La formulation classique de la théorie de PRANDTL reste valable, soit:

$$(54) \qquad Cz = \pi \, \lambda_A \, A_1$$

b) *Expression du coefficient de traînée induite*

$$(55) \qquad Cx = -2 \, \lambda_A \sum_{n=1}^{N} A_n \int_0^\pi \delta\alpha_A(\theta) \sin n\theta \sin \theta \, d\theta$$

Il est encore possible d'écrire la traînée comme une fonction de la portance; il vient:

$$(56) \qquad Cx = Cz\alpha - 2 \, \lambda_A \sum_{n=1}^{N} A_n \int_0^\pi \left[\alpha_{0A}(\theta) - \alpha_{vA}(\theta)\right] \sin n\theta \sin \theta \, d\theta$$

c) *Expression du coefficient de moment de tangage*

La formule ci-dessous définit le coefficient de moment de tangage par rapport à un point A correspondant à la projection dans le plan xy du point situé à 25% de la corde aérodynamique moyenne notée L_A.

$$(57) \qquad Cm = -\pi \frac{x_A}{L_A} \lambda_A \, A_1 + \frac{b_A}{S_{ref} L_A} \int_0^\pi Cm_F(\theta) l^2(\theta) \sin \theta \, d\theta + 2 \frac{\lambda_A}{L_A} \sum_{n=1}^{N} A_n \int_0^\pi x_F(\theta) \sin n\theta \sin \theta \, d\theta$$

où $x_F(\theta)$ et $Cm_F(\theta)$ représentent respectivement la position du foyer de chaque profil, et le coefficient de moment de tangage du profil par rapport à ce point.

L'effet de l'apparition d'une circulation sur les carénages amont est obtenu en faisant la différence des coefficients calculés successivement en présence et en l'absence de ces carénages. Les corrections ainsi déterminées seront notées par la suite $\Delta Cz_{PRANDTL}$, $\Delta Cx_{PRANDTL}$ et $\Delta Cm_{PRANDTL}$.

5. Correction des coefficients aérodynamiques

Soit Fz, la force de portance s'exerçant sur la maquette en présence des carénages, Cz_b le coefficient sans dimension associé à cet effort et rapporté à la pression cinétique de référence q_c, et enfin $(Cz_c)_q$ le coefficient obtenu en rapportant l'effort à la pression cinétique exacte q_b. On peut écrire:

$$(58) \qquad Fz = q_c S_{ref} Cz_b = q_b S_{ref} \left(Cz_c\right)_q$$

ou encore, avec $\Delta Cz_q = Cz_b - \left(Cz_c\right)_q$: $\qquad \Delta Cz_q = \dfrac{q_b - q_c}{q_b} Cz_b$

On obtient ainsi la correction ΔCz_q qui doit être appliquée à la mesure brute du coefficient de portance pour le dégager des perturbations de vitesse axiale induite par les carénages (avec $\Delta q/q_\infty$ défini en (38)):

$$(59) \qquad \Delta Cz_q = K_q Cz_b \qquad \text{avec } K_q = \frac{\Delta q}{q_\infty}\left\{1 - \frac{1}{S_{ref}}\left[\iint_{S_A} (Cp_{eA})_b(x, H_A, z)dS + \int_0^L \int_0^{2\pi} (Cp_F)_b(x, \theta)dxd\theta\right]\right\}$$

Le coefficient de portance étant rapporté à la pression cinétique exacte, il convient alors de le corriger de l'ascendance induite par les carénages, qui se traduit, à iso-Cz, par une modification de l'incidence effective de la maquette. Il vient, en notant α_c l'incidence corrigée, $(Cz_c)_{EPAIS}$ le coefficient de portance corrigé des effets de volume des carénages, et en désignant par $(\partial Cz/\partial\alpha)_q$ la pente de la courbe $Cz_b(\alpha)$ corrigée de l'effet sur la pression cinétique:

$$(60) \qquad \left.\begin{aligned} \left(Cz_c\right)_q &= \left(\frac{\partial Cz}{\partial \alpha}\right)_q (\alpha_c + \Delta\alpha - \alpha_0) \\ (Cz_c)_{EPAIS} &= \left(\frac{\partial Cz}{\partial \alpha}\right)_q (\alpha_c - \alpha_0) \end{aligned}\right\} \qquad \text{d'où} \qquad \Delta Cz_{\Delta\alpha} = \left(\frac{\partial Cz}{\partial \alpha}\right)_q \Delta\alpha$$

Le principe de la méthode simplifiée repose sur une décomposition de l'effet total des carénages en un effet à incidence nulle fourni par la résolution du problème épais, et un effet d'incidence obtenu à l'aide du calcul des interférences mutuelles sur les lois de circulation. Finalement, la correction totale à appliquer à la mesure brute du coefficient de portance s'écrit:

$$(61) \qquad \Delta Cz = Cz_b - Cz_c = K_q(Cz_b)_{\alpha=0} + (1 - K_q)\left[\left(\frac{\partial Cz}{\partial \alpha}\right)_b\right]_{\alpha=0} \Delta\alpha + \Delta Cz_{PRANDTL}$$

Le coefficient de traînée est corrigé selon le même schéma; il faut cependant tenir compte d'un terme correctif supplémentaire: l'existence d'une ascendance ayant pour conséquence une rotation du repère aérodynamique, la nouvelle composition des forces se traduit par une correction $\Delta Cx_r = -Cz_b \sin\Delta\alpha$ (la correction correspondante sur le Cz est négligeable). Il vient finalement:

$$(62) \qquad \Delta Cx = Cx_b - Cx_c = K_q(Cx_b)_{\alpha=0} + (1 - K_q)\left[\left(\frac{\partial Cx}{\partial \alpha}\right)_b\right]_{\alpha=0} \Delta\alpha - (Cz_b)_{\alpha=0} \sin\Delta\alpha + \Delta Cx_{PRANDTL}$$

En ce qui concerne le coefficient de moment de tangage, il semble qu'une méthode de correction basée sur une notion de perturbation moyenne de la pression cinétique et de l'ascendance ne soit pas adaptée à la résolution du problème. La confrontation des résultats théoriques issus de la méthode simplifiée, et expérimentaux, ne portera donc que sur les coefficients de portance et de traînée.

B. ETUDE EXPERIMENTALE

L'étude de l'effet du support 3 mâts a donné lieu à une campagne d'essais dans la soufflerie F1 de l'ONERA sur une maquette à l'échelle 1/14ème de l'AIRBUS A310 (ref. [6]). La soufflerie F1 est une soufflerie pressurisée à circuit aérodynamique fermé dont la veine d'essais, de section 4.5m x 3.5m, permet de recevoir des maquettes de 3 mètres d'envergure.

Cette série d'essais a porté sur une configuration "aile + fuselage" avec et sans empennage horizontal. La détermination des effets du montage sur les caractéristiques aérodynamiques de la maquette a été effectuée suivant le procédé conventionnel: les interactions sont obtenues par différence entre les pesées de la maquette tenue par un dard en présence et en l'absence d'un mannequin du support 3 mâts. Divers aspects ont été explorés: effet du montage complet, effet des 2 mâts amont, effet des 3 carénages, effet des carénages amont et enfin effet du carénage arrière uniquement. Tous les essais ont été effectués à la pression génératrice maximale Pi = 3.85 bars pour un nombre de MACH de 0.12 ou 0.2.

La figure 2 présente la configuration de base de ces essais dite "maquette seule": celle-ci est montée par l'intermédiaire d'une balance interne sur un dard Z tourné à l'envers devenant ainsi un dard dérive. Des calculs préalables à l'aide de la méthode AM37 ont permis de vérifier que les perturbations propres à ce montage étaient négligeables relativement au niveau des perturbations induites par le 3 mâts.
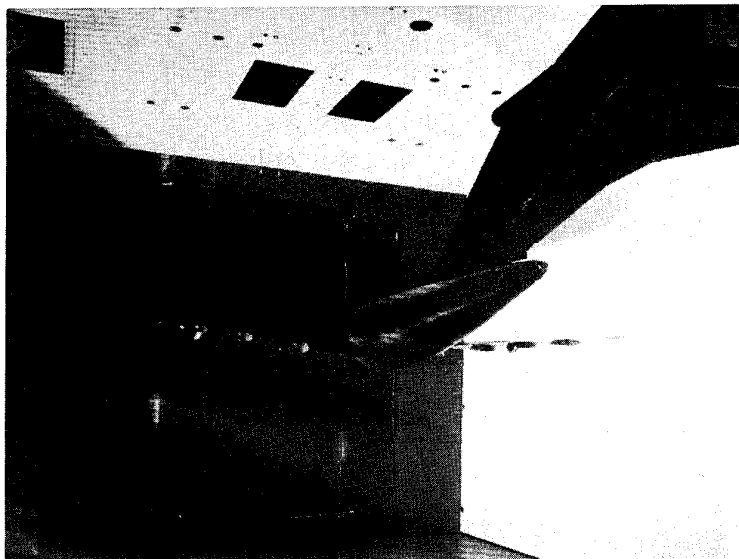
Figure 2 - Configuration de base des essais "maquette seule"

La figure 3 présente la maquette montée sur le dard en présence des éléments du montage 3 mâts, tenus dans la veine sans aucune liaison avec la maquette. Les mâts sont représentés par des mannequins de bois mais les carénages réels ont été conservés. L'un des mannequins des mâts amont et le mât aval sont équipés d'une petite balance, afin de pouvoir mesurer la tare du montage en présence de la maquette.

La figure 4 montre la configuration en veine adoptée pour la mesure de l'effet des carénages uniquement.
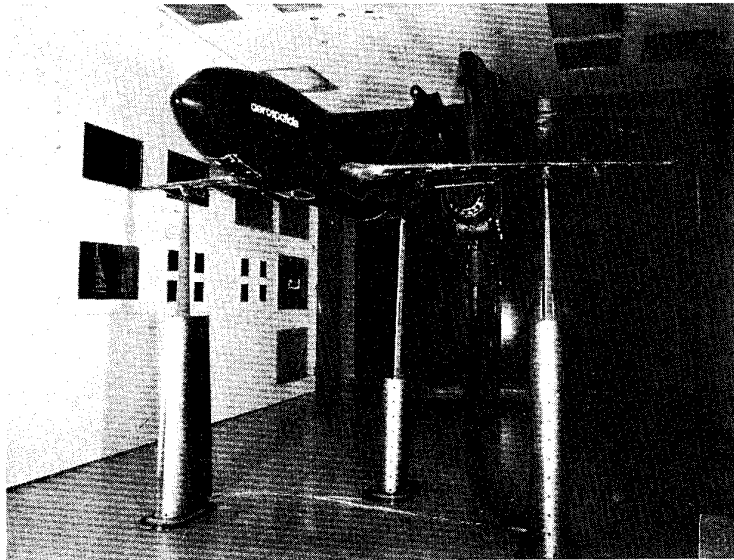
Figure 3 - Mesure des interactions du montage 3 mâts de F1
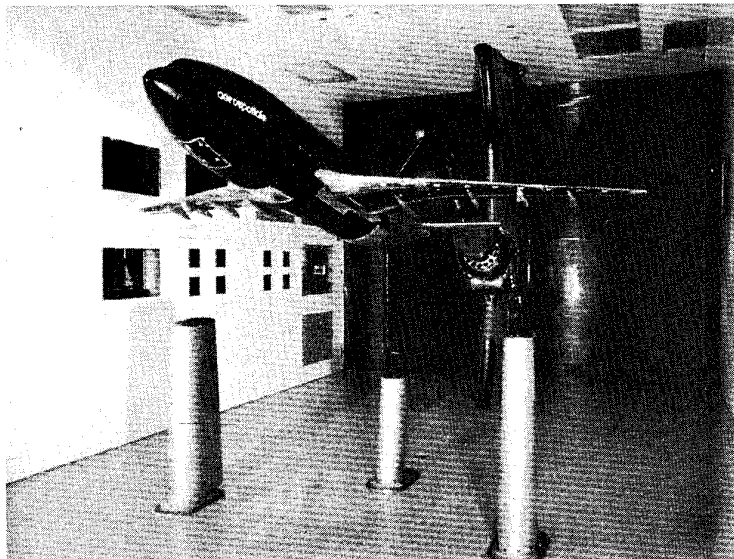
Figure 4 - Mesure des interactions des carénages du montage 3 mâts de F1

La plage d'incidence à explorer était limitée par la condition suivant laquelle le décrochage de la voilure ne devait pas être atteint, afin que la maquette ne touche pas les mâts et fausse ainsi les mesures de la balance interne. D'autre part, le centre de rotation de la maquette montée sur dard ne coïncidant pas exactement avec celui de la même maquette montée sur la balance de paroi par l'intermédiaire du support 3 mâts, les mesures en présence de celui-ci ont été effectuées par palier, chaque palier nécessitant un repositionnement correct des mâts ou des carénages par rapport à la

maquette. La longueur du mât arrière variant considérablement avec l'incidence, des lames différentes ont dû être utilisées.

Le shéma figure 5 présente l'ensemble du montage "maquette + dard + 3 mâts" réalisé.
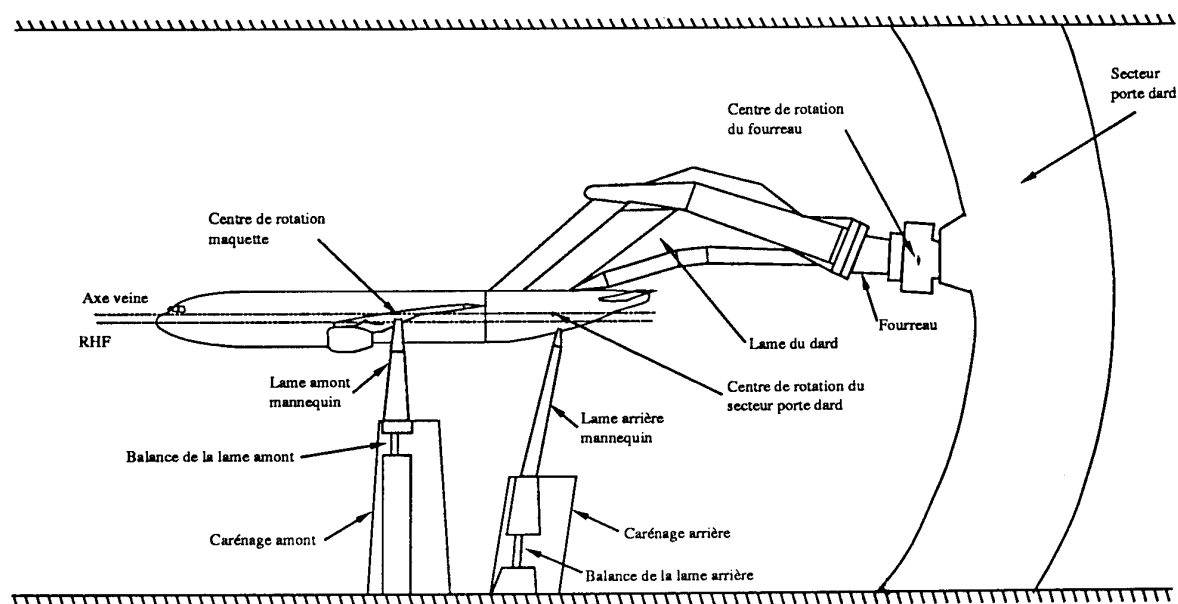
Figure 5 - Shéma du montage en veine

C. EFFET DES CARENAGES DU MONTAGE 3 MATS DE F1
COMPARAISON DES RESULTATS THEORIQUES ET EXPERIMENTAUX

1. Conditions et données géométriques des calculs théoriques

Les calculs théoriques de l'influence des carénages ont été effectués dans des conditions identiques à celles de l'étude expérimentale, soit pour un MACH à l'infini amont égal à 0,2 autour d'une configuration fuselage+voilure becs et volets rentrés (les effets de l'empennage horizontal et de l'hypersustentation ne font pas l'objet de cet exposé). Les variations de pression cinétique et d'ascendance dues à l'effet d'épaisseur des carénages sont issues d'un calcul à incidence nulle. Un balayage degré par degré de 0° à 12° a été effectué pour la résolution du problème portant. Par contre, les temps de calcul propres à la méthode des singularités surfaciques étant relativement élevés, seules les incidences suivantes ont été étudiées: α=0°, 5° et 10°.

On a d'autre part opté pour une représentation fine des formes des obstacles. Les maillages ont été définis comme suit:
• Méthode des singularités surfaciques: l'étude portant sur des cas de vols longitudinaux, seul le maillage d'une demi-maquette a été défini en raison de la symétrie de l'écoulement. Le fuselage et la voilure ont été modélisés à l'aide d'environ 8000 panneaux. Quelques 1000 panneaux supplémentaires furent nécessaires pour représenter les carénages, le plafond et les parois verticales; le plancher était obtenu à l'aide d'une symétrie supplémentaire.
• Méthode simplifiée: prise en compte de 10 images pour la modélisation des parois de la veine d'essais.
Résolution du problème épais: axe du fuselage: 50 points, voilure: 50 sections de 69 points, carénages amont: 30 sections de 21 points, carénage arrière: 20 sections de 16 points.
Résolution du problème portant: 50 sections pour une demi-voilure, 32 sections pour les carénages amont.

2. Traitement et précision des mesures expérimentales

Les mesures brutes de pesées n'ont subi aucune correction préalable. Ceci est justifié par le fait que les corrections de support sont les premières corrections à appliquer aux résultats bruts de soufflerie, dans la mesure où les études sur les effets de paroi sont faites sur une maquette seule en veine, dégagée de toute influence extérieure.

Les coefficients aérodynamiques servant de base à la confrontation théorie/expérience sont le résultat de la moyenne, à incidence donnée, de 20 mesures acquises au cours d'un même essai en palier stabilisé; de plus, chacun de ces essais a été au minimum doublé. Malgré le soin particulier apporté durant cette campagne, il faut tenir compte de la précision de la balance utilisée: les valeurs suivantes peuvent être retenues comme valeurs d'incertitude sur les effets mesurés: ± 0.003 sur le ΔCz, ±0,0005 sur le ΔCx et ±0,0010 sur leΔCm.

3. Comparaison des résultats

3.1. Influence des carénages sur le coefficient de portance

La comparaison des résultats théoriques et expérimentaux sur le coefficient de portance, présentée figure 6, est satisfaisante: compte tenu de la dispersion associée à la courbe expérimentale, le niveau de l'effet des carénages et son évolution avec l'incidence sont correctement prédits à l'aide des calculs d'écoulement de fluide parfait, quelle que soit la méthode utilisée.

On observe que la présence des carénages se traduit par une augmentation pratiquement linéaire de la portance; l'expérience montre que cet effet s'attenue sensiblement au delà d'un Cz_b inférieur au Cz de décrochage de la maquette dans cette configuration. Les méthodes théoriques, basée sur une linéarisation des effets, ne permettent pas de retrouver ce phénomène; elles fournissent cependant une explication: la figure 7, issue des calculs à l'aide de la méthode simplifiée, montre notamment les modifications de la direction locale de l'écoulement sur l'aile dues aux effets de portance. On constate ainsi que les angles induits augmentent avec l'incidence, c'est à dire qu'ils dépendent de la position relative de la maquette par rapport aux carénages. Les incidences locales étant plus élevées en présence des carénages, les décollements à l'extrados de la voilure apparaissent prématurément, d'où une diminution du gradient $\partial Cz/\partial\alpha$ impliquant une chute de l'effet ΔCz.
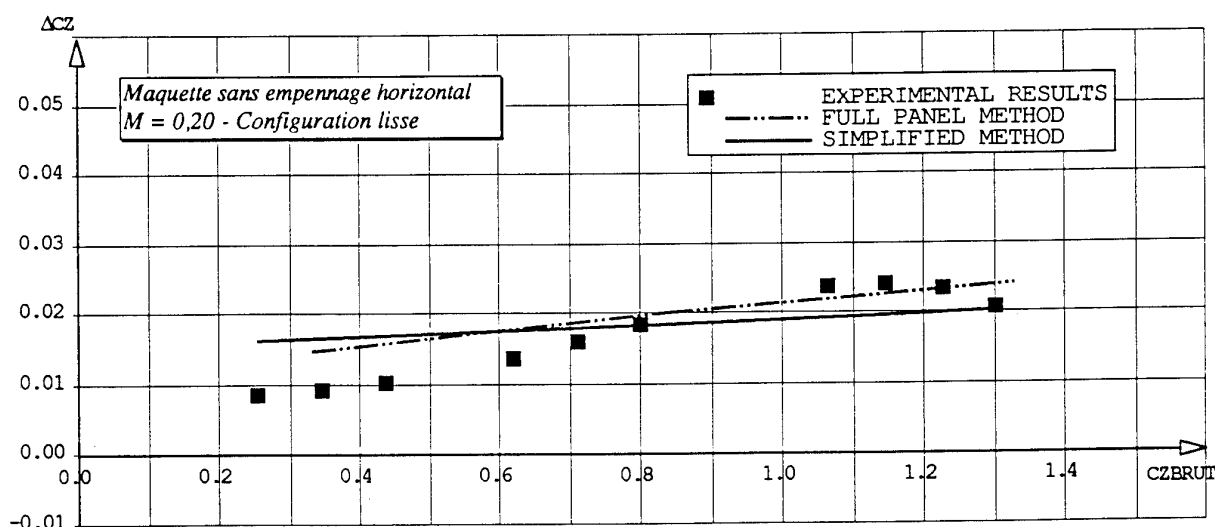
Figure 6 - Effet des carénages sur le coefficient de portance
Comparaison théorie/expérience
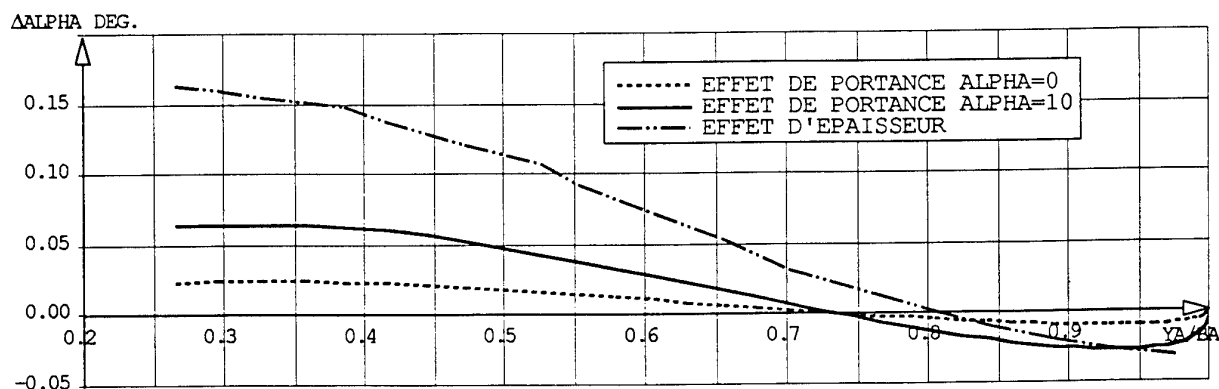
Figure 7 - Ascendance induite par les carénages (méthode simplifiée)

Les modifications de la loi de circulation de l'aile induites par ces angles induits sont fournies figure 8; la figure 9 montre les circulations créées sur le carénage amont gauche par la portance de la voilure.
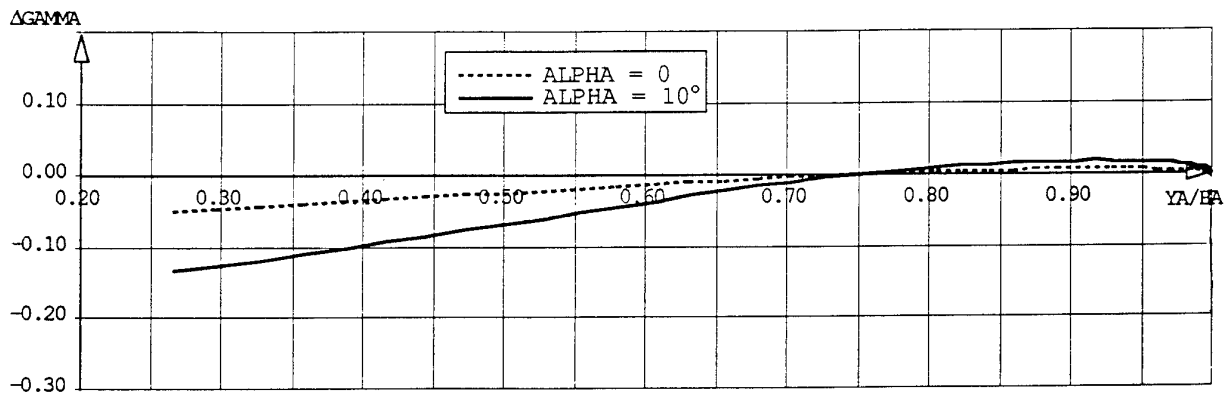
Figure 8 - Effet des tourbillons des carénages amont sur la circulation de l'aile
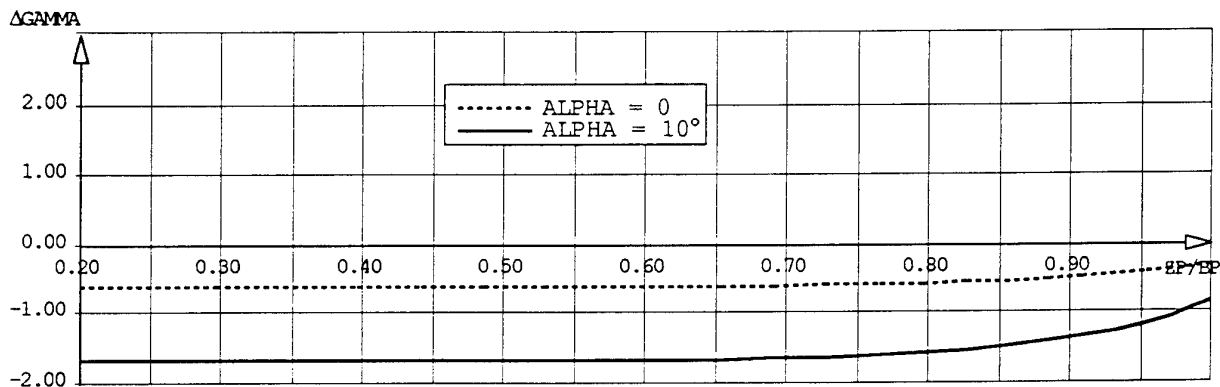
Figure 9 - Circulation sur le carénage amont gauche induite par l'aile

3.2. Influence des carénages sur le coefficient de traînée

L'effet des carénages sur le coefficient de traînée de la maquette est présenté figure 10 en fonction du coefficient de portance brut. On observe que lorsque la portance de la maquette augmente, l'accroissement de la traînée va de pair avec la diminution de la correction globale ΔCx à appliquer aux mesures.

Le résultat de la comparaison théorie/expérience sur la correction de traînée, plus délicate à obtenir, est moins satisfaisant que dans le cas du coefficient de portance. Les écarts restent cependant acceptables, compte tenu des incertitudes liées d'une part à la précision de la balance, et d'autre part aux difficultés pratiques propres à la mise en oeuvre de tels essais. Le fait que les ΔCx expérimentaux, relatifs à la traînée totale de la maquette, soient proches des valeurs théoriques issues des calculs de fluide parfait, semble montrer que seule la traînée induite est affectée par la présence des carénages; la portance générée par l'aile peut ainsi être considérée comme le facteur majeur responsable du niveau des interactions.

A noter d'autre part que l'évolution expérimentale en fonction du Cz est respectée. Les résultats issus de la méthode simplifiée, plus proches de l'expérience, dans le domaine d'incidence utile, que ceux obtenus à l'aide de la méthode globale, montrent que la décroissance des effets est due d'une part au terme lié à la rotation des axes aérodynamiques, et d'autre part aux interférences de portance entre l'aile et les carénages amont (variation de 0 à -10 points sur le domaine étudié).
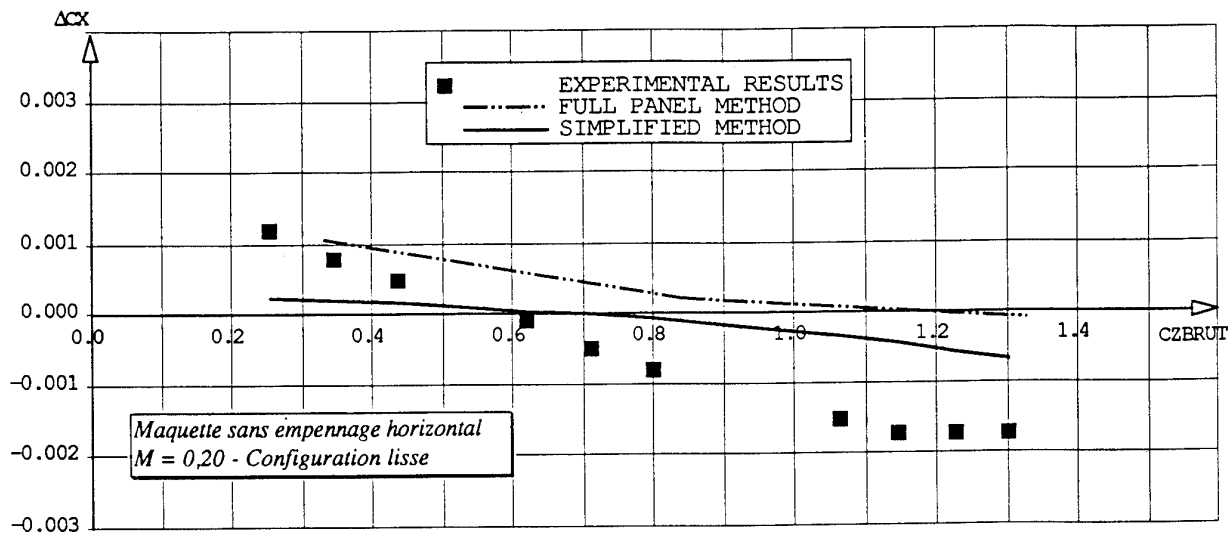
Figure 10 - Effet des carénages sur le coefficient de traînée
Comparaison théorie/expérience

3.3. Influence des carénages sur le coefficient de moment de tangage

Les modifications des directions locales de l'écoulement dues aux effets de volume et de portance induits par les carénages se traduisent principalement par une ascendance sur l'aile interne et une déflexion sur l'aile externe (figure 7), d'où l'existence d'un moment cabreur supplémentaire. Cet effet est faible pour une maquette non empennée. On a vu que la méthode simplifiée, basée sur une représentation schématique de l'écoulement perturbé, ne permettait pas de retrouver le niveau expérimental; en contrepartie, la comparaison des mesures aux résultats issus de la méthode globale est satisfaisante (figure 11).
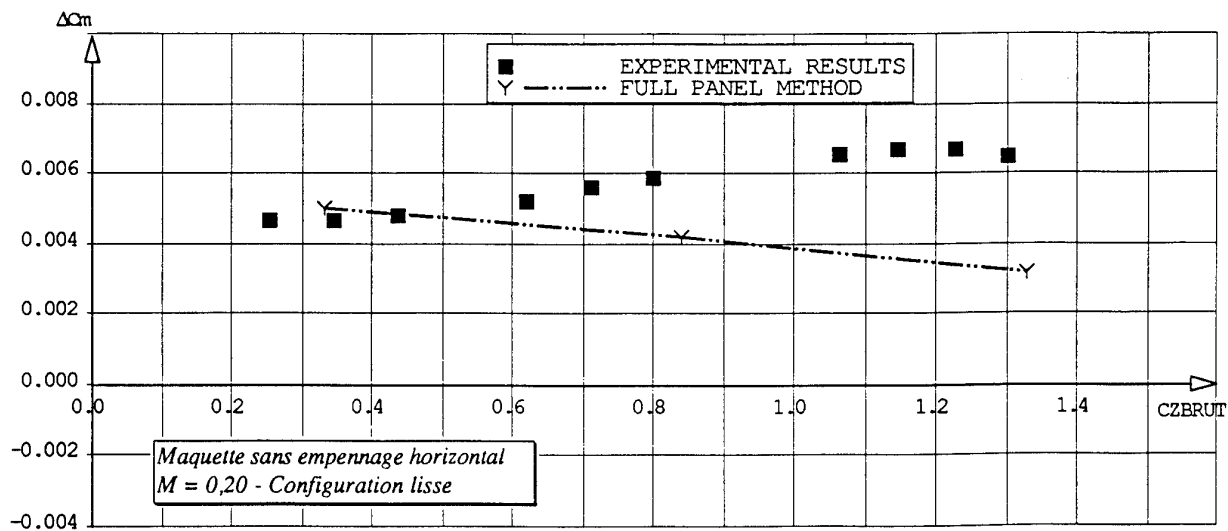
Figure 11 - Effet des carénages sur le coefficient de moment de tangage
Comparaison théoric/expérience

D. EFFET EXPERIMENTAL DES LAMES DU SUPPORT 3 MATS

L'effet des lames sur la maquette est obtenu en differenciant les mesures effectuées en présence du montage complet et en présence des 3 carénages uniquement. Le nombre de MACH de 0.2 prévu à l'origine n'a pu être atteint en raison de l'apparition d'oscillations de la lame du mât amont, dues à la souplesse de sa propre balance. Les résultats sont présentés pour M = 0.12.

Les figures 12 à 14 fournissent la comparaison de l'influence du montage complet avec celle des carénages, en fonction du coefficient de portance non corrigé de la maquette. On observe que l'allure générale des courbes est identique à celle relative aux carénages seuls; l'effet des lames se traduit par un incrément supplémentaire pratiquement indépendant de la portance.

L'hypothèse généralement faite que l'effet d'interférence des lames est petit comparé à celui des carénages n'est pas vérifié sur le coefficient de traînée (effet constant de l'ordre de 10 points correspondant, à incidence nulle, à une augmentation d'environ 50% de l'effet des carénages). En contrepartie, cette hypothèse reste valable sur le coefficient de portance (effet des lames de l'ordre de +0.004), et sur le coefficient de moment de tangage (environ +0.002). Bien que faible, l'effet des lames est d'une nature plus complexe que celui des carénages: les lames amont s'étendent jusqu'à la voilure et leurs sillages interactionnent avec l'écoulement visqueux sur l'aile. Les essais en présence uniquement des mâts amont ont montré que les lames amont étaient responsable de pratiquement la totalité de l'effet. Il s'ensuit que la position du mât arrière, dont la longueur correspond à une incidence donnée de la maquette, ne joue qu'un rôle secondaire.
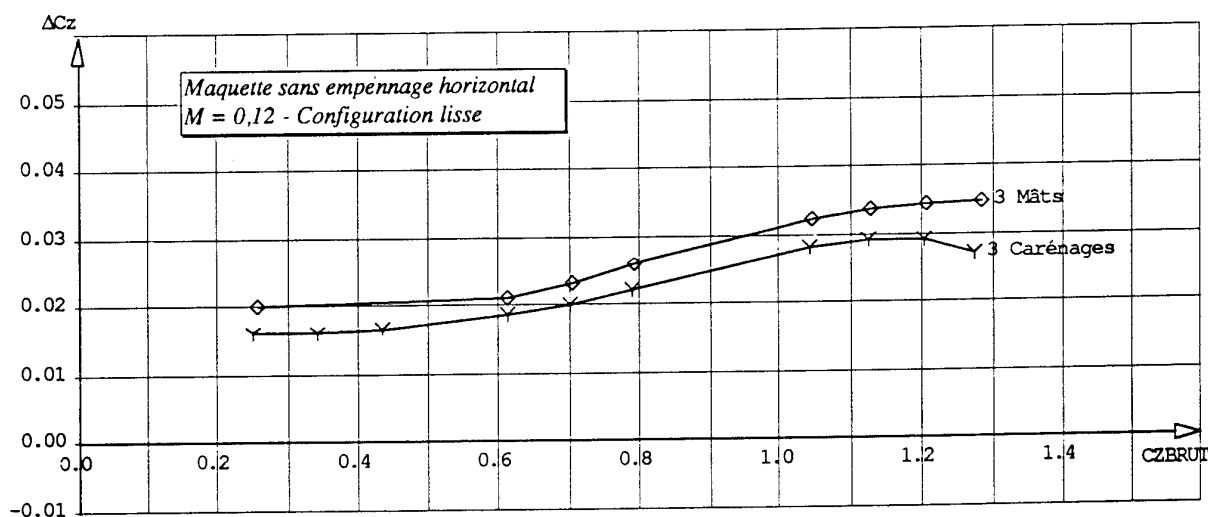
Figure 12 - Effet des lames sur le coefficient de portance
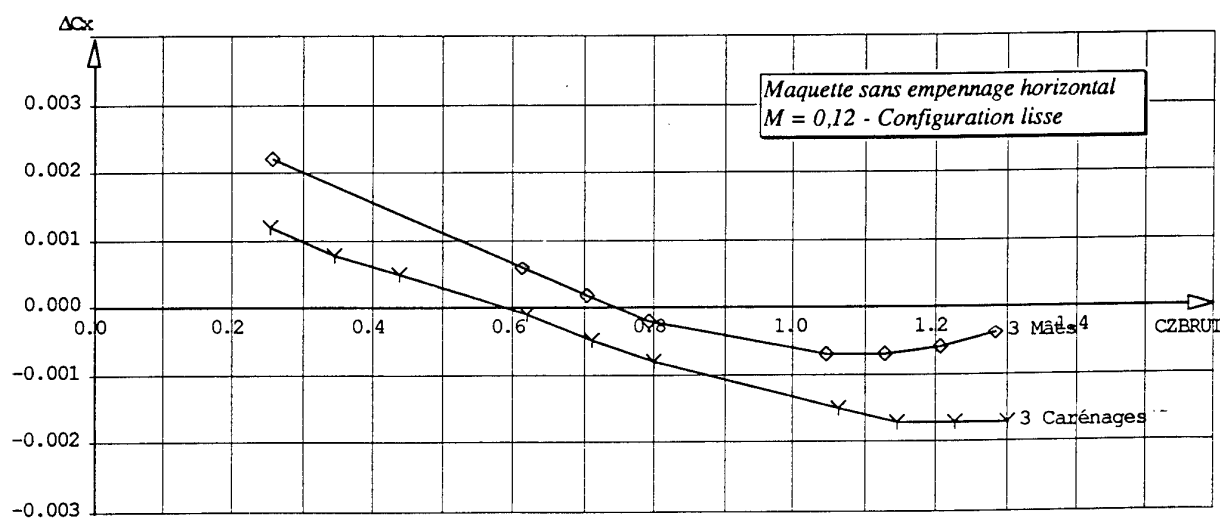
Figure 13 - Effet des lames sur le coefficient de traînée
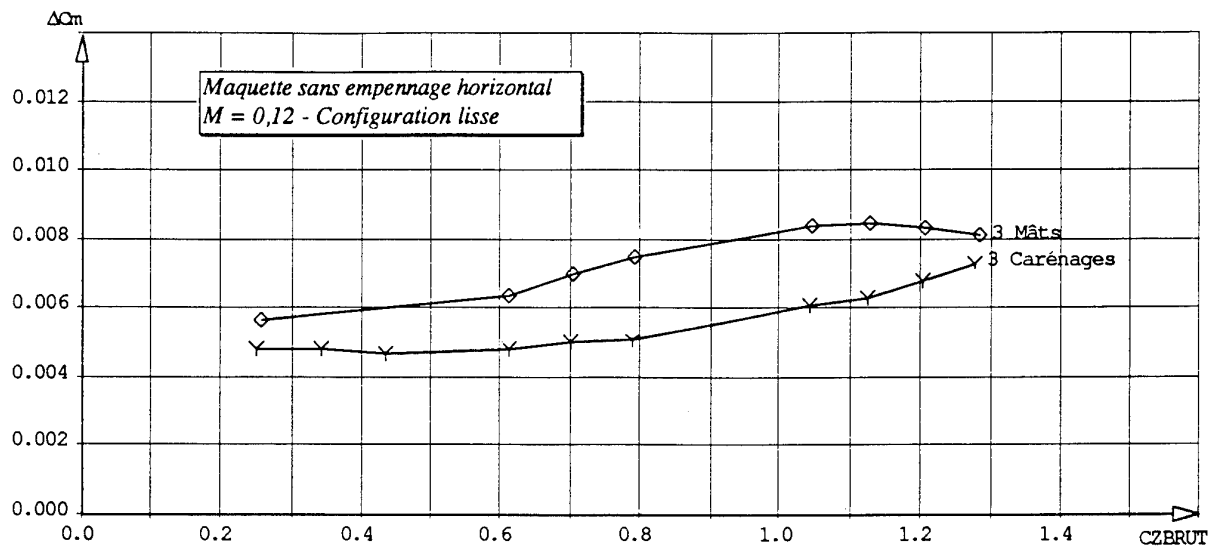
Figure 14 - Effet des lames sur le coefficient de moment de tangage

E. INFLUENCE DE LA MAQUETTE SUR LE TARAGE DU MONTAGE

Nous rappelons que la procédure normale d'essais sur 3 mâts consiste à monter la maquette sur la balance de paroi par l'intermédiaire de ce support; les lames, exposées au vent, sont soumises à des forces dont les mesures par la balance viennent s'ajouter à celles relatives à la maquette.

Un tarage préalable du montage est donc nécessaire afin d'identifier ces efforts et de les déduire des mesures globales. La détermination du tarage et la correction conséquente ont longtemps été obtenus à l'aide d'essais effectués sur le support en l'absence de la maquette, ce qui supposait que l'écoulement autour des mâts n'était pas perturbé par celle-ci. L'utilisation, au cours de cette campagne d'essais, de petites balances situées à l'intérieur des mâts a permis d'accéder aux efforts et d'isoler les modifications de la tare induites par la présence de la maquette.

Les figures 15 à 17 présentent respectivement les 3 coefficients longitudinaux caractérisant les efforts qui s'exercent sur le montage complet en l'absence et en présence de la maquette non empennée. Les mesures présentées sont adimensionnées avec les longueurs de référence de l'A310 et le moment de tangage est ramené au point situé à 25% de la corde moyenne aérodynamique.

Ces figures montrent tout d'abord que la tare du montage en présence de la maquette est indépendante de l'incidence, c'est à dire qu'elle est peu sensible aux variations de la longueur du mât arrière. D'autre part, la présence de la maquette entraîne une diminution des efforts s'exerçant sur les lames; ainsi, l'application de corrections issues d'un tarage "montage seul en veine" avait pour conséquence une sous-estimation des coefficients longitudinaux de la maquette.
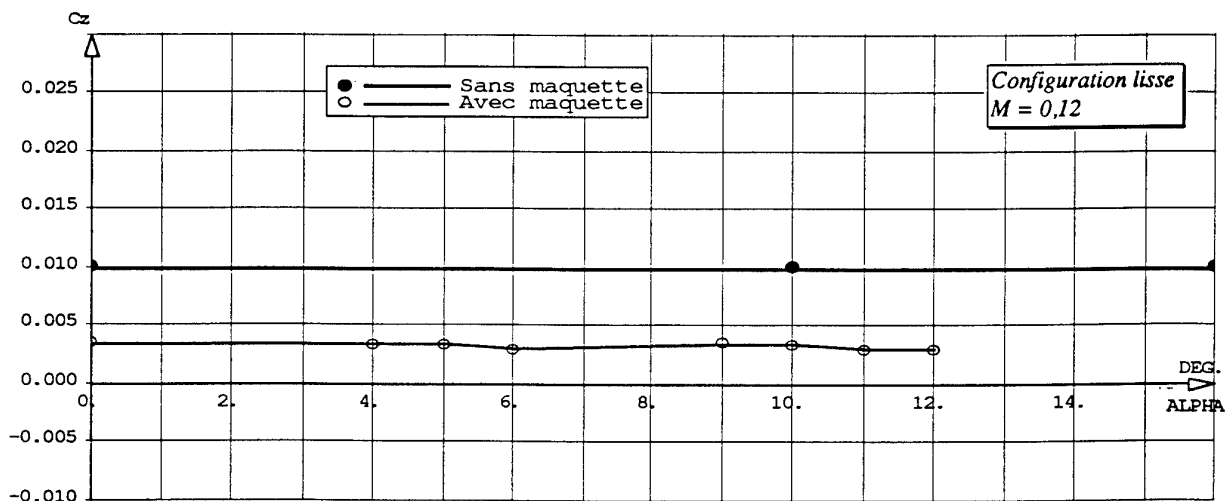
Figure 15 - Effet de la maquette sur la tare du montage 3 mâts de F1
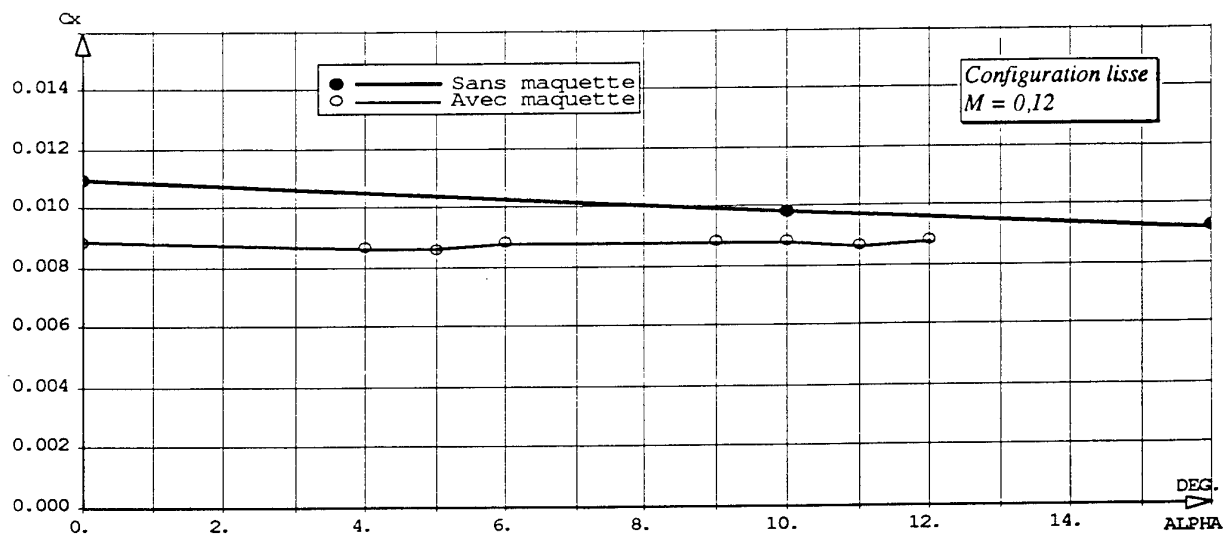
Figure 16 - Effet de la maquette sur la tare du montage 3 mâts de F1 - Coefficient de traînée
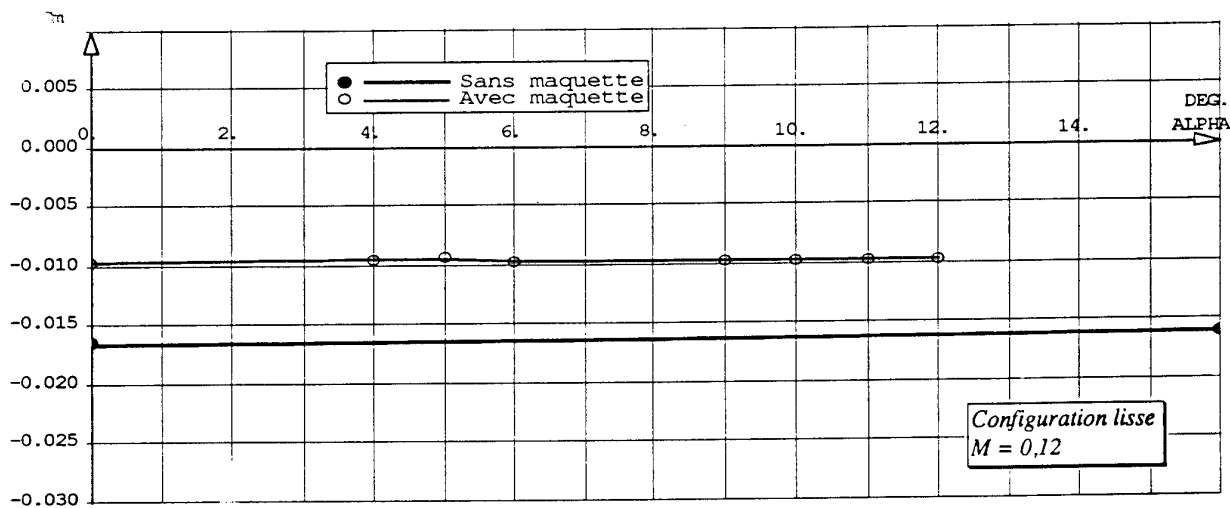
Figure 17 - Effet de la maquette sur la tare du montage 3 mâts de F1 - Coefficient de moment de tangage

Le coefficient le plus affecté est le coefficient de traînée pour lequel on observe un écart décroissant avec l'incidence de 40 à 10 points. L'effet sur la correction du moment de tangage, sans être aussi conséquent (de l'ordre de 0.005), doit cependant être pris en compte. L'effet sur le coefficient de portance est faible; en ce qui le concerne, notons que les mesures effectuées rendent compte d'une force verticale qui ne correspond pas à la portance latérale induite par la voilure étudiée précedemment.

CONCLUSION

Les deux méthodes théoriques proposées pour la détermination de l'effet des carénages d'un support de type 3 mâts, basées sur des calculs d'écoulement de fluide parfait, prévoient correctement l'évolution des phénomènes globaux et fournissent des corrections du même ordre de grandeur que celles obtenues au cours d'une campagne d'essais dans la soufflerie F1 de l'ONERA.

La méthode simplifiée sera privilégiée pour le calcul des interactions sur les coefficients de portance et de traînée, en raison d'une part de sa facilité de mise en oeuvre (réduction des temps de préparation des données), et de ses

faibles durées de calcul. Cette méthode ne permettant pas actuellement de définir correctement la correction sur le coefficient de moment de tangage, il faudra appliquer la méthode globale de singularités surfaciques.

Les essais ont permis d'autre part de montrer que les lames du montage, bien que discrètes dans l'écoulement, induisaient un effet sur la traînée de niveau pratiquement identique à celui des carénages.

De plus, négliger l'influence de la maquette sur la tare du support entraîne une erreur sur le coefficient de traînée et le coefficient de moment de tangage d'un ordre de grandeur équivalent à l'effet global du montage sur la maquette.

REFERENCES BIBLIOGRAPHIQUES

[1]   C. QUEMARD - Influence des supports de maquette à F1 - ONERA R.T. 12/3236 GN Octobre 84

[2]   J. BOUSQUET - Aérodynamique: Méthode des singularités - CEPADUES Editions - Septembre 90

[3]   J. L. HESS / A. M. O. SMITH - Calculation of non-lifting potential flow about arbitrary three dimensionnal bodies - DOUGLAS AIRCRAFT Co Report N°E.S. 40622 - Mars 62

[4]   J. L. HESS - Calculation of potential flow about arbitrary three dimensionnal lifting bodies - DOUGLAS Report MDC Jo545 - Décembre 69

[5]   A. BONNET / J. LUNEAU - Aérodynamique: Théories de la dynamique des fluides - CEPADUES Editions - Septembre 89

[6]   C. QUEMARD / D. CARUANA - Mesure de l'interaction du montage 3 mâts de la soufflerie F1 - ONERA PV 1/8475 GY - Mars 89

INTERFERENCE CORRECTIONS FOR A CENTRE-LINE PLATE MOUNT IN A POROUS-WALLED TRANSONIC WIND TUNNEL

Richard J.D. Poole
Senior Research Engineer, Aerodynamic Research and Development,
Mail Stop N18-06, de Havilland Inc.,
Garratt Blvd., Downsview, Ontario, Canada. M3K 1Y5

Robin D. Galway
Research Council Officer, Institute for Aerospace Research,
High Speed Aerodynamics Laboratory, National Research Council,
Montreal Road, Ottawa, Ontario, Canada. K1A 0R6

1.   SUMMARY

A programme of collaborative research between the National Research Council of Canada, Institute for Aerospace Research (I.A.R.) and de Havilland Inc. included the design and manufacture of a slim centre-line plate mount model support for installation in the I.A.R. 1.5m. Trisonic Wind Tunnel. The primary objective of the collaborative research program was to provide a mounting method suitable for accurate measurement of the drag increments resulting from configuration changes on typical transport aircraft models. The secondary objective was to derive the tare effect of the model mounting plate so that datum aerodynamic parameters could be measured.

To obtain the tare effect of the mounting plate on a model, an alternative mount from the tunnel ceiling was designed and built. The "Y-Mount" allowed the model to be held in close proximity to a dummy plate and also to be tested without the plate in the tunnel. Comparative plate in and plate out measurements were made for a range of Mach numbers and model incidences to obtain the plate tares.

2. LIST OF SYMBOLS

C_{D_π}	Drag / $(q * S_\pi)$
C_{L_π}	Lift / $(q * S_\pi)$
C_{M_π}	Pitching moment / $(q * S_\pi * 1)$
1	Fuselage length
M	Mach number
q	Tunnel dynamic pressure
S_π	Fuselage cross sectional area
R_{Ec}	Reynolds Number based on wing mean aerodynamic chord
Δ	Increment

3.   INTRODUCTION

The wind tunnel model research programs conducted by de Havilland Inc. have been concentrated at the National Research Council of Canada (N.R.C.C.). The tunnels, operated by the Institute for Aerospace Research (I.A.R.), employ a variety of model mounting systems.

The Low Speed tunnels employ the "traditional" three strut system for three dimensional models, for which there are conventional strut tare procedures (either dummy/image struts or an added ventral stut). Both the Low Speed and High Speed tunnels have well developed mounting systems for reflection plane models (Reference 1.). These have been extensively used to obtain incremental data for high lift (Low Speed Tunnel) and Cruise (High Speed, Trisonic Tunnel) configurations. A sting mount with combined pitching and rolling motions was the standard method for mounting complete three dimensional models in the 1.5m Trisonic tunnel prior to the development of the plate mount described in this paper.

Correct matching of Mach number and an adequate test Reynolds number are essential for predicting aircraft cruise performance from wind tunnel data. Wind tunnel tests which provide incremental data are normally adequate for development work on existing aircraft configurations. However, when significant changes in aircraft configuration are to be examined, it becomes highly desirable that the measured aerodynamic parameters be known not just as increments but also as absolute values. To get as close as possible to the aircraft datum values requires a knowledge of the interference between the model and the mounting system.

A plate mount was selected as the optimum solution for obtaining fully tared data from three dimensional models at zero yaw in the I.A.R. Trisonic tunnel. The plate mount was designed by de Havilland Inc. as a self-contained unit attached to the floor of the porous-walled transonic section of the tunnel. The systems design and the plate mount manufacture were carried out jointly by de Havilland Inc. and I.A.R.

To investigate the plate mount interference, an alternative ceiling-mounted model support, the Y-Mount, was designed and built by de Havilland Inc. as part of the second phase of the collaborative program between I.A.R. and de Havilland Inc. The tare/interference evaluation involved a regional transport aircraft configuration, with the model mounted from the ceiling support through a fin/sting combination. The interference was determined from measurements made with a dummy plate installed in the plate support but not contacting the model and also with the plate removed, for a range of Mach numbers and model angles of attack.

4.   MODEL MOUNTING SYSTEMS

In order to validate the decision to design and build the plate mount, it was necessary to evaluate the alternatives available at the I.A.R. Trisonic tunnel.

Sting Mount

Transport aircraft typical to de Havilland Inc. have tapered rear fuselages and frequently some upsweep. A rear sting mount destroys any attempt at accurate modelling of the flow in this region and can significantly effect longitudinal stability data. On fighter-type aircraft, with jet exhausts at the aft end of the fuselage, wake filling by a sting mount may be considered of less critical importance.

A dual sting mount for the acquisition of tares and uncontaminated rear fuselage data was considered to be too complex and possibly lacking in structural integrity for use in the high load environment of the I.A.R. tunnel.

Blade Mount

Slim blades mounted off a sting and entering the model rear fuselage can be employed, but are generally less stiff and less suited for high Reynolds number testing in blowdown tunnels. Pressure distributions on the rear fuselage are usually incorrect

due to the thickness of the blade. Lateral/directional cross-coupling of models with asymmetries limit model size and the available Reynolds number for this type of mounting.

Fin Mount

Reservations regarding a fin mount were similar to those encountered with a blade mount. Blade thickness is usually greater then that of a fin, causing errors in the rear fuselage pressure distribution. Structural stiffness considerations made this a second choice option.

Centre-line plate

The centre-line plate mount method has been employed successfully in other tunnels (for example, Calspan and Boeing (BTWT) with an underfloor balance). The influence of the mount on the model is restricted to a narrow strip along the fuselage surface. Due to the low thickness/chord ratio of the plate, no unwanted transonic flow effects occur. Additional tunnel blockage effects are small and local flow irregularities are minimal. The major shortcoming is, of course, the inability to do tests with significant yaw angles.

5.   CENTRE-LINE PLATE - DESIGN CRITERIA

The requirements for correct matching of Mach number and an adequate test Reynolds number are most closely met at I.A.R. by the 1.5m Trisonic Blowdown Tunnel. The blowdown tunnel presents the model designer with several specific problems, primarily associated with the brevity of the run. Pressurised tunnels also exert high transient and steady state loads requiring very robust models and mounting systems.

Since the plate mount was designed by de Havilland Inc. for installation in an I.A.R. tunnel, one design criterion was to minimise modifications to the existing tunnel structure. This was accomplished by using the existing points of attachment of the porous floor to the test section backup structure. Longer bolts through the plate mount footplate secured both it and the floor to the structure. The design also made use of two existing observation ports in the test section floor, to provide access from the plate mount box into the tunnel plenum chamber for instrumentation cables and hydraulic hoses.

To minimise the effect of the plate mount on flow quality in the tunnel working section, the box started well upstream. CFD calculations provided guidance in determining the required length (References 2 and 3). Blockage effects were minimised by keeping the box as slim as possible (7.6cm), the width and height selected giving a 1.6% area blockage. Figure 1 shows a model in the tunnel on the plate mount. Figure 2 is a diagram of the plate mount, showing the internal rocking horse and hydraulic drive jack. The Y-Mount is also shown.

To achieve the maximum possible Reynolds numbers, models were as large as practical for the tunnel. This gave wing spans in the 106cm to 114cm range in a 1.5m wide tunnel. The models have an internal body axis balance, and the plate is non-metric, unlike the Boeing BTWT arrangement with a metric plate and underfloor balance. Though the use of a 6-component body axis balance can degrade the accuracy of drag coefficients away from incidences near to zero, the absence of a metric plate removes a significant factor in the accuracy (magnitude) of measured drag quantities. Instrumentation leaves the model through a hollow aft fairing on the plate.

A total pitch angle range of 28 degrees is available, and the design of the model mounting plate can be varied to bias the model zero angle of attack anywhere within this range (e.g., -8 to +20 degrees or -14 to +14 degrees). The pitching centre for the model is on the centre-line of the tunnel. The pitch drive system has the capability for a wide range of computer commanded pitch rates for use during runs (typically 2 to 3 degrees per second) and at run termination (or "alarmed" shut-down) when the model returns to a safe position at maximum rate (15 degrees per second). Plate incidence was read from a gear driven potentiometer mounted at the back of the plate mount rocking horse. The model incidence was read from a fuselage installed Sundstrand accelerometer.

6. Y-MOUNT DESIGN

The ceiling mount was selected for use in tare evaluation only after alternatives had been considered and discarded. The dominating criterion was to have minimal relative movement between the model and the dummy plate. The stiffness of the tare mounting was critical to the success of the investigation. For this reason, a sting mount using the existing tunnel equipment was rejected. Similarly, the choice of a single ceiling attachment was rejected, because the Y-

Mount had more stiffness than a single mount of the same blockage bulk, thus preventing lateral interference between the model and the plate and the possibility of a balance overload.

Figure 3 shows the model mounted on the Y-Mount, with the dummy plate installed. Figure 4 is a diagram of the Y-Mount, showing the geometry of the mounting system. The location of the Y-Mount is also shown on Figure 2.

The fin and sting from the Y-Mount entered the top of the metric model rear fuselage, with clearances which were confirmed during pre-test loading calibrations.

The dummy plate entered the fuselage lower surface in the same way as the regular plate, but stopped short of the balance carrier. The seals used to prevent flow into the model (spring loaded teflon along the sides and soft foam at the front) were the same as used in regular "plate mount" testing. When the dummy plate was removed, the slit in the lower surface of the fuselage was filled to profile with an aluminum strip and the slit in the top of the box was covered.

Static load calibrations were performed in the wind tunnel to determine the stiffness constants for the complete model, balance and roof-mount support system. During subsequent tunnel runs, the balance signals proportional to normal force and pitching moment (suitably scaled using the balance factors and calibrated support stiffness constants), were used to modulate the signal to the plate incidence servo. This caused the angle of the dummy plate to track the deflection of the model under load. From Reference 4, - a fuselage alone test - it was known that unporting of the plate from the front fuselage had a measurable effect on drag.

The final Y-Mount design had an incidence range from -4 degrees to +10 degrees in two degree increments. Incidences could only be changed between runs.

During the calibrations, it was found that the Y-Mount always had an initial movement under load as the slack was taken out of the tolerances in the system. A diagonal turn-buckle strut from the Y-Mount to the ceiling was used to "pre-tension" the rig and take out the slack. This had a useful side benefit, as it was possible to pre-bias the model incidence, so that the wind-on/load-on incidence was repeatable between runs.

7. TEST FACILITY

The I.A.R. Trisonic Wind Tunnel is of the pressurized blowdown type, and is capable of operating at high Reynolds numbers in the subsonic, transonic and supersonic flow regimes, at Mach numbers between 0.10 and 4.25 (Figure 5 and Reference 5.) Within the range of Mach numbers covered by the present test ($0.35 \leq M \leq 0.76$), a Reynolds number of 40 million per metre was obtained for a run duration of approximately 12 seconds. Higher Reynolds numbers are possible, but at the expense of reduced run time.

The basic test section is 1.5m square with solid walls for measurements in subsonic and supersonic flow. A separate test section having all four walls perforated with 60 degree inclined holes, and being contained within a pressure tight plenum chamber, provides for subsonic-transonic flow (References 6 and 7). The wall porosity is variable in a range between 1% and 6% open. Control is by sliding throttle plates behind the walls, in which the slanted hole pattern is replicated. The porosity holes in the walls (but not in the throttle plates) are equipped with integral streamwise splitter plates for suppression of edgetone noise.

Microcomputers are used extensively to control various wind tunnel functions, such as the stream stagnation pressure, Mach number and the model attitude. For example, the Mach number control system alters the Mach number (through the adjustment of the second throat area or plenum ejection flow), so as to compensate for changing blockage and wall interference corrections when model attitude is varied. During a blowdown, variations in stagnation pressure and Mach number are typically of the order of ± 0.5kPa (± 0.07 psi) and ± 0.001 respectively

The data acquisition system used for recording nominally steady state information is built around DEC PDP and VAX computers with extensive disc storage. Because of the limited run time, it is normal to record all data channels continuously during the blowdown, usually at a 100 Hz rate. A modern high speed data acquisition system, (with 192 channel capacity and sampling rates to 40 kHz per channel), is also available for making measurements involving unsteady phenomena, but it was not used during the test reported here.

In addition to the measurement of model forces and moments using an internal strain gauge balance, the streamwise pressure distributions on the test section

walls were recorded using Electronic Pressure Scanning (ESP) techniques. These pressure distributions are recorded routinely during all tests, to provided the boundary conditions for computation of wall interference corrections to Mach number, incidence and drag (buoyancy) - References 8 and 9. The internal fuselage cavity pressure, referred to in Section 8, was measured using one 'port' on the ESP module assigned to the ceiling pressure measurements.

8. TEST PROGRAM and MODEL

A range of Mach numbers and incidences were tested, as applicable to a high speed propeller driven transport aircraft (Table 1). The model, Figure 1, had been tested previously, so that the expected model loads were known. The model represented a current transport aircraft in a cruise configuration. The wings had transition fixed on both surfaces at 15% chord using discrete cylinders, and the fuselage had transition fixed one inch back from the nose. The internal balance was a 2.0 inch diameter Task Mk.VIIA. All the cabling for the balance was taken from the model through the hollow sting and fin.

MACH NUMBER	R_{Ec} millions	NOMINAL INCIDENCES (degrees)				
0.35	3.65	0.0	2.0	4.0	6.0	8.0
0.50	4.00	0.0	2.0	4.0	6.0	8.0
0.60	4.00	0.0	2.0	4.0	6.0	-
0.70	4.00	0.0	2.0	4.0	-	-
0.76	4.00	0.0	2.0	4.0	-	-

TABLE 1. TEST CASES

The model incidence was recorded from a calibrated Sundstrand accelerometer mounted inside the fuselage.

The static pressure inside the fuselage was recorded for some runs, to measure differences that occurred with the plate in and plate out. The open clearance area in the rear fuselage where the fin/sting entered, was parallel to the fuselage datum, so no significant effects were expected on drag, but the impact on lift and pitching moment required monitoring.

Plate tare increments were determined by subtracting the dummy plate in and dummy plate out runs, using data without tunnel wall interference corrections. Such corrections are a function of lift coefficient which did not change significantly plate in/plate out.

9. RESULTS

The maximum difference in test incidence between plate in and plate out runs was less than 0.05 degrees. Figure 6 shows the increments in lift, drag and pitching moment coefficients due to the presence of the plate, non-dimensionalised with reference to the fuselage cross sectional area and length.

Lift coefficient increments due to the plate were very small, with a ΔC_{L_π} range within a ± 0.2 band (approximately 0.02 based on wing area).

Drag coefficient increments due to the plate decreased with increasing incidence at low Mach number from 0.030 to -0.008. As Mach number increased, the increments reached a minimum at $M=0.60$. From the repeat cases over the range of Mach numbers at zero incidence, it was noted that the scatter band width on the increments was of the order of ± 0.004. This represented about $\pm 10\%$ of the fuselage alone drag, or about ± 4 drag counts based on the wing area. At typical cruise incidences, the total drag tare of the plate had a magnitude of about 20% of the fuselage drag.

Pitching moment increments were affected by the changes in internal static pressure, plate in and plate out. After corrections for the internal pressure changes were applied, the pitching moment increments generally decreased as incidence increased, with very little change due to Mach number. The exceptional case was at $M=0.35$, where the pitching moment increments did not follow the common pattern.

10. CONCLUSIONS

The interference corrections for a centre-line plate mount were measured for a model of a propeller driven transport aircraft. The Y-Mount system gave a rigid alternative model mount which repeatably held the model in close proximity to the original plate mount.

Subtracting data obtained from plate in and plate out tunnel runs showed that:-

(1)   Lift increments due to the plate were small, less than 0.02 based on wing area.

(2)   Drag increments decreased with increasing incidence and Mach number, from 30 aircraft drag counts at $M=0.35$ and zero degrees incidence to effectively zero at $M=0.60$ and 4 degrees incidence.

(3)   Pitching moment increments varied almost linearly with incidence, from positive at zero incidence to very small at four degrees. The data for $M=0.35$ showed inconsistencies which could not be immediately explained.

In the future, some cases will have to be repeated to resolve the anomalies in the pitching moment increments.

The scatter band width on the drag tare needs to be refined. The internal balance used in the tare test had a wider load range than required, because it was selected for, and carried over from a previous full flight envelope test. Also, the Mach number range should be extended to cover high speed transport aircraft configurations.

11. REFERENCES

1.   B.Eggleston, R.J.D.Poole
     High Lift Systems for Transport Aircraft
     with Advanced Airfoils
     AGARD 71st Fluid Dynamics Panel
     Meeting and Symposium on High Lift
     Aerodynamics, Banff, Alberta, Canada.
     October 1992

2.   M. Mokry (I.A.R.),
     G.Waller (de Havilland Inc.)
     Unpublished correspondence.
     CFD Analysis of a Porous Tunnel and a
     Plate Mount

3.   M.Mokry
     Evaluation of Combined Wall and Support
     Interference on Wind Tunnel Models.
     AGARD. 73rd Fluid Dynamics Panel
     Meeting and Symposium on Wall
     Interference, Support Interference and Flow
     Field Measurements,
     Brussels, Belgium. October 1993

4.   Unpublished de Havilland Inc. report
     Fuselage Alone Tests on a Plate Mount

5.   D.Brown (Editor).
     Information for Users of the National
     Research Council's 5-Ft. x 5-Ft. Blowdown
     Wind Tunnel at the National Aeronautical
     Establishment (3rd Ed.)
     LTR-HA-6, National Aeronautical Est.
     National Research Council. (Sept. 1977)

6. L.H.Öhman et al
   New Transonic Test Sections for the
   NAE 5Ft. x 5Ft. Trisonic Wind Tunnel
   First Canadian Symposium on
   Aerodynamics
   Paper No.34, CASI, Ottawa, Dec. 1989
   also NAE-AN-62, N.R.C.C. Jan. 1990

7. L.H.Öhman, D.Brown
   Performance of the New Roll-In Roll-Out
   Transonic Test Sections of the NAE 1.5m
   Blowdown Wind Tunnel ICAS-90-6.2.2,
   Stockholm, Sweden.   Sept. 1990

8. M.Mokry
   Evaluation of Three Dimensional Wall
   Interference Corrections from Boundary
   Pressure Measurements   LTR-HA-51,
   NAE, N.R.C.C. November 1980

9. M. Mokry
   Subsonic Wall Interference Corrections for
   Finite-Length Test Sections using Boundary
   Pressure Measurements. AGARD-CP-335.
   Fluid Dynamics Panel SpecialistsMeeting on
   Wall Interference in Wind Tunnels.
   London, U.K. May 1982

Acknowledgements
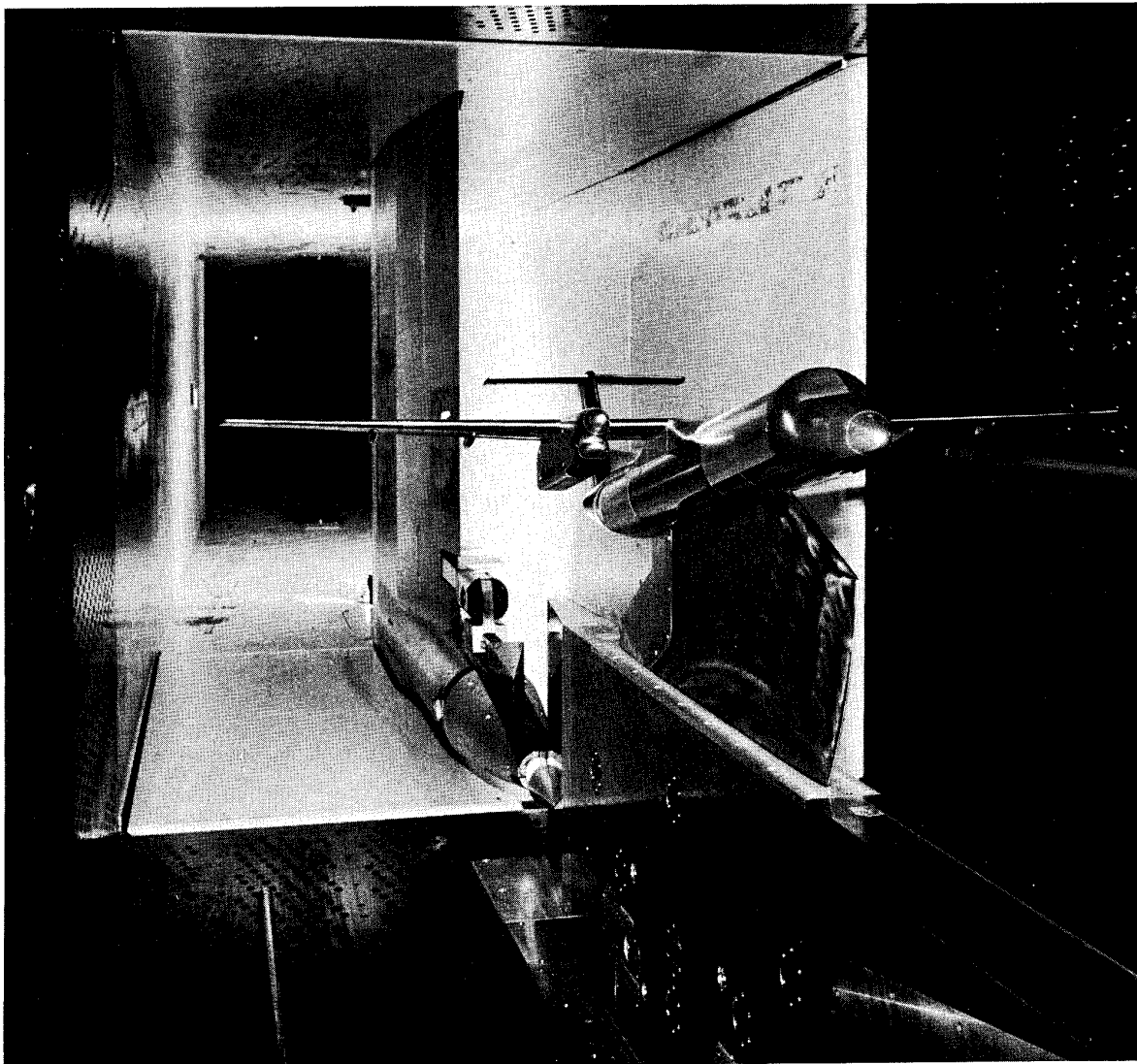
FIGURE 1.   COMMUTER AIRCRAFT MODEL ON PLATE MOUNT
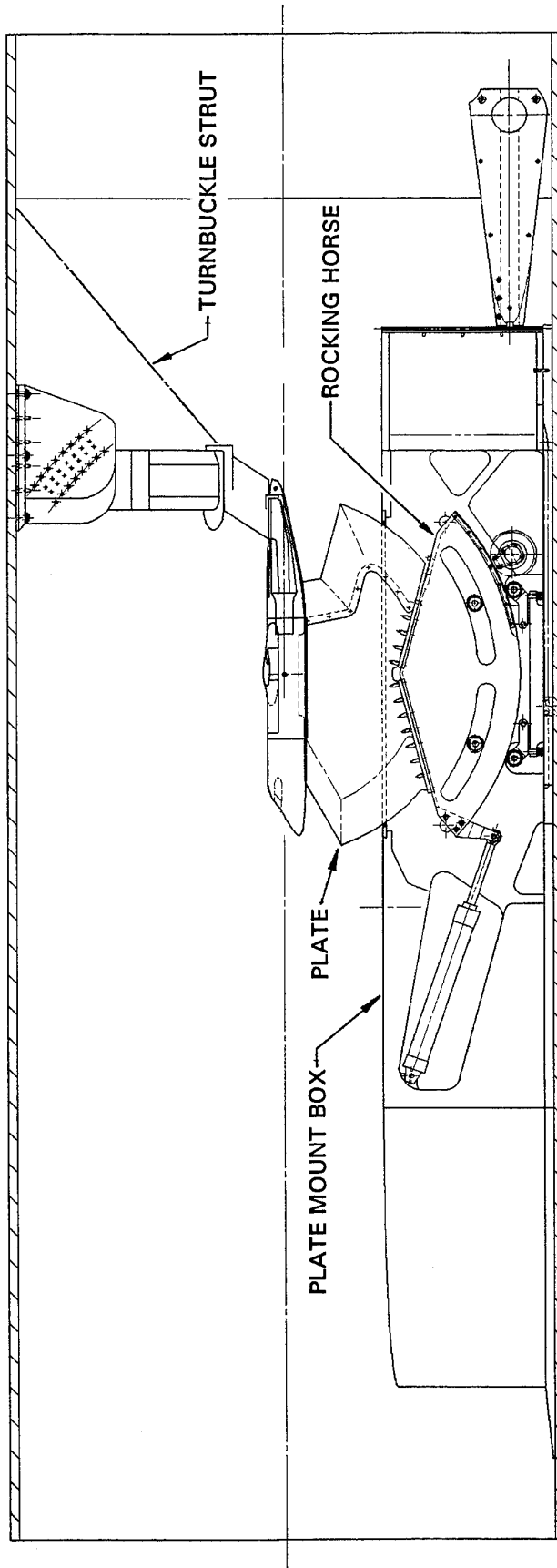
FIGURE 2. PLATE MOUNT SCHEMATIC With Y-Mount Added
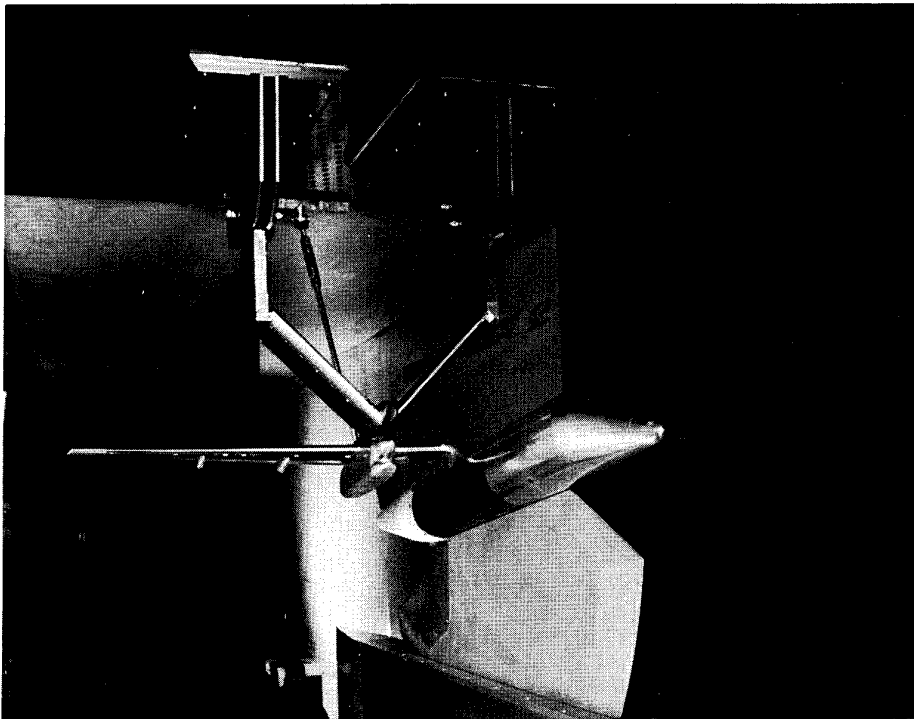
FIGURE 3. **MODEL: ON Y-MOUNT**
With Dummy Plate Installed
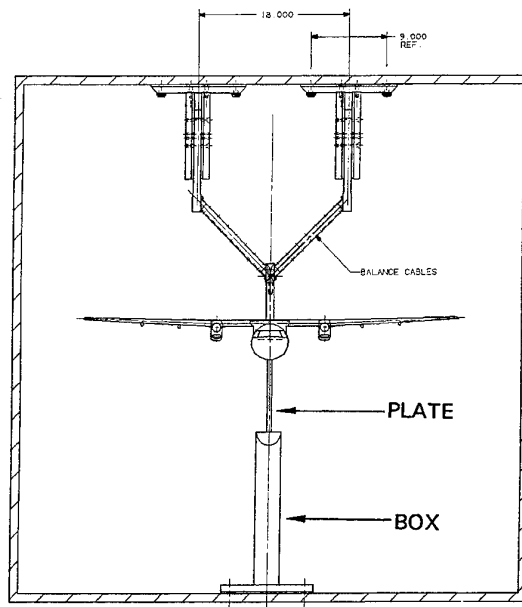
FIGURE 4. **FRONT VIEW OF Y-MOUNT**
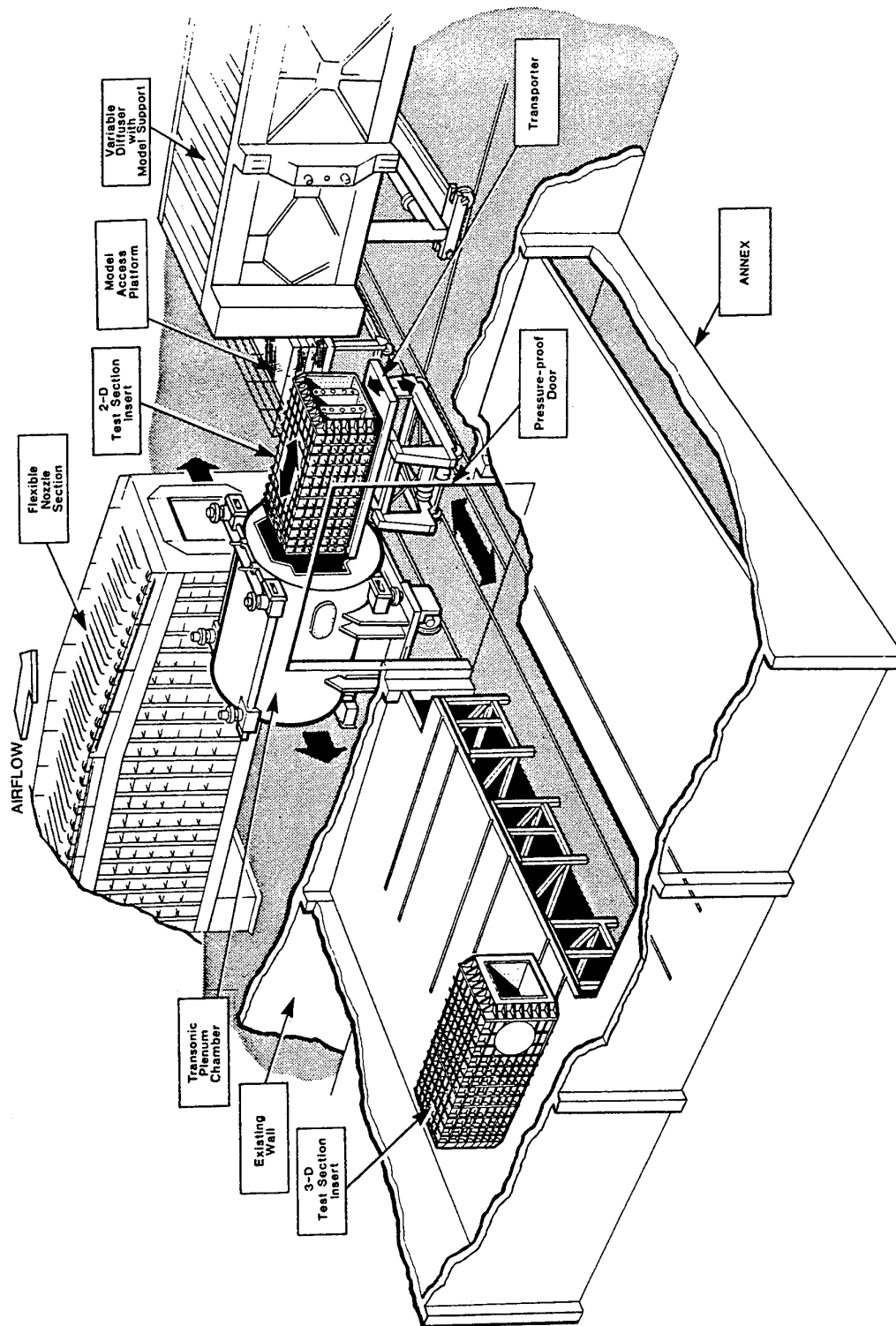
FIGURE 5.   I.A.R. 1.5m TRISONIC TUNNEL
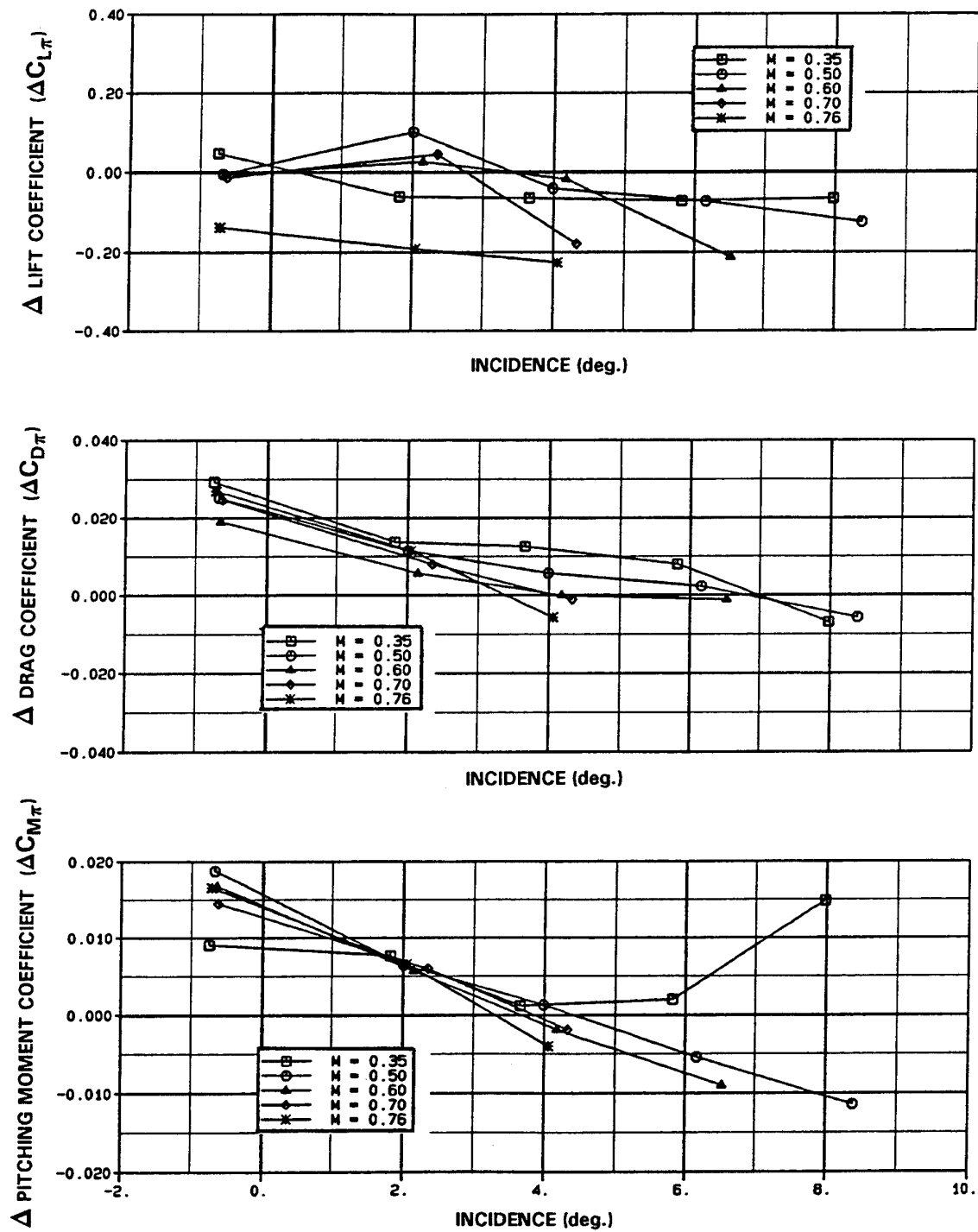
FIGURE 6.   PLATE MOUNT TARE CORRECTION INCREMENTS
(Plate In - Plate Out)

CORRECTION OF SUPPORT INFLUENCES ON MEASUREMENTS WITH STING MOUNTED WIND TUNNEL MODELS

D. Eckert
German-Dutch Wind Tunnel (DNW)
P.O. Box 175
8300 AD EMMELOORD
The Netherlands

SUMMARY

The structures of wind tunnel model supports always penetrate the so-called near field of the flow around the model. Therefore, support corrections of aerodynamic coefficients, evaluated either by measurement or by calculation, depend on the specific configuration of the model and of the model/support intersection. As a consequence support influences known for the correction of a wind tunnel measurement with one model are, in general, not transferable to another configuration. Nevertheless, such a generalization, at least between models of the same aircraft family, would in principle be very helpful in avoiding the time consuming measurements or the viscous flow calculations necessary for the evaluation of support corrections.

To this end, at DNW a comprehensive data-base of measured influences of three sting support types on different low-speed aircraft models was analyzed. The aim was to split up the total support effects in terms representing the effect of support volumes located in the far field of the model and in terms representing the effect of support elements located in the near field of the model.

The data-base has been analyzed with the aid of a physical model which interprets support influences as flow perturbations relevant for the wing, the fuselage and the tail of the model.

This analysis showed that for some fuselage/sting arrangements the near field effects may be considered small compared with the far field effects and independent of the wing's slat/flap configuration.

These findings offered the important possibility of using near field dependent correction terms known for one model configuration for measurements with new configurations (e.g. new wing slat/flap combination). In order to determine the far field influence on new configurations, the physical model mentioned before is used in DNW's on-line data processing system to calculate the support corrections by combining previously determined flow perturbations with the actual measurements during routine tests. Examples show the successful application of the method to measurements with different models.

LIST OF SYMBOLS

C	coefficient of aerodynamic load component
C_D	drag coefficient
C_L	lift coefficient
C_I	coefficient of interference load
C_M	pitching moment coefficient
C_N	normal force coefficient
C_{NT}	coefficient of normal force disturbance
C_P	pressure coefficient
C_{TT}	coefficient of axial force disturbance
c	mean aerodynamic chord
Δq_w	wing kinetic pressure disturbance
q	kinetic pressure
X_I	polynomial coefficients
X_T	axial distance
Z_T	normal distance
α	angle of attack
$\Delta \alpha_w$	wing angle of attack disturbance
σ	standard deviation

1. INTRODUCTION

The flow field around wind-tunnel models is influenced by the presence of a model support and test section walls. For this imperfect simulation of the free-flight situation wind-tunnel measurements have to be corrected if their results are used for the prediction of the aerodynamic performances at free flight.

In the past the development and improvement of the accuracy and applicability of correction methods for the test section wall constraint have been a continuous challenge to take benefit of the developments of analytical and numerical potential flow methods. This can only

partly be said about the development of corrections for the influences of support structures on wind tunnel measurements. The reason for this fact is well-known: test section walls are normally completely situated in the so-called far field of the model, whereas support structures always penetrate the near field of the model flow, changing the pressure and the boundary layer development at least in the neighbourhood of the model/support inter-section. This fact has two troublesome consequences: firstly, for the determination of support corrections either viscous flow calculations or time consuming measurements using combinations of support/dummy support configurations are necessary, and secondly, if support influences are known they are relevant as corrections only for the specific model/support configuration used during the interference measurements or calculations. Normally, no generalization for use with other models is possible, although such a generalization of support corrections, at least between models of the same aircraft family, would be very helpful during the wind tunnel development of new aircraft configurations.

To investigate the transfer problem, a data-base of measured influences of three sting support types on different models was created and analyzed at DNW.

The analysis was based on a physical model of support influences, separating these effects on the model flow in near field effects, mentioned above, and in far field effects, being model flow perturbations caused by support volumes located outside the pressure near field of the model. Both effects were expected to vary with the movement of the support elements relative to the model and to the test section walls during angle of attack measurements, see Figure 1.

The above mentioned physical model may be only realistic for support configurations which do not intrude the wing boundary layer like struts of an external balance. To avoid these near field flow disturbances, which can affect the wing high lift system in a direct way, models at DNW are supported via an internal balance by a dorsal, rear or ventral sting, penetrating the model fuselage in the rear part.

In the following sections the measurement and the evaluation process used to define the data-base of support influences are described and an analysis method is given, which allows the separation of the far field from the near field effects.

2. MEASUREMENT OF SUPPORT INTERFER-ENCES

In the closed wall 8x6 m^2 test section of DNW two series of support interference measurements were carried out with a 1:7.5 scaled A320 low-speed model. The measurements were part of the A320 low speed development test program of Deutsche Airbus, Bremen. In one series of measurements the influences of a dorsal and a ventral sting support on the model were evaluated. In a second series the influences of a rear sting support were determined in combination with the effects of the same dorsal sting used during the first test phase.

Figure 2 presents seven different support arrangements used for the determination of the support influences C_I, incorporated in the measured load components C_i of each configuration. The loads were measured by an internal balance and rotated to the wind axes system using the model's angle of attack measured by a three inclinometer system located in the model fuselage.
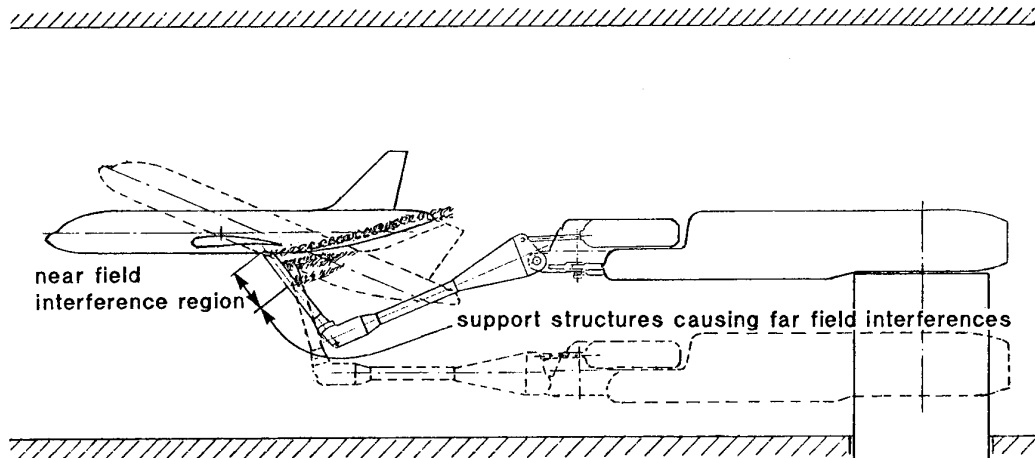
Fig. 1 Near field and far field support interference regions

According to the formulae given in Figure 2, a linear combination of four different measurements defines the support influences which can be used as correction terms to correct the measurements with a model supported by one of the three alternative sting arrangements. This means that the accuracy bandwidths of the corrections will be two times the standard deviations known for the evaluation of load coefficients. Table 1 lists the combined standard deviations of the corrections for the longitudinal coefficients, which are evaluated per data-point using the standard DNW data measuring and processing system.

	Deviation	Single polar	Combination of four polars
lift	$\sigma (C_L)$	$0.6 \cdot 10^{-3}$	$1.2 \cdot 10^{-3}$
drag	$\sigma (C_D)$	$3.0 \cdot 10^{-4}$	$6.0 \cdot 10^{-4}$
pitching moment	$\sigma (C_M)$	$0.4 \cdot 10^{-3}$	$0.8 \cdot 10^{-3}$

Table 1 Standard deviations of data

The interference measurements were carried out with nine different slat/flap settings each combined with four setting angles of the horizontal stabilizer and without stabilizer.

For stiffness reasons the dummy dorsal sting (see Fig. 2) was fixed at the non-weighted balance adapter during the measurements with the dummy arrangement. A membrane sealing was then installed around the dummy sting fuselage intersection to avoid flow leakage through the fuselage from one sting access to the other forming plume wakes. For the resulting membrane loads corrections for the normal force and pitching moment coefficients were evaluated from pressure measurements. Both corrections turned out to be less than 10^{-3}. A tangential membrane load could not be detected (Ref. 1).

After the completion of the measurements all data were smoothed per polar by means of a least square method. Data-points measured at angles of attack beyond the stall onset were not used in the smoothing process. The next step was to apply the formulae given in Figure 2 to prepare a data-base of angle of attack dependent support influences on the longitudinal coefficients for the different wing slat/flap configurations and the stabilizer settings. With equation (1) to (4) the support

$$C_4 = C + C_{IV,R} + C_{ICV,R} + C_{ISV,R} + C_{IT} + C_{ID} + C_{ICD} + C_{ICW} \qquad (C_{ICW} \approx C_{ISD})$$

$$C_3 = C + C_{IV,R} + C_{ICV,R} + C_{ISV,R} + C_{IT}$$

$$C_2 = C + C_{IV,R} + C_{ICV,R} + C_{ISV,R}$$
corrected coefficient $C = C_2 - (C_4 - C_1) - (C_3 - C_2)$

$$C_1 = C + C_{ID} + C_{ICD} + C_{ISD}$$
corrected coefficient $C = C_1 - (C_4 - C_2) - (C_3 - C_2)$
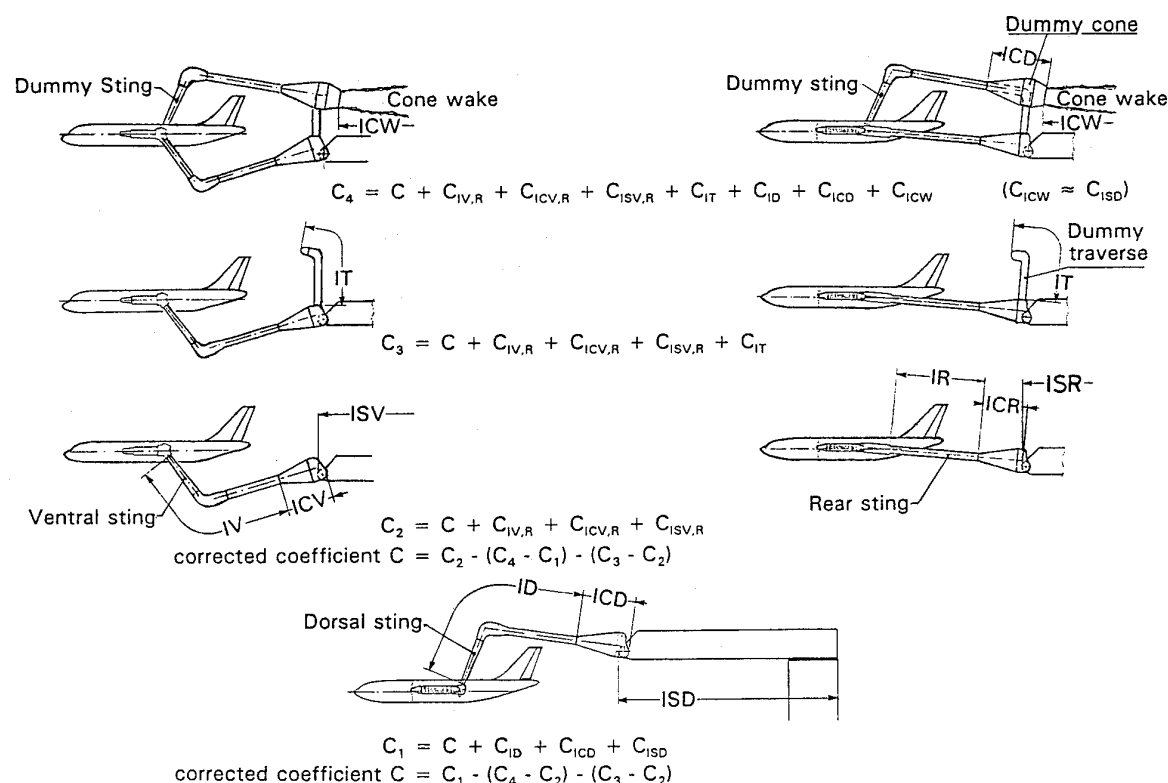
Fig. 2 Support arrangements for interference measurements

influences can be used in a direct way as corrections of the measured coefficients C_M.

$$\Delta C_{ID} = (C_{ID} + C_{ICD} + C_{ISD}) \qquad (1)$$

$$\Delta C_{IV} = (C_{IV} + C_{ICV} + C_{ISV}) \qquad (2)$$

$$\Delta C_{IR} = (C_{IR} + C_{ICR} + C_{ISR}) \qquad (3)$$

$$C = C_M - \Delta C_{I,D,V,R} \qquad (4)$$

3. PRESENTATION OF SUPPORT INFLUENCES

3.1 Effects on Lift
Figure 3 illustrates the effects of a selection of slat/flap settings on the lift interferences for three different sting supports.
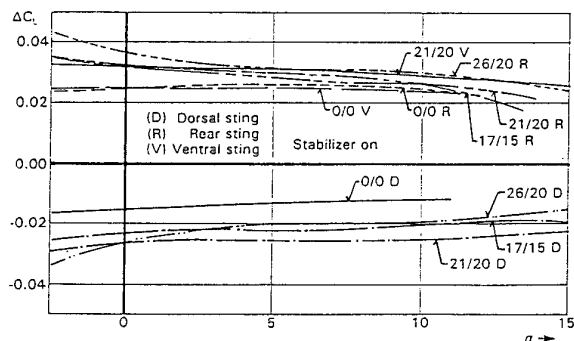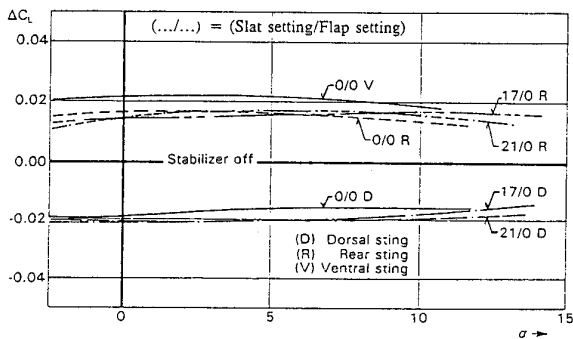
Fig. 3 Support effects on lift

Typically it turned out that the lift effects were of the same order of magnitude for all supports but of opposite sign for the dorsal sting. This corresponds with the movement of the so-called torpedo of the support system representing the biggest volume of the different supports (see Fig. 2). During an angle of attack polar with the dorsal sting mounted model the torpedo moves in the upper test section half and with the test section, thereby inducing a downwash or upwash effect on the wing, respectively. This consequence of the support movement becomes more clear in the next chapter.

Figure 4 shows stabilizer installation effects on the lift influences which are obviously the smallest for the dorsal sting and relatively large for the rear sting configuration.
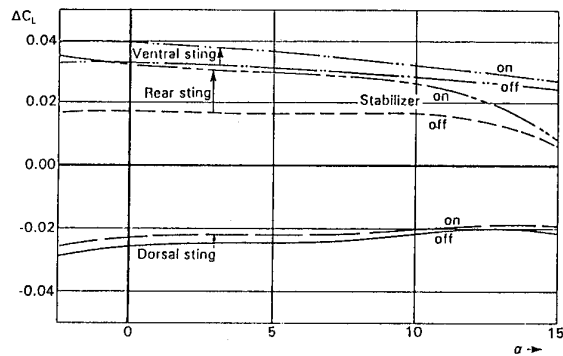
Fig. 4 Support influence on lift (stabilizer installation effect)

3.2 Effects on Drag
For the same selection of slat/flap combinations as shown in Figure 3 the effects of different supports on the drag are plotted in Figure 5. It turned out that the influences are of the same order of magnitude but of different signs.
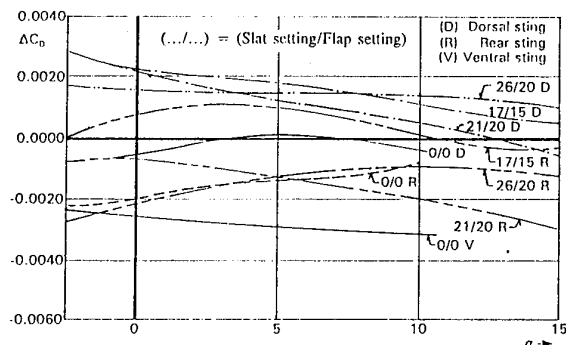
Fig. 5 Support effect on drag

3.3 Effects on Pitching Moment

Figure 6 presents support effects on the pitching moment of the model with installed horizontal stabilizer.

The effects on the dorsal sting mounted model show relatively little variation during an angle of attack polar. Similarly the variation with the slat/flap configuration is small compared to the effects induced by the rear sting. This is probably a consequence of the fact that there is a relatively large direct influence of the wing

Fig. 7 Support influence on pitching moment (stabilizer installation effect)

Fig. 6 Support effect on pitching moment (stabilizer on)

downwash on the fuselage/rear sting intersection and the nearby located stabilizer.

The comparison in Figure 7 shows clearly for the three support configurations that the dorsal sting causes the smallest stabilizer installation effects on pitching moment measurements. For the stabilizer-off measurements the corrections are of the same order of magnitude. This means that the large extra effects measured with the stabilizer-on configurations with the ventral and rear sting, respectively, are a consequence of a stronger variation of the disturbance field of the support along the model tail. Using the known stabilizer effectiveness $(\partial C_M/\partial \alpha_H)$ the arrows (see Fig. 7), symbolizing the extra influences acting on the stabilizer, would correspond with an equivalent change $\Delta \alpha_H$ of the angle of attack at the tail by

$$\Delta \alpha_H = \Delta(\Delta C_M)/(\partial C_M/\partial \alpha_H) \approx \begin{array}{l} 0.2° \text{ (dorsal sting)} \\ 0.4° \text{ (ventral sting)} \\ 1.1° \text{ (dorsal sting)} \end{array}$$

4. ANALYSIS OF MEASURED SUPPORT INFLUENCES

4.1 Configuration Dependence

Figures 3 to 7 show a significant dependence of the support effects on the type of the sting support and on the model configuration, which was varied by different wing slat/flap combinations and tail on/off investigations.

Looking at the slat/flap setting dependence the question arises if there exist relative simple rules for the interpolation of interference data. Such rules would be very helpful solving the typical problem to prepare support corrections applicable to wing slat/flap configurations which are different from those represented in the database of measured interferences.

From Fig. 3 it becomes obvious that, for example, an interpolation rule like 'the same lift coefficient causes the same lift interference' cannot be used.

Therefore, in the next chapter a set of formulae will be derived dealing in a more detailed manner with the physical mechanisms which generate support interferences.

4.2 Support Effects on Wing Fuselage Combinations

4.2.1 Analytic model representing support effects

Figure 8 provides a sketch of the physical model used at DNW for the interpretation of support effects of a dorsal sting on a wing/fuselage model. Principally the modelling is based on two different interference mechanisms and should in this way be applicable to all three sting types used at DNW:

The wing of the model is only affected by far field support influences represented by a ro-

Wing body configuration

Dorsal sting support

$$\left(\frac{\partial C_L}{\partial \alpha} + C_D\right) \Delta \alpha_W + C_L \frac{\Delta q_W}{q} + \cos\alpha\ C_{NT} - \sin\alpha\ C_{TT} = \Delta C_L \quad (5)$$

$$\left(\frac{\partial C_D}{\partial \alpha} - C_L\right) \Delta \alpha_W + C_D \frac{\Delta q_W}{q} + \sin\alpha\ C_{NT} + \cos\alpha\ C_{TT} = \Delta C_D \quad (6)$$

$$\frac{\partial C_M}{\partial \alpha} \Delta \alpha_W + C_M \frac{\Delta q_W}{q} - \frac{X_T}{\bar{c}} C_{NT} + \frac{Z_T}{\bar{C}} C_{TT} = \Delta C_M \quad (7)$$

substitution set

$$\left[\begin{array}{l} \Delta \alpha_W = X_1 + X_2\alpha + X_3\alpha^2 \\[2ex] \dfrac{\Delta q_W}{q} = X_4 + X_5\alpha + X_6\alpha^2 \\[2ex] C_{NT} = X_7 + X_8\alpha + X_9 \left(\dfrac{C_N}{\alpha}\right) \\[2ex] C_{TT} = X_{10} + X_{11}\alpha + X_{12} \left(\dfrac{C_N}{\alpha}\right) \end{array}\right. \quad (8)$$
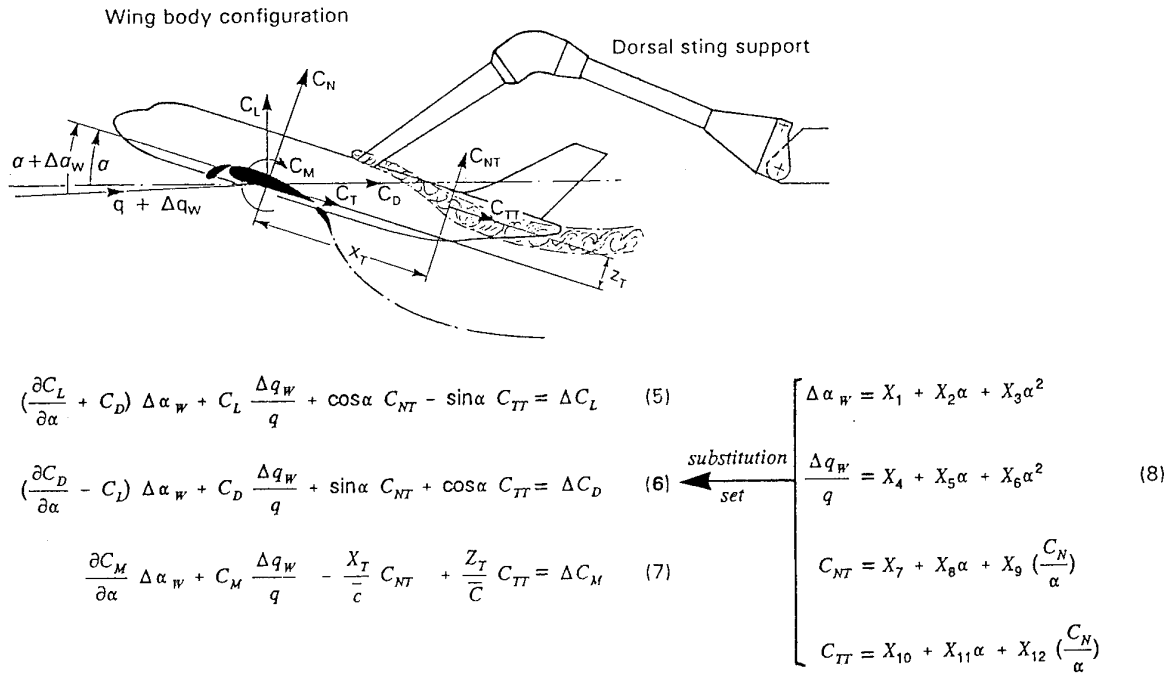
Fig. 8 Analysis of support effects on the longitudinal coefficients

tation $\Delta\alpha_w$ and a change of the kinetic pressure Δq_w of the undisturbed flow. In this sense $\Delta\alpha_w$ and Δq_w are wing averaged values.

The fuselage of the model is affected by far field influences in combination with near field effects as a consequence of the inhomogeneous pressure field induced at the model by the support volumes which are moving relative to the model and to the test section walls during an angle of attack polar. The far field effect will result in an axial buoyancy load on the fuselage. Near field effects act at the fuselage tail. The wake of the dorsal sting affects the vertical tail, and the trace of the horseshoe vortex around the sting/fuselage intersection influences the fuselage aft part.

For the analysis of the data-base the far and the near field effects on the fuselage/vertical fin combinations are represented by concentrated loads C_{NT} and C_{TT} acting at unknown distances X_T and Z_T from the model aerodynamic centre. C_{NT} and C_{TT} depend on the angle of attack and on the wing configuration since the wing downwash will affect the sting wake geometry. In the wind axis system the balance of the interference contribution to the longitudinal coefficients is described by the formula set (5) to (7) in Figure 8. This set has been applied to the interference data of all slat/flap configurations represented in the data-base. With the three equations (5) to (7) the four

unknown functions of the angle of attack $\Delta\alpha_w$, $\Delta q_w/q$, C_{NT} and C_{TT} and the two unknown constants X_T and Z_T have to be defined. This is in principle possible if there are at least six sets of data per angle of attack α which are linearly independent from each other. For at least two measurements with two different wing configurations this is the case and the system consisting then of two times the equations (5) to (7) becomes solvable. Since the available database incorporated nine independent sets of measurements, a least square method has been used to find the best solution of (5) to (7) for the complete data-base.

For the stability of the iteration process it turned out to be advantageous to substitute the unknown variables in (5) to (7) by polynomial expressions (8). In the polynomials far field effects are supposed to vary with the movement of the support volumes inside the test section walls which is defined by α. The variation of near field effects is described by the terms $X_i (C_N/\alpha)$, where (C_N/α) represents a combined measure for the variation of the geometrical extension of the horseshoe vortex trace on the afterbody. The distances X_T and Z_T have been found by variation of the parameters and looking for the smallest total error of the polynomial fit. Typically, the plausible values $X_T/c = 3.5$ and $Z_T/c = 0.5$ turned out to give the best results throughout the whole data-base.

4.2.2 Comparison of results

In Figure 9 the variation of the mean angle of attack and kinetic pressure disturbances ($\Delta\alpha_w$ and $\Delta q_w/q$) are given as functions of α. For comparison, measured disturbances are also presented.
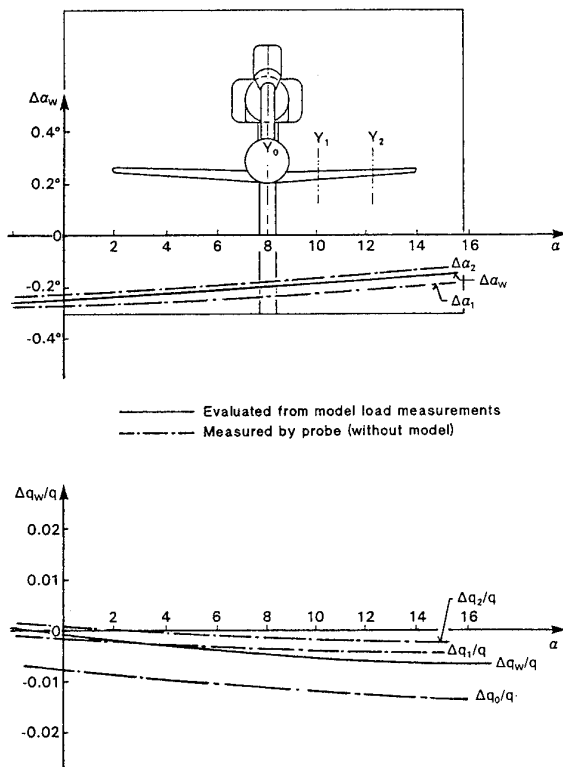
Fig. 9   Flow disturbances at different wing stations versus angle of attack

Fig. 10 Fuselage support disturbance loads

This buoyancy load is a consequence of the fact that the support volumes introduce a stagnation effect along the fuselage which increases during an angle of attack movement since the support torpedo volume is then moving from a position above the model to a position behind the model. The difference C_{TT} - $C_{TT,B}$ could be interpreted as a near field effect of the dorsal sting wakes on the vertical fin and of the horseshoe vortex on the fuselage tail.

These measured data have been obtained using a 6-hole probe located at different positions on the fuselage axis and on the quarter chord line of the wing, respectively. No model was installed for the measurements, but the dorsal sting support arrangement was moved in the same way as during an angle of attack polar.

Figure 10 presents the fuselage disturbance loads C_{TT} and C_{NT} which were calculated from the data-base. The component in normal direction turned out to be small compared with the lift measurement accuracy in Table 1. The axial interference load C_{TT} may be interpreted to be primarily determined by the buoyancy effect of the support disturbance pressure field on the fuselage. For comparison, in Figure 10 the pure buoyancy effect is also presented, evaluated by use of the probe measurements of the kinetic pressure disturbance along the fuselage axis.

4.2.3 Verification of the numerical analysis

Figures 11 to 13 present comparisons of measured and recalculated dorsal support effects on the A320 model. For the recalculation equations (5), (6) and (7) have been used with the results ($\Delta\alpha_w$, $\Delta q_w/q$, C_{TT}, C_{NT}) of the analysis of the measured data as input. The derivatives ($\partial C/\partial\alpha$) were calculated using numeric differential schemes. As can be seen in Figures 11 to 13, the deviations of the recalculated data from the measured data are one order of magnitude smaller than the influences themselves.

In Figure 14 a detailed comparison is shown of the measured and recalculated lift interference effect on a high-lift configuration of the A320 model.

As described in chapter 2 the measured data are evaluated according to the formula set given
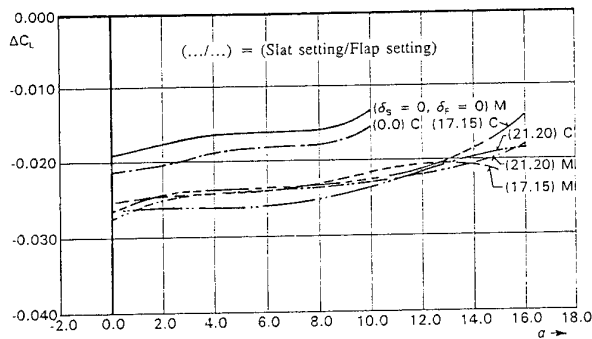
Fig. 11 Measured (M) and recalculated (C) effects on lift
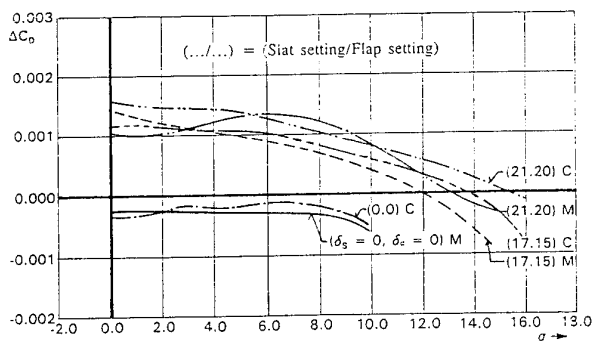
Fig. 12 Measured (M) and recalculated (C) effects on drag

Fig. 14 Lift interference analysis

$$\Delta C_L = (\frac{\partial C_L}{\partial \alpha} + C_D)\, \Delta \alpha_w + C_L\, \frac{\Delta q_w}{q} + \cos\alpha\, C_{NT} - \sin\alpha\, C_{TT} \qquad (5)$$

Fig. 13 Measured (M) and recalculated (C) effects on pitching moment

in Figure 2. The measurement scatter was suppressed applying a numerical smoothing procedure after throwing away the strong varying data at negative angles of attack where the slat is starting to work and at the end of the polar where the beginning wing stall is observed. So, only the data in between the hatch marks were used for the analysis resulting in the disturbance data presented in Figures 9 and 10.

These data were the input for the on-line interference calculation procedure using the formula set (5) to (7) in combination with the measured data of a polar. The procedure has been implemented in the standard DNW data processing software. Since this on-line program is structured under the condition that for the processing of a data-point only information may be used of the data-point itself and the previously measured data-points of the same polar the calculation of the gradients $(\partial C_L/\partial \alpha)$, $(\partial C_D/\partial \alpha)$, and $(\partial C_M/\partial \alpha)$ forms a special problem. Comparing the $(\partial C_L/\partial \alpha)$ versus angle of attack of a typical slat/flap combination with the on-line calculations of ΔC_L, it becomes obvious that the $(\partial C_L/\partial \alpha)$ gradient is dominating formula (5), see Figure 14. Therefore, the quality of the on-line calculated support corrections will primarily be defined by the quality of the numerical differentiation method. As a consequence of this problem, the sharp, slat induced dip of the lift interference in Figure 14 is somewhat weakened by the on-line differentiation process. A better attack of this difficulty would be possible applying an off-line support correction procedure.

4.3 Support Effects on the Horizontal Stabilizer

In analogy to the numerical method for the wing/fuselage configuration as outlined in Figure 8, an analysis of the extra support effects on the horizontal stabilizer was made.

In order to determine these extra effects on the measurements with the same wing configuration, the stabilizer-off influences were subtracted from the stabilizer-on data, see for instance Figures 4 and 7. After this step the data were analyzed using a formula set derived from formulae (5) to (8) by adding terms which account for mean angle of attack and mean kinetic pressure disturbances relevant for the test section volume where the stabilizer is moving during an angle of attack polar. From the analysis mean disturbance terms experienced by the stabilizer were evaluated.

The results of the analysis for the ventral/dorsal sting interference measurement cycle are in good agreement with probe measurements of the local angle of attack and kinetic pressure disturbances at the stabilizer's location. For the data from rear/dorsal sting cycle of measurements the agreement was very poor. This suggests that stabilizer interference measurements with the rear sting support configuration cannot be analyzed with the classical linear method as described in Figure 2.

5. APPLICATION OF THE SUPPORT CORRECTION METHOD

5.1 Improvement of Measured Interference Data

In Table 1 figures are given of the expected error bandwidth of correction data evaluated from interference measurements. These errors are the result of the inaccuracies of the combined interference polars and are therefore larger than the errors relevant for the data of a single production polar which has to be corrected for support influences.

Thus, it seems to be attractive to use the above described method of analyzing a measured data-base and the recalculation of the support influences before using the measured data for the correction of measurements with a model configuration represented in the data-base. In this way the measured influences, which could at random be infected with the maximum error, can be improved with the aid of better measurements involved in the same data-base. Therefore, the deviations of the recalculated data in Figures 11 to 14 should not be interpreted as inaccuracies of the numerical process or a principal drawback of the method.

5.2 Calculation of Corrections for Wing Configurations not Available in the Data-Base

With the formula set (5) to (7) the calculation of support corrections becomes possible for slat/flap settings which were not realized during the interference measurements with a certain model. At DNW the correction terms are determined during the on-line processing of a measurement by calculating the derivatives $(\partial C/\partial a)$ for each new data-point using the information of a maximum of ten previously measured data-points. Together with the angle of attack dependent disturbances of the relevant support configurations Δa_w, Δq_w. C_{NT} and C_{TT}, stored as polynomials in the computer, the actual corrections of the longitudinal coefficients can be calculated and applied per data-point.

In this sense the method developed at DNW represents a very effective process to calculate support corrections by physically meaningful interpolation between measured support interference data.

5.3 Calculation of Corrections for Models of the Same Family

The wing-configuration independent flow disturbances of Figure 9 show that the wing of sting supported models is only affected by far field influences which vary relatively little in that part of the test section volume where the wing is located during angle of attack movements of the model. So, it should be possible to use the same sting configuration defined wing disturbance functions Δa_w (a), Δq_w (a), evaluated for a basic model configuration also for new configurations with a modified wing (e.g. extended wing) if the position of the aerodynamic centre relative to the support structure and the support itself is not changed. Support corrections for new configurations with fuselage extensions can be calculated using an increased distance X_T. The fuselage interference load C_{TT} has then to be modified by an increase of the buoyancy load as a consequence of the closer location of the fuselage tail relative to the support. This increase can be defined by use of the measurements of the support pressure field or by potential flow calculations using a panelled model of the support structure.

5.4 Calculation of Corrections Using Measured Support Disturbances

The good agreement of the measured support induced flow disturbances with the mean disturbances experienced by the model (see Figs. 9 and 10) offers the possibility to prepare the input for the correction formulae (5) to (7) by simple flow disturbance measurements.

Figure 15 shows as an example the support arrangement for a blade sting mounted model. Without the model installed, flow disturbances at different spanwise and streamwise locations of the model wing and fuselage geometry have been measured using a 6-hole probe during the angle of attack movement of the support. From these measurements the input $\Delta\alpha_w$, Δq_w and C_{TT} has been prepared and used for the calculation of the on-line corrections. The normal disturbance load C_{NT} was neglected. The axial disturbance load C_{TT} was calculated as buoyancy load from the static pressure disturbance along the fuselage axis.
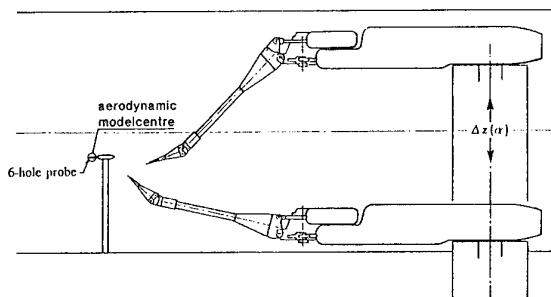
Fig. 15 Support disturbance measurement

In Figure 16 uncorrected and corrected lift coefficients are compared with corrected measurements with the same model in a wind tunnel with a slotted roof and floor test section and a different support system. The model blade sting and its adapter were identical, which means that the near field interference load on the fuselage rear end was the same in both wind tunnels.
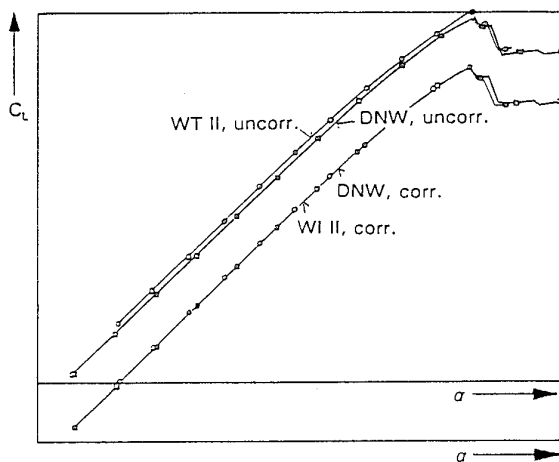
Fig. 16 Support corrections of lift

The lift as well as the drag comparison in Figure 17 show the rather good agreement of the measurements. The obvious descrepancies of the uncorrected data show the importance of the application of support corrections
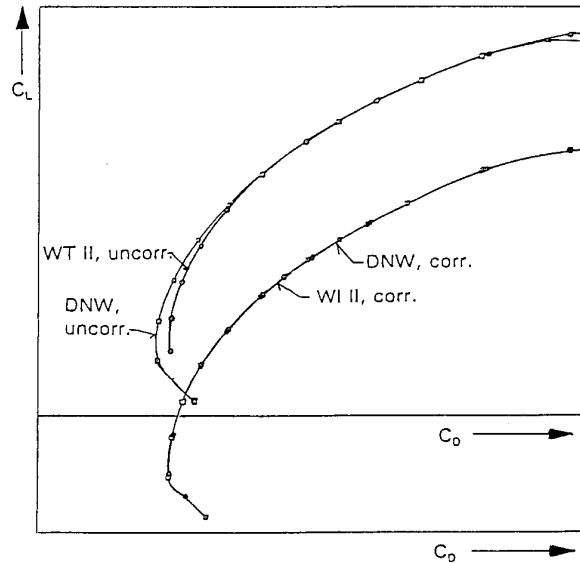
Fig. 17 Support corrections of lift and drag

5.5 Correction Calculations Using Numerically Calulated Support Disturbances

Instead of measuring the support disturbances in that volume of the test section where the model is located during the measurement of a polar, numerical methods may be used to calculate the flow disturbances of an actual support configuration. At DNW a panel method developed by NLR was used to calculate the input for the formulae (5) to (7). Figure 18 shows as an example the panel representation of the support configuration for tests of a propeller driven aircraft model. The figure presents also a comparison of the calculated pressure distribution along the fuselage axis with the fuselage pressure disturbance evaluated by the combination of two measurements with support arrangements shown in Figure 19. Since for both measurements the model was supported by the same ventral sting, only the far field effect of the main support structure is presented in Figure 18.

An integration of the pressure disturbance along the fuselage results in a buoyancy load of ΔC_D = -0.0017. The evaluation of formulae (5) to (7) using the measured interference loads of the

arrangement shown in Figure 19 results in C_{TT} = -0.0020. Also the mean wing upwash angle $\Delta\alpha_w$ = 0.10° resulting from the evaluation of (5) to (7) seems to be in good agreement with
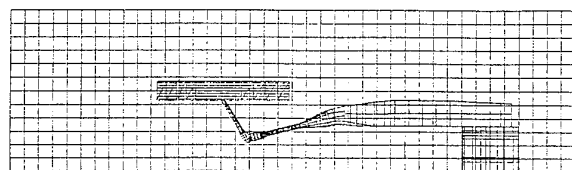
panel representation of support / test section geometry

ΔC_p ↑ support pressure disturbance along fuselage axis

measured
panel calculation
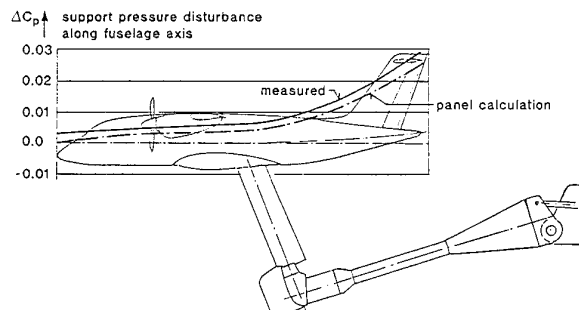
Fig. 18 Comparison of measured and calculated pressure disturbance

the upwash angle determined by the panel method calculations.

So, numerical calculation of the disturbance quantities $\Delta\alpha_w$, $\Delta q_w/q$, C_{NT} and C_{TT} necessary for the application of formulae (5) to (7) is useful provided that an adequate geometrical representation of the support structure in combination with the test section wall geometry is used.

Since the panel method cannot calculate the near field effects on the fuselage its contribution to C_{TT} should be known. For a

$C_1 = C + C_V + C_{VC} + C_{VS}$

$C_2 = C + C_V + C_{VC}$
$C_{VS} = C_1 - C_2$

Fig. 19 Interference measurement arrangement for $\alpha = 0°$

fuselage/sting intersection like in Figure 19, a systematic investigation [Ref. 2] turned out that the near field effect is small (ΔC_{TT} = 0.0003) if the sting intersects the cylindrical part of the fuselage and larger (ΔC_{TT} = 0.0030) if the sting intersects the tailored aft part of the fuselage. Investigations at DNW revealed the sensitivity of the near field effects to the sting intersection details. An increase of the gap between the fuselage and the sting from 3 to 12 mm caused an increase of C_{TT} by 0.0020.

6. CONCLUSIONS

The analysis and recalculation of measured influences on sting mounted models proved the following:

o The near field dependent contributions to the support corrections are small compared to the far field effects.

o The far field effects might be determined using support dependent flow direction and kinetic pressure disturbances relevant for wing and fuselage.

o The far field disturbances may be evaluated either from classical interference measurements with the model presented, or without the model by 6-hole probe measurements, or by panel method calculations.

o The calculation of influences using the developed disturbance formulation allows for an on-line support correction of measurements.

7. ACKNOWLEDGEMENT

The author would like to thank his colleagues D. Ehlen and C. Jutten for the enthusiastic help during the numerical analysis of the data-base.

8. REFERENCES

[1] Eckert, D.
"Interference Investigations with the Sting Supported A320 8D Model in the DNW", DNW-TR-86.06, November 1986.

[2] Veldhuis, L.L.M.
"Support Interference Effects of a Ventral Sting on a Body of Revolution", Internal Report LSN 89-2, Delft University of Technology, 1989.

CALCULATION OF SUPPORT INTERFERENCE IN DYNAMIC WIND-TUNNEL TESTS

D. Almosnino
Senior Research Scientist
Analytical Methods, Inc.
2133 - 152nd Avenue, N.E.
Redmond, Washington, 98052, U.S.A.

SUMMARY
An unsteady, subsonic flow panel method is applied to predict the support interference effects in dynamic wind tunnel test simulation. Interference effects are calculated by simulating the unsteady flow around the aircraft model, both in the presence and absence of the support system, unlike common experimental techniques that try to measure these effects. The present study uses the Standard Dynamics Model (SDM) in pitch oscillations as a test case. Calculated results for free flight conditions are compared with results obtained when simulating the presence of an existing side-wall-mounted support system in a dynamic wind-tunnel test facility. The calculated results are also compared with experimental data available from different dynamic wind-tunnel test facilities.

NOMENCLATURE

b	Wing span
$\bar{c}$	Mean aerodynamic chord
C_D	Drag coefficient $(D/q_\infty S)$
C_L	Lift coefficient $(L/q_\infty S)$
C_l,CMX	Rolling moment coefficient $(\mathcal{L}/q_\infty S\, b/2)$
C_m,CMY	Pitching moment coefficient $(M/q_\infty S\bar{c})$
C_{mq}	Damping in pitch $(M_t/q_\infty S\, \bar{c}f\, \Delta\theta)$
C_n,CMZ	Yawing moment coefficient $(N/q_\infty Sb/2)$
C_y,CS	Side force coefficient $(Y/q_\infty S)$
C_z	Normal force coefficient $(Z/q_\infty S)$
D	Drag force
f	Frequency of oscillation in pitch (H_z)
$\bar{f},OM,\bar{\omega}$	Reduced frequency of oscillation $(\omega\bar{c}/2V_\infty)$
L	Lift force
$\mathcal{L}$	Rolling moment
M	Pitching moment or Mach number
N	Yawing moment
p,q,r	Angular velocities around corresponding x,y,z axes
q_∞	Free stream dynamic pressure
S	Reference area
t	Time
τ,T	Normalized time $(V_\infty t/\bar{c})$
V_∞	Free stream velocity
Y	Side force
x,y,z	Body coordinates
Z	Normal force
α, ALPHA	Angle of attack (deg.)
$\Delta\theta$	Amplitude of oscillation in pitch (deg.)
ω	Angular velocity $(2\pi f,\ \text{rad./sec.})$

Subscripts

I	Imaginary component
R	Real component
∞	Of the free stream

1. INTRODUCTION
The unsteady aerodynamic characteristics of modern flight vehicles play an important role in their design and optimization process. One of the most common tools used to predict unsteady aerodynamic coefficients is dynamic wind-tunnel testing. In these tests, a model of the flight vehicle is placed on a specially designed movable support system, or rig, and undergoes a prescribed set of motions. The cost of such tests is usually high because of the complex apparatus involved and the huge amount of data to be accumulated. The accuracy and reliability of the experimental results, which are crucial for the designers, are affected by several factors. One of these is the interference of the support system used in the experiment. Model support systems used in dynamic testing (see, for example, Refs. 1-6) are usually very rigid, to avoid measurement errors due to structural flexibility. As a result, both the size of a support system and the way it is constructed introduce a significant flow disturbance, which in turn affects the measured characteristics of the model being tested, as noted in Refs. 1-4 and discussed in detail in Refs. 7-11.

Computational methods can simulate a prescribed motion of an aircraft without the interfering presence of a support system or the wind tunnel walls, and without the need to construct special apparatus to carry out the dynamics. The common limitations on computational studies are computer resources, and inaccuracies associated with the underlying assumptions of the method used. It is therefore important to validate the results of computational methods against as many as possible existing results obtained by experiments or by other methods of calculation. Such validation runs are essential to prove the reliability and estimate the accuracy of any particular computational method.

The present calculations make use of an unsteady doublet panel computer program[12,13] to calculate the aerodynamic characteristics of a fighter-type model (the Standard Dynamics Model (SDM)) in pitch oscillations. The mathematical model and numerical procedure used in the present method are detailed in Refs. 12 and 13.

The SDM has been studied extensively in several dynamic wind-tunnel test facilities since the early 1980's.[1,2,4,14-20] The experimental program involved small oscillations in pitch, roll and yaw about pre-defined nominal angles of attack and yaw. Other parameters varied were the Mach number (from low subsonic to high transonic), the reduced frequency of the oscillations and, to a limited extent, the Reynolds number. The aerodynamic data generated in the SDM wind-tunnel tests serve as a broad base for the validation of the computational method used in the present study.

2. METHOD OF CALCULATION AND SDM MODEL

2.1 General Description

The calculations in the present study use an unsteady, inviscid doublet panel method described in detail elsewhere.[12,13] The surface of the aircraft model, as well as the wind-tunnel support system (when present) is divided into "patches", and each patch is further divided into elemental doublet panels. Patches are assigned to user-defined dynamic frames of reference, so that a complete and accurate set of motions simulates the actual movement of the aircraft model and the different parts of the support system attached to it. Vortex wakes are shed from the wing, tail and fin surfaces, from the base of the body, and from the strake leading edge (at $\alpha > 8°$). The doublet distribution and wake geometry are updated every single time step. The number of finite time steps from which a prescribed motion is comprised is defined by the user. The number of time steps is usually a practical tradeoff between computer CPU time and storage demands, and the accuracy of the dynamic model of the motion as well as the wake roll-up process. The present calculations do not include any boundary layer corrections at this stage of the study.

2.2 Details of SDM and Support System Models

The SDM is described in Fig. 1 (adapted from Ref. 1), while Fig. 2 shows the schematics of the sidewall-mounted support system used in the Canadian NAE dynamic wind-tunnel pitch oscillation tests.[16] A model of that support system is used in the present study. The SDM computational model uses 1,384 panels to describe the aircraft geometry, and 626 panels to describe the geometry of the sidewall-mounted support system, as described in Figs. 3(a) and (b).

2.3 Calculation Procedure

The SDM model is set at a nominal angle of attack (up to 10° in the present set of calculations), and then is oscillated at a small amplitude around the pitch axis ($\Delta\theta = \pm 1°$, typically). When simulating the presence of the support system, the frames of reference are defined such that the support system parts move exactly as they do in the wind-tunnel test, to keep the center of rotation of the aircraft model at the point defined in Fig. 1. The reduced frequency of the oscillation matches that used in the Ref. 16 experiments ($\bar{f}$ = 0.045 for the NAE tests), and the free stream Mach number is 0.6. Every run covers a full time period of oscillation, divided into 80 discrete time steps. Since the motion
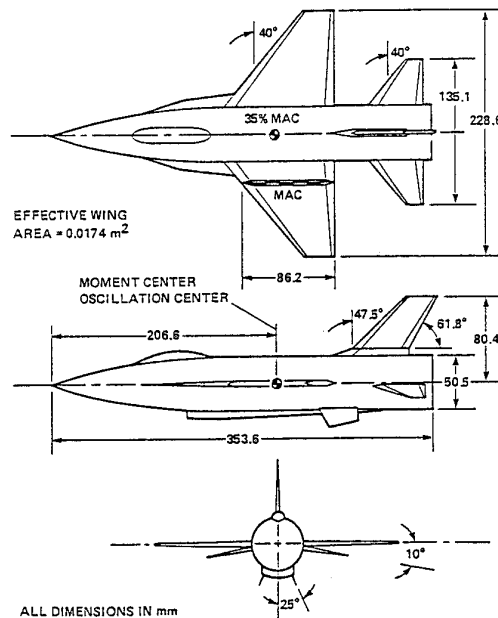
Fig. 1. Standard Dynamics Model (Adapted from Ref. 1).
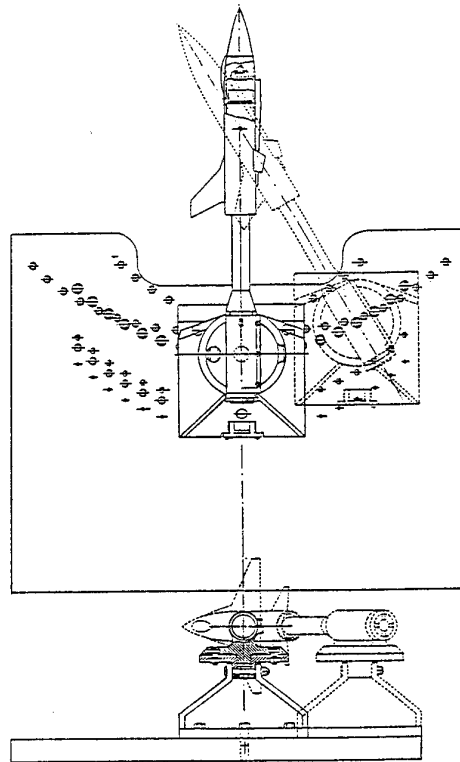
Fig. 2. Sidewall-Mounted Support System (Ref. 16).
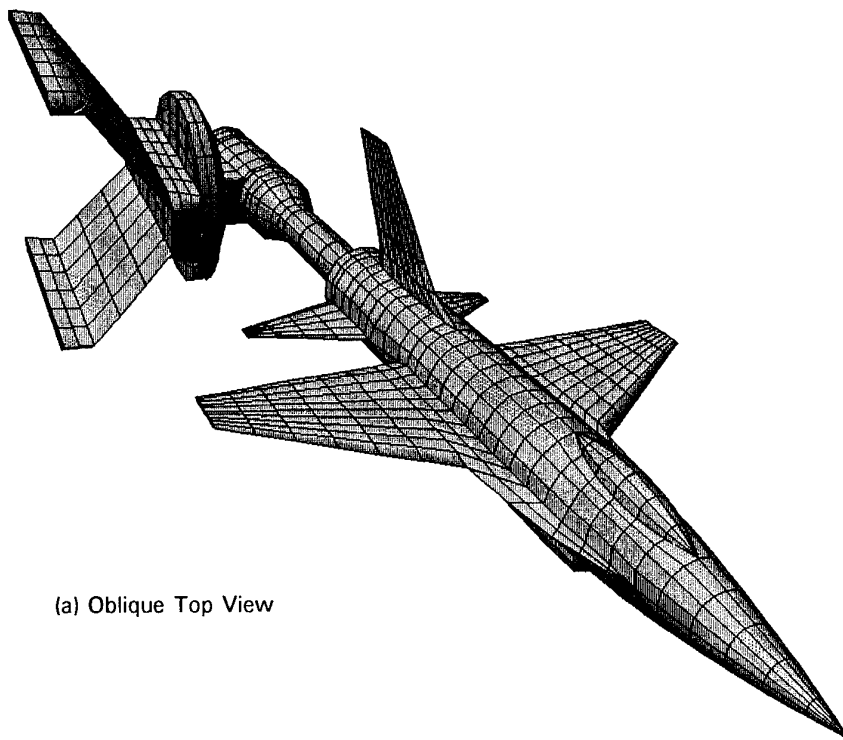
(a) Oblique Top View
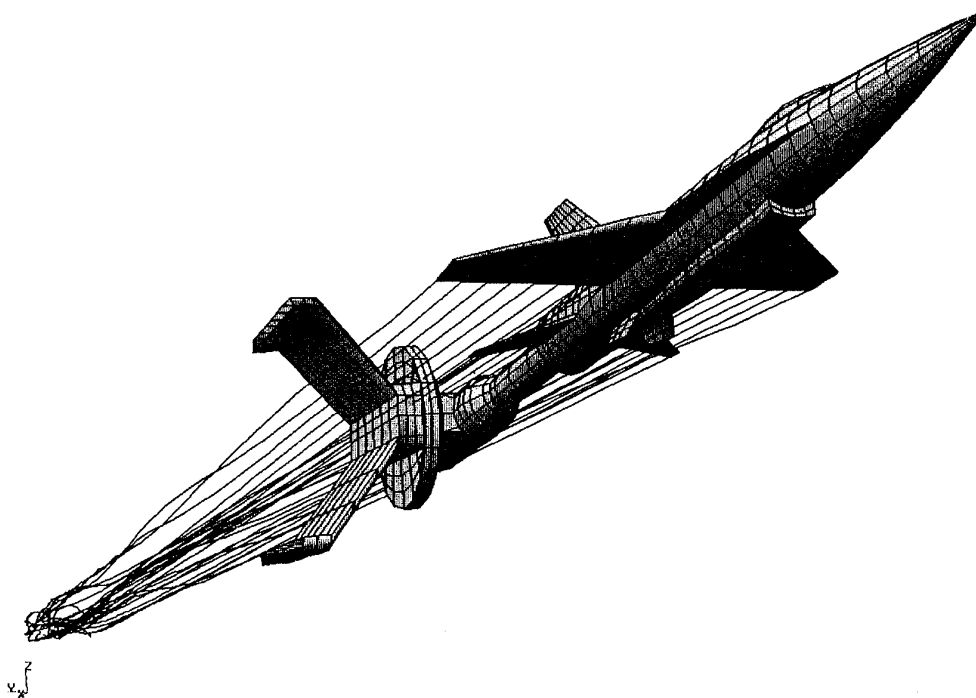
(b) Oblique Bottom View, Including Wake Filaments

Fig. 3. Computational Model of SDM on Sidewall Mount.

of the model is harmonic by definition, the dynamic derivatives are calculated using a Fourier analysis over a full period of the oscillation. The actual calculation spans more than one period to allow the initial vortex wake (starting vortex) to clear the configuration and the Fourier analysis is performed over a full period of motion in the last part of the calculated motion. The Fourier analysis is a built-in feature of the present method of calculation, as described in Refs. 12 and 13. One sequence of calculations is carried out in the presence of the support system model, while another is carried out in "free flight" conditions, with the support system absent. Tunnel walls are not modeled in the present study.

3. RESULTS

3.1 Time History of the Aerodynamic Coefficients

An example of the time history for the lift, pitching moment and induced drag coefficients at $\alpha = 5°$ is presented in Figs. 4 and 5, with and without the effect of the support system. The time span in these figures is 1¼ periods of oscillation, showing the indicial response of the aerodynamic coefficients as well. The support system has very little effect on the lift coefficient, C_L, as shown in Fig. 4. The effect of the support system on the pitching moment coefficient is to shift the C_m curve down by about $\Delta C_m \approx -0.01$. Note the phase difference between the C_L and C_m curves, both with or without the presence of the support system. The phase shift is not significant between the lift and the induced drag curves (Fig. 5).

Fig. 5. Time History of the Lift and Drag Coefficients at $a = 5°$.
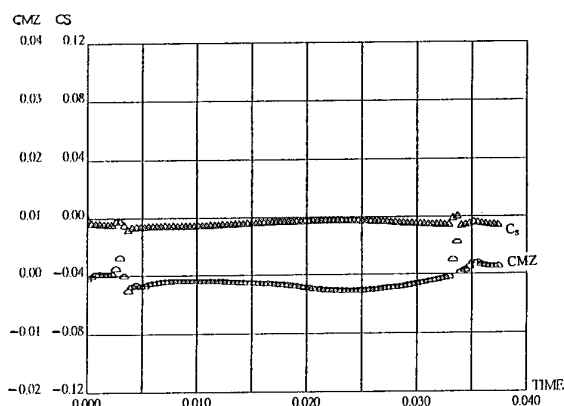
Fig. 6. Time History of the Side Force and Yawing Moment Coefficients at $a = 5°$ in Presence of Support System.

Fig. 4. Time History of the Lift and Pitching Moment Coefficients at $a = 5°$.

The support system seems to increase the induced drag, as shown in Fig. 5, although there is some uncertainty as to the accuracy of the base drag in both cases. The asymmetry of the support system at $\alpha = 5°$ induces residual amounts of side force and yawing moment, and almost no rolling moment, as shown in Figs. 6 and 7.
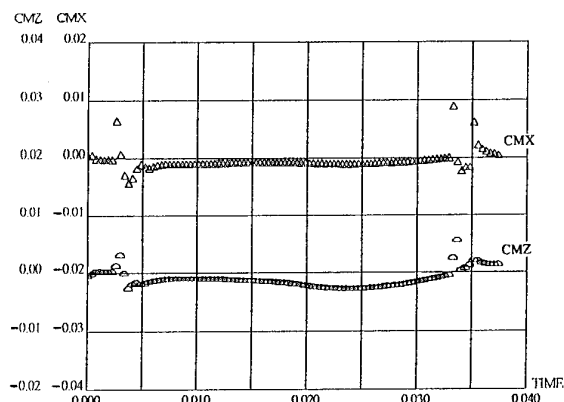
Fig. 7. Time History of Rolling and Yawing Moment Coefficients at $a = 5°$ in Presence of Support System.

3.2 Time-averaged Normal Force and Pitching Moment Coefficients

The average normal force coefficient, C_z, is plotted for various angles of attack in Fig. 8, and the corresponding pitching moment coefficient, C_m, is depicted in Fig. 9. Shown in these figures are the calculated results with and without the presence of the support system model, as well as experimental data from different test facilities.[4,16,18] The calculated results for C_z (Fig. 8) show very little effect of the support system up to about $\alpha = 8°$. At $\alpha = 10°$, the calculation in the presence of the support system produces a higher than expected C_z value, possibly because of the coarse description of the various wakes detaching from the aircraft in the present study. Other than at this point, there is good agreement between the calculated results and the experimental data.
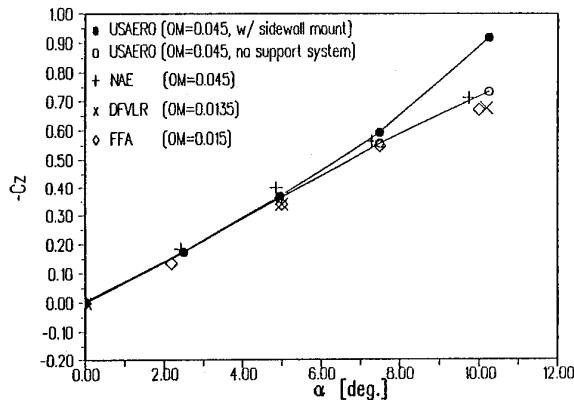
Fig. 8. Average Normal Force Coefficient in Pitch Oscillations.
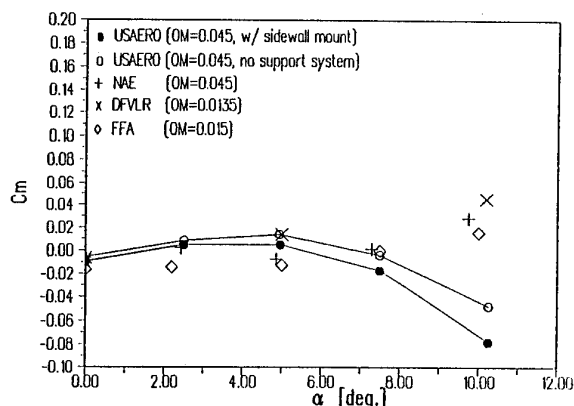
Fig. 9. Average Pitching Moment Coefficient in Pitch Oscillations.

The calculated results for C_m, Fig. 9, show that the presence of the support system tends to shift down the pitching moment. Up to $\alpha = 5°$, this trend brings the calculated results closer to the NAE data used for the simulation.[16] The calculation does not pick up the correct trend, as the angle of attack increases towards $\alpha = 10°$. This fact strengthens the assessment that the possible cause for the $\alpha = 10°$ discrepancy is due to coarse wake modeling, which can produce inaccurate interactions with the aircraft and its support system. Note that the same discrepancy exists even without the presence of the support in the calculation.

3.3 Fourier Analysis for Damping in Pitch

Figure 10 shows the damping in pitch coefficient, C_{mq}, for various angles of attack. This coefficient is obtained in the present calculations via a Fourier analysis performed over one period of oscillation. The calculated C_{mq} values in the presence of the support seem to be more damped than the corresponding values obtained without the support. The values of the calculated results fall generally within the scatter of the experimental data in Fig. 10; however, the shape of the curve does not closely match the NAE results[16] upon which the calculation is based. An improved wake model and possibly better paneling of the aircraft and support system may improve the results in future calculations. Note that C_{mq} is a dynamic derivative quantity, and as such, it is more sensitive to accumulating errors and local disturbances in the time-stepping calculation than are the time-averaged coefficients.
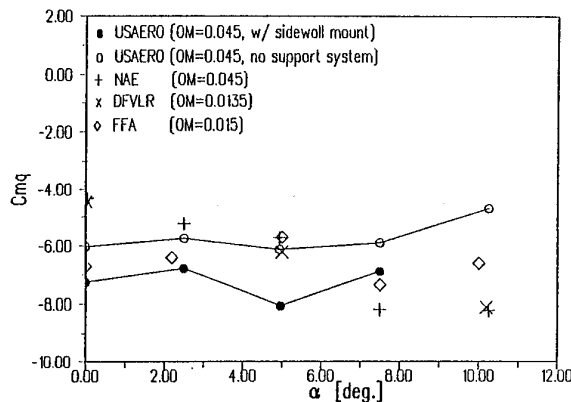
Fig. 10. Damping in Pitch Derivative, Cmq.

4. CONCLUSIONS

The results of the present preliminary study show that an unsteady doublet panel method is capable of predicting effects of support interference in dynamic wind tunnel tests, in subsonic flow and at low angles of attack. Time-averaged coefficients, such as C_L and C_m, seem to be predicted

more accurately than derivatives such as C_{m_q}, when compared with experimental data. The present calculation method has the potential to predict interference trends of dynamic support systems during their design phase. As a result, the present method can be used to design supports with minimum interference, or to estimate the interference effects of existing support systems by calculating an aircraft configuration with and without the presence of supports. As indicated by the results of the present work, further studies are needed to examine the effects of several parameters on the accuracy of the method. Parameters that should be considered include the number of panels used to model the geometry, the effects of refining the wake representation, as well as the effects of varying the time-step size and the period of motion involved. Another topic for future study is the effect of including the tunnel walls in the model. Such studies are essential for establishing further confidence in the method, while at the same time extending its usable domain to higher angles of attack, different flow conditions and complex geometries and dynamics.

Acknowledgements

5. REFERENCES

1. Beyers, M.E. and Moulton, B.E., "Stability Derivatives Due to Oscillations in Roll for the Standard Dynamics Model at Mach 0.6", NAE Report LTR-US-64, Jan. 1983.

2. Malcolm, G.N. and Schiff, L.B., "Recent Developments in Rotary-Balance Testing of Fighter Aircraft Configurations at NASA Ames Research Center", AGARD CP-386, Paper 18, May 1985.

3. O'Leary, C.O. and Rowthorn, E.N., "New Rotary Rig at RAE and Experiments on HIRM", AGARD CP-386, Paper 19, May 1985.

4. Schmidt, E., "Standard Dynamics Model Experiments with the DFVLR/AVA Transonic Derivative Balance", AGARD CP-386, Paper 21, May 1985.

5. Rohlf, D., "Identification of Aircraft Characteristics Including Gust-Induced Dynamic Effect", AGARD CP-386, Paper S-4, May 1985.

6. Tristrant, D. and Renier, O., Récents Développements des Techniques de Simulation Dynamique Appliquées à L'Identification des Paramètres de Stabilité", AGARD CP-386, Paper 22, May 1985.

7. Ericsson, L.E. and Reding, J.P., "Review of Support Interference in Dynamic Tests", AIAA J., Vol. 21, No. 12, Dec. 1983.

8. Beyers, M.E., "Direct Derivative Measurements in the Presence of Sting Plunging", J. Aircraft, Vol. 23, No. 3, Mar. 1986.

9. Ericsson, L.E. and Reding. J.P., "Dynamics Support Interference in High-Alpha Testing", J. Aircraft, Vol. 23, No. 2, Dec. 1986.

10. Beyers, M.E., "Unsteady Wind-Tunnel Interference in Aircraft Dynamic Experiments", J. Aircraft, Vol. 29, No. 6, Nov.-Dec. 1992.

11. Beyers, M.E., "Some Recent NAE Experiences of Support Interference in Dynamic Tests", NAE Report LTR-UA-83, Ottawa, Ontario, Canada, Nov. 1985.

12. Maskew, B., USAERO—A Time-Stepping Analysis Method for the Flow about Multiple Bodies in General Motion, Users' Manual, Version C.3, Analytical Methods, Inc., Redmond, Washington, 1991.

13. Almosnino, D. and Maskew, B., Non-linear Stability Derivatives of Fighter/Attack Aircraft at High Angles of Attack", Analytical Methods Report No. 9301, July 1993.

14. Coulter, S.M. and Marquart, E.J., "Cross and Cross-Coupling Derivative Measurements on theStandard Dynamics Model at AEDC", AIAA 82-0596, 12th Aerodynamic Testing Conf., 1982.

15. Beyers, M.E., "Subsonic Roll Oscillation Experiments on the Standard Dynamics Model", AIAA Paper 83-2134, 10th Atmospheric Flight Mech. Conf., 1983.

16. Beyers, M.E., Kapoor, K.B. and Moulton, B.E., "Pitch and Yaw Oscillation Experiments on the Standard Dynamics Model at Mach 0.6", NAE Report LTR-US-76, Ottawa, Ont., Canada, June 1984.

17. Jermey, C. and Schiff, L.B., "Aerodynamic Characteristics of the Standard Dynamics Model in Coning Motion at Mach 0.6", NASA TM-86717, July 1985.

18. Jansson, T., and Torngren, L., "New Dynamic Testing and Related Results at FFA", AGARD CP-386, Paper 20, May 1985.

19. Huang, X.Z. and Beyers, M.E., "Subsonic Aerodynamic Coefficients of the SDM at Angles of Attack up to 30°", NAE Report LTR-UA-93, Ottawa, Ont., Canada, 1990.

20. Guglieri, G. and Quagliotti, F.B., "Determination of Dynamic Stability Parameters in a Low Speed Wind Tunnel", AIAA Paper 91-3245, in AA 9th Appl. Aero. Conf. Proc., Vol. 1, Sept. 1991.

GENERAL DISCUSSION

Dr. D. Woodward, DRA, UK

I am your chairman for this last session. You have now heard all the technical papers and the time has come to evaluate what we have learned from those papers, to discuss and maybe agree, maybe not agree on the outcome. To help us in that discussion it is my great pleasure to welcome Mark Goldhammer from Boeing who is going to evaluate the papers that we have heard. Mark graduated from Renselaer Polytechnic Institute in 1970 and got his Masters from the University of Southern California in 1974. He has worked for Douglas Aircraft for 6 years in aerodynamics design, but now works for the Boeing Aircraft Company. He has worked for them for 17 years, specializing in configuration aerodynamics, transonic wing-design, CFD applications and wind tunnel testing. He has tested in wind tunnels in the USA, the UK, Japan and Canada. At the present time he is supervisor for the aerodynamic design for the Boeing 777 program, a new large-capacity, long-range, twin-jet airplane. You can see from those qualifications that he is eminently well qualified to be our technical evaluator today. So, I introduce to you, Mark Goldhammer.

Mr. M. Goldhammer, Boeing, USA

Thank you very much, David. First of all I would like to start by thanking the Fluid Dynamics Panel of AGARD for the honor of being selected as the Technical Evaluator and also to thank the authors and presenters for their fine written and oral reports which made the job easier. I hope that I can live up to the expectations of the FDP, especially after the exceptionally well presented keynote address by Frank Lynch. Frank's presentation and paper are an excellent portrayal of the needs of the aircraft industry which is the primary beneficiary of this research. You will hear me repeat him frequently. I would also like to start with a few apologies, apologies for speaking mostly from the application side of the house, because that is where my experience lies, and the academic researchers that we have heard should not feel this as a put-down to the fundamental fluid dynamics research which often forms the basis for the practical test or computational techniques we use in industry. We in industry just like to be able to see the tie between the fundamentals and eventual application. As of yet I have no formal text, and mercifully so I have no vu-foils, so I will speak slowly so that the translators can keep up. I apologize in advance, despite 4 years of high school french, je ne parle pas le francais.

My presentation plan today is to give a short review of the industry needs from my perspective, but you will find that I repeat Frank Lynch quite a bit. Then I am going to go into a review of what I thought we heard, mainly the key aspects. I apologize again for omissions and for misinterpretations. I would also like to discuss what, in my opinion, we did not hear and some of that will be industry priorities. I plan to have a written report ready in 6 weeks; that is my assignment. In that report, I hope to have an extension of what I said today, but not a report-by-report critique.

Now for the industry overview: To industry the windtunnel was merely a tool to develop airplane configurations with minimum cost. Minimum cost can be regarded, for example, relative to a flight demonstrator, which is very costly; minimum risk - we want to minimize the risk of financial ruin by a bad design, and also, the human risk inherent in flight; minimum time, cost and schedule, which translates into money; and maximum benefits in terms of airplane performance and airplane handling characteristics, loads prediction, return on investment, and so on. Much of what we heard in this conference were academic studies that often find their way into the industrial world. That is good. Hopefully, AGARD and the FDP is a useful body for providing the aeronautical community with visibility towards maximizing the applications and utility of these studies. I think that is why Frank Lynch and I were selected to open and close this conference, to bring that reality of industry to this meeting. However, we in industry must have sufficient vision to encourage the broad-based research and not be too constrained by near-term requirements or a myopic view of profit-oriented industrialists. There is a delicate balance to be had there. With regard to wall interference, support interference, and flow field measurement, industry is looking for, in my opinion, accurate validated techniques, ease of application, flexibility, low cost and short flow time. To elaborate, accurate validated techniques means that we don't have time during an airplane development program to de-bug methodology, whether it be wind tunnel methodology, CFD or the like. We have to use validated methodology and tools that we can trust right from the outset. Ease of application means simple algorithms that we can use on-line in a wind tunnel test, processing them on-line. We don't have the time, nor can we afford to go back and run big CFD analyses on tens of thousands of test points. We often run our wind tunnel tests with relatively low experienced engineers who have to be able to understand what they are doing. Flexibility - that applies mainly to flow field modelling, but also to wind tunnel corrections. We don't

always know where the problems are going to be when we go into a wind tunnel test, so we have to be flexible. Certain techniques are more amenable to flexibility than others. Low-cost airplanes cost too much. That is one of the biggest problems we have in the commercial transport business right now, and anything we can do to lower that cost is useful. So the techniques that we need to apply to develop airplanes should be low cost. Cost is also related in time, and short flow time lowers cost. A program cannot continue in the design phase until the aerodynamic lines are defined and frozen. Change is bad, so we have to get into the wind tunnel, do our work, design the lines and then let the people who design the material to build the airplane have on with it. We cannot change our minds. So much for a short industry overview. For more of it, I refer you to Frank's excellent paper.

Now I would like to move on to what we heard and what we did not hear. First of all I will start with the wall effects. It is not necessary for me to review the fundamentals of modern wind tunnel wall correction methodologies. The invited paper presented by Dr. Pat Ashill is another of his wonderful papers that clearly discusses the concepts in terms that even an applied aerodynamicist such as myself can understand. I applaud his efforts and the wisdom of the FDP in inviting him, along with Frank Lynch, to summarize this topic. I predict that their papers from this forum will be referenced for years to come. It is clear from Pat's paper that the world of wind tunnel wall corrections is in the midst of transition, from handbook corrections based on the method of images to empirical methods based on measured boundary values and CFD. The transition is being caused by an improved understanding of the flow physics, improved mathematical and computational capability for on- line processing, improved wind tunnel instrumentation, things such as electronic pressure scanning, improved flow field measurement and perhaps most importantly, an increased need mandated by the larger wind tunnel models intended to obtain higher Reynolds numbers. It is also clear from Pat's paper that those who envision constructing new wind tunnels should understand the implications of test-section cross section, wall porosity distribution and type, wall adaptability, etc. on wall effects correctability. To carry that step one further, proprietors of existing wind tunnels may want to reconsider reconfiguring their test section walls to improve correctability of their data through improved ventilation techniques, adaptability, and so on, perhaps even improved support systems. If there is one area of disagreement to be raised with the Ashill paper, it is in the utility of adaptive wall wind tunnels in the environment of aircraft development. To date, at least to my knowledge, no major aircraft development has been conducted routinely in an adaptive wall facility. It is probably a combination of a misunderstanding or a lack of confidence in the concept by aircraft aerodynamicists in the practicality of taking literally thousands of runs and tens of thousands of test points in a typical aircraft development program in an adaptive wall facility. I am personally not optimistic about seeing a change in this area during the remainder of my career, but I could be proved wrong. The TSAGI T-2surp128 tunnel is an example where adaptability is close to routine application. I don't want to discourage the use of adaptive wall wind tunnels. It is a wonderful tool and will aid in research, particularly in validating CFD codes where you need that perfect answer. But in the day-to-day practical wind tunnel test environment of an aircraft development program, I am skeptical about its application.

We saw a number of excellent presentations of the application of relatively new boundary value measurement techniques to wind tunnel wall corrections. Researchers are clearly finding new applications to allow better CFD solutions, to understand complex, high blockage flows, such as separated flows and vectored jet flows, for which we saw several presentations. But there is clearly more work to be done here. Several papers we heard explored the two-variable approach to the wall effects correction procedure. I am discouraged, but not surprised, by what I have seen. Determining wall tangential velocities from wall or rail static pressures is a difficult enough challenge in practice. But to apply a two-variable technique and to take model geometry out of the picture, especially for transonic flow, you have to measure the velocity normal to the ventilated walls. That will have to become a routine and accurate procedure. This will, in my opinion, get into the nasty flow details through slots or holes, which is a highly viscous flow phenomena involving complex flow physics that are beyond the state of the art and may not be worth solving. The fine work presented by Prof. Freestone was both encouraging and discouraging in this regard. However, the paper by Agrell of FFA, to me anyway, suggested that new knowledge about optimizing slot geometries may be on the horizon. The industry has been confused about this issue for years - holes versus slots, few big slots versus many narrow slots, tapered versus constant width slots, baffled slots, and so on. I would hope that improved understanding gained from this research, possibly coupled with slot flow field measurements using PIV or DGV or whatever, could shed new light on improved wall configurations. Goodness, we need this issue cleaned up. I recommend to the FDP that work be encouraged in this area.

The concept of modifying the measured forces and moments for wall corrections, as we heard in a paper by McDonnell Douglas, rather than correcting the free stream conditions, is relatively new and different. To

me, it seems diametrically opposed to the two boundary value approach which tries to eliminate the need for model representation. This technique calls for increased CFD fidelity on the model, in my opinion. I am confident that this will pose a technical debate for some time and a real technical challenge. This may be one area where the needs of the commercial transport industry and the military airplane industry are different. I also was excited to see a paper regarding ground effects wind tunnel testing. This often-ignored subject needs increased attention. Most flaps-down testing is done in so-called free air, in other words, not near the ground plane although inside a wind tunnel. But the real flaps-down performance from a design standpoint is mostly involved in ground effect. Besides the ground/boundary layer issues discussed in the paper, it should also be recognized that rarely do airplanes fly both close to the ground and parallel to the ground. The one exception, obviously, is the Miss Budweiser. The real simulation requires an inflow or outflow from the ground to represent ascent or descent. These effects are not negligible, but they are generally ignored. A real wind tunnel challenge is to attack this problem.

There is a topic that Frank Lynch and I discussed during a number of the coffee breaks that I just have to bring up, that is, adaptive walls and cryogenic wind tunnels. Our opinion is, "don't bother". We have discussed this at length and we agree. Cryogenic tunnels allow small models relative to the size of the tunnel. The reason that is good is you can minimize wall effects and then you can easily calculate them. It is tough enough testing in cryogenic conditions and making things work. To us the concept of having adaptive walls in cryogenics is abhorent.

Moving on to two-dimensional air foil testing, the wall effects there continues to be studied and improved. Clearly floor and ceiling issues are well understood. More and more is being learned about the sidewall effects, and perhaps this issue will be concluded by the next FDP meeting on this subject. The key issues seem to be the sidewall boundary layer treatment and the two dimensional aspect ratio, a contradiction in terms, by the way.

The presentations by ONERA and IAR were very consistent with each other, and industry has both supported and accepted these findings. This is an example of a good cooperative spirit between labs, universities and industry internationally.

Now a little bit about what we did not hear on wall effects. In my opinion the high-lift, flaps-down wall effects is not getting enough attention. Why do we tend to test large models in solid wall wind tunnels, flaps down, when the flow field around the model is very severe? Perhaps we may learn some lessons from transonic testing and Frank Lynch did touch on this. Flow field curvature due to walls can effect optimum flap setting, tail increments and so on. Our high-lift mounting systems tend to have very high interference because of model loads. Another area that I think was neglected is half models. Half models are like taxes, nobody likes them but we have to have them because we need them. Besides all the often exaggerated normal wall effects issues, the so-called plane of symmetry in half model testing also imposes a set of wall effects challenges that must be better understood. This includes testing on a splitter plate versus testing on the tunnel wall or floor, boundary layer suction, boundary layer blowing, offset plates and so on. This is a very challenging area. This subject was touched on both by the TSAGI presentation of Neyland and the Dehaviland presentation of Poole. Another area that was not discussed at length was stability and control testing. Stability and control uses most of the test time in the commercial airplane development. They test to the extremes of the flight envelope to buffet and beyond, they test in yaw, they test with large control surface deflections and huge wakes. Because of the massive quantities of data required, S&C engineers tend to use the wind tunnel as a simulator. What they see is what they get, and they need simple, reliable correction techniques.

Moving on to mounting system interference, two major themes came through to me. People in the Symposium seem to feel that wall effects and support effects are intimately related, and to that I agree. They also seem to be on the track that CFD is used to develop support corrections. It sounds great, but it is not reality in industry, at least, at Boeing. We at Boeing probably spend more time and more money on mounting system effects than anybody else. Our reality, and I believe that for much of the industry, is this: when support interference effects are considered, and it is only considered periodically during the development of an airplane, there is really no tie to wall interference. We tend to treat them separately. That is not necessarily right, it is just reality. With regard to how we determine support interferences, it is almost exclusively by tests. We do occasionally cross check with CFD to understand the reasonableness of our answers, but in general, we test and test and test. We test and demand high quality. For high speed drag, we tend to develop our support interferences so we have confidence within one or two drag counts. We do that by using two separate supports and doing what we call a closure exercise, which is getting the same

answer from two mounting systems. We also look for angle of attack within one or two hundredths of a degree. For flaps down testing, we tend to get poorer correlation, but it is mainly because that is what we get, not because that is what we want. Some specifics on what we heard at the Conference: the work presented by Aerospatiale on three strut support interference and by DNW on stings is typical in my opinion of what the industry approach is. A little bit more CFD flavor to that work which is good, but in reality, both companies seem to rely, as we do, on testing. Bram Elsenaar made a comment during one of the presentations on the drag results being frightening, and I agree with him, and that is not a criticism of the work presented, it is just reality - drag is hard. Wall effects, mounting system effects are done for drag, and again, I'll say that the way we attack that problem is to test and test and test. I was very happy to see the report today on plate mounts. We have used that mounting system for years at Boeing with great success. It is a mounting system that is very stable, repeatable, and low interference. The only downside to it, and that is the way we use it at Boeing, is that it has a large plate tare as we use a balance outside the tunnel. But that tare turns out to be invariant with flight condition. The other downside is that you can't use a mounting system such as that for yaw testing.

I don't want to discourage CFD work on mounting systems, but there just may be some higher priorities. What are those higher priorities? I think companies around the world need to make better selections on mounting systems. Industry is quite inconsistent in this regard, and opportunities are being missed. Companies like Boeing who tend to test around the world find it difficult in going from tunnel to tunnel that there is no consistency in mounting systems. Perhaps an AGARDOGRAPH on how to mount models and various scenarios for corrections is recommended. Another higher priority, and I have already mentioned this in regard to wall effects, is half models.

Finally, on to flow field measurement. I guess that this is the one criticism in my talk and that is to me the relationship between the wall and support interference portions of this Conference and the flow field measurement portions of this Conference were not very well defined. Before I arrived, I was expecting to see utilization of flow field measurements near ventilated wind tunnel walls to aid in developing wall interference correction techniques and perhaps to develop low interference wall geometries, like slots and holes. I didn't see much of this. This may be a useful application of these flow field measurement techniques. What we did see was a wide variety of flow field measurement techniques, both intrusive and non-intrusive. We saw new applications of intrusive techniques such as the 5 and 7 hole probes to determine velocity fields as well as some hot wire work. These studies were both to develop and demonstrate specific flow probe devices plus to investigate certain flow phenomena around vehicle geometries. It was good work, interesting presentation, relatively routine. We also saw new applications of non-intrusive techniques, primarily based on LDV technologies and schlieren. Applications were both aeronautical and otherwise, going as far as biomedical and turbomachinery. The objectives were to demonstrate the technology, understand flow physics around various configurations, including delta wings and afterbodies, for CFD validation, and the like. It is good fundamental work which does support industry in my opinion. We also saw a talk on pressure-sensitive paint which is a new and emerging technology. I was a little disappointed not to see high value airplane design oriented diagnostic flow field measurement techniques, the type of techniques used by the airplane design community. Especially since a number of these techniques are relatively new and emerging and should be heard by a technical advisory board such as AGARD. Included in that would be transition detection devices. A key to developing a laminar flow aircraft, whether it be natural or hybid laminar flow, is transition detection. The technologies in vogue are primarily infra red imaging, but also liquid crystals and hot film methods. The laminar flow airplane may come someday and it may be the technical breakthrough similar to the swept wing, so it is something we should not ignore. Pressure-sensitive paint is at near breakthrough status as well, with tremendous potential for improved design diagnostic capability, and it meets the need of, "it's something you don't need in advance". If you run into a problem, you can use it. There are some exciting possibilities for its use as well, and this is far out thinking, in terms of a flight vehicle where you encounter a problem. It also may have utility in wind tunnel wall effects methodology in seeing what is happening on the walls. Another key area that I didn't hear much on was wake surveying. That is a key technique to understanding the origins of drag of an aircraft, at least in the commercial field. We at Boeing have work by Jim Crowder on something he calls his Wake Imaging System, and from personal experience I can tell you it has provided great value in both qualitative and quantitative understanding of airplane flows. There is also multi-element applications which will be a key to improve CFD models. We heard a little bit from Frank Lynch and some others on particle imaging velocimetry and Doppler global velocimetry, and I must admit that this is an area that I have not been very familiar with. I would have like to have heard more because it looks exciting.

To conclude my talk I would like to say that the Symposium was useful for focussing the activities on wind

tunnel issues, especially wall interference and support interference. I commend the FDP's effort to involve industry. The bias towards the transport industry having Frank Lynch and me talk is probably OK because the transport industry is probably the most challenging technical application of these wind tunnel methodologies. I admit confusion as to the combination of the wall and support work with the flow field measurement work, but that is probably OK too. However, the wall and support information work is a big enough topic that it could have filled the entire Symposium itself.

Dr. D. Woodward, DRA, UK
Thank you very much for that marvelously detailed and excellent evaluation. I would particularly like to thank you, because I know that you have been working late at night and eating on your own in order to achieve that excellent summary of what has been going on. Now I throw the meeting open for discussion. Perhaps you would like to remember to state your name and origin. Let's see what you all have to say.

Prof. G.E.A. Meier, DLR, Germany
The review was very excellent and also the Conference gave a very good picture of the present state of the art. But I would like to take the opportunity to emphasize some problems that are, in my opinion, still left. Additionally, I would like to mention some future areas of research for the three topics of the Conference.

With respect to wall interference, I think there should be special attention given to the problem of transonic adaptation or correction, because this is a highly non-linear problem and the ambiguity of the flow field equations needs special treatment. Another problem in the area of wall interference is the acoustic lining of tunnels. This has not been tackled very much in the Conference, but I think that it is the central problem of quiet tunnels. It is also very important with respect to the receptivity problem of boundary layer transition and with respect to unsteady flow measurements. In tunnels, the acoustic resonance effects may disturb unsteady flows strongly. The acoustic problems are also very important with respect to airframe noise measurement. This problem has to be taken into consideration, because it is also a major topic in the future. The shock reflection problem in supersonic tunnels can also be put in this general area of acoustic lining problems.

With respect to tunnel boundary layer interaction, not only the problem of boundary layer thickness has to be taken into account, but I think all kinds of secondary flow. In some contributions they have been mentioned here, but I think all the vortices, wakes and separations in the wind tunnels are very problematic, and each wind tunnel is an individual with respect to this. Here we have another problem of correction and adaptation. Not very much treated during the conference was the unsteady flow in all the slots and plenum chambers of the tunnels due to shear layer instability which I think is present in most wind tunnels and gives rise to noise and other problems. I also mention here the suction problem which was emphasized by Mrs. Neyland as a special topic of interference with the tunnel flow. At least I would like to make one short remark with respect to support interference. There are not only blockage effects but also unsteady wakes and flutter instabilities with the consequence of model vibrations and influence on dynamic measurements in wind tunnels.

Finally, some short comments about flow field measurements. The three-dimensional and surface measurements methods dealt with in the Conference are highly appreciated, but I feel that they have to fulfill some additional requirements. Two main points are simplicity and applicability in almost all kinds of wind tunnels. Further there is the question of accuracy for validation purposes. For instance, the results with pressure-sensitive paint and other optical field methods could be increased if one uses a loose net of reference points equipped with ordinary pressure probes or alike. Also the point of integrability into the running test is very important. This means on one side the immediate applicability of measurement results for overlooking the state of the test on the other side, the feedback into control and adaptation procedures and the immediate comparison with numerical results. This leads finally to a hybrid kind of testing with online computer controlled interaction between wind tunnel measurement and correction or adaptation methods and flow field calculations.

Dr. D. Woodward, DRA, UK
You highlighted adaptation, which was the point that Mark was a bit controversial about. Mrs. Neyland, would you like to make a comment on the operation of adaptive wall wind tunnels and do you think it is a technique which can be applied to an industrial tunnel for routine testing.

Mrs. V. Neyland, TSAGI, Russia
The answer is quite obvious. Yes, we believe it might be a productive testing technique. We are working in

this direction. For instance, we have equipped our wind tunnel with electronic scanivalves. We have developed new software and next month we are supposed to repeat half model testing with adaptation in an on-line mode, so that we can adjust whole polars, not only one or two points on the polar, but whole polars. I believe that at the next Conference of this type, we will be able to show you productive testing of that kind.

Mr. B. Elsenaar, NLR, Netherlands

I might join in a little bit in the controversial remarks. On the one hand, like Mark said, the future of the two variable method for ventilated walls doesn't look very bright because of the difficulty of measuring V in a proper way. So you have to go to a one variable method in order to apply adaptation for porous type of walls, and in that situation, you have to have a very accurate model representation in order to get the accuracy. In my view, it is not quite clear if you are ever able in tunnels with porous walls, adaptable or not adaptable, to calculate the wall-induced upwash within one-hundredth of a degree. And that is what you need for accurate drag testing. That is a very demanding requirement. Personally, I have almost the feeling that it is too much to ask for. I was even more pessimistic about it after listening to some of the contributions. That leads to the question that if you want high accuracy data, you have to go to closed wall wind tunnels. It can still be and has to be adaptive, but with flexible and solid walls. In that situation you can very accurately measure both the U and the V component on the walls and calculate the residual interference if this is still left, or adjust your flexible walls in such a way that you are virtually interference free. I think that there is a future for adaptive walls if it is proven to be productive, but I wouldn't be astonished if the future is more in solid type of walls rather than porous type of walls. So I am on a different track than Mrs. Neyland.

Mr. M. Goldhammer, Boeing, USA

I agree with your comments mostly, but the one concern I have is with regard to choking of the tunnel. I am not sure adaptivity is going to get you around that problem. For the higher Mach number type subsonic transport, as an example, you are going to either have a severe restriction on model size, which goes into Reynolds number, or you are going to have a severe restriction on Mach capability. Once you have a 0.8 Mach or higher airplane, you are really very limited in a solid wall tunnel.

Mr. N. Taylor, DRA, UK

In my view, the control of wall-induced blockage does not pose a problem when testing in adaptive flexible-walled test sections: I have tested two-dimensional lifting models through the speed of sound (including at Mach 1.0) with solid blockage ratios of 8% (and ratios of test section depth to model chord only just in excess of unity). In fact, by identifying several new freedoms that may become available to operators of flexible-walled test sections, the novel insights provided by recent developments in adaptive wall technology have not simply overcome, but actually reversed many of the constraints imposed by more conventional transonic wind tunnel testing technology.

For instance, you will be aware that when testing at Mach 1, the regions of the near-sonic flow in the immediate vicinity of the model are remarkably small - these acutely sensitive portions of the flowfield are almost entirely confined to the far-field. This leads us to believe that, with the powerful control over wall-induced blockage afforded by diverging the flexible liners adjacent to the model, we should utilise larger rather than smaller models when testing through the speed of sound. This will also allow us to take full advantage of the Mach freeze phenomenon, particularly in two-dimensional testing, where the flow throughout the test section may be expected to be insensitive to variations in freestream Mach number over a wide band of near-sonic environments. We have already demonstrated that vast quantities of high quality sonic and near-sonic test data may be acquired rapidly (effectively on a one-shot basis), with minor adjustments to the wall contours.

I would also like to make a few additional comments on the subject of adaptive wall technology. To date, adaptive wall research has been almost exclusively concerned with demonstrating the ability to minimise the effects of wall interference - a step made necessary by the need to overcome deeply rooted objections (many of which are ill-conceived) that have been allowed to become widespread throughout the aerospace community. For example, holding developments that preceded the adoption of transonic ventilated test sections in abeyance, it is often stated (note: not claimed) that problems associated with wall-induced blockage and shock reflection preclude the use of closed test sections as platforms for transonic wind tunnel testing. Activities in flexible-walled test sections have repeatedly been successful in overcoming these objections. However, almost entirely as a consequence of this emphasis (with the exceptions of the research conducted in the T2 Tunnel at ONERA/CERT, the T-128 facility at TSAGI and TSWT at the University of Southampton), relatively little effort has been directed towards addressing the issues associated with

tunnel productivity.

Furthermore, the emphasis that has been placed on the requirement to minimise the effects of wall interference appears to have unduly confined the scope of our expectations for the potential benefits that may arise from future developments in adaptive wall technology. I would like to stress that adaptive flexible-walled test sections provide powerful control over the test section environment: you may choose to utilise this control to minimise the effects of wall interference if you like, or you may decide to exploit it for other purposes. For example, you may wish to alleviate the effects of sting, strut or sidewall support interference in addition to alleviating the distortion of the flow produced by the walls of the test section. It may even be possible to contrive to simulate the variations in aerodynamic performance that may occur in flight, such as the spanwise variations in twist that occur during long-range cruise or high-g manoeuvres. These are only a few of the freedoms that we at Southampton believe may emerge as being uniquely available to operators of adaptive flexible-walled test sections. It seems reasonable to expect that more will arise as the aerospace community improves its familiarity and becomes increasingly involved with the technology.

Given the current status of the technology supporting the minimisation of the effects of wall interference, we are now in a strong position to begin exploiting some of these novel freedoms. Moreover, in the light of the rate at which progress has been made in flexible-walled test sections (which, unlike their ventilated couterparts, provide environments in which the boundary conditions may be swiftly and accurately acquired, thereby enabling high quality test data to be procured without invoking any assumptions about the geometry or aerodynamic behaviour of the walls or model), the prospects for future developments appear to be good. Consequently, while adaptive wall technology may not yet have reached the stage where it is widely acknowledged as being competitive in production testing environments, it is possible that, given appropriate levels of financial support, the capabilities of flexible-walled test sections may soon surpass those of their ventilated competitors in virtually all measures of productivity and performance.

Dr. D. Almosnino, Analytical Methods, USA
I would like to say a few words about the combination of CFD methods and wind tunnel testing. It seems that in the views expressed by the distinguished speaker there is a source of contradiction, regarding two things. One has to recognize the limitations of any method. Both CFD methods and wind tunnel tests have their own limitations. I think that what the distinguished speaker said about wind tunnel production policy, which is to "test and test and test", clearly contradicts the other thing that he had said that production facilities, and big companies like Boeing, would like to save money and cut costs for aircraft development. "Test and test and test" doesn't go together with that. "Test and test and test" is basically another way of saying "bounce your head against the wall". So, I think that large companies should be more flexible in their thinking, combining disciplines when possible, and maybe it's time to spend some effort in that direction. This is a typical problem between research effort and the amount of spending that large companies are willing to commit for doing some research efforts in order to enhance the capability of its other facilities. From what I have learned in this Conference, I think that the Canadian efforts are a remarkable example of what seems to be a reasonable balance between CFD methods and wind tunnel testing.

Mr. M. Goldhammer, Boeing, USA
I finally had a short response there. Apparently, I have been successful in what I was charged to do which is to develop a little controversy, and it is always nice to know that you are successful. I didn't want to give the impression, so I want to make this comment, that we at Boeing don't combine wind tunnel testing and CFD, because we do, quite dramatically. In fact, the work that was presented by IAR on the two-dimensional wall effects was done in cooperation with Boeing, so I feel that we have a major contribution there. In addition, we have been using CFD along with measured wall pressures in three-dimensional wind tunnel testing for a number of years now, and we reported on that in ICAS Conference in 1990. My comments were mainly towards support interference and I am familiar with work we have done at Boeing on that subject, both testing- and CFD-wise, and to date the CFD has not emulated the test very well and that is why we test and test and test. What we call tare and interference testing, to get out the effects of support interferences, is a very lengthy complex process. It is expensive and we tend to do it only once or twice in the life of a given airplane program because it is so expensive. Most of our testing is done on what we call an incremental basis, starting with a known baseline and looking at design options and then finally, when you have a complete configuration, doing a tare and interference determination test to come up with your final predictions of the flight characteristics. With regard to adaptive wall wind tunnels, most of the successful work has been in 2 dimensions. But when we talk about a three-dimensional model, not just near its long range cruise Mach number, but at 20 degrees angle of attack at its maximum operating Mach or its dive Mach

number, where the flow is separated in some unpredictable way, it is hard to imagine that we can build the degrees of freedom into an adaptive wall wind tunnel that will handle those cases. So, for those cases, as an example, you are looking at building a smaller model to fit in a tunnel and not have unacceptable wall effects and then you are starting to get into the question of multiple sets of models for the same program which becomes prohibitive in itself.

D. Stanniland, Aircraft Research Association, UK

We have heard frequent comments about separated flow, flow at high incidence, and the problems associated with that, often with the reference to the global cure that the Navier-Stokes equations will give us the perfect answer. One of the problems with both CFD models and wind tunnel models is that the geometry is not representative. When you talk about flow breakdown, you are talking about fine details in the geometry. CFD models use perfectly smooth representation of wings; they are not. Wind tunnel models tend to ignore details, which, when you look at the flow breakdown, are significant. The obvious aspects are things like vortex generators, but you also go down to details like gaps between flaps on the wing leading edge. They are frequently not represented in the model, either CFD or wind tunnel. In a particular case we have looked at recently, we have had a Navier-Stokes code which gave us a perfect single vortex breakdown on a highly swept wing. When you look at the model, it has got a segmented leading edge, smooth to the touch, but there is sufficient unsmoothness to trigger part-span vortices. I suspect that the free air case would be more like the wind tunnel model, but probably different again. We must bear in mind exactly what we are modelling, particularly considering fine details, to ensure that the geometry that we are representing is an accurate representation of the aircraft.

Dr. V. Atli, Istanbul Technical University, Turkey

In the flow field measurement presentations, the works mainly were concentrated on the mean velocity measurements, but however, the turbulence is another main parameter on the flow field. Also, turbulence is one of the main parameters effecting the flow quality and the test quality. In the future, we have to concentrate on the turbulence measurements and maybe this is because of the test facilities quality or achievement of the instrumentation.

Mr. D. Stanniland, ARA, UK

A quick response to that. Yes, I would certainly agree that the tunnel turbulence is a significant parameter, but we do need to be careful on how we interpret this. Certainly, in the ARA tunnel we have what appears to be a peak in the free stream turbulence level, the empty tunnel turbulence level, which has been published in many papers, both for our tunnel and similar effects for other tunnels. This is not present when the model is in the tunnel. So, we need to be careful about precisely what the interpretation of turbulence is.

Dr. D. Woodward, DRA, UK

I would like to take you back to support interference, if you don't mind.

Dr. Freestone, City University, UK

I noted you were both encouraged and discouraged by our work at City. I don't know whether I should be encouraged by that myself or discouraged, perhaps I should be encouraged. What I would suggest is that we shouldn't give up on measuring slot flows. I think that slot flows when a transport configuration is under test will probably be very mild, and should be readily capable of measurement, so that the test section upwash can be determined to something of the order of a hundredth of a degree. This only requires determination of the slot flow to an accuracy of about one degree, which I don't think should be out of court. Even for cases where this high standard is not achieved, I think that it is still worth pursuing because, at the very worst, it will provide a parallel method of determining wall interference. I think that engineers like to know that measurements can be checked and they like to see a check. If there are two independent methods of getting an answer they would like to employ both methods and see if the answers agree. If they disagree, they can scratch their heads and try to find out why. So, perhaps you could also be encouraged by our wall interference work.

Mr. M. Goldhammer, Boeing, USA

If I could make one comment there. I didn't want to discourage the work from continuing, that was not my intention. I just wanted to raise the caution that to see a technique like that in day-to-day production wind tunnel testing seems like a remote possibility to me, not to say that it would not be a good technique to develop that perfect set of test data, for example for CFD validation, and there it may have some value. In a similar vein, I felt that some of the charts shown by Pat Ashill that implied that there was a certain geometry of wind tunnel cross section and perhaps porosity that would yield the most correctible data is something

that should be pursued, especially as new wind tunnels are being conceived around the world. To me, that would be a high value effort to help guide these new wind tunnel developments. I was hoping to hear a comment from the audience with regard to my concern about the lack of understanding of wall configurations, slots, holes and the like. I was hoping that it was just my lack of knowledge on the field rather than a generally agreed perception, that we don't know much about that. I am not aware of much work in that area since maybe the 1940's or early 1950's when ventilated tunnels were first being conceived, and I would sure like to hear some encouragement that we know more than I do.

Dr. D. Woodward, DRA, UK
Perhaps I could interject a specific situation into that. You mentioned testing high-lift flaps-down models in the solid wall tunnels, and that certainly is a severe flow environment, and yet you almost never, (and I am saying almost never because I am not sure I am right), but you almost never see a low speed tunnel with either a porous or a slotted wall. I hadn't ever thought about it very much, I accepted that low speed tunnels had solid walls, but it is an interesting point. Does anyone have any comment about it? It is something that low speed tunnels ought to be thinking about, moving into the uncertainties involved in measuring the flows through the slots.

Dr. Ashill, DRA, UK
I was just wanting to add that there is another option for low-speed, high-lift testing: adaptive walls. I would like to respond, if I may, to Bram's pessimistic outlook for wind tunnels with porous walls. I believe he is saying that, for tunnels of this type, he is doubtful that we will be able to determine wall-induced upwash to the required accuracy of 0.01 degrees with one-variable methods. This is a concern that has to be taken very seriously, given the number of tunnels of this type in use in various parts of the world. The long term hope is that work on two-variable methods of the type described by Dr. Freestone will help. In the meantime, however, consideration needs to be given to the sources of error in one-variable methods. Confining our attention to methods of the Dirichlet type, one source of error comes from the measurement and treatment of 'wall' pressures. It would have been very useful to have had papers in this Symposium from users of methods of this type, indicating how accurately it is necessary to measure 'wall' pressures and how many measurements it is necessary to have to achieve the required accuracy. Model representation remains a significant source of error, and in my own paper I indicated possible ways of minimising errors from this source, but it is clear that this is an important area for future study. Perhaps I am not quite as pessimistic as Bram, but it would be good if there could be more papers in future dealing with this really central issue of the accuracy of the wall-interference methods.

Mrs. V. Neyland, TSAGI Russia
I would like to return again to CFD and its role in all questions arising here. There were some comments about flexible walls and very valuable estimations from Mr. Goldhammer on porous walls adaptation. In my opinion, the next restriction in this wall adaptation of different schemes will not be productivity, not blockage, but will be CFD methods for transonic flows, because in every adaptive wall approach the main part which determines the adaptation is the transonic calculation. Up to now, we have not had adequate theoretical calculations for three-dimensional flow fields. That is why, I suppose, it will be very useful to create special computational approaches to simulate transonic flows in a wind tunnel. You see the history of all CFD calculations developed in such a way that at first these CFD methods were developed for free flow and only after this were they adapted to wind tunnel conditions. This adaptation sometimes is not good enough to describe all the small features of wind tunnels and wind tunnel geometry. That is why, I suppose, the development of special testing programs, special simplified models to be tested and to be compared with CFD approaches, would be useful. These models and this experiment might be so-called computable, so that we would have 100% confidence in the computation and in the experiment. Only in this way, can we develop good mathematical and computational models of three-dimensional transonic flows. Only after this, can productivity be achieved in wall adaptation, either flexible or porous or some other kind.

Dr. D. Woodward, DRA, UK
Would somebody from the CFD community like to respond to that suggestion?

Dr. H. Korner, DLR, Germany
I think that the CFD methods already have reached a certain maturity, although we are not able to give the values overall of C_L, C_D and so on, for full configurations at this time. But with an Euler method, for example, we can compute full configurations approximately. I see also in the future, say three years from now, the full configuration with RANS. There is then no reason why wall-interference of solid or flexible walls will not be computed with high accuracy.

Mr. M. Goldhammer, Boeing, USA

If we get to the point where CFD can predict wall effects so accurately, then you have to ask yourself why you are wind tunnel testing. I don't expect to see that in my lifetime. With regard to Dr. Neyland's comment on transonic CFD, it is a good comment, I agree with it entirely. I did want to point out that we have a technology at Boeing called Tranair which is a transonic panel method which we use routinely to compute wall effects. It actually provides panels on the models and on the wind tunnel walls. It is restricted only in so far as it requires a porosity model for the flow through the ventilated walls.

Dr. W.J. McCroskey, NASA Ames, US

Those of you who attend AGARD meetings regularly will hear the broken record starting to sound again about CFD versus wind tunnels. I think that there has been entirely too much an adversarial relation between the CFD community and the wind tunnel community that has discouraged specialized use of CFD methodology to help improve wind tunnel testing techniques. I would hope that the situation might change in the future, but if you look in any of these methodologies, whether it is wind tunnel testing or CFD or any other engineering method, success is dependent upon lots and lots of experience and trial and error and learning from those experiences. The total accumulation of either person hours or CPU hours in the area of modelling experimental difficulties with CFD is very much less than either the total number of hours devoted to developing wind tunnel techniques or the total number of hours devoted to developing better algorithms, turbulence models or whatever. I think it has been a failure of our community to encourage the two separate groups to work together for specialized applications where the wind tunnel alone clearly is not producing the half-a-count in drag accuracy, or the 0.01 of a degree accuracy in flow angularity. You cannot get that kind of accuracy out of either one alone, but there should be ways of combining the advantages of each of these techniques in some meaningful way that will lead to good production methods in the future.

Mr. M. Goldhammer, Boeing, USA

It might make you feel better to know that the transonic wall corrections we used to guarantee the Boeing 777 are based on CFD, so we have put CFD to work. We have actually staked our company position on it.

Prof. J. Slooff, NLR, Netherlands

First of all I got the impression that Mrs. Neyland on the one hand, and Dr. Korner and Mark Goldhammer on the other hand were talking about different things. I think Mrs. Neyland meant the kind of computational methods that are needed to calculate the residual corrections in an adaptive wall situation or in a measured boundary condition situation, which is something different than trying to simulate as well as possible a complete aircraft configuration in free air or in a wind tunnel. I am not so much concerned about the speed or the productivity of the residual wall corrections type of computations. I think that methods and computer hardware are available that would create a sufficiently fast environment to do that sort of thing without hampering the productivity of the whole system.

I have a few other things that I would like to communicate to the audience. When I came to this meeting, I had the impression that there are a number of challenges in the various areas that we have here as a subject of this Conference. As far as wall interference is concerned, it is obviously the challenge of trying to bring maturity to the measured boundary condition approach; in particular the one requiring two variables for ventilated wind tunnels. The other one of course is the challenge of developing technology that is sufficiently productive in an adaptive environment, be it either with solid walls or porous walls. I think as far as the porous walls are concerned, it will be very interesting to see what will come out of the demonstrater type tests at TSAGI. There is a good hope that we may be able to satisfy that challenge in the future. As far as the measured boundary condition challenge is concerned, I did not see until this meeting, any real hope of being able to bring that to maturity, in particular in the sense that it will lead to sufficiently productive correction procedures. I learned of one new measurement technique here at this meeting that might be developed into the kind of measurement technique that one needs in a measured boundary condition approach.

I am referring to the Doppler Global Velocimetry technique. I still don't quite understand how it works and what its productivity limits are, but it seems worthwhile to investigate its potential for measuring the U's and V's and W's in a plane somewhere away from the wall since it would not be necessary to know all the details of the slot flow to determine the wall corrections. This might be a light at the end of the tunnel, but I am hesitant to say so, and I would like to have some comments from somebody in the audience who knows more about Doppler global velocimetry than I do.

As far as support interference is concerned, there is still no hope for a real solution in my perspective. I

agree completely with you that the only thing we can do is test and test and test. Perhaps CFD may help, not in the sense that it can be an actual part of the productivity chain to get data, but in the sense that it may help in understanding better what is going on and to learn to better shape the support and the attachment of the supports to the aircraft model. This means that non-viscous CFD is not going to do the job here. I am tempted to say that it would probably have to be almost full Navier-Stokes, and that of course cannot not be done in a real production environment. However, it might help in trying to learn how to improve the model mountings and that sort of thing.

The third aspect of this Symposium was non-intrusive measurement techniques. As you have already pointed out a new, fast technique for measuring velocity components in planes is really needed and Doppler Global Velocimetry may have a potential as such. I suspect that the wake imaging technique that you are using at Boeing, is not all that fast. Wake imaging is something that is very much needed for drag diagnostics for example, where you want to be able to split up between wave drag, induced drag and boundary layer drag. Perhaps DGV has the potential to develop into a technique that is fast enough to utilize in a high productivity wind tunnel environment.

Mr. R. Bengelink, Boeing, USA

I would like to follow up a little bit more on the comment that Jim McCroskey made about the fact that we see showing up again this adversarial or at least paranoid relationship between the CFDers and the experimentalists. I think that we should recognize that there are really three aspects to aerodynamics; one is the theory, the other side is the application and in between are the tools and methods needed to get from the theory to an application that produces the product. CFD and experiment are just two different tools and methods, that is all. But unless every aerodynamicist is properly motivated and has the capability and resources available to use both of those tools, and to use them in the proper combination for that particular task, then we are going to be in trouble. Folks are coming from different backgrounds who are working in those fields. I think some of what we see is left over from maybe 15 years ago when there was an understanding among a lot of people that CFD was going to do the whole job and we didn't need experimental facilities anymore. I don't think anybody sees it that way now. We should all accept the fact that both are going to continue to exist and both are going to continue to improve. As we figure out the best combination for a given task of those two tools and get them to work together, we are all going to get more efficient. I point out that laser methods, even pressure paint, require a certain blend of the traditional experimental and computer-based techniques to get to the right answer. CFD is just another aspect of that. Maybe we can get less paranoid. In fact, maybe I will go so far as to suggest that when you look at the subcommittees in this Panel, we have sort of encouraged this when we have differentiated between test and experiment and CFD. Maybe we ought to turn our committees around a little bit too, and have one on theory and one on methods and one on applications or applied aerodynamics.

Dr. D. Woodward, DRA, UK

Thank you very much. We are now approaching the time to draw this session to a close and invite Professor Slooff to make his closing comments to the Conference.

Prof. Slooff, NLR, Netherlands

Thank you David. It is me again. It is with some reluctance that I have to bring this meeting and your stay in Brussels to an end. I hope that you found it an interesting meeting and that you also enjoyed Brussels. I think that the Round Table Discussion that we just had indicates that there is still a large interest in this subject and that there are still several challenges to be pursued. I am also particularly glad with some of the recommendations for future AGARD activities that Mark Goldhammer provided us with.

This meeting, of course, would not have been possible without the help of several people. First of all, we thank the Program Committee, and in particular its two co-chairmen, David Woodward and Bram Elsenaar for their initiative and for setting up the program and the sessions. The person who had the most difficult job of all of us this week is the Technical Evaluator, Mark Goldhammer. I think he did a very good job and I am always personally very happy if we have a Technical Evaluator from industry because it is their needs, eventually, or the military's, that we have to take into account in our future activities. Of course, we also have to thank all the people who provided the material for Mark to be evaluated, that is you, the authors and all of you in the audience who participated in the discussions. Special thanks go to the invited speakers, Frank Lynch, Michel Riethmuller, Pat Ashill, Mrs. Neyland and also to the other speaker from TSAGI, Mr. Phonov. On the local arrangements side, we thank the Belgian National Coordinator, Major Lecluyse for all the work he did for making this meeting possible. We also had the indispensable help, as usual, from the interpreters, (SP) Madame Celier, Madame Couedic and Madame Vioche for their very difficult work and I

hope you will join me in an applause for them. Also, the assistance from the technicians from the Royal Military Academy and the SHAPE technicians, Mr. Brolet and Mr. Holthaus, and also the assistance of Mrs. Devinck and Adjutant De Luyck from the Etat Major de la Force Aerienne is of course highly appreciated. A person who has done a tremendous amount of work is Professor Decuypere, our local coordinator and Panel Member who is also a professor here at the Military Academy. He certainly deserves a big applause. So does his wife, as a matter of fact, who together with Madame Ginoux put a lot of work into setting up the companions program. Last but not least, we had the usual support from our Panel Executive Jack Molloy and his secretary Anne-Marie Rivault. As always, they have done a perfect job and made things run smoothly. We also should thank them. Finally, of course, the audience, all of you who have been here and have participated in the discussions. Before we leave, I would like to bring you up to date with some of the future activities of the Fluid Dynamics Panel. If you enjoyed this meeting, perhaps you might consider participating in some of the 1994 activities that we are planning, and communicate the information to colleagues who might also be interested. It remains for me to thank you all for your attendance and your patience and to wish you a safe journey home.

REPORT DOCUMENTATION PAGE

1. Recipient's Reference	2. Originator's Reference	3. Further Reference	4. Security Classification of Document
	AGARD-CP-535	ISBN 92-835-0756-8	UNCLASSIFIED/ UNLIMITED

5. Originator	Advisory Group for Aerospace Research and Development North Atlantic Treaty Organization 7 rue Ancelle, 92200 Neuilly sur Seine, France

6. Title	WALL INTERFERENCE, SUPPORT INTERFERENCE AND FLOW FIELD MEASUREMENTS

7. Presented at	the 73rd Fluid Dynamics Panel Symposium held in Brussels, Belgium, 4th–7th October 1993.

8. Author(s)/Editor(s)	9. Date
Various	July 1994

10. Author(s)/Editor's Address	11. Pages
Various	452

12. Distribution Statement	There are no restrictions on the distribution of this document. Information about the availability of this and other AGARD unclassified publications is given on the back cover.

13. Keywords/Descriptors

Wind tunnels	Support interferences
Aerodynamics	Wall interferences
Flow field measurements	

14. Abstract

The 31 papers prepared for the AGARD Fluid Dynamics Panel (FDP) Symposium on "Wall Interference, Support Interference, and Flow Field Measurements", which was held 4th–7th October 1993 in Brussels, Belgium, are contained in this report. In addition, a Technical Evaluator's Report aimed at assessing the success of the Symposium in meeting its objectives, and an edited transcript of the General Discussion held at the end of the meeting are also included.

The primary objective of this Symposium was to report on recent developments from research and technology programmes aimed at reducing test data errors caused by wind tunnel walls, model supports, and intrusive flow field measurement devices. The scope of papers included wall interference correction methods based on measured data at the walls and methods to eliminate wall interference through adaptive and/or ventilated walls, support interference calculations and corrections methods, and recent advances in flow field measurement techniques.

AGARD-CP-535	AGARD Conference Proceedings 535	AGARD-CP-535	AGARD Conference Proceedings 535
Wind tunnels Aerodynamics Flow field measurements Support interferences Wall interferences	Advisory Group for Aerospace Research and Development, NATO WALL INTERFERENCE, SUPPORT INTERFERENCE AND FLOW FIELD MEASUREMENTS Published July 1994 452 pages The 31 papers prepared for the AGARD Fluid Dynamics Panel (FDP) Symposium on "Wall Interference, Support Interference, and Flow Field Measurements", which was held 4th–7th October 1993 in Brussels, Belgium, are contained in this report. In addition, a Technical Evaluator's Report aimed at assessing the success of the Symposium in meeting its objectives, and an edited transcript of the General Discussion held at the end of the meeting are also included. P.T.O.	Wind tunnels Aerodynamics Flow field measurements Support interferences Wall interferences	Advisory Group for Aerospace Research and Development, NATO WALL INTERFERENCE, SUPPORT INTERFERENCE AND FLOW FIELD MEASUREMENTS Published July 1994 452 pages The 31 papers prepared for the AGARD Fluid Dynamics Panel (FDP) Symposium on "Wall Interference, Support Interference, and Flow Field Measurements", which was held 4th–7th October 1993 in Brussels, Belgium, are contained in this report. In addition, a Technical Evaluator's Report aimed at assessing the success of the Symposium in meeting its objectives, and an edited transcript of the General Discussion held at the end of the meeting are also included. P.T.O.
AGARD-CP-535	AGARD Conference Proceedings 535	AGARD-CP-535	AGARD Conference Proceedings 535
Wind tunnels Aerodynamics Flow field measurements Support interferences Wall interferences	Advisory Group for Aerospace Research and Development, NATO WALL INTERFERENCE, SUPPORT INTERFERENCE AND FLOW FIELD MEASUREMENTS Published July 1994 452 pages The 31 papers prepared for the AGARD Fluid Dynamics Panel (FDP) Symposium on "Wall Interference, Support Interference, and Flow Field Measurements", which was held 4th–7th October 1993 in Brussels, Belgium, are contained in this report. In addition, a Technical Evaluator's Report aimed at assessing the success of the Symposium in meeting its objectives, and an edited transcript of the General Discussion held at the end of the meeting are also included. P.T.O.	Wind tunnels Aerodynamics Flow field measurements Support interferences Wall interferences	Advisory Group for Aerospace Research and Development, NATO WALL INTERFERENCE, SUPPORT INTERFERENCE AND FLOW FIELD MEASUREMENTS Published July 1994 452 pages The 31 papers prepared for the AGARD Fluid Dynamics Panel (FDP) Symposium on "Wall Interference, Support Interference, and Flow Field Measurements", which was held 4th–7th October 1993 in Brussels, Belgium, are contained in this report. In addition, a Technical Evaluator's Report aimed at assessing the success of the Symposium in meeting its objectives, and an edited transcript of the General Discussion held at the end of the meeting are also included. P.T.O.

The primary objective of this Symposium was to report on recent developments from research and technology programmes aimed at reducing test data errors caused by wind tunnel walls, model supports, and intrusive flow field measurement devices. The scope of papers included wall interference correction methods based on measured data at the walls and methods to eliminate wall interference through adaptive and/or ventilated walls, support interference calculations and corrections methods, and recent advances in flow field measurement techniques.

The primary objective of this Symposium was to report on recent developments from research and technology programmes aimed at reducing test data errors caused by wind tunnel walls, model supports, and intrusive flow field measurement devices. The scope of papers included wall interference correction methods based on measured data at the walls and methods to eliminate wall interference through adaptive and/or ventilated walls, support interference calculations and corrections methods, and recent advances in flow field measurement techniques.

The primary objective of this Symposium was to report on recent developments from research and technology programmes aimed at reducing test data errors caused by wind tunnel walls, model supports, and intrusive flow field measurement devices. The scope of papers included wall interference correction methods based on measured data at the walls and methods to eliminate wall interference through adaptive and/or ventilated walls, support interference calculations and corrections methods, and recent advances in flow field measurement techniques.

The primary objective of this Symposium was to report on recent developments from research and technology programmes aimed at reducing test data errors caused by wind tunnel walls, model supports, and intrusive flow field measurement devices. The scope of papers included wall interference correction methods based on measured data at the walls and methods to eliminate wall interference through adaptive and/or ventilated walls, support interference calculations and corrections methods, and recent advances in flow field measurement techniques.

AGARD

NATO ⊕ OTAN

7 RUE ANCELLE · 92200 NEUILLY-SUR-SEINE

FRANCE

Télécopie (1)47.38.57.99 · Télex 610 176

DIFFUSION DES PUBLICATIONS
AGARD NON CLASSIFIEES

Aucun stock de publications n'a existé à AGARD. A partir de 1993, AGARD détiendra un stock limité des publications associées aux cycles de conférences et cours spéciaux ainsi que les AGARDographies et les rapports des groupes de travail, organisés et publiés à partir de 1993 inclus. Les demandes de renseignements doivent être adressées à AGARD par lettre ou par fax à l'adresse indiquée ci-dessous. *Veuillez ne pas téléphoner.* La diffusion initiale de toutes les publications de l'AGARD est effectuée auprès des pays membres de l'OTAN par l'intermédiaire des centres de distribution nationaux indiqués ci-dessous. Des exemplaires supplémentaires peuvent parfois être obtenus auprès de ces centres (à l'exception des Etats-Unis). Si vous souhaitez recevoir toutes les publications de l'AGARD, ou simplement celles qui concernent certains Panels, vous pouvez demander à être inclu sur la liste d'envoi de l'un de ces centres. Les publications de l'AGARD sont en vente auprès des agences indiquées ci-dessous, sous forme de photocopie ou de microfiche.

CENTRES DE DIFFUSION NATIONAUX

ALLEMAGNE
Fachinformationszentrum,
Karlsruhe
D-7514 Eggenstein-Leopoldshafen 2

BELGIQUE
Coordonnateur AGARD-VSL
Etat-Major de la Force Aérienne
Quartier Reine Elisabeth
Rue d'Evere, 1140 Bruxelles

CANADA
Directeur du Service des Renseignements Scientifiques
Ministère de la Défense Nationale
Ottawa, Ontario K1A 0K2

DANEMARK
Danish Defence Research Establishment
Ryvangs Allé 1
P.O. Box 2715
DK-2100 Copenhagen Ø

ESPAGNE
INTA (AGARD Publications)
Pintor Rosales 34
28008 Madrid

ETATS-UNIS
NASA Headquarters
Code JOB-1
Washington, D.C. 20546

FRANCE
O.N.E.R.A. (Direction)
29, Avenue de la Division Leclerc
92322 Châtillon Cedex

GRECE
Hellenic Air Force
Air War College
Scientific and Technical Library
Dekelia Air Force Base
Dekelia, Athens TGA 1010

ISLANDE
Director of Aviation
c/o Flugrad
Reykjavik

ITALIE
Aeronautica Militare
Ufficio del Delegato Nazionale all'AGARD
Aeroporto Pratica di Mare
00040 Pomezia (Roma)

LUXEMBOURG
Voir Belgique

NORVEGE
Norwegian Defence Research Establishment
Attn: Biblioteket
P.O. Box 25
N-2007 Kjeller

PAYS-BAS
Netherlands Delegation to AGARD
National Aerospace Laboratory NLR
P.O. Box 90502
1006 BM Amsterdam

PORTUGAL
Força Aérea Portuguesa
Centro de Documentação e Informação
Alfragide
2700 Amadora

ROYAUME UNI
Defence Research Information Centre
Kentigern House
65 Brown Street
Glasgow G2 8EX

TURQUIE
Millî Savunma Başkanlığı (MSB)
ARGE Daire Başkanlığı (ARGE)
Ankara

Le centre de distribution national des Etats-Unis ne détient PAS de stocks des publications de l'AGARD.
D'éventuelles demandes de photocopies doivent être formulées directement auprès du NASA Center for AeroSpace Information (CASI) à l'adresse ci-dessous. Toute notification de changement d'adresse doit être fait également auprès de CASI.

AGENCES DE VENTE

NASA Center for
  AeroSpace Information (CASI)
800 Elkridge Landing Road
Linthicum Heights, MD 21090-2934
United States

ESA/Information Retrieval Service
European Space Agency
10, rue Mario Nikis
75015 Paris
France

The British Library
Document Supply Division
Boston Spa, Wetherby
West Yorkshire LS23 7BQ
Royaume Uni

Les demandes de microfiches ou de photocopies de documents AGARD (y compris les demandes faites auprès du CASI) doivent comporter la dénomination AGARD, ainsi que le numéro de série d'AGARD (par exemple AGARD-AG-315). Des informations analogues, telles que le titre et la date de publication sont souhaitables. Veuiller noter qu'il y a lieu de spécifier AGARD-R-nnn et AGARD-AR-nnn lors de la commande des rapports AGARD et des rapports consultatifs AGARD respectivement. Des références bibliographiques complètes ainsi que des résumés des publications AGARD figurent dans les journaux suivants:

Scientifique and Technical Aerospace Reports (STAR)
publié par la NASA Scientific and Technical
Information Program
NASA Headquarters (JTT)
Washington D.C. 20546
Etats-Unis

Government Reports Announcements and Index (GRA&I)
publié par le National Technical Information Service
Springfield
Virginia 22161
Etats-Unis

(accessible également en mode interactif dans la base de données bibliographiques en ligne du NTIS, et sur CD-ROM)

SPS

Imprimé par Specialised Printing Services Limited
40 Chigwell Lane, Loughton, Essex IG10 3TZ